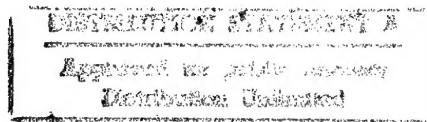


AGARD

ADVISORY GROUP FOR AEROSPACE RESEARCH & DEVELOPMENT

7 RUE ANCELLE, 92200 NEUILLY-SUR-SEINE, FRANCE



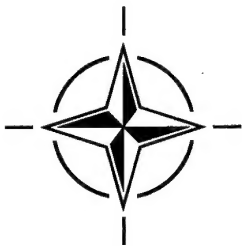
CONFERENCE PROCEEDINGS 584

The Characterisation & Modification of Wakes from Lifting Vehicles in Fluids

(la Caractérisation et la modification des sillages créés dans
les fluides par des véhicules portant)

*Papers presented at the Fluid Dynamics Panel Symposium held in Trondheim, Norway, from
20-23 May 1996.*

19970117 218



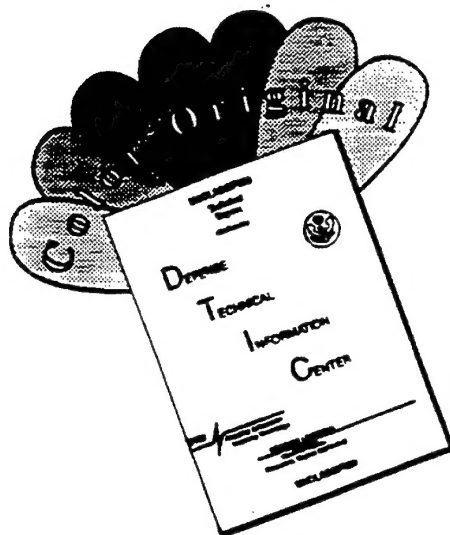
NORTH ATLANTIC TREATY ORGANIZATION

Published November 1996

Distribution and Availability on Back Cover

QUALITY INSPECTED

DISCLAIMER NOTICE



THIS DOCUMENT IS BEST QUALITY AVAILABLE. THE COPY FURNISHED TO DTIC CONTAINED A SIGNIFICANT NUMBER OF COLOR PAGES WHICH DO NOT REPRODUCE LEGIBLY ON BLACK AND WHITE MICROFICHE.

AGARD

ADVISORY GROUP FOR AEROSPACE RESEARCH & DEVELOPMENT

7 RUE ANCELLE, 92200 NEUILLY-SUR-SEINE, FRANCE

CONFERENCE PROCEEDINGS 584

The Characterisation & Modification of Wakes from Lifting Vehicles in Fluids

(la Caractérisation et la modification des sillages créés dans les fluides
par des véhicules portant)

Papers presented at the Fluid Dynamics Panel Symposium held in Trondheim, Norway, from
20-23 May 1996.



North Atlantic Treaty Organization
Organisation du Traité de l'Atlantique Nord

The Mission of AGARD

According to its Charter, the mission of AGARD is to bring together the leading personalities of the NATO nations in the fields of science and technology relating to aerospace for the following purposes:

- Recommending effective ways for the member nations to use their research and development capabilities for the common benefit of the NATO community;
- Providing scientific and technical advice and assistance to the Military Committee in the field of aerospace research and development (with particular regard to its military application);
- Continuously stimulating advances in the aerospace sciences relevant to strengthening the common defence posture;
- Improving the co-operation among member nations in aerospace research and development;
- Exchange of scientific and technical information;
- Providing assistance to member nations for the purpose of increasing their scientific and technical potential;
- Rendering scientific and technical assistance, as requested, to other NATO bodies and to member nations in connection with research and development problems in the aerospace field.

The highest authority within AGARD is the National Delegates Board consisting of officially appointed senior representatives from each member nation. The mission of AGARD is carried out through the Panels which are composed of experts appointed by the National Delegates, the Consultant and Exchange Programme and the Aerospace Applications Studies Programme. The results of AGARD work are reported to the member nations and the NATO Authorities through the AGARD series of publications of which this is one.

Participation in AGARD activities is by invitation only and is normally limited to citizens of the NATO nations.

The content of this publication has been reproduced
directly from material supplied by AGARD or the authors.

Published November 1996

Copyright © AGARD 1996
All Rights Reserved

ISBN 92-836-0034-7



*Printed by Canada Communication Group
45 Sacré-Cœur Blvd., Hull (Québec), Canada K1A 0S7*

The Characterisation & Modification of Wakes from Lifting Vehicles in Fluids

(AGARD CP-584)

Executive Summary

The aim of this Symposium was to bring together researchers, engineers, and civil aviation representatives working in the field of aircraft wakes. Aircraft wake research has been supported by many organizations such as FAA, NASA, DLR, ONERA, aircraft manufacturers and others, and significant advances have been made in prediction, methodology, and experimental techniques. A review of the state-of-the-art was appropriate.

The aircraft separation necessary to avoid the hazard of vortex encounters must be maintained despite the increasing number of airports and of commercial aircraft per airport. In addition, wakes are becoming more and more important in the detection of military aircraft. Techniques leading to a premature vortex decay or breakdown are of great interest. Economically efficient aircraft spacing requires an accurate prediction of vortex formation, evolution, decay and breakdown. Presentations focused on the following areas: Regulatory Viewpoints, Aircraft Spacing Considerations, Vortex Wake Structure, Vortex Instabilities and Breakdown, Aircraft/Vortex Interactions, and Atmospheric Effects on Wakes.

Currently, operators and regulators are concerned with improved detection and avoidance procedures as a means to allow reduced aircraft separation near airports. The fluid dynamics community can contribute by providing better approximate models of wake decay, better models of rolling moments for various generating aircraft, and better predictions and means of detecting vortex wakes. All segments of the scientific and technological communities must continue to work together to attain a better world-wide air traffic system in the 21st Century.

La caractérisation et la modification des sillages créés dans les fluides par des véhicules portant (AGARD CP-584)

Synthèse

Ce Symposium a eu pour objectif de rassembler des chercheurs, des ingénieurs et des représentants de l'aviation civile travaillant dans le domaine des sillages des aéronefs. Des travaux de recherche dans le domaine des sillages des aéronefs ont été entrepris par bon nombre d'organisations telles que le FAA, le NASA, le DLR, l'ONERA, ainsi que par des avionneurs et d'autres intervenants et de réels progrès ont été réalisés dans la prévision, la méthodologie et les techniques expérimentales. L'examen de l'état actuel des connaissances dans ce domaine semblait donc nécessaire.

La séparation entre les vols, qui est indispensable pour éviter toute possibilité de contact avec les tourbillons de sillage, doit être maintenue en dépit du nombre croissant d'aéroports et d'avions de ligne par aéroport. En outre, les tourbillons de sillage deviennent de plus en plus importants pour la détection d'avions militaires. Les techniques permettant de provoquer l'amortissement ou l'éclatement prématuré des tourbillons sont d'un grand intérêt. Pour être rentable, l'espacement des avions passe par le calcul précis de l'établissement, de l'évolution, de l'amortissement et de l'éclatement des tourbillons. Les présentations ont porté sur les domaines suivants : les aspects réglementaires, l'espacement des avions, la structure des tourbillons de sillage, les instabilités et l'éclatement des tourbillons, les interactions aéronef/tourbillons et les effets atmosphériques sur les sillages.

A l'heure actuelle, les exploitants et les services officiels s'intéressent à l'amélioration des procédures de détection et d'évitement en vue de réduire l'espacement des aéronefs dans la zone d'approche des aéroports. La communauté de la dynamique des fluides a la possibilité de participer à ces efforts en fournissant des modèles améliorés de l'amortissement des sillages et des moments de roulis pour les différents aéronefs générateurs, ainsi que de meilleures prévisions et des moyens plus performants pour la détection des tourbillons de sillage. Tous les composants des communautés scientifiques et techniques doivent continuer à travailler ensemble pour améliorer le système global de circulation aérienne au 21^{ème} siècle.

Contents

	Page
Executive Summary	iii
Synthèse	iv
Recent Publications of the Fluid Dynamics Panel	viii
Fluid Dynamics Panel	x
	Reference
Technical Evaluation Report by W.J. McCroskey	T
KEYNOTE SESSION Chairman: G.E.A. Meier	
Vortex Wakes in Aerodynamics by H.W.M. Hoeijmakers	1
Wake Vortices' Effects and the Need for Prompt Action — A U.S. View by G.R. Mack	2
Wake Vortices — A European Regulatory View by K. Koplin	3
Air Traffic Control Procedures for the Avoidance of Wake Vortex Encounters Today and Future Developments by Deutsche Flugsicherung GmbH by F. Brenner	4
Structure of a Transport Aircraft-Type near Field Wake by K. Huenecke	5
The Interaction between an Injected Vortex and a Rolling up Vortex Sheet by M.R. Dhanak and K.S. Vishwanthan	6
Flowfield Prediction of Three-Dimensional Wing Trailing Vortices Using Advanced Turbulence Models by J.A. Eaton and M.P. O'Flaherty	7
An Unsteady Vortex Wake Model for Maneuvering Vehicles by M.R. Mendenhall and S.C. Perkins, Jr.	8
Experimental Assessment of the Extended Betz Method for Wake Vortex Prediction by W.R. Graham	9
Structure, Trajectory and Strength of B747 Aircraft Wake Vortices Measured by Laser by J.M. Vaughan, D.W. Brown, G. Constant, J.R. Eacock and R. Foord	10

Wake Vortex Decay Near the Ground Under Conditions of Strong Stratification and Wind Shear	11
by R.P. Rudis, D.C. Burnham and P. Janota	
Wake Turbulence Training and Regulation: An Industry Team Approach	12
by D.C. Carbaugh and W.D. Forsythe	
Ground-Based Anemometer Measurements of Wake Vortices from Landing Aircraft at Airports	13
by S. Abramson and D.C. Burnham	
The Dynamic Response of a Twin-Engine, Commercial Jet Transport to Wake Vortex Encounters	14
by J. Vasatka	
Experimental Analysis of the Vortex Wake Structure behind a Propeller-Wing Configuration	15
by L.L.M. Veldhuis and D.W.E. Rentema	
Flowfield of a Wing Embedded in the Wake of a Bursted Vortex	16
by J.M.A. Longo, M. Orlowski and D. Strohmeier	
Stability of Multiple Trailing-Vortex Pairs	17
by J.D. Crouch	
Initiation of the Crow Instability by Atmospheric Turbulence	18
by P.R. Spalart and A.A. Wray	
Simulation numérique directe de l'instabilité sinusoïdale	19
by D. Sipp, L. Jacquin and P. Sagaut	
Stability Theory for Two Wingtip Vortices Behind Cruising Aircraft	20
by T. Ehret	
Analysis of UK Encounters 1982-1990	21
by D.C. Burnham	
A Simulation-Based Study of the Impact of Aircraft Wake Turbulence Weight Categories on Airport Capacity	22
by J.J. Robinson	
An Aircraft Vortex Spacing System (AVOSS) For Dynamical Wake Vortex Spacing Criteria	23
by D.A. Hinton	
On the Interaction between Topographical Wind and Landing Aircraft	24
by N. Kubberud, I. Øye and H. Nørstrud	
Flow Field Survey in Trailing Vortex System behind a Civil Aircraft Model at High Lift	25
by A.C. de Bruin, S.H. Hegen, P.B. Rohne and P.R. Spalart	
Measurements in Vortex Wakes Shed by Conventional and Modified Subsonic Aircraft	26
by V.J. Rossow	
Natural and Forced Growth Characteristics of the Vortex Wake of a Rectangular Airfoil	27
by J.D. Jacob, D. Liepmann and Ö. Savaş	

Three-Dimensional Direct Numerical Simulations of Wake Vortices: Atmospheric Turbulence Effects and Rebound with Crosswind	28
by A. Corjon, F. Risso, A. Stoessel and T. Poinso	
Caractérisation et Modélisation du Sillage d'un Avion à partir d'Essais en Vol de Maquettes en Laboratoire	29
by P. Coton	
Direct Numerical Simulation of the Breakdown of Aircraft Wake Vortices	30
by S.C. Rennich and S.K. Lele	
The Inviscid Motion of a Vortex Pair in a Compressible and Stratified Atmosphere	31
by R. Stiff	
Experimental and Numerical Results on Spiral Vortex Breakdown	32
by S.H. Backstein	
Computational and Experimental Investigation of the Wakes shed from Flapping Airfoils and their Wake Interference/Impingement Characteristics	33
by C.M. Dohring, M.F. Platzer, K.D. Jones and I.H. Tuncer	
Recent Laboratory and Numerical Trailing Vortex Studies	34
by D.P. Delisi, G.C. Greene, R.E. Robins and R. Singh	
Wake Dynamics and Exhaust Distribution behind Cruising Aircraft	35
by T. Gerz and T. Ehret	
The Use of Aircraft Wakes to Achieve Power Reductions in Formation Flight	36
by D. Hummel	
On the Dynamics of Engine Jets behind a Transport Aircraft	37
by L. Jacquin and F. Garnier	
General Discussion	GD

Recent Publications of the Fluid Dynamics Panel

AGARDOGRAPHS (AG)

Turbulent Boundary Layers in Subsonic and Supersonic Flow

AGARD AG-335, July 1996

Computational Aerodynamics Based on the Euler Equations

AGARD AG-325, September 1994

Scale Effects on Aircraft and Weapon Aerodynamics

AGARD AG-323 (E), July 1994

Design and Testing of High-Performance Parachutes

AGARD AG-319, November 1991

Experimental Techniques in the Field of Low Density Aerodynamics

AGARD AG-318 (E), April 1991

Techniques Expérimentales Liées à l'Aérodynamique à Basse Densité

AGARD AG-318 (FR), April 1990

A Survey of Measurements and Measuring Techniques in Rapidly Distorted Compressible Turbulent Boundary Layers

AGARD AG-315, May 1989

Reynolds Number Effects in Transonic Flows

AGARD AG-303, December 1988

REPORTS (R)

Aerothermodynamics and Propulsion Integration for Hypersonic Vehicles

AGARD R-813, Special Course Notes, to be published in the fall of 1996

Parallel Computing in CFD

AGARD R-807, Special Course Notes, October 1995

Optimum Design Methods for Aerodynamics

AGARD R-803, Special Course Notes, November 1994

Missile Aerodynamics

AGARD R-804, Special Course Notes, May 1994

Progress in Transition Modelling

AGARD R-793, Special Course Notes, April 1994

Shock-Wave/Boundary-Layer Interactions in Supersonic and Hypersonic Flows

AGARD R-792, Special Course Notes, August 1993

Unstructured Grid Methods for Advection Dominated Flows

AGARD R-787, Special Course Notes, May 1992

Skin Friction Drag Reduction

AGARD R-786, Special Course Notes, March 1992

Engineering Methods in Aerodynamic Analysis and Design of Aircraft

AGARD R-783, Special Course Notes, January 1992

Aircraft Dynamics at High Angles of Attack: Experiments and Modelling

AGARD R-776, Special Course Notes, March 1991

ADVISORY REPORTS (AR)

Cooperative Programme on Dynamic Wind Tunnel Experiments for Manoeuvring Aircraft

AGARD AR-305, Report of WG-16, to be published in the fall of 1996

Hypersonic Experimental and Computational Capability, Improvement and Validation

AGARD AR-319, Vol. I, Report of WG-18, May 1996

Aerodynamics of 3-D Aircraft Afterbodies

AGARD AR-318, Report of WG-17, September 1995

A Selection of Experimental Test Cases for the Validation of CFD Codes

AGARD AR-303, Vols. I and II, Report of WG-14, August 1994

Quality Assessment for Wind Tunnel Testing

AGARD AR-304, Report of WG-15, July 1994

Air Intakes of High Speed Vehicles

AGARD AR-270, Report of WG-13, September 1991

Appraisal of the Suitability of Turbulence Models in Flow Calculations

AGARD AR-291, Technical Status Review, July 1991

Rotary-Balance Testing for Aircraft Dynamics

AGARD AR-265, Report of WG11, December 1990

Calculation of 3D Separated Turbulent Flows in Boundary Layer Limit

AGARD AR-255, Report of WG10, May 1990

Adaptive Wind Tunnel Walls: Technology and Applications

AGARD AR-269, Report of WG12, April 1990

CONFERENCE PROCEEDINGS (CP)

Progress and Challenges in CFD Methods and Algorithms

AGARD CP-578, April 1996

Aerodynamics of Store Integration and Separation

AGARD CP-570, February 1996

Aerodynamics and Aeroacoustics of Rotorcraft

AGARD CP-552, August 1995

Application of Direct and Large Eddy Simulation to Transition and Turbulence

AGARD CP-551, December 1994

Wall Interference, Support Interference, and Flow Field Measurements

AGARD CP-535, July 1994

Computational and Experimental Assessment of Jets in Cross Flow

AGARD CP-534, November 1993

High-Lift System Aerodynamics

AGARD CP-515, September 1993

Theoretical and Experimental Methods in Hypersonic Flows

AGARD CP-514, April 1993

Aerodynamic Engine/Airframe Integration for High Performance Aircraft and Missiles

AGARD CP-498, September 1992

Effects of Adverse Weather on Aerodynamics

AGARD CP-496, December 1991

Manoeuvring Aerodynamics

AGARD CP-497, November 1991

Vortex Flow Aerodynamics

AGARD CP-494, July 1991

Missile Aerodynamics

AGARD CP-493, October 1990

Aerodynamics of Combat Aircraft Controls and of Ground Effects

AGARD CP-465, April 1990

Computational Methods for Aerodynamic Design (Inverse) and Optimization

AGARD CP-463, March 1990

Applications of Mesh Generation to Complex 3-D Configurations

AGARD CP-464, March 1990

Fluid Dynamics of Three-Dimensional Turbulent Shear Flows and Transition

AGARD CP-438, April 1989

Validation of Computational Fluid Dynamics

AGARD CP-437, December 1988

Aerodynamic Data Accuracy and Quality: Requirements and Capabilities in Wind Tunnel Testing

AGARD CP-429, July 1988

Aerodynamics of Hypersonic Lifting Vehicles

AGARD CP-428, November 1987

Aerodynamic and Related Hydrodynamic Studies Using Water Facilities

AGARD CP-413, June 1987

Applications of Computational Fluid Dynamics in Aeronautics

AGARD CP-412, November 1986

Fluid Dynamics Panel

Chairman: Prof. Dr. C. ÇIRAY
Aeronautical Eng. Department
Middle East Technical University
Inonu Bulvari PK: 06531
Ankara, Turkey

Deputy Chairman: Prof. B. CANTWELL
Stanford University
Dept. of Aeronautics & Astronautics
Stanford, CA 94305
United States

PROGRAMME COMMITTEE

Professor Dr. G.E.A. MEIER (Chairman)
Direktor des Institutes für Stromungsmechanik der DLR
Bunsenstrasse 10
D-37073 Göttingen — Germany

Professor Dr. Ir.J.L. van INGEN
Dept. of Aerospace Engineering
Delft University of Technology
Kluyverweg 1, 2629 HS Delft — Netherlands

Professor R. DECUYPERE
Ecole Royale Militaire
Avenue de la Renaissance 30
B-1040 Brussels — Belgium

Professor Dr. H. NØRSTRUD
Department of Applied Mechanics
Thermo-and Fluid Dynamics
Norwegian University of Science & Technology
N-7034 Trondheim — Norway

Professor R.J. KIND
Department of Mechanical and Aerospace Engineering
Carleton University
Ottawa, Ontario K1S 5B6 — Canada

Professor D.I.A. POLL
Head of the College of Aeronautics
Cranfield University
Cranfield
Bedford MK43 OAL — U.K.

M.A. BONNET
Professeur au Dept. Aérodynamique
Ecole Nationale Supérieure
de l'Aéronautique et de l'Espace
10 Avenue Edouard Belin, BP 4032
31055 Toulouse Cedex — France

Mr. R.L. BENGELINK
Boeing Commercial Airplane Group
P.O. Box 3707 M/S 67-WH
Seattle, WA 98124-2207 — U.S.A.

Dr. B. WAGNER
Dornier Luftfahrt GmbH (DASA-LR)
Aerodynamics TE-2 — Bldg 318
P.O. Box 1103
82230 Wessling — Germany

Dr. L.P. PURTELL
Program Officer — Mechanics and Energy
Conversion Division
Code 333 - Office of Naval Research
800 North Quincy Street
Arlington, VA 22217-5660 — U.S.A.

Professor F. SABETTA
Universita di Roma "La Sapienza"
Dipartimento di Meccanica E Aeronautica —
Via Eudossiana 18
00184 Roma — Italy

PANEL EXECUTIVE

Mr. J.K. MOLLOY

Mail from Europe:
AGARD-OTAN
Attn: FDP Executive
7, rue Ancelle
92200 Neuilly-sur-Seine
France

Mail from USA and Canada:
AGARD-NATO
Attn: FDP Executive
Unit PSC 116
APO AE 09777

Tel: 33 (1) 47 38 57 75

TECHNICAL EVALUATION REPORT

AGARD Fluid Dynamics Panel Symposium on

"THE CHARACTERISATION AND MODIFICATION OF WAKES FROM LIFTING VEHICLES IN FLUIDS"

W.J. McCroskey

U.S. Army Aeroflightdynamics Directorate, AVRDEC

NASA Ames Research Center, Moffett Field, California 94035, USA

SUMMARY

The Fluid Dynamics Panel of AGARD arranged a Symposium on "The Characterisation and Modification of Wakes from Lifting Vehicles in Fluids," on 20-23 May 1996 in Trondheim, Norway. The purpose of the Symposium was "... to review and discuss recent developments in wake research for aircraft and the implications for air traffic regulations," with a clear emphasis on the hazard of vortex encounters in civil aviation. Sessions were devoted specifically to operational procedures and aircraft spacings in airport terminal areas; to the aerodynamic interactions between trailing vortices and following aircraft; to trailing vortex structures, instabilities, atmospheric effects on wakes, and vortex breakdown; and to miscellaneous issues, such as vortices generated by other vehicles and the interactions between vortex wakes and engine exhausts. The Symposium was unclassified, and it was rather unusual with respect to the broad range of interests of the active participants: representatives of regulatory agencies; aircraft manufacturers and operators; and research scientists engaged in flight tests, flight simulations, and basic experimental and theoretical fluid dynamics. Thirty-seven papers were presented at the meeting. An overview of the Symposium and some general conclusions and recommendations are given in this Evaluation Report.

1. INTRODUCTION

Vortical aerodynamic flows comprise an important and on-going part of the AGARD Fluid Dynamics Panel's terms of reference, activities, and expertise. In 1990, the Panel held a Symposium on "Vortex Flow Aerodynamics" [1],

which was primarily concerned with near-field vortical flows and separation on military aircraft and missiles. That meeting emphasized leading-edge vortices of highly-swept wings and slender bodies at high angles of attack, and their effects on performance, stability, control, and structural design loads. Figure 1, from Paper No. 1 of the present Symposium, schematically indicates some of the basic features of this class of problems. On the other hand, the present conference focused mostly on the vortex wakes of large civil jet transports (represented by Fig. 2 from Paper 26), and on the hazards that they present to following aircraft. Both practical problems share many common fluid dynamic aspects, of course; and both meetings included papers on fundamental aspects of vortical flows and their control that are applicable to all classes of flight vehicles.

The theme of the present Symposium was listed in the program as follows:

"The aim of the symposium is to review and discuss recent developments in wake research and the implications for air traffic regulations. The aircraft separation necessary to avoid the hazard of vortex encounters must be realized despite the increasing number of airports and of commercial aircraft per airport. Economically efficient aircraft spacing requires an accurate prediction of vortex formation, evolution, decay and breakdown. Atmospheric stratification and compressibility affect aircraft wakes at cruising altitude and also near the ground during takeoff and landing. In addition, wakes are getting more and more

important in the detection of military aircraft. Therefore, techniques leading to a premature vortex decay and breakdown are of great interest. New experimental techniques and theoretical methods have been developed for the improvement of wake prediction. These tools include Direct Numerical Simulation (DNS) and inflight measurements."

This statement is an effective synopsis of the Symposium, except for a few papers that were given on other, closely related topics. Also, it may be mentioned that contributions were solicited on the role of vortex wakes in the detection of military aircraft and submarines, but none was offered to the Program Committee. On the other hand, papers on helicopter wakes, which share many vortical features with aircraft wakes, were not solicited. Thirty-seven papers were presented in eight technical sessions that spanned 3-1/2 days, and the meeting concluded with the Technical Evaluator's preliminary comments and a general discussion.

2. THE VORTEX WAKE PROBLEM AND ITS CONSEQUENCES

As noted above, the primary problems that were addressed by the Symposium stem from the safety hazard of an aircraft encountering the strong vortex wake generated by a large aircraft flying ahead of it. It is well known that the trailing wake of a lifting body rolls up into a pair of strong, counter-rotating longitudinal vortices that persist for *many* body dimensions downstream. The strength of these trailing, ribbon-like vortices is approximately proportional to the weight of the aircraft that generated them, and they represent a severe atmospheric disturbance to other aircraft that happen to traverse their path -- accidents have resulted and lives have been lost. This vortex-wake problem and the associated safety issues came to the fore in the late 1960s with the introduction of "jumbo jets" that were much larger and heavier than other aircraft in common service.

A flurry of basic and applied research activity in the 1970s produced a better understanding of the far-wake structure and its perverse persistence, and of the magnitude of the forces and moments experienced by aircraft encountering trailing vortex wakes. However, little success was achieved in reducing this invisible hazard, other than avoiding the flight path of large aircraft.

But since aircraft must share the airspace near airports, the only solution up to now has been to maintain a suitably-large spacing between aircraft during takeoff and landing. This spacing requirement, especially for landings, constrains the operational capacity at a growing number of congested commercial airports around the world, and future aircraft of even greater size and weight will exacerbate the costly delays between landings. Therefore, there is a keen practical interest in the fluid dynamics of almost all aspects of vortex wakes. This includes their formation, control, evolution, transport, decay, and breakdown; the interactional aerodynamic effects on aircraft that encounter vortex wakes; meteorological and ground-interaction effects on vortex structure and breakdown; and modeling, computing, detecting, and measuring trailing wakes.

The first two papers set the stage for the Symposium very well by defining and explaining (1) the relevant fluid dynamic phenomena of trailing vortical wakes, (2) the effects of vortex encounters by following aircraft, and (3) the practical, operational consequences of assuring that severe vortex encounters are avoided. The third point is brought out very clearly by Mr. Gerald Mack in Paper 2, describing the commercial air traffic control procedures and separation criteria that have evolved in the United States to avoid unsafe vortex encounters.

Mack notes that the majority of wake vortex, or wake turbulence, encounters occur during final approach, which is characterized by airplanes flying through a relatively narrow corridor. Both the "leader" and "follower" aircraft in the U.S. are classified as "heavy," "large," or "small." Different minimum separation distances are in effect for each combination of aircraft. Different operating environments, *i.e.*, instrument or visual meteorological conditions (IMC and VMC, respectively), also affect the flight paths. For example, Air Traffic Control maintains horizontal and vertical separation between airplanes under instrument flight rules (IFR), whereas the pilot of the following airplane is responsible for maintaining safe separation under visual flight rules (VFR). The prescribed IFR horizontal separation distances are typically larger than those maintained by pilots for VFR landings. Significantly, there have been *no* accidents in the US while IMC operations were in effect and the prescribed procedures were followed, and none have occurred during VMC operations *when the following pilot flew at or above the flight path of the leading aircraft.*

The prescribed IFR horizontal separation distances in the U.S. now range from 3 to 6 miles, depending on the sizes of the two aircraft. These minimums represent a key limiting factor at many congested airports, and travelers know from practical experience that delays at one airport often ripple throughout the entire air traffic system. Therefore, pressure is mounting to reduce the existing separation criteria, without compromising safety. Although much has been learned over the past 25 years, Mack points out that:

"... Refining existing separation criteria requires consideration not only of wake turbulence-related aircraft categories, ATC procedures, and piloting procedures, but also of a variety of issues such as radar limitations, runway occupancy time, flight path constraints, airport configuration, and traffic mix."

According to Mack, the most important unresolved wake issues are:

- "1. The near-field characteristics of a wake and how these influence the far-field characteristics;
2. The influence of meteorological conditions on the far-field characteristics of a wake."

Subsequent papers addressed these points in some detail, but they remain poorly understood.

Finally, Paper 2 introduces an automated-system concept that is designed to adjust dynamically and adaptively the separation criteria based on more detailed information about the participating aircraft, and on measurements of local meteorological conditions and trajectories of wake vortices during flight operations. The program is called "Aircraft Vortex Spacing System (AVOSS)," and it is described in more detail in Paper 23 by D.A. Hinton.

Comments on the European regulatory viewpoint are given in Paper 3 by Mr. Klaus Koplin, who describes the activities of the 26-member Joint Aviation Authorities (JAA) and its relationship with other European organizations concerned with civil aviation regulations. Wake vortex hazards are worrisome in Europe and must be considered in planning for air traffic growth, but JAA does not consider this an urgent safety problem at present. Paper 4 describes the

International Civil Aviation Organization (ICAO) size classifications and separation distances, which are slightly different from those of the US Federal Aviation Administration (FAA). The author also discusses how a vortex detection and warning system could be used to improve the situation.

Papers 12, 14, 21, 22, and 23 also help to define more clearly the vortex hazard problem by analyzing actual and theoretical rates of encounters; by addressing training, simulation, and regulation issues and their consequences; and by discussing ways of improving operational efficiency and airport capacity. These papers contain important considerations for future courses of action, which will be mentioned again in Section 4.2

3. THE PHYSICS OF VORTEX WAKES

In simple terms, the generation of lift by an aircraft creates strong concentrated trailing vortices, which should be avoided by other aircraft. The Keynote Speaker points out in Paper 1 the distinction between vortex wakes created by flow separation from highly-swept leading edges, such as delta wings (see Fig. 1), and vortex wakes typical of subsonic transport aircraft; e.g., Figs. 2 and 3. The former wakes dominated the 1990 Symposium [1], whereas the present Symposium strongly emphasized the latter. The majority of the present papers address some aspects of vortex aerodynamics, and they can be grouped for discussion into the five subcategories listed below.

3.1 Initial Wake Formation and Rollup

Papers 5, 9, 15, 25, and 27 present detailed wake survey measurements in the initial rollup region (see Fig. 4). Paper 29 contains smoke flow visualizations behind a free-flight model of an Airbus A300-B2 aircraft, extending beyond the wake-rollup region. Paper 27 reports on the effects of mass injection near the origin of the tip of a simple rectangular wing, resurrecting an idea promoted in the early 1970's [2] with limited success. Papers 5, 9, 25, and 29 provide data for wings with flaps deployed, which produce the multiple-vortex patterns indicated in Fig. 3, and Paper 15 analyzes the measurements behind a wing, nacelle, and propeller combination. These data should be especially valuable data for checking theoretical and numerical methods.

Papers 6, 7, 8, 9, 20, and 25 contain theoretical or numerical methods for analyzing initial wake rollup. Paper 6 analyzes in the Trefftz plane the interaction between a pair of concentrated longitudinal vortices and the vortex sheet rolling up behind an elliptically loaded wing, with a view toward determining the effectiveness of large vortex generators on the upper surface of the wing in destabilizing the vortex wake downstream. Paper 7 is a Computational Fluid Dynamics (CFD) study, using two different turbulence models, of (1) tip vortex formation and (2) the decay of an axisymmetric vortex in the far field. Although good qualitative results are obtained, neither turbulence model produces the high levels of suction observed on the wing tip (see Fig. 7 of Paper 7). However, it may be mentioned in passing that Dacles-Mariani, *et al* [3] attained excellent quantitative results for this same case using many more grid points and a higher-order CFD algorithm.

3.2. Instability, Decay, and Breakdown

This topic comprised the largest component of the symposium, representing the primary focus, or at least a significant element, of Papers 6, 10, 11, 17-20, 30-32, 34, and 35. Considerable theoretical research has been expended over the past 25 years since the landmark paper by Crow [4], which predicted the growth of sinusoidal instabilities in trailing vortex pairs. The Crow Instability is generally accepted as the mechanism for the observed transformation of contra-rotating straight trailing vortices into a wavy pattern, and eventually into a train of vortex rings that quickly disintegrates.

As noted in the previous section, Paper 6 analyzes the interaction between prescribed concentrated longitudinal vortices and the trailing vortex sheet of an elliptically-loaded wing. The authors report on the optimum location and strength of the prescribed vortices for promoting the Crow instability far downstream. Paper 17 analyzes the linear stability, *à la* Crow, and nonlinear transient growth of *two* vortex pairs, representing an aircraft with high-lift flaps deployed. The author finds additional modes for the periodic instabilities produced by the addition of flap-edge vortices, and indicates that the spanwise location of the outboard edge of the flap is an important parameter in controlling the wake breakdown.

Papers 18, 19, 28, and 30 present impressive Direct Numerical Simulations (DNS) of the Crow

Instability in the Decay Region (see Fig. 4). This is done in Paper 18 by immersing several pairs of theoretical line vortices in a large "box" of three-dimensional atmospheric turbulence. Each individual vortex is close enough to its own "partner" to interact with and develop sinusoidal instabilities, but the vortex pairs are far enough apart to not interact with other pairs. Owing to the randomness of the turbulence in the box, the different pairs develop into different detailed trains of vortex rings, replicating what is observed in actual contrails. Paper 19 is a two-dimensional DNS simulation of the time-evolution of a pair of ideal vortices with laminar viscous cores, subjected to a small perturbation disturbance. Marching the calculations forward in time, the authors are able to link the vortex pair behavior with the Crow instability. Paper 28 studies the effects of atmospheric turbulence, ground interference, and crosswinds on vortex instability and decay. Large-scale atmospheric turbulence is found to promote an inviscid, long wave-length instability, whereas small-scale turbulence increases the diffusion of the viscous core.

Paper 30 uses a new laminar three-dimensional method, periodic in the streamwise direction, to study some properties of the Crow Instability in concentrated pairs and rolling-up pairs of trailing vortices. Paper 34 includes a numerical study of Reynolds number on the evolution of pairs of laminar trailing vortices; the Crow Instability is also reproduced.

Paper 20 is also able to reproduce the Crow instability by superimposing small perturbations on a quasi-steady flow field that is constructed by three-dimensional vortex filaments with analytical viscous cores. The author cites the results for sensitivity to wave number and insensitivity to Reynolds number as evidence that the Crow instability is purely kinematic kind, and an absolute instability. Paper 35 uses the vortex filament technique of Paper 20 to compute the initial rollup of the vortex wake behind a Boeing 747 aircraft in cruise, *including* the entrainment (or non-entrainment in some cases) of the engine exhaust. A Large Eddy Simulation (LES) technique carries the solution far downstream to the initial collapse of the vortex pair. The role of buoyancy, stratification, and atmospheric and aircraft boundary-layer turbulence on the onset of tip vortex decay is investigated, in what appears to be the first attempt to study the lifespan of the wake from formation to breakdown with all these effects included.

Paper 31 is an analytical two-dimensional, inviscid study of the basic effects of atmospheric compressibility and density stratification (buoyancy) on the vertical motion of a vortex pair. Examples representing the wake of a Boeing 747 aircraft show how the descent of the vortex pair can be accelerated or decelerated by atmospheric effects.

Experimental results related to vortex decay and breakdown are presented in Papers 10, 11, 13, 32, and 34. However, there is no counterpart for the Decay Region of the detailed data of Papers 5, 9, and 25 in the Wake Rollup Region (see Fig. 4); only Paper 34 directly complements the theoretical and numerical studies mentioned above. Paper 34 includes Digital Particle Image Velocimetry measurements of the decaying wake vortex of a wing in a towing tank, through the onset of the Crow Instability, and some information is given concerning the effects of drag-producing devices on the far-wake development. Paper 32 studies the spiral breakdown of a wing tip vortex in the presence of an adverse axial pressure gradient downstream of the wing, tested in a water tunnel. A numerical study of the three-dimensional Euler equations provides some additional physical insight into the vortex breakdown for this special problem. The impressive field measurements described in Papers 10, 11, and 13 were made near the ground; therefore, they are discussed in Section 3.3 below.

3.3. Ground and Crosswind Interactions

Papers 10 and 13 contain field measurements of the structure, trajectory, and strength of transport aircraft wakes near the ground during normal landing operations. Paper 11 examines wakes of Boeing 727, 757, and 767 aircraft during low-altitude flyovers, with and without flaps deflected, and mostly under conditions of persistent crossflow. The ground-based measurement techniques include hot wire and propeller anemometers mounted on towers (Papers 11 and 13, respectively), a form of Laser Doppler Velocimetry called coherent laser radar, or LIDAR (Papers 10 and 11), and an acoustic Doppler backscatter system called Monostatic Acoustic Vortex Sensing System, or MAVSS (Paper 11). Results in all three papers appear to correspond to the Vortex Region and Decay Region of Fig. 4 (note that in Fig. 4 the *distances* are typical for *cruise*, not landing conditions).

The large data base described in Paper 11 provides some information on the effect of meteorological conditions on vortex lifetime. Paper 10 reports on data collected at five sites near Heathrow Airport for a range of atmospheric conditions and aircraft heights. More complex vortex velocity profiles were measured in the Boeing 747 wakes than in the conventional ones of the B-757, and this deserves further attention. The authors also report occasional instances of vortices rebounding after descending normally. Paper 13 also reports rebounding, which is attributed to ground boundary layer effects and the creation of secondary vortices.

The impressive DNS calculations reported in Paper 28 (see Section 3.3) reproduce this rebounding phenomenon and the creation of secondary vortices, and Paper 34 gives some indication of the large effects of vertical wind shear on the Crow Instability. Thus the numerical tools to study ground and interactions in more detail seem to be available, although further validations and algorithm improvements are still required.

3.4 Forces and Moments on Following Aircraft

The fundamental characteristics of wake formation and decay are important ingredients in the vortex hazard problem, but the hazard manifests itself in the response of the aircraft that encounters the wake. Furthermore, changes in the detailed structure of the vortex in the Rollup Region (see Fig. 4) do not always significantly affect the total angular momentum in the wake. Unfortunately, the important topic of the forces and moments on following aircraft did not receive much attention at the present Symposium, addressed only in Papers 14 and 26.

Paper 14 is a flight simulator study of the response of a Boeing 737 aircraft to a variety of prescribed vortex wakes and operational assumptions. The aerodynamic interaction is modeled rather simply; but trends were obtained for stick-free response, the response of the aircraft controlled only by the autopilot, and response with a "math pilot" designed to keep the wings level.

Paper 26 summarizes extensive recent test results obtained in the largest NASA wind tunnel, in which simplified wing models of various spans were mounted at one-half and one mile scale distances downstream of 0.03 scale

models of B-747 and DC-10 aircraft. For these two generating models, conventional landing configurations, unconventional flap configurations, and several candidate vortex-alleviation devices were tested. The lift and rolling-moment data on the following models are used to validate a vortex-lattice prediction method. The reader is referred to Ref. 5 by the same author for a more complete review of some of the successes and failures of past attempts to reduce the rolling moment response. In some cases, significant reductions have been obtained in rolling moment induced on the following wings, but unfortunately, not without performance penalties.

3.5 Exhaust/Vortex Interactions

The interaction of the engine exhausts with the trailing vortex wake does not appear to contribute significantly to the wake vortex hazard problem, although the possibility of triggering wake instabilities remains somewhat open. On the other hand, exhaust/vortex interactions can be important in assessing the impact of aircraft emissions and in the infrared detection of aircraft. Also, at high altitude, water vapor in the exhaust often provides an effective visualization of the wake location and breakdown.

As noted in Section 3.2, Paper 35 uses a vortex filament technique to compute the initial rollup of the vortex wake behind a Boeing 747 aircraft in cruise, and an LES technique carries the solution far downstream to the initial collapse of the vortex pair. Passive tracers released in the turbine core and in the bypass region show that the engine exhaust does not always become completely entrained in the trailing tip vortices within the Rollup Region (see Fig. 4). This calculated result agrees with and helps explain recent flight measurements.

The last paper of the Symposium, Papers 37, studies the dynamics of jet/wake interaction in the Rollup Region of cruising flight. Arguments based on characteristic interaction parameters lead to the conclusion that the jets have almost no effect on the vortex wake. The authors then use a one-dimensional integral model for the jet and a fully-developed vortex model for the wake. These models lead to complete entrainment of the engine exhausts into the wake vortices. The authors conclude that distortion of the jet plume by vortex shearing becomes important as the jets are drawn into the center of the vortices, and that this effect should be investigated.

4. ALLEVIATING THE PROBLEM

At the present time, there are three ways to alleviate the hazard of encounters between an aircraft and a trailing vortex wake. The first is to wait, passively; that is, to maintain a suitably-large separation distance between aircraft. The consensus of Papers 1-4 seems to be that today's separation standards and procedures are adequate, *if followed*. However, economic pressures to *decrease* separations will inevitably grow over time. On the other hand, the introduction of even larger aircraft will exacerbate the vortex hazard, necessitating *increased* separations and offsetting some of the economic advantages of the larger vehicles. The alternatives in the highly-competitive area of air transportation are to either (1) modify the vortices without sacrificing performance, or (2) modify the flight procedures without compromising safety.

4.1 Modifying the Vortices.

Papers 6, 17, 26, 27, 30, 34 join the fluid dynamics research community's perennial crusade to modify the vortices. Techniques considered include generating additional longitudinal vortices to destructively interfere with the tip vortices, altering the spanwise extent of the flaps, altering the flap deflections in different spanwise segments, injecting air at the wing tip to destabilize the vortices, perturbing over time the spanwise circulation distribution, and altering the spanwise drag distribution. Physical understanding is improving with the aid of advanced CFD techniques and new detailed measurements, and promising results are shown. However, modern jet transports are highly optimized for weight, cost, and performance, and a practical solution that does not sacrifice these parameters has yet to emerge.

4.2 Modifying the Flight Procedures.

Current air traffic procedures for aircraft spacing are essentially statistically designed to preclude a dangerous aircraft-wake encounter under worst-case conditions. An alternative is to adapt the flight procedures case by case, on the basis of better knowledge of the potential hazard in individual flight situations and/or of the particular meteorological conditions at the time. Some aspect of this general theme is addressed in Papers 2-4, 12, 14, 21-23. In particular, Paper 23 describes an Aircraft Vortex Spacing System (AVOSS) under development by NASA that dynamically integrates current and predicted

local weather conditions, wake vortex transport and decay information, wake vortex sensor data obtained within the flight corridors, and knowledge of acceptable vortex strengths to produce appropriately-reduced separation distances.

Ideally, the AVOSS system would provide time-dependent spacing criteria to automated Air Traffic Control systems with sufficient lead time to influence aircraft arrival scheduling. The paper describes the overall concept and the challenges of the various subsystems, such as weather prediction, vortex detection, and hazard prediction or assessment. CFD simulations of wake vortex and development and meteorological forecasts are being used to develop fast prediction algorithms, and LIDAR and other (unspecified) ground-based sensor technologies are being investigated for detecting and tracking wake vortices. A field demonstration is planned for the year 2000.

If successful, and if adapted, AVOSS could enable airport capacities to be increased in the next century by means of the weather-dependent reduced aircraft spacings. On the other hand, past studies [6] at one major European airport, Schiphol/Amsterdam, indicate that the variability in winds and the uncertainties in predicting them may well force the air traffic controllers to apply the standard, large separations most of the time, thus negating the potential advantage of a vortex advisory system.

Finally, other new technologies, such as Global Positioning System (GPS), are developing rapidly, and these developments may present new opportunities for varying the flight procedures advantageously. For example, Rossow [7] has recently suggested that the aircraft separation distances could be reduced by using GPS to constrain the flight paths to corridors more narrow than the present ones. The argument is that AVOSS, or other vortex-avoidance systems, could be simplified by limiting where the wake vortices are located and where aircraft that might encounter them can fly.

5. RELATED TOPICS

Roughly 20% of the papers in the Proceedings of the Symposium are on other, but closely related, topics. Paper 8 summarizes the combination of discrete vortex and vortex lattice design and analysis methods for unsteady problems, including practical examples such as

maneuvering aircraft, missiles, and submarines. Paper 15 gives a detailed analysis of experimental flow field surveys behind a propeller-wing configuration in low speed flow. Paper 16 is a numerical study, using an Euler CFD code, of the flowfield of a delta wing embedded in the wake of a bursting vortex generated by another delta wing. Performance enhancements by vortical effects are considered in Papers 33 and 36. Wakes shed from flapping airfoils and their interactions with shear layers are studied in Paper 33, and favorable interference effects of wing vortices in formation flight, such as the V-shaped formations of migrating birds, are described in Paper 36. Finally, Paper 24 presents a detailed study and analysis of the shifting winds surrounding the airport for the Symposium and the effects on the final stages of landing there. Most of the participants at the Symposium were glad they heard about this situation only *after* they arrived.

6. SUMMARY AND CONCLUSIONS

As noted in the Abstract, this Symposium was especially noteworthy for the wide range of authors and active participants, which included both research scientists and customers; *i.e.*, representatives of regulatory agencies, airlines, and manufacturers. However, it is somewhat surprising that little mention was made of a similar, and larger, international conference in 1991, the Aircraft Wake Vortices Conference [8], sponsored by the FAA. Nevertheless, the present Symposium disseminated more widely, and reinforced, the following existing knowledge about the vortex wake hazard of transport aircraft and their implications for air traffic regulations:

First, there is a *hazard*, and avoiding this hazard creates airport congestion, air traffic restrictions, and delays. These problems translate into higher costs for air transportation.

Second, the relevant *physics* is that aircraft produce strong vortices, whose strength is approximately proportional to the weight of the aircraft, and these vortices are perniciously persistent. Much is known about the fundamental fluid dynamics, and the Symposium participants contributed impressive new field and laboratory experiments and numerical simulations that were not available at the time of the 1991 FAA Conference. However, the details of vortex decay and breakdown are still

not fully understood. Even less is known about the influence of meteorological conditions on the far-field characteristics of a vortex wake.

Third, vortex decay *can* be enhanced, although not easily. More importantly, the far-wake structure, and its induced forces and rolling moments (the hazard), *can* be modified. However, this is also difficult to accomplish, especially without adding unacceptable weight or performance penalties that outweigh the savings of closer aircraft spacings. In other words, a practical, *engineering* solution has not yet been found.

Collectively, this knowledge would lead the optimist to conclude that aerodynamics is not a fully mature technology.

Looking ahead, short-term gains seem most likely to come from refinements to the existing systems, such as improved training, especially with respect to vertical separations, and possibly changing the weight categories (see Paper 12). These refinements can be supported by additional simulation studies, such as those reported in Paper 22.

The fluid dynamics community remains ever optimistic that a better fundamental understanding of vortex formation, decay, and breakdown will lead to practical modifications of aircraft that will reduce the hazard of vortex wake encounters. Forecasting technological progress is risky, but it seems to the writer that the ongoing search for and implementation of an *aerodynamic* solution remains a long-term challenge. Newly-emerging CFD tools revealed at the Symposium should help accelerate the process, but the numerical simulations have not been adequately validated for the most part, and the enormous new data bases are just beginning to be digested. Nevertheless, CFD appears mature enough today to complement laboratory experiments and flight tests in evaluating methods for modifying the wake vortex formation and initial rollup. The next few years should see these numerical simulations for real, complex geometries extended to the far wake. There are risks involved because of the cost of such CFD solutions, but they will still be economical compared to flight tests. In any case, they will prove to be worth the price by generating new ideas and by obtaining meaningful evaluations of vortex-alleviating devices.

The operators and regulators are more skeptical, and they are far from ready to modify air traffic

control procedures based on fluid dynamics research. Understandably, they are more concerned with improved detection and avoidance procedures as a means to allow reduced aircraft separation near airports. In fact, these are the measures that are more likely to provide mid-term relief. The fluid dynamics community can help by providing better approximate models of wake decay; better models of rolling moments for various generating aircraft; better predictions and means of detecting of vortex wakes; and cheaper, more reliable weather data. Emerging information systems technology should help gather, process, and disseminate the enormous amount of data that will be generated in aircraft terminal operations.

Ultimately, the economics of airport congestion will have to be weighed against the performance penalty of modifying the vortices and the cost and complication of implementing a safe and reliable system to vary aircraft spacing dynamically. All segments of the scientific and technological communities must continue to work together to attain a better world-wide air traffic system in the 21st Century.

7. REFERENCES

1. Symposium on "Vortex Flow Aerodynamics," AGARD CP-494, July 1991.
2. White, R.P., Jr., and Balcerak, J.C., "The Nemesis of the Trailing Tip Vortex -- Is It Now Conquered?" in *Proceedings of the American Helicopter Society 28th Annual Forum*, May 1972, Paper No. 624.
3. Dacles-Mariani, J.S., Kwak, D., and Zilliac, G., "Accuracy Assessment of a Wingtip Vortex Flowfield in the Near-Field Region," *AIAA Paper 96-0208*, Jan. 1996.
4. Crow, S.C., "Stability Theory for a Pair of Trailing Vortices," *J. AIAA*, 8, 12, Dec. 1970, pp. 2172-2179.
5. Rossow, V.J., "Prospects for Alleviation of Hazards Posed by Lift-Generated Wakes," in *"Proceedings of the Aircraft Wake Conference,"* J.N. Hallock, ed., DOT/FAA/SD/92-1.1, June 1992, Paper 22.
6. van Woortman, H.J.B., and Polak, F.R., "A Vortex Advisory System at Schiphol/Amsterdam Airport: Feasible and Meaningful?", in *"Proceedings of the Aircraft Wake Conference,"*

J.N. Hallock, ed., DOT/FAA/SD/92-1.1, June 1992, Paper 5.

8. J.N. Hallock, ed., "Proceedings of the Aircraft Wake Conference," Vol. 1 and 2, DOT/FAA/SD/92-1.1 & .2, June 1992.

7. Rossow, V.J. "Wake-Separation Distances when Flight-Path Corridors are Constrained," J. Aircraft, 33, 3, May-June 1966, pp. 539-546.

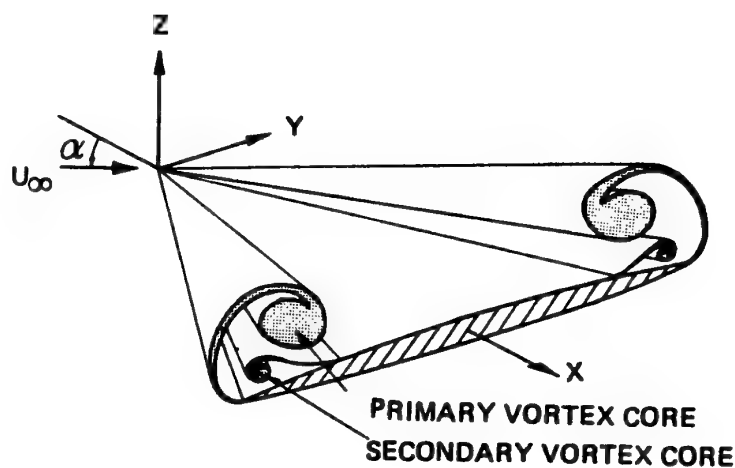


Figure 1. Schematic of flow on a delta wing with leading-edge vortices. (from Paper 1)

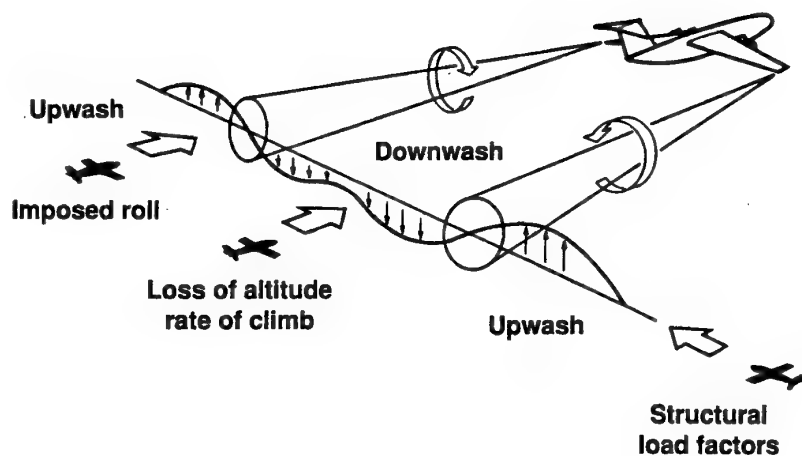


Figure 2. Schematic of generation of wake vortices from wing tips and possible encounters by following aircraft. (from Paper 26)

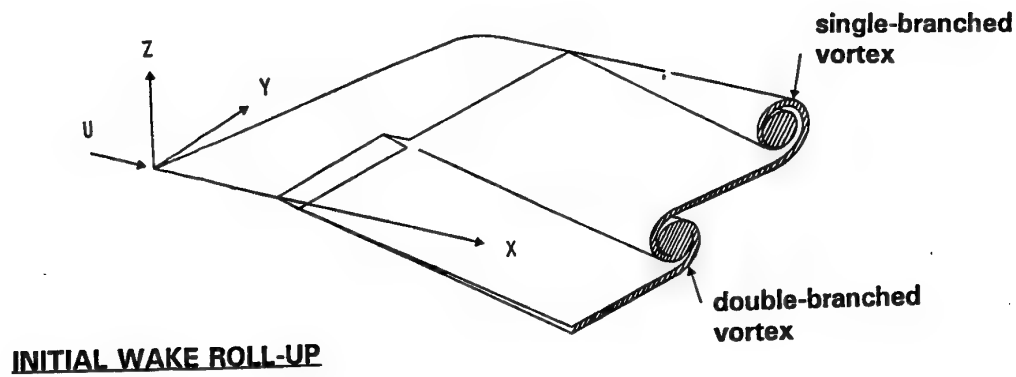
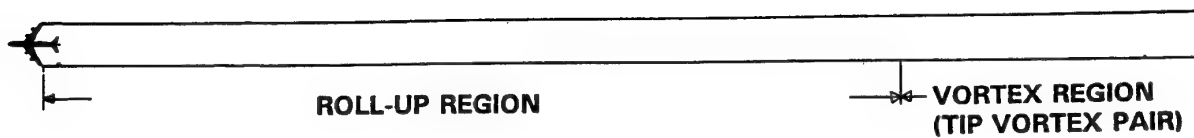


Fig. 3. Vortex wakes from a wing with flaps (from Paper 1)



- **ROLL-UP REGION**
~ 20 spans, 5 sec flying time, 1 km
- **VORTEX REGION**
≤ 400-500 spans, 1.5 min flying time, 20 km
- **DECAY REGION**

DANGEROUS WAKE HAZARD: 4-5 km,
strongly dependent on atmospheric conditions

Fig. 4. Wake regions for a transport aircraft in cruise. (from Paper 1)

VORTEX WAKES IN AERODYNAMICS

H.W.M. Hoeijmakers
Department of Aerospace Engineering
Delft University of Technology
Kluyverweg 1
2629 Delft, The Netherlands

SUMMARY

A survey is presented of the physics of vortex wakes as occur in the flow about aircraft configurations. The emphasis is on fundamental aspects of the flows and on the assessment of the mathematical models that can be used for numerically simulating vortex wakes.

INTRODUCTION

In aircraft aerodynamics flows involving free shear layers and vortex cores, generally termed vortex flows, play an important role (Küchemann, 1973). At the high Reynolds numbers pertinent to aircraft aerodynamics free shear layers form whenever the flow encounters a sharp edge such as the trailing edge. The vorticity contents of the (thin) shear layer is determined by the conditions that at the edge (a geometrical singularity) the velocity remains finite and that vorticity is convected away from it, i.e. in inviscid flow enforced by the Kutta condition. In three-dimensional high-Reynolds-number flow the vorticity contents of the shear layer is *primarily* determined by change in the direction, i.e. the shear, of the velocity vector across the separation line, not by the vorticity already present within the viscous layers meeting at the separation line (Hirschel, 1986).

Away from the edge the shear layer is subject to its self-induced velocity field, usually causing it to roll up into one or more vortex cores which accumulate vorticity of equal sign. These finite-cross-sectional-area regions with a high concentration of vorticity remain embedded within the shear layer and are continuously fed with vorticity convected from the shear layer to the vortex cores. Sooner or later most of the vorticity generated at the edge will be concentrated in these regions with distributed vorticity. In general the effects of viscosity counteract the effects of the stretching of the vorticity and the resulting vortical flow structure is often well-ordered, steady and persistent.

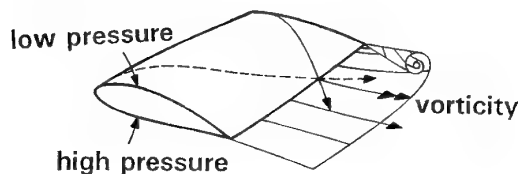


Fig. 1 Separation at the trailing edge

On an aircraft configuration the flow may separate before a sharp edge is reached, i.e. at a smooth portion of the surface. In contrast to the separation at a sharp edge the location of the smooth-surface separation depends, for given Mach number and incidence, on parameters such as Reynolds number and state of the boundary layer, and is not known a priori. In three-dimensional flow this type of separation (i.e. specifically the so-called "open" type of separation) may result in another

well-defined and steady vortical flow structure, which itself is not very dependent on Reynolds number.

A different type of ordered vortical flow may occur downstream of oblique shocks of varying strength, such as the cross-flow shock which appears in the flow field of a slender body at high angle of attack at supersonic speed. This inviscid flow phenomenon is caused by the vorticity produced along the shock wave, which subsequently gets concentrated in vortex cores.

Other separations such as "closed" type of separations involve regions with recirculating flow. This type of vortex flow is largely dominated by viscous effects, often occurs at off-design conditions and has associated with it a usually unsteady and not-well-ordered vortical flow structure.

Two types of vortex flow may be distinguished, vortex flow where there is a *weak* and vortex flow where there is a *strong* interaction between the vortical flow structures and the flow over the surface of the configuration.

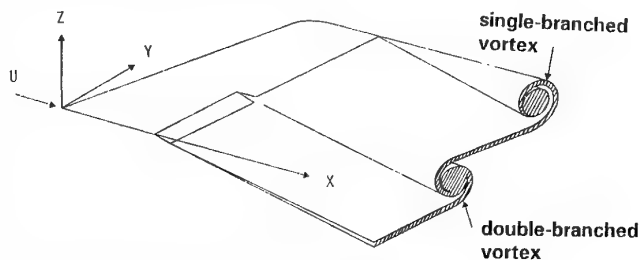


Fig. 2 Vortex wake: Weak-interaction vortex flow

The flow in the wake downstream of the trailing edge of a transport type of wing is usually a weak-interaction type of vortex flow. In this case the vorticity vector is in a direction approximately perpendicular to the separation line, i.e. in this case the trailing edge (Fig. 2). This means that the region with vortical flow is not in close proximity of the configuration and that the direct influence of the vorticity on the velocity and pressure distribution on the surface of the configuration will be small. For weak-interaction vortex flow the lift increases approximately linearly with incidence, at least until on the configuration viscous flow effects become significant. The total amount of vorticity generated at the trailing edge is directly related to the *lift* of the wing, while the velocity field induced on the surface of the wing (in subsonic flow) by the vorticity in the wake is the source of the *induced drag* of the wing.

Strong-interaction vortex flow can occur when the flow separates at the side edge of a low-aspect-ratio wing of low sweep or at the highly swept leading edge of a slender wing (Fig. 3) and also when the flow separates from the smooth surface of the forebody of a fighter aircraft or the elongated body of a missile configuration. In these cases the vorticity vector is ap-

proximately parallel to the separation line. A strong interaction also takes place when the vortex wake of one component of the configuration closely approaches another component of the aircraft. Examples are the interaction of the wake of the wing with the flow about the tail surfaces, the flow about a "close-coupled" canard-wing configuration and the flow about a strake-wing configuration. In the case of strong interaction the rotational flow region(s) are close to the surface of the configuration. The local surface velocity and pressure distribution and the overall characteristics of the configuration are affected considerably, in some cases favourably in other cases unfavourably. For strong-interaction vortex flow typically the lift increases nonlinearly with incidence, and if favourable effects are induced up to higher incidences than without vortex flow. Ultimately a limit to the favourable effects is reached when large-scale vortex burst occurs above the configuration and eventually the steady and ordered vortex-flow pattern is destroyed.

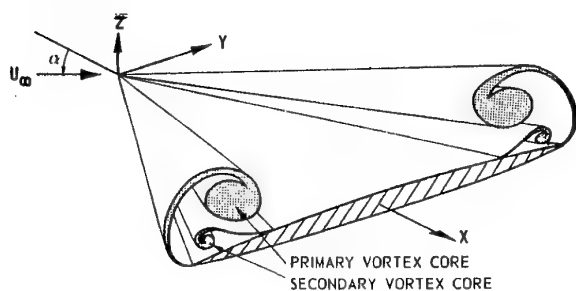


Fig. 3 Delta wing with leading-edge vortices: Strong-interaction vortex flow.

Well-known are the favourable effects induced by the leading-edge vortices on highly swept wing and strake-wing configurations (Fig. 4) at high incidence, resulting in a substantial increase of their lift capability (e.g. Polhamus, 1984). This is of great practical importance for configurations employing these wings with their relatively small lift slope ($\partial C_L / \partial \alpha$). Other details of the vortex flow characteristics of fighter aircraft are still emerging, as demonstrated by Lamar et al. (1986), Campbell et al. (1988), Erickson et al. (1990) in several flow visualization investigations.

Another class of strong-interaction vortex flows are those generated by the rotor of a helicopter and those produced by a propeller. In these cases the wake of one blade of the rotor or propeller passes close to the surface of the next one, which leads to a strong interaction. Also the vortical wake of the (tractor) propeller intersects with the wing which leads to further strong interactions. Likewise the wake of the rotor of a hovering helicopter will intersect the fuselage, giving rise to another strong interaction type of vortex flow.

WEAK AND STRONG INTERACTION ORDERED VORTEX FLOWS

In this section the physical features of a number of vortex flows are described. In all cases we will deal exclusively with flows that will be termed ordered vortex flows. Ordered vortex flows are flows with a topologically well-defined, steady and stable flow pattern, which is maintained within a sizable range of flight parameters (Mach number, incidence, sideslip, Reynolds number, etc.). This implies that most cases consid-

ered here are vortex flows associated with "controlled" flow separation, i.e. flow separating at "aerodynamically" sharp edges.

Vortex wakes - Weak interaction

At the trailing edge of a wing of finite span at incidence the velocity on the lower wing surface and the velocity on the upper wing surface differ in direction (Fig. 1). Actually in steady flow the static pressure should be continuous at the trailing edge, which for incompressible inviscid flow and for compressible inviscid flow without shocks results in the velocity vectors at the trailing edge being equal in magnitude but different in direction. This three-dimensional flow effect, caused by the air tending to flow around the wing tip from the lower ("pressure") side to the upper ("suction") side of the wing, results in the generation of vorticity and the formation of the vortex wake. In the vortex wake the vortex lines are approximately directed in free-stream direction, i.e. away from the trailing edge, and they are not located near the surface of the generating wing, resulting in a "weak interaction" between the vortex wake and the surface pressure distribution.

Since the Reynolds number is large, convection is much larger than diffusion and the vorticity remains within a thin free shear layer. Due to the velocity induced by the vorticity contained within the layer, the layer tends to roll up into vortex cores. This rolling-up may occur in various ways. The most well-known is the tip vortex. It is the single-branched vortex that forms at the free edge of a shear layer (Fig. 2). In case the trailing wake contains vorticity of both signs, vorticity of equal sign will roll-up into separate vortices. Examples of this are the wake of a highly swept wing and the wake of a wing with deployed part-span flaps. Such wakes contain both single-branched (at the edges) and double-branched vortex cores. Even if the shed vorticity is of one sign one or more double-branched vortices may be formed (see Fig. 2). Whether or not multiple centers of roll-up develop is not always a priori evident. For a single straight trailing edge the local extrema of the trailing vorticity (inflection points in the spanwise loading) act often as a center of roll-up, but for more complex shapes the situation is less clear.

In downstream direction vorticity from the shear layer is continuously fed into the vortex core(s), resulting into a growth of the vortex core(s), both in strength and usually also in cross-sectional dimension. The stretching of the shear layer associated with the roll-up process counteracts the effect of viscous diffusion, so that quite often one observes that the shear layer remains relatively thin up to several spans downstream of the trailing edge.

Further downstream of the configuration the roll-up process will be completed, most of the vorticity residing within a limited number of vortex cores (e.g. the trailing vortex pair). The concentration of vorticity into these relatively compact regions of rotational flow is probably responsible for their surprisingly stable and persistent character. The strong and persistent trailing vortex system of large transport aircraft has proven to present a possible hazard for other air traffic, which has resulted in stringent rules imposed at present on air traffic involving large aircraft.

Still further downstream, cores with vorticity of the same or opposite sign, if close enough to each other, start to merge, accompanied by viscous diffusion and decay. Alternatively,

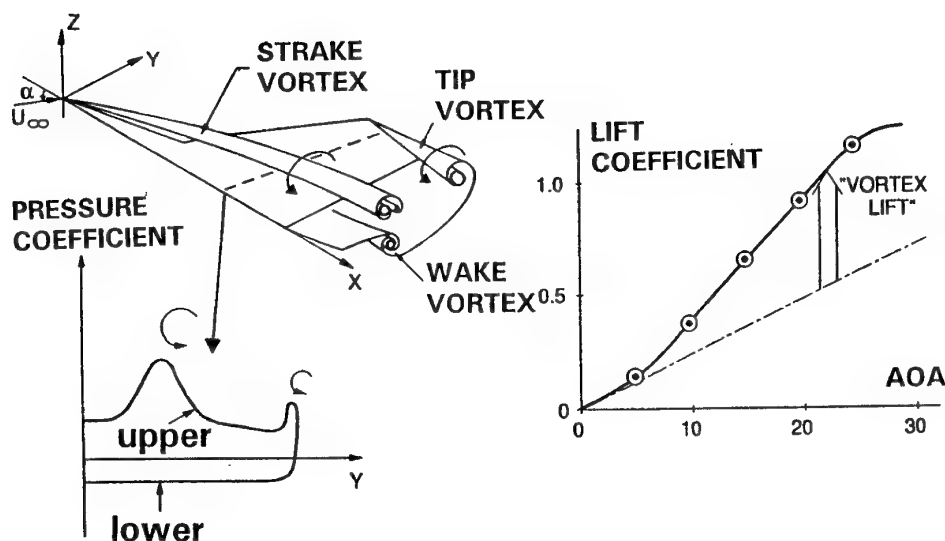


Fig. 4 Strake-wing configuration

complicated longitudinal instabilities may be triggered before the merging or decay process has started, resulting in a somewhat earlier break-up of the trailing vortex system.

Delta-wing leading-edge vortex flow - Strong interaction

The low speed high-angle-of-attack flow about low-aspect-ratio highly swept wings with leading-edge vortex separation has been described extensively in the literature. Based primarily on experimental investigations by amongst others Legendre (1952), Earnshaw (1962), Wentz & McMahon (1966), Fink & Taylor (1967), Hummel (1979) and others the topology of the high-Reynolds number flow about these wings is well-established. At moderate to high angles of attack the flow separates at the leading edge, resulting in a free shear layer emanating from the edge (Fig. 3).

Under influence of the vorticity contained within it, the free shear layer rolls up in a spiral fashion to form a relatively compact single-branched core with distributed vorticity, the so-called leading-edge vortex. The presence of this core in the proximity of the wing surface affects the pressure distribution on the wing to a large extent, the predominant effect being a low pressure region underneath the position of the vortex core. It is this suction peak that is mainly responsible for the increment in the lift due to the vortex flow, the so-called vortex lift. Depending on the leading-edge sweep a stable vortex-flow pattern can persist up to incidences as high as 25 to 35 deg.

It has also been observed in experiments that the adverse pressure gradient in the region just outboard of the lateral position of the center of the leading-edge vortex core causes a so-called secondary separation. The free shear layer emanating smoothly at the line of secondary separation rolls up in a vortex core also, its vorticity being of opposite sign compared to that of the vorticity within the leading-edge vortex core. The extent of the effect of secondary separation on the surface pressure distribution has been observed to depend strongly on whether the boundary layer is laminar or turbulent (Hummel, 1979). It appears that secondary separation effects are largest for the laminar case. Generally for both lami-

nar and turbulent flow they become relatively more important for cases with narrower suction peaks, i.e. for wings at smaller incidences or for wings with lower leading-edge sweep.

Viewed in downstream direction, the leading-edge vortex is continually being fed with vorticity generated at the leading edge which is transported through the free shear layer to the vortex core, so that the latter is increasing in strength as well as in cross-sectional dimension. Downstream of the trailing edge, i.e. in the wake, the free shear layer continues to feed vorticity into the leading-edge vortex core. In the wake the vorticity of sign opposite to that within the leading-edge vortex core, which is generated along almost all of the trailing edge between the plane of symmetry and the wing tip, starts to roll up in a double-branched, so-called trailing-edge vortex core. This two-vortex system, mushroom shaped, has first been observed experimentally by Maltby (1962) and more recently by Hummel (1979), Verhaagen (1983, 1989), Kjellgaard et al. (1986), Solignac et al. (1989) and others. The latter few references also provide detailed surface and flow-field data.

A limit to the favourable effects induced by the vortex flow is reached when large-scale vortex breakdown occurs above the wing. Vortex breakdown manifests itself as an abrupt increase in the cross-sectional area of the vortex core, a decrease in the magnitude of axial and circumferential velocity components near the center of the vortex core and in an increase in the turbulence level in the vortex core. However, the global strong circulatory flow pattern does not disappear abruptly at the point where vortex breakdown occurs, it still persists. Upstream of this point the vortex is hardly affected. Vortex breakdown has first been identified in experimental investigations by e.g. Peckham (1957, 1958), Elle (1958)) and Lambourne & Bryer (1961) in the late fifties. The mechanism underlying vortex breakdown is still unclear, e.g. Hall (1972) and Delery (1994). However, vortex breakdown does appear to depend rather weakly on Reynolds number. The latter may suggest that in essence it is an inviscid flow phenomenon. It has been observed that with increasing angle of attack vortex

breakdown progresses in upstream direction and that it occurs in regions where there is an increase in the pressure along the core, e.g. Erickson (1982). Part of the increase in core dimension may possibly be explained as the response of the inviscid outer part of the rotational core to a pressure rise. Further experimental investigations have been carried out by Kegelmann & Roos (1989, 1990) and Roos & Kegelmann (1990) who measured at a low free-stream Mach number the flow field above 60- and 70-deg delta wings employing a Laser-Doppler-Velocimeter (LDV) and a 7-hole probe. In the case of vortex breakdown they found from the LDV measurements that on the vortex axis the axial component is about constant up to the breakdown location where the axial component of the velocity decreases abruptly and asymmetrically, but stays positive. The probe measurement showed that in the vortex core the total-pressure loss is also about constant up to the breakdown location where it increases sharply. The portion of the vortex core with high losses in total pressure decreases up to the burst location, increases abruptly at the location of the burst and then starts to fill the entire vortex core. In this area the total-pressure losses start to decrease again.

At the higher incidences vortex breakdown is often accompanied by an asymmetric flow pattern. For simple delta wings asymmetric flow patterns without vortex breakdown have been observed for leading-edge sweep angles in excess of 80 degrees.

Strake-wing vortex flow - strong interaction

For wings with low or moderate leading-edge sweep favourable vortex flow effects can be invoked by adding a relatively small, highly swept leading-edge extension, commonly named a "strake". The vortex flow above strake-wing configurations is more complex than the delta-wing vortex flow. Investigations by amongst others Wentz & McMahon (1966), Luckring (1979), Brennenstuhl & Hummel (1982, 1983) have provided valuable insight into the vortex layer structure above strake-wing configurations. Verhaagen (1989), employing a laser-light-sheet flow visualization technique, has acquired additional valuable topological information. Thompson (1985) has also provided such information from water-tunnel studies. From these investigations it follows that above a strake-wing configuration the (single-branched) leading-edge vortex, originating at the leading edge of the strake continues above the wing. The vortex modifies the wing flow field considerably inducing in addition to the favourable effects on the strake itself, favourable effects on the main wing as well. In case of sufficiently (depending on leading-edge sharpness, etc.) swept wing leading edges and at high angle of attack the flow separates also at the wing leading edge. The shear layer emanating from the wing leading edge constitutes the downstream continuation of the shear layer emanating from the strake leading edge. In this single shear layer a double-branched vortex develops. This so-called wing vortex starts close to the kink in the leading edge and viewed in downstream direction, travels along the shear layer, looping around the (single-branched) strake vortex. At some point downstream of the kink the two cores (with distributed vorticity of the same sign) merge into one core. At smaller wing sweep angles and at lower incidences the flow does not separate at the wing leading edge. In this case the flow picture is not yet completely clear. Mostly it is assumed that the shear layer detaches (from the leading edge) at the kink, as proposed by Küchemann (1978, p. 254), see Fig. 4. It might also be hypothesized that downstream of the kink the strake leading-edge shear layer continues as a

shear layer that is attached to the wing upper surface, now emanating from some separation (?) line (see also the discussion in Smith (1984).

For the case of simple delta wings the angle of attack at which vortex breakdown reaches the trailing edge depends strongly on the sweep of the leading edge. For double-delta wings and strake-wing configurations such a simple correlation can not be obtained. Depending on the magnitude of the kink in the leading edge the wing vortex may burst long before the strake vortex breaks down.

DYNAMICS OF VORTEX WAKES

The persistent vortices in the trailing wake generated by large aircraft during cruise and specifically during take-off and landing can be very hazardous to other aircraft. The strength of the vortices is proportional to the weight of the aircraft. The safe longitudinal separation distance between consecutive aircraft is in part determined by the time it takes for the vortices to dissipate and decay, or to break up due to the onset of an instability, or to be convected out of the flight path of the next airplane by the combined action of the self-induced velocity and the wind. These processes are strongly influenced by atmospheric conditions such as ambient turbulence, wind shear and stratification, which can half the 'life time' of the vortices.

Also of great practical interest are the effects of the hot exhaust plumes of the jet engines of the aircraft on the dynamics of the vortex wake, including the way in which the exhaust gases entrain into, and sometimes detrain again out of the vortex wake.

Description

An aircraft moving through the atmosphere leaves behind a so-called vortex wake. The vortex wake originates at the trailing edge of the wing, the horizontal and the vertical tail surfaces and consists initially of a thin (shear) layer across which the velocity changes direction rapidly, i.e. constituting a thin region with high values of vorticity, with the vorticity being directed more or less in the direction of flight (weak interaction, see Fig. 1). Under influence of the self-induced velocity the wake shear layer starts to roll up immediately downstream of the trailing edge, resulting in compact regions with vorticity, so-called vortex cores, embedded within the shear layer. These vortex cores continue to accumulate vorticity rapidly until eventually most of the vorticity resides in a finite number of cores. The resulting topology of the vortex wake depends, in a highly nonlinear fashion, on the initial distribution of the vorticity, i.e. the distribution of the vorticity generated at the trailing edges of the aircraft.

The most well-known topology is the single tip vortex pair. It consists of one starboard and one counter-rotating port-side vortex, separated by a distance of about three-quarter of the span of the aircraft, which descend parallel to each other through the atmosphere.

The single tip vortex pair is the typical topology associated with aircraft in cruise flight, where the variation in initial vorticity distribution is rather smooth, with most trailing-edge vorticity being generated near the wing tips. During landing and take-off high-lift devices (e.g. part-span flaps) are deployed which result in an initial vorticity distribution with multiple extrema, each of which may act as a center of attraction where vorticity of equal sign concentrates into a vortex core,

see Fig. 2. Clearly the dynamics of such a wake is much more complex than that of a single tip-vortex pair.

Typically the roll-up is completed at about 20 spans downstream of the aircraft, which for a B-747 amounts to a distance of about 1 km, or 5 seconds flying time. The concentration of vorticity into relatively compact vortex cores, where viscous diffusion and vortex stretching counteract each other, is responsible for the surprisingly stable and persistent character of wake vortices. The (invisible) strong and persistent trailing vortices of large transport aircraft have proven to present a serious hazard to other air traffic, which has resulted in the present stringent Air-Traffic-Control (ATC) rules imposed on air traffic involving large aircraft. Typically the "vortex regime" can stretch to hundreds of spans (e.g. 20km or 1.5min flying time), where a region of 4 to 5 km behind a B-747 is still to be considered dangerous for subsequent aircraft.

In a quiet atmosphere wake vortices may indeed persist very long and the decay through molecular dissipation may take tens of kilometers. However, triggered by atmospheric perturbations, the trajectories of the vortex cores may be prone to linear, sinusoidal, instability waves. Through a rapid nonlinear amplification process this then results in a violent instability in which:

- "vortex breakdown" of the separate vortices occurs; or,
- the line vortices disrupt, break-up and connect up with each other forming a series of three-dimensional vortex rings.

For a single tip vortex pair the latter type of instability is the so-called Crow instability, Crow (1970). In the Crow instability the most amplified wave has a length of about 8 wing spans. The process of nonlinear development of instabilities into vortex breakdown or vortex break-up and vortex connection and the subsequent more rapid decay and dispersion of kinetic energy does alleviate the vortex wake hazard. However, this process is not understood at all, not for a single tip vortex pair and certainly not for a multiple vortex system relevant for an aircraft during landing.

In summary, in the vortex wake three regions can be distinguished:

(1) *Roll-up region* (≈ 20 spans, 5 sec flying time, 1 km)

In this initial region the vortex cores are formed and most vorticity is accumulated in vortex cores, resulting in a certain topology of the vortex wake. In this region the jet exhaust plumes and the vortex wake may interact and the condensation trails (contrails) are formed. In this region also the entrainment/detrainment of the exhaust gases in the vortex wake may occur and the chemistry of the gas-phase reactions in the exhaust will be of importance;

(2) *Vortex region* (≈ 500 spans, 1.5 min flying time, 20 km)

In this vortex regime the vortex system will gradually drift downward. In this process the vortex cores interact mutually and instabilities, triggered by atmospheric disturbances, are instrumental in prompting the process of nonlinear break-up, i.e. vortex breakdown of individual vortices or the breakup and connection of vortices (Crow instability). Atmospheric conditions (ambient turbulence, wind, stratification) will have a strong influence on the life time of the vortices;

(3) *Decay region* (> 500 spans)

In this region the (remnants of the) vortices disperse through viscous dissipation.

Ground effect

For an aircraft in landing configuration the extended flaps will result in variations in the spanwise circulation distribution, which will result in a multi-vortex wake topology. The proximity of the ground, cross-winds, etc. have a profound effect on the development of this already complex vortex wake and ground effect should be taken into account. Near the ground the vortices interact strongly with the earth's boundary layer and vortices may cause flow separation on the ground surface, where the latter will result in additional (ground) vortices. The ground vortex and the wake vortex may form a vortex dipole which through its self-induced velocity moves away from the ground rapidly (vortex bouncing). It will be clear that the determination of a safe aircraft separation distance is very difficult and requires meteorological data as input.

The atmosphere has a strong influence on the distance (time) it takes for the vortex wake to break-up or decay, actually it has been observed that a factor of two in the life time is not uncommon. This implies that in the study of vortex wakes one has to account for ambient turbulence, effects of wind, effects of stratification (temperature distributions), etc.

Exhaust plumes

The presence of the exhaust plumes from the jet engines will have an effect on the development of the vortex wake. In the near field (about 100 jet diameters) the jets will influence the formation of the vortex cores, but wake roll-up will be complete before the exhausts and the wake begin to merge. In the far field, where the exhaust will be trapped in the vortex cores one can distinguish three regions:

- (1) the region where the jet expands due to the turbulence generated at the interface of the plume and the external flow;
- (2) the region where the jet deflects due to the velocity field induced by the vortex wake;
- (3) the region where the jet convects more or less passively towards the center of the vortices, by the velocity field induced by the vortices and by buoyancy.

The exhaust-wake interaction is very complex, and the detailed modelling of this phenomenon has not yet been achieved. Though it is generally assumed that the exhaust of the jet engines is trapped by the vortices, not necessarily the complete exhaust is entrained by the vortex cores. The portion not trapped by the vortices remains at the initial flight level in relatively quiet air and diffuses only very slowly. Contrails captured by the vortices experience a completely different history. First they remain highly concentrated without much mixing with air, next when the vortices are disrupted and burst, they are suddenly released and dissolved.

In this whole process, depending on the flight level and the meteorological conditions, also phase transitions, cloud-forming micro-physics and (heterogenous) chemistry of the constituents of the exhaust take place.

Wake hazard alleviation

Wake vortex alleviation has been a topic for a long time. However, thus far it has proven impossible to modify the vortex wake generating aircraft such that it produces less hazardous wakes, without affecting the performance of the aircraft. Measures attempted are the injection of turbulence, the addition of devices to reduce or recover the swirl of tip vortices and changes in the geometry of wing tips. However, so far design guide lines to tailor the aircraft design such that it produces a benign vortex wake have not been formulated.

The relation between details of the roll-up process and the details of the spanwise circulation distribution is highly indirect, nonlinear and not fully understood. This implies that changes in the aircraft geometry and changes in the topology of the vortex wake and its dynamics are not related very directly. So, this author wonders whether there will be ever found a satisfactory solution to the wake hazard alleviation problem.

Experiment and numerical simulation

The knowledge of the physics of vortex wakes is far from complete. This is due to the complexity of the processes that play a role in the vortex wake and also because of the inaccessibility of the vortex wake of an aircraft to experimental techniques. In flight tests only the wake very close to the aircraft can be observed and measured (preferably non-intrusively) in detail, which is already very difficult and expensive. Experiments using small-scale models in (big, low-speed) wind tunnels have been carried out, but suffer from scale effects (too low Reynolds number, too low Mach number, inappropriate ambient turbulence) and from wind-tunnel-wall interference. Phenomena important in the vortex wake processes can better be studied using computational methods based on accurate models of the flow physics. These methods can provide crucial information to improve the prediction of the process of vortex formation, nonlinear break-up and subsequent decay.

The numerical simulation of the vortex wakes employing high-level flow models should address:

- the initial development of the vortex wake, i.e. the formation of the vortex cores and the topology of the vortex wake, including the distribution of the three components of the velocity and the vorticity;
- the trajectory and strength of the vortex cores for given meteorological conditions;
- statistical characteristics of vortex curvature, displacement, decay and life time;
- the history of the enstrophy of the vortex wake, specifically during the nonlinear break-up process;
- the effects of stratification (Brunt-Vaisala frequency, Froude number) and of the wind, the effects of the proximity of the ground.
- the effects of Reynolds number, i.e. to enable comparison of the physics of full-scale with results of sub-scale wind-tunnel experiments, so that their value can be assessed;
- simulations of the interaction of vortex wakes with the dynamics of exhaust jets;

Computational Methods

A distinction must be made between the region close to the aircraft and the region further away, i.e. the near wake and the far wake.

Near wake In the near wake the topology of the wake is established.

- The classical Betz's method for determining the topology of the wake from the spanwise circulation distribution is not robust for general circulation distributions and does not yield the details of the early and intermediate stages of the roll-up, where also the interaction with the exhaust plumes is of importance.
- The Euler and Navier-Stokes methods used for simulating the flow about aircraft configurations are at the other end of the spectrum of computational methods. These methods are focused on accurately simulating the flow about the aircraft

itself, and *capture* the vortex wake as part of the solution. However, the grid in the wake region is usually rather coarse, while also the 'far-field' boundary extends typically only a few spans behind the aircraft. Refining the grid and extending it to hundreds of spans behind the aircraft would increase the computation time enormously, without providing more accuracy in the flow solution on the aircraft. A more efficient method would be obtained by coupling the Euler/Navier-Stokes method with some parabolized method for the vortex wake, say starting at one span downstream and using the result of the Euler/Navier-Stokes method as 'initial' boundary condition.

- Potential-flow methods (panel methods) *fit* the wake vortex sheets, which constitutes a nonlinear boundary-value problem. None of the existing wake-relaxation procedures used to solve this boundary-value problem, however, is robust enough to treat general aircraft configurations. This implies that most panel methods employ the *rigid-wake approximation*, which is adequate for obtaining an accurate solution on the configuration.

With the spanwise circulation distribution determined in that way the parabolization for the wake roll-up is obtained by replacing the streamwise coordinate x by $U_\infty \tau$ and employing the two-dimensional time-dependent analogy of the three-dimensional steady flow problem to compute wake roll-up.

An example of a method for computing the 2D time-dependent wake roll-up is NLR's VOR2DT method (Hoeijmakers, 1989). This method can handle general spanwise circulation distributions of multiple lifting components. It recognizes single- and double-branched vortex cores, employs a second-order accurate (2D) panel method with adaptive, curvature-dependent, paneling and an adaptive time-step Euler scheme. At free edges of wake vortex sheets Pullin's (1978) self-similar solution is used as initial shape for the tip vortex. The method is computationally very fast and robust.

Consider the generic example of a straight trailing edge with an elliptic circulation distribution augmented by a distribution due to the deflection of a part-span flap (see Fig. 5). For this case multiple centers of roll-up are expected.

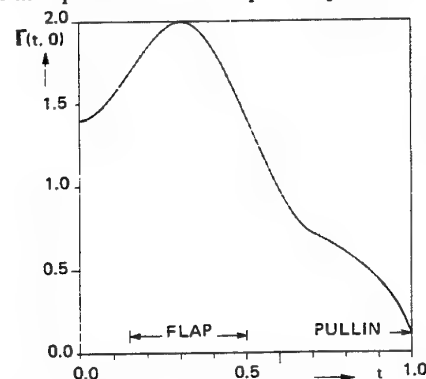


Fig. 5 Spanwise circulation distribution for wing with deployed part-span flap

The results for the wake roll-up computation are shown in Fig. 6 for a number of times τ . Here $\tau - \tau_0$ corresponds to:

$$x - x_{TE} = 2.8 \frac{c(0)}{c_f(0)} \left(\frac{1/2 b}{c(0)} \right)^2 (\tau - \tau_0), \text{ with } x - x_{TE} \text{ the distance behind the trailing edge. For a span of 60m, a root chord of 3m and a root lift coefficient of 0.8 we find } x - x_{TE} \approx 10^3 (\tau - \tau_0) \text{ m.}$$

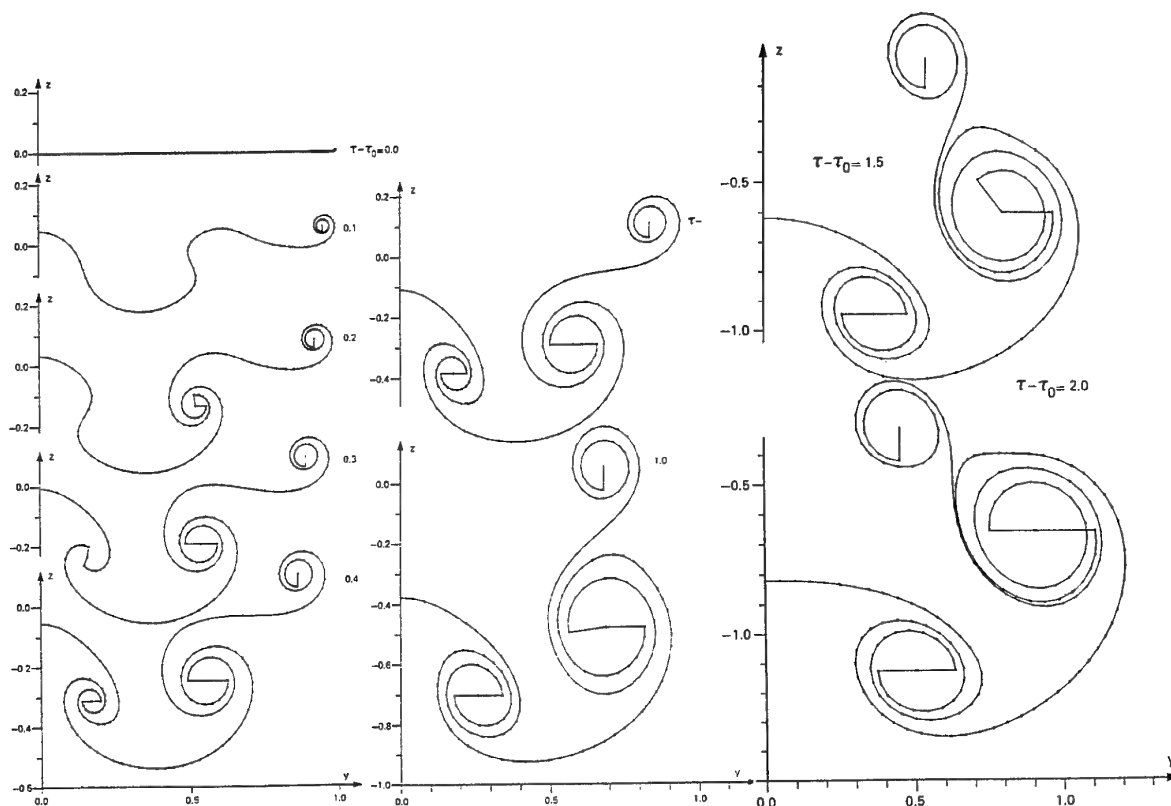


Fig. 6 Roll-up of the wake of a wing with a deployed part-span flap

Three vortices appear:

- the *tip vortex*, appearing instantaneously at $\tau = 0^+$, which is already incorporated in the initial data at the start of the computation $\tau = \tau_0 = 0.0027$;
- the *outboard flap vortex* appears at $\tau - \tau_0 = 0.125$, as the replacement of a at that time highly rolled-up region of the vortex sheet by a double-branched isolated vortex;
- the *inboard flap vortex* appears at $\tau - \tau_0 = 0.268$, again as the replacement of a highly rolled-up region by a double-branched isolated vortex.

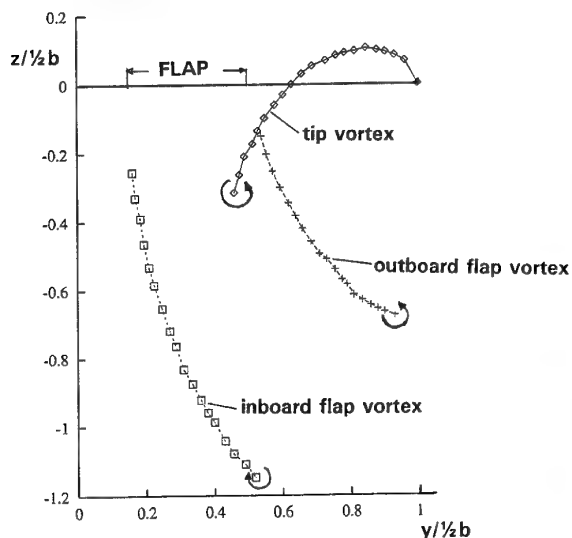


Fig. 7 Trajectory of vortex cores in wake of wing with deployed part-span flap

Upon the emergence of the three vortex cores the computation has been continued up to $\tau - \tau_0 = 2.0$. Fig. 7 shows, up to this distance (time), the trajectory of the three vortex cores in the (y,z) -plane. The strongest vortex is the outboard flap vortex, which ultimately contains 85 percent of the circulation. The inboard flap vortex contains -30 percent of the total circulation and the tip vortex has 45 percent of the total circulation. Note that the tip vortex first moves upwards before moving downward.

Far wake The vortex wake concerns three-dimensional, unsteady, viscous and turbulent, compressible flow. At the in-flow boundary of the far wake domain the result of the simulation of the flow around the aircraft is used.

To model this flow the full Navier-Stokes equations have to be solved at full-scale Reynolds number. The level of model to be used as base line probably should be the so-called Direct-Numerical-Simulation (DNS) method, which solves the full Navier-Stokes equations without approximation, i.e. fully resolves all the relevant spatial and time scales of the flow field. However, at the relevant Reynolds numbers the computational cost of DNS are still prohibitive at present.

The alternatives would be a method based on the Reynolds-Averaged version of the Navier-Stokes equations (RANS) or one based on the Large-Eddy-Simulation (LES) approximation of the Navier-Stokes equations. Employing the RANS version of the Navier-Stokes equations for such a complex flow would require sophisticated turbulence models, since conventional turbulence models cannot adequately capture the anisotropic turbulence field associated with the strongly swirling flow. The LES approximation of the full Navier-Stokes equations would allow higher Reynolds numbers than DNS, it is able to capture the large eddies, but requires a Sub-Grid-Scale (SGS) model to account for the effects of the small-scale eddies. It is not clear whether state of the art SGS models apply to the present type of flow.

The minimum spatial resolution to be considered for the DNS method applied to study the onset of the break-up process is estimated as follows. The most amplified wave length of the Crow instability is of the order of 8 spans. Using 4 periods and 10 points per span leads to 320 planes in flight direction. The boundary conditions at the border of the computational domain requires special attention. To limit the computational domain an analytic matching technique must be used, which will allow the lateral dimensions to be not more than about 5 spans, which allows sufficient resolution in cross-flow planes and renders the computational effort feasible.

In the break-up process three stages can be distinguished: (1) the initiation of the perturbations, i.e. the receptivity problem;

(2) the growth of the initial perturbations in the linear regime; (3) bifurcations and nonlinear breakdown.

For stage (1) it might be expected that for predicting the distance to breakdown the wave length is not the critical item, but rather the initial amplitude of the atmospheric disturbance. This means that the intensity of the ambient turbulence plays a decisive role. In strong turbulence phase (2) might even be "by-passed".

For the background turbulence in first instance isotropic homogeneous turbulence would be taken.

Discussion

● It might be expected that in future results of wake vortex dynamics research could be incorporated in an ATC (Air-Traffic-Control) advisory system based on forecast meteorological parameters. This system could indicate the recommended safe separation distance, so that the separation distance could be reduced to specified radar minima, increasing airport capacity.

An automatic system, integrated in ATC systems, could optimize the separation distances between aircraft, incorporating more parameters than just the presently used Maximum Take-Off Weight (MTOW).

● Similarly, results of the vortex wake research could be used for developing vortex wake models suited for incorporation in flight simulators for training pilots to safely engage active vortex wakes. This requires that using results of the detailed vortex wake research empirical relations are derived to be used, in prediction methods that can be used real time. Clearly much validation will be required to develop a simple representative model which incorporates all important parameters.

● Knowledge on the entrainment of exhausts plumes into the wake vortices, its subsequent detrainment in the atmosphere, its mixing and final distribution could be used as the initial condition for (much-longer-time) atmosphere dispersion models used in climatological studies of the impact of air traffic, or for models that predict the dispersion of emitted species near airports.

● Knowledge on the interaction of the exhaust plumes with the vortex wake could be used in the infra-red detection of aircraft.

VORTEX BREAKDOWN

In experiments vortex breakdown, or burst, is characterized by a sudden expansion and a change in the coherent structure of the vortex core. Two types of breakdown have been identified, bubble-type and spiral-type (see Fig. 8), though some investigators argue that this distinction cannot really be made,

while others find even more types. Experimental evidence indicates that vortex breakdown, at least its onset, depends only weakly on Reynolds number, so indeed, there may be some possibility that it can be modeled by Euler's equations.

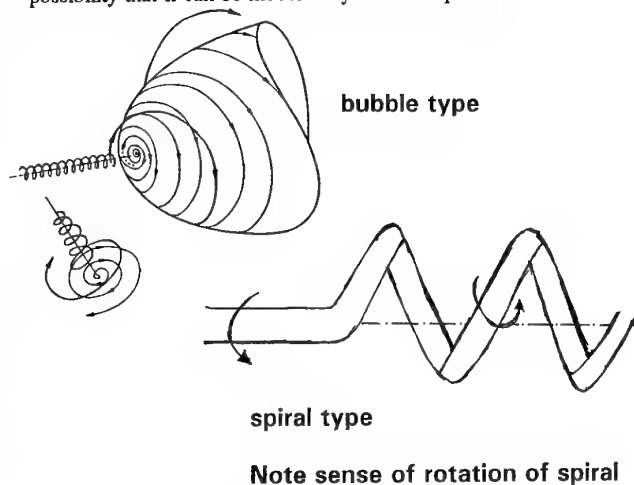


Fig. 8 Types of vortex breakdown

For the Reynolds numbers of interest here usually the spiral type of breakdown occurs. For both types the axial component of the velocity decelerates and stagnates on the vortex axis and a region with reversed flow appears apparently with (bubble) or without (spiral) a zone with recirculating flow, i.e. in the vortex core the flow changes from a jet-like to a wake-like type of flow. Downstream of the stagnation point the flow usually becomes unsteady and turbulent. Vortex breakdown occurs above a critical value of the angle of attack, or swirl ratio defined as $S = (u_\theta/u_x)_{edge} \sim \Gamma_\theta/2\pi r_\theta u_x = 1/2\pi Ro$, where Ro is the so-called Rossby number.

The process of leading-edge vortex breakdown is three-dimensional, unsteady and highly nonlinear and is not yet fully understood, e.g. Hall (1972), Leibovich (1984), Delery (1994). Important ingredients appear to be:

- (i) an in axial direction adverse external pressure gradient
- (ii) the strength (circulation) or rather the swirl ratio (circumferential u_θ /axial component u_x of the velocity) at the edge of the core. If there is an adverse pressure gradient and the swirl ratio exceeds a critical value (slightly above 1.0) vortex breakdown will occur.

The role of the total-pressure losses at the center of the vortex core in the breakdown process is not clear. However, if these total-pressure losses play an important role (as conjectured by Lambourne & Bryer, 1961) it might also be expected that viscosity and the Reynolds number would play an equally important role, precluding an inviscid model to be used for predicting vortex breakdown. This appears to be the case when (bubble-type) vortex breakdown is explained in terms of an analogy with boundary-layer separation, i.e. the flow with low total-pressure encountering an adverse external pressure gradient. However, also note that in the case of the boundary layer the pressure through the layer is constant and the velocity near the wall is low, while in case of the vortex core the pressure decreases rapidly towards the axis and the velocity is high although both quantities are lower than they would have been in an inviscid flow where a singularity is present at the axis.

Quite some research on vortex breakdown (e.g. Pagan & Benay, 1987; Lê et al., 1989), both experimental and theoretical, has concentrated on confined vortex flow inside a tube (see Hall, 1972 and review by Leibovich, 1984). However, it must be realized that this type of vortex does not have the same characteristics as a leading-edge vortex resulting from the roll-up of a free shear layer, the main difference being that a leading-edge vortex is continually fed with vorticity.

Experimental investigations including flow-field surveys on delta wings, above the incidence at which vortex breakdown starts, have been pursued, at low speed, by amongst others Kegelmann & Roos (1989, 1990), Roos & Kegelmann (1990), Payne et al. (1987, 1988) and others. In some of these investigations the spiral-type of instability has been observed.

The effect of the Reynolds number is indirect through the velocity distribution in the vortex core. For lower Reynolds number the azimuthal velocity component u_θ will be lower, so that the swirl number S will be lower and the onset of vortex breakdown will be delayed. The effect of the pressure gradient is that when the pressure gradient increases, such as is associated with an increase of the incidence, the location of the vortex breakdown will be shifted in upstream direction.

Theory and computation

The theoretical approaches to the problem of vortex breakdown can be listed as:

- Quasi-cylindrical approach, which seeks the onset of breakdown in terms similar to the ones for boundary-layer separation;

- The method of critical states due to Squire and Benjamin concerns a search for the existence of long standing waves, which enable disturbances to travel upstream provoking breakdown. In the case of so-called supercritical flow the upstream travelling wave has $c_{wave} < u$, the flow is subcritical and subject to breakdown when $c_{wave} > u$. Using this theory it can be shown that for inviscid flow in a cylinder the flow will be subcritical for $S > 1.2$;

- The theory of hydrodynamic instabilities (Ludwig, Leibovich) involves the linear stability characteristics for axisymmetric, laminar Navier-Stokes equations.

Each of these theories has its shortcomings and is mathematically quite complex.

- A number of investigators have applied the axisymmetric Navier-Stokes equations for laminar (incompressible) flow in an isolated vortex. This is a viable approach because experimental evidence suggests that turbulence is not a key factor in vortex breakdown itself. Also, for Reynolds numbers above 200 to 300 vortex breakdown simulated using the Navier-Stokes equations appear to be independent of Reynolds number. Most methods are hampered by the circumstance that when the bubble forms that it tends to move to the inflow boundary. Also the pseudo-time procedure to march the solution to steady state does not converge beyond the stage of the onset of vortex breakdown.

- The application of DNS and LES to the problem of the breakdown of an isolated vortex has begun.

It must be remarked that all theory and most computations

have been carried out for the case of an isolated vortex, while most computations consider confined vortex flows, i.e. cases where the vortex does not increase in strength due to vorticity being fed into the vortex core. These studies are therefore not applicable to the breakdown of a leading-edge vortex.

- As far as the question of whether or not computational methods based on the Euler equations can simulate vortex breakdown (of leading-edge vortices) is concerned, the following can be remarked:

- If the driving mechanism for (the onset of) vortex breakdown is inviscid in nature Euler methods should be capable of simulating vortex breakdown;

- In inviscid flow the solution is singular at the axis of the vortex core, which causes difficulties mathematically, while computationally numerics-induced total-pressure losses will be unavoidable. The latter will de-singularize the solution;

- Most Euler methods seek a steady-state solution and fail to converge above some critical value of the incidence. This critical incidence appears to depend on the grid, as well as on other numerical parameters. In the author's opinion this phenomenon, which does have strong similarities with the real, physical vortex breakdown, could best be phrased "**SOLUTION BREAKDOWN**". Prior to the critical incidence a dramatic changes in the internal structure of the vortex core appear: a deficit in the axial component of the velocity, converting the familiar jet-like velocity distribution into a wake-like velocity distribution; a switch in the direction of the azimuthal component of the vorticity with a change in sign of the helicity density (Hoeijmakers (1992), van den Berg et al. (1992, 1993). It has also been found that, carefully choosing a solution-continuation procedure, close to the critical incidence two different solutions can be found, one with jet-like vortex cores and one with wake-like vortex cores.

The question to be posed is whether "solution breakdown" indeed indicates vortex breakdown. Time-accurate simulation with Euler methods are required to make progress in this matter.

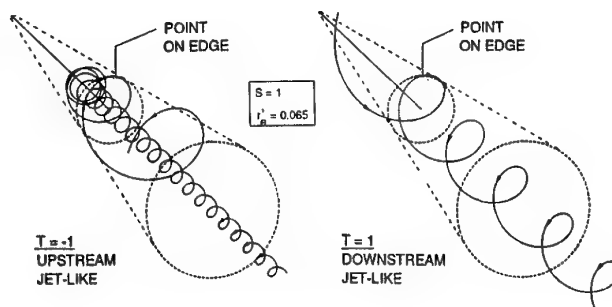


Fig. 9 Streamline for two closed-form solutions of the Euler equations in a conical vortex core

A non-unique solution of the Euler equations for an isolated vortex core

Stewartson & Hall (1963) presented an exact closed-form solution of the Euler equations for the steady, incompressible, axisymmetric, swirling flow in a conical geometry, assuming conical similarity. The boundary condition along the boundary of the vortex core are: $u_x = U_c$, $u_\theta = V_c$ and $p = P_c$. This

solution has the (downstream) jet-like characteristic typical for a leading-edge vortex far removed from vortex breakdown. Recently, a second, exact, closed-form, solution was discovered satisfying identical boundary conditions. This second solution has a wake-like (upstream jet-like) axial velocity distribution. For the two solutions the streamline is shown in Fig. 9.

PROPELLER SLIPSTREAM

An isolated propeller generates a helicoidal vortex wake. The vorticity produced at the trailing edge of a propeller blade in the form of a shear layer rolls up quickly into a tip vortex and depending on the blade loading a finite number of other vortices. These vortices follow the helicoidal path indicated in Fig. 10.

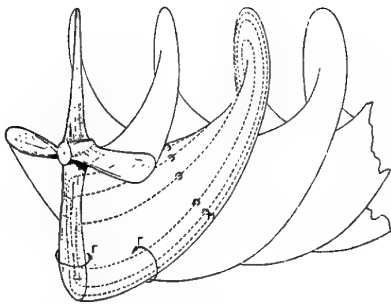


Fig. 10 Sketch vortex wake isolated propeller

In the case of the propeller there is a stronger interaction between the vortex wake and the flow about the generating blade than in the case of a conventional wing. In the case of the isolated propeller the flow field is steady in a coordinate system fixed to the propeller blade. The propeller imparts an increase in the axial velocity component and a swirl, related to the azimuthal and axial vorticity component, respectively.

In case the propeller operates upstream of a wing the flow field is unsteady, quasi-periodic, which however is usually treated as time-averaged over one revolution of the propeller. Obviously the blade vortex wake collides with the wing. Though it must be emphasized very explicitly that 3D vortex lines and smoke or dye streak lines are *not* identical (e.g. Kida, 1994), smoke pictures as in Johnston & Sullivan (1992) and condensation trails in pictures presented in Campbell et al. (1988), strongly suggest that the blade-tip vortex is cut by the wing. However, it also appears that the vortex is apparently not much affected by the cutting and seems to reconnect downstream of the wing trailing edge. The question is: are vortex lines really cut by the wing?

The surface of a vortex tube V consists of vortex lines, all passing through a closed contour, implying that the normal component of the vorticity vector is zero. According to Helmholtz and Kelvin we have that in an inviscid flow a vortex tube remains a vortex tube for all times, as is a vortex line. This means that in general, again in inviscid flow, vortex lines cannot be cut, nor reconnected. In this context it is interesting that Lanchester (1907) suggests that a vortex line resembles a rope or a steel cable, once more indicating the difficulty with the wing cutting the vortex lines in the slipstream of the propeller.

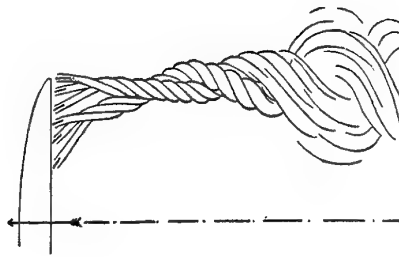


Fig. 11 Sketch vortex lines in wake of wing (Lanchester, 1907)

Above does imply that for cutting/reconnecting vortex lines viscosity is required, or alternatively, that a singularity in the inviscid flow solution develops, which anyway would invalidate the inviscid flow model.

After Marshall (1994) (and somewhat similar with the Kutta condition for the inviscid flow separating at a sharp edge) it is suggested that: the viscous effects are strictly confined to the collision/cutting process; following cutting the flow is again inviscid.

The following model would then be a consistent inviscid flow model (see Fig. 12):

- As the vortex line hits the leading edge it connects up, instantly, with the vortex lines in the *surface* vortex distribution, which, in order to keeping the zero-normal-velocity boundary condition on the wing satisfied, was already adjusting due to the approaching vortex line.
- As soon as the other part of the spiral vortex line hits the leading edge a similar process takes place and the two parts are linked through the surface vorticity distribution, forming one spiral above the upper wing surface and one spiral below the lower wing surface, i.e. the original spiral has split into two spirals.
- The surface boundary conditions cause the vortex lines near the wing surface to slow down, resulting in inclined spiral vortex lines.
- The surface boundary conditions also cause on the upper and lower wing surface an outboard and inboard drift, respectively, so that at the trailing edge there is a chordwise as well as a spanwise shift of the two spirals. However, since both spiral vortex lines are continuous Helmholtz's vortex laws are still satisfied.

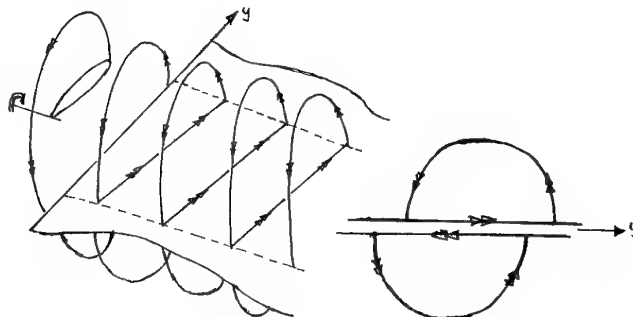


Fig. 12 Sketch vortex line from propeller cutting wing

CONCLUDING REMARKS

- Many aspects of the characteristics of vortex wakes are still unclear, in particular vortex breakdown and the cutting and reconnection process of vortices.

- The modification of vortex wakes cannot be pursued rationally unless its physics is understood. Direct interpretation of flow visualisation using particles or smoke is not always simple.

- The prediction of the effect of the vortex wake on the dispersion and chemistry of exhaust gases in engine plumes is an important field of research.

- The behaviour of aircraft wakes near the ground under realistic conditions needs further research.

- The application of Direct Numerical Simulation (DNS) and Large Eddy Simulation (LES) to vortex wakes could lead to more insight in the evolution and decay of vortex wakes in the atmosphere.

ACKNOWLEDGEMENT

The author likes to acknowledge Mr. A. Elsenaar of NLR, Amsterdam, the Netherlands for presenting the paper at the Symposium in Trondheim. The author would also like to thank Mr. N.B.M. van Noordenburg for contributing to the vortex flow research.

REFERENCES

- Benjamin, T. (1962): Theory of the Vortex Breakdown Phenomenon. *JFM*, Vol. 14, pp. 593-629.
- Berg, J.I. van den, Hoeijmakers, H.W.M., Sytsma, H.A. (1992): Numerical Investigation into High-Angle-of-Attack Leading-Edge Vortex Flow. *AIAA Paper 92-2600*.
- Betz, A. (1932): Verhalten von Wirbelsystemen. *ZAMM*, Vol. XII, No. 3, pp. 164-174.
- Brennenstuhl, U., Hummel, D. (1982): Vortex Formation over Double-Delta Wings. *ICAS Paper 82-6.6.3*.
- Brennenstuhl, U., Hummel, D. (1987): Experimentelle und Theoretische Untersuchungen über die Wirbelbildung an Doppeldeltaflügeln. *ZFW*, Vol. 11, pp. 37-49.
- Brown, G.L., Lopez, J.M. (1990): Axisymmetric Vortex Breakdown Part 2. Physical Mechanisms. *JFM*, Vol. 221.
- Campbell, J.F., Chambers, J.R., Rumsey, C.L. (1988): Observations of Airplane Flow Fields by Natural Condensation Effects. *AIAA Paper 88-0191*.
- Corjon, A., Poinso, T. (1995): A Model to Define Aircraft Separations due to Wake Vortex Encounter. *AIAA Paper 95-1776*.
- Crow, S. (1970): Stability Theory for a Pair of trailing Vortices. *AIAA Journal*, Vol. 8, No. 12, pp. 2172-2179.
- Darmofal, D.L. (1996): Analysis of a Conservation Law Model for Axisymmetric Vortices in Pressure Gradients with Application to Vortex Breakdown. *AIAA Paper 96-0800*.
- Delery, J.M. (1994): Aspects of Vortex Breakdown. *Prog. Aerospace Sci.* Vol. 30, pp. 1-59.
- Doligalski, T.L., Smith, C.R., Walker, J.D.A. (1994): Vortex Interactions with Walls. *Annu. Rev. Fluid Mech.* 1994, Vol. 24, pp. 573-616.
- Dunham, R.E. Jr., Stuever, R.A., Vicroy, D.D. (1993): The Challenges of Stimulating Wake Vortex Encounters and Assessing Separation Criteria. *AIAA Paper 93-3568*.
- Earnshaw, P.B. (1962): An Experimental Investigation of the Structure of a Leading-Edge Vortex. *ARC R&M No. 3281*.
- Elle, B.J. (1958): An Investigation at Low Speed of the Flow Near the Apex of Thin Delta Wings with Sharp Leading Edges. *ARC Rep. R&M No. 3176*.
- Erickson, G.E. (1982): Water-Tunnel Studies of Leading-Edge Vortices. *J. of Aircraft*, vol. 19, No. 6, pp. 442-448.
- Erickson, G.E., Schreiner, J.A., Rogers, L.W. (1990): Multiple Vortex and Shock Interactions at Subsonic, Transonic and Supersonic Speeds. *AIAA Paper 90-3023*.
- Fink, P.T., Taylor, J. (1967): Some Early Experiments on Vortex Separation. *ARC R&M No. 3489*.
- Greene, G.C. (1986): An Approximate Model of Vortex Decay in the Atmosphere. *J. of Aircraft*, Vol. 23, No. 7, pp. 566-573.
- Hall, M.G. (1972): Vortex Breakdown. *An. Rev. of Fl. Dyn.*, Vol. 4, pp. 195-218.
- Hirschel, E.H., Rizzi, A. (1986): The Mechanism of Vorticity Creation in Euler Solutions for Lifting Wings. In: *Proceedings of Symposium on "International Vortex Flow Experiment on Euler Code Validation"*, ed. by A. Elsenaar and G. Eriksson. FFA, Stockholm, October 1-3 1986, pp. 127-161 (1986).
- Hoeijmakers, H.W.M. (1989): Computational Aerodynamics of Ordered Vortex Flows. *NLR Report TR 88088*.
- Hoeijmakers, H.W.M. (1992): Aspects of the Modelling and Numerical Simulation of Leading-Edge Vortex Flow. In: *Proceedings IUTAM Symposium Fluid Dynamics of High Angle of Attack*, Tokyo, Japan, September 13-17 1992, Eds. R. Kawamura, Y. Aihara, Springer Verlag, 1993.
- Hummel, D. (1979): On the Vortex Formation Over a Slender Wing at Large Incidence. *AGARD CP-247*, Paper 15.
- Johnston, R.T., Sullivan, J.P. (1992): Unsteady Wing Surface Pressures in the Wake of a Propeller. *AIAA Paper 92-0277*.
- Kärcher, B., Fabian, P. (1994): Dynamics of Aircraft Exhaust Plumes in the Jet-Regime. *Ann. Geophysicae*, Vol. 12, pp. 911-919.
- Kegelman, J.T., Roos, F.W. (1989): Effects of Leading-Edge Shape and Vortex Burst on the Flowfield of a 70-degree-sweep Delta Wing. *AIAA Paper 89-0086*.
- Kegelman, J.T., Roos, F.W. (1990): The Flowfields of Bursting Vortices over Moderately Swept Delta Wings. *AIAA Paper 90-0599*.
- Kida, S. (1994): Vortex Reconnection. *Annu. Rev. Fluid Mech.* 1994, Vol. 26, pp. 169-189.
- Kjelgaard, S.O., Sellers III, W.L., Weston, R.P. (1986): The Flow Field over a 75 Degree Swept Delta Wing at 20.5 Degrees Angle of Attack. *AIAA Paper 86-1775*.
- Küchemann, D. (1978): *The Aerodynamic Design of Aircraft*. Pergamon Press.
- Lamar, J.E., Bruce, R.A., Pride, J.D., Smith, R.H., Brown, P.W., Johnson, T.D. (1986): In-Flight Flow Visualization of F-106B Leading-Edge Vortex Using the Vapor-Screen Technique. *AIAA Paper 86-9785*.
- Lambourne, N.C., Bryer, D.W. (1961): The Bursting of Leading-Edge Vortices - Some Observations and Discussion of the Phenomenon. *ARC Rep. R&M No. 3282*.
- Lanchester, F.W. (1907): *Aerodynamics*. Constable & Company, London.
- Lê, T.H., Mège, P., Morchoisne, Y. (1989): Simulation Numérique de L'éclatement Tourbillonnaire par Résolution des Équations D'Euler en Fluide Incompressible. *Rech. Aérosp.*, No. 1989-5, pp. 35-49.

- Legendre, R. (1952): Écoulement au Voisinage de la Pointe Avant d'une Aile à Forte Flèche aux Incidences Moyennes. *La Rech. Aéron.* Vol. 30, pp. 3-8; Vol. 31, pp. 3-6; Vol. 35, pp. 7-8.
- Leibovich, S. (1984): Vortex Stability and Breakdown. AGARD CP-342, Paper 23 (1983). See also AIAA J. Vol. 22, No. 9, pp. 1192-1206.
- Luckring, J.M. (1979): Aerodynamics of Strake-Wing Interactions. *J. of Aircraft*, Vol. 16, No. 11, pp. 756-762.
- Lopez, J.M. (1990): Axisymmetric Vortex Breakdown Part 1. Confined Swirling Flow. *JFM*, Vol. 221.
- Ludwig, H. (1965): Erklärung des Wirbelauflaufplatzens mit Hilfe der Stabilitätstheorie für Strömungen mit schraubenlinienförmigen Stromlinien. *ZFW*, Vol. 13, No. 12.
- Maltby, R.L. (1962): Flow Visualization in Wind Tunnels Using Indicators. AGARDograph No. 70.
- Marshall, J.S. (1994): Vortex Cutting by a Blade, Part I: General Theory and a Simple Solution. *AIAA J.* Vol. 32, No. 6, pp. 1145-1150.
- Marshall, J.S., Yalamanchili (1994): Vortex Cutting by a Blade, Part II: Computations of Vortex Response. *AIAA J.* Vol. 32, No. 7, pp. 11428-1436.
- Melville, R., MacCormack, R.W. (1996): Free Vortex Burst Simulations with Compressible Flow. AIAA Paper 96-0805.
- Olsen, J.H., Goldburg, A., Rogers, M. (eds) (1970): *Aircraft Wake Turbulence and its Detection*. Proceedings of Symposium on Aircraft Wake Turbulence, held in Seattle, USA, September, 1970. Plenum Press, 1971.
- Pagan, D., Benay, R. (1987): Vortex Breakdown Induced by an Adverse Pressure Gradient: Experimental and Numerical Approaches. AIAA Paper 87-2487.
- Payne, F.M., Ng, T.T., Nelson, R.C., Schiff, L.B. (1986): Visualisation and Flow Surveys of the Leading-Edge Vortex Structure on Delta-Wing Planforms. AIAA Paper 86-0330. See also AIAA J. Vol. 26, No. 2, pp. 137-143 (1988).
- Payne, F.M., Ng, T.T., Nelson, R.C. (1987): Experimental Study of the Velocity Field on a Delta Wing. AIAA Paper 87-1231.
- Peckham, D.H., Atkinson, S.A. (1957): Preliminary Results of Low Speed Wind Tunnel Tests on a Gothic Wing of Aspect Ratio 1.0. ARC Rep. CP-508.
- Peckham, D.H. (1958): Low Speed Wind Tunnel Tests on a Series of Uncambered Slender Pointed Wings with Sharp Edges. ARC Rep. R&M No. 3186.
- Polhamus, E.C. (1984): Applying Slender Wing Benefits to Military Aircraft. *J. of Aircraft*, Vol. 21, No. 8, pp. 545-559.
- Pullin, D.L.I. (1978): The Large-Scale Structure of Unsteady Self-Similar Rolled-Up Vortex Sheets. *JFM*, Vol. 88, pp. 401-430.
- Quackenbush, T.R., Teske, M.E., Bilanin, A.J. (1996): Dynamics of Exhaust Plume Entrainment in Aircraft Vortex Wakes. AIAA Paper 96-0747.
- Risso, F., Corjon, A., Stoessel, A. (1996): Direct Numerical Simulation of Trailing Vortices in Homogeneous Turbulence. AIAA Paper 96-802.
- Roos, F.W., Kegelmann, J.T. (1990): An Experimental Investigation of Sweep-Angle Influence on Delta Wing Flows. AIAA Paper 90-0383.
- Rossow, V.J., Saco, J.N., Askins, P.A., Bisbee, L.S., Smith, S.M. (1995): Measurements in 80- by 120-Foot Wind Tunnel of Hazard Posed by Lift-Generated Wakes. *AIAA Journal*, Vol. 32, No. 2, pp. 278, 284.
- Rusak, Z., Wang, S., Whiting, C. (1996): Numerical Computations of Axisymmetric Vortex Breakdown in a Pipe. AIAA Paper 96-0801.
- Saffman, P.G. (1992): *Vortex Dynamics*. Cambridge University Press.
- Sarpkaya, T. (1983): Trailing Vortices in Homogeneous and Density-Stratified Fluid. *J. of Fluid Mechanics*, Vol. 136, pp. 85-109.
- Schumann, U. (1990): *Air Traffic and its Environment - Background, Tendencies and Potential Global Atmospheric Effects*. Lecture Notes in Engineering, Vol. 60, Springer.
- Schumann, U., Wurzel, D. (1996): Aircraft and Air Pollution - Research in Europe on Atmospheric Effects of Aviation. AIAA Paper 96-0744.
- Smith, J.H.B. (1984): Theoretical Modelling of Three-dimensional Vortex Flows in Aerodynamics. AGARD CP-342, Paper 17 (1983). See also *Aeron. J.*, April 1984, pp. 101-116.
- Solginac, J.-L., Pagan, D., Molton, P. (1989): Experimental Study of Incompressible Flow on the Upper Surface of a Delta Wing. *Rech. Aérop.* No. 1989-6, pp. 47-65.
- Spall, R.E. (1996): Transition from Spiral to Bubble-type Vortex Breakdown. *Phys. Fluids*, Vol. 8., No. 5, pp. 1330-1332.
- Stewartson, K., Hall, M.G. (1963): The Inner Viscous Solution for the Core of a Leading-Edge Vortex. *JFM*, Vol. 15, pp. 306-318.
- Thompson, D.H. (1985): A Visualization Study of the Vortex Flow Around Double-Delta Wings. ARL-AERO-R-165.
- Verhaagen, N.G. (1983): An Experimental Investigation of the Vortex Flow over Delta and Double-Delta Wings at Low Speeds. AGARD CP-342, Paper 7.
- Verhaagen, N.G., Naarding, S.H.J. (1989): Experimental and Numerical Investigation of the Vortex Flow Over a Yawed Delta Wing. AIAA Paper 88-2563 (1988). See also *J. of Aircraft*, Vol. 26, No. 11, pp. 971-978.
- Visbal, M. (1995): Computational and Physical Aspects of Vortex Breakdown on Delta Wings. AIAA Paper 95-0585.
- Wentz, W.H., McMahon, M.C. (1966): An Experimental Investigation of the Flow Fields about Delta and Double-Delta Wings at Low Speeds. NASA CR 521.
- Zeman, O. (1995): The Persistence of Trailing Vortices. A Modeling Study. *Phys. Fluids*, Vol. 7, pp. 135-143.
- Zheng, Z.C., Ash, R.L., Greene, G.C. (1994): A Study of the Influence of Cross-Flow on the Behavior of Aircraft Wakes near the Ground. In *Proceedings 19th Congress International Council of Aeronautical Sciences*.

Wake Vortices' Effects and the Need for Prompt Action--A U.S. View

Gerald R. Mack
 Director of Airplane Certification
 Boeing Commercial Airplane Group
 P. O. Box 3707, MS 67-UM
 Seattle, WA 98124-2207
 USA

Summary

The growth of commercial aviation has placed such demand on the air traffic system that many major U.S. airports are capacity limited and are experiencing significant traffic delays. These delays inconvenience passengers, cost the aviation industry hundreds of millions of dollars each year, and limit further growth of traffic. The existing wake-turbulence separation distances represent a major challenge in ameliorating this congestion.

To facilitate the introduction of the airplanes now categorized as "heavy," U.S. manufacturers worked with the Federal Aviation Administration (FAA) to conduct flight-test evaluations of the hazards of wake turbulence. These tests underscored, among other things, the necessity of three-dimensional flight path control. In light of the flight test findings, the FAA's effort focused on three areas: aircraft categories, air traffic control (ATC) procedures, and piloting procedures.

In the U.S., ATC provides the lateral and vertical separation between airplanes during instrument meteorological conditions (IMC). Piloting and ATC procedures used during visual meteorological conditions (VMC) provide the pilot and ATC more flexibility than available during IMC. Once the pilot accepts a visual clearance, it is the pilot's responsibility to avoid a wake-turbulence encounter. Pilots operate at significantly smaller separation distances during VMC operations. Refining existing separation criteria requires consideration not only of wake turbulence-related aircraft categories, ATC procedures, and piloting procedures, but also of a variety of issues such as radar limitations, runway occupancy time, flight path constraints, airport configuration, and traffic mix.

As we approach the next century, wake vortices have become one of the key limiting factors in airport capacity. Despite the significant effort expended on wake vortices over the years, several issues remain unresolved. The major issues that must be resolved before separation criteria can be refined are as follows: 1) defining the basis for wake turbulence

separation; 2) determining the far-field characteristics of the wake; 3) understanding the influence of meteorological conditions on these characteristics; 4) evaluating the significance of the wake characteristics to safety of flight; and 5) developing the technology required to mitigate capacity constraints associated with wake turbulence.

Regulatory agencies, airlines, manufacturers, the piloting and ATC communities, and research institutions must team together to ensure that the affected segments of the industry are engaged together, using their collective skills to achieve both the highest possible safety level and the most efficient operational procedures to meet travel demand.

1 Introduction

In the U.S., the air traffic system operates under two sets of rules. ATC is responsible for maintaining horizontal and vertical separation between airplanes operating under instrument flight rules (IFR). The pilot is responsible for maintaining safe separation under visual flight rules (VFR).

Until 1970, ATC maintained at least a three-nautical-mile separation between all airplanes during IMC conditions. This standard was based largely on radar-system operating limits.

To facilitate the introduction of the airplanes now categorized as "heavy" (airplanes with maximum takeoff gross weights greater than 300,000 lbs.) into the national airspace system, the FAA, the National Aeronautics and Space Administration (NASA), and U.S. manufacturers conducted flight-test evaluations of the hazards of wake turbulence (Reference 1). These tests underscored, among other things, the necessity of three-dimensional flight path control. In light of the flight test findings, the FAA's effort focused on the following three areas:

- **Aircraft Categories:** To create workable aircraft categories, the key factor of the difference between the leader's and follower's wing span had to be reflected in

the division of the aircraft fleet. Maximum takeoff weight generally relates to span and thus was chosen by the FAA as the most workable parameter for establishing the aircraft categories.

- **ATC Procedures:** ATC procedures and air traffic separation distances were refined by the FAA on the basis of the test results and experience. For many aircraft, the then existing IFR separation distance of three miles was determined adequate. Distances greater than this were considered necessary when the follower's wing span was significantly smaller than the leading aircraft's span.
- **Piloting Procedures:** Piloting procedures were identified as a significant opportunity for reducing the chance of a wake turbulence encounter. Because of the wake's characteristic descent, the follower aircraft should fly on or above the flight path of the leader aircraft.

With this framework in mind and cognizant of the need to address both IMC and VMC operations, the FAA developed wake turbulence avoidance procedures (Reference 2). During IMC, ATC provides horizontal and vertical separation. During VMC, piloting procedures developed by the FAA are intended to provide the separation for avoiding an encounter.

The FAA has made several refinements to wake-turbulence related IFR separation distances since the introduction of those distances. In 1972, a DC-9 accident prompted an FAA re-evaluation of the separation distances. The re-evaluation resulted in increased separation behind DC-10s and L1011s. In 1975, the FAA refined the IFR separation distances for airplanes following "heavies." In 1986, the FAA revised the IFR separation distances to allow the separation distance to be reduced to 2.5 nautical miles for certain aircraft pairs. In June 1994, the FAA made an interim modification to the IFR separation distances in response to certain NTSB recommendations resulting from a special investigation into wake turbulence-related accidents and incidents.

A comparison of the IFR prescribe separation distances to observed VFR separation distances is presented in Table 1. VFR landings typically occur with significantly smaller separation distances than required for IFR landings.

Table 1
A Comparison of Prescribed IFR Separation
Distances to measured VFR Separation Distances

IFR

Leader Follower	Heavy	Large	Small
Heavy	4	3	3
Large	5	3	3
Small	6	4	3

Source: Reference 2

Note: As an interim measure, the separation distance behind a 757 is 4 n.mi. for all aircraft

VFR

Leader Follower	Heavy	Large	Small
Heavy	2.7	1.9	1.9
Large	3.6	1.9	1.9
Small	4.5	2.7	1.9

Source: Reference 3

2 The Basis for IFR Wake Turbulence Separation

Before the existing wake turbulence separation distances can be refined, the basis used for determining such distances must be clearly defined. One would think that this definition is a rather straight forward proposition. History has shown us otherwise.

In February 1970, the FAA, NASA, and industry initiated a test program to establish logical terminal area spacing criteria. The conclusions reached by the analysis of the three-phase program were unanimous and non-controversial (Reference 1). Key findings of the test were:

1. Short-spanned aircraft rolled out of the vortices, whereas large-spanned aircraft were pushed out of the vortices. Subsequent to this test it had been assumed that roll would be the obvious result of a wake turbulence encounter for all aircraft.
2. Both the 737 and CV 990 experienced similar dynamic encounters from the 747 and 707.
3. The sink rate of the wake was consistent with theoretical prediction.

However, the recommendations concerning the applications of these findings were not unanimous and generated considerable controversy. In the end, the responsibility for determining the separation strategy was with the FAA and was based on the available facts, data and experience up to that time.

In April 1995, the FAA, Air Transport Association (ATA) and Boeing sponsored an industry-wide team with the following objectives: 1) evaluate available data; 2) determine if revisions to wake turbulence classifications and separations are appropriate; and 3) identify specific revisions, if required. The following conclusions (Reference 4) were drawn:

A review of wake turbulence related accidents and incidents in the U.S. shows that there have been no accidents while IMC operations were in effect and the appropriate procedures were followed.

Piloting and ATC procedures used during VMC operations provide the pilot and ATC more flexibility than available during IMC operations. Once the pilot accepts a visual clearance, it is the pilot's responsibility to avoid a wake-turbulence encounter. Separation distances during VMC operations are significantly less than IMC operations. A review of wake turbulence related accidents and incidents in the U.S. shows that there have been no accidents during VMC operations when the pilot flew at or above the flight path of the leading aircraft. Maintaining vertical separation of the follower relative to the leader appears to be the most significant factor for preventing these types of accidents and incidents during VMC operations.

The concerns associated with the multiple interpretations of the results of the 1970 flight test program remain today. The wake characteristics and airplane responses constituting a hazard are still not well defined. An additional challenge is a lack of understanding of the existing fleet's far-field

wake characteristics. However, sufficient evidence exists to suggest refinements to the boundary between the small and large weight category.

This subcommittee concluded, however, that refining the IMC weight categories and separation distances will not address the vertical separation issue associated with VMC operations.

3 Wake Characteristics

There is a significant amount of published information describing the characteristics of airplane wakes (References 5, 6 and 7). The present understandings of the characteristics of wake vortices include:

1. The initial strength as measured by circulation can be calculated using theoretical methods;
2. The initial sink rate of the wake can be calculated using theoretical methods;
4. The far-field characteristics of a wake are strongly influenced by meteorological conditions.

The key issues that must be resolved before wake turbulence separation criteria can be refined include developing a better understanding of:

1. The near-field characteristics of a wake and how these influence the far-field characteristics;
2. The influence of meteorological conditions on the far-field characteristics of a wake.

4 The Significance of the Wake Characteristics

The majority of wake turbulence encounters occur during final approach. This region of flight is characterized by the airplane flying through a relatively narrow corridor. The existing wake turbulence avoidance procedures were developed assuming conservative meteorological conditions, where a vortex might stall in the approach corridor. Under many meteorological conditions, the wake is quickly transported away from the approach corridor or decays at a much faster rate than under calm conditions. An opportunity to improve capacity may be available by including the effect of the actual meteorological conditions on vortex transport and decay when determining aircraft separation distances. Providing separation distances in such an adaptive manner requires focusing on the following questions:

Is the wake in the flight path of the following airplane?

Under many meteorological conditions, the wake is quickly transported away from the flight path. Having the ability to predict or track wake location would allow reduced separation distances when the flight path is clear.

Is the wake alive?

Under some meteorological conditions, the wake may stall in the approach corridor. The ability to evaluate the "aged" characteristics of the wake allows for a circumspect determination of separation.

What is the significance of the wake's characteristics?

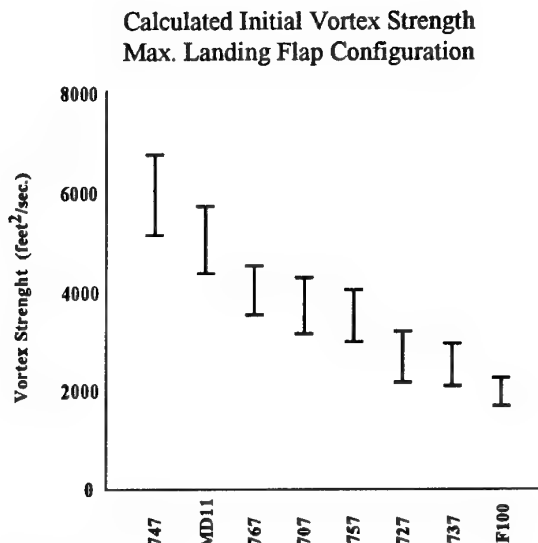
In the event that a wake stalls in the corridor and is still alive, the significance of these aged characteristics on the following aircraft must be assessed for a circumspect determination of separation.

With the latter element comes one of the most challenging issues in determining wake turbulence related separation distances: defining *operationally acceptable wake characteristics*. This subject has prompted hot debate ever since the 1970's flight test program—debate that may be amplified by modern considerations. The development of "Airplane Families" has created additional challenges. Calculated initial vortex strength for a sample of commercial jet transports is shown in Figure 1. Considering this characteristic of the wake, there are no obvious breaks for categorizing aircraft, but instead a continuum. In the end, the strategy used for determining separation lies with the regulatory agencies and will be based on available facts, data and experience.

5 Road Map for Wake Turbulence Work

The growth of commercial aviation has led to congestion at many major airports. There are presently 33 U.S. airports that are capacity-limited and many more experience significant traffic delays. The limitations and delays experienced at a particular airport are not limited to that airport, but instead ripple through the entire air traffic system. The results of these delays are inconvenienced passengers, increased cost to the aviation industry, and limited air traffic growth. The existing IFR wake turbulence separation distances represent a major roadblock in ameliorating airport congestion.

Figure 1



The goal of NASA's Advanced Subsonic Technology (AST) Program is to develop, in cooperation with the FAA and industry, viable technologies to enable a safe, highly productive global air transport system. NASA's vision of the ATC system of the future includes an automated system that maximizes airport operating efficiency through dynamic, adaptive separation criteria (Reference 8). This requires that the aviation industry exploit technology that minimizes inefficiencies in the system. Addressing these issues requires an integrated approach with participation from all affected segments of the aviation industry.

Developing, validating, and implementing an automated spacing system, such as the one proposed by NASA, requires:

1. Developing a better understanding of the far-field characteristics of wake vortices, and the influence of meteorological conditions on these characteristics;
2. Evaluating how the following airplane will respond to far-field characteristics;
3. Determining the significance of the following airplane's response;
4. Developing sensor technology to track wake vortices;
5. Assessing the impact of making changes to the system;
6. Integrating such a system into existing or new air traffic management systems.

NASA has made significant contributions to this subject; however, no single organization has the

expertise or resources required to address all the issues associated with developing and implementing AVOSS.

To mitigate the capacity limitations placed on the system due to wake vortices will require participation from all the affected segments of the industry. Regulatory agencies, airlines, manufacturers, the piloting and ATC communities and research institutions must combine their efforts to ensure that an industry-wide, wake-turbulence plan is implemented and that it has constancy of purpose, clear and attainable goals, strong leadership, and adequate resources.

Urgency is required in this activity considering the rapid development and implementation of new air traffic concepts using Global Positioning Satellite Technology and associated equipment. It would be a tremendous set back to have future ATC system enhancements not fully used due to the current limitations based on wake vortices.

References

1. Rudolph, J. F., "A Compilation of Working Papers Concerning the Wake Turbulence Tests," FAA report, April 30, 1970
2. Federal Aviation Administration, "Airman's Information Manual," FAA Publication, June 1995
3. Haines, A. C. , "Parameters of Future ATC Systems Relating to Airport Capacity Delays," DOT/FAA/EM-78-8A, June 6, 1978
4. Wake Turbulence Industry Team, "Science of Separation Distances Subcommittee, Final Recommendations," June 9, 199
5. Hallock, J. N, "Aircraft Wake Vortices: A State-of-the-Art Review of the United States R&D Program," FAA Report No. FAA-RD-77-23, February 1977
6. Hallock, J. N, "Aircraft Wake Vortices: An Assessment of the Current Situation," DOT-FAA -RD-90-29, January 1990
7. Hallock, J. N., "Aircraft Wake Vortices: An Annotated Bibliography (1923 - 1990)," U.S. Dept. of Transportation Report DOT-FAA-RD-90-30, January 1991
8. Hinton, D. A., "Aircraft Vortex Spacing System (AVOSS) Conceptual Design," NASA TM 110184, August 1995

Klaus Koplin
Secretary General, Joint Aviation Authorities
Saturnusstraat 8-10, P.O. Box 3000
2130 KA Hoofddorp, the Netherlands

1. **Introduction**

Jerry Mack, the previous speaker, expressed his view from the US side and stressed the need for prompt action concerning the effects of wake vortices. I admire his (usually) strong position whereby he can draw from his former insider knowledge of the FAA, and from his long industry experience. The FAA has developed in their Aviation Safety Plan a program that is based on the knowledge of a large nation with a large aviation transport system and driven/supported by a strong aviation safety watch dog - the National Transport Safety Board (NTSB).

We do not have such a strong institution in Europe. We are organised individually in more than 30 countries with a similar number of aviation authorities, air traffic control organisations and accident investigation institutions. The two European organisations, EUROCONTROL and Joint Aviation Authorities are not yet fully developed and are sometimes a toothless tiger.

Therefore my position is from a weaker stand-point than Jerry's. You would need more than 50 speakers to present a comprehensive European view. I am happy that the next speaker comes from the German ATC organisation, Deutsche Flugsicherungs GmbH. He will explain to us - I believe - today's ATC procedures to avoid wake vortices and future developments by the DFS. I can circumvent this chapter in my presentation.

I cannot add anything to the very comprehensive presentation of Jerry and looking into the program of the Symposium I see that many more technical views will be presented which reflect also the European activities.

I will try to analyse on the safety situation for aviation as a whole and the importance of problems created by wake vortices. I will further try to draw a model to organise improvements through coordinated research, rulemaking and training. I believe that this is an area that shall not be solved through regulation alone. The industry - manufacturer and operators - have to take their own responsibilities and initiate their own activities. You shall now wait for the "Regulator" always.

I have mentioned the JAA before, an organisation which might not be known to all of you. I am the Secretary General of this organisation and feel obliged to make it known to a wider public. Therefore I take the liberty to give you a short introduction into the JAA. A comprehensive paper about JAA is available here and should the copies available not be sufficient, please leave your business card with me and a copy will be sent to you.

2. JAA - A European Organisation

WHAT IS JAA?

The Joint Aviation Authorities (JAA) are an associated body of the European Civil Aviation Conference (ECAC) representing the civil aviation regulatory authorities of a number of European States who have agreed to co-operate in developing and implementing common safety regulatory standards and procedures. This co-operation is intended to provide high and consistent standards of safety and a "level playing-field" for competition in Europe. Much emphasis is also placed on harmonising JAA regulations with those of the USA.

The JAA's objectives and functions may be summarised as follows:

- To ensure, through cooperation on regulation, common high levels of aviation safety within the Member States.
- Through the application of uniform safety standards, to contribute to fair and equal competition within the Member States.
- To aim for cost-effective safety and minimum regulatory burden so as to contribute to the European industries' international competitiveness.

JAA originated as the Authorities' response to the technical and economic needs of the European Aviation Industry. However, since 1 January 1992 JAA codes, as they are completed, are referenced in the European Community Regulation on Harmonised Technical Standards and become law in the EC States.

Industry is fully represented in committees and working groups developing requirements and procedures and in a Joint Assembly and Joint Boards where policy issues are debated ensuring a democratic rulemaking process.

The JAA, as presently constituted, carry out their tasks of approval, certifications and safety monitoring using the staff of the national authorities, who also retain the responsibility for the legal findings, granting of licences and certificates, etc.

The JAA Headquarters are responsible for the process of rulemaking, harmonisation and standardisation, (using specialist staff from the national authorities), the decision-making system, the "infrastructure" and various related tasks.

GENERAL ORGANISATION OF THE JAA

Membership

Membership is open to States who are members of the European Civil Aviation Conference (ECAC), which currently has 33 member countries, and JAA are an "associated body" of ECAC. Membership takes effect when the 1990 "Arrangements" are signed. Twenty-six countries are members of the JAA today - *see Figure 1*. At present there are 18 full members and 8 candidate members of JAA.

Structure of the JAA

The JAA are run by the JAA Committee (JAAC) which is comprised of one member from each member State - generally the person responsible for all the safety regulatory functions covered by JAA in each authority. Broad policy decisions and final approval of the budget are decided by the JAA Board which comprises the Directors General of Civil Aviation of the JAA member states.

The Headquarters staff are headed by a Secretary-General and has six divisions - certification, regulation, maintenance, operations, licensing, and administration (support services). In 1996 there will be 33 staff members appointed at HQ. This number is planned to increase to 36 in 1997. The HQ budget is 3.1 million ECUs in 1996 and planned to rise to around ECU 3.6 million in 1997.

Funding of JAA HQ

At present JAA are funded by national contributions (85-90%), plus income from the sale of publications and training (10-15%).

BRIEF OUTLINE OF JAA WORK

Certification

JAA are committed to the joint certification of new aircraft, engines and propellers. They are finalising a joint system for the approval, using a multinational Team or local Authority, according to the complexity, of these products, Auxiliary Power Units (APUs) and equipment coming under the JTSO system. Almost all major products are certified using this joint system (all Airbus Products, Boeing 777, 737 New Generation etc).

Maintenance

JAR-145 : "Approved Maintenance Organisations" was issued in July 1991 and adopted on 1 January 1992. All organisations carrying out maintenance

on aircraft used for Commercial Air Transportation were required to be in compliance with JAR-145 by 31 December 1994. Today some 2.448 approvals / acceptances have been issued of which 1.428 are in Europe, 927 in the USA, 57 in Canada and 36 in the rest of the world.

The JAA concept for the approval of maintenance organisations is that this is the responsibility of the national authorities; however, an important foundation for the mutual acceptance of maintenance approvals is the use of Maintenance Standardisation Teams (MAST). Three such teams are operating and so far three visits have been completed to all "full" JAA members and the fourth round of visits has commenced.

Operations

JAR-OPS Parts 1 and 3 (covering Commercial Air Transportation by aeroplanes and helicopters respectively) were adopted by the JAA Committee at the end of March 1995, the first issue being published on 22 May. JAR-OPS must be implemented no later than 1 April 1998 and this will occur, initially, under national legislation.

JAR-OPS 1 will be subject to "phased implementation" with the operators of large aeroplanes (those over 10 tonnes MTOM or with 20 or more passenger seats) and mixed fleets of large and small aeroplanes being affected first, followed 1 year later (1 April 1999) by those AOC Holders operating small aeroplanes only. Some of the provisions in JAR-OPS have later compliance dates to alleviate the practical difficulties for industry of implementing certain requirements.

Licensing

Licensing deals with the drafting of common Standards and Joint Implementation Procedures (JIP) for these standards in the field of Personnel Training, Testing and Licensing in Aviation.

Current activities for JAR-FCL covers Flight Crew Licensing and is divided into 3 Parts: Part 1 is Aeroplane, Part 2 is Helicopter, and Part 3 is Medical. These parts are planned to be adopted in 1996 and after a transition period of two years to be implemented in mid 1998.

Research

Most JAA Member States perform research work for aviation safety and also the European Union is organising such research on their own. To coordinate the aviation safety research of the JAA members a specific Committee has been set up.

The JAA Research Committee's primary task is to define, promote and co-ordinate research activities in the fields of design, manufacture, operations,

maintenance, personnel licensing and the environment (noise and emissions) where these are expected to lead to safety or environmental improvements through changes to requirements and guidance material. The Research Committee should develop its role from co-ordinating national programmes to developing a Joint Research programme.

The Research Committee is comprised of members from the NAA and, reports to the Secretary General and, through him, to the JAAC. The Committee shall meet regularly with industry representatives and any other interested parties. It has established meanwhile a close link with the EU to coordinate aviation research.

OUTLOOK

The current draft JAA Convention will give JAA a formal European legal basis and might be the first step to a Single European Aviation Safety Authority. As this can be a lengthy process and furthermore needs a careful balance with the European Union an assumption of the time needed cannot be made. However JAA will continue with its work and will without doubt be the genesis of a European Authority.

3. Wake Vortex and Aviation Safety

When we take a regulatory view into an aviation problem we have to review first of all the implication of aviation safety. Before discussing the safety related to wake vortex we have to look into aviation safety as a whole.

Over the last 30 years the number of flights have increased (more than doubled), the number of passengers have increased (with a factor of 10), whilst the number of accidents and the number of persons killed has been rather constant. That means that the relative accident rate was almost reduced by a factor of three.

If the civil air traffic increases as forecasted by 6 to 7% annually, it will have doubled in the next ten to twelve years. In order to keep the present accident rate and the possible number of accidents and fatalities we have to halve the accident rate, or in other words we have to ensure that every second possible accident must be avoided.

In the available documentation from the US it can be seen that there were, prior to the implementation of wake vortex related avoidance procedures, on average 15 wake turbulence related accidents per year (reference 1). The corresponding fatal accident rate was three per year.

After implementation of wake vortex related avoidance procedures, there were on average five wake turbulence related accidents per year. The corresponding fatal accident rate was less than one per year (reference 2). None of these accidents occurred when the pilot and ATC followed the appropriate procedures. I was not able to find similar specific data for Europe nor for other areas of the world.

R Ashford, my predecessor, made an analysis in 1994 - Causal Factors Attributed to Fatal Accidents of the period 1984 to 1993 - (Reference 3). From this document we see that only 1 fatal accident occurred where wake turbulence was the main cause or contributing factor.

I do not wish to be misunderstood. I still believe that wake turbulence is a safety problem but not an urgent one which requires immediate actions from the Regulator. It is a general safety problem which must be solved or at least be minimised. It might be sufficient for the problem of wake vortex to be taken care of by the operators and manufacturers. This is not valid for the questions of separation and wake turbulence classification. Necessary steps have to be taken by ATC.

On the other hand there are two fatal accidents with the same type of aircraft of which the reasons for the accident have not been found yet. Wake vortices could have been, in both cases, the initiation of the problem the pilots were not able to cope with.

In the US, the FAA has agreed that wake turbulence is a major safety problem and has incorporated in their Aviation Safety Plan (Reference 4) a program item related to that problem. One of the significant changes of the Plan from 1995 was the following item:

Wake Vortex Advisory System

"To enable accurate prediction of the wake vortex hazard and use of appropriate procedures for avoidance"

The plan itself reads now:

<i>Approach</i>	<i>4.1 D</i>	<i>Reduce Wake Vortex Vulnerability</i>
<i>Initiative</i>	<i>4.1.20</i>	<i>Revise recommended standards for Wake Vortex separation</i>
		<i>Completion Date FY 1996</i>
<i>Issue 4.8</i>		<i>Turbulence Detection</i>
<i>Initiative 4.8.1</i>		<i>Explore technologies, such as LIDAR, which can detect clear air turbulence (including wake vortices and mountain wave turbulence) on the ground and in-flight. If practical and effective, certify such systems for use on aircraft and deploy at airports which are particularly susceptible to clear air turbulence.</i>

Jerry Mack has mentioned the joint program of FAA and US Industry which was the basis for this part of the Aviation Safety Plan.

In Europe Wake Vortices are obviously not a major safety problem as nobody has defined comparable safety goals as the FAA did in their Aviation Safety Plan.

4. **A European Road Map for Wake Vortex Work**

We heard from Jerry what consequences have been drawn in the US and what he believes has to be done urgently to solve the safety problems coming from wake vortex.

Here in Europe there seems, outside ATC, no need to discuss and solve the wake vortex problems. I have explained that it is not an urgent problem but a problem! Therefore I propose that we tackle it in the following way:

Research

We have to understand better the characteristics of wake vortices, the meteorological influence and the responses of aircraft. We also have to develop better sensor technology and to integrate wake vortex avoidance into air traffic management systems. All items have been mentioned by Jerry and I agree with them. These items will initially need to be researched and we in Europe shall put the necessary resources into that. I look forward to the presentations which will be made later in the Symposium, also from the European research establishments. However, I believe that more efforts will be needed to be the equal partner to the US as we always claim to be.

We cannot rely on our colleagues from the US to a large extent. Such research needs to be coordinated between the participants, not only through the scientific links and symposia like this, but also through the aviation safety administrations. Wake vortex was never an item during the annual conferences of JAA and FAA! Wake vortex is not a discussion subject of the JAA Research Committee and we have, despite the activities of the Research Committee, a lot of programmes of the individual states and of the EU which are still uncoordinated.

A better coordination is needed and cooperation and coordination between JAA and FAA is an urgent item.

Regulation

What about the new rule to improve safety. As I said before we should not always ask immediately for the "Regulator" when we believe we are facing a safety problem. Nevertheless we shall not exclude it. We have to review airworthiness and operational requirements.

In relation to the discussed subject we have today in JAR-25 (Joint Aviation Regulation, Large Aeroplanes) the following paragraph:

JAR 25X261 Flight in rough air

Procedures for flight in turbulence must be established. (See ACJ 25X261.)

*ACJ 25X261
Flight in Rough Air (Interpretative Material)
See JAR 25X261*

The procedures should give the maximum protection against loss of control and against structural damage occurring either directly as the result of turbulence or occurring in the recovery from any disturbance of the flight path. The procedures should, where necessary, distinguish also between the procedure to be followed when deliberately entering an area of known turbulence and that to be followed when the encounter is unexpected.

I do not think we have to change or add something to this. The manufacturer can easily take into account the additional knowledge we gain from research and the certifying Authority can ask for such "taken into account".

There are no specific requirements concerning wake vortex in the Operation Requirements of the JAA. The code JAR-OPS contains only general requirements which indicate having an Operation Manual which must contain all the necessary information for the Operation of the aircraft. It usually contains information about operations on how to avoid the encounter of wake vortices. It might be necessary in future to rethink this situation when we might know more about definitive possibilities to identify wake vortices and when equipment is developed to indicate them to the crews.

Training seems to me the most important possibility to reduce the effects of wake turbulences when you encounter them. We should make sure that specific knowledge is kept current with the pilots and that they are aware of the possible effects of wake turbulences on the aircraft model they are operating. The European Code, JAR-FCL (Flight Crew Licenses) does require that training includes "wake turbulence awareness" (Flight Training Syllabus in Section 2). We have at least to ask if it is sufficient in future.

As already mentioned before there is a responsibility of the manufacturers and operators to take all the available knowledge into account when they design and operate aircraft. We shall not always ask for the regulator.

One specific task is with the equipment industry. They have to strengthen their efforts to find methods to identify wake turbulences so that the crew can actively avoid them in their flight. This could be of a great advantage also during other flight phases so that it would be possible to identify all turbulences and give early warning to the crews.

Conclusions

Wake vortex is not the main concern for aviation safety but it is a safety problem. We have to review the effects carefully and study the effects of it and the possibilities to avoid their encounter in flight. It is a problem that is not unique only in the US. We can have it at any airport of the world and we have to solve it world wide.

We can solve the problem only with joint efforts and I would like to repeat the challenging remarks of Jerry Mack. "Regulatory agencies, airlines, manufacturers, the piloting and ATC communities and research institutions must combine their efforts to ensure that an industry-wide, wake-vortex plan is implemented and that it has constancy of purpose, clear and attainable goals, strong leadership and adequate resources".

We need research for this phenomena and this must be done in cooperation between Europe and the US. Therefore such symposia like this are of the utmost importance.

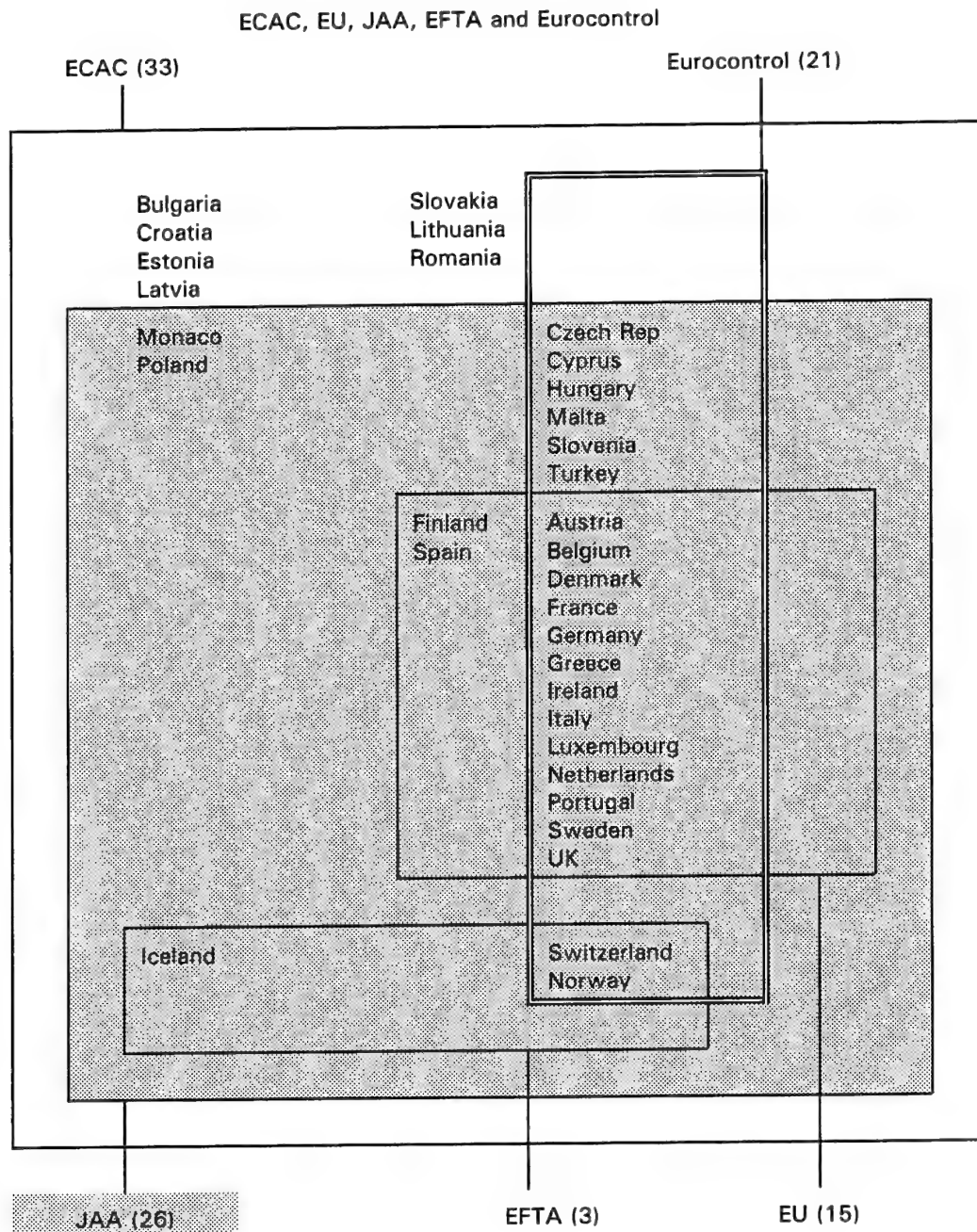
I think that the Regulator is only asked for further developed ATC procedures. We have to rethink the aircraft classification and the necessary separation of aircraft.

Finally we - the regulatory bodies - have to ensure that the authorities cooperate more. There is only one aviation safety and that has to be ensured world wide.

References

1. FAA Report No FAA-RD-77-23, Aircraft Wake Voctices: A State-of-the-Art Review of the United States R&D program, 1977.
2. Federal Aviation Administration Report FAA-EM-75-6, Vortex-Related Accidents Over the Ten year period 1964 - 1973, dated April 1975.
3. Ronald Ashford, Causal Factors Attributed to Fatal Accidents Civil Turbojet/Turbofan Aeroplanes, Worldwide, 1984-93, Issue 1, September 1994.
4. Aviation Safety Plan - February 1996. Published by the US Department of Tranportation Federal Aviation Administration, Washington, DC 20591.

Figure 1



Air Traffic Control Procedures for the Avoidance of Wake Vortex Encounters

Today and Future Developments by Deutsche Flugsicherung GmbH

Frank Brenner

Head of ATC Operations

DFS Deutsche Flugsicherung GmbH

Kaiserleistr. 29-35

63067 Offenbach/Main

Germany

Introduction

The contents of the following paragraphs were presented by Frank Brenner, Head of Current ATC Operations at Headquarters of DFS Deutsche Flugsicherung GmbH, Offenbach on the occasion of the AGARD meeting on May 20th-23rd in Trondheim, Norway.

DFS Deutsche Flugsicherung GmbH, the corporized provider of air traffic control services in Germany is responsible for the development and application of air traffic control procedures. The control procedures are applied at the 17 international airports, the 15 regional airports working under the supervision of DFS and in the 7 area control centers, responsible for the enroute, approach and departure control of aircraft.

In the following the present control procedures are explained and compared to the ICAO procedures. Future developments of DFS procedures are shown.

Present Situation

An increasing number of movements of flights leads to the necessity to space aircraft more and more often with the minimum values in order to avoid delays in air traffic. The question is: What are the minimum values? Are the minima established a long time ago by ICAO still valid? On the one hand trials have shown that these values need not necessarily to be obtained if special conditions prevail and the pilot of a succeeding aircraft is able and willing to adjust his flight path in such a way that the safety of the aircraft is not endangered by wake vortices produced by the preceding aircraft. This means the pilots and the air traffic controllers need to understand the behaviour of wake vortices and closely cooperate in achieving a high throughput of traffic whilst minimizing the risk of wake vortices encounters.

On the other hand incidents have been reported in which the ICAO minima have been maintained.

So the situation must be regarded as complex and only specific solutions

might lead to the results commonly wished.

Information to pilots and controllers

In order to make the partners involved to understand the dangers of wake vortices and to react in a proper way applying the present control procedures information need to be published. The following information taken out of the ICAO supporting documentation DOC 9426 (Annex 1) is also part of the operations manual for our controllers the Manual of Operation for Air Traffic Control Service (BA-FVK) (Annex 2) as well as the Aeronautical Information Publication (AIP Germany) (Annex 3).

Generation of Wake Vortices

Foil 1

Wake vortices are generated whenever an aircraft wing produces lift and are related to the aircraft gross mass, airspeed configuration and wingspan. Vortex strength increases proportionally to weight and is greatest when the generating aircraft is heavy, in a clean configuration and is flying slowly. They originate because of pressure equalizing from the partial vacuum at the upper side of the wing and the excess pressure at the lower side of the aircraft wing. Wake vortices are always generated at both wing tips and are two counter-rotating cylindrical air masses trailing aft of the aircraft. Wake vortices are present behind every aircraft, but are particularly severe when generated by a large and widebody aircraft.

Helicopters produce wake vortices when in flight and there is some

evidence that, per kilogram of gross mass, their vortices are more intense than those of fixed wing aircraft.

Wake Vortex Behaviour

Foil 2

In still air vortices descend at a speed of 400-500 ft/min, except when in ground effect (ie within about 100ft of the ground). They tend to level off after a descent of about 900ft and travel away from each other at 3-5kt, transversely to the flight path. On entering ground effect vortices may 'bounce', and vortices which are generated close to the ground may rise by approximately 100ft. Vortices are transported by wind, and the local wind velocity must be added to the motion just described.

Foil 3

Vortices generally dissipate or break up in one of three ways:

- a) over a long period of time, turbulent diffusion can enlarge each wake so that the wakes merge and dissipate;
- b) disturbances along the length of the vortices become unstable and sinuous oscillations develop which cause the vortices to touch and link together;
- c) a sudden structural change known as vortex breakdown or bursting can abruptly widen the vortex core.

Turbulence hastens the decay of vortices. High winds create turbulence which causes vortices to decay more rapidly.

The Dangers of Wake Vortices

There are three basic effects of wake vortex or wake turbulence on a following aircraft:

- induced roll
- loss of height or rate of climb
- possible structural stress

The greatest danger is the roll induced on the penetrating aircraft to the degree that it exceeds the counter control capability of the aircraft concerned. Should the wake turbulence occur in the approach area, its effect is greater because the following aircraft is in a critical state with regard to speed, thrust, altitude and reaction time.

Wake vortices are most dangerous to following aircraft during take-off, initial climb, final approach and landing phase. It is very dangerous on take-off when there is a crosswind component of 3-5kt, since this may hold the upwind vortex of the preceding aircraft over the runway when it is in ground effect.

Avoidance of Wake Turbulence incidents

Beyond the pilots responsibility to avoid areas where wake turbulence could be present, ATC has also procedures to minimize the risk of wake turbulence incidents.

ICAO categorized all aircraft into wake turbulence categories according to the maximum certificated take-off mass:

Foil 4

ICAO gives separation minima for each aircraft constellation:

Foil 5

These separation minima should be applied when:

- an aircraft is operating directly behind another aircraft at the same altitude or less than 1 000 ft below;

or

- both aircraft are using the same runway, or parallel runways separated by less than 760 m;

or

- an aircraft is crossing behind another aircraft, at the same altitude or less than 1 000 ft below.

Wake Turbulence Separation Procedures in Germany

The German wake turbulence separation minima are in compliance with those prescribed by ICAO. Yet, in Germany, it is possible to deviate from these values. In this case, the obligation and the responsibility for providing wake turbulence separation is delegated to the pilot.

Foil 6

During final approach, the competent controller may give the pilot of the following and lighter aircraft information about the position of the preceding and heavier aircraft. As soon as the pilot of the following aircraft has the preceding aircraft in sight, the controller may leave it to the pilot's discretion to either proceed behind the heavier aircraft maintaining the standard wake turbulence

separation minima or to apply reduced wake turbulence separation minima on his own responsibility.

Foil 7

This procedure asks for a sound knowledge about the creation and behaviour of wake vortices on behalf of the pilots: Information as presented above or as contained in the FAA documentation "Wake Turbulence Training Aid" are a prerequisite.

Foil 8

For departures, it is also possible to leave it to the discretion of the pilot of the following aircraft to provide his own wake turbulence separation from the preceding aircraft of a higher weight category, provided that the additional information listed below has been transmitted to the pilot together with the take-off clearance:

Foil 9

Pilots will then be fully responsible for wake turbulence avoidance and will not be required to conform to the normal wake turbulence separation minima for departing aircraft.

This departure procedure has already been incorporated in the ECAC APATSI Manual on Mature ATC Procedures (Annex 4) and has been submitted to ICAO for incorporation in DOC 7030 on the initiative of the Federal Republic of Germany.

German plans for a Wake Vortex Warning System

The DFS Deutsche Flugsicherung GmbH plans to instal a wake vortex warning system at Frankfurt Airport in 1996 with the intention to increase safety and capacity.

Foil 10

This project will be carried out in cooperation with Deutsche Lufthansa AG and the Flughafen Frankfurt/Main AG.

Purpose

The purpose of the Wake Vortex Warning System (WVWS) is to increase the approach capacity by reducing the wake turbulence separation and to increase the safety by forecast of the wake vortex danger.

Wake Vortex Warning System

The Wake Turbulence Warning System gives, on the basis of measured data, a prognosis about the drift of wake vortices. This prognosis determines whether a wake vortex can, with a determined probability, reach the safety area of the parallel runway (the safety area is the area in which drifting or remaining wake vortices might endanger landing aircraft). The Wake Turbulence Warning System takes into account the cross wind speed, the vortex speed, the vortex life and the critical vortex drift.

Foil 11

A reduced wake vortex separation is only recommendable if the calculated vortex drift is smaller than the critical vortex drift. The critical vortex drift for Frankfurt Airport is 458 metres. It is derived from the distance between the parallel runways in Frankfurt (518 metres) and reduced by a possible lateral deviation from the extended centre line (2 x 15 metres) as well as by the critical distance of the vortex core from the body of the aircraft. The following picture illustrates the critical vortex drift.

This means that for the calculation of the risk involved in the operational use of the Wake Turbulence Warning System, it is only necessary to determine the danger of leeward vortices drifting to the respective parallel runway. For this reason, the Wake Turbulence Warning System cannot be used yet to determine the potential risk involved in approaches to one runway (single runway operation) since in this case the danger caused by windward wake vortices would be important. Up to now, it has not been possible to develop a drift model for windward wake vortices; this means that for single runway operations, the conventional wake vortex separation procedures must be maintained.

3. Description of the procedures when using Wake Turbulence Warning System

3.1 General

ICAO Doc. 9426-AN924 provides the possibility to deviate from the wake vortex separation minima when the necessary technical preconditions are ensured.

New technical systems, scientific research and a risk analysis carried out specifically for this problem area are planned to enable DFS to deviate from the prescribed separation minima since the Wake Turbulence Warning System can predict for a certain period of time whether drifting wake vortices might be a potential hazard on the parallel runway.

Foil 12

The air traffic controller may deviate from the prescribed wake vortex separation and apply the procedures described under 3.2 and 3.3 (staggered, modified staggered) if the system predicts for a time horizon of at least six minutes that the wake vortices of approaching aircraft will not reach the safety area of the aircraft approaching the parallel runway. The Wake Turbulence Warning System gives a new prognosis every minute. With a certain frequency, it can be the case that for predictions given immediately after each other, the predicted time horizon for the application of a reduced wake vortex separation decreases by more than one minute. This is called a prognosis breakdown. When the prognosis horizon is reduced by two minutes or more within the time horizon of six minutes, this is called a critical prognosis breakdown. If the predicted time horizon is reduced by one minute within the period of six minutes, this is called a change in the prognosis period. Therefore, the question arises as to the development of operational procedures for prognosis breakdowns, critical prognosis breakdowns and missed approach procedures. Furthermore, procedures for changes in the prognosis horizon below six minutes must be defined.

3.2 Staggered approach

The Aircraft approach the two runways in a staggered mode, regardless of their weight categories.

Foil 13

The Wake Turbulence Warning System will indicate whether it is possible to use a staggered procedure.

3.3 Modified staggered approach

Aircraft approach the two runways in turn. The aircraft of the higher weight category are always on the lee side. This procedure allows either modified staggered 25L or modified staggered 25R, depending on the direction of the wind.

Foil 14

The Wake Turbulence Warning System will indicate whether it is possible to use a modified staggered procedure.

3.4 Procedure

If the predicted time horizon is less than six minutes, no reduced wake vortex separation will be applied.

If the prognosis is below the time horizon of six minutes, no matter whether by one minute or more, the following procedure shall be applied.

This procedure is based on two advisory opinions:

Aircraft that will reach the runway threshold within 6 minutes shall proceed on final approach (this is equivalent to a distance of approximately 12 NM, even for slower aircraft). The pilots concerned will be informed about the reduced prognosis horizon and taken out of the approach sequence on their request.

Aircraft that are more than 12 NM away from the runway threshold will be separated according to the prescribed wake vortex separation.

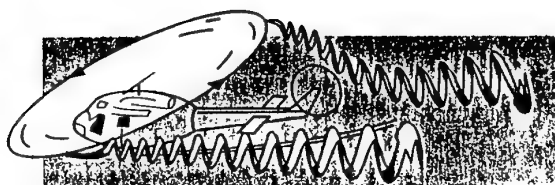
Summary

- ➔ As there is no possibility to build additional runways in Germany, the predicted capacity increase has to be handled with the present infrastructure
- ➔ Wake turbulence separation criteria as established by ICAO a long time ago have to be validated
- ➔ The transfer of responsibility and separation in visual conditions to the pilot of the succeeding aircraft as laid down in the ECAC-APATSI programme is supported by the DFS
- ➔ Advanced technology to predict wake turbulence is needed. An approach to tackle the problem has been undertaken by DFS with the planned operational testing of the Wake Vortex Warning System at Frankfurt Airport

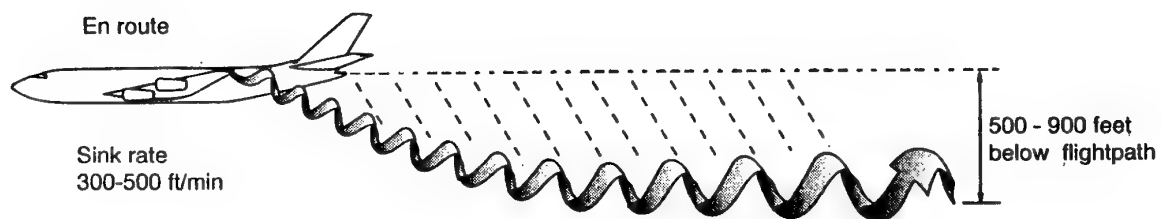
References

1. ICAO DOC 9426 (Annex 1)
2. German Manual of Operations BA-FVK 328, 435 of DFS Deutsche Flugsicherung GmbH (Annex 2)
3. Aeronautical Information Publication (AIP) Germany (Annex 3)
4. Air Traffic Control at International Airports in the Federal Republic of Germany 1995 Edition by DFS Deutsche Flugsicherung GmbH
5. ECAC APATSI (Airports/Air Traffic System Interface) Manual on Mature ATC Operations (Annex 4)
6. Betriebliche Verfahren während der Nutzung des Wirbelschleppenwarnsystems (WSWS) für Anflüge auf das Parallelbahnsystem 25 am Flughafen Frankfurt

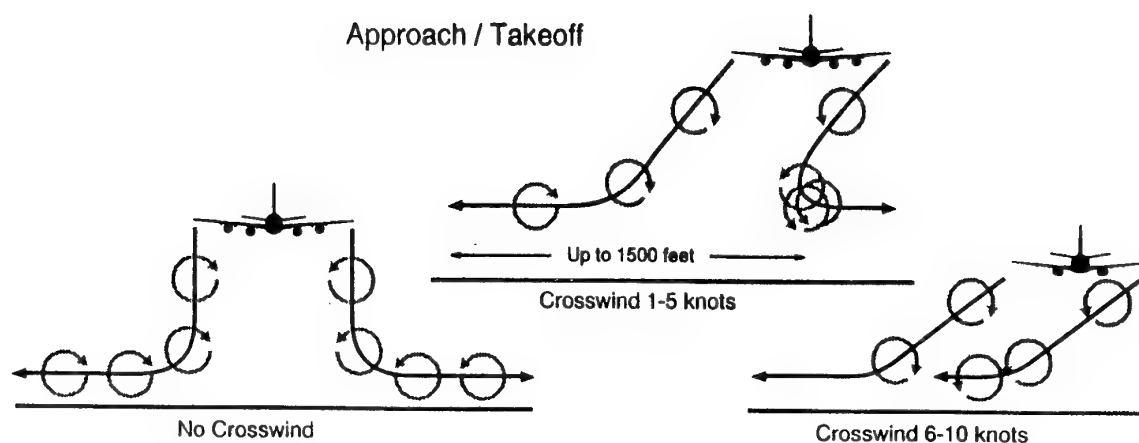
Generation of Wake Vortices



Wake Vortex Behaviour



Wake Vortex Behaviour



ICAO Wake Vortex Categories

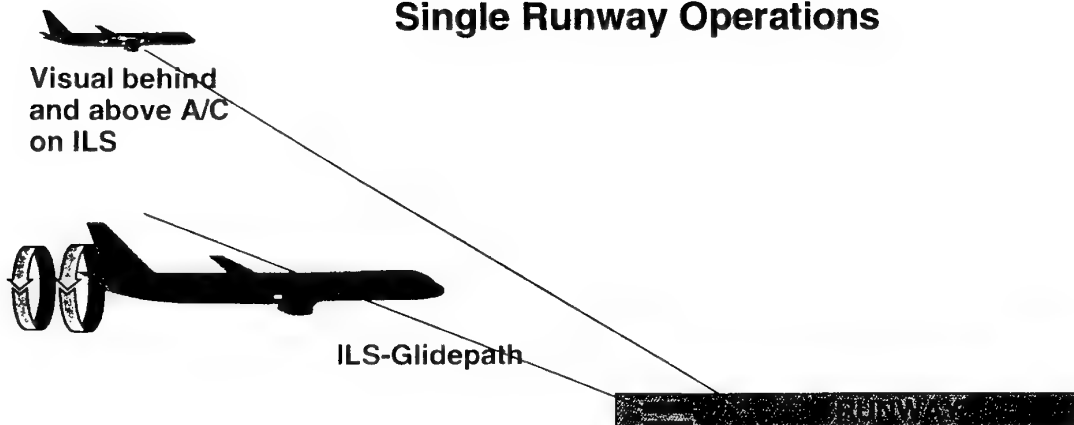
H - HEAVY	all aircraft types of 136 000 kg or more
M - MEDIUM	aircraft types less than 136 000 kg and more than 7 000 kg
L - LIGHT	all aircraft types of 7 000 kg or less

ICAO Wake Vortex Separation

Leading Aircraft	Following Aircraft	Separation
HEAVY	HEAVY	4 NM
	MEDIUM	5 NM
	LIGHT	6 NM
MEDIUM	LIGHT	5 NM

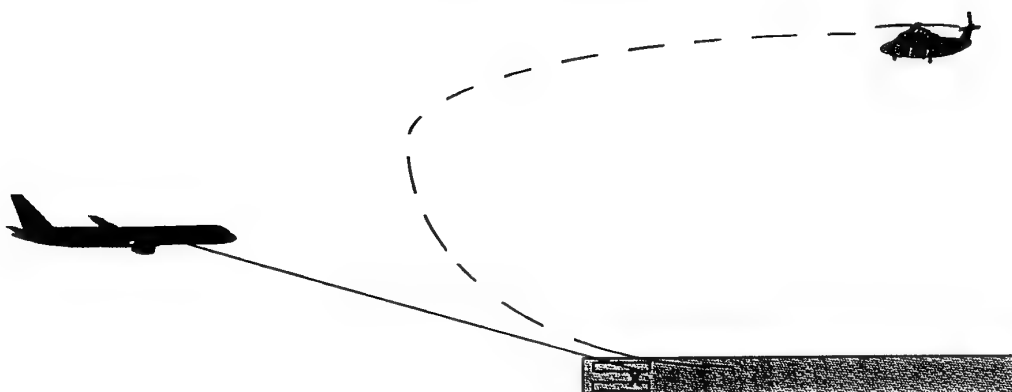
Avoidance Procedure: Landing

Single Runway Operations



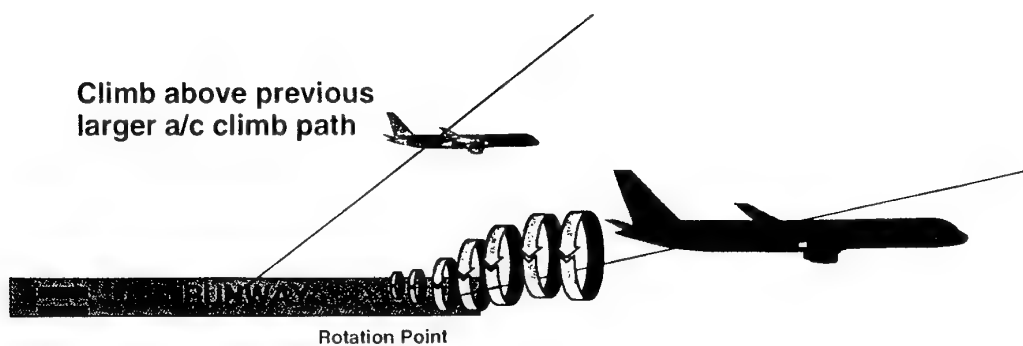
Avoidance Procedure: Landing

Visual Approach



Avoidance Procedure: Take Off

Single Runway Operations



Contents of a Take-Off Clearance

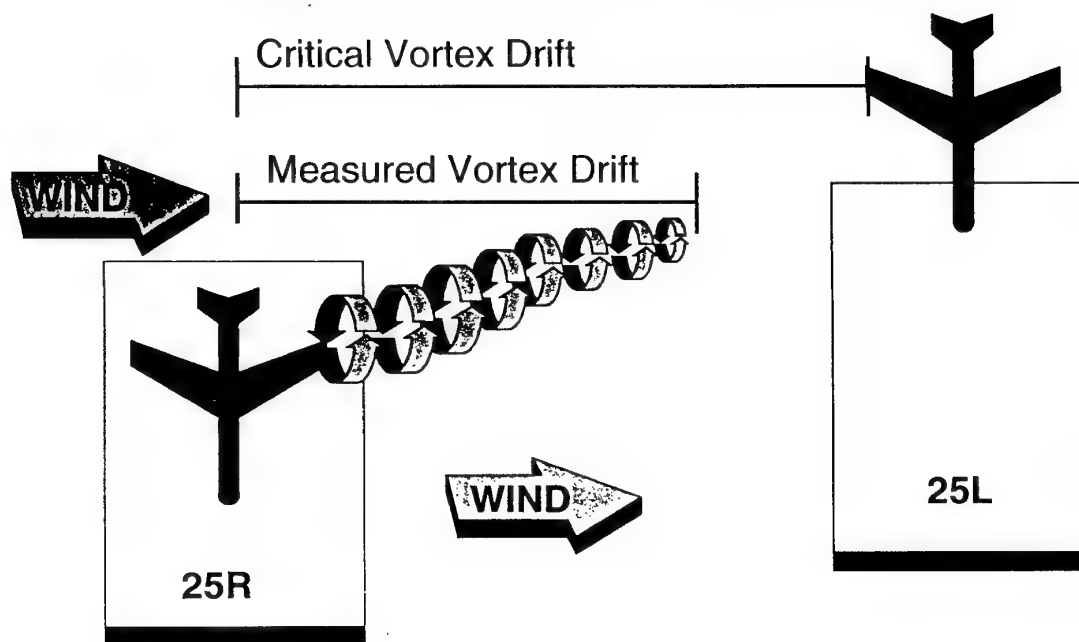
- Type of Previously Departed Aircraft
- Elapsed Time of the Distance of the Previously Departed Aircraft
- Actual Wind
- A Warning of the Possible Occurance of Wake Turbulence

Wake Vortex Warning System

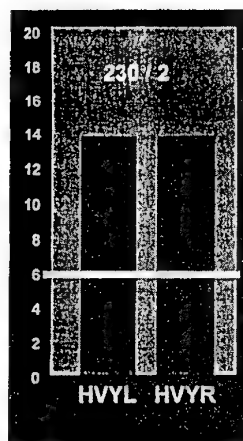
Purpose

- Increase safety by forcast of wake vortex danger
- Increase capacity by reducing wake vortex separation

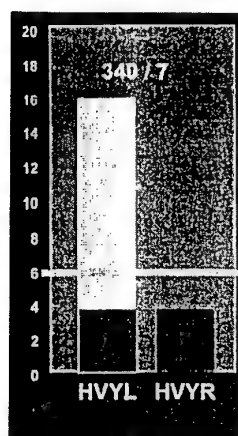
Wake Vortex Warning System



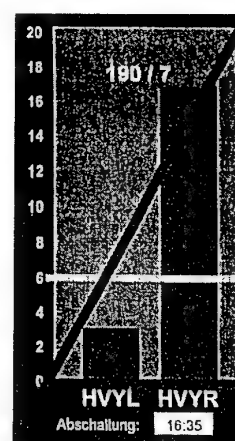
WWWS Displays



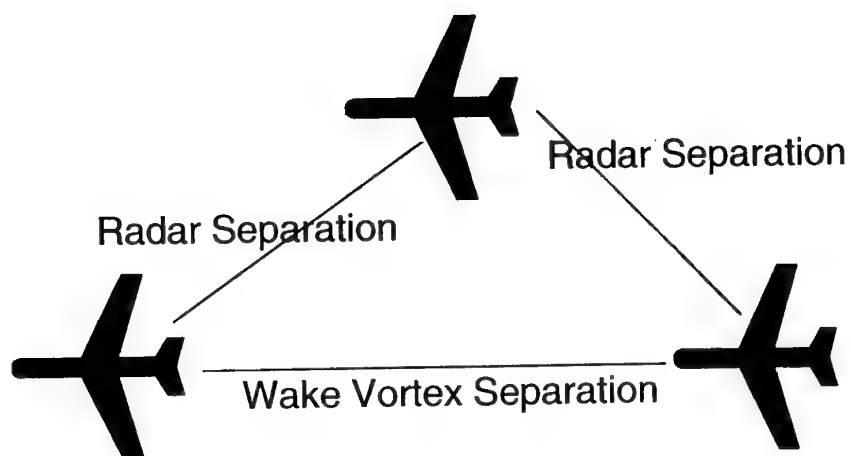
Staggered Approach



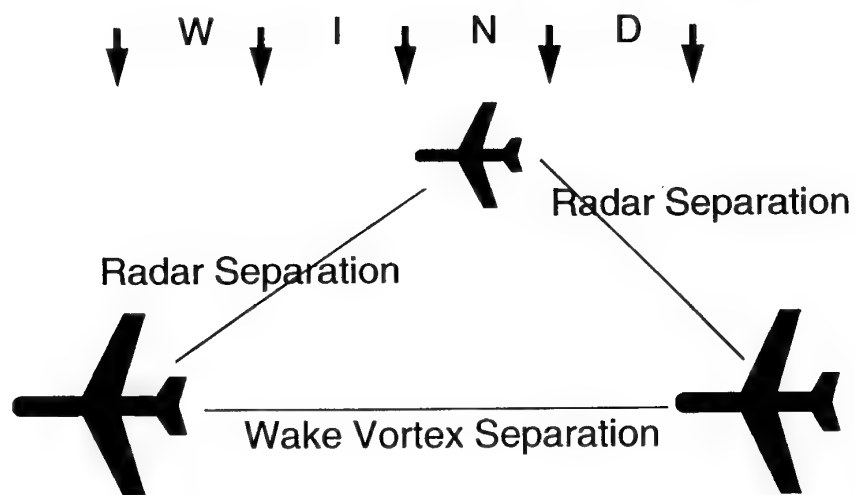
Modified Staggered Approach



Staggered Approach



Modified Staggered Approach



Structure of a transport aircraft-type near field wake

Klaus Huenecke
DASA Airbus, Dept. EFP
Huenefeld St. 1-5, D-28199 Bremen
Germany

Introduction

The wake vortex issue has raised widespread concern to commercial aviation because of its hazardous effects on flight safety, and as a limiting factor to increase airport capacity and aircraft efficiency.

It is found, however, that surprisingly little is known about wakes trailing behind aircraft. Major reason behind the inadequate knowledge of the physical appearance of a wake is the complexity of the flowfield, together with its behaviour in time and space, and a general lack of adequately accessing such flowfields by experimental or theoretical methods.

As a consequence of the wake hazard, typical aircraft separation distances have been imposed in the seventies which are believed to provide adequate safety to air traffic (**Fig.1**). The major parameter dictating separation distance, and classifying aircraft accordingly, is aircraft weight. Separation distances extend from 3 to 6 nautical miles which equate to 1.3 to 2.6 flight minutes when aircraft are on the approach path.

Urgency to solve present-day wake vortex problems, and possible threats looming behind outsize future transport aircraft, have renewed interest in wake research throughout the world. At *Daimler-Benz Aerospace Airbus*, the wake vortex issue is addressed within a government-cofunded research program on high-lift.

Investigations carried out were purely experimental, utilizing the 2m x 2m low-speed wind tunnel at Bremen, with wind tunnel models available from industrial projects. Tests comprised near-field wake flow surveys using a five-hole probe. Data processing was accomplished by utilizing advanced visualization tools.

Results reveal the structure of a near field wake to be of complex nature, even though only the steady-state sector of the flow was accessible with the available testing gear.

Flowfield evaluation focused on

- vortex relative motion
- streamwise vortex development
- crossflow velocity structure
- streamwise velocity structure
- total pressure loss
- streamwise vorticity redistribution.

Testing technique and model

At present, fairly reliable results appear to be gained only from experiments in wind tunnels. Length limitations inherent to tunnel test sections, however, will allow only the near field, and the extended near field, of a wake to be accessed. In practice, this covers about 0.03 flow seconds, contrasting a wake lifetime of 2 minutes for which a reliable prediction is sought.

The assumption is made that significant characteristics of a wake originate from nearfield phenomena of the nearby aircraft. By "nearfield" is meant a wake length of one half to one wing span, a distance accessible by the majority of existing wind tunnels, with models of sufficient scale with respect to tunnel size.

With this assumption it appears justifiable, that by investigating the near field, a sufficient characterization of a wake is possible. Results gained from such investigations may also serve as a basis for far field wake research, once experimental and numerical techniques have matured.

Within the framework of the specific tests carried out by DASA Airbus, two high-lift configurations of a twin-engined aircraft model were investigated in the low-speed wind tunnel at the Bremen facility of DASA Airbus. Testing was done with a representative half model of a medium-range passenger transport aircraft (**Fig.2**).

Model scale was 1/13.6 (7.35% of actual size),

featuring a high-lift configuration with the following characteristics:

- slat 26°
- single-slotted, continuous-length flap at 34°
- symmetric aileron (aileron droop) 5°
- through-flow nacelle representing high-bypass ratio turbofan at flight idle
- nacelle strake off
- fuselage representative of actual medium-range 150-seat passenger transport aircraft
- tailplane off

For investigations with a double-slotted flap system, the same wind tunnel model was used. Trailing-edge flaps of this model were replaced by a double-slotted type flap, but model was otherwise identical. Characteristics of this model were:

- main flap 34°
- inner tab 19° , outer tab 23.8°

The model was mounted on the ceiling of the test section and set at 7 degrees incidence.

Tunnel freestream velocity was 60 m/s (Mach 0.18), Reynolds number based on mean aerodynamic chord 1.27×10^6 .

Data acquisition was by a conventional 5-hole probe mounted on a rod that could be rotated for probe vertical positioning.

Flow surveying was made at five planes perpendicular to freestream direction (Fig. 3). Streamwise positions of surveying planes were at 7%, 18%, 37%, 75%, and 95% of wing half span, respectively.

Structure of crossflow velocity field

With all 5 surveying planes arranged together, an impression may be gained of the flowfield volume, relative to the model size, that has been surveyed in the nearfield (Fig. 4). Effects of both tip and flap vortices, together with spatial streamlines, indicate the highly three-dimensional character of the wake. Magnitude of the crossflow velocity is represented as shaded areas on the planes.

Crossflow velocity is defined as the vectorial sum of both vertical and lateral components of the velocity vector (Fig. 5).

Arranging surveying planes separately, vortex development and positions become apparent (Fig. 6). While the flap vortex becomes the dominant part of the vortical system, with its position stabilizing in downstream direction, the tip vortex, on the other hand, exhibits a rotational motion about the stronger flap vortex, like a planet around the sun. Initial rotational velocity of the tip vortex was found to be 7.3 revolutions per second with the double slotted model (lift coefficient $C_L = 2.3$), whereas rotation was only 5.3 revolutions per second with the single-slotted model (lift coefficient $C_L = 1.76$).

Three-dimensional nature of the wake appears concealed when representing tunnel data by the flat shading technique. Therefore, carpet plots were used which ideally indicate high and low crossflow velocity areas (Fig. 7). Crossflow velocities peak at flap and tip vortices, attaining maximum values as high as 57% of freestream velocity [1]. Originating from the nacelle, a crossflow velocity peak results from the through-flow type used. Effect will be different on a real aircraft with a propulsive jet issuing from the nozzles.

Between vortices, crossflow velocity is close to zero (Fig. 8). Highly asymmetric character of vortices becomes apparent on the flat shading representation of data. At the flap vortex, crossflow velocity peak is bounded by two high-speed shoulders, with the advancing shoulder higher than the preceding one. Note that the vortex system rotates about the flap vortex at 7.3 revolutions per second in downstream direction (like a corkscrew), whereas an observer on the airplane would always view the same structure at this position.

Structure of streamwise velocity field

The streamwise velocity flowfield is dominated by the development of the velocity deficit resulting from the wing boundary layer and local flow separations from flap track fairings (Fig. 9). Vortical effects appear to be small supporting the general assumption that such effects are found mainly perpendicularly to freestream direction.

However, on a carpet plot, the initial stage of the tip vortex reveals a large, needle-shaped deficit in V_x (Fig. 10). This effect continues in

downstream direction (**Fig. 11**). Streamwise velocity deficit is more pronounced at the inner wing, the downward motion of which initially is strongly influenced by wing downwash. At a later stage, this reduced-energy low-speed pocket slowly rotates about the flap vortex eventually merging with it further downstream.

Total pressure loss

Total pressure losses usually are associated with aircraft drag. Sources that contribute to aircraft drag may easily be traced by wake surveying. With respect to vortex development, total pressure loss shows marked peaks near vortex cores, though areas affected are small initially (**Fig. 12**). Further downstream, total pressure losses accumulate at vortex core areas and close to the fuselage (**Fig. 13**).

Structure of wake vorticity

Vorticity resulting from wing lift is generally considered to be the single most important quantity responsible for wake characteristics. Wake vorticity is frequently described by the streamwise component ξ of the vorticity vector:

$$\xi = \frac{\partial V_z}{\partial y} - \frac{\partial V_y}{\partial z}$$

V_y , V_z are crossflow components of the velocity vector; y , z define cartesian coordinates that correspond to grid points of the surveying planes.

Vorticity was calculated from measured crossflow components, and then made non-dimensional with wing half span and tunnel freestream velocity [2].

Vorticities so calculated show typical concentrations after vortices have formed, with the flap vortex dominating (**Fig. 14**). At a closer view, such a structure, at this particular streamwise position, gives a clue to wake formation and decay at the same time (**Fig. 15**).

It was found that after excluding all vorticity below a value of one vorticity unit, and applying the thresholding technique to data visualization, a low-vorticity redistribution path emerged which apparently is the highway along which vorticity is transported. As both flap and tip vortices rotate in the same direction, a vorticity

"foothill" is formed at the flap vortex where low-vorticity streams from wing and tip vortices join. Also, the low-vorticity path crosses over to the flap vortex where crossflow velocity V_θ is lowest (cf. **Fig. 15**, bottom).

Low-vorticity foot regions of vorticity peaks, together with edges of the low-vorticity path are bounded by close-to-zero vorticity areas where gradual decay occurs. This mechanism is presently little understood and may require non-steady effects to be taken into account.

Wake characterization parameters

A comprehensive characterization of wakes requires a large number of parameters to be recognized. The following list was found useful and may serve as a guideline for wake research (**Table 1**):

- Crossflow velocity V_θ
- Streamwise velocity V_x
- Downwash velocity V_z
- Vorticity vector, at least its streamwise component ξ
- Total pressure loss ΔP_t
- Crossflow energy E_θ
- Change in total energy ΔE
- Divergence
- Pressure coefficient (static) C_p

Conclusion and outlook

High-lift configurations of a 1/13.6 scale passenger transport aircraft were investigated in the near field up to one half wing span. Results so far showed unexpected flow phenomena which may contribute to shed more light on the wake vortex problem. Objective of this investigation was to get better insight into the wake structure. Additionally the results may foster theoretical modelling.

Recently, a new investigation was carried out in the DNW tunnel which allowed the wake to be measured for as long as 7 wing spans with great accuracy, using the same model as before. Results will be presented in due course.

Acknowledgement

This investigation was made possible by support from the German Ministry of Research and Technology.

All data processing and visualization was performed by Caren Huenecke, DASA-Airbus, utilizing the CFView software package developed by Numeca, Brussels (Belgium) [3].

References

- [1] Huenecke, K.
Wake vortex investigations of transport aircraft
 AIAA paper 95-1773
 AIAA 13th Applied Aerodynamics Conference, San Diego, June 19-22, 1995

[2] Brune, G.W., Hallstaff, T.H.

Wing Span Loads of Complex High-lift Systems from Wake Measurements

J. Aircraft, Vol.22, NO.9, Sept. 1985

[3] D. Vucinic, M. Pottiez, V. Sotiaux, C. Hirsch
CFView - an Advanced Interactive Visualization System based on Object-oriented Approach

AIAA paper 92-0072

30th Aerospace Sciences Meeting and Exhibit, Reno, NV, January 6-9, 1992

- Crossflow velocity $V_\theta = \sqrt{V_y^2 + V_z^2}$ (referenced to V_∞)
- Streamwise velocity V_x (referenced to V_∞)
- Vorticity vector $= \left[\left(\frac{\partial V_z}{\partial y} - \frac{\partial V_y}{\partial z} \right); \left(\frac{\partial V_x}{\partial z} - \frac{\partial V_z}{\partial x} \right); \left(\frac{\partial V_y}{\partial x} - \frac{\partial V_x}{\partial y} \right) \right]$ (3-D, referenced to $\frac{b/2}{V_\infty}$)
- Streamwise component of vorticity vector $\xi = \left(\frac{\partial V_z}{\partial y} - \frac{\partial V_y}{\partial z} \right) * \frac{b/2}{V_\infty}$
- Total pressure loss $\frac{\Delta P_t}{P_{t\infty}} = 1 - \frac{P_t}{P_{t\infty}}$ (Crowder)
- Crossflow energy $E_\Theta = \frac{V_y^2 + V_z^2}{V_\infty^2}$
- Change in total energy $\Delta E = \frac{V_x^2 + V_y^2 + V_z^2}{V_\infty^2} - 1$
- Divergence $\frac{\partial V_x}{\partial x} = - \left(\frac{\partial V_y}{\partial y} + \frac{\partial V_z}{\partial z} \right) * \frac{b/2}{V_\infty}$
- Pressure coefficient $C_p = \frac{p - p_\infty}{q_\infty}$

Table 1 Wake characterization parameters

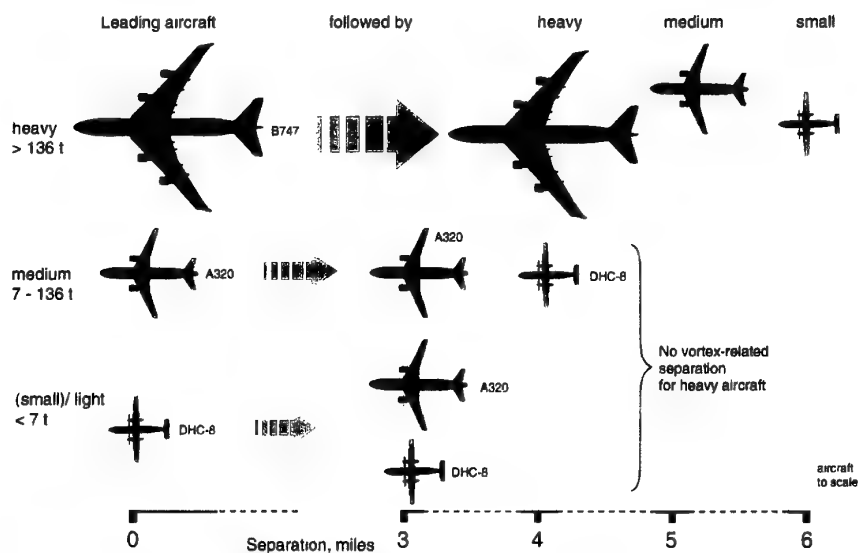


Fig. 1 Air traffic wake turbulence separations

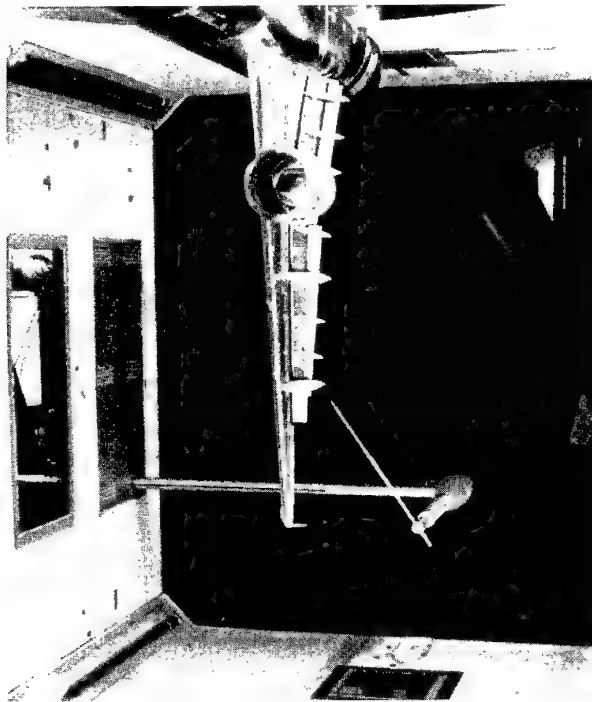
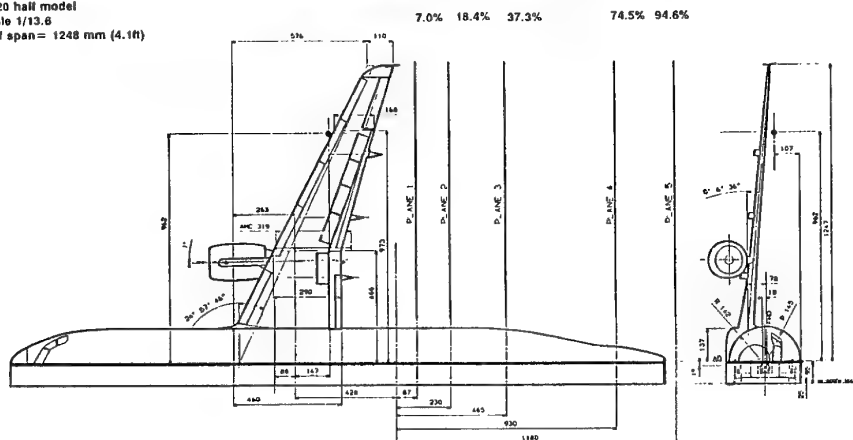


Fig. 2 A321 model in Bremen wind tunnel

Fig. 3 Nearfield surveying planes A320/ A321

A320 half model
scale 1/13.8
half span = 1248 mm (4.1ft)



Distance of planes in percentage of half span
and referenced to trailing-edge of wing tip



Fig. 4 Crossflow velocity and streamlines

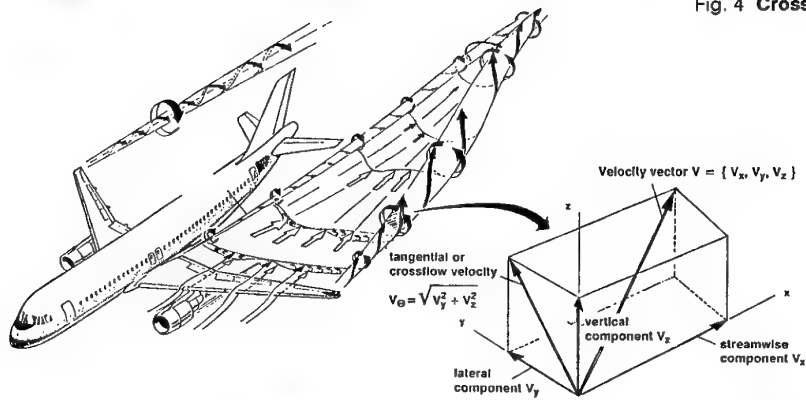


Fig. 5 Crossflow velocity definition

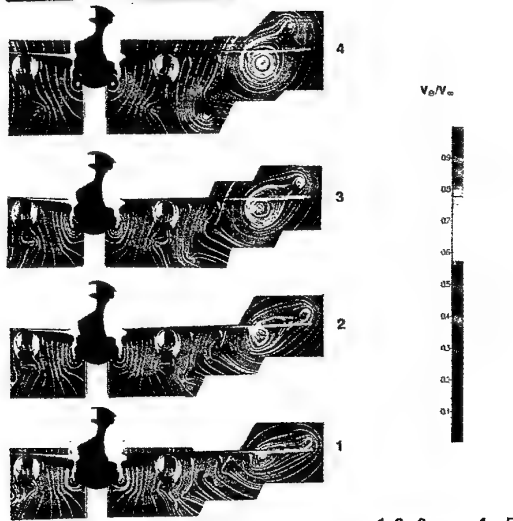
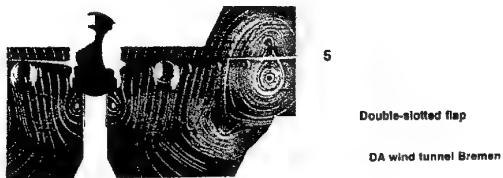


Fig. 6 Nearfield vortex motion

Aircraft configuration:
 slat 26° / flap 34° / aileron droop 5°
 inner tab 19° / outer tab 34.8°
 $\alpha = 7^\circ$
 $C_L = 2.18$
 freestream velocity 60 m/s

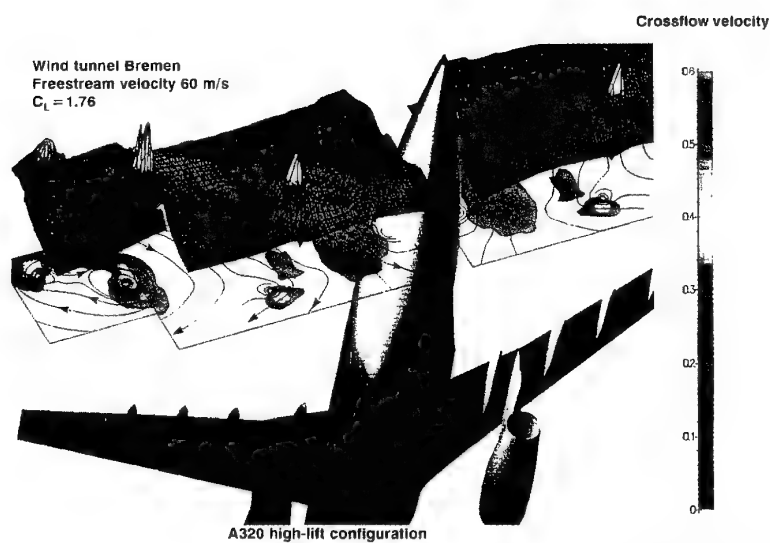
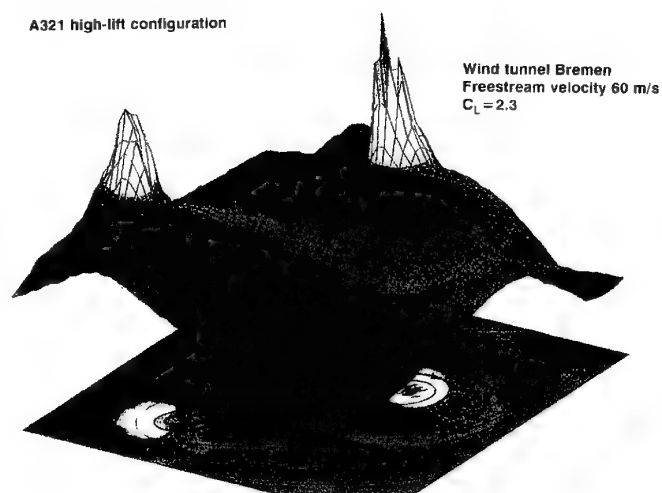
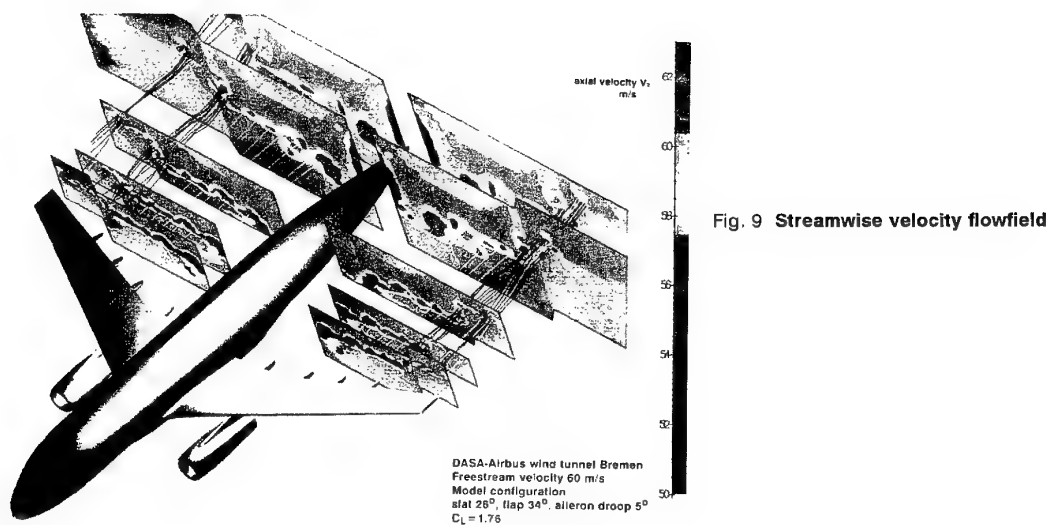
Fig. 7 Crossflow structure at $x/b=0.19$ Fig. 8 Crossflow structure of A321 at $x/b=0.19$ 

Fig. 9 Streamwise velocity flowfield

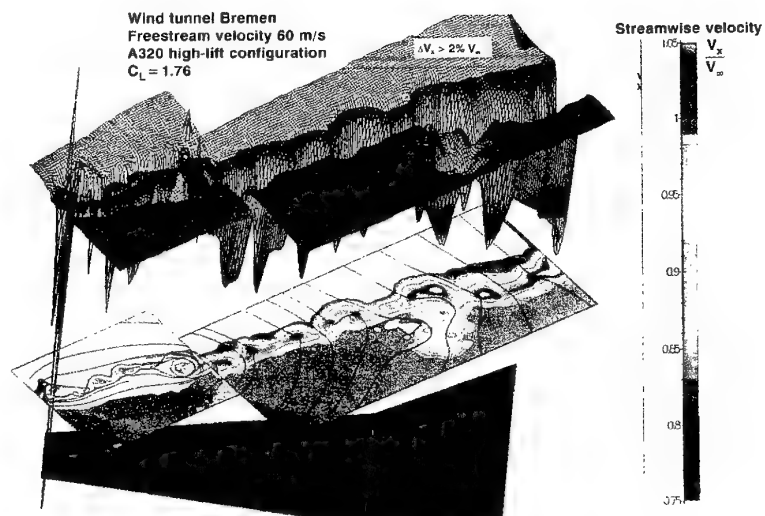


Fig.10 Streamwise velocity field at initial stage

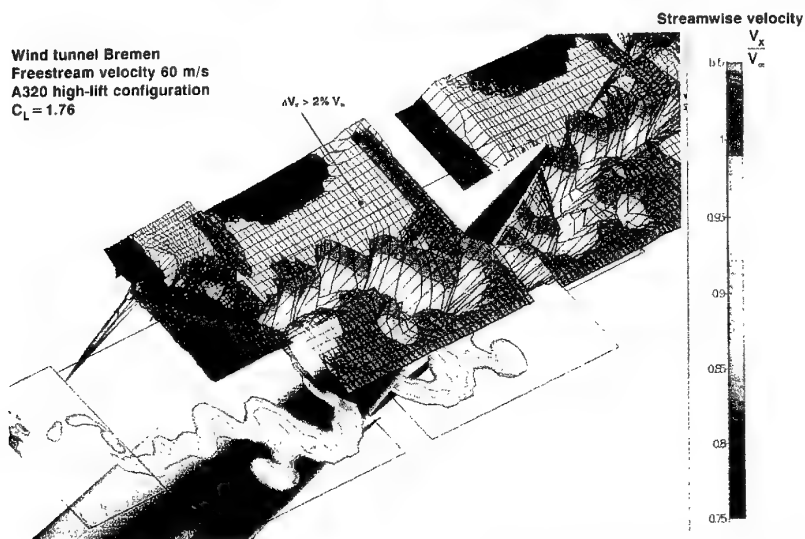
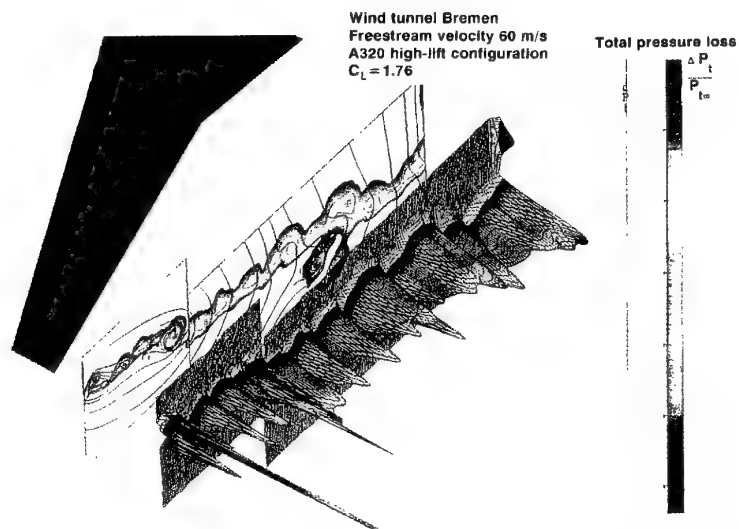
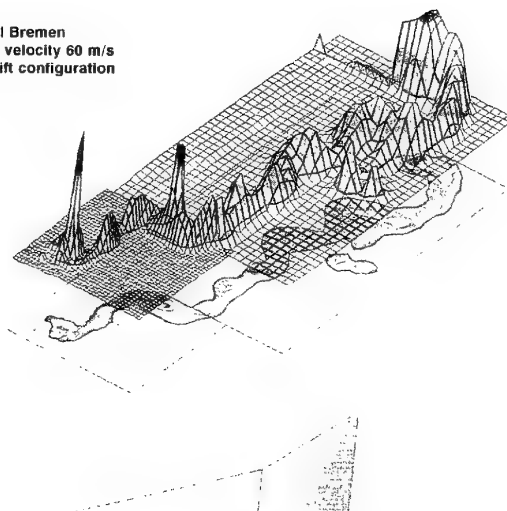
Fig.11 Streamwise velocity field at $x/b=0.19$ 

Fig.12 Total pressure loss at initial stage of wake

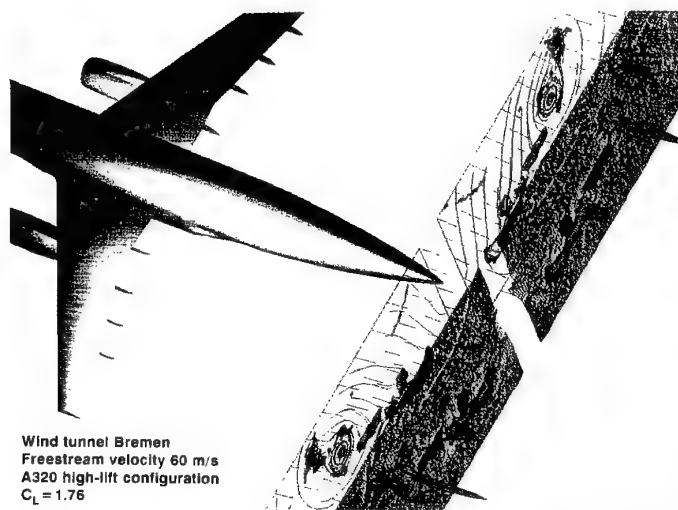
Wind tunnel Bremen
Freestream velocity 60 m/s
A320 high-lift configuration
 $C_L = 1.76$



Total pressure loss

$$\frac{\Delta P_t}{P_{t\infty}}$$

Fig.12 Total pressure loss at $x/b=0.19$



Vorticity units

Wind tunnel Bremen
Freestream velocity 60 m/s
A320 high-lift configuration
 $C_L = 1.76$

Fig.14 vorticity structure at $x/b=0.47$

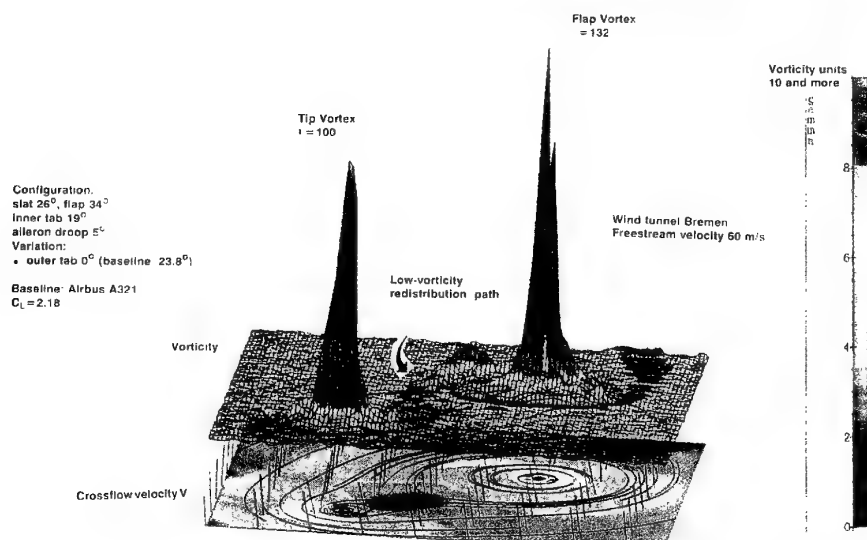


Fig.15 vorticity structure at $x/b=0.37$

The Interaction between an Injected Vortex and a Rolling Up Vortex Sheet

M R Dhanak and K S Vishwanthan
Florida Atlantic University
Boca Raton, Florida FL 33431

ABSTRACT

The interaction between two symmetrically located finite Rankine vortices and an elliptically loaded vortex sheet is examined in the Trefftz plane for a range of flow parameters. The Rankine vortices, which are placed over the sheet, have vorticity of opposite sign to that of the adjacent section of the vortex sheet. They may be considered to represent, in the Trefftz plane, vortices 'injected' into the flow from an upstream location. It is shown that there are in general three types of interactions which significantly affect the rolling up process. Accordingly, an interaction can result in straightforward merging, formation of subsidiary structures or considerable inboard displacement of the rolling up tip vortex. In the last case, the process should help to enhance the onset of the Crow instability considerably.

1. INTRODUCTION

The hazard presented by the vortex trail of a large aircraft such as a B-747 during landing at busy airports is well known. Under normal conditions, such a trail can persist for a considerable distance downstream of the aircraft and migrate across runways preventing hazard-free take-offs of other aircraft. Considerable experimental and theoretical efforts have been made in alleviating vortex wakes (Rossow, 1991). Rossow describes a vortex injection method, which involves use of vertical fins on the top surface of the wings to generate subsidiary vortices which then interact with the developing vortex wake of the wing; the injected vortex has vorticity of opposite sign to that in the adjacent section of the developing vortex sheet. Although this appears to be an effective method, resulting in reduction in the strength of the ensuing tip vortices, at least to the extent corresponding to that of the injected vortex, there is at present a lack of sufficient understanding of the basic interactions that occur between the injected vortex and the developing wake. For example, experimental results (Wittmer et al, 1994) suggest that the presence of the injected vortex close to the surface of the wing may have a significant effect on the strength distribution of the ensuing vortex sheet.

Here, a parametric numerical investigation of a model,

inviscid, incompressible problem aimed at obtaining a better understanding of the interactions in the developing wake is described. Specifically, a study of the interaction between two symmetrically located finite Rankine vortices and an elliptically loaded vortex sheet in the Trefftz plane is described. The vorticity in each finite vortex is uniform and of opposite sign to that of the sheet. The finite vortices are located over the sheet. Although viscous effects are important in producing the vorticity cancellation that ensues in the vicinity of vortices of opposite sign, it is expected that the initial redistribution of vorticity takes place on a sufficiently fast time scale so that the initial dynamics are well described by inviscid equations of motion. However, once the injected vortex is sufficiently distorted, viscosity would need to be accounted for and we indicate the effect of this on our results and on the wake development. Further, the present work ignores three-dimensional effects. Such effects are expected to be important in inducing Crow-type instability through interaction of the trailing vortices with the injected vortices. However, in the vicinity of the wing, these development also occur on a slower time scale and we expect the description in the Trefftz plane to be fairly representative of the initial development in the wake.

A preliminary study of the problem using point vortices to represent the injected vortices and the vortex sheet was carried out by Rossow (1978). However, when the injected vortex is in the vicinity of the vortex sheet, its structure, as we indicate, plays an important role in the interaction and needs to be accounted for. In the present study, the structure of the injected vortex is assumed to comprise of a core of uniform vorticity. In practice, the distribution of vorticity in the core of the injected vortex is non-uniform and a future study will address this aspect of the structure. However, experience with similar vortex interaction problems in which the influence of non-uniform vorticity distribution is considered suggest that a uniform vorticity distribution gives a fairly good approximation to the interaction. We therefore expect the present results to be a good approximation to the interaction although refinements can be achieved by allowing for variation of vorticity in the core of the injected vortex.

2. FORMULATION AND NUMERICAL METHOD

We choose Cartesian co-ordinates Oy^*z^* to describe the flow in the Trefftz plane, with Oz^* along the span-wise direction. Initially, the plane vortex sheet is located along the z^* -axis between $-b \leq z^* \leq b$ and a circular Rankine vortex is introduced symmetrically above the sheet on either side of the center-line (figure 1). Length and time variables are respectively non-dimensionalized with respect to the semi-span b and b^2/Γ_s , where Γ_s is the total strength of the section $0 \leq z^* \leq b$ of the vortex sheet; thus $t^* = b^2/\Gamma_s t$, $z^* = bz$ and $y^* = by$. We consider the case of a vortex sheet associated with an elliptically loaded wing so that the non-dimensional vortex sheet strength is given by

$$\gamma = z(1 - z^2)^{-1/2}, \quad -1 \leq z \leq 1 \quad (1)$$

or, introducing $z = -\cos \alpha$, $0 \leq \alpha \leq \pi$,

$$\gamma = -\cot \alpha; \quad 0 \leq \alpha \leq \pi. \quad (2)$$

It is convenient to represent the vortex sheet in terms of the Lagrangian circulation parameter Γ and consider the flow in terms of the complex variable, $Z = z + iy$. Γ denotes the fixed circulation around a curve enclosing the section between a point on the sheet and the end point at $z = -1$, with the aerodynamic convention that clockwise rotation denotes positive circulation. Since Γ is fixed, it can be expressed in terms of the parameter α as

$$\Gamma = \sin \alpha \quad (3)$$

so that $\Gamma(0) = \Gamma(\pi) = 0$ and $\Gamma = -d\gamma/ds$ where s is the arc-length.

At any time t , the vortex sheet is given by the parametric curve $Z = Z_s(\Gamma(\alpha), t)$ and the motion of the vortex sheet is governed by the Birkhoff-Rott equation

$$\frac{\partial \bar{Z}_s}{\partial t}(\alpha, t) = \frac{-1}{2\pi i} \int_0^\pi \frac{\gamma(\alpha') d\alpha'}{Z_s(\alpha, t) - Z_s(\alpha', t)} + Q_E(Z_s, t) \quad (4)$$

where \oint denotes a Cauchy-Principal value integral, the bar denotes complex conjugate and $Q_E(Z_s, t)$ is the external complex velocity induced by sources other than the vortex sheet. This equation is exact. However, attempts to integrate it numerically invariably leads to development of spurious short-wave instability associated with the singular nature of the integrand, requiring use of approximate smoothing techniques. Most successful and convenient approach is that given by Krasny(1987). In this approach, the integrand in the Birkhoff-Rott equation is replaced by one which renders the integral non-singular. Thus (4) is replaced by the approximate equation

$$\frac{\partial \bar{Z}_s}{\partial t}(\alpha, t) = \frac{-1}{2\pi i} \int_0^\pi \frac{(\bar{Z}_s(\alpha, t) - \bar{Z}_s(\alpha', t))\gamma(\alpha') d\alpha'}{|Z_s(\alpha, t) - Z_s(\alpha', t)|^2 + \delta^2} + Q_E(Z_s, t). \quad (5)$$

Here, δ is essentially a smoothing parameter, taken to be constant. The method relies on suppression of growth of spurious short-wave disturbances on the sheet which are expected in any numerical calculation, akin to the suppression of growth of such disturbances on a vortex layer of finite thickness. In fact, as pointed out by Krasny(1987), the inclusion of δ may be approximately regarded as representing a non-singular distribution of vorticity in the form of a layer; the larger the value of delta, the thicker the layer.

The external velocity in (5) is due to the presence of the finite vortices in the Trefftz plane. We consider the vorticity in the core of these vortices to be uniform, given by $\omega = \omega_0$, so that the external velocity is given by

$$Q_E(Z, t) = \frac{\omega_0}{4\pi} \oint \left(\frac{Z - Z_c}{\bar{Z} - \bar{Z}_c} - \frac{Z + \bar{Z}_c}{\bar{Z} + Z_c} \right) d\bar{Z}_c \quad (6)$$

where $Z_c(\beta, t)$ parametrically represents the curve enclosing the finite uniform vortex in the first quarter of the Z plane. The second term in the integrand represents the contribution due to the identical vortex in the second quarter. $Z_c(\beta, t)$ is governed by the contour-dynamics equation

$$\begin{aligned} \frac{\partial \bar{Z}_c}{\partial t}(\beta, t) = & \frac{\omega_0}{4\pi} \oint \left(\frac{Z_c(\beta, t) - Z_c(\beta', t)}{\bar{Z}_c(\beta, t) - \bar{Z}_c(\beta', t)} \right. \\ & \left. - \frac{Z_c(\beta, t) + \bar{Z}_c(\beta', t)}{\bar{Z}_c(\beta, t) + Z_c(\beta', t)} \right) dZ_c \\ & + \frac{-1}{2\pi i} \int_0^\pi \frac{(\bar{Z}_c(\beta, t) - \bar{Z}_s(\alpha', t))\gamma(\alpha') d\alpha'}{|Z_c(\beta, t) - Z_s(\alpha', t)|^2 + \delta^2}. \end{aligned} \quad (7)$$

Initially, $Z_s(\alpha, t)$ and $Z_c(\beta, t)$ are given by

$$\begin{aligned} Z_s(\alpha, 0) &= -\cos(\alpha); \quad 0 \leq \alpha \leq \pi \\ Z_c(\beta, 0) &= d + ih + Re^{i\beta}; \quad 0 \leq \beta \leq 2\pi \end{aligned} \quad (8)$$

where d denotes the distance of the center of the finite vortex from the centerline, h denotes its initial height above the plane vortex sheet and R is the radius of the vortex.

Starting from the initial configuration, (5) and (7) were integrated in time using a 4th-order Runge-Kutta integration. The interval $0 \leq \alpha \leq \pi$ was divided into $N - 1$ portions of the vortex sheet by N equally spaced grid points. The contour of the finite uniform vortex

was discretized using M equally spaced points. The spatial derivatives were obtained using five-point centered-difference formulae and the integrals in (5) and (7) were evaluated using the trapezoidal rule. An adaptive scheme was employed whereby points were inserted by linear interpolation between nodes if the spacing between nodes increased beyond a prescribed value, ϵ , and intermediate nodes were removed if the distance between nodes decreased by $\epsilon/2$.

The Fortran code developed was checked by successfully reproducing the results given by Krasny (1987) for the evolution of a vortex sheet and by Pullin (1981) for an interacting pair of uniform vortices.

3. RESULTS

The parameters of the problem, with length non-dimensionalized with respect to the semi-span b of the vortex sheet and time with respect to b^2/Γ_s , are (i) the strength Γ_c of the injected vortex, (ii) its initial radius R , (iii) its initial span-wise location d and (iv) its initial height h above the sheet. These parameters were systematically varied in order to examine their influence on the interaction. The choice of the value of δ in (5) has a significant bearing on the number, N , of nodes on the sheet and the time step δt required to accurately follow the evolution of the vortex sheet. Although a small value of δ is required, practical consideration necessitates use of a finite value of δ . Physically, as shown by Krasny (1987), a smaller value of δ implies that the vortex sheet stretches and rolls up at a faster rate forming tighter turns in the vortex spiral. Thus, the smaller the value of δ , the larger the value of N and the smaller the value of δt is required to accurately follow the evolution, with a correspondingly larger demand on computer time. For example, for $\delta = 0.0003$, $N = 2000$ and $\delta t = 0.005$ would be required. For a parametric study, this is prohibitively expensive. Therefore, in order to study the relative merits of the various other flow parameters, we restrict attention here to a particular moderate value of $\delta = 0.04$. With this value of δ , an initial value of $N = 200$ nodes on the vortex sheet and a time step of $\delta t = 0.01$ were, in general, found to be adequate; for the present choice of maximum node separation distance of $\epsilon = 0.01$, the number of nodes typically increased to approximately $N = 1000$ at the end of a run. As indicated in section 2, a smaller value of δ may also be considered to imply a smaller initial thickness of the vortex sheet or a larger flow Reynolds number. Consideration of a range of such values of δ is left as part of future work. The number of nodes $M = 30$ were chosen to discretize the initial contour of the finite vortex. This number increased to $M = 1000$ at the end of a typical run. Typical cases took approximately 50 CPU minutes to run on a Cray Y-MP.

In the absence of the injected vortex, the vortex sheet rolls up in the normal manner as shown in figure 2(i). By the non-dimensionalized time $t = 2.5$, 95% of the

vorticity is contained within the center and the last turn of each spiral. The injected vortex and the vortex sheet typically undergo severe distortion. Figures 2(ii) - (iv) illustrate the effect of the interaction in one of three basic types of general interactions which can be identified. Over each semi-span, either (a) the injected vortex is completely 'devoured' by the rolling up tip vortex, resulting in a straightforward net vortex of correspondingly reduced strength, or (b) the injected vortex gives rise to secondary roll-up features on the sheet resulting in a weaker tip vortex and development of weaker subsidiary vortices or (c) the injected vortex is partially 'devoured' by the rolling up vortex sheet and the resulting 'vortex pair' of unequal vortices is drawn considerably inboard.

Krasny (1987) defines a 'vorticity distribution' associated with the δ -approximation. Taking account of the finite uniform vortices, the vorticity $\Omega(y, z, t)$ can be expressed as

$$\Omega(y, z, t) = -\frac{\delta^2}{\pi} \int_0^\pi \frac{\partial \Gamma / \partial \alpha'}{|Z - Z_s'|^2 + \delta^2} d\alpha' + \frac{\omega_0}{2\pi i} \oint_C \frac{dZ_c}{Z - Z_c}.$$

The local 'vortical energy' per unit area can be defined as $T(y, z, t) = \Omega \Psi$ where Ψ is given by

$$\Psi = \text{Im} \left[\frac{-1}{2\pi i} \int_0^\pi \frac{(\bar{Z} - \bar{Z}_s') \Gamma \partial Z_s' / \partial \alpha'}{|Z - Z_s'|^2 + \delta^2} d\alpha' \right. \\ \left. + \frac{\omega}{4\pi} \oint_C [(Z - Z_c) \ln(Z - Z_c) + (Z + \bar{Z}_c) \ln(Z + \bar{Z}_c)] dZ_c \right]. \quad (9)$$

In figures 3 (i)-(iv), we show the span-wise distribution of 'vortical energy' per unit length given by $\int T(y, z, t) dy$ in the wake corresponding to the the final stage shown in each of figures 2(i)-(iv) respectively; the use of the δ cut-off method is equivalent to considering a finite distribution of the sheet vorticity. The figures help to identify the principal regions of vortical activity during the interaction and in particular the effect of the interaction on the tip vortices. In figure 4, we show the time development of the strength of the rolling up vortex sheet for representative cases. Γ_a is the circulation round a curve enclosing a region in the Trefftz plane so as to include the last turn of the vortex sheet spiral and any vorticity of opposite sign entrained by the spiral. The wake development is significantly affected by either through amalgamation of vorticity of opposite sign or through formation of secondary structures along the span or through considerable in-board displacement of the developing vortex. When secondary structures are formed, it is expected that these will eventually amalgamate to form a single vortex of appropriately reduced strength in each span-wise region,

the interaction acting to delay the formation of this vortex. The in-board displacement seen in figure 2(iv) will significantly reduce the distance between the resulting trailing vortices and promote three-dimensional interaction associated with the Crow instability. For the time scale associated with the Crow instability for a pair of vortices is $O(D^{*2}/\Gamma_s)$, where D^* is the separation distance between the vortices, so that a reduction in D^* by a factor of two, for example, implies a reduction in this time scale by a factor of four.

Application to Aircraft Wake

It is expected that the vortex injection will take place during landing, possibly using retractable vertical fins; for example, of the type suggested by Rossow. Introduction of such fins, which shed vorticity of opposite sign to that of the wing, would result in loss of lift, as would be the case in switching on landing gears. Such fins may be regarded as part of the overall design of the landing gear system, their inclusion contributing to a favorable wake manipulation. On the other hand, if it is desired that the lift of the aircraft be unaffected or only partially affected, then the loss of lift associated with the presence of the fins would need to be compensated for, by an increase in speed of the aircraft or the angle of attack or both, say. In order to illustrate the application of the non-dimensional results presented above, we consider the latter case here, comparing the case with and without the injected vortices. The results given in figures 2-4 have been non-dimensionalized with respect to the semi-span b and the associated total strength Γ_s of the primary vortex sheet. Suppose that in the absence of the injected vortices, $\Gamma_s = \Gamma_{s0}$ so that the lift is $L_0^* \propto \rho^* U_0^* \Gamma_{s0} b$, approximately, where ρ^* is the density of air and U_0^* is the speed of the aircraft. In the presence of the injected vortices, suppose the semi-span b is the same and $\Gamma_s = \Gamma_{s1}$, so that the associated lift is correspondingly $L_1^* \propto \rho^* U_1^* \Gamma_{s1} (1 + \Gamma_c) b$; note that $\Gamma_c < 0$. If we require that there be no loss in lift in the presence of the injected vortices, we must have $U_1^* \Gamma_{s1} = U_0^* \Gamma_{s0} / (1 + \Gamma_c)$. The non-dimensional time scale in the second case, t_1 , is related to the first (t_0) by $t_1 = (\Gamma_{s1}/b^2) t^* = U_0^* t_0 / (U_1^* (1 + \Gamma_c))$. Thus the developments seen in figures 2(ii)-(iv) occur over a time scale which is greater by a factor of $1.33 U_0^* / U_1^*$ in cases (ii) and (iii) and by a factor of $2 U_0^* / U_1^*$ in case (iv). The strength Γ_a of the net tip vortex, as given in figure 4, is also greater by a factor of $1.33 U_0^* / U_1^*$ in cases (ii) and (iii) and by a factor of $2 U_0^* / U_1^*$ in case (iv). This implies that in case (iv), for example, the final strength of the net tip vortices, which result following the roll up of the vortex sheet, may be of the same order as in the

absence of the injected vortices, although their separation distance is significantly smaller. This will have a bearing on the Crow instability of the ensuing trailing vortex system. As stated above, the instability acts to annihilate a coherent pair over a time $O(D^{*2}/\Gamma_s)$, where D^* is the distance of separation between the two vortices. Assuming that this separation distance is $D^* = D_0^* = O(2b)$ in the absence of the injected vortices, and from figure 2, it is approximately $D^* = D_1^* = 0.5b$ in case (iv), we expect that the time over which Crow instability acts to annihilate the coherent vortex system in the latter case, in the presence of the injected finite vortices, will be $O(32 U_0^* / U_1^*)$ faster. That is, the vortices will persist as a coherent, rolling moment generating, system over a downstream distance $O(U_1^{*2} / 32 U_0^{*2})$ shorter than in the absence of the injected vortices. Depending on how the loss of lift is compensated for, this suggests that the downstream persistence distance can be shorter approximately by a factor $1/16$ to $1/32$.

Similar considerations apply if vortex moment, instead of lift, is required to be conserved or if the vortex injection is regarded as part of the landing gear system, requiring the loss of lift to be only partially compensated for.

4. CONCLUSIONS

The principal characteristics of the interaction have been identified. For an elliptically loaded wing, the optimum effect on the development of the strength of the tip vortices is produced with $d \sim 0.7$, $\Gamma_c \sim -0.25$, $R \sim 0.05$ and $h \sim 0.06$, while significant detrimental in-board displacement of the tip vortices occurs with $d \sim 1.0$, $\Gamma_c \sim -0.5$, $R \sim 0.1$ and $h \sim 0.15$.

The work was supported by NSF grant BCS-9211847. The computations were performed on Florida State University's Cray-YMP.

REFERENCES

- Krasny, R. Computation of vortex sheet roll-up in the Trefftz plane, *J. Fluid Mech.* Vol. 184, pp. 123- 155, 1987.
- Rossow, V. J., Prospects for Alleviation of Hazard Posed by Lift-Generated Wakes, *Proc. Aircraft Wake Vortices Conf.* Vol. 1, Washington, October, 1991.
- Rossow, V. J., Effect of Wing-fins on Lift-Generated Wakes, *J. Aircraft* Vol. 15, No. 3, 1978.
- Wittmer, K S, Devenport, W J, Rife M C and Glegg, S A. 1994. AIAA paper 94-0526. 32nd Aerospace Sciences meeting, Reno, NV.

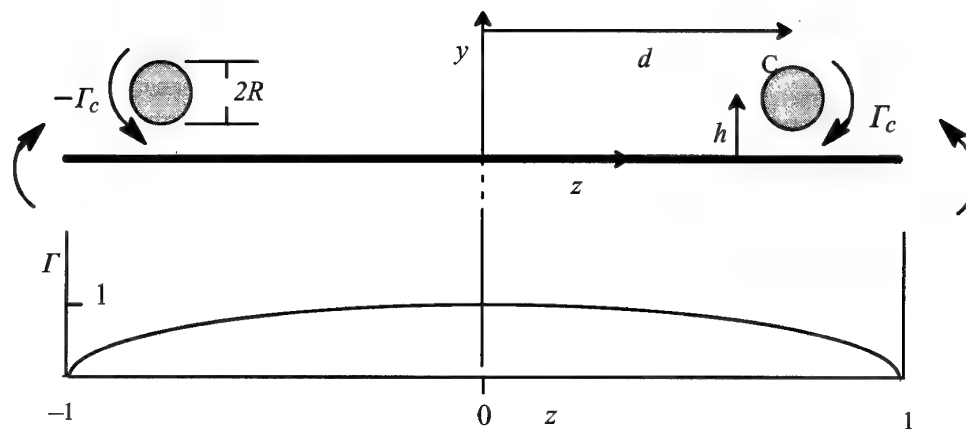


Figure 1. Schematic of the problem showing finite vortices over an elliptically loaded vortex sheet.

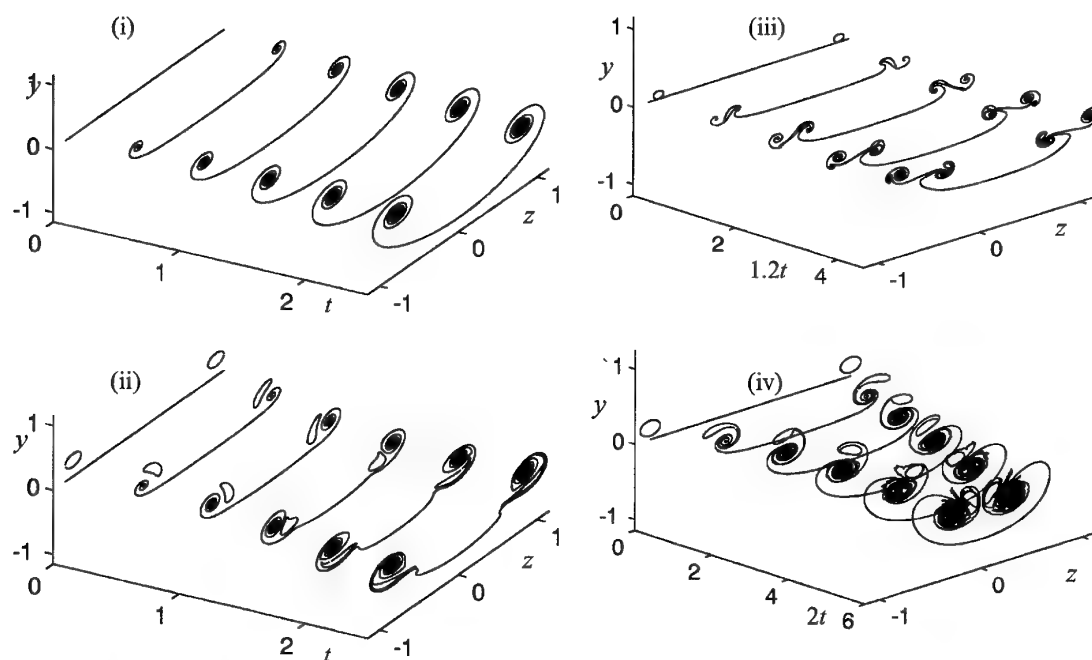


Figure 2. Interaction in the Trefftz plane between a finite vortex and a rolling up vortex sheet. Roll up in (i) the absence of the vortex sheet, and in the presence of a finite vortex with (ii) $\Gamma_c = -.25$, $R = 0.1$, $d = 0.9$ and $h = 0.25$, (iii) $\Gamma_c = -.25$, $R = 0.05$, $d = 0.9$ and $h = 0.055$ and (iv) $\Gamma_c = -.5$, $R = 0.1$, $d = 1.0$ and $h = 0.15$.

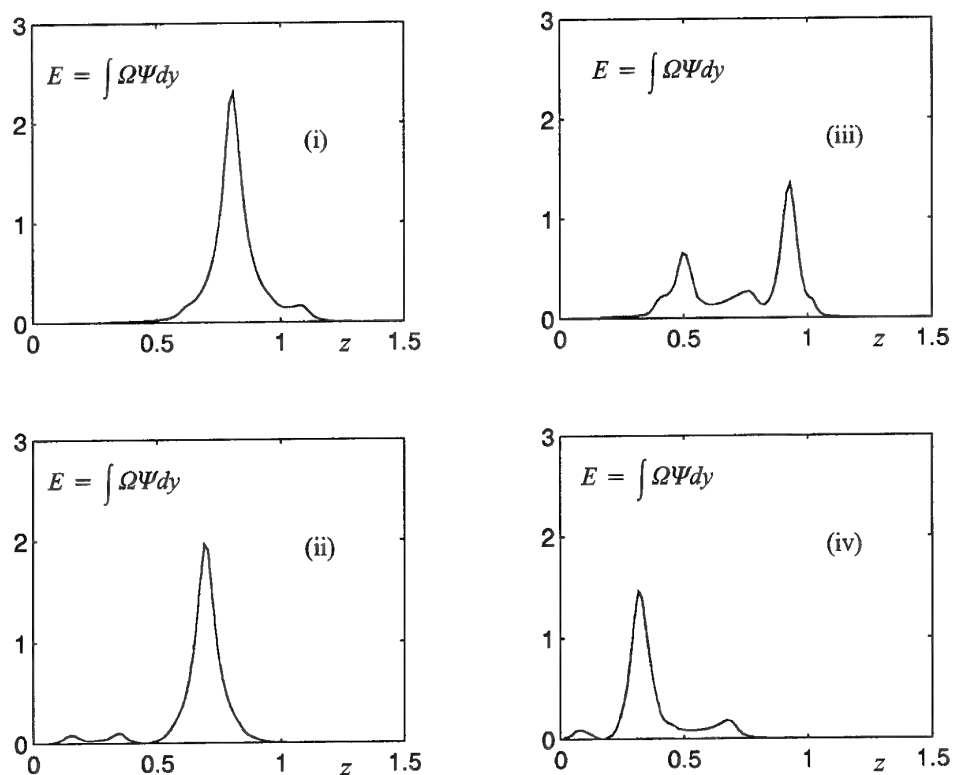


Figure 3. Spanwise distribution of 'vortical energy' per unit length, $E = \int \Omega \Psi dy$ in semi-span region corresponding to the final time ($t = 2.5$) shown in each of the figures 2(i)–(iv) respectively.

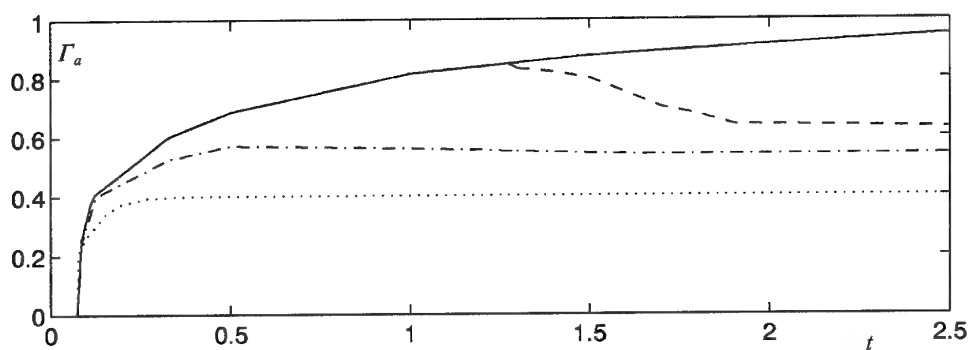


Figure 4. Effect on the development of the strength Γ_a of the tip vortex in the cases shown in figure 2: — case (i); - - case (ii); ··· case (iii); · - · - case (iv). Γ_a is the strength of that fraction of the evolving vorticity which forms the tip spiral.

FLOWFIELD PREDICTION OF THREE-DIMENSIONAL WING TRAILING VORTICES USING ADVANCED TURBULENCE MODELS

J.A. Eaton

M.P. O' Flaherty

Aerospace Research Unit, University College Galway, Ireland.

SUMMARY

The feasibility of employing a general-purpose Navier-Stokes code, in conjunction with a Reynolds stress transport turbulence model, for predicting wake vortex flow fields is investigated. Two test cases are considered, each employing two different turbulence models, a $k-\epsilon$ model, which is isotropic, and an anisotropic, differential Reynolds stress model. First the flow field around a low aspect ratio wing in a wind tunnel is computed to assess the influence of the turbulence model on the solution. Pressure distributions on the surface and velocity distributions in the wake, particularly the streamwise component, are compared with measurements. Although the grids used are suboptimal, predictions indicate a qualitative improvement for the anisotropic model, in particular where the swirl component of the flow is greater, such as in the vortex core. Next, wind tunnel data are used as a starting point for an axisymmetric model of a free vortex with axial flow. These computations allow the effects of choice of turbulence model on the aging and decay of a vortex in the far field to be observed. The $k-\epsilon$ model predicts a rapid growth of the vortex, whereas the differential Reynolds stress model results in a more realistic, almost uniform evolution of the core radius.

LIST OF SYMBOLS

c_p	static pressure coefficient
C_μ	constant in eddy viscosity formula
D	hydraulic diameter: $4A/P$
k	turbulent kinetic energy
p	pressure
P	stress production tensor
r	radius
r_θ	vortex core radius, radius at which maximum v_θ occurs
r_r	radius at which maximum v_r occurs
U	mean velocity vector
u_∞	inlet axial velocity
u, v, w	x, y and z components of U
v_θ	rotational velocity, $r\omega$
v_r	radial velocity component
x'	streamwise displacement for axisymmetric analysis. $x' = 0$ is at outlet of wing tip flow field
ϵ	turbulent energy dissipation rate
ζ	bulk viscosity
μ	viscosity
ρ	density
ρ_0	reference density
ω	angular velocity
$a \otimes b$	tensor cross product of a and b

1 INTRODUCTION

Aircraft wake vortices pose a threat to air traffic in general, and especially in the vicinity of airports. Where an aircraft onboard system is employed to detect, during the aircraft approach and landing phase, aircraft wake vortices laid by earlier aircraft, the line of sight of the sensor (e.g. lidar (1), radar) will be more or less aligned with the streamwise direction of the target vortex pair. The component of the vortex field velocity that is required to be detected is therefore this streamwise (or 'axial') component. It is not clear from published information whether there exists a sufficient signature in the streamwise component of a far-field vortex wake to be detectable at a reasonable downstream range. The aim of this work, in the near term, is to establish the feasibility of employing a general-purpose Navier-Stokes code, and in particular of applying more sophisticated, anisotropic turbulence models, for wake vortex prediction. The long term aims are to develop a validated CFD method for predicting realistic near-field wake vortex flow fields, with particular reference to resolving streamwise velocity and turbulence fields, as a precursor to reliable far-field predictions; to verify the potential benefits afforded by using advanced turbulence models; and to understand the factors affecting the far field development of wake vortices.

Recent measurements by Chow (2) show that in the near field the wake vortex flow is quite complex. The upper and lower wing surface boundary layers, which feed into the vortex, separate and roll up to form a spiralling flow centred around a highly viscous and turbulent core region. Depending on the tip configuration and flow conditions, secondary separations and flows may also be induced. Local axial velocities in the core can peak at nearly 1.8 times freestream value, and compressibility effects may be important there. The 'wake' region contains a longitudinal vortex embedded in a free shear layer; and wake vortices are highly energetic and persist for considerable distances behind an aircraft. The flow is rotational, and streamlines near the core are strongly curved, which has a stabilising influence on turbulence in this region. Significant mean velocity gradients and extra strain rates thus arise locally throughout the domain, and these are coupled non-linearly to the turbulent field.

Computing a fully three-dimensional viscous flow field of such a complex nature, with a view to resolving the different near field features, is a challenge, particularly in respect of the turbulence modelling (2,3). Short of direct numerical simulation, which would be prohibitively costly in computational terms, use of more advanced turbulence models appears to be the most promising approach. It is known that the use of isotropic, eddy viscosity based, turbulence models, such as $k-\epsilon$, greatly overpredict vortex diffusion and decay rates due to the absence of flow rotation (or streamline curvature) effects in the turbulent kinetic energy equation (3). Zeman's (3) calculations with a line vortex indicate that the mean swirling flow suppresses the Reynolds shear stress production within the vortex core, so that the core growth rate is controlled only by viscous (molecular) stress, and the vortex turbulence decays since the produc-

tion rate is nearly zero. Moreover, for the wing tip vortex field measured by Chow, Zeman also compared components of the mean strain rate tensor with the corresponding Reynolds stress components, and found a 45 deg. shift between the two; the conclusion is that use of (isotropic) eddy viscosity models are invalid in such flows.

In the present paper the results of some preliminary computations performed using a Reynolds stress transport model, as well as datum results for a $k-\epsilon$ model, are presented. Two distinct computational analyses are performed. The first case models the experimental arrangement used by Chow, consisting of a low aspect ratio wing in a wind tunnel, for which extensive, high-quality mean flow and turbulence data are available. The second case is a simplified model of the evolution of a free vortex with axial flow, in the far-field, obtained using an axisymmetric, analytical vortex model based on Dosanjh's (4) solution to the Navier-Stokes equations in combination with input velocity profiles from Chow's data.

2 COMPUTATIONAL MODEL

The code used for all analyses is CFDS-FLOW3D, a three-dimensional Navier-Stokes solver. This is an implicit, finite volume method which uses a primitive variable formulation solved on a generalised curvilinear coordinate system. A body-fitted, multi-block arrangement is used in conjunction with a structured, collocated grid approach based on the Rhie-Chow algorithm. Algebraic multigrid (AMG) is employed for convergence acceleration. Various pressure-velocity coupling algorithms are available, and flows may be treated as compressible and unsteady. A broad range of turbulence models are implemented, ranging from various scalar models through to full Reynolds stress transport models, including rotation effects.

For the computations reported here the objective was to obtain preliminary, stable solutions, and the choice of solution method options was taken primarily on pragmatic, rather than purist, grounds.

2.1 Differencing Schemes

Although the code offers several differencing schemes which range from first- to third-order accurate, for expediency in this preliminary analysis it was decided to use lower-order differencing schemes for the treatment of advection terms. Initial trials with higher-order schemes tended to result in divergence and instability in the solution, perhaps not surprising given the coarse meshes under consideration. Dacles-Mariani (5) et al. found that up to fifth-order differencing produces improvements in accuracy for the vortex core. Since one of the primary objectives of the present analysis was to assess the feasibility of applying the method to this type of problem, as well as examining the effects of turbulence modelling, it was deemed preferable to begin with the more robust lower order schemes. In conjunction with more realistic mesh densities, higher-order differencing such as QUICK, CCCT, CONDIF, and different TVD schemes will be explored later when suitable processing power is available.

Hybrid differencing (6) has been used here for all terms except pressure. In this scheme upwinding is used for the convection term in regions where the mesh Peclet number is greater than 2; central differencing is applied where the value is less than 2. Formally, at high Peclet numbers the accuracy is only first-order, except across streams and in areas of low speed where second order accurate central differencing is used. Central differencing is used as the default for pressure terms (7).

2.2 Turbulence Models

There is a range of turbulence models implemented in CFDS-FLOW3D. Two different turbulence models were used in the analysis, the standard $k-\epsilon$ model and the differential Reynolds stress model (DSM) (7).

2.2.1 The $k-\epsilon$ model

The $k-\epsilon$ is an isotropic, eddy viscosity based model. The continuity and momentum equations, assuming steady incompressible flow, are:

$$\nabla \cdot (\rho U) = 0 \quad (1)$$

and

$$\begin{aligned} \nabla \cdot (\rho(U \otimes U)) - \nabla \cdot (\mu_{eff} \nabla U) \\ = -\nabla p' + \nabla \cdot (\mu_{eff} (\nabla U)^T) \end{aligned} \quad (2)$$

where μ_{eff} , the effective viscosity is given by:

$$\mu_{eff} = \mu + \mu_T \quad (3)$$

μ_T , the turbulent viscosity is a scalar defined by:

$$\mu_T = C_\mu \rho \frac{k^2}{\epsilon} \quad (4)$$

2.2.2 Differential Reynolds Stress Model

In Reynolds stress models, of which the differential stress model is one, transport equations are solved for the individual components of the Reynolds stress tensor. The momentum equation for the Reynolds stress model is given by:

$$\nabla \cdot (\rho U \otimes U) - \nabla \cdot (\mu \nabla U) = -\nabla p'' - \nabla \cdot (\rho \overline{u \otimes u}) \quad (5)$$

where p'' is related to the true pressure by:

$$p'' = p + \left(\frac{2}{3} \mu_{eff} - \zeta \right) \nabla \cdot U - \rho_0 \phi \quad (6)$$

Jacquin (8) notes that models such as $k-\epsilon$ cannot correctly describe the effects of rotation where production is present. For rotating flows the differential stress model implemented in the present code differs from $k-\epsilon$ and other Reynolds stress models because it has an additional rotational term added in its stress production tensor, P , which is given by:

$$P_{rot} = -\rho \omega \otimes \overline{u \otimes u} \quad (7)$$

Although the rotational effect is not explicitly active in the predictions presented here, its later incorporation in the analyses should make the DSM particularly suitable for modelling the swirling flows found in a trailing vortex (7,9).

3 WING TIP GEOMETRY CASE

The wing tip configuration examined by Chow consists of a NACA 0012 section, with a chord of 1.22 m, an aspect ratio of 0.75 and a rounded tip set at a geometric incidence of 10 deg. The wind tunnel, Figure 1, has a 1.22 m x 0.81 m cross section and is 2.21 m long in the streamwise direction. The origin is at the root, quarter chord point. The x direction is the flow direction, z is out towards the tip and y is up. The flow field stretches for 1.73 m downstream and 0.48 m upstream of the origin. The reference inlet velocity, u_∞ , is 51.8 m/s and the Reynolds number based on chord (Re_c) is 4.6×10^6 .

3.1 Grid

The grid used consists of two zones. The first, an O-type zone surrounds the wing, and a simple H-type box models the domain from just downstream of the wing to the downstream

boundary (Figure 2). This configuration leads to some slight skewing of the grid around the trailing edge of the wing, however, the area downstream of the wing where the vortex develops is virtually free of distortion. A body fitted grid is generated around the geometry using a combination of algebraic and elliptic interpolation. A total of 1.2×10^5 cells was used. A grid spacing of about $3.0 \times 10^{-3}c$ was used near the surface, which results in rather marginal y^+ values for the log-law approximation (10).

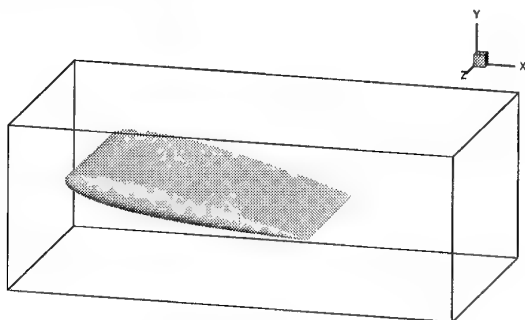


Figure 1: Wind tunnel configuration

3.2 Boundary Conditions

The upwind boundary is specified as a Dirichlet condition, with a uniform axial velocity distribution of 51.8 m/s specified over this plane. There are upwash effects in this region, and measured values for the velocity vector distribution over the inlet plane will be used in later analyses. The values of the turbulence variables k and ϵ on the inlet are set based on mean flow characteristics. Uniform profiles for k and ϵ are approximated as: (7)

$$k_{inl} = 0.002u_{\infty}^2 \quad (8)$$

$$\epsilon_{inl} = \frac{k_{inl}^{1.5}}{0.3D} \quad (9)$$

The tunnel walls and wing surface are specified as no slip boundaries with logarithmic wall profiles.

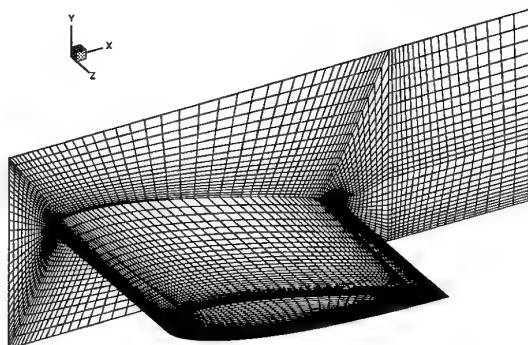


Figure 2: Grid used for computational analysis

Two different types of boundary condition were tried on the downstream plane. The first was a mass flow boundary, implemented as a Neumann condition (all normal gradients set to zero). The second type used was a pressure boundary, where a Dirichlet condition is set for pressure and Neumann for all other variables, velocity, k , ϵ etc. (7). A pressure distribution

based on the experimental results was specified at this boundary. The curve fit used for this distribution is:

$$c_p = -3.679[\exp(-30r)] \quad (10)$$

Figure 3 shows a comparison of the outlet pressure profile from the experiment and that derived from the equation. This arrangement was found to be more accurate than the full Neumann condition and was used for all subsequent analyses. The next stage will be to specify measured outlet, as well as input, data directly into the computational model, but the approach used to date represents a useful first step.

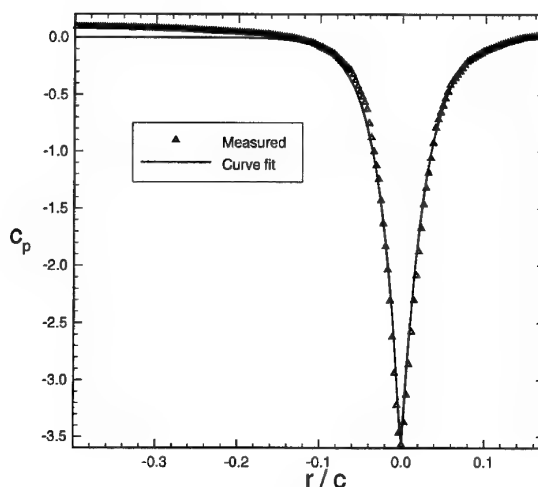


Figure 3: Outlet pressure profile and analytical curve fit used as input for axisymmetric model

3.3 Solvers

The analysis used assumed steady, viscous, incompressible flow. The SIMPLEC algorithm is used for the coupling of velocity and pressure (11).

The block structure used for this geometry consists of a total of six blocks. There is a low proportion of well ordered connections between these blocks and for this reason the algebraic multi-grid solver option was used for the pressure and momentum equations. AMG was not used for the turbulence equations, as it is possible for this method to produce negative values for k and ϵ , which must always remain positive. For this reason the line solver option is used for k and ϵ (7).

3.4 Results and discussion

The results of the two computational analyses are now compared with each other, to show the effect of the different turbulence models on the solutions, as well as with measurements obtained by Chow.

3.4.1 Surface Results

Comparison of surface friction is important to measure the validity of Navier-Stokes computations (5). Figure 4 (top) shows the computed surface friction lines, for the differential stress model calculation. The particles are released in a row near the leading edge, on both the suction and pressure surfaces. It can be seen that the particle paths go around the tip to a point of convergence near the trailing edge. This convergence suggests departure of the shear layer from the surface. The oil flow visualisation (bottom) shows similar patterns in the shape of the lines. In particular both sets of lines curve into the tip

trailing edge.

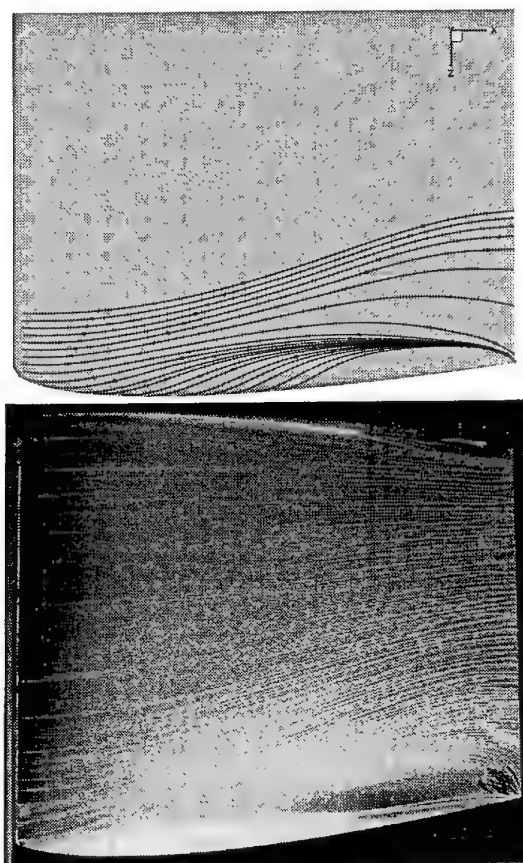


Figure 4: Computed surface pathlines for wing geometry and experimental oil flow visualisation (suction side)

Figure 5 is a sectional c_p plot comparing the computed solutions. The slice is located at the area of separation of the vortex, found from the experimental results ($z/c = 0.667$). The comparison is good at the leading edge and on the lower surface. The experimental results show that there is a large suction peak located here. The predictions show a very small suction peak at the trailing edge, however the peak calculated by the differential stress model is larger than the $k-\epsilon$ one, which is an improvement.

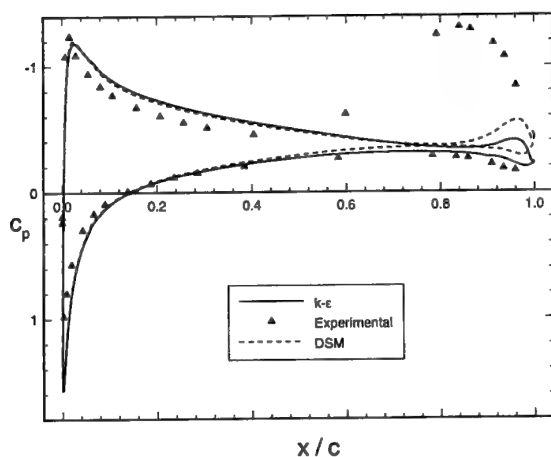


Figure 5: Sectional c_p plot at $z/c = 0.667$

Figure 6 shows a comparison of the surface pressure contour distributions obtained on the suction side of the wing. The results compare very well over most of the surface, in particular at the leading and trailing edges inboard of the tip. Two areas on the measured plot are of particular interest. The first is at the root leading edge where an area of high suction ($c_p = -2.40$) occurs, and the second is at the trailing edge just slightly inboard of the tip where another suction peak ($c_p = -1.20$) occurs. Neither of the computational analyses picked up the second suction peak, which is positioned where the vortex separates from the wing. The differential stress model, however, has captured most of the suction area on the leading edge.

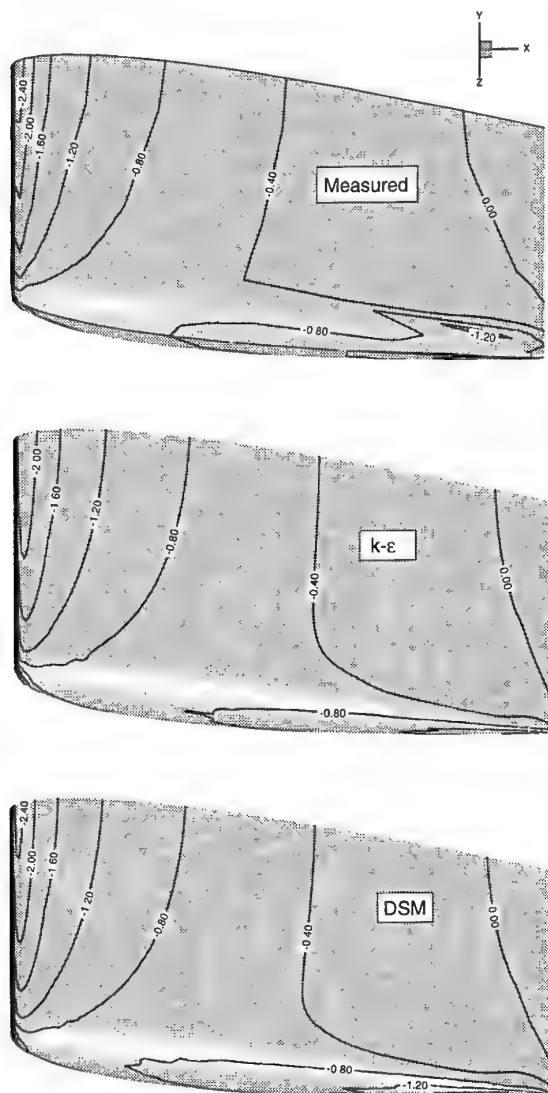


Figure 6: Comparison of surface static pressure coefficient

3.4.2 Wake Results

A comparison of the normalised axial velocity is shown in Figure 7. The measurements show that at all stages the core is very concentrated and has a very high velocity magnitude at its centre. This suggests a strong axial velocity signature for the vortex, at least in the near field. Both sets of computed results show a similar axial velocity distribution at the outlet. However it can be seen that the core of the experimental vortex is more

concentrated than both computed ones. This may be due to the coarse mesh, or to excessive turbulent diffusion in the core. It has been shown (3) that vortex decay is not influenced strongly by turbulent diffusion and this could explain the difference in the computed cores. The wind tunnel wall boundary layers are also evident in the computed plots, where the effects of mean flow diffusion can be seen in the thickening of the upper wall layer.

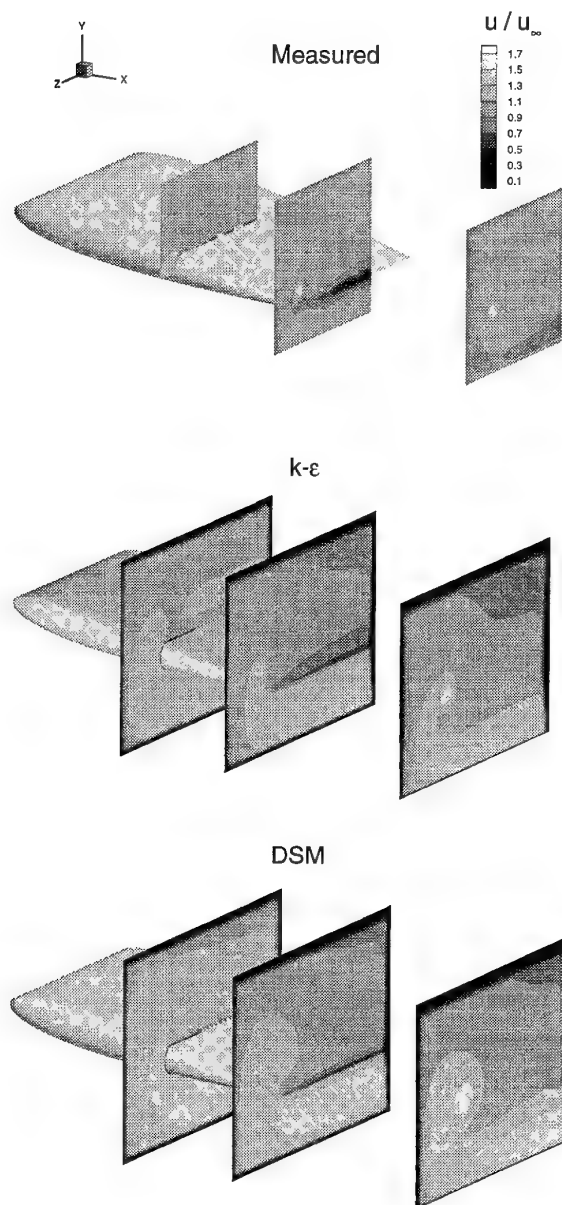


Figure 7: Comparison of computed and measured axial velocity contours

Figure 8 shows the streamwise velocity profiles taken through the vortex centres at plane $x/c = 1.727$. It was found that, initially, the pressure boundary condition caused divergence of the $k-\epsilon$ solution. This was solved by specifying that the cross derivative diffusion terms in the k and ϵ equations be effectively under-relaxed. The pressure boundary condition results

in the peak streamwise velocity being matched in the vortex core, but both numerical models give a velocity profile which is more diffused than the measurements, most likely due to the relatively coarse grid employed across the wake region. There is little difference between results for the two turbulence models.

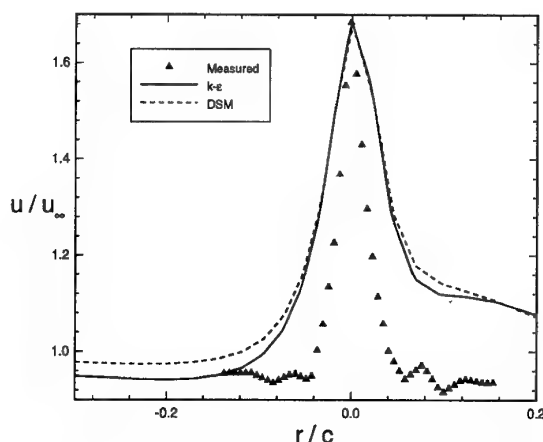


Figure 8: Streamwise velocity profiles in the vortex core

4 AXISYMMETRIC FREE VORTEX CASE

In order to examine the development of the vortex further downstream an axisymmetric model of the wing tip vortex was implemented. This provides a low cost yet useful way of modelling the vortex as it decays.

4.1 Grid

A fully axisymmetric grid with cylindrical polar coordinates is used. This gives a cell distribution of $186 \times 53 \times 1$ in the streamwise, radial and rotational directions, respectively. The outer radius of the grid, shown in Figure 9, is 100 (experimental) core radii, and the grid extends for eight wing chords in length. There is a geometric progression, of 1.1, in the radial direction in order to concentrate the cells towards the axis. There are 20 cells across the vortex core and the maximum aspect ratio, $\Delta x / \Delta r$, of the cells is 25, along the centreline.

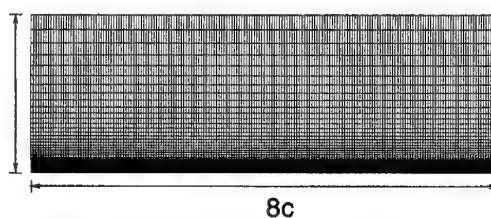


Figure 9: Computational grid for axisymmetric case

4.2 Boundary Conditions

A solution of the Navier-Stokes equations for an axisymmetric vortex with axial flow, formulated by Dosanjh et al. (4) was used to model the outflow velocity profiles from the flow field of the wing case. These velocity profiles were curve-fitted as follows:

$$v_{\theta} = \frac{1.4r_{\theta}(v_{\theta})_{max}}{r} \left(1 - \exp \left[-1.26 \left(\frac{r}{r_{\theta}} \right)^2 \right] \right) \quad (11)$$

$$v_r = \frac{1.65r(v_r)_{max}}{r_r} \left(\exp \left[-0.5 \left(\frac{r}{r_r} \right)^2 \right] \right) \quad (12)$$

$$u - u_\infty = (u_{max} - u_\infty) \left(\exp \left[\frac{-1514.195r^2}{u_\infty} \right] \right) \quad (13)$$

Figure 10 shows the measured and curve-fitted profiles. These profiles were used as input to an axisymmetric flow field.

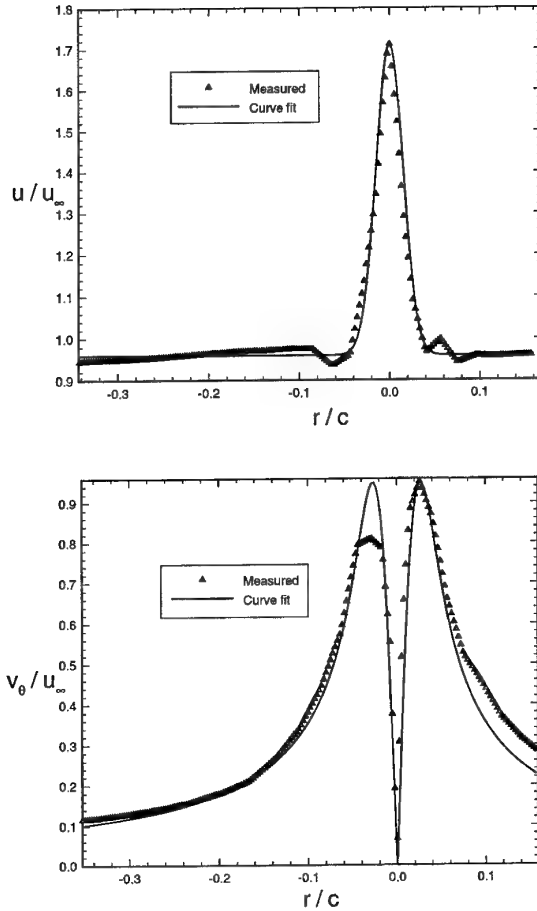


Figure 10: Measured axial and rotational velocity profiles at the outlet and analytical curve fits used as input to axisymmetric analysis

The upstream face is an inlet, with the previously mentioned axial, rotational and radial velocity profiles specified along it. The downstream face is specified as a uniform pressure boundary. The centreline of the domain is a symmetry boundary condition. The outer radial face of the domain is a pressure boundary. It was felt that this would be preferable to a solid boundary condition, as it would allow radial outflow from the domain, a factor which contributes to vortex decay and breakdown (12). Finally the domain was specified to be periodic in the rotational direction.

4.3 Solvers

Since this is a single block, single zone flow domain, a line relaxation solver was used for solution of all the terms in the transport equations.

4.4 Results and discussion

Figure 11 shows the centre-line axial velocity. The upstream boundary conditions used give rise to a local perturbation in the form of a rapid deceleration at the entrance to the flow field. This is followed by an acceleration of the flow back up to the freestream value u_∞ . When this is compared to the radial velocity profile in Figure 12, it can be seen that the deceleration near the start causes the radial velocity to go from negative to positive (negative indicates inflow). This suggests that vorticity is being convected outward by turbulent diffusion. The axial velocity returns to its freestream value eventually and the radial flow drops to zero. At this point the radial diffusion of the vortex is balanced by axial convection, which results in spreading of the vortex and a subsequent decrease in the rotational velocity seen in Figure 13 (12). The radial and rotational profiles are taken at $r = 0.032$ m, which corresponds to the value of r_θ at the inlet.

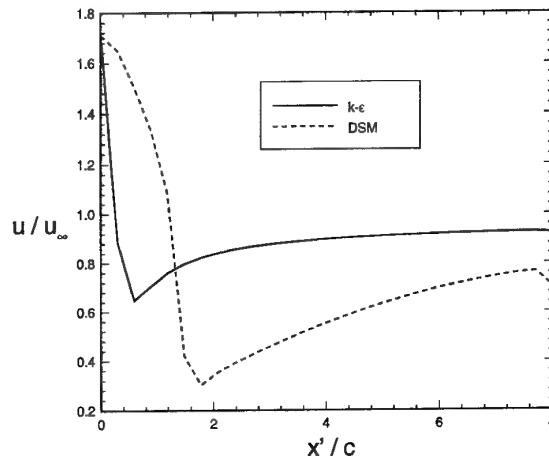


Figure 11: Centreline Axial velocity for axisymmetric case

The $k-\epsilon$ solution predicts a much quicker decay of the vortex than the DSM. It can be seen that the rotational velocity for $k-\epsilon$ drops off rapidly to almost zero, indicating negligible swirl in the flow. The DSM prediction shows a more gradual decay in the rotational velocity. The plots of the vortex core radii shown in Figure 14, confirms that the $k-\epsilon$ vortex decays rapidly while the DSM vortex is more persistent. This is due to better representation of the turbulent diffusion afforded by the anisotropic nature of DSM (3)

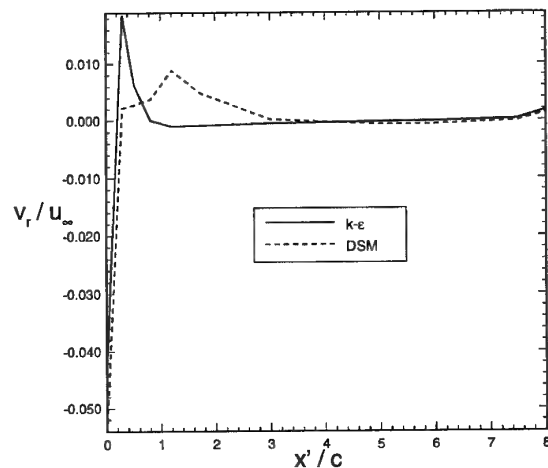


Figure 12: Radial velocity component for axisymmetric case at $r = r_\theta$

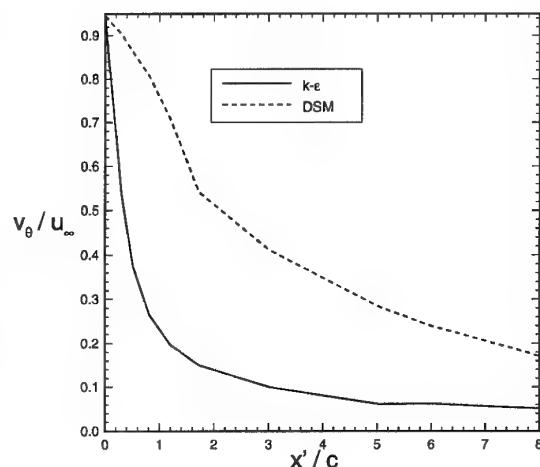


Figure 13: Peak rotational velocity for axisymmetric case

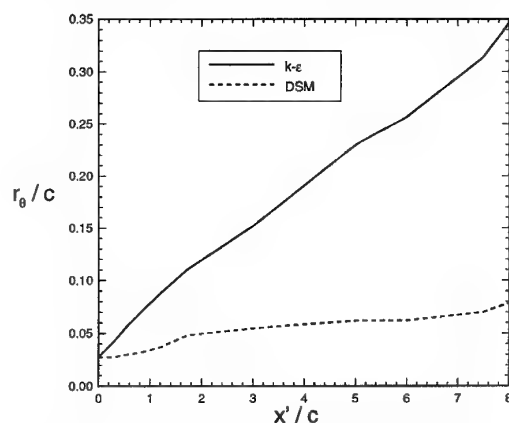


Figure 14: Predicted Growth of vortex core radius

5 CONCLUSIONS

The feasibility of employing a general-purpose Navier-Stokes code, in conjunction with a Reynolds stress transport turbulence model, for predicting wake vortex flow fields has been demonstrated. Numerical predictions have been obtained for a developing vortex in the near-field and for an axisymmetric free vortex with axial flow in the far-field. The effects of choice of turbulence model were assessed for both cases. Preliminary results suggest that the use of an anisotropic turbulence model, while computationally more expensive, produced improvements in the quality of results obtained, particularly in pressure and vortex core decay predictions. An interactive use of experimental data, such as in specifying boundary conditions, also produced benefits in terms of accuracy and realism. These are

the results of preliminary computations, and clearly there is scope for considerable improvement. Future work on the wingtip model will concentrate on grid refinement and optimisation, the incorporation of wind tunnel data as upstream and downstream boundary conditions, higher-order differencing schemes, and different turbulence models in combination with activation of rotational effects in the turbulence models.

6 ACKNOWLEDGMENTS

The authors would like to thank Peter Bradshaw and Greg Zilliac for providing the wing tip experiment data, also Jim Chow for permission to publish the oil flow picture.

REFERENCES

1. Mandle, J., "Future Laser Atmospheric Measuring Equipment", Aerodays '93, Second Community Aeronautics RTD Conference, Naples, 4-5 October 1993, pp457-463.
2. Chow, J.S., "Turbulence Measurements in the Near Field of a Wingtip Vortex", Stanford University, Department of Mechanical Engineering, Thermosciences Division, report No. MD-69, August 1994.
3. Zeman, O., "The Persistence of Trailing Vortices: a Modelling Study", *Phys. Fluids* 7 (1), 1995.
4. Dosanjh, D.S., Gasperek, E.P., Eskinazi, S., "Decay of a Viscous Trailing Vortex", *RAeS Aero. Quarterly*, May 1962, pp 167-188.
5. Dacles-Mariani, J., Zilliac, G.G., Chow, J.S., Bradshaw, P., "Numerical/Experimental Study of a Wingtip Vortex in the Near Field", *J. AIAA*, 33, 9, Sept. 1995, pp 1561-1568.
6. Spalding, D.B., "A novel finite difference formulation for differential expressions involving both first and second derivatives", *Int. J. Num. Meth. Eng.*, 4, 1972, pp551-559.
7. Anon., "CFDS-FLOW3D Release 3.3 User Guide", AEA Technology, Oxfordshire, UK, June 1994.
8. Jacquin, L., "Developed Turbulence in Rotating Flows", Euroconference on "Flows dominated by effects of system rotation, curvature or density stratification", Paris, Nov. 9-10, 1995.
9. Clarke, D.S., Moore, J.R., Wilkes, N.S., "Prediction of Turbulent Swirling Flows through Quarled Burners using Reynolds Stress Turbulence Models", United Kingdom Atomic Energy Authority, AERE R 13726, February 1990, p4.
10. Dacles-Mariani, J., Kwak, D. and Zilliac, G.G., "Accuracy Assessment of a Wingtip Vortex Flowfield in the Near Field Region", *AIAA Paper 96-0208*, 34th Aerospace Sciences Meeting & Exhibit, Jan. 1996.
11. Van Doormal, J.P., Raithby, G.D., "Enhancements of the SIMPLE Method for Prediction of Incompressible Fluid Flows", *Numerical Heat Transfer*, 7, 1984, pp 147-163.
12. Roberts, L., "Persistence and Decay of Wake Vorticity", AGARD conference on Ground/Flight Testing facilities Correlation, 1975, pp 9.1-9.10.

AN UNSTEADY VORTEX WAKE MODEL FOR MANEUVERING VEHICLES

M. R. Mendenhall

S. C. Perkins, Jr.

Nielsen Engineering & Research

526 Clyde Ave.

Mountain View, CA 94043 USA

1. SUMMARY

A preliminary-design prediction and analysis capability applicable to vehicles in unsteady maneuvers involving nonlinear, time-dependent flow conditions is described. The approach is a direct coupling of fluid dynamics and flight mechanics for use in the flight regimes where the flow phenomena are dominated by vorticity and separation associated with high angles of attack and rapid motions. The modularized computer algorithm is based on mathematical flow models, supplemented by empirical information where necessary, which accurately represent the physics of complex flows. This physics-based method is applicable to generic configurations, it is not dependent on specific empirical information, and it is economical to use. The resulting method can be used as a prediction capability for specified vehicle motions or flow conditions, or it can be coupled with a six-degree-of-freedom equation-of-motion solver to predict flight trajectories and transient performance characteristics.

2. LIST OF SYMBOLS

c_n	section normal force coefficient
C_l	rolling moment coefficient
C_N	normal force coefficient
D	body diameter
F_A	axial force
F_N	normal force
F_Y	side force
L	body length
m	mass
p, q, r	roll, pitch, yaw rates
r'	dimensionless yaw rate, rL/V_∞
t	time
V_∞	free stream velocity
δ	control surface deflection
Δt	time increment
Γ	vortex strength
ω	coning rate

3. INTRODUCTION

Many modern high-performance vehicles, either aircraft¹ or submersibles,² have mission requirements which necessitate rapid maneuvers at high angles of attack and large angular rotation rates. Under these flow conditions, the vehicle may operate in a flow regime in which the aerodynamic or hydrodynamic characteristics are dominated by unsteady nonlinear effects induced by flow separation, vortex shedding, and vortex lag effects (Fig. 1). During extreme

multiple-axis maneuvering conditions, the dynamic and time-dependent effects of these nonlinear flow characteristics contribute significantly to the behavior and maneuvering capability of the vehicle.

Since many new vehicles and concepts are being designed with maneuverability as a high priority, it is essential that analytical methods which consider these important flow regimes be available for dynamic analyses early in the design cycle. These methods should correctly represent the physics of the complex flow phenomena associated with rapid maneuvers to predict the time history of the forces and moments, and they should require moderate and reasonable resources to be practical and economic in the preliminary design and analysis phase.

A physics-based engineering prediction method applicable to the unsteady and nonlinear flow conditions associated with maneuvering vehicles at high angles of incidence is described. The method, using a unique unsteady discrete vortex wake model, has been applied to a number of different aircraft, missile, and submarine configurations under unsteady flight conditions in incompressible flows. It requires reasonable computer resources, provides an accurate representation of flow field details in unsteady flows, and predicts the unsteady forces and moments on a variety of vehicles in unsteady motions. A secondary result from these unsteady calculations is detailed information on the strength and position of the trailing vortex wake behind the maneuvering vehicle for use in detection models.

The purpose of this paper is to present a wide range of model-scale and full-scale results from the two related prediction methods, SUBFLO³ for submersible vehicles and SHAMAN^{4,5} for flight vehicles.

4. TECHNICAL APPROACH

Unsteady motions of a maneuvering vehicle involve time histories of the translational velocity components (u, v, w) and of the angular rotation (p, q, r) around the center of gravity. As illustrated in Fig. 1, extensive wake regions surround the submersible and flight vehicles and dominate the induced aerodynamic^{5,6} and hydrodynamic³ characteristics. The wake is typically made up of body vortices from the forebody, vortices associated with the wing leading and side edges, and lifting surface trailing vortices. In the case of submarines, the vortex field from the body aft of the sail is an essential element in the prediction method.

The presence of the vortex wake introduces memory into the flow problem, and the nonlinear forces and moments on the vehicle depend on the time history of the motion and the wake development. For example, vorticity shed from the nose of the vehicle will pass downstream to influence the loads on the wing and tail surfaces.⁷ The vortex-induced loads depend on the motion of the vehicle and the vortex wake during the time it takes the vorticity to be transported from the nose to the tail.

4.1 Vortex Wake Model

The key to the prediction method is the accurate modeling and representation of the forebody and lifting surface trailing vortex field using discrete vortices. The discrete vortex or vortex cloud approach has been used by a number of investigators to successfully predict nonlinear vortex-induced aerodynamics and hydrodynamics for vehicles in steady flows.⁸

The steady vortex wake represents the initial step of the unsteady calculation. At some Δt increment later, a new set of flow conditions are either specified or determined from the integration of the equations of motion of the vehicle. The vortex wake moves downstream during the interval Δt under the influence of the new local flow conditions. New forces and moments are computed at each time interval under the effects of the changing vortex field. This time-marching approach continues, and the vortex wake forms the historical lag in the flow field. As time passes, the wake shed at some earlier time is swept downstream past the tail, and the influence on the vehicle gradually diminishes.

For the lifting surfaces modeled with a vortex lattice panel model, the changing flow conditions result in a changing loading which modifies the trailing vortex wake. The unsteady loading requires a spanwise vortex be shed to represent the change in bound vortex strength in the interval Δt . These spanwise vortex filaments are included as part of the total trailing vortex field, and they are tracked downstream as part of the complete vortex wake to interfere on the tail regions of the vehicle.

4.2 Static and Dynamic Stall Models

The flow regimes of interest for vehicles maneuvering at high incidence angles will undoubtedly produce stall on the various lifting surfaces. The vortex lattice panel method used to represent the lifting surfaces presumes attached flow; consequently, the predicted loading will exceed the actual loading in the post-stall regime. A stall model which provides reasonable estimates of the loss of loading is needed, but the model should not dominate the computation. The selected approach is based on empirical corrections to the attached-flow solutions.

Assuming the local loading on a lifting surface at each spanwise location can be treated as a two-dimensional loading, the attached-flow normal force coefficient is

compared with measured normal force data on a two-dimensional airfoil section with similar geometric characteristics. If the predicted normal force is greater than that on the airfoil section, the predicted value is reduced to agree with the section data at an equivalent angle of attack. This correction procedure is applied to each spanwise segment of the lifting surface. The bound and trailing vortex strengths on the surface are adjusted to match the correct loading, and these modified strengths define the lifting-surface wake.

This approach for representing a stalled lifting surface requires experimental data on a selection of airfoil sections. SHAMAN includes flat plate and standard airfoil information, and it has the capability of including specific airfoil data should it be available.⁵

An aircraft undergoing rapid maneuvers at high angles of attack will experience the phenomenon of dynamic stall (or dynamic lift); that is, the higher than expected lift generated on a wing pitching to an angle well beyond the static stall angle. This is a critical phenomenon which must be included in the flow model for accurate prediction of maneuvering aerodynamic characteristics. An empirical correlation model similar to that used for the static stall model was selected.

Using airfoil data for positive pitch rates⁹ and negative pitch rates,¹⁰ a correlation was developed for a correction factor which is a function of pitch rate and Mach number. This factor modifies the value of maximum c_n at the end of the linear range. This empirically-based model, while obviously not definitive for all configurations, provides a reasonable means for estimating the dynamic overshoot and undershoot of normal force which can be encountered during rapid, high- α maneuvers.

4.3 Trajectory Simulations

The prediction method can be used for unsteady trajectory simulations in two distinct ways. First, the vehicle motion can be calculated by integrating the six-degrees-of-freedom equations-of-motion with a direct simulation approach. This method does not require a priori knowledge of the vehicle stability derivatives. Instead, the method accepts the instantaneous forces and moments on the vehicle as provided by the analysis to produce the translational and rotational accelerations at the specified time. The three forces and three moments, including apparent mass effects, become the right-hand side of the six equations of motion. Integration over a specified Δt produces the translational and angular velocities which can be integrated to determine the position and attitude of the vehicle. This approach has been successful in wing-rock prediction of fighter aircraft^{4,5} and maneuvering trajectories of submarines.³

Similarly, the method can also be used in an unsteady calculation by specifying the motion of the vehicle as a function of time. For example, the unsteady flight conditions

of a model undergoing forced oscillations in a tow-tank test were replicated in Ref. 6. This technique has also been used to model the trajectories of an aircraft in flight tests to examine the resulting flow field associated with the motions.⁵

5. RESULTS

A variety of results are presented to illustrate the importance of the vortex wake on the predicted forces and moments of a maneuvering vehicle. The implication is that if the vortex-induced forces and moments are predicted accurately, then the predicted vortex wake is a reasonable representation of the actual wake associated with the vehicle in unsteady motion.

5.1 Submersible Vehicles

Submarines in both steady and unsteady flows exhibit a number of complex fluid mechanics problems simply because of their geometry (Fig. 1). The presence of the sail creates an asymmetry in the geometry which gives submarines interesting hydrodynamic characteristics. The trailing vorticity from the sail causes an asymmetric flow field aft of the sail which has a significant influence on the loading distribution on the hull and the tail surfaces. When the flow is further complicated with separation from the body, the mutual interactions between the hull vorticity and the sail trailing vorticity cause a complex flow field which induces nonlinear forces and moments which can dominate the motion behavior of the maneuvering vehicle. Both sub-scale models and full-scale vehicles are considered below.

5.1.1 Sub-scale models

The measured and predicted normal force coefficients on a tail fin as it rolls through the wake shed from a submarine hull are shown in Fig. 2. This model is rotating in the horizontal plane at a constant yaw rate ($r'=0.193$) while keeping a constant 15-deg. angle of sideslip.¹¹ This is a steady flow condition with nonuniform flow along the body, and it illustrates the influence of hull vorticity on a tail fin emerged in the lee side wake. The discrete vortex wake at the tail fin is illustrated in the figure. The comparison of measured and predicted fin force is very good, even in the region of largest vortex interference. Notice that the prediction method reproduces the loading reversal on the fin near $\phi_t = 15$ deg.

Forces and moments on a hull-sail configuration on a rotating-arm test facility at constant yaw rate ($r'=0.25$) and varying angles of sideslip (β) are available.¹² These flow conditions represent a steady turn in a horizontal plane. Measured and predicted forces and moments are compared in Fig. 3. The in-plane side force and yawing moment coefficients are in good agreement for $\beta < 15$ deg., but at greater angles, sail stall begins to dominate the forces and moments. The stall model described above was not applied in this calculation.

Although the vehicle is moving in a horizontal plane at combined β and r' , the vortex wake-induced effects cause significant out-of-plane normal force (Z') and pitching moments (M'). Since these forces and moments are a direct result of the interaction of the vortex field from the sail and afterbody, the prediction method seems to correctly represent the general effects. The details of the results at higher angles are affected by sail stall.

Measured forces and moments on an axisymmetric submarine hull in coning motion in a water tunnel are available.¹³ The body is at a constant angle of attack with combined roll ($p=\omega\cos\alpha$) and yaw ($r=\omega\sin\alpha$) rates. Comparison of measured and predicted forces and moments are shown in Fig. 4. Predicted results with and without hull vorticity illustrate the importance of an accurate wake model on the induced forces and moments. The predicted vortex wake is also shown in Fig. 4 for two angles of attack. Notice that the vortex field is asymmetric on this axisymmetric body because of the combined roll and yaw rates. At incidence angles less than 6 degrees, the vortex wake induces small nonlinear effects, but at higher angles, the vortex field is stronger, and its effect begins to dominate the forces and moments.

5.1.2 Full-scale submarine

To illustrate the trajectory prediction capability of SUBFLO, the motion of a typical full-scale submarine configuration in a specific maneuver is presented. No experimental data are available for comparison purposes. The selected maneuver is a stern-plane jam simulation. Beginning from a trimmed condition, the horizontal tail planes are deflected to produce a nose-down pitching moment. Holding these fins deflected throughout the maneuver, the recovery procedure involves movement of the rudder and sail planes in a predetermined manner. The motion of the control planes is shown in Fig. 5.

The calculation starts with a 12-sec. approach to develop the steady trimmed wake. The speed of the submarine and the control fin deflections are specified at the proper time. Key times in the deflection schedule are denoted by arrows on the time axis to identify major control events. The hydrodynamic forces and moments are calculated, and these values are used with apparent mass, buoyancy, and inertia characteristics to integrate the equations of motion of the submarine.

Predicted histories of the submarine angles of attack and sideslip and angular rates are shown in Figs. 6 and 7, respectively. The pitch rate (q) indicates a nose-down rate at the start of the maneuver, but this levels to a constant rate after the rudders and sail planes are deflected. The roll rate (p) begins positive, but it changes sign during recovery. The yaw rate (r) is slightly negative from the start of the maneuver, but it increases significantly during the recovery phase. This explains the increasing sideslip angle shown in Fig. 6.

The history of the predicted hydrodynamic forces and moments on the submarine is shown in Fig. 8. The normal force coefficient is upward ($Z' < 0$) for a short period of time because of the normal force on the horizontal tail fins; however, it changes sign because of the pitch-down attitude of the submarine. The side force coefficient (Y') is nearly zero until the sideslip angle begins to build up.

The total forces and moments dictate the motion of the submarine, but they provide only minimal information on the fluid mechanic details associated with the motion. To understand the behavior of the vehicle, it is necessary to examine the details of the flow field and the loading distributions on the vehicle components. For example, the history of the pitching moment on the vehicle components show the forebody and sail regions to be moderately loaded, but the afterbody and tail regions exhibit more extreme behavior during the course of the maneuver.³ This is obviously caused by the interference of the wake on the aft regions of the submarine.

Details of the wake phenomena in the tail region are described in Ref. 3 where the individual tail surfaces are examined with relation to the wake vorticity. There it can be seen how the tail loading changes as the wake becomes more asymmetric. For example, the upper rudder and starboard tail plane are subject to minor interference from the hull wake throughout the motion. The lower rudder experiences large interference effects from the negative vorticity shed from the hull.

The simulation of the sternplane jam maneuver just described has been observed in real time by displaying the predicted motion and vortex fields in a video. The added dimension of time and the use of advanced graphics techniques increase understanding of the flow phenomena which dominate the motion of submarines.

5.2 Flight Vehicles

In this section, results are presented for unsteady motion of both wind tunnel models and a full-scale flight test vehicle. The code SHAMAN⁵ was used to produce the following results.

5.2.1 Wind tunnel models

A simple wing-body configuration representing a generic fighter aircraft model exhibited limit cycle wing rock motion in a wind tunnel.¹⁴ Similar unpublished data from NASA/Langley Research Center for a circular cross section forebody are shown in Fig. 9 for $\alpha = 35^\circ$. These data exhibit wing rock with amplitude of approximately 30 degrees at a frequency of 0.5 Hz.

The prediction method applied to this configuration without forebody vortex shedding does not develop the limit cycle motion, even if an initial perturbation is used to start the motion. When forebody separation is included, with forced

asymmetry based on either static wind tunnel data or on estimated moving wall effects,⁴ a limit cycle motion develops. Using test data to define the appropriate level of forebody vortex asymmetry, predicted wing-rock motion is shown in Fig. 10. The rolling moment coefficients are also shown. The roughness in the rolling moments is caused by the sensitivity of the vortex-induced effects on the wing. The predicted amplitude is approximately 45 degrees, and the oscillation frequency is about 13% lower than that measured in Fig. 9, but the general character of the predicted wing rock is similar to that measured. The predicted result could be improved if more accurate information on the inertial characteristics of the model and rolling friction in the test mechanism were known.

The predicted vortex fields at the leading edge of the wing root chord are shown in Fig. 11. The details of the flow field and the instantaneous roll rates and rolling moments are shown for one complete cycle of wing rock. The lag effect of the forebody vortex is the driving force for the wing rock motion.⁴

Another example of wing rock is shown in Fig. 12 for a 2% subscale model of an X-31 configuration.¹⁵ The inboard and outboard leading-edge flaps were deflected -40° and -32° , respectively, and the trailing-edge flaps were set to 0° deflection. The angle of incidence was 32° , and the canards were deflected -39° . The model exhibits two limit cycle motions (small and large amplitude motion), and it oscillates about a nonzero roll angle.

Data were not available to calibrate the asymmetry of the forebody vortex field on this model; therefore, a moderate level of asymmetric separation was specified in the predictions to provide the necessary asymmetry to sustain wing rock. Two wing rock calculations were carried out for this configuration, and a comparison of the time histories of roll amplitude is shown in Fig. 13. The only difference between the two calculations is the initial roll angle ($\phi_0 = 0$ and 20°) of the configuration. The predicted wing-rock motion is approaching the same limit cycle amplitude ($\sim 3.5^\circ$) for each case. The use of a somewhat larger perturbation for the forebody vortex asymmetry could produce a larger limit cycle amplitude.

The predicted forebody vortex fields at the wing leading edge at various times during the last complete cycle of the predicted rolling motion are presented in Fig. 14. The roll angle time history for this cycle is also shown. In this figure, the $+\Gamma$ and $-\Gamma$ forebody vorticity is indicated by square and circle symbols, respectively, and the right and left canard vorticity is indicated by the triangle and diamond symbols, respectively. In each figure, the strengths of the vortex fields are noted. Note that relatively small asymmetries in the vortex strength and position are sufficient to start and sustain wing rock.

5.2.2 Flight test aircraft

The prediction method has been applied to the X-31 fighter aircraft in several different flight test maneuvers involving angles of attack up to 70 degrees.⁵ In the pitch-up maneuver, the aircraft is initially trimmed at a steady 6 deg. angle of attack, and the motion is initiated with the thrust vectoring vanes. It accomplishes a rapid pull-up to 70 deg. angle of attack where it holds steady for a period of time as shown in the inset in Fig. 15. Throughout the maneuver, the canard, wing leading edge flaps, wing trailing edge flaps, and thrust vectoring vanes are all moving in a prescribed manner. For this forced-motion calculation, the aircraft attitude and rates are specified from the flight test data, and the method predicts the unsteady flow field and associated aerodynamic forces and moments.

Comparisons of measured and predicted normal forces in Fig. 15 indicate good agreement over much of the maneuver. The solid curve is Flight Test data, and the dashed curve is the SHAMAN unsteady result. The solid symbols represent steady, relaxed-wake calculations with SHAMAN. There is a slight underprediction of normal force at the beginning of the maneuver, during which time the angle of attack is building up, and the pitch rate is slowly increasing. During the time when the angle of attack is moderate to high and the pitch rate is highest ($t = 2.5-3.0$ sec.), the normal force is somewhat overpredicted. This is likely due to an overestimation of dynamic lift effects from the dynamic stall model.

It is interesting that the steady calculations produced results which are nearly identical to the unsteady forced motion results. This would indicate that the time-lag effects of the vorticity have a relatively small effect on the overall loads in this particular case.

Next, the analysis was applied to the so-called departure maneuver of the X-31. Prior to the start of the maneuver, the X-31 is flying in trim at $\alpha \approx 25^\circ$. The intended maneuver is a complete roll around the velocity vector to a roll angle of approximately 180° , followed by a rapid pull-up. In the actual maneuver, the roll to 180° is achieved, but the maneuver *departs* from the intended trajectory during the pull-up at $\alpha \approx 55^\circ$ at $t \approx 15$ sec. SHAMAN was applied to this maneuver using the actual flight conditions in anticipation that the results may provide some insight into the flow phenomena causing the departure.

Comparisons of measured and predicted forces are shown in Figure 16. In this figure, the solid curve is Flight Test data, the dashed curve is the SHAMAN forced maneuver results, and the solid symbols are the steady calculations for selected times. Up to the time of departure ($t \approx 15$ sec), all predicted force components are in good agreement with the flight values. After departure, the normal force is first under-predicted and later over-predicted, the axial force is under-

predicted, and the predicted side force is often opposite in sign to that indicated by the flight data.

The predicted lateral aerodynamic characteristics immediately after the estimated time of departure are opposite in sign to the flight test data. During this time period, the flight test yaw rate and angular acceleration are positive and, up to $t \approx 17$ sec., the yaw angle is negative, indicating an axial center of pressure due to side force which is aft of the CG. This implies that either the rudder or the body near the wing/rudder, or both, are experiencing a negative side force and contributing to the positive yaw angular acceleration. It is suspected that the negative side force experienced by the rudder and/or body in the wing-rudder region is caused by the interaction of these aircraft components with forebody and/or wing vorticity.

As part of this investigation, the predicted flow field was studied in detail before and after departure to look for possible sources of side force and yawing moment which could contribute to the departure phenomena. The predicted vortex field is shown in Fig. 17 to illustrate the X-31 flow field before departure. At the very high incidence angle at this time, the vortex field is moving away from the vehicle at a high angle, but there are still significant interference effects of the vorticity on the aircraft. The forebody and wing vorticity at $t = 14$ sec. may have a strong interference effect on the wing/rudder loading, and small perturbations in the strength and position could change the predicted results.

Note that at $t = 14$ sec., the rudder is engulfed in part of the forebody vortex field. If the trailing vortex field from the stalled wing leaves the wing ahead of the trailing edge (instead of at the trailing edge in the present model), the interference effects of this field on the rudder loading, in combination with the strong forebody vortex field, could be the cause of the departure. Additionally, a situation in which a wing leading-edge vortex bursts on one side of the rudder could have strong interference effects on rudder loading.

6. CONCLUSIONS

The application of a physics-based prediction method to predict the nonlinear behavior of maneuvering vehicles in unsteady flows is described. The key feature of the prediction method is the accurate modeling of the complex vortex wake flow field in the vicinity of the vehicle. Knowledge of the time history of the vortex wake associated with the vehicle motion is shown to be an essential part of the total flow model and prediction method.

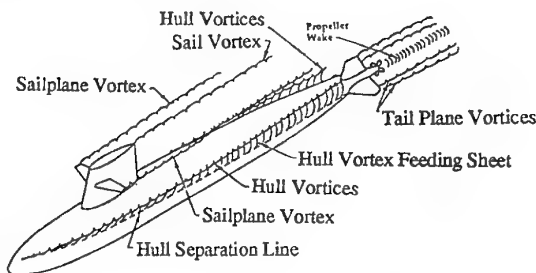
The technical approach has practical application to preliminary design studies of maneuvering vehicles prior to wind tunnel or flight testing, and it provides increased understanding of the physics of vortex wake interference effects. The resulting information on the vortex wake resulting from maneuvering vehicles can be used for investigations into wake-detection methods.

7. ACKNOWLEDGEMENTS

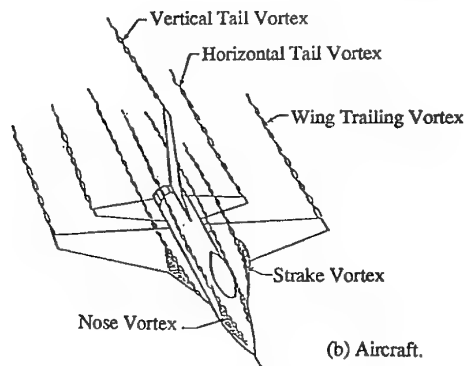
The authors would like to acknowledge ARPA for support of the high- α fighter analysis. Col. Michael S. Francis is the technical monitor for this continuing work, and his contributions through numerous technical discussions are greatly appreciated. Dr. Lars E. Ericsson assisted with the dynamic stall model. The unsteady submarine analysis was also sponsored by ARPA.

8. REFERENCES

1. Lang, J. and Francis, M. S.: Unsteady Aerodynamics and Dynamic Aircraft Maneuverability. AGARD-CP-386, May 1985.
2. Mendenhall, M. R. and Perkins, S. C., Jr.: Prediction of the Unsteady Hydrodynamic Characteristics of Submersible Vehicles, Fourth International Conference on Numerical Ship Hydrodynamics, National Academy of Sciences, Washington, DC, Sept. 24-27, 1985.
3. Mendenhall, M. R. and Perkins, S. C., Jr.: Prediction of Vortex-Induced Fluid Mechanics of Maneuvering Submarines. AIAA 93-0638, Jan. 1993.
4. Mendenhall, M. R., Perkins, S. C., Jr., and Ericsson, L. E.: Prediction of Forebody Vortex-Induced Wing Rock on Wing-Body Configurations. AIAA 93-3451, Aug. 1993.
5. Mendenhall, M. R. and Perkins, S. C., Jr.: Computational Methodology for Maneuvering Aircraft at High Angles of Attack. NEAR TR 508, Mar. 1996.
6. Mendenhall, M. R. and Perkins, S. C., Jr.: Analysis of Dynamic Maneuver Performance of Fighter Aircraft at High Angles of Attack. AFWAL-TR-88-3048, July 1988.
7. Mendenhall, M. R., Perkins, S. C., Jr., and Lesieutre, D. J.: Prediction of the Nonlinear Aerodynamic Characteristics of Maneuvering Missiles. Journal of Spacecraft and Rockets, Vol. 24, Sept.-Oct. 1987, pp. 394-402.
8. Mendenhall, M. R., Perkins, S. C., Jr., and Lesieutre, D. J.: Vortex Cloud Model for Body Vortices and Tracking. Tactical Missile Aerodynamics: Prediction Methodology, Vol. 142 of Progress in Astronautics and Aeronautics, ed. by M. R. Mendenhall, AIAA, 1992, pp. 225-285.
9. Carr, L.W. and Chandrasekhara, M. S.: An Assessment of the Impact of Compressibility on Dynamic Stall. AIAA Paper No. 95-0779, Jan. 1995.
10. Niven, A. J. and Galbraith, R. A. McD.: Experiments on the Establishment of Fully Attached Airfoil Flow from the Fully Stalled Condition During Ramp-Down Motions. ICAS Paper 90-3.4.3, Sept. 1990.
11. Lewandowski, E. M.: Tests Employing Instrumented Appendages and Flow Visualization to Study the Hydrodynamics of a Maneuvering Submarine. Report SIT-DL-86-9-2544, Feb. 1986.
12. Klosinski, W. E. and Lewandowski, E. M.: Tests on Low Fineness Ratio Submarine Model to Investigate the Effects of Fairwater Size and Location on Hydrodynamic Coefficients. SIT-DL-85-9-2537, Nov. 1985.
13. Eccles, T. J.: Measurements of Hydrodynamic Forces and Moments and Flow Field Mapping of a Model in Coning Motion. MIT Report 90-10, June 1990.
14. Brandon, J. M. and Nguyen, L. T.: Experimental Study of Effects of Forebody Geometry on High Angle of Attack Static and Dynamic Stability. Journal of Aircraft, Vol. 25, No. 7, July 1988, pp. 591-597.
15. Williams, D. L., II, Nelson, R. C., and Fisher, D. F.: An Investigation of X-31 Roll Characteristics at High Angle-of-Attack Through Subscale Model Testing. AIAA 94-0806, Jan. 1994.



(a) Submarine.



(b) Aircraft.

Fig. 1 - Vortex wake near maneuvering vehicles.

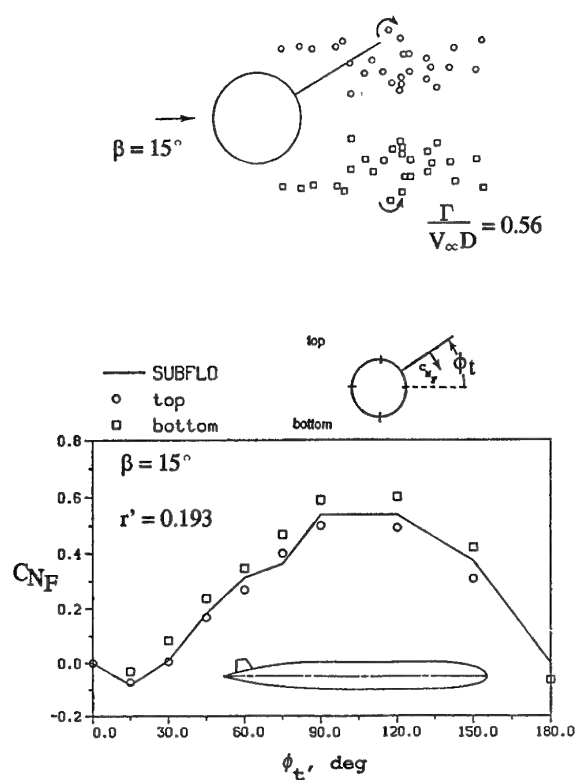


Fig. 2 - Measured and predicted tail fin normal force, $r' = 0.193$, $\beta = 15^\circ$.

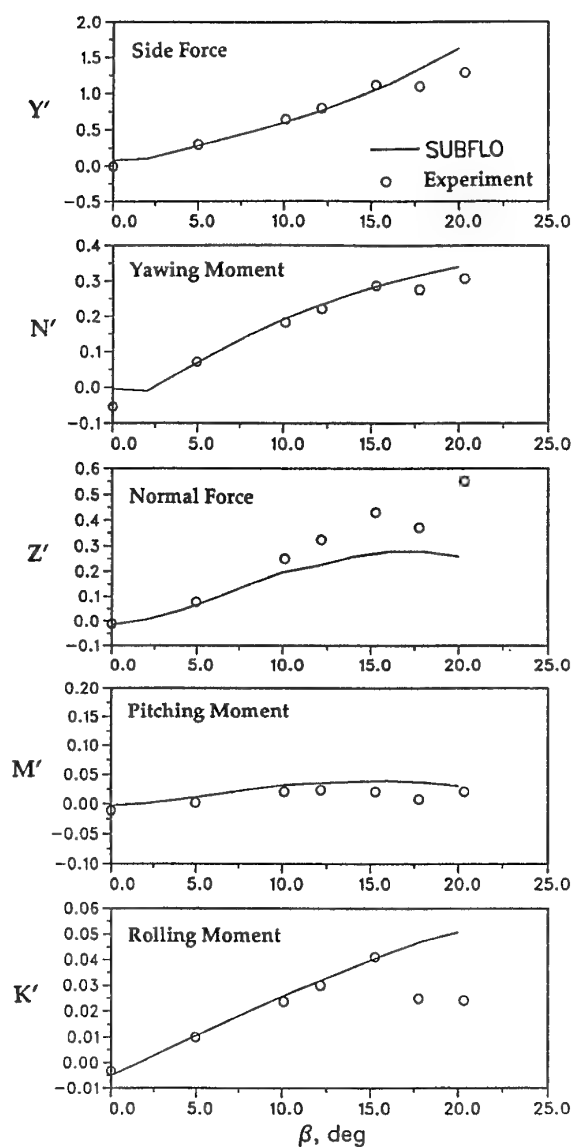


Fig. 3 - Measured and predicted forces and moments on a hull-sail configuration, $r' = 0.25$.

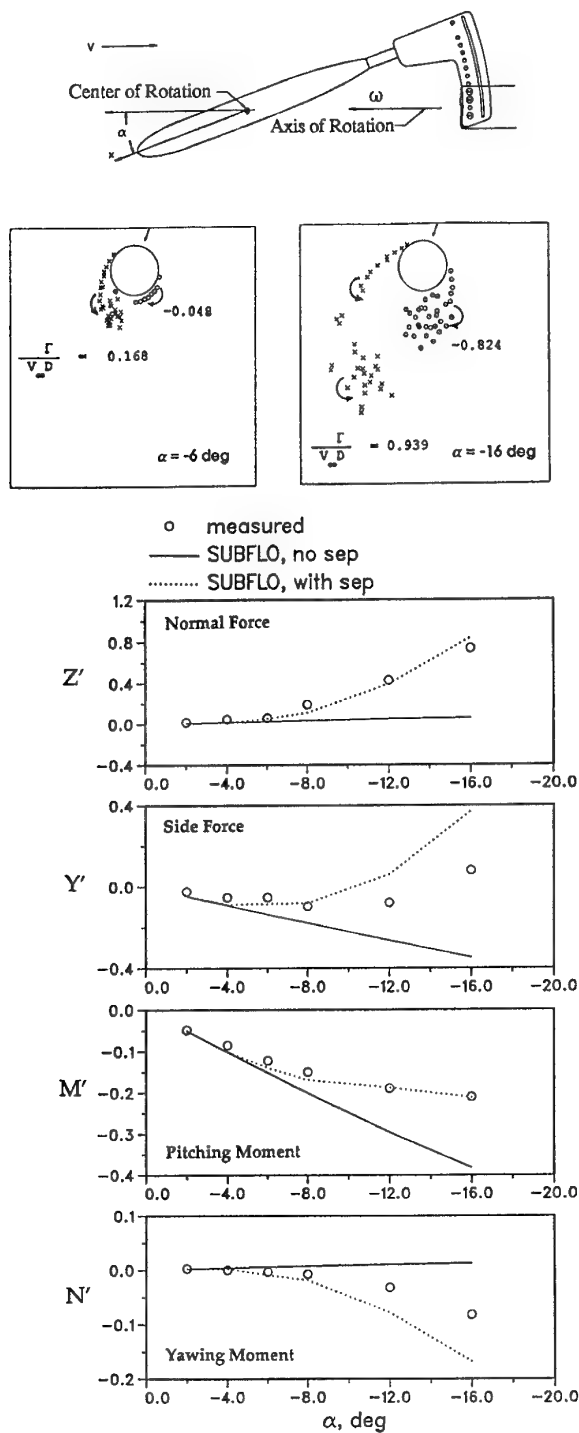


Fig. 4 - Measured and predicted forces and moments on a hull alone in coning motion, $\omega' = 0.715$.

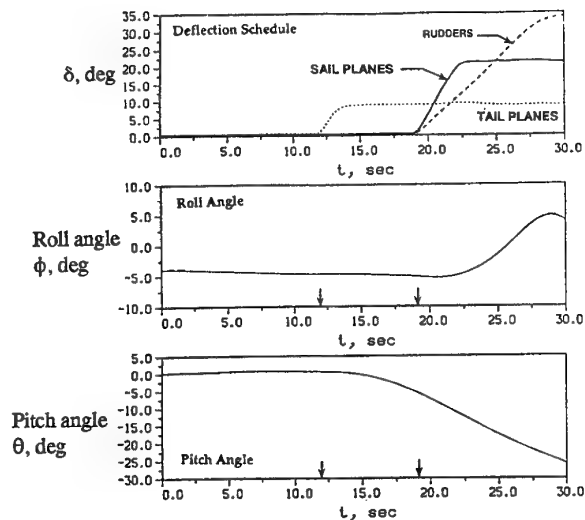


Fig. 5 - Trajectory parameters for a submarine in a sternplane jam maneuver.

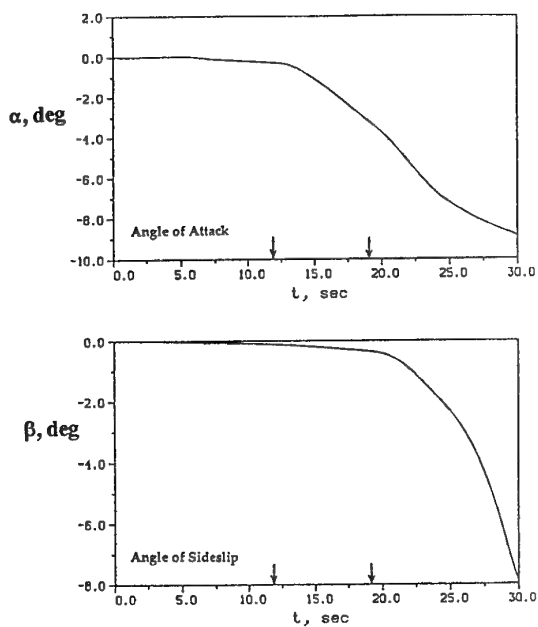


Fig. 6 - Time history of flow angles on a maneuvering submarine.

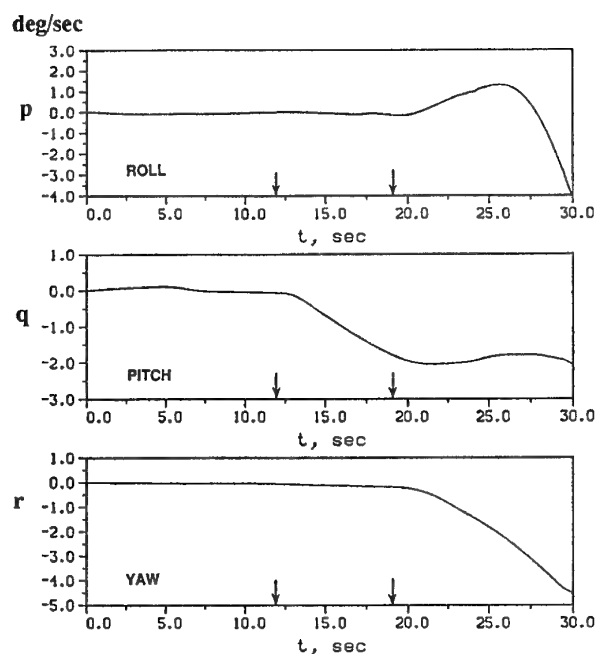


Fig. 7 - Time history of rotation rates on a maneuvering submarine.

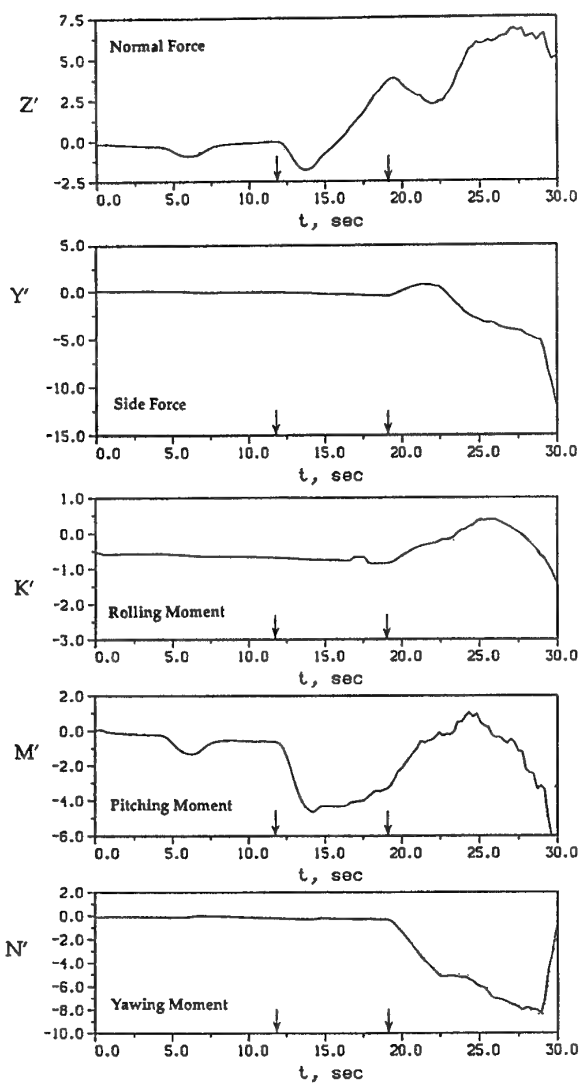


Fig. 8 - Time history of predicted forces and moments on a maneuvering submarine.

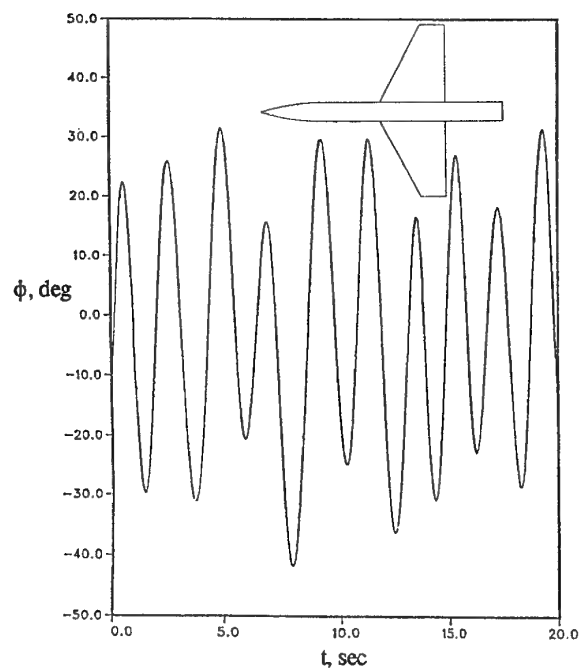
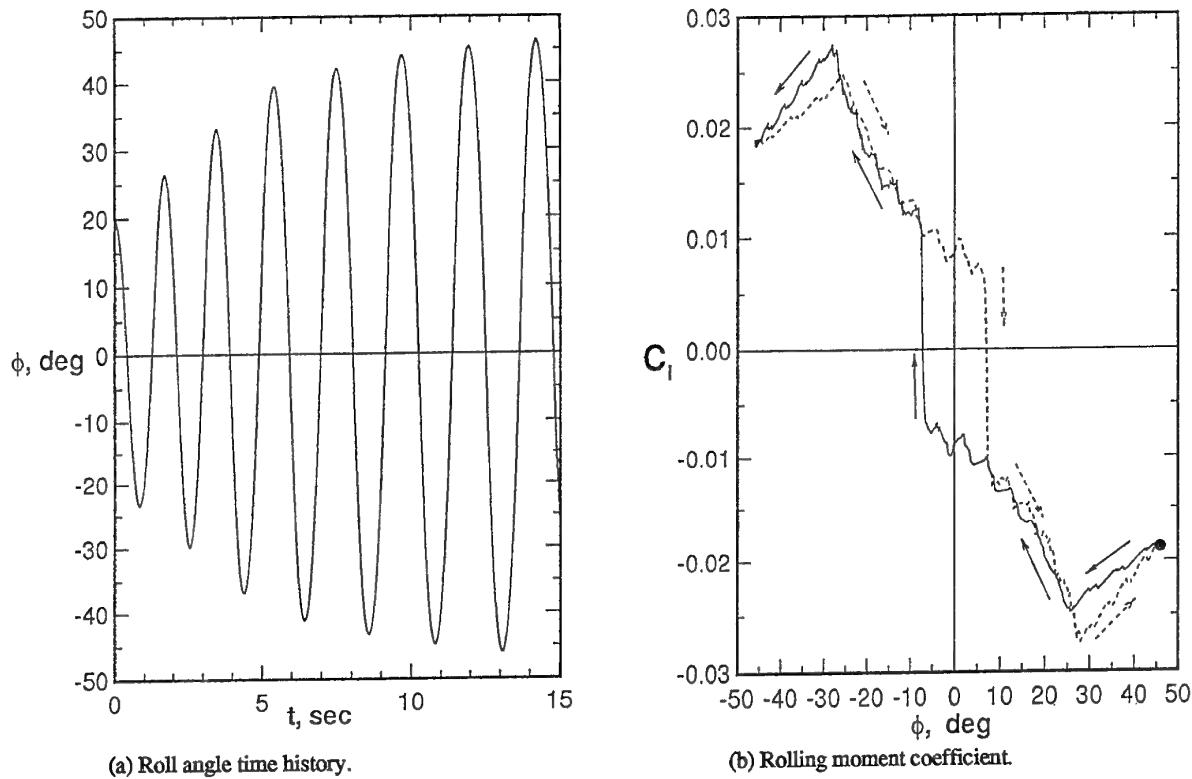
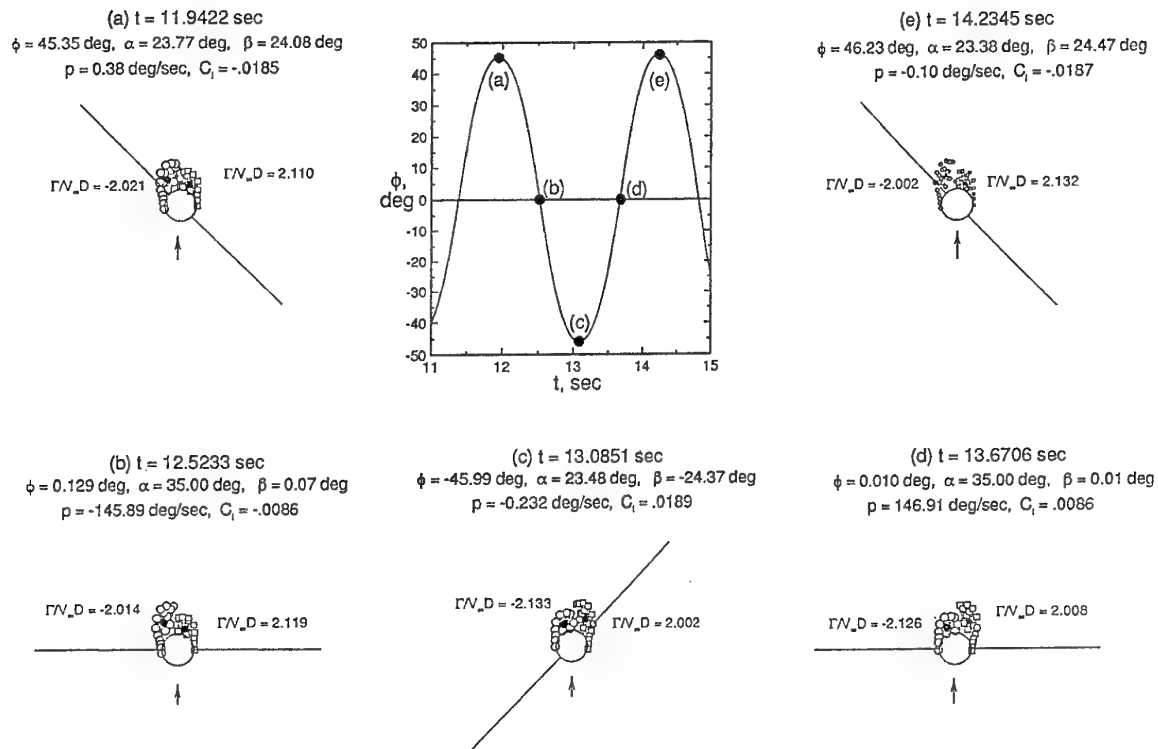


Fig. 9 - Measured wing rock on a generic fighter model, $\alpha = 35^\circ$.

Fig. 10 - Predicted wing rock on a generic fighter model, $\alpha = 35^\circ$.Fig. 11 - Predicted vortex field at the wing leading edge of a generic fighter model during wing rock motion, $\alpha = 35^\circ$.

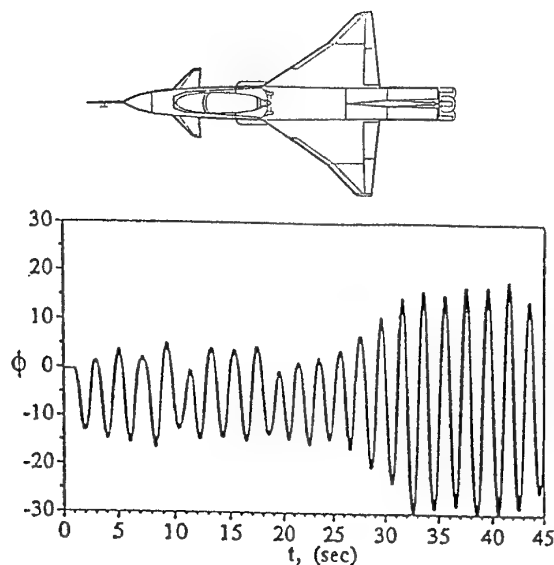


Fig. 12 - Measured wing rock on an X-31 model,
 $\alpha = 35^\circ$.

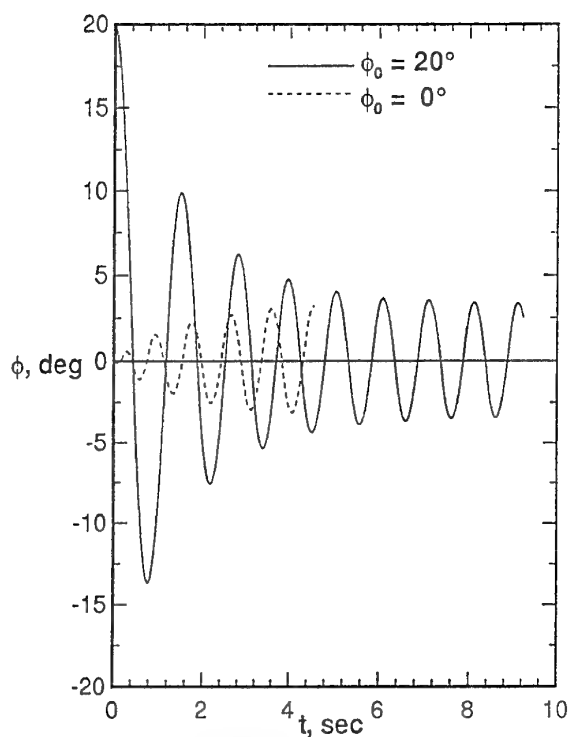


Fig. 13 - Predicted wing rock on an X-31 model,
 $\alpha = 35^\circ$.

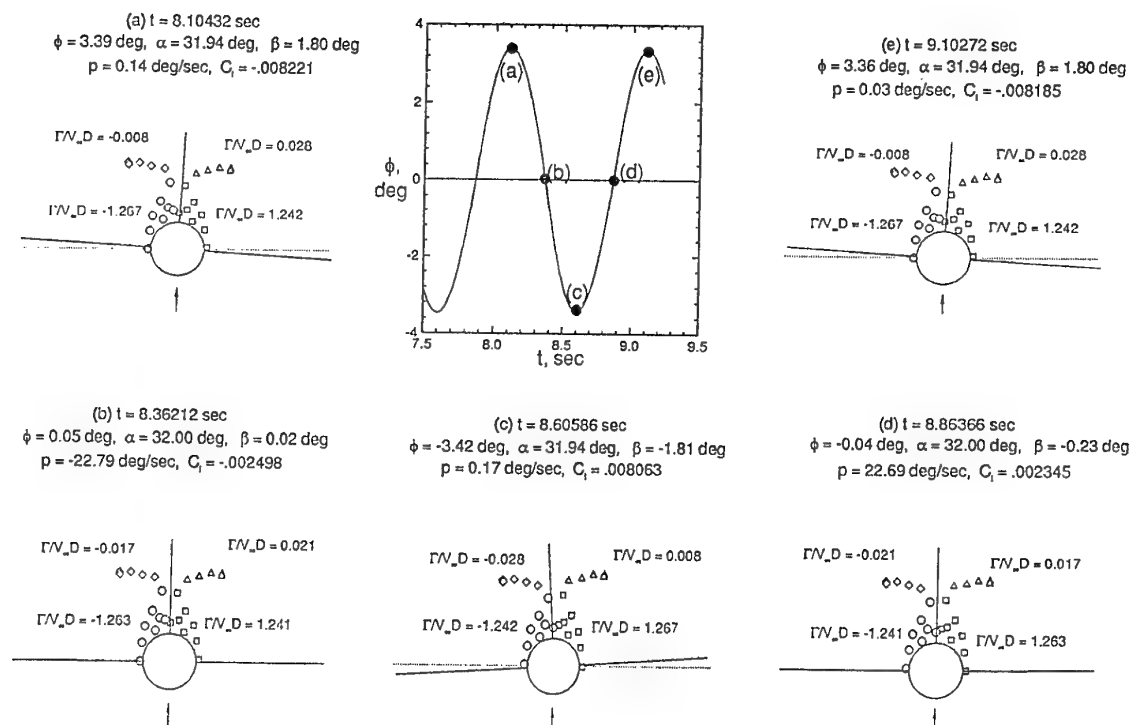


Fig. 14 - Predicted vortex field at the wing leading edge of an X-31 model during wing rock motion, $\alpha = 35^\circ$.

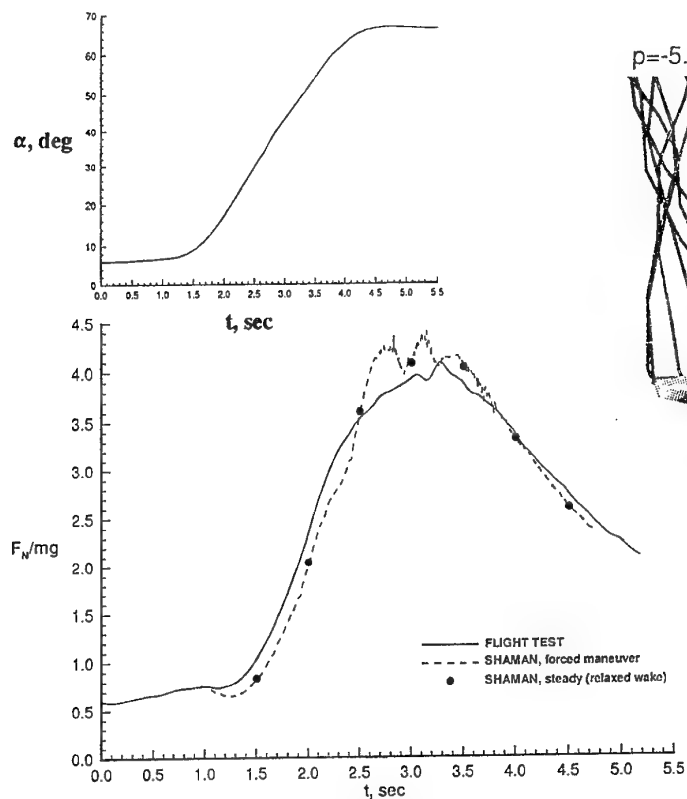


Fig. 15 - Measured and predicted normal force on an X-31 during a pull-up maneuver.

$\alpha = 44.67$ deg, $\beta = -2.82$ deg
 $p = -5.78$ deg/sec, $q = 30.54$ deg/sec, $r = -0.33$ deg/sec

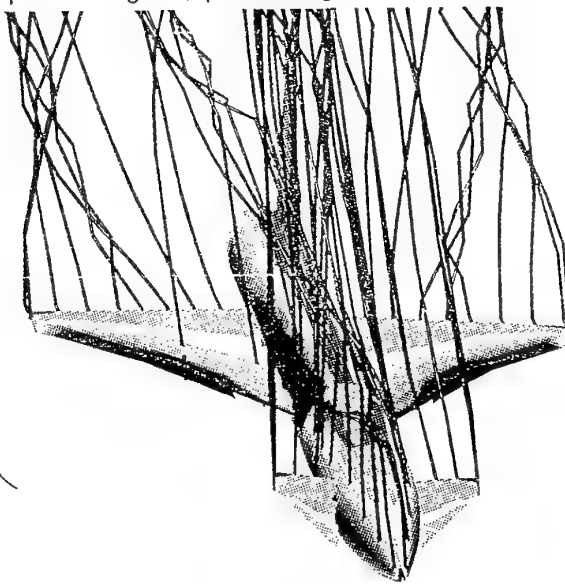


Fig. 17 - Predicted vortex field near an X-31 in a departure maneuver, $t = 14$ sec.

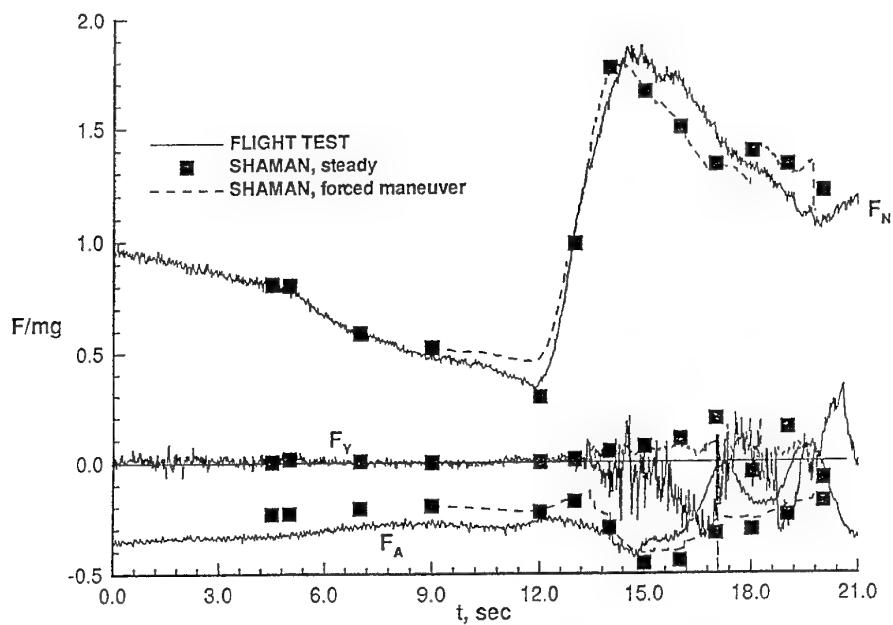


Fig. 16 - Measured and predicted forces on an X-31 in a departure maneuver.

Experimental Assessment of the Extended Betz Method for Wake Vortex Prediction

W R Graham

Cambridge University Engineering Department
Trumpington Street
Cambridge CB2 1PZ
England

1. SUMMARY

The extended Betz method, whereby wake vortex velocity predictions are obtained from a given wing lift distribution, is assessed by comparison with experimental results for wake cross-flow velocities behind a wing model with flaps. The required lift distributions are found from overall lift data and a lifting-line calculation, and the comparison is made for both clean and high-lift configurations. In each case it is found that the fundamental Betz assumption of effectively two-dimensional, inviscid flow in the wake is well supported, but that a proposed approximate invariant, the second moment of vorticity, is not conserved. In spite of this, the theoretical predictions for the single vortex shed by each half of the clean wing are found to be accurate. However, the multiple vortices arising from the wing in high-lift configuration are not as well predicted, and in this case the usefulness of the method seems to be restricted to providing estimates of the number of vortices, and their overall circulations.

2. LIST OF SYMBOLS

a_m	Fourier coefficient (equation (6.11))
A_R	wing aspect ratio, $2s/c$
b	tunnel breadth
b_m	Fourier coefficient (equation (6.14))
c	wing chord
$c_L(y)$	section lift coefficient (= section lift/ $\frac{1}{2}\rho_0 U^2 c$)
C_L	overall lift coefficient (= lift/ $\frac{1}{2}\rho_0 U^2 S$)
D/Dt	material time derivative
$G(y)$	section lift curve slope, $\partial\Gamma/\partial y$
G_m	coefficient of Fourier expansion for $G(y)$
h	tunnel height
I_{mnp}	see equation (6.8)
$m_0(y)$	section lift curve slope
m_m	coefficient of Fourier expansion for $m_0(y)$
M_1	spanwise first moment of vorticity
M_2	second moment of vorticity
n_m	Fourier coefficient (equation (6.16))
r	radial distance variable in wake vortex
R	radius of rolled-up wake vortex
s	wing semi-span
S	wing planform area in clean configuration
t	time
u_θ	vortex tangential velocity ($=\Gamma_v(r)/2\pi r$)
U	free-stream velocity
y	spanwise distance variable
y_{n1}, y_{n2}	spanwise vortex boundary locations in roll-up
\bar{y}	overall spanwise centre of vorticity
$\bar{y}_p(y)$	partial spanwise centre of vorticity
$\alpha(y)$	section geometric incidence angle
$\alpha_{df}(y)$	free-field section downwash angle
$\alpha_{di}(y)$	wall interference section downwash angle
$\alpha_0(y)$	section zero-lift incidence angle

$\Gamma(y)$	wing circulation
Γ_m	coefficient of Fourier expansion for $\Gamma(y)$
$\Gamma_v(r)$	circulation distribution in wake vortex
Γ_w	overall half-wake circulation
η	spanwise integration variable
ρ	radial integration variable
ρ_0	fluid density
ω	streamwise vorticity

3. INTRODUCTION

It has long been known that the wake behind an aircraft wing rolls up into trailing vortices, and that these vortices are associated with part of the drag experienced by the aircraft. More recently, the safety implications of such wake vortices have become important, in particular on the approach to landing. This problem was first recognised around 1970, with the advent of the Boeing 747; lately plans for a new 'Super-Jumbo' and attempts to improve airport capacity by reducing minimum separation distances have again raised the issue.

If wake vortex effects are to be minimised, a prediction method for their formation, evolution and decay is required. Despite advances in computing power, there is currently no question of being able to perform a single calculation covering the entire process, and instead it must be broken into separate stages, each of which is susceptible to certain simplifying assumptions. A key component here is the formation, or roll-up, process, which is typically complete around 10 chord lengths behind the wing. Even this flow alone is difficult to simulate in its entirety, and the problem tends to be broken down into first calculating the wing lift and then the wake roll-up. For design purposes one would like to be able to carry out the latter task very rapidly, and there is thus a need for a computationally inexpensive approach to roll-up prediction. One such approach, based on an extension of a method formulated by Betz [1], has been proposed by Donaldson *et al* [2]. In addition to developing the theory, these authors tested its predictions against data obtained from aircraft tower fly-by tests, with generally good results. However, if the method is to be used with confidence, a detailed comparison with data taken under more controlled conditions must be carried out. This is the aim of the current work.

The layout of the paper is as follows. In Section 4, the Betz method and Donaldson *et al*'s extension are briefly summarised to provide the background for the subsequent discussion. The experimental approach, and examples of the data obtained, are presented in Section 5. Then, in Section 6, we describe how the experimental wing lift data may be used, in conjunction with lifting-line theory, to obtain estimates of the wing lift distribution. Given these estimates, predictions of wake vortex profiles may be obtained via the extended Betz method, and these predictions are compared with processed results from the experimental data in Section 7. Our conclusions on the applicability of the extended Betz method for wings in clean and high-lift configurations are then summarised in Section 8.

4. THE BETZ METHOD AND ITS EXTENSION

4.1 Introduction

As a starting point for wake vortex calculations, it is usual to assume that the wing may be modelled as a 'lifting line', supporting a circulation $\Gamma(y)$ at a spanwise location y , and thus shedding a vortex sheet of strength $-d\Gamma/dy$ [8]. This sheet then rolls up to form the wake vortices. Viscous effects are expected to be small in the relatively rapid roll-up process, and a common further approximation is the neglect of streamwise velocity fluctuations in the wake. The roll-up is then governed by the two-dimensional convective vorticity equation

$$\frac{D\omega}{Dt} = 0, \quad (4.1)$$

which states that the streamwise vorticity ω is simply convected by the wake cross flow velocity components. An early attempt to solve this equation numerically was made by Clements and Maull [3], and recently Krasny [4] has taken advantage of improved computing power to calculate solutions with a high degree of resolution. This method remains, however, numerically intensive, and a more economical approach is desirable for preliminary design purposes. The extension of the Betz method proposed by Donaldson *et al* [2] is an attempt to provide such an approach. In this section we briefly describe first the original Betz method, and then its extension to cope with complex lift distributions. The presentation essentially follows that of [2], where a more detailed account may be found.

4.2 The Original Betz Method

The approach taken by Betz [1] was to assume a final, axisymmetric form for the rolled-up vortices, and then to relate their circulation distributions to the wing circulation and associated vortex sheet via conservation statements. Specifically, he required that the circulation, spanwise centre of vorticity and second moment of vorticity of each half of the wake be conserved during the roll-up process. If each rolled-up vortex has an axisymmetric circulation distribution $\Gamma_v(r)$, these conditions become

$$\Gamma_v(R) = \int_0^R \frac{d\Gamma_v}{dr} dr = \int_0^s -\frac{d\Gamma}{dy} dy = \Gamma(0), \quad (4.2)$$

$$y(r=0) = \bar{y} = \frac{1}{\Gamma(0)} \int_0^s -\frac{d\Gamma}{dy} y dy, \quad (4.3)$$

$$\int_0^R \frac{d\Gamma_v}{dr} r^2 dr = \int_0^s -\frac{d\Gamma}{dy} (y - \bar{y})^2 dy. \quad (4.4)$$

(Note that the condition of zero circulation (loading) at the wing tip, $\Gamma(s) = 0$, has been used in deriving (4.2).)

In themselves, these equations are not sufficient to define $\Gamma_v(r)$. Betz therefore introduced the additional piecewise conservation requirements

$$\Gamma_v(r) = \int_0^r \frac{d\Gamma_v}{d\rho} d\rho = \int_y^s -\frac{d\Gamma}{d\eta} d\eta = \Gamma(y), \quad (4.5)$$

$$\int_0^r \frac{d\Gamma_v}{d\rho} \rho^2 d\rho = \int_y^s -\frac{d\Gamma}{d\eta} (\eta - \bar{y}_p(y))^2 d\eta, \quad (4.6)$$

$$\text{where} \quad \bar{y}_p(y) = \frac{1}{\Gamma(y)} \int_y^s -\frac{d\Gamma}{d\eta} \eta d\eta. \quad (4.7)$$

These expressions specify conservation of *local* circulation and second moment of vorticity as the vortex rolls up from the wing tip.

At this point it is instructive to consider the approximations inherent in this proposed solution to (4.1). Conservation of circulation, (4.2), follows from Kelvin's circulation theorem [5], and conservation of spanwise centre of vorticity, (4.3), can be proved for a flow obeying (4.1) and having $y=0$ as a symmetry axis. Equations (4.4)–(4.7), however, are approximations and, as they stand, have little obvious physical justification. Donaldson *et al* [2] do not address this issue, but the results of their analysis of (4.2)–(4.7) show that the approximations made are synonymous with a kinematic assumption for the roll-up process, illustrated in Fig 4.1. The partially rolled-up vortex, of radius r , is attached to the remainder of the initial vortex sheet, which is assumed undeformed. On applying the exact conditions of conservation of circulation and spanwise centre of vorticity to this kinematic model, we obtain

$$\Gamma_v(r) = \Gamma(y) \quad (4.8)$$

$$r = \bar{y}_p(y) - y, \quad (4.9)$$

which are the conditions that Donaldson *et al* derived from (4.2)–(4.7). For the simple lift distributions typical of clean wing configurations, these equations suffice to define the circulation distribution in the rolled-up vortex.

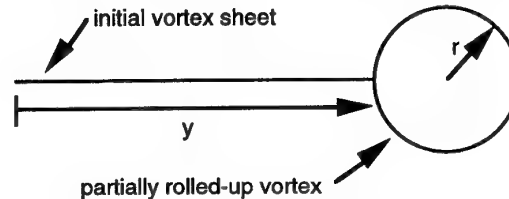


Figure 4.1 Kinematic model for wing-tip roll-up.

Problems with this recipe arise if the radius variable r ceases to increase monotonically as y decreases from s . Such problems occur with the more complicated lift distributions typical of wings in landing configuration, and indicate that the assumed roll-up into a single vortex is not feasible. Instead, multiple vortices will be formed from each half of the wake, and a more sophisticated analysis is required.

4.3 The Extended Betz Method

The first step in developing a formulation for complex lift distributions is the identification of points where roll-up commences. Donaldson *et al* propose that these should be the positions of maximum shear in the shed vortex sheet, ie points of maximum $|d\Gamma/dy|$. Having identified these locations, it is simplest to proceed on the basis of the kinematic model shown in Fig. 4.2—the obvious

extension of the kinematic assumption described previously. Since Kelvin's circulation theorem applies around any contour in the cross flow plane, we have piecewise conservation of circulation; ie, for vortex n :

$$\Gamma_{vn}(r_n) = \Gamma(y_{n1}) - \Gamma(y_{n2}), \quad (4.10)$$

while conservation of the overall spanwise centre of vorticity implies

$$\sum_{n=1}^N \int_{y_{n1}}^{y_{n2}} -\frac{d\Gamma}{d\eta} \eta d\eta = \sum_{n=1}^N (y_{n1} + r_n) \Gamma_{vn}(r_n). \quad (4.11)$$

This expression is not sufficient to specify individual vortex circulation distributions, and Donaldson *et al* make the further assumption that conservation of centre of vorticity applies in a piecewise sense, ie

$$\int_{y_{n1}}^{y_{n2}} -\frac{d\Gamma}{d\eta} \eta d\eta = (y_{n1} + r_n) \Gamma_{vn}(r_n), \quad (4.12)$$

which, in conjunction with (4.10) and the kinematic relation $y_{n2} - y_{n1} = 2r_n$, yields a roll-up recipe similar to (4.8) and (4.9).

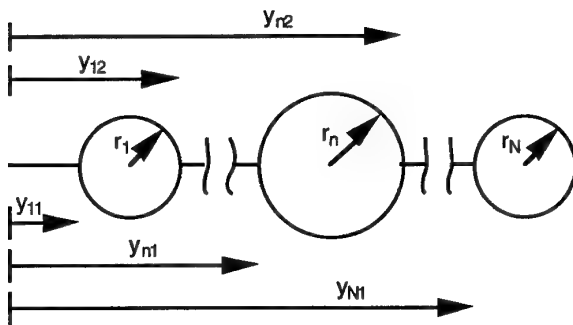


Figure 4.2 Kinematic model for multiple vortex roll-up.

Finally, it is necessary to define vortex boundaries, since (4.10) and (4.12) give no information about where the roll-up process stops for a given vortex. Donaldson *et al* suggest points of minimum or zero shear, and give a prescription for continuing the roll-up if one boundary is reached before the other. The latter is inconsistent with our kinematic assumption, but the effects of this *ad hoc* approach are usually small (since it is applied to regions of low vorticity).

The extended Betz method can thus be seen as the upshot of two exact conditions (conservation of circulation and spanwise centre of vorticity) applied to a kinematic model, with a further assumption, (4.12), made in order to obtain a solution. It therefore manifests an additional level of approximation compared to the original method, whose sole assumption was the kinematic model.

4.4 Wall Interference Effects

Since our experimental assessment of the Betz method will be based on wind tunnel data, we conclude this section with a discussion of how wall interference effects influence the preceding analysis. For a rectangular tunnel cross-section, the rigid walls effectively introduce the infinite array of images shown in Fig. 4.3 [6], all of which induce velocities in the working section. The most important

question is how these velocities affect the exact conditions of conservation of circulation and spanwise centre of vorticity.

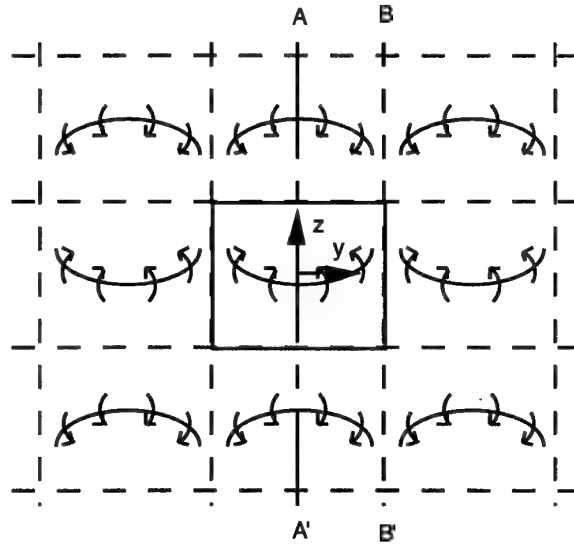


Figure 4.3 Image array for wake roll-up in a wind tunnel.

As noted previously, Kelvin's circulation law states that circulation is conserved around any material contour. Since there is no fluid transport across the tunnel walls, we conclude that circulation is still conserved on each side of the wake. More complicated is the issue of the spanwise centre of vorticity. Here we must exploit the symmetry of the array of images. In particular, we can say that the spanwise first moment of vorticity M_1 (= total circulation \times spanwise centre of vorticity), is conserved to the right of axes AA' and BB', since both are planes of symmetry. Therefore, M_1 is conserved for the region AA'B'B. Now consider estimating M_1 for this region, starting with the wake itself, giving $M_1 = M_{1w}$ say. Adding the first two images gives $M_1 = -M_{1w}$, the next two $M_1 = M_{1w}$, and so on. The centre of vorticity remains fixed at M_{1w}/Γ_w , where Γ_w is the overall half-wake circulation. Thus, even if wall interference effects are significant, the exact results for a free two-dimensional wake remain valid in the wind tunnel.

It remains to consider the influence of wall interference on the kinematic models of Figs. 4.1 and 4.2. This is much harder to quantify but if, as we shall find, wall interference effects are relatively small, one would not expect them to alter the validity (or otherwise) of such models. We therefore conclude that wind tunnel based assessments of the accuracy of the Betz method and its extension will genuinely reflect their validity in free-field conditions.

5. EXPERIMENTAL INVESTIGATIONS

5.1 Apparatus

The work described in this section was carried out in the Cambridge University Engineering Department $5\frac{1}{2}$ ft x 4 ft (1.67m x 1.22m) low speed wind tunnel. The tunnel is equipped with a three component force balance and an automated wake traverse mechanism, which may be positioned approximately 0.7m or 1.2m downstream of the balance attachment points. A single-tube yaw meter, or 'Chu-tube' [7] is mounted on the wake transverse, and the

output from its pressure transducer is recorded by a data-logging system. Figure 5.1 shows the tunnel layout.

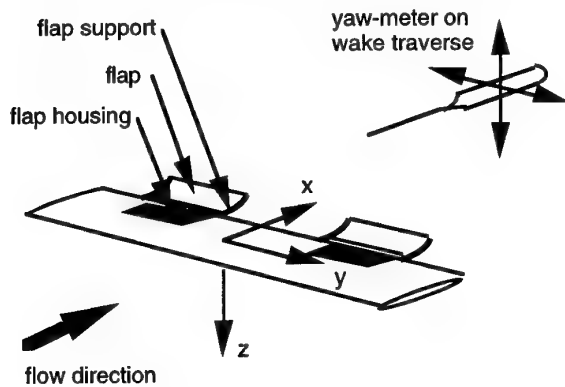


Figure 5.1 Wind tunnel layout.

The wing model used consists of a basic section (NACA 23012) and two symmetrically-placed flaps, cut out from the underside of the wing. The flaps can be replaced in the cut-outs, giving a clean configuration with a rectangular planform of 1m x 0.125m, or deployed in the slotted supports shown in Fig. 5.1. The supports are equispaced, at 0.2m, and the flap chord is 31mm.

5.2 Calibration of the Chu-tube

The Chu-tube probe consists of two concentric tubes, the inner having a chamfered face. By rotating the inner tube, and then bringing the outer tube forward to act as a pitot, the Chu-tube effectively performs as a five-hole yaw meter, but with a significantly smaller measuring area. The first such device is described in detail by Chu *et al* [7], and our design is identical in its essential aspects.

Before use, the probe must be calibrated. This is achieved by taking measurements in a free-stream of known pressure and velocity, with the probe oriented at a series of yaw and pitch angles between $\pm 40^\circ$. Once this procedure is complete, the flow angle, overall velocity and static pressure at the probe tip may be calculated from its five measured pressures. The calibration method described by Chu *et al* [7] was followed here, with the exception that interpolated values from raw calibration data, rather than least squares polynomial fits, were used in the subsequent data analysis. This choice was made because polynomial fitting was found to be unsatisfactory in some regions of the calibration space.

5.3 Experimental Procedure

All tests were carried out with the wing model hanging from the force balance. Two wing configurations were investigated: clean (flaps in), and flaps out, with the flap leading edge approximately level with the wing trailing edge. Lift vs incidence curves were obtained for the two configurations at a Reynolds number based on chord of 3.7×10^5 (free-stream velocity 45ms^{-1}); in the subsequent traverse tests the free-stream velocity and Reynolds number were reduced to 41ms^{-1} and 3.4×10^5 to keep oscillations of the model at a low level. Wake traverses were carried out for the two wing configurations, at 5° and 10° incidence, with the traverse in the forward and back positions; giving eight runs in all. Each traverse covered an area of $0.6\text{m} \times 0.4\text{m}$ on one side of the wake, at a resolution of 10mm.

5.4 Experimental Results

5.4.1 Lift curves

The lift curves for the two wing configurations are plotted in Fig. 5.2, which shows that the effect of the flaps is to raise the lift curve, with essentially no change in its slope. In each case, the curve is linear up to about 5° , after which it increases less rapidly up to a maximum around 15° . The least squares straight line fits to the linear regions are:

$$\text{flaps in: } C_L = 0.086 + 5.26\alpha, \quad (5.1)$$

$$\text{flaps out: } C_L = 0.339 + 5.20\alpha, \quad (5.2)$$

where α is expressed in radians.

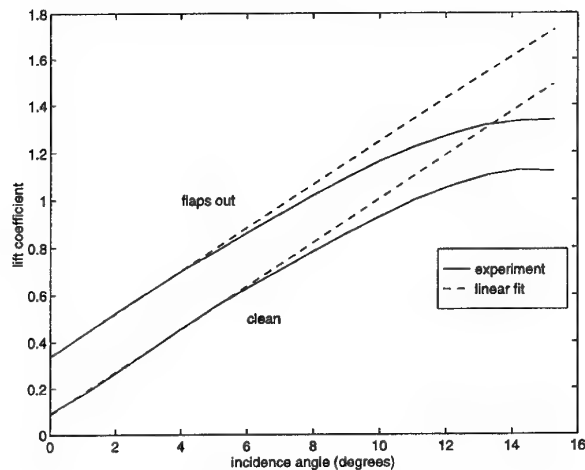


Figure 5.2 Lift curves for the wing model

5.4.2 Wake velocities

Figures 5.3 and 5.4 show velocities in the cross-flow plane, obtained with the wing at 5° incidence and the traverse in the back position. The axes correspond to those indicated on Fig. 5.1. In Fig. 5.3 the flaps are in, and a single rolled-up vortex, originating at the wing-tip, is clearly visible. A similar tip vortex is also seen in Fig. 5.4, where the flaps are out, but here we also observe two flap vortices, of opposite sign, confirming our earlier assertion that wings in landing configuration tend to produce multiple rolled-up vortices.

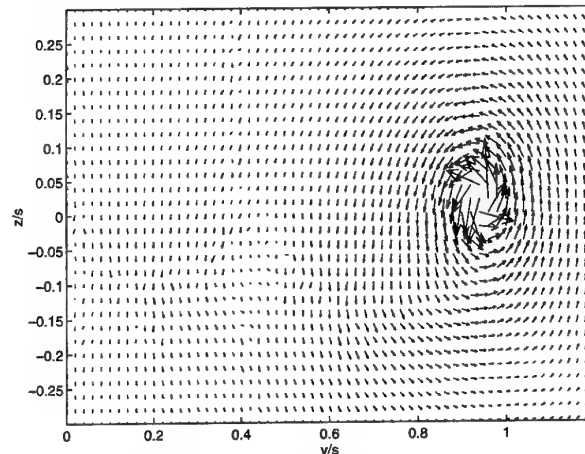


Figure 5.3 Cross-flow velocities, 5° , clean configuration.

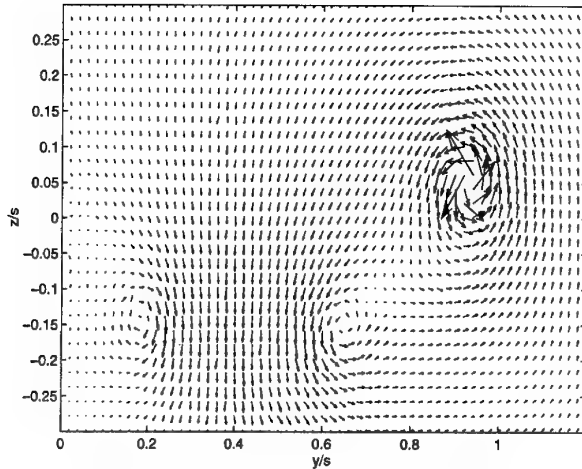


Figure 5.4 Cross-flow velocities, 5°, flaps out.

The corresponding plots for the other test cases are qualitatively similar, and the velocity data considered here must be processed further before they can be easily differentiated. The results of this analysis are presented in Section 7, where the experimental results are compared with the predictions of the Betz method. To obtain these predictions, however, we require a knowledge of the wing lift distribution, and this calculation is the subject of the following section.

6. CALCULATION OF THE WING LIFT DISTRIBUTION

6.1 Introduction

Given the underlying 'lifting-line' assumption of the theory described in Section 4, it is consistent to calculate the wing lift distribution using this approach. Here (see, for example, [8]), one treats the flow at each spanwise station of the wing as quasi-two-dimensional, and obtains the local lift from a knowledge of the local angle of attack and section properties. This approach could be taken for our clean wing, whose section properties are documented, but not the flaps out configuration. Instead, then, we use an alternative method whereby the local section properties are *deduced* from our knowledge of the planform geometry and the overall wing lift curve. This method is described in 6.2.

A further difficulty is the interference effect from the wind tunnel walls, which will alter the shape, as well as the magnitude of the lift distribution. In 6.3 we describe an iterative technique which takes the free-field lift distribution calculated in 6.2, and corrects it to the enclosed wind tunnel lift distribution. The latter forms the basis of the Betz method estimates for vortex circulations presented in Section 7.

6.2 The Free-Field Lift Distribution

6.2.1 Formulation

Our starting point in the calculation of the free-field lift distribution is the lifting-line equation

$$c_L(y) = m_0(y) [\alpha(y) - \alpha_0(y) - \alpha_{df}(y)], \quad (6.1)$$

which states that the local lift coefficient, c_L , is equal to the local lift curve slope, m_0 , times the local effective

incidence angle. Here α is the geometric incidence, α_0 the zero lift incidence and α_{df} the reduction in incidence due to the trailing vortex downwash. In terms of the wing circulation, $\Gamma(y)$, this equation becomes

$$\frac{2\Gamma(y)}{Uc} + \frac{m_0(y)}{4\pi U} \int_{-s}^s -\frac{d\Gamma}{d\eta} \frac{d\eta}{\eta - y} = m_0(y) [\alpha(y) - \alpha_0(y)], \quad (6.2)$$

where c is the wing chord. Furthermore, if we differentiate with respect to α , and write $\partial\Gamma/\partial\alpha = G$, we obtain

$$\frac{2G(y)}{Uc} + \frac{m_0(y)}{4\pi U} \int_{-s}^s -\frac{dG}{d\eta} \frac{d\eta}{\eta - y} = m_0(y) \quad (6.3)$$

Equations (6.2) and (6.3) allow us to find the clean and flaps out lift distributions as follows. Since $m_0(y)$ is constant for the clean wing (Fig. 6.1(a)) we can enter a trial value in (6.3), solve for $G(y)$ and then find the associated overall lift curve slope. A few iterations of this process yield the value of m_0 which corresponds to the experimental lift curve slope. We also note from (6.2) that, since $\alpha_0(y)$ is constant for the clean wing, it must be equal to the overall zero lift angle. Thus the clean wing lift distribution may now be calculated from (6.2) for any value of α .

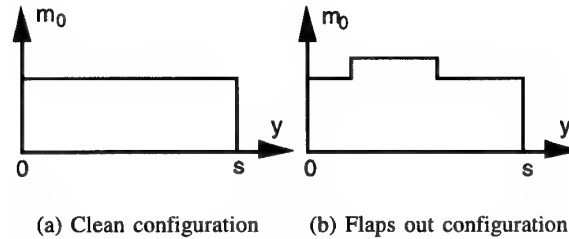


Figure 6.1 Wing section lift curve slopes.

Turning to the flaps out configuration, m_0 is no longer constant, but we know that it consists of the clean wing value, plus a constant difference over the spanwise extent of the flaps (Fig. 6.1 (b)). We can again iterate (6.3) for different values of this constant until the correct overall lift curve slope is obtained. Similarly, α_0 may be found from (6.2) by noting that it too consists of the known clean wing value plus a constant difference over the flaps, and varying this constant (for a given α) until the correct value of C_L is obtained.

Thus, in principle, we can obtain the desired lift distributions from our knowledge of the wing geometry and overall lift curves. We now describe how this is achieved in practice.

6.2.2 Fourier series solutions

As described in [8], solutions to equations (6.2) and (6.3) may be obtained by expanding $\Gamma(y)$ and $G(y)$ as Fourier series, ie

$$\Gamma(\theta) = \frac{Uc}{2} \sum_{n \text{ odd}} \Gamma_n \sin n\theta, \quad G(\theta) = \frac{Uc}{2} \sum_{n \text{ odd}} G_n \sin n\theta, \quad (6.4)$$

with θ defined by

$$y = s \cos \theta. \quad (6.5)$$

Equation (6.3) then becomes

$$\sum_{n \text{ odd}} G_n \sin n\theta + \frac{m_0(\theta)}{4A_R} \sum_{n \text{ odd}} n G_n \frac{\sin n\theta}{\sin \theta} = m_0(\theta), \quad (6.6)$$

and (6.2) takes essentially the same form. If we now also expand $m_0(\theta)$ in Fourier series form, $m_0 = \sum m_p \sin p\theta$, with p odd, multiply by $\sin m\theta$ and integrate over the range 0 to π , we obtain

$$G_m + \frac{1}{4A_R} \sum_{n,p} n G_n I_{mnp} m_p = m_m, \quad (6.7)$$

$$\text{where } I_{mnp} = \frac{2}{\pi} \int_0^\pi \frac{\sin m\theta \sin n\theta \sin p\theta}{\sin \theta} d\theta. \quad (6.8)$$

The numerator of this integral may be split into individual trigonometric functions, and each subsequent integral evaluated from standard formulae [9], with the result

$$\begin{aligned} I_{mnp} &= 0, & p < |m-n|, & p > m+n, \\ I_{mnp} &= 1, & |m-n| < p < m+n. \end{aligned} \quad (6.9)$$

Since the cases $p = |m-n|$, $p = m+n$ do not occur for our odd summation indices, (6.9) allows us to evaluate the summation over p in (6.7) very easily, leaving a matrix equation for the G_n . The corresponding equation arising from (6.2) is

$$\Gamma_m + \frac{1}{4A_R} \sum_{n,p} n \Gamma_n I_{mnp} m_p = a_m, \quad (6.10)$$

$$\text{where } a_m = \frac{2}{\pi} \int_0^\pi m_0(\theta) [\alpha(\theta) - \alpha_0(\theta)] \sin m\theta d\theta. \quad (6.11)$$

The solution process described in 6.2.1 is now straightforward to implement. The Fourier coefficients m_p and a_m can be calculated in terms of the unknown constants defining the section lift curve slopes and zero-lift incidence angles for the two wing configurations and, given trial values for these constants, the predicted overall lift curve slope and lift coefficients then follow from the G_n and the Γ_n . Only a few iterations of this process are required in order to find the values that yield agreement with the experimental results of 5.4.1.

When applied to the experimental results, this approach was found to lead to higher than expected values of the section lift-curve slope. The likely cause of this problem was identified as tunnel wall interference, and an iterative technique, described in the following, was developed to take this effect into account.

6.3 Correction for Tunnel Wall Interference

The effect of the tunnel walls is to introduce the array of wake images shown in Fig. 4.3. For the purpose of calculating their influence on the lift distribution, we make the same assumption as the free-field lifting-line

calculation and neglect any roll-up. Then [6] the overall downwash angle is given by $\alpha_{df} + \alpha_{di}$, where

$$\alpha_{di}(y) = \frac{1}{4\pi U} \sum_{m,n=-\infty}^{\infty} (-1)^n \int_{-s}^s \frac{d\Gamma}{d\eta} \frac{mb + \eta - y}{(mb + \eta - y)^2 + n^2 h^2} d\eta, \quad (6.12)$$

(the prime indicating that $(m,n) = (0,0)$ is excluded from the summation). When this term is included in the lifting-line analysis, equation (6.10) becomes

$$\Gamma_m + \frac{1}{4A_R} \sum_{n,p} n \Gamma_n I_{mnp} m_p = a_m - b_m, \quad (6.13)$$

$$\text{where } b_m = \frac{2}{\pi} \int_0^\pi m_0(\theta) \alpha_{di}(\theta) \sin m\theta d\theta, \quad (6.14)$$

and (6.7) takes the similar form

$$G_m + \frac{1}{4A_R} \sum_{n,p} n G_n I_{mnp} m_p = m_m - n_m, \quad (6.15)$$

$$\text{where } n_m = \frac{2}{\pi} \int_0^\pi m_0(\theta) \frac{\partial \alpha_{di}}{\partial \alpha} \sin m\theta d\theta. \quad (6.16)$$

The correction terms b_m and n_m are small, rendering (6.13) and (6.15) amenable to iterative solution. First the free-field values for $G(\theta)$ and $\Gamma(\theta)$ are calculated, as previously. These are then used to provide initial approximations to b_m and n_m , which in turn may be used to update the estimates for $G(\theta)$ and $\Gamma(\theta)$ via (6.15) and (6.13). Equations (6.14) and (6.16) must be evaluated numerically, but the rapid convergence of the iterative procedure, and the use of the identity [9]

$$\frac{1}{\pi} \sum_{n=-\infty}^{\infty} (-1)^n \frac{x}{x^2 + n^2} = \text{cosech}(\pi x) \quad (6.17)$$

result in an inexpensive computation, which yields the section lift curve slopes and zero lift angles in exactly the same way as before.

6.4 Results

The estimated values of m_0 and α_0 for the clean wing and flaps out sections are given in Table 6.1. Note that m_0 is actually reduced for the wing section with flaps out; this follows from the slightly lower experimental lift curve slope found for the flaps out configuration (see equations (5.1) and (5.2)). Note also that the values of m_0 are somewhat *higher* than the theoretical, thin aerofoil value of 2π . Estimates of the influence of tunnel blockage effects [6] were generally significantly lower than the observed difference, and no satisfactory explanation has yet been found for this discrepancy.

	m_0 (rad ⁻¹)	α_0 (rad)
Clean wing section	6.68	-0.016
Flaps out section	6.48	-0.129

Table 6.1 Estimated wing section properties

The calculated lift distributions for the clean and flaps out configurations at 5° incidence are shown in Figs 6.2 and 6.3. Also plotted are the corresponding free-field lift distributions, showing that the image system upwash increases the wing circulation by about 4%, on average.

The clean configuration plot for 10° incidence is of identical shape to Fig. 6.2, and the flaps out configuration plot is similar to Fig. 6.3. (Here the shape is not identical, due to differing relative contributions from the clean and flaps out sections.) These lift distributions may now be used as the input to the Betz method, and the associated wake vortex circulations predicted.

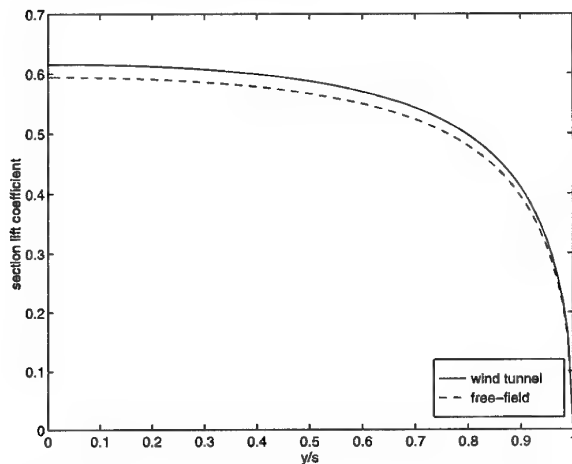


Figure 6.2 Wing lift distribution, 5° , clean configuration.

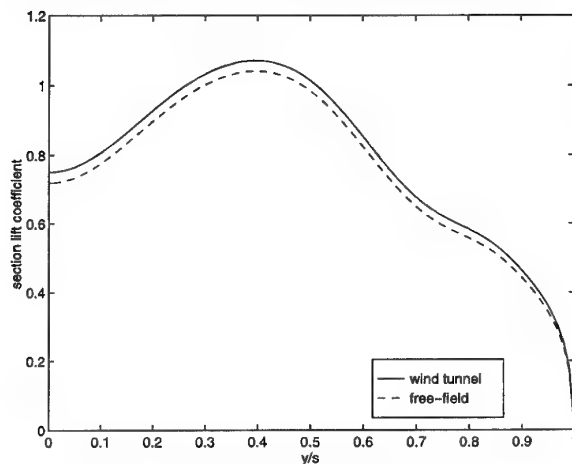


Figure 6.3 Wing lift distribution, 5° , flaps out.

7. COMPARISON OF EXPERIMENTAL AND THEORETICAL RESULTS

7.1 Implementation of the Betz Method

The lift distributions found in Section 6 yield lift coefficients obeying the straight line fits (5.1) and (5.2). These are in good agreement with experimental results at 5° but overpredict C_L at 10° . Thus, before applying the Betz method, all lift distributions were scaled to match the lift coefficient measured during the relevant wake traverse run. The largest scalings applied were just over 5%.

A weakness of the Betz method, as far as numerical implementation is concerned, is the need for gradient

information from the lift distribution data. Here this difficulty was solved by generating a least squares cubic spline fit to the lift distribution curve. This fit represents the lift distribution by a set of cubic polynomials in y/s , joined to one another at 'knots', where continuity is enforced up to second derivative. Satisfactory fits to the clean and flaps out lift distributions were obtained with six and seven knots respectively; in each case, once the knot positions were optimised the plotted fit was found to overlay the lift distributions (e.g. Figs. 6.2, 6.3) exactly.

Once the cubic spline fit is obtained, the gradient of the lift distribution follows from the polynomial coefficients, and the roll-up points and vortex boundaries specified by Donaldson *et al* may be found. The recipe for the vortex circulation distributions, defined by (4.10) and (4.12), can then be implemented, starting from the roll-up positions and using the cubic spline representation for $\Gamma(y)$ to evaluate the component expressions. The result is a set of predicted vortex circulation distributions, and spanwise vortex locations, which may be compared with the experimental data. This comparison is carried out in 7.3; first, though, we assess the validity of the conservation assumptions leading to the detailed predictions.

7.2 Experimental Assessment of the Invariance Assumptions

The invariance assumptions we shall consider here are those of overall conservation of circulation, spanwise centre of vorticity and second moment of vorticity. The first two follow from the approximation that the wake behaviour is two-dimensional and inviscid, and the third from the kinematic model (Figs. 4.1 and 4.2) and (when applicable) the assumption of piecewise conservation of centre of vorticity, equation (4.12).

The values of the three quantities in the vortex sheet immediately behind the wing can easily be calculated from the cubic spline fit to the lift distribution. The experimental values are less straightforward to obtain, requiring an initial estimate of the streamwise vorticity in the wake. Here the velocity gradients required are calculated directly from the experimental cross-flow velocity data. Examples of the resulting vorticity fields (corresponding to the velocity fields of Figs. 5.3 and 5.4) are shown in Figs. 7.1 and 7.2. The tip vortex is immediately obvious in each plot, and two counter-rotating flap vortices are also clearly visible in Fig. 7.2. Estimates of the required invariants may then be obtained from these fields.

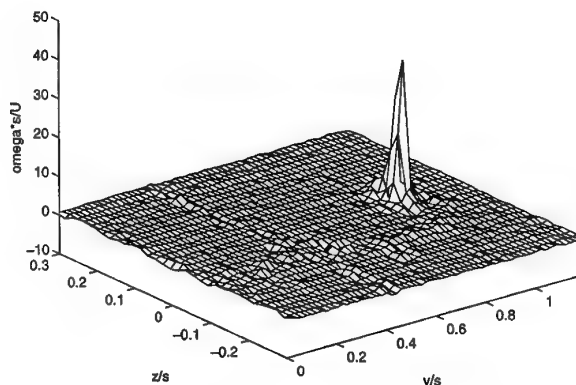


Figure 7.1 Vorticity field, 5° , clean configuration.

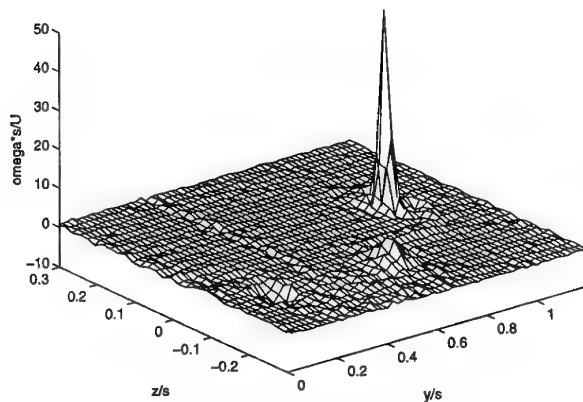


Figure 7.2 Vorticity field, 5°, flaps out.

The results of the calculations described above are summarised in Tables 7.1–7.3. Here we see that the overall circulation is close to being constant during the roll-up process, and that, in general, the deviation from the initial value is a reduction in the downstream direction. The results also seem to bear out the second assumption, conservation of spanwise centre of vorticity, the largest discrepancy being 7% of the predicted value (in the forward measurement for the clean configuration at 5° incidence).

The same cannot be said, though, for the second moment of vorticity, which shows considerable variation throughout the results (although it does appear to remain almost constant between the forward and back traverse locations when the flaps are out). Not too much weight can be placed on the exact experimental values here, as 'noise' in the vorticity estimation at locations far from the centre of vorticity can give contributions approaching 10^{-3} ; however the discrepancies between the estimates calculated from the lift distributions and from experiment indicate that the second moment of vorticity is not conserved during the roll-up process.

7.3 Vortex Circulation Distributions

The calculation of vortex circulations from the experimental data is not entirely straightforward, as the measured velocities are the result of contributions from all the vortices in the wake. To find individual circulations, either the influence of other vortices must be removed, or a line integral around the relevant vortex must be calculated. The latter approach was found to be most suitable, and the integral was estimated for successive circular integration paths around a given vortex to yield the variation of circulation with radius. The velocity at each point on the integration path was calculated from the experimental data using bilinear interpolation, and initial estimates of the vortex centre location were refined numerically (to maximise the circulation at a chosen radius) before the circulation distribution was calculated. The best radius for this optimisation was found to correspond to the peak vortex tangential velocity (defined by $u_\theta = \Gamma_v(r)/2\pi r$), and this value was identified in each case from a preliminary analysis.

	Vortex sheet	Forward location	Back location
Clean configuration			
5° incidence	0.080	0.075	0.072
10° incidence	0.134	0.132	0.125
Flaps out configuration			
5° incidence	0.095	0.094	0.091
10° incidence	0.149	0.141	0.142

Table 7.1 Overall circulation Γ_w/Us

	Vortex sheet	Forward location	Back location
Clean configuration			
5° incidence	0.885	0.947	0.924
10° incidence	0.885	0.906	0.911
Flaps out configuration			
5° incidence	1.056	1.055	1.060
10° incidence	0.985	1.004	1.003

Table 7.2 Spanwise centre of vorticity \bar{y}/s

	Vortex sheet	Forward location	Back location
Clean configuration			
5° incidence	4.07×10^{-2}	-1.53×10^{-3}	2.46×10^{-5}
10° incidence	6.79×10^{-2}	2.89×10^{-3}	1.37×10^{-3}
Flaps out configuration			
5° incidence	3.86×10^{-2}	-1.56×10^{-2}	-1.60×10^{-2}
10° incidence	6.79×10^{-2}	-1.35×10^{-2}	-1.45×10^{-2}

Table 7.3 Second moment of vorticity M_2/Us^3

Plots of the predicted and measured tip vortex tangential velocity for the clean configuration, at 5° and 10° incidence, are shown in Figs. 7.3 and 7.4. For small radii a viscous core is clearly visible in the experimental results, and for $r/s \geq 0.1$ the measured velocities drop below the predictions (this is more clearly seen if circulation is plotted). However, the agreement in the intermediate region is remarkably good in all cases.

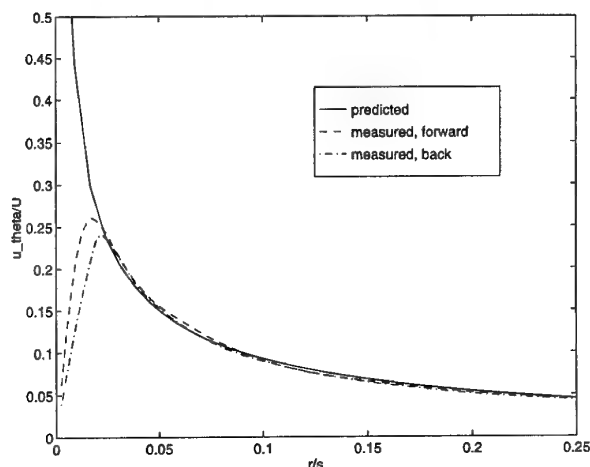


Figure 7.3 Measured and predicted vortex velocities at 5° .

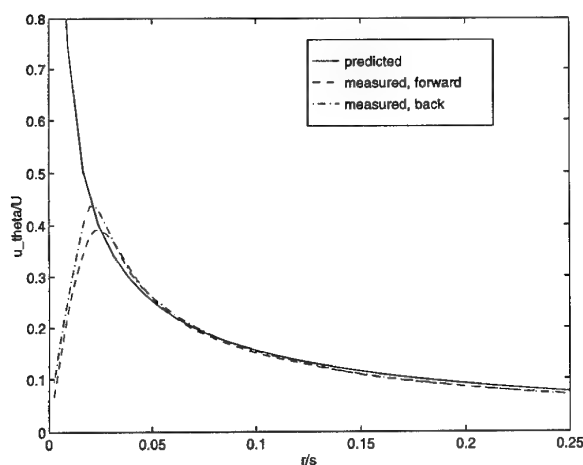


Figure 7.4 Measured and predicted vortex velocities at 10° .

The corresponding plots for the flaps out configuration are shown in Figs. 7.5 and 7.6. Here we find generally less good agreement than for the clean configuration—although the tip vortex velocities are still quite well predicted, the flap vortices show higher velocities than their theoretical counterparts at small radii, and then tend to drop below them at larger distances.

Further insight into this behaviour may be gained by considering vortex circulations, rather than velocities. Figure 7.7 shows the circulations for 5° incidence; those for 10° exhibit a similar pattern. Here we see that the relative overall circulations for each vortex are quite accurately predicted by the extended Betz method, although the lower overall circulation in the experimental results and the presence of some residual vorticity outside the vortices are reflected in lower absolute values. However, the distribution of the circulation in the flap vortices is

markedly different from the predictions; hence the lack of agreement in the velocity profiles.

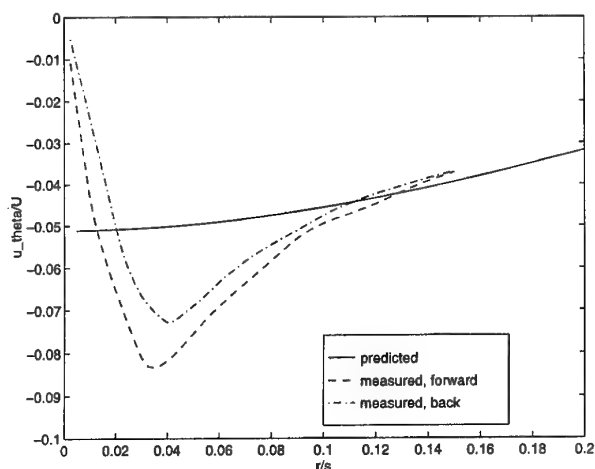


Figure 7.5(a) Measured and predicted inner flap vortex velocities at 5° .

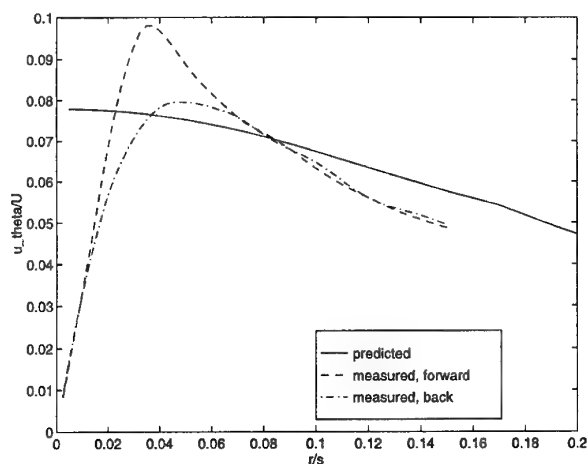


Figure 7.5(b) Measured and predicted outer flap vortex velocities at 5° .

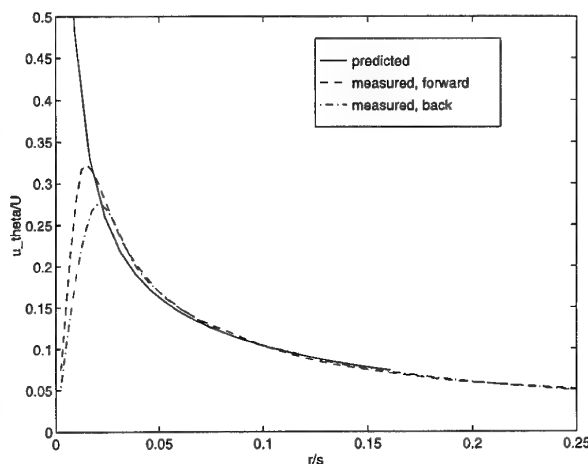


Figure 7.5(c) Measured and predicted tip vortex velocities at 5° .

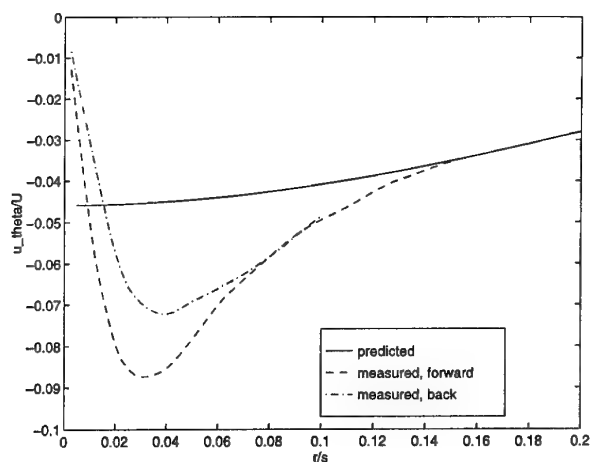


Figure 7.6(a) Measured and predicted inner flap vortex velocities at 10° .

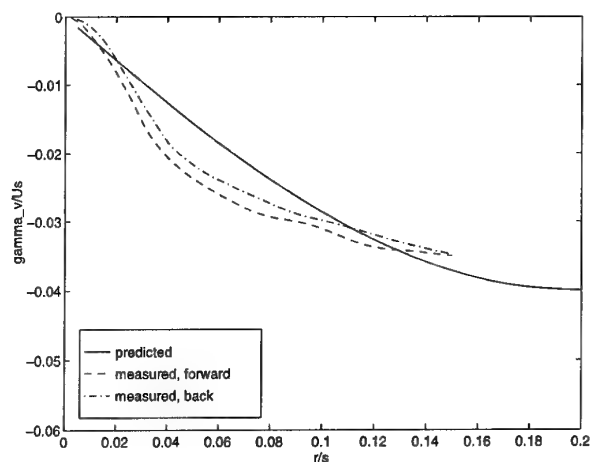


Figure 7.7(a) Measured and predicted inner flap vortex circulation distribution at 5° .

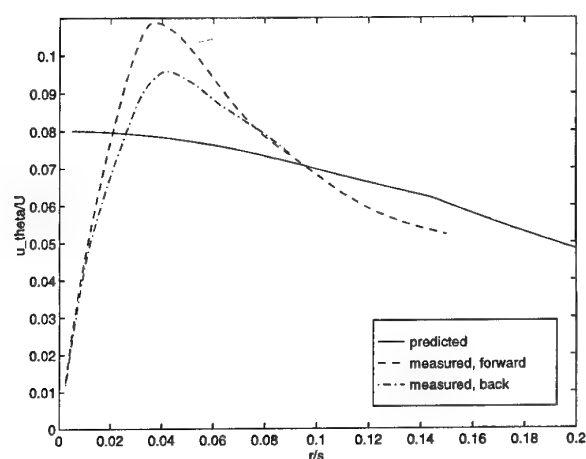


Figure 7.6(b) Measured and predicted outer flap vortex velocities at 10° .

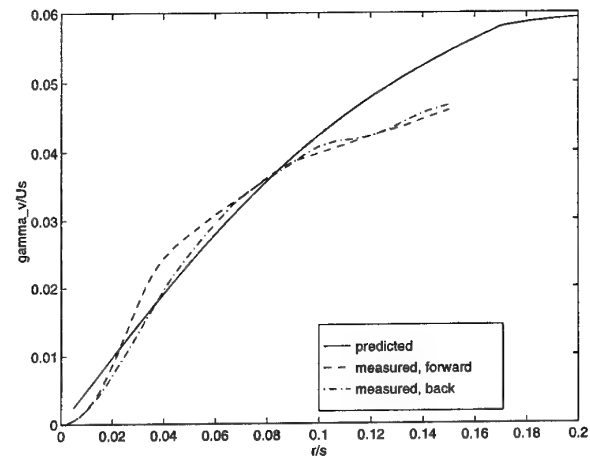


Figure 7.7(b) Measured and predicted outer flap vortex circulation distribution at 5° .

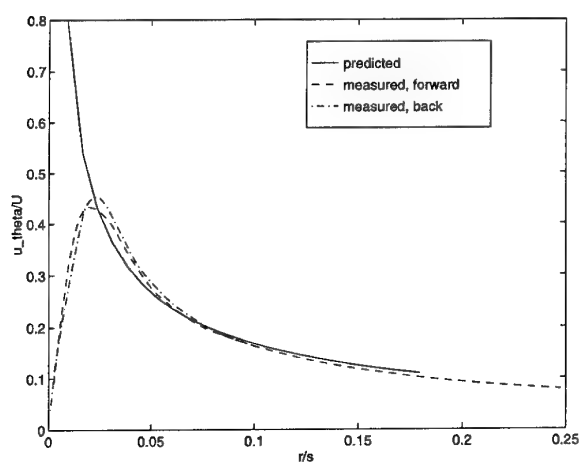


Figure 7.6(c) Measured and predicted tip vortex velocities at 10° .

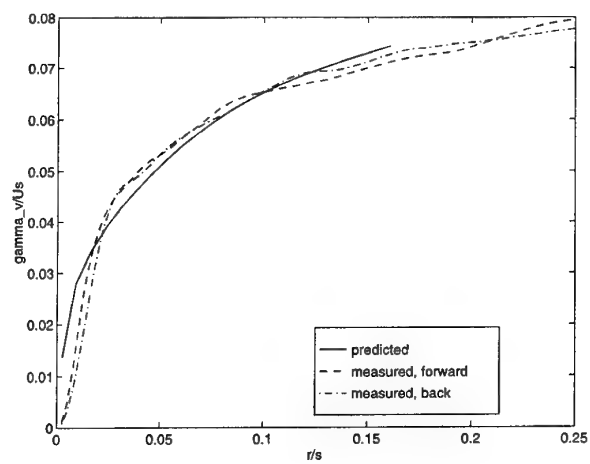


Figure 7.7(c) Measured and predicted tip vortex circulation distribution at 5° .

7.4 Discussion

The results presented in 7.3 show varying degrees of success for the Betz method and its extension. While the tip vortex velocity profile is excellently predicted for the clean configuration, and still well predicted for the flaps out configuration, the flap vortices are less accurately described. To understand the reasons for this, we must return to the assumptions inherent in the theory.

Firstly, the two-dimensional, inviscid flow assumption, according to which the overall circulation and spanwise centre of vorticity of each half of the wake are conserved, is quite well borne out by the results presented in 7.2. The further assumption of conservation of second moment of vorticity cannot be justified, but interestingly the original Betz method nonetheless predicts accurate tip vortex velocity profiles for the clean configuration. We postulate that this is because the kinematic roll-up model (Fig. 4.1), which arose from the third conservation assumption, still gives a good representation of the roll-up process, even though the conservation assumption itself is violated. Furthermore, the 10° incidence results imply that this holds true some way into the non-linear region of the lift curve, even though lifting-line theory itself is strictly only valid in the linear regime.

Given the success of the Betz method for the clean configuration, it is tempting to accept it for the flaps out configuration too, and blame the discrepancies on the lift distribution calculation. Thus, one could claim that the calculated lift distribution, represented by the full line in Fig. 7.8, should be replaced by the dashed line, which has the same lift and would give steeper velocity profiles in the flap vortices. The total wake circulation, which is defined by $\Gamma(0)$, would then be lower, in agreement with experimental results. However, the overall circulations of the flap vortices (Γ_{f1} and Γ_{f2} on Fig. 7.8) would increase, and this is not borne out by experiment. It therefore seems more plausible to attribute the lower experimental value for circulation to departures from the two-dimensional, inviscid model and accept the calculated lift distribution.

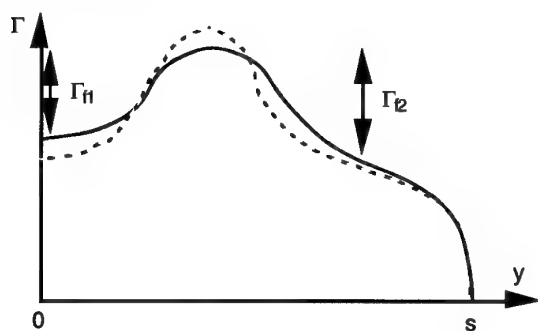


Figure 7.8 Lift distributions producing differing vortices for the same overall lift.

This leaves the kinematic model, Fig. 4.2, and the piecewise conservation of centre of vorticity assumption to be examined. Again, given the success of the clean configuration kinematic model, one is led to question the latter. However, it is straightforward to show that, for small radii, where the lift distribution can be expanded in a Taylor series about the roll-up point, the prescription given by (4.10) and (4.12) maximises the predicted vortex circulation for a given radius. We therefore conclude that

the main source of the inaccuracies in the extended Betz method is the kinematic model, Fig 4.2.

This statement should be qualified by noting that, if one vortex is dominant, the kinematic model seems to yield quite good results for that vortex. This would explain the agreement between theory and experiment found here for our tip vortices, and by Donaldson *et al* [2] for aircraft flap vortices in tower fly-by tests. However, smaller vortices will not be well predicted and, by implication, the theory will be generally suspect in cases where multiple vortices of similar strengths are shed. In such cases, its applicability will be restricted to predicting the number of shed vortices, and their overall circulation, which seem to be quite accurately determined by Donaldson *et al*'s criteria for vortex boundaries.

8. CONCLUSIONS

In this paper, we have presented an experimental assessment of the validity of the Betz method, and a proposed extension [2], for wake vortex prediction. The Betz method and its extension have been briefly described, and their approximations identified. Additionally, the concept of a kinematic model for the wake roll-up process, implicit in the method, has been explicitly introduced, aiding physical understanding of the approximations involved. The extent to which these are justified has been discussed with reference to an experimental study on a wing with a simple, generic representation of a high-lift system with flaps. Cross-flow velocities in two planes downstream of the wing have been obtained using a 'Chutube' yaw-meter and compared with the predictions of the Betz method, based on wing lift distributions derived from lifting-line theory. The comparisons show good agreement when the wing is in the 'clean' configuration, and only a single, tip vortex appears on each side of the wake, but are less satisfactory with the wing in the 'flaps out' configuration, when two additional vortices are generated by each flap. However, overall invariants derived from the fundamental assumption of two-dimensional, inviscid wake roll-up are still conserved, to a good approximation.

We conclude that, in general, the two-dimensional, inviscid approximation to the wake flow is valid, and furthermore that the simple kinematic model implied by the original Betz method (Fig. 4.1) is a good approximation for single vortex roll-up. These observations hold even at higher wing loadings, where the lift curve is non-linear and the lifting-line theory which forms the basis of this approach is strictly invalid. However, for wakes rolling up into multiple vortices, the extended Betz method will only give accurate velocity profile predictions for the dominant vortex, if one exists. The reason for the diminished accuracy in this case is most likely to be the inapplicability of the generalised kinematic roll-up model (Fig. 4.2), as the other assumptions of the method still appear to be satisfied. In particular, Donaldson *et al*'s [2] criteria for vortex roll-up centres and boundaries seem valid and, in conjunction with the condition of piecewise conservation of circulation, will give reasonable predictions for overall vortex circulations, even when the radial distributions are not reliable. If greater accuracy is required in this case, recourse to numerical simulations will probably be necessary.

ACKNOWLEDGEMENTS

This work has been greatly facilitated by the availability of the experimental apparatus described in 5.1, which was developed by F. Lam and Simon Burnell. In addition, David

Mauil has been a ready source of useful advice and apposite comment on the wake vortex problem.

REFERENCES

- [1] Betz A, 'Behaviour of vortex systems', *Zeitschrift für angewandte Mathematik und Mechanik* **12**(3), June 1932.
- [2] Donaldson C duP, Snedeker R S and Sullivan R D, 'Calculation of aircraft wake velocity profiles and comparison with experimental measurements', *J. Aircraft* **11**(9), 547-555.
- [3] Clements R R and Mauil D J, 'The rolling-up of a trailing vortex sheet', *Aero. J. Royal Aero. Soc.*, Jan. 1973, 46-51.
- [4] Krasny R, 'Computation of vortex sheet roll-up in the Trefftz plane', *J. Fluid Mech.* **184**, 123-155.
- [5] Batchelor G K, 'An introduction to fluid mechanics', Cambridge University Press 1985, 273ff.
- [6] Garner H C, Rogers E W E, Acum W E A and Maskell E C, 'Subsonic wind tunnel wall corrections', *AGARDograph* 109, 1966.
- [7] Chu J K, Rios-Chiquette E, Sarohia S and Bernstein L, 'The 'Chu-tube': a velocimeter for use in highly-sheared, three-dimensional steady flows', *Aero. J. Royal Aero. Soc.*, March 1987, 142-149.
- [8] Katz J and Plotkin A, 'Low-speed aerodynamics: from wing theory to panel methods', McGraw-Hill 1991, 193ff.
- [9] Gradshteyn I S and Ryzhik I M, 'Table of integrals, series and products', 4th ed., Academic Press 1980.

STRUCTURE, TRAJECTORY AND STRENGTH OF B747 AIRCRAFT WAKE VORTICES MEASURED BY LASER

J M Vaughan, D W Brown, G Constant, J R Eacock and R Foord

Electronics Sector, Defence Research Agency
St Andrews Road, Gt Malvern
Worcs. WR14 3PS, UK

1. SUMMARY

Wake vortices of aircraft landing at Heathrow have been measured with a coherent laser radar. Analysis of the vortex velocity profiles from B747 aircraft shows a series of symmetrical dips or inversions on approach to the central core. Such inversions are not predicted theoretically and contrast with the uniformly increasing velocity profiles observed from other aircraft. Vortex trajectories may also be reconstructed; in one case a B747 vortex, after initial descent, returned to the glideslope with undiminished strength over a minute later.

2. INTRODUCTION

In the process of generating lift all aircraft create transverse rotational flow in the air that has passed over each wing. This rotational flow rapidly evolves into two powerful, counter-rotating, vortices that extend as a pair of trailing ribbons behind the aircraft [1,2]. The characteristics of these wake vortices - their formation, strength, evolution, persistence, trajectory, mode of decay etc. - have been studied for many years; a comprehensive assessment of the state of knowledge in 1991 was given by Hallock [3], together with an extensive annotated bibliography [4]. The initial separation of the vortices is typically about 80% of the wing span; their rotational sense produces a strong downdraft in the region between them, and in free air they tend to sink at a rate of $1-2\text{ms}^{-1}$. Their trajectory is of course largely determined by the prevailing meteorological conditions; on approach to the ground the sink rate is reduced and the vortices tend to separate.

The existence of such vortices represents a potential hazard to following aircraft, particularly for smaller aircraft behind larger. Many studies in the 1970s, including laser measurements, helped to define separation minima between various categories of aircraft arriving at and departing from airports. Such separation minima limit the capacity for the world's busier airports; in consequence in the last few years there has been increased interest in the problem of wake vortices.

The present work derives from measurements at Heathrow with a coherent, continuous CO_2 laser radar

operating at $10.6\mu\text{m}$ wavelength; the equipment had both high spatial resolution and high Doppler frequency (hence velocity) resolution, and also high sensitivity. It was thus possible to measure precise velocity profiles of the vortices close to their central cores. Usually the peak Doppler shift rises monotonically on approach to the vortex core with increasing velocity gradient. However for the B747 aircraft the Doppler shift, and corresponding tangential velocity, increase towards the core but then undergo a series of inversions - dips in the usual increase of velocity - which are approximately symmetrical on either side of the centre. Such structures have not been observed previously; the most credible interpretation is of annular rings or flow lines of reduced speed around a higher speed central core. The strength and trajectory of B747 vortices have also been examined. In one remarkable case a vortex, after initial descent to $\sim 40\text{m}$, returned close to the aircraft glideslope at $\sim 85\text{m}$ altitude, over 60secs after passage of the generating aircraft. Analysis shows that the vortex had undiminished strength at this stage but in the next 15 seconds weakened rapidly in the core.

3. LASER MEASUREMENT OF WAKE VORTICES

In coherent laser radar (also known as lidar, ladar and Laser Doppler Velocimetry - LDV) the Doppler frequency shift in light scattered from a laser beam by small particles (aerosols) is measured. In the lower levels of the atmosphere, signal strength is generally high due to an abundance of aerosols and it is possible to measure atmospheric properties such as windspeed and direction, windshear, turbulence, and of course the air motion due to aircraft wake vortices. During the early 1970's and 1980's several investigations of wake vortices by laser radar at $10.6\mu\text{m}$ wavelength were conducted in Federal Aviation Agency (FAA) and NASA sponsored programmes and are documented in papers, reports and conference and workshop proceedings [5-12]. In other programmes in the late 1980's lidar measurements were made at Frankfurt Airport [13], in the United States at the NOAA Test Facility in Idaho Falls and also at Dallas Fort Worth [14,15]. Work is currently being carried out at Memphis Airport [16]; measurements have also been made with pulsed 1 and $2\mu\text{m}$ wavelength lidars [17,18].

In a recent experimental and theoretical paper [19] the interaction of a lidar beam with a rotational flow was analysed. It was shown that the most significant feature is a high frequency Doppler peak due to scattering from the immediate tangent region. As the beam gets closer to the vortex core, the Doppler shift of this peak rapidly increases and its intensity falls. A novel colour display of successive Doppler spectra was introduced which traces out the profile of wake vortices in a characteristic cusp-like form. Good agreement was found with experimental spectra recorded on aircraft vortices at Bedford Airfield.

4. MEASUREMENTS AT HEATHROW

The coherent lidar is similar to those described in several publications [19,20,21], and incorporates an eye-safe, stable CO₂ laser of ~8 Watt power output at 10.6µm and a 30cm diameter telescope. The continuous wave laser beam is brought to a focus, at ranges usually between 40m and 400m, which defines the pencil-like probe volume of greatest sensitivity to aerosol scattering. Typically at 100m focal range this probe volume is about 12m long and 1cm diameter. The Doppler shifted signal at frequency $\Delta\nu$ is generated in the lidar by light beating (heterodyne) techniques and analysed with a surface acoustic wave (SAW) spectrum analyser. At wavelength λ the line-of-sight velocity component V is given by the expression $(\lambda\Delta\nu/2)$; the available SAW bandwidth of 0-6MHz thus permits velocity measurements up to 31.8ms⁻¹ (equivalent to ~65 knots of air speed), with an instrumental accuracy of ~0.08ms⁻¹.

The Wake Vortex lidar was deployed at 5 sites near Heathrow airport over 28 days in December 1994, February/March 1995 and September/October 1995. Nearly 3000 records were obtained, in a wide range of atmospheric conditions, showing vortices generated by arriving aircraft at heights between 30m and 150m above ground level. Figures 1a-d show colour-coded spectra where the lidar beam was static and pointing upwards. Figure 2 is a lengthy record where the lidar beam scanned rapidly to the side in a plane normal to the glideslope. It should be noted in these records that the magnitude of the velocity component is shown and not its direction or sense. In Figures 1a,b, for example, the direction of flow between the cores is downward and outside them it is upward.

5. STRUCTURE IN THE B747 VORTEX

In Figure 1a the peak Doppler shift for the B757 vortices rises very sharply as it approaches the core with increasing velocity gradient. In Figures 1c-d for B747 aircraft the Doppler profiles are very different: the peak velocity increases towards the core but then undergoes a series of inversions, or dips, which are approximately symmetrical on either side of a sharper central core. It is worth emphasising a number of points. Firstly, the records shown are not unusual examples. All measurements examined to date of B747

aircraft show comparable features. This includes both B747-200 series aircraft and the newer B747-400 series with tip winglets. Secondly, the structures are not transient phenomena during the process of the initial wrapping up of the component elements of vorticity. The records shown, and many others, relate to fully mature vortices. Thirdly, because of the observed symmetry about the vortex core (which for Figures 1c and 1d extends over a period >4s), it is difficult to explain the observations by a mechanism involving two or more separate vortices interacting (eg. rotating around one another) to form a major vortex, or by some form of secondary minor vortex.

The most credible interpretation of the vortex spectra is of annular rings or flow lines, around the central core, of reduced speed. This is further supported by the positions of at least some of the subsidiary peaks within the individual Doppler spectra; close observation (of eg. Figure 1d) shows that these are approximately aligned and fall towards the centre of vortex. The situation may be analysed with reference to Figure 3a showing successive positions of a lidar beam interacting with an idealised rotational structure with flow inversion at radius i . The beam at tangent distance i will have a Doppler-shifted peak at frequency $V(i).(2/\lambda)$. Similarly the beam at tangent distance x will have a peak Doppler shift at $V(x).(2/\lambda)$ with an additional subsidiary peak due to scattering from the region 'A' (and also 'A¹') where the beam intersects the flow inversion. It is readily shown that such a velocity inversion leads to an increase (and peak) in the spectral density [19]. The Doppler shift of this subsidiary peak is derived from the line-of-sight velocity component at 'A' and is given by $V(i)\cos\theta(2/\lambda)$ where $\cos\theta$ is equal to x/i . The subsidiary peak shift is thus proportional to x/i and may be expected to fall linearly to zero at the centre of the vortex where x is zero. This situation is illustrated schematically in Figure 3b. In practice some distortion may be expected with flow lines not perfectly circular and symmetric and possibly having some helical character around the vortex core. Nevertheless the experimental measurements shown in Figure 3c give reasonable agreement with this model. Simple analysis also shows that, if the linear pattern on one side extends close to the centre and the cross wind is V_c , the inversion ring has an angular size of at least $V(i)/V_c$ radians. For the positions 1 ($V(i) \approx 13\text{ms}^{-1}$) and 2 ($V(i) \approx 8\text{ms}^{-1}$) marked on Figure 3b this corresponds to ~4 rads and ~2.5 rads respectively.

Further extending the profile analysis to the vortex core shows that for Figure 1c the diameter of the inner core region (where rotational speed falls towards the centre from a peak of ~20ms⁻¹) is ~1.0m, with an estimated error limit of ±0.2m. Outside this is a rotational sheath (particularly obvious on Figure 1c) where over a radial distance of ~0.5m the speed falls by ~5ms⁻¹. Analyses of several other records, have given similar values with inner core diameters in the range 0.8-1.3m.

Such clear persistent inversions and structure have not been observed previously [eg. 22,23], although something much weaker was observed in the early stages of an A320 vortex [19]. In early measurements with acoustic scattering, Burnham and Sullivan [23], distinguished between tubular and nontubular vortices, for which the general forms of Figures 1a and 1b provide obvious examples. Two recent theoretical papers [24,25] appear to indicate phenomena that may be related. Spalart [24] describes a tip vortex which may be surrounded by satellites for span loadings with 'steps'. Sreedhar and Ragab [25] using large-eddy simulation have described ring-shaped structures appearing around the core when the vortex is unstable.

Finally the question arises why such structures are evident in the vortices of B747 aircraft and are either absent, or less evident, from other aircraft. The answer must lie in the complex interaction of flap, wing tip and other vortex elements created by the individual aircraft type and the precise landing configuration. It is also evident that while having similar features the records of Figures 1b,c,d and Figure 3c are not identical and this must be due to the landing weight, airspeed, flap settings etc. of the individual B747 aircraft on those specific occasions.

6. TRAJECTORY OF B747 VORTICES

On most occasions wake vortices are advected away from the aircraft glideslope under the influence of the prevailing wind and their natural sink rate and divergence. Analysis of Figure 2 provides however a most unusual example of a long-lived vortex returning close to the glideslope over 60s after passage of the generating aircraft. Figure 4 was constructed on the basis of measurements off an enlarged record, and the further evidence provided by relative signal strength, cross wind and rotational sense, together with requirements for consistency in successive positions of the vortices. After ~25s the near-wing vortex is 40m above ground but in the presence of tall trees up to 20-25m. The vortex may thus be expected to be well into ground effect with reduced sink rate and tendency to diverge from its partner. It is also apparent on the Doppler record that at this stage the cross wind has fallen away. This evidence forces the conclusion that the vortex traverses the loop shown in Figure 4 from 24s to 53.5s. It then ascends steadily between 53.5s and 74s, passing through the focal region close to the glideslope. The final signature at 86s is at the very top of the scan and the vortex core has almost certainly passed out of the scan sector.

It is worth seeking some physical basis for this complex trajectory in order to develop more confidence in predictions of vortex behaviour. The initial sink rate, which from 4s to 24s is $\sim 1.6\text{ms}^{-1}$, is much as expected for two B747 vortices interacting in a free atmosphere (see next section). The move upwind from 24s to 39s averages $\sim 0.7\text{ms}^{-1}$ horizontal velocity and

may be ascribed to the natural divergence of the vortices in ground effect and a falling away of the light and variable cross wind. After 39s the vortex rises steadily at $\sim 1.2\text{ms}^{-1}$ and moves to the south (downwind) at $\sim 0.7\text{ms}^{-1}$. A possible explanation for its ascent may be available from the meteorological conditions. The weather was cold but the vortex may have entrained warmer air - from engine exhaust or due to a natural temperature gradient - when it formed at 85m. It descended to 40m under the influence of its 'twin', but as the vortices separated this interaction would weaken and the warmer air trapped in the vortex would lead to its subsequent rise. While extremely rare it should be emphasised that this is not an isolated result; appraisal of other records taken on the same morning shows vortices, that initially sank but then returned to a position high in the scan.

7. STRENGTH OF B747 VORTICES

The strength of vortex circulation or vorticity $\Gamma(r)$ is given by the expression

$$\Gamma(r) = 2\pi r V(r) \quad m^2 s^{-1} \quad \dots 1$$

where $V(r)$ is the rotational speed at radius r . From measurements with a static, upward-looking lidar, a particularly convenient way to derive a value of vorticity is to consider the velocity field mid-way between the vortices. If the vertical downward velocity in this region is measured as V_v then one half is due to each vortex. With the corresponding vortex separation of $2s$ the vorticity $\Gamma(s)$ is thus simply given by $\pi s V_v$. At large distances $V(r)$ will be generally proportional to r^{-1} . Thus the downdraft at distance $2s$ (and hence the sink rate of each core) will be given by $V_v/4$.

To complete the measure of vortex circulation one needs to convert the horizontal time scales of Figures 1a,b to distance scales in order to obtain a value s . This requires a measure of the effective cross wind, which can be derived in a number of ways: 1) from ancillary measurements of wind speed and direction by other local equipments - in the present case an adjacent Doppler wind lidar; 2) from a line-of-sight wind component if measured by the vortex lidar immediately prior to the vortex arrival; and 3) from the transit time of the vortices as they move the known distance from near the centre line to the lidar beam. These three methods have been found to give fair agreement - generally within 10-15%. For the records of Figures 1a,b values of core separation $2s$ of 28.6m and 44.8m were derived, compared with initial values of 29.8m and 46.8m expected for these aircraft under the assumption of elliptical wing loading [2]. The corresponding values of vorticity are for the B757 vortex $\Gamma(14.3\text{m}) = 331\text{m}^2\text{s}^{-1}$ (at mean age 16s) and for

the B747 vortex $\Gamma(22.4\text{m}) = 545\text{m}^2\text{s}^{-1}$ (at mean age 17s), in reasonable agreement with expectation.

Considering the scanned records, it is obvious from the Doppler spectra of Figure 2 that the vortex remains strong at least up to signature k at 74s. From this record vortex diameters $D(V)$ have been evaluated, from successive profiles, at the tangent velocity components of 6,8,10, and 12ms^{-1} and are plotted in Figures 5. The results show that $D(V)$ remains constant, within experimental error, over the period 4 to ~60 secs. After this $D(V)$ reduces, particularly near the core, where at 74 secs $D(12\text{ms}^{-1})$ has approximately halved, from 9.1m to 4.6m. Changes of $D(V)$ are less marked at lower velocities; $D(6\text{ms}^{-1})$ remains close to 27m out to 70s. The corresponding value of circulation $\Gamma(13.5\text{m})$ is $509\text{m}^2\text{s}^{-1}$ which is comparable with the value above from Figure 1b.

These present results on vortex decay are not altogether consistent with previous observations [eg. 7,8]. Burnham and Hallock [7] showed (their figure 9) a fairly uniform decay of vortex strength with age at 3 radii: 5,10 and 20m for B707 and DC8 aircraft, measured with acoustic sensing. Burnham [8] similarly showed (his figures 19 and 25-27) a generally uniform decay at 4 radii: 5,10,15 and 20m for a B747 in landing configuration, with measurements made by an LDV. Over the years many theoretical studies have been made of wake vortex decay and the contributing mechanisms of diffusion, turbulence and density stratification [eg. 26-30]. In the prevailing conditions of record 80039 (Figure 2) vortex decay commencing at ~60 secs is consistent with these treatments. The present results, with decay starting at the centre, have some correspondence in the change of velocity profile with the recent calculations of Sreedhar and Ragab [25] (as shown in their figure 18). Woodfield has suggested that in fact better agreement could be obtained with a modified form of profile combined with the slower development and decay associated with smaller (negative) gradients of velocity (A. Woodfield - private communication, January 1996).

8. CONCLUSIONS

Laser Doppler measurements made with high spatial and spectral resolution have revealed several novel features of the B747 wake vortex. LDV techniques offer the prospect of quantitative measurement of highly complex phenomena in a real, flying environment as opposed to reduced scale, wind-tunnel testing. Analysis of such LDV data should permit both precise comparison with theoretical studies and improved understanding of vortex evolution as an aid to safe operation of airports.

Acknowledgements.

Most of the experimental work at Heathrow and some of the analysis was undertaken under contract for the Chief Scientist's Division of the UK National Air Traffic Services as part of their R&D programme to support the safe improvement of airport capacity. We are greatly indebted to J Greenwood of NATS(CAA) and A Woodfield for many valuable discussions of these problems.

REFERENCES

1. Lamb, H., "Hydrodynamics", 6th Ed., Cambridge University Press, Cambridge, 1932.
2. Glauert, H., "The Elements of Aerofoil and Airscrew Theory", 2nd Ed., Cambridge University Press, Cambridge, 1959.
3. Hallock, J.N., 1991, "Aircraft wake vortices: An assessment of the current situation", Report No. DOT-FAA-RD-90-29, DOT-VNTSC - FAA- 90-6 (available through: National Technical Information Service, Springfield, Virginia 22161, USA).
4. Hallock, J.N., 1991, "Aircraft wake vortices: An annotated bibliography (1923-1990)", Report No. DOT-FAA-RD-90-30, DOT-VNTSC-FAA-90-7 (available as ref. 3).
5. Huffaker, R.M., Jelalian, A.V. and Thomson, J.A.L., 1970, "Laser- Doppler system for detection of aircraft trailing vortices", Proc. IEEE, 58, 322. Huffaker, R.M., Jelalian, A.V., Keene, W.H. and Sonnenschein, S.M., 1971, in "Aircraft Wake Turbulence and its Detection", edited by J.H. Olson, A. Goldburg and M. Rogers, (New York: Plenum), pp. 113-124: see also: Jelalian, A.V., 1992, Laser Radar Systems (Boston: Artech), p.195.
6. Huffaker, R.M., Jeffreys, H.B., Weaver, E.A., Bilbro, J.W., Craig, G.D., George, R.W., Gleason, E.H., Marrero, P.J., Reinbolt, E.J. and Shirey, J.E., 1975, "Development of a laser Doppler system for the detection, tracking, and measurement of aircraft wake vortices", Report No: FAA - RD - 74 - 213 (available as ref. 3).
7. Burnham, D.C. and Hallock, J.N., 1981, "Chicago monostatic acoustic vortex sensing system, Vol. II: decay of B707 and DC-8 vortices", Report No. FAA-RD-79-103.II. (available as ref. 3).

8. Burnham, D.C., 1982, "B-747 vortex alleviation flight tests: Ground-based sensor measurements", Report No. DOT-FAA-RD-81-99. (available as ref. 3).
9. Hallock, J.N., (editor), 1977, Proceedings of the Aircraft Wake Vortices Conference, FAA-RD-77-68, Cambridge, Mass., (available as ref. 3).
10. Wood, W.D., (editor), 1979, Proceedings of FAA/NASA Workshop on Wake Vortex Alleviation and Avoidance, FAA-RD-79-105, Cambridge, Mass., (available as ref. 3).
11. Wilson, D.J., Zalay, A.D., Brashears, M.R., Craven, C.E., Shrider, K.R. and Jordan, A.J., 1979, "Full-scale wake flow measurements with a mobile laser Doppler velocimeter", *J. Aircraft*, 16, 155-161.
12. Hallock, J.N., (editor), 1991, Proceedings Aircraft Wake Vortices Conference, Vols. 1 and 2, DOT/FAA/SD-92/1.2; DOT-VNTSC-FAA-92-7.2, Washington D.C., (available as ref. 3).
13. Koepp, F., 1994, "Doppler lidar investigation of wake vortex transport between closely spaced parallel runways", *AIAA Journal*, 32, 805-810.
14. Rudis, R.P., (editor), 1990, Wake Vortex Research Data Package, Volpe National Transportation System Center; Report No. VNTSC/IDF-1, (available Volpe NTSC, Kendall Square, Cambridge, MA02142, USA).
15. Rudis, R.P., 1991, Wake Vortex Research Data Package, Volpe National Transportation System Center. Vol. I, II and III; Report Nos. VNTSC/IDF-A, 2B, 2C (available as ref. 14).
16. Heinrichs, R.M., Freehart, R.E., Dasey, T.J. and Mandra, R.S., 1995, "Development and performance of a cw coherent laser radar for detecting wake vortices", OSA Technical Digest Series Vol. 19, Paper TuD3, p. 186-189.
17. Hannon, S.M. and Thomson, J.A., 1994, "Aircraft wake vortex detection and measurement with pulsed solid-state coherent laser radar", *J. Mod. Opt.* 41, 2175-2196.
18. Hannon, S.M., Henderson, S.W. and Thomson J.A., "Recent 2 μ m Doppler lidar measurement results", OSA Technical Digest Series, Vol. 19, Paper TuD2, p. 182-185.
19. Constant, G.D.J., Foord, R., Forrester, P.A. and Vaughan, J.M., 1994, "Coherent laser radar and the problem of aircraft wake vortices", *J. Mod. Opt.* 41 2153-74.
20. Woodfield, A.A. and Vaughan, J.M., 1993, "Airspeed and wind shear measurements with an airborne CO₂ cw laser", *Int. J. Aviat. Safety*, 1, 207-224.
21. Vaughan, J.M. and Forrester, P.A., 1989, "Laser Doppler velocimetry applied to the measurement of local and global wind", *Wind Engineering*, 13, 1-15.
22. McCormick, B.W., Tangler, J.L. and Sherrieb, H.E., 1968, "Structure of trailing vortices", *J. Aircraft*, Vol. 5, No. 3, 260-267.
23. Burnham, D.C. and Sullivan, T.E., 1974, "Influence of flaps and engines on aircraft wake vortices", *J. Aircraft Eng. Notes*, Vol 11, No 9, 591-2.
24. Spalart, P.R., "On the motion of aircraft wakes in a stably stratified fluid", paper in preparation, 1996.
25. Sreedhar, M.K. and Ragab, S.A., 1994, "Large eddy simulation of a longitudinal vortex", AIAA 94-0529, 1-17.
26. Crow, S.C., 1970, "Stability theory for a pair of trailing vortices", *AIAA Journal*, Vol. 8, No. 12, 2172-2179.
27. Crow, S.C. and Bate Jr, E.R, 1976, "Lifespan of trailing vortices in a turbulent atmosphere", *J. Aircraft*, Vol. 13, No. 7, 476-482.
28. Greene, G.C., 1986, "An approximate model of vortex decay in the atmosphere", *J. Aircraft*, Vol. 23, No. 7, 566-573.
29. Neuhart, D.H., Greene, G.C., Satran, D.R. and Holbrook, G.T, 1986, "Density stratification effects on wake vortex decay", *J. Aircraft*, Vol. 23, No. 11, 820-824.
30. Sarpkaya, T. and Daly, J.J., 1987, "Effect of ambient turbulence on trailing vortices", *J. Aircraft*, Vol. 24, No. 6, 399-404.

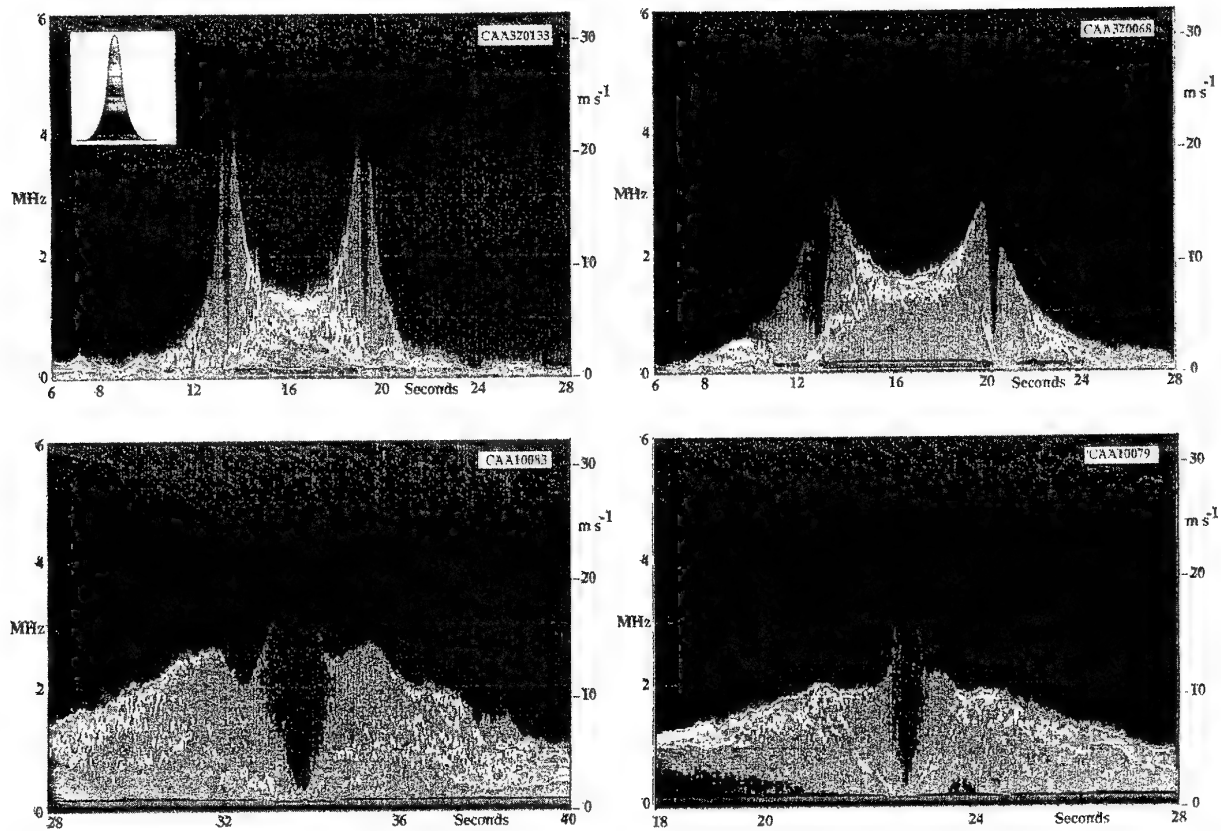


Figure 1 Doppler spectra (recorded at 25s^{-1}) from wake vortices carried by the prevailing cross wind through a static, upward looking lidar. Each spectrum is plotted vertically and colour coded for amplitude as shown by the insert. The time after passage of the generating aircraft is shown on the horizontal scale, the Doppler frequency (left hand) and equivalent velocity component (right hand) are on the vertical scales. a) Pair of vortices from a B757 aircraft (CAA 320133, 3 Oct. 1995); lidar elevation 90° and focal range 110m. The cross wind was 4.9ms^{-1} ; note the very sharp profiles of the vortices, rising close to the top of the scale, on either side of the cores. The downflow midway between the vortices is 7.4ms^{-1} . b) Pair of vortices from a B747-200 aircraft (CAA 320068, 3 Oct. 1995); lidar elevation 90° and focal range 115m.

The cross wind was 6.0ms^{-1} and downdraft $\sim 0.7\text{ms}^{-1}$. Note the characteristic shape with broad, steadily rising profile up to $\sim 12\text{ms}^{-1}$ and then rounding over into a series of inversions. The corrected downflow V_v between the vortices is 7.75ms^{-1} . c) Single vortex from a B747-200 (CAA 10083, 2 Dec. 1994) on enlarged scale to show the detail at the top of the vortex profile; lidar elevation 80° and focal range 70m, the light and variable cross wind was $\sim 1.8\text{ms}^{-1}$. Note the very marked inversions on either side of the sharp inner core. d) Single vortex from a B747-400 (CAA 10079, 2 Dec. 1994); lidar elevation 90° and focal range 70m; the cross wind was $\sim 4.3\text{ms}^{-1}$ and updraft $\sim 0.8\text{ms}^{-1}$. In this case the inversions are less marked on either side of the inner core.

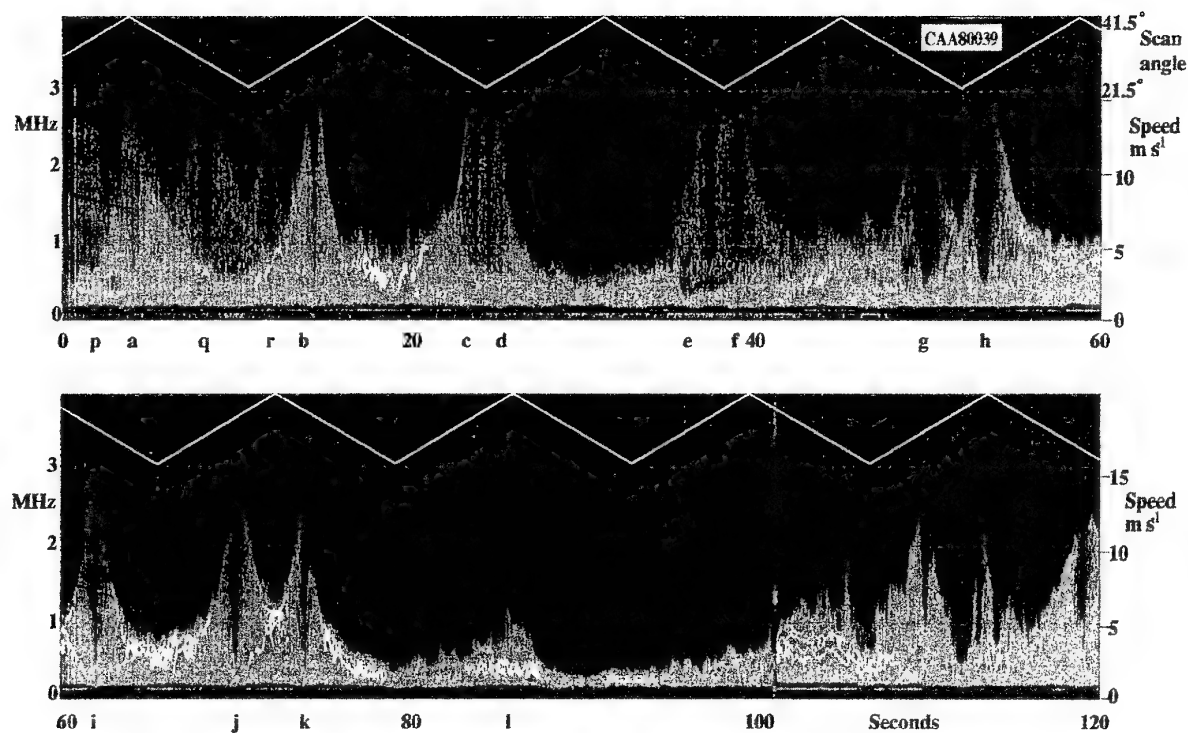


Figure 2 Temporal record (CAA 80039, 12 Dec. 1994) of Doppler spectra similar to Figure 1 but with a scanning lidar beam. The saw-tooth scan ($31.5^\circ \pm 10^\circ$) is shown in the upper white trace; the scan rate was $\sim 3^\circ \text{s}^{-1}$. The lead aircraft was a B747-200 followed by a second B747 at 102s which passed through the lidar beam and gave the strong return evident at that time. In the record there are at least 12 signatures due to the lead aircraft. The initial appreciation was that the first group (labelled a-d) was from the far-wing vortex, followed by a second group from the near-wing vortex (for the aircraft and lidar geometry see Figure 4). More careful inspection showed that this could not provide the explanation. The overlapping set of faint vortex spectra at p,q,r are due to the far vortex and all the others are due to the near-wing vortex. The vortex trajectory is reconstructed in Figure 4.

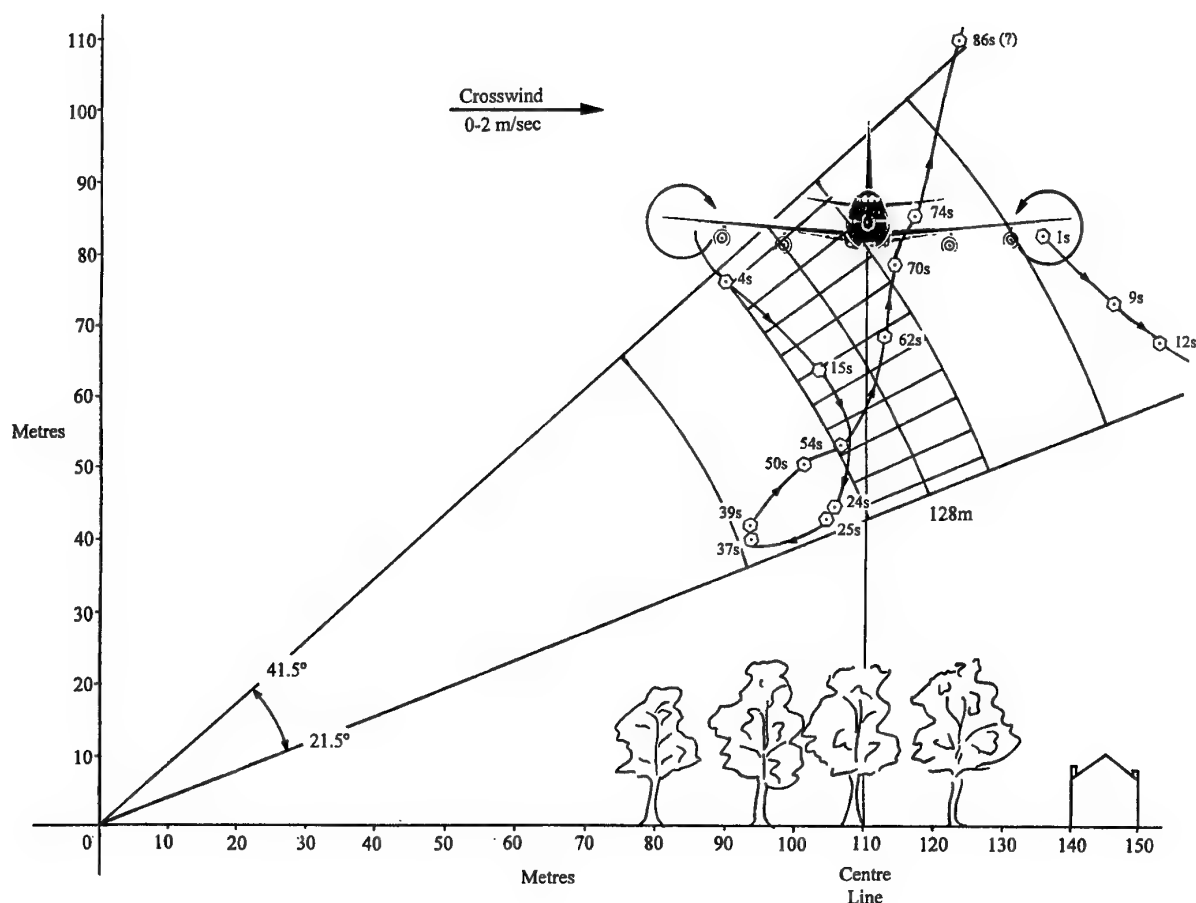


Figure 4 Reconstruction of vortex trajectories for record CAA 80039 (Figure 2). The lidar was sited at a position ~110m north of the centre line with the aircraft (B747-200) ~85m above ground flying E to W. The lidar was set to focus at ~128m range and the scan in the N-S plane is shown extending over $31.5 \pm 10^\circ$. The wind was WNW, about $5-6\text{ms}^{-1}$ at $\sim 295^\circ$ at a height of 75m, giving a variable cross wind of $0-2\text{ms}^{-1}$ from the north. The weather was cold ($3-5^\circ\text{C}$) with occasional rain and sun. The vortex signatures p,q,r (Figure 2) are ascribed to the far wing vortex and shown plotted at their corresponding angles at 1s, 9s and 12s. Signatures a,b and c-d are plotted (at 4s, 15s and 24-25s) with b (15s), the strongest return, closest to the focal range of 128m. Analysis of signatures e to k shows the vortex hovering in the lower part of the scan (e,f,g,h at time 37s, 39s, 50s and 54s) then rising rapidly (i,j,k - 62s, 70s, 74s) and also increasing in signal intensity from e to i (37s to 62s). The final signature at 86s is at the very top of the scan.

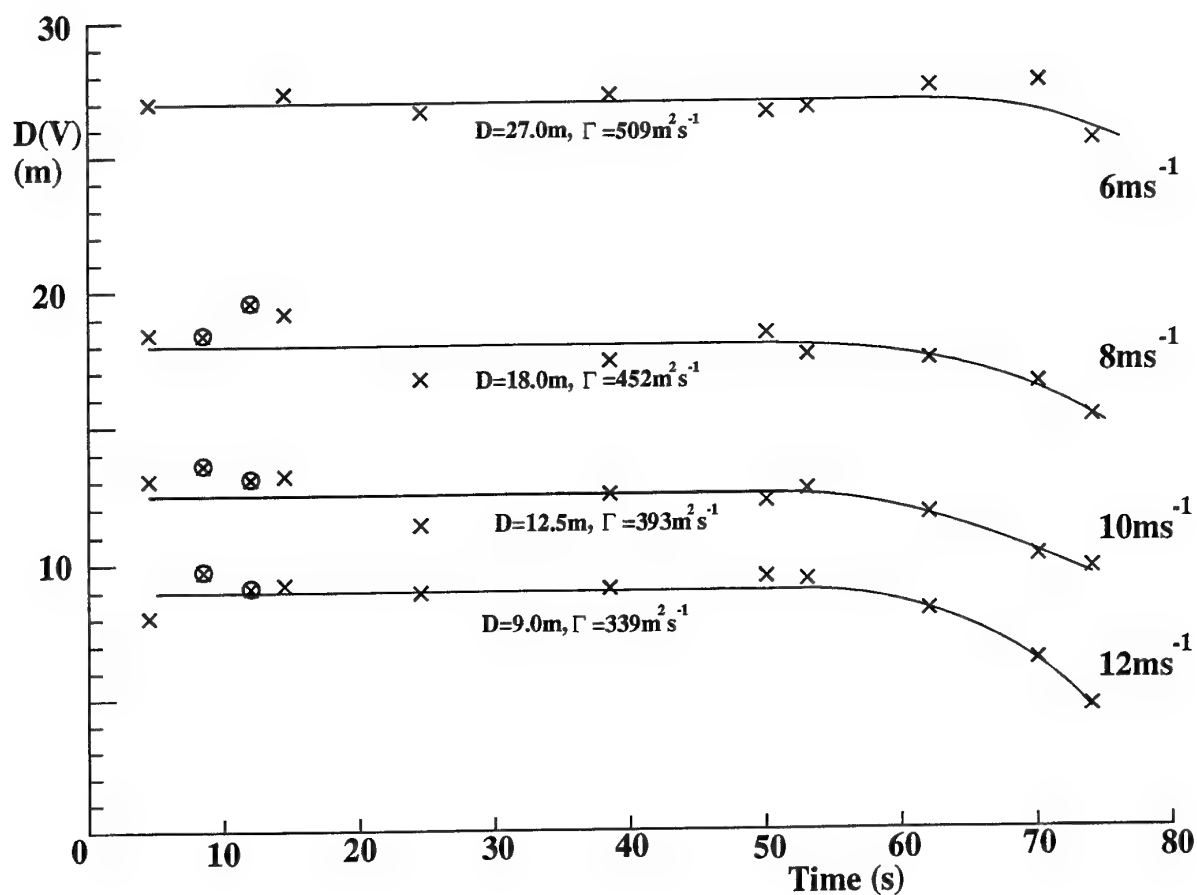


Figure 5 Vortex diameters $D(V)$ at four different values of tangent velocity V derived from the successive vortex records of Figure 2. Allowance has been made for the relative angular movement of each vortex and the lidar scan and also the changing range to the vortex (Figure 4). The circled crosses are from the far-wing vortex. The experimental (limit) error on individual points is up to about $\pm 1.5\text{m}$ for the weaker spectra. Within experimental error the vortex diameters are constant up to 60s and reduce thereafter.

Wake Vortex Decay Near the Ground Under Conditions of Strong Stratification and Wind Shear

R. P. Rudis

Volpe National Transportation Systems Center
Kendall Square
Cambridge MA 02142
USA

D. C. Burnham

Scientific and Engineering Solutions, Inc.
P. O. Box 64
Orleans MA 02653
USA

P. Janota

System Resources Corporation
128 Wheeler Road
Burlington MA 01803
USA

1. SUMMARY

Using the tower fly-by method, decay measurements were made on wake vortices generated by B-727, B-757 and B-767 aircraft. In addition to a 60-meter instrumented tower, two remote sensing systems were deployed: (1) Laser Doppler Velocimeter (LDV) (high resolution vortex profiles at ranges of 40-200 meters) and (2) Monostatic Acoustic Vortex Sensing System (MAVSS) (lower resolution profiles up to 500 meters beyond the tower location). Typical early morning meteorology during the test period consisted of stratified drainage flows. Because of the persistent crosswind, the MAVSS gave the most complete vortex decay information. Meteorological conditions were measured by instruments on the tower and on a tethered sonde. The analysis looked for statistical relationships between vortex lifetime and several meteorological parameters, treated independently. Due to the meteorological conditions of stratification, low turbulence and wind shear, the upwind vortex lasted longer than the downwind vortex; the circulation remained above $140 \text{ m}^2/\text{s}$ for up to 125, 150 and 170 seconds for the B-727, B-757 and B-767, respectively. However, in every case, the crosswind was strong enough to sweep both wake vortices away from the generating location; in some cases the vortices traveled more than 500 meters laterally. Although these durations are much longer than the normally observed vortex lifetimes, they are related, according to the analysis, to strong crosswind shear coupled with low turbulence levels. While this long vortex migration at the observed strength levels might represent a potential vortex encounter hazard for operations on a downwind parallel runway, the drainage flow conditions which led to this unusual vortex behavior would be unlikely to occur at most airports.

2. INTRODUCTION

In September 1990 wake vortex decay measurements were made at the Idaho National Engineering Laboratory (INEL) in Idaho Falls, Idaho. Apart from helicopter wake tests conducted in the mid 1980s, this test was the first major wake vortex test conducted by the Federal Aviation Administration since the extensive airport data collection efforts of 1973-1980. Previous reports provided an overview of the test¹ and a detailed analysis of the instrumented tower data². This paper is the first detailed presentation of the MAVSS decay measurements.

2.1 Test Goals

Three goals were defined for the test:

1. Characterize the wakes of aircraft introduced into service since 1980.
2. Compare the vortex measurements from the three measurement techniques used in the 1970s.
3. Study the effects of meteorological conditions on the decay of wake vortices.

This paper addresses the third test goal.

2.2 Sensor Selection

The three methods used to measure wake vortices in the 1970s were deployed at Idaho Falls to make the first simultaneous measurements on the same wake vortices:

1. Tower instrumented with hot-wire anemometers²,
2. Laser Doppler Velocimeter (LDV)³, and
3. Monostatic Acoustic Vortex Sensing System (MAVSS)⁴.

The instrumented tower was installed and operated by Idaho Falls NOAA personnel. The Volpe Center installed and operated the LDV and the MAVSS. Because of the differences in coverage of the three techniques, simultaneous measurements had never been made before. Table 1 summarizes the characteristics of the three techniques.

Table 1. Characteristics of Measurement Techniques

Characteristic	Tower	LDV	MAVSS
Measurements per vortex	1	Unlimited	up to 8
Measure stationary vortex?	No	Yes	No
Maximum vortex height (m)	61	250	70*
Vortex radius resolution (m)	0.6	0.3-1.0	3-6
Direction of vortex scan	Vertical	Diagonal	Horizontal

* Double range returns detected in some cases

3. TEST DESCRIPTION

3.1 Configuration

Figure 1 shows the configuration of the Idaho Falls test. The layout was designed for the early morning conditions when, in September, the wind is typically from the northeast because of drainage flows from nearby mountains.

Tower - For most runs the aircraft flight path was selected to optimize the tower measurements. The aircraft flew upwind of the 60-meter tower at an altitude above the top of the tower (75 to 110 meters above the ground). The distance of the

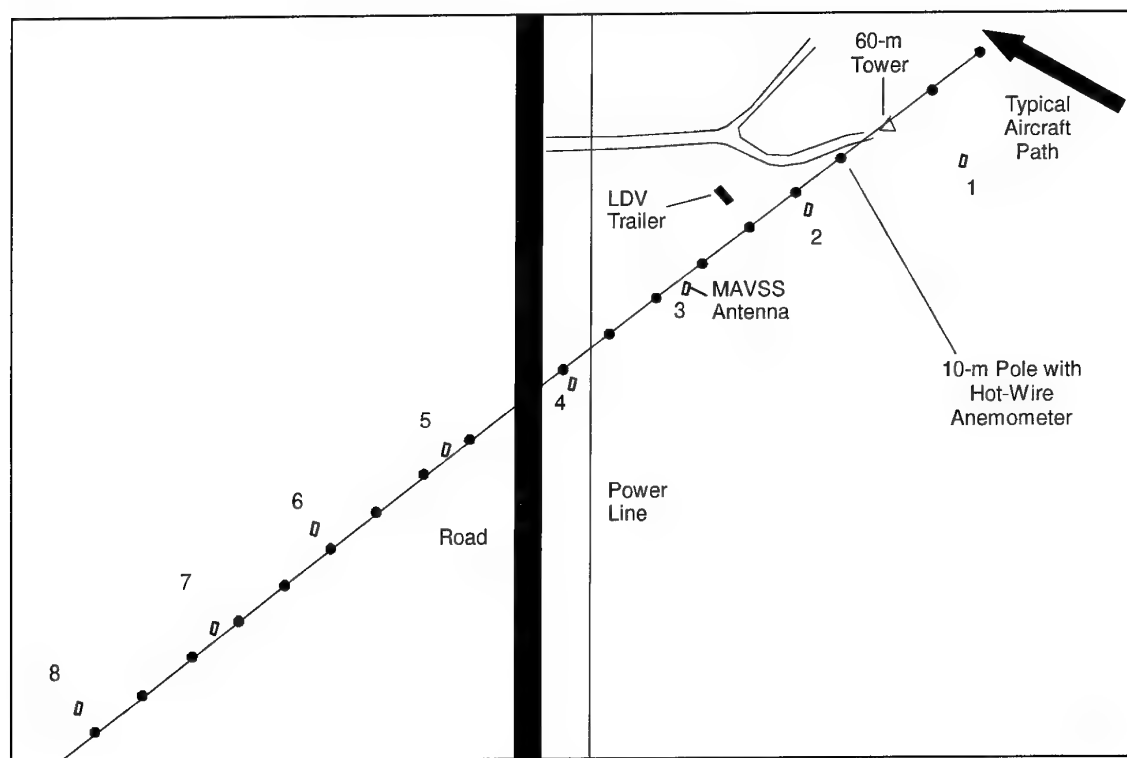


Figure 1. Idaho Falls Test Layout. The aircraft flew at a compass heading of 300 degrees.

aircraft from the tower was adjusted so that the wake vortices would hit the upper half of the tower, to minimize the effects of the ground on the vortices measured by the tower. The tower hot-wire anemometers were supplemented by an array of hot-film anemometers on 10-meter poles at 30-meter spacing (black circles in Figure 1).

LDV - The LDV (useful range of 40-200 meters) was located downwind of the tower at a distance that gave good measurements at the range of the tower, but could also measure vortices downwind of the LDV location.

MAVSS - Eight MAVSS antennas were located along the array of 10-meter poles at a spacing of 75 meters.

The tower made at most a single measurement of each vortex. The LDV made many measurements of each vortex. However, for most early morning runs the crosswind transported the vortices beyond the range of the LDV before they had completely decayed. Consequently, for most runs, the MAVSS measurements give the most complete picture of vortex decay. For this reason, this paper will concentrate on MAVSS data.

3.2 Sensor Descriptions

Hot-wire anemometer - The hot-wire anemometers were installed at 0.6-meter spacing on the tower. The anemometer wires were oriented parallel to the aircraft flight path. They therefore measured the magnitude of the wind in the plane perpendicular to the flight path; this plane contains the wake vortex tangential velocity. Unfortunately, the ambient crosswind is also in this plane and must therefore be accounted for in analyzing the hot-wire anemometer measurements.

LDV - The cw LDV achieves range resolution by focusing its beam at a selected range. The LDV scan plane was oriented to be perpendicular to the aircraft flight path. The LDV scan pattern consists of 3 to 5 arcs at different focal ranges. The

vortex tangential velocity is measured as the maximum Doppler shift. The LDV provides high resolution (0.5-meters) vortex tangential velocity profiles (0.55 m/s resolution, 30 m/s maximum velocity).

MAVSS - The MAVSS measures the vertical profile of the vertical wind component above each MAVSS antenna. The ambient wind, which is horizontal near the ground, is not measured. Thus, the Doppler shifts measured by the MAVSS are direct measurements of the wake vortex tangential velocity. The maximum range was set at 70 meters for the Idaho Falls test. The pulse width used gives 3.3-meter vertical resolution; the data were analyzed with range gates spaced at 2.7 meters. Separate transmit and receive antennas are used to minimize antenna ringing that would otherwise limit the minimum range of the measurement. The two antennas are oriented to overlap at 23-meter range.

A wake vortex is measured every time it passes over a MAVSS. The vortex tangential velocity is taken as the vertical velocity from the range gate with the highest velocities. [This algorithm underestimates the tangential velocity for early vortex ages when the vortex is descending through several range gates while it is being measured.] The velocity versus time data is converted to velocity versus radius data by measuring the vortex transport speed (from arrival times at successive MAVSS antennas). The measurements near the vortex core are smeared by the limited spatial resolution of the MAVSS (3-6 meters depending on the range) and by two anomalies associated with small vortex cores:

1. Noise generated by the vortex, and
2. Acoustic reflections from the core.

3.3 Test Aircraft

Two new-generation aircraft were leased for the tests: Boeing 757 and 767. In order to relate the results to previous studies,

a Boeing 727 was also leased. Each aircraft was operated on two test days. Table 2 lists characteristics of the three test aircraft.

Table 2. Test Aircraft Characteristics

Parameter	B-727-222	B-757-200	B-767-200
Wingspan (m)	32.9	37.9	47.6
Max Landing Weight (kg)	64,800	90,000	109,100
Max. Takeoff Weight (kg)	68,200	122,700	140,900

3.4 Meteorological Measurements

Seven levels of the tower were instrumented to measure temperature, dew point, wind speed, and wind direction. In addition, a tether sonde, operated about one half kilometer upwind of the tower, measured the same parameters from ground level to 200 meters above the ground.

4. MORNING TEST RESULTS

This section presents the combined test results for all morning runs, separated by aircraft type. Sections 5 and 6 will present an analysis of all runs that processes each run individually and then combines the results from all aircraft types.

4.1 Circulation Estimation Method

The normal way of specifying the vortex strength is in terms of its circulation Γ . For an axially symmetric vortex the circulation is a function of the vortex radius r and is related to the tangential velocity $v(r)$ by: $\Gamma(r) = 2\pi r v(r)$. The circulation profile $\Gamma(r)$ starts at zero for $r = 0$ and increases to an asymptotic value $\Gamma(\infty)$ which is a characteristic of the vortex; its initial value can be calculated from aircraft and atmospheric parameters. Measuring $\Gamma(\infty)$ is a compromise between (1) using a large radius where the full value is observed but the velocities are small and therefore prone to error and (2) using a small radius where the velocity is better defined but the asymptotic value may not yet be reached. A practical estimate of $\Gamma(\infty)$ can be obtained from the vortex velocity profile by averaging $\Gamma(r)$ over a range of radii r where (1) the velocity data are valid, (2) the radii are as large as practical without including the other vortex and (3) the number of data points included is as large as possible to average away random errors. Both sides of the vortex must be included in the average to eliminate the effects of the ambient wind and vortex motion. For LDV data a practical averaging range which avoids velocity errors is 4.5 to 7.5 meters. Because the MAVSS has lower spatial resolution but no low velocity limits, slightly larger radii (6 to 10.5 meters) are more appropriate.

4.2 MAVSS Circulation Measurements

The MAVSS circulation measurements for the morning runs are plotted in Figures 2-4 for the B-727, B-757 and B-767, respectively. A variety of flap settings were used for the various runs; more than half the runs used landing flaps. The detection reliability of the MAVSS becomes uncertain when the circulation falls significantly below 100 m^2/s . The MAVSS vortex detections were reviewed for reasonableness (especially for consistent lateral transport) before being included in Figures 2-4. The measurements for each vortex are connected with lines. The two vortices are distinguished by the sign of the circulation (negative for the first or downwind vortex and positive for the second or upwind vortex). Under the morning conditions of the tests (strong

wind shear and low turbulence) the second or upwind vortex lasted significantly longer. Note that the upwind vortex has the same sign vorticity as the wind shear while the downwind vortex has opposite sign vorticity. The wind shear thus tends to enhance the upwind vortex and annihilate the downwind vortex.

The initial circulations are similar for the B-757 and B-767 but smaller for the B-727. The vortex decay appears as expected, with the vortices lasting longer for the larger aircraft. Section 4.3 will present the same data of Figures 2-4 in a normalized form that will elucidate how the results scale with aircraft size.

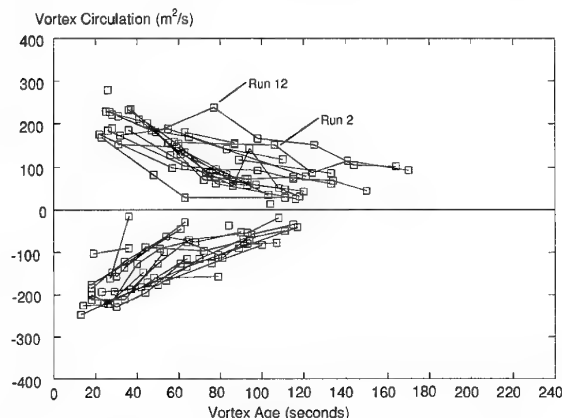


Figure 2. Circulation Measurements for B-727 Morning Low-Altitude Runs

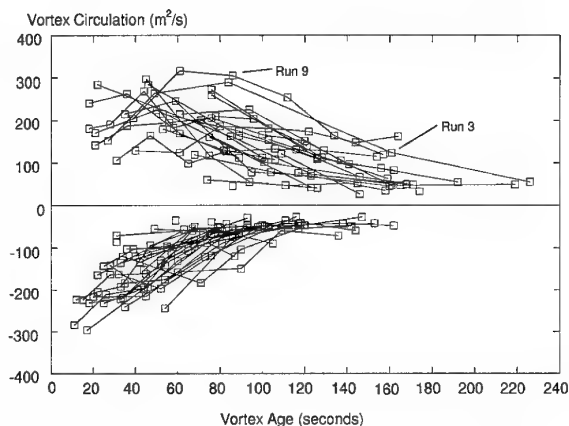


Figure 3. Circulation Measurements for B-757 Morning Runs

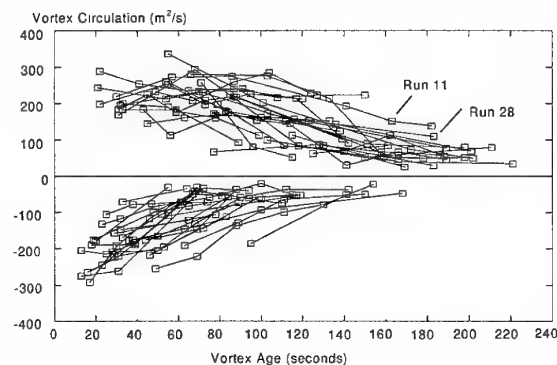


Figure 4. Circulation Measurements for B-767 Morning Runs

A static model⁵ of a wake vortex encounter using strip theory can relate the maximum induced roll on the wing of a following aircraft to the vortex circulation. For example, a vortex circulation 140 m²/s can induce a rolling moment greater than the typical roll control authority for a following aircraft with a span of 28 meters (e.g., DC-9). Under the morning conditions of the Idaho Falls tests, vortex circulations above 140 m²/s are observed to last for approximately 125, 150 and 170 seconds for the B-727, B-757 and B-767, respectively.

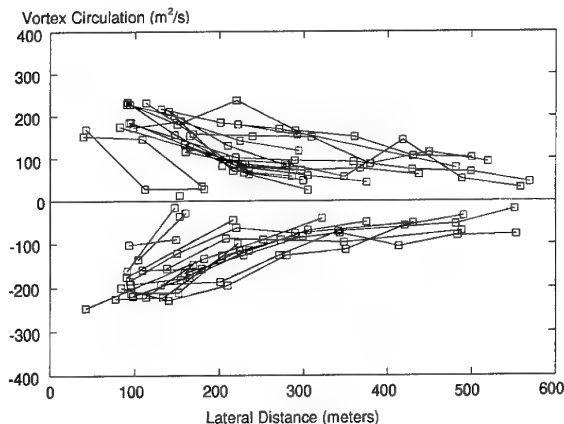


Figure 5. Circulation vs. Lateral Position for B-727 Morning Low-Altitude Runs

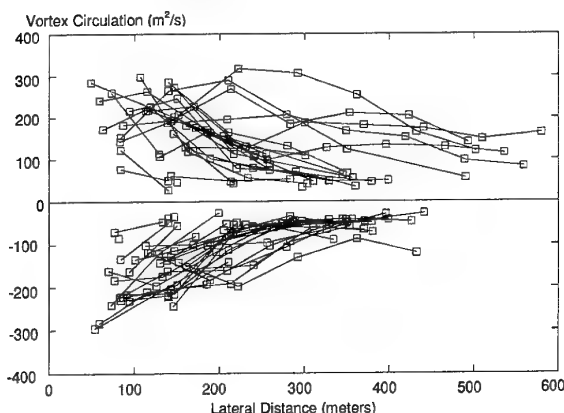


Figure 6. Circulation vs. Lateral Position for B-757 Morning Runs

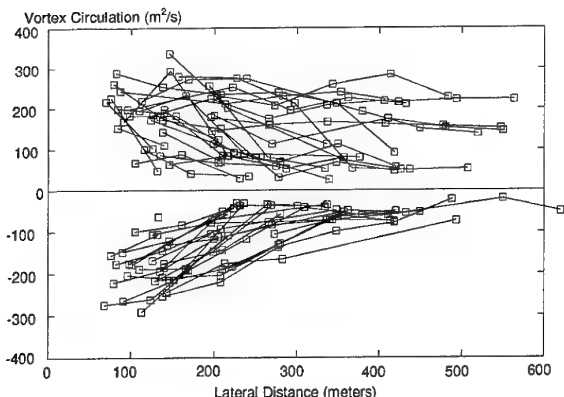


Figure 7. Circulation vs. Lateral Position for B-767 Morning Runs

Figures 5-7 replot the data of Figures 2-4 as a function of lateral transport distance rather than vortex age. The lateral distance is taken perpendicular to the aircraft path and the lateral position of the aircraft is defined as the origin. Few of the B-727 vortices appear to reach the end of the MAVSS array. Some of the B-757 vortices have significant circulation when they reach the end of the MAVSS array. Many B-767 vortices have more than one third of their initial circulation when they reach the end of the MAVSS array. For these B-767 runs the vortex time decay in Figure 4 is therefore truncated by the limited length of the MAVSS array. Consequently, the test results may not accurately represent the actual maximum duration of B-767 wake vortices.

4.3 Normalized MAVSS Circulation Measurements

Greene⁶ introduced a method for normalizing circulation decay measurements. The circulation is normalized to the initial circulation $\Gamma_0(\infty)$ which is given by the equation:

$$\Gamma_0(\infty) = KW/\rho Vb, \quad (1)$$

where the parameters are:

K = constant related to the lift distribution on the wing

K = 1 for uniform lift, K = 4/π for elliptic loading.

W = Aircraft weight

ρ = Air density

V = Airspeed

b = Wingspan

The spacing b' between the two vortices is given by:

$$b' = b/K. \quad (2)$$

The descent rate w of the vortices is given by:

$$w = \Gamma_0(\infty)/2\pi b'. \quad (3)$$

The vortex age is normalized by the time T it takes for the vortices to descend their separation distance:

$$T = b'/w. \quad (4)$$

Figures 8-10 show the data from Figures 2-4 in normalized form. The maximum normalized circulations are somewhat below one. Using larger radii (9-18 meters) for the circulation estimate gives maximum values close to one. The normalization does not give similar decay curves for the three aircraft types. In particular, the B-767 appears to show shorter vortex lifetimes, perhaps because of the limited length of the MAVSS array discussed in Section 4.2. The array-length limit becomes more significant as the aircraft size is increased. In addition to this systematic measurement effect, the observed differences may (1) reflect subtle differences in the meteorology on the test days for the three aircraft or (2) may imply that the normalization process does not adequately represent the way vortices from different sized aircraft decay near the ground. An example of the second issue is that, for aircraft at the same altitude, a smaller aircraft will take more normalized time to descend close to the ground.

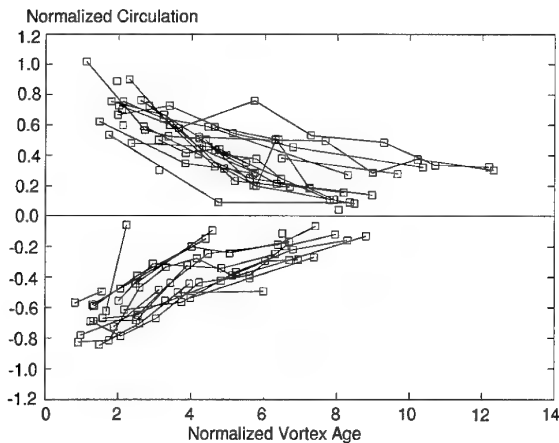


Figure 8. Normalized Circulation Decay for B-727 Low-Altitude Morning Runs

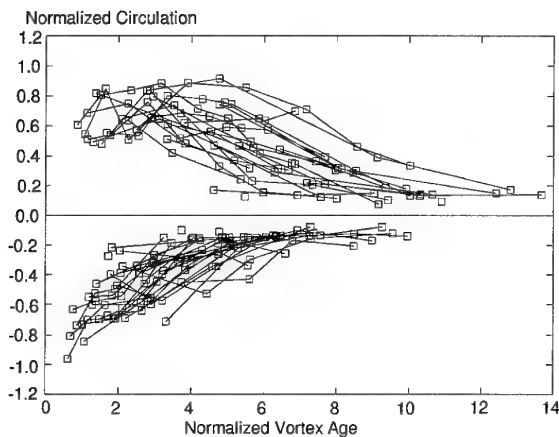


Figure 9. Normalized Circulation Decay for B-757 Morning Runs

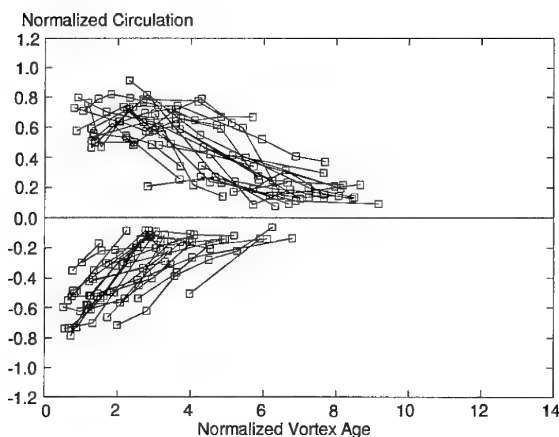


Figure 10. Normalized Circulation Decay for B-767 Morning Runs

4.4 LDV Circulation Measurements

For two B-767 runs the crosswind was low enough that the upwind vortex remained within the LDV range until it decayed. Figure 11 shows the circulation decay for these two runs. The vortex tangential velocity was taken as the highest velocity peak in the Doppler spectrum. Figure 12 presents the data of Figure 11 in normalized form. These two runs are at the upper limit of vortex duration for the MAVSS runs in Figure 10.

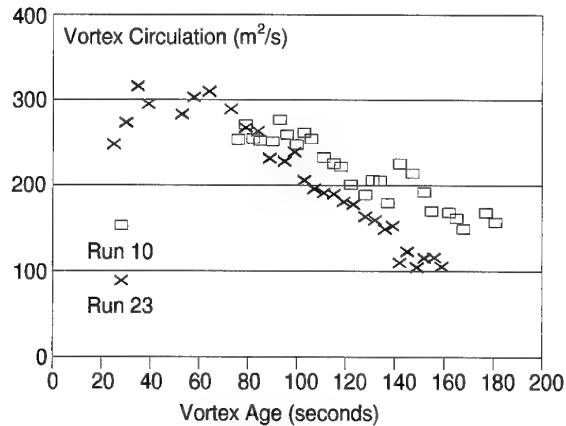


Figure 11. LDV Circulation Measurements for Two B-767 Runs

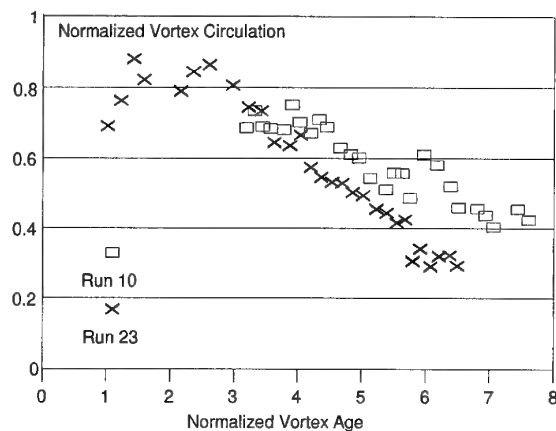


Figure 12. Normalized Circulation Decay for Two B-767 Runs

5. METEOROLOGICAL EFFECTS ON DECAY

Section 4 presented the overall results of the Idaho Falls test for the morning runs. This section and the next will examine the results in more detail for all runs, with an emphasis on the changes in vortex behavior for changes in meteorological conditions. Specifically, the lifetimes of the vortices will be related to measured and derived atmospheric variables. The analysis results (Section 6) will be graphical comparisons of vortex lifetime to individual atmospheric variables.

The typical meteorology of the test site during September consists of stratified drainage flows from the northeast during the early morning. Later in the morning the stratified layer is dissipated by heating of the ground and the flow reverses to southwest winds.

5.1 Background

The Greene⁶ model of vortex decay describes vortex decay away from the ground; two atmospheric parameters are considered: (1) turbulence and (2) stability, which are assumed to be uniform in the volume where the vortices move. Stratification limits the descent of the vortices and causes vortices to disintegrate as they reach their maximum descent distance. Two additional effects must be considered near the ground: (3) interaction with the ground boundary layer and (4) vertical wind shear.

In some of the Idaho Falls runs the upwind vortex stopped descending well above its normal ground-effect height, but without significant decay. Two explanations are possible for

this observation, which is inconsistent with the effects of atmospheric stability away from the ground:

- 1) Non-uniform stability may affect vortex decay differently from uniform stability. For example, a strongly stable layer extending to a height h above the ground could be equivalent to raising the ground to height h as far as vortex behavior is concerned.
- 2) Strong crosswind shear may counteract the normal stability-induced vortex decay.

5.2 Outline of Analysis

The analysis here will be restricted to runs at low enough altitudes that the vortices would normally descend into ground effect. Some B-727 runs during the first test morning were flown at 181-meter altitude above the ground and will not be included in this analysis. These runs could be studied further as a special class of flights since preliminary analyses suggest that they may be useful for testing Greene's predictions⁶ in the free atmosphere.

In the spirit of Greene's model, vortex lifetimes should change as air mass characteristics change. Possibly significant parameters are static stability, turbulence, time-of-day, windspeed, and vertical wind shear. In this dataset, unfortunately, no direct turbulence measurements are available. Consequently, various surrogates (e.g., time of day) were tried. In particular, more rapid vortex breakup should occur by midday due to increased solar heating and associated turbulence. Wind speed and vertical wind shear are also possible turbulence indicators. Vertical crosswind shear also creates a horizontal vorticity field that can potentially enhance (same sign as) or diminish (opposite sign as) the vorticity of each member of the wake vortex pair.

5.3 Vortex Lifetimes

For this analysis, vortex lifetime is defined as the time required for the circulation of the vortex to drop to 25 percent of its initial calculated circulation $\Gamma_0(\infty)$ given by Equation 1 assuming elliptic loading. This analysis was carried out before the development of the method for estimating circulation described in Section 4.1. Consequently, the circulation estimate used averaging radii from 0 to 15 meters for both LDV and MAVSS data, rather than the values recommended in Section 4.1. Note that, at a level of 25-percent, the lifetime threshold is near the detection threshold of the both the LDV and the MAVSS.

The lifetimes of the two vortices from each run were manually selected from graphs of circulation versus vortex age using both LDV and MAVSS data. The selection was frequently difficult because of discontinuities in the data and disagreements between the two measurements methods. Lifetime estimation errors could be in the range of 10 to 20 seconds out of typical lifetimes of 60-180 seconds. Nevertheless, this method was the only practical approach since it included quality control by a human during the estimation process, and many runs were eliminated. Out of 189 possible cases, fewer than 100 survived for the meteorological study (see Table 3).

Table 3 summarizes the normalized lifetime statistics for vortices 1 and 2 (the downwind and upwind vortices, respectively). Lifetimes are normalized as in Section 4.3 by dividing the lifetime by the characteristic time T given by Equation 4 (approximately 16, 18, and 24 seconds for the B-727, B-757, and B-767, respectively). Note from the table that, except for the 21 B-727 runs used, the mean lifetimes

for vortex 1 are significantly shorter than for vortex 2, as discussed in Section 4.2

Table 3. Summary of Non-Dimensional Vortex Lifetime Data

A/C Type	Runs	Vtx.	Runs			Standard Deviation
			Used	Mean	Min.	Max.
B-727	60	1	21	4.07	1.12	6.02
		2	21	4.21	1.49	6.57
B-757	70	1	36	3.55	1.03	5.92
		2	35	6.00	1.21	10.23
B-767	59	1	35	2.52	0.57	4.80
		2	38	4.32	0.94	8.43
ALL	189	1	92	3.28	0.57	6.02
		2	94	4.92	0.94	10.23

5.4 Integrated Meteorological Database

The meteorological data from the tower and tether sonde were integrated into a consistent format. Tower data consisted of three-minute averages at 7 levels up to 60 meters, taken before each flyby (about every six minutes). The tether sonde sampled various levels from 30 to 215 meters with a settling time of about 10 seconds and a periodicity of about 12 minutes. The tether sonde was operated about 600 meters northeast of the tower. After testing for upwind data lags when the wind was in line with the tower and sonde, it was concluded that, for this dataset, spatial separation of the observations was not a concern. Therefore, a Barnes⁸ analysis algorithm was developed to interpolate the observations from the sonde and tower onto gridded height vs. time cross sections of wind components relative to the aircraft track and temperature. The grid dimensions are 15m (vertically) by five minutes (horizontally), except below 15m where data were recorded at the surface, 1.9, 3.8, and 7.5 m. From these arrays, cross sections of potential temperature, Brunt-Vaisala frequency (which is a measure of a stable atmosphere's restoring force), and gradient Richardson number (a commonly used measure of turbulence potential) were derived.

5.5 Scaling of Meteorological Variables

Wind components (e.g., u) are normalized by the descent speed w of the wake vortices given by Equation 3:

$$U = u/w \quad (5)$$

Vertical wind shear components (vws) (units of 1/second) are normalized using the characteristic vortex time T (units of seconds) from Equation 4:

$$VWS = T vws \quad (6)$$

The Brunt-Vaisala Frequency (bvf) (units of 1/second) is similarly normalized as:

$$BVF = T bvf \quad (7)$$

Unless otherwise stated, normalized, i.e. non-dimensionalized, variables will be used in the following plots and tables.

5.6 Vertical Wind Shear Sign Adjustment

Horizontal ambient wind components (u, v) are based on a coordinate system defined relative to the aircraft. The along

track component (u) is defined as positive toward the tail of the aircraft (positive u is a headwind). The crosswind (v) is positive toward the starboard (right-hand) wing. Since the flybys were on a heading of 300 degrees true, southwesterly winds give positive relative crosswinds at Idaho Falls.

Wake vortex decay is found to depend upon the vortex position relative to the crosswind. The upwind vortex (termed vortex 2) typically decays (see Section 4.2) more slowly than the downwind vortex (termed vortex 1). Since the vortex number will be used to distinguish the two vortices in the following analyses, it is appropriate to adjust the sign of the crosswind shear according to the sign of the crosswind. The crosswind shear will be defined as positive if the magnitude of the crosswind increases with height, as is the normal case. With this definition, the vertical crosswind shear has the same sign vorticity as vortex 2 and the opposite sign vorticity from vortex 1.

5.7 Sample Meteorological Data

Figure 13, taken from the integrated meteorological database for the morning of September 25, 1990, is a vertical cross-section of *dimensional* Brunt-Vaisala (B-V) frequency vs. time of day. The height units are feet (0.3048 meters). Note the deep layer of large (stable) values during the early hours, and the rapid formation of a deepening neutrally stable mixed layer after about 0808 Mountain Daylight Time (MDT). This transition was a common event during the other early morning test periods as well. Figure 14 shows a vertical cross-section of relative crosswinds from the same period. The negative values indicate flow from the northeast; note the strong vertical wind shear prior to 0815, and how it rapidly weakens after that time below 30 m (100 feet). Typically, vertical wind shear was strongest early in the day with stable stratification, and weakened as the neutral mixed layer developed. This was particularly true for the B-757 and B-767 test days.

Figure 15 plots non-dimensional Brunt-Vaisala frequency (BVF) at 30 m against time-of-day (TOD) which shows a correlation in that most cases were stable (positive) prior to about 1030 MDT, and unstable thereafter. Strictly speaking, the BVF is imaginary for unstable cases; since real BVF are positive, Figure 15 plots imaginary BVF as the negative of the magnitude of BVF.

Figure 16 plots the non-dimensional adjusted vertical crosswind shear at 30 m against TOD, and shows that the strongest shears occur before about 0815 MDT (a predominantly stable regime), while in the later (less stable) hours, shears are significantly smaller. In simple terms, essentially all of the relevant meteorological parameters were more or less linked to time of day, and, therefore, to each other.

Although vortex lifetimes appear to be sensitive to variations in some of the meteorological variables taken individually, which may suggest physical relationships, the difficulty is that these effects are not independent due to the diurnal linkages noted above, and it is possible that many of the relationships are merely surrogates for one another. The effect of diurnal warming, which produces an increase in turbulence, and the probable effect of vertical wind shear on vortex lifetimes may be the only real physical relationships that can be identified.

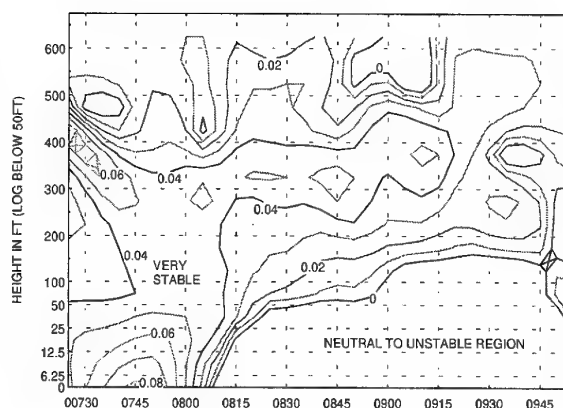


Figure 13. Time vs. Height Crossection of B-V Frequency on 9/25/90 (First B-757 Test Day)

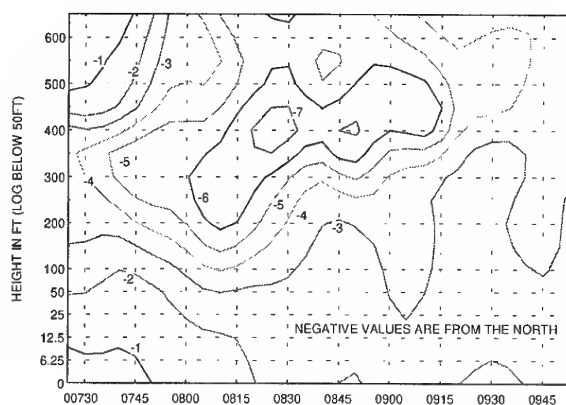


Figure 14. Time vs. Height Crossection of Crosswind (m/s) on 9/25/90 (First B-757 Test Day)

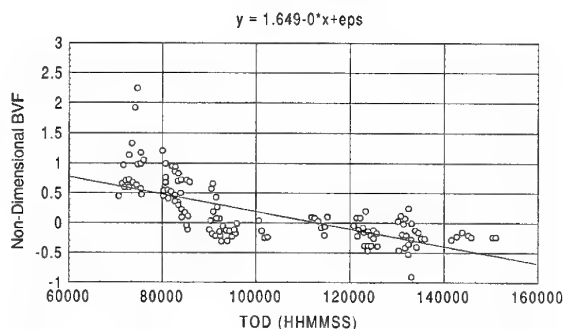


Figure 15. Non-Dimensional B-V Frequency at 30 m vs. Time of Day for All Runs

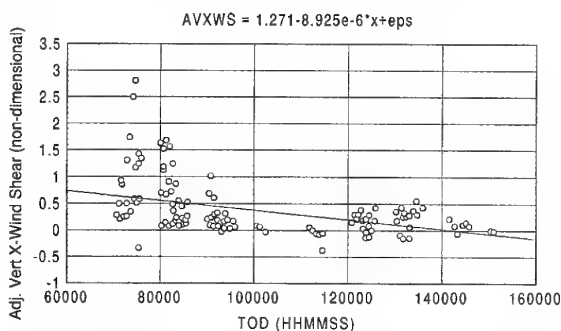


Figure 16. Adjusted Vertical Crosswind Shear at 30 m vs. Time of Day for All Runs

6. RELATIONSHIP OF VORTEX LIFETIMES TO METEOROLOGY

In this section, we associate the non-dimensional vortex lifetimes of vortex 1 and vortex 2 (T1, T2) with selected atmospheric variables for the purpose of possibly identifying statistical relationships. The graphical scatter plots (Figures 15-20) presented in the following sections will (1) contain data from all three aircraft types, (2) include linear regression lines giving the average relationship between lifetime and the variable and (3) present the regression equations at the top of the plot. Because of the small sample and the cross correlations among many of the variables, it is not generally possible to assert that the relationships are mutually independent. In spite of the small sample size and large scatter, this statistical analysis provides behavioral clues that may stimulate future in-depth analyses of individual classes (e.g., all B-757s in level flight before 0830 MDT), or even specific runs. However, much more data from future experiments will be needed to define vortex behavior algorithms that will be useful for routine airport operations.

Assuming the absence of turbulence, Greene's⁶ model predicts that the lifetime of a vortex pair will be reduced in a statically stable environment compared to its value in a less stable or neutrally stable environment. In unstable atmospheres, one would expect the lifetime to be shortened by the inevitable occurrence of convective turbulence. The effects of wind and wind shear are not treated in Greene's model; however, it will be shown that these effects can be important, especially near the ground.

6.1 Time of Day

Time of Day (TOD) is not strictly a meteorological variable; however, it is related to solar heating and correlates strongly with other meteorological variables in the Idaho Falls dataset. In particular, it is a reasonable surrogate for turbulent activity as the ground heats up and generates convective eddies by mid-morning. Figure 17, plotting T1 and T2 against TOD, shows a striking contrast in behavior between the morning and afternoon runs. Both vortices show similar lifetime distributions after 1200 MDT with mean values near 3 units (about 54 seconds for a B-757), and variations from about 1 to 5 units. There are no "long" lifetimes during the afternoon; this result is entirely consistent with the hypothesis that convective turbulence is the controlling factor.

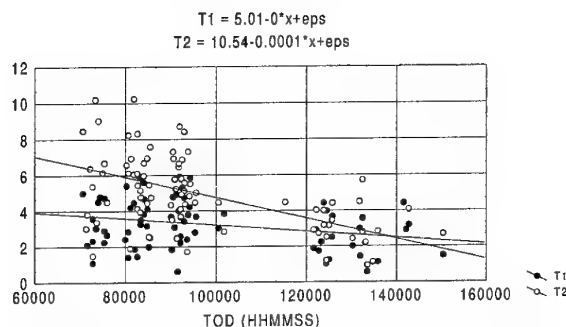


Figure 17. Normalized T1 (solid) and T2 (open) vs. Time of Day

However, T1 prior to about 1000 MDT shows a mean of only about 3.5 units versus about 5.5 units for T2. The range of T2 is also substantially greater than that of T1 in the morning. All of the longest lifetimes are associated with vortex 2 in the morning, which is a period of strong static stability and

laminar shearing flow. From the linear regression, T2 drops from about 6.5 units at 0700 to about 2.5 units by 1400 MDT, a decrease of 62 percent. T1 only drops about 28 percent during the same period.

Since stability and turbulence should act the same on the lifetimes of both vortices, there must be another effect present in the morning to account for such asymmetric behavior.

6.2 Vertical Crosswind Shear

Figure 18 plots T1 and T2 vs. Adjusted Vertical Crosswind Shear that has been non-dimensionalized and adjusted for wind direction (Section 5.6). For small shear values, T1 and T2 vary randomly. For stronger positive shears, T1 is seen to decrease on the order of 50 percent, while T2 tends to increase by about the same fraction. The T2 plot has considerable scatter, and the two longest lifetimes were with only moderate shear, but the trend is reasonable, and the shortest T2 values are all with minimum shear. This result is consistent with the concept of adjusting the signs of the vertical crosswind shear (Section 5.6). After adjustment, positive crosswind shear depresses T1 and enhances T2. Vertical crosswind shear is negatively correlated with TOD (larger values in the early morning, and only small values during the later flights) and Figure 17 shows that the two largest T2 values occurred on very early runs in stable air.

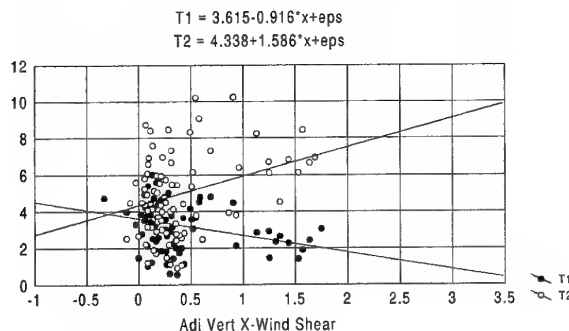


Figure 18. Normalized T1 and T2 vs. Adjusted Crosswind Shear at 30 m

6.3 Windspeed

Windspeed itself should be a factor in vortex lifetime in the sense that stronger winds are generally associated with stronger turbulence; therefore, if turbulence is predicted by windspeed, both T1 and T2 should decrease with increasing windspeed. Figure 19 plots T1 and T2 against non-dimensional windspeed at 30 m. The regressions lines for both T1 and T2 indicate a general tendency for the longer lifetimes to occur for lower windspeeds and vice versa.

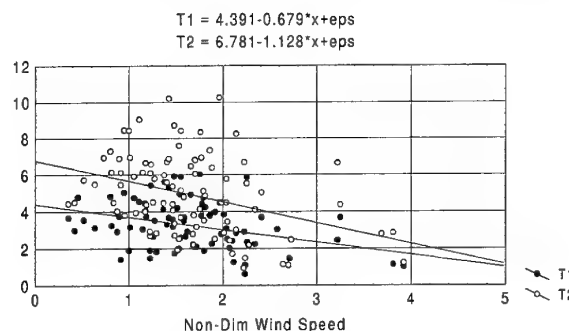


Figure 19. Normalized T1 and T2 vs. Non-Dimensional Wind Speed at 30 m

6.4 Brunt-Vaisala Frequency

The Brunt-Vaisala Frequency (BVF) measures atmospheric stability in terms of the frequency with which a vertically displaced "parcel" of air would oscillate about its original position after release. Three categories of stability can be defined:

- Stable - BVF is positive. High frequencies indicate very stable conditions; flow is probably laminar, and vertical wind shears can be large. Stable conditions dominated the early morning hours at Idaho Falls.
- Neutral - BVF is exactly zero. A vertically displaced parcel will continue to drift without restraint. Neutral conditions are often turbulent, and vertical wind shears in non-stormy conditions are reduced due to turbulent exchange. A neutral surface layer tended to form and deepen each day with increased heating at Idaho Falls (e.g., see Figure 13 after 0808 MDT). Vertical wind shear weakened in the same region at about the same time (e.g., see Figure 14).
- Unstable - BVF is imaginary. A vertically displaced parcel will *accelerate* in the direction of its displacement. Unstable conditions are turbulent, and, at Idaho Falls, are generally found near the surface due to strong heating (the area beneath the BVF = 0 contour in Figure 13 actually becomes slightly unstable up to as high as 30-46m by mid morning).

Figure 20 plots T1 and T2 vs. non-dimensionalized BVF at 30 m above the ground. On these plots, remember that negative values of BVF are the negative magnitudes of imaginary BVF values, which result from unstable atmospheric conditions. The relationships shown at 30 m were very representative of 15 and 46 m as well. One expects to find that lifetime vs. BVF is roughly the inverse of lifetime vs. TOD, and that is indeed the case.

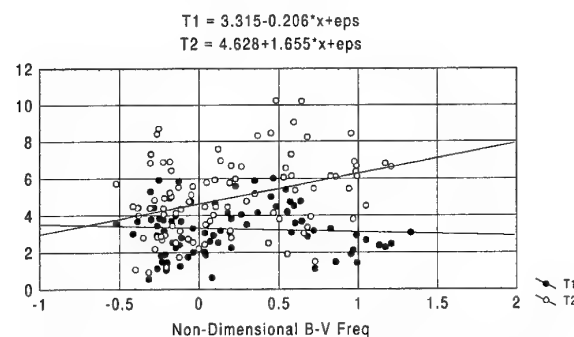


Figure 20. Normalized T1 and T2 vs. B-V Frequency at 30 m

Note that, in Figure 20, both the longest and shortest T1 values occurred in the slightly unstable to slightly stable range where most T1 cases were clustered. According to Greene⁶, longest lifetimes should occur near neutral stability, providing there is little turbulence. However, near-neutral atmospheres also increase the likelihood of turbulence outbreaks. Perhaps the wide T1 distribution near neutral stability at Idaho Falls demonstrates that with BVF near zero, the large T1s were in smooth conditions (following Greene), while the small T1s were reduced by turbulence.

Since BVF and TOD are negatively correlated, the generally longer T2s at higher BVFs occurred in the early morning during periods of probable laminar flow with strong vertical

crosswind shear having the same sign vorticity as the upwind vortex.

6.5 Summary of Graphical Comparisons

The reader should note that the data sample of fewer than 100 runs during a few days of highly correlated weather in September of 1990 is a weak statistical basis upon which to base general conclusions. This limitation is reflected, in part, by the considerable scatter in the comparative plots. Estimating the lifetimes of the vortex pairs had the highest potential for observational error, and must have contributed strongly to the data scatter in spite of a considerable quality assurance effort. However, the following tentative results are worthy of discussion.

With the exception of windspeed, the measured and derived meteorological variables were significantly correlated with time-of-day (TOD). Therefore, the comparisons of vortex lifetimes with these variables could also be illustrated with respect to TOD. The group of vortex lifetimes from flights after about 1030 MDT were relatively short regardless of which vortex was being measured. This observation indicates that, during this time frame, convective turbulence is probably the controlling mechanism. However, in the early morning, vortex 2 (upwind) had mean lifetimes nearly double those of vortex 1, and also double those of both vortices during the later flights. The only other variable that seems to be able to explain this asymmetry is the vertical crosswind shear which is strongest in the early morning during stable, laminar conditions, and tends to strengthen the upwind vortex while weakening the downwind vortex due to the relative sign of the vorticity in the shearing flow. By the time of the later flights, turbulence seems to take control such that the lifetimes of both vortices are similarly shorter. Another variable that could partially account for reducing vortex lifetimes is the windspeed which is logically proportional to the growth of turbulence. However, windspeed alone cannot account for the asymmetry in lifetimes between vortices 1 and 2.

6.6 Some Special Cases

Table 4 summarizes a brief look at a few runs that exhibited sustained large circulations; these were all upwind vortices. The integrated database was used to deduce dimensional values of BVF and adjusted vertical crosswind shear averaged between 15 and 76m at run time. These variables tend to have large values which is consistent with the statistical plots previously analyzed. These selected runs are identified in Figures 2-4, which show the slow decay of vortex 2.

Table 4. Selected Long-Lived Runs

A/C Type	727	727	757	757	767	767
Run	2	12	3	9	11	28
Day	9/23	9/23	9/25	9/25	9/29	9/30
Hour	0723	0836	0734	0818	0820	0905
Lifetime	174	190	180	160	200	175
BVF	0.06	0.04	0.04	0.03	0.04	0.025
AVWS	0.044	0.044	0.04	0.046	0.072	0.026

7. SUMMARY AND CONCLUSIONS

7.1 Meteorological Effects

The analysis approach was to look for statistical relationships between non-dimensional vortex lifetimes and a number of meteorological variables treated independently. The analysis qualitatively supported predictions relative to the impact of turbulence on shortening vortex lifetimes. However, the hypothesis that strong atmospheric stability also shortens lifetimes was not supported in the IDF dataset. Greene's work⁶, for example, specifically applies to the "free atmosphere" with uniform values of stability and turbulence, and not when the vortices are forced by the ground surface to cease their descent. Another parameter of importance appears to be the vertical crosswind shear which seems to account for the long lives of the upwind vortices (while weakening the downwind vortices) in strongly stratified (non-uniform) stable conditions.

7.2 Limitations of Idaho Falls Tests

Some vortex durations observed at Idaho Falls in the morning are much longer than the normally observed vortex lifetimes. An analysis of the effects of meteorological conditions on vortex decay suggested that these long durations are related to strong crosswind shear coupled with low turbulence levels. The conditions of the Idaho Falls tests were generated by drainage flows and would be unlikely to occur at most airports where atmospheric stability and significant crosswinds normally do not occur at the same time. However, if they did occur, the crosswind should be strong enough to sweep both wake vortices away from the generating runway so that the potential vortex encounter hazard would be for operations on a downwind parallel runway. In spite of these limitations, the Idaho Falls site provided a useful range of meteorological conditions for studying wake vortex behavior; some of the test results should be transferable to other locations.

Vortices from flybys do not simulate the effects of actually landing where the vortices disappear when the lift disappears after touchdown. Thus, they may have longer lifetimes than those of a landing aircraft under otherwise identical conditions. Therefore, data from operational settings are needed to assess the effects of vortex termination on vortex decay at locations up the glideslope.

7.3 Recommendations

More analysis of the Idaho Falls data could still be accomplished by studying and explaining individual cases. For example, the unique behavior (T1 and T2 often equal) of the B-727 lifetimes compared to the B-757 and B-767 warrants further analysis.

In order to quantify the effect of the ground on vortex decay, it would be worthwhile to compare the Idaho Falls results with Greene's model of vortex lifetime as a function of viscosity, atmospheric stability and turbulence.

The understanding of vortex decay would benefit from additional excellent quality vortex circulation vs. time histories accompanied by comprehensive meteorological measurements.

ACKNOWLEDGEMENTS

This work was supported by the United States Federal Aviation Administration. L. Osovski assisted in analyzing the MAVSS data. G. Thokar carried out the Barnes analysis.

REFERENCES

1. Page, R.D., Clawson, K.L., Garodz, L.J. and Rudis, R.P., "Panel Discussion on Tower Fly-By Testing - 1990 Fall Series," Proceedings of the Aircraft Wake Vortices Conference - Vol. 2, October 29-31, 1991, DOT/FAA/SD-92/1.2, June 1992, pp 49-(1-53).
2. Garodz, L.J. and Clawson, K.L., "Vortex Wake Characteristics of B575-200 and B767-200 Aircraft Using the Tower Fly-By Technique," NOAA Technical Memorandum ERL ARL-199, January 1993.
3. Burnham, D.C., "B-747 Vortex Alleviation Flight Tests: Ground-Based Sensor Measurements," Report No. DOT-FAA-RD-81-99, February 1982.
4. Burnham, D.C., "Chicago Monostatic Acoustic Vortex Sensing System, Volume 1: Data Collection and Reduction," Report No. FAA-RD-79-103,I, October 1979.
5. Burnham, D.C. and Hallock, J.N., "Chicago Monostatic Acoustic Vortex Sensing System, Volume IV: Wake Vortex Decay," Report No. DOT/FAA/RD-79-103,IV, July 1982.
6. Greene, G.C., "An Approximate Model of Vortex Decay in the Atmosphere," J. Aircraft, Vol. 23, No. 7, July 1986, pp. 566-573.
7. Delisi, D.P., Robins, R.E., and Fraser, R.B., "The Effects of Stratification and Wind Shear in the Evolution of Aircraft Wake Vortices Near the Ground," NWA-87-R006, April 1987, Northwest Research Associates, Bellevue WA.
8. Barnes, S.L., "Technique for Maximizing Details in Numerical Weather Map Analysis," J. Applied Meteorology, Vol. 3, No. 4, August 1964.

Wake Turbulence Training and Regulation: An Industry Team Approach

Capt. David C. Carbaugh and W. Douglas Forsythe
Boeing Commercial Airplane Group
P.O. Box 3707, MS 20-87
Seattle, Washington USA 98124

Summary

This paper describes the development and content of the industry endorsed Wake Turbulence Training Aid and industry's input to regulators regarding wake turbulence efforts. The Wake Turbulence Training Aid is a safety document aimed at both pilots and air traffic controllers. The aid consists of a manual with pull out sections for easy use and a video of about 25 minutes in length. The reason for developing the aid is discussed. Increased traffic, mixed traffic, accidents and incidents, ASRS reports, and calls for action all culminated in needing training to step up to the need for more awareness and education for pilots and controllers. Who was involved in the development of the aid is discussed to highlight its international scope, as well as the time progression towards completion. The content of the aid is then discussed in detail. Lastly, the efforts of the industry team to make specific inputs to the FAA regarding efforts to reduce wake turbulence encounters and to improve safety is presented.

Introduction

Wake turbulence has been known since the early days of aviation. The introduction of wide-body aircraft and the wake turbulence associated with their heavy weights, an increase of air traffic, and safety concerns, prompted industry and government interest. Much investigation and analysis was done by industry and government in the 1960's and 1970's. It was during this time that the ground rules, or to be more precise, air rules were established so that this usually invisible hazard could be avoided.

The Past

During the introduction of the airplanes now categorized as "heavy", manufacturers worked with the Federal

Aviation Administration (FAA), the National Aeronautics and Space Administration (NASA), and the Air Force to conduct flight-test evaluations of the hazards of wake turbulence. These tests underscored, among other things, the necessity of three-dimensional flight path control. In light of the flight test findings, the FAA developed air traffic control (ATC) and piloting procedures designed to avoid the hazard (References 1 through 3).

- **ATC Procedures:** ATC procedures and air traffic separation distances were refined by the FAA on the basis of the test results and experience. For many aircraft, the existing IFR separation distance of three miles was determined adequate. Distances greater than this standard IFR separation distance were considered necessary when the follower's aircraft span was significantly smaller than the leading aircraft's span.

- **Piloting Procedures:** Piloting procedures were identified as a significant opportunity for reducing the chance of a wake turbulence encounter. Because of the wake's characteristic descent, the follower's aircraft should fly on or above the flight path of the leader aircraft.

With this framework in mind and cognizant of the need to address both instrument meteorological conditions (IMC) and visual meteorological conditions (VMC) operations, the FAA developed wake turbulence avoidance procedures. Under IMC, ATC provides horizontal and vertical separation for avoiding an encounter. Under VMC piloting procedures developed by the FAA are intended to provide the vertical separation for avoiding an encounter.

The Present

Wake turbulence accidents and incidents have been and continue to be a

contributor to the worldwide safety statistics. The National Transportation Safety Board (NTSB), in a report on safety issues related to wake turbulence encounters (Reference 4), stated that data show that between 1983 and 1993 there was a combined total of 51 accidents and incidents in the United States that resulted from probable encounters with wake vortices. As a result of these accidents and incidents, 27 people were killed, 8 were seriously injured, and 40 aircraft were damaged or destroyed. In their report, the NTSB raised concern over "the adequacy of air traffic control procedures" and "pilot knowledge related to the avoidance of wake vortices."

A review of wake turbulence related accidents and incidents in the U.S. (References 4 through 7) shows that there have been no accidents during IMC or VMC operations when the pilot and air traffic control followed the appropriate procedures. Maintaining **vertical separation of the follower relative to the leader** appears to be the most significant factor for preventing these types of accidents and incidents during VMC operations.

The Future

The growth of commercial aviation has placed such demand on the air traffic system that many major U.S. airports are capacity limited and are experiencing significant traffic delays. These delays inconvenience the airline's passengers, cost the aviation industry hundreds of millions of dollars each year, and limit the growth of traffic at these airports. The existing wake vortex separation distances represent a major challenge in relieving airport congestion.

Lessons from the U.K.

In 1972, the United Kingdom Civil Aviation Authority (CAA) implemented a voluntary reporting system for pilots experiencing a wake turbulence encounter. The database from this system has become a most authoritative source for statistics on wake turbulence encounters.

Analyses of encounters from 1982 to 1993 are presented in References 9 through 12. Key findings from these analyses include:

- 1) The annual rates of reported encounters are subject to large statistical fluctuations because the encounter frequency is low.
- 2) Aircraft which report encounters above 300 feet AGL are consistently positioned below the flight path of the leader.
- 3) Pilots often knowingly place their aircraft below the glideslope during final approach.
- 4) Examination of available radar data identified approach patterns that can place follower aircraft below the flight path of the leader.

Based on the data presented in References 9 through 12, piloting and ATC procedures appear to be the determining factors for wake turbulence encounters above 300 feet AGL. Analysis of encounter data provides a method for evaluating the effectiveness of weight categories, separation distances, and piloting and ATC procedures. One issue not addressed in References 9 through 12 is whether these encounters are safety of flight issues or merely uncomfortable events.

Wake Turbulence Training Aid

In April 1994 an industry team was formed to address training needs and to make regulatory recommendations regarding wake turbulence. The industry team was formed for a variety of reasons. The team principally addressed the kinds of issues raised in a National Transportation Safety Board (NTSB) special investigation report into wake-turbulence related accidents and incidents. This report issued March 2, 1994 identified the following issues:

- The adequacy of the existing weight category matrix for establishing wake turbulence separation criteria

- The adequacy of ATC procedures related to visual approaches and visual flight rules operations involving a mix of lighter and heavier airplanes
- Pilot knowledge related to the avoidance of wake turbulence
- The lack of available data on wake turbulence encounters in the United States

Additional reasons for forming the team were: to evaluate recent accidents and incidents, respond to a call for action from the government and private sectors, and to address the lack of change in separation criteria because of the growth in traffic volume and mix of airport traffic.

At the request of the FAA Associate Administrator for Regulation and Certification, a wake turbulence industry team formed in April 1994. The team consisted of airframe manufacturers, pilot and traffic controller groups, NASA and other scientific organizations, FAA and European aviation regulatory agencies, and other industry organizations and individuals. The purpose of the team was to develop a wake turbulence training package for pilots and air traffic controllers. This was later expanded to provide recommendations to the FAA regarding wake turbulence aircraft classification and separation standards.

A very comprehensive training package was developed first because the industry team felt by increasing knowledge and awareness it would have the greatest short term impact. This "Wake Turbulence Training Aid" is intended to be one-stop shopping for pilots and controllers. Designated for mass distribution, the training aid was developed in CD-ROM, written, and video formats. It is written for an audience of both pilots and controllers because they play an equal role in the prevention of encounters.

The "Training Aid" is presented in four major sections: an overview for management, a pilot and air traffic controllers guide, a sample training program, and background data. The

overview for management paints a broad review of the training aid, its benefits and costs, and management's role in increasing safety in this area. It points out that the training aid may be used in its entirety or as a supplement to existing training.

The Pilot and Controller's Guide is the major section of the training aid. It first addresses what we presently know about wake vortex behavior and characteristics. A discussion is given regarding scientific efforts to understand wake vortices and the limitations of those studies as well as forecasting difficulties. Various accidents and incidents are reviewed and common problems of the IMC and VMC environment discussed. Wake Vortex avoidance techniques are reviewed from both the pilot and controller aspect as well as vertical and longitudinal separation standards from a worldwide perspective. Lastly, future efforts regarding scientific efforts and equipage are discussed.

The next section of the training aid is the sample training program. This section offers an example of classroom material, a script of the video, instructor guides, and quizzes of the previously introduced material. It is intended that the users incorporate this material as necessary in their pilot or controller training programs. Lastly, in the background data section additional detailed information is given for the use of instructors or those desiring additional information.

Recommendations of the Industry Team

In early 1995 the industry team was asked to prepare recommendations to the FAA wake turbulence steering committee regarding wake turbulence aircraft classifications and separation standards(Reference 13). The team formed three subcommittees to address the major areas of piloting procedures, ATC procedures, and the science of Separation distances. With the welcomed assistance of international experts and regulatory bodies the following conclusions were made and recommendations given.

General Conclusions

A review of wake turbulence related accidents and incidents and scientific data shows that current aircraft weight categories and separation standards, pilot procedures and air traffic control (ATC) procedures used during instrument meteorological conditions (IMC) operations have prevented wake turbulence accidents. However, a review of available flight test and statistical data coupled with the existing aviation environment, produces some merit for modifying the current IFR standards. During visual meteorological conditions (VMC) operations, accidents and incidents have resulted because of the lower vertical positioning of the follower aircraft relative to the leader's flight path. Improvements in vertical positioning during both IMC and VMC should be given a priority, as well as longitudinal separation, in preventing wake turbulence accidents and incidents.

The wake turbulence avoidance criteria, pilot procedures, and ATC procedures used during VMC operations provide pilots and controllers with greater flexibility and airport efficiency than during IMC operations. Separation distances significantly less than the IMC standards typically occur during VMC operations. A review of wake turbulence related accidents and incidents in the U.S. shows that there have been no accidents during VMC operations when the pilot flew in-trail at or above the flight path of the leading aircraft. The NTSB special investigation, as well as other data highlights the difficulties of determining the leading aircraft's flight path during VMC operations. Therefore, as longitudinal separation decreases, consideration of vertical positioning of the follower relative to the leader may provide the greatest potential for preventing accidents resulting from wake turbulence.

Avoiding wake turbulence by staying on or above the flight path of the leader aircraft, requires trailing pilots to make assumptions on where the leader has flown since there is no available visual references. Pilots can make better judgments and decisions if they are

provided with more flight path information.

Recommendations

The following recommendations are made to improve flight safety:

1. Steps should be taken to assure wide spread availability and incorporation or adoption of the education and training promoted in the Wake Turbulence Training Aid.
2. FAA Handbook 7110.65 Air Traffic Control should be amended to assure that Air Traffic Controllers consider the impending vertical positioning and overtake situation when clearing aircraft to proceed visually. Procedures should also be established to require controllers to inform the following pilot of separation distance, overtaking situation and potential vertical problems.
3. FAA/Air Traffic should critically evaluate all current airport arrival and departure paths and procedures. A four-dimensional (time, location, altitude, and speed) analysis should identify and eliminate potential wake turbulence traps caused by established IMC and visual routings or radar vector flight paths that place follower aircraft below and/or downwind of a leader's flight path. Procedures should be established to reduce or eliminate situations that routinely require the pilot to lose excessive amounts of altitude during arrivals resulting in abnormally steep descents.
4. The FAA should establish procedures to permit and require pilots to adjust aircraft flight paths to be established on a 300 feet per nautical mile flight path, or the electronic glide slope, 3 flight path miles from the runway threshold. Communication procedures should be developed for pilots to report if they are unable to comply.
5. The FAA should take steps to promote the development and use of equipment that allows a pilot to better determine the flight path of the leader aircraft.

6. The FAA should establish a government industry team to study how ATC procedures are being applied for visual separation or visual approaches when wake vortex avoidance is required. The team should study several operating locations and make recommendations to pilot and controller procedures based on observed operations.

7. Ensure that the NASA/FAA Integrated Wake Vortex Program has constancy of purpose, a clear and obtainable goal, strong leadership, adequate resources and involvement of all affected segments of industry. The FAA/NASA/Industry should conduct a piloted study to define the hazard from the aspect of wake turbulence encounters in the aircraft flare and final approach segments. This data will greatly help NASA determine appropriate spacing recommendations.

8. The FAA should revise the present wake turbulence data collection system to provide meaningful data for determining the causes of encounters. This action should be coordinated with other agencies in order to establish common worldwide reporting standards. The U.K. has developed a system for collecting and analyzing wake turbulence encounters. The analysis of the incidents in the U.K. from 1990 through 1993 illustrates the value of a refined reporting system for identifying piloting issues, ATC issues and aircraft differences. The wake turbulence data collection system should also include the radar traces and appropriate, available aircraft electronic flight information. Because of the logistics associated with this recommendation, a limited number of key airports should be chosen for implementing these refinements.

9. The Team recommends that changes be made to the existing weight categories. Available data suggests that the current Large weight category presents a risk to the short span aircraft at the low end of the range. The same data also suggests that distances may be reduced between some aircraft pairs. This information suggests the three-category weight system in Table 1. A four-category system is presented in Table 2. Under certain assumptions, the four-category system may offer improvements in

capacity relative to the proposed three category system without adversely affecting wake turbulence criteria.

Testing and operational experience has demonstrated that a break in the large category at between 75,000 lbs and 88,500 lbs may be considered appropriate because of the differences in wingspan loading and wingspan ratio. In order to more adequately address the wake vortex issues and avoid the limitations of just using wingspan and weights in Tables 1 and 2, a possible solution is presented in Table 3.

Table 1
Three-category System

Category	Approximate Wingspan (ft)	Wingspan roughly equates to these weights (lbs)
Heavy	> 120/130	255,000
Large	60/70 - 120/130	41,000 - 255,000
Small	< 60/70	< 41,000

Note: The existing fleet represents a continuum of aircraft, and therefore, there is flexibility in setting the categories near these boundaries.

Table 2
Four-category System

Category	Approximate Wingspan (ft)	Wingspan roughly equates to these weights (lbs)
Heavy	> 170	460,000
Large	120/130 - 170	255,000-460,000
Medium	60/70-120/130	41,000-255,000
Small	< 60/70	< 41,000

Table 3
A Modified Three-Classification System

Classification	Wingspan/Takeoff Grossweight
A	12,500 lbs or <75,000-88,500 lbs/90-60 wingspan
B	Aircraft not in Classification A and C
C	>255,000 lbs

A more detailed analysis needs to be performed to determine where the specific boundaries of each category should be placed. In addition, the impact on airport capacity must be developed for consideration.

Leader Aircraft

C (Heavy)	B (Medium)	A (Light)
-----------	------------	-----------

Follower Aircraft

C (Heavy)	4 NM	Standard	Standard
B (Med)	5 NM	Standard	Standard
A (Light)	6 NM	5 NM	Standard

A capacity analysis should be made using representative airports in order to determine the effect of implementing recommendations.

Conclusion

Many challenging issues remain to be solved, not the least of which are defining operationally acceptable wake characteristics, accurate forecasting and detection of wakes, and further understanding of wake decay. To mitigate the capacity limitation placed on the system due to wake vortices, the regulatory agencies, airlines, manufacturers, the piloting and ATC communities and research institutions must team together to ensure that the effected segments of the industry are involved in the solutions.

References

- 1) Federal Aviation Administration -- Flight Standards Service, *A Compilation of Working Papers Concerning the Wake Turbulence Tests*, dated 30 April 1970
- 2) FAA memo from FS-1 to OP-1, *Interim Report -- Wing Tip Vortices Test Program*, dated 9 March 1970
- 3) Airman's Information Manual
- 4) National Transportation Safety Board Special Investigation Report NTSB/SIR-94-01, *Safety Issues Related to Wake*

Vortex Encounters During Visual Approach to Land, February 1994

- 5) Federal Aviation Administration Report FAA-EM-75-6, *Vortex-Related Accidents Over the Ten Year Period 1964 - 1973*, dated April 1975

- 6) FAA Report No. FAA-RD-77-23, *Aircraft Wake Vortices: A State-of-the-Art Review of the United States R&D Program*, 1977

- 7) Wake Turbulence Industry Team, *Science of Separation Distances Subcommittee, Final Recommendations*, dated June 9, 1995

- 8) ATCEU Memorandum 177, *The Wake Vortex Reporting Programme: A Brief History and Explanation of Incident Reporting and Data Capture*, dated July 1991

- 9) CAA Paper 91015, *United Kingdom Civil Aviation Authority Wake Vortex Database: analysis of Incidents Reported between 1982 and 1990*, dated August 1991.

- 10) ATCEU Memorandum 184, *The Wake Vortex Reporting Programme: Analysis of Incidents Reported Between January 1990 and December 1991*, dated June 1992

- 11) ATCEU Memorandum 197, *The Wake Vortex Reporting Programme: Analysis of Incidents Reported Between January and December 1992*, dated October 1993

- 12) ATCEU Memorandum 213, *The Wake Vortex Reporting Programme: Analysis of Incidents Reported Between January and December 1993*, dated August 1994

- 13) Wake Turbulence Industry Team, *Position Paper: Wake Turbulence Weight Classification and Separation Standards*, dated 6 June 1995

GROUND-BASED ANEMOMETER MEASUREMENTS OF WAKE VORTICES FROM LANDING AIRCRAFT AT AIRPORTS

S. Abramson

Volpe National Transportation Systems Center
Kendall Square
Cambridge MA 02142
USA

D. C. Burnham

Scientific and Engineering Solutions, Inc.
P. O. Box 64
Orleans MA
USA

1. SUMMARY

In 1994 an array of two-axis propeller anemometers was installed at 10-meter height under the approach to Runway 31R at Kennedy Airport. Since the aircraft are typically 50 meters above the ground at the test location, the wake vortices rapidly descend toward the ground where they are readily detected and measured by the anemometers. In 1995 a similar installation was made on Runway 27 at the Memphis Airport. The ultimate goal of this study is to better understand when wake vortices remain in the flight path of following aircraft. The data collection system operates automatically and hence provides wake vortex data under all weather conditions and at all times of day and night with minimal cost. Real-time remote display of the vortex locations was implemented. The anemometers are augmented with additional weather sensors to provide meteorological data with greater detail than the standard surface weather observations. New processing methods for the anemometer data were developed to determine vortex height and strength in addition to the lateral position that was traditionally obtained from ground-based anemometers. The anemometer array is particularly appropriate for studying the interaction of wake vortices with the ground. It readily detects the secondary vortices detached from the boundary layer by the influence of the primary wake vortices; these secondary vortices produce the well known vortex bouncing. Such secondary vortices have not been seen by any other sensing system.

2. INTRODUCTION

Airport measurements of wake vortices from landing aircraft have concentrated on the region between the middle marker and touchdown where vortices can stall on the extended runway centerline and remain on or rise into the flight path of a following aircraft. During the 1970s the Volpe Center deployed¹ anemometer arrays in this region at many airports to detect wake vortices. Normal vortex descent brings the vortex pair down to the ground where the vortex flow field can be readily measured by single-axis propeller anemometers oriented perpendicular to the flight path and mounted on 3-meter poles. The two vortices produce opposite sign crosswinds. Validation tests² showed that the anemometers showing the highest and lowest crosswind components give reasonable estimates of the lateral positions of the two vortices.

The ground based anemometers were useful for detecting and tracking wake vortices. However, no practical methods were

developed for estimating vortex circulation. A second limitation of the 1970s tests was that the data collection system was operated only during normal working hours.

In the mid 1980s German studies³ of vortex transport between parallel runways showed that improved vortex tracking and measurement can be achieved by increasing the height of the anemometers to 10 meters and including vertical wind and headwind measurements in addition to the crosswind measurements. The improved vortex tracking from the German configuration is presumably due to the lower turbulence level farther away from the ground and the fact that vertical vortex wind measurement is not affected by the ambient wind which is horizontal.

3. CURRENT INSTALLATIONS

The Volpe Center recently adapted the German configuration to study wake vortices stalled on the extended runway centerline. Anemometer arrays were installed 120 meters inside the middle marker (50 meter aircraft height) at two airports (JFK in 1994 and MEM in 1995).

The immediate goal of the New York Kennedy Airport (JFK) installation on Runway 31R was to provide reference vortex location information for evaluating a radio acoustic sensing system (RASS) for detecting and tracking wake vortices. The data acquired at JFK were then used to develop new processing algorithms that show promise for measuring vortex circulation and height.

An additional system was installed at the Memphis Airport (MEM) Runway 27 to support NASA's Memphis studies and to collect concurrent data with a cw lidar that will be used to validate the new processing algorithms.

The ultimate goal of the current study is a better understanding of when wake vortices remain in the flight path of following aircraft. The data collection system operates automatically and hence provides wake vortex data under all weather conditions and at all times of day and night with minimal cost. Aircraft arrivals are detected by aircraft noise. Real-time remote display of the vortex data is provided via dial-in modems. The anemometers are augmented with additional weather sensors to provide meteorological data with greater detail than the standard surface weather observations.

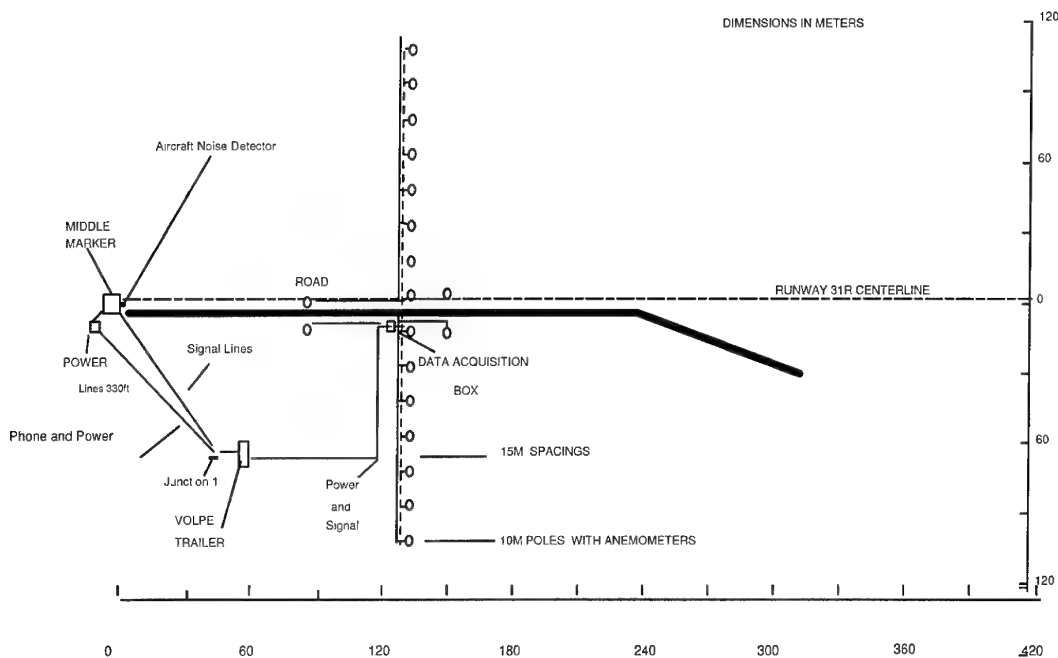


Figure 1. JFK Test Site

3.1 JFK Installation

The present test was conducted at the same site (middle marker region of JFK Runway 31R) used extensively for wake vortex studies in the early 1970s. The installation, shown in Figure 1, was designed to be an enhanced version of prior airport data collection efforts:

1. The German anemometer configuration was adopted. Vertical and horizontal anemometers were installed on 10-meter poles (15-meter spacing covering ± 107 meters perpendicular to the extended runway centerline) on the main baseline 122 meters inside the middle marker. Since wake vortices have little axial flow outside the

vortex core, headwind anemometers were installed only at both ends of the sensor line to obtain a measurement of the ambient wind that is not corrupted by wake vortices.

2. Prior tests generally measured a single crosssection through a vortex and hence could not detect vortex distortion (i.e., Crow instability) which may reduce the vortex hazard. This installation made a limited effort to detect distortion for stalled vortices by installing two additional poles (on centerline and 15 meters to one side) at 61 and 137 meters inside the middle marker. Note that airport obstruction rules would mandate shorter poles at

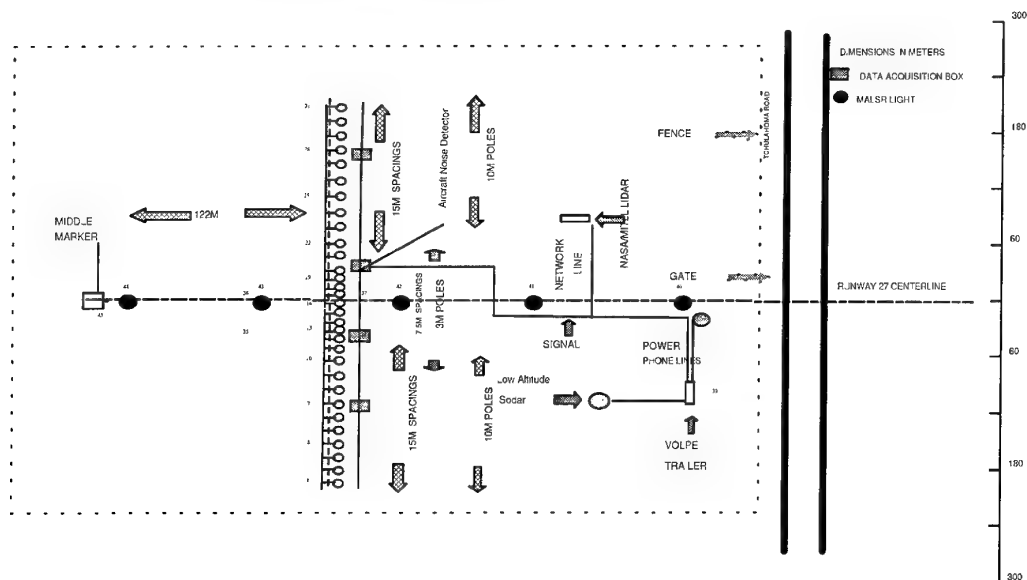


Figure 2. Memphis Test Site

- locations closer to touchdown.
3. The data collection was made completely automatic. Aircraft arrivals were detected by aircraft noise which triggered:
 - a) A video frame grabber to take a picture of the airplane for type identification, and
 - b) The run start procedure for data collection and real-time data processing.
4. Local measurements of temperature and humidity were made 2.5 meters above the ground.

Although the JFK Runway 31R site offers ideal real estate for sensor installation and a high proportion of Heavy aircraft, it was eventually abandoned in the 1970s because it appeared to be used only under high wind conditions when vortex lifetime is short. The current test shows substantial runway traffic at night and early in the morning when winds and turbulence are low; these arrivals would have been missed during the earlier tests.

3.2 MEM Installation

The MEM installation, shown in Figure 2, covered a wider distance (± 198 meters) than at JFK in order to reduce the likelihood of vortices transporting off the end of the anemometer array. Lower poles (3 meters) had to be used within ± 30 meters of the extended runway centerline at MEM to avoid interference with the MALSER approach lighting system. To compensate for the lower poles, the pole spacing was cut in half (to 7.5 meters) near the middle of the array.

4. DATA COLLECTION

The anemometers are digitized at a 10 Hz rate and averaged for two-seconds before being transferred to the data collection computer which operates under a multitasking environment that permits real-time processing. The data collection computer is attached to a PC based computer network for remote access and for additional real-time processing.

A variety of data files are generated:

1. Complete daily files of two-second averaged data are archived on the data collection computer.
2. A reduced daily file of two-second data (one minute before an aircraft arrival and five minutes after) is saved on the network fileserver.
3. Each one-minute block of two-second data is processed by a second task on the data collection computer into daily files (both local and fileserver storage) of one-minute means and standard deviations.
4. For each aircraft arrival a run file is saved on the fileserver containing two-second data from 10 seconds before the arrival until 180 seconds after the arrival or the next aircraft arrival.
5. The current run is also saved in a separate file that can be used for real-time processing.
6. Each two-second data block is saved in a file on the fileserver for real-time processing and display.

4.0 DATA ANALYSIS

Eventually all the collected wake vortex data will be incorporated into a database of wake vortex behavior as a function of weather conditions, both those measured by the local wind, temperature and humidity sensors and those reported by the standard airport surface observations. The MEM data set will also incorporate sodar wind profiles and NASA meteorological data.

4.1 Data Screening

At present, interesting runs have been selected for conditions not present in previous studies, namely low winds and/or low turbulence at night or early in the morning which may lead to long-lived vortices remaining near the runway centerline. The screening process is based on 24-hour plots of the one-minute means and standard deviations of the wind. Aircraft arrivals can be readily detected in these plots because their wake vortices cause larger than ambient variances in the crosswind and the vertical wind, especially the latter. The variations in vertical wind variance across the anemometer array coupled the measurements of the mean crosswind permit an estimate of which vortices are stalling near the runway centerline.

4.2 Velocity Profiles

Figure 3 shows a sample vortex velocity profile observed 18 seconds after the arrival of a B-747 aircraft under low turbulence and low crosswind conditions. The bottom of Figure 3 shows the velocity vectors measured at each anemometer position. The two top plots show, respectively, the variation of the vertical wind and crosswind components across the array (in these plots the lines simply connect the data points). The vortex pair generates a downwash between the vortices, an upwash outside the vortices, and an outwash under each vortex. Two of the anemometers show three wind vectors (0 and ± 15 meters); these are the lateral locations with anemometers at three longitudinal positions.

4.3 Crosswind Tracking Algorithm

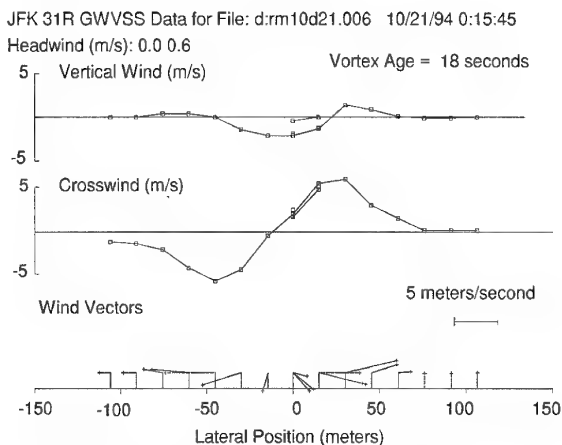


Figure 3. Velocity Profile: B-747 Run at JFK

The first analysis of the JFK data used the traditional crosswind tracking algorithm that assigns the lateral position of the two wake vortices to the anemometers showing the maximum and minimum crosswind component (see middle plot in Figure 3). Figure 4 shows the results from this algorithm for all vortex ages for the same run shown at age 18 seconds in Figure 3. The data from the traditional tracking algorithm are plotted as lines. [The points in Figure 4 will be discussed in Section 4.4.] The top plot in Figure 4 shows the lateral position of the two vortices as a function of vortex age. The bottom plot of Figure 4 shows values of the two vortex crosswinds (maximum and minimum) and the median crosswind. These parameters were not used in the traditional analysis of ground wind anemometer data. The median crosswind gives an estimate of the ambient crosswind and the vortex peak velocity is taken as the difference between the minimum or maximum crosswind and the median crosswind.

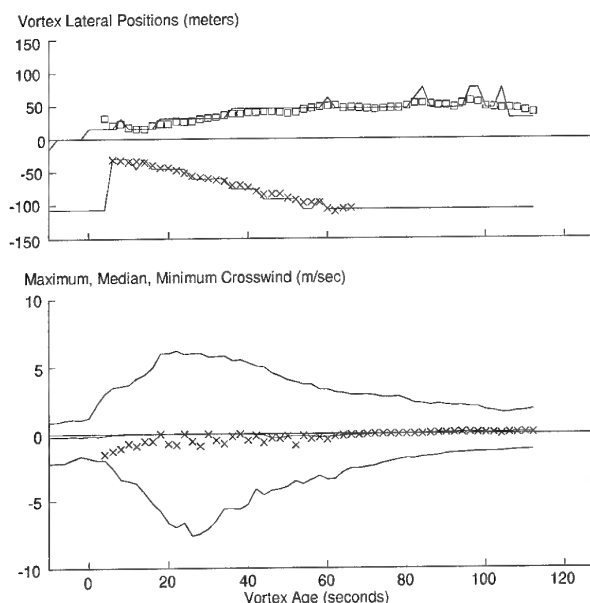


Figure 4. Traditional Tracking of B-747 Run

Vortex tracking is initiated when the vortex peak velocity is above a fixed threshold (currently set at 2.0 m/s). When a vortex drifts off the end of the array (± 107 m), its position track is terminated (e.g., note vortex marked with x's in top plot of Figure 4). Otherwise, the vortex track is terminated when the vortex peak wind drops below a fixed threshold (currently set at 1.0 m/s). The run in Figure 4 was actually terminated by the arrival of the next aircraft. Future processing algorithms should track the vortices until they disappear even if another aircraft arrives.

The start-track and stop-track vortex velocity limits should actually be adjusted according to the ambient turbulence level (as was done effectively in earlier analyses). However, the use of fixed velocity limits for defining the vortex lifetime may be appropriate to study the effect of turbulence on vortex lifetime.

4.4 Least-Square-Fit Algorithm

A least-square-fit algorithm was developed to analyze both the horizontal and vertical winds measured by the JFK anemometers. The goal of this analysis is to extract vortex height and circulation values from the data. The parameters of the fit are the ambient crosswind and the height, lateral position and circulation of each vortex included in the fit. The classical image model is used to represent the interaction of the vortices with the ground; image vortices are included to satisfy the boundary condition of no vertical wind at the ground. The horizontal and vertical wind at each anemometer location is calculated by adding the vortex induced winds to the ambient crosswind. The stall response of the propeller anemometer is modeled simply by setting the calculated horizontal and vertical winds to zero if both are less than 0.5 m/s.

The results of the conventional tracking algorithm are used to decide how many vortices to include in the fit (i.e., those being tracked) and to obtain initial estimates of the vortex parameters:

- The lateral positions are used directly.

- The ambient crosswind is taken as the median crosswind.
- The ratio of circulation to height is taken from the measured vortex peak velocity (correct for an isolated vortex).
- The vortex height is the least sensitive parameter and is taken as 30 meters.

The ratio of circulation to height is used as one parameter of the fit to avoid the strong interaction between height and circulation in specifying the measured vortex velocity. Once the largest measured vortex crosswind is specified, the height of the vortex determines the width of the observed crosswind peak; an intermediate value of 30 meters is used for the initial vortex height. The parameters of the fit are varied by specified increments (0.7 m/s for crosswind, 8 meters for lateral position and 20 percent for circulation/height and height) until a minimum sum of squares of the 30 errors (i.e., the difference between calculated and measured horizontal or vertical wind component at each of the 15 lateral positions) is obtained. The increments are then divided by two and the minimization repeated. After three divisions the process is terminated. The fit is abandoned if it does not converge after 30 incremental changes.

Figure 5 shows the fitted vortex locations (large squares) and velocity profiles for the data shown in Figure 3. Note that the vertical and horizontal distance scales of the wind vector plot (bottom of Figure 5) are the same so that the vortex positions are to scale in the plane perpendicular to the aircraft path. In contrast to Figure 3, plots in Figure 4 plot the measurements as points and the fitted profiles as lines. The fitted wind profiles are in excellent agreement with the measurements. As expected, the vortices are located over the anemometers having the highest and lowest crosswinds.

The fitted vortex parameters are plotted (x or square) as a

JFK 31R GWVSS Data for File: d:rm10d21.006 10/21/94 0:15:45

Headwind (m/s): 0.0 0.6

Vortex Age = 18 seconds

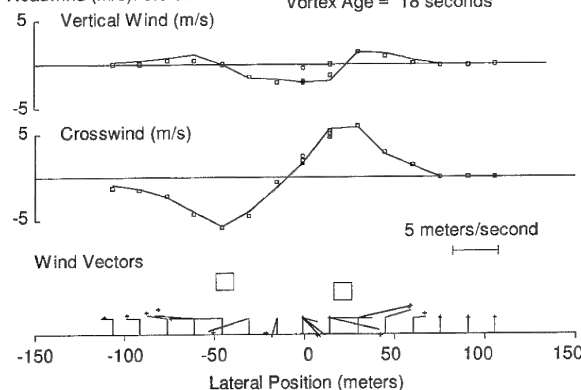


Figure 5. Fitted Vortex Positions and Wind Field at Vortex Age = 18 seconds

function of vortex age in Figures 4 and 6. The fitted lateral positions in Figure 4 vary more smoothly than the traditional tracks (lines). The two vortices separate because of their interaction with the ground. The fitted ambient crosswind is plotted as x in the bottom plot of Figure 4. The slightly negative ambient crosswind is consistent with the general vortex drift toward negative lateral positions.

The bottom plot of Figure 6 shows the variation in the mean square error of the fit (averaged per pole, with one horizontal wind error and one vertical wind error). The error for age 18 seconds is quite low, as would be expected for the excellent fit observed in Figure 5. Significantly larger errors are noted around age 38 seconds (see flow field in Figure 7), where the classical image model does not fit the flow field as well. A large jump in the error is noted at age 68 seconds when the fit no longer includes the vortex plotted as an x. The error slowly decays as this vortex moves farther away from the anemometer array.

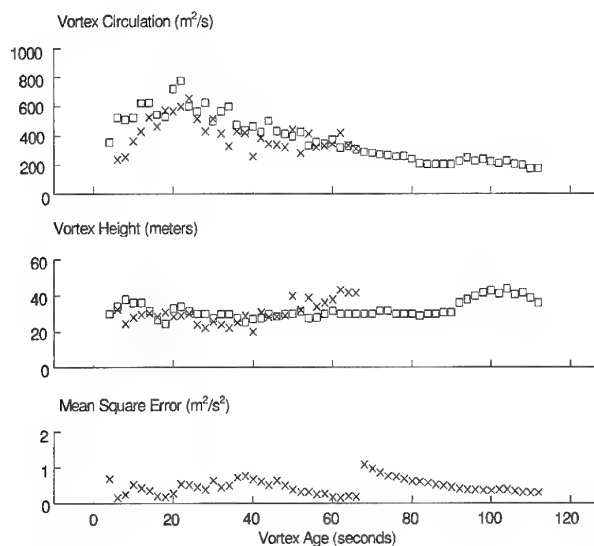


Figure 6. Least-Square Fit (Two Vortices) for B-747 Run

The height and circulation of the vortices in Figure 6 are the new parameters of the fit. The initial height should be 50 meters and initial strength should be about $600 \text{ m}^2/\text{s}$. The initial descent rate should be about 2 m/s . The fitted values are consistent with these values after about 10 seconds, but have low heights and circulations at earlier times. The vortices descend as expected to a minimum height of about 25

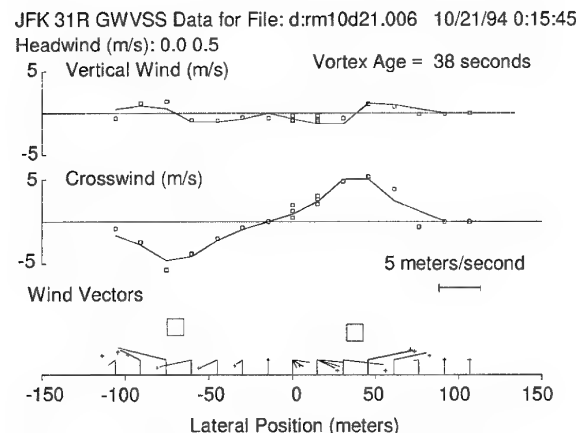


Figure 7. Fitted Vortex Positions and Wind Fields at Vortex Age = 38 seconds

meters and then rise somewhat from their lowest height. The downwind vortex rises more rapidly than the upwind vortex. The vortex circulation starts to decay at about 30 seconds and reaches about one third of its initial value at 112 seconds. The data points for the vortex remaining near the runway centerline are fairly consistent from one 2-second wind field to the next. Although the random error is small, the systematic errors may be large if the flow field is not well represented by the classical image model (as in Figure 7)

4.5 Secondary Vortices

The interaction of a wake vortex with the ground is not accurately represented by the image-vortex approach which generates high crosswinds at ground level. In fact, the proper treatment of the vortex-ground interaction must deal with a boundary layer of opposite sign vorticity that has zero crosswind at ground level. Under light crosswind conditions, the strong vortex lateral velocity near the ground detaches this boundary layer into secondary vortices which are located outside the primary wake vortices. These vortices cause the primary vortices to rise or "bounce."

Secondary vortices are regularly seen in the ground-based anemometer data. The primary and secondary vortices produce converging crosswinds (as in Figure 7 to the right of the right vortex) and an upward vertical wind in between. The least-square fit algorithm was modified to include secondary vortices when their expected location is within the anemometer array. Figure 8 shows the results of adding a secondary vortex (smaller square) to the fit shown in Figure 7. The fitted secondary vortex turns out to have the same height as the primary vortex. The fitted velocity profiles are significantly improved in the region where the secondary vortex is located. Surprisingly, the fit around the other vortex (left) is also somewhat improved.

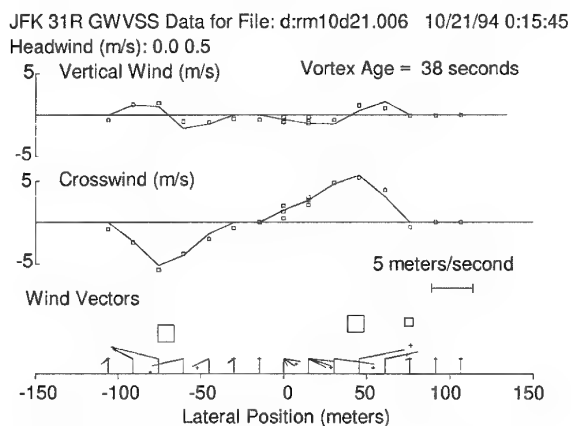


Figure 8. Fitted Vortex Positions and Wind Fields at Vortex Age = 38 seconds, with Secondary Vortex

Figure 9 shows the results of fitting secondary vortices to the entire run, starting at vortex age 20 seconds. The secondary vortices are plotted as small pluses or diamonds. No validity criteria were applied to the secondary vortices other than the requirement for convergence of the fit (e.g., no convergence was obtained for age 22 seconds). The corresponding results without secondary vortices are shown in Figures 4 and 6. The five plots of Figure 9 will be discussed from bottom to top:

- The fitted crosswind is steadier with the secondary vortices.
- The lateral positions of the secondary vortices are outside the primary vortices, as would be expected, since their initial locations were assigned at 25 meters outside the primary vortices. The secondary vortex positions are closer (pluses) to the primary vortex that is moving more rapidly laterally than (diamonds) to the main vortex moving more slowly.
- The mean square errors are significantly reduced only over vortex ages from 24 to 48 seconds. The secondary vortices are therefore more likely to be real for these times.
- The secondary vortex heights are more consistent over the ages where the fit was improved (24 to 48 seconds) than at later times. Over this age range, the plus vortices were located at about half the primary vortex height while the diamond vortices were close to the primary vortex height.
- The addition of secondary vortices generally increased the circulation values of the primary vortices. Since the net effect of the secondary vortices, which have opposite circulation, is to subtract from the winds induced by the main vortices, this result is as expected. Note that the secondary vortices similarly reduce the effect of the vortices on an encountering aircraft. The plus secondary vortices have about one sixth the circulation of the primary vortex. The diamond secondary vortices are stronger (one fourth of the primary vortex circulation).

4.6 MEM Sample Run

Many of the aircraft using Runway 27 at Memphis are small twin-propeller aircraft. Since the vortices from such aircraft descend closer to the ground than vortices from jet transport aircraft, they can still be readily detected by the ground-based anemometers even though their circulations are much smaller. The lower, denser anemometer array at MEM facilitates this detection. Figure 10 shows a sample vortex wind profile with fitted vortices for such an aircraft (Saab340). The wind vector plot at the bottom of Figure 10 shows the shorter poles and closer spacing within ± 50 meters of the extended runway centerline. The crosswind plot (middle of Figure 10) shows two vortices that are well fitted by the image vortex model. In addition, there is a crosswind gust between +50 and +100 meters that will cause difficulties with the fit at later times.

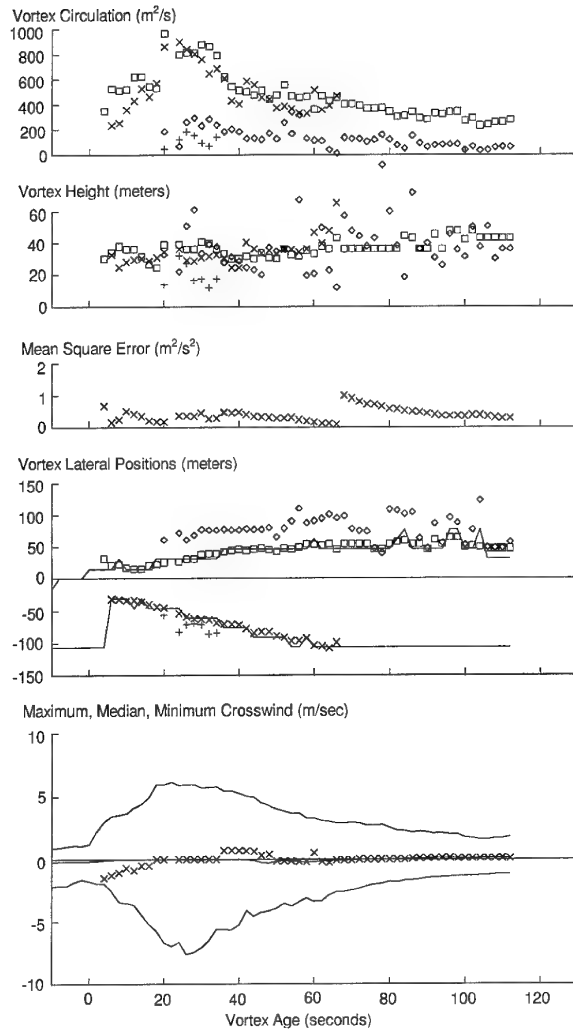


Figure 9. Fitted Parameters of B-747 Run with Secondary Vortices

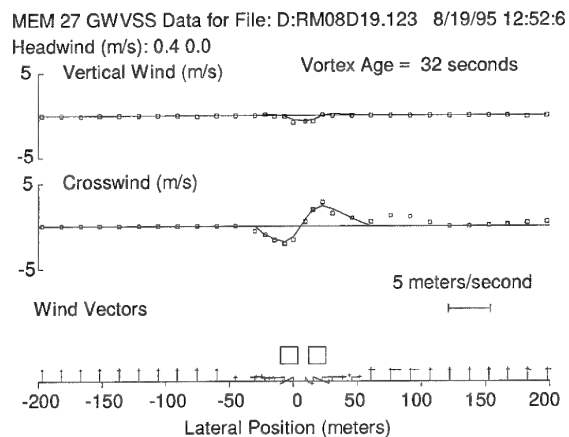


Figure 10. MEM Wind Field for Saab340 Aircraft at Age 32 Seconds

Figure 11 shows the complete vortex history for this same run. The vortex descent down to about 10 meters height is clearly tracked for vortex ages of 28 to 48 seconds (with outliers at 38 and 40 seconds). The fitted circulations decrease from 200 to about 60 m^2/s during this age period. At age 50 seconds large jumps in fitted height and circulation occur. The velocity plots show that the crosswind gust observed in Figure 8 contributes to this change in the fit. Thus, in this run the least-square-fit results are unreliable after 48 seconds.

4.7 Future Development

The least-square analysis will be improved by:

1. Developing criteria for when to include secondary vortices in the fit,
2. Determining the accuracy of the fitted vortex heights and circulations by comparison with concurrent lidar data from Memphis
3. Developing criteria for deciding when the vortex measurements are no longer valid,
4. Optimizing the processing under varying turbulence levels,
5. Fitting the early vortex history to the dynamics of the classical image theory, and
6. Studying vortex distortion in stalled vortices (Crow instability) in the JFK data by taking the vortex circulation from the least-square fit for the main sensor baseline and then adjusting its position to fit the data at the two locations on the two displaced baselines.

CONCLUSIONS

Ground-based anemometers have always been a low-cost, all-weather method of detecting and tracking aircraft wake vortices. The application of state-of-the-art (1) data processing, (2) computer networking and (3) communication technology to this venerable measurement technique has greatly improved its capabilities. When the limitations of the new data processing algorithms have been determined, ground-based anemometers will provide automatic, real-time measurements of wake vortex location and circulation in the most critical region of the final approach path.

ACKNOWLEDGEMENTS

This work was sponsored by the United States Federal Aviation Administration Wake Vortex Program Office.

REFERENCES

1. Hallock, J.N. and Eberle, W.R., editors, "Aircraft Wake Vortices: a State-of-the-Art Review of the United States Program," Report No. FAA-RD-77-23, February 1977, Transportation Systems Center, Cambridge MA and Lockheed Missiles and Space Company, Inc., Huntsville AL
2. Sullivan, T.E. and Burnham, D.C., "Ground Wind Sensing System Calibration Tests," Report No. FAA-RD-80-13, February 1980, Transportation Systems Center, Cambridge MA.
3. Tetzlaff, G., Franke, J. and Schilling, V., "Wake Vortex Propagation in the Atmospheric Boundary Layer," Proceedings of the Aircraft Wake Vortices Conference, Washington DC, October 29-31, 1991, Report No. DOT/FAA/SD-92/1.2, pp 47-(1-19).

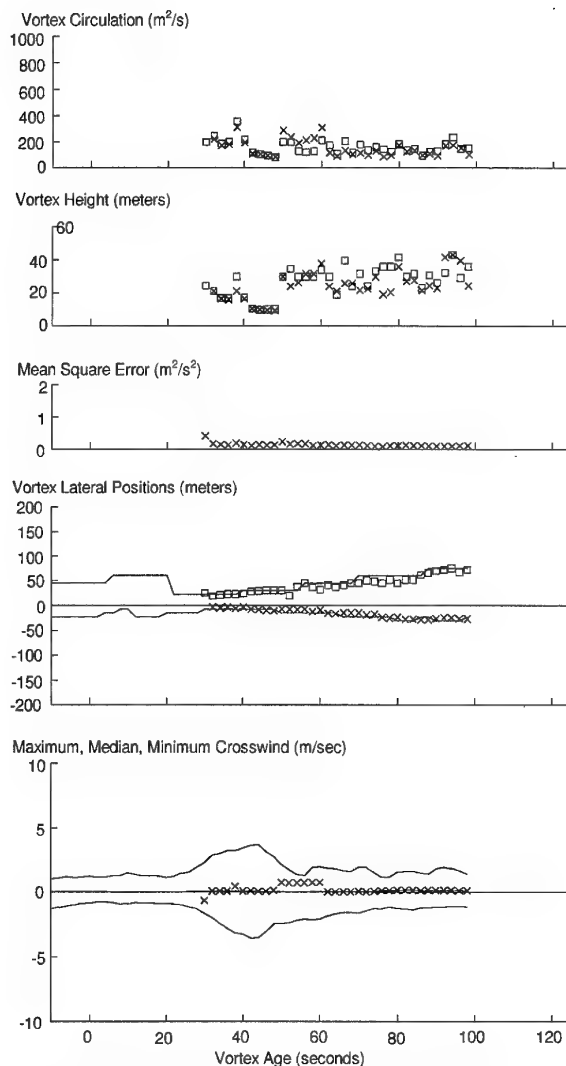


Figure 11. MEM Fitted Data for MEM Run:Saab340 Aircraft

The Dynamic Response of a Twin-Engine, Commercial Jet Transport to Wake Vortex Encounters

Mr. James Vasatka
Principal Engineer, Aerodynamics Engineering
Boeing Commercial Airplane Group
P. O. Box 3707, MS 67-63
Seattle, WA 98124-2207
USA

Summary

In order to refine existing wake-vortex separation distances through the application of technology, the issues associated with defining the basis for separation criteria must be addressed. This includes understanding the *significance* of a wake vortex encounter.

To further the process of understanding the *significance* of such encounters, a flight simulator was used to evaluate the response of a jet-transport aircraft to wake-vortex encounters. The objective was to evaluate the response of a twin-engine, commercial jet transport to a variety of wake characteristics and operational assumptions. The study was conducted using a modified simulation of a twin-engine, commercial jet transport. The simulations included: 1) the free response of a trimmed airplane encountering a wake; 2) the response of an airplane controlled by only the autopilot; and 3) the response of an airplane controlled by a "math pilot" designed to maintain wings level. The latter two modes of airplane control were chosen in order that the airplane response could be evaluated without incurring the variation associated with pilot-in-the-loop simulations.

The results from this study suggest that the airplane's response is dependent on the flight path through the wake.

Further work is required in 1) defining the "aged" characteristics of a wake, 2) validating the effects of a vortex flow field on the aerodynamic characteristics of an airplane, 3) modeling the vortex-induced aerodynamic characteristics in the simulator, and 4) defining an operationally acceptable airplane response.

Fully addressing these issues will require participation from all the affected segments of the industry, attainable goals, strong leadership, and adequate resources.

Symbols

- b Wing Span (feet)
- C_l Rolling moment coefficient induced by the wake
= $\frac{\text{rolling moment}}{q S b}$
- C_n Yawing Moment Coefficient = $\frac{\text{yawing moment}}{q S b}$
- p Roll Rate (deg/s)
- \dot{p} Roll Acceleration (deg/s²)
- q Dynamic Pressure (lbs/feet²)
- r Radius of the Vortex Core (feet)
- S Wing Reference Area (feet²)
- W Weight of the Generating Airplane (lbs)
- V Velocity of the Generating Airplane (feet/s)
- β Sideslip Angle (deg)
- Φ Bank Angle (deg)
- ρ Density (slugs/feet³)

Introduction

Many major U.S. airports are capacity limited and are experiencing significant traffic delays. These delays result in substantial cost increases and limit the growth of traffic at these airports. The existing wake-vortex separation distances represent *one* of the major opportunities for mitigating airport congestion. The goal of NASA's Advanced Subsonic Technology (AST) Program is to develop, in cooperation with the FAA and industry, viable technologies to ensure a safe, highly productive global air transport system. The conceptual design of a system that alleviates capacity limitations related to wake vortices through the application of technology is presented in Reference 1. The system, as conceptualized, would track the wake's position, evaluate its characteristics, assess its potential effect on the following aircraft, and provide spacing guidance to the controller. The concept offers significant potential for enhancing safety in the air

The author is indebted to H. B. Dellicker, M. D. Ingham, J. W. Kerrigan, S. A. Lewis and J. E. Wilborn for their assistance.

traffic control (ATC) system while minimizing capacity constraints associated with wake vortices.

There are many challenges associated with the AST research effort. One of the challenges is defining the basis for separation criteria. This issue is still debated much as it has been since the 1970s flight test program (Reference 2). Refining the present wake vortex separation criteria requires that the following three questions be addressed:

Is it there? Under many meteorological conditions, the wake is quickly transported away from the approach corridor. The ability to track wakes would allow reduced separation distances when the approach corridor is clear.

Is it alive? Under some meteorological conditions, the wake may stall in the approach corridor. The ability to evaluate the "aged" characteristics of the wake would allow for a circumspect determination of separation.

Does it matter? In the event that a wake stalls in the corridor and is still alive, the *significance* of these aged characteristics on the following aircraft must be assessed for a prudent determination of separation.

An aircraft encountering the wake of the preceding aircraft can be disturbed by the resultant forces induced by the vortical flow field of the wake. The elements necessary to determine the significance of a wake turbulence encounter--and thus answer the question of "Does it matter?"--include the following:

Wake Characteristics. Understanding the "aged" characteristics of wakes is necessary in order to assess the dynamics of a wake encounter.

Response dynamics. The response of an airplane to the wake of the preceding airplane is related to the characteristics of the wake, the location of the wake, the flight path, and the aerodynamics and inertial characteristics of the encountering airplane.

Human Factors. Understanding the spectra of human factors associated with the pilot's response to the motions of the aircraft is essential for defining operationally acceptable characteristics.

The objective of this study was to evaluate the response of a twin-engine, commercial jet transport to a variety of wake characteristics and operational assumptions. The simulations included: 1) the free response of a trimmed airplane encountering a wake; 2) the response of an airplane controlled by only the autopilot; and 3) the response of an airplane

controlled by a "math pilot" designed to maintain wings level. The latter two modes of airplane control were chosen in order that the airplane response could be evaluated without incurring the variation associated with pilot-in-the-loop simulations. This study differs from past simulation-based studies, References 3 through 5, in that the focus is on assessing variance in operational assumptions and in lateral and vertical positioning of the encountering airplane relative to the wake.

The Airplane Simulation Model

The baseline simulation used for the study was a six-degree-of-freedom simulation validated through an extensive flight test program. Sketches of the airplane used in the study are presented in Figure 1. The simulation includes modeling of applicable airplane systems. The "math" pilot used in this study was designed to maintain wings level.

Simulations are typically developed for a uniform wind field acting on the airplane. The three commonly used methods for assessing the effects of a vortex flow field on the aerodynamic characteristics of an airplane are: 1) linear rotary approximation; 2) strip theory calculation; and 3) vortex lattice and paneling technique. Each of these methods has specific limitations, which are discussed in Reference 6.

This simulation, which was originally developed for a uniform wind field acting on the airplane, was modified using strip theory to include the variations in flow field induced by the vortex. The incremental forces and moments acting on the airplane were calculated for each strip. The forces and moments were then summed and added to the baseline simulation. Each wing was divided into forty chordwise strips of equal width. The horizontal and vertical tails were each divided into twelve chordwise strips of equal width.

Wake Model used in the Simulations

It is well-known that the non-uniform lift distribution on a finite span wing results in a trailing vortex sheet. The roll-up of this sheet into vortices was recognized as early as 1911 by Lanchester. A significant amount of work describing the characteristics of airplane wakes has been published over the years. An annotated bibliography of the reference material from 1911 through 1990 is presented in Reference 7. A summary of the understanding of the wake vortex phenomenon is presented in References 8 and 9. The present understanding of wake characteristics is summarized as follows:

- 1) The initial strength as measured by circulation can be calculated using theoretical methods;
- 2) The initial sink rate of the wake can be calculated using theoretical methods;
- 3) The far-field characteristics of a wake are strongly influenced by meteorological conditions.

The strength of the vortices in this discussion refers to circulation, where circulation is defined as:

$$\Gamma = \text{Constant} \frac{W}{\rho V b}$$

The tangential velocity distribution used in the simulation is as follows outside the core.

$$V_{\text{tan}} = \frac{\Gamma}{2 \pi r}$$

Inside the core, the velocity varies linearly.

The ability to reliably predict the characteristics of wake vortices as they age is a challenging task. The effects of atmospheric stratification, wind shear, and atmospheric turbulence are not easily predicted. The most conservative answer is a vortex pair that does not decay or decays very slowly. Therefore, the initial strength of the vortices is the strength used for this study.

The core diameter was defined as ten percent of the wake's span. The wake characteristics used in these simulations are summarized in Tables 1-A and 1-B. It is important to note that the wake characteristics used in this study represent a subset of the wake characteristics that are possible in an operational environment.

Table 1.A
Wake Characteristics for Transition Flaps

Γ (ft ² /sec)	Wake Span (feet)	Core Dia. (feet)
1000	75	7.5
2000	75	7.5
3000	116	11.6
4000	158	15.8
5000	158	15.8

Table 1.B
Wake Characteristics for Landing Flaps

Γ (ft ² /sec)	Wake Span (feet)	Core Dia. (feet)
2000	75	7.5
3000	93	9.3
4000	116	11.6

5000	158	15.8
6000	158	15.8

Determining the Significance of an Encounter--The parameters used for evaluating the trends of the encounters with a wake were Φ_{max} , p_{max} , \dot{p}_{max} , and $C_{t \text{ max}}$. These parameters provide a reasonable measure of the airplane's response to the matrix of conditions studied. There are other characteristics of the encounter, including $C_{n \text{ max}}$ and β_{max} , that may also provide a measure of the significance of the encounter. These latter two characteristics are not presented in this paper for the sake of brevity.

Entry Scenarios--The entry paths used in this study were an entry from the side of the wake and an entry from below the wake. The location and orientation of the airplane were established with respect to the wake. The airplane was initially positioned outside the influence of the wake on an intersecting flight path. The two entry paths are described in Figures 2-A and 2-B.

Airplane Enters from the Side of the Wake--The following scenarios were studied with the airplane entering from the side of the wake: 1) the response of a trimmed airplane with no additional control inputs; 2) the response of the airplane with only the control inputs from the autopilot; and 3) the response of the airplane with the control inputs of a math pilot designed to maintain wings level. Each simulation was initialized with the airplane center of gravity (C.G.) at the same height as the center of the vortices. The airplane was positioned outside the wake on a five-degree intercept heading. Five degrees was chosen since it was large enough to assure that the airplane penetrated the wake, and yet small enough that the airplane did not transit the wake too quickly.

Airplane Enters from below the Wake--The following scenarios were studied with the airplane entering from below the wake: 1) the response of a trimmed airplane with no additional control inputs; 2) the response of the airplane with only the control inputs from the autopilot; and 3) the response of the airplane with the control inputs of a math pilot designed to maintain wings level. Each simulation was initialized with the airplane C.G. below the center of the port vortex. The airplane was positioned outside the wake in level flight on the same heading as the wake. The wake was positioned on a three-degree glide slope.

Encounters with a Trimmed Airplane and No Additional Control Inputs--The characteristics of the encounters with no additional control inputs are presented in Figures 3-A, 3-B, 4-A and 4-B for

initial approach flaps and landing flaps, respectively. The typical flight path for this type of encounter is presented in Figures 5-A and 5-B. For this scenario, the forces and moments induced by the vortex pair tend to raise the airplane over the first vortex and then pull the airplane below the second vortex.

These results are in reasonable agreement with the trends from the 1970s flight test of a 737-100 (Reference 9).

Encounters with Control Inputs from the Autopilot--

The characteristics of the encounters with control inputs from only the autopilot are presented in Figures 6 and 7 for transition flaps and landing flaps, respectively. The typical flight path for this type of encounter is presented in Figure 8. One of the trends indicated from these simulations is that for entries from the side, the Φ_{\max} tends to be sensitive to the strength of the vortex. This trend results from the autopilot trying to maintain the established flight path through the wake, resulting in a flight path near the cores.

The encounter characteristics for the entry from below are relatively small compared to the entry from the side and are not presented for brevity.

The entry height of the airplane relative to the wake was also studied. The characteristics of these encounters are presented in Figure 9 as a function of entry height. These simulations show two significant trends. The first trend is that Φ_{\max} is rather sensitive to entry height. The maximum Φ_{\max} tends to occur at an entry height of -25 feet. For this condition, the airplane is drawn up through the core of the first vortex.

It is also interesting to note the bimodal nature of the curves. For airplanes entering below the wake, the airplane is drawn up into the first vortex. For airplanes entering above the wake, the airplane is drawn down into the second vortex. When the airplane enters the wake at the same altitude, the airplane is drawn over the first vortex and below the second.

The second trend indicated from the results of this study is that, as the airplane passes over a vortex, it experiences significant yawing moments. This result is expected, considering that the vortex-airplane interaction model used in the simulation superimposes the vortex flow field on the airplane. However, this trend does not agree with the flight test results presented in Reference 9. Accurately modeling the vortex-airplane interaction will require a more sophisticated model than presently exists.

Encounters with Control Inputs from a Math Pilot--

The characteristics of the encounters with control inputs from a math pilot designed to maintain wings level are presented in Figures 10 and 11 for transition flaps and landing flaps, respectively. The typical flight path for this type of encounter is presented in Figure 12. One of the trends indicated from these simulations is that the Φ_{\max} tends to be insensitive to the strength of the vortex up to a threshold level. This trend results from math pilot's authority to control the C_l induced by most of the wakes studied.

The encounter characteristics for the entry from below are relatively small compared to the entry from the side and are not presented for brevity.

Conclusions

The strip theory used in the study provides a reasonable simulation of the forces and moments for many encounters; however, the method overestimates the yaw moments induced by the vertical tail when the airplane passes through or above the wake.

The results also suggest that the dynamic response of an airplane to an encounter with a wake is dependent on the flight path through the wake. However, the limited nature of this study precludes a conclusive determination of the sensitivity of the aircraft's dynamic response to parameters such as entry height, intercept angle, and Γ .

Road Map to Future Simulation Work

In order to refine existing wake-vortex separation distances through the application of technology, the issues associated with defining the basis for separation criteria must be addressed. In the event that a wake stalls in the corridor and is still alive, the *significance* of these aged characteristics on the following aircraft must be understood. This will require 1) defining the "aged" characteristics of a wake, 2) validating the effects of a vortex flow field on the aerodynamic characteristics of an airplane, 3) modeling the vortex-induced aerodynamic characteristics in the simulator, 4) expanding the simulation studies to include an assessment of the human factors, and 5) defining an operationally acceptable airplane response.

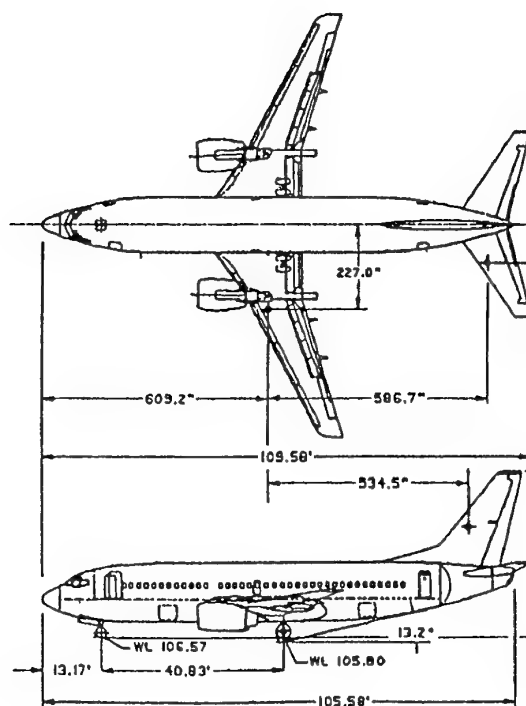
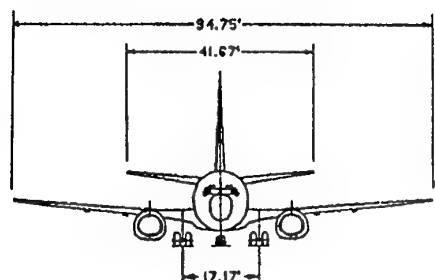
Fully addressing these issues will require participation from all the affected segments of the industry. Regulatory agencies, airlines, manufacturers, the piloting and ATC communities and research institutions must combine their efforts to ensure that an industry-wide wake-vortex plan is

implemented and that it has constancy of purpose, clear and attainable goals, strong leadership, and adequate resources.

References

- 1) Hinton, D. A., "Aircraft Vortex Spacing System (AVOSS) Conceptual Design," NASA TM 110184, August 1995
- 2) Rudolph, J. F., "A Compilation of Working Papers Concerning the Wake Turbulence Tests," FAA report, April 30, 1970
- 3) Hastings, E. C. et al., "Simulated Vortex Encounters by a Twin-Engine Commercial Transport Aircraft During Final Approach," SAE Technical Paper 800775, May 1980
- 4) Sammonds, R. I. et al., "Criteria Relating Wake Vortex Encounter Hazard to Aircraft Response," Journal of Aircraft Vol. 14, No. 10, pg. 981, October 1977
- 5) Nelson, R. C., "Dynamic Behavior of an Aircraft Encountering Aircraft Wake Turbulence," Journal of Aircraft Vol. 13, No 9, pg. 704, September 1977
- 6) Dunham, R. E. et al., "The Challenges of Simulating Wake Vortex Encounters and Assessing Separation Criteria," Paper 93-3568, August 9, 1993
- 7) Hallock, J. N., "Aircraft Wake Vortices: An Annotated Bibliography (1923 - 1990)," U. S. Dept. of Transportation Report DOT-FAA-RD-90-30, January 1991
- 8) Hallock, J. N., "Aircraft Wake Vortices: A State-of-the-Art Review of the United States R&D Program," FAA Report No. FAA-RD-77-23, February 1977
- 9) Hallock, J. N., "Aircraft Wake Vortices: An Assessment of the Current Situation," DOT-FAA -RD-90-29, January 1990

Figure 1
Three-view Sketch of the Aircraft
Simulated in the Investigation



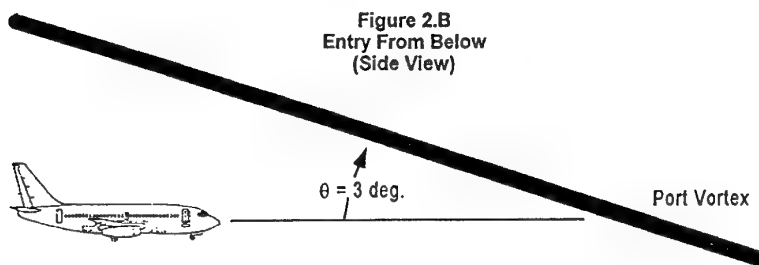
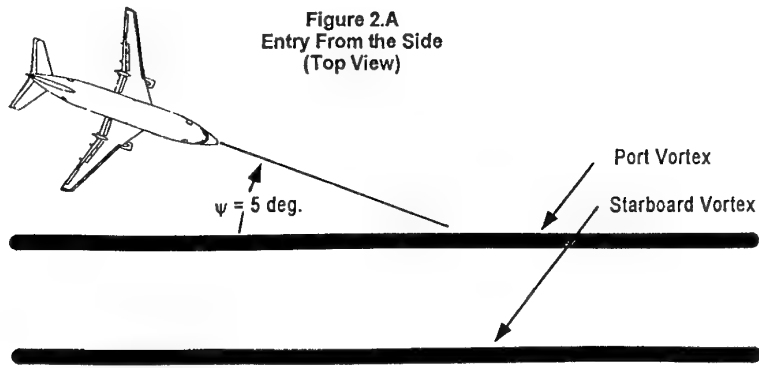


Figure 3.A
Encounter Characteristics for a Free Response
Trimmed for Level Flight
Transition Flaps Configuration
Entry from the Side, Del Alt. = 0

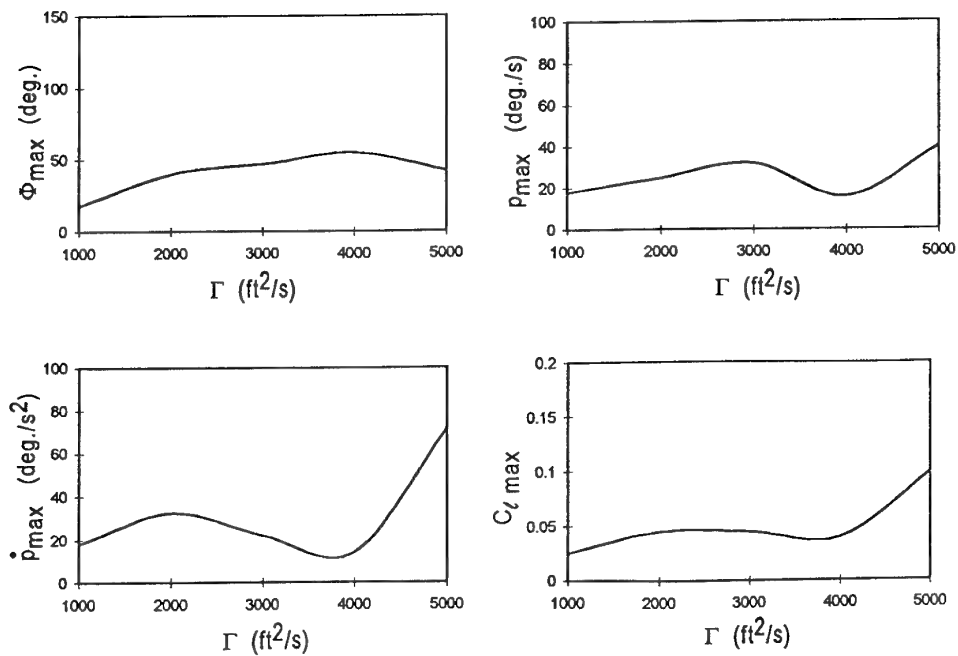


Figure 3.B
 Encounter Characteristics for a Free Response
 Trimmed for Level Flight
 Transition Flaps Configuration
 Entry from Below

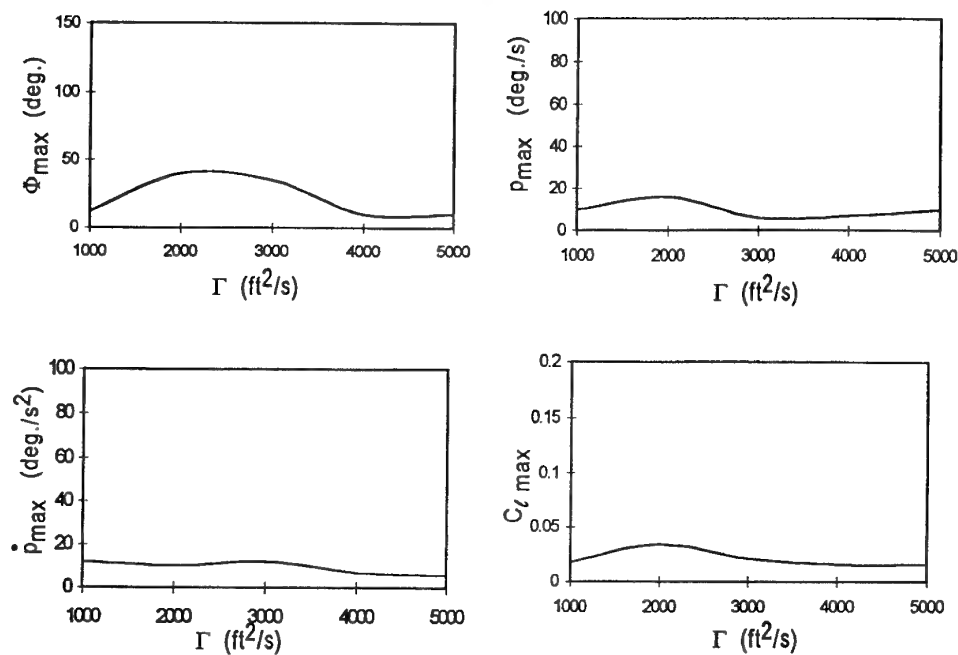


Figure 4.A
 Encounter Characteristics for Free Response
 Trimmed for Level Flight
 Landing Flaps Configuration
 Entry from the Side, Del Alt. = 0

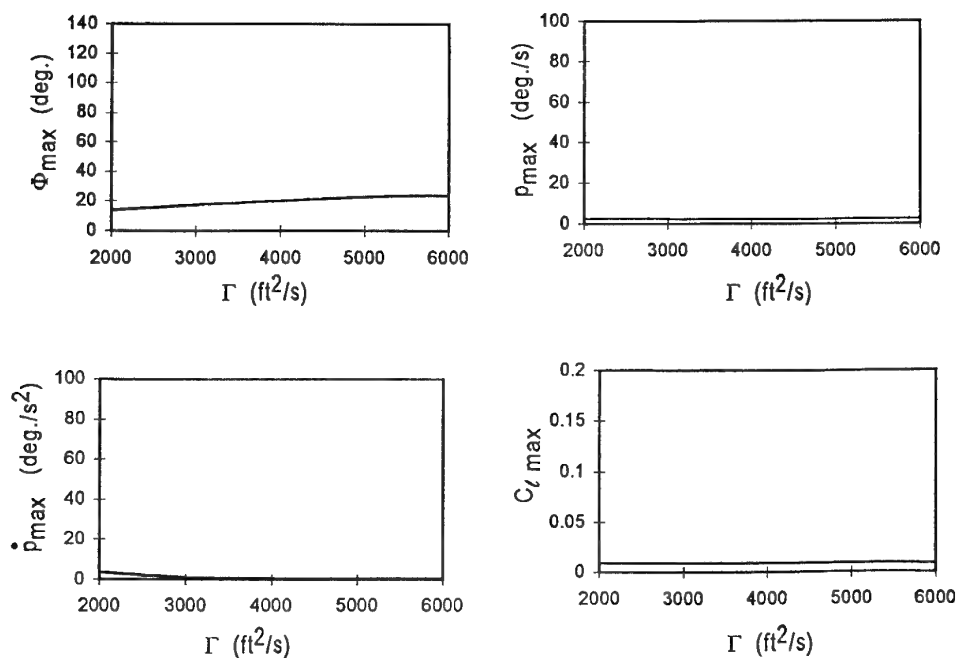


Figure 4.B
 Encounter Characteristics for a Free Response
 Trimmed for Level Flight
 Landing Flaps Configuration
 Entry from Below

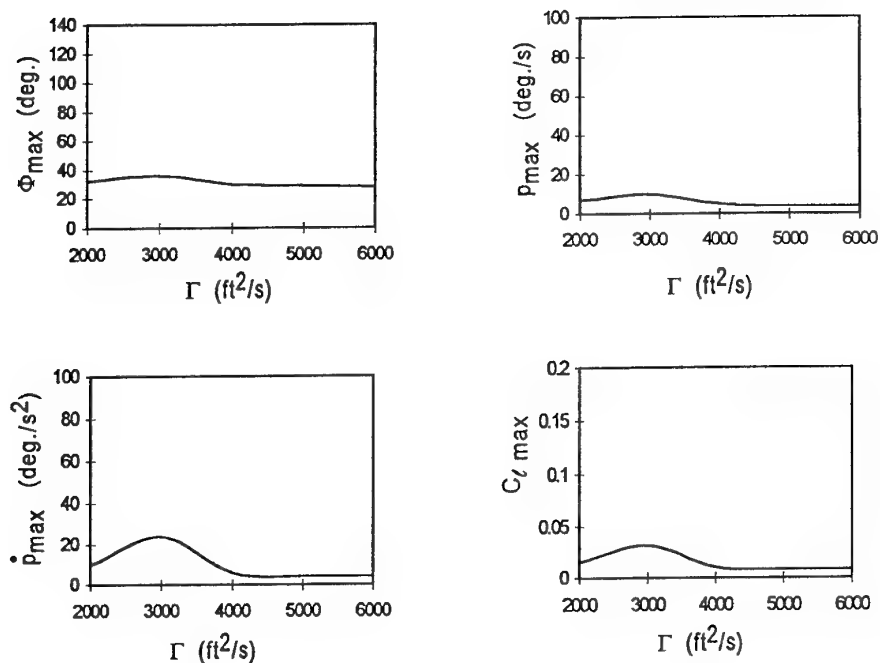


Figure 5.A
 Typical Flight Path for Entry from the Side
 Trimmed for Level Flight
 No Additional Control Surface Inputs
 (Rear View)

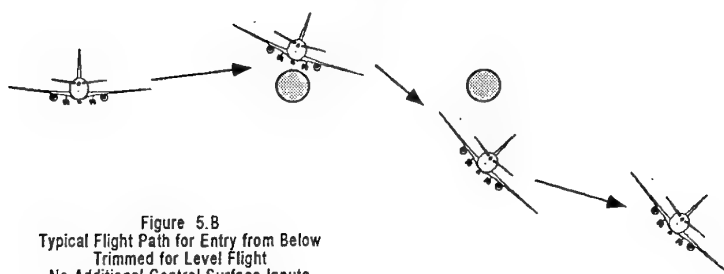


Figure 5.B
 Typical Flight Path for Entry from Below
 Trimmed for Level Flight
 No Additional Control Surface Inputs
 (Rear View)

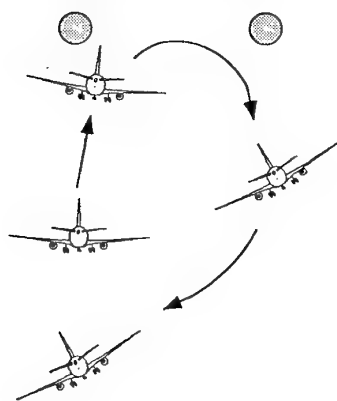


Figure 6
 Encounter Characteristics vs Wake Strength
 Autopilot Inputs Only
 Transition Flaps Configuration
 Entry from the Side, Del Alt. = 0

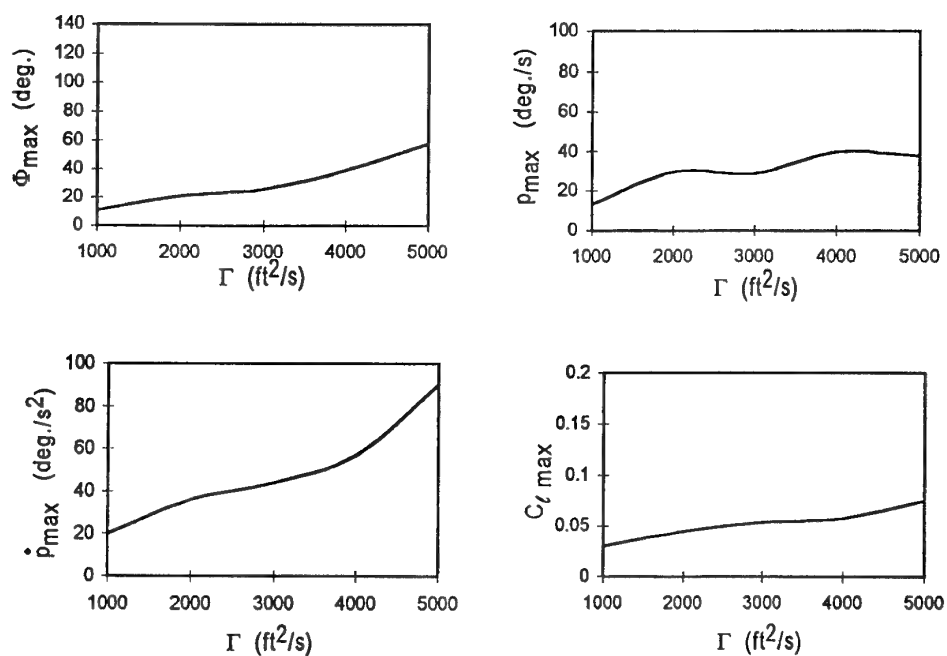


Figure 7
 Encounter Characteristics vs. Wake Strength
 Autopilot inputs Only
 Landing Flaps Configuration
 Entry from the Side, Del Alt. = 0

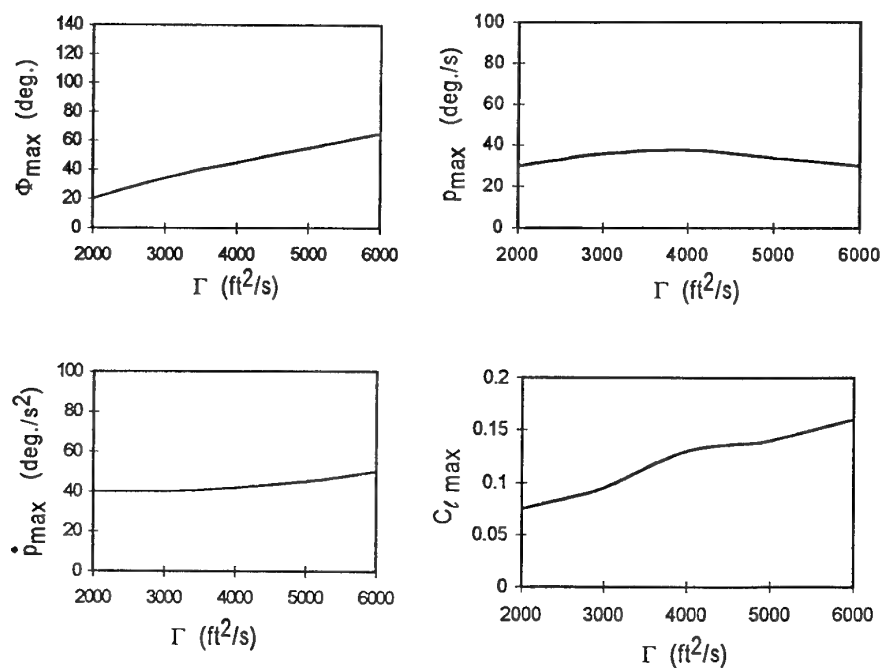


Figure 8.A
Typical Flight Path for Entry from the Side
Autopilot Inputs Only
(View from the Rear)

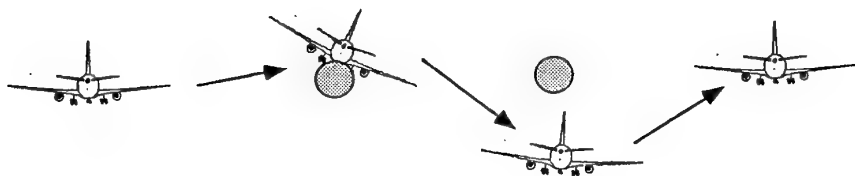


Figure 8.B
Typical Flight Path for Entry from Below
Autopilot Inputs Only
(View from the Rear)

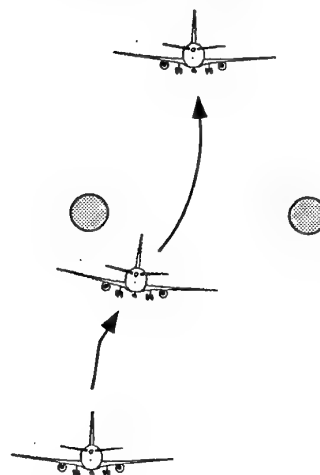


Figure 9
Encounter Characteristics vs Entry Height
Autopilot Inputs Only
Transition Flaps Configuration
Entry from the Side

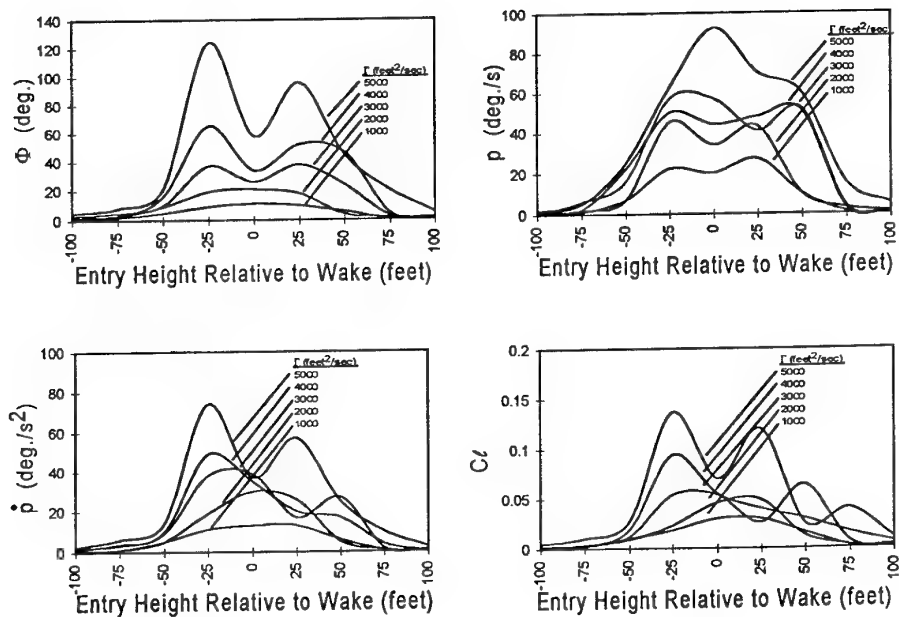


Figure 10
 Encounter Characteristics vs. Wake Strength
 Math Pilot
 Transition Flaps Configuration
 Entry from the Side
 Del Alt. = 0

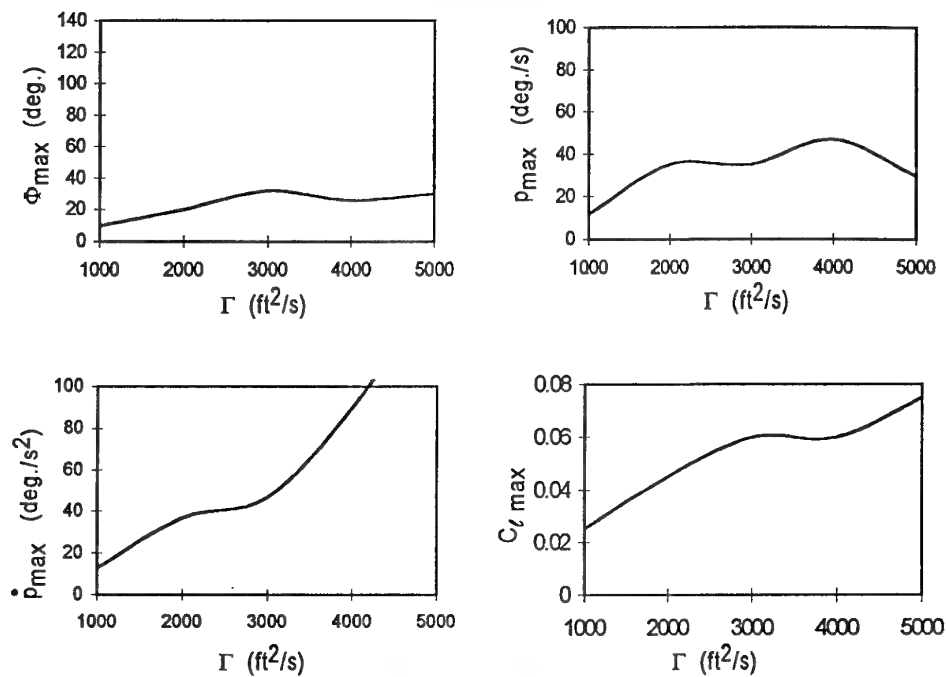


Figure 11
 Encounter Characteristics vs Wake Strength
 Math Pilot
 Landing Flaps Configuration
 Entry from the Side
 Del Alt. = 0

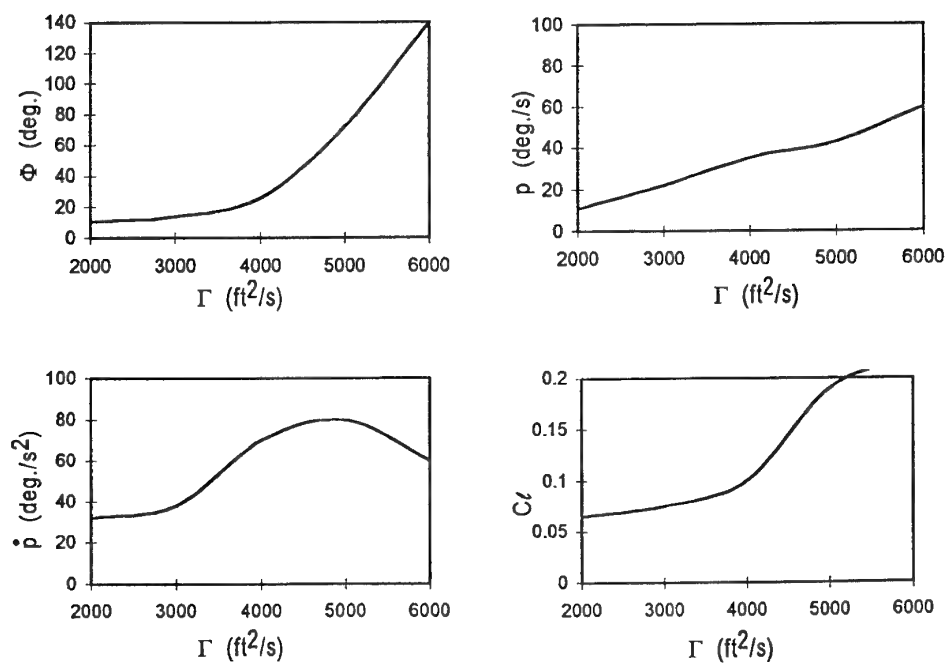


Figure 12.A
Typical Flight Path for Entry from the Side
Math Pilot On

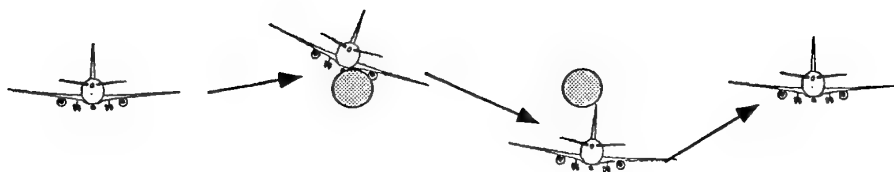
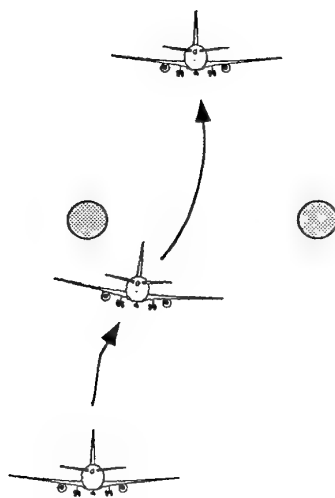


Figure 12.B
Typical Flight Path for Entry from Below
Math Pilot On



Experimental Analysis of the Vortex Wake Structure behind a Propeller-Wing Configuration

L.L.M. Veldhuis

D.W.E. Rentema

Low Speed Aerodynamics Laboratory

Delft University of Technology

Kluyverweg 1, 2629 HS Delft, the Netherlands

Summary

A flow field survey was performed with a 5-hole pressure probe at 1 chord length behind a propeller-wing configuration revealing important qualitative and quantitative information on the propeller dominated interactive flow field. The model, that consists of a low aspect ratio semi-span wing model combined with a 4 bladed tractor propeller, was tested at several low subsonic flow conditions in the Delft University Low Speed Windtunnel.

The distribution of total pressure and axial vorticity show, besides the well-known spiral tip vortex, a strong deformation of the slipstream structure. The deformation of the vortex wake is strongly related to the spanwise lift distribution of the propeller/wing configuration which might be used as a starting point for prediction of vortex formation and decay. It also determines the magnitude of the overall induced drag and the deformation process therefore has implications for the proper modelling of slipstreams used within theoretical prediction codes for the analysis of airplane performance. To obtain quantitative information from the field data the theory of Betz and Maskell was applied to determine the lift, the profile drag and the induced drag for both the model with and without running propeller. Comparison of these results with external balance measurements shows a good agreement. The lift distributions which were compared with surface pressure measurements reveal that a considerable amount of swirl is left in the slipstream after passage of the wing; an important observation for future optimisation of propeller-wing configurations. In general the flow field survey with traversing 5 hole probe appears to be a powerful technique to better understand propeller/wing interactive flows.

SYMBOLS AND UNITS

b	wing span [m]
c	wing chord [m]
C_{P_t}	total pressure coefficient ($= (P_t - P_{t_\infty}) / q + 1$)
C_D	drag coefficient
C_L	lift coefficient
C_x	tangential force coefficient ($X / \frac{1}{2} \rho V^2 S$)
D	drag force ; propeller diameter (=0.236 m)
H	total pressure
L	lift force
P_c	power coefficient ($= P / \rho V^3 D^2$)
R	propeller radius [m]
Re	Reynolds number based on wing MAC
S	wing area [m]
T_c	thrust coefficient ($= T / \rho V^2 D^2$)

U	axial flow velocity [m/s]
U_∞	undisturbed flow velocity [m/s]
u,v,w	flow velocity in x-, y- and z-direction
x,y,z	flow axis system
x_p	streamwise propeller position [m]
α_p	propeller angle of attack [°]
ΔP_t	total pressure jump across propeller plane [Pa]
ξ	axial vorticity ($= \partial w / \partial y - \partial v / \partial z$)

Indices

∞	undisturbed flow situation
1,2	at survey plane 1 and 2

1. INTRODUCTION

Wake vortices are generated whenever a three-dimensional body generates forces which have a component perpendicular to the undisturbed flow direction. Particularly the vortex system generated by a lifting wing is of great importance with respect to the problem of aircraft separation in the vicinity of airports with high traffic intensity. The problem might increase in the near future due to the development of large aircraft which produce a wake in which larger amount of energy is dispersed.

Not only this "far field effect" of the vortex structure is of importance, also the "near field" interference effect on the aircraft itself plays a significant role; the latter mainly with regard to the performance and aerodynamic behaviour of the wing and the empennage. A further exploration into the aerodynamic phenomena which occur in this process is the basis of this paper. It is part of a research program that was set up, at the Low Speed Aerodynamics laboratory of Delft University of Technology, to derive a better fundamental understanding of the interactive flows causing propeller-airframe interaction, based on theoretical as well as experimental methods.

Since modern turboprop aircraft tend to have higher disk loading the aerodynamic behaviour of propeller powered aircraft has become more complex. This has accentuated the need to optimise the integration of the propulsion system in connection with the strong influence of the propeller slipstream on other aircraft components and the wake structure that is formed.

During the last decade several innovations like utilisation of : blade sweep, advanced blade airfoil sections, counter-rotation and spinner area ruling have increased the fuel efficiency of the propeller. Generally however, the propeller is active in a flow field where strong interactions with its supporting structure, like a wing, play a role. Consequently, the combined performance of the propeller plus other aircraft parts should be examined.

The interaction between a propeller and wing and the associated vortex flow field is very complex. Therefore an optimisation of the configuration with theoretical prediction techniques will only be successful if quite detailed data are available on the characteristics of the slipstream/wing interactive flow. For that reason a fundamental flow field survey at 1 chord length behind a low aspect ratio wing with tractor propeller was performed. One of the earlier attempts to explain the different phenomena that occur when a propeller slipstream interacts with a trailing wing was made by Aljabri and Hughes [4.]. Their analysis is however restricted to a 2-dimensional wing thus omitting the (strong) effect of the wing tip vortex. Besides this, the flow field characteristics were mainly presented in the form of cross-flow vector plots. Although this is done by many authors, unfortunately this type of data not always contains enough information or may even produce a wrong perception of the real flow structure, as was shown by Krämer et al. [5].

The flow field surveys that are described hereafter exhibit some interesting perspectives :

- Three dimensional visualisation of the flow field reveals important qualitative information on the deformation process of the wake which can be important for the aerodynamic design of the wing and trailing surfaces and for the modelling of vortex formation in CFD-codes.
- The components of drag can be measured separately. Thus the quantitative results of the wake survey may be of use for the validation of codes where the calculation of profile drag and induced drag are generally performed with different calculation models.

The aim of this paper is to present a part of the experimental program namely a flow field survey that was performed on a tractor propeller wing configuration. The main objectives of this work are:

- to learn more about the ability of a quantitative wake survey to accurately produce lift and drag information when a propeller slipstream interacts with a wing
- to improve the understanding of the complex vortex wake structure as it is important for future optimisation of propeller-wing configurations.

The theory and experiments described hereafter are presented in detail by Rentema [6].

2. THEORETICAL BACKGROUND

In this section a brief review of the theory behind the quantitative wake analysis method is given. A more comprehensive discussion is given by Maskell [4], Betz [7], Rentema [6] and Wu et al. [9]. First of all the assumptions that were made should be outlined :

- The flow is assumed to be steady (time-averaged) and incompressible at the field survey plane (FSP) which is positioned somewhere behind the model
- The closed windtunnel has a uniform effective cross section which means that the effective boundary of the stream is defined as the displacement surface of the boundary layer on the wind tunnel walls.

2.1 Wake drag integrals

The drag of a body positioned in a control volume as depicted in fig. 1 can be found from the change in momentum in the direction of the undisturbed flow.

Considering the conditions at plane S1 and S2 upstream and downstream of the body respectively the drag may be written as :

$$D = \iint_{S_1} (p_1 + \rho u_1^2) dydz - \iint_{S_2} (p_2 + \rho u_2^2) dydz \quad (1)$$

Introducing the total head H :

$$H = p + \frac{1}{2}\rho(u^2 + v^2 + w^2) \quad (2)$$

equation (1) may be rewritten as :

$$D = \iint_W (H_\infty - H_2) dydz + \frac{1}{2}\rho \iint_S \{ (u_1^2 - v_1^2 - w_1^2) - (u_2^2 - v_2^2 - w_2^2) \} dydz \quad (3)$$

Since the total head is constant everywhere outside the vortical area of the flow the first integral is limited to the wake downstream of the object. To limit the second integral to the wake also Betz [7] introduced an artificial velocity-component u^* which differs from u only in the wake area :

$$H_\infty = p + \frac{1}{2}\rho(u^{*2} + v^2 + w^2) \quad (4)$$

The difference between Betz' velocity and the undisturbed flow velocity is called the perturbation velocity u'' :

$$u'' = u^* - U_\infty \quad (5)$$

Substituting (4) and (5) into the drag relation (3) results in :

$$D = \iint_W \{ (H_\infty - H_2) + (u_2^* - u_2) (u_2^* + u_2 - 2U_\infty) \} dydz + \frac{1}{2}\rho \iint_S \{ (u_1^2 - v_1^2 - w_1^2) - (u_2^2 - v_2^2 - w_2^2) \} dydz \quad (6)$$

This equation holds for any steady incompressible flow of a fluid with constant viscosity. To express the contribution of the perturbation velocity Maskell [8] introduced the wake integral for the wake-blockage velocity u_b :

$$u_b = \frac{1}{2S} \iint_W (u_2^* - u_2) dydz \quad (7)$$

The perturbation velocity u'' can be considered as a constraint correction to the Betz' formula, due to the presence of the windtunnel walls. Maskell [8] derived the relation between u'' and u_b by considering a system of a bound vortex and a source-sink combination in the flow :

$$\frac{1}{2} \rho \iint_S (u_1'^2 - u_2'^2) dydz = -2\rho u_b^2 S \quad (8)$$

Substituting (8) into (6) leads to :

$$D = \iint_W \{ (H_\infty - H_2) + \frac{1}{2} \rho (u_2^* - u_2) (u_2^* + u_2 - 2U_\infty) \} dydz \\ - 2\rho u_b^2 S + \frac{1}{2} \rho \iint_S \{ (v_2^2 + w_2^2) - (v_1^2 + w_1^2) \} dydz \quad (9)$$

The first two terms are considered by Betz as the profile drag while the last term is supposed to be the vortex drag or induced drag. It should be noted that for the case where a propeller is running the energy supply to the flow increases the value of H_2 which means that the profile drag may become negative.

In this investigation the induced drag is defined as being the result of local non-viscous normal forces, such as lift, generated by the windtunnel model. The remainder is defined as the profile drag.

The problem with formulation of the last integral of (9) is that it must be evaluated over the entire cross section of the windtunnel. This can however be solved in the following way (ref. Wu et al. [9]). Introduce the continuity equation :

$$\frac{\partial v}{\partial y} + \frac{\partial w}{\partial z} = -\frac{\partial u}{\partial x} = f \quad (10)$$

the vorticity vector :

$$\vec{\omega} = \vec{i}\xi + \vec{j}\eta + \vec{k}\omega \quad (11)$$

and two scalar functions $\phi(y, z)$ and $\psi(y, z)$ such that the following conditions are satisfied :

$$v = \frac{\partial \psi}{\partial z} + \frac{\partial \phi}{\partial y} \quad (12)$$

$$w = -\frac{\partial \psi}{\partial y} + \frac{\partial \phi}{\partial z} \quad (13)$$

When equations (12) and (13) are substituted in (10) and (11) we obtain :

$$\frac{\partial^2 \psi}{\partial y^2} + \frac{\partial^2 \psi}{\partial z^2} = -\xi ; \quad \frac{\partial^2 \phi}{\partial y^2} + \frac{\partial^2 \phi}{\partial z^2} = f \quad (14)$$

With known values of ξ and f in the windtunnel cross section the values of the scalars ϕ and ψ can be calculated applying the right boundary conditions (Rentema [6]).

Returning to the last integral of (9), Maskell [8] and Wu et al [9] succeeded in rewriting this part as an integral that is partly taken over just the viscous wake. Without further mathematical explanation their result is given :

$$\iint_S \{ (v_2^2 + w_2^2) - (v_1^2 + w_1^2) \} dydz = \iint_W \psi_2 \xi_2 dydz + \\ \iint_S (\phi_1 f_1 - \phi_2 f_2) dydz \quad (15)$$

When the survey plane S_1 is taken far upstream f_1 vanishes thus simplifying the vortex drag as :

$$D_v = \frac{1}{2} \rho \iint_W \psi_2 \xi_2 dydz - \frac{1}{2} \rho \iint_W \phi_2 f_2 dydz \quad (16)$$

In general the contribution of the second integral is negligible outside the wake thus integration is performed over the wake only. De Leeuw [3] verifies this vortex drag formula with experiments on a simple half-wing model. He concludes that for the clean wing configuration the transverse vorticity contribution is very small (0.04%-0.13% of the vortex drag).

2.2 Wake Lift integral

Following the classical wing theory the lift of the complete model (wing+propeller) can also be evaluated from the quantities measured in the wake survey plane. Following an analysis similar to that employed in the derivation of the drag relation (9) Maskell [8] determines the lift integral :

$$L = \rho U_e \iint_W \xi y dydz + \rho \iint_W (u_2^* - u_2) w_2 dydz \quad (17)$$

where the contribution of the second term turns out to be negligible in practice. It represents the loss of momentum due to the energy loss in the wake, expressed by $(u^* - u)$.

The local lift coefficient can be found following the classical wing theory. When a planar wake is assumed, and this is essential, the local lift coefficient can be found from :

$$c_l = -\frac{2}{U_c} \int_{y_1=y}^{\infty} \int_{z=-\infty}^{\infty} \xi dz dy_1 \quad (20)$$

Of course the integration can be restricted to the vortical wake since outside this area ξ becomes zero. One important remark should be made regarding equation (20). Since the wake behind the wing deforms, the assumption of a planar wake is not correct. This means that from the shed vorticity the direction and the location of the inducing (lift) force acting locally on the wing can not be determined exactly. Therefore calculation of the integral in (20) through succes-

sive integration in z - and y -direction produces a wrong picture in areas where the vortex sheet has rolled up.

In fact the integration should be performed first in s - and then in t -direction which are locally perpendicular and parallel to the vortex sheet respectively. This is practically unrealisable in a fully developed tip vortex where the sheet is stretched in lateral direction and rolled up into one vortex core. Although this is a clear limitation in the use of (20) a reasonable representation of the local lift distribution will be obtained using the classical wing theory. Further discussion on possible solutions for this problem is needed but is felt to be beyond the scope of this report.

3. EXPERIMENTS

3.1 Experimental set-up

3.1.1 Model and Instrumentation

The windtunnel model (fig. 2) called PROWIM (propeller wing interference model) consists of a straight wing of aspect ratio 5.33 with no twist, constant chord and airfoil section (NACA 64-A015). It is equipped with a 4-bladed metal propeller of 0.236m diameter was driven by a 5.5kW electrical 3-phase induction motor contained inside the nacelle. The propeller speed setting of this motor was controlled using a 200-per-revolution optical encoder mounted on the rotor. The axi-symmetrical nacelle was build as a "minimum body" mounted with its rotation axis on the MAC-line and at 0.3 m from the wing root. During all tests the $\frac{3}{4}$ R blade angle was set to 25° . The model was attached to an external 6 component balance through a turntable which is flush with the image plate situated at 0.3 m from the upper wall.

To perform surface pressure measurements with PDCR-22 transducers, the wing contains a total of 918 pressure orifices located in 18 rows. In the vicinity of the nacelle, where the slipstream washes the wing, a closer spacing was used than outside this area. Two pitot tubes were installed at a small distance behind the propeller to determine the total pressure jump ΔP_t across the propeller plane which is a measure for T_c .

3.1.2 The test facility

The windtunnel used during these investigations was the Delft University Low Turbulence Tunnel (LTT) which has an octagonal test section of $l \times w \times h = 2.60 \times 1.80 \times 1.25$ m. To compensate for the wall boundary layer displacement effect the test section is slightly divergent. Maximum speed is 120 m/s and the turbulence level ranges from 0.025 % at 40 m/s to 0.085 % at 100 m/s. A general description of this facility is given by Veldhuis [1].

3.1.3 Five hole probe and traversing mechanism

To acquire velocity field data at 1 chord length behind the wing, 5-hole probe measurements were performed.

The purpose of these surveys was :

1. to explore the geometry of the deformed slipstream and vortex wake downwind of the wing

2. to calculate the lift, profile drag and induced drag of the model following a procedure similar to the one presented by Brune & Bogataj [2] and de Leeuw [3].

The five-hole probe that was used for all wake surveys has a diameter of 1.65 mm diameter with a conical head (fig. 3). All test data were reduced on-line yielding the three components of wake velocity, from which circulation, and total pressure within the slipstream/wake were calculated.

Traversing of the probe was done through a system consisting of a diffuser mounted x, y, z slide and a adjustable sting connected to it. To reduce time needed for measuring several model configurations, the pressure measurements were done with the probe in non-nulling mode using a fast pressure transducer reading while the probe was traversing at low speed (5 mm/s). The number of samples per pressure hole was fixed at 10 and the sample rate at 10000 Hz. The complete measurement cycle of one survey point took 24 ms. This means that the displacement effect ($0.024 \times 5 = 0.12$ mm) of the traversing probe is negligible compared to the probe diameter. For all flow conditions the measurement grid was build with its borders as closely as possible to the Poisson area to prevent acquisition of unnecessary data. Typically, the total measurement grid behind the model contains about 30,000 to 40,000 data points.

3.1.4 Test conditions

The test were performed at a Reynolds number (based on the MAC) of $0.82 \cdot 10^6$, with the propeller running at a constant advance ratio of $J=0.85$. This results in a rather low thrust coefficient of $T_c=0.168$. Measurements with and without the propeller installed were performed at 3 angles of attack : 0° , 4° and 10° .

3.1.5 Data reduction

To work out the lift and drag formulae practically all variables were first non-dimensionalized. The profile drag (the first integral in eq. (9)) can simply be resolved from integration in the survey plane. Determination of the vortex drag though, requires calculation of the axial vorticity ξ and the axial velocity gradient $\partial U / \partial x$. Since the survey plane was build up with a very fine mesh size no attempt was made to fit cubic splines through the data points as suggested by Brune [2]. Instead a simple and straightforward five point difference scheme was used to acquire the velocity derivatives.

The Poisson equations (14) and (15) were solved on a rectangular domain using the Poisson solver HWSRPT from the well known FISHPAK library. All calculations were performed on a local workstation (Hewlett Packard 9000-720).

4. RESULTS AND DISCUSSIONS

4.1 Overall behaviour

4.1.1 Balance measurements

As part of an earlier investigation on propeller/wing interference balance measurements were performed to acquire

the overall characteristics of the model. These data were generated during a separate measurement period (Philipsen [10]). Several parameters were changed like : wing angle of attack, propeller thrust and flap deflection. Since the forces on the propeller could not be measured separately the effective thrust was determined through a simple bookkeeping procedure. In this case the thrust of the propeller is defined as the difference in tangential force between the prop on (wnp) and prop off (wn) configuration. In coefficient form :

$$T_c = \left(C_{T_{wn}} - C_{T_{wnp}} \right) \frac{S}{2D^2} \quad (21)$$

Some of the results of the balance measurements are presented together with the flow field results furtheron.

4.1.2 Pressure measurements

To get some indication about the extent of the slipstream influence on the wing, surface pressure measurements were carried out as well. In fig. 4 typical chordwise pressure distributions show the effect of the increase in axial and swirl velocity in the propeller slipstream. The increase in local lift for the upgoing blade side (UBS), due to increased dynamic pressure and increased local angle of attack, is clearly visible. As shown in the 3-dimensional representation of the pressure distribution for the prop off case the nacelle influences the local onflow of the wing. Due to the increased velocity on both sides of the nacelle peaks in the local pressure distribution are found.

Due to both the effects of total pressure rise within the slipstream and the propeller induced swirl velocity the distribution of normal force coefficient and tangential force coefficient is strongly distorted. Fig. 5 shows that a negative overall drag contribution is possible for the inboard up rotating propeller due to increased leading edge suction (negative C_l -contribution) visible especially at the UBS of the nacelle.

A more detailed description of this phenomenon is given by Veldhuis [11]. For $\alpha=10^\circ$ the decrease of the wing normal force is at the DBS small if not absent due to the opposite effects of the axial velocity and rotational velocity contributions.

4.2 Flow field survey

To be able to analyse slipstream influence on wing profile drag, induced drag and lift distribution a grid spacing of only 2 mm was chosen in both directions. This very fine grid, was selected to uncover enough detail of the flow field to draw qualitative conclusions. To check the necessity of taking this many data points some calculations with fewer data points were performed afterwards. By skipping measurement data the effect of grid density on the calculated axial vorticity was found. Some examples are presented in fig. 6 for the tip vortex region at $\alpha=10^\circ$. It is remarkable that even for a very coarse grid, were only 1 in every 5 datapoints was used (SKIP=5), the tip vortex structure is still clearly recognisable. Apparently quite coarse measurement grids can be used if only qualitative data are requested. The variables however that depend on the value of ξ like the local lift coefficient C_l and the induced drag coefficient show a clear effect of grid density as indicated by table 1 and fig. 7

Thus the choice of the 2mm grid spacing seems to be appropriate to ensure accurate integration of flow data over the wake area.

4.2.1 Flow structure for the prop off case

Fig. 8 displays the total pressure coefficient for the propeller off case at $\alpha=0^\circ, 4^\circ$ and 10° . The strong deficit which occurs in the wing wake and the wing tip vortex are clearly visible. Besides the total head loss behind the nacelle with the pressure tubes installed, there is a distinct effect of the horseshoe vortex at the wing/wall junction. For $\alpha=4^\circ$ and 10° , when the wing generates lift the total head loss in the tip vortex core becomes very pronounced. The wake starts to deform significantly for the higher angles of attack which has consequences for the theory applied above where a planar wake was assumed. Near the root, the wake of the wing shows a disturbance (see arrow in fig. 8b) which becomes larger at higher angles of attack. This is caused by a small streamwise gap between the trailing edges of the inboard flap and the wing. The fact that this small geometrical disturbance generates a measurable effect demonstrates the power of the flow field analysis. In fig. 9 the cross flow vectors are depicted. Although this type of graph is easily generated, even on-line during the measurements, it exhibits no significant additional information on the flow field compared to the axial vorticity plots shown further on. In fact the interpretation of the cross flow vectors may result in a completely wrong perception of the real flow field since distinct vortices can not be distinguished. An example of this problem is given in fig. 10 where the cross flow seems to be produced by a single vortex where in fact several distinct vortices are active.

A more interesting way of looking at the flow field is to consider the axial vorticity ξ as presented in fig. 12. Now all important vorticity confined in either sheets or distinct vortices becomes visible. Also the total pressure loss sometimes forms a good indicator for the presence of vortical flow as long as the position of the viscous wake (with lower C_{pt} as well) is known and taken into account. An example is given in fig. 11 where the flow structure of both ξ and C_{pt} show a clear resemblance.

For $\alpha=0^\circ$ two vortex pairs are discernible originating from the horseshoe vortices generated by the nacelle/wing connection. At $\alpha=4^\circ$ the vortices with negative ξ merge and the field rotates in anti-clockwise direction due to the cross flow induced by the wing. Since the wing now produces lift the wake rolls up resulting in a strong vortex with very high ξ -value at the tip. Moving from the tip to the root the trailing vorticity becomes weaker. This is easily explained by considering the spanwise gradient of the lift which decreases when moving rootward.

4.2.2 Flow structure for the prop on case

With the propeller running the structure of the flow field changes radically. As can be seen in the C_{pt} -plots of fig.

13 a strong total head rise occurs in the slipstream. There are remarkable strong spatial gradients in total pressure towards the slipstream boundary.

Apparently the decay of the vorticity between the propeller position and the survey plane is limited. This can also be seen in the axial vorticity plots of fig. 15 where distinct boundaries are visible. The wake of the nacelle is completely embedded in the slipstream which is substantially distorted by the wing, as expected.

Though hard to see in the 3D view of the data in fig. 14 for $\alpha=10^\circ$, the total pressure rise is higher at the side of the downgoing propeller blade due to the increased local blade angle of attack.

Due to the swirl introduced by the propeller the slipstream rotates resulting in a displaced total pressure field. This is clearly shown in fig. 13c where at $\alpha=10^\circ$ the peak total pressure value has moved in the propeller rotational direction. This, of course has implications for the aerodynamic load on trailing surfaces.

Returning to equation (9), the second integral generally represents approximately 2% of the total induced drag (de Leeuw [3]), which means that strong axial vorticity (in the first integral) is indicative for a high induced drag contribution (fig. 15). Although it is impossible to relate a ξ -peak in the survey plane to a corresponding spanwise co-ordinate on the wing, due to (unknown) wake deformation between the wing and the survey plane, the effects of the propeller blade tip vortices and the wing tip vortex can be clearly detected.

When viewed from behind, the tips of the propeller blades produce anti-clockwise vortices. These vortices create a narrow zone with high positive ξ -values at the outer border of the slipstream. The root parts of the propeller blades produce negative vorticity which is spread out inside the nacelle wake area.

As can be seen in fig. 13 for $\alpha=0^\circ$ the rotational symmetry of the slipstream is clearly influenced by the presence of the wing. The boundary seems to be sheared at the passage of the wing so that the slipstream boundaries at the upper and lower wing surface are at different spanwise stations. A convenient explanation of this phenomenon can be found in the way the slipstream influences the wing lift distribution. Fig. 15 shows that strong vorticity is shed from the junction of the wing surface and the edge of the slipstream, which is indicative of the high gradient of spanwise load on the wing. To explain the effect the vorticity is considered as being contained in 3 discrete vortices (fig. 16). As a result both slipstream halves shift in opposite spanwise directions near the intersections between the wing and the slipstream outer boundary. The areas with negative ξ -values at these locations confirm this explanation. Also the clockwise rotating centre vortex with positive ξ is clearly visible in fig. 15. At $\alpha=10^\circ$ both slipstream halves have shifted in opposite directions due to the strong influence of the wing tip vortex.

Although the 5-hole probe measurements were all performed at a rather low thrust coefficient the contraction of the slipstream is still visible, especially at $\alpha=0^\circ$ in fig. 13a.

Summarising these results it should be stated that the deformation which occurs in the wake is strongly related to the lift distribution of the propeller/wing combination. Therefore further research is recommended to analyse the effects of different slipstream geometry's on the calculation results of CFD-codes which incorporate propeller flow.

4.2.3 Comparison with surface pressure measurements

Although the wing has some straightening effect on the flow the basic circular shape of the slipstream is maintained and substantial swirl velocities remain within the slipstream downstream of the wing. This becomes clear when the lift distribution found from integration in the wake is examined.

In fig. 17 the distribution of the local lift, represented by eq. (20), is presented for $\alpha=4^\circ$ and $\alpha=10^\circ$ together with the results of the integrated surface pressure measurements. A small difference between the lift acquired with both techniques outside the slipstream area is notable in all figures. The reason for this discrepancy is still unclear but is expected to be a result of a cumulation of several small errors within both measurements. Further research will be performed to improve both experimental techniques. The most striking difference however between the flow field survey curves and the results of the surface pressure measurements is the opposite effects in the area washed by the slipstream. The latter represents the pressure effects at the wing only, hence no contribution of the lift forces that act on the propeller blades are incorporated in the data. The flow field data however contain the lift contribution of the complete configuration. Obviously the normal forces acting in the propeller plane exceed the lift variations at the wing which are generated by the slipstream. This means in fact that a considerable swirl is still present in the slipstream after passage of the wing. Here again it is important to note that the wake position, where a certain value of the local lift is found, cannot be directly connected to a known wing spanwise location. On the other hand, a separate investigation of the uninstalled propeller with a numerical code indicated that the changes in C_n -values in the slipstream indeed provide a reasonable representation of the normal force acting on the propeller.

The increased loading at the downgoing blade is clearly visible as the peak in the local lift coefficient becomes higher than the values at the inboard side. From these figures it is reasonable to conclude that optimisation of the wing alone with prescribed propeller input data, as suggested by Kroo [12], Miranda [13] and Veldhuis [14] should be replaced by an optimisation of the complete propeller/wing combination in which all the interaction effects are integrated.

4.2.4 Comparison with balance measurements

The final results of the wake surveys are compared with the balance measurements in fig. 19 and 20.

If we look at the effect of the propeller on the separate contributions of induced drag and profile drag we see that mainly the profile drag component is influenced as a result of the strong positive P_i -effect. The results of the calculations for $\alpha=4^\circ$ and 10° are presented in table 2.

It is clear that the drag found in the case of a running propeller includes the thrust component and therefore becomes negative (fig. 20). From table 2 it can be concluded that the favourable effect of the propeller, a negative $\Delta(C_{dp})_{prop}$, becomes slightly less (about 14 counts) when the angle of attack is increased from 4° to 10° . It is however impossible to determine whether this is caused by a change of the wing profile drag or by a change in the slipstream characteristics due to angle of attack. Separate measurement of the propeller thrust with an internal balance will be necessary to draw conclusions in this respect.

Although the flow field surveys produce a drag coefficient that is slightly smaller than the drag from the external balance measurements the agreement between the two techniques is quite good. The comparison of the overall lift coefficients, as presented in fig. 19, is even better. The agreement is better for the prop-off case (maximum difference of 2%) than for the prop-on case (maximum difference

of 5%). No convenient explanation for this phenomenon is available at this moment.

5. CONCLUSIONS AND RECOMMENDATIONS

The following conclusions can be drawn from the experimental investigations:

- Flow field surveys with a 5 hole probe behind the propeller/wing configuration with a fine grid spacing reveals valuable information on the vortex wake structure of the propeller and the wing
- Lift and drag characteristics of the complete configuration can be determined from a quantitative wake survey
- The slipstream structure distorts significantly when it passes the wing. This complex flow forms an interesting testcase for CFD-codes that are used in situations where strong vorticity occurs.
- Most of the vorticity generated by the propeller is confined to a small "tubular-like" area coming from the propeller blade tips. This means that in most cases it is probably acceptable to model the propeller generated vorticity as a more or less deformed singularity sheet. The vorticity that is generated by the wing is concentrated in a strong wing tip vortex
- As indicated by the lift distribution with running propeller, a strong normal force exists on the propeller blades at positive angles of attack. The swirl recovery is only very limited since a significant tangential velocity component is left in the slipstream.
- When comparing the results of the integrated surface pressure measurements, the balance measurement and the flow field surveys generally a good agreement is found.

The results might be used as a reference database to get a better understanding of the interaction between propellers and wings and the complex vortical flow they produce.

6. ACKNOWLEDGEMENTS

The authors wish to thank I. Philipsen for his support in producing part of the data presented in this paper.

7. REFERENCES

1. Veldhuis, L.L.M., "Capabilities for testing 3D propeller powered windtunnel models at the Low Speed Laboratory of Delft University of Technology", Internal Report LSW 92-8, 1992, Fac. of Aerospace Engineering, Delft University of Technology.
2. Brune, G.W. and Bogataj, P.W., "Induced drag of a simple wing from wake measurements", AIAA-90-1934, 1990
3. Leeuw, A. de, "Induced drag ; theory, measurements and calculations", Graduate thesis, Fac. of Aerospace Engineering, Delft University of Technology, 1993
4. Aljabri, A.S and Hughes, A.C., "Wind tunnel investigation of the interaction of propeller slipstream with nacelle/wing/flap/combinations", AGARD, FDP, Aerodynamics and Acoustics of propellers, AGARD DCP 366, paper nr. 21, Toronto, oct 1984
5. Krämer, E., Hertel, J. and Wagner, S., "Euler procedure calculation of the steady rotor flow with emphasis on wake evolution", AIAA-90-3007-CP, 1990
6. Rentema, D.W.E., "Drag and lift calculations based on wake surveys of a propeller-wing combination at several angles of attack", Graduate thesis, Fac. of Aerospace Engineering, Delft University of Technology, 1994
7. Betz, A., "Ein verfahren zur direkten Ermittlung des Profielwiderstandes", Zeitschrift für Flugtechnik und Motorschiffahrt", Vol. 16, p.42, 1925
8. Maskell, E.C., "Progress towards a method for the measurement of components of the drag of a wing of finite span", RAE TR-72232, jan. 1973
9. Wu, J.C., Hackett, J.E., Lilley, D.E., "A generalized wake-integral approach for drag determination in three-dimensional flows", AIAA 79-0279, jan. 1979
10. Philipsen, I., "Analysis of Propeller/Wing Interference on a Straight Half Wing and Tractor propeller", Graduate thesis, Fac. of Aerospace Engineering, Delft University of Technology, 1993
11. Veldhuis, L.L.M., "Experimental Analysis of Tractor Propeller Effects on a Low Aspect Ratio Semi-Span Wing", Second Pacific International Conference on Aerospace Science and Technology & the Sixth Australian Aeronautical Conference, Vol. 2, p. 491-498, Melbourne, 20-23 march 1995.
12. Kroo, I., "Propeller-wing interaction for minimum induced loss", J of Aircraft, Vol. 23, No. 7, July 1986, p. 561-565
13. Miranda, L.R. and Brennan, J.E., "Aerodynamic effects of wingtip-mounted propellers and turbines", AIAA 86-1802, 1986
14. Veldhuis, L.L.M. "Optimisation of tractor propeller/wing configurations", Internal Report LSW 93-4, Oct. 1993, Fac. of Aerospace Engineering, Delft University of Technology.

SKIP*	$\Delta C_{di}/(C_{di})_{SKIP=1}$
1	0.00
2	-0.37
3	-3.60
5	-13.0

* SKIP=1 means that all data were used (grid spacing= 2mm)

Table 1 Effect of grid density on the overall induced drag at $\alpha=10^\circ$, prop off.

		α	
		4°	10°
C_{Dp}	prop on	-0.10609	-0.09411
	prop off	+0.01600	+0.02661
	$\Delta(C_{Dp})_{prop}$	-0.12209	-0.12072
C_{Dv}	prop off	+0.00717	+0.02774
	prop on	+0.00324	+0.01935
	$\Delta(C_{Dv})_{prop}$	+0.00393	+0.00839
C_D	prop on	-0.09893	-0.06637
	prop off	+0.01924	0.04596
	$\Delta(C_D)_{prop}$	-0.11817	-0.11233
C_L	prop on	0.3302	0.7328
	prop off	0.2917	0.6618
	$\Delta(C_L)_{prop}$	+0.0385	+0.0710

Table 2 Propeller influence on wing lift and drag.

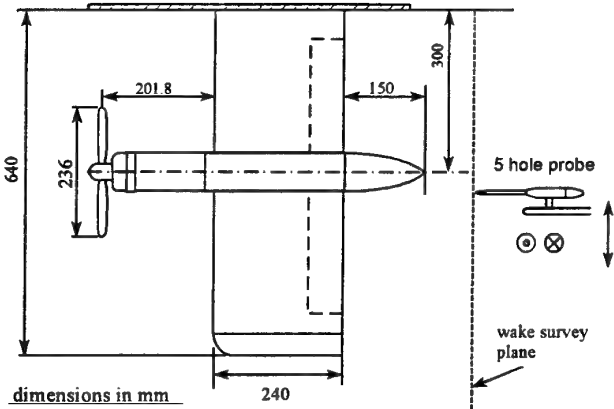


fig. 2 Layout of the windtunnel model with 5 hole probe.

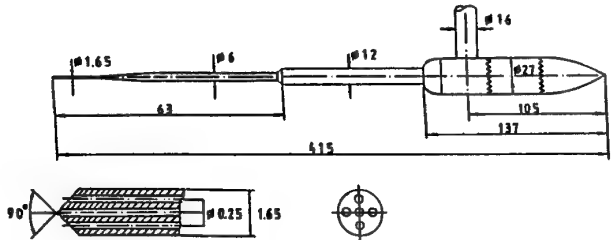


fig. 3 Geometry and dimensions of the 5-hole probe.

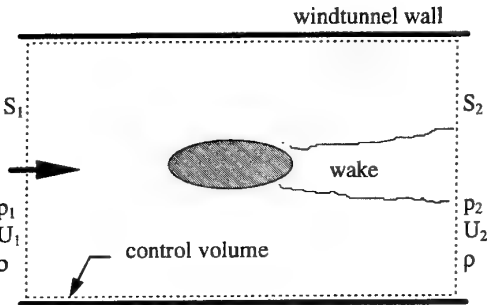


fig. 1 Body in the windtunnel with enclosing control volume

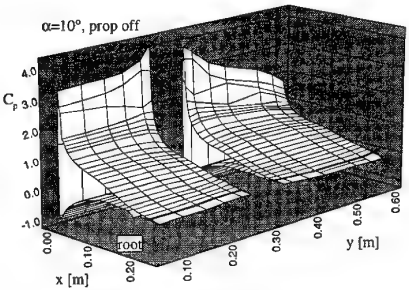
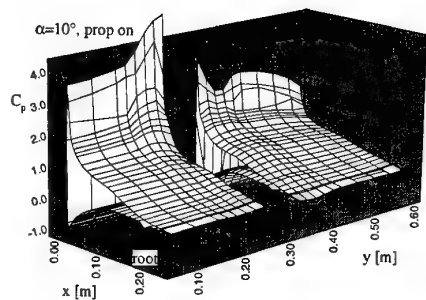
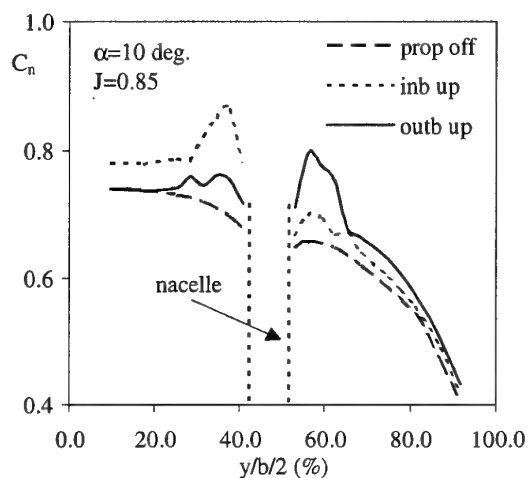


fig. 4 (a) continued

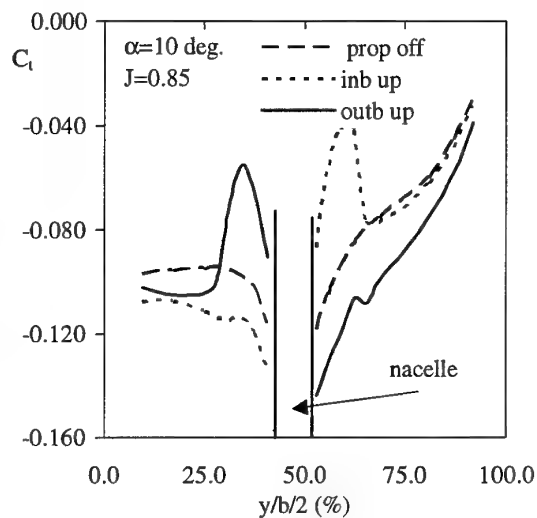


(b)

fig. 4 Wing surface pressure distribution; $\alpha=10^\circ$
(a) prop off, (b) prop on

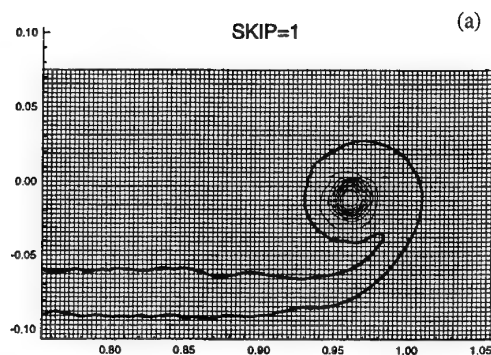


(a) normal force coefficient

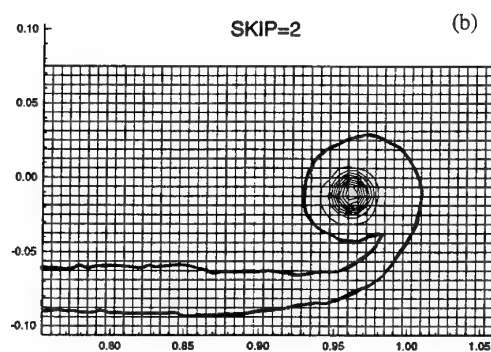


(b) tangential force coefficient

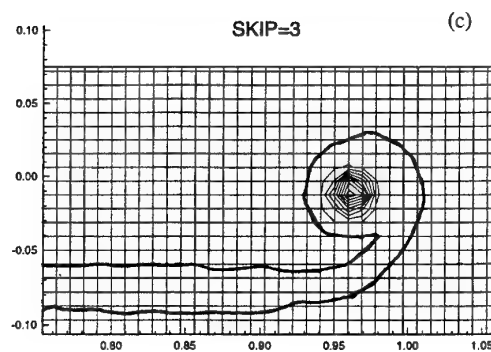
fig. 5 Normal (a) and tangential (b) force coefficient from integrated surface pressure measurements; $\alpha=10^\circ$, $J=0.85$



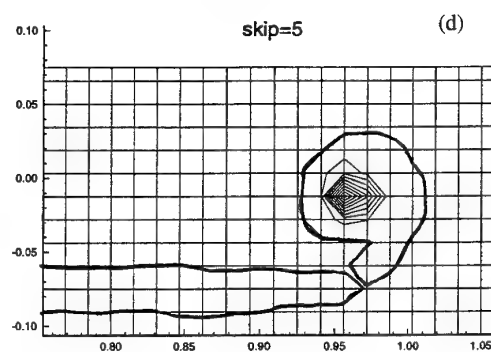
(a)



(b)



(c)



(d)

fig. 6 Effect of grid density on measured tip vortex structure (axial vorticity); $\alpha=10^\circ$, prop off.

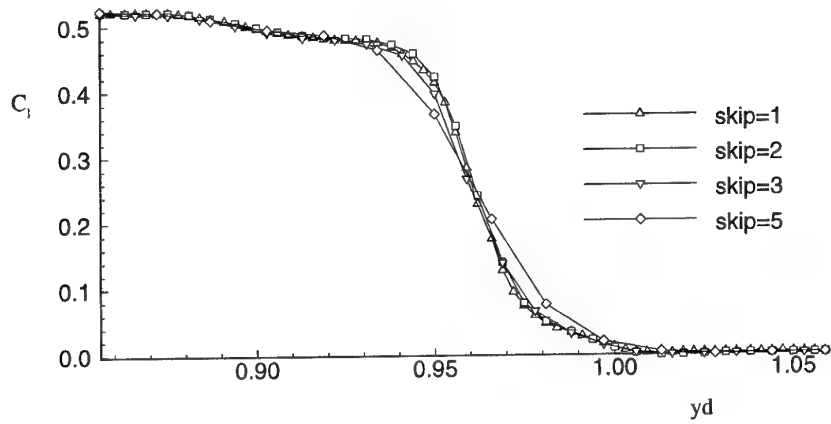


fig. 7 Effect of grid density on the lift distribution in the wing tip area ; $\alpha=10^\circ$, prop off.

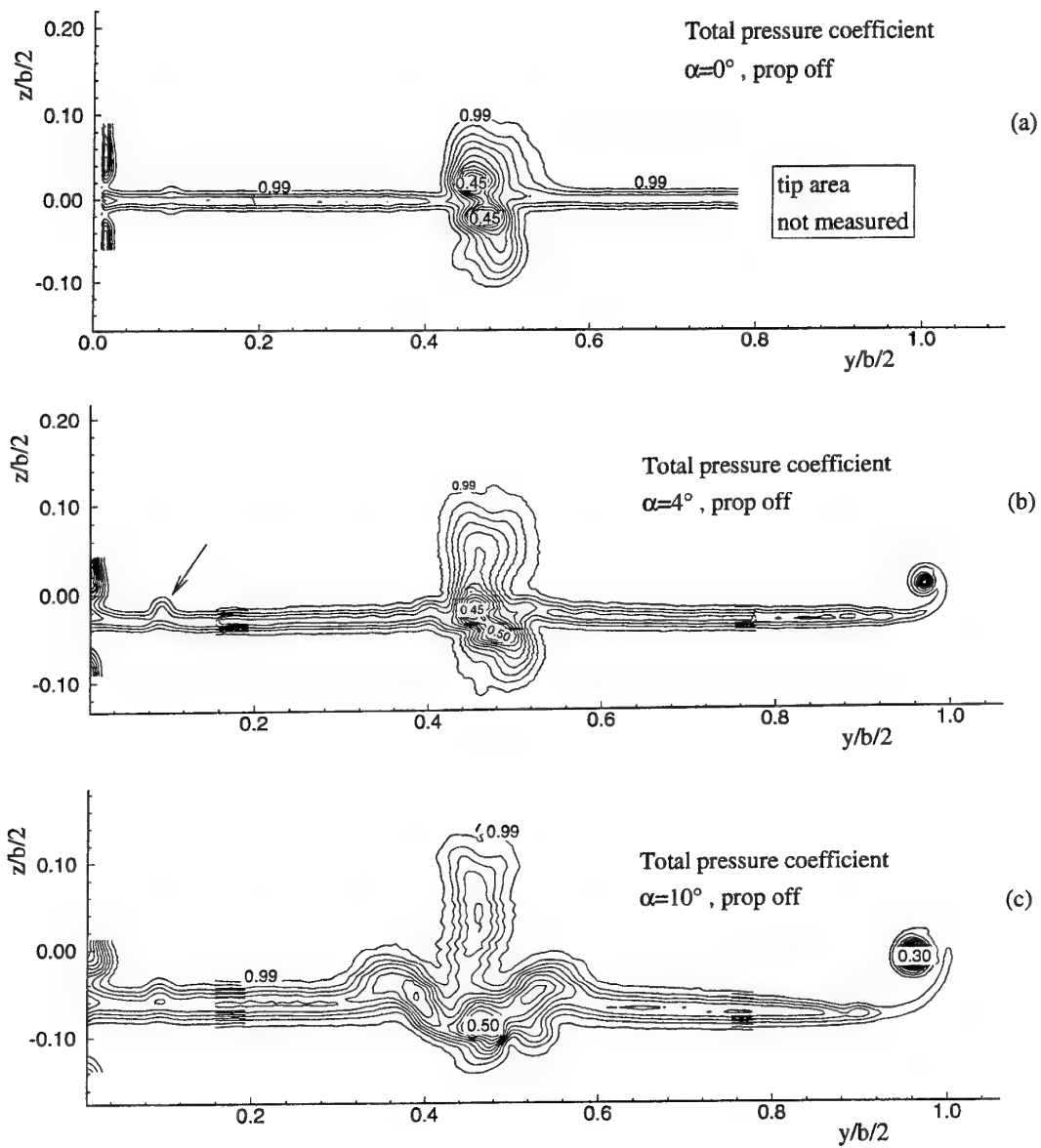
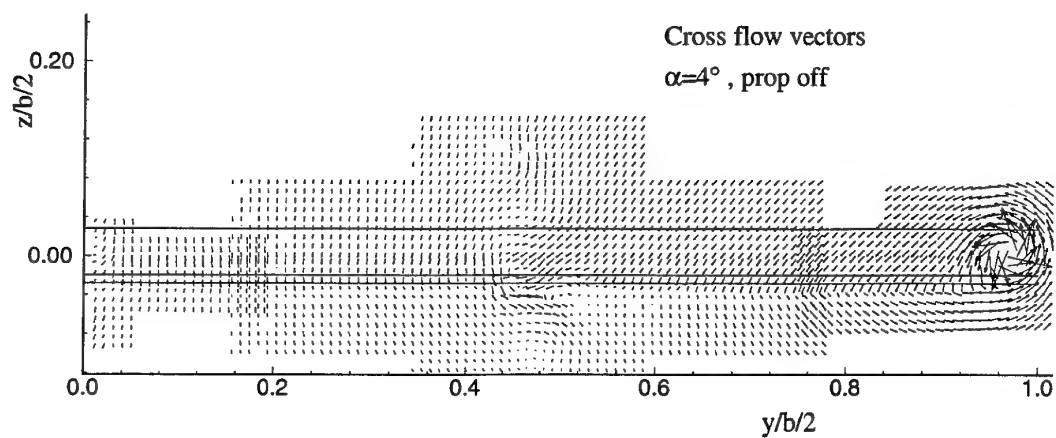
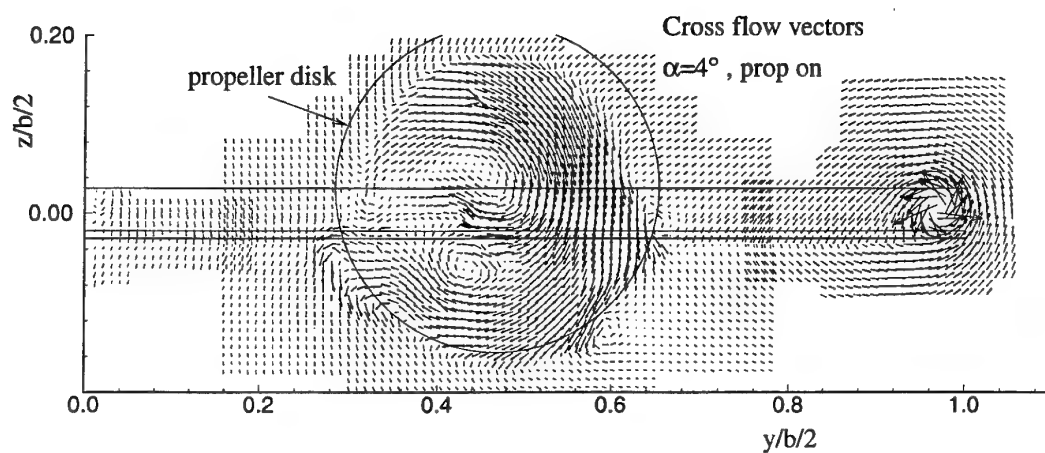


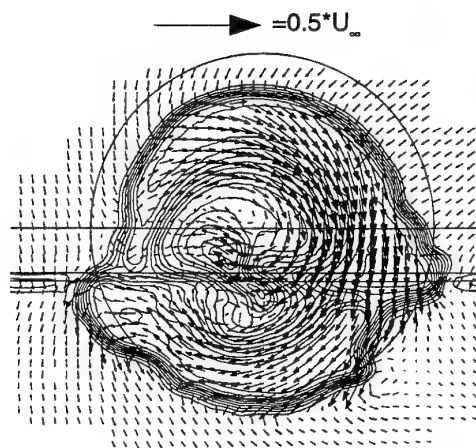
fig. 8 The total pressure coefficient for the propeller of f case. The pressure loss at the center of the figure is the result of the wake of the nacelle with installed total pressure probes.



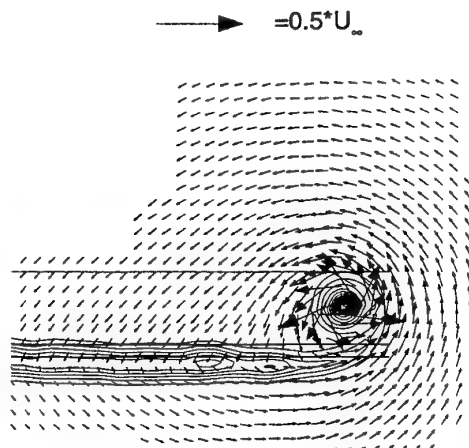
(a)



(b)



(c) the slipstream region



(d) the tip vortex region

fig. 9 Cross flow vectors for $\alpha=4^\circ$; (a) prop off, (b) prop on, (c) and (d) details combined with total pressure contours.

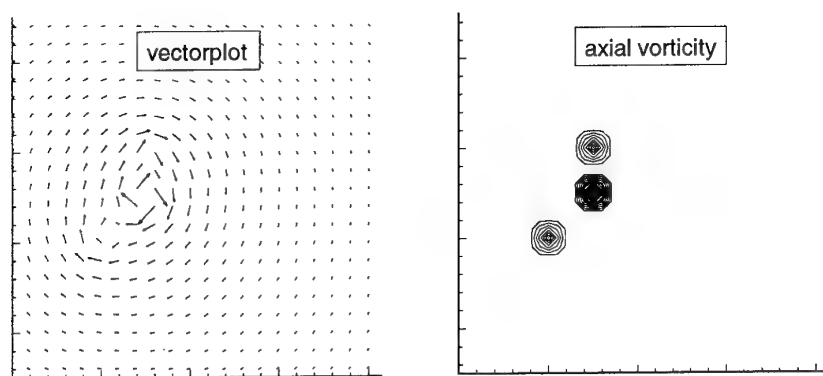


fig. 10 Possible mis-interpretation of the structure of a flow field through the usage of a vector plot instead of an axial vorticity plot. The flow contains 3 distinct vortices.

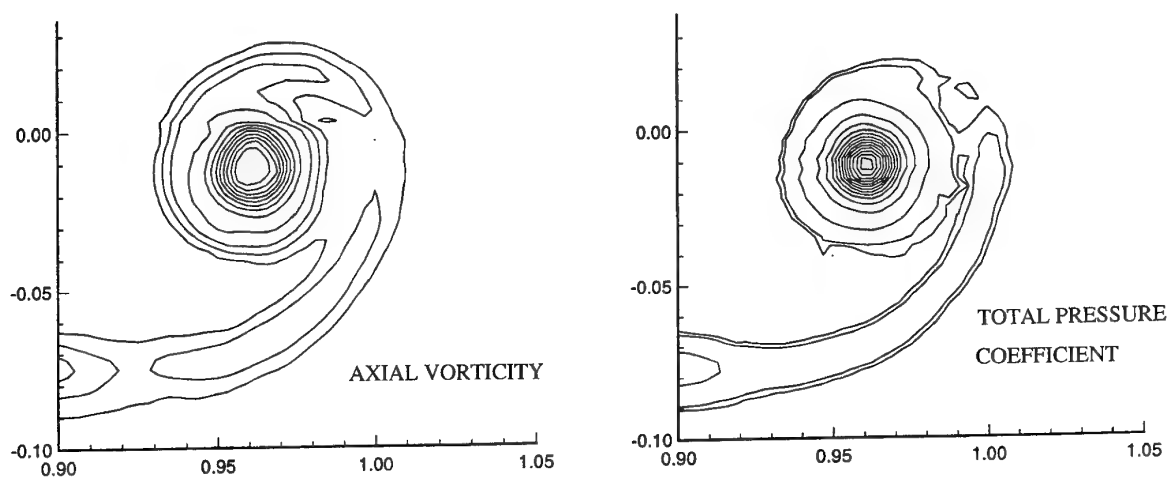


fig. 11 Comparison of axial vorticity (a) and total pressure coefficient (b) contour lines in the tip area ; $\alpha=10^\circ$, prop off

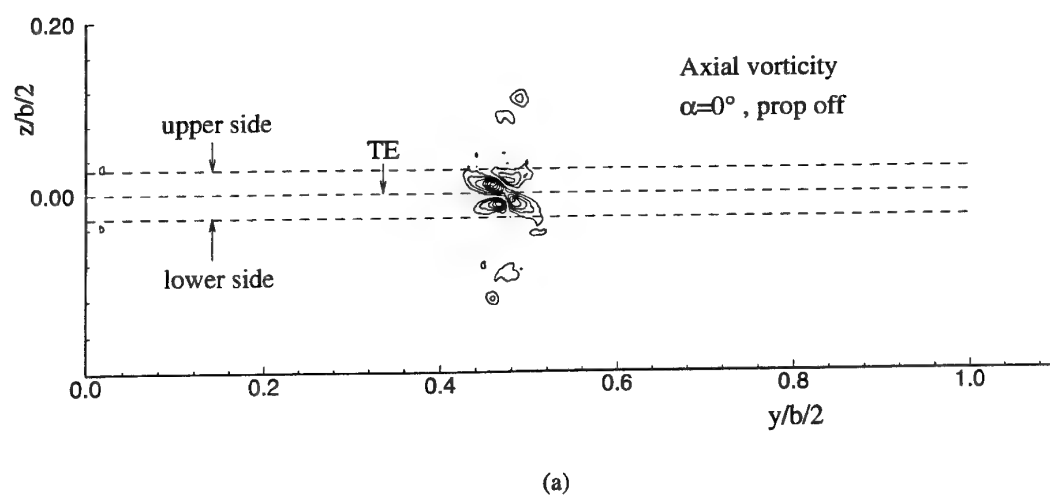
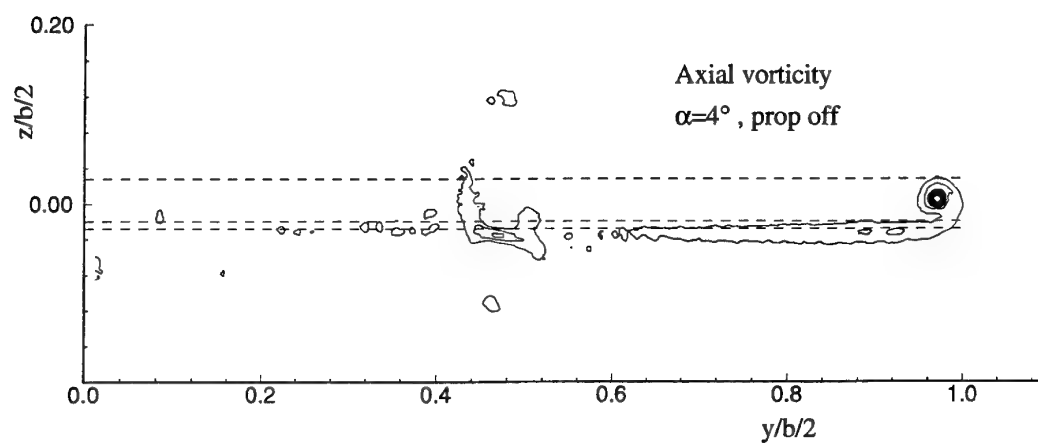
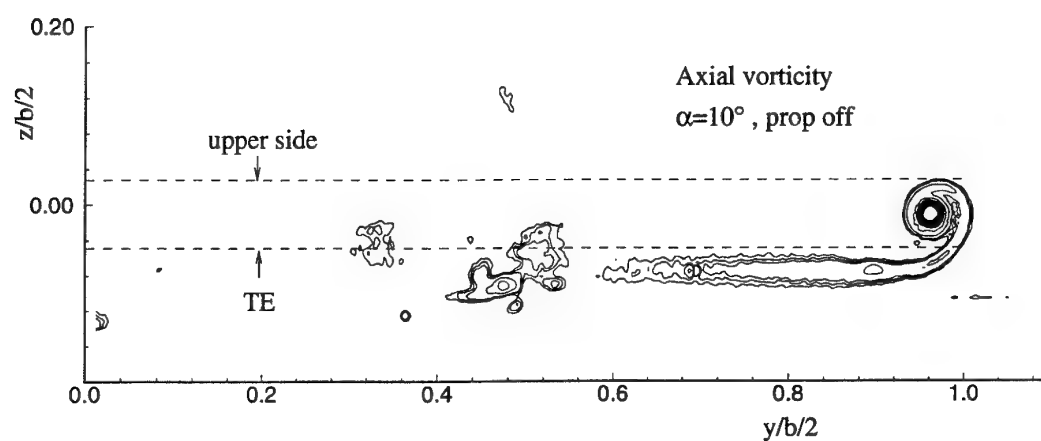


fig. 12a (continued)



(b)



(c)

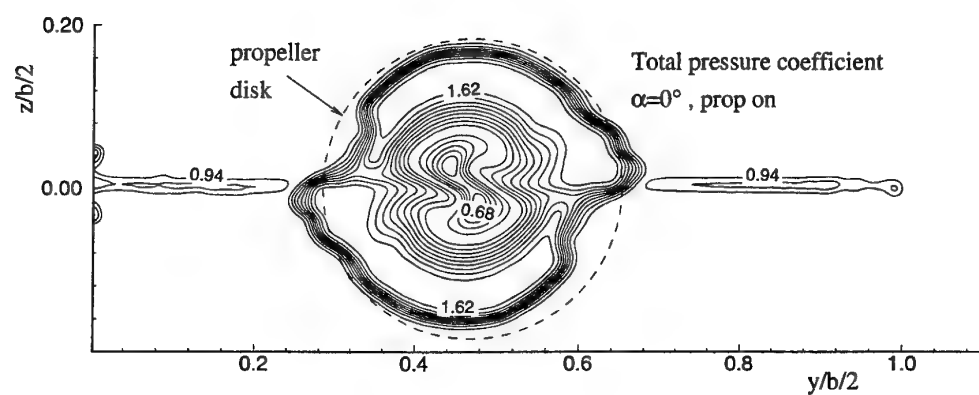
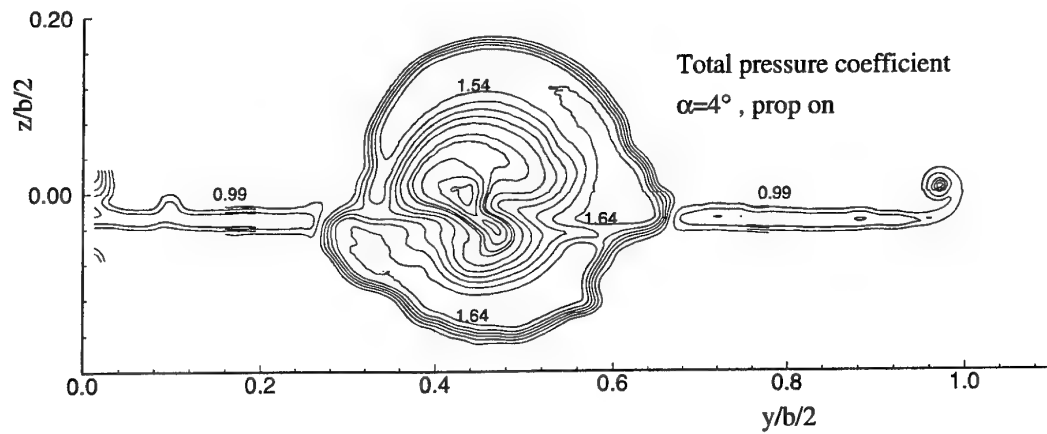
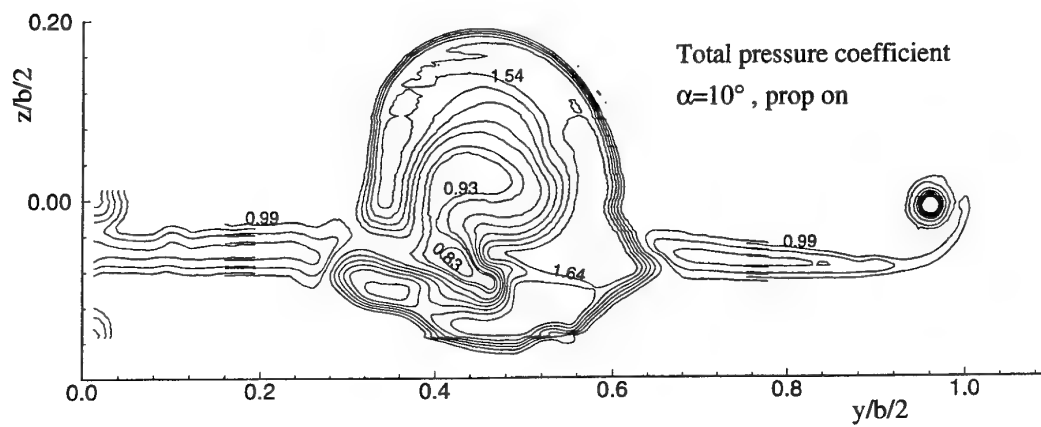
fig. 12 The axial vorticity $\tilde{\xi}$ for the propeller off case.

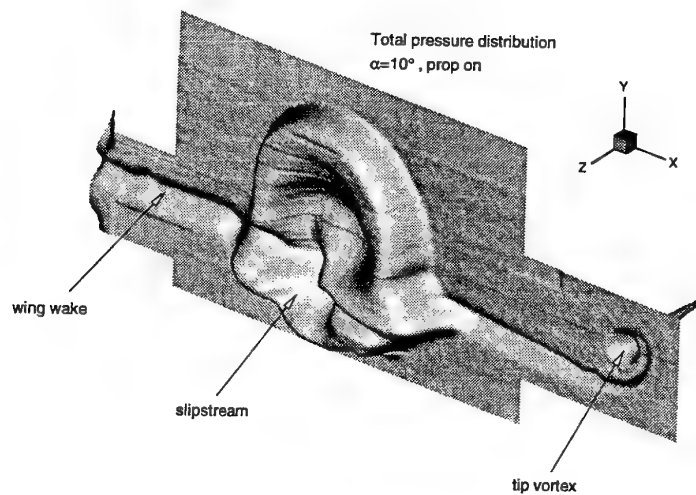
fig. 13a (continued)



(b)



(c)

fig. 13 The total pressure coefficient C_{pt} for the propeller on case.fig. 14 3-Dimensional view of the pressure distribution at $\alpha = 10^\circ$ showing the effect of the wing wake, the slipstream and the tip vortex.

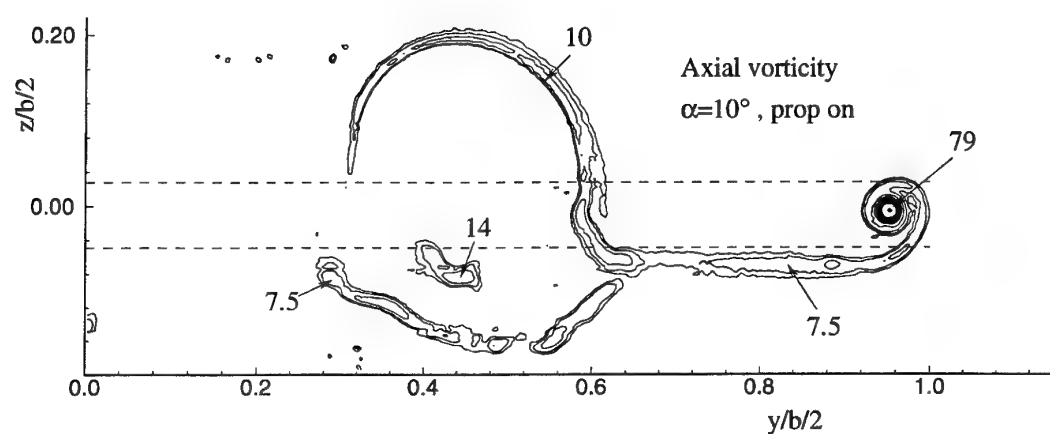
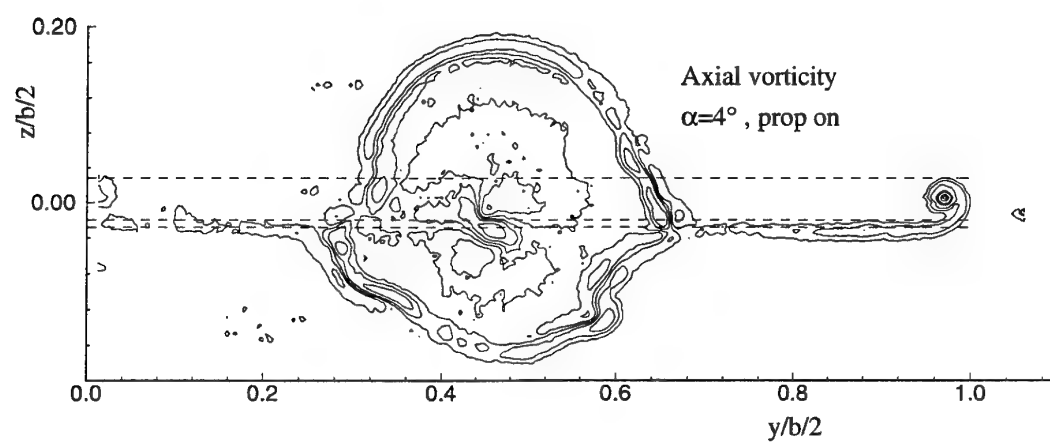
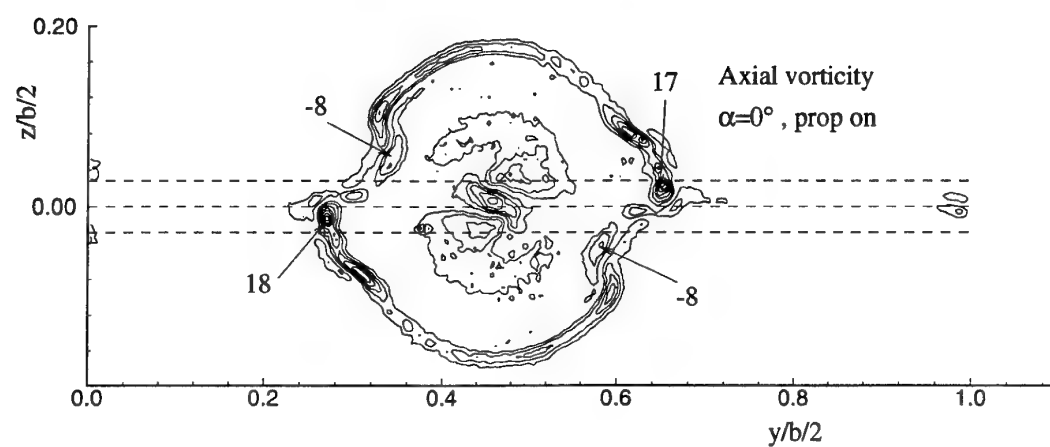


fig. 15 The axial vorticity $\tilde{\xi}_z$ for the propeller on case.

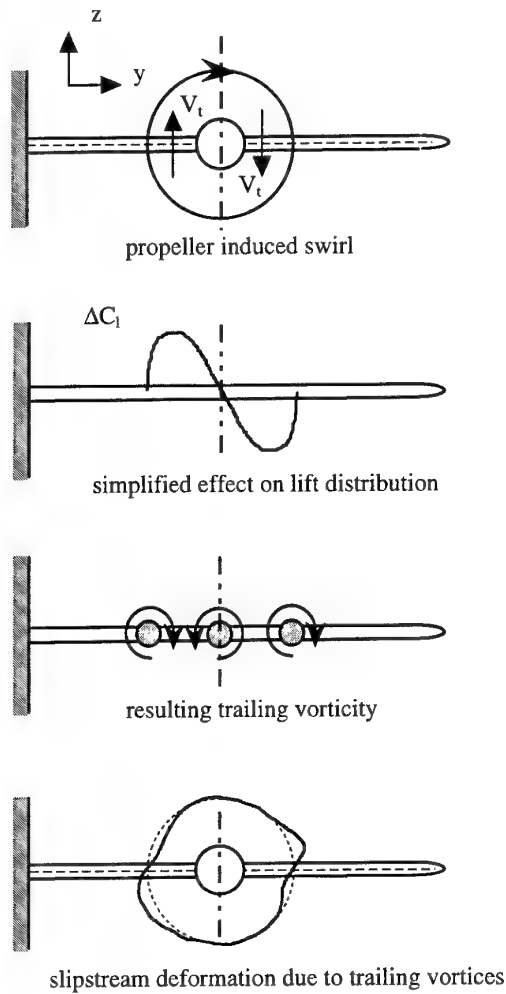


fig. 16 Simple explanation for the spanwise shearing of the propeller slipstream induced by trailing vorticity.

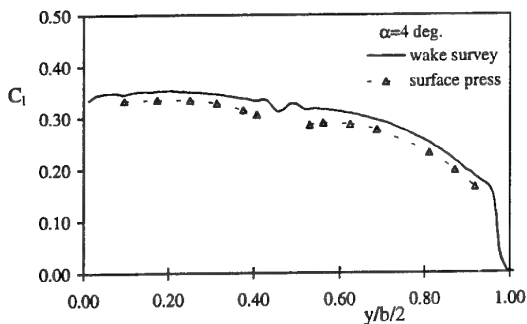


fig. 17a (continued)

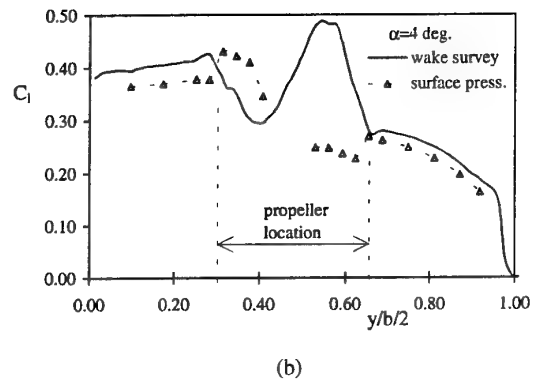


fig. 17 Comparison of the lift distribution found from integrated surface pressure and from the flow field method at $\alpha = 4^\circ$; (a) prop off, (b) prop on

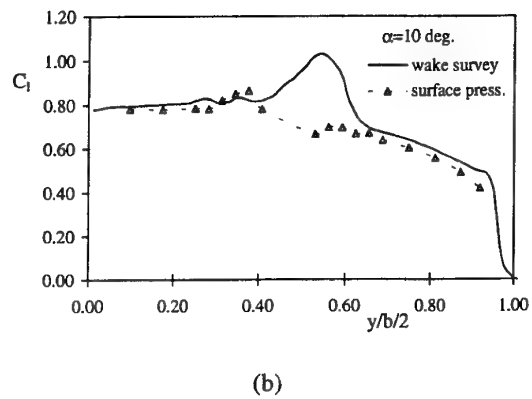
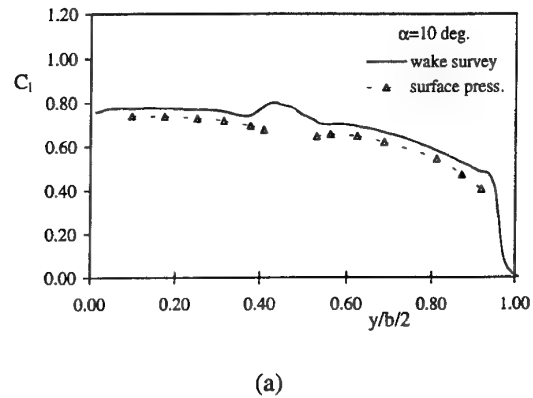


fig. 18 Comparison of the lift distribution found from integrated surface pressure and from the flow field method at $\alpha = 10^\circ$; (a) prop off, (b) prop on

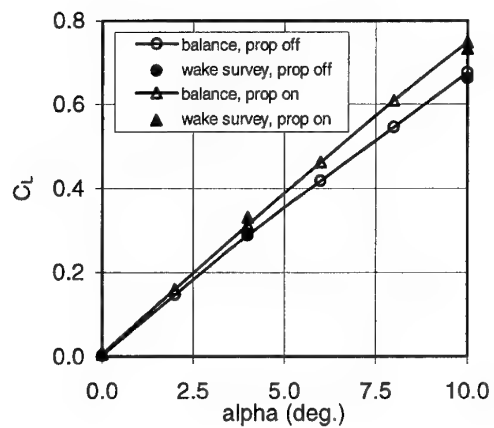


fig. 19 Comparison of lift coefficients found from external balance measurements and wake surveys.

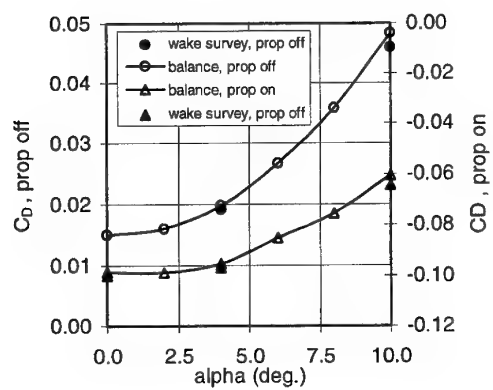


fig. 20 Comparison of drag coefficients found from external balance measurements and wake surveys.

FLOWFIELD OF A WING EMBEDDED IN THE WAKE OF A BURSTED VORTEX

J.M.A. Longo, M. Orlowski, D. Strohmeier

Institute of Design Aerodynamics, DLR, 38108 Braunschweig, Fed. Rep. of Germany

Abstract

In the present paper the flowfield around a delta wing partially embedded in the wake of a bursted vortex is numerically studied at $M_\infty = 0.4$. The simulation is carried out solving the Euler equations on two structured grids of about 2.3 million points and 300000 points respectively. Due to the lack of experimental results, special emphasis is put on the analysis of the effect of grid fineness on the wake-flow. The present investigation indicates that the spiraling flow of a vortex continues after breakdown with a swirl velocity comparable to that of a non-burst vortex generated at lower angles of attack and hence interference effects coming from its wake persist long downstream.

Introduction

Since 1986 the DLR Institute of Design Aerodynamics is carrying out an intensive program for the prediction of vortical-flow-aerodynamics by the numerical solution of the Euler equations. This research program is focused on the determination of the capability of Euler codes to be used as reliable tool within the aerodynamic design process of flight vehicles. Up to now advantages and constraint of this approach have been well established for the evaluation of aerodynamic forces generated by vortical flows which emanate from the sharp edges of delta wings¹⁻⁴. Flow solutions involving vortex-vortex and shock-vortex interaction phenomena on more complex geometries like canard-wing, strake-wing and missile configurations have been successfully simulated⁵⁻⁹. The aerodynamic of delta wing configurations under asymmetric flow conditions has been investigated at different freestream Mach numbers¹⁰⁻¹¹. Furthermore the ability of Euler codes to predict vortex-breakdown phenomena has been well established in recent papers¹²⁻¹⁵.

Most of these investigations have been performed restricted due to a lack of computer capacity and computer speed, to the effects occurring above the lifting surface from which the vortical flow emanate. With the research program progressing in time, the computers became more powerful allowing to increase the complexity of the problems under consideration. Wake-flow aerodynamics corresponds to this kind of problems. They require a large amount of grid points and need a lot of computational time and computer memory.

The strong interaction which takes place when the wake flow of one aircraft closely approaches another, plays an important role in aircraft aerodynamics. In the present paper this problem is simulated based on the vortical flowfields of two sharp-edged delta wings. The primary aim of this investigation is to determine the effects of the numerical dissipation on this type of simulation, allowing to size the problem for future systematic studies. The present results have been obtained with the DLR code CEVCATS¹⁶ at a freestream Mach number $M_\infty = 0.4$ and angles of attack up to maximum lift.

Numerical Simulation

Computer code

The numerical simulation is based on the solution of the three-dimensional, compressible Euler equations in integral form. The computational scheme employs a finite-volume spatial discretization in which the discrete values of the flow quantities are located at the vertices of the grid cell. Artificial dissipative terms (also known as artificial viscosity) based on the work of Jameson et al.¹⁷ are added to the governing discrete equations. The magnitudes of these terms depend on the pressure gradients in the flow and on the damping coefficients $k^{(2)}$ and $k^{(4)}$ specified by the user. The values used in the present investigation for these coefficients are $k^{(2)} = 1/4$ and $k^{(4)} = 1/32$. Small values imply less numerical dissipation on the solutions but also a reduced stability margin of the numerical scheme. Earlier studies on vortical flow simulation with Euler codes showed that a high amount of numerical dissipation produces solutions with a large error concerning the values of the density. The system of ordinary differential equations which is obtained by the discretization in space is advanced in time with a five stage Runge-Kutta scheme. Three methods are used to accelerate the convergence to steady state: local time stepping, implicit smoothing of the residuals and a multigrid method. The code allows multi-block decomposition of the computational domain and is therefore grid topology independent. The criterion used to determine whether a solution has converged to the steady state is the residual convergence of the continuity equation, namely the L_2 -Norm. Converged solutions are assumed once the L_2 -Norm has drops at least through three orders of magnitude, as shown in Fig. 1. The required computer time per grid point and multigrid cycle is 65 μ s

on a CRAY-90 supercomputer. This time includes the time required to read and write data files and the time required to perform the calculations.

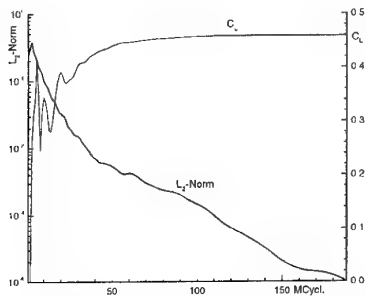


Fig. 1 Convergence history, single wing, $\alpha = 10$ deg.

Configuration and grid

The two wings used in this investigation are cropped delta wings of 65 deg. sweep angle as shown schematically in Fig. 2. Both have a symmetric cross section profile with sharp leading edges. Due to the fact that the flowfield of the wings, one behind the other, is to be compared with that of a wing alone, a H-H grid-topology has been selected since the same grid structure can be also retained for the wing alone case. This has been realized reducing the thickness of the backward wing to zero and allowing the flow to go through its cells. Thus, the use of H-H grids provides essential simplicity in the construction of the meshes and also uniformity in the simulation of the flow around the wing without and with interference effects. In order to achieve higher precision in the flow resolution, especially in the region between both wings where spiraling flows and high flow gradients occurs, a large number of grid points has to be provided. In the simulation the position of the backward wing remained always parallel to the freestream flow while the orientation of the forward wing and its surrounding grid was changed according to the specific angle of attack. This procedure guarantees a minimum influence of the angle of attack on the resolution of the wake-flow of the forward wing. In addition it reduces the possibility of changes in the flow-field of the forward wing due to undesirable interference effects coming from the backward wing. The computational domain is subdivided into ten symmetric blocks, five for the flowfield above and five for the flowfield below the wing. In streamwise direction these blocks are: incoming flow, forward wing, wake, backward wing and outgoing flow. Each block contains 48 volumes in streamwise direction, 72 volumes in spanwise direction and 64 volumes normal to the wing midsurface, thus amounting to a total of more than 2.3 million points. Due to symmetric onflow ($\beta = 0$ deg.), the computational domain is restricted to only one half of the physical domain. The grid generation is based on transfinite interpolations coupled with an optimization procedure for orthogonality. In

order to determine the sensitivity of the computed solutions to mesh fineness, a second grid has been derived deleting every second grid point in each coordinate direction leading to a grid of about 300000 points. The farfield of the computational domain extends two root chord lengths in all directions. The clustering of the grid lines in direction normal to the surface of the configuration is characterized by a minimum spacing of the first mesh layer of about 10^{-3} root chord lengths.

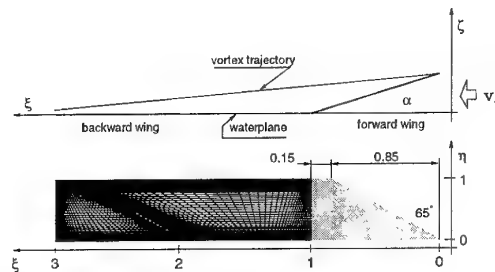


Fig. 2 Configuration arrangement and surface grid.

Results and Discussion

For the present investigation four angles of attack are considered: 10, 15.5, 21, and 35 deg. The first two angles correspond to conditions without vortex breakdown, while vortical flow with vortex bursting is observed for the large angles of attack. The first part of the study is devoted to the analysis of the wake flow of the forward wing in absence of the backward wing.

Wake flow of a delta wing

Figure 3 shows, for both grids, the pressure distribution induced by the vortex on the wing surface and on the water plane, i.e. a plane oriented with the freestream flow which contains the backward wing in the second part of the study. The position of the backward wing is also indicated in the figure. Both grid solutions have common features: on the wing surface no vortex breakdown is observed at $\alpha = 10$ and 15.5 deg. At $\alpha = 21$ deg. the vortex burst upstream the wing trailing edge, while at $\alpha = 35$ deg. vortex breakdown occurs close to the wing apex. Maximum lift is achieved at this incidence. Also in both grid solutions the wake-flow consists of two vortices of different strength: the leading-edge vortex, which is the stronger one, and the trailing-edge vortex. The region of the wake influenced by the vortices wide linearly with increasing angle of attack even after vortex breakdown. For the case of massive vortex breakdown ($\alpha = 35$ deg.), the extension of the vortex induced pressure field in the wake is wider than a wing semispan. It can also be observed that the strength of the pressure field increases approximately linear with the angle of attack up to $\alpha = 21$ deg. There are differences between the results coming from both grids as well: for all angles of attack the fine grid results exhibit larger peak

values than the coarser one at the wing surface. In the wake, the differences tend to reduce as the angle of attack increases. At $\alpha = 35$ deg. the wake-flow resulting from both grid solutions is very similar.

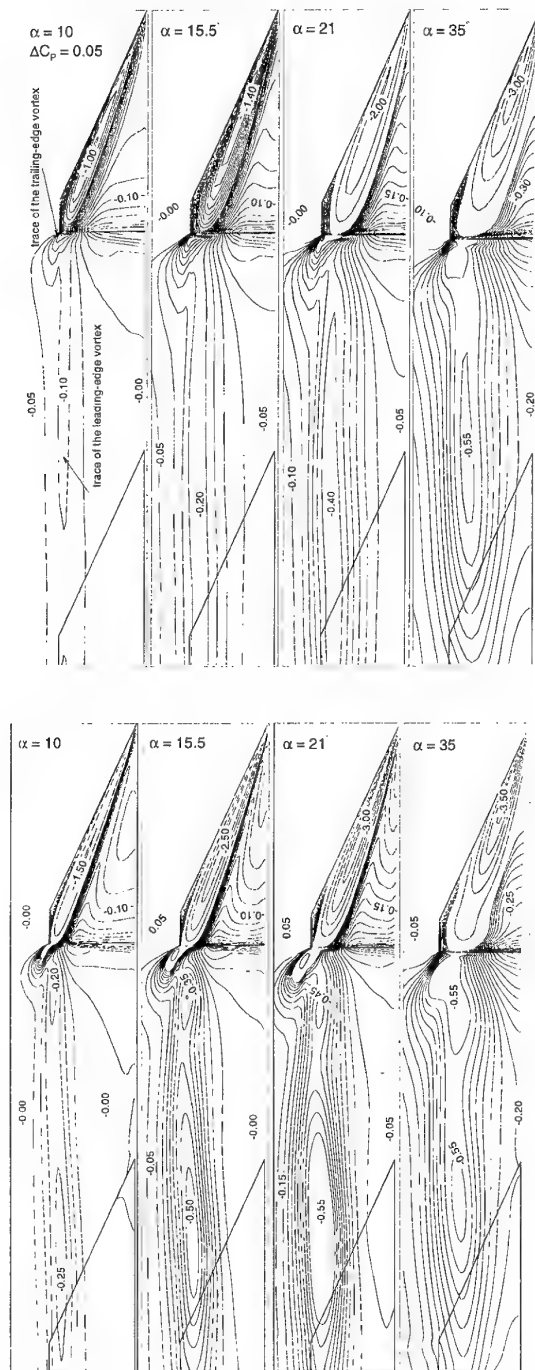


Fig. 3 Static pressure coefficient on the forward wing and on the water plane for different angles of attack. Coarse grid results (top). Fine grid results (bottom).

The downstream development of the wake-flow is shown in Figs. 4 and 5 in terms of swirl $[(v^2 + w^2)^{0.5}]$ and axial velocity components, at $\alpha = 10$ deg. Figure 4 shows results obtained on the coarse grid and Fig. 5 on the fine grid. They include one wing station ($\xi = 0.9$) also to allow comparisons of vortex strength (in terms of velocity components) above and behind the wing. Both grid solutions show the classical features of wake-flow velocity profiles: a deficit of the axial velocity in the vortex core and the two relative maxima of the swirl velocity close to the vortex axis. Furthermore the interaction process between the leading and the trailing edge vortex is captured by both grid solutions. The trailing-edge vortex moves around the leading-edge vortex when travelling downstream due to the opposite sense of rotation. This movement is faster for the fine grid solution compared to the coarse grid solution. Unfortunately, for both grid solutions, the strength of the trailing-edge vortex decays up to disappearance before finalizing the interaction process with the leading-edge vortex. Due to the fact that the vortices resolved on the coarse grid are in general weaker than those obtained on the fine grid, they orientate earlier with the freestream flow. As indicated in the figures 4 and 5 at $\xi = 3.0$ the vortex core observed on the fine grid is more inboard and downward than that on the coarse grid.

Finally the lift coefficients obtained on both grid solutions are compared in Tab. 1. For low angles of attack the coefficients obtained on the fine grid are larger than the values resulting on the coarse grid. The differences between both grid results start to decrease as the breakdown of the vortex moves upstream. At $\alpha = 35$ deg. both solutions provide almost the same lift coefficient.

Delta wing embedded in a wake flow

For the investigation of wake-flow interference effects a second wing is placed one root chord length behind the forward wing. As mentioned above this wing is orientated parallel to the freestream flow, i.e. $\alpha = 0$ deg., in order to avoid changes in the upstream pressure field (see chapter configuration and grid). Figure 6 shows the influence of the angle of attack on the forward wing wake-flow in terms of swirl velocity, in the plane $\xi = 1.5$ without and with the backward wing. It turns out that at this location and upstream of it the backward wing has no effect on the wake-flow of the forward wing. For all investigated angles of attack the trailing-edge vortex lies outboard the leading-edge vortex at this location. Having opposite sense of rotation, both vortices contribute to a resulting upwash, which is therefore larger than the downwash. As the angle of attack increases the leading-edge vortex moves away from the water plane and upward relative to the trailing-edge vortex, hence reducing the increment of the upwind velocity. At $\alpha = 35$ deg. downwash and upwash are of the same magnitude and, despite the reduction in intensity, the wake-flow is still comparable to one resulting for a small angle of attack ($\alpha = 15$ deg.). In Fig. 7 the pressure field induced by the vortices on both wings and on the water

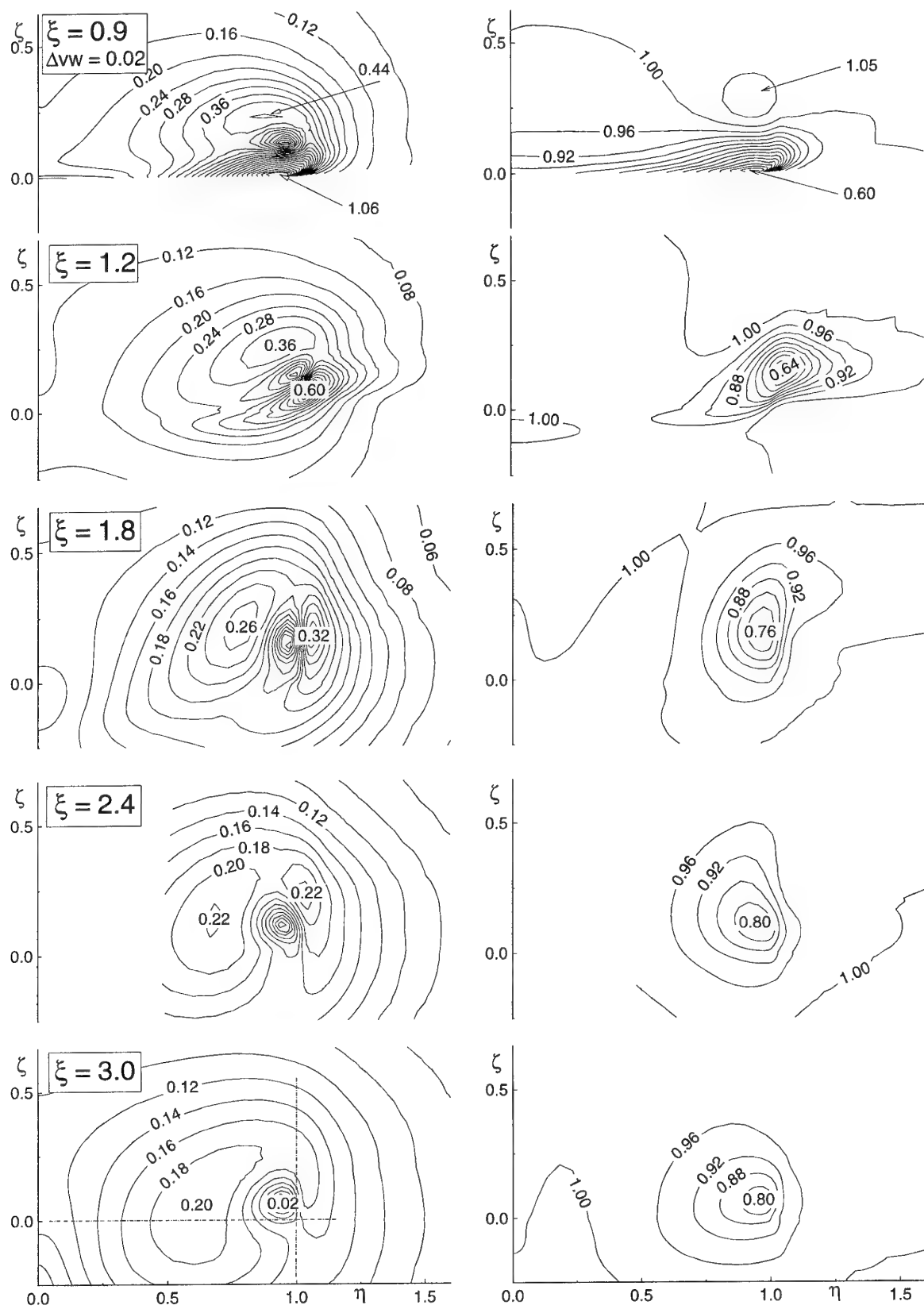


Fig. 4 Spatial development of the wake-flow at $\alpha = 10^\circ$, coarse grid. Swirl velocity (left). Axial velocity (right).

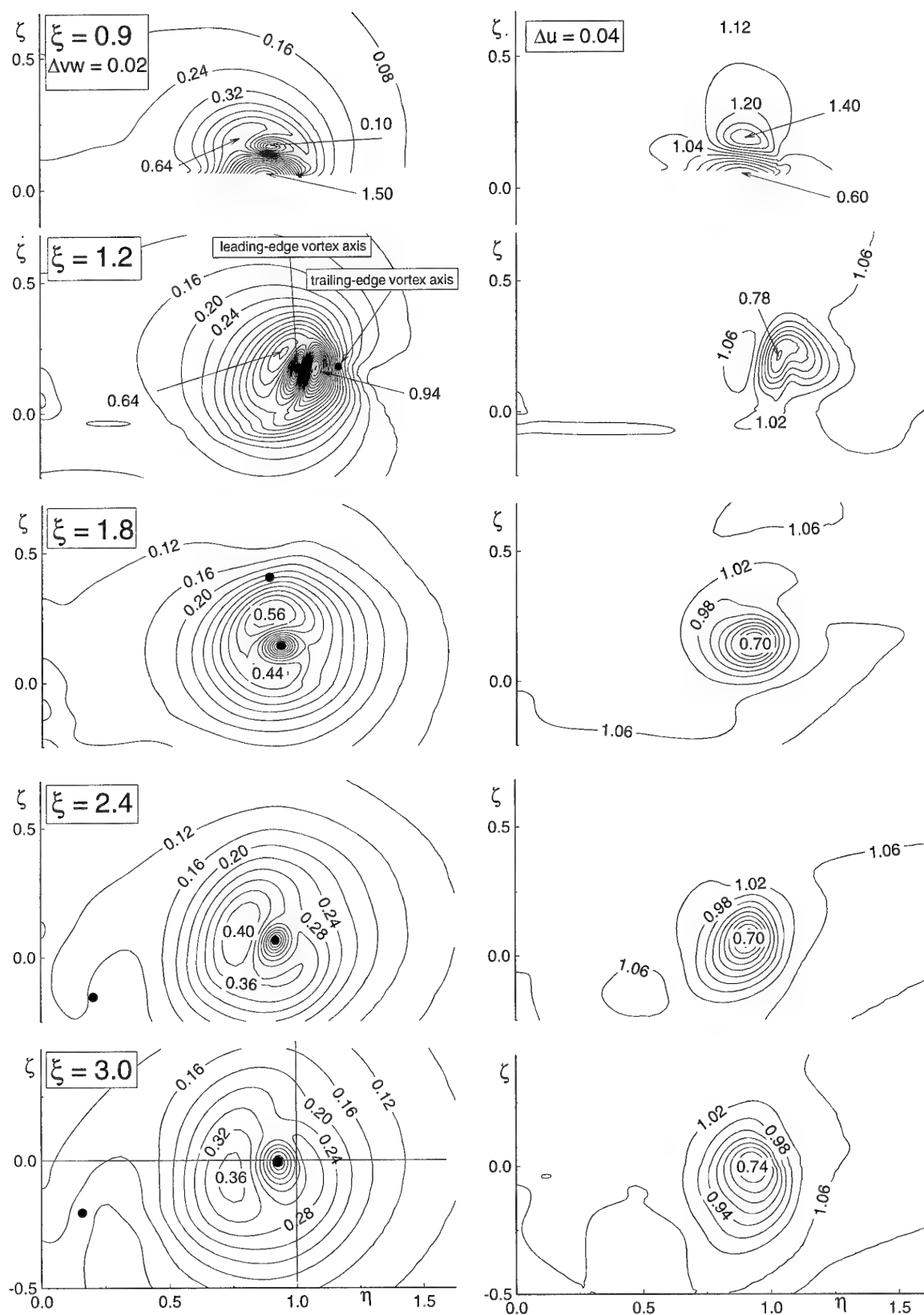


Fig. 5 Spatial development of the wake-flow for $\alpha = 10^\circ$, **fine grid**. Swirl velocity (left). Axial velocity (right).

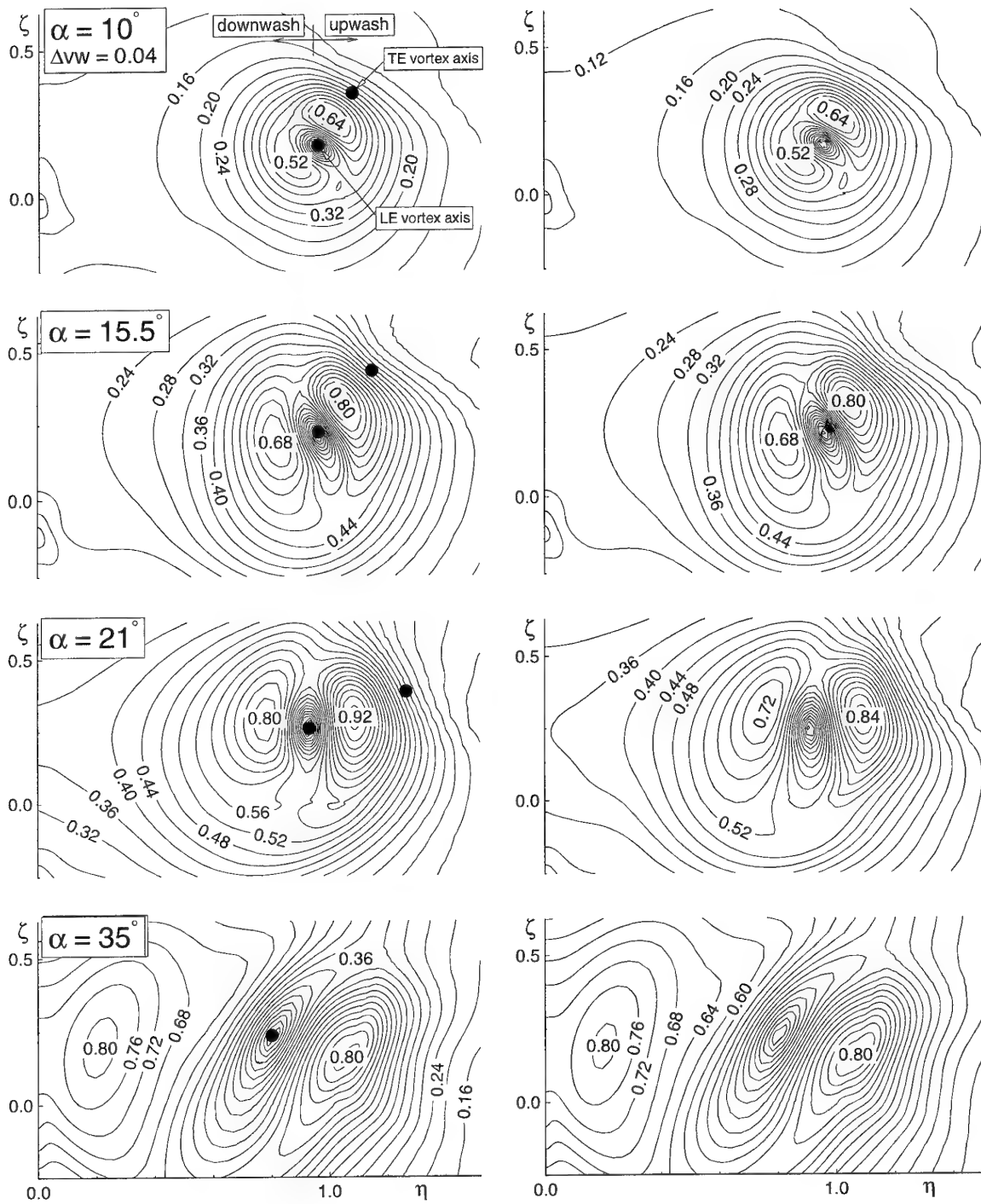


Fig. 6 Development of the wake-flow with angle of attack in terms of swirl velocity at $\xi = 1.5$, **fine grid**. Single wing (left). Two wings case (right).

plane is shown. While the presence of the backward wing does not influence the pressure field above the forward wing (see also fig. 3), the wake-flow leads to dramatic changes in the pressure field surrounding the backward wing. Due to the fact that the backward wing is embedded in the downwash part of the wake, the wake-flow induces flow separation on the lower surface of the backward wing. A sparsan type of vortex is generated on its lower surface, extending in upstream direction with increasing angle of attack of the forward wing. It turns out that the effective angle of attack of the backward wing is negative. Figure 8 shows iso-lines of the swirl velocity in two cross planes of the backward wing, indicating the position of the sparsan vortex for the $\alpha = 10$ deg- case. The consequence of this wake-induced vortical flow are displayed in Tab. 1 in terms of the lift coefficient: the larger the positive angle of attack of the forward wing, the larger is the negative angle of attack experienced by the backward wing, leading to the observed negative lift coefficient. Once the leading-edge vortex of the forward wing bursts, the effective angle of attack of the backward wing decreases, but is still larger than the resulting lift coefficient for a single wing at $\alpha \approx 7$ deg.

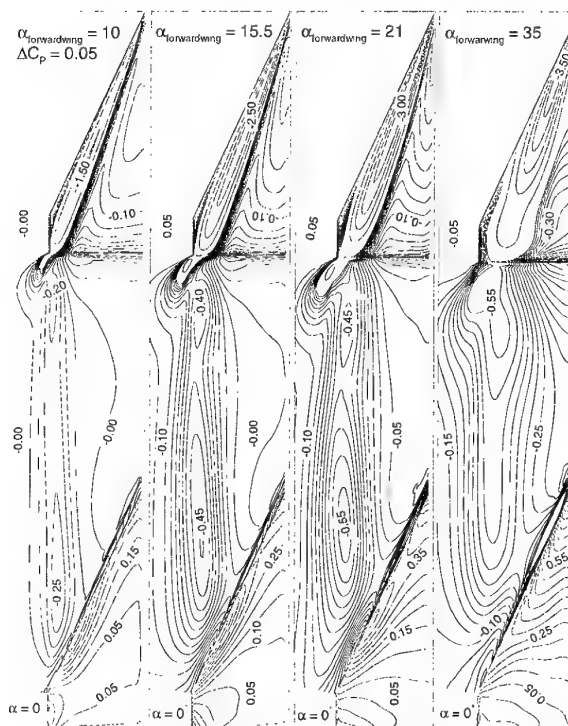


Fig. 7 Static pressure coefficient on the upper surfaces of the wings and on the water plane, for different angles of attack of the forward wing, **fine grid**.

Final Comments

In the present paper the flowfield around a delta wing partially embedded in the wake of a bursted vortex has been

numerically studied at $M_\infty = 0.4$. The simulation has been carried out solving the Euler equations on two structured grids of about 2.3 million points and 300000 points respectively. The first part of the study has been devoted to the effect of the grid fineness on the wake-flow emanating from a delta wing. Besides quantitative effects all essential flow features captured on the fine grid are also reproduced on the coarse grid. Classical axial and swirl velocity wake-flow profiles are found in both grid solutions. Furthermore, the observed quantitative differences tend to reduce with increasing angle of attack. The wake flow becomes wider and stronger linear with the angle of attack until the occurrence of vortex breakdown. Then, the strength of the vortex decays while the wake continues to wide. Furthermore the spiraling flow of the wake continues long after vortex breakdown inducing strong up- and downwash flows. In the case of a second wing approaching to this kind of wake, the interference effect coming from the spiraling flow induces large (and therefore dangerous) effective angles of attack on the backward wing. A difficulty observed in this study is the rapid decay of secondary vortices due to numerical diffusion, which leaves the interference process between vortices uncompleted. For a detailed simulation of the flowfield it is essential to consider also viscous effects and to model the decay of vortex strength with time and its evolution along large downstream distances. However, the amount of effort to solve the whole problem is at the present time too high. Having this objective in mind the present study can be considered as preliminary.

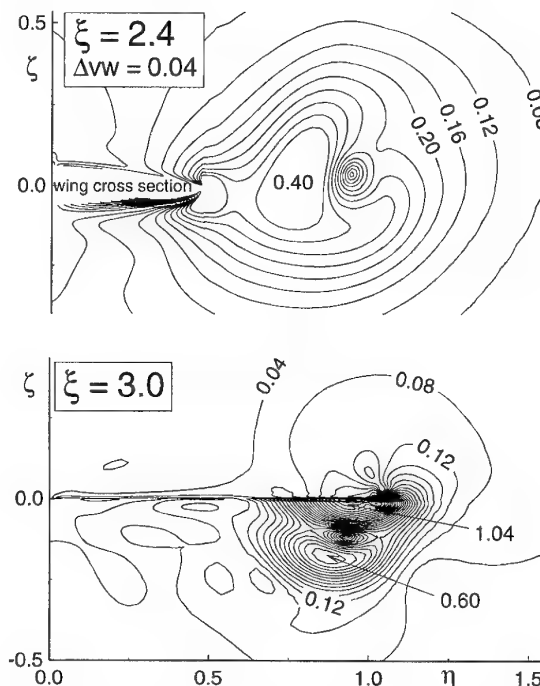


Fig. 8 Iso-lines of swirl velocity on two cross planes of the backward wing, for an angle of attack of the forward wing $\alpha = 10$ deg.

References

- ¹Kumar, A. and Das, A., "Computation of Vortex Flow on a Delta Wing at Transonic Speed", *IUTAM Symposium Transonicum III*, Springer-Verlag, Berlin, 1988, pp.317-328.
- ²Longo, J.M.A., "The Role of The Numerical Dissipation on The Computational Euler Equations Solutions for Vortical Flows", AIAA paper 89-2232, July 1989.
- ³Das, A., "Analysis of Spiraling Vortical Flows Around Slender Delta Wings Moving in an Inviscid Medium", *ZAMM*, Vol.71, No.11, 1991, pp.465-471.
- ⁴Strohmeier, D. and Longo, J.M.A., "Aerodynamische Untersuchungen einer Wellenreiterkonfiguration im Unter- und Transschall", *DGLR-Fachsymposium*, Arbeitsgemeinschaft STAB, Erlangen, October 1994.
- ⁵Scherr, S. and Das, A., "Basic Analysis of The Flow Fields of The Slender Wings Using The Euler Equations", *Proceedings of the 16th Congress of the International Council of the Aeronautical Sciences*, Vol.2, 1988, pp.1428-1436.
- ⁶Longo, J.M.A. and Das, A., "Numerical Simulation of Vortical Flows over Close-Coupled Canard-Wing Configuration", AIAA paper 90-3003, Aug. 1990.
- ⁷Das, A., and Longo J.M.A., "Numerical Computation of Vortical Flow Fields of Double-Delta Wings Moving in a Compressible Medium", *ZAMM*, Vol.74, No.10, 1994, pp.475-486.
- ⁸Streit, Th., "Euler and Navier-Stokes Solutions for Supersonic Flow Around a Complex Missile", *Journal of Spacecraft and Rockets*, Vol.31, No.4, 1994, pp.600-608.
- ⁹Burggraf, U., and Ehlers, T., "Aerodynamische Untersuchungen an Doppeldeltaflügelkonfigurationen mit Seitenkante", *DGLR-Fachsymposium*, Arbeitsgemeinschaft STAB, Erlangen, October 1994.
- ¹⁰Longo, J.M.A. and Das, A., "Numerical Study of a Delta Wing in Sideslip", *Arbeitsgemeinschaft STAB Jahresbericht*, 1992, pp.101-102.
- ¹¹Herrmann, U., "Vortex Flow on a Hypersonic Spaceplane Configuration", *Proceedings of the xxth Congress of the International Council of the Aeronautical Sciences*, , paper 94-4.4.2, August 1994.
- ¹²Longo, J.M.A., "Simulation of Complex Inviscid and Viscous Vortex Flow", *IUTAM Symposium on Fluid Dynamics of High Angle of Attack*, Springer-Verlag, Berlin, 1992, pp.363-373.
- ¹³Longo, J.M.A., "Compressible Inviscid Vortex Flow of a Sharp Edge Delta Wing", *AIAA Journal*, Vol.33, No.4, 1995, pp.680-687.
- ¹⁴Das, A. and Longo, J.M.A., "Numerical Analysis of The Vortical Flow Around a Delta Wing-Canard Configuration", *Journal of Aircraft*, Vol.32, No.4, 1995, 716-725.
- ¹⁵Strohmeier, D., Orlowski, M., Longo, J.M.A., Hummel, D. and Bergmann, A., "An Analysis of Vortex Breakdown Predicted by The Euler Equations", *Proceedings of the 20th Congress of the International Council of the Aeronautical Sciences*, paper 96-2.4.1, Sorrento, Italy, 1996.
- ¹⁶Kroll, N., Radespiel, R., Rossow, C.C., "Accurate and Efficient Flow Solvers for 3D Applications on Structured Meshes", VKI Lecture Serie *Computational Fluid Dynamics*, Brussels, 1994.
- ¹⁷Jameson, A., Schmidt, W., and Turkel, E., "Numerical Solutions of the Euler Equations by Finite Volume Methods Using Rung-Kutta Time Stepping Schemes", AIAA Paper 81-1259, June 1981.

Tabelle 1: Lift coefficients (C_L)

	Wing alone (coarse grid)	Wing alone (fine grid)	Forward W. (fine grid)	Backward W. (fine grid)
10	0.4227	0.4582	0.4582	-0.1711
15.5	0.6874	0.7417	0.7417	-0.2444
21	0.9496	0.9778	0.9778	-0.2802
35	1.2693	1.2696	1.2696	-0.3361

Stability of Multiple Trailing-Vortex Pairs

J. D. Crouch

Boeing Commercial Airplane Group
P.O. Box 3707, MS 67-LF
Seattle, WA 98124-2207
U. S. A.

1. SUMMARY

The stability of two vortex pairs is analyzed as a model for the vortex system generated by an aircraft in flaps-down configuration. The co-rotating vortices on the starboard and port sides tumble about one another as they propagate downward. This results in a time-periodic basic state. The instabilities are periodic along the axes of the vortices with wavelengths that are large compared to the size of the vortex cores. The results show symmetric instabilities that are linked to the long-wavelength Crow instability. In addition, new symmetric and anti-symmetric instabilities are observed at shorter wavelengths. These instabilities have growth rates 60-100% greater than the Crow instability. The system of two vortex pairs also exhibits transient growth which can lead to growth factors of 5 or 10 in one fourth of the time required for the same growth due to instability.

2. INTRODUCTION

Instability is one of the dominant mechanisms affecting the persistence of trailing vortices in the wake of an aircraft. The growth of sinusoidal instabilities along the axis of the vortices leads to points of connection between the counter-rotating vortices. This results in the formation of vortex rings which then degenerate into smaller-scale turbulence. The evolution of the sinusoidal instabilities on a single pair of trailing vortices was analyzed by Crow [3]. Predictions from Crow's analysis are in general agreement with observations of aircraft in flight.

For an aircraft with an elliptically-loaded wing, Crow estimates the most-amplified wavelength to be about 8 times the vortex spacing. The instability growth is relatively weak from a practical point of view; the instability amplitude increases by a factor of 2.3 during the time the vortices propagate a distance equal to their spacing. This leads to a strong sensitivity to the initial amplitudes of disturbances. Nonetheless, the instability can breakup the vortices well before they are expected to decay due to other means. Under natural conditions, the vortices are excited due to turbulence in the atmosphere. The time required

to breakup the vortices then depends on the strength of the atmospheric turbulence in addition to the instability growth rate [5].

In order to reduce the time to breakup (as well as its variability), Crow [4] has suggested a means for directly exciting the vortex-pair instability using a periodic variation of the span loading. The total lift can be kept constant while the circulation and vortex positions are changed with a frequency chosen to excite the most unstable wavelength. Bilanin & Widnall [1] successfully demonstrated this concept experimentally in a towing tank. Chevalier [2] used variations in aircraft pitch to demonstrate direct excitation of the instability in flight. The ability to excite the Crow instability, however, does not imply the viability of the concept for practical applications. The demand for large initial amplitudes, for example, may preclude its application to commercial aircraft.

These earlier studies did not account for the multiple vortices that exist for some distance behind aircraft during take off and landing. Commercial aircraft under high-lift conditions may produce a number of vortices along the span. Many of these vortices quickly merge due to their close proximity and large effective core sizes. However, distinct vortices associated with the outboard-edge of the inboard flap and the wing tip can persist much longer.

The time to merger is still not well predicted for realistic configurations at flight Reynolds numbers. Inviscid studies predict an infinite time to merger for a co-rotating vortex pair with core sizes which are small relative to the separation distance [12]. Observations based on tracer materials in towing-tank experiments show merger of the flap-edge and tip vortex after the vortices propagate a distance of approximately one span [7]. The early merger observed in these experiments is likely due to large core sizes resulting from lower Reynolds numbers and turbulence in the initial shear layer. Some flight tests show distinct vortices after a propagation distance of approximately three spans [14]. In other cases, only a single pair is detected. The time to merger depends on the configuration and the size of the vortex cores (among other factors).

Independent of the actual time to merger, the initial development of perturbations occurs on the system of multiple vortices. We consider the stability of a vortex system with two dominant vortex pairs. Consideration of the two vortex-pair system offers the potential for identifying new instabilities and growth mechanisms which may be exploited to enhance the breakup of the vortices. Klein, Majda, and Damodaran [9] have developed a general formulation for the stability of an arbitrary number of vortex filaments. Their detailed analysis and results, however, focus on the linear and nonlinear stability of a single vortex pair. Their linear results are in agreement with Crow's analysis for counter-rotating vortices and with Jimenez's results for co-rotating vortices [8]. Following the formulation of Crow [3], we provide a detailed analysis of the two vortex-pair system – including both linear stability and transient growth.

3. STABILITY ANALYSIS

The motion of the vortex pairs can be characterized by a mean propagation and a co-rotation, resulting in a tumbling effect. For real configurations, the co-rotation begins as the vortices role up – producing helical structures along the line of the circulation centroids on the starboard and port sides. The wavelength of the helix is $2\pi\tilde{V}_A/\tilde{\omega}$, where $\tilde{\omega}$ is the vortex-pair rotation frequency and \tilde{V}_A is the aircraft speed. Our analysis assumes the helix wavelength is large relative to the instability wavelength and thus the helical variation can be neglected. The relative position of the vortices is then independent of the axial distance and dependent only on time.

The dynamics of the trailing vortices are modeled using thin vortex filaments. The formulation follows the original work of Crow for the stability of a single vortex pair [3]. Figure 1 is a schematic of the trailing-vortex system. The local coordinate system moves with the mean position of the vortices. The vortices that are initially outboard are designated by 1 and 2, and the inboard vortices by 3 and 4. The total positive circulation (produced by one wing) is given by $\tilde{\Gamma}_0 = \tilde{\Gamma}_2 + \tilde{\Gamma}_4$, where $\tilde{\Gamma}_2$ and $\tilde{\Gamma}_4$ characterize the strengths of the two vortex pairs and $\tilde{\Gamma}_1 = -\tilde{\Gamma}_2$, $\tilde{\Gamma}_3 = -\tilde{\Gamma}_4$. The circulation centroids on the starboard and port sides are separated by a distance \tilde{b} and the co-rotating vortices are separated by a distance \tilde{d} . All quantities are nondimensionalized by the length scale \tilde{b} and time scale $2\pi\tilde{b}^2/\tilde{\Gamma}_0$. This leads to two key parameters characterizing the system, $\Gamma = \tilde{\Gamma}_4/\tilde{\Gamma}_2$ and $\delta = \tilde{d}/\tilde{b}$.

When δ is small the vortices rotate in a near-circular path (in the local frame) with frequency $\omega = 1/\delta^2$. As δ is increased, the vortex trajectories become distorted and the frequency is reduced below $1/\delta^2$. The vortices are perturbed by an axially periodic disturbance with wavelength $\lambda = 2\pi/\alpha$. Neglect-

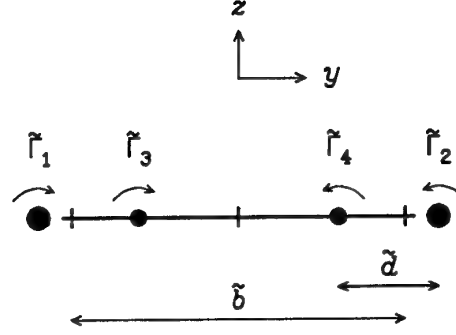


Figure 1: Schematic showing the initial positions of the vortices.

ing the helical variation of the vortices requires that $1/(V_A\alpha\delta^2) \ll 1$, where V_A is the aircraft speed nondimensionalized by the mean vortex propagation velocity; a typical value is $V_A \approx 50$.

Equations for the propagation and stability of the vortices are derived by matching the induced velocities from Biot-Savart with kinematic equations obtained by temporal differentiation of the vortex position vectors. The position vector representing the location of induced velocity on vortex n is given by

$$\mathbf{r}_n = x_n\hat{i} + (y_n + \eta_n e^{i\alpha x_n})\hat{j} + (z_n + \zeta_n e^{i\alpha x_n})\hat{k}, \quad (1)$$

with n taking values from 1 to 4. The position vector representing the induction source has the same form but the subscript n is replaced by m . The induced velocity at \mathbf{r}_n is given by

$$\mathbf{v}_n = \sum_{m=1}^4 \frac{\Gamma_m}{4\pi} \int_{-\infty}^{\infty} \frac{(\mathbf{r}_m - \mathbf{r}_n)}{|\mathbf{r}_m - \mathbf{r}_n|^3} \times \frac{\partial \mathbf{r}_m}{\partial x_m} dx_m, \quad (2)$$

where

$$\begin{aligned} \mathbf{r}_m - \mathbf{r}_n = & x_{mn}\hat{i} + (y_{mn} + \eta_m e^{i\alpha x_m} - \eta_n e^{i\alpha x_n})\hat{j} \\ & + (z_{mn} + \zeta_m e^{i\alpha x_m} - \zeta_n e^{i\alpha x_n})\hat{k}, \end{aligned} \quad (3)$$

and $x_{mn} = x_m - x_n$, $y_{mn} = y_m - y_n$, $z_{mn} = z_m - z_n$. Expanding the integrand of eq. (2), the induced velocity can be written in the form

$$\begin{aligned} \mathbf{v}_n = \sum_{m=1}^4 \left\{ V_{0mn}\hat{j} + W_{0mn}\hat{k} + \right. \\ \left. (V_{1mn}\zeta_n + V_{2mn}\zeta_m + V_{3mn}\eta_n + V_{4mn}\eta_m)e^{i\alpha x_n}\hat{j} + \right. \\ \left. (W_{1mn}\eta_n + W_{2mn}\eta_m + W_{3mn}\zeta_n + W_{4mn}\zeta_m)e^{i\alpha x_n}\hat{k} \right\}. \end{aligned} \quad (4)$$

Equation (4) is linearized based on the assumption that the perturbation amplitudes are small relative to the minimum separation distance of the vortices ($|\eta_n|/\delta \ll 1$, $|\zeta_n|/\delta \ll 1$ for the range of parameters considered). The velocity components V_{imn} and W_{imn} are determined from integrals that are defined

in the appendix. The analysis assumes thin vortex filaments and uses a cutoff distance x_0 to account for the finite core effects when calculating the self induction. The cut-off distance is related to the effective core diameter c_e by the expression $x_0 = 0.3210c_e$ [3]. The core size is scaled with the strength of the vortex based on the assumption that the peak-vorticity level is constant. For vortices 1 and 2, $x_0 = \epsilon$, and for vortices 3 and 4, $x_0 = \Gamma^{1/2}\epsilon$. Thus the core characteristics are represented by a single cut-off parameter ϵ .

The induced motion of the trailing vortices satisfies a kinematic condition derived from the temporally varying position vector. In the absence of any constraints on the vortex motions,

$$\frac{\partial \mathbf{r}_{Fn}}{\partial t} = W_0 \hat{k} + \frac{\partial \mathbf{r}_n}{\partial t} = \mathbf{v}_n. \quad (5)$$

The vector \mathbf{r}_{Fn} is measured from a fixed frame and W_0 is the propagation velocity for the local reference frame (i.e. $W_0 = 1$, the small- δ mean propagation velocity of the vortices). Differentiating (1) with respect to t yields

$$\frac{d\mathbf{r}_n}{dt} = \left(\frac{dy_n}{dt} + \frac{d\eta_n}{dt} e^{i\alpha x_n} \right) \hat{j} + \left(\frac{dz_n}{dt} + \frac{d\zeta_n}{dt} e^{i\alpha x_n} \right) \hat{k}. \quad (6)$$

Combining eqs. (4)-(6), the equations for the mean vortex positions become

$$\frac{dy_n}{dt} = \sum_{m=1}^4 V_{0mn}, \quad (7)$$

$$\frac{dz_n}{dt} = \sum_{m=1}^4 W_{0mn} - W_0, \quad (8)$$

with initial conditions defined as

$$y_2(0) = .5 + \delta\Gamma/(1 + \Gamma), \quad y_4(0) = .5 - \delta/(1 + \Gamma),$$

$$y_1(0) = -y_2(0), \quad y_3(0) = -y_4(0), \quad z_n(0) = 0, \quad n = 1, 4. \quad (9)$$

The perturbation amplitudes are governed by

$$\frac{d\eta_n}{dt} = \sum_{m=1}^4 (V_{3mn}\eta_n + V_{4mn}\eta_m + V_{1mn}\zeta_n + V_{2mn}\zeta_m), \quad (10)$$

$$\frac{d\zeta_n}{dt} = \sum_{m=1}^4 (W_{1mn}\eta_n + W_{2mn}\eta_m + W_{3mn}\zeta_n + W_{4mn}\zeta_m), \quad (11)$$

with initial conditions

$$\eta_n(0) = \eta_{n0}, \quad \zeta_n(0) = \zeta_{n0}. \quad (12)$$

The amplitude equations (10) and (11) are a set of eight coupled differential equations. The coefficients (V_{imn} , W_{imn}) are periodic functions of time due to the co-rotation of the vortex pair. When $\Gamma = 0$, the equations reduce to those considered by Crow [3].

4. FLOQUET THEORY

Equations (7)-(12) can be solved by a combination of analytical and numerical methods to yield the stability characteristics for the system of two vortex-pairs. Introducing the disturbance vector $\phi = (\eta_1, \eta_2, \eta_3, \eta_4, \zeta_1, \zeta_2, \zeta_3, \zeta_4)^T$, equations (10) and (11) can be written in the compact form

$$(d/dt)\phi = [\mathbf{F}(t)]\phi. \quad (13)$$

The elements of the matrix $[\mathbf{F}(t)]$ depend on time through the changing vortex positions given by eqs.(7)-(9). Thus $[\mathbf{F}(t)]$ satisfies the condition $[\mathbf{F}(t+T)] = [\mathbf{F}(t)]$, where T is the rotation period for the co-rotating pair; $T \approx 2\pi\delta^2$ for small δ . The vortex positions and the coefficient matrix $[\mathbf{F}(t)]$ are characterized by the parameters Γ , δ , and ϵ .

The growth rate for instability can be determined from eq. (13) using the Floquet theory [10]. We first define a nonsingular constant matrix $[\mathbf{A}]$ by numerically integrating eq. (13) over one period of the vortex rotation. Using $\phi(0) = (1, 0, 0, 0, 0, 0, 0, 0)^T$ as an initial condition, the resulting vector after integration provides the first column of $[\mathbf{A}]$, $a_1 = \phi(T)$. Likewise, setting the k th element of $\phi(0)$ to 1 with all others zero yields the k th column a_k . The disturbance vector after one period of evolution $\phi(t+T)$ can then be related to the disturbance vector $\phi(t)$ through the relation

$$\phi(t+T) = [\mathbf{A}]\phi(t). \quad (14)$$

Introducing $\phi(t) = [\mathbf{P}]\psi(t)$ into (14) leads to

$$\psi(t+T) = [\mathbf{P}]^{-1}[\mathbf{A}][\mathbf{P}]\psi(t) = [\mathbf{S}]\psi(t), \quad (15)$$

where the columns of $[\mathbf{P}]$ are unit norm eigenvectors of $[\mathbf{A}]$. Assuming the eigenvalues of $[\mathbf{A}]$ are distinct, the matrix $[\mathbf{S}]$ is diagonal with the eigenvalues σ as its entries. For a given eigenvalue, $\psi(t+nT) = \sigma^n \psi(t)$, or more generally,

$$\psi(t+nT) = [\mathbf{S}]^n \psi(t). \quad (16)$$

The function ψ can be written in the normal form by introducing $\gamma = \ln(\sigma)/T$,

$$\psi(t) = \exp(\gamma t)\chi(t). \quad (17)$$

$\chi(t)$ is a periodic function and γ is the characteristic exponent. The condition for instability then has the usual form $\gamma > 0$.

The eigenvectors corresponding to different values of σ describe the relative magnitudes and orientations of the perturbations on each of the vortices. Following Crow [3], we classify the modes as symmetric or anti-symmetric based on their appearance from the ground. A mode which is symmetric with respect to the vortices 1 and 2 satisfies the condition $\eta_1 = -\eta_2$ and $\zeta_1 = \zeta_2$. The corresponding anti-symmetric mode satisfies the condition $\eta_1 = \eta_2$ and $\zeta_1 = -\zeta_2$.

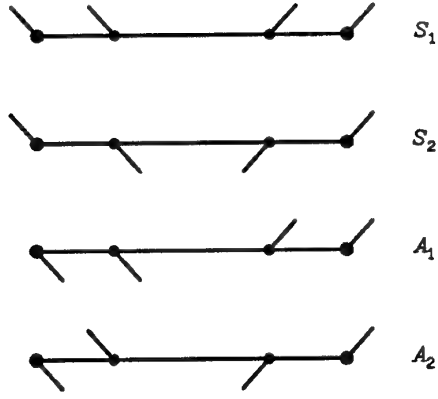


Figure 2: Schematic of the instability mode shapes as observed at a fixed x position.

Considering the complete system of four vortices, we define two symmetric modes S_1 , S_2 , and two anti-symmetric modes A_1 , A_2 , as shown in figure 2. The diagrams show the relative orientation of the disturbances at a single x location at a time nT , $n \geq 1$. This is quantified by the angles $\theta_2 = \tan^{-1}(\zeta_2/\eta_2)$ and $\theta_4 = \tan^{-1}(\zeta_4/\eta_4)$. The relative magnitudes are given by the ratio $|\eta_4/\eta_2|$.

The modes S_1 and A_1 are generalizations of the Crow modes. The vorticity centroids are perturbed in a direction consistent with a single vortex at the centroid location. The modes S_2 and A_2 are perturbations about the centroids. The centroid locations are only weakly perturbed.

5. STABILITY CHARACTERISTICS

The mean-position and perturbation equations are integrated numerically in order to define the matrix $[A]$. The first few points are evaluated using forth-order Runge Kutta; the remaining steps are evaluated using the Adams-Bashforth predictor scheme. The stability results are based on a time step of $\Delta t = 0.01$. Further reduction in Δt changes the growth rate by less than 1%. Smaller time steps are used for studying transient behavior.

Figure 3 shows the variation of the growth rate γ with the wavenumber α for different values of the spacing parameter δ . The circulation ratio $\Gamma = 0.5$ and cut-off parameter $\epsilon = 0.05$ are constant. The results show three unstable modes S_1 , S_2 , and A_2 . The variation of the growth rate for the S_1 mode is similar to the long-wavelength Crow instability for a single vortex pair placed at the vorticity centroids. This mode is only weakly affected by changes in the co-rotating-vortex spacing δ . The maximum growth rate is approximately 0.8. For $\delta = 0.3$ and $\alpha = 0.8$, the orientation of the S_1 mode after $t = nT$ is given by $\theta_2 = 45^\circ$, $\theta_4 = 52^\circ$, $|\eta_4/\eta_2| = 0.9$. The orientation does not change significantly during the rotation period T .

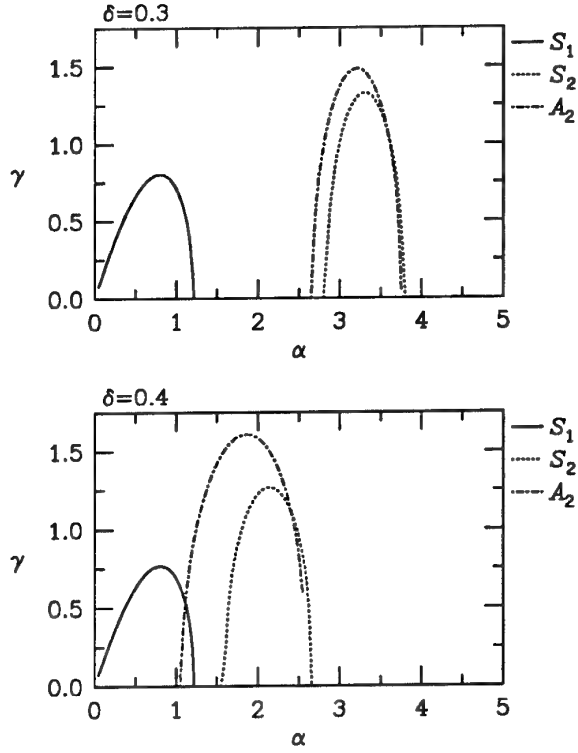


Figure 3: Growth rate γ as a function of wavenumber α for different values of the vortex-spacing parameter δ ($\Gamma = 0.5$, $\epsilon = 0.05$).

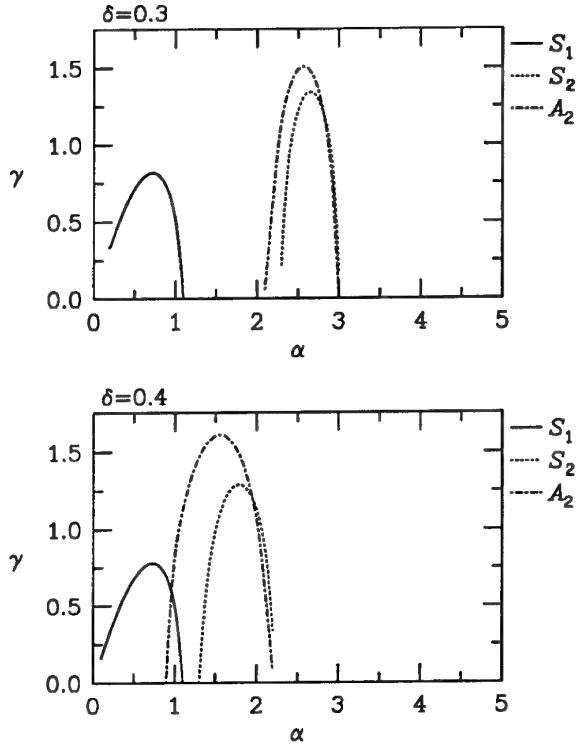


Figure 4: Growth rate γ as a function of wavenumber α for different values of the vortex-spacing parameter δ ($\Gamma = 0.5$, $\epsilon = 0.02$).

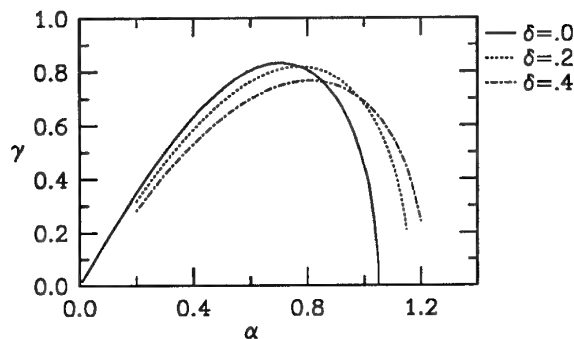


Figure 5: Growth rate γ for the mode S_1 as a function of wavenumber α for different values of the vortex-spacing parameter δ ($\Gamma = 0.5$, $\epsilon = 0.05$).

The modes S_2 and A_2 are shorter wavelength instabilities. These modes are quite sensitive to the vortex-spacing parameter δ . The most unstable wavenumbers decrease from 3.3 at $\delta = 0.3$ to approximately 2 at $\delta = 0.4$. The anti-symmetric mode A_2 has a maximum growth rate of approximately 1.5 and the symmetric mode S_2 has a maximum growth rate close to 1.3. For $\delta = 0.3$ and $\alpha = 3.3$, the orientation of the S_2 mode after $t = nT$ is given by $\theta_2 = 67^\circ$, $\theta_4 = -110^\circ$, $|\eta_4/\eta_2| = 2.6$. The orientation of the A_2 mode with $\alpha = 3.2$ is given by $\theta_2 = 68^\circ$, $\theta_4 = -111^\circ$, $|\eta_4/\eta_2| = 3.0$. The orientation of these modes changes significantly over the rotation period T . When the vortices are aligned along $z = 0$ (i.e. $t = nT/2$), the ζ perturbation is larger than the η perturbation. When the vortices are aligned along $y = 0.5$ (i.e. $t = T/4 + nT/2$), the η perturbation is largest.

Figure 4 shows growth-rate curves for a smaller core size, $\epsilon = 0.02$. The S_1 mode is relatively unaffected by the reduced ϵ . The wavenumbers of the unstable S_2 and A_2 modes decrease with decreasing core size. The maximum growth rates show no significant variation with ϵ . Variation of the circulation ratio Γ has a similar effect to changing ϵ . For $\epsilon = 0.2$, increasing Γ from 0.5 to 1 shifts the wavenumber for maximum growth of the S_2 and A_2 modes by $\Delta\alpha \approx -0.1$. Decreasing Γ from 0.5 to 0.25 shifts the wavenumber for maximum growth by $\Delta\alpha \approx 0.5$. Part of the effect of changing Γ is due to the change in the cut-off length for the vortices 1 and 3 as discussed in the appendix.

The S_2 and A_2 modes look similar to the spurious short-wavelength modes found by Crow [3] for $\alpha\epsilon \approx 1$ (using our notation). Widnall, Bliss & Tsai [16] show that the thin-filament analysis is limited to wavelengths which are large compared to the core size $\alpha\epsilon \ll 1$, and that spurious instabilities are predicted for $\alpha\epsilon \approx 1$. In the current analysis, the shorter wavelength modes are observed at $\alpha\epsilon \approx 0.05$ (from figure 4), which is within the range of validity of the long-wavelength approximation.

Figure 5 shows a detailed comparison of the growth

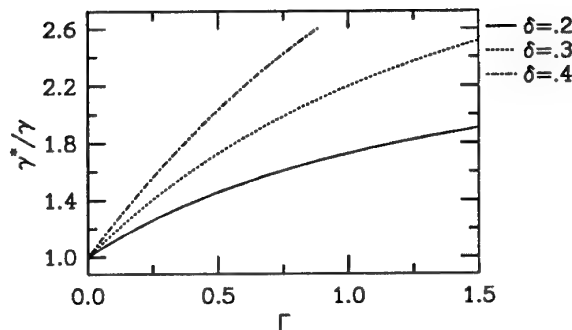


Figure 6: Ratio of growth rates γ^* and γ .

rates for the S_1 mode and the Crow instability ($\delta = 0$). The maximum growth rate is slightly reduced and the most unstable wavenumber is slightly increased due to increased δ . These quantities are nondimensionalized by the total circulation $\tilde{\Gamma}_0$ and the spacing between vorticity centroids \tilde{b} . To estimate the effects of Γ and δ on the physical growth rate we consider lift distributions with the tip vortices separated by a fixed distance \tilde{b}^* (i.e. constant span). As the strength and position of the flap vortex is changed, the total lift is held constant. For $\Gamma = 0$, there is a single vortex pair of strength $\tilde{\Gamma}_0^*$ separated by \tilde{b}^* . For $\Gamma \neq 0$, constant lift requires $\tilde{\Gamma}_0\tilde{b} = \tilde{\Gamma}_0^*\tilde{b}^*$. This provides a relationship between \tilde{b}^* and \tilde{b} and $\tilde{\Gamma}_0^*$ and $\tilde{\Gamma}_0$. The physical growth rate γ^* (nondimensionalized by fixed values $\tilde{\Gamma}_0^*$ and \tilde{b}^*) is related to the growth rate parameter γ through the relation $\gamma^*/\gamma = [1 + 2\delta(\Gamma/(1+\Gamma))]^3$; this ratio is plotted in figure 6 for different values of Γ and δ . For $\delta = 0.3$, an increase in Γ from 0.25 to 0.75 results in a 40% increase in the physical growth rate. Although the growth rate parameter γ is relatively unchanged with Γ and δ , the physical growth rate for a constant-lift/constant-span configuration can change by more than a factor of 2.

6. TRANSIENT GROWTH

The temporal evolution of the vortex positions and the disturbance amplitudes can be studied by numerically integrating the initial-value problem (7)-(12). A combination of Runge-Kutta and Adams-Bashforth schemes are used with a time step $\Delta t = 0.001$. Figure 7 shows the evolution of the mean positions and perturbations for the vortices 2 and 4. The circulation ratio is $\Gamma = 0.5$ and the spacing is $\delta = 0.3$. The initial positions are consistent with figure 2. The vortices follow a nearly circular orbit about $(y = 0.5, z = 0)$ in the local reference frame. The period of orbit is $T = 0.634$; this is larger than $2\pi\delta^2 = 0.565$ due to the interaction with the vortices 1 and 3. The smaller vortex follows a larger trajectory around the vorticity centroid.

The perturbation amplitudes correspond to a wave

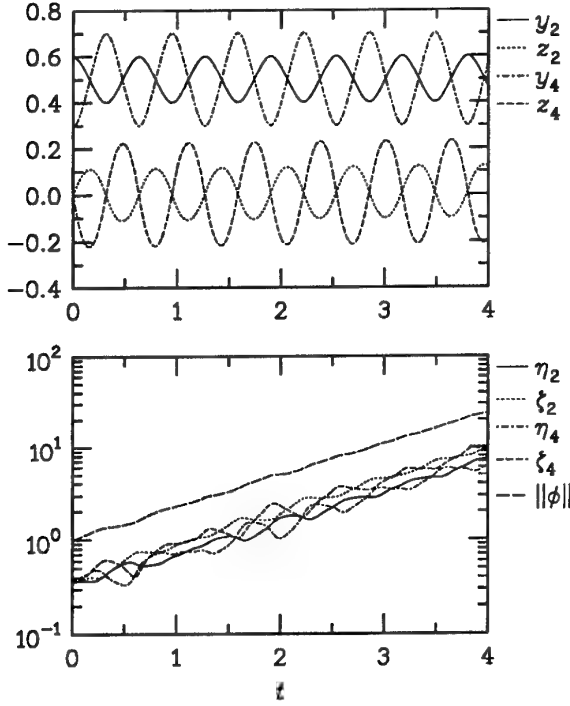


Figure 7: Temporal evolution of the vortex positions and disturbance amplitudes for the conditions $\Gamma = 0.5$, $\epsilon = 0.05$, $\delta = 0.3$, and $\alpha = 0.7$.

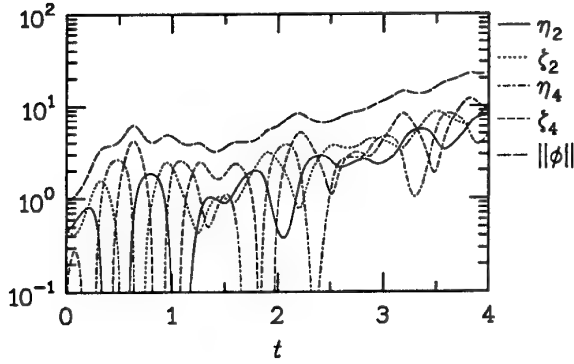


Figure 8: Temporal evolution of the disturbance amplitudes for the conditions $\Gamma = 0.5$, $\epsilon = 0.05$, $\delta = 0.3$, and $\alpha = 0.7$.

number $\alpha = 0.7$, which is an S_1 symmetric mode. The initial condition is symmetric with $\theta_2 = \theta_4 = 45^\circ$, $\eta_4/\eta_2 = 1$ and $\|\phi(0)\| = 1$. After some initial adjustment, the disturbance growth is characteristic of the predicted unstable eigenmode for these conditions. At $t = 2$ (after the vortex centroids have propagated a distance $2\bar{b}$), the disturbance has grown by a factor of 5.

Figure 8 shows the disturbance-amplitude evolutions for the same conditions as figure 7 except with $\eta_4/\eta_2 = 0.1$. These initial conditions lead to transient growth which amplifies the disturbance by a factor of 5 from $t = 0$ to $t = 0.55$. Thus the transient

growth produces the same level of amplification as the instability in approximately 25% of the time. At large times, the disturbance amplitudes vary in accordance with the unstable eigenmode. By exciting only the outboard vortices (1 and 2), the short-term growth is dramatically increased.

Transient growth has been observed in conjunction with a number of hydrodynamic instabilities, including: plane channel flow, boundary layers, and isolated line vortices [11], [13]. Transient growth can amplify small disturbances leading to nonlinear interactions in systems which are stable ($\gamma < 0$) [15]. The transient growth stems from the non-normality of the linear operator governing the disturbance evolution; the operator eigenvectors are non-orthogonal. An initial condition of small magnitude can produce large expansion coefficients when projected onto the non-orthogonal eigenvectors since the eigenvectors can partially cancel each other. As the eigenmodes grow and/or decay at varying rates, the eigenvector cancellation is reduced resulting in transient growth.

The potential for transient growth can be estimated by considering the upper bound on the energy amplification [6]. For a given initial condition $\phi(0)$, the response after n periods can be obtained by rewriting (16) in the form

$$\phi(nT) = [\mathbf{P}][\mathbf{S}]^n[\mathbf{P}]^{-1}\phi(0). \quad (18)$$

The maximum energy amplification after n periods $G(nT)$ for an initial input of unit norm $\|\phi(0)\| = 1$ is

$$G(nT) = \sup_{\|\phi(0)=1\|} \|\phi(nT)\| = \|[\mathbf{P}][\mathbf{S}]^n[\mathbf{P}]^{-1}\|. \quad (19)$$

The maximum energy amplification over all time is given by

$$G_{max} \equiv \sup_{n \geq 0} G(nT), \quad (20)$$

which is bounded by

$$1 \leq G_{max} \leq \kappa(\mathbf{P})\sigma_{max}^n. \quad (21)$$

$\kappa(\mathbf{P})$ is the condition number of the matrix \mathbf{P} and σ_{max} is the maximum eigenvalue of $[\mathbf{A}]$.

The condition number $\kappa(\mathbf{P})$ provides a measure of the potential for transient growth. When $\kappa(\mathbf{P}) = 1$, the eigenvectors are orthogonal and there is no transient growth. The maximum energy amplification is then completely governed by instability. For $\kappa(\mathbf{P}) > 1$, transient growth can occur; the greater the value of $\kappa(\mathbf{P})$, the greater the energy amplification. Figure 9 shows the condition number as a function of α for different values of ϵ and δ . For $\epsilon = 0.05$, the condition number (and therefore the level of transient amplification) shows a general increase with decreasing δ . At smaller values of δ , the smaller wavenumbers can exhibit the largest transient growth. For $\epsilon = 0.02$, the α which produces the largest condition number depends on δ . Smaller wavenumbers exhibit the strongest transient growth for small δ compared to larger wavenumbers at larger δ .

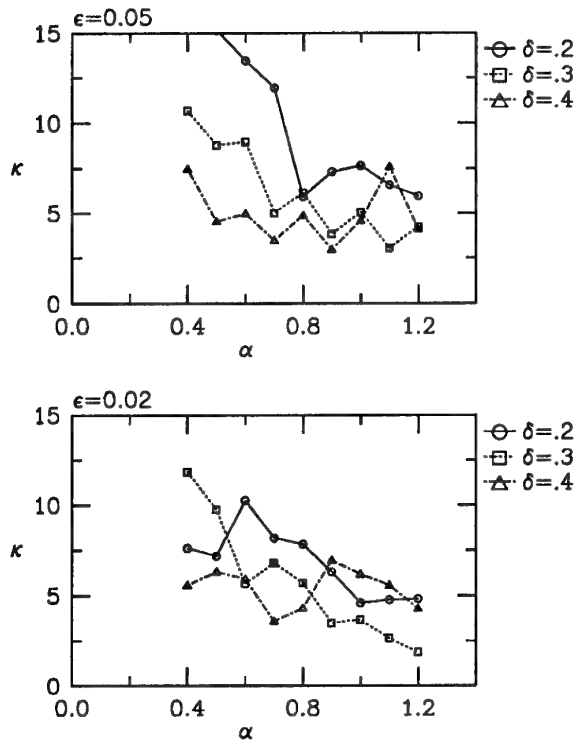


Figure 9: Condition number $\kappa(P)$ as a function of wavenumber α for different values of the cut-off parameter ϵ and the vortex-spacing parameter δ ($\Gamma = 0.5$).

7. CONCLUSIONS

Analysis of the stability of two trailing-vortex pairs suggests that the vortex system produced by flaps-down high-lift configurations provides other mechanisms for breaking up the vortices in addition to the Crow instability. These include new instability modes and the potential for amplification due to transient growth. Although most of the results are presented for a tip vortex which is twice as strong as the flap-edge vortex ($\Gamma = 0.5$), they can be generalized to the full range of practical values of Γ .

The two vortex pairs are unstable to a symmetric mode at wavelengths greater than five times the vorticity centroid spacing \tilde{b} . This mode is characterized by displacement of the vorticity centroids as predicted by the Crow instability for a single vortex pair. Maximum growth rates, nondimensionalized by the total circulation and the centroid spacing, are approximately 0.8. This results in a five-fold growth in the disturbance amplitude in the time it takes the vorticity centroids to propagate a distance of $2\tilde{b}$. The growth rates are in close agreement with those predicted for a single vortex pair. The spacing and relative circulation between the flap and tip vortices provides only a small modification of the nondimensional growth rate. However, the physical growth rate (for a constant-lift/constant-span configuration)

can vary by more than 50% for different values of the spacing and relative circulation. This results from the changes in the vorticity centroid spacing and the total circulation.

The two vortex-pair system is also unstable to shorter-wavelength symmetric and anti-symmetric modes. These modes are characterized by displacements about the vorticity centroids, with the centroid locations relatively unperturbed. The band of unstable wavelengths for these modes depends on the vortex-core size and the flap- and tip-vortex spacing and circulation ratio. For the parameters considered, the symmetric-mode wavelength lies between $1.5\tilde{b}$ and $4\tilde{b}$. The anti-symmetric mode wavelength lies between $1.5\tilde{b}$ and $6\tilde{b}$. Although these wavelengths are shorter than the symmetric Crow mode, they are long relative to the effective vortex-core size. Maximum growth rates are approximately 1.3 for the symmetric mode and 1.6 for the anti-symmetric mode. The symmetric mode grows by a factor of five in the time required for the vorticity centroids to propagate a distance of $1.2\tilde{b}$.

The y perturbation (which is the relevant quantity for predicting connection of the counter-rotating vortices) is a maximum when the co-rotating vortices 1,3 and 2,4 are nearly aligned at $y = -\tilde{b}/2$ and $y = +\tilde{b}/2$, respectively. Connection occurs when the y perturbation reaches $0.5\tilde{b}$. At the initial position with the vortices aligned along $z = 0$, most of the instability-mode energy is in the z perturbation. Thus an initial z perturbation of $0.1\tilde{b}$ (or approximately 6% of the span) would lead to a breakup of the vortices after they have propagated a distance of approximately $1.2\tilde{b}$. This assumes that the nonlinear effects do not weaken the instability growth.

The two vortex-pair system exhibits transient growth as demonstrated by numerical integration of the initial-value problem. This is further substantiated by an analysis of the linear operator governing the disturbance evolution. Transient growth can amplify an initial disturbance by a factor of five in the amount of time the vorticity centroids propagate a distance $0.5\tilde{b}$ (one fourth of the time required for comparable growth due to instability at the same wavelength). The strength of the transient growth increases as the spacing between the flap and tip vortices is reduced. The amount of amplification depends on the initial conditions. Exciting both vortex pairs, so that the distribution of the initial perturbation is close to the most unstable mode, results in very little transient growth. If, however, only one vortex pair is excited, the level of transient growth is close to the theoretical maximum.

Acknowledgements

Philippe Spalart and Byram Bays-Muchmore of Boeing and Peter Schmid of the University of Washington provided a number of helpful discussions.

References

- [1] Bilanin, A. J. and Widnall, S. E. 1973 "Aircraft wake dissipation by sinusoidal instability and vortex breakdown", AIAA Paper No. 73-107.
- [2] Chevalier, H. 1973 "Flight test studies of the formation and dissipation of trailing vortices", *J. Aircraft*, **10**, pp. 14-18.
- [3] Crow, S. C. 1970 "Stability theory for a pair of trailing vortices", *AIAA J.*, **8**, pp. 2172-2179.
- [4] Crow, S. C. 1971 Panel Discussion in: *Aircraft Wake Turbulence and Its Detection*, ed. J. Olsen, A. Goldburg, M. Rogers, pp. 551-582.
- [5] Crow, S. C. and Bate, E. R. Jr. 1976 "Lifespan of trailing vortices in a turbulent atmosphere", *J. Aircraft*, **13**, pp. 476-482.
- [6] Darmofal, D. L. and Schmid, P. J. 1995 "The importance of eigenvectors for local preconditioners of the Euler equations", AIAA Paper No. 95-1655-CP.
- [7] Dunham, R. E., Jr. 1974 "Model tests of various vortex dissipation techniques in a water towing tank", NASA LWP-1146.
- [8] Jimenez, J. 1975 "Stability of a pair of co-rotating vortices", *Phys. Fluids*, **18**, pp. 1580.
- [9] Klein, R., Majda, A. J. and Damodaran, K. 1995 "Simplified equations for the interaction of nearly parallel vortex filaments", *J. Fluid Mech.*, **288**, pp. 201-248.
- [10] Nayfeh, A. H. and Mook, D. T. 1979 *Nonlinear Oscillations*, Wiley & Sons, New York.
- [11] Reddy, S. C. and Henningson, D. S. 1993 "Energy growth in viscous channel flows", *J. Fluid Mech.*, **252**, pp. 209-238.
- [12] Rossow, V. J. 1976 "Convective merging of vortex cores in lift-generated wakes", AIAA Paper No. 76-415.
- [13] Schmid, P. J., Henningson, D. S., Khorrami, M. R. and Malik, M. R. 1992 "Sensitivity analysis of hydrodynamic stability operators", ICASE Report No. 92-33.
- [14] Snedeker, R. S. and Bilanin, A. J. 1975 "Analysis of the vortex wakes of the Boeing 727, Lockheed L-1011, McDonnell Douglas DC-10, and Boeing 747 Aircraft", Aeronautical Research Associates of Princeton, Inc. Report No. 245.
- [15] Trefethan, L. N., Trefethan, A. E., Reddy, S. C. and Driscoll, T. A. 1993 "Hydrodynamic stability without eigenvalues", *Science*, **261**, pp. 578.
- [16] Widnall, S. E., Bliss, D. B. and Tsai, C. Y. 1974 "The instability of short waves on a vortex ring", *J. Fluid Mech.*, **66**, pp. 35-47.

APPENDIX A

The velocity components introduced in eq. (4) are given by:

$$V_{0mn} = \frac{\Gamma_m}{2\pi} \int_{x_0}^{\infty} r^{-3} z_{mn} dx, \quad (22)$$

$$W_{0mn} = \frac{\Gamma_m}{2\pi} \int_{x_0}^{\infty} -r^{-3} y_{mn} dx, \quad (23)$$

$$V_{1mn} = \frac{\Gamma_m}{2\pi} \int_{x_0}^{\infty} (-r^{-3} + 3r^{-5} z_{mn}^2) dx, \quad (24)$$

$$V_{2mn} = \frac{\Gamma_m}{2\pi} \int_{x_0}^{\infty} (r^{-3}(1 - i\alpha x) - 3r^{-5} z_{mn}^2) e^{i\alpha x} dx, \quad (25)$$

$$V_{3mn} = \frac{\Gamma_m}{2\pi} \int_{x_0}^{\infty} 3r^{-5} y_{mn} z_{mn} dx, \quad (26)$$

$$V_{4mn} = \frac{\Gamma_m}{2\pi} \int_{x_0}^{\infty} -3r^{-5} y_{mn} z_{mn} e^{i\alpha x} dx, \quad (27)$$

$$W_{1mn} = \frac{\Gamma_m}{2\pi} \int_{x_0}^{\infty} (r^{-3} - 3r^{-5} y_{mn}^2) dx, \quad (28)$$

$$W_{2mn} = \frac{\Gamma_m}{2\pi} \int_{x_0}^{\infty} (-r^{-3}(1 - i\alpha x) + 3r^{-5} y_{mn}^2) e^{i\alpha x} dx, \quad (29)$$

$$W_{3mn} = \frac{\Gamma_m}{2\pi} \int_{x_0}^{\infty} -3r^{-5} y_{mn} z_{mn} dx, \quad (30)$$

$$W_{4mn} = \frac{\Gamma_m}{2\pi} \int_{x_0}^{\infty} 3r^{-5} y_{mn} z_{mn} e^{i\alpha x} dx, \quad (31)$$

where $r = [x_{mn}^2 + y_{mn}^2 + z_{mn}^2]^{1/2}$ and $x = x_{mn}$. The coefficient $\Gamma_m/(4\pi)$ in eq. (2) is replaced by $\Gamma_m/(2\pi)$ and the integration is nominally from 0 to ∞ . The lower limit of integration x_0 is introduced as a cutoff to account for the non-physical singularity when $n = m$,

$$x_0 = \begin{cases} 0 & n \neq m \\ \epsilon (|\Gamma_m|/\Gamma_2)^{1/2} & n = m \end{cases}$$

The parameter ϵ is the nondimensional cutoff distance for the outboard vortices (1 and 2). The cutoff distance for the inboard vortices (3 and 4) is scaled in relation to their circulation. This assumes that differences in circulation are due to differences in the core size, and that the peak vorticity and vorticity distribution are fixed.

Initiation of the Crow instability by atmospheric turbulence

P. R. Spalart*

Boeing Commercial Airplane Group
P.O. Box 3707
Seattle, WA 98124-2207

A. A. Wray

NASA Ames Research Center
Moffett Field, CA 94035
U. S. A.

1. SUMMARY

The interaction between vortex pairs and well-developed isotropic turbulence is studied by Direct Numerical Simulation. It is a model of the effect of *natural* environmental disturbances on airplane wakes. The nondimensional turbulence intensity η is in the range $[0.02, 0.5]$, typical of airplanes. The most-amplified wavelength of the Crow instability is placed within the inertial range of the turbulence, which is typical in the atmosphere and fits the theoretical setting of Tombach and Crow & Bate. The vorticity peaks in cross-flow planes are tracked to reveal the deformation of the vortices. In agreement with visual observations, the Crow instability dominates in weak turbulence, whereas chaotic deformations are seen in stronger turbulence. The average wavelength is about 27% shorter than the most amplified one. The beginning of destruction is identified with the first changes in the connectivity of the lines; identifying the end of destruction is more elusive. The wake lifespans overlap those from flight tests, laboratory tests, and the theory of Crow & Bate. However, in strong turbulence, theory and simulation both predict shorter average lifespans than the tests do. The scatter in lifespans is almost as large in simulations as in flight tests; thus, the intermittency of turbulence appears to explain the scatter even without any other differences in conditions. We conclude that the predictability of wake destruction by this mechanism is very poor.

2. INTRODUCTION

The presence of trailing, or wake, vortices is an important consideration in Air Traffic Control (ATC) particularly during the approach to an airport. While the descent of the wakes is fairly predictable (barring strong vertical currents or stratification [1]), the time required for the wakes to effectively disappear exhibits wide variations, even for the same airplane model in the same

configuration. This variability constitutes a major obstacle to an optimal ATC strategy.

Having recognized that the destruction of wakes depends strongly on ambient perturbations such as wind shear, stratification, and atmospheric turbulence, an approach can be envisioned in which the relevant environmental parameters are known in addition to those of the airplane, and the wake lifespan variations are both physically explained and predictable. The current effort in this direction of a "dynamical" ATC spacing criterion at NASA is the Aircraft Vortex Spacing System (AVOSS, [2]). It would use a wake-prediction model similar to that developed by Greene [3], also at NASA. Similar work is under way in other countries, notably in India with CAA sponsorship and in Europe. The deployment of such a system will hinge on a widely accepted physical model for a host of complex fluid-dynamical phenomena and on the extensive, concrete demonstration of a much reduced scatter in the wake locations and/or lifespans when all the agreed-upon airplane and atmospheric parameters are held constant.

Whereas others expect a gradual "decay" of the vortices until their strength is below some acceptable level, we believe the wake vortices propagate with a fairly constant strength and then self-destruct rather rapidly [4]. We denote these events with the brief terms "lifespan" and "destruction". In this study, we use Direct Numerical Simulation (DNS) to isolate and quantify one of the triggers of wake destruction, namely atmospheric turbulence. We examine the DNS results for consistency with theoretical models and experimental observations, as well as to estimate the residual scatter. The setting is that of Crow & Bate [5] (hereafter CB): generic wakes are immersed in generic turbulence and the destruction is simulated. Two decades ago, they applied a purely theoretical approach; we'll return to the advantages of the three-dimensional time-dependent simulations that have now become possible.

The wakes are represented by single vortex pairs with circulation $\pm\Gamma$ and spacing b without attention to the details of the vorticity profile in their cores, except for

*Mainframe computer time donated by NAS

ensuring that the cores remain small enough not to overlap until three-dimensional deformations draw them into proximity. There is no imposed axial flow. The surrounding turbulence is isotropic and was allowed to develop under forcing at the low wave numbers [6] before the wakes were added. This leads to a short Kolmogorov inertial range, which contains the expected wavenumber range of the instability, with the result that the turbulence is characterized only by its dissipation rate ϵ , as first postulated by Tombach [4]. The total kinetic energy of the turbulence is dominated by contributions from smaller wavenumbers, and therefore not taken into account. The turbulence-wake interaction then contains only one non-dimensional parameter $\eta \equiv 2\pi\epsilon^{1/3}b^{4/3}/\Gamma$, once the vortex core structure is given. CB produce a curve for the non-dimensional lifespan $\tau \equiv t\Gamma/(2\pi b^2)$, as a function of η , based on attractive asymptotic arguments. They distinguish a regime of “weak turbulence” with $\eta < 0.1$, and “strong turbulence” with $\eta > 0.5$, and collect flight-test results with $0.03 < \eta < 0.4$. The test-theory agreement is encouraging, at least with logarithmic axes. The scatter of the flight results for the normalized lifespan τ is a factor of 3 if η is fixed, compared with about 6 if it is not. Earlier, Tombach [4] had a factor of 5. This scatter could originate in other influences that are uncorrelated with η , such as stratification, but this has not been demonstrated.

The experimental study of Sarpkaya & Daly [7] had the same goals as ours and confirmed the dissipation ϵ as the dominant turbulence parameter. Unless it is small, the integral length scale of the turbulence plays no role. Their η range, $[0.01, 2]$, was much wider than expected for airplanes. Their results had somewhat less scatter (a factor of about 2.3, η fixed), an encouraging trend since uncorrelated factors were avoided. However, such a scatter would still far exceed the tolerance of a purely “lifespan-based” ATC system.

The DNS study of Risso, Corjon, & Stoessel [8] is very close to ours in its formulation. However, their much smaller domain size supports only small-scale instabilities, whereas we pursue the (large-scale) Crow instability. We also have concerns about the apparently very large spectral energy density (and therefore dissipation rate) and lack of maturity of the surrounding turbulence; we have spent much effort on these two aspects. These authors have a new paper at this symposium. Their code is also much more general than ours, as it includes compressibility, multiple species, and chemistry. In any case, some duplication of thinking and effort is useful.

3. PROBLEM FORMULATION, NUMERICAL METHOD, ANALYSIS

3.1 Formulation

The flow domain is a periodic “box” of size λ in each direction and the basic DNS code is that of Rogallo [9]. It solves the incompressible Navier-Stokes equations us-

ing Fourier series. All lengths are non-dimensionalized with b ; then $\lambda = 8\pi$. While it is computationally costly compared with, for instance, the $\lambda = 3.5$ value of Risso *et al.* [8], this relatively large value is essential for two reasons. It places the Crow most-amplified wavelength (about 8.6, [10]) away from the lowest Fourier modes of the simulation, which are less realistic. It also gives the deformations some broad-band character, allowing the dynamics to select natural wavelengths. The selection reflects not only the instability growth rates, but also the “receptivity” (the channeling of perturbations from the surrounding turbulence to the unstable modes), which is an essential objective of our study.

Two simulations were run, one for $\eta \leq 0.1$ with $256 \times 512 \times 512$ grid points and the other for $\eta \geq 0.1$ with 384^3 points. This was necessary to avoid extreme values of the circulation Reynolds number $Re = \Gamma/\nu$. Wakes with different values of η and Re have slightly different grid requirements, and 512^3 is just out of reach for such lengthy simulations (close to 20,000 time steps). The initial turbulence field is produced by an extension of the Rogallo code as in Jiménez *et al.* [6]. The Fourier modes with wavelength larger than 10.05 are artificially boosted, in a sustained manner, and the simulation brought to statistically steady state. Figure 1 shows the one-dimensional spectrum before and after the injection of the wakes. A fair inertial range with $E(k)k^{5/3}\epsilon^{-2/3} \approx 1.7$ is present; $E(k)$ is the spectral kinetic-energy density at wavenumber k . The small turn-up of the spectrum beyond $kb \approx 40$ is considered as benign [6], and is dwarfed by the energy of the wakes. The wakes greatly increase the kinetic energy and especially the dissipation of the field. The dissipation rate *before* the injection of wakes is used throughout this paper; the dissipation rate after injection is irrelevant, as it depends on the distance between wakes. The spectrum shows the wakes to be well resolved. At the same time, the viscosity is increased by up to 50% over its value during the preparatory run. This is in an attempt to compensate for the increased energy at small length scales. Figure 1 indicates that the theoretical conditions of CB are quite well satisfied, even though an extension of the inertial range in both directions would of course be desirable.

The DNS code we used contains other minor additions to Rogallo’s. The vortices are super-imposed to the turbulence field by adding a body force for one time step. This amounts to an airplane rapidly flying across the periodic box of the DNS, and the initial roll-up of its vortex sheet also being completed rapidly, relative to the turbulence time scale. The vorticity field of each vortex is given by a Gaussian distribution:

$$\omega_x = \frac{\Gamma}{\pi\sigma^2} \exp\left(-\frac{r^2}{\sigma^2}\right)$$

where r is the distance to the vortex center; σ is a core radius, equal to 0.08; and x is the flight direction. Vortices with circulation $\pm\Gamma$ are placed at $y = \pm b/2$ from the wake centerline. The Reynolds number Re ranges

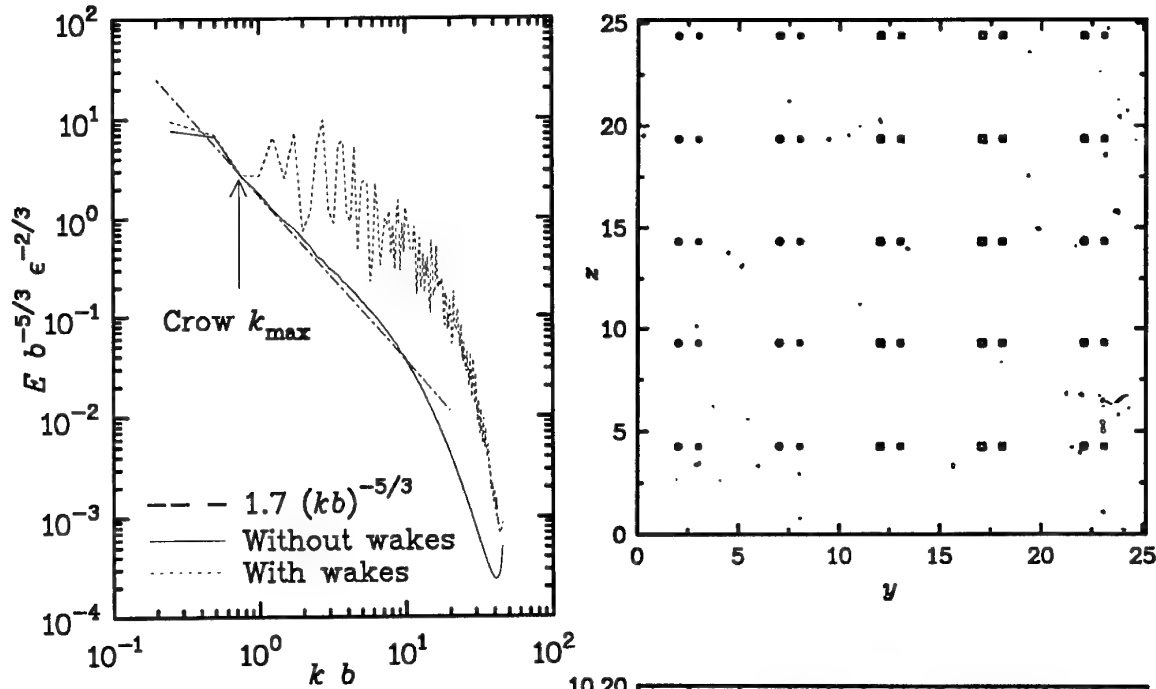


Figure 1: One-dimensional energy spectrum before and after the injection of the vortex pairs.

from about 1,700 to 9,000; the variation in η is obtained by varying the circulation, not the pair spacing. Although the core structure is not exactly that of a full-size airplane and the Reynolds number is considerably lower (even if an effective turbulent Reynolds number were invoked), the cores do not dominate the dynamics and, with these values of σ and Re , do not touch even at the time of destruction. The initial kinetic energy per unit length, normalized by Γ^2 , is close to that of a wing. More complex wake structures such as multiple pairs may be treated in the future, but only at an even higher cost. Our study consumed over 1,000 CPU hours on a Cray C-90, representing close to 2×10^{15} floating-point operations.

A benefit of the large period $\lambda = 8\pi$ is that many wakes can co-exist in the box. A five-by-five array of pairs is simulated, putting them about $5b$ apart. This is an acceptable separation for vortex pairs, because the strain rate due to neighboring pairs is only a few percent of that exerted by one vortex on the other in the pair (this latter strain controls the Crow instability). Each of the two simulations covers five values of η , and there are five wakes for each η . Wakes with the same circulation (and therefore descent velocity) are stacked vertically to avoid collisions. These five wakes produce a total of about twenty destruction events, which is the beginning of a statistical sample. The average wavelength is about 2π which is smaller than the most-amplified Crow wavelength [10]. This pushes the most relevant wavenumber a little to the right in Fig. 1. This is consistent with some flight tests, but not Chevalier's [11].

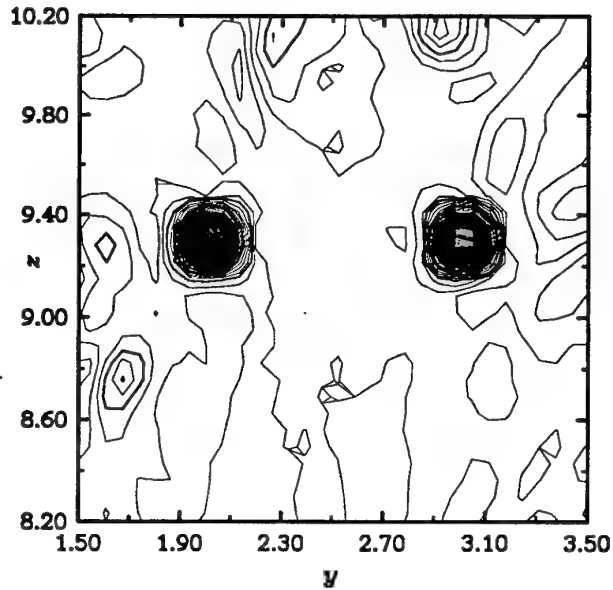


Figure 2: Vorticity field in a cross-stream plane. a) whole field; b) detail near one vortex pair.

Figure 2 shows the initial vorticity field. Figure 2a outlines the arrangement in the DNS itself; later results will have the wakes repositioned to provide clear views. The array of wakes is apparent, and the contour levels were chosen to bring out spots of the background turbulence. Even the weakest wakes ($\eta = 0.506$), which form the left-most column, stand out from the turbulence, as shown in Fig. 2b (which is a detail of Fig. 2a, with finer contour levels). The rather small value of the core radius σ is apparent.

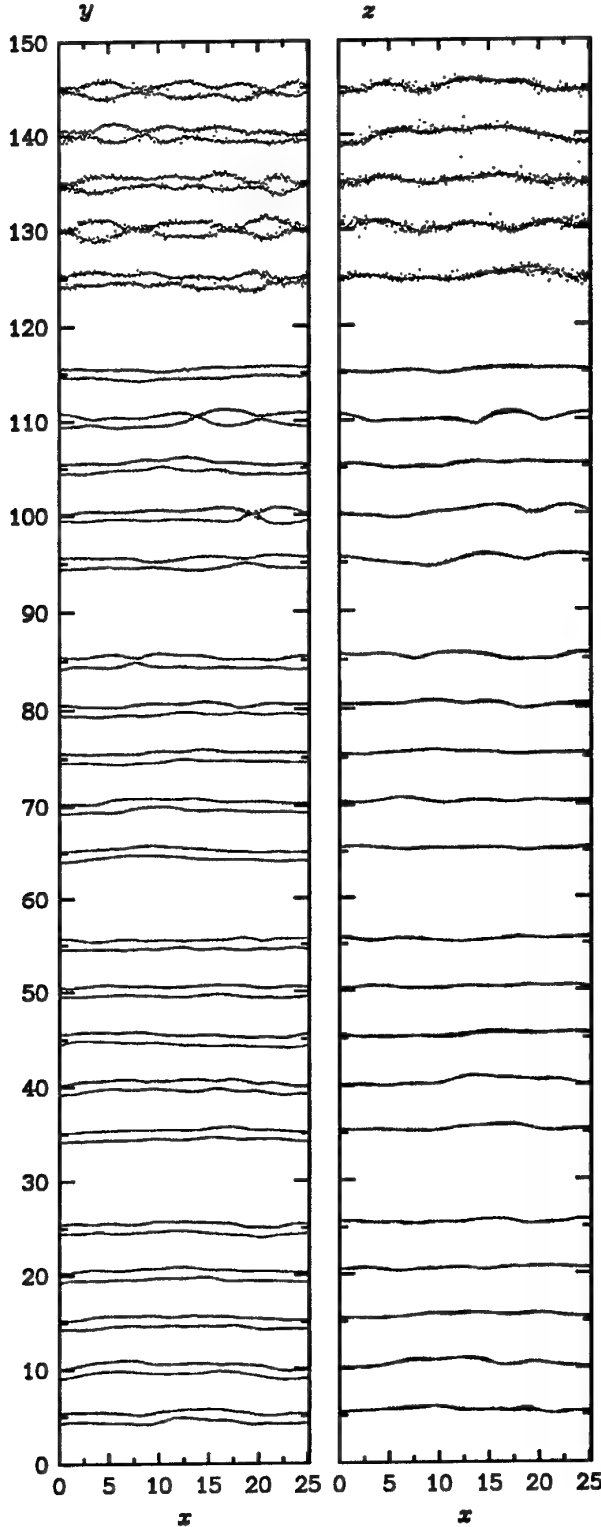


Figure 3: Wakes with $\eta = 0.0198$ (highest five pairs), 0.0296 (next five), 0.0444 (next five), 0.0667, and 0.1. Time is $\eta\tau = t\epsilon^{1/3}b^{-2/3} = 0.11$. Left, bottom views; right, side views.

3.2 Analysis

The exploitation of the simulation is primarily through visualization. Subsets of the velocity fields may be used for encounter simulations in the future. However, for our purpose here, an encounter model would introduce so many approximations and parameters that simple conclusions would be difficult to reach.

A collection of marker points, evenly spaced in the flight direction x , is associated with each vortex; they are defined as follows. They mark local maxima of $|\omega_x|$ in y - z planes. In addition, at each time step the points are first moved with the local velocity, and then corrected to the closest local maximum of $|\omega_x|$. As long as the vorticity peak is much above the background, "the vortex" can be recognized unambiguously (for instance in vorticity contours such as Fig. 2) and the marker follows it. The purpose is very similar to smoke visualization in flight tests, or condensation. Those markers respond both to the local velocity and to the low-pressure conditions that exist in the vortex; often we trust that they mark the vortex largely because of the absence of gyrations or helical shapes.

This hybrid definition of the vortex markers is needed for two reasons. Simply following material particles initially placed at the vortex centers would give an equivalent answer in principle, but poses deep difficulties for the time integration. Errors would make the particle orbit the vortex center, especially considering that for some cases the core fluid undergoes over 100 revolutions. Conversely, simply producing local maxima of $|\omega_x|$ would forfeit the continuity in x and in t , and require arbitrary thresholds to weed out peaks that belong to the surrounding turbulence.

Our marker collections are ordered, periodic in x , and identified with an initial vortex, properties which could be used to define amplitudes, mode shapes, and spectra of the deformations $y(x, t)$ and $z(x, t)$. The use of the absolute value $|\omega_x|$ for local maxima has the advantage that when "pinching", or "reconnection", occurs the marker coming with the lower peak jumps to the higher peak, thus clearly changing the connectivity of the lines. These "events" or "incidents" are recorded and taken to signal the beginning of the destruction. Pinching is typical in weak turbulence, when the Crow instability dominates. In stronger turbulence, the lines do not always approach each other, but become so distorted they lose continuity. Again, these "snipping" events define the beginning of destruction. Examples will be given.

The principal result of the study is a collection of "event times" τ for each value of η . The event times have a statistical distribution, or "pdf", inherited from the statistical properties of the turbulence and the selection by the vortex pair as an amplifier. CB produced a single time, while recognizing the statistical aspect. Although they were not very specific about the relation between that time and the pdf, it is fair to assume it approximates the mean time to destruction. The standard deviation of the pdf is of value; unfortunately, from a

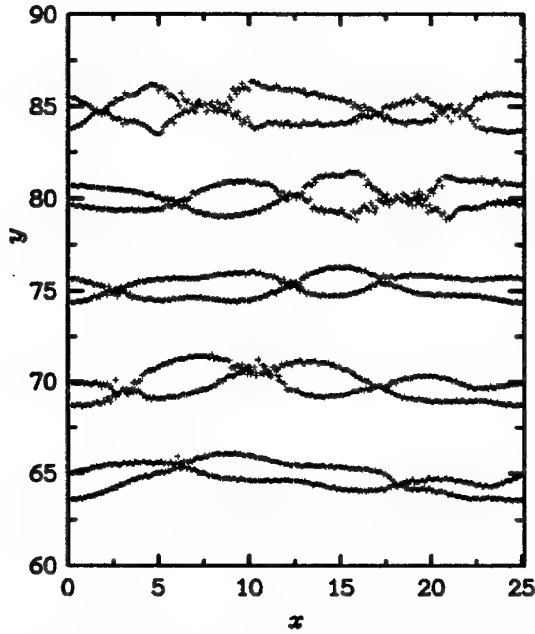


Figure 4: Wakes with $\eta = 0.0444$, $\tau = 4.26$. Bottom view.

practical point of view, its “tail” for large τ is quite important and is not accurately provided by a sample of size 20. The simulations are continued until no nearly straight vortex sections of length more than a few times b remain. In that sense, the destruction event that is recorded last occurs during the last identified breakup of the wake. The idea is that a wake that is distorted to that extent is of much less significance to a following airplane (especially if the leading and following airplane have approximately the same heading, which is the more relevant situation). “Complete destruction” is more difficult both to define and to simulate. In particular, the reconnection involves so much stretching of the vortices that it taxes the numerical resolution. It is also more sensitive to viscous or small-scale turbulent mixing, and vortex core structure.

4. RESULTS

4.1 Examples

We begin with visualizations to gain confidence by comparison with observations, and to establish the meaning of the destruction times presented later (Fig. 7). Bottom and side views of the wakes are shown, with x , y , and z representing the streamwise, spanwise, and vertical directions respectively. Recall that they have been re-arranged from their position in the DNS (Fig. 2a). Figure 3 shows the stronger wakes, relative to the turbulence (lower η). The five families are shown at the same turbulence time, and therefore different τ . The strongest wakes, $\eta = 0.0198$, are highest (centered at $y = 125, 130, 135, 140$, and 145) and have achieved many reconnections. Their wake time is $\tau = 5.6$; events will

be recorded until $\tau \approx 8$. The average wavelength is 2π , as mentioned above. The roughness of the curves is suggestive of physical core breakup, but in fact reflects numerical truncation errors. These wakes have the highest Reynolds number and non-dimensional time step (CFL number). A decisive improvement of the resolution would increase the simulation cost by an order of magnitude, which is not feasible. Based on this and similar figures, we believe the reconnection events are indicated well enough to be used, and we note that the other wake families in the box were not “polluted”.

The next family has $\eta = 0.0296$ and is found between $y = 95$ and 115 . Some reconnections have taken place, but the need for a statistical description is clear, as some wake sections are still essentially intact (e.g., that at $y = 115$). The agreement in mode shape and wavelength with observations of airplanes is quite satisfactory. The still weaker wakes ($\eta \approx 0.0444, 0.067$ and 0.1) are “younger” (for the last one, $\tau = 1.1$) and reveal a mix of apparently passive parallel displacements and of Crow instability, the latter well indicated by antiparallel shapes in the bottom view and “arches” in the side view. End views would exhibit the familiar V shape. We note that little “rolling” of the pairs to one side is observed; there is debate about the cause of such rolling in some experiments and in flight tests.

Figure 4 shows reconnections in more detail for $\eta = 0.0444$, $\tau = 4.26$, including the merging of the two lines of markers and the formation of “hammer heads” which recede from the merged regions. The broad-band character of the distortions is again evident. In this figure, twelve reconnection events have already been recorded (for Fig. 7); three events are imminent; a further five will eventually occur.

Figure 5 is extracted from the second simulation. The $\eta = 0.1$ family (now the highest one in the figure instead of the lowest) is more mature than in Fig. 3: $\tau = 1.8$ instead of 1.1 . Accordingly, it displays larger deformations. Again, truncation errors are apparent (as for $\eta = 0.0198$ in the first simulation), and these five wakes were not used. The weaker wakes, with η ranging from 0.15 to 0.506 , are useable. Although weaker, their vorticity peaks do not become confused with the background vorticity. They look similar, as expected in the strong-turbulence approximation of CB—namely, they appear to be passively convected by the turbulence. The weaker wakes even appear to show more distortion as a result of “remaining in the same eddy for a longer time”, as discussed by CB. It turns out that they all break up at approximately the same “turbulence time” $\tau \times \eta$, as predicted by CB.

In the family with the highest non-dimensional turbulence level, $\eta = 0.506$, Fig. 6 reveals losses of connectivity of the marker lines, but not by reconnection with the partner vortex. It is most dramatic near $(x, y) = (16, 18)$. Of course, both the vortex lines and the material lines remain continuous, but must be similarly distorted so that the implications for the velocity field are clear. In this figure, six disconnection events

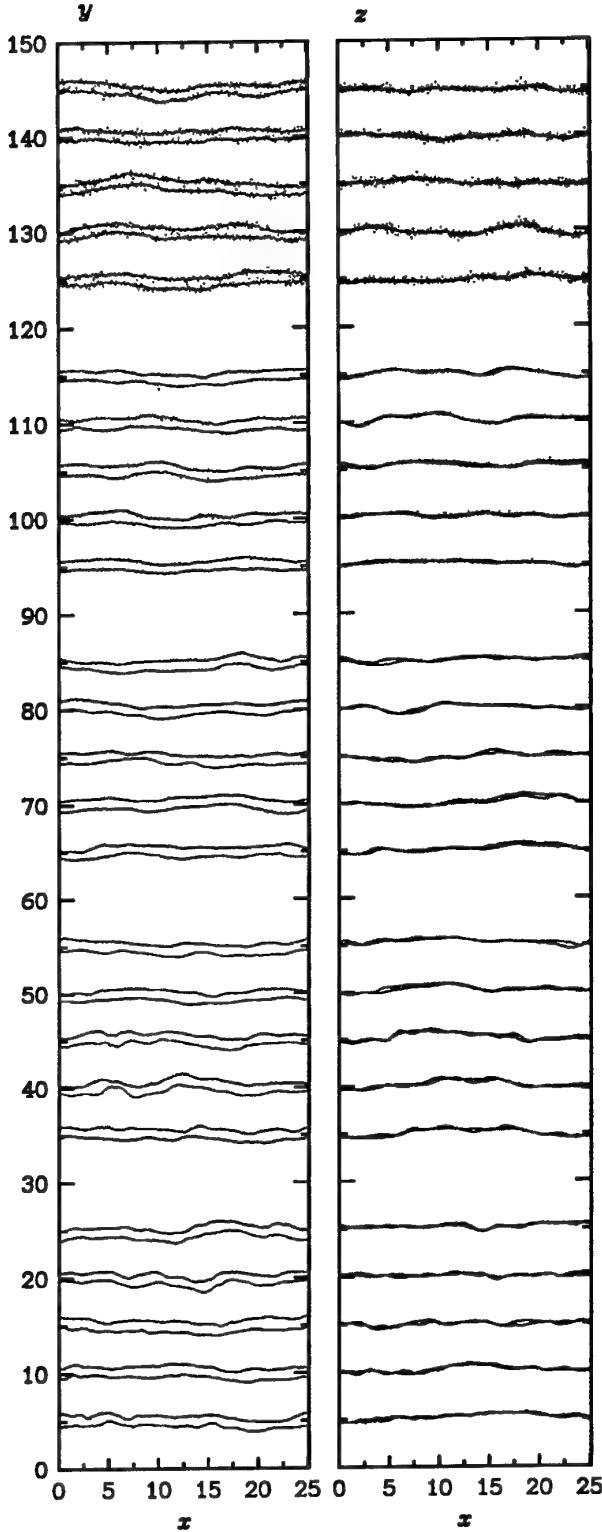


Figure 5: Wakes with $\eta = 0.1$ (highest five pairs), 0.15, 0.225, 0.337, and 0.506. Time is $\eta\tau = t\epsilon^{1/3}b^{-2/3} = 0.18$. Left, bottom views; right, side views.

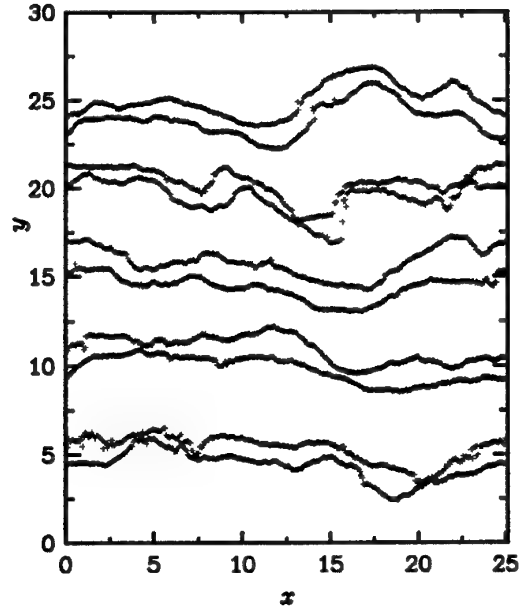


Figure 6: Wakes with $\eta = 0.506$, $\tau = 1.15$. Bottom views.

have already been recorded; seven events are imminent; a further nine will eventually occur.

4.2 Compendium

Figure 7 encapsulates our knowledge of the “CB problem”. As “theory” it shows the single curve of CB; as “flight tests” it shows the perimeter of the flight observations [4, 5]; as “lab tests” it shows the band of the tow-tank results [7]. All the events within the simulations, discussed in §4.1, are shown as discrete points. The set of flight-test results has rather fewer points than the simulations; therefore, if anything its coverage of the pdf tails would be sparser. It is also biased towards larger values of η which occur for slower airplanes; such aircraft are more easily available for tests. This could well explain why it is wider, vertically, for larger η . The lab tests are not biased, and have about half as many points as the simulations. One of the simulation sets is biased towards low τ , the one with $\eta = 0.1$. This is because these were the last to break up and the cost of completing them did not seem justified. The bias is obvious in the figure, by comparison with the neighboring sets. At least six additional events would occur in a continued simulation.

All sources agree within statistical scatter for η up to about 0.2. Beyond that, the simulations follow the theoretical trend which is $\tau \propto \eta^{-1}$, whereas the experiments almost continue the less steep trend that prevails for smaller η . Unpublished results of Sarpkaya (personal communication, 1996) for $\eta \geq 0.1$ indicate much better agreement if the *initial* tearing or bursting is recorded in the experiment as in the simulation, instead of the final destruction [7]. The CB curve is consistently about 20%

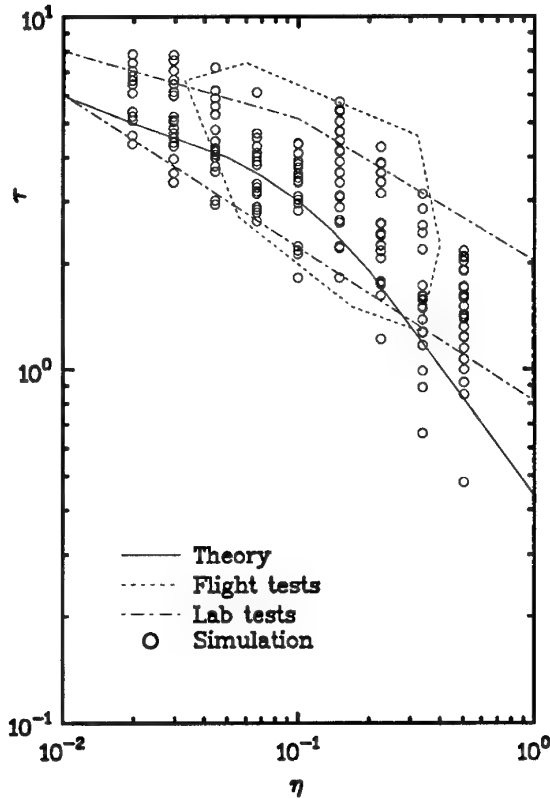


Figure 7: Non-dimensional wake lifespans.

lower than the average (whether arithmetic or geometric) of the simulations. This aspect of the agreement is good indeed, and the shortcoming of the theory resides instead in the lack of measures of the pdf (using the average curve for lifespan prediction in ATC would not make sense). The standard deviation of the simulation results increases from about 20% of the mean for small η to 40% of the mean for large η , with the total scatter increasing from a factor of about 2 to about 4. This is our principal finding: *the scatter due solely to the statistical fluctuations of the turbulence is still large*. It is likely that an improved simulation with a larger period (spectrum higher for $kb < 0.5$ in Fig. 1) would produce slightly more scatter.

The simulation results are shown again in Fig. 8, made dimensional with common airliner parameter values and with a linear scale for the lifespan, converted to a distance, so as to reiterate the practical implication of the large scatter. We consider generic airliners in early approach, flying at a speed $U = 123\text{m/s}$ (240kt), with a root circulation $\Gamma = Ub_w/21$ where b_w is the full span of the wing, $b_w = 4b/3$. For the dissipation we take $\epsilon = 10^{-4}\text{m}^2/\text{s}^3$, the threshold between “negligible” and “light” turbulence [4]. Interpolating the scatter for a Boeing 747 ($b_w \approx 60\text{m}$, $\eta \approx 0.13$) gives wake lengths from about 4 to 13 nm. Incidentally, the figure illustrates how for given weather conditions and *under this destruction mechanism alone* the lifespan increases with

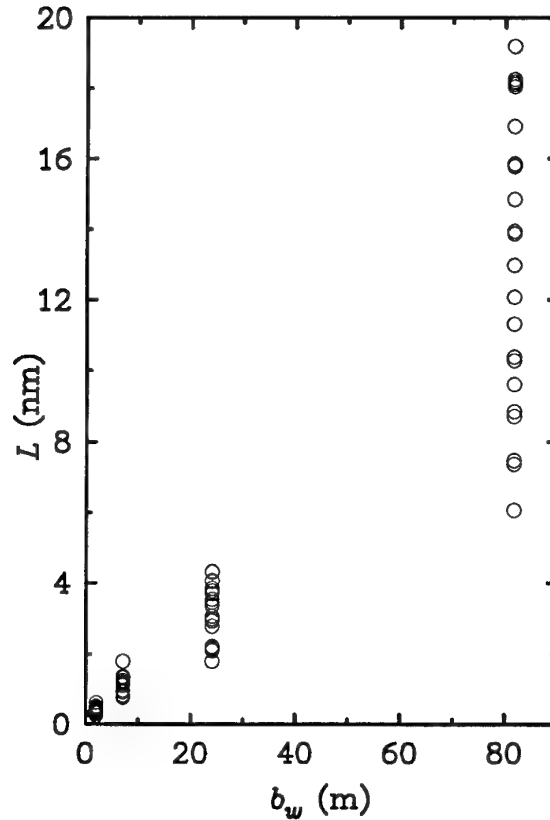


Figure 8: Dimensional wake length as a function of span. Very light turbulence, $\epsilon = 10^{-4}\text{m}^2/\text{s}^3$, flight speed 240kt, typical wing lift coefficient and aspect ratio.

the size of the airplane (see also CB, Fig. 9). Both the length itself and the extent of the scatter are roughly linear in b_w .

Because of the low value of ϵ , the high speed for an approach, and the absence of any other destruction mechanism (such as stratification), Fig. 8 is close to the worst-case situation. At 120kt in the same weather the range would be roughly 1.5 to 3.5 nm; the length is less than half as a result of halving the speed and doubling the circulation (which reduces the duration in time). At 240kt but with $\epsilon = 5 \times 10^{-3}\text{m}^2/\text{s}^3$ (the border between “light” and “moderate” turbulence [5]), the length would be between about 1.1 and 5.5 nm. In addition, we show in Fig. 9 the $\eta = 0.225$ wakes shortly before the last recorded destruction events. The wake sections $0 \leq x \leq 15$, $y \approx 77$, and $10 \leq x \leq 15$, $y \approx 98$, are not considered as destroyed. A pinching event is imminent near $x = 7.5$, $y = 77$. This figure shows that our analysis of the results is rather conservative. These wakes are “mostly destroyed” but two sections, 1/6 of the total length of all five wakes, have lost little of their upset potential for a follower airplane. The application of findings such as those presented here to ATC will require much thought.

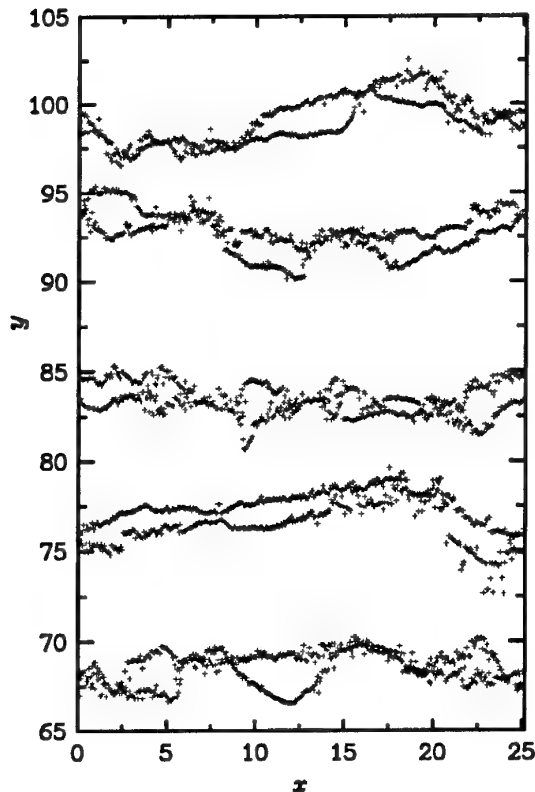


Figure 9: Wakes with $\eta = 0.225$, $\tau = 3.6$. Bottom view.

References

- [1] Spalart, P. R. 1996 "On the motion of aircraft wakes in a stably stratified fluid". Submitted to *J. Fluid Mech.*
- [2] Hinton, D. A. 1995 "Aircraft Vortex Spacing System (AVOSS) conceptual design". NASA TM 110184.
- [3] Greene, G. C. 1986 "An approximate model of vortex decay in the atmosphere." *J. Aircraft* **23**, 7, 566-573.
- [4] Tombach, I. 1973 "Observations of atmospheric effects on vortex wake behavior". *J. Aircraft* **10**, 11, 641-647.
- [5] Crow, S. C. & Bate, E. R. 1976 "Lifespan of trailing vortices in a turbulent atmosphere". *J. Aircraft* **13**, 7, 476-482.
- [6] Jiménez, J., Wray, A. A., Saffman, P. G., & Rogallo, R. S. 1993 "The structure of intense vorticity in isotropic turbulence". *J. Fluid Mech.* **255**, 65-90.
- [7] Sarpkaya, T. & Daly, J. J. 1987 "Effect of ambient turbulence on trailing vortices". *J. Aircraft* **24**, 6, 399-404.
- [8] Risso, F., Corjon, A., & Stoessel, A. 1996 "Direct numerical simulation of trailing vortices in homogeneous turbulence". AIAA-96-0802.
- [9] Rogallo, R. S., 1981 "Numerical Experiments in Homogeneous Turbulence". NASA TM-81315.
- [10] Crow, S. C. 1970 "Stability theory for a pair of trailing vortices". *AIAA J.* **8**, 2172-2179.
- [11] Chevalier, H. 1973 "Flight test studies of the formation and dissipation of trailing vortices". *J. Aircraft* **10**, 1, 14-18.

Simulation numérique directe de l'instabilité sinusoïdale

D.SIPP, L.JACQUIN et P.SAGAUT

Office National d'Etudes et de Recherches Aérospatiales
29, avenue de la Division Leclerc, 92320 Châtillon-France

1 Résumé

On présente les résultats d'une simulation directe temporelle de l'instabilité sinusoïdale qui se développe dans une allée tourbillonnaire composée de deux tourbillons contrarotatifs. Les résultats sont confrontés à la théorie d'instabilité linéaire développée par Crow([1]). On étudie en particulier l'effet de la densité du maillage, des conditions aux limites et de la forme de la perturbation initiale sur la qualité de la solution.

2 Introduction

L'instabilité sinusoïdale ou instabilité de Crow est l'un des mécanismes qui engendrent la dispersion des sillages d'avion. Elle se déclenche après une phase de diffusion 'régulière' des deux tourbillons qui composent ce sillage. Il semble qu'un affaiblissement préalable de l'intensité des tourbillons, par la diffusion moléculaire, voire turbulente, soit nécessaire avant que ce type d'instabilité puisse se développer. On attribue alors son déclenchement à la turbulence atmosphérique. Mais aucune corrélation définitive n'a pu être établie sur ce point. Le développement d'instabilités secondaires, e.g. instabilité elliptique, pourrait également participer au phénomène. La compréhension des lois dynamiques qui régissent ce type d'écoulement présente un intérêt général qui dépasse le problème particulier des sillages d'avion.

La simulation directe constitue un outil privilégié pour l'étude de ces phénomènes(cf. [5]). Cet article présente un ensemble de résultats qui prouvent la faisabilité d'une simulation directe des équations de Navier-Stokes appliquée au problème de l'instabilité sinusoïdale et qui fixent certaines des conditions nécessaires pour arriver à ce but. Ce travail constitue la première phase d'une étude numérique générale des mécanismes fondamentaux de la dynamique des tourbillons de sillage.

On présente tout d'abord les caractéristiques du code de simulation directe utilisé pour cette étude. Ce code est développé à la Direction de l'Aérodynamique de l'ONERA([4]) dans l'objectif de simuler des écoulements turbulents tridimensionnels de complexité quelconque. L'un des objectifs de la présente étude était de valider cet outil sur un problème possédant des solutions théoriques connues en régime linéaire.

3 Présentation du code numérique

3.1 Généralités

Le code utilisé permet de résoudre les équations de Navier-Stokes tridimensionnelles instationnaires et incompressibles.

Il utilise des maillages cartésiens et des schémas de type 'différence finie' d'ordre 2 en espace et en temps.

Les termes de convection sont écrits sous forme semi-conservative avec un schéma d'ordre 2 centré pour la partie conservative et d'ordre 3 décentré pour la partie non conservative. La partie temporelle est traitée par un schéma d'Adams-Bashforth.

La diffusion est calculée à l'aide du schéma de Crank-Nicholson.

Une méthode itérative Bi-CGSTAB avec préconditionnement par la méthode de Jacobi est utilisée pour le calcul de la pression.

3.2 Maillage et conditions aux limites.

Les écoulements étudiés dans cet article sont des tourbillons étroits (épaisseur faible devant l'allongement). Le développement temporel de ces tourbillons est simulé en imposant une périodicité dans la direction d'allongement axiale Oy . Les conditions aux limites dans les deux autres directions sont des conditions de symétrie (vitesse normale nulle, dérivée de la vitesse tangentielle nulle) et/ou de sortie (vitesse tangentielle interpolée, vitesse normale déterminée par la pression).

Typiquement, on utilise 46 points répartis de façon régulière dans la direction Oy et 100 à 200 points dans les deux autres directions. Le maillage est raffiné dans la région des tourbillons. Il est également resserré aux frontières de la boîte de calcul afin de confiner les perturbations induites par les conditions aux limites. L'un de ces maillages est présenté sur la figure 1.

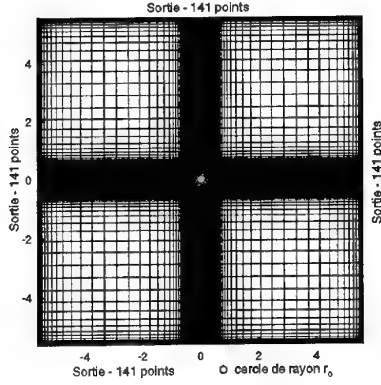


Figure 1: Maillage dans les directions Ox et Oz.

4 Simulation bidimensionnelle des tourbillons de Lamb-Oseen.

4.1 Simulation d'un tourbillon de Lamb-Oseen.

On présente ici une simulation d'un tourbillon de Lamb-Oseen, qui constitue l'écoulement de référence pour le problème étudié. Ce tourbillon d'axe Oy est une solution exacte des équations de Navier-Stokes bidimensionnelles. La composante de la vorticité ω_y , la vitesse tangentielle v , la circulation $\Gamma(r)$ autour d'un cercle de rayon r , le rayon visqueux r_0 , lieu du maximum de vitesse tangentielle et les moments de vorticité sont définis par :

$$\omega_y(r, t) = \frac{\Gamma_0}{4\pi\nu t} \exp\left(-\frac{r^2}{4\nu t}\right) \quad (1)$$

$$v(r, t) = \frac{\Gamma(r, t)}{2\pi r} \quad (2)$$

$$\Gamma(r, t) = \Gamma_0 \left(1 - \exp\left(-\frac{r^2}{4\nu t}\right)\right) \quad (3)$$

$$r_0(t) = 2.24\sqrt{\nu t} \quad (4)$$

$$\langle \omega_y \rangle(t) = \Gamma_0 \quad (5)$$

$$\langle x\omega_y \rangle(t) = C_1 \quad (6)$$

$$\langle z\omega_y \rangle(t) = C_2 \quad (7)$$

où $\langle \rangle = \iint dx dz$, C_1, C_2 , la circulation Γ_0 et la viscosité ν sont des constantes. Les barycentres de vorticité, définis par :

$$x_c = \frac{\langle x\omega_y \rangle}{\langle \omega_y \rangle} \quad (8)$$

$$z_c = \frac{\langle z\omega_y \rangle}{\langle \omega_y \rangle} \quad (9)$$

sont donc fixes.

Toutes les grandeurs sont adimensionnées par une échelle de longueur L et une échelle de temps T arbitraires. Le nombre de Reynolds vaut $Re = \frac{L^2}{\nu T} = 5026$, ce qui correspond par exemple à $\Gamma_0 = 2\pi L^2 T^{-1}$ et $\nu = 0.00125 L^2 T^{-1}$. Le rayon caractéristique initial $r_0(t=0)$ est pris égal à $0.15L$.

On compare les résultats de la simulation aux solutions théoriques du problème. La figure 2 présente l'évolution temporelle du maximum de ω_y pour deux densités de maillage différentes, correspondant à 5 ou à 10 points dans les directions Ox et Oz à l'intérieur du rayon visqueux initial $r_0(t=0)$. La figure 3 montre l'erreur sur ω_y dans un plan $y = cte$ à $t = 1.1T$. Sur la figure 4, on a tracé l'erreur obtenue sur ω_y et sur la circulation Γ en fonction du rayon r à $t = 1.1T$. Enfin, la figure 5 évalue l'erreur commise sur le rayon visqueux $r_0(t)$.

Ces résultats montrent les faits suivants :

- la diffusion numérique affecte le niveau de la vorticité du tourbillon. Cet effet est illustré sur les figures 2 et 3. La figure 2 montre que ce phénomène peut-être logiquement réduit moyennant l'utilisation d'un maillage suffisamment dense. Cette figure indique qu'à $t = 1.1T$, le maximum de vorticité est sous-estimé de 20 pourcents pour le maillage le plus lâche et de 7,5 pourcents pour le maillage le plus dense. Par la suite, l'atténuation des gradients, qui résulte de la diffusion, entraîne un amortissement de la diffusion numérique.
- la figure 4 montre que la diffusion numérique transfère la vorticité du centre vers la périphérie, et que la circulation est peu affectée dans la mesure où l'on considère des rayons suffisants.
- enfin, la figure 5, montre que le rayon visqueux est assez fidèlement reproduit.

En ce qui concerne les moments de la vorticité (non montré ici), la simulation respecte strictement les relations de compatibilité définies ci-dessus, dans la mesure où l'on considère initialement un tourbillon centré dans le plan Oxz. Dans le cas contraire, on observe une décroissance des moments $\langle x\omega_y \rangle$ et $\langle z\omega_y \rangle$. Ce phénomène doit être attribué à l'influence des conditions aux frontières.

4.2 Simulation de deux tourbillons contrarotatifs de Lamb-Oseen.

On considère maintenant deux tourbillons contrarotatifs d'axes parallèles situés de part et d'autre du plan $z = 0$. L'écoulement est supposé symétrique par rapport à $z = 0$:

$$u_x(x, -z) = u_x(x, z) \quad (10)$$

$$u_z(x, -z) = -u_z(x, z) \quad (11)$$

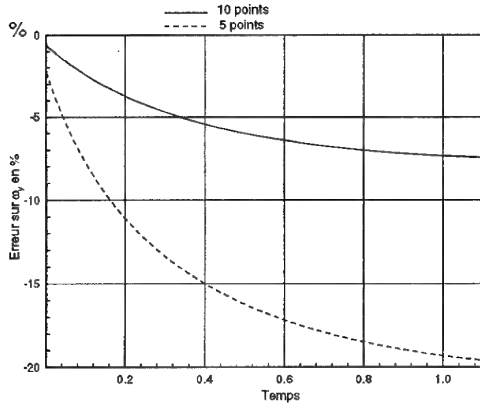


Figure 2: Erreur sur le maximum de ω_y pour deux maillages différents.

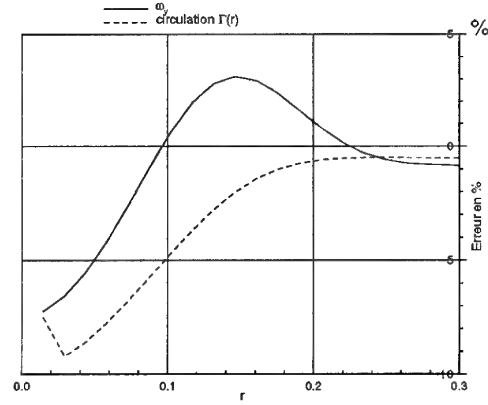


Figure 4: Erreur sur ω_y et Γ en fonction du rayon r à $t = 1.1T$.

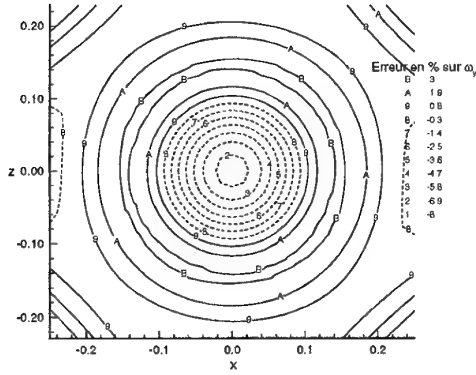


Figure 3: Erreur sur le champ ω_y à $t = 1.1T$.

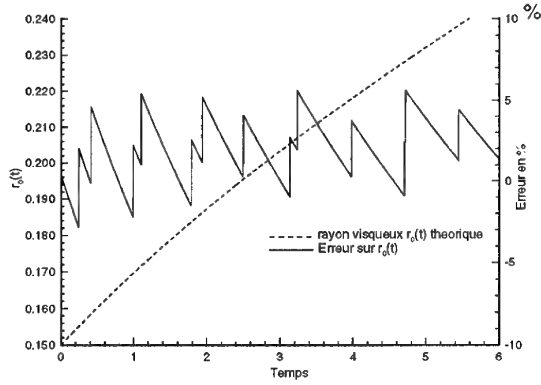


Figure 5: Rayon visqueux théorique $r_0(t)$ et erreur commise sur celui-ci.

On considère deux situations (voir figure 6). Dans la première, seul le domaine $z > 0$ est calculé, le plan $z = 0$ étant traité par une condition de symétrie. Dans le deuxième cas, la totalité du domaine est prise en compte.

Les paramètres Re , Γ_0 , ν et $r_0(t = 0)$ sont identiques au cas précédent. La distance de séparation des deux tourbillons vaut $b = 1$. Les tourbillons dérivent avec une vitesse $u_0 = 1$ vers les x négatifs, et on les stabilise en superposant une vitesse uniforme opposée.

Pour cet écoulement, on a (voir [3]):

$$\langle \omega_y \rangle^+(t) = -\langle \omega_y \rangle^-(t) \quad (12)$$

$$\langle x\omega_y \rangle^+(t) = -\langle x\omega_y \rangle^-(t) \quad (13)$$

$$\langle z\omega_y \rangle^+(t) = \langle z\omega_y \rangle^-(t) = Cte \quad (14)$$

avec $\langle \rangle^+ = \iint_{z>0} dx dz$ et $\langle \rangle^- = \iint_{z<0} dz dz$. On consid-

ère les barycentres de vortacité définis par :

$$x_c^+ = \frac{\langle x\omega_y \rangle^+}{\langle \omega_y \rangle^+} \quad (15)$$

$$z_c^+ = \frac{\langle z\omega_y \rangle^+}{\langle \omega_y \rangle^+} \quad (16)$$

Sur le long terme, $\langle \omega_y \rangle^+$ décroît sous l'effet de la diffusion de la vortacité à travers le plan $z = 0$. Dans les conditions de notre simulation ($r_0(t) \ll b$), ce phénomène est négligeable. Dans ce cas $\langle \omega_y \rangle^+(t)$, $\langle x\omega_y \rangle^+(t)$, $\langle z\omega_y \rangle^+(t)$, $x_c^+(t)$ et $z_c^+(t)$ doivent être constants.

La figure 7 présente l'erreur obtenue sur $\langle x\omega_y \rangle^+$, $\langle z\omega_y \rangle^+$, $\langle \omega_y \rangle^+$, en fonction du temps, dans les deux cas (symétrisé et non symétrisé). On observe que les moments $\langle x\omega_y \rangle^+$ et $\langle z\omega_y \rangle^+$ décroissent. Le moment $\langle x\omega_y \rangle^+$ est par exemple sous-estimé de 22

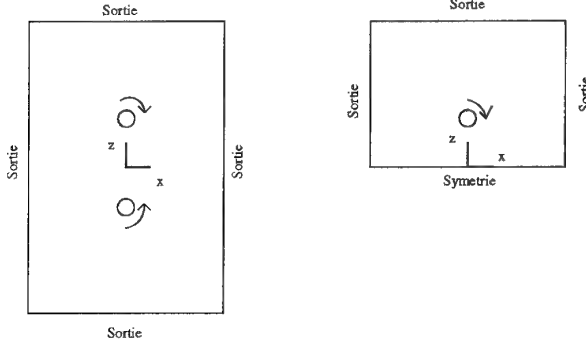


Figure 6: Conditions aux limites utilisées dans les cas non symétrisé et symétrisé.

pourcents à $t = 6T$ dans le cas symétrisé. Ce comportement résulte d'une dérive des tourbillons induite par des effets de conditions aux limites. On constate que ce défaut est atténué dans le cas d'un calcul sans condition de symétrie.

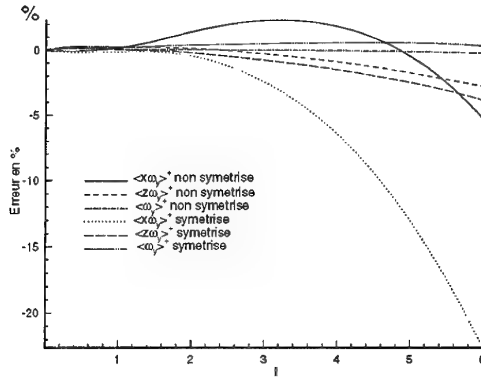


Figure 7: Erreur sur les moments de vorticité $\langle \omega_x \rangle^+, \langle \omega_y \rangle^+, \langle \omega_z \rangle^+$ dans les cas symétrisé et non symétrisé.

5 Simulation d'un tourbillon de forme sinusoïdale.

On considère, de nouveau, un seul tourbillon, que l'on déforme de façon transitoire, dans le plan $z = 0$, en appliquant le champ de vitesse suivant :

$$u_x^D(x, y, z) = u_x^0 \cos(ky) \quad (17)$$

$$u_y^D(x, y, z) = 0 \quad (18)$$

$$u_z^D(x, y, z) = 0 \quad (19)$$

où k représente le nombre d'onde de la sinusoïde et u_x^0 l'intensité du champ de déformation.

On montre que le plan de ce tourbillon sinusoïdal doit tourner avec un taux de rotation de module $\Omega = \frac{\Gamma_0}{4\pi} k^2 (\ln \frac{1}{kr_0} + A + \ln 2 - \gamma)$ et de signe opposé à celui de la rotation du tourbillon (voir [2]). Dans cette formule $A = -0.058$, $\ln 2 - \gamma = 0.1159$. Cette expression est valable dans la limite $\epsilon = \frac{r_0}{R} \rightarrow 0$, où R est le rayon de courbure en un point de la sinusoïde. Dans la pratique, le rayon visqueux $r_0(t)$ augmentant au cours du temps, le taux de rotation $\Omega(t)$ diminue. Ces résultats théoriques sont représentés sur la figure 8 pour une perturbation de nombre d'onde $k = \frac{2\pi}{L}$.

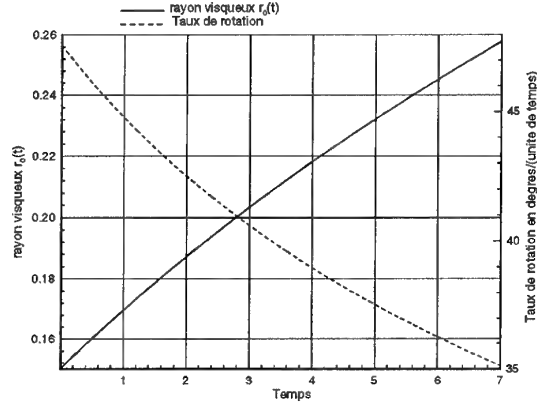


Figure 8: Rayon visqueux $r_0(t)$ et taux de rotation Ω du plan de la sinusoïde en fonction de t .

Les résultats de la simulation de ce cas sont présentés sur les figures 9, 10 et 11. Les calculs ont été réalisés en imposant 10 points de maillage dans un rayon visqueux. Sur la figure 9, on montre la position du plan de la sinusoïde projeté sur Oxz à diverses époques. La figure 10 montre le taux de rotation du plan. Après un transitoire relativement long (environ 4 temps physiques), on observe que le taux de rotation tend vers sa valeur théorique. La phase transitoire est mieux illustrée sur la figure 11 qui concerne le cas d'une déformation initiale de nombre d'onde $k = 2\pi L^{-1}$.

L'utilisation d'une autre méthode de déformation des tourbillons, en l'occurrence celle consistant à initialiser directement le calcul par un tourbillon sinusoïdal, aboutit au même résultat. Ce transitoire présente donc un caractère physique.

Un calcul avec un maillage plus lâche (non montré ici) donne sensiblement les mêmes résultats.

6 L'instabilité de Crow

6.1 Rappel.

On revient ici au cas de deux tourbillons contrarotatifs d'axe parallèle et de séparation b . L'instabilité de Crow se déclenche lorsqu'on perturbe cet écoulement. Les principaux résultats théoriques sur cette instabilité

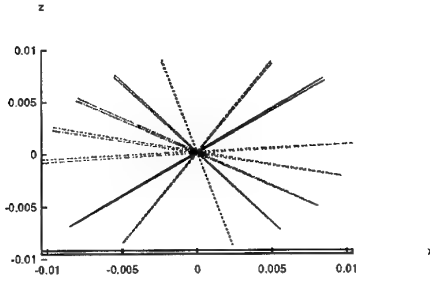


Figure 9: Représentation de la sinusoïde dans le plan Oxx.

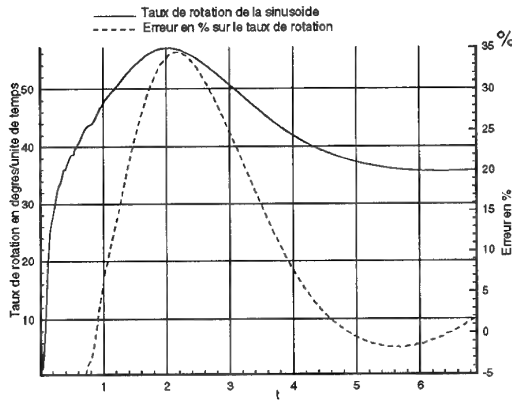


Figure 10: Taux de rotation de la sinusoïde et erreur commise sur celui-ci pour $k = \frac{2\pi}{7} L^{-1}$.

sont rappelés ici en considérant le cas d'une configuration symétrique. On note par $x_c(y, t)$ et $z_c(y, t)$ la position du centre du tourbillon dans un plan Oxx (voir figure 12). Ces variables sont supposées de la forme :

$$x_c(y, t) = \Re(x(t) \exp(iky)) \quad (20)$$

$$z_c(y, t) = \Re(z(t) \exp(iky)) \quad (21)$$

où k est le nombre d'onde de l'instabilité.

A partir de la linéarisation de la loi de Biot-Savart et de l'équation de la vorticité pour un fluide non visqueux, on obtient (voir [1]) :

$$\begin{pmatrix} \dot{x} \\ \dot{z} \end{pmatrix} = \frac{\Gamma_0}{2\pi b^2} \quad (22)$$

$$\begin{pmatrix} 0 & 1 + \chi - \beta^2 \phi \\ 1 - \psi + \beta^2 \phi & 0 \end{pmatrix} \begin{pmatrix} x \\ z \end{pmatrix}$$

où $\beta = kb$ est le nombre d'onde adimensionnel et :

$$\chi(\beta) = \beta K_1(\beta) \quad (23)$$

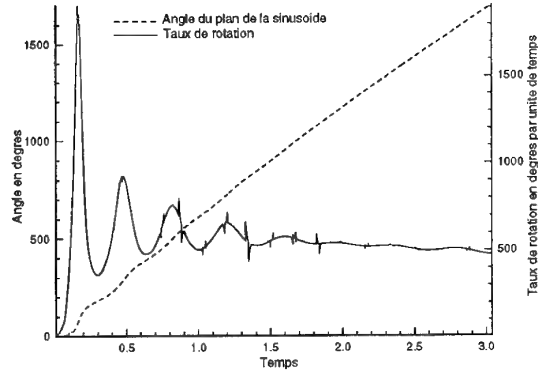


Figure 11: Angle et taux de rotation de la sinusoïde pour $k = 2\pi L^{-1}$.

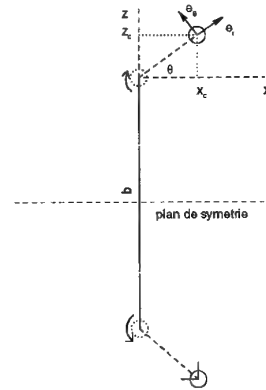


Figure 12: Définitions utilisées.

$$\psi(\beta) = \beta^2 K_0(\beta) + \beta K_1(\beta) \quad (24)$$

$$\phi(\beta) = \frac{1}{2} \left(\ln \frac{1}{\beta} + \ln \frac{b}{r_0} + A + \ln 2 - \gamma \right) \quad (25)$$

$K_0(\beta)$ et $K_1(\beta)$ sont les fonctions de Bessel modifiées de deuxième espèce. L'expression de ϕ est due à Widnall, Bliss et Zalay (voir [2]). On pose alors : $x(t) = x_0 \exp(at)$ et $z(t) = z_0 \exp(at)$ où a est le taux d'amplification de l'instabilité. On considère le taux d'amplification adimensionnel $\alpha = \frac{2\pi b^2}{\Gamma_0} a$. Le système différentiel (22) admet une valeur propre réelle positive (dans le cas $\alpha^2 > 0$) :

$$\alpha = \sqrt{(1 - \psi + \beta^2 \phi)(1 + \chi - \beta^2 \phi)} \quad (26)$$

L'angle de calage $\Theta = \arctan \frac{z_0}{x_0}$ vérifie :

$$\tan \Theta = \sqrt{\frac{1 - \psi + \beta^2 \phi}{1 + \chi - \beta^2 \phi}} \quad (27)$$

Le cas calculé correspond à $k = \frac{2\pi}{7}L^{-1}$, $r_0(t=0) = 0.15L$, $b = 1L$, $A + \ln 2 - \gamma = 0.0579$. Les résultats théoriques obtenus pour ce cas sont tracés sur la figure 13. Ces courbes tiennent compte de l'évolution du rayon visqueux au cours du temps (r_0 intervient dans l'expression de $\phi(\beta)$ ci-dessus).

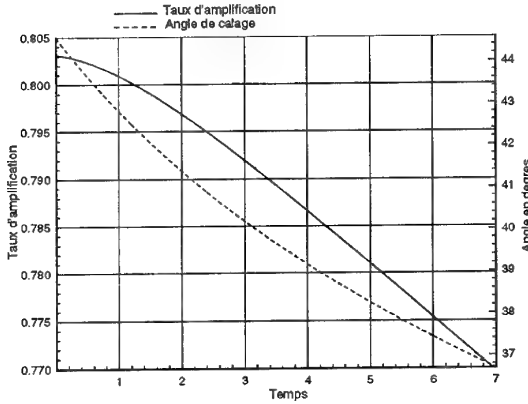


Figure 13: Valeurs théoriques du taux d'amplification α et de l'angle de calage Θ en fonction du temps t .

6.2 Caractérisation des trois mécanismes de base de l'instabilité de Crow

On définit ici, sur un plan physique, les principaux mécanismes qui participent à l'instabilité de Crow. Le système différentiel (22) traduit trois effets :

1. Une déformation pure, correspondant au champ de composantes

$$\begin{pmatrix} \dot{x} \\ \dot{z} \end{pmatrix} = \begin{pmatrix} z \\ x \end{pmatrix} \quad (28)$$

et dont les lignes de courant sont des hyperboles d'équation $x^2 - z^2 = cste$ (voir figure 14).

2. Une rotation 'elliptique' :

$$\begin{pmatrix} \dot{x} \\ \dot{z} \end{pmatrix} = \begin{pmatrix} +\chi z \\ -\psi x \end{pmatrix} \quad (29)$$

Les lignes de courant de ce champ sont des ellipses d'équation $\psi x^2 + \chi z^2 = cste$ avec $\psi > \chi$ (voir figure 14).

3. Une rotation de corps solide de taux $\beta^2\phi$:

$$\begin{pmatrix} \dot{x} \\ \dot{z} \end{pmatrix} = \begin{pmatrix} -\beta^2\phi z \\ +\beta^2\phi x \end{pmatrix} \quad (30)$$

dont les lignes de courant sont des cercles d'équation $\beta^2\phi x^2 + \beta^2\phi z^2 = cste$ (voir figure 14).

Le sens de cette rotation est inverse par rapport à celui du cas précédent. La déformation et la rotation elliptique résultent de l'influence d'un tourbillon sur l'autre. Il s'agit là donc, d'un effet de 'champ lointain'. Par contre, la rotation de corps solide est un effet auto-induit propre à chaque tourbillon (cf. paragraphe 5), et présente donc un caractère plus local.

Si l'on introduit le vecteur radial \vec{e}_r et le vecteur angulaire \vec{e}_Θ (cf. figure 12), alors :

$$\vec{e}_r = \frac{1}{r} \begin{pmatrix} x \\ z \end{pmatrix} \quad (31)$$

$$\vec{e}_\Theta = \frac{1}{r} \begin{pmatrix} -z \\ x \end{pmatrix} \quad (32)$$

où $r = \sqrt{x^2 + z^2}$. La décomposition des trois champs précédents sur ces deux vecteurs aboutit aux relations suivantes :

$$\begin{pmatrix} z \\ x \end{pmatrix} = \frac{1}{r} (-z^2 + x^2) \vec{e}_\Theta + \frac{1}{r} (2xz) \vec{e}_r \quad (33)$$

$$\begin{pmatrix} +\chi z \\ -\psi x \end{pmatrix} = \frac{1}{r} (-\psi x^2 - \chi z^2) \vec{e}_\Theta + \frac{1}{r} ((\chi - \psi)xz) \vec{e}_r \quad (34)$$

$$\begin{pmatrix} -\beta^2\phi z \\ +\beta^2\phi x \end{pmatrix} = \frac{1}{r} (\beta^2\phi(x^2 + z^2)) \vec{e}_\Theta + 0 \cdot \vec{e}_r \quad (35)$$

Au cours du développement de l'instabilité de Crow, le plan de chaque tourbillon se cale dans une direction fixe correspondant à l'annulation de la somme des composantes azimuthales de ce système. On obtient alors :

$$(1 + \chi - \beta^2\phi)z^2 + (-1 + \psi - \beta^2\phi)x^2 = 0 \quad (36)$$

Soit :

$$\frac{z}{x} = \sqrt{\frac{1 - \psi + \beta^2\phi}{1 + \chi - \beta^2\phi}} \quad (37)$$

On retrouve bien l'expression (27).

Par suite, pour la composante \vec{e}_r , il reste :

$$\begin{pmatrix} z \\ x \end{pmatrix} + \begin{pmatrix} +\chi z \\ -\psi x \end{pmatrix} + \begin{pmatrix} -\beta^2\phi z \\ +\beta^2\phi x \end{pmatrix} = \frac{(2 + \chi - \psi)xz}{r^2} \begin{pmatrix} x \\ z \end{pmatrix} \quad (38)$$

ou encore :

$$\begin{pmatrix} (1 + \chi - \beta^2\phi)z \\ (1 - \psi + \beta^2\phi)x \end{pmatrix} = \alpha \begin{pmatrix} x \\ z \end{pmatrix} \quad (39)$$

dont les lignes de courant sont des cercles avec $\alpha = \sqrt{(1 - \psi + \beta^2\phi)(1 + \chi - \beta^2\phi)}$. D'où l'expression (26).

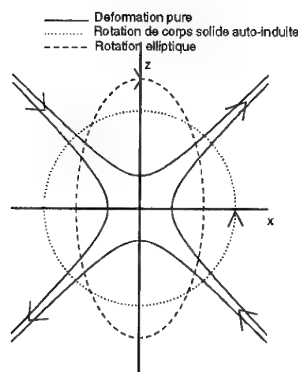


Figure 14: Lignes de courant du champ de déformation, du champ de rotation elliptique et du champ de rotation pure.

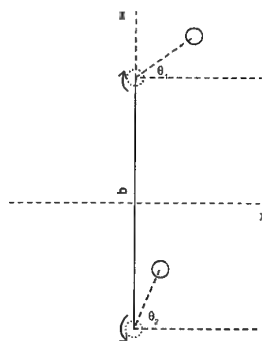


Figure 15: Définition des angles Θ_1 et Θ_2 .

6.3 Résultats de la simulation.

On déforme les tourbillons dans des plans suivant des angles Θ_1 et Θ_2 définis sur la figure 15.

6.3.1 Etude du cas $\Theta_1 = \Theta_2 = 0^\circ$

Les tourbillons ont été déformés suivant les angles $\Theta_1 = \Theta_2 = 0^\circ$. Les calculs sont menés en utilisant 5 ou 10 points dans un rayon visqueux et en choisissant l'une des deux configurations symétrisée ou non symétrisée (voir figure 6).

L'influence du maillage et des conditions aux limites est illustrée sur la figure 16. Quatre courbes sont présentées : la courbe de calage théorique $\Theta(t)$ et trois courbes résultant d'un calcul non symétrisé à 10 points, d'un calcul symétrisé à 10 points et d'un calcul symétrisé à 5 points. On observe que le code reproduit assez fidèlement l'angle de calage. Celui-ci est sures-

timé dans une proportion inférieure à 5 pourcents.

L'utilisation de 5 ou 10 points dans le rayon visqueux ne change pas ces résultats. Cette invariance vis-à-vis de la densité du maillage s'explique par le caractère essentiellement non local des mécanismes qui engendrent l'instabilité de Crow (cf. paragraphe 6.2). La conservation de la circulation (voir figure 4) assure une bonne représentation de la déformation pure et de la rotation elliptique. L'utilisation de 5 points dans le rayon visqueux suffit pour rendre compte de la contribution de la rotation auto-induite sur l'issue de l'instabilité de Crow.

La figure 17 montre les résultats sur le taux d'amplification. L'erreur par rapport à la valeur théorique varie de nouveau autour de 5 pourcents.

Jusque-là tous les résultats étaient construits à partir des barycentres de vorticité (15) et (16). On peut aussi considérer le maximum de vorticité pour définir le centre tourbillonnaire. Cependant, les angles de calage Θ_1 et Θ_2 obtenus avec cette nouvelle définition sont calculés avec une précision égale à la taille d'une maille. Sur la figure 18, on compare les erreurs sur Θ_1 selon les deux définitions. Bien que l'angle construit à partir des maxima de vorticité soit mal défini, sa valeur moyenne coïncide avec la valeur précédente.

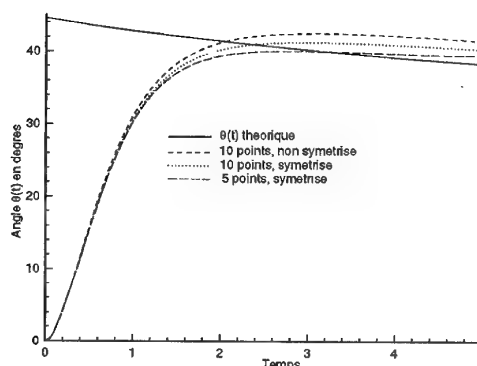


Figure 16: Angles $\Theta_1(t)$ pour des initialisations différentes.

6.3.2 Autres initialisations

On étudie maintenant le comportement de la solution numérique pour plusieurs types de déformations initiales :

1. $\Theta_1(0) = 0^\circ, \Theta_2(0) = 0^\circ$;
2. $\Theta_1(0) = 45^\circ, \Theta_2(0) = -45^\circ$;
3. $\Theta_1(0) = 90^\circ, \Theta_2(0) = -90^\circ$;
4. $\Theta_1(0) = 45^\circ, \Theta_2(0) = 45^\circ$.

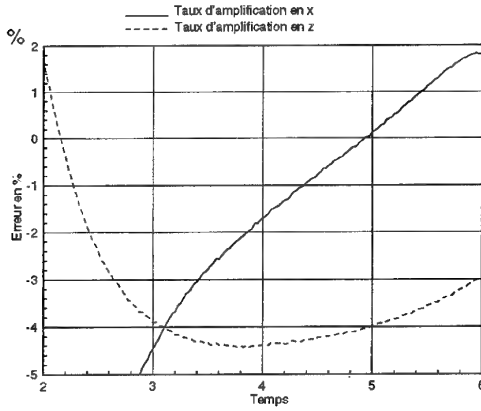


Figure 17: Erreur sur le taux d'amplification en x, en z dans le cas $\Theta_1 = -\Theta_2 = 0^\circ$.

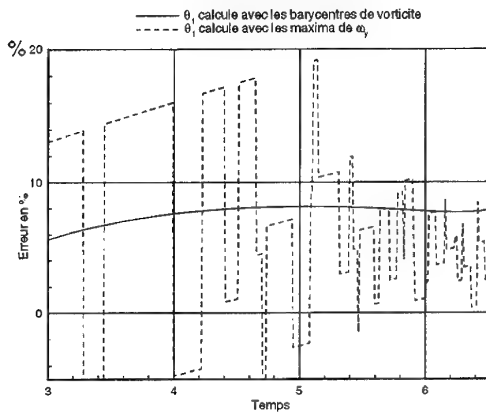


Figure 18: Erreurs sur l'angle Θ_1 selon les deux définitions.

L'ensemble des résultats est présenté sur la figure 19. Ils comprennent :

- l'angle de calage $\Theta(t)$ théorique ;
- l'angle $\Theta_1(t)$ pour les trois cas de déformation initiale symétrique ;
- les angles $\Theta_1(t)$ et $|\Theta_2(t)|$ pour le cas $\Theta_1(0) = 45^\circ$, $\Theta_2(0) = 45^\circ$.

On obtient des résultats analogues aux précédents (figure 16) : tous les angles convergent vers la valeur théorique à 5 pourcents près.

Sur la figure 20 le calcul a été poussé jusqu'au contact des deux tourbillons ('linking'). Pour ce faire, la perturbation $\Theta = 0^\circ$ a été amplifiée pour obtenir ce phénomène dans des temps raisonnables (environ 3 temps physiques). On a représenté sur cette figure la

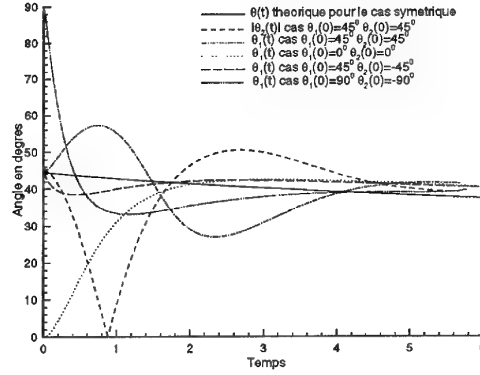


Figure 19: Angles $\Theta_1(t)$ et $\Theta_2(t)$ pour des initialisations différentes.

projection sur Oxz de la sinusoïde à trois instants successifs. L'amplitude des deux sinusoïdes croît jusqu'à ce que les deux tourbillons se touchent. On assiste alors à un repliement des deux tourbillons sur eux-mêmes.

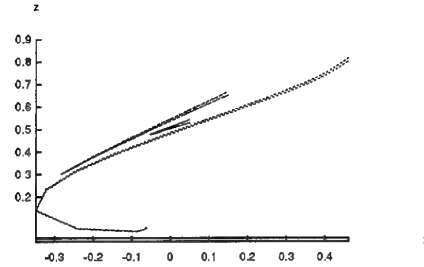


Figure 20: Linking.

7 Conclusion

L'instabilité de Crow a été simulée à l'aide d'un code de résolution directe des équations de Navier-Stokes (DNS). Des confrontations ont été faites entre les résultats numériques et ceux de la théorie linéaire du problème. L'effet de la densité du maillage et des conditions aux limites classiques ont été discutés. On a montré que si des maillages relativement denses (au moins 10 points dans le rayon visqueux) sont nécessaires pour représenter correctement la structure interne des tourbillons, les mécanismes de l'instabilité de Crow peuvent être capturés avec des maillages plus lâches (5 points).

Ces mécanismes ont été rappelés et quantifiés. Dans l'ensemble, les résultats prouvent que le code utilisé permet de simuler très correctement le phénomène.

References

- [1] S.C. Crow, *The stability theory for a pair of trailing vortices*, AIAA Journal, Vol 8, No 12, Dec 1970, pp 2172-2179.
- [2] S.E. Widnall, D. Bliss and A. Zelay, *Theoretical and experimental study of the stability of a vortex pair*, Aircraft wake turbulence and its detection, Plenum Press, 1971, pp 305-338
- [3] L. Ting, R.Klein *Viscous Vortical flows*, Lecture Notes in Physics No 374, Springer-Verlag, 1991.
- [4] P. Sagaut, *Simulations numériques d'écoulements décollés avec des modèles de sous-maille*, Juin 1995.
- [5] R.E. Robins, P.Delisi, soumis à l'AIAA.

Stability Theory for two Wingtip Vortices behind Cruising Aircraft

Thorsten Ehret

Institut für Strömungslehre und Strömungsmaschinen

Universität Karlsruhe (TH)

Kaiserstr. 12

D - 76128 Karlsruhe

Germany

1 Summary

To perform a stability analysis on an interesting flow field, an undisturbed quasi steady basic velocity profile of the concerned flow field must be provided. In case of wake vortices behind cruising aircraft, the velocity distribution within the vortices has to be evaluated as a function of the height coordinate z and the spanwise coordinate y . A three-dimensional vortex filament method was used to calculate the velocity field of the wake flow, because it is an efficient tool for flows consisting of large regions of vorticity.

Vortex filament methods simulate such a flow field by discretizing the regions behind the aircraft wing which contain vorticity, and tracking this discretization in a Lagrangian reference frame. The velocity field behind the aircraft is determined kinematically from the given vorticity field and computed by an application of the Biot-Savart-law. Small perturbations are then superimposed on the given quasi steady base flow and this sum is then substituted into the governing equations. After a linearization process, two fourth order perturbation differential equations are found. They give rise to an eigenvalue problem with a complex eigenvalue ω and eigenfunctions for the amplitudes of the disturbances.

2 List of Symbols

- a real wave number, $a = 2\pi/\lambda$
- b span of aircraft wing
- c vortex core radius
- i complex unit, $i = \sqrt{-1}$

r filament radius variable

Δt time step

$\mathbf{u} = (u, v, w)$ velocity vector

u velocity component in x -direction

v velocity component in y -direction

w velocity component in z -direction

$\mathbf{x} = (x, y, z)$ position vector

x downstream coordinate

y spanwise coordinate

z height coordinate

L_w length of the wake

M_∞ flight Mach number

N_s number of filament segments

N_t number of time steps

N_v number of filaments on one wing

Re Reynolds number

U_∞ flight velocity

V integration volume

V_g group velocity

$\alpha = 0.413$, constant formfactor

λ wavelength in x -direction

ν kinematic viscosity

σ filament core radius

$\boldsymbol{\omega} = (\omega_x, \omega_y, \omega_z)$, vorticity vector

$\omega(r)$ vorticity distribution over radius r

$\omega = \omega_r + i \cdot \omega_i$, complex frequency

$\omega_i = Im(\omega)$, temporal amplification rate

$\Gamma(y)$ circulation distribution over aircraft wing

Γ_0 maximum circulation over aircraft wing

3 Introduction

Viscosity is not the only reason leading to the decay of trailing vortices in the atmosphere behind a large civil aircraft. This mechanism is described by the decay-law of a so called

Hameln-Oseen vortex, which is an exact solution of the Navier-Stokes equations (Zierep, J. 1982). If just vortex diffusion caused by viscosity was present, the trailing vortices, whose motions sometimes become visible in form of condensation trails, would exist for a very long time (Scorer, R. and Davenport, L.J. 1970). But very often trailing vortices undergo a symmetric instability after about half a minute in the early stages of its growth, before they would decay just by simple vortex diffusion. This kind of instability is known as Crow instability (Crow, S. C. 1970). According to Crow's model the cause of the instability is a small displacement of the two originally parallel trailing vortices, which amplifies under mutual induction. Crow's model is based on two nearly parallel vortex lines interacting in neutrally stable air, because at that time he had no information about the velocity distribution within the vortices and only an estimation about the vortex cores. The present work is based on Crow's ideas and the first steps towards a modification and refinement of his theory lie in the calculation of the quasi steady velocity profile in the wake of a large airliner.

4 Vortex Filament Method

A vortex filament is nothing more than a vortex line with a finite core radius σ (Leonard, A. 1980). This is necessary for 3D simulations, because a curved vortex line with an infinite small core radius would lead to a singularity by inducing itself an infinite velocity (Meiburg, E. 1986). To avoid this, a form function $\omega(r)$ for the vorticity distribution over the filament radius r is used:

$$\omega(r) = \frac{\alpha}{\pi\sigma^2} \frac{1}{\left(\frac{r^2}{\sigma^2} + \alpha\right)^2} \quad (1)$$

This formula can be found in the literature by Nakamura et al. where the variable $\alpha = 0.413$ denotes a constant formfactor (Nakamura, Y. et al. 1982). The required velocity field of the aircraft wake $\mathbf{u}(\mathbf{x}, t)$ at a position \mathbf{x} is then computed by applying the pure kinematic Biot-Savart-Law on a given vorticity field $\omega(\mathbf{x}', t)$ at a position \mathbf{x}' :

$$\mathbf{u}(\mathbf{x}, t) = -\frac{1}{4\pi} \int \frac{(\mathbf{x} - \mathbf{x}') \times \boldsymbol{\omega}(\mathbf{x}', t)}{|\mathbf{x} - \mathbf{x}'|^3} dV(\mathbf{x}') \quad (2)$$

The Biot-Savart-integration along the filament volume dV is carried out over all elements of the flow field containing vorticity. It should be noted that the Biot-Savart-law, which has its origin rather in electro dynamics than in fluid mechanics, normally is only valid for inviscid and incompressible flows (Leonard, A. 1985). The concerned flow field here is the vortex wake flow behind an aircraft with $M_\infty = 0.82$ and transonic flows are of course compressible. But the characteristic velocity describing the vortex flow is the maximum circumferential velocity of a wake vortex in the y, z -plane and not the speed of the aircraft in downstream direction x . This maximum circumferential velocity is of order 20m/s and so the flow within the vortex can be regarded as being incompressible.

Viscosity effects are taken into account using a finite vortex core σ for each filament. This vortex core σ is a pure numeric parameter and must be validated after the calculations by comparisons with results from experiments or such taken from the literature. Still it is not possible to calculate 'real' viscous flows using a Biot-Savart-integration, because the velocity profiles obtained with a finite vortex core σ for each filament do not decay or change their shape with time. So, the result of the vortex filament calculation of the wake vortices behind an aircraft is a steady velocity distribution at each certain distance in downstream direction x .

It must also be pointed out, that the flow behind an aircraft flying with transonic speed is turbulent. According to Crow's model, turbulence may be the cause for small displacements of the two originally parallel trailing vortices, but it is not important for the velocity profile itself as a basic solution for the stability analysis. After the displacements, the two trailing vortices amplify under mutual induction and this leads to instability. The Biot-Savart-integration doesn't take turbulence into consideration. In this sense, the solution of the

Biot-Savart-calculation is a quasi steady velocity profile and can be viewed as a time averaged profile. As a starting point for the vortex filament calculations, a given circulation distribution over the wing of the concerned aircraft is needed. We assume a nearly elliptically loaded aircraft wing with a circulation distribution $\Gamma(y)$ along the span coordinate y of the wing, see Figure 1. According to the theorems

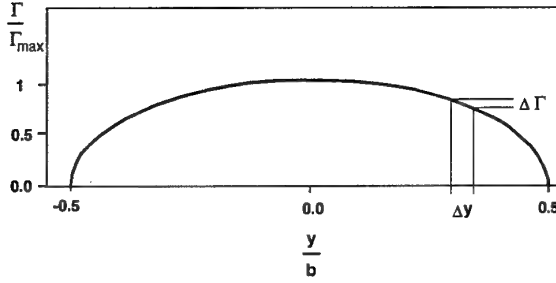


Figure 1: Circulation distribution over aircraft wing

of Kelvin and Helmholtz, a change in the circulation along the span $d\Gamma/dy$ is modelled by proper positioning the vortex filaments along the wing. Each vortex filament on one wing has the same circulation $\Delta\Gamma = \Gamma_0/N_v$ where N_v is the number of vortex filaments on one wing and $\Gamma_0 = 700\text{m}^2/\text{s}$. During the calculations the circulation $\Delta\Gamma$ as well as the filament core radius σ and the vorticity ω remain constant for each filament. The horizontal distance Δy between two neighboured vortex filaments along the span coordinate y of the wing is determined by $\Delta y = \Delta\Gamma/(d\Gamma/dy)$. On positions along the trailing edge, where there are strong gradients of the circulation along the span $d\Gamma/dy$ the vortex filaments are close to each other and Δy is small. The highest concentration of vortex filaments can therefore be found near the wing tip, where the gradient $d\Gamma/dy$ reaches its maximum.

The vortex filaments point in the downstream direction x against the flight direction and lie in the x, y -plane at the beginning of the calculations forming a vortex sheet. Due to the mutual induction influence from each filament upon each other filament the vortex sheet rolls

up into two trailing vortices. Each filament is divided into a number of segments N_s of equal length and after each timestep Δt one more segment is taken into account for the calculation, see Figure 2. In this sense, the integration proceeds in time according to the cruising velocity of the aircraft and the length of the segment. Starting the simulation, the required local velocity field in the aircraft wake

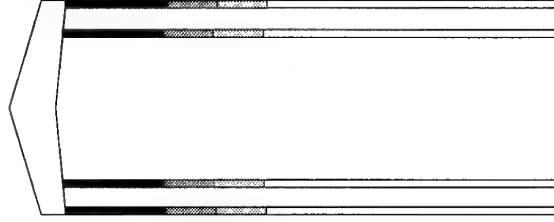


Figure 2: Sketch of filament segments

is computed by integrating the Biot-Savart-law and the motion of the filaments can be studied looking at the change of their positions with each time step in a Lagrangian reference frame. The new positions of the filament segments are calculated using an explicit predictor-corrector-method of second order accuracy:

$$\mathbf{x}_p = \mathbf{x}(t) + \mathbf{u}(\mathbf{x}, t) \cdot \Delta t \quad (3)$$

$$\mathbf{x}(t + \Delta t) = \mathbf{x}(t) + \frac{1}{2} \cdot (\mathbf{u}(\mathbf{x}, t) + \mathbf{u}_p(\mathbf{x}_p)) \Delta t \quad (4)$$

Numerical stability constraints as well as conditions for convergence define connections between the numerical parameters as follows:

$$U_\infty \cdot \Delta t \cdot N_s = L_w \quad (5)$$

$$2 \cdot \sigma \cdot N_s / L_w > 0.4 \quad (6)$$

$$N_s / N_t < 3/4 \quad (7)$$

The flight velocity U_∞ of the aircraft is a given parameter and serves as input data for the initialization of the vortex filaments. Before the beginning of the calculations, the length of the considered vortex wake L_w in downstream direction x , which is equal to the length of the vortex filaments, must be determined. Typical time steps Δt used for vortex filament calculations are of order $\Delta t = 0.05\text{s}$. Equation (5) is then a condition to determine the number of vortex segments N_s . An example: The

flight velocity of a transonic aircraft with a Mach number $M_\infty = 0.82$ at cruising altitude is about $U_\infty = 250 \text{ m/s}$. If one is interested in the early state of the wake evolution 1s after the fly over of the aircraft, the wake length L_w has to be chosen to $L_w = 250 \text{ m}$. With a typical time step $\Delta t = 0.05 \text{ s}$ the number of filament segments of each filament according to Equation (5) is then $N_s = 20$.

Equation (6) is a relation for an appropriate value of the filament core radius σ . If a chosen σ is too small and doesn't fulfill equation (6), the calculation becomes unstable because the self induction influence leading to singularities, is not damped. Equation (7) is a condition to obtain steady velocity profiles at the considered distance L_w behind the wing. Due to the addition of one more filament segment after each time step, a stable solution for the velocity is obtained, if the calculation is extended to a number of time steps greater than the number of filament segments. Figure 3 shows the

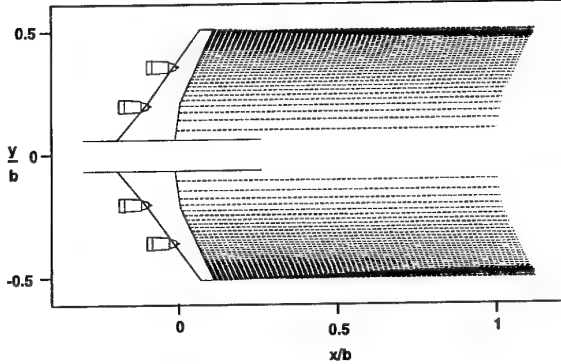


Figure 3: Vortex filament distribution in the jet regime

wake in a distance of one span $b = 60 \text{ m}$ behind the wing computed with a number of 80 filaments, 40 on each wing. The filaments represent the roll up process from a vortex sheet to a wake vortex behind each wing. According to the flight velocity of $U_\infty = 250 \text{ m/s}$, the horizontal distance $x/b = 1$ corresponds to a time $t = 0.24 \text{ s}$. The roll up process starts at the wing tips with a large number of filaments because of the strong circulation gradients $d\Gamma/dy$. The filaments near the body of the

airplane do not roll up but move downwards in z -direction in their induced velocity field. The roll up process is said to be finished when the two wake vortices have a constant downwash velocity. Further calculations show that this happens between 2 and 3 seconds or at a horizontal distance between 500 m and 800 m behind the wing (Ehret, T., Oertel, H. 1994).

5 Velocity Profiles

After the end of the roll up process, we assume two parallel counter rotating trailing vortices which move downwards in negative z -direction in their own induced velocity field. In this case, the axial velocity component u in downstream direction x can be neglected. Figure 4 shows the profile of the vertical velocity component w of two trailing vortices after 4 seconds at an x -position 1000 m behind the wing. $w = w(y)$ is here a function of the spanwise coordinate y , whereas the centers of the trailing vortex cores with $w = 0$ are at a position $z < 0$ in relation to the airplane wing at $z = 0 \text{ m}$. The horizontal distance in y -direction between the two

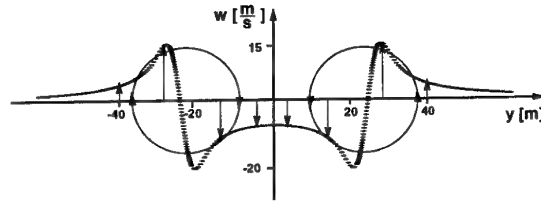


Figure 4: Vertical velocity profile $w(y)$

centers of the vortex cores is 47 m , which is $\pi/4$ of the wingspan $b = 60 \text{ m}$. This corresponds to a value given by an analytic formula for an exactly elliptically loaded wing. The w -profile is not point symmetric with respect to the center of the vortex core with $w = 0$ on each side because of the downward induction influence of the respective other vortex, which amplifies the maximum value w_{max} of w -component in the inner part of the wake up to $w_{max} = -20 \text{ m/s}$ while diminishing it in the outer half to about $w_{max} = 15 \text{ m/s}$.

The velocity profile of the wake vortices was

calculated as a result of an integration of the Biot-Savart-law. It is notable that this numerically computed velocity distribution $w(y)$ is quite similar to the velocity profile $w(r)$ of a so called Hameln-Oseen-vortex, which is an exact solution of the Navier-Stokes equations. Both show the behaviour of a solid body rotation near the vortex center, where the velocity is proportional to the distance from the vortex center, and the behaviour of a potential flow away from the vortex center, where the velocity is proportional to the reciprocal value of the distance. Figure 4 also shows a steady and smooth transition from the solid body flow area in the middle of the vortex core to the potential flow area outside. This is a consequence of the use of a finite filament core radius σ , which allows to take viscosity effects into account.

Figure 5 shows the profile of the horizontal velocity component $v(z)$ as a function of the height coordinate z , also at an x -position $1000m$ behind the wing. The centers of the vortex cores with $v = 0$ are located at spanwise positions $y = -23.5m$ for the vortex on the left side and $y = 23.5m$ for the vortex on the right side, respectively. According to the downwash influence, these vortex core centers have moved downwards to positions $z = -5.8m$ in relation to the airplane wing at $z = 0m$. The veloc-

ity in a non symmetry for the $w(y)$ velocity profile. As a definition for the core radius c of a trailing vortex we take the distance between the vortex core center with $v = 0$ and the maximum circumferential velocity $v_{max} = 18m/s$ and find a value of $c = 3.2m$. Summing up the results so far, we state that the velocity distribution within a trailing vortex is not symmetric to the vortex core center. Therefore the velocity distribution can not be described in terms of a circumferential velocity $V_\varphi(r)$ where the velocity is only a function of a radius r and independent of the rotation angle φ .

For this reason the velocity components v and w are described and calculated in a cartesian coordinate system using y and z as independent variables, where both v and w are functions of the spanwise coordinate y and the height coordinate z , so it becomes $v = v(y, z)$ and $w = w(y, z)$. Figure 6 shows the velocity profile $w(y, z)$ of the vortex on the right in Figure 4 in a dimensionless form. The independent variables y and z are transformed onto intervals $y \in [-1, 1]$ and $z \in [-1, 1]$. This is necessary for the numerical derivation of $v(y, z)$ and $w(y, z)$ later on, using a high order Compact-Finite-Difference-Method with a spectral like solution (Lele, S.K. 1992). The velocities are normalized with the maximum velocity and the

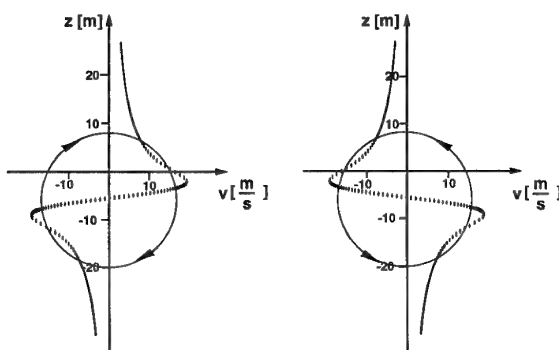


Figure 5: Horizontal velocity profile $v(z)$

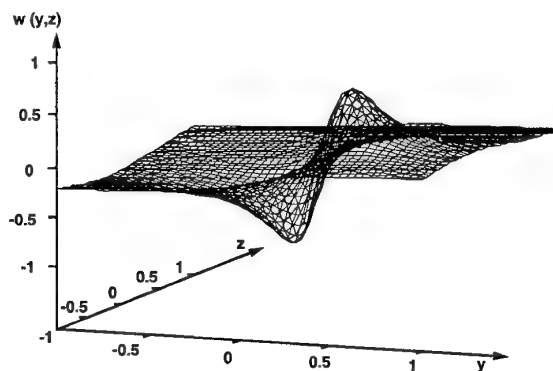


Figure 6: Normalized velocity profile $w(y, z)$

ity profiles $v(z)$ are symmetric to the vortex core centers, because the mutual induction influence in y -direction of the two trailing vortices is equalized, in comparison to the mutual induction influence in z -direction, which results

independent variables y and z are normalized with half of the horizontal distance $47m$ between the two vortex core centers. Additionally, the independent variables are transformed along their axes in a way that the vortex core

centers with vanishing velocities have dimensionless positions $y = 0$ and $z = 0$. In this sense, the dimensionless coordinate $y = -1$ in Figure 6 corresponds to a position $y = 0m$ and the dimensionless coordinate $y = 1$ corresponds to a position $y = 47m$. Beside $w(y, z)$, also the horizontal velocity component $v(y, z)$ must be considered. Figure 7 shows the velocity profile $v(y, z)$ of the vortex on the right in Figure 5 in a dimensionless form. Here, the di-

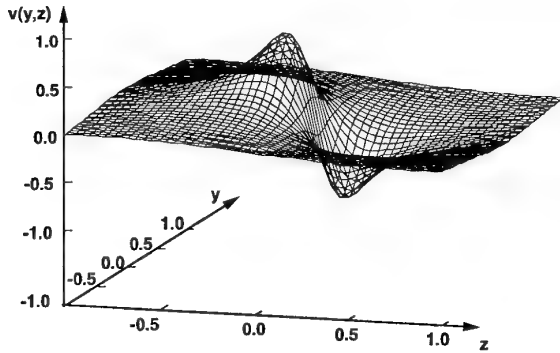


Figure 7: Normalized velocity profile $v(y, z)$

dimensionless coordinate $z = -1$ in Figure 7 corresponds to a position $z = -23.5m - 5.8m = -29.3m$ and the dimensionless coordinate $z = 1$ in the same figure corresponds to a position $z = 23.5m - 5.8m = 17.7m$. These two velocity profiles $v(y, z)$ and $w(y, z)$ then serve as an approximate base flow for the derivation of the perturbation differential equations. In the ongoing text they will be denoted with an index 0 to indicate the undisturbed, quasi steady solution $v_0(y, z)$ and $w_0(y, z)$ of the governing equations of fluid mechanics.

The question to be answered we were interested in, is whether the Crow instability can be viewed as absolutely or convectively unstable. In case of an investigated time averaged velocity profile one uses the terms of absolute or convective sensitivity rather than instability which is normally only used for undisturbed laminar flows. Here, the results of the Biot-Savart calculation for an in reality turbulent flow are viewed as time averaged profiles, but with respect to the well established term Crow instability, we make a distinction between ab-

solute or convective instability rather than sensitivity (Oertel jr. H., Delfs, J. 1996).

6 Stability Theory

First, we calculate the neutral curve $\omega_i = 0$ with respect to the equations in Crow's original paper (Crow, S.C. 1970). As a difference, while Crow worked with a cut-off-distance δ in order to avoid self induction singularities, we used our vortex core radius c to define a Reynolds number Re and computed the curve of vanishing temporal amplification rates $\omega_i = 0$ in the (Re, a) -plane. The characteristic velocity is the maximum velocity v_{max} of a trailing vortex, the characteristic length is the vortex core radius c and ν denotes the kinematic viscosity $\nu = 3.53 \cdot 10^{-5} \frac{m^2}{s}$ in a height of $10 km$. The Reynolds number then becomes $Re = v_{max} \cdot c / \nu$. The variable a here denotes a dimensionless real wave number $a = (2\pi/\lambda) \cdot b$, normalized with the wingspan b . Figure 8 shows that the Crow instability is of pure kinematic origin, because the neutral curve $\omega_i = 0$ divides the entire (Re, a) -plane for all Reynolds numbers in a stable and an unstable region. Only the value of the dimensionless wave number a is important for the onset of the Crow instability. Small wave numbers lead to instability. Typical values under cruising conditions $U_\infty =$

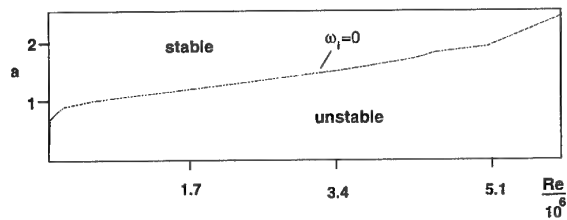


Figure 8: Neutral curve $\omega_i = 0$

$250m/s$ and $\Gamma_0 = 700 \frac{m^2}{s}$ are circumferential velocities $v_{max} = 18m/s$ and a core radius of about $\sigma = 3.3 m$. The Reynolds number describing the vortex motion in a height of $10 km$ is then $Re = 1.68 \cdot 10^6$. At this Reynolds number standing waves with wave numbers $a < 1$ or wave lengths $\lambda > 2\pi b = 377m$ are unstable, which is in good conformity with observations.

The derivation of the perturbation differential equations starts with the assumption of a given quasi steady base flow in the (y, z) -plane with the velocity components $v_0(y, z)$, $w_0(y, z)$ and the pressure $p_0(y, z)$. The governing equations for the disturbed base flow are the continuity equation and the Navier-Stokes equations for an unsteady, incompressible flow:

$$\nabla \cdot \mathbf{u} = 0 \quad (8)$$

$$\frac{\partial \mathbf{u}}{\partial t} + (\mathbf{u} \cdot \nabla) \mathbf{u} = -\frac{1}{\rho} \nabla p + \nu \Delta \mathbf{u} \quad (9)$$

Small perturbations $u'(\mathbf{x}, t)$, $v'(\mathbf{x}, t)$, $w'(\mathbf{x}, t)$ and $p'(\mathbf{x}, t)$ are superimposed on the given quasi steady flow field:

$$u = u'(\mathbf{x}, t) \quad (10)$$

$$v = v_0(y, z) + v'(\mathbf{x}, t) \quad (11)$$

$$w = w_0(y, z) + w'(\mathbf{x}, t) \quad (12)$$

$$p = p_0(y, z) + p'(\mathbf{x}, t) \quad (13)$$

The small displacements of the two originally parallel trailing vortices lead to a velocity disturbance in x -direction and therefore $u'(\mathbf{x}, t)$ has to be taken into consideration. Equations (10)-(13) are then substituted into the governing equations (8) and (9). After a linearization process, we find:

$$\frac{\partial u'}{\partial x} + \frac{\partial v'}{\partial y} + \frac{\partial w'}{\partial z} = 0 \quad (14)$$

$$\frac{\partial u'}{\partial t} + v_0 \frac{\partial u'}{\partial y} + w_0 \frac{\partial u'}{\partial z} = -\frac{1}{\rho} \frac{\partial p'}{\partial x} + \nu \Delta u' \quad (15)$$

$$\begin{aligned} \frac{\partial v'}{\partial t} + v' \frac{\partial v_0}{\partial y} + v_0 \frac{\partial v'}{\partial y} + w' \frac{\partial v_0}{\partial z} + w_0 \frac{\partial v'}{\partial z} = \\ -\frac{1}{\rho} \frac{\partial p'}{\partial y} + \nu \Delta v' \end{aligned} \quad (16)$$

$$\begin{aligned} \frac{\partial w'}{\partial t} + v' \frac{\partial w_0}{\partial y} + v_0 \frac{\partial w'}{\partial y} + w' \frac{\partial w_0}{\partial z} + w_0 \frac{\partial w'}{\partial z} = \\ -\frac{1}{\rho} \frac{\partial p'}{\partial z} + \nu \Delta w' \end{aligned} \quad (17)$$

Note, that the pressure $p_0(y, z)$, which can not be computed using a Biot-Savart-integration, could be eliminated during the linearization. As a result of the mutual velocity induction of the two displaced trailing vortices as cause for

the instability, the perturbations turn out to be standing waves in the downstream direction x . So, we can use a normal mode ansatz for the perturbation functions:

$$u'(\mathbf{x}, t) = \hat{u}(y, z) \cdot \exp(i(ax - \omega t)) \quad (18)$$

$$v'(\mathbf{x}, t) = \hat{v}(y, z) \cdot \exp(i(ax - \omega t)) \quad (19)$$

$$w'(\mathbf{x}, t) = \hat{w}(y, z) \cdot \exp(i(ax - \omega t)) \quad (20)$$

$$p'(\mathbf{x}, t) = \hat{p}(y, z) \cdot \exp(i(ax - \omega t)) \quad (21)$$

The amplitudes of the disturbances are denoted with a hat and they are functions of the same independent variables y and z as the corresponding base flow. The normal mode ansatz is then substituted into equations (14)-(17) and after eliminating u' and p' we find two fourth order partial differential equations for the unknown amplitude functions $\hat{v}(y, z)$ and $\hat{w}(y, z)$:

$$\begin{aligned} \omega \left[-i \cdot a^2 \hat{v} + i \cdot \frac{\partial}{\partial y} \left(\frac{\partial \hat{v}}{\partial y} + \frac{\partial \hat{w}}{\partial z} \right) \right] = \\ -a^2 \left[\hat{v} \frac{\partial v_0}{\partial y} + v_0 \frac{\partial \hat{v}}{\partial y} + \hat{w} \frac{\partial v_0}{\partial z} + w_0 \frac{\partial \hat{v}}{\partial z} \right] \\ + \frac{\partial}{\partial y} \left[v_0 \frac{\partial}{\partial y} \left(\frac{\partial \hat{v}}{\partial y} + \frac{\partial \hat{w}}{\partial z} \right) + w_0 \frac{\partial}{\partial z} \left(\frac{\partial \hat{v}}{\partial y} + \frac{\partial \hat{w}}{\partial z} \right) \right] \\ - \nu \left[\left(-a^2 + \frac{\partial^2}{\partial y^2} + \frac{\partial^2}{\partial z^2} \right) \frac{\partial}{\partial y} \left(\frac{\partial \hat{v}}{\partial y} + \frac{\partial \hat{w}}{\partial z} \right) \right] \\ + \nu \left[-a^4 \hat{v} + a^2 \left(\frac{\partial^2 \hat{v}}{\partial y^2} + \frac{\partial^2 \hat{v}}{\partial z^2} \right) \right] \end{aligned} \quad (22)$$

$$\begin{aligned} \omega \left[-i \cdot a^2 \hat{w} + i \cdot \frac{\partial}{\partial z} \left(\frac{\partial \hat{v}}{\partial y} + \frac{\partial \hat{w}}{\partial z} \right) \right] = \\ -a^2 \left[\hat{w} \frac{\partial w_0}{\partial y} + v_0 \frac{\partial \hat{w}}{\partial y} + \hat{w} \frac{\partial w_0}{\partial z} + w_0 \frac{\partial \hat{w}}{\partial z} \right] \\ + \frac{\partial}{\partial z} \left[v_0 \frac{\partial}{\partial y} \left(\frac{\partial \hat{v}}{\partial y} + \frac{\partial \hat{w}}{\partial z} \right) + w_0 \frac{\partial}{\partial z} \left(\frac{\partial \hat{v}}{\partial y} + \frac{\partial \hat{w}}{\partial z} \right) \right] \\ - \nu \left[\left(-a^2 + \frac{\partial^2}{\partial y^2} + \frac{\partial^2}{\partial z^2} \right) \frac{\partial}{\partial z} \left(\frac{\partial \hat{v}}{\partial y} + \frac{\partial \hat{w}}{\partial z} \right) \right] \\ + \nu \left[-a^4 \hat{w} + a^2 \left(\frac{\partial^2 \hat{w}}{\partial y^2} + \frac{\partial^2 \hat{w}}{\partial z^2} \right) \right] \end{aligned} \quad (23)$$

In the equations (22) and (23), the base flow appears, beside the given real wave number a and the kinematic viscosity ν , as $v_0(y, z)$ and $w_0(y, z)$ and only in a derivation of first order. To get more insight, the equations (22)

and (23) can be written in a matrix form using two matrices **A** and **B**:

$$\mathbf{A} = \begin{pmatrix} A_{11} & A_{12} \\ A_{21} & A_{22} \end{pmatrix}, \quad \mathbf{B} = \begin{pmatrix} B_{11} & B_{12} \\ B_{21} & B_{22} \end{pmatrix}$$

The elements of matrix **A** are then:

$$\begin{aligned} A_{11} &= a^2 \left(\frac{\partial v_0}{\partial y} + v_0 \frac{\partial}{\partial y} + w_0 \frac{\partial}{\partial z} \right) - \\ &\left(\frac{\partial v_0}{\partial y} \frac{\partial^2}{\partial y^2} + v_0 \frac{\partial^3}{\partial y^3} + \frac{\partial w_0}{\partial y} \frac{\partial^2}{\partial y \partial z} + w_0 \frac{\partial^3}{\partial y^2 \partial z} \right) \\ &+ \nu \left(a^4 - \frac{2a^2 \partial^2}{\partial y^2} - \frac{a^2 \partial^2}{\partial z^2} + \frac{\partial^4}{\partial y^2 \partial z^2} + \frac{\partial^4}{\partial y^4} \right) \\ A_{12} &= a^2 \frac{\partial v_0}{\partial z} - \\ &\left(\frac{\partial v_0}{\partial y} \frac{\partial^2}{\partial y \partial z} + v_0 \frac{\partial^3}{\partial y^2 \partial z} + \frac{\partial w_0}{\partial y} \frac{\partial^2}{\partial z^2} + w_0 \frac{\partial^3}{\partial y \partial z^2} \right) \\ &+ \nu \left(-a^2 \frac{\partial^2}{\partial y \partial z} + \frac{\partial^4}{\partial y \partial z^3} + \frac{\partial^4}{\partial y^3 \partial z} \right) \\ A_{21} &= a^2 \frac{\partial w_0}{\partial y} - \\ &\left(\frac{\partial v_0}{\partial z} \frac{\partial^2}{\partial y^2} + v_0 \frac{\partial^3}{\partial y^2 \partial z} + \frac{\partial w_0}{\partial z} \frac{\partial^2}{\partial z \partial y} + w_0 \frac{\partial^3}{\partial z^2 \partial y} \right) \\ &+ \nu \left(-a^2 \frac{\partial^2}{\partial z \partial y} + \frac{\partial^4}{\partial y^3 \partial z} + \frac{\partial^4}{\partial z^3 \partial y} \right) \\ A_{22} &= a^2 \left(\frac{\partial w_0}{\partial z} + v_0 \frac{\partial}{\partial y} + w_0 \frac{\partial}{\partial z} \right) - \\ &\left(\frac{\partial v_0}{\partial z} \frac{\partial^2}{\partial y \partial z} + v_0 \frac{\partial^3}{\partial y \partial z^2} + \frac{\partial w_0}{\partial z} \frac{\partial^2}{\partial z^2} + w_0 \frac{\partial^3}{\partial z^3} \right) \\ &+ \nu \left(a^4 - \frac{2a^2 \partial^2}{\partial z^2} - \frac{a^2 \partial^2}{\partial y^2} + \frac{\partial^4}{\partial y^2 \partial z^2} + \frac{\partial^4}{\partial z^4} \right) \end{aligned}$$

The elements of matrix **B** are:

$$\begin{aligned} B_{11} &= i \cdot \left(-a^2 + \frac{\partial^2}{\partial y^2} \right) \\ B_{12} &= i \cdot \frac{\partial^2}{\partial z \partial y} \\ B_{21} &= i \cdot \frac{\partial^2}{\partial z \partial y} \\ B_{22} &= i \cdot \left(-a^2 + \frac{\partial^2}{\partial z^2} \right) \end{aligned}$$

After discretizing the matrix elements, using a high order Compact-Finite-Difference-Method

(Lele, S.K. 1992), the equations (22) and (23) give rise to a generalized matrix eigenvalue problem consisting of the complex eigenvalue ω and the real eigenfunctions $\hat{v}(y, z)$, $\hat{w}(y, z)$ (Gourlay, A.R., G.A. Watson, 1973):

$$(\mathbf{A} + (\omega_r + i \cdot \omega_i) \mathbf{B}) \begin{pmatrix} \hat{v}(y, z) \\ \hat{w}(y, z) \end{pmatrix} = \begin{pmatrix} 0 \\ 0 \end{pmatrix} \quad (24)$$

Equation (24) shows that the real part ω_r of the complex frequency must be zero, because all elements of matrix **A** are purely real and all elements of matrix **B** are purely imaginary. The definition of the group velocity V_g , which is the velocity of the propagation of disturbance energy, yields a criterion to find out, whether the Crow instability is absolutely or convectively unstable (Oertel jr. H., Delfs, J. 1995). The group velocity is defined as the partial derivative $\partial \omega_r$ over the real wave number ∂a for maximum amplification rate $(\omega_i)_{max}$:

$$V_g = \frac{\partial \omega_r}{\partial a} \Big|_{(\omega_i)_{max}} \quad (25)$$

If V_g is zero, the disturbance remains local and is amplified, then the flow field is absolutely unstable. Otherwise, the disturbance energy is convected away and the flow field is convectively unstable. According to the vanishing real part ω_r in equation (24), for all wave numbers a it is $\omega_r = 0$ and with respect to equation (25), $V_g = 0$, which means that the Crow instability is absolutely unstable.

7 Conclusions

A vortex filament method was developed to simulate the roll up process in the wake behind a cruising aircraft. The velocity field of two parallel counter rotating trailing vortices after the end of the roll up process was calculated by means of a Biot-Savart integration. This velocity field served as a base flow to perform a stability analysis. It was confirmed that the Crow instability is of pure kinematic kind, because there are stable and unstable regions for all Reynolds numbers, only depending on the wave number. The perturbation differential equations, based on an undisturbed quasi

steady velocity field were derived and transformed to a generalized matrix eigenvalue problem. The matrix eigenproblem was discussed with respect to the complex frequency ω and the definition of the group velocity V_g . As a result, the Crow instability was identified as an absolute instability.

Acknowledgement

The work was supported by the Deutsche Forschungsgemeinschaft (DFG) within the priority program 'Impact of Emissions from Aircraft and Spacecraft upon the Atmosphere'

References

- Crow, S. C. 1970: Stability Theory for a Pair of Trailing Vortices *AIAA Journal* **8**, 2172-2179.
- Ehret, T., Oertel, H. 1994: Numerical Simulation of the Dynamics and Decay of Trailing Vortices including Pollutants from Air Traffic. In: *Impact of Emissions from Aircraft and Spacecraft upon the Atmosphere* (U. Schumann and D. Wurzel, eds.), DLR Mitteilung 94-06, Köln, 268-273.
- Gourlay, A.R., G.A. Watson, 1973: Computational Methods for Matrix Eigenproblems, John Wiley & Sons
- Lele, S.K. 1992: Compact Finite Difference Schemes with Spectral-like Resolution. *J. Comput. Phys.* **103**, 16-42
- Leonard, A. 1980: Vortex Methods for Flow Simulation, *J. Comp. Phys.* **37**, 289-335
- Leonard, A. 1985: Computing Three-Dimensional Incompressible Flows with Vortex Elements, *Ann. Rev. Fluid Mech.* **17**, 523-559
- Meiburg, E. 1986: Numerische Simulation der zwei- und dreidimensionalen Strukturbildung in Scherschichten und Nachläufen. *DFVLR-FB 86-10*
- Nakamura, Y., Leonard, A., Spalart, P., 1982: Vortex Simulation of an Inviscid Shear Layer, AIAA-paper 82-0948 presented at AIAA/ASME 3rd Joint Thermophysics, Fluids, Plasma and Heat Transfer Conf., 1982, St. Louis, Mo.
- Oertel jr. H., Delfs, J. 1995: Mathematische Analyse der Bereiche der reibungsbehafteten Strömung, *Z. angew. Math. Mech.* **75** 7, 491-505
- Oertel jr. H., Delfs, J. 1996: Strömungsmechanische Instabilitäten, Springer Verlag, Berlin Heidelberg
- Scorer, R. and Davenport, L.J. 1970: Contrails and aircraft downwash. *J. Fluid Mech.* **43** 451-464
- Zierep, J. 1982: Ähnlichkeitsgesetze und Modellregeln der Strömungslehre, Braun Verlag, Karlsruhe

Analysis of UK Encounters 1982-1990

D. C. Burnham

Scientific and Engineering Solutions, Inc.
P. O. Box 64
Orleans MA
USA

1. SUMMARY

Wake vortex separation standards are used to limit the frequency and severity of wake vortex encounters under instrument flight rules (IFR). One of the goals of wake vortex research is to develop models that can specify the safe separation for any aircraft pair and hence can be used to judge the safety of proposed changes in separation standards. A direct approach to defining a safe separation model is presented in this paper. The observed UK vortex encounter rates are fitted to a model that defines equal-encounter-rate (EER) separations as a function of the parameters of the leading and following aircraft (specifically their wingspans). Safety is specified by defining the acceptable encounter rate. The first analysis fits the EER separation to powers of the wingspans of the leading and following aircraft. When these powers (1.13 and -0.95, respectively) are found to be close to one, the analysis is repeated using the leader-follower span ratio.

2. INTRODUCTION

Wake vortex separation standards are used to limit the frequency and severity of wake vortex encounters under instrument flight rules (IFR). Current standards assign aircraft to classes and then specify the minimum spacing permitted between members of each pair of classes. This spacing is then provided by air traffic control. Perhaps the most familiar standards are the spacings assigned to aircraft on final approach to a single runway, which will be the subject of this paper. Section 3 reviews the requirements for separation systems.

The critical requirement for a separation system is that the assigned separations be *safe*. Consequently, one of the goals of wake vortex research is to develop models that can specify the safe separation for any aircraft pair. One approach¹ to defining a safe separation model is to combine a vortex decay model (e.g., based on decay measurements) and an encounter hazard model. The validity of such a safe separation model depends upon the validity of each part of the model. A more direct approach to defining a safe separation model is presented in this paper. The observed vortex encounter rates are fitted to a model that defines equal-encounter-rate (EER) separations as a function of the parameters of the leading and following aircraft. Safety is specified by defining the acceptable encounter rate.

3. SEPARATION SYSTEM REQUIREMENTS

A wake vortex aircraft classification/separation system must meet the requirements discussed in the following sections. The primary focus of these requirements is the separation standards themselves, not the operational procedures making use of the standards.

3.1 Safety

The primary requirement is that the system be safe. This general requirement translates into the specific requirement that no wake vortex caused accidents will occur when the system is used. For example, the current US IFR landing separations have been used for 20 years with no accidents when the

required procedures are followed. This observation implies an accident rate of less than one per 20 years. If an accident were to occur, it is likely that the separation standards would be increased. In fact, in 1994 some US spacings were increased in response to several accidents that occurred under visual flight rules (VFR).

A secondary requirement is that wake vortex encounter incidents be infrequent. When such incidents are reported systematically, the safety level can be defined by the observed incident rate.

3.2 Efficiency

The system must use available airspace efficiently. The separations used must not be overly conservative. The separations should reflect the actual duration of the wake vortex hazard for each generator/encounterer pair as closely as possible, so that unnecessarily large separations are avoided. The efficiency of the system is optimized when:

- Enough wake vortex classes are used to accurately fit the actual hazard duration.
- Separations are reduced until the maximum acceptable incident rate is reached.

3.3 Fairness

A fair system will result in a wake vortex incident probability per operation that is comparable for all classes of following aircraft. A system is not acceptable if the overall incident rate is acceptable, but most of the incidents occur for one class of aircraft. It should be noted that a fair system is also likely to be efficient, within the constraints of this discussion, since the prescription for efficiency in Section 3.2 would lead to the same incident rate for all aircraft.

3.4 Complexity

The system must not be too complex to be used operationally. At present the number of classes and separations must be small enough for easy use by air traffic controllers. Eventually air traffic control automation will permit (and then require) fine-grained separations that can treat every aircraft pair differently.

4. ENCOUNTER STATISTICS

This analysis is based on the UK wake vortex encounter statistics collected² between 1982 and 1990. Separation standards and procedures were stable during this period. Table 1 shows the basic statistics that will be used to develop the analysis method. The notable feature of Table 1 is the similarity of the encounter rates for "Medium" class aircraft (mostly B737 and DC9 aircraft) behind the B747 at the Heavy-Medium separation of five miles and behind the B757 at the Medium-Medium separation of three miles. This similarity suggests that the separations are "fair" or "balanced" since the encounter rates are similar behind the largest aircraft in the Heavy and Medium classes. Note that the UK Medium class represents the upper portion of the US Large class.

Table 2. Equal Encounter Rate Separations (nmi) for a Follower Wingspan Power $n = 0.95$

		Follower																		
Span		B7474	B777	A340	B747	MD11	DC10	DC10	L1011	L1011	B767	A300	A310	B757	B727	A320	MD80	B737	DC9	F100
Leader (m)		64.92	60.93	60.30	59.60	52.00	50.40	47.30	50.00	47.30	47.60	44.80	43.90	37.90	32.90	33.91	32.87	28.30	28.00	28.08
B747-4	64.92	2.48	2.63	2.66	2.69	3.06	3.15	3.35	3.17	3.35	3.33	3.52	3.59	4.13	4.72	4.59	4.73	5.45	5.51	5.49
B777	60.93	2.31	2.45	2.47	2.50	2.85	2.93	3.12	2.96	3.12	3.10	3.28	3.34	3.84	4.40	4.27	4.40	5.07	5.13	5.11
A340	60.30	2.28	2.42	2.44	2.47	2.81	2.90	3.08	2.92	3.08	3.06	3.24	3.30	3.80	4.35	4.22	4.35	5.02	5.07	5.05
B747	59.60	2.25	2.39	2.41	2.44	2.78	2.86	3.04	2.88	3.04	3.02	3.20	3.26	3.75	4.29	4.17	4.29	4.95	5.00	4.99
MD11	52.00	1.93	2.05	2.07	2.09	2.38	2.45	2.60	2.47	2.60	2.59	2.74	2.80	3.21	3.68	3.57	3.68	4.24	4.29	4.27
DC10	50.40	1.86	1.98	2.00	2.02	2.30	2.37	2.51	2.38	2.51	2.50	2.65	2.70	3.10	3.55	3.45	3.55	4.10	4.14	4.13
DC10	47.30	1.73	1.84	1.86	1.88	2.14	2.20	2.34	2.22	2.34	2.33	2.46	2.51	2.89	3.30	3.21	3.31	3.81	3.85	3.84
L1011	50.00	1.84	1.96	1.98	2.00	2.28	2.35	2.49	2.36	2.49	2.48	2.62	2.67	3.08	3.52	3.42	3.52	4.06	4.10	4.09
L1011	47.30	1.73	1.84	1.86	1.88	2.14	2.20	2.34	2.22	2.34	2.33	2.46	2.51	2.89	3.30	3.21	3.31	3.81	3.85	3.84
B767	47.60	1.74	1.85	1.87	1.89	2.15	2.22	2.36	2.24	2.36	2.34	2.48	2.53	2.91	3.33	3.23	3.33	3.84	3.88	3.87
A300	44.80	1.63	1.73	1.75	1.77	2.01	2.07	2.20	2.09	2.20	2.19	2.32	2.36	2.72	3.11	3.02	3.11	3.58	3.62	3.61
A310	43.90	1.59	1.69	1.71	1.73	1.97	2.02	2.15	2.04	2.15	2.14	2.26	2.31	2.65	3.04	2.95	3.04	3.50	3.54	3.53
B757	37.90	1.35	1.43	1.45	1.46	1.66	1.72	1.82	1.73	1.82	1.81	1.92	1.96	2.25	2.57	2.50	2.57	2.97	3.00	2.99
B727	32.90	1.15	1.22	1.23	1.25	1.42	1.46	1.55	1.47	1.55	1.54	1.63	1.67	1.92	2.19	2.13	2.19	2.53	2.55	2.55
A320	33.91	1.19	1.26	1.28	1.29	1.47	1.51	1.61	1.52	1.61	1.60	1.69	1.72	1.98	2.27	2.20	2.27	2.62	2.64	2.64
MD80	32.87	1.15	1.22	1.23	1.25	1.42	1.46	1.55	1.47	1.55	1.54	1.63	1.66	1.91	2.19	2.13	2.19	2.53	2.55	2.55
B737	28.30	0.97	1.03	1.04	1.05	1.20	1.23	1.31	1.24	1.31	1.30	1.38	1.41	1.62	1.85	1.80	1.85	2.13	2.16	2.15
DC9	28.00	0.96	1.02	1.03	1.04	1.18	1.22	1.29	1.23	1.29	1.29	1.36	1.39	1.60	1.83	1.78	1.83	2.11	2.13	2.12
F100	28.08	0.96	1.02	1.03	1.04	1.19	1.22	1.30	1.23	1.30	1.29	1.37	1.39	1.60	1.83	1.78	1.83	2.11	2.14	2.13

Table 1. UK Encounter Statistics 1982-1990

Case Leader//Follower	Separation (nmi)	Encounter Rates*	
		Total	Severe
B747//Medium	5	176	27
L1011//Medium	5	86	13
A300/310//Medium	5	41	7
B757//Medium	3	194	27
B747//Heavy	4	79	6

* Per 100,000 queued arrivals

5. ANALYSIS ASSUMPTIONS

The goal of the analysis is to define a separation model that will give *equal encounter rates* (EER) for each leader-follower pair, namely those obtained for the B737 and DC9 following the B747 and B757. This model then meets the fairness requirement in Section 3.3. The level of safety then depends upon the selected equal encounter rate.

5.1 Leading Aircraft Dependence

The first assumption of the analysis is that the EER separation S behind an aircraft depends upon the wingspan b_L of the leading aircraft. A power law is assumed and fitted to give EER separations of three and five miles for the DC-9 behind the B757 and B747, respectively:

$$S = 5(b_L/59.6)^{1.13} \quad (1)$$

This equation was used to define the separations in the DC-9 follower column of Table 2. The B747 and B757 leader entries are bolded (4th and 13th rows) to indicate that they are the values used to define the EER separations.

The selection of wingspan to characterize the leading aircraft is a matter of convenience. The purpose is to define the size of the aircraft in a simple fashion. The aircraft weight could have been selected instead. In general, the design of jet transport

aircraft yields a well-defined relationship between span and weight, with a few exceptions where the span was kept small to fit preexisting gates. To first approximation the encounter risk is proportional to the wake vortex circulation. The initial circulation is proportional to weight divided by span. In normalized decay models³ the decay time is inversely proportional to the cube of the span. Thus, if significant decay is needed to reach the equal encounter rate, then wingspan is perhaps a better parameter than weight.

5.2 Following Aircraft Dependence

The second assumption of the analysis is that the EER separation for a following aircraft depends upon its wingspan b_F . Although other parameters may also play a role, all encounter models treat the follower wingspan as the primary determinant of the severity of a wake vortex encounter. Again a power law is assumed:

$$S = 5(b_L/59.6)^{1.13}(28/b_F)^n \quad (2)$$

Since there is no *a priori* correct value for the power n , various values were used; Table 2 is for $n = 0.95$ (found to be the optimum choice in Section 5.3). Since some choices for n were based on an assumed safe separation for a B-747 following another B-747, this entry in Table 2 has also been bolded. Table 3 shows the variation in the B-747/B-747 EER separation for different values of n .

Table 3. Relationship between Power n and B747-B747 EER Separation (nmi)

Power n	0.30	0.50	0.67	0.95	1.00
Separation	3.99	3.43	3.01	2.44	2.35

5.3 Functional Dependence of Encounter Rate

The third assumption of the analysis is that the encounter rate R depends upon the ratio of the EER separation S to the actual separation A (which is equal to the separation standard for the queued arrivals used to calculate the rates in Table 1):

$$R = F(S/A) \quad (3)$$

The entries in Table 1 were used to explore this dependence. As before, the B737 and DC9 are taken as the aircraft for the Medium follower. For the last entry in the Table it is assumed that the smallest Heavies (B767, A310 and A300) are the aircraft experiencing the encounters. The safe separation distance was averaged for the three aircraft types. The calculations for $n = 0.95$ are presented in Table 4. Table 4 includes some additional cases with smaller incident rates than those in Table 1. Figure 1 shows how the functional dependence in Equation 3 depends upon the power n selected. Since the values for Medium follower are independent of n , those points are fixed for all values of n . The last entry in Table 1 thus gives the only incident rate above 50 that can be used to define the best choice for n ; the results are quite sensitive to n and $n = 0.95$ is the best value. For clarity, Figure 2 shows just the data for $n = 0.95$ (i.e., all the cases in Table 4). The straight line gives a surprisingly good fit to the data, although there is some spread for encounter rates below 15.

5.4 Summary of Analysis

The three assumptions have led to a definitive model that predicts the encounter rate to be expected for each aircraft pair as a function of: (1) wingspan of the leading aircraft, (2) wingspan of following aircraft and (3) assigned separation distance (Table 2 combined with straight line in Figure 2).

Table 4. Relationship between Encounter Rate R and Ratio of EER Separation S to Standard Separation A

Leader//Follower	R	A	S	S/A
B747//Medium	176	5 nmi	5 nmi	1
B757//Medium	194	3	3	1
L1011//Medium	86	5	4	0.8
A300/310//Medium	41	5	3.58	0.716
B747//Heavy	79	4	3.17	0.793
B737//Medium	7	3	2.15	0.717
B757//Heavy	10	3	1.9	0.633
L1011//Heavy	8	4	2.5	0.625
A300/310//Heavy	12	4	2.28	0.57

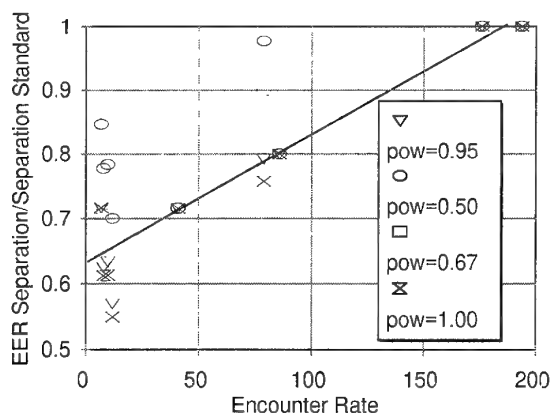


Figure 1. Functional Results for Four Choices of Power

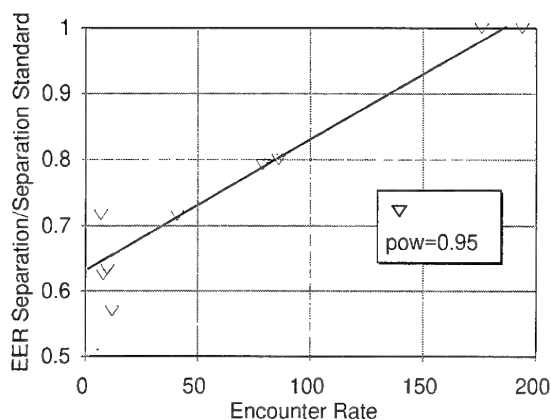


Figure 2. Functional Results for Power = 0.95

6. SPAN RATIO MODEL

The fitted powers for Equation 2 are very close to one. If they were exactly one, the safe separations would depend upon the span ratio between the leader and the follower, which is a popular assumption. Equation 2 becomes:

$$S = 5(b_L/59.6)(28.0/b_F) \quad (4)$$

The factor for normalizing S is selected to give a separation of five miles for the DC-9 behind the B-747. Table 6 shows the separation matrix for this choice. Table 5 and Figure 3 show the relationship between encounter rate and separation that result from this choice. The fit is just as good as, if not better than, that for the powers of 1.13 and 0.95. The functional dependence of Equation 3 is well represented by a straight line for all high encounter rate data. The functional form of Equation 3 becomes:

$$R = 479(S/A - 0.645) \quad (5)$$

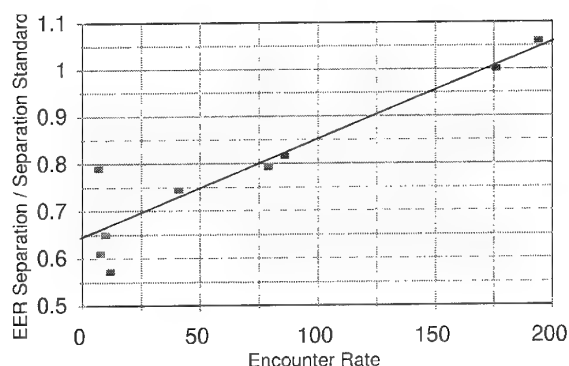
The equation corresponds to an encounter rate for $S/A = 1$ of 170 per 100,000 queued landings.

Table 5. Relationship between Encounter Rate R and Ratio of EER Separation S to Standard Separation A

Leader//Follower	R	A	S	S/A
B747//Medium	176	5 nmi	5 nmi	1
B757//Medium	194	3	3.18	1.06
L1011//Medium	86	5	4.08	0.816
A300/310//Medium	41	5	3.72	0.744
B747//Heavy	79	4	3.17	0.793
B737//Medium	7	3	2.37	0.790
B757//Heavy	10	3	1.95	0.650
L1011//Heavy	8	4	2.544	0.610
A300/310//Heavy	12	4	2.29	0.573

Table 6. Equal-Encounter-Rate Separation Matrix using Wingspan Ratio of Leader to Follower

Leader	Span (m)	Follower																		
		B747-4	B777	A340	B747	MD11	DC10	DC10	L1011	L1011	B767	A300	A310	B757	B727	A320	MD80	B737	DC9	F100
		64.92	60.93	60.30	59.60	52.00	50.40	47.30	50.00	47.30	47.60	44.80	43.90	37.90	32.90	33.91	32.87	28.30	28.00	28.08
B747-4	64.92	2.35	2.50	2.53	2.56	2.93	3.03	3.22	3.05	3.22	3.20	3.40	3.47	4.02	4.64	4.50	4.64	5.39	5.45	5.43
B777	60.93	2.20	2.35	2.37	2.40	2.75	2.84	3.03	2.86	3.03	3.01	3.19	3.26	3.78	4.35	4.22	4.35	5.06	5.11	5.10
A340	60.30	2.18	2.32	2.35	2.38	2.72	2.81	2.99	2.83	2.99	2.98	3.16	3.23	3.74	4.31	4.18	4.31	5.01	5.06	5.04
B747	59.60	2.16	2.30	2.32	2.35	2.69	2.78	2.96	2.80	2.96	2.94	3.13	3.19	3.69	4.26	4.13	4.26	4.95	5.00	4.99
MD11	52.00	1.88	2.00	2.03	2.05	2.35	2.42	2.58	2.44	2.58	2.57	2.73	2.78	3.22	3.71	3.60	3.72	4.32	4.36	4.35
DC10	50.40	1.82	1.94	1.96	1.99	2.28	2.35	2.50	2.37	2.50	2.49	2.64	2.70	3.12	3.60	3.49	3.60	4.18	4.23	4.22
DC10	47.30	1.71	1.82	1.84	1.86	2.14	2.20	2.35	2.22	2.35	2.33	2.48	2.53	2.93	3.38	3.28	3.38	3.93	3.97	3.96
L1011	50.00	1.81	1.93	1.95	1.97	2.26	2.33	2.48	2.35	2.48	2.47	2.62	2.68	3.10	3.57	3.46	3.57	4.15	4.19	4.18
L1011	47.30	1.71	1.82	1.84	1.86	2.14	2.20	2.35	2.22	2.35	2.33	2.48	2.53	2.93	3.38	3.28	3.38	3.93	3.97	3.96
B767	47.60	1.72	1.84	1.85	1.88	2.15	2.22	2.36	2.24	2.36	2.35	2.50	2.55	2.95	3.40	3.30	3.40	3.95	3.99	3.98
A300	44.80	1.62	1.73	1.75	1.77	2.02	2.09	2.22	2.10	2.22	2.21	2.35	2.40	2.78	3.20	3.10	3.20	3.72	3.76	3.75
A310	43.90	1.59	1.69	1.71	1.73	1.98	2.05	2.18	2.06	2.18	2.17	2.30	2.35	2.72	3.13	3.04	3.14	3.64	3.68	3.67
B757	37.90	1.37	1.46	1.48	1.49	1.71	1.77	1.88	1.78	1.88	1.87	1.99	2.03	2.35	2.71	2.63	2.71	3.15	3.18	3.17
B727	32.90	1.19	1.27	1.28	1.30	1.49	1.53	1.63	1.55	1.63	1.62	1.73	1.76	2.04	2.35	2.28	2.35	2.73	2.76	2.75
A320	33.91	1.23	1.31	1.32	1.34	1.53	1.58	1.68	1.59	1.68	1.67	1.78	1.81	2.10	2.42	2.35	2.42	2.81	2.84	2.84
MD80	32.87	1.19	1.27	1.28	1.30	1.48	1.53	1.63	1.54	1.63	1.62	1.72	1.76	2.04	2.35	2.28	2.35	2.73	2.76	2.75
B737	28.30	1.02	1.09	1.10	1.12	1.28	1.32	1.41	1.33	1.41	1.40	1.48	1.51	1.75	2.02	1.96	2.02	2.35	2.37	2.37
DC9	28.00	1.01	1.08	1.09	1.10	1.26	1.30	1.39	1.32	1.39	1.38	1.47	1.50	1.74	2.00	1.94	2.00	2.32	2.35	2.34
F100	28.08	1.02	1.08	1.09	1.11	1.27	1.31	1.39	1.32	1.39	1.39	1.47	1.50	1.74	2.00	1.95	2.01	2.33	2.36	2.35

**Figure 3.** Model Results Using Span Ratio

7. DISCUSSION OF RESULTS

After the 1982-1990 period analyzed here, the UK decided that the encounter rate for the B737/DC9 behind the B757 was too high (highest rate in Figure 3 with $S/A = 1.06$) and raised the required spacing from 3 to 4 nautical miles. The impact of this change can be estimated using Table 6 and Equation 5. The new value of S/A is $3.18/4.00 = 0.795$, which leads to a predicted incident rate of 72 per 100,000 queued arrivals. Changes in approach procedures since 1990 may affect the validity of this prediction.

The UK statistics combine encounter data from two regions of airspace:

- 1) Near the ground, < 100 meters AGL
- 2) Away from the ground, > 500 meters AGL

which would be expected to have different encounter probabilities. If aircraft all fly the same glideslope, encounters away from the ground are prevented by normal vortex descent; encounter probabilities therefore depend upon how well the aircraft fly the glideslope. Vortices near the ground can, however, be stalled on the runway centerline by a crosswind

and may bounce back up into the glideslope because of interactions with the ground boundary layer. Consequently, it would be desirable to repeat this analysis separately for the two encounter regions.

It would be desirable to extend this analysis to smaller aircraft types. Unfortunately, the UK encounter is too sparse to provide much guidance. The UK aircraft spacings for small following aircraft are significantly greater than those used in the US. Simply extending the equations developed for jet transport aircraft in this paper leads to separation requirements for small aircraft that are even greater than used in the UK.

ACKNOWLEDGMENTS

This work was supported by the Federal Aviation Administration, the Volpe National Transportation Systems Center, Cambridge MA and the System Resources Corporation, Burlington MA. G. Greene suggested the use of span ratio in the analysis.

REFERENCES

1. Burnham, D.C., "How to Use Wake Vortex Measurements to Set Separation Standards," Proceedings of the Aircraft Wake Vortices Conference, Washington DC, October 29-31, 1991, DOT/FAA/SD-92/1.2, pp 53-(1-11).
2. "United Kingdom Civil Aviation Authority Wake Vortex Database: Analysis of Incidents Reported between 1982 and 1990," CAA Paper 91015.
3. Greene, G.C., "An Approximate Model of Vortex Decay in the Atmosphere," J. Aircraft, , 23, 7, July 1986, pp 566-573.

A Simulation-Based Study of the Impact of Aircraft Wake Turbulence Weight Categories on Airport Capacity

Jerry J. Robinson
Air Traffic Management Research
Boeing Commercial Airplane Group
P.O. Box 3707, M/S 02-60
Seattle, WA 98124-2207, USA

1. SUMMARY

The Federal Aviation Administration (FAA) is considering revising the current aircraft wake turbulence weight categories and the associated separation standards during instrument meteorological conditions (IMC). Various proposals have been submitted to the FAA with regard to this revision. This paper presents the results and conclusions of a capacity study conducted by The Boeing Company. This study examined the impact of these proposed changes on airport capacity during IMC.

The approach taken for this study was to simulate arrival and departure operations at ten major US airports by employing a database derived from the 1993 Official Airline Guide (OAG) traffic schedule. Simulations were conducted for the traffic mix at each airport utilizing one standard, representative runway configuration. The aircraft wake vortex separation requirements were changed according to the various proposed weight categories; these separations were then applied to the particular traffic set at each airport. In general, it was found that current capacity levels could be reduced by as much as 4%.

This approach provides a consistent comparison of capacity results. It is hoped that the results from this study will provide useful information to assist in assessing the capacity impact of a modification to the existing aircraft wake turbulence weight categories and their associated separation standards during IMC.

2. INTRODUCTION

A Wake Turbulence Industry Team was formed in April 1994 at the request of the FAA Associate Administrator for Regulation and Certification. The Team consisted of representatives from airframe manufacturers, industry groups, US government and regulatory agencies, and other organizations and individuals.

The purpose of the Team was to develop a wake turbulence training package for pilots and air traffic controllers. The training package was submitted to the FAA in December 1994 and later released for publication (Ref. 1). This same Team reconvened in April 1995 with added participation from European aviation regulatory agencies. The Team was directed at that time to provide the FAA Wake Vortex Steering Committee with recommendations on aircraft wake turbulence weight classifications and separation standards.

On 5-6 June 1995, the Team met in Washington DC to discuss wake vortex decay and its relation to airborne separation between aircraft. It was concluded at that meeting (Ref. 2) that airborne separations should be dependent on the parameters of the wingspan and weight of the leading aircraft.¹ In addition, several aircraft weight classification schemes (Ref. 3) were discussed. For example, the Team discussed changing the *Small* category maximum of 12,500 lbs to something between 29,000 and 88,500 lbs, as well as changing the *Heavy* category minimum to something greater than 255,000 lbs, but not more than 300,000 lbs. After discussions it was suggested that further capacity studies be conducted to address the impact of these changes on the operational environment in the terminal area. The author was thereafter authorized by an FAA representative to conduct such capacity studies utilizing the weight categories and the associated separations discussed at the meeting.

¹ The classical formula for these parameters in determining vortex strength for an elliptically loaded wing is: $\Gamma = 4W / \pi b \rho V$ where W is weight, b is wingspan, ρ is air mass density, V is leading aircraft speed, and Γ is the circulation about the shed vortex.

3. DEVELOPMENT OF CURRENT WAKE TURBULENCE SEPARATION STANDARDS

As early as 1947, the US Civil Aeronautics Administration (CAA), in a publication known as *Facts of Flight* (Ref. 4), warned owners of private aircraft about the possibilities of 'stall' during landing or take-off behind multi-engine transports. This publication, subtitled *Practical Information About Operation of Private Aircraft*, noted that "[t]he turbulence created by the propellers may extend to the rear for a mile or more, and will affect a light airplane in much the same way as violent gusts." The phenomenon known today as *wake turbulence*, at that time was commonly attributed to the effects of 'propeller wash' (also called 'propwash'), 'jet blast,' or 'thrust stream turbulence.'

About the same time, researchers were investigating the motion of trailing vortices² associated with the wing of an aircraft so as to estimate the effects of aircraft-induced vortices (Ref. 5). They found that the strength of the vortex wake was directly proportional to the weight, inversely proportional to the forward speed, and, approximately, inversely proportional to the wingspan of the generating aircraft.

In 1952, the CAA determined that a pilot educational program might be needed due to the increasing number of reported incidents of turbulence encountered by small aircraft "following or crossing the thrust streams of multi-engine or jet type aircraft" (Ref. 6). In 1955, in *Aviation Safety Release No. 399*, the CAA informed the pilot community that "[s]evere vortex turbulence has a duration of from 30 to 60 seconds (1 to 3 miles) after the passage of the large airplane which caused it, and may persist much longer under favorable conditions" (Ref. 7).

Though no separation requirements due to wake turbulence were imposed at that time, aircraft were required to maintain a minimum longitudinal separation of 3 nautical miles (nm) during Instrument Flight Rules (IFR) because of radar

² The earliest works on the trailing vortex system for a wing are credited to Frederick W. Lanchester (*Aerodynamics*, 1907), and Ludwig Prandtl (*Tragflügeltheorie*, 1918 and *Generation of Vortices in Fluids of Small Viscosity*, Wilbur Wright Memorial Lecture, 1927).

operating considerations and runway occupancy limitations³. Moreover, air traffic controllers were required to issue cautionary advisories.⁴

As early as 1961, an accident in Hawaii was attributed to the wake turbulence of a DC-8 (Ref. 8). A federal trial court opinion in 1969, later reversed by the appellate court, suggested that a separation time of 12½ minutes should be applied to smaller airplanes landing behind a 707 aircraft (Ref. 9). The Air Traffic Control Association (ATCA) reaction following the trial court opinion was that if the decision was sustained on appeal, then the government would have to ban smaller aircraft at air carrier airports--a move unacceptable to ATCA. (However, as indicated above, the trial court decision was overturned on appeal in 1972.)

Nine hours before the Boeing 747 entered commercial service on 21 January 1970, the FAA adopted an interim requirement that all aircraft trailing a 747 or C-5A maintain 10 nm (4 minutes) separation due to wake turbulence concerns (Ref. 10). Meanwhile, the FAA was conducting flight tests to collect data for determining separation standards for aircraft trailing a 747 in the terminal area (Ref. 11). The flight test program was expedited on 13 February to address French objections to the adverse effect on air traffic that would be caused by a 747 under the interim rules (Ref. 11). The flight test program was completed by 21 February 1970.

³ In 1967, the Fifth ICAO Air Navigation Conference noted that the then current separation minima "...were based on the principal that, normally, no more than one aircraft at a time should occupy the runway in use and [it was] recognized that this was a limiting factor on runway capacity," (Document 8720.AN-CONF/5, p. 1-18, *Report of the Fifth Air Navigation Conference*, ICAO, 14 November - 15 December 1967)

⁴ In fact, section 411.7 of the Air Traffic Manual (ATM-2-A) stated: "When controllers foresee the possibility that departing or arriving aircraft might encounter rotorcraft downwash, thrust stream turbulence or wing tip vortices from preceding aircraft, cautionary information to this effect should be issued to pilots concerned." This statement was found in Air Traffic Manuals in the 1960s.

Thereafter, the FAA, on 1 March 1970, introduced the *Heavy* category of aircraft (the *Large*⁵ and *Small* aircraft categories already existed). *Heavy* aircraft referred to all aircraft capable of takeoff at weights of 300,000 lbs or more; *Large* continued to denote aircraft weighing more than 12,500 lbs, (but less than 300,000 lbs), while *Small* described aircraft weighing 12,500 lbs or less. The FAA also issued wake turbulence separation standards between aircraft. It required controllers to ensure in IFR that all non *Heavy* aircraft following a *Heavy* maintain at least a 5-nm separation distance, while a *Heavy* following a *Heavy* was separated by at least 3 nm (or a 7-nm reduction compared to the interim restriction) (Refs. 12 and 13). In 1973, the FAA increased the separation distance for a *Heavy* following a *Heavy* to 4 nm, and, in 1975, increased the separation distance for a *Small* following a *Heavy* to 6 nm. The international community formally adopted these separation standards in 1978 through the International Civil Aviation Organization (ICAO) (Ref. 14). Tables 1a and 1b provide a summary of selected changes in separation standards for both the US and United Kingdom (UK). Tables 2 and 3 provide information on the current aircraft weight categories and separation criteria for the US, UK, and ICAO.

The increasing number of capacity-constrained airports brought on by the traffic growth in the 1980s has prompted a resurgence in wake turbulence research by the FAA. According to the FAA 23 US airports were capacity-constrained in 1993 (i.e., exceeding 20,000 hours of annual flight delays), with 32 airports anticipated to be capacity-constrained by 2003 (*Section 1.4.5* in Ref. 15). The FAA is currently funding research efforts to better understand wake-vortex strength, duration, and transport characteristics, in part to determine if aircraft separation standards can be safely reduced. Such reductions, the FAA estimates, may increase airport capacity by 15% in IMC (*Section 5.2.5 of Appendix H.2.7* in Ref. 15).

⁵As early as 1961, the *Large* aircraft category was defined as "[a]ircraft of more than 12,500 pounds maximum certificated takeoff weight" (*FAA Civil Air Regulations Part 60 - Air Traffic Rules*, 15 May 1961). This definition, as originally formulated, appears to have been unrelated to wake turbulence.

4. STUDY METHODOLOGY

This paper examines the operational impact of the current and proposed aircraft wake turbulence weight categories on airport capacity. The airports used in this study were the top ten US airports experiencing operational delays of 15 minutes or more in 1993 (refer to *Table 1-3* in Ref. 15): Newark (EWR), Chicago O'Hare (ORD), Boston Logan (BOS), New York LaGuardia (LGA), Los Angeles (LAX),⁶ New York John F. Kennedy (JFK), Dallas Fort Worth (DFW), San Francisco (SFO), Atlanta Hartsfield (ATL), and St. Louis Lambert Field (STL).

The approach employed herein was to examine the scheduled traffic operations at these airports using a standard, representative runway configuration to determine the influences the proposed weight classifications would have on traffic mix and airport capacity. Two runways at LAX were selected as the representative runway configuration. The LAX configuration (Figure 1) features parallel runways (Runway 25L was used for arrivals and Runway 25R for departures), eight exits located along the runway, and runway lengths that are adequate for *Heavy* departure operations.⁷

The four aircraft classification proposals used for this study were: 1) standard radar separation without application of wake turbulence procedures ("*Weight Classification 0*," or "*WC0*")--that is, 3 nm separation for successive departures⁸ and 2.5 nm separation for successive arrivals;⁹ 2) the current FAA weight classification scheme (*WC1*); 3) raising the boundary between *Large* and *Small*

⁶Even though Denver Stapleton International (DEN) was number five of the top ten in 1993, LAX replaced it for this study because DEN was closed in 1995 and LAX has a more representative runway configuration.

⁷Both dependent and independent simultaneous runway operations were considered for this study.

⁸In the simulation all successive departure-departure operations are assumed to be on the same course. Current FAA procedures permit a one nautical mile separation between successive departures if courses diverge immediately after takeoff (*Section 5-112a* in Ref. 16).

⁹Current air traffic control procedures permit a 2.5-nm separation between aircraft established upon the final approach course within 10 nm of the landing runway under certain conditions. (*Section 5-72f* in Ref. 16).

aircraft to 29,000 lbs maximum takeoff weight (WC2); and 4) raising the boundary between *Large* and *Small* aircraft to 75,000 lbs maximum takeoff weight (WC3). The representative traffic mix for each of these classification proposals was obtained by averaging the traffic mixes of all ten airports.

The WC2 and WC3 weight classification proposals are based on discussions at the June 1995 Industry Team Meeting. Table 3 summarizes the weight classification proposals WC2 and WC3 as addressed in the study.

The simulation employed for this study was a computer model developed by The Boeing Company known as *CAPACITY*.¹⁰ This simulation model was used to conduct the analysis of the impact of the proposed aircraft wake turbulence weight categories on airport capacity. Once the mixes were determined, capacity simulations for each mix were executed and the results compared. The variation in capacity was then plotted as a function of the percentage of arrival operations to provide a detailed depiction of the traffic characteristics influencing capacity.

5. AIRPORT CAPACITY AND DELAY FACTORS

Herein, *practical* airport capacity refers to the expected hourly operations rate when the average delay per operation is six minutes. Simple analytical formulas, assuming an infinite stream of traffic, exist to calculate the maximum hourly capacity (infinite delay) for a single runway configuration and traffic mix employing first-come/first-served operational procedures. More complex runway configurations and operational procedures require non-analytical and computer simulation techniques to estimate the hourly capacity as a function of average aircraft delay.

The airport capacity and delay factors (Figure 2) used for this analysis were: weather, traffic characteristics, terminal airspace route structure, airplane performance, runway separation minimums, Air Traffic Control (ATC) system performance,

pilot response characteristics, and airport runway configuration.

Current methods of increasing airport capacity involve improving the airfield, airport facilities and equipment, and operational procedures. Such improvements include: constructing a new runway, improving runway exits to reduce runway occupancy time, relocating an existing runway, upgrading the navigational landing aids and weather observing equipment, reducing separation, improving the sequencing of departures, etc.

5.1 Weather

Figure 3 indicates that 72% of all delays were attributed to weather in the US during 1993 (refer to Table 1-1 in Ref. 15). Typically, weather dictates the type of procedures that will be in effect; for example, visual approaches for visual meteorological conditions (VMC) or instrument approaches for IMC. The declaration of VMC or IMC is determined by field instrumentation that measures ceiling and visibility. Under VMC and upon acceptance of a visual approach,¹¹ the separation between arrivals on approach is the pilot's responsibility. On average, arrival longitudinal separation is closer in VMC than in IMC, and thus provides greater capacity.

5.2 Airport Runway Configuration

Airport runway configuration is defined as the way in which the runways are aligned or positioned. Some common configurations are parallel runways, crossing runways, converging runways, and diverging runways. In addition, the location and design of runway exits have a significant influence on runway occupancy time for an operation. For example, departing aircraft wait until arriving aircraft have exited the runway to avoid conflict with a missed approach or a touch and go operation. Moreover, closely spaced parallel runways (i.e., when the centerline spacing between parallel runways is 2500ft/760m or less) must be treated as a single runway due to wake vortex considerations--specifically, the concern that wake vortices may transport laterally from an adjacent runway due to both ground effect and crosswind.

¹⁰ *CAPACITY* is a fast-time computer program that simulates arrival and departure operations of an airport runway for estimating average delays and airfield operational capacity (Ref. 17).

¹¹ During a visual approach in the US, the reported weather at the airport must be a ceiling at or above 1,000 feet and visibility of three miles or greater.

5.3 Traffic Characteristics

Aircraft are grouped into categories of maximum takeoff weight since *weight* is a significant factor in calculating the vortex strength (circulation). Examples of weight-related factors that can significantly influence airport capacity are the percentage of *Heavy* aircraft (e.g., Boeing 747, Airbus 340, and McDonnell Douglas DC-10) and the percentage of arrival operations.

5.4 Terminal Airspace Route Structure

The terminal airspace route structure influences the number of traffic streams arriving and departing an airport. The sequencing of aircraft is dependent upon the endpoints of standard procedures and directions of traffic flow operations. For example, the use of alternating departure routes enables fanning in back-to-back departure operations so as to reduce the separation between departures to one nautical mile unless wake vortex rules apply. Airspace route structure contributes to operational efficiency by influencing runway assignments. Also, noise abatement requirements strongly influence airspace route structure and may negatively influence capacity.

5. Airplane Performance

Airplane performance influences airport capacity. For example, climb rates are important to the clearing of runways during departure. Controllers use proper sequencing and spacing of aircraft to take full advantage of airplane performance.

5.6 Terminal Area Separation Minima

Terminal Area Separation or runway spacing protect: slower aircraft from being overtaken by a faster following aircraft, a following aircraft from losing roll control due to wake vortex encounters, and aircraft from entering into conflicts due to flight path convergence. Runway spacing must take into account the limits and uncertainties of traffic monitoring equipment (e.g., radar), and runway occupancy limitations (Figures 4 and 5).

5.7 ATC System Performance

ATC system performance refers to various factors such as controller response times, the sequencing and spacing of aircraft onto final approach, the precision of maintaining the nominal separation of aircraft at the threshold and at the final approach fix (FAF), and balancing runway utilization.

5.8 Pilot Response Characteristics

Pilot response, with regard to the *CAPACITY* simulation analysis, refers to issues relating to braking times, spoiler deflection response time, and departure release response time.

6. OAG ANALYSIS

Tables 4(a-c) list the traffic mix at the ten airports along with the *practical* capacity value where the percentage of arrivals is 50%. On average, *Heavy* aircraft constitute about 12% of the traffic mix.¹² The airports with a large percentage of *Heavy* aircraft are: JFK with 43%, LAX with 19%, SFO with 17%, and ATL with 13%. Since JFK and LAX have the highest percentage of *Heavy* aircraft and consistently the lowest capacity value, it would seem that the application of wake turbulence procedures has a more significant impact on reducing capacity at these airports than the other airports.

Tables 4(a-c) indicate that the percentage of *Large* aircraft in the mix positively influences the capacity in contrast to the percentage of *Heavy* and *Small*. Furthermore, since these Tables indicate that the capacity values corresponding to the representative (averaged) traffic mix represent the average capacity values for the ten airports, it can be assumed that those values are representative for comparison purposes. Table 5 indicates the type of aircraft found in the OAG affected by changing the *Small* category as proposed.

The effect of raising the upper limit of the *Small* category to 29,000 lbs results in an increased separation for aircraft following certain heavier aircraft (e.g., Learjet and some Dassault jets) as well as the addition of several turbo props to this classification. The impact to capacity is related primarily to the increased separation. Increasing the *Small* category weight range to include aircraft weighing less than 75,000 lbs primarily results in combining the turbo props and single-engine aircraft into the *Small* category.

7. CAPACITY RESULTS

Figure 6 illustrates the impact of the current wake turbulence separation standards on *practical* ca-

¹² No scheduled traffic at the ten airports studied weighed more than 255,000 lbs and less than 300,000 lbs; thus, WC2 and WC3 retain the 300,000 lbs boundary line dividing the *Heavy* and *Large* aircraft categories.

capacity for the airport configuration and averaged traffic mixes used in this study. It was assumed that if wake turbulence procedures are not applied, then the only separation requirement would be due to radar procedures.¹³ Figure 6 indicates that there is a 12% loss in capacity when current FAA separations are employed and arrivals comprise 50% of the operation. This loss changes according to the percentage of arrivals (from 6% for no arrivals to 20% for all arrivals) and is attributed to the difference in the successive arrival separation being less than the successive departure separation. Fanning of successive departure operations will provide even more capacity.

Figure 7 shows a comparison between the simulation results for the current FAA weight classification scheme (WC1) and the weight classification schemes (WC2 and WC3) used in the study. Figure 7 suggests that WC3 consistently results in the greatest reduction in capacity relative to the current FAA capacity levels. Generally, this loss is about two operations per hour. Even though Figure 7 shows that this reduction in capacity may be only about 4%, the key inquiry may be to determine the impact at a hub airport. Though it is difficult to measure the impact of losing one or two operations per hour, such a small loss may be deemed critical at a hub airport during peak periods where one flight serves a bank of connecting flights. This scenario has the potential of propagating delays through the system. However, such disruptions might be avoided through scheduling changes.

Table 6 lists the capacity results for all four weight classification proposals studied. The table indicates that capacity decreases as the *Small* category becomes more inclusive (i.e., includes aircraft of 75,000 lbs or less in contrast to 29,000 lbs or less). Though the results for WC2 and WC3 are very similar, it appears that WC3 would increase the (longitudinal) separation of turbo props behind *Heavy* aircraft, and therefore result in a decrease in capacity. WC3 consistently shows the largest decrease in capacity. Since the simulation indicates that capacity decreases occur most frequently at airports where there are a large percentage of *Heavy* aircraft (e.g., JFK and LAX),

¹³ Successive arrival operations were separated by 2.5 nm, successive departure operations by 3 nm, and a departure followed by an arrival was separated by 2 nm.

it is surmised that these airports are the ones which would experience more delays during peak hours.

Study results indicate that if it were possible to operate closely-spaced parallel runways as though they were independent runways, an even larger gain in capacity would result. The *practical* capacity increased to 62 operations per hour for the independent runway configuration. This showed a gain of 28% when the runways were operated independently,¹⁴ with arrivals and departures on separate runways, and using the WC1 (current FAA) traffic mix.

Understanding the lateral transport of wake vortices would therefore also likely contribute to increasing capacity. Accordingly, researching the use of communication, navigation, and surveillance (CNS) technologies to foster increased use of parallel runways for conducting simultaneous operations may lead to capacity gains.

8. CONCLUSION

This study has examined the impact of the current FAA wake turbulence aircraft weight categories on airport capacity. Computer simulation results indicate that the current wake turbulence separation standards have reduced airport capacity by about 12% during IMC relative to the standard radar separation (2.5nm between arrivals and 3nm between departures). In addition, these results indicate that a further decrease of about 4% could occur by revising the *Small* aircraft category to include aircraft of 75,000 lbs or less, and revising the *Heavy* aircraft category to include aircraft weighing more than 255,000 lbs (see also footnote 12).

The study also indicated that decreased capacity typically occurs during the hours in which a majority of the operations are arrivals. These decreases could be mitigated through scheduling. In addition, further study is needed to understand how delays are propagated through a network of

¹⁴ In the US, independent runways have a centerline separation of 4,300 feet or more. When a Precision Runway Monitor (PRM) is present, independent runways may have a centerline separation down to 3,400 feet (refer to Sections 5-126a2 and 5-127a in Ref. 16).

airports when there is a loss of operations at major hubs - even of one or two operations per hour.

Furthermore, this study indicates that the greatest gain (i.e., a potential 28% increase) in airport capacity may be derived from the increased use of parallel runways for simultaneous operations.

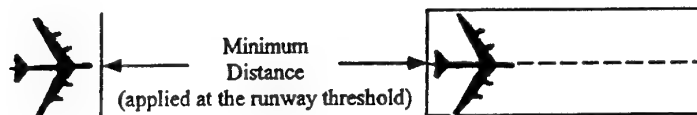
ACKNOWLEDGMENTS

The author is indebted to M. A. Aslin, L.W. Barnes, B. Bays-Muchmore, Y.S. Ebrahimi, J.F. Haydon-Hawkins, R.W. Schwab, C.M. Stafford, and J. Vasatka (The Boeing Company); M.S. Alcabin (formerly of The MITRE Corporation); and G.P. Lawing (retired Chief of FAA Wash. DC Terminal Operations and Procedures Branch) for their assistance.

REFERENCES

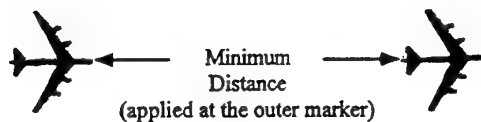
1. *FAA Wake Vortex Training Aid Document*, DOT/FAA/RD-95-6, DOT-VNTSC-FAA-95-4, Final Report, February 1995.
2. *Position Paper for Wake Turbulence Weight Classification And Separation Standards*, The Wake Turbulence Industry Team, June 1995.
3. *Final Recommendations*, Science of Separation Distances Subcommittee, Wake Turbulence Industry Team, June 1995.
4. *Facts of Flight: Practical Information About Operation of Private Aircraft*, p. 11, Civil Aeronautics Administration, Department of Commerce, Washington DC, March 1947.
5. *The Rolling Up of the Trailing Vortex Sheet and Its Effect on the Downwash Behind Wings*, Spreiter, J.R., Sacks, A., p.21-32, 72, *Journal of the Aeronautical Sciences*, 18, 1 (January 1951).
6. Circular Letter W-380-105, *Effect of Large - Plane 'Turbulence' on Small Aircraft*, Civil Aeronautics Administration, Department of Commerce, Washington DC, 3 March 1952; Circular Letter W-380-213, Civil Aeronautics Administration, Department of Commerce, Washington DC, 28 August 1952.
7. *Hazards to Small Aircraft Flown in the Wake of Large or Heavy Jet and Propeller Driven Aircraft - Aviation Safety Release No. 399*, Civil Aeronautics Administration, Department of Commerce, Washington DC, 19 December 1955.
8. *Furumizo v. United States*, 245 F. Supp. 981 (D. Haw. 1965), aff'd, 381 F.2d 965 (9th Cir. 1967)
9. *Lightenburger v. United States*, 298 Supp. 813 (C.D. Cal. 1969), rev'd, 460 F.2d 391 (9th Cir.), cert. denied, 409 U.S. 983 (1972).
10. *Aviation Week & Space Technology*, p. 20, 26 January 1970.
11. *Aviation Week & Space Technology*, p. 25-26, 23 February 1970.
12. *Aviation Week & Space Technology*, p. 225, 227, 9 March 1970.
13. FAA General Notice ("GENOT"), 26 February 1970.
14. PANS-RAC/Document 4444, *Amendment 10 to the ICAO Procedures or Navigation Services - Rules of the Air and Air Traffic Services*, ICAO, 1978.
15. *1994 FAA Aviation Capacity Enhancement (ACE) Plan*.
16. FAA Order 7110.65H, *AIR TRAFFIC CONTROL*, Change 5, 30 March 1995.
17. D6-55558, *PC Capacity User's Guide*, J.J. Robinson, Boeing, 13 October 1990.

**Table 1a Selected Developments in FAA
Wake Turbulence Separation Standards**



Period	FAA	
Pre - 1970	All Aircraft	3nm
January 1970	All Aircraft following a 747 or C-5A	10nm
March 1970	<i>Heavy</i> followed by <i>Large / Small</i>	5nm
	<i>Heavy</i> followed by <i>Heavy</i>	3nm
1973	<i>Heavy</i> followed by <i>Heavy</i>	4nm
1975	<i>Large</i> followed by <i>Small</i>	5nm
	<i>Heavy</i> followed by <i>Small</i>	6nm
1994	All Aircraft following a 757	4nm

**Table 1b Selected Developments in UK CAA
Wake Turbulence Separation Standards**



Period	UK CAA	
Pre - 1972	All Aircraft	(3nm separation)
1972	Larger followed by Smaller	(5nm separation)
	UK Introduces Wake Turbulence Incident Reporting Program	
1978*	UK Adopts ICAO Aircraft Classification Scheme <i>Heavy, Medium, Light</i>	
1982	UK Introduces the <i>Small</i> Aircraft Category	
1983	UK Commissions Wake Turbulence Incidence Database	
1993	UK Commissions Trials of Revised Wake Turbulence Separation Minima	

* Wake Turbulence Separation Standards are internationally adopted with approval of Amentment 10 to the ICAO PANS-RAC 4444 Document.

Table 2 Current Separation Standards

WEIGHT CLASSIFICATIONS (lbs)			
CATEGORY	FAA (WC1)	UK CAA	ICAO
Heavy	≥300,000	≥300,000	≥300,000
Large	<300,000 >12,500	n/a	n/a
Medium	n/a	<300,000 >88,200	<300,000 >15,500
Small	≤12,500	≤88,200 >37,500	n/a
Light	n/a	≤37,500	≤15,500

300,000 lbs = 136,000kg
 88,200 lbs = 40,000kg
 37,500 lbs = 17,000 kg
 15,500 lbs = 7,000 kg
 12,500 lbs = 5,700 kg

GROSS WEIGHT CATEGORIES		MINIMUM SEPARATION DISTANCE (nm)		
LEADING AIRCRAFT	FOLLOWING AIRCRAFT	FAA	UK CAA	ICAO
Heavy	Heavy	4	4	4
	Large	5	n/a	n/a
	Medium	n/a	5	5
	Small	6	6	n/a
	Light	n/a	8	6
Large	Large	3*	n/a	n/a
	Small	4	n/a	n/a
Medium	Medium	n/a	3	3
	Small	n/a	4	n/a
	Light	n/a	6	5
Small	Light	n/a	4	n/a

* As an interim measure, the FAA implemented procedures effective July 1, 1994 to require 4 nautical miles separation for small, large and heavy category aircraft following B-757.

n/a (Not applicable) Separation not based on wake turbulence.

Table 3 Separation Standards Used in Capacity Study

WEIGHT CLASSIFICATIONS -lbs		
CATEGORY	(WC2)	(WC3)
Heavy	≥300,000	≥300,000
Large	<300,000 ≥29,000	<300,000 ≥75,000
Small	<29,000	<75,000

300,000 lbs = 136,000kg
 75,000 lbs = 34,000kg
 29,000 lbs = 13,200kg
 12,500 lbs = 5,700kg

GROSS WEIGHT CATEGORIES		MINIMUM SEPARATION DISTANCE (nm)
LEADING AIRCRAFT	FOLLOWING AIRCRAFT	WC2 / WC3
Heavy	Heavy	4
	Large	5
	Small	6
Large	Large	3
	Small	4
Small	Small	3

NOTE: Successive departure operations are separated by the standard radar separation of 3 nm, except where the leading departue is a *Heavy* aircraft, then the separation is increased to 5 nm for wake turbulence considerations.

Table 4a Traffic Mixes - Top Ten Airports vs. WC1 (Current FAA) Weight Categories with Resultant Practical Capacity

	EWR	ORD	BOS	LGA	JFK	DCA	SFO	ATL	STL	LAX	Representative Mix ²
Heavy	8.6 %	10.6 %	7.5 %	3.7 %	42.8 %	7.0 %	16.6 %	12.6 %	2.8 %	19.4 %	12.2 %
(757) ¹	4.6 %	9.4 %	6.0 %	7.6 %	5.0 %	7.5 %	10.5 %	9.1 %	0.3 %	7.4 %	7.1 %
Large	86.2 %	80.0 %	84.7 %	88.6 %	51.6 %	85.1 %	72.6 %	76.8 %	96.8 %	72.0 %	80.0 %
Small	0.6 %	0.0 %	1.8 %	0.1 %	0.6 %	0.4 %	0.3 %	1.5 %	0.1 %	1.2 %	0.7 %
ops/hr	49.21	49.59	47.39	49.99	46.27	49.49	48.54	48.30	50.20	47.29	48.17

Table 4b Traffic Mixes - Top Ten Airports vs. WC2 Weight Categories (Small < 29,000 lbs) with Resultant Practical Capacity

	EWR	ORD	BOS	LGA	JFK	DCA	SFO	ATL	STL	LAX	Representative Mix ²
Heavy	8.6 %	10.6 %	7.5 %	3.7 %	42.8 %	7.0 %	16.6 %	12.6 %	2.8 %	19.4 %	12.3 %
Large	75.8 %	84.9 %	48.7 %	79.1 %	36.6 %	70.1 %	55.9 %	66.6 %	76.4 %	44.7 %	65.3 %
Small	15.6 %	4.5 %	43.8 %	17.2 %	20.6 %	22.9 %	27.5 %	20.8 %	20.8 %	35.9 %	22.4 %
ops/hr	47.32	49.95	45.79	48.79	45.25	47.58	47.22	48.03	48.52	45.88	46.71

Table 4c Traffic Mixes - Top Ten Airports vs. WC3 Weight Categories (Small < 75,000 lbs) with Resultant Practical Capacity

	EWR	ORD	BOS	LGA	JFK	DCA	SFO	ATL	STL	LAX	Representative Mix ²
Heavy	8.6 %	10.6 %	7.5 %	3.7 %	42.8 %	7.0 %	16.6 %	12.6 %	2.8 %	19.4 %	12.3 %
Large	56.9 %	72.7 %	42.4 %	74.0 %	20.8 %	68.0 %	55.9 %	65.5 %	69.5 %	44.7 %	59.0 %
Small	34.5 %	16.7 %	50.1 %	22.3 %	36.4 %	25.0 %	27.5 %	21.9 %	27.7 %	35.9 %	28.7 %
ops/hr	47.04	49.55	46.66	49.76	45.18	48.49	47.45	48.10	49.64	46.66	46.40

¹ Although this is a Large category aircraft, the FAA implemented procedures effective 1 July 1994 as an interim measure, to require 4 nm separation for Small, Large, and Heavy category aircraft following a B-757.

² The 'Representative Mix' is the average of the traffic mixes for all ten airports.

Table 5 Scheduled Aircraft Impacted by Changing *Small* Category to Include Aircraft Weighing Less than 75,000 lbs

OAG Code	Weight (lbs)	Wingspan (feet)	Speed (knots)
BANDAI	12,500	50.3	92
DHTOTT	12,500	65.0	75
SWMETR	12,500	46.3	112
DORNER	12,183	55.7	87
J31BAE	14,550	52.0	99
BCH 19	16,600	54.5	116
J41BAE	22,377	60.0	99
SHTBRO	26,000	74.9	104
S/F 340	27,000	81.2	121
DHC-8	33,200	85.0	90
ATR42	34,700	80.6	105
DHC-7	44,000	93.0	83
CONVAR	46,200	91.8	107
FOK-28	65,000	77.3	119

**Table 6 Traffic Mix and Capacity Comparison
(50% Arrivals and Dependent Runway Configuration)**

Category	Radar* (WC0)	Current FAA (WC1)	Small <29,000 lbs (WC2)	Small <75,000 lbs (WC3)
Heavy	12%	12%	12%	12%
757		7%		
Large	87%	80%	65%	59%
Small	1%	1%	23%	29%
Operations per Hour	54	48	47	46
% Change	+12%	Baseline	-2%	-4%

* Radar separations without application of wake turbulence procedures.

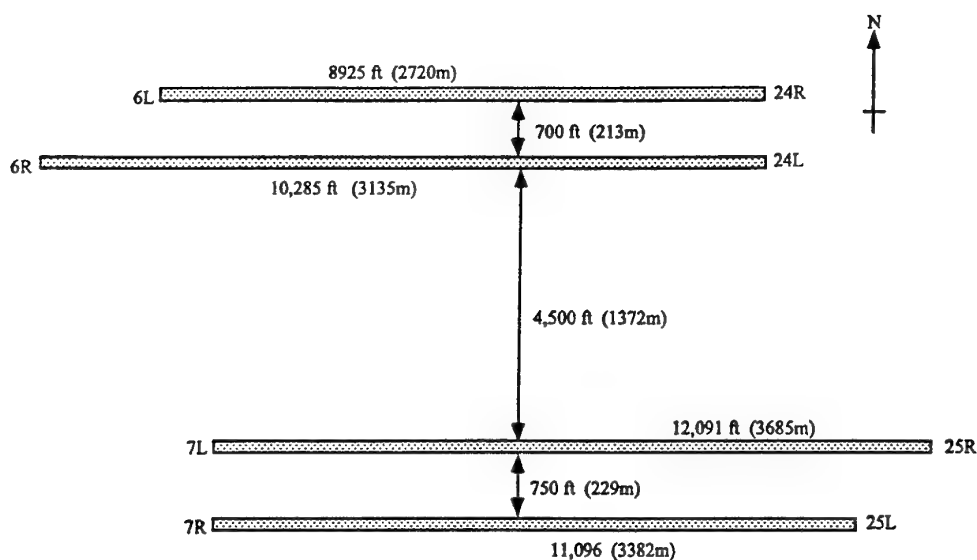


Figure 1 LAX Runway Configuration

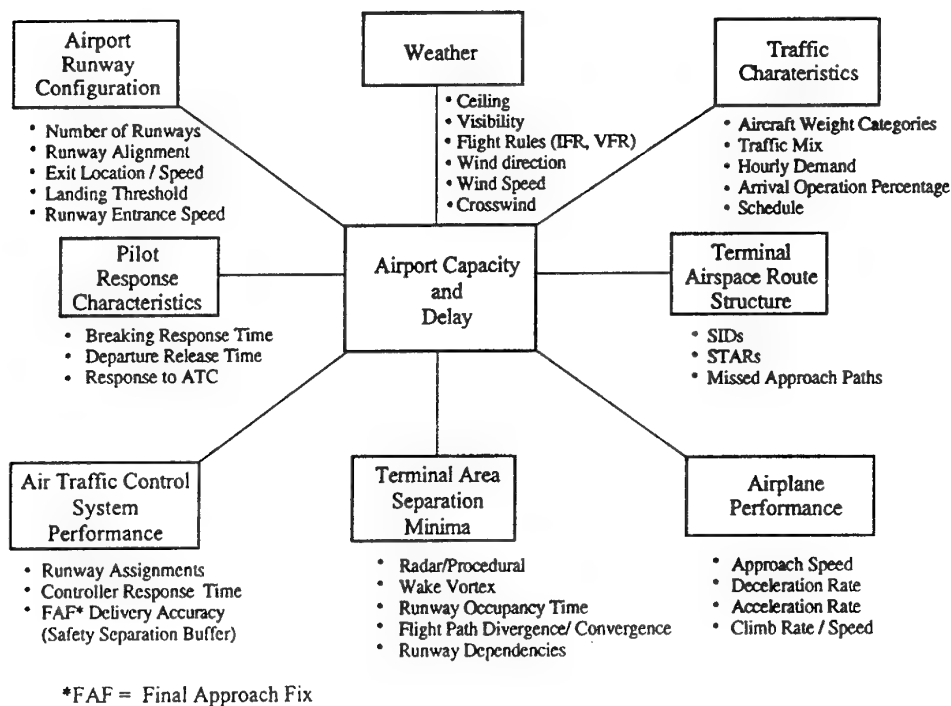
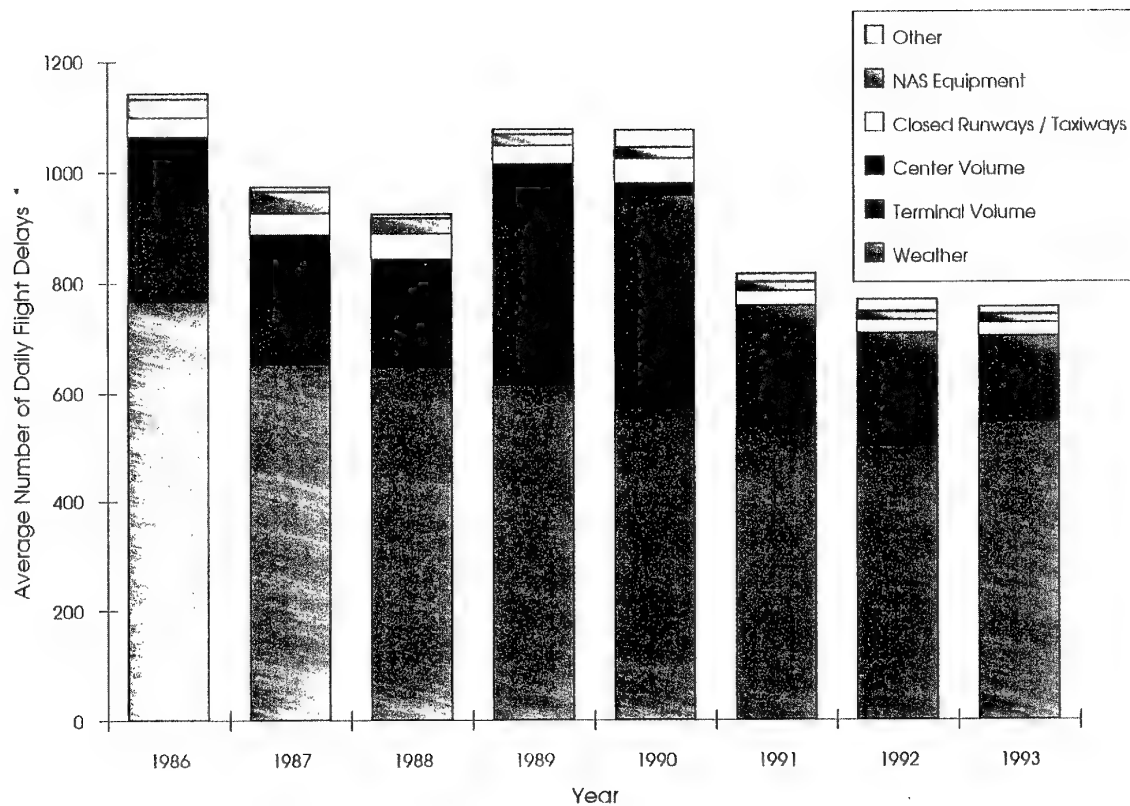


Figure 2 Factors Influencing Airport Capacity and Delay



* Delay exceeding 15 minutes

Source: FAA 1994 ACE Plan, Table 1-1

Figure 3 Causes of Air Traffic Systems Delay for All US Airport

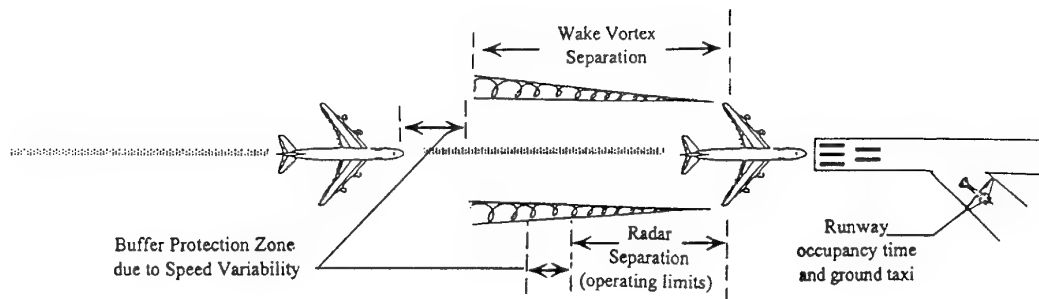


Figure 4 Aircraft Separation Standards Criteria for Approach Single Runway

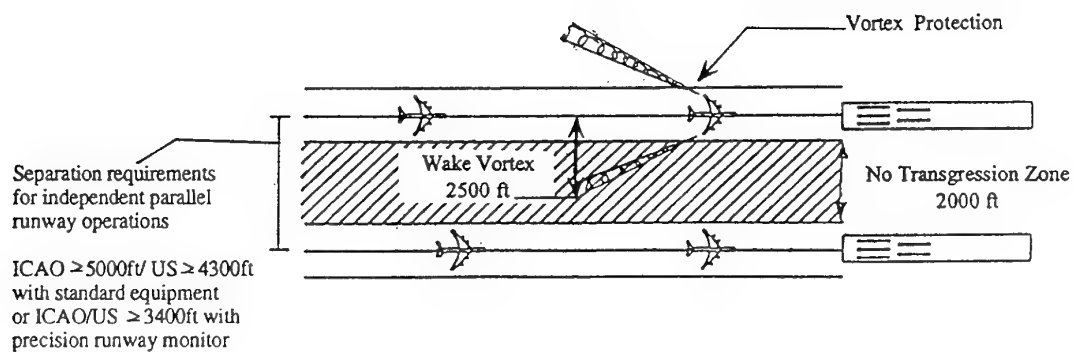
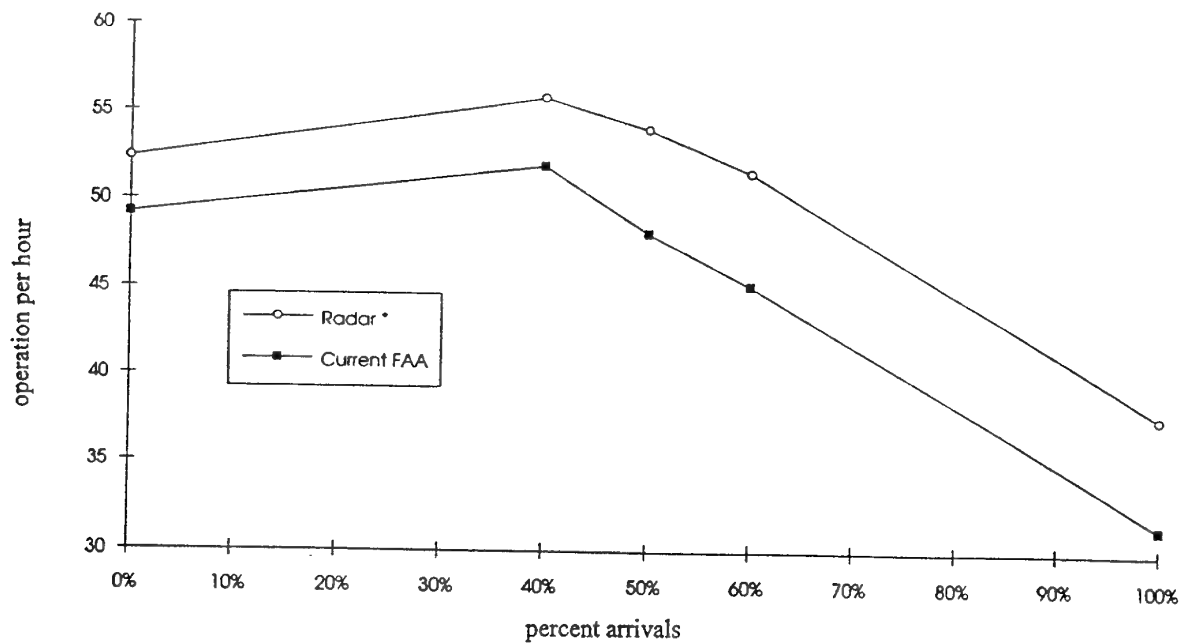


Figure 5 Aircraft Separation Standards Criteria for Approach Parallel Runway



* Radar separations without application of wake turbulence procedures.

Figure 6 Wake Turbulence Impact on Airport Capacity

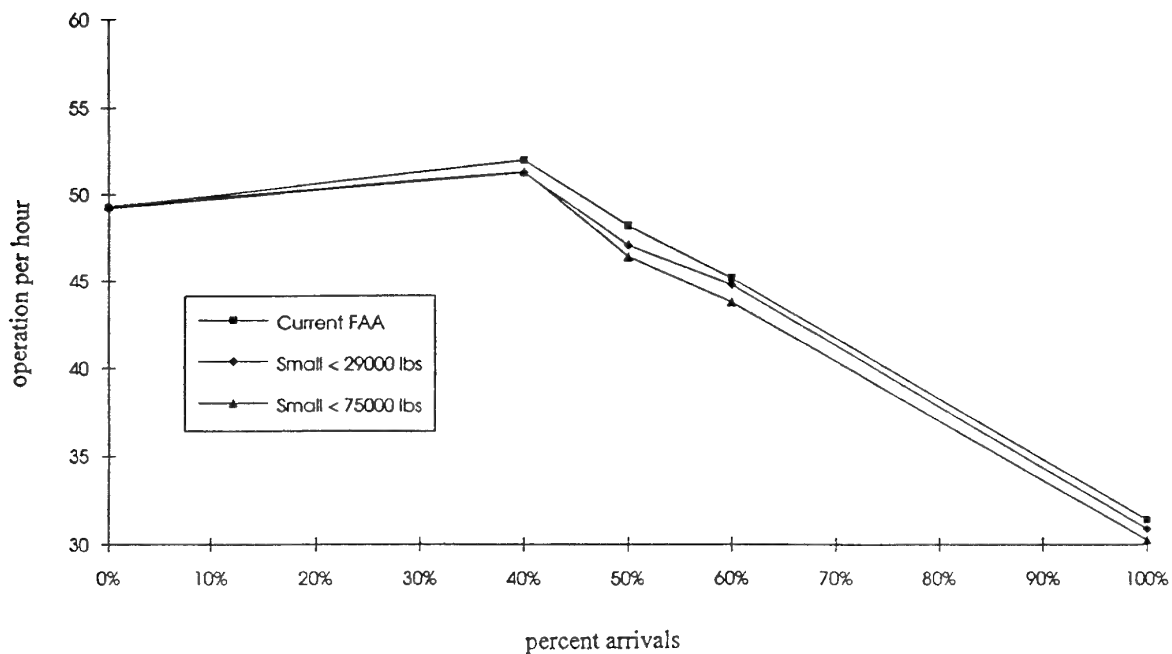


Figure 7 Airport Weight Classification Impact on Airport Capacity

An Aircraft Vortex Spacing System (AVOSS) For Dynamical Wake Vortex Spacing Criteria

D.A. Hinton
NASA, Langley Research Center
Mail Stop 156-A
Hampton, VA 23681-0001, USA

Preface

A trend for increased air travel has led to more frequent flight delays and associated costs to the traveling public and to the air carriers. One response is an increased interest in maximizing the efficiency of available runway capability. Under current airport operations a degradation in weather conditions from clear to poor seriously degrades capacity. The National Aeronautics and Space Administration is addressing the problem through its Terminal Area Productivity (TAP) Program. The major goal of the TAP program is to provide the technology base and systems to permit the same airport capacity levels during instrument meteorological conditions that are presently available during visual airport operations. Two major initiatives under TAP are the development of advanced ATC automation systems and wake vortex systems to improve terminal area efficiency and capacity. NASA Ames is the responsible center for development and demonstration of a Center-TRACON Automation System (CTAS). This automation provides aids to the controller to effectively schedule and sequence arrivals and minimize variations in desired interarrival spacing. The automation provides an opportunity to dynamically alter the wake vortex separation constraint as a function of the weather. NASA Langley is performing the research and development to develop the automated wake system, known as the Aircraft Vortex Spacing System (AVOSS).

During instrument flight conditions ATC has direct responsibility for aircraft separation and applies wake vortex constraints that are not weather dependent. Separation must therefore be based on worst case weight differences between and within aircraft weight categories and wake persistence observed during weather conditions favorable for long vortex life. In the United States, responsibility for final approach separation may be given to the pilot in visual meteorological conditions. There are no minimum following distances that must be applied during visual operations and, in many cases, the primary constraint on following distance is runway occupancy time. In visual conditions that are favorable for rapid vortex demise or drift, or when following aircraft of very similar size and weight, pilots frequently apply less separation than would be required in instrument conditions. There is no fundamental reason to believe that vortices behave differently in visual and instrument meteorological conditions. By quantifying the atmospheric effects on wake behavior, the same reduced spacing should be possible in instrument conditions.

The purpose of the AVOSS is to integrate current and predicted weather conditions, wake vortex transport and decay knowledge, wake vortex sensor data, and operational definitions of acceptable strengths for vortex encounters to produce dynamical wake vortex separation criteria. By considering ambient weather conditions the wake separation distances can be relaxed during appropriate periods of airport operation. With the appropriate interface to CTAS, spacing can be tailored to specific generator/follower aircraft types rather than several broad weight categories of aircraft. In a manual ATC, a simplified form of the AVOSS concept may be used to inform ATC when a fixed alternate, reduced separation standard may be used for the "large" and "heavy" aircraft categories. Work is currently underway to address the critical disciplines and knowledge needs to demonstrate a prototype AVOSS in the 1999 time frame. This paper describes the concept of an operational AVOSS system, system ground rules and requirements, research needs, and the development efforts being followed.

Summary

A concept is presented for the development and implementation of a prototype Aircraft Vortex Spacing System (AVOSS). The purpose of the AVOSS is to use current and short-term predictions of the atmospheric state in approach and departure corridors to provide, to ATC facilities, dynamical weather dependent separation criteria with adequate stability and lead time for use in establishing arrival scheduling. The AVOSS will accomplish this task through a combination of wake vortex transport and decay predictions, weather state knowledge, defined aircraft operational procedures and corridors, and wake vortex safety sensors. Work is currently underway to address the critical disciplines and knowledge needs so as to implement and demonstrate a prototype AVOSS in the 1999/2000 time frame.

1. Introduction

A continuing trend for increased air travel, combined with severe environmental restrictions on expansion or new airport construction, has led to more frequent flight delays and associated costs to the traveling public and to the air carriers. One response has been an increased interest in maximizing the efficiency of the runway capability that is available. The National Aeronautics and Space Administration is addressing the problem through its Terminal Area Productivity (TAP) Program. The major goal of the TAP program is to provide the technology base and systems to permit the same airport capacity levels during instrument meteorological conditions that are presently experienced during visual airport operations. Two major initiatives under TAP are the development of advanced Air Traffic Control (ATC) automation tools (reference 1) and wake vortex systems to improve terminal area efficiency and capacity. NASA Ames Research Center is the responsible center for development, testing, and demonstration of a Center-TRACON Automation System (CTAS), which includes a Traffic Management Advisor (TMA), a Descent Advisor (DA), and a Final Approach Spacing Tool (FAST). This automation provides aids to the controller to effectively schedule and sequence arrivals and minimize variations in desired inter-arrival spacing. This automation provides an opportunity to dynamically alter the wake vortex separation constraint as a function of the weather and the actual aircraft pair type (as opposed to broad weight categories). NASA Langley Research Center is performing the research and development to develop the automated wake system, known as the Aircraft Vortex Spacing System (AVOSS).

The impact of wake vortex on aircraft separation standards under instrument conditions results from multiple factors. During instrument flight conditions ATC has direct responsibility for aircraft separation and applies wake vortex constraints that are not weather dependent. Separation must therefore be based on worst case weight differences between and within aircraft weight categories and wake persistence observed during weather conditions favorable for long vortex life. Under visual conditions, responsibility for separation may be given to the pilot during the final approach phase. There are no minimum following distances that must be applied during visual operations and, in many cases, the primary constraint on following distance is runway occupancy time. In visual conditions that are favorable for rapid vortex demise or drift, or when following aircraft of very similar size and weight, pilots frequently apply less separation than would be required in instrument conditions. There is no fundamental reason to believe that vortices behave differently in visual and instrument meteorological conditions. By quantifying the atmospheric effects on wake behavior, the same reduced spacing should be possible in instrument conditions.

The purpose of the AVOSS is to integrate current and predicted weather conditions, wake vortex transport and decay knowledge, wake vortex sensor data, and operational definitions of acceptable strengths for vortex encounters (acceptable vortex strength definition) to produce dynamical wake vortex separation criteria. By considering ambient weather conditions the wake separation distances can be relaxed during appropriate periods of airport operation. With the appropriate interface to planned ATC automation (CTAS), spacing can be tailored to specific generator/follower aircraft types rather than several broad weight categories of aircraft. In a manual ATC, a simplified form of the AVOSS concept may be used to inform ATC when a fixed alternate, reduced separation standard may be used for the "large" and "heavy" aircraft categories.

2. Prior Research

The AVOSS prototype development will build on prior wake vortex research activities conducted by the Federal Aviation Administration (FAA), Volpe National Transportation Systems Center, and industry. In particular, reference 2 provides a system concept that forms the foundation of the current system development. A detailed bibliography of prior research activities and a summary of the knowledge

gained can be found in references 3 and 4. A number of developments have occurred since the earlier system concept definition that enhance the opportunity to realize a practical system. The current development effort is being conducted in a strong meteorological frame work. Many advances in weather sensors, wake sensors, computer capability required for computational fluid dynamic modeling, and ATC automation have occurred which will aid development and implementation of an Aircraft Vortex Spacing System.

3. AVOSS Concept

The philosophy behind the AVOSS system is to avoid aircraft encounters with vortices above an "operationally acceptable strength." This avoidance is obtained through consideration of two factors, wake vortex motion away from the flight path of following aircraft and wake vortex decay. Since these factors are highly dependent on ambient meteorological conditions, as well as the generating aircraft position and type, the wake vortex constraints on aircraft separation are expected to vary significantly with the weather. Since terminal area metering to meet airport acceptance rates occurs well before final approach, the AVOSS system must provide a predictive capability to realize reduced approach spacing. Initial predictions of wake vortex separation constraints 30 to 50 minutes in advance of the actual approach may be required to take full advantage of reduced wake constraints. This predictive requirement will drive all efforts in the primary work areas of meteorological sensors, ATC procedures, and system architecture.

The potential for an encounter will be determined through consideration of vortex motion and boundaries of the approach and departure corridors used by the aircraft. The approach corridor concept is required since wake separation requirements must be established well before the approach. This requirement does not allow use of actual aircraft

position to provide separation between specific aircraft pairs.

The approach and departure corridors are sliced into a series of cross-sectional "windows", where the aircraft altitude varies at each window. The window concept provides a computational frame work for computing the varying vortex behavior at different heights above ground and for utilizing the varying meteorological conditions at those altitudes. The altitude or location on the approach or departure path with the longest lasting hazard will determine the separation required for the entire approach.

The term "operationally acceptable strength" indicates that vortex encounters will be permitted if the strength of the encountered vortex will have no adverse operational effect (pilot or passenger concern, increase in touchdown point dispersion, need to disengage autopilot, etc.) on the trailing aircraft. Such would be the case, for example, of a large turbojet transport encountering the wake of a small business-class jet. While the research is yet to define "operationally acceptable strength", this strength will be well below the strength required to produce an upset. FAA and industry consensus will be essential to the establishment of this strength limit.

The general AVOSS structure is shown in figure 1. The meteorological subsystem provides current and expected atmospheric state to the predictor subsystem. The predictor subsystem, to be discussed in detail below, utilizes the meteorological data, airport configuration, and aircraft specifications to predict the separation time required for a matrix of aircraft. The sensor subsystem monitors actual wake vortex position and strength to provide feedback to the predictor subsystem and to provide a warning to ATC if a spacing is sufficiently in error to require a wave-off.

Ground rules have been established for the development of

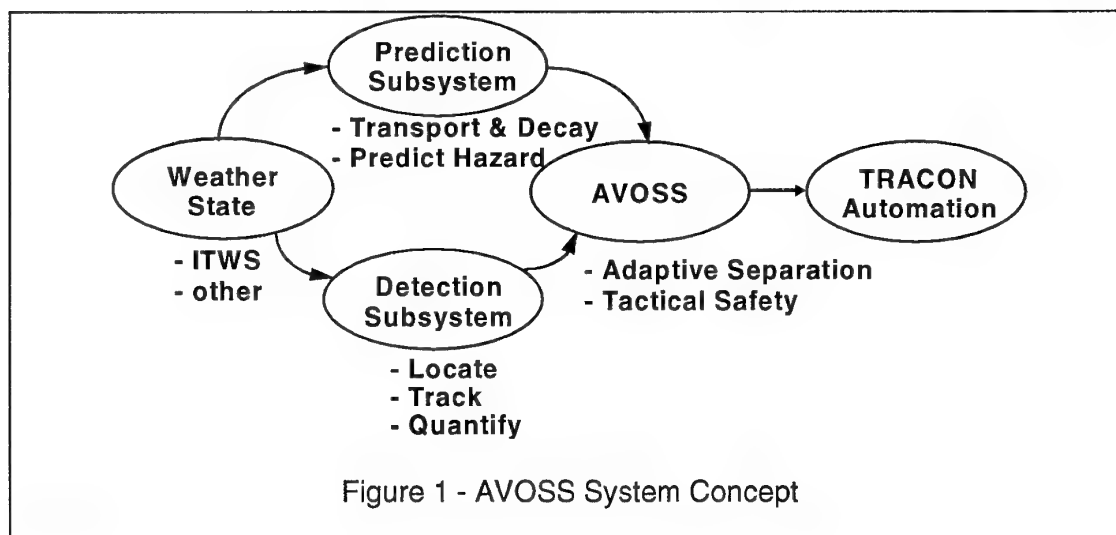


Figure 1 - AVOSS System Concept

an AVOSS. The ground rules are:

1. The development effort will be focused on a system that can be approved for operational use. This will require a large degree of robustness, reliance on readily available meteorological and wake sensors, graceful system degradation when sensors or subsystems fail, and cost realism.
2. The safety provided will be equal to or greater than the currently operational system.
3. The AVOSS will not require an increment in pilot skill levels or training requirements.
4. No aircraft structural or systems modifications will be required.
5. The AVOSS will not alter current pilot functions nor change airborne/ground responsibilities.
6. "Vortex-limited" spacing operations may require special ATC or flight procedures compatible with current skill levels. Examples may include executing straight-in Instrument Landing System (ILS) approaches and no intentional operations above glide slope by large or heavy aircraft.

As suggested above, the AVOSS system and ATC interface will require both technical processes and integration with operational practices. The technical aspects include understanding of vortex behavior under various atmospheric conditions, aircraft encounter dynamics, and sensor systems. The operational aspects include runway configuration and usage at a specific airport, the aircraft mix arriving during peak traffic periods, and procedures for vectoring aircraft to the localizer and on departure. The operational factors must be considered in the AVOSS implementation. For example, when all aircraft are constrained to full ILS approaches the precise knowledge of expected aircraft trajectory may allow AVOSS to provide the minimal spacing. When visual approaches are in use the relative uncertainty in aircraft trajectory may require reversion to a default spacing, or a less optimum spacing based only on vortex decay rates.

3.1 Predictor Subsystem Requirements and Architecture

The core of the AVOSS system is the predictor subsystem. This subsystem will accept weather state, a matrix of generating aircraft characteristics that relate to initial wake strength, dimensions of the operational corridor, and a matrix of limiting vortex strength for encounters with following aircraft. This data will be used in real-time to predict the inter-arrival time interval required, by the wake vortex constraint only, for each aircraft pair in the aircraft matrix. When weather conditions predicted to exist 20 to 50 minutes in the future are input, the predictor algorithms will provide the required spacing at that time. Uncertainty in weather state estimation and aircraft parameters must also be considered to provide an appropriately conservative separation prediction. The ATC system will use this data along with other constraints such as runway occupancy time

and radar control precision to establish actual aircraft pair spacing. Two prediction horizons are required, an 30 to 60 minute prediction for flow rate metering and a shorter time prediction for final approach and departure control use.

The AVOSS predictor subsystem is being designed to the following requirements. The adequacy of these requirements will be substantiated or changed as required during the development process.

1. The predictor algorithm must provide separation of aircraft from significant vortices along the entire final approach path, from glide slope intercept to the runway. This range is needed due to the differences in atmospheric state and vortex behavior at various altitudes. The required aircraft separation must be predicted for a series of "windows" along the approach path. An approximately logarithmic altitude selection is suggested, with windows spaced to intersect the approach path at altitudes of 25, 50, 100, 200, 400, 800 feet, and the glide slope intercept altitude. The development research may indicate the need for greater or fewer windows.
2. The predictor algorithm must function without detailed knowledge of aircraft approach flap setting, airspeed, or weight. Only aircraft type and whether the operation is a takeoff or a landing will be used. The reason for this requirement is that predicting aircraft speed, weight and configuration 30 minutes in advance would require mandating speeds for the crews and/or a modification to procedures and systems to permit data link of each aircraft operating weight and planned approach configuration to the ATC system. This violates the proposed ground rules. Since the predictor algorithm will not have complete knowledge of aircraft initial wake conditions the predictions provided will be based on the potential range of initial wake conditions. This should not incur a severe penalty on the system, since transport aircraft generally fly similar speeds in high density operations and most operators will use a narrow range of flap settings for a particular operation.
3. The predictor is not being used to predict the actual movement of any particular wake vortex. This would require exact, and unavailable, knowledge of atmospheric state at each spatial and temporal location on the flight path. Instead the predictor will estimate the range of expected wake behavior given the uncertainties in aircraft and atmospheric parameters.
4. The prediction algorithms will operate on a matrix of individual aircraft types, rather than the current 3 or 4 element matrix of aircraft weight categories.
5. The predictor algorithm must accommodate feedback from wake vortex sensors. The sensed wake behavior will be used to ensure system safety through mechanisms such as increasing uncertainty buffers when the wake behavior deviates from predictions, to revert to a default spacing criteria when a threshold of prediction errors is crossed, or to provide a time critical

alert to ATC if a wake persists long enough in the corridor to be a hazard to the following aircraft. The anticipated system will combine weather-based predictions with wake sensor feedback to reduce the level of uncertainty.

6. The predictor algorithm must be based on wake vortex knowledge that is or will be available in the near term, while accommodating increments in this knowledge.
7. The operational domain of the AVOSS will be the approach corridor and the initial climb corridor only. The purpose of AVOSS is not to reduce the number of wake encounters that currently exist in the initial descent and terminal area regions before beginning the approach. Operational procedures alone will be used prior to glide slope intercept for wake avoidance purposes.
8. The predictor algorithms must function in a sufficiently wide range of airport and meteorological conditions to improve airport capacity, but are not required to function in all conditions. Under conditions that do not permit accurate wake vortex predictions the AVOSS may provide existing manual ATC separation criteria as the "default" spacing.
9. The predictor algorithms and AVOSS operation will be tailored to commercial turboprop commuter and turbojet aircraft. The traffic mix at busy hub airports contain very few small aircraft during peak demand, and the airport capacity will be little effected by maintaining current separation standards for those aircraft. The technical risks and development schedule for AVOSS should be greatly enhanced by tailoring sensor development, wake studies, aircraft/wake interaction investigation, and operational procedures to these larger

commercial aircraft.

Given the basic predictor algorithm requirements, the structure of the predictor algorithms are suggested. Figure 2 shows the expected structure. The predictor subsystem will ingest meteorological data and projections, an aircraft specifications matrix, and airport configuration data. The meteorological data and projections will not only include the actual parameters of interest, but must also include the confidence intervals on those parameters. By combining meteorological data and airport configuration data AVOSS will establish data such as head wind and cross wind components at each corridor window.

The aircraft matrix will include that data required for each operational aircraft type to predict the initial wake characteristics. The first order wake data expected to be required includes the spacing of the wake cores and total circulation strength. First order estimates of these values can be calculated from aircraft wing span, weight, speed, and air density. Other factors, such as flap setting also affect the initial wake structure but initial examination of wake data, taken from a B727, B757, and B767 during tower flybys at Idaho Falls in 1990 (reference 5) suggest that a close approximation to the initial behavior can be estimated from span, weight, and speed alone. Initial AVOSS predictor algorithm development will proceed under the hypotheses that basic aircraft parameters are adequate for estimating the initial wake characteristics. Further research, some of which is described below, is needed to assess the need for detailed configuration data and more refined initial wake estimates. Under this assumption the speed of the aircraft can be predicted based on a nominal approach speed for the aircraft

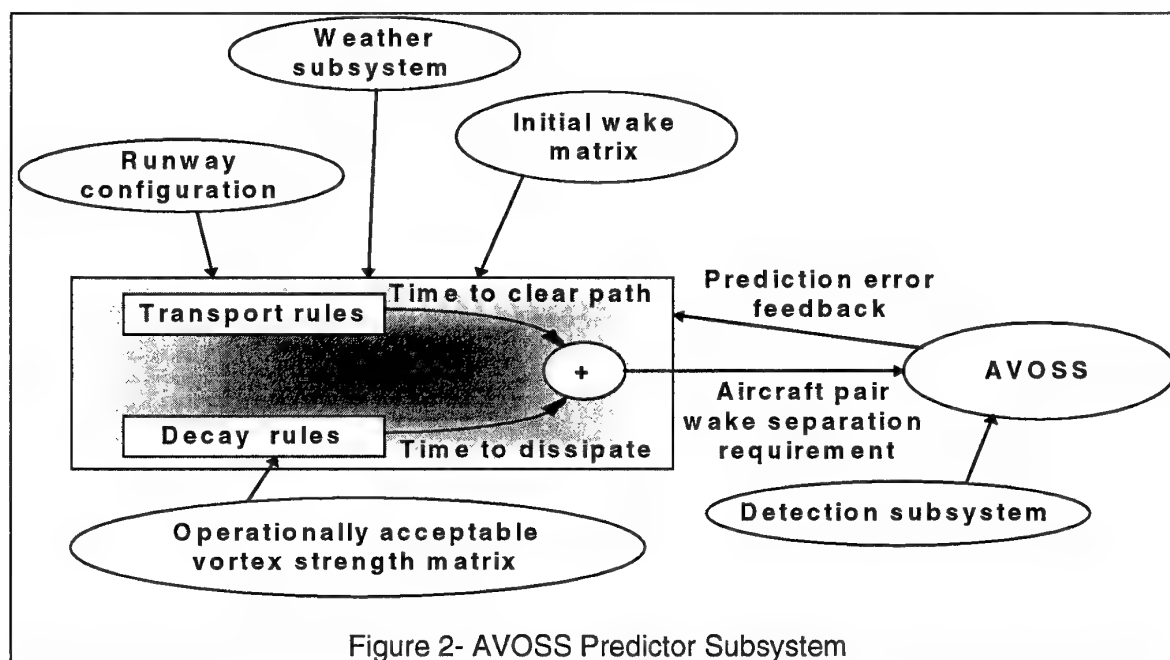


Figure 2- AVOSS Predictor Subsystem

type and the speeds actually being used on final during the high traffic period. Expected weights of the aircraft can be estimated from statistical distribution of takeoff and landing weights at a particular terminal.

After ingesting the required meteorological and aircraft data, the predictor will perform a set of computations for each window along the approach path. The first set of computations will determine, for each aircraft type, the time required for its vortices to exit the approach corridor. Consistent with the terminology of reference 2, this time is referred to as the "transport time" for the vortex in that window. Second, the predictor will determine the time required for the vortex of each aircraft to decay below a specified acceptable encounter strength for each following aircraft type. This calculation is also performed for each window along the approach and the time is referred to as the "decay time". This calculation requires, in addition to the meteorological and initial wake estimations, an acceptable vortex strength definition against which vortex strength can be compared. Next, the predictor compares the transport time and decay time for each aircraft pair at each window and takes the minimum value as an acceptable aircraft time spacing. This time is referred to as the vortex "residence time" at each window. Finally, the predictor compares each window residence time and chooses the maximum value as the predicted acceptable time spacing for the entire approach. Following application of an appropriate uncertainty buffer the aircraft time separation matrix is provided to the ATC interface.

3.1.1 Approach Corridor Dimensions

The corridor to be protected will be subject to FAA and industry consensus. The AVOSS can be designed to any specified criteria for the approach and departure corridors, and the choice will affect the capacity gains that can be realized. Candidate protected corridor dimensions for the AVOSS system are presented. The rationale for these dimensions are described in greater detail in reference 6. Consideration of previous wake vortex efforts, actual flight technical error observed in service (reference 7), FAA standards for instrument approach obstacle clearance (reference 8) and the limits of the ILS path itself were used to establish the candidate corridor dimensions. For example, reference 2 defined a corridor width of 300 feet (150 feet each side of the runway centerline) from the middle marker to the runway. This was based on statistical data showing 3-s aircraft variation from centerline at the middle marker to be about 50 feet and research showing that a vortex separated laterally from the aircraft by 100 feet "cannot significantly affect aircraft motion".

Equation 1 provides a definition of the candidate AVOSS approach corridor width between the outer and middle marker. The width is a constant 91.5 m (300 feet) from the

runway touchdown zone to the middle marker. The middle marker is assumed to be located 859 m (2816 feet) from the runway threshold. In this equation, D represents the distance from the landing runway in units of feet. The width of the AVOSS corridor beyond the middle marker is roughly 6 to 7 standard deviations of the observed traffic in reference 7 and 1/2 to 1/3 the width of the localizer course.

Equation 2 provides a definition of the candidate AVOSS approach corridor floor between the outer and middle marker. The equation provides the distance from the glide slope to the corridor floor and assumes that the glide slope angle is three degrees and the glide slope altitude is 61 m (200 feet) at the middle marker. This provides a very conservative floor that does not reduce separations for vertical wake motion at all inside the middle marker, and requires the vortex to be 61 to 122 m (200 to 400 feet) below glide slope at all other locations. This distance is always greater than a full scale deviation from the glide slope guidance. Equation 3 provides a second option of the corridor floor. The floor is still at ground level from the runway to the middle marker, but rises to 21.3 m (70 feet) below glide slope at the middle marker and increases to 61 m (200 feet) below glide slope at the outer marker. Although 61 m is only 1/2 scale glide slope guidance deviation at the outer marker, this represents considerable aircraft altitude error at glide slope intercept. At the middle marker this option places the AVOSS floor 150 percent deviation below the glide slope guidance. These and other corridor floor options will be tested during AVOSS development and final industry acceptance will involve a safety assessment and consensus process.

$$\text{Width} = 91.4 + 0.02539(D - 859) \quad (1)$$

$$\text{Floor1} = 61 + 0.00725(D - 859) \quad (2)$$

$$\text{Floor2} = 21.3 + 0.00471(D - 859) \quad (3)$$

Table 1 summarizes the corridor dimensions at several approach windows. The "ILS Limit" column represents full scale deviation from the localizer guidance assuming a runway length of 2439 m (8000 feet), or full scale glide slope deviation. The "AVOSS" columns are the recommended AVOSS corridor width or floor dimensions. Table 1 also gives the time required for a vortex to transport vertically and laterally outside the corridor at a sample translation speed. An initial vortex pair spacing of 30.5 m (100 feet) is assumed for computing the lateral transport time. The table is for illustration only and does not include many factors that will be modeled in AVOSS, such as changes in vortex drift rate at various altitudes and assumed flight technical error on the part of the generating aircraft.

<u>Position</u>	<u>ILS Limit Width</u>	<u>AVOSS Corridor Width</u>	<u>ILS Limit Below Glide Slope</u>	<u>AVOSS Corridor Floor, Option 1</u>	<u>AVOSS Corridor Floor, Option 2</u>	<u>Lateral Transport Time at 5.1 m/s (10 knot) drift rate</u>	<u>Vertical Transport Time at 1 m/s (200 foot/min) sink rate, Floor Option 2</u>
Runway Threshold	213m (700 ft)	91.5 m (300 ft)	3.7 m (12 ft)	15.9 m (52 ft)	15.9 m	12 sec	16 sec
Middle Marker	283 m (929 ft)	91.5 m	14.3 m (47 ft)	61 m (200 ft)	21.3 m (70 ft)	12	21
3.7 km (2 nm) from runway	515 m (1689 ft)	164 m (537 ft)	49.1 m (161 ft)	81.6 m (267 ft)	34.7 m (114 ft)	19	35
9.27 km (5 nm) from runway	967.7m (3174 ft)	304.9 m (1000 ft)	117 m (385 ft)	122 m 400 ft	61 m (200 ft)	33	61

Table 1 - AVOSS Corridor Dimensions and Example Transport Times

The takeoff case presents additional challenges for the corridor concept in that the altitude profile of departing aircraft vary widely, as opposed to the precise altitude profile of an aircraft during an instrument landing system (ILS) approach. This factor may be accommodated in several ways. One is to establish a takeoff corridor to accommodate expected variations in aircraft liftoff point, climb gradient, and departure vectors. This would make the takeoff spacing criteria aircraft pair specific since a range of expected climb gradients can be predicted for each aircraft type. Another approach is to ignore the sinking motion of the vortices and depend on lateral transport only. Yet a third method is to ignore vortex transport and depend only on the decay predictions. Evaluation of these techniques will be made during AVOSS design.

3.2 Weather Subsystem Requirements

While the core of the AVOSS system is the predictor subsystem, the predictions and system effectiveness will only be as good as the nowcast, or near-term weather prediction, provided by the meteorological subsystem. Initial requirements for this subsystem can be derived from the AVOSS system concept and previous wake studies. Separation criteria predictions are required as aircraft are metered into the terminal area, requiring 20 to 50 minute weather state predictions. The meteorological subsystem information will have a statistical element. There will be no attempt to predict the actual wind that any single vortex would experience at a later time. Instead the mean and standard deviation of the winds over a suitable interval will be used by the predictor algorithm to estimate the range of expected wake transport and decay intervals. The weather system will also be required to advise AVOSS when weather phenomena exists that make accurate wind predictions impractical, such as convective cell activity, or that a discrete event that will affect the weather state, such as cold fronts or gust fronts, will arrive. Finally, predictable changes in the planetary boundary layer occur in the morning and evening

hours which affect stratification and the low altitude wind structure. Due to the need to adjust traffic flow in advance of the weather change, some prediction capability for this effect must be included. This is particularly critical in the evening when the formation of a temperature inversion may reduce surface winds and tend to increase wake separation requirements.

Some of the required weather capabilities can be provided by the Integrated Terminal Weather System (ITWS) program (reference 9) under development by the FAA and Massachusetts Institute of Technology (MIT) Lincoln Laboratory. Coordination with that program has begun to provide weather information to AVOSS. Additional products, such as nowcast wind and lapse rate products will be developed.

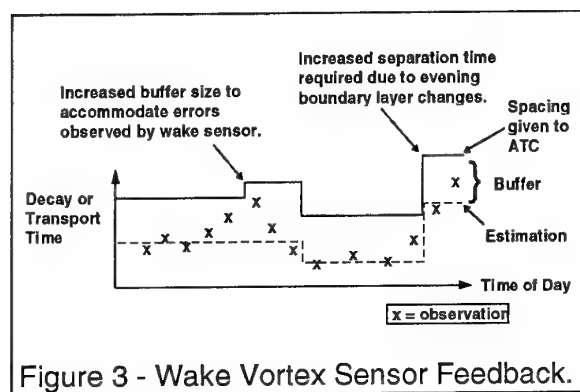
3.3 Wake Vortex Sensor Subsystem Requirements

Although various capability levels of AVOSS may be implemented, some of which would not require a wake vortex sensing subsystem, the AVOSS concept includes a wake sensor. As is the case for the weather subsystem, only general sensor requirements will be stated at this time. Detailed sensor requirements will be defined during the course of the research and development.

To be operationally useful to the AVOSS system the sensor must be capable of detecting, tracking, and quantifying the strength of wakes. Operation must be highly reliable and automated. The tracking domain should cover at least the protected corridor. Atmospheric stratification could potentially lead to accurate predictions at one altitude and large prediction errors at nearby altitudes. The volumetric domain of a wake sensor will be defined based on the criticality of prediction errors at each location and the confidence of predictions. Operational evidence (reference 10) and vortex sink characteristics suggest that the most critical domain for protection will be at relatively low

altitudes close to the airport environment, perhaps from the runway to a distance of about 3.7 km (2 nm) from the runway.

Figure 3 shows a concept for the use of position and strength feedback. As time of day progresses the predictor algorithm will produce an estimate of transport time and decay time, and the confidence intervals for these values, at various windows on the approach path. The sensor system will provide actual transport and decay times to the predictor so that the buffer and values provided to ATC can be adjusted whenever the actual data deviates from the predicted. With appropriate buffer size choices this adjustment will occur before any aircraft are exposed to a potential hazard. In the sudden event of a vortex persisting much longer than expected a message can be provided to ATC to command a go-around procedure for the following aircraft. Other uses of



the sensor data would be to allow AVOSS to default to standard separation criteria when specified prediction errors or variations in successive vortices develop.

The wake vortex sensor subsystem will be required to operate both in visual and in instrument meteorological conditions appropriate to the approach minima at a particular airport. The sensor or sensors will not be required to operate in conditions where accurate wake predictions are not likely to be achieved or where the wake is not likely to be the primary constraint in airport operations. Examples of these conditions include convective storm activity, extremely strong winds, heavy snow or freezing rain. The default vortex spacing criteria may be applied during these periods.

3.4 AVOSS Operational Integration

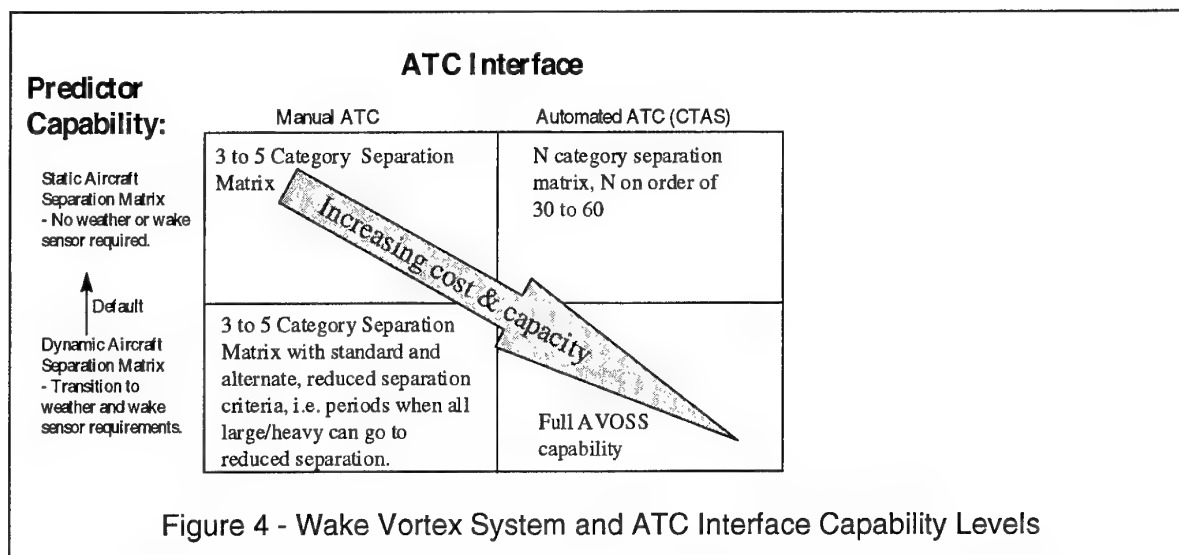
The AVOSS concept described above will be validated for operational readiness and integrated into automated and manual ATC systems. This will require interfaces beyond the minimum required for experimental testing. The interfaces will include those required for matching the AVOSS output to the ATC system expectations and for operational safety and redundancy. The rate at which separation criteria updates are provided to ATC (i.e. once every 30 minutes or once every 3 hours), the maximum

changes permitted between updates (i.e. 10 seconds, 30 seconds, or no limit), the resolution provided (i.e., 5, 10, or 15 seconds) can all be refined for controller and ATC automation acceptance. Due to the statistical nature of the wake predictions and increasing uncertainty in atmospheric state as forecast time increases, frequent updates could increase the maximum potential acceptance rate of the runway. Too frequent updates would also have negative impact on controller workload and possibly create system problems as the traffic flow adjustments ripple back into the TRACON and center airspace.

The size of the separation matrix and translation into separation distance will also be adjusted for the ATC system in use. Internally the AVOSS will operate with individual aircraft pair types, such as B-727 or DC-10, perhaps with grouping of the small aircraft category. A highly automated ATC system may be capable of directly using this matrix for highly efficient aircraft scheduling and sequencing. A less capable system, or a manual ATC environment, may require that the aircraft be grouped into three or four major groups for actual use. The AVOSS could provide output in this grouped format. All AVOSS provided wake constraints will be time based and indicate the minimum separation time between airplane pairs anywhere on the approach or initial departure path. Planned ATC automation tools can directly use this time matrix for separation, although controller interface issues would need to be addressed. A manual system would require output in a distance format for direct application by the controllers. Operational procedures and aircraft speed at various positions along the approach path must be considered in this translation of time into distance.

3.5 AVOSS System Tradeoffs

The general AVOSS concepts outlined above cover a wide range of possible system implementations, ranging from a simple system that advises a manual ATC system when a specific reduced separation matrix can be used to a multiple sensor system interfaced to an automated ATC system to optimize spacing between individual aircraft pairs. Figure 4 suggests four possible wake system implementations that vary in cost and capability. At one extreme (upper row of figure 4) a static separation matrix determined from a large matrix of aircraft, potentially with one matrix element per aircraft type, can be collapsed into a 3 to 5 category system for manual ATC use. NASA Langley has taken this approach in response to a FAA request for a scientific basis for revised separation standards and aircraft classifications. No dedicated weather or wake sensors would be required for this system, and this is considered to be the "default" AVOSS spacing when weather conditions are changing too rapidly for accurate dynamical wake predictions. A fully automated ATC system could use the full separation matrix for more efficient operations. The lower row in figure 4 represents dynamical spacing interfaced to either a manual or an automated ATC system. The manual ATC system would employ a relatively simple procedure that provides for



a fixed, reduced separation matrix under certain weather conditions. An example of this procedure would be to allow less than current standard spacing between all large and heavy aircraft pairs when the atmospheric conditions permit. Dynamical separation standards require a dedicated weather subsystem and, for maximum capacity, a dedicated wake sensor subsystem. The level of AVOSS complexity to be applied at a given airport will be a function of the capability of the ATC system at that facility and tradeoff studies that show the capacity gain expected with various AVOSS levels.

4. Current Research Activities

The NASA is addressing the development and demonstration of a prototype AVOSS through a combination of analytical, wind tunnel, field and flight tests. Critical activities underway include the following.

4.1 Numeric Wake Vortex Modeling

The Terminal Area Simulation System (TASS) large-eddy simulation code of reference 11, proven highly effective in the successfully completed NASA/FAA wind shear program, is being modified to model the effect of various atmospheric conditions on the behavior of aircraft vortices. Modifications include the required wake initialization routines, regridding and grid nesting, and post-processing software to diagnose vortex core location and strength. A related effort is developing the ability to model the evolution of the planetary boundary layer (PBL) with changes in sun angle, cloud cover, and terrain (reference 12). Both 2-dimensional and full 3-dimensional modeling of wake behavior are being conducted. Emphasis will be placed on validation of the model behavior against observed wake data prior to using TASS for AVOSS predictor algorithm development. Following validation of TASS, parametric studies will be performed to quantify the effects of stratification, wind speed and vertical shear, and various turbulent scale lengths on the transport and decay of the

vortices from various sized aircraft. Once TASS is validated within a given envelope of weather and terrain conditions, these parametric studies should provide more information than could be feasibly gathered from field experiments where multiple factors are usually changing with each observed wake and a limited subset of possible atmospheric conditions can be expected to occur. TASS results will be useful not only for predictor algorithm development, but also as numeric simulation data for developers of wake vortex sensors.

4.2 Field Measurements of Aircraft Wake Vortices

Crucial to the validation of TASS, prediction algorithm development, and full system testing and demonstration is a field effort sponsored by NASA Langley and conducted by the MIT Lincoln Laboratory (reference 13 & 14). This field effort serves multiple purposes:

1. Provide a comprehensive data collection suite to gather meteorological, aircraft, and wake data at a major airport.
2. Provide the above data for validation of wake models and direct use by predictor algorithm developers.
3. Establish the required field facilities and system interfaces for predictor algorithm and AVOSS prototype testing and demonstration.

The Lincoln effort has established a facility at the Memphis International Airport that provides the most complete wake vortex data facility established to date in an operational setting. Aircraft wake vortex data was collected with a 10.6 micron continuous wave laser mounted in a mobile van. The van could be driven to various airport locations as runway operations changed or to collect data at different airplane crossing altitudes. The lidar was implemented with real-time wake vortex identification and tracking algorithms to optimize data quality (reference 15).

A 150 foot tower measured wind direction, temperature, and humidity at five elevations. Solar flux, soil temperature, and soil moisture are measured for correlation with the atmospheric boundary layer characteristics and validation of PBL models. A radar profiler with a radio acoustic sounding system (RASS) provided winds aloft from approximately 100 meters above ground level (AGL) to about 2500 meters AGL with a vertical resolution of 100 meters and a 25 minute averaging period. The RASS provided temperature up to about 1000 meters AGL at a 5 minute averaging period. Also employed was an acoustic sodar that provided 10-minute average winds with a vertical resolution of 20 meters from an altitude of 20 meters up to about 300 meters AGL. Dedicated rawinsonde balloon launches were made from the airport during the tests. Lincoln was responsible for total system integration but the National Atmospheric and Oceanic Administration and the Volpe National Transportation Systems Center assisted with radar profiler and sodar installations. NASA Langley deployed an OV-10A aircraft to Memphis during measurement periods to collect meteorological data over spatially diverse regions to augment the fixed meteorological site measurements. Wind, turbulence, pressure, temperature, and dew point measures were taken by the OV-10.

Lincoln also collected extensive aircraft data for most aircraft being observed through agreements with the major aircraft operators at Memphis. The operators provided the actual approach weight of each aircraft observed and information on flight procedures required to estimate flap setting from airspeed and weight. Air Traffic Control beacon data provided the altitude, aircraft type, and ground speed of each aircraft crossing the laser facility. Lincoln uses this data and the meteorological data to estimate the aircraft airspeed and correlate individual arrivals to the operator-provided weight data. This processing provides detailed information on the aircraft generating each observed wake.

The initial Memphis deployment occurred between November 15 and December 14, 1994. During this deployment all systems were operated together for the first time and the lidar wake tracking software was refined and brought to an operational status by Lincoln. Approximately 600 aircraft wakes were observed, with about 100 observed with the lidar tracking algorithms functioning. A second deployment was conducted in August of 1995 (reference 14). High quality wake vortex data was taken in a wide domain of initial wake altitudes and atmospheric conditions required for TASS validation efforts and AVOSS development. Three altitude bands were selected, out-of-ground (OGE) effect to validate previous models of vortex behavior in that domain (reference 16) and well as the TASS model, near-ground-effect (NGE) to capture vortices generated out of ground effect and quickly descending into surface interaction, and in-ground-effect (IGE) to capture vortices generated at altitudes less than $\frac{1}{2}$ wing span above ground. These altitude bands were chosen due to the requirement to validate vortex models at all altitude regimes for an operational system, limitations in previous vortex transport models in ground effect, and a relative lack of quality wake and meteorological data collected at low altitudes. During the 1995 deployment over 600 wakes were observed by the Lincoln lidar, with about 400 cases surviving data quality checks. Data was collected at varied hours of the day from early morning to midnight, in stable and unstable atmospheric conditions, and in both calm and light to moderate ambient wind shear conditions. Numerous high interest wake tracks were collected in conditions that caused the wakes to either sink vertically through the corridor with little drift, or to stall near or on the runway centerline at low altitudes. Stalled vortices lasting over a minute at the runway threshold were observed, as were vortices that were formed in ground effect then gained in altitude. These are critical environments in which to validate the Langley numeric models and in which to understand and

Local Time	Cloudy, Windy	Cloudy, Calm	Clear, Windy	Clear, Calm
6:00 AM - 8:30 AM			10 OGE	17 OGE 17 NGE 11 IGE
11:00 AM - 5:00 PM		35 NGE	8 IGE	38 OGE 22 NGE 8 IGE
5:00 PM - 7:30 PM		7 OGE 36 NGE	14 OGE	33 OGE 12 NGE
10:30 PM - 12:00 AM			16 OGE 1 NGE	56 OGE 24 IGE
12:00 AM - 1:00 AM			19 OGE	71 OGE 6 IGE

TABLE 2 - Approximate List of 1995 Memphis Wake Vortex Measurements
 Cloudy indicates more than 5/10 sky cover. Windy indicates more than 5 m/s (10 knots) surface wind or significant vertical shear. OGE = Out-of-Ground Effect, NGE = Near-Ground-Effect, IGE = In-Ground-Effect.

quantitatively predict vortex behavior. Table 2 represents a list of wake cases collected by time of day, wind condition, and initial wake altitude region. This table represents field notes collected by Langley personnel in August and may have slightly different numbers than the final data set, which has been delivered but not fully analyzed at this time. Analysis and TASS validation is continuing at this time and future deployments will be conducted as required to develop and test AVOSS subsystems and the integrated AVOSS system.

4.3 Operationally Acceptable Vortex Strength Definition Requirements

The transport rule component of the AVOSS system is not dependent on knowledge about wake vortex interaction with the following aircraft. The decay rule component of the predictor, however, must predict when the wake of any given aircraft has decayed to an operationally acceptable strength for an encounter by any given following aircraft. Work is currently ongoing at NASA Langley and Ames Research centers, using combinations of analytical, wind tunnel, and flight test techniques to develop and validate tools that predict the dynamics of aircraft wake encounters (reference 17). Industry and FAA Flight Standards involvement will also be required to provide the appropriate consensus on the results. The output of this activity will be a sensor-observable wake vortex "strength definition" and acceptable encounter values for various aircraft types in the commercial fleet.

4.4 Wake Vortex Sensors

Efforts are in progress at Langley to develop and demonstrate ground based sensor technologies to support the AVOSS concept. Both radar and laser technologies are being examined for operational feasibility. A technology selection is scheduled to take place in 1996. The selected technology will be further developed and fielded as early as 1997 for field tests and initial AVOSS integration. The goal of the sensor development effort is to provide the wake sensor subsystem requirement for an AVOSS prototype demonstration in the 1999/2000 time frame.

References

1. Erzberger, Heinz; Davis, Thomas J.; and Green, Steven; "Design of Center-TRACON Automation System" NASA Ames Research Center, Presented at AGARD Guidance and Control Symposium on Machine Intelligence in Air Traffic Management, 11-14 May, 1993, Berlin, Germany.
2. Eberle, W.R.; Brashears, M.R.; Zalay, A.D.; Shrider, K.R.; and Love, D.A.; "Aircraft Wake Vortex Characteristics from Data Measured at John F. Kennedy International Airport", Lockheed Missiles and Space Co., FAA-RD-78-47, March 1978.
3. Hallock, J.N., "Aircraft Wake Vortices: An Annotated Bibliography (1923-1990)", Volpe National Transportation Systems Center, DOT-FAA-RD-90-30, DOT-VNTSC-FAA-90-7, January 1991.
4. Hallock, J.N., "Aircraft Wake Vortices: An Assessment of the Current Situation", Volpe National Transportation Systems Center, DOT-FAA-RD-90-29, DOT-VNTSC-FAA-90-6, January 1991.
5. Garodz, Leo J. and Clawson, Kirk L., "Vortex Wake Characteristics of B757-200 and B767-200 Aircraft Using the Tower Fly-By Technique" 2 Volumes, NOAA Technical Memorandum ERL-ARL-199, January 1993.
6. Hinton, "Aircraft Vortex Spacing System (AVOSS) Conceptual Design", NASA TM-110184, August 1995.
7. Owen, M.R., "The Memphis Precision Runway Monitor Program Instrument Landing System Final Approach Study", MIT Lincoln Laboratory Project Report ATC-194, DOT/FAA/NR-92/11, May 24, 1993.
8. "United States Standard for Terminal Instrument Procedures (TERPS)", FAA 8260.3B, July 1976 with changes through #15 dated September 1993.
9. Cole, Rodney E. and Wilson, F. Wesley Jr., "ITWS Gridded Winds Product", Presented at the Sixth Conference on Aviation Weather Systems, January 15-20, 1995, Dallas, TX.
10. Critchley, J.B. and Foot, P.B., "United Kingdom Civil Aviation Authority Wake Vortex Database: Analysis of Incidents Reported Between 1982 and 1990", CAA Paper 91015, August 1991.
11. Proctor, F. H., "The Terminal Area Simulation System", 2 Volumes, NASA CR-4046 and CR-4047, April 1987.
12. Showalter, D.G.; DeCroix, D.S.; Lin, Y.L.; Proctor, F.H.; Arya, S.P.; and Kaplan, M.L.; "Turbulent Statistics in the Atmospheric Boundary Layer: A Comparison of Large Eddy Simulation with Observations", North Carolina State University, Presented at the 11th Symposium on Boundary Layers and Turbulence, March 27-31, 1995, Charlotte, NC.
13. Campbell, Steven D.; Dasey, Timothy; Heinricks, Richard; and Matthews, Michael P.; "Overview of 1994 Memphis Wake Vortex Testing Program", MIT Lincoln Laboratory, Presented at the Sixth Conference on Aviation Weather Systems, January 15-20, 1995, Dallas, TX.

14. Campbell, S., Dasey, T.; Freehart, R.; Heinrichs, R.; Matthews, M.; and Perras, G.; "Wake Vortex Field Measurement Program at Memphis, TN", MIT Lincoln Laboratory, AIAA Paper 96-0399, Presented at the 34th Aerospace Sciences Meeting & Exhibit, Reno, NV, January 15-18, 1996.
15. Dasey, Timothy J. and Heinrichs, Richard, "An Algorithm for the Recognition and Tracking of Aircraft Wake Vortices with a Continuous Wave Coherent Laser Radar", MIT Lincoln Laboratory, Optical Society of America Coherent Laser Radar Topical Meeting, Keystone, CO., July 23-27, 1995.
16. Greene, George C., "An Approximate Model of Vortex Decay in the Atmosphere" in *Journal of Aircraft*, Vol. 23, No. 7, July 1986.
17. Vicroy, Dan; Bowles, Roland; Brandon, Jay; Greene, George; Jordan, Frank, Jr.; Rivers, Robert; Stewart, Eric; Stough, H. Paul III; and Stuever, Robert; "NASA Wake Vortex Research", ICAS-94-6.2.2, Presented at the 19th Congress of the International Council of the Aeronautical Sciences, Anaheim, CA, September 19-23, 1994.

On the Interaction between Topographical Wind and Landing Aircraft

Nils Kubberud and Ivar Øye

CFD norway as
Professor Brochsgt. 6
N-7030 Trondheim, Norway

Helge Nørstrud

Norwegian University of Science and Technology
Department of Applied Mechanics, Thermo and Fluid Dynamics
N-7034 Trondheim, Norway

SUMMARY

Trondheim airport at Værnes (located 2 km from Hell) is characterised by winds from the southeast which creates strong vortical flow around the airport due to mountainous topography on the southern side of the glide slope. This leads to a rapid change of flow conditions for an aircraft in the landing phase approaching from the west.

The present paper gives a qualitative study of the flow interaction between a representative landing aircraft and the wind induced vortical flow. Separate numerical analysis for the wind flow over the given terrain and the flow structure around the lifting airplane is given. The interaction is performed by superposing the two solutions in various crossflow planes along the glide path direction of the aircraft. This leads to an estimate of the change of circulation for the lifting body and the associated need for corrective control forces.

1. INTRODUCTION

A lifting vehicle such as an aircraft produces its lift force by the generation of a downward momentum of the surrounding fluid or air. This can be described through a system of vorticities and for the case of an aircraft this consists of a bound vortex representing the wing and a vortex system trailing behind. Early theoretical analysis of the roll-up of the vortex sheet behind a lifting wing is found in references [1], [2], [3] and [4]. Wind effects on such vortex systems have been addressed in various connections [5], [6] and are mostly concerned with wake effects on following aircrafts. The present paper deals with wind effects on a medium class aircraft in the landing phase toward a specific airport. It also gives a simplified method to characterise the trailing vortex as a function of wing span and aircraft lift. An analysis of the various elements connected to an aircraft in a wind environment points toward a critical phase just before touch-down for the selected runway. This phase starts at a height of 150 ft and 0.5 nm from the runway.

2. WIND CONDITION AT REFERENCE AIRPORT

The airport selected for the present study is Trondheim airport at Værnes, Norway with the European Datum of $63^{\circ} 27' 29''$ N and $10^{\circ} 55' 3''$ E, see figure 1 which is taken from the Instrument Approach Chart - ICAO. The selected flight path for the final approach to runway 09 will follow a glide slope of 5,3 % (3°) from FAF and passes over the fjord from west.

Winds from southeast are dominant during the fall and winter season and will create strong influence on landing aircrafts. This is primarily due to topographical interactions from numerous hills (heights in the order of 300-400 metres) which are located to the south of the reference flight path. For this reason an overall wind direction of 157.5° was adopted for a numerical wind analysis of the area around the Værnes airport. Figure 2 illustrates the results with a vector plot of the local wind velocity in a plane 10 m above ground level. Note the location of the air traffic controller wind velocity meter at the runway indicated by a filled circle. At this spot the analysis yields a wind direction which can be termed as headwind for the pilot of a landing aircraft.

2.1 Numerical wind analysis

The computer code employed is based on a time-marching, finite-volume technique and solves the Euler equations in three dimensions. The surface grid for the topographical area (19 x 20 km) is obtained from digital map data and extended to a vertical space of 1 km. Approaching global wind as boundary condition input is specified by the power law

$$u(z) = U_{\text{ref}} \left(\frac{z}{10} \right)^{0.11} \quad (1)$$

where the reference velocity U_{ref} is defined as 12 m/s in a height of $z = 10$ m above ground level.

The general wind distribution for a height of $z = 10$ m above ground level is shown in figure 3. Furthermore, streamlines are traced from points in the terrain south-west of the runway. The flow pattern to the north (upper left side of the figure) clearly shows the direction of the global, approaching wind.

A vertical cut through the flight path, figure 4, indicates the wind shear to be expected from 5 km west of the runway or from the touch-down point. In order to illustrate the crossflow pattern for various positions along the flight path reference is made to figure 5.

For each of these stations the circulation is evaluated along the sides of a rectangle encompassing the aircraft

and the mean flux of vorticity is calculated for the left- and right side of the flight direction, i.e.

$$\bar{\zeta} = \frac{\Gamma}{F_{\text{ref}}}$$

where the respective areas of integration are depicted in figure 6. It should be noted that in the above given relation the Stoke's theorem has been used to relate the mean flux of vorticity through the area enclosed by the circulation path and the associated value for the circulation.

The obtained values are given in Table 1 below.

POSITION		MEAN FLUX OF VORTICITY, $\bar{\zeta}$ [1/s]			
ℓ [km]	z [m]	N_1	S_1	N_2	S_2
0.5	26.2	0.04618	0.04816	0.05652	0.05700
1.0	52.4	0.05010	0.05197	0.05648	0.05772
1.5	76.8	0.04935	0.04976	0.05060	0.05028
2.0	104.8	0.04599	0.04585	0.03596	0.03952
2.5	131	0.03205	0.03103	0.02844	0.02748
3.0	157.2	0.01910	0.01938	0.01802	0.01813
3.5	183.4	0.02915	0.02721	0.02764	0.02876
4.0	209.6	0.03179	0.03225	0.03144	0.03148
4.5	235.8	0.02995	0.03106	0.03144	0.03316
5.0	262.0	0.03145	0.03227	0.03124	0.03216

Table 1 - Mean flux of vorticity through vertical planes at points on the flight path

As can be observed from the table the two fluxes $\bar{\zeta}_1$ and $\bar{\zeta}_2$ have similar distribution in the flight direction and there are little variation with regard to the left (N) and right (S) side.

Figure 7 gives an overall picture of the wind components to be found along the flight path and for the convenience of discussing wind behaviour along the glide slope three critical points are defined as

CRITICAL POINT DESIGNATION	POSITION		COMMENTS
	ℓ [m]	z [m]	
A	3300 (1.78 NM)	173 (568 FT)	Sudden increase of side wind and head wind
B	2421 (1.31 NM)	127 (417 FT)	Decrease of side wind and head wind
C	864 (0.47 NM)	45 (148 FT)	Change of side wind direction

Table 2 - Critical point definition

It should be mentioned that the critical point A corresponds to a minimal value of the mean flux of vorticity which occurs 46 s before touchdown. When the side wind changes sign (critical point C) the pilot has 12 s left before landing.

3. AIRCRAFT CONFIGURATION AND FLOW FIELD

The geometry adopted for the simulation of a landing aircraft corresponds to the DFVLR - F4 wing-body configuration [7], see figure 8. At an angle of attack of 6° this generic configuration, with a wing span equal 30 m, will produce a lift force and a wake field similar to a Boeing 737 medium class aircraft which is typical for the commercial air traffic at Värnes. Furthermore, a landing speed of $V = 140$ knot ($= 72$ m/s) is adopted throughout the study.

3.1 Numerical aerodynamic analysis

With the surface grid structure of the wing-body configuration shown in figure 8 and a solution space (approximately 150 000 nodal points) extended three spanwidths downstream from the body aft point an Euler flow calculation yields a total lift coefficient of $c_L = 1.1$. Hence, the resulting liftforce is evaluated to

$$\begin{aligned} L[N] &= \frac{1}{2} c_L A_p V^2 \\ &= 330\,830 \text{ N } (= 33\,724 \text{ kg}) \end{aligned} \quad (2)$$

where the air density is set to $\rho = 1.225 \text{ kg/m}^3$. The corresponding circulation is found from integrating over a crossplane located one halfspan behind the fuselage (see figure 9), i.e.

$$\begin{aligned} \Gamma_0 &= \oint \vec{v} \cdot d\vec{\ell} \\ &= 151 \text{ m}^2/\text{s} \end{aligned} \quad (3)$$

The circulation is defined positiv counterclockwise as seen in the flight direction and with an enclosing area of $18 \times 18 \text{ m} = 324 \text{ m}^2$ the average vorticity flux will be $\zeta_0 = 0.466 \text{ s}^{-1}$. This value is an order of magnitude larger than the wind induced fluxes in

equivalent cross planes and will be used as the reference value in chapter 4.

The normalized downwash w/V [-] is evaluated along a line going through the trailing vortex core, see figure 9, and the spanwise distribution is given in figure 10. Note that the core centre (indicated as point P'' in the figure) is located at 91% of the halfspan. This value is reduced to 86% at a crossplane station 5 times the halfspan.

Writing the Kutta-Joukowski theorem as

$$L = \rho V \Gamma_0 \quad (4)$$

and in combination with equation (2) we will obtain the relation

$$c_L \bar{c} = \frac{2\Gamma_0}{V} = 4.19 \quad (5)$$

for the local load distribution at midspan. This value is indicated in figure 11 where the numerical obtained load distribution is shown. Furthermore, rewriting equation (5) will yield

$$\frac{c_\epsilon}{c_L} = \frac{2\Gamma_0}{c_L V \bar{c}} = 1.06 \quad (6)$$

for the midspan station.

3.2 Simplified analytical wake model

Consider a wing of infinite span or aspect ratio in a uniform stream characterised by the velocity components u_∞ , v_∞ in a xy-plane [8] and let the wing profile be a flat plate with a chordwise distribution of vorticity given by

$$\gamma(x) = \left(\frac{1-x}{x} \right)^{1/2} \quad 0 \leq x \leq 1 \quad (7)$$

The flowfield induced by this relation (which satisfies the Kutta condition at the trailing edge) is evaluated for small α as

$$\frac{u(x, \pm y) - u_\infty}{u_\infty} = \pm \frac{\alpha y}{2q_2 \left\{ [x(1-x) - y^2]^2 + y^2 \right\}^{1/2}} \quad (8)$$

$$\frac{v(x, \pm y) - v_\infty}{u_\infty} = \mp \frac{\alpha}{(x-1)^2 + y^2} \left\{ \frac{x}{2pq_2} + \frac{p - 2q_2 + 1}{2q_2(2p - 4q_1^2 - 1 - p^2)} \right\} \quad (9)$$

where

$$p_1 = \frac{x(1-x) - y^2}{(x-1)^2 + y^2} \quad q_1 = [0.5(p + p_1)]^{1/2}$$

$$p_2 = \frac{|y|}{(x-1)^2 + y^2} \quad q_2 = [0.5(p - p_1)]^{1/2}$$

$$p = (p_1^2 + p_2^2)^{1/2}$$

Equations (8) and (9) are presented in graphical form in figure 12. It should be noted that the Prandtl factor $\beta = (1 - M_\infty^2)^{1/2}$ could be included in the analysis presented above, however, for our case of landing speed at $M_\infty = 0.25$ we let $\beta = 0.968 \Rightarrow 1.0$.

If we consider the lifting wing theory with its simplified horseshoe vortex structure we can extend the above analysis to the vortex pattern downstream of the wing, see figure 13. The wing to be discussed is defined as a rectangular flat plate of 30 m spanwidth and a constant chord length equal to the mean aerodynamic chord of our reference aircraft (or wing-body configuration).

Combining the flat plate unit area lift coefficient

$$c_l = 2\pi\alpha \quad (10)$$

which is a consequence of equation (7), with equation (5) we can write

$$\alpha = \frac{\Gamma_0}{\pi V C} = 0.185 \quad (\text{or } \alpha = 10.5^\circ)$$

Hence, we have now defined a flat plate wing configuration which produces the same amount of circulation Γ_0 as evaluated for the wing-body, equation (3). Here α [-] represents the geometric angle of attack for the wing of infinite span. Since a finite wing of elliptic loading will induce a downwash at the trailing edge of the constant value

$$w = \frac{\Gamma_0}{2b} = 2.25 \text{ m/s}$$

the associated induced angle of attack will give

$$\alpha_i = \alpha - \alpha_{\text{eff}} \approx w/V$$

$$= 0.035 \quad (\text{or } \alpha_i = 2^\circ)$$

For a vertical distance of 0.75 ($\alpha - \alpha_i$) = 0.11 with reference to a chordlength of unity, see figure 14, the

downwash distribution will take the form as shown in figure 15. Hence, the similarity to the downwash pattern from the reference wing-body configuration (figure 10) should be noted. At this point reference is also made to the ratio $b'/b = \pi/4$ where b' represents the distance between the two rolled-up vortices far behind a elliptical loaded wing [1], [3]. The present simplified analysis indicates a ratio of $b'/b = 3/4$.

4. INTERACTION ANALYSIS

We have selected a certain wind condition for Trondheim Airport at Værnes and calculated the local wind distribution due to topography. Furthermore, a representative aircraft has been selected for the landing approach to the airport and a numerical analysis has been presented for the determination of the associated vortex system or lift distribution.

A simplified interaction model is now introduced in order to give a first approximation to the wind effects on the simulated aircraft. In this context an average value of the mean flux of the wind generated vorticity has been adopted (see table 1) and introduced as corrections to the circulation (or vorticity flux) for the undisturbed wing lifting system. Hence, we write

$$\frac{\Delta L(\ell)}{L} = \frac{\bar{\zeta}(\ell)}{\zeta_0}$$

where $\zeta_0 = 0.466 \text{ s}^{-1}$, see page 24-4. Table 3 gives the following results for the gain of lift for the right wing which is equal to the loss of lift for the left wing, i.e.

POSITION	VORTICITY FLUX	LIFT GAIN/LOSS
ℓ [km]	$\bar{\zeta}[\text{s}^{-1}]$	$\Delta L/L[\%]$
0.5	0.0568	12.2
1.0	0.0571	12.3
1.5	0.0504	10.8
2.0	0.0377	8.1
2.5	0.0280	6.0
3.0	0.0182	3.9
3.5	0.0282	6.1
4.0	0.0315	6.8
4.5	0.0323	6.9
5.0	0.0317	6.8

Table 3 - Wind effects on lift for each half wing

The distribution of the induced wind effects on lift is plotted in figure 16 together with a reference to the critical point locations. As can be seen critical point A indicates a rapid change of lift distribution over the whole wing, critical point B represents the state of condition in the early approach phase and point C determines a definite critical point along the glide slope just before landing. This is finally shown in figure 17 which illustrates the action to be taken by the pilot, i.e. the flying into the wind in order to oppose the sidedrift. Just before touch-down he has to use rudder to align the aircraft with the runway (kicking off drift).

5. CONCLUSIONS

A simplified analytical model is proposed for the interaction between atmospheric wind and the lifting vortex system of an aircraft in the landing phase. For a specific airport it is shown that this wind effect will introduce a critical situation for the aircraft just before touch-down. Furthermore, the associated change of lift for the wing can be formulated as a function of downwash and then traced to the vortex structure behind the wing.

6. ACKNOWLEDGEMENT

The authors wish to acknowledge the discussion with retired flight captain Hans Gunnar Bakken who gave his invaluable experience from numerous windy landings at Værnes airport.

REFERENCES

- [1] Kaden, H., «*Aufwicklung einer unstabilen Unstetigkeitsfläche*», Ingenieur-Archiv, Band 11, 1931, pp. 140-168.
- [2] Betz, A., «*Verhalten von Wirbel-systemen*», Zeitschrift für angewandte Mathematik und Mechanik (ZAMM), Band 12, 1932, pp. 164-174.
- [3] Spreiter, J.R. and Sacks, A.H., «*The Rolling Up of the Trailing Vortex Sheet and Its Effect on the Downwash Behind Wings*», Journal of the Aeronautical Sciences, 1951, pp. 21-32, 72.
- [4] Rossow, V.I., «*On the Inviscid Rolled-Up Structure of Lift-Generated Vortices*», Journal of Aircraft, Vol. 10, 1973, pp. 647-650.
- [5] Robins, R.E. and Delisi, D.P., «*Potential Hazard of Aircraft Wake Vortices in Ground Effect with Crosswind*», Journal of Aircraft, Vol. 30, No. 2, 1993, pp.201-206.
- [6] Spilman, D.R. and Stengel, R.F., «*Jet Transport Response to a Horizontal Wind Vortex*», Journal of Aircraft, Vol. 32, No. 3, May-June 1995, pp. 480-485.
- [7] Redeker, G. et al, «*Experiments on the DFVLR-F4 Wing-Body Configuration in Several European Wind Tunnels*», AGARD CP-240, 1987, pp. 2-1 to 2-14.
- [8] Nørstrud, H., «*Zur angestellten Platte in einer unendlichen Strömungsebene*», Zeitschrift für angewandte Mathematik und Mechanik (ZAMM), Band 52, 1972, pp. 247-248.

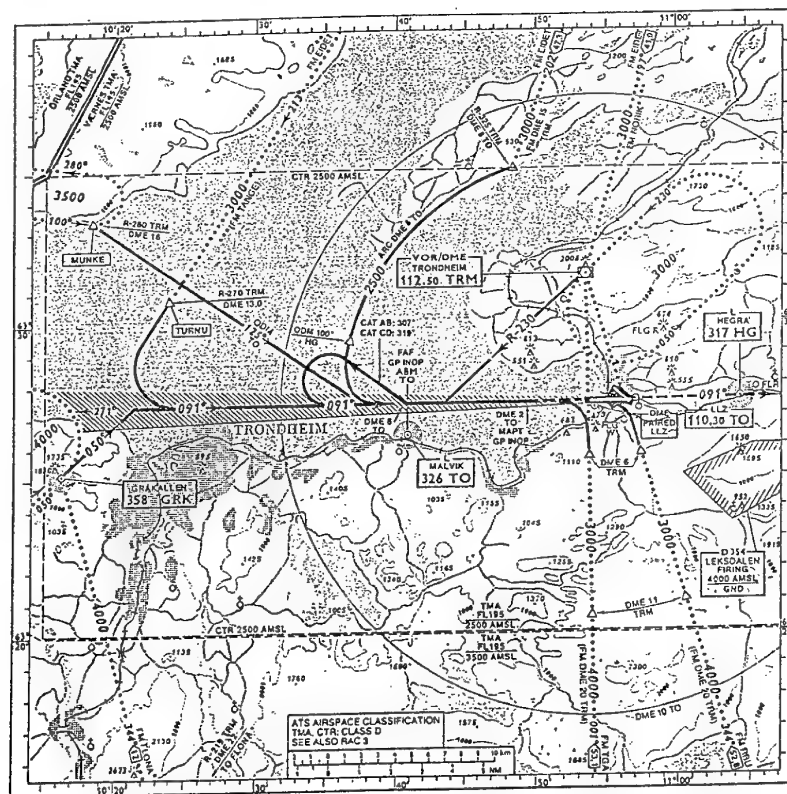


FIGURE 1 - Instrument approach chart for Trondheim airport, Værnes

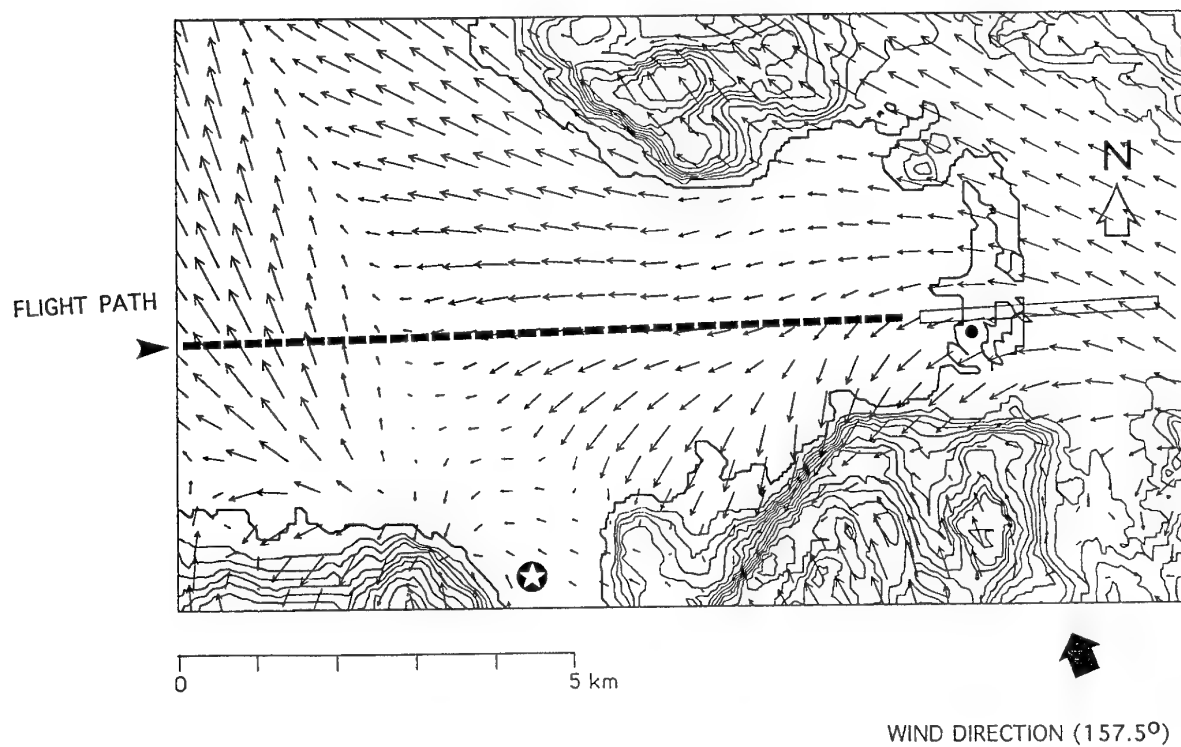


FIGURE 2 - Local wind velocity distribution for 10 m above ground level



FIGURE 3 - Velocity plot and streamlines for wind at 10 m height

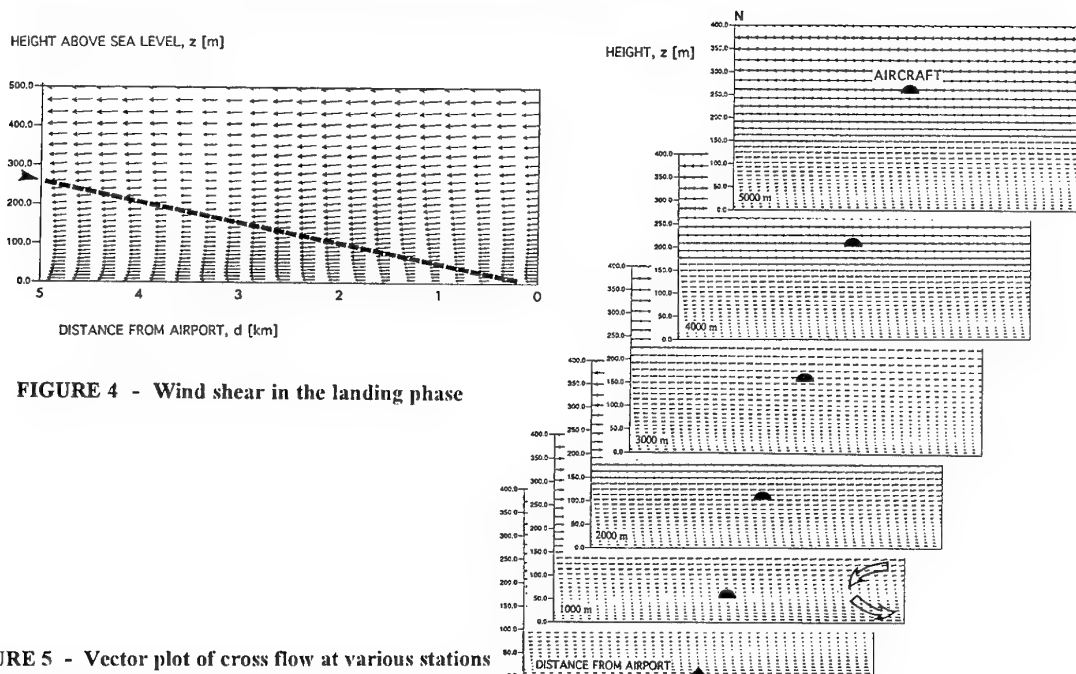


FIGURE 5 - Vector plot of cross flow at various stations

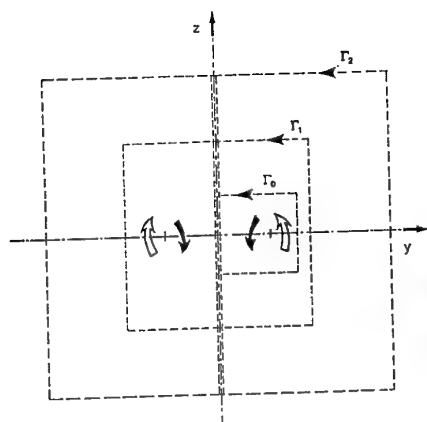


FIGURE 6 - Enclosed area for circulation evaluation

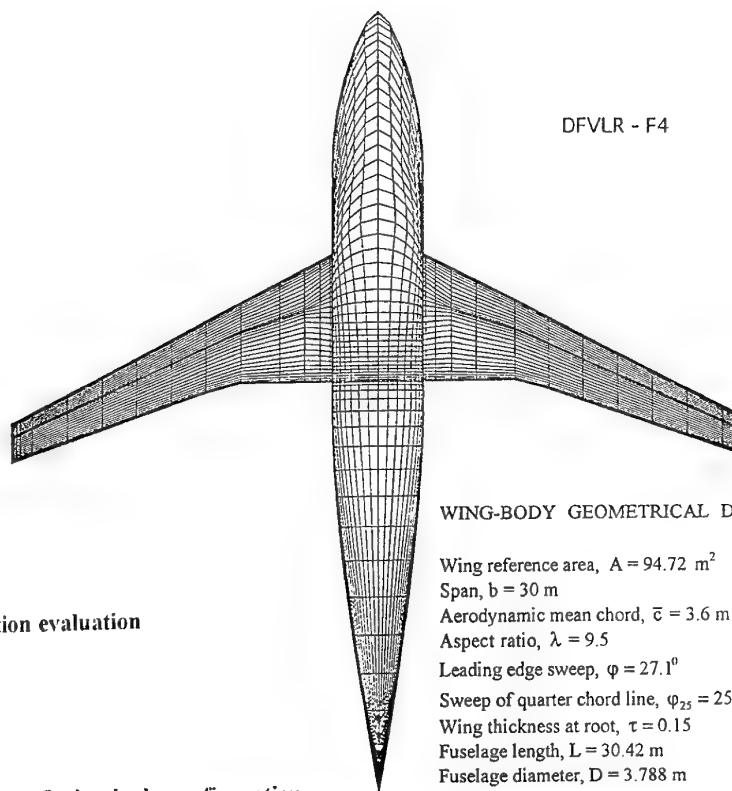


FIGURE 8 - Geometry of wing-body configuration

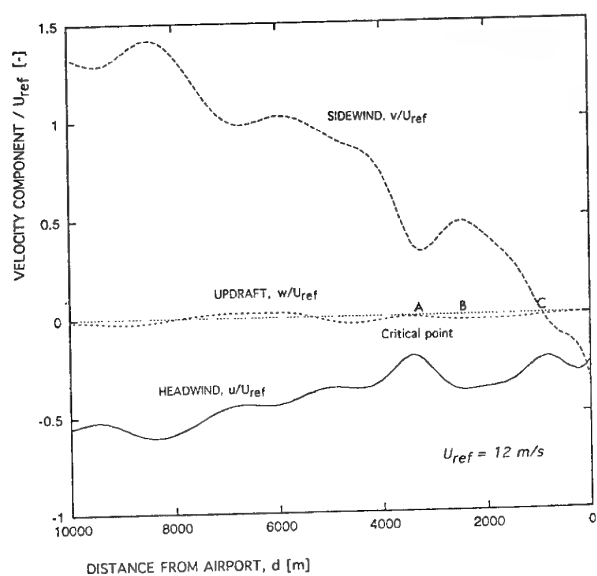
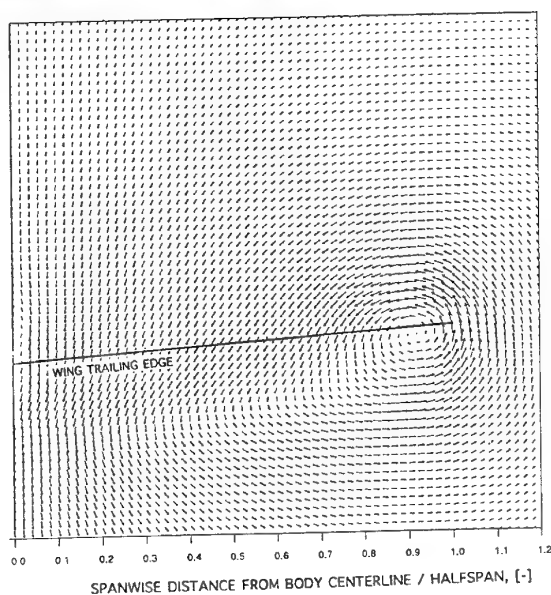


FIGURE 7 - Normalized velocity components along flight path

FIGURE 9 - Vector plot of cross flow at $x = b/2$

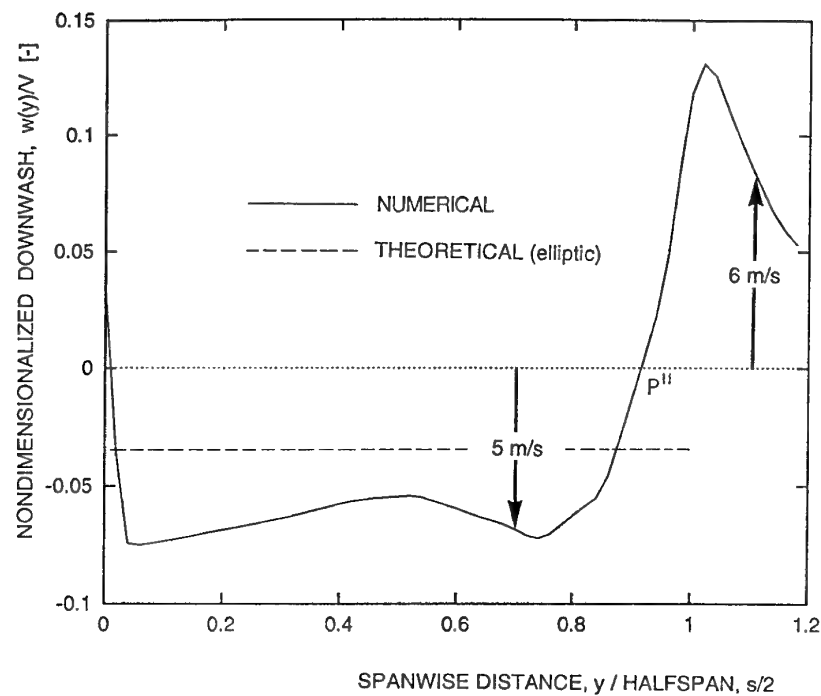
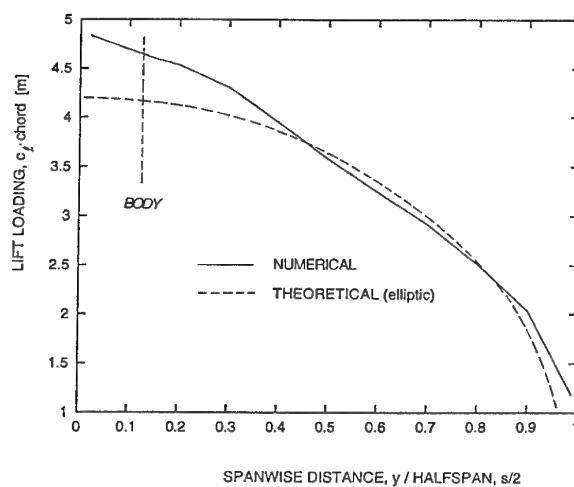
FIGURE 10 - Downwash behind wing-body at $x = b/2$ 

FIGURE 11 - Spanwise lift distribution of wing-body combination

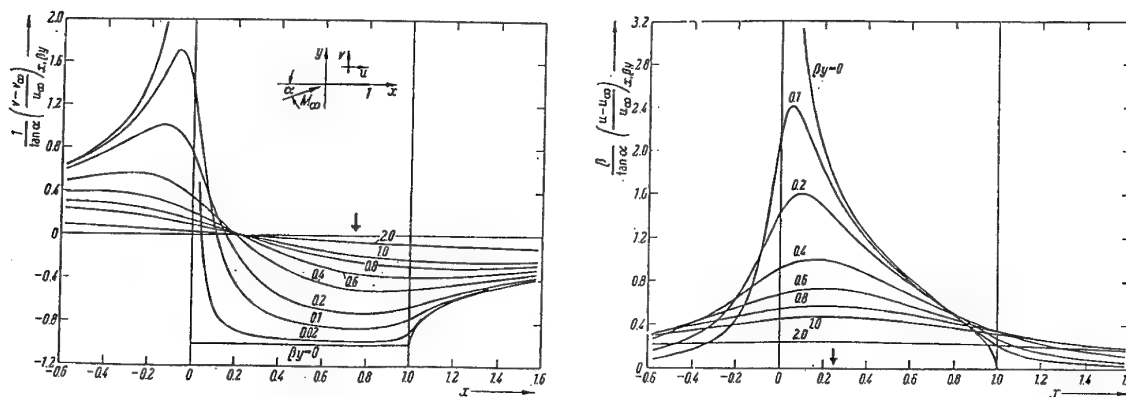


FIGURE 12 - Velocity distribution of a flat plate in uniform flow [8]

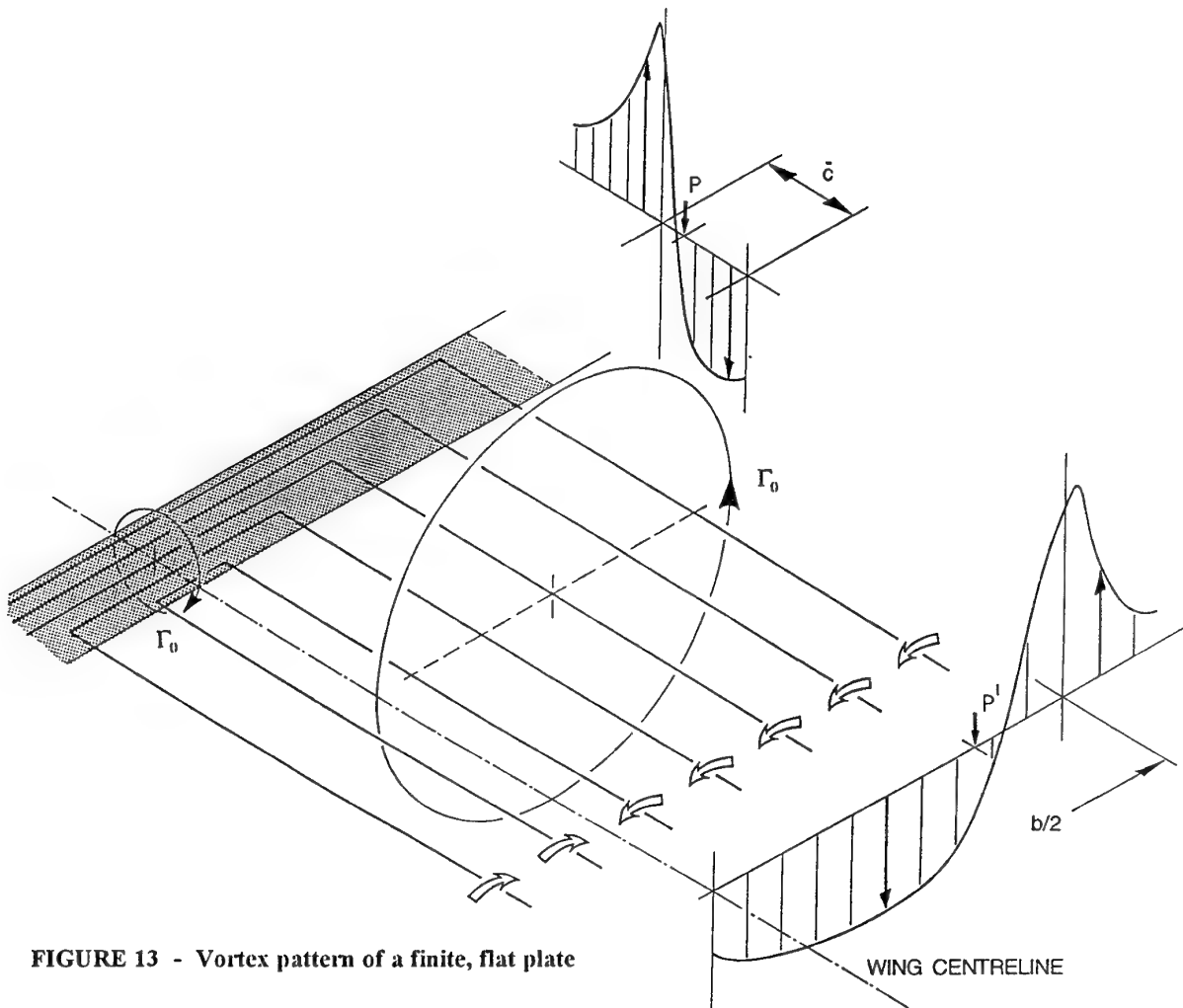


FIGURE 13 - Vortex pattern of a finite, flat plate

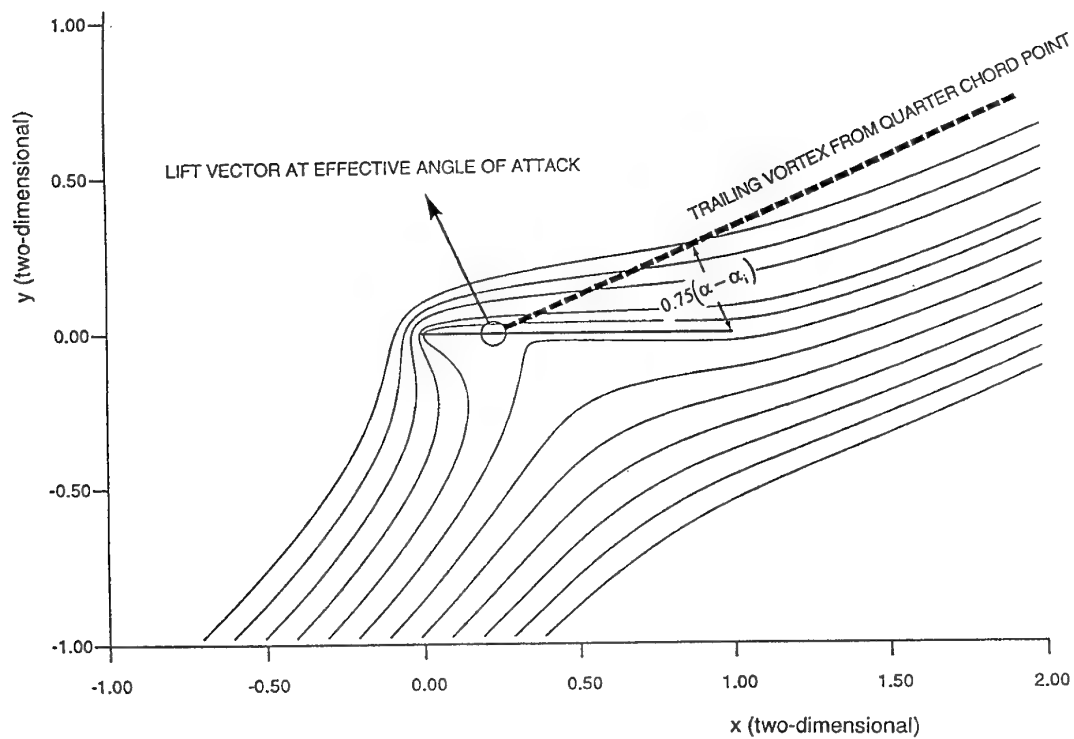


FIGURE 14 - Streamline pattern around a flat plate in planar flow

FIGURE 15 - Downwash distribution behind an elliptical loaded wing

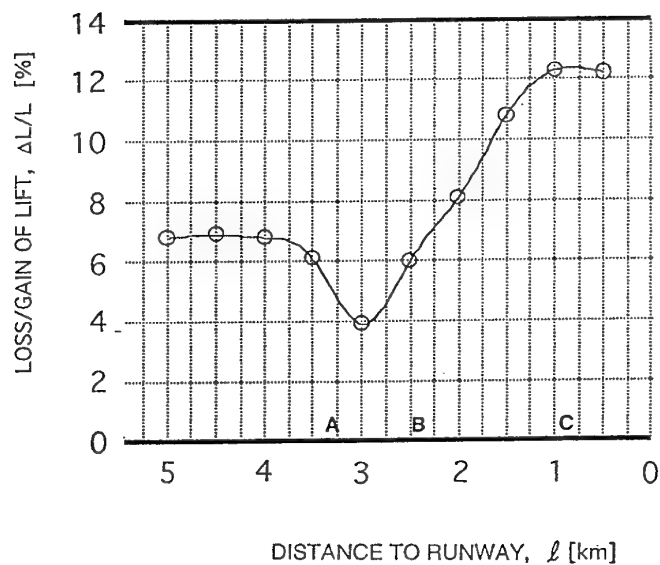
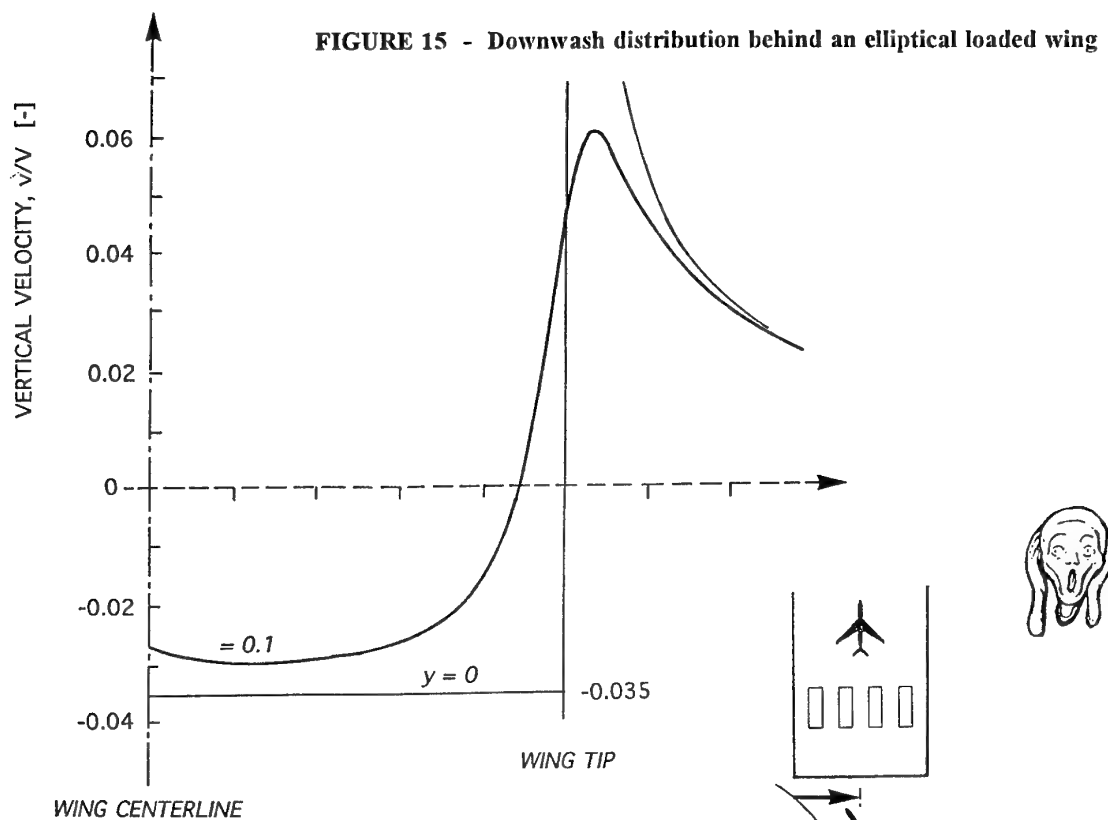


FIGURE 16 - Change of lift along the glide slope

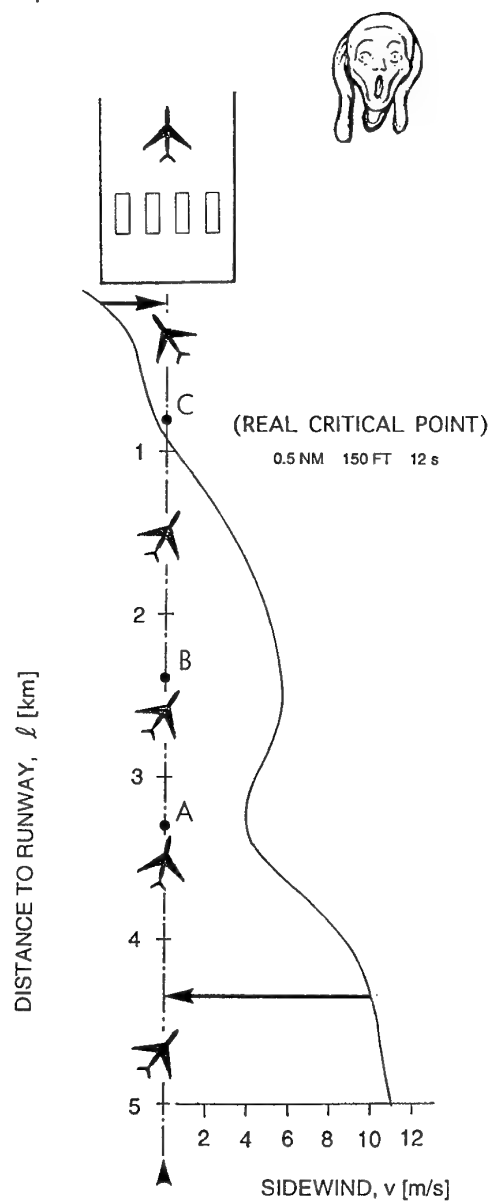


FIGURE 17 - Aircraft flight correction due to sidewind

Flow field survey in trailing vortex system behind a civil aircraft model at high lift

Anton C. de Bruin, Sinus H. Hegen, P. Bernd Rohne
National Aerospace Laboratory NLR
Voorsterweg 31, 8316 PR Marknesse, the Netherlands
and
Philippe R. Spalart
Boeing Commercial Airplane Group
P.O. Box 3707, M/S 67-LM, Seattle WA 98124-2207, USA.

SUMMARY

The roll-up of the trailing vortex system behind a generic civil aircraft windtunnel model with extended flaps and slats is studied up to 5 wing spans downstream. A laser light sheet flow visualisation technique is used and detailed flow field measurements are made with a spanwise traversable rake with five-hole probes. The measurement results are compared against calculations with the 2D vorticity transport equation.

LIST OF SYMBOLS

b	wing span of the model ($b=1.3565$ m)
u, v, w	non-dimensional velocity components
c_l	local wing load
r	non-dimensional distance to vortex core
C_L	lift coefficient
MRP	Model Reference Point
Re_b	Reynoldsnumber
S	wing area
X_{MRP}	position of MRP at $\alpha=0$ deg
X_b	downstream position in wake ($X-X_{MRP}$)/ b
Y_b, y	spanwise position (Y/b)
Z_b, z	vertical position (Z/b)
α	angle of attack of model (deg)
ω_x	non-dimensional streamwise vorticity
Γ	non-dimensional bound circulation
Ψ	streamfunction for crossflow velocity components

1. INTRODUCTION

The trailing vortex system behind civil aircraft may have important implications for trailing aircraft. In particular during the take-off and landing phase where, due to increased airport congestion, separation distance between individual aircraft tends to be small. In the present study the development of the wake roll-up behind a high-lift model with part-span flaps and slats is followed up to 5 wing spans downstream. Flow visualisations with the laser light sheet method reveal a stable vortex system with vortices emanating from the wing tip, the edge of the outboard flap and the edge of the inboard flap. In addition detailed flow field measurements with a rake with five-hole probes enable a more quantitative analysis of the wake roll-up process. Measured data-fields are analysed for the downstream development of axial velocity, streamwise vorticity and circulation. Measured streamwise vorticity fields are used to check the validity of the two-dimensional vorticity transport equation. Additional experiments are planned in the large low speed windtunnel DNW, to obtain data up to about 13 wing spans downstream of the model.

2. EXPERIMENTAL SET-UP

2.1 Windtunnel

The Phase I and Phase II experiments were performed in NLR's closed circuit low speed windtunnel LST which has a cross section of 3.0×2.25 m² and a test section length of 8.75 m with excellent visual accessibility through removable transparent side panels. The LST windtunnel has a remarkably low free stream turbulence level of about .025%. It is equipped with a remote controlled Y-Z traversing mechanism, allowing manual movements in X-direction over most of the test section length. Additional Phase III experiments are planned in the large (8×6 m²) low speed tunnel DNW. All tests are made at 60 m/s.

2.2 Model

An existing generic civil aircraft model was used, it consists of a fuselage and a wing only (fins and engines were not mounted). Figure 1 gives a sketch of wing planform and the flap and slat system. The measurements concentrate on a model geometry with a strong 35 degrees deflected inboard flap. The aft part of the flap has an extra flap partition, the inboard part has an extra deflection of 10 deg. The outboard flap was deflected either 5 or 15 degrees. Table 1 gives a summary of the investigated model configurations. To give an impression of measured lift coefficients for the various model configurations investigated, C_L - α polars are shown in figure 2. The maximum lift coefficient is about 2 with flaps extended, while with flaps and slats a value of about 3 is reached. Flow field measurements concentrate on model configurations 2 and 5.

Table 1 Model configurations

Conf.	Test Phase		deflection (deg)	
			slat	flap
	I	II	inner/outer	inner/outer
7	X	-	0 / 0	0 / 0
2	X	X	0 / 0	35-10/0 / 5
3	X	-	0 / 0	35-10/0 / 15
5	X	X	10 / 20	35-10/0 / 5
6	X	-	10 / 20	35-10/0 / 15

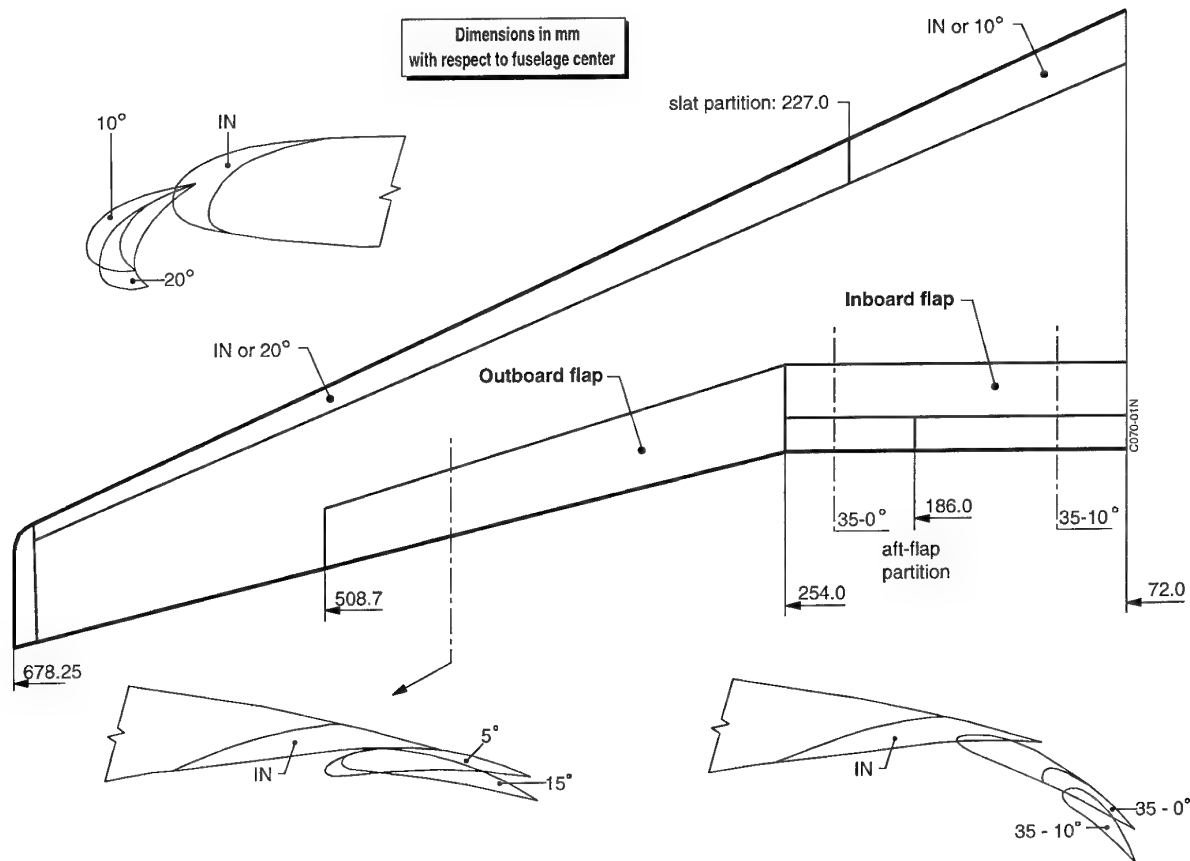
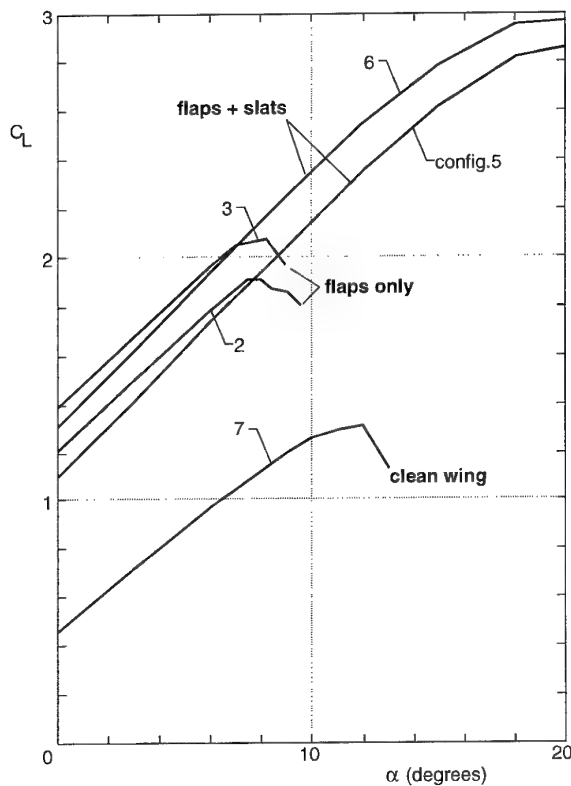


Fig. 1 Sketch of available high lift devices

Fig. 2 $C_L - \alpha$ curves

The model is mounted on a subsonic sting support connected to the wind tunnel floor via a manually controlled alpha mechanism interface. Model forces are measured with an internal balance. The model is positioned close to the test section entrance to obtain maximum distance downstream of the model. Only symmetric flow conditions are considered. Non-dimensional downstream position in the wake is referenced to the nominal ($\alpha=0$ deg) position of the Model Reference Point: $Xb=(X-X_{MRP})/b$. At $\alpha=0$ deg the fuselage centerline is at $Zb=0.153$ above the windtunnel centerline.

2.3 Laser screen flow visualisation

In the Phase I tunnel entry, a laser light sheet flow visualisation method was used. Smoke is injected at an appropriate location just upstream of the model. By moving the smoke tube progressively in-board, the individual vortices emanating from the wing tip and the flap edges are identified, even at

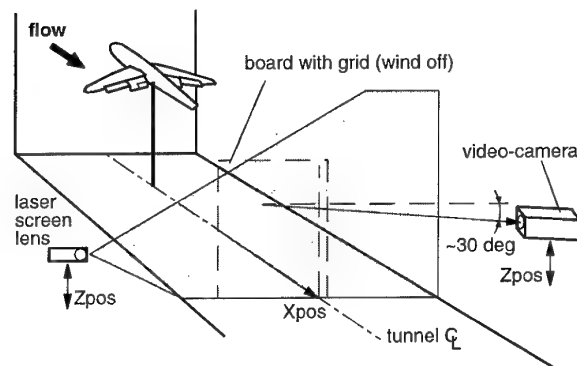


Fig. 3 Set-up for laser screen visualization in LST

Table 2 Visualisation tests (Phase I)

Conf.	Xb	α (deg)
2	.68, 1.2, 2.0, 3.3, 5.0	7
5	.68, .86, 1.2, 2.0, 3.3, 5.0	18
6	.86, 1.2, 2.0, 3.3, 5.0	18
3	.68, .86, 1.2, 2.0, 3.3, 5.0	7
3	5.0	4, 5, 6
7	.68, .86, 1.2, 2.0, 3.3, 5.0	10

long distances downstream of the model. The video camera and the screen emitting lens are mounted on the traversing mechanism, but at opposite sides of the tunnel test-section (see Fig. 3). Individual vortex cores appear as black holes in the video images. At the Xb locations given in table 2 the Yb and Zb position (with respect to the tunnel axis) of the individual vortex cores is evaluated from video-still images.

2.4 Flow field measurements

Preliminary flow field measurements were made during Phase I, while more extensive flow field measurements were made in the Phase II tunnel entry (see Tab. 3). A NLR designed and built rake equipped with 18 miniature five-hole probes with spherical heads is used ($\varnothing 2.5$ mm, probe pitch of 15 mm, see Fig. 4). Probe pressures are electronically scanned (with the electronically scanned pressure units placed inside the rake support sting) yielding high data rates with on-line pressure calibration abilities. The rake sting is mounted on a streamlined horizontal strut, which penetrates the windtunnel side walls, and is fixed to the Y-Z traversing mechanism (see Fig. 5). The rake is continuously traversed in spanwise Y-direction (traversing speed 5 mm/s), while taking measurements every

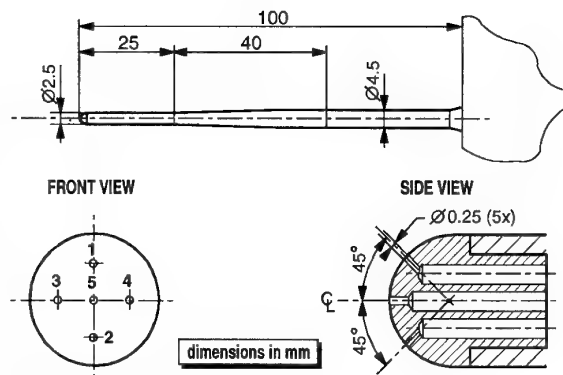


Fig. 4 Five-hole probe geometry

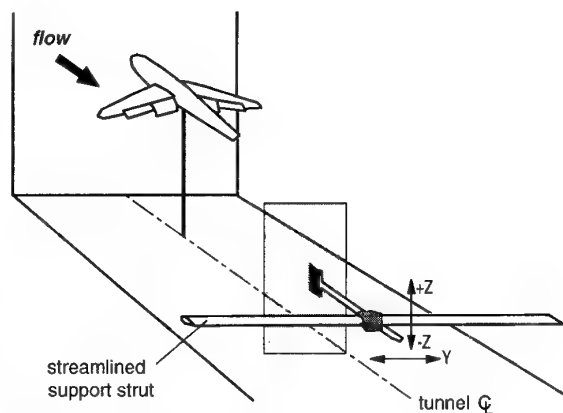


Fig. 5 Model and five hole rake in LST

second. With intermediate traversements at half probe pitch a fine grid ($\Delta Y \times \Delta Z = 5 \times 7.5$ mm) is obtained. Dedicated data handling software and interpolation in the calibration data base guarantees a nearly on-line presentation of measured data.

Table 3 Flow field measurements (Phase II)

Conf.	α (deg)	Xb			
		.67	2.00	3.53	4.69
2	3	.34/.53	-	-	.37/.33
2	5	.34/.53	-	-	.34/.34
2	7	.34/.55	.35/.50	.33/.46	.35/.39
2	9	.33/.59	-	-	.35/.39
5	9	.33/.55	-	-	.33/.38
5	12	.33/.55	-	-	.31/.42
5	15	.33/.59	-	-	.29/.44
5	18	.32/.60	.28/.52	.27/.47	.26/.45

Note: tabulated data refer to non-dimensional distance of tip and inboard flap vortex and maximum cross-flow velocity.

3. DISCUSSION OF RESULTS

3.1 Flow visualisation results

The flow visualisation tests give mainly a qualitative impression of the wake roll-up process up to 5 wing spans downstream of the model. The vortex core trajectories for configurations 2 and 5 are shown in figure 6 and 7, while remaining vortex trajectories in the Yb-Zb cross-plane are shown in figure 8. Concentrated vortices develop from the inboard flap edge, the outboard flap edge and the wing tip. In general the "tip" and "outboard flap" vortex become trapped in a helical motion or even merge at more downstream locations. For high lift (higher angle of attack) the merging process is more rapid than for comparatively low lift cases. However, the vortex from the inboard flap remains well separated from the other two vortices in all cases.

3.2. Flow field measurements

Preliminary (Phase I) flow field measurements confirmed the adequacy of the measurement method. However, the measured cross of flow angles (up to 35 deg near vortex cores) were well out of the available calibration range which covered flow angles up to 20 deg. It was therefore decided to recalibrate the rake up to flow angles of 45 deg before the next tunnel entry.

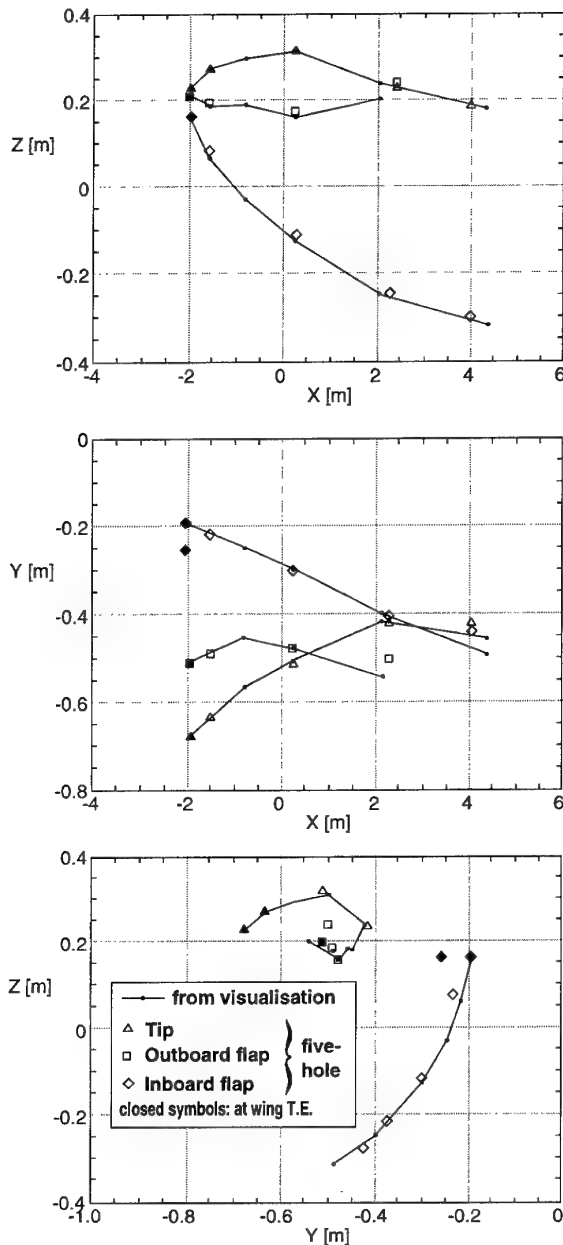


Fig. 6 Location of vortex with respect to test section center for configuration 2, $\alpha = 7^\circ$

Measurement planes are traversed over two, three or even four rake heights, depending on the vertical extent of the wake region. In total twenty planes were measured, some containing nearly 30000 data points. Though pre-test runs confirmed that the results were not sensitive to traversing direction, all traverses were made starting near $Y = -9$ m in the potential flow region outside the wing tip area. Figure 9 shows measured cross flow vectors is a small portion of a measured flow field. It gives a good impression of the observable flow details and the consistency of the measured data. Vortex cores are typically only 20 mm (about 1 % of wing span) in diameter and, despite the small size of the probes, one can not expect very accurate results in the vortex cores.

Prior to further analysis of the measured data, the three components of the non-dimensional velocity vector were linearly

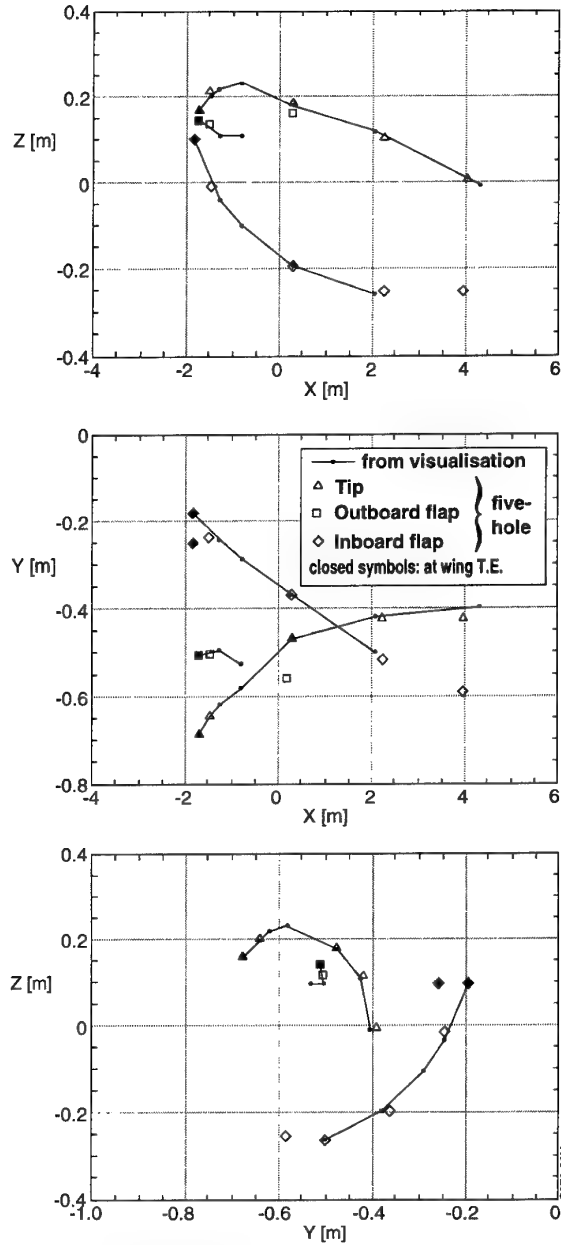


Fig. 7 Location of vortex with respect to test section center for configuration 5, $\alpha = 18^\circ$

re-interpolated in spanwise direction to obtain data on a regular rectangular grid ($\Delta Y \times \Delta Z = 5 \times 7.5$ mm). A small spanwise invariant correction on measured velocity components was applied as well (corrections typically 0.5 deg or less). The non-dimensional streamwise vorticity component ω_x (scaling factor U_∞/b):

$$\omega_x = \frac{\partial w}{\partial y} - \frac{\partial v}{\partial z} \quad (1)$$

was computed with central differencing in velocity components.

Plots 1 and 2 show the downstream development of crossflow velocity and streamwise vorticity fields for configuration 2 ($\alpha = 7^\circ$) and configuration 5 ($\alpha = 18^\circ$). Note that only a

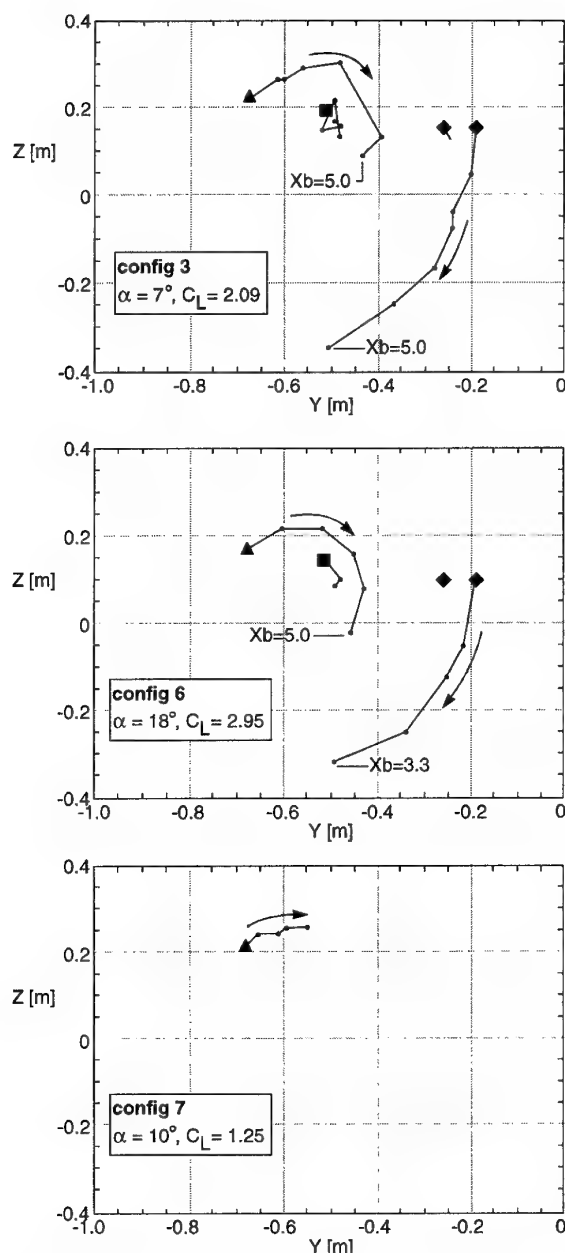


Fig. 8 Vortex core trajectories from flow visualisations

quarter of the available cross-flow vectors is shown for clarity. The position of the vortex cores is in good agreement with the flow visualisation results (see Fig. 6 and 7). Maximum crossflow velocity is seen to grow with model angle of attack (up to 60 % of free-stream velocity for configuration 5, $\alpha=18$ deg at $Xb=0.67$, see Tab. 3) and decreases in downstream direction. At $Xb=0.67$ the thin vorticity layer emanating from the wing trailing edge and the counter rotating region from the inboard flap edge are clearly visible, while the spanwise position of the individual vortices is still well related to the flap partition geometry of the model. At more downstream stations the vorticity becomes more and more concentrated in individual isolated vortices, though some remnants of the vorticity layer are still seen spiraling around the vortex cores. The weak straight horizontal vorticity layers are clearly unphysical and caused by small probe dependent errors ($\Delta\alpha$ and/or $\Delta\beta$ errors of order one deg, probably due to small oil and/or dust particles occasionally attaching to the probe heads). At more down-

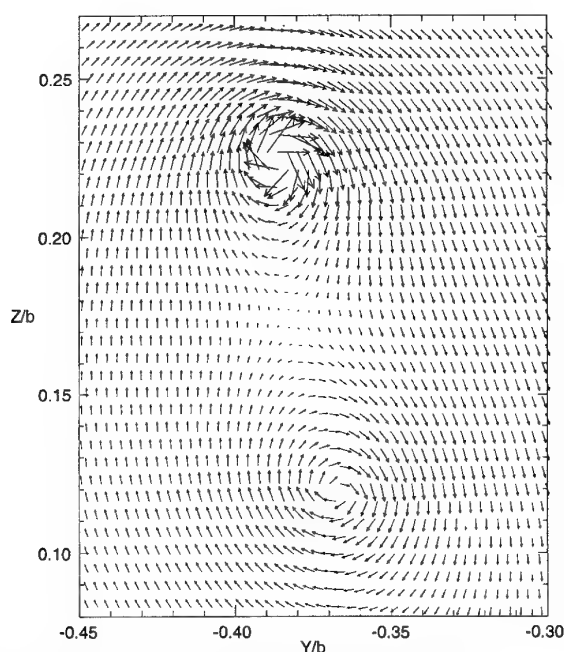


Fig. 9 Measured cross-flow vectors, configuration 2, $Xb = 2.0$, $\alpha = 7^\circ$

stream locations the tip and outboard flap vortex tend to merge. The inboard flap vortex and the tip vortex remain however well separated, though for configuration 5, starting from $\alpha=12$ deg, the distance between these two vortices decreases in downstream direction and with the angle of attack of the model (see Tab. 3).

A good impression of the position of the wake can be obtained by plots of axial velocity. For configuration 5, $\alpha=18$ deg, results are shown in plot 3. At $Xb=0.67$ the compartmentation of the flow (high velocities above and low velocities below the wing) is still clearly visible. Just as in Huenneke (Ref. 1) the tip vortex is partly surrounded by a region with comparatively large axial velocity, especially at initial station $Xb=0.67$ ($u_{max} \approx 1.07$). At the $Xb=0.67$ station the large wake region emanating from the fuselage is clearly visible. At more downstream locations the inboard flap vortex remains embedded in a large region with low speed flow.

3.3. Spanwise wing load and total lift force.

The strength of the trailing vortex system downstream of the configuration is proportional to the wing lift, while its topology will largely depend on the spanwise lift distribution of the wing. According to Maskell (Ref. 2) and Brune (Ref. 3) the total lift and spanwise wing load can be obtained from wake measurements. The contribution of the measured portion of the wake plane to the total lift coefficient becomes (see Fig. 10):

$$C_L = \frac{4b^2}{S} \int_{y_{min}}^{y_{max}} \int_{z_{min}}^{z_{max}} (y\omega_x) dy dz, y_{max} \leq 0 \quad (2)$$

With Yb in the integrand and no large concentrated vorticity to be expected near the model symmetry plane, Eq. 2 should give a fair approximation of total lift even at $Xb=0.67$ where $y_{max} < 0$ due to the presence of the fuselage. Instead of solving Eq. 2 directly, we may also refer to the circulation $\Gamma(y)$ of the bound and trailing vortices. To first order the spanwise wing load is directly related to $\Gamma(y)$:

$$c_l c(y) = 2b\Gamma(y). \quad (3)$$

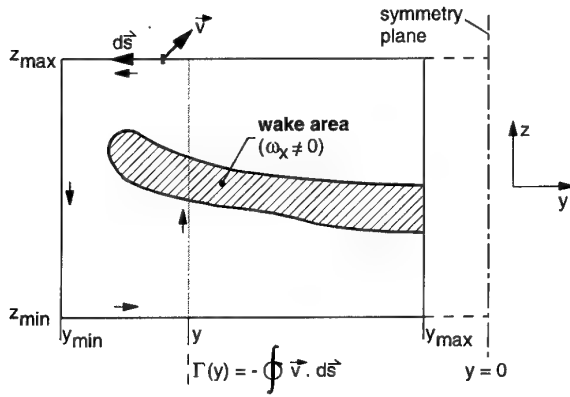


Fig. 10 Domain of integration for model lift

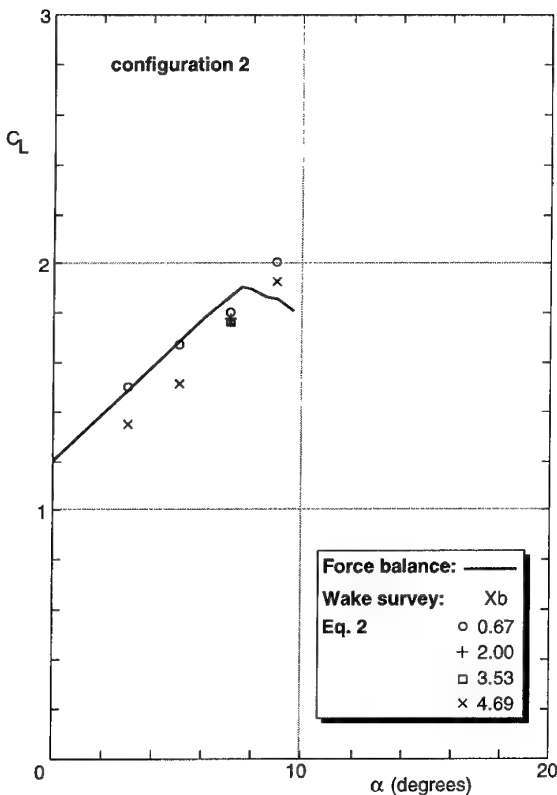
This relation is generally lost at more downstream stations due to the wake roll-up process. Two alternative methods were used to determ $\Gamma(y)$. In the first method, with $d\Gamma = -\omega_x dydz$, the following expression for $d\Gamma/dy$ is found:

$$\frac{d\Gamma}{dy} = - \int_{z_{min}}^{z_{max}} \omega_x dz. \quad (4)$$

Integration in y -direction (taking $\Gamma=0$ at $y=y_{min}$) yields $\Gamma(y)$. In the second method the circulation is determined from a closed contour integration of velocities (see Fig. 10). Eq. 2 can be rewritten to obtain the lift coefficient from a spanwise integration of $\Gamma(y)$:

$$C_L = -\frac{4b^2}{S} \int_{y_{min}}^{y_{max}} \left(y \frac{d\Gamma}{dy} \right) dy \quad (5)$$

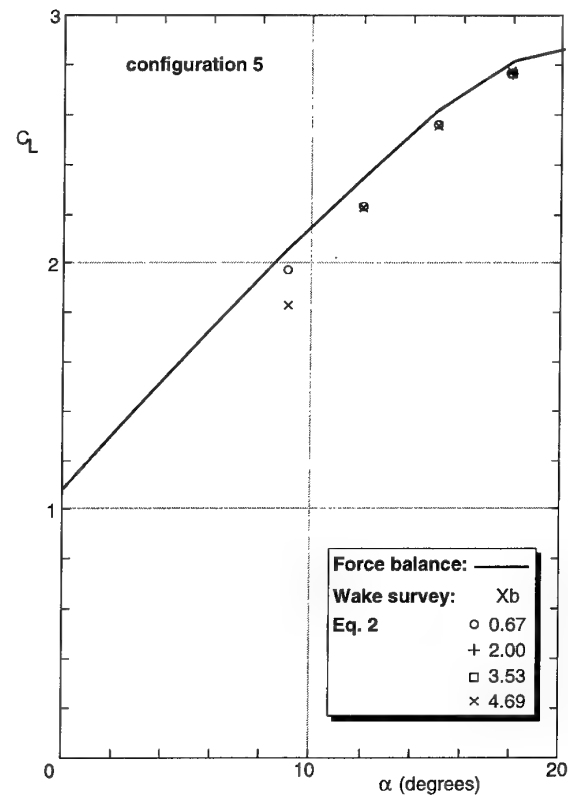
$$= \frac{4b^2}{S} \left(-y\Gamma \Big|_{y_{min}}^{y_{max}} + \int_{y_{min}}^{y_{max}} \Gamma(y) dy \right),$$

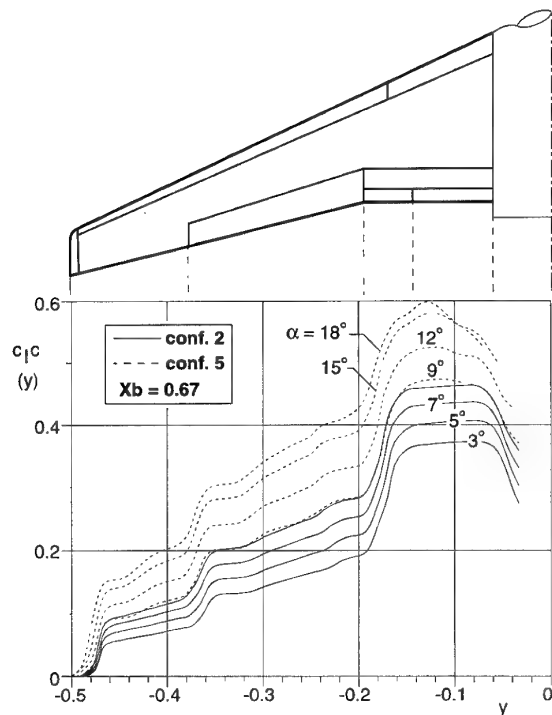
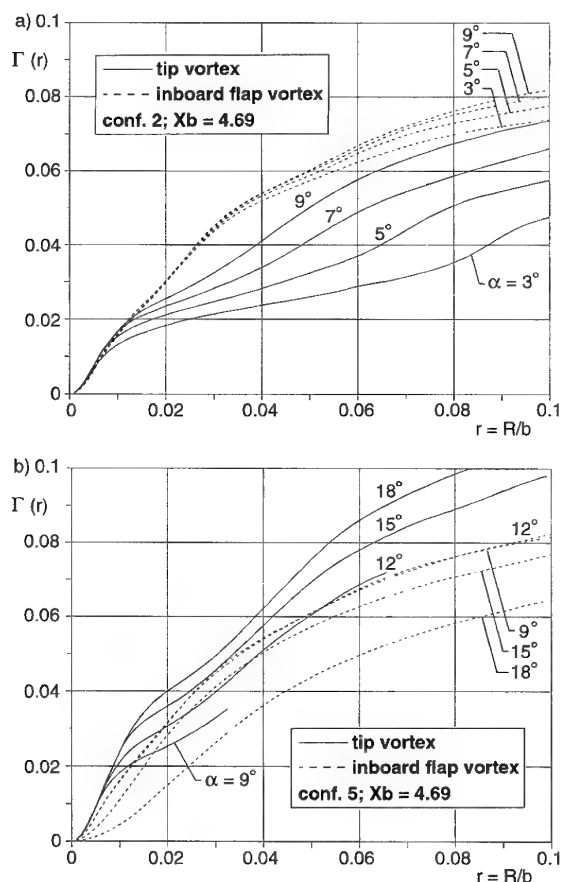
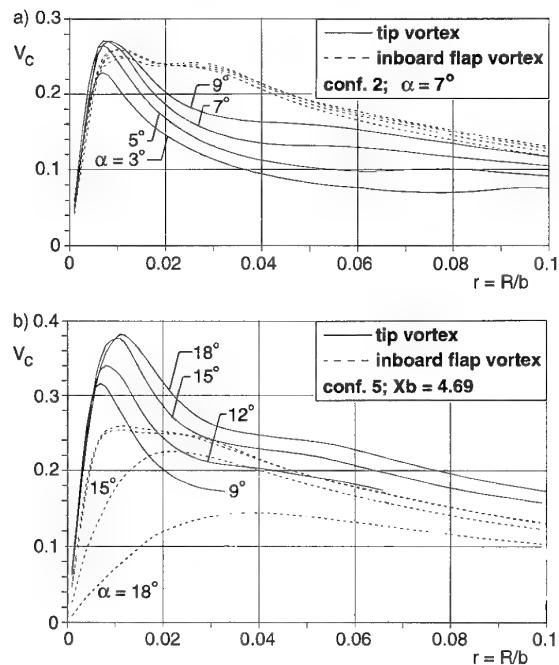
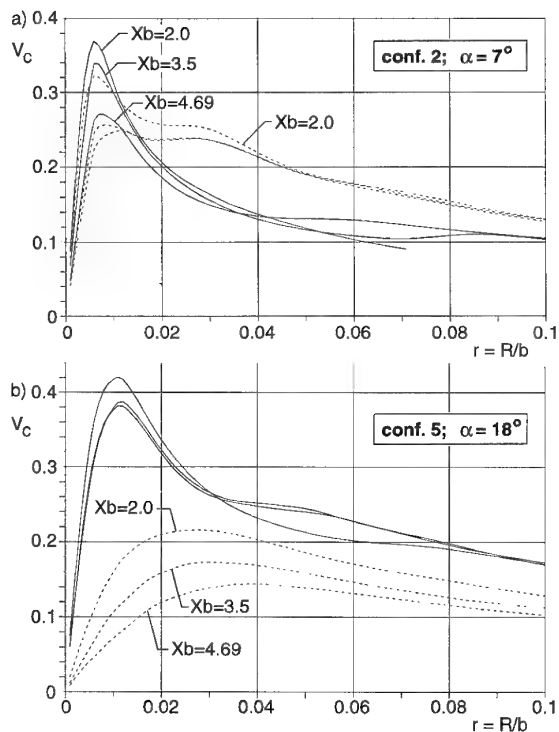
Fig. 11a $C_L - \alpha$ curve, configuration 2

where $y_{min} \Gamma(y_{min}) = 0.0$. The total lift was computed with these three alternative methods and differences were less than a few percent, demonstrating the consistency of the present data. Results are compared against direct balance measurements in figure 11. For model configuration 5 the computed lift is largely independent of the measurement plane and the results compare quite well with the direct force measurements. However, less satisfactory results are observed for configuration 2. Spanwise wing load distributions at $Xb=.67$ are shown in figure 12. The jumps in span-load are an indication for the strength of individual vortices at this position. Note that the spanwise positions of the jumps in circulation do not match with flap partition locations since already some wake roll-up occurred. At low angles of attack the inboard flap vortex is relatively strong, while at high angles of attack the tip vortex gains more importance. Further note that a change of model configuration at $\alpha=9$ deg (with and without slats extended) hardly affects the wing load distribution.

3.4. Vortex strength

Once the individual vortices are sufficiently separated, an impression of their strength can be obtained by calculating the circulation $\Gamma(r)$ and the average circulation velocity $V_c(r) = \Gamma(r)/(2\pi r)$ on circular contours around the vortex core (here defined as point with maximum vorticity). For $Xb=4.69$, the circulation strength variation with angle of attack is shown in figure 13, while V_c is shown in figure 14. Note that lines stop when the circular contour touches the edge of measurement domain. The tip vortex strength continuously increases with angle of attack (partly by the merging process with the outboard flap vortex), but the strength of the inboard flap vortex remains rather constant up to $\alpha=12$ degrees and then starts to diminish in strength considerably. At $Xb=4.67$ the non-

Fig. 11b $C_L - \alpha$ curve, configuration 5

Fig. 12 Spanwise "wing loads" at $X_b = 0.67$ Fig. 13 Vortex strength, variation with α Fig. 14 Mean circulation velocity, variation with α Fig. 15 Mean circulation velocity, variation with X_b

dimensional viscous core diameter of the tipvortex is about 0.015 (20 mm) and largely independent of model angle of attack. On the other hand the viscous core diameter of the inboard flap vortex increases considerably above $\alpha = 12^\circ$. The downstream development of V_c , shown in figure 15, reveals a particularly rapid increase of vortex core diameter for the inboard flap vortex (configuration 5, $\alpha = 18^\circ$).

4. WAKE ROLL-UP CALCULATIONS

Assuming flow turbulence and vortex stretching effects to be small, the wake roll-up can be described with the two-dimensional vorticity transport equation (Spalart, Ref. 4 and Fell, Ref. 5):

$$\begin{aligned} \frac{D\omega_x}{Dt} &= \frac{\partial\omega_x}{\partial t} + v \frac{\partial\omega_x}{\partial y} + w \frac{\partial\omega_x}{\partial z} \\ &= \frac{1}{Re_b} \left(\frac{\partial^2\omega_x}{\partial y^2} + \frac{\partial^2\omega_x}{\partial z^2} \right), \end{aligned} \quad (6)$$

with $t \sim x/u_\infty$ and v and w are obtained from a Poisson equation for the stream function Ψ :

$$\begin{aligned} \frac{\partial^2\Psi}{\partial y^2} + \frac{\partial^2\Psi}{\partial z^2} &= -\omega_x, \text{ with:} \\ v &= \frac{\partial\Psi}{\partial z}; w = -\frac{\partial\Psi}{\partial y} \end{aligned} \quad (7)$$

Tunnel walls can be simulated by using proper inviscid boundary conditions on Eq. 7. Calculations were initiated with the experimentally determined (unsmoothed) vorticity field at $Xb=2.0$. For configuration 5 calculations proceed up to $Xb=4.69$ (with and without tunnel walls) and to $Xb=17.5$ (without tunnel walls), results are shown in plot 4. At $Xb=4.69$ only a modest effect of the tunnel walls is observed, leading to a small upward shift of the vortex system ($\Delta z=0.065$). The computed vortex locations with tunnel walls are in very good agreement with the measurements. Between $Xb=4.69$ and $Xb=17.5$ a continued downward movement of the vortices and a diminishing distance between the two vortices is observed (non-dimensional distance goes from .26 at $Xb=4.69$ to .18 at $Xb=17.5$). Calculation results for model configuration 2, $\alpha=7$ deg., also show a vertical shift ($\Delta z=.06$) due to the tunnel wall effect (see plot 5). Again the calculation with tunnel walls shows good overall agreement with experimental results, though there are some differences in the merging of the tip and outboard flap vortex. It should however be noted that, with these vortices being so close together, the flow becomes particularly sensitive to the initial conditions.

5. CONCLUDING REMARKS

The wake roll-up process behind a high lift configuration of a civil aircraft model with a relatively strong inboard flap was studied up to 5 wing spans behind the model. Mainly model configurations with a powerful 35 deg deflected inboard flap and a mildly 5 deg deflected outboard flap were studied. With slats extended, a rather large lift coefficient was reached ($C_L \approx 3.0$).

Flow visualisation studies with the laser light sheet method reveal a rapid roll-up of the vorticity layer into individual vortices, emanating from the wing tip, the outboard flap edge and the inboard flap edges. At more downstream locations the wing tip and outboard flap vortices tend to merge, especially for the high lift cases. The wing tip and the inboard flap vortices remain however well separated, though for the higher lift coefficients their mutual distance seems to decrease downstream.

Five hole probes were used to measure the three components of velocity. Twenty planes were measured, each containing 15000 to 30000 individual data points on a fine measurement grid (5×7.5 mm). Crossflow vector plots reveal a complicated structure of the flow field, with small sized vortex cores (typically 20 mm in diameter or even less). Contrary to the tip

vortex the inboard flap vortex is imbedded in an area with comparatively low speed flow, especially at higher angles of attack.

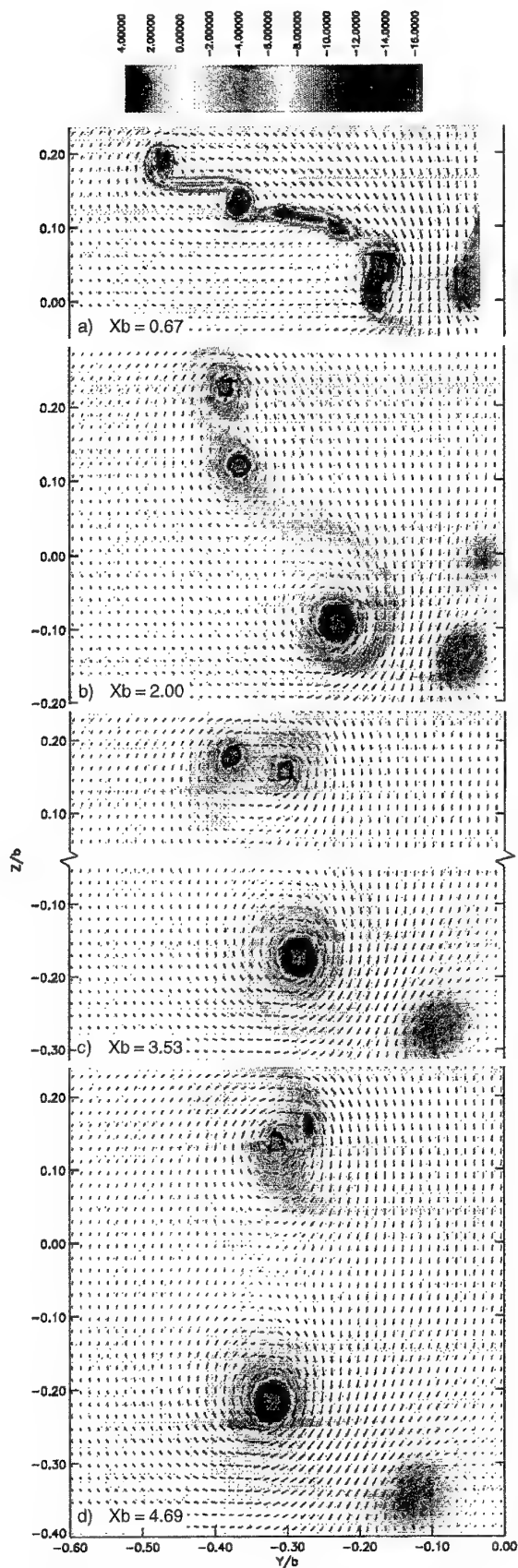
Streamwise vorticity was evaluated and Maskell's method was applied to determine the total lift and the spanwise wing load of the model. Results agree reasonably well with force balance measurements. Spanwise lift loadings and detailed analysis of the strength of individual vortices reveal a growing importance of the tip vortex for higher angles of attack. On the other hand the strength of the inboard flap vortex remains fairly constant. However, above $\alpha=12$ deg the core diameter of the inboard flap vortex rapidly increases downstream.

Measured streamwise vorticities at $Xb=2.0$ were used as initial data field for wake roll-up calculations with a two-dimensional vorticity transport equation. At $Xb=4.69$ calculation results with windtunnel walls included are in excellent agreement with experimental vortex locations. Calculations confirm that the disturbing effects due to the tunnel walls are relatively small. For model configuration 5, $\alpha=18$ deg, calculations were continued up to $Xb=17.5$ (no tunnel walls). A decrease of distance between the tip and inboard flap vortices is noted (non-dimensional distance decreases from 0.26 to 0.18 between $Xb=4.69$ and 17.5), but further analysis is needed whether this is due to a cyclic variation or not.

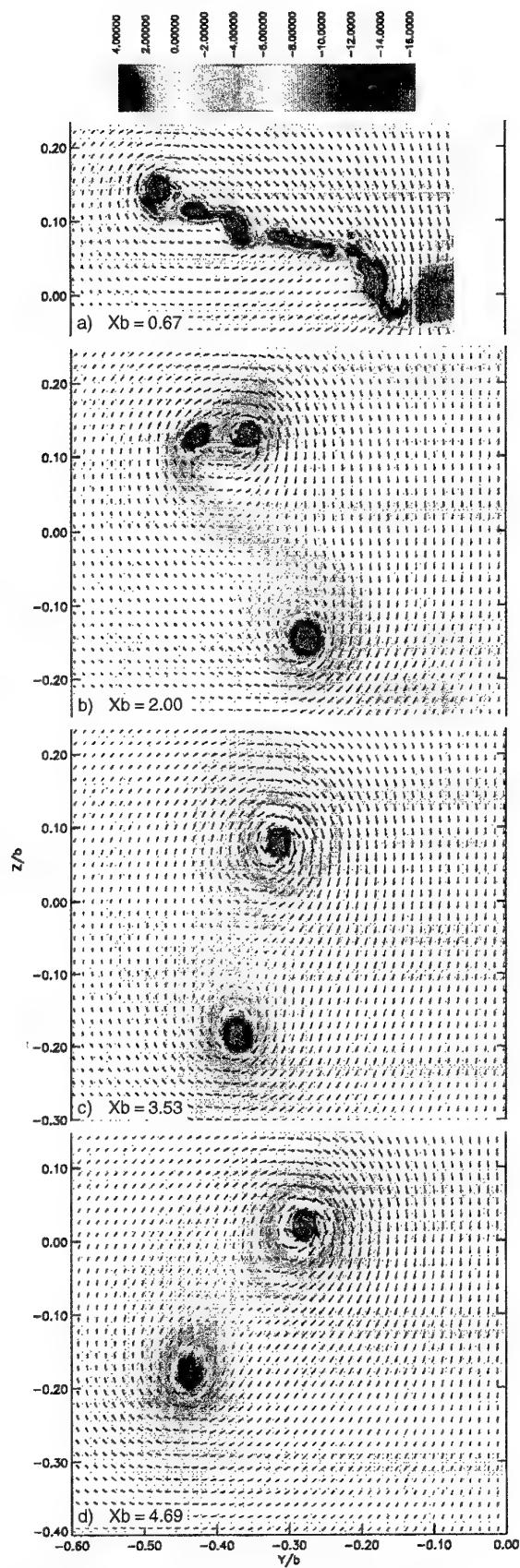
Additional measurements, up to about $Xb=13$, are planned in the large low speed windtunnel DNW to increase confidence in the idea that vortices can remain separated up to large distances downstream.

6. REFERENCES

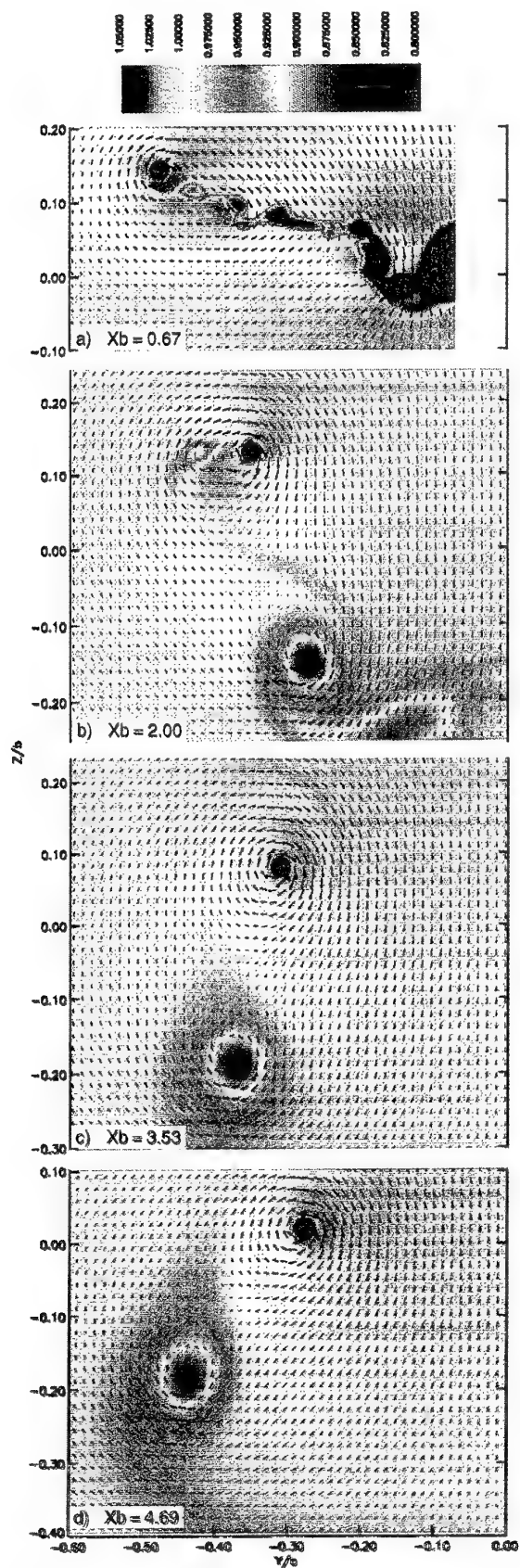
1. K. Huenecke, "Wake vortex investigations of transport aircraft", AIAA-95-1773-CP, 1995.
2. E.C. Maskell, "Progress towards a method for the measurement of the components of the drag of a wing of finite span", RAE Technical Report 72232, 1972.
3. G.W. Brune, "Quantitative low-speed wake surveys", Journal of Aircraft, Vol. 31, No. 2, March-April 1994.
4. Ph. R. Spalart, "On the motion of aircraft wakes in a stably stratified fluid", submitted to JFM.
5. St. Fell and R. Staufenbiel, "Formation and structure of vortex systems generated by unflapped and flapped wing configurations", Z. Flugwiss. Weltraumforsch. 19(1995),



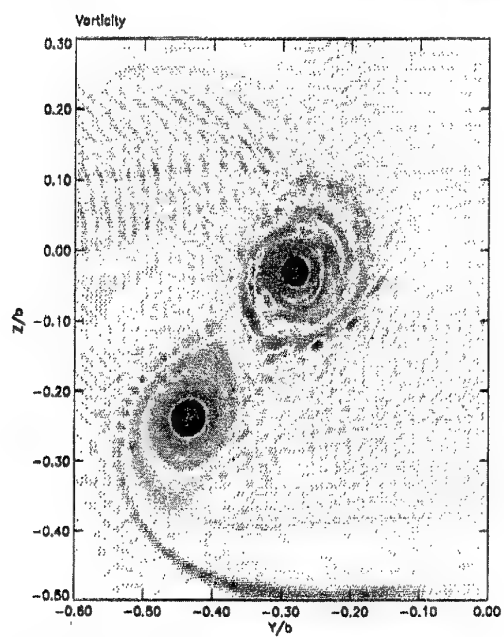
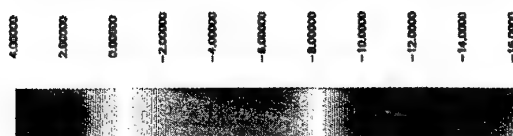
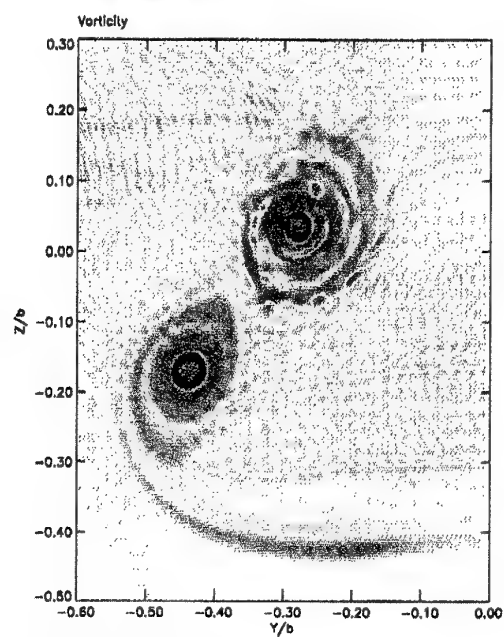
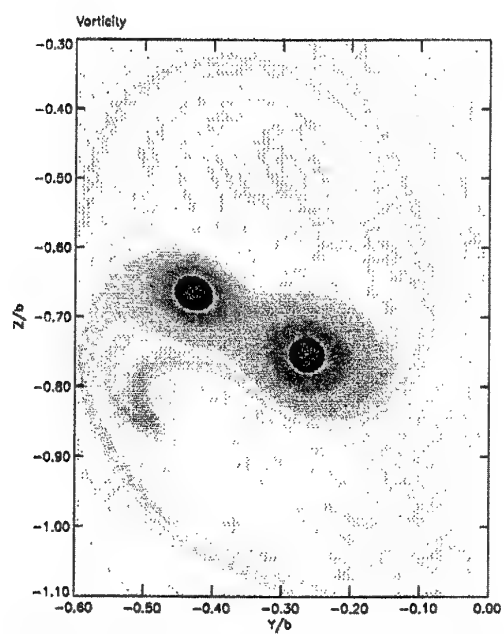
Plot 1 Downstream development of streamwise vorticity, configuration 2, $\alpha = 7^\circ$



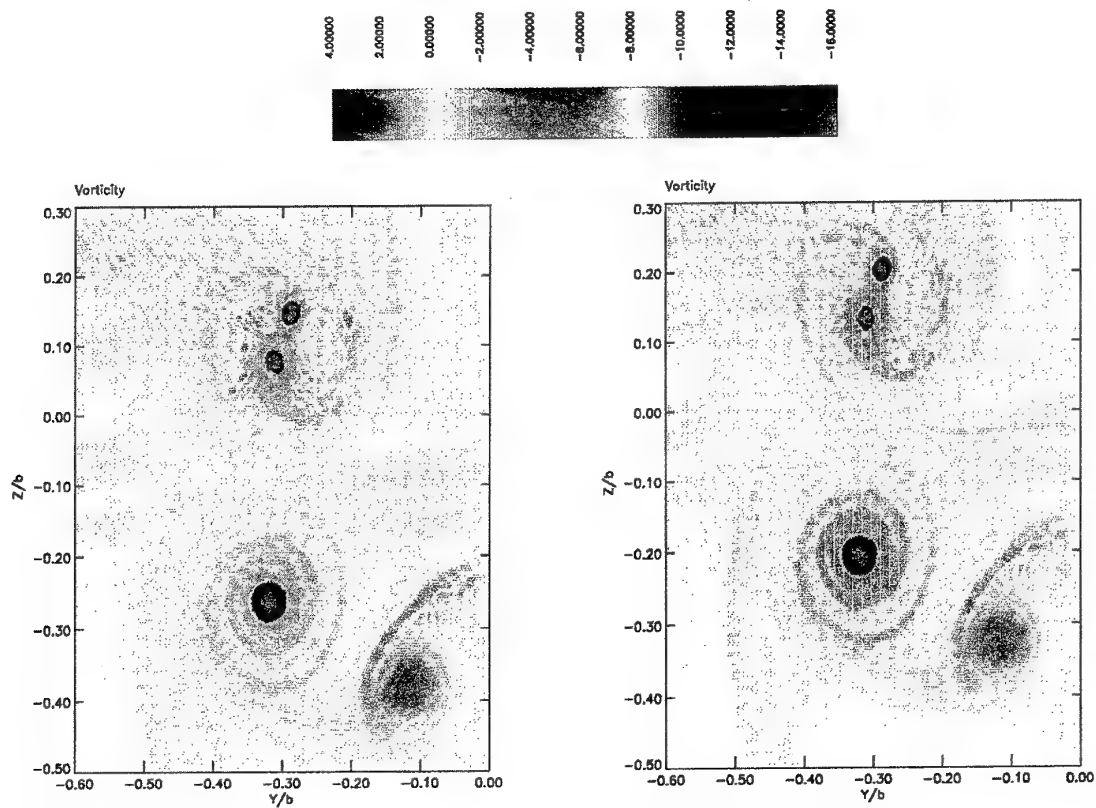
Plot 2 Downstream development of streamwise vorticity, configuration 5, $\alpha = 18^\circ$



Plot 3 Downstream development of axial velocity, configuration 5, $\alpha = 18^\circ$

a) $Xb = 4.69$, no tunnel wallsb) $Xb = 4.69$, with LST tunnel wallsc) $Xb = 17.5$, no tunnel walls

Plot 4 Computed vorticity fields, configuration 5, $\alpha = 18^\circ$



Plot 5 Computed vorticity fields, configuration 2, $\alpha = 7^\circ$

MEASUREMENTS IN VORTEX WAKES SHED BY CONVENTIONAL AND MODIFIED SUBSONIC AIRCRAFT

Vernon J. Rossow
Low Speed Aerodynamics Branch
NASA Ames Research Center
Moffett Field, CA 94035-1000

SUMMARY

A theoretical and experimental program is underway at NASA Ames Research Center to first obtain a better understanding of the hazard posed by the vortex wakes of subsonic transports, and then to develop methods on how to modify the wake-generating aircraft in order to make the vortices less hazardous. This paper summarizes results obtained in the 80- by 120-Foot Wind Tunnel at NASA Ames Research Center on the characteristics of the vortex wakes that trail from 0.03 scale models of a B-747 and of a DC-10. Measurements are first described that were taken in the wakes with a hot-film anemometer probe, and with wings that range in size from 0.2 to 1.0 times the span of the wake-generating models at downstream distances of 81 ft and 162 ft. behind the wake-generating model; i.e., at scale distances of 0.5 and 1.0 mile. The data are then used to evaluate the accuracy of a vortex-lattice method for prediction of the loads induced on following wings by vortex wakes.

LIST OF SYMBOLS

AR	=	aspect ratio
b	=	wing span
c	=	chord
C_L	=	lift coefficient = L/qS
C_l	=	rolling-moment coefficient = M/qSb
L	=	lift
M	=	rolling moment
q	=	dynamic pressure = $\rho U_\infty^2/2$
r	=	radial distance from axis of vortex
S	=	wing planform area
u, v, w	=	velocity components in x, y, z directions
U_∞	=	velocity of aircraft
W	=	weight
x	=	distance in flight direction
y	=	distance in spanwise direction
z	=	distance in vertical direction
α	=	angle of attack
β	=	yaw angle
ρ	=	air density

Subscripts

av	=	averaged over time at a given point
f	=	following model
g	=	wake-generating model
max	=	maximum on one side of centerline
mi	=	minimum at a given point
mx	=	maximum at a given point
p	=	pitch
r	=	roll

1 INTRODUCTION

After 25 or more years of research on the wake-vortex problem, Fig. 1, a satisfactory set of guidelines for the modification of the vortex wakes of subsonic transport aircraft have not yet been developed. However, the information presented in several overviews of the status of the research sponsored by the Federal Aviation Administration (FAA) and National Aeronautics and Space Administration (NASA) of the United States indicates that some progress has been made by both industry and government groups working on the problem¹⁻⁶. It is noted in these overviews that a great deal of effort has gone into the use of ground-based facilities. Only a limited number of flight tests were carried out because they are expensive to conduct and

present experimental difficulties^{7,8} when detailed measurements are desired on the characteristics of vortex wakes. The use of ground-based facilities gained support when it was found that they could produce results that were in good agreement with the results from flight tests⁷⁻⁹.

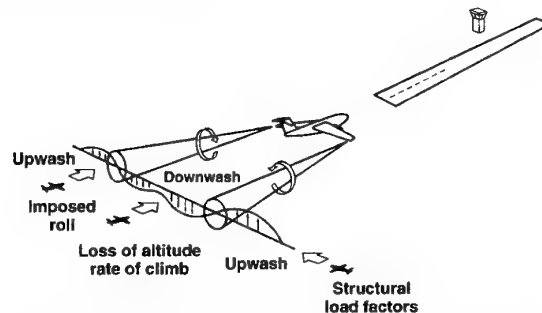


Fig. 1 Schematic of possible encounters with a lift-generated wake by a following aircraft.

The first work in the large wind tunnels at NASA began in the 40- by 80-Foot Wind Tunnel¹⁰⁻¹⁸ in the early 1970's because the larger 80- by 120-Foot Wind Tunnel was not available until the late 1980's. In the early 1990's, the 80- by 120-Foot Wind Tunnel was chosen as the facility for the investigation of wake vortices because it is the largest NASA facility, and, consequently, has the greatest downstream test distance, Table I. The test section alone is about 200 ft. long so that wake measurements can be made at downstream distances that simulate scale distances up to one mile when models of 0.03 scale are used; Fig. 2. The first test in the 80- by 120-Foot Wind Tunnel¹⁷, made at 81 ft. or one-half mile scale distance, showed that the measured results in the two large wind tunnels are in good agreement. The second wind tunnel test¹⁸ provided data on various configurations of models of the Boeing B-747 and the McDonnell Douglas DC-10, Table II, at downstream distances in the wake at 81 and 162 feet; i.e., one-half and one mile scale distances for the 0.03 scale models used in the test. In order to assess the characteristics of vortex wakes, following wings were tested that range in size from 0.186 to 1.0 times the span of the wake-generating model; Table III. A two-component hot-film anemometer probe was used to determine the up- and down-wash distributions in the wake at both the 81 and 162 ft. downstream measuring stations. The end objective of the research is, of

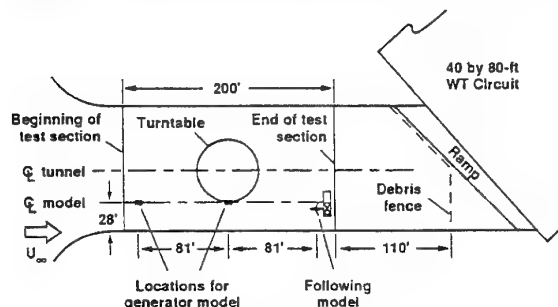
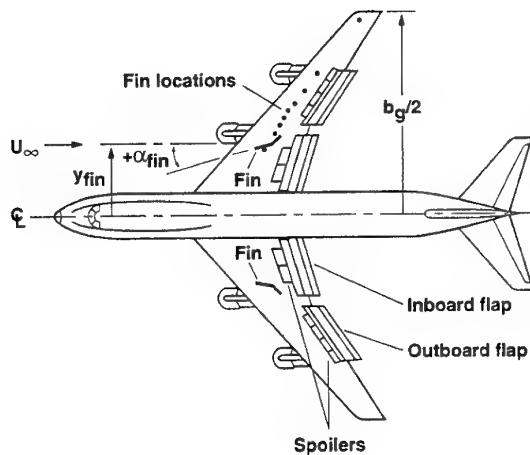
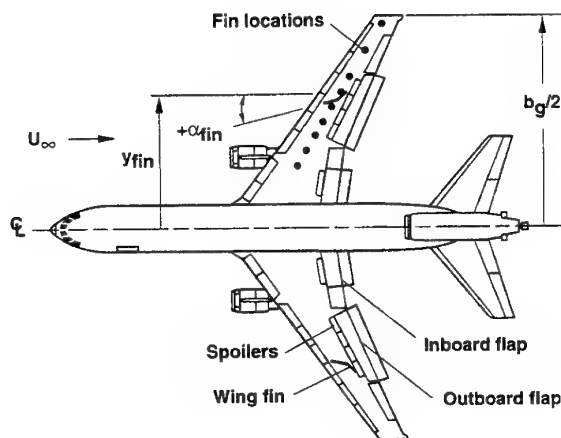


Fig. 2 Plan view of experimental setup in 80- by 120-Foot Wind Tunnel.



(a) B-747



(b) DC-10

Fig. 4 Wake-generating models in plan view to illustrate flap arrangements and locations of wing fins.

models are constructed of wood and aluminum, and then covered with fiberglass to ensure a smooth, durable finish along with structural rigidity and adequate frequency response. As a result, the natural frequencies in roll and pitch of the model-balance combinations are several times larger than the wake-induced lift and rolling-moment frequencies encountered. The trailing model or wing is mounted on a sting, Fig. 3, that can be raised and lowered over a height range of about 8 ft. The vertical traverse mechanism is attached to a tower that can be translated laterally, or spanwise, across the airstream over a range of about 20 ft. The follower model is attached to its sting through a strain-gage balance located inside the centerbody of the wing so that the wake-induced lift and rolling moment can be measured.

The procedure used to measure the rolling moment on each following wing consists of several steps. The generator model is first set up in its desired configuration and angle of attack. After the time-averaged loads on the wake-generating model are recorded, the following wing is placed at various locations in the vortex wake of the generator model. Since the airstream is not perfectly uniform, the position of the vortex wake moves about with time to cause different amounts of lift and rolling moment to be induced on the following wing. In order to obtain a measurement of the variation of these quantities with time and to find the maximum at each location, the time-varying rolling moment indicated by the strain-gage instrumentation is recorded. The data is processed by first calculating the value of each

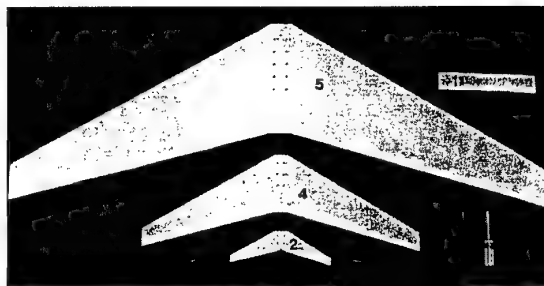


Fig. 5 Overhead photograph of following wings.

parameter when time-averaged over 0.1 second. In order to obtain one full minute of data, 600 such samples are recorded end-to-end. The permanent record consists of the maximum and the minimum of all of the 0.1-second values that occurred during the one minute test interval, and also the average or mean value of all 600 samples. A total sample of about one minute in duration was found to be long enough that two to four peak values of about the same magnitude would occur. These data are taken at a number of spanwise and vertical positions of the following model until the entire active wake region has been surveyed¹⁴⁻¹⁸ for the maximum or most intense value of the rolling moment on both sides of the wake centerline. If the span of the following model is small relative to the span of the generator model, the largest rolling moment is assumed to occur when the centerline of the following model coincides with the axis of one of the vortices in the wake. These locations were then used as the elevations at which spanwise surveys were conducted with various following wings or with a hot-film anemometer probe. Since the vortex centers occur at different elevations on each side of the centerline, the survey elevation on each side of the wake was changed at the centerline so that both surveys pass through the vortex center for their respective sides.

3 CONVENTIONAL CONFIGURATIONS

The presentation of the results for the two wake-generating models is divided into two groups. The first group, which will be discussed in this section, includes the conventional landing configurations. The second group, which will be discussed in the next section, includes those configurations wherein modifications were applied to the wings of the wake-generating models in an effort to reduce the magnitude of the rotary velocities in the wake in order to alleviate the wake hazard for aircraft which might encounter them.

3.1 Up- and Down-wash Distributions

The up- and down-wash distributions are discussed first because their characteristics illustrate several features that affect the discussions of the rolling-moment measurements. Since the vertical velocity surveys require a large amount of time to acquire, they were restricted to only a few configurations. In order to choose the best configurations for survey with a hot-film probe, the surveys were taken near the end of each test sequence with each model and separation distance to make available the characteristics of the wakes shed by the configurations tested.

Consider first the distributions of flow-field angularity, w/u , behind the standard landing configurations of both wake-generating models at the two separation distances, $x_f=81$ ft. and 162 ft.; Figs. 6a and 6b. In this paper, only the lines connecting the measured data and not the data points themselves are presented to reduce the clutter on the graphs. Even though the data in Fig. 6 at $x_f=162$ ft. is not as smooth as the data at $x_f=81$ ft., several observations can be made with regard to changes in the vortex wakes with downstream distance. (On the basis of data presented in Ref. 18, the differences between the port and starboard sides of the wake are not due to a slight yaw of the model relative to the free-stream. The port and starboard asymmetries in the data are attributed to differences in the aerodynamic structure of the wings of the models that occurred when there were built.) The increased size of the fluctuations in

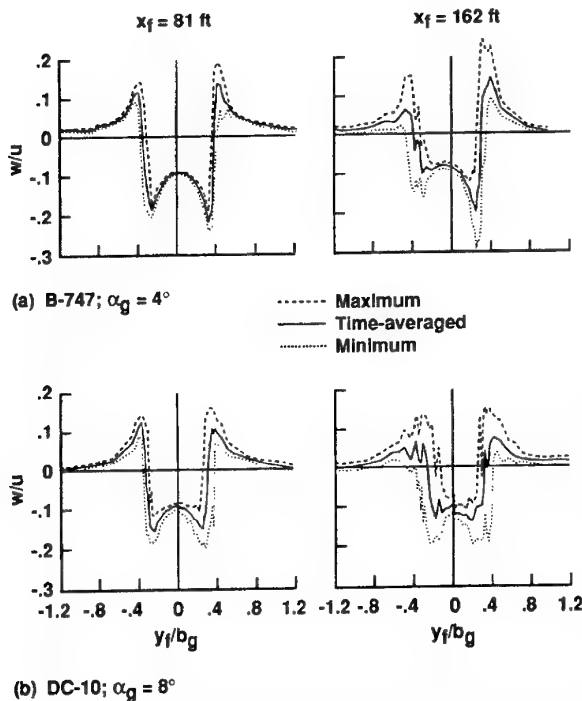


Fig. 6 Comparison of downwash distributions in wakes of transport models at two downstream distances.

the velocity distributions at $x_f=162$ ft. are believed to be caused by the larger meander distances of the vortices at the greater downstream distance. Less erratic data profiles can probably be achieved by use of data sampling intervals longer than one minute at $x_f=162$ ft. As in the data presented previously¹⁷, the differences between the maximum and minimum data curves indicate not only the variations in the velocity at a given point in the flow field, but also the lateral or spanwise displacement of the vortex center as it meanders about due to background turbulence in the airstream. Examination of the maximum and minimum curves in the vortex core region indicates that the vortex meanders about 4 inches (i.e., over about a 2 in. radius) at the 81-ft. station and about 8 inches (or over a 4 in. radius) at the 162-ft. station. Such a variation is expected because the greater downstream distance allows twice as much time for the turbulent eddies to convect, and distort, the vortices from their time-averaged locations. Since the analog data coming from the hot-film anemometer is filtered at 0.1 Hz, vortex excursions with a higher frequency do not appreciably influence the recorded data. At 0.1 Hz, the wave length of an eddy in the airstream is about 13 ft. (i. e., between 2 and 3 spanlengths).

After the data was plotted, it was quite surprising to find that some of the up- and down-wash velocities in the vortices were noticeably higher at $x_f=162$ ft. than at $x_f=81$ ft.; Figs. 6a and 6b. These increases in the swirl velocity indicate vortex intensification rather than decay²⁰. In contradiction, the maximum measured rolling moments to be presented in figures to follow were always less at the $x_f=162$ ft. station than at the $x_f=81$ ft. station, which is an indication of some vortex decay. Therefore, the two sets of data appear to be inconsistent because rolling moments calculated by use of the measured velocity distributions would be significantly larger than the measured ones at either the $x_f=162$ ft. station or at the $x_f=81$ ft. station. Several explanations for this inconsistency in the measured data were explored. The one that seemed to best represent the observed characteristics of the data appears to be related to the way in which the hot-film anemometer data were taken, and to possible vortex stretching by the turbulence eddies in the free-stream flow field. It is recalled that the time-averaged data presented in Fig. 6 represents the measurements taken during a one-minute interval at a given point, while the vortex center

moves about randomly. In the data taking process, the one-minute interval is divided into 0.1 sec. intervals to yield 600 data samples. The maximum and minimum data points are obtained as the two extremities of the 600 samples taken during the one minute. If the wind tunnel airstream had no turbulence, the time-averaged, maximum and minimum data would all be the same. But since the wind tunnel airstream does contain turbulence, the vortex moves about (meanders), and is stretched and compressed to change the magnitude of the swirl velocities in the vortex; thereby leading to the three curves in each part of Fig. 6.

In order to understand the effect of the meander and of the stretching processes, consider the hypothetical case where the vortex meanders but does not stretch or compress to change its intensity. If such a situation existed, the peak magnitudes of the maximum (and the minimum) curves would be the same over a lateral distance equal to the meander distance. This points out the fact that the maximum and minimum curves represent the envelope of velocity profiles for all possible meander locations of the vortex and not the instantaneous downwash profile. As the meander distance increases, the flat top and bottom of the two extremity curves also increase in the lateral direction, but not in magnitude. If the total area under the velocity curves is used to compute rolling moment, a sizeable error will occur if the lateral offsets due to meander are not removed.

Now consider the second hypothetical case wherein the vortex is stretched but its center is not displaced from the measuring point during the measuring interval. Such a situation arises whenever eddies in the airstream combine to bend and stretch the vortex locally but do not move the vortex center from its time-averaged location. In that case, a lateral spreading of the velocity curves does not occur. However, both extremities of the velocity curves increase because vortex stretching reduces the core radius and increases the swirl velocity because the angular momentum of the flow field is conserved. The imposed rolling moment is not changed appreciably, if at all, even though the maximum swirl velocity has been increased because the intensification occurs within the core at a small radius so that the following wing does not experience much increase in torque if its span is more than several core diameters. (Large amounts of vortex curvature and stretching can change the vortex structure substantially, but amounts that large are not expected for ordinary wind tunnel turbulence, at the distances used in the present test.) Since the maximum and minimum curves in Fig. 6 are made up of the envelopes of the extremities of the data taken at each survey point, they would include all of the enhanced velocity variations due to vortex motion and stretching.

The complexity of the interaction of the vortices with the airstream turbulence makes it difficult to estimate the amount of vortex enhancement to be expected, but it seems that the process could account for the larger velocities at the $x_f=162$ ft. station. That is, it is conjectured that both meander and vortex stretching occur to form an envelope of the maximum and minimum velocity curves. As the amplitude of vortex meander increases, the amplitude of the velocity extremes also increases. Further evidence of vortex stretching was believed to occur in the data when values of rolling moment were found at the periphery of the meander region rather than at the time-averaged location of the vortex center. On-line observation of the data indicated that the analog signals were much more erratic at the $x_f=162$ ft. station than at the $x_f=81$ ft. station, just as illustrated in Fig. 6. It is believed that a series of experiments designed to explore the foregoing conjectures will clarify the various characteristics in the data associated with vortex meander and stretching, and resolve the inconsistencies in the data. It should be remembered that, as aggravating as vortex meander is in the wind tunnel when valid measurements are desired, the same or similar phenomenon is present in the atmosphere. An improved understanding of how turbulence affects the intensity and decay of vortices²⁰ is therefore needed in order to predict their behavior in the airport environment.

3.2 Effect of Angle of Attack of the Wake-Generating Model

As indicated in Figs. 7a and 7b, and as expected, the magnitude of the rolling moments induced on following wing #1 by the

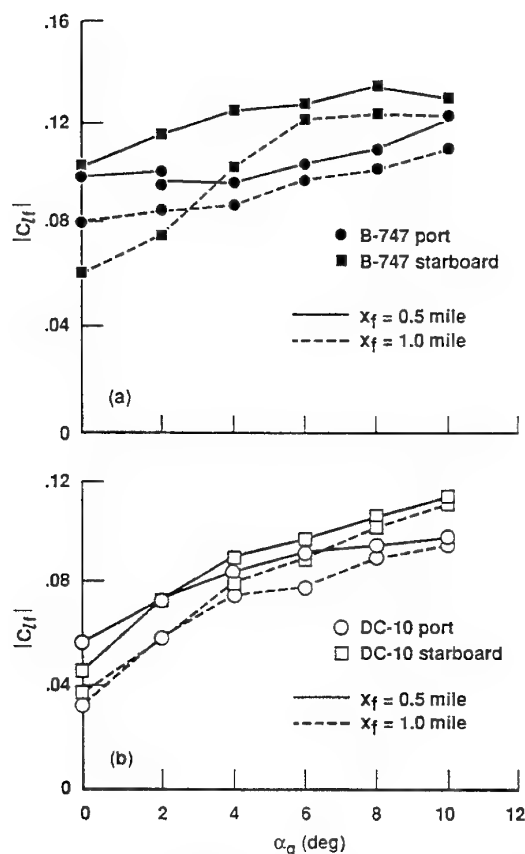


Fig. 7 Maximum rolling moment, $|C_H|$, induced on following wing #1 by wakes of the standard landing configurations as a function of angle of attack.

wake increase as the angle of attack, and lift, of the wake-generating model increases. The results for both the B-747 and the DC-10 at $x_f = 81$ ft. and 162 ft. are offset indicating that some wake decay has occurred. Some of the spread between the data at the two downstream stations at the lower angles of attack are believed to be caused by the turbulence introduced into the wake by the slats and flaps which operate there at significantly off-design conditions. Past experience has shown that introduction of turbulence into the wake causes the measured rolling moments to decrease significantly. Unfortunately, a limit appears to exist beyond which further introduction of turbulence does not reduce the wake hazard but does significantly affect the performance of the generator aircraft¹²⁻¹³. At the upper end of the angle of attack range, the rolling moments are about the same at the two downstream stations, indicating that wake decay is small²⁰ when the wake-generating wing is operating at near-design conditions. The large differences that occur at small angles of attack may not be present at full scale where the Reynolds number of flow over the wings is much larger.

A characteristic not observed in previous tests is a small amount of hysteresis that occurs in the lift on the generator model as the angle of attack is approached from above rather than from below. Once this characteristic was identified, the angle of attack on the generator model was set by approaching the desired angle from above. In this way, the lift at a given angle of attack was the greatest obtained at a given angle of attack. The angle of attack is determined by an indicator fastened to the inside of the wake-generating model in order to eliminate uncertainty in the angle of attack due to freedom of movement in the drive linkage. Once again, it is believed that the hysteresis is caused by the low Reynolds number (i.e., $Re \approx 600,000$) of the test.

Since the inboard parts of wings have large flap deflections and the outboard parts do not, the span loading is a function of angle

of attack causing the intensity of the shed vortices to change with angle of attack. The maximum rolling moment induced on a following wing is not then expected to be proportional to the lift on the wake-generating wing. In order to explore how the lift and rolling moment are related, the ratio of rolling moment to lift, $|C_H|/C_{Lg}$, is plotted as a function of the angle of attack, Fig. 8. For both models, a linear relationship appears not to exist. Some of the reason for the non-linearity may be caused by flow separation on the wake-generating wings at low angles of attack. It is believed however, that the primary cause is attributable to the changes in span loading as the angle of attack changes.

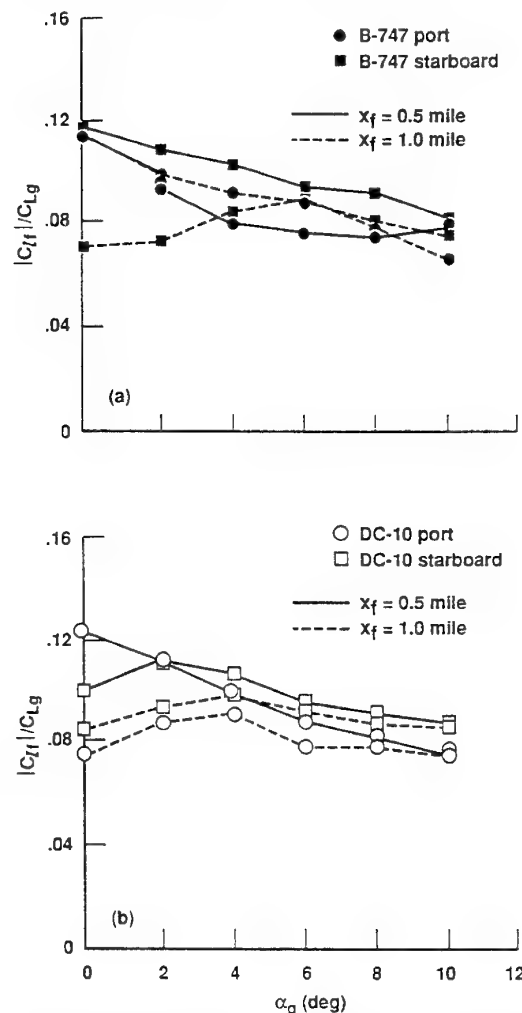


Fig. 8 Reduced maximum rolling moment, $|C_H|/C_{Lg}$, induced on following wing #1 by wakes of the standard landing configurations as a function of angle of attack.

A direct comparison of the wake-induced rolling moments of the two wake-generating models suggests that, at a given angle of attack, the larger B-747 has a somewhat more intense wake than the DC-10; Fig. 9a. The more appropriate way in which to compare the results is to plot the rolling moment coefficient, $|C_H|$, as a function of the lift on the wake-generating wing; Fig. 9b. The rolling-moment intensity of the two wakes then appears to be comparable.

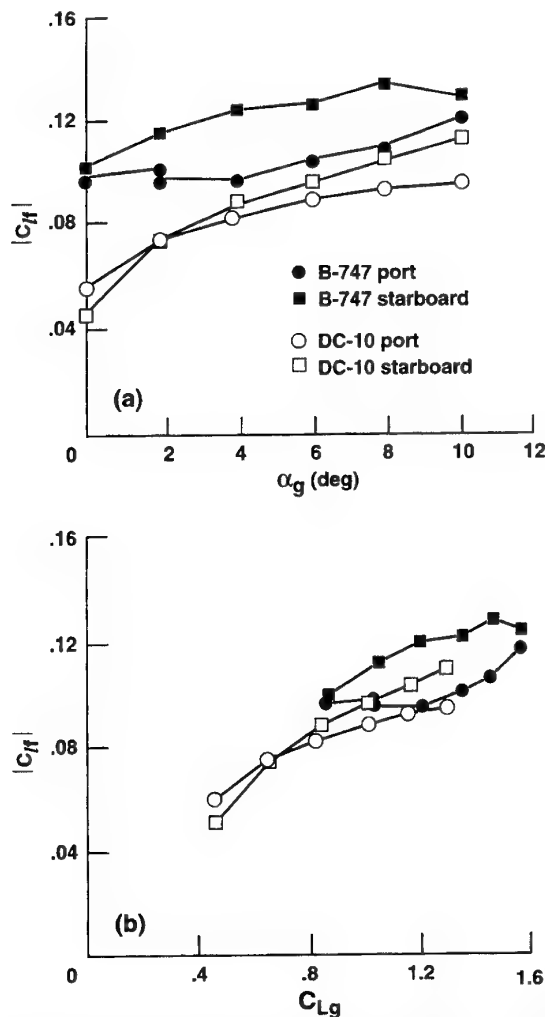


Fig. 9 Comparison of maximum rolling moments induced on following wing #1 by wakes of the two wake-generating models in their standard landing configuration; $x_f = 81$ ft.; a) As a function of α_g . b) As a function of C_{Lg} .

4 ALLEVIATED LANDING CONFIGURATIONS

Another way in which to compare the wakes of aircraft is to explore how sensitive or susceptible their lift-generated wakes are to changes in the planform of, or to devices attached to, their wings. The objective here is to determine whether changes in the B-747 that were found to be successful in previous tests¹⁴⁻¹⁸ would also be successful in reducing the intensity of the rotary velocities in the wake of the DC-10 model. The use of such devices is only of interest when the aircraft is in its landing or takeoff configuration because reduction of the wake hazard is only needed in the vicinity of airports while aircraft are landing or departing, which is when they are constrained to the same flight corridor. The primary purpose of the tests is to determine the mechanism that brings about the reduction in the intensity of the vortex wakes.

In addition to the configurations to be discussed in the following paragraphs, tests were also conducted with the wing planform modified by adding extensions to the leading-edge of the wing of the B-747 model¹⁸. Each extension was of constant chord (i.e., streamwise extent) and segmented so that its spanwise extent from the fuselage outboard to a sharp cutoff could be varied from about 0.2 to 0.3 of the wing span; i.e., ending between the two engine nacelles. The outboard end of each leading-edge extension was chosen to correspond to a series of spanwise

locations near the point where the wing-mounted fins were found to be particularly effective, and where the outboard flap is located. It was found that only a minor decrease in the wake-induced rolling moments were obtained¹⁸. It was concluded that such a device was relatively ineffective or that it was improperly applied, and therefore the data are not presented here.

4.1 Effect of Span of Trailing-Edge Flaps

Early in the wake-vortex research program of the 1970's, it was discovered that the wake intensity of the B-747 could be substantially reduced by changing the standard landing configuration to the so-called (30°,0°) flap configuration^{3-8,14}. The configuration is achieved by placing the inboard flaps in their standard landing configuration and the outboard flaps in their stowed position. In order to study the concept further, configurations were tested on both the B-747 and the DC-10 models wherein the spanwise extent of the outboard flap was varied from the stowed to the fully deployed status. Intermediate flap sizes that were tested include spanwise lengths that extended from the inboard end outboard to 25%, 50%, and 75% of the standard span shown in Fig. 4. Once again, in order to reduce the influence of the magnitude of the lift on the rolling-moment, the data is presented as $|C_H|/C_{Lg}$ in Fig. 10. The measured data shows that, for both aircraft models, the maximum value of the induced rolling moment is a minimum when the outboard flap is completely stowed (i.e., the (30°,0°) flap configuration of the B-747). The higher value of rolling moment on the port side is consistently observed with this model, and is believed to be caused by the fact that the alleviation mechanism did not go to completion within the 81 ft. distance from the generator to the following model. That is, data taken on the port side indicated the presence of two vortex centers rather than the one that occurs when the alleviation has gone to completion. The maximum rolling moments are noted to be largest when both flaps are fully deployed. The test results indicate that intermediate flap sizes do not perform as well as the fully stowed flap configuration. It was not possible to determine whether the vortex-linking mechanism²¹ attributed to the alleviation on the B-747 also applies to the DC-10.

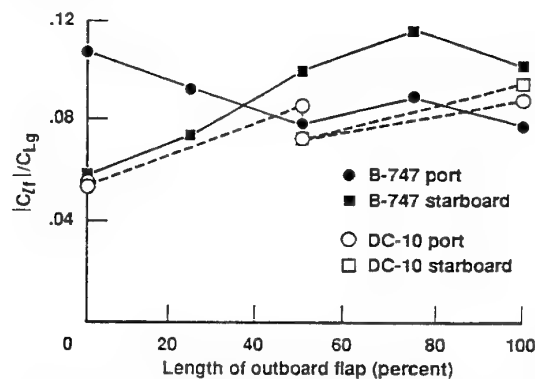


Fig. 10 Variation of wake-induced rolling moment with spanwise size of outboard trailing-edge flaps; following model #1, $x_f = 81$ ft.; B-747, $\alpha_g = 4^\circ$; DC-10, $\alpha_g = 6^\circ$ and 8° .

4.2 Effect of Wing Fins

The mechanism by which lift-generated wakes are alleviated when vertical surfaces (wing fins) are placed on the upper surface of the wake-generating wings is not clearly understood, nor has a way been found to make the penalties in performance negligible. It is, however, the one wake-alleviation scheme that has produced substantial reductions in the wake-induced rolling moments that are proportional to its design parameters; namely, the size and angle of attack of the fin¹⁵⁻¹⁸. The curve in Fig. 11 for the rolling moment as a function of spanwise location of a fin on the B-747 wing indicates that the optimum location for a fin is near the half-way point between the wingtip and centerline¹⁴⁻¹⁶.

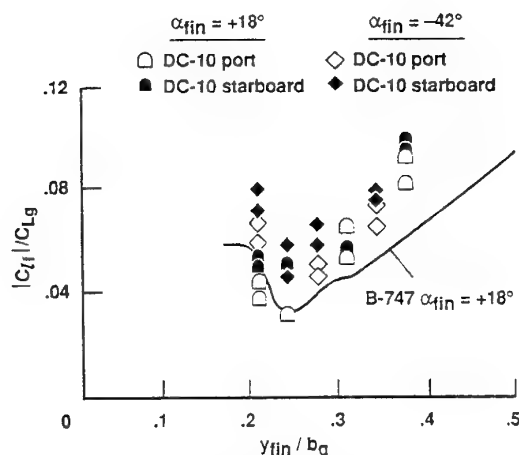


Fig. 11 Variation of wake-induced rolling moment with spanwise location of fins mounted on upper surface of wings; following model #1, $x_f = 81$ ft.

A similar result is found for the DC-10 model, Fig. 11, whether the fin is at a positive or negative angle of attack. Even though a range of fin angles of attack were tested, only the results for the most effective positive and negative angles are presented to reduce the clutter in the figure. A difference occurs in the optimum magnitude of the positive and negative angles of attack of the fin because, due to wing sweep, the flow direction over the upper surface of the wing where the fin is located has a strong inboard component. The optimum spanwise location is about the same on both aircraft models but the magnitudes differ. The different amounts of alleviation may be due to the nature of the two wings, but it is believed to be more likely due to a difference in the relative sizes of the two sets of fins used in the experiment. That is, when the B-747 model was tested, the fin size was $0.0567 b_g$ by $0.0851 b_g$. When the DC-10 model was tested, the fin size was $0.0336 b_g$ by $0.0672 b_g$. The smaller relative fin size was used on the DC-10 because larger sizes degrade the performance a disproportionate amount. It is concluded that the mechanism of wake alleviation by wing fins is probably the same on the two wake-generating models, and that the magnitudes can be made comparable by changes in the fin design. The approximately equal effectiveness of the fins on the two models is not surprising. Although the two wing planforms appear to differ somewhat, both were probably designed for minimum weight at a given lift to yield quite similar span-load distributions. If such is the case, the span loadings and the vortex wakes shed by the two models are similar enough that they are about equally influenced by wing fins.

4.3 Effect of Span of Following Model

The ability of a following aircraft to cope with the rolling moment induced on it by a vortex wake is well known to depend on the span of its wing. In order to illustrate the susceptibility of a wing to a vortex wake, the most intense, or maximum, rolling moments found in the port and starboard portions of vortex wakes are presented in Fig. 12 as a function of the span ratio, b_f/b_g . The data shown were taken at $x_f = 81$ ft. in the wakes of three of the configurations of the B-747 model. The following wings used in the evaluation include the three swept wings, #2, #4 and #5, that all have the same planform (which is a generic average of many of the subsonic transports now in service). A dashed line at $|C_{l_f}| = 0.06$ is used to indicate the approximate rolling-moment capability typical of subsonic transport aircraft. Any points above the $|C_{l_f}| = 0.06$ line indicate situations where a following aircraft would not have sufficient roll-control capability to resist wake-induced rolling moments. In fact, an analysis²² of results obtained with flight simulators suggests that an encounter with a wake near the ground is probably unsafe unless the imposed rolling moment is down to about half of the roll authority on board the following aircraft. Such a restraint leaves a reserve of control power available to compensate for the pilot's

reaction time and to bring the following aircraft back to a level attitude.

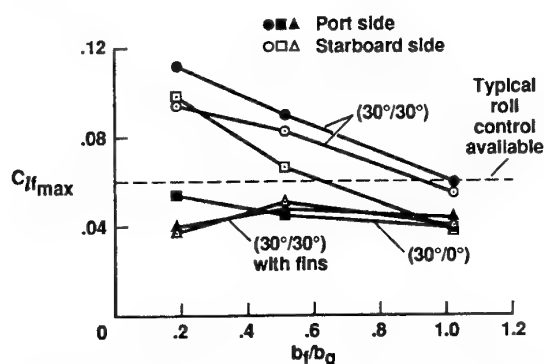


Fig. 12 Comparison of wake-induced rolling moments on swept following-wing nos. 2, 4 and 5 as a function of span ratio; $x_f = 81$ ft.

When the wake-generator is in its conventional landing or $(30^\circ, 30^\circ)$ configuration, the rolling-moment coefficients are noted to decrease markedly as the span ratio, b_f/b_g , increases. Instead, when the wake is shed by a configuration presented in Fig. 12 show that the wake-induced rolling-moment coefficients do not change significantly with span ratio. The general trend of the plotted results indicates that if an alleviated wake is safe for small following aircraft it is also likely to be safe for larger aircraft. Another observation to be noted in the data presented in Fig. 12 is the fact that when the following wing is the same size as the span of the wake-generator, the imposed roll is about the same as the typical roll control available. This characteristic of wake encounters has been noted in the past by test pilots flying in the wake-vortex program. When the encounter of the aircraft with a vortex is of short duration or intermittent, a follower of the same size as the generator (or larger) will probably not experience overpowering rolling moments. A sustained encounter could, however, be judged to be marginally safe or unacceptable during landing or takeoff. Finally, since the results for the DC-10 model are about the same as for the B-747 model, the curves in Fig. 12 are representative of both models¹⁸.

5 COMPARISON OF PREDICTED AND MEASURED LOADS

5.1 Lift

The spanwise distributions of up- and down-wash angle as measured in the 80- by 120-Foot Wind Tunnel¹⁷ were used as input into a vortex-lattice code²³ to predict the lift on following wings #1, #4, and #5, Fig. 13, as they encounter the vortex wake shed by the full landing configuration of the B-747 wake-generating model. In each part of the figures, the computed time-averaged distributions (solid lines), are compared with the measured time-averaged distributions (data shown as open-circle symbols). It is to be noted that the comparisons have been restricted to the time-averaged data because their use is more straightforward than a combination of the maximum and minimum data sets.

In general, the comparisons in Fig. 13 indicate that the lift distributions computed by use of the vortex-lattice method are in good agreement with the measured values. The agreement of the results in Fig. 13a for following model #1 are very good considering the complexity and unsteady character of the flow field. The comparisons made for the larger following models, #4 and #5, are not as good in the region between the vortex centers. A systematic effort was made to be sure that the discrepancy between the results was not due to misalignments or adjustments in the data or to approximations in the mesh size, spacings, etc. in the vortex-lattice code. Predictions made for following model #1 follow the measured data within experimental accuracy thereby indicating that the assumptions made in order to apply the

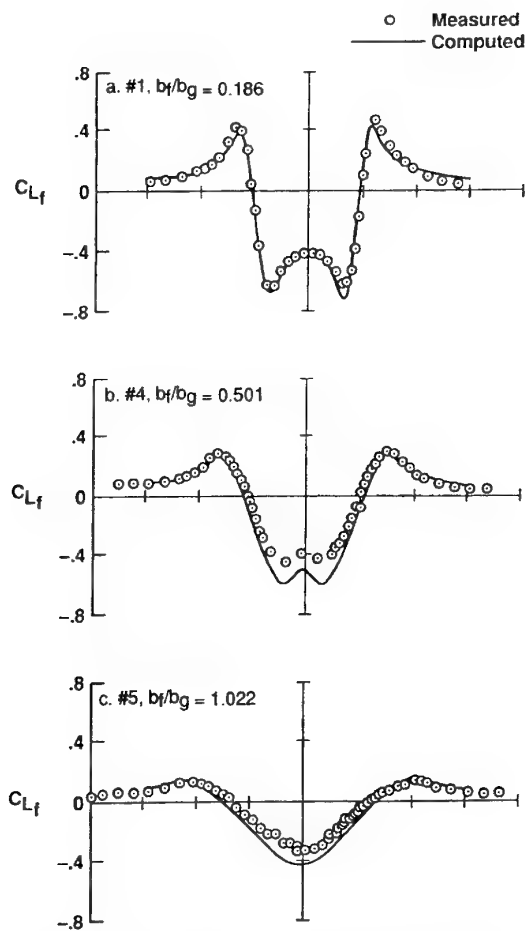


Fig. 13 Comparison of measured and predicted lift induced on following wings as they traverse laterally through the wake of the model of the landing configuration of B-747; $x_f = 81$ ft., $\alpha_g = 4^\circ$.

potential-flow vortex-lattice method to the rotational flow field of vortex wakes are valid. Furthermore, since following model #1 is the smallest of the three following wings, it is the one expected to suffer most from flow separation or stall whenever the vortex flow field impresses a large angle of attack on the following wing. Since no such deviation is noted for following model #1, flow separation probably is not the cause of the discrepancies that appear for following models #4 and #5 in Figs. 13b and 13c. It is concluded therefore, that the differences between the computed and measured data are due to some characteristic of the flow field that is not included in the vortex-lattice method or in the application of the boundary conditions. Since the agreement of the predicted and measured data for following wing #1 is very good, it is also concluded that the experimental and data-reduction techniques are adequate and produce reliable results.

5.2 Rolling Moment

The comparisons presented in Fig. 14 for rolling moment parallel those presented previously for lift. Once again the rolling-moment distributions computed for following model #1, Fig. 14a, are in very good agreement with the measured data. The values computed for following model #4, Fig. 14b, are also in quite good agreement in most regions except near the vortex centers, where the magnitude of the predictions are again too large. The same comments can be made for the comparisons presented for following model #5, Fig. 14c, but the magnitude of the discrepancy has increased over that observed for the two smaller encountering wings. Once again, the discrepancies are believed to be due not to flow separation, nor to lack of accuracy of the application of the vortex-lattice method, but due to a flow-

field characteristic not included in the method.

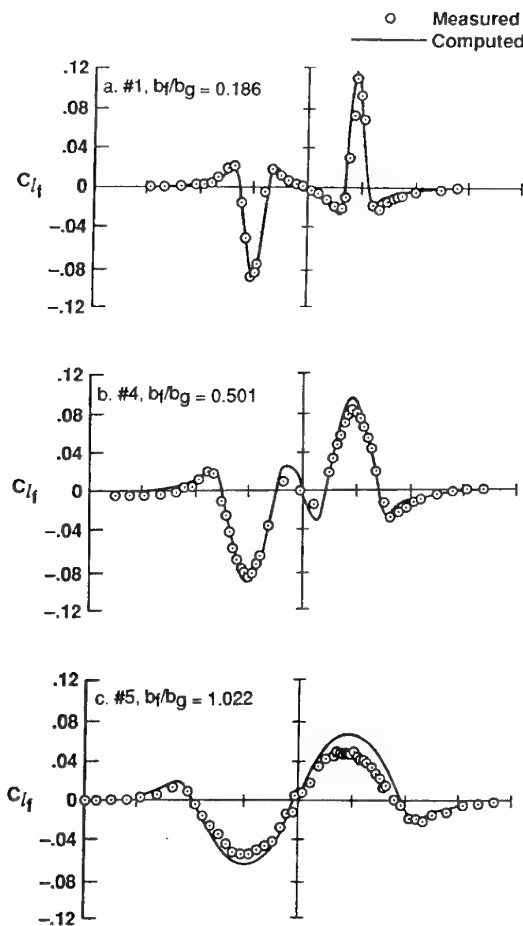


Fig. 14 Comparison of measured and predicted rolling moment induced on following wings as they traverse laterally through the wake of the model of the landing configuration of B-747; $x_f = 81$ ft., $\alpha_g = 4^\circ$.

5.3 Distortion of Rotational Flow Field by Wing

As mentioned previously, a systematic effort was made¹⁹ to be sure that the discrepancies between the results for the larger following wings were not due to misalignments or adjustments in the data nor to approximations in the mesh size, spacings, etc. in the vortex-lattice code. It was found that the computed results usually changed less than 1 % at any place through the wake due to any of the items tried. After these possibilities had been tested and eliminated as responsible for the discrepancy between computed and measured distributions, the assumption made in the application of the vortex-lattice method regarding the streamwise downwash distribution was investigated. That is, when the vertical velocity at each control point is set, it is assumed that the value is the same as the free-stream value for all control points at the same spanwise station. In other words, the downwash is assumed to be the same for each set of streamwise panels or lattices and an allowance for distortion of the oncoming vorticity distribution by the following wing is not made. It is believed that this approximation is the most logical reason for the discrepancy between the computed and measured lift and rolling-moment distributions¹⁹. In support of this conjecture, it is again noted that the vortex-lattice method was quite accurate when the following wing was small, and that the error increased as the following wing increased in size. This observation is supported by the fact that small following wings, like following wing #1, cause small or negligible distortions to a vortex wake, and the comparisons in Figs. 13 and 14 indicate that the vortex-lattice method yields reliable results with only small or negligible error.

Large wings, like #4 and #5, however, cause larger distortions to the structure of the vortex wake so that the resulting downwash distribution and predicted loads are expected to differ by larger amounts from the measured values.

An estimate of the distortion that can be brought about by a wing/vortex-wake interaction was obtained by use of a Trefftz-plane type of analysis¹⁹. Although these new computations are approximate, they do demonstrate that the vorticity in the wake is redistributed when it interacts with the following wing so that the downwash in the spanwise region between the two vortex centers is reduced, just as observed with the lift for the larger following wings. Furthermore, the outboard distributions of downwash are slow to be altered, just as observed with the lift comparisons. It is concluded that the changes in downwash distribution caused by the presence of the encountering wing are important for encountering wings larger than about one-fourth the span of the generating wing. Therefore, the ingredient left out of the current vortex-lattice method is the distortion of the vorticity distribution in the vortex wake that is brought about by the presence of the encountering wing. It remains then to develop an effective method to properly analyze the wing/vortex-wake interaction and apply it to the test configurations studied here.

6 CONCLUDING REMARKS

The data presented on the two wake-generating models indicates that their vortex wakes are comparable when the size of the aircraft and the lift on the wings are taken into consideration. It is also found that the vortex wakes of both models are susceptible to alleviation in about the same way and to about the same degree when the trailing-edge flaps or wing fins are employed for optimum effectiveness.

In general, the large wind tunnels appear to produce reliable results. However, as measurements and their analysis accumulate, questions or concerns about the data and its interpretation occur. For example:

1. Turbulence in the freestream of the wind tunnel causes vortex meander and stretching (similar to atmospheric turbulence) which complicates the acquisition and interpretation of the data.
2. An apparent contradiction between measured and predicted loads on wings encountering vortices is probably attributable to the interaction of the following wing with the wake.
3. A more complete explanation for the alleviation brought about by wing fins is needed to determine whether adequate alleviation can be obtained with smaller penalties.
4. How does the small scale of the test and the differences in Reynolds number affect the application of the results to flight hardware?

7 REFERENCES

- 1 Hallock, J. N., "Aircraft Wake Vortices: An Annotated Bibliography (1923-1990)", Rept. No. DOT-FAA-RD-90-30, DOT-VNTSC-FAA-90-7, U. S. Dept. of Transportation, John A. Volpe National Transportation Systems Center, Cambridge, MA, Jan. 1991.
- 2 Olsen, J. H., Goldburg, A., and Rogers, M., eds., *Aircraft Wake Turbulence and its Detection*, Plenum Press, 1971.
- 3 NASA Symposium on Wake Vortex Minimization, NASA SP-409, 1976.
- 4 Hallock, J. N., ed., *Proceedings of the Aircraft Wake Vortices Conference*, Report No. FAA-RD-77-68, U. S. Dept. of Transportation, March 15-17, 1977.
- 5 Wood, William D., ed., *FAA/NASA Proceedings Workshop on Wake Vortex Alleviation and Avoidance*, Report No. FAA-RD-79-105, U. S. Dept. of Transportation, Nov. 28-29, 1978.
- 6 *Proceedings of the Aircraft Wake Vortices Conference-Vol. 1 and 2*, J. N. Hallock, ed., U. S. Dept. of Transportation, Federal Aviation Admin., DOT/FAA/SD-92/1.1, DOT-VNTSC-FAA-92-7.1, Washington, D. C., October 29-31, 1991.
- 7 Smith, Harriet J., "A Flight Test Investigation of the Rolling Moments Induced on a T-37B Airplane in the Wake of a B-747 Airplane", NASA TM-56031, April 1975.
- 8 Jacobsen, R. A., and Short, B. J., "A Flight Investigation of the Wake Turbulence Alleviation Resulting from a Flap Configuration Change on a B-747 Aircraft", NASA TM-73,263, July 1977.
- 9 Barber, Marvin R., and Tymczyszyn, Joseph J., "Wake Vortex Attenuation Flight Tests: A Status Report", 1980 Aircraft Safety and Operating Problems Conf., Part 2, NASA Langley Research Center, NASA CP-2170, March 1981, pp 387-408.
- 10 Corsiglia, V. R., Schwind, R. G., and Chigier, N. A., "Rapid Scanning, Three-Dimensional Hot-Wire Anemometer Surveys of Wing Tip Vortices", *AIAA Journal of Aircraft*, Vol. 10, No. 12, Dec. 1973, pp 752-7.
- 11 Rossow, V. J., Corsiglia, V. R., and Philippe, J. J., "Measurements of the Vortex Wakes of a Subsonic and a Supersonic-Transport Model in the 40- by 80-Foot Wind Tunnel", NASA TM X-62,391, September 1974.
- 12 Rossow, V. J., Corsiglia, V. R., Schwind, R. G., Frick, J. K. D., Lemmer, O. J., "Velocity and Rolling-Moment Measurements in the Wake of a Swept-Wing Model in the 40- by 80-Foot Wind Tunnel", NASA TM X-62,414, April 1975.
- 13 Corsiglia, V. R., and Rossow, V. J., "Wind-Tunnel Investigation of the Effect of Porous Spoilers on the Wake of a Subsonic Transport Model", NASA TM X-73,091, January 1976.
- 14 Corsiglia, V. R., Rossow, V. J., and Ciffone, D. L., "Experimental Study of the Effect of Span Loading on Aircraft Wakes", *AIAA Journal of Aircraft*, Vol. 13, No. 12, Dec. 1976, pp. 968-973.
- 15 Rossow, V. J., "Effect of Wing Fins on Lift-Generated Wakes", *AIAA Journal of Aircraft*, Vol. 15, No. 3, March 1978, pp 160-7.
- 16 Rossow, V. J., "Experimental Investigation of Wing Fin Configurations for Alleviation of Vortex Wakes of Aircraft", NASA TM 78520, Nov. 1978.
- 17 Rossow, V. J., Sacco, J. N., Askins, P. A., Bisbee, L. S., and Smith, S. M., "Measurements in 80- by 120-Foot Wind Tunnel of Hazard Posed by Lift-Generated Wakes", *AIAA Journal of Aircraft*, Vol. 32, No. 2, March/April 1995, pages 278-284.
- 18 Rossow, V. J., Fong, R. K., Wright, M. S., and Bisbee, L. S., "Vortex Wakes of Two Transports Measured in 80- by 120-Foot Wind Tunnel", *AIAA Journal of Aircraft*, Vol. 33, No. 2, March/April 1996, pages 399-406.
- 19 Rossow, V. J., "Validation of Vortex-Lattice Method for Loads on Wings in Lift-Generated Wakes", *AIAA Journal of Aircraft*, Vol. 32, No. 6, Nov./Dec. 1995, pages 1254-1262.
- 20 Zeman, O., "Persistence of Trailing Vortices: A Modeling Study", *Physics of Fluids*, Vol. 7, No. 1, January 1995, pp.135-143.

21 Rossow, V. J., "Prospects for Alleviation of Hazard Posed by Lift-Generated Wakes", J. N. Hallock, ed., Proceedings of the Aircraft Wake Vortices Conference-Vol.1, U. S. Dept. of Transportation, Federal Aviation Admin., DOT/FAA/SD-92/1.1, DOT-VNTSC-FAA-92-7.1, Washington, D. C., October 29-31, 1991, pp. 22-1-40.

22 Rossow, V. J., and Tinling, B. E., "Research on Aircraft/Vortex-Wake Interactions to Determine Acceptable Level of Wake Intensity", AIAA Journal of Aircraft, Vol. 25, No. 6, June 1988, pp. 481-492.

23 Hough, Gary, "Remarks on Vortex-Lattice Methods", AIAA Journal of Aircraft, Vol. 10, No. 5, May 1973, pp 314-317.

Natural and Forced Growth Characteristics of the Vortex Wake of a Rectangular Airfoil

J. D. Jacob
D. Liepmann
Ö. Savas

Department of Mechanical Engineering
University of California at Berkeley
Berkeley, CA 94720-1740, USA
savas@euler.me.berkeley.edu

Abstract

The forced trailing vortex wake of a rectangular NACA 0012 airfoil with an aspect ratio of 8 is investigated experimentally. The experiments include limited five-hole probe measurements in the near wake in a wind tunnel and extensive DPIV measurements in the far wake in a tow tank. Measurements are conducted on the natural wake and the forced wake at chord Reynolds numbers from $2 \cdot 10^4$ to $6 \cdot 10^4$. The wake is forced by axial jets located on each wing-tip injecting fluid into the vortex cores. The forcing is steady or pulsatile. Pulsatile forcing is varied from 1 Hz to 40 Hz and with the wing-tip jets in phase, out of phase, or one on/one off. Relevant parameters, including vortex separation, vorticity, circulation, and core size, are measured up to 1000 chord lengths behind the wing. Forcing increases both the separation of the vortex pair and the growth rate of the vortex core size. At low frequencies, these effects are monotonic with increasing forcing frequency. At high frequencies, the measurements suggest a complex response to forcing. Based on measurements and observations, some parameters of importance are suggested in exploring possible means of controlling the behavior of the vortex wake. The complexity of the problem dictates that any search for identifying practical solutions must be a concerted effort among experiments, analyses and numerics.

1 Introduction

This paper describes research exploring means of altering the evolution of the vortex wake from a rectangular airfoil. The physics of vortex wakes are not trivial, particularly when devices are added to modify the wake behavior, such as those designed to *alleviate* the vortex wake. In order to reduce the risk of a vortex wake through alleviation, it is necessary to understand how

the wake behaves in complex geometries and flow conditions. The behavior in question includes the roll-up process for the near wake and the decay process of the mid and far wake. Thus it is necessary to have detailed observations of all wake regions and relations sufficient to explain the character of the entire wake. In this work, dual experiments are conducted in a wind tunnel with a five-hole probe for near wake measurements and in a tow tank with digital particle image velocimetry (DPIV) for mid and far wake measurements. The wind tunnel allows detailed measurements of the near wake in a plane fixed relative to the wing while the tow tank allows measurements of the entire evolving wake in a plane fixed relative to an observer. Our previous work has shown this method to be applicable to the problem [1, 2, 3].

The first scientific explanation of the vortex wake was given by F. W. Lanchester in his presentation to the Birmingham Natural History Society in 1894, explaining the ideas of circulation as the cause of lift and tip vortices as the cause of induced drag [4, 5]. Several review articles and symposium proceedings have been published over the recent years, offering a variety of details and viewpoints about both the physical and engineering aspects of the vortex wake [6, 7, 8, 9, 10, 11, 12, 13, 14, 15]. In addition, a comprehensive bibliography containing all of the relevant archival abstracts on the subject since 1923 is available from the United States Department of Transportation [16].

Previous experiments of wings at large downstream distances have been conducted in water tunnels using other experimental methods. Using LDV, Ciffone and Orloff [17] found two characteristic regions in the wake, the first with little or no decay and the second where the maximum azimuthal velocity decayed inversely proportional to the square root of downstream distance ($t^{-1/2}$). Using a hydrogen bubble technique, Lezius [18] measured temporal decay rates proportional to $t^{-7/8}$. The rate of vortex decay was largely dependent upon the level of turbulence introduced into the system due to the effects

of Reynolds number and angle of attack. It was cautioned, however, that due to the low Reynolds number, the rate of decay measured would not correctly predict that of full-scale aircraft, though results from Iverson [19] might indicate otherwise. Sarpkaya [20] performed a number of experiments examining the effects of wing and tip geometry and stratification on wake evolution of short aspect ratio wings. Detailed measurements of the near-field vortex wake have recently been made using both particle displacement velocimetry and laser-Doppler velocimetry [21, 22, 23]. These have yielded important information on the initial roll-up process of the vortices, but are nominally limited to measurements a few chords downstream of the airfoil. Recent measurements of the wakes of aircraft models and their effects on following wings have been made in the 80×120 foot wind tunnel at NASA-Ames Research Center [24]. Results indicate that angle of attack has a large effect on both the intensity of the vortex and the induced rolling moment on following aircraft, though the effects are not entirely predictable. Available data for full-scale aircraft are often measurements made by tower fly-by techniques or ground anemometers [25, 26, 27]. While important, these experiments complicate the fundamental flow problem with the ground effects. There is also concern about the interference from the tower affecting the structure of the vortex core [28]. The cost and repeatability of these experiments are also a major factor in their limitations. It must be noted, however, that systems such as these are currently being used as vortex tracking systems, which while lacking the ability to effectively determine velocity fields, can measure the path of the vortices and thus offer a possible warning mechanism at airports [29, 26].

Various methods of vortex alleviation have been tested. These include control surface oscillations, wingtip devices, multi-wake interactions, thermal forcing, and mass/momentum injection. Tests with tip devices and wing/stator combinations found a reduction in maximum tangential velocity, which the authors state would result in lower rolling moments on following aircraft from the vortex [22]. Other tests of tip devices and varied methods of injecting fluid into the vortex core had similar effects, though actual measurements on wing models placed in the wake found no substantial decrease in rolling moment coefficients [30]. The same study tried to induce vortex instabilities with a variety of active and passive devices, with no observed success, though the research did verify that several concepts reduced the induced drag for improvement of cruise performance. Wu and Gilliam also investigated the effect of wing-tip jets on the development of the vortex pair [31]. It was found that a small jet had a large influence on the spanwise pressure distribution, affecting the wing performance. Multiple induced secondary vortices was observed. The wake vortices were dispersed, though total circulation was increased. It appears that at the time of this writ-

ing, no effective method of trailing vortex mitigation has been successfully implemented.

2 Experimental Apparatus

2.1 Facilities and Hardware

Wing Model: The test wing is shown in figure 1. It is a NACA 0012 section with span $b = 30.5$ cm and chord $c = 3.81$ cm ($R=8$). It is constructed of stainless steel on an EDM with grooves in the upper surface at the station of maximum thickness. The endcaps are NACA 0012 elliptical contours with a 2:1 ratio. Another NACA 0012 section is used as the strut with a length of 15 cm which is connected to a larger hollow strut which, in turn, is fastened to a support mechanism. The angle of attack is variable from -12° to $+12^\circ$ in 2° increments. In this study, negative angles are used on the symmetric wing in the tow tank experiments to increase the allowable measurement time of the vortex wake. The wing is located approximately 0.6 m below the surface of the water. Stainless steel tubes with an inner diameter of $d = 0.635$ mm are placed in the airfoil leading from the supporting strut to the the wing-tips such that they inject axially into the tip vortex cores. The tubes fit into the grooves of the wing which are smoothed to match the section. The tubes are connected to miniature solenoid valves located in the strut which can be pulsed up to a frequency of 60 Hz. The valves are operated independently so that the jets can be in phase, out of phase, or one on/one off. The valves are pulsed at 50% duty cycle. Fluid is driven through the valves by a pressurized reservoir. The pressure is maintained at a constant 100 kPa in the tow tank experiments. The mass ($C_m = \dot{m}/\rho SU$) and momentum coefficients ($C_\mu = 2\dot{m}U_j/\rho SU^2$) are $9 \cdot 10^{-5}$ and $6 \cdot 10^{-4}$ for $U = 50$ cm/s, respectively, and $3 \cdot 10^{-5}$ and $6 \cdot 10^{-5}$ for $U = 160$ cm/s. In the definition of C_m and C_μ , \dot{m}

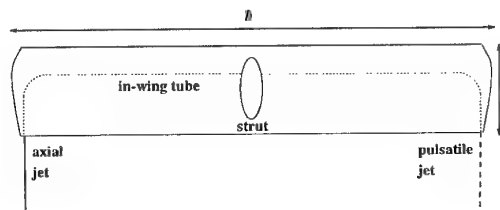


Figure 1: Airfoil with axial injectors. The wing is a NACA 0012 section with $b = 30.5$ cm and $c = 3.81$ cm. Two identical wings have been constructed: one with injectors and one without.

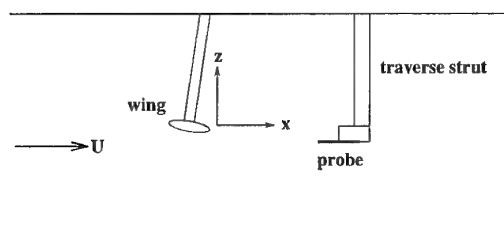


Figure 2: Wind tunnel set-up.

Side-view of the U.C. Berkeley low-turbulence wind tunnel.

is the mass flow rate through the tube, ρ the density of water, $S = bc$ the wing area, U the wing velocity, and $U_j = 4\dot{m}/\pi\rho d^2$ the mean jet velocity, ~ 1.7 m/s. Note that $C_\mu = (8/\pi)(S/d^2)C_m^2$. The jet fluid is colored with red fluorescent dye for flow visualization. This scheme served well for marking the core and observing instabilities and vortex bursting which manifests itself as an increase in sudden redistribution of the dye.

Wind Tunnel: The five-hole probe measurements are conducted in the University of California at Berkeley low-turbulence subsonic wind tunnel (figure 2). The tunnel has a square test section measuring $0.81\text{m} \times 0.81\text{m}$ and is 3.7 m long. The tunnel velocity is controlled through a feedback loop and is capable of speeds up to 25 m/s. The five-hole probe is a conical type probe 3.8 mm in diameter and is mounted on a computer controlled traverse mechanism. The pressure ports are connected to a barocel via a computer actuated valve relay bank, enabling two ports to be measured differentially simultaneously. The wake is first mapped using a low resolution large window pass. Once the location of the vortices is determined, the region around a single vortex is mapped at a grid resolution of 1.9 mm.

Tow Tank: The DPIV measurements are conducted in the University of California at Berkeley Richmond Field Station towing tank (figure 3). The tank is approximately 2.4 m wide, 1.7 m deep, and 61 m long. The nominal water depth is 1.5 m. The tank has a vertical bulkhead at one end and a sloping beach at the other. A viewing section is located near the center of the tank with windows 3 m long and extending the height of the tank. The towing carriage moves along rails above the tank with a variable speed from 0.1 m/s to 1.6 m/s with an accuracy better than 1% .

A 10 W argon-ion laser is used to generate a laser sheet spanning the cross section of the tank at the viewing station. A 1 m wide region surrounding the vicinity of the light sheet is seeded with 40 μm silver-coated hollow

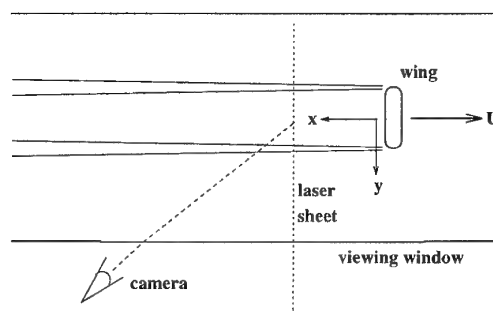


Figure 3: Tow tank set-up.

Top-view of the U.C. Berkeley tow tank.

glass spheres. A non-interlaced CCD camera is used to image the region at 30 Hz and the resulting images are stored on a laser video recorder at $512\text{H} \times 480\text{V}/\text{frame}$ pixels to be retrieved for processing later. A single image frame contains approximately 10^4 particles.

2.2 Data Processing and Reduction

Five-Hole Probe: The probe is calibrated in the yaw and pitch axis from -40° to $+40^\circ$ yielding a linear pressure-velocity relationship for each axis. Resulting pressure fields from runs are converted to give a three-dimensional velocity field in a plane. The cross-stream components are examined to determine quantities such as vortex core size and circulation. (It should be noted that the possible increase of core size due to the probe intrusion was not in any way accounted for [32]). While the streamwise component gives the velocity deficit. Quantities such as lift and drag can be estimated by methods given in Brune [33].

DPIV: The DPIV algorithm employs an iterative scheme that allows for the reduction in size of the interrogation windows, resulting in smaller resolvable length scales [34]. In the present implementation, the final window size is half the initial window size, doubling the spatial resolution. In this study, an initial window size of 8×8 is used. A median filter removes spurious vectors based on a local threshold. The resulting velocity field is corrected for distortion from viewing the image plane at an angle and scaled to dimensional units. Circulation is calculated along rectangular paths of the velocity field using

$$\Gamma = \sum_i u_i dl \quad (1)$$

and vorticity is calculated using

$$\omega = \frac{\Gamma}{\delta y \delta z} \quad (2)$$

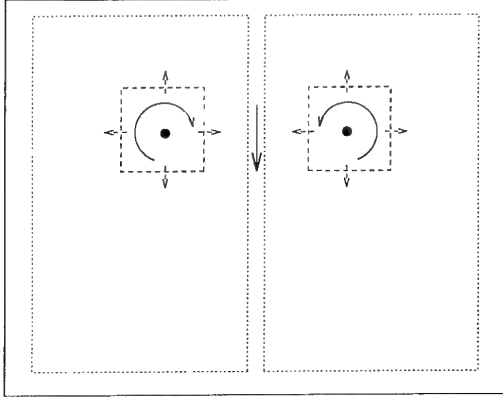


Figure 4: Circulation calculation.

Circulation is estimated along a rectangular path around the region of interest, both for global circulation and for local circulation (vorticity) with the path perimeter approaching the minimum value.

Quantities such as the core size are determined by locating the peak of vorticity within the core and marching radially outward to locate the maximum tangential velocity. Separation distance is determined by the distance between the positive and negative vorticity peaks.

DPIV is still a relatively new measurement technique and care must be taken when examining complex flow regimes with this method. In the particular case presented here, difficulties arise due to the size of the vortices in relation to the remainder of the image. For an elliptically loaded wing, we can expect the vortices to have a radius of $r \approx 0.1b$ [35]. If the full span of the wing is $2/3$ of the image plane, then the vortex radius will approximately be 30 pixels for an image width of 512 pixels. This is an upper bound, however, and we can expect the vortex radii to be smaller. The resolution of DPIV is limited to an order of the window size of the integration area. For the data presented herein, window sizes of 8×8 with 50% overlap are used, approximately $1/2$ to $1/3$ the size of the vortex core. To test the algorithm, false data are generated with two opposite signed Rankine vortices of approximate size, location, and strength expected in the tow tank tests. Comparisons with the given velocity field show errors of approximately 2-5% for velocities with the error being highest near the vortex cores. The vortex radii are estimated to within 10% with the error increasing as the cores become smaller. To determine the core size, slices are taken at several different angles across the vortex cores and the resulting profiles are splined to help minimize discretization. The radius is then determined by the average distance of maximum azimuthal velocity from the peak vorticity.

run	Re_c [$\times 10^{-4}$]	Re_{Γ_o} [$\times 10^{-4}$]	x/c_{max} [$\times 10^{-3}$]	f [Hz]
1	2.0	0.84	0.9	—
2	2.0	0.84	0.9	0
3	2.0	0.84	0.9	1
4	2.0	0.84	0.9	2
5	2.0	0.84	0.9	10
6	2.0	0.84	0.9	20
7	2.0	0.84	0.9	40
8	6.1	2.67	1.4	—
9	6.1	2.67	1.4	0
10	6.1	2.67	1.4	1
11	6.1	2.67	1.4	2
12	6.1	1.34	1.4	—
13	6.1	1.34	1.4	0
14	6.1	1.34	1.4	1
15	6.1	1.34	1.4	40

Table 1: Tow tank data.

3 Discussion

3.1 Scaling Parameters

Eleven tow tank runs are used in this study and are shown in table 1 and sample wind tunnel runs are given in table 2. The airfoil chord $c = 3.9$ cm is used as the length scale. Both the chord based Reynolds number

$$Re_c = \frac{Uc}{\nu} \quad (3)$$

and the vortex Reynolds number using

$$Re_{\Gamma_o} = \frac{\Gamma_o}{\nu} \quad (4)$$

are used here. The ratio of these numbers is

$$\frac{Re_{\Gamma_o}}{Re_c} = \pi\alpha \quad (5)$$

if ones assumes that the wing can be modeled as a lifting vortex line of strength $\Gamma_o = \pi\alpha Uc$. For the wind tunnel runs, Re_c was closely matched, also matching Re_{Γ_o} .

run	Re_c [$\times 10^{-4}$]	Re_{Γ_o} [$\times 10^{-4}$]	x/c [$\times 10^{-3}$]	f [Hz]
A	2.5	1.1	4	—
B	2.5	1.1	20	—
C	2.5	1.1	40	—

Table 2: Wind tunnel data.

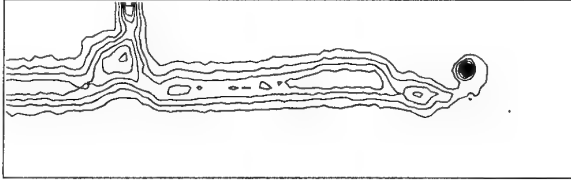


Figure 5: Wind tunnel wake survey data.

Pressure deficit for NACA 0012 wing in wind tunnel at $U = 10$ m/s, $\alpha = 8^\circ$. Constant lines of $(p_t - p_{t\infty})/q_\infty$ are shown.

The vortex core radius r_c is scaled as

$$r^* = \frac{r_c Re_c^{1/2}}{c} \quad (6)$$

whose dependence on the “age” of the vortex is calculated by Moore & Saffman [36] as

$$r^* = 2.92 \left(\frac{x}{c} \right)^{1/2} \quad (7)$$

Velocity and vorticity are scaled by U and c/U , respectively, and the characteristic time scale is given by

$$t^* = tU/c = x/c \quad (8)$$

3.2 Wake Evolution

Sample raw data from wind tunnel experiments are shown in figure 5. Contours of the pressure difference between the center port of the five-hole probe and the static port of the free stream Pitot-static tube are plotted. The data are taken near the wing at $x/c \approx 4$. The contours indicate an early phase of the vortex sheet roll up. The wake of the strut is also observable. Sample data from tow tank experiments are shown in figure 6 and 7. Figure 6 shows the vorticity contours at about $x/c \approx 75$ where the roll up of the sheet is complete and the vortices are clearly formed and descending under the influence of each other. (The plots have been vertically transposed to show downward moving vortices.) The wake of the strut is also clearly visible, though does not seem to be interfering with the descent of the vortex pair. Vertical velocity v/U and streamwise vorticity profiles $\omega c/U$ in figure 7 correspond to the data in figure 6. Vorticity is concentrated at vortex locations.

The roll-up process is dependent upon both the wing geometry and flow conditions, though in most cases the process is complete within a few chord lengths of the trailing edge. Once completely rolled up, the vortex pair is characterized by the strength of the vortices, Γ , and the separation distance, s , between them. At far distances downstream of the wing ($x/c \gg 1$), s asymptotes

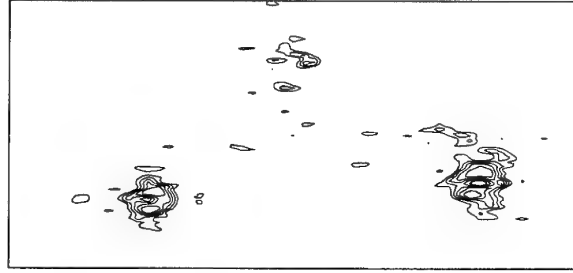


Figure 6: Tow tank vorticity data.

Lines of constant vorticity for run 8 at $x/c \approx 75$. The strut wake is visible in the center of the figure.

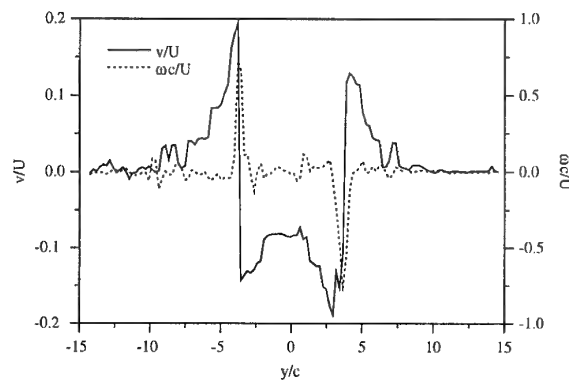


Figure 7: Velocity and vorticity profile.

Corresponding velocity and vorticity profiles for figure 6.

to $\pi b/4$ for an elliptically loaded wing. Figure 8 shows the vortex core separation distance for runs 8–11. The distance is determined by the extrema of the vorticity distribution and is non-dimensionalized by wing span b . The figure includes results from both unforced and forced wakes. Forcing includes steady and pulsatile jets. Despite the large scatter, the vortex core separation decreases from unity to above $\pi/4$. Since the current wing is of rectangular planform, the vortex separation is expected to remain slightly larger than $\pi/4$. The scatter in the figure obscures the effect of forcing on the core separation. As a simple method of quantifying the trends, parabolic lines $((x/c)^{-1/2})$ are fitted to the data in the figure over the range of measurements. From these curve fits, the ratio of the final to initial separation s_f/s_i are plotted in figure 9. Data indicate that forcing increases vortex separation. s_f/s_i is less than unity for the data shown in figure 8, as observed in natural wakes. Forcing at high frequencies cause the vortices to separate. Instantaneous separations can be larger than the wing

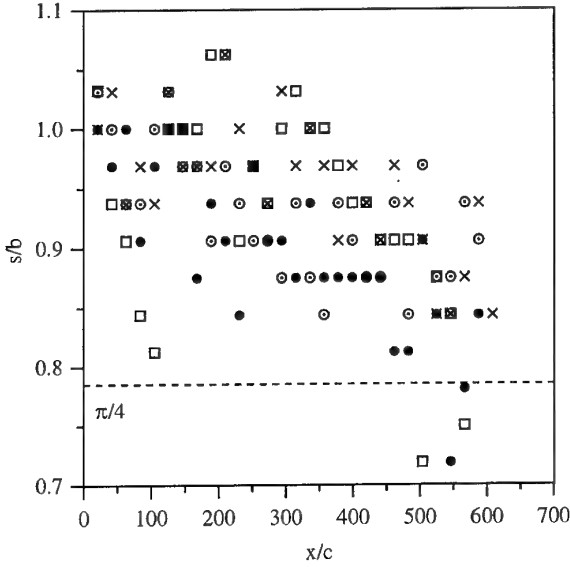


Figure 8: Vortex core separation distance.

Dimensionless vortex core separation versus downstream distance for runs 8-11. •, 8; ○, 9; □, 10; ×, 11.

span b as observed in figure 8. The increase appears to be monotonic for steady or low forcing frequencies. The reaction to higher forcing frequencies appears to be more complicated, however. This change in separation may be connected to a possible change in the lift characteristics of the airfoil, which remains to be explained.

Crow [37] gives the time scale for the onset of the Crow instability to be the inverse of the rate of amplification,

$$a^{-1} = 9.4(AR/c_l)(s/U) \quad (9)$$

For the largest value of U used here, this gives $a^{-1} = 13$ seconds. The entire measurement period is just over 30 seconds, indicating that if the Crow instability were to form, it would still be in the early stages and might not be recognized as such.

Effect of forcing on circulation is shown in figure 10. The percent change in circulation is shown for the average of the left and right vortices. As shown by the figure, no clear trend is evident. The least difference, however, is shown by the pinch in the middle of the plot around $x/c = 300$. This is where the vortices are in the middle of the image plane and the circulation calculation is most accurate. There appears to be a general decrease in the circulation strength for the forced cases in this region, though the decrease is small and well within the measurement error.

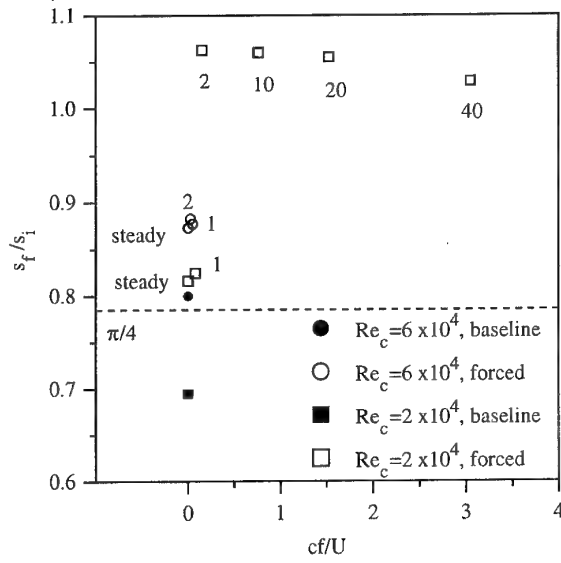


Figure 9: Wake convergence trends.

Ratio of final separation distance s_f to initial separation distance s_i of the wing tip vortices for runs 1-11. Number adjacent to symbols indicate forcing frequencies.

3.3 Vortex Core Growth

Non-dimensional vortex core evolution is shown in figure 11 for run 8. The vortices are not forced. In examining this example, it must be noted that the radii are instantaneous snapshots of the vortex core. Thus, the radii shown here reveal large (and discrete) fluctuations in the core size which is confirmed by flow visualization. The measurements are taken over a wide range of the axial distance (x/c). Near-wake measurements are not as accurate as those farther downstream, due to tighter streamline curvatures in the flow. Equation 7 from Moore & Saffman [36] for laminar flow is shown in the figure. Both vortices show growths which are smaller than predicted for laminar vortices. The rate of this growth is determined from a curve fit to the *average* radii of the left and right vortices. Following Zeman [38], the vortex core growth parameter is defined as

$$\sigma = \frac{\Delta r}{\Delta(\Gamma_o t)^{1/2}} = \frac{\Delta r^*}{\Delta(x/c)^{1/2}} (\Gamma_o)^{-1/2} \quad (10)$$

Figure 12 summarizes the effect of forcing on the growth of the vortex core size. The solid circles are the unforced (baseline) values for $Re_c = 2 \cdot 10^4$ and $6 \cdot 10^4$. The growth rate is about an order of magnitude lower for the higher Reynolds number case. The first observation in the figure is that a steady jet injected into the vortices increases their growth rate. This increase is higher for

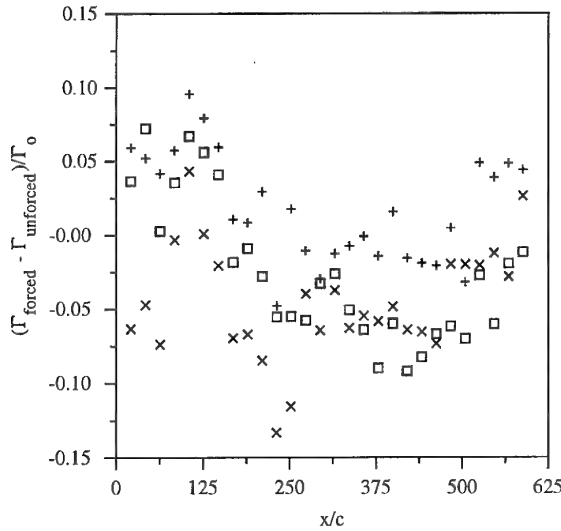


Figure 10: Circulation difference.

Effect of forcing on circulation in runs 8-11. Difference in average circulation (of left and right vortices) from forced to unforced case. \times , run 9; $+$, run 10; \square , run 11.

the low Re_c case. The mechanism for this increase is not clear. One may attribute this to changing the stability characteristics of the core flow. Forcing at low frequencies ($f = 1$ and 2 Hz) causes a monotonic increase in growth rates for both cases. The response of the core, thus, to low frequencies is well behaved. Forcing at high frequencies (shown only for the $Re_c = 2 \cdot 10^4$ case) increases the growth rate, though the dependence shows no particular tendency for the frequencies used. Given the possibility of an almost infinite number of modes, this behavior is not unusual. It points to the complexity of the problem. For example, one may speculate that $f \rightarrow \infty$ should mimic the steady flow result.

A laminar vortex is expected to grow by viscous diffusion. At high Reynolds numbers however, turbulence must be considered though its precise role in the evolution of the vortex is unclear. There is experimental and numerical evidence that trailing vortices at high Reynolds numbers persist for inordinately long times. Our experiments as well as the recent flight tests at NASA Langley Research evidence of this persistence [41]. Zeman's turbulent vortex calculations provide numerical evidence of the extreme longevity of the vortices [38].

Zeman's calculations show that when turbulence is modeled by a Reynolds stress closure model, the growth rate is found to be close to that determined by the molecular viscosity. Thus the vortex core size should grow as (νt)

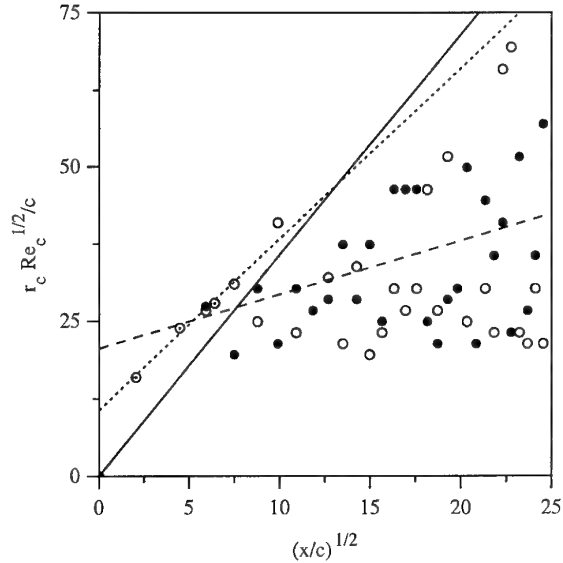


Figure 11: Dimensionless core radius.

Dimensionless core radius versus downstream distance for run 8. \bullet , right vortex; \circ , left vortex; \odot , wind tunnel; dotted line, curve fit to wind tunnel data; broken line, curve fit to the average vortex radii of run 8; solid line, predictions from Moore and Saffman [36].

where t is the age of the vortex. Zeman's main conclusion is that turbulence is only a secondary influence on the longevity of the vortices. He based this conclusion on a comparison in his figure 2 of his numerical results with some experimental data where the measurements from Baker *et al.* [39] are misplaced.

Figure 13 compares numerous findings on the growth rate of the vortices as a function of the vortex Reynolds number (Γ_0/ν) . The growth rate is defined as the rate of change of the radius where the azimuthal velocity is at its maximum. The experimental points consist of those by Baker *et al.* [39], those compiled by Govindaraju & Saffman [40], and the current ones. The current results are extracted from vortex size histories as that shown in figure 11. The growth rate of a viscous vortex core determined by the analysis of Moore & Saffman [36], $2.92(\Gamma_0/\nu)^{-1/2}$, is also shown in the figure. Zeman's Reynolds stress closure model is also shown in the figure. The experimental data suggests a viscous behavior of the vortex. In view of this close agreement, Moore & Saffman's analytic result may be considered a good prediction of the vortex growth rate in the wake of a lifting body when the interaction between the vortices has not developed yet. That Zeman's Reynolds stress closure model gives a similar behavior may be interpreted either

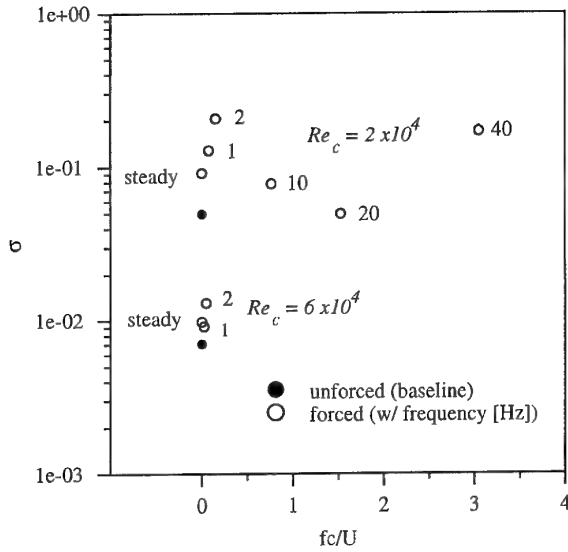


Figure 12: Forcing effect on growth rate.

The effect of forcing on growth rate. At low forcing frequencies ($f = 0 - 2$ Hz), the growth rate is monotonic increasing. Higher frequencies do not give a clear trend, however.

as a confirmation of this result if the modeling is assumed to be indisputable or a confirmation of the suitability of the modeling for this particular case. The latter is more likely. Zeman finds that results based on the $k-\epsilon$ turbulence model are poor. More recently, Dacles-Mariani *et al.* [42] find that a modified Baldwin-Barth one-equation algebraic turbulence model gives good agreement with experiments in the very near region of the wake vortex ($x/c < 2$). The modification to the original model seems to have been guided by desire to match their experiments. Its applicability to the far field, however, remains untested.

3.4 Observations

Observations of the wake vortices in the towing tank as marked by the dyed fluid forced out of the jets at the wing tips point toward the complexity of the problem. When the dye is allowed to seep from the jet ports without any significant reservoir pressure, the dye traces may be assumed to be indicative of the behavior of the natural wake vortices. No Crow rings are formed within the period of the experiments described here even though there are some hints of an early stage of the instability. The vortices are highly sensitive to fossil turbulence in the tank. Further, the left and right vortices respond differently to fossil turbulence. One of the vortices may be

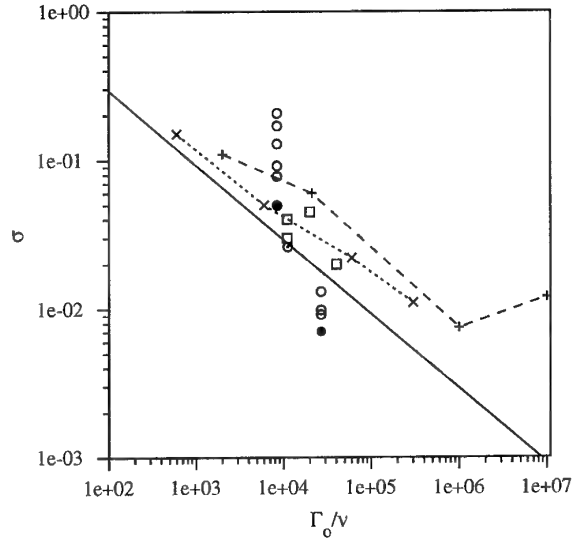


Figure 13: Vortex core growth rate.

The core growth rate σ vs vortex Reynolds number Γ_0/ν for experiments here and elsewhere. \bullet , baseline (unforced) runs 1 and 8; \circ , forced runs 2-7 and 9-11; \odot , wind tunnel run; \square , Baker *et al.* [39]; $+$, Govindaraju and Saffman [40]; \times , Zeman's Reynolds Stress Closure model [38]; solid line, prediction from Moore and Saffman [36].

undergoing a local bursting indicated by a sudden and localized dispersion of the dye while the other remains intact or shows a similar behavior far away from the site of local bursting of the former. Local bursting seems to be in a mode reminiscent of the centrifugal instability. Propagating bursts on the other hand appear to have helical structures.

The behavior of the vortices is observed to be even more complex when forced. Slight differences due to manufacturing tolerances seems to make the vortex behavior different, as well. For example, at steady forcing, increasing the flow rate can cause one of the vortices to burst immediately, while causing the other to become more stable (inhibit bursting, for example). Another example is that at a given frequency, one vortex may be stable while the other is bursting and a change in the forcing frequency or the amplitude changes the responses completely or makes both behave similarly. A close examination of the jet nozzles showed that the two are not identical, hence the different behaviors may be attributed to the particulars of the forcing jets. These observations point to the richness or the complexity of the short-wave stability characteristics of the vortices.

It has been previously demonstrated that various methods of blowing (both spanwise and chordwise) change the lift characteristics of the wing [30] and that the degree to which a vortex rolls up is dependent upon the lift coefficient, span loading, and aspect ratio of the wing [35]. The question then arises: do the jets affect the evolution of the vortices directly by altering the vortex structure already under formation or indirectly by appearing as an alteration in the lift characteristics of the wing? The direction of axial velocity in a trailing vortex filament is dependent upon the tip loading distribution on the wing [36]. In this study the jet velocity U_j is comparable to U and, hence, should be dominant in the immediate wake of the wing. A likely scenario here is that the jets both modify the lift distribution and, depending on their direction and frequency, implant seeds of instability into the vortex cores. It should be noted that stratification effects due to temperature differences have not been taken into consideration.

An estimate of resource requirements for forcing: On the untested assumption that similar forcings on a full scale aircraft can achieve similar modifications to the wake vortices as the kind we have observed in our experiments, we may estimate the resource requirements for a full scale implementation. Taking the larger of the mass and momentum coefficients used in this study,

$$C_m = \dot{m}/\rho S U \sim 10^{-4}$$

and

$$C_\mu = 2\dot{m}U_j/\rho S U^2 \sim 10^{-3},$$

we estimate that for a wide body transport which has a wing area of $S \sim 500\text{m}^2$ and velocity of $U \sim 200\text{m/s}$, we have a mass flux rate of $\dot{m} \sim 10\text{kg/s}$ and a momentum flux of $\dot{m}U_j \sim 10^4\text{N}$. The momentum flux is the most critical parameter since it represents a drain from the engine thrust. For a wide body aircraft, a typical total engine thrust is $\sim 10^6\text{N}$. We observe that, an engine bleed ratio of $\sim 10^{-2}$ seems plausible for an implementation of a scheme similar to what has been described here.

The ratio of the jet momentum flux $\dot{m}U_j$ to the lift of the wing may be taken as a design parameter instead of the momentum coefficient C_μ defined earlier. This new parameter will be higher by a factor of the inverse of the lift coefficient of the wing. These two will be comparable at takeoff or landing as the lift coefficient then is order unity.

Some wake forcing issues:

Control of wake requires the control of both the individual vortices and their interaction. The control of a vortex is usually a question of controlling its breakdown. There is currently no single theory that adequately describes this phenomenon in its entirety. The state of affairs is similar for the control of the vortex wake. This is due to the extreme complexity of the problem. Based

on our limited observations, we list below issues that an experimentalist should be mindful of when exploring the means of controlling the vortex wake by jet injectors.

1. The location of injection with respect to the vortex core vorticity distribution seems to be of utmost importance. This essentially gives a mechanism to sow seeds of instability selectively. The radial location of injection jet with respect to the vortex core determines the length and time scales of the local stability problem. Ratios of vortex azimuthal velocity to jet velocity u_θ/U_j versus to vortex axial velocity u_θ/u_x determines whether a disturbance has a advance or a retrograde helix with respect to the shell of the core where it is injected. Based on our visual observations, this seems to be an important parameter of the stability problem.
2. The result of vortex bursting is to redistribute the vorticity, circulation remaining unchanged. This amount to an increase in the size of the vortex core. In the development of Crow instabilities, the mutual induction term remains unaffected by bursting. The self induction contribution is, however, affected due to the increased size of the vortex core. Further, local time scales are also changed due to the increase in the core size [43]. It is likely that these affects can be exploited for controlling the instability.
3. The Crow instability of the vortex pairs is a long wave instability and a direct forcing requires comparable wave lengths. Two possibilities are:
 - (a) Forcing vortices with equal continuous jets whose magnitudes are the same, yet helix angles are out of phase. This configuration should modify the onset of the instability.
 - (b) Forcing vortices with in-phase, axial intermittent pulses. Our experiments with 50% duty-cycle pulses near the Crow wave lengths showed signs of early instability.
4. The role of the injection-to-free stream velocity ratio U_j/U is not obvious. This parameter all by itself is not sufficient to modify effectively the behavior of the core. We expect that the local velocity ratio at the injection location must be important since this will determine the helix angle of the disturbance seeded into the core of a vortex. However, there is no guarantee that its influence is monotonic. Concerns about noise generation may limit U_j to subsonic domain.
5. Background conditions have strong effects on the behavior of the wake. We have earlier pointed out to the independence of the response of vortices to fossil turbulence. Another equally important factor is the the background shear. A lateral shear field will effect the vortices asymmetrically depending on whether a vortex is cyclonic or anticyclonic

with respect to the background shear. The behavior of wake vortices under these conditions is largely unexplored. Finally, there is the question of extrapolating what is known at laboratory scales to larger Reynolds numbers. It is very likely that there will be substantial differences [44].

The number of parameters to be considered are many. Even a programmatic schedule of experiments seems inordinately long. Analysis provides valuable insight albeit it is usually restricted to idealized cases. Numerical schemes on the other hand are very versatile and can be used to test complex conditions. We deem imperative that further work on exploring possible means of vortex wake control be done in close collaboration with numerical and theoretical works. We conclude with a quote from Donaldson and Bilanin [6]:

Each wake will, in general, be a thing unto itself, and methods which recognize this individuality of wakes should be used in their analysis.

4 Summary

The behavior of the undisturbed and the forced vortex wake of a wing is investigated experimentally. The study is motivated by a desire to find methods of controlling the evolution of the wake. In particular, it is motivated by a desire to find a practical means of mitigating the potential hazard posed by intense vortices on trailing aircraft both during airport operations and in flight. Pulsatile jets of low mass and momentum coefficients are explored as possible means of achieving this goal. A rectangular NACA 0012 wing with an aspect ratio of 8 is used in both wind tunnel and tow tank experiments. The measurement tools are a 5-hole probe for the wind tunnel experiments and digital particle image velocimetry (DPIV) for the tow tank. DPIV proved to be an effective new tool in making instantaneous velocity field measurements in the far wake. Measurements are conducted on the natural, or undisturbed, wake and the forced wake at chord Reynolds numbers from $2 \cdot 10^4$ to $6 \cdot 10^4$. Steady or pulsatile jet forcing is used in tow tank experiments only. Pulsatile forcing is varied from 1 Hz to 40 Hz and with the wing-tip jets in phase, out of phase, or one on/one off. Numerous quantities, including vortex separation, vorticity field circulation, core size, and core growth rate are determined up to 1000 chord lengths behind the wing. Forcing increases both the separation of the vortex pair and the growth rate of the vortex core. At low frequencies, these effects are monotonic with increasing forcing frequency. At high frequencies, the measurements suggest a complex response to forcing. This complexity arises from the multitude of possible modes of excitation of the vortices at both short and long wave

lengths. Based on measurements and observations, some parameters of importance are suggested in exploring possible means of controlling the behavior of the vortex wake. It seems imperative that search for controlling the behavior of the vortex wake should be done in coordination among experimental, analytical and numerical researches to identify practical control parameters.

5 Acknowledgments

We would like to thank P. Marcus, D. Fabris, A. Chen and T. Matsushima of U.C. Berkeley and B. Bays-Muchmore of the Boeing Commercial Aircraft Group for their valuable discussions. This work was supported by California Department of Transportation, contract RTA-65V749.

References

- [1] J. D. Jacob. *Experimental investigation of the trailing vortex wakes of rectangular airfoils*. PhD thesis, University of California at Berkeley, 1995.
- [2] J. D. Jacob, D. Liepmann, and Ö. Savaş. Experimental investigation of the trailing vortex wake of a rectangular wing. In *AIAA 13th Applied Aerodynamics Conference Proceedings*. AIAA, 1995. Paper 95-1841.
- [3] J. D. Jacob, Ö. Savaş, and D. Liepmann. Trailing vortex wake growth characteristics of a high aspect ratio rectangular airfoil. In review for *AIAA Journal*.
- [4] F. W. Lanchester. *Aerodynamics*, volume 1. D. Van Nostrand, New York, NY, 1908.
- [5] L. M. Milne-Thomson. *Theoretical Aerodynamics*. Dover, New York, NY, 1958.
- [6] C. duP. Donaldson and A. J. Bilanin. Vortex wakes of conventional aircraft. In R.H. Korkegi, editor, *AGARDograph No. 204*. AGARD, 1975.
- [7] M. Escudier. Vortex breakdown: Observations and explanations. *Progress in Aerospace Sciences*, 25:189-229, 1988.
- [8] A. Gessow, editor. *Symposium on Wake Vortex Minimization*. NASA, 1976. NASA SP-4096.
- [9] M. G. Hall. Vortex breakdown. In *Annual Review of Fluid Mechanics*, volume 4, pages 775-802. Annual Reviews Inc., Palo Alto, CA, 1972.
- [10] J. N. Hallock. Aircraft wake vortices: An assessment of the current situation. Technical Report DOT-FAA-RD-90-20, DOT-VNTSC-FAA-90-6, U.S. Department of Transportation, John A. Volpe National Transportation Systems Center, Cambridge, MA, 1991.

- [11] S. Leibovich. The structure of vortex breakdown. In *Ann. Rev. Fluid Mech.*, volume 10, pages 221-246. Annual Reviews Inc., Palo Alto, CA, 1978.
- [12] J. H. Olsen, A. Goldburg, and M. Rogers, editors. *Aircraft Wake Turbulence and its Detection*. Plenum Press, 1971.
- [13] P. G. Saffman and G. R. Baker. Vortex interactions. In *Annual Review of Fluid Mechanics*, volume 11, pages 95-122. Annual Reviews Inc., Palo Alto, CA, 1979.
- [14] J. H. B. Smith. Vortex flows in aerodynamics. In *Annual Review of Fluid Mechanics*, volume 18, pages 221-242. Annual Reviews Inc., Palo Alto, CA, 1986.
- [15] S. E. Widnall. The structure and dynamics of vortex filaments. In *Annual Review of Fluid Mechanics*, volume 6, pages 141-165. Annual Reviews Inc., Palo Alto, CA, 1974.
- [16] J. N. Hallock. Aircraft wake vortices: An annotated bibliography (1923-1990). Technical Report DOT-FAA-RD-90-30, DOT-VNTSC-FAA-90-7, U.S. Department of Transportation, John A. Volpe National Transportation Systems Center, Cambridge, MA, 1991.
- [17] D. L. Cifone and K. L. Orloff. Far-field wake-vortex characteristic of wings. *Journal of Aircraft*, 12(5):464-470, 1975.
- [18] D. T. Lezius. Water tank study of the decay of trailing vortices. *AIAA Journal*, 12(8):769-779, 1974.
- [19] J. D. Iverson. Correlation of turbulent trailing vortex decay data. *Journal of Aircraft*, 13(5):338-342, 1976.
- [20] T. Sarpkaya. Trailing vortices in homogeneous and density stratified media. *Journal of Fluid Mechanics*, 136:85-100, 1983.
- [21] A. Shekariz, T. C. Fu, J. Katz, and T. T. Huang. Near-field behavior of a tip vortex. *AIAA Journal*, 31(1):112-118, 1991.
- [22] R. Staufenbiel and T. Vitting. Formation of tip vortices and vortex wake alleviation by tip devices. In *Proceedings of the 17th ICAS Congress, Sweden*, pages 279-291. AIAA, 1990.
- [23] J. Szafruga and B. R. Ramaprian. Lda measurements over the tip region of a rectangular wing. In *AIAA 13th Applied Aerodynamics Conference Proceedings*. AIAA, 1995. Paper 95-1780.
- [24] V. J. Rossow, R. K. Fong, M. S. Wright, and L. S. Bisbee. Vortex wakes of two subsonic transports as measured in 80- by 120-foot wind tunnel. In *AIAA 13th Applied Aerodynamics Conference Proceedings*. AIAA, 1995. Paper 95-1900.
- [25] L. Garodz and K. Clawson. Vortex wake characteristics of b757-200 and b767-200 the tower fly-by technique. Technical Report NOAA-TM-ERL-ARL-199-V1, NOAA, 1993.
- [26] F. Kopp. Doppler lidar investigation of wake vortex transport between closely space parallel runways. *AIAA Journal*, 32(4):805-810, 1994.
- [27] M. E. Teske, A. J. Bilanin, and J. W. Barry. Decay of aircraft vortices near the ground. *AIAA Journal*, 31(8):1531-1532, 1993.
- [28] J. H. Olsen, A. Goldburg, and M. Rogers, editors. *Aircraft Wake Turbulence and its Detection*. Plenum Press, 1971.
- [29] M. Balser, C. A. McNary, and A. E. Nagy. Acoustic backscatter radar system for tracking aircraft trailing vortices. *Journal of Aircraft*, 11(9):556-562, 1974.
- [30] R. E. Dunham. Unsuccessful concepts for aircraft wake vortex minimization. In A. Gessow, editor, *Symposium on Wake Vortex Minimization*, pages 221-249. NASA, 1976. NASA SP-4096.
- [31] J. M. Wu and F. T. Gilliam, Jr. A flow visualization study of the effect of wing-tip jets on wake vortex development. In *Flow Visualization III: Proceedings of the Third International Symposium*, pages 387-391. Hemisphere Publishing Corp., September 1985.
- [32] S. I. Green and A. J. Acosta. Unsteady flow in trailing vortices. *Journal of Fluid Mechanics*, 227:107-134, 1991.
- [33] G. W. Brune. Quantitative low-speed wake surveys. *Journal of Aircraft*, 31(2):249-255, 1994.
- [34] D. Fabris. *Experimental and Computational Investigation of Vortex Rings*. PhD thesis, University of California at Berkeley, 1996.
- [35] J. R. Spreiter and A. H. Sacks. The rolling up of the trailing vortex sheet and its effect on downwash behind wing. *Journal of the Aeronautical Sciences*, 18:21-32, 1951.
- [36] D. W. Moore and P. G. Saffman. Axial flow in laminar trailing vortices. *Proceedings of the Royal Society of London A*, 333:491-508, 1973.
- [37] S. C. Crow. Stability theory for a pair of trailing vortices. *AIAA Journal*, 8:2172-2179, 1970.
- [38] O. Zeman. The persistence of trailing vortices: a modeling study. *Physics of Fluids*, 71(1):135-143, 1995.
- [39] G. R. Baker, S. J. Barker, K. K. Bofah, and P. G. Saffman. Laser anemometer measurements of trailing vortices in water. *Journal of Fluid Mechanics*, 65(2):325-336, 1974.
- [40] S. P. Govindaraju and P. G. Saffman. Flow in a turbulent trailing vortex. *Physics of Fluids*, 14(10):2074-2080, 1971.

- [41] NASA Langley Research Center. Radar detection of wake vortices at wallops, 1995. Video Production Center, Hampton, VA.
- [42] J. Dacles-Mariani, G. G. Zilliac, J. S. Chow, and P. Bradshaw. Numerical/experimental study of a wingtip vortex in the near field. *AIAA Journal*, 33(9):1561–1568, 1995.
- [43] P. G. Saffman. *Vortex Dynamics*. Cambridge University Press, New York, NY, 1992.
- [44] T. Sarpkaya. Turbulent vortex breakdown. *Physics of Fluids*, 7(10):2301–2303, 1995.

Three-Dimensional Direct Numerical Simulations of Wake Vortices: Atmospheric Turbulence Effects and Rebound with Crosswind

Alexandre Corjon

C. E. R. F. A. C. S. - CFD project

42, Avenue Gustave Coriolis

31057 Toulouse Cedex France.

Frédéric Risso*

Alain Stoessel†

Thierry Poinso†

SUMMARY

This paper presents three-dimensional direct numerical simulations of a vortex pair. Two types of computations are conducted. The first type considers a vortex pair placed in an homogeneous turbulent field. The phenomenon of interaction between the vortices and the turbulence is analysed in details from two simulations calculated on a 135^3 nodes mesh grid (one case with axial core velocity, the other without). The results show that the role of large and small turbulent eddies can be separated into two fairly independent mechanisms. The large structures are stretched by velocity gradients induced by the vortex pair. That leads to the formation of both tubes of vorticity spinning azimuthally around each vortex and associated axial velocity sheets. These turbulent structures cause a strong decrease of the maximal velocity and curvature of the vortices. These deformations of the vortex induced by the turbulence initiate an antisymmetric long-wave instability of the pair which will probably lead to the collapse of the vortices. Concurrently, the small structures can enhance the diffusion of the vorticity out of the vortex core. From this analysis and dimension considerations, the correct form for a model of decay of the vortices is derived. On the other hand, nine simulations on a 81^3 nodes mesh grid are used to determine the sensibility of the results upon the random turbulent initial conditions.

The second type of computations considers a vortex pair placed in a laminar flow field near the ground. This laminar flow is representative of a neutral surface boundary layer. The effect of variable crosswind shear is studied with the effect of an axial wind. A comparison between the two-dimensional and the three-dimensional results shows that the main phenomenon is not modified but that the altitude of rebound depends on the three components of the wind. Furthermore, the curvature of the secondary vortices

due to long wavelength crosswind variation leads to their reconnection with the primary and makes them burst.

LIST OF SYMBOLS

a	= sound celerity
b	= wingspan
b_0	= spacing between vortices at $t = 0$.
	$b_0 = \pi/4b$ for an elliptically loaded wing
d_0	= spacing between vortices at $h \rightarrow \infty$.
	$d_0 = 2b_0 h_0 / \sqrt{b_0^2 + 4h_0^2}$
E	= energy spectral density
K	= wavenumber
k	= kinetic energy of turbulence
h	= altitude of the vortices
L	= size of the computational domain
P	= pressure
q	= coefficient of q-vortex
Re	= Reynolds number
Re_Γ	= circulation based Reynolds number
r	= distance from vortex centre
r_c	= core radius
r_0	= initial core radius
t	= time
U_θ	= azimuthal velocity
u'	= rms velocity (m/s)
u_f	= friction velocity at the wall
V_{max}	= maximal azimuthal velocity
V_0	= V_{max} at $t = 0$
w_0	= crosswind magnitude at initial height
W_{max}	= maximal axial velocity
r, θ, z	= cylindrical coordinate
x, y, z	= ground coordinate
y_r	= roughness height
ϵ	= turbulence dissipation rate
Γ	= circulation of individual vortex
Γ_0	= initial circulation
κ	= the Von Karman constant $\kappa = 0.4$

*present address: I. M. F. T., avenue C. Soula, 3 1400 Toulouse, FRANCE

†I. F. P., 1-4 av. de Bois Préau, 92506 Rueil-Malmaison, France

‡I.M.F.T./C.E.R.F.A.C.S.

Λ	= integral length of turbulence
ν	= kinematic viscosity
Ω	= vorticity
ρ	= density
σ	= wind shear
<i>subscripts</i>	
0	= initial
c	= core
d	= dissipation spectrum
e	= energy spectrum
p	= primary
s	= secondary

1 INTRODUCTION

In this introduction, after the general context of the study, we will present the complexity of the wake vortex studies due to the atmospheric environment in distinguishing the causes and their effects.

General context

The first problems due to wake vortices appeared near 1970 at the Boeing 747 arrival. Many accidents due to wake vortices encounter by following aircraft occurred, killing people. The importance of the wake shedded by the Boeing 747 is not due to any particularity in the aircraft design but only to its size which was a lot higher than any other aircraft.

A first study program was launched by the Federal Aviation Administration between 1969-1970 to solve the problem of wake vortex encounter. An extensive data collection effort (flight and ground test and incidents analysis) led to the definition of aircraft separation standards edited by International Civil Aviation Organization (ICAO) and applied by many countries (a 3×3 matrix based on the Maximum Take-Off Weight (MTOW) of the aircrafts). The objective of this categorization is to ensure safety by avoiding any encounter between wake vortices and a following aircraft. But, with the constant traffic growth, these separations worked towards the main airport congestion. Then, all the subsequent studies try to recover some of the capacity lost in optimizing the separations or the MTOW categorization of the aircrafts but with the same level of safety.

The actual separation are not adapted to ensure hundred percent of safety (incidents at Heathrow¹ or accidents²) or to ensure the operational efficiency (significantly more traffic in Visual Flight Rules in USA³). To improve the safety, the separation matrix is modified in several countries like in England where the number of incidents were too high. The more recent studies have shown that there is no homogeneous hazard with the ICAO standards. Some proposals are made to create a new class and modify the limits of the others.

The operational efficiency of a new categorization needs a better knowledge of the effects of meteorological

conditions on the lifetime and decay of wake vortices. Since 1970, the main phenomena are identified: turbulence and stratification. Since, a lot of studies have tried to parametrize these effects.

More than the meteorological phenomena, it is of first importance to consider the behavior of the vortices near the ground. As shown by the UK Civil Aviation Authority¹, there is two ranges of altitude where the potential hazard is maximum. The first is located between 600 and 900 meters and the second between 30 and 60 meters. This last altitude range is the most hazardous because of the short recovery time. At this altitude, all the aircrafts are on the same flight path while vortices may bounce on the ground. Therefore, the behavior of the wake vortices strongly depends on the velocity of the crosswind.

All the results of the studies should be simplified in model with real-time capability to be used on the airport. The most widely used engineering model was developed by Greene in 1986⁴. In his model, Greene sums up several studies made between 1970 and 1980 and is able to simulate the effects of the atmospheric turbulence and stratification on the vortex decay. On this basis, we have tried to add the effects of the ground and the crosswind to extend the range of application of the model⁵. But these models should be the quintessence of more important studies that should be continued to improve their results.

Wake vortex phenomenon

As said before, the external conditions act on the wake vortex decay. The causes are: turbulence, stratification, ground effect and wind. These causes have several effects on the stability, decay and trajectories (rebound) of the vortices. In the following, we will present the main literature on the subject, categorized by effect, and the links with our work.

Stability: The main mechanisms of instability are the bursting (for an isolated vortex) and the reconnection (for a vortex pair) which are initiated by the turbulence. The initial work on the trailing vortices instability is due to Crow^{6,7}. Crow has defined the linking time of a vortex pair as a function of turbulent energy dissipation rate. These theoretical works were confirmed by many experimental studies in towing tank in neutral medium (Sarpkaya and Daly⁸, Liu⁹) or in stratified fluid (Sarpkaya⁸) or even in the atmosphere (Tombach¹⁰). The results of Sarpkaya and Daly⁸ have shown that the Crow formula is not valid for the high Reynolds number where the demise of the vortices is essentially due to the bursting phenomenon. Moreover, the reconnection of the vortices does not imply the absence of hazard for the following aircraft. Some recent stability studies divide the effects due to short and long wavelength instabilities (Klein and Majda¹¹, Klein, Majda and Demoran¹²) and find the Crow theory as an application case of a more general theory. They show that a vortex pair is always unstable when their circulation ratio is negative. The bursting phenomenon is

not yet well understood. The reconnection implies bursting but not the contrary. The work done on this subject focuses on the stability of one isolated vortex (Rayleigh¹³, Lessen and Paillet¹⁴, Ragab and Sreedhar¹⁵).

The constant power increase of the computer and the improvement of the numerical scheme permit to study these complex phenomena by the use of DNS. For example, the vortex pair reconnection is studied by Virk, Hussain and Kerr¹⁶ in the framework of fundamental turbulence studies but the results could apply to wake vortices. Another application of DNS for trailing vortices will be presented by Spalart and Wray¹⁷. They will give new insights on Crow instability initiated by the atmospheric turbulence and the operational interest of these results. We will also deal with these instabilities in section 4.1.4.

Decay due to turbulence: The Crow instability or the bursting are not the only effects of the atmospheric turbulence on the wake vortices. An important work has been made by Donaldson and Bilanin¹⁸. More than a very complete review of existing results, they proposed a model of diffusion for the aging of a vortex pair in the atmospheric turbulence. This model depends on the aircraft wingspan and the r.m.s. velocity of turbulence (see equation 19). These theoretical results are based on experimental results and dimension analysis. They have also done some numerical simulations with Reynolds Averaged Navier-Stokes Solver (RANSS)¹⁹ which have been recomputed with more powerful computers (Robins and Delisi²⁰ and Zheng and Ash²¹). They perform two-dimensional studies of the effect of a neutral atmospheric turbulence on wake vortices for three cases: constant turbulent bath, mean crosswind shear and ground effect. No improvement to the model proposed by Donaldson and Bilanin in 1975 was obtained due to these new results.

The work done by Squire²² is also very used. He proposed to model the effect of the turbulence on the trailing vortices with an equivalent eddy viscosity, which is proportional to the circulation of an ideal laminar vortex. Owen²³ proposed an extension to this theory and both these theories were experimentally studied by Iversen²⁴. Some recent work, like Philipps²⁵ have shown the relaminarization of the vortex core and Zeman²⁶ has shown that the evolution of the core radius is locally controlled by viscous effects like in laminar. In this paper, we will try to give some new insights on the turbulent mechanism of wake vortex aging.

As said previously, not only the atmospheric turbulence but also the stratification play a major role in the decay of real vortices. The main studies on this field are due to Hill²⁷, Sarpkaya²⁸, Saffman²⁹, Scorer and Davenport³⁰ and more recently Spalart¹⁷.

Rebound: Few of these references take into account the effects of the ground on the wake vortices behavior. Some experiments have shown that the

Crow instabilities are no more relevant to define the lifetime of the vortices near the ground^{31,32} and that this lifetime is shorten in this case.

The main phenomenon is the rebound of the vortices. This vortex bouncing was explained first by Harvey and Perry³³ and confirmed by many experiments (e.g. Liu⁹). During their descent, each primary vortex is inducing a boundary layer and a strong vorticity sheet due to the adverse pressure gradient. As they continue to descent this vorticity sheet becomes unstable and detaches from the wall creating a secondary vortex. This secondary vortex rolls over the primary one and makes it rise up. Therefore, the behavior of the wake vortices strongly depends on the velocity of the crosswind. Several authors have published papers on vortex rebound with crosswind for bidimensional flowfield in laminar (Peace and Riley³⁴, Zheng and Ash^{35,21}, Schilling³⁶ and Teske and al.³⁷) or even in turbulent (Ash and Zheng^{38,39}, Robins and Delisi⁴⁰) but none had given relationships between the altitude of rebound and the meteorological conditions. As mentioned in section 5.1, Corjon and Poinso⁴¹ provided a correlation law between the altitude of rebound and the crosswind shear. Finally, to our knowledge, only Dommermuth⁴² and Sarpkaya⁴³ have dealt with the three-dimensional interaction of a vortex pair with a free surface.

Several authors give important informations on the vortex rebound near the ground with totally different aim. Many studies have concentrated on vortex ring interacting with the ground. For experimental work, we can refer to the works of Chu and Falco⁴⁴, Walker and al.⁴⁵ and Doligalski, Smith and Walker⁴⁶. In all these experiments secondary vortices are created and even tertiary vortices leading to complex behavior. There are also several numerical studies; Orlandi⁴⁷, Smith and al.⁴⁸, Swaeringen, Crouch and Handler⁴⁹ give informations of the evolution of the secondary vortex size and the decay of the primary and secondary vortices.

Present work

This paper will present direct numerical simulations (DNS) used to study complex phenomena. It will deal with two points: the effect of the atmospheric turbulence on the wake vortices decay and the effect of the wind on three-dimensional rebound of the vortices. These works follow two already published studies^{41,50}.

This article is divided into two parts. The same numerical tool is used in both parts (Section 2). We will present DNS of a vortex pair embedded either in homogeneous isotropic turbulence (Section 4) or in a neutral surface boundary layer (Section 5).

The aim of the study of atmospheric turbulence effects is to define a model of decay (Section 4.3) which could replace the model presented by Donaldson and Bilanin in 1975. The well known Crow instabilities will be just mentioned (Section 4.1.4). To reinforce

our conclusions, a statistical study of our turbulent results will be presented in Section 4.2.

Further, we will deal with the three-dimensional rebound in laminar flows. First of all, we will recall the two-dimensional results (Section 5.1). Then results with variable crosswind will be presented before considering an axial component of the wind and its effect on the altitude of rebound (Section 5.2). Finally, we will conclude and draw the perspectives of these works.

2 NUMERICAL TOOL

The present *NTMIX3D* code⁵¹ is solving 3D unsteady compressible Navier-Stokes equations with multi-species, transport and chemistry. Obviously, for this study, multi-species and chemistry capabilities are not used.

A highly accurate finite difference method over a cartesian grid is used to fully handle most of the different scales in the 3D flow: spatial derivatives are computed with a 6th order compact scheme (Padé scheme)⁵² which has the property of being low-dispersive and non-dissipative. These schemes are allowing some quasi-spectral accuracy. Time advancement is achieved with a 3rd order Runge-Kutta method. The code is supporting different types of boundary conditions thanks to the use of the NSCBC method⁵³. In particular, non-reflecting open boundary conditions as well as adiabatic or isothermal solid walls are implemented.

The cost in CPU and memory of a 3D simulation is so high that it requires the use of MPP computers to be affordable. Thus, the code has been written in parallel with a Message Passing Paradigm. Specific domain decomposition methods have been developed for the parallel treatment of compact schemes⁵⁴ and are allowing the availability of a highly efficient version of the code on a wide range of distributed memory parallel computers such as IBM SP2, Fujitsu VPP500 and Cray T3D. For instance, on a Fujitsu VPP500 with 18 nodes, a 210^3 grid is handled in less than 200 Mwords of memory and with a cost of $0.33 \mu\text{s}/\text{GridPoint}/\text{TimeStep}$. The simulations presented in the following have been run either on a VPP, a Meiko CS2 or a Cray T3D.

3 PRESENTATION OF THE SIMULATIONS

All the simulations presented here have been performed on a regular grid. The initial conditions have been built by the superimposition of the two flow fields induced by a vortex pair and either an homogeneous and isotropic turbulence (Section 4) or a laminar boundary layer (Section 5). Then, the time evolution of the whole flow field has been calculated by solving the full compressible Navier-Stokes set of equations with the numerical tool presented in section 2.

3.1 The vortex pair

To define the initial conditions for the simulations, we have used analytic expressions for the vortices. The Lamb-Oseen vortex was chosen. It is an unsteady solution of the Navier-Stokes equations for the evolution of an initial line vortex characterised by a circulation Γ (see Lamb⁵⁵, pp. 592). It models well the vortices shed by an aircraft: quasi-solid rotation into the core and constant circulation at the infinity. If the cylindrical coordinates (r, θ, z) are considered, the induced velocity \vec{U} is only azimuthal and its spatial distribution depends only on r :

$$\frac{U_\theta \left(\frac{r}{r_c} \right)}{V_{max}} = \alpha \frac{r_c}{r} \left(1 - \exp \left(-\beta \left(\frac{r}{r_c} \right)^2 \right) \right) \quad (1)$$

The magnitude of the velocity circulation which could be obtained from the integration of (1) never decreases, thus the criterion of Rayleigh¹³ is satisfied and stability is ensured. The pressure P is given by the integration of:

$$\frac{dP}{dr} = \rho \frac{U_\theta^2}{r} \quad (2)$$

As it is shown in equation (1), the spatial structure of the Lamb-Oseen vortex is function of two parameters. To show the maximal azimuthal velocity V_{max} and the core radius where V_{max} is reached ($U_\theta(r_c) = V_{max}$), the two constants α and β have been introduced. They are solutions of the following equations:

$$1 + 2\beta = \exp(\beta) \implies \beta \cong 1.2544 \quad (3)$$

$$\alpha = \frac{1}{1 - \exp(\beta)} \implies \alpha \cong 1.40 \quad (4)$$

Time evolution does not modify the structure of the velocity distribution given by equation (1). In consequence, the conservation of the kinetic momentum imposes that the circulation at infinity remains equal to the initial value Γ . The aging of the vortex can be expressed by the evolution of r_c and V_{max} which depends on the cinematic viscosity ν :

$$r_c(t) = \sqrt{4\beta\nu t} \quad (5)$$

$$V_{max}(t) = \frac{\Gamma}{2\pi\alpha r_c} = \frac{\Gamma}{2\pi\alpha\sqrt{4\beta\nu t}} \quad (6)$$

For the Lamb-Oseen vortex, the maximal value of the vorticity magnitude Ω_{max} varies as the inverse of time:

$$\Omega_{max}(t) = \frac{2\alpha\beta V_{max}(t)}{r_c(t)} = \frac{\Gamma}{4\pi\nu t} \quad (7)$$

As shown by Batchelor⁵⁶, the process of formation of the wake vortices leads to the existence of an axial velocity in the core region. Lessen and Paillet¹⁴ have proposed a simpler expression than those of Batchelor. They approximated the radial profile of the axial velocity by a Gaussian law and introduced a parameter called q proportional to the ratio between the azimuthal and radial maximal velocity :

$$\frac{U_z \left(\frac{r}{r_c} \right)}{W_{max}} = \exp \left(-\beta \left(\frac{r}{r_c} \right)^2 \right) \quad (8)$$

with

$$W_{max} = \frac{\alpha \sqrt{\beta}}{q} V_{max}$$

In the present work, the simulations referred as G_1 , P_1 to P_9 and P_{lam} (see table 1) used the Lamb-Oseen type vortex (eq. 1) without axial velocity. For the case G_2 , the q-vortex was chosen (eq. 1 and 8). In all cases, no initial radial velocity was present and the flow field was homogeneous in the axial direction. The pressure field corresponding of each vortex was computed by integrating equation (2) considering the fluid at rest at the infinity. The vortex pair consisted in two vortices parallel to the z-axis with a spacing d_0 in the x-direction. The flow field of a pair is obtained by the linear superimposition of the velocity and pressure fields induced by each vortex, this superimposition being valid until the distance d_0 is equal to several core radii.

For the cases without axial velocity, the initial vortex pair is entirely defined by three dimensionless parameters:

- $Re = \frac{V_0 r_0}{\nu} = 600 = \frac{\Gamma}{2\pi\alpha\nu} = \frac{1}{2\pi\alpha} Re_\Gamma$
- $d_0^* = \frac{d_0}{r_0} = 8$
- $Ma = \frac{V_0}{a} = 0.2$

The Reynolds number is small in comparison with real phenomenon (about four orders of magnitude). The spacing chosen is a typical value observed behind aircraft⁵⁷. The Mach number is sufficiently small for all the compressible effects can be neglected. In the following, all quantities marked with a star (*) are normalized using the reference scales built on V_0 and r_0 .

For the case G_2 , the magnitude of the initial maximal axial velocity appearing in (8) has also to be fixed. Lessen and Paillet¹⁴ have studied the stability of an isolated q-vortex. Their results shows that the flow is stable for all modes of perturbations until $q > 1.5$, which has been confirmed by the study of Mayer and Powell⁵⁸. In view to emphasis the difference with the case without axial velocity, we choose a value of the

initial axial velocity close to the upper limit allowed by the criterion of stability:

$$W_0^* = \frac{W_0}{V_0} = 1.0 \implies q \cong 1.57$$

3.2 The ambient turbulence

The turbulence flow field is initialized considering an isotropic homogeneous turbulence. This field is built in the spectral plane from a given spectrum with random phases for each mode. The formulation derived from the spectrum of Von Karman and Pao (see Hinze⁵⁹) is used for the energy spectrum $E(k)$:

$$E(K) = \frac{2^{3/2} k^{5/2}}{3} \frac{(K/K_e)^4}{\epsilon \left(1 + (K/K_e)^2 \right)^{17/6}} \exp \left(-\frac{9}{4} (K/K_d)^{4/3} \right) \quad (9)$$

Thus, the generated flow field stands for a classical developed turbulence. K_e is the peak wave number for the energy spectrum, K_d the peak wave number for the dissipation spectrum, and $k = \frac{1}{2} \left(\overline{u_x'^2} + \overline{u_y'^2} + \overline{u_z'^2} \right)$. The turbulence characteristics in the atmospheric boundary atmospheric boundary layer are described by Donaldson and Bilanin¹⁸. They proposed an approximate relation for Λ :

$$\begin{aligned} \Lambda &= 1.3y \quad \text{for } y \leq 169m \\ \Lambda &= 220 \quad \text{for } y > 169m \end{aligned} \quad (10)$$

In the numerical simulations, the value of the maximum length scale for turbulent eddies was limited by the computational domain size L . Here two size of domain were used. In the simulations referred as G_1 and G_2 , the side length of the cubic domain was $L^* = 46.9$ on a 135^3 nodes grid. In all other simulations, it was $L^* = 28$ on a 81^3 nodes grid. To simulate the same turbulence field in all cases, the mesh size was the same: $\Delta x^* = \Delta y^* = \Delta z^* = 0.35$ and the minimal value of L was used to determine L_e from the following criterion:

$$L_e = \frac{2\pi}{K_e} \leq \frac{1}{2} L = 14r_c \quad (11)$$

Thus, we retained $L_e^* = 14$ which implied for the given spectrum (9) an integral scale $\Lambda^* = 2.87$. As the core radius behind typical aircraft is between 1 to 3 m, this value is less than those observed in real atmospheric turbulence. Nevertheless, it ensures that the length scale characteristic of the most energetic eddies ($L_e^* = 14$) is larger than the vortex spacing ($d_0^* = 8$). This point is of major importance to mimic the real situation as we will see later. Considering measurements of atmospheric turbulence presented by Donaldson and Bilanin¹⁸, one notices that in the case of strong turbulence, the root mean square velocity of the turbulent fluctuation is about 10 % of the maximal velocity induced

Cases	Mesh grid	Domain size L^*	Re	$u'^*, \epsilon^*, \Lambda^*, Re_T = \Lambda u' / \nu$	Ke^*, Kd^*	Remarks
G_1	135*135*135	46.9	600	0.108, 4.7 10 ⁻⁵ , 2.85, 185	0.45, 4.5	Lamb-Oseen
G_2	135*135*135	46.9	600	0.108, 4.7 10 ⁻⁵ , 2.85, 185	0.45, 4.5	q-vortex ($W_0/V_0 = 1$) (init. turb. like G_1)
P_{1-9}	81*81*81	28	600	0.108, 4.7 10 ⁻⁵ , 2.85, 185	0.45, 4.5	Lamb-Oseen (init. turb. random)
P_{lam}	81*81*81	28	600	undefined		Lamb-Oseen 2D (laminar case)
P_{thi}	81*81*81	28		0.108, 4.7 10 ⁻⁵ , 2.85, 185	0.45, 4.5	without vortex (init. turb. like P_9)

Table 1: characteristics of the simulations of turbulence effects

by a vortex. For all present simulations we put $\sqrt{2k} = 0.108V_0$ which leads for the given spectrum to a dissipation of $\epsilon = 4.710^{-5}V_0^3r_0^{-1}$ and to a size of the eddies corresponding to the peak in the dissipation spectrum four time larger than the resolution ($2\pi/K_d = 4\Delta x$).

The turbulence field generated at $t = 0$ is not artificially maintained during the computation and its intensity will decay with time. To study the effect of this decay, it is possible to compare the time scale of the turbulence and the time scale of the vortices. A characteristic time for the turbulence is the eddy turn-over time T_t defined by the ratio of the integral length scale to the r.m.s. velocity. The corresponding characteristic time for the vortices T_V could be similarly defined by the ratio of the core radius to the maximal velocity. The comparison of these two characteristics times gives:

$$\frac{T_t}{T_V} = \frac{\Lambda V_0}{r_c \sqrt{\epsilon}} = 26 \quad (12)$$

Turbulence decay is sufficiently slow in comparison to the vortices dynamic to obtain the main characteristics of the effects of the atmospheric turbulence on the wake vortices.

3.3 Surface boundary layer

This section is related to the initialization of the computations of three-dimensional rebound of a vortex pair studied in Section 5. The initialization involves four vortices (see Figure 1): two real vortices and their mirror images to ensure a zero normal velocity at the wall (the no-slip condition is imposed by setting a zero parallel velocity at the wall). No turbulence is added for this case

The boundary conditions are:

- inlet: subsonic inlet or non reflecting

$$u = U(y) = \frac{u_f}{\kappa} \log \left(\frac{y + y_r}{y_r} \right)$$

or

$$u = U(y) = \frac{U(y_{max})}{\log \left(\frac{y_{max}}{y_r} \right)} \log \left(\frac{y + y_r}{y_r} \right) \quad (13)$$

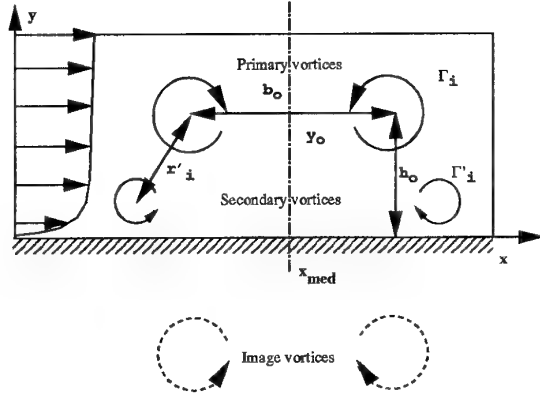


Figure 1: Computation domain

- outlet: non reflecting
- bottom: non slip wall
- top: non reflecting

The inlet wind profile is given by the Monin-Obukhov similarity theory for the surface boundary layer³¹. It corresponds to neutral condition in the surface boundary layer ($y \leq 100\text{m}$).

All lengths are normalized using the wingspan b . The initial spacing b_0 is set to $0.8b$ which is the same as for a wing with an elliptical loading ($b_0 = (\pi/4)b$, Betz⁵⁷). The domain size for all the computations is ($0 < x^* < 6, 0 < y^* < 2$).

Velocities will be scaled using V_0 and the computation Reynolds number is $Re = V_0 r_0 / \nu = 600$ (dimensionless variables using this normalization are written with a star (*) in section 5). To obtain a variation of the crosswind u along the z -axis, we multiply equation 13 with:

$$c(z) = 1 + (1 - \cos(2\pi z/z_{max})/2) u'_{inf} \quad (14)$$

We assume that the axial component w has a similar profile to u and that there is no vertical wind $v = 0$. The computation domain is periodic in the z -direction.

4 ATMOSPHERIC TURBULENCE EFFECTS

All the computations have been performed in a domain periodic in all directions.

4.1 Results and discussion of one turbulent computation

In this section, we present the results obtained from the two simulations G_1 and G_2 on the large computational domain. The objective is to understand the mechanisms of interaction between vortices and turbulence, and to obtain quantitative results about the aging process. These results will be compared with the laminar case (P_{lam}). And for the analysis of the turbulence, the case without vortices (P_{thi}) is used as reference.

4.1.1 Qualitative description of the phenomenon

Figure 2 shows the evolution of the vortex pair in the case without axial velocity (G_1). On the figures 2.a to 2.d is drawn one iso-surface of the vorticity magnitude ($\Omega^* = 0.06$) for different instants. The right vortex has a positive vorticity, the left one has negative vorticity. At $t^* = 0$ (Figure 2.a), the iso-surface are rectilinear cylinders. In the surrounding turbulent field, no eddy with a vorticity magnitude as intense as $\Omega^* = 0.06$ is present. The high levels of vorticity are concentrated inside the two vortices. For greater times, tubes with a vorticity greater than $\Omega^* = 0.06$ appear. These structures roll around the vortices in the same direction as the swirling velocity of each vortex. The vorticity direction in these tubes is in the cross planes normal to the z-axis, rather parallel to the azimuthal direction of the corresponding vortex, without preferential sense. Consequently the axes of the vortices are no more rectilinear. Their curvature seems to be more important in the direction joining the two vortices (x-direction) and increases with the time. Similar structures have been evidenced by Melander and Hussain⁶⁰. In their study of helical wave decomposition they show the creation of polarized threads surrounding coherent structures. As in our case these secondary structures spun azimuthally around the column vortex.

Figures 3.e and 3.f show two iso-surfaces of axial velocity (z-direction) and one iso-surface of vorticity magnitude respectively at the instant $t^* = 0$ and $t^* = 96$. This latter iso-surface $\Omega^* = 0.15$ shows the location of the two wake vortices. The two iso-surfaces of axial velocity correspond respectively to the values $u_z^* = -0.035$ and $u_z^* = 0.035$. At $t^* = 96$ some axial velocity sheets have appeared, they roll around the vortices. These structures which do not exist at the beginning of the simulation are created by the action of the vortices on the ambient turbulence. The phenomenon is antisymmetric: sheets of opposite sign alternate along each vortex; their sign is directly related to the axis curvature of the related vortex. Later, these structures of axial velocity disappear.

4.1.2 Action of the vortices on the turbulence

To explain the mechanism involved in the process just described, let us consider a fluid element initially located above the vortices (see Figure 4). This element is entrained between the vortices by the mean flow they induced. The vorticity related to the vortices is localized in the near core region. Thus, so long as the fluid element is far the vortices, all the vorticity it contains is due to the turbulent eddies. Later, its evolution is driven by the equation of vorticity which is in Cartesian coordinates (using the Einstein convention):

$$\frac{D\Omega_i}{Dt} = \frac{\partial\Omega_i}{\partial t} + U_j \frac{\partial\Omega_i}{\partial x_j} = \Omega_j \frac{\partial U_i}{\partial x_j} + \nu \frac{\partial^2 \Omega_i}{\partial x_j \partial x_j} \quad (15)$$

Here, the main process is the vortex stretching mech-

	near zone	far zone
Mesh	7x32x32	32x32x32
size	2.1x10.85x10.85	10.85 ³
limits relative to the pair center		
x_{min}^*, x_{max}^*	-1.05, 1.05	-5.25, 5.60
y_{min}^*, y_{max}^*	-5.25, 5.60	12.60, 23.45
z_{min}^*, z_{max}^*	-5.25, 5.60	-5.25, 5.60

Table 2: Far and near zones definition

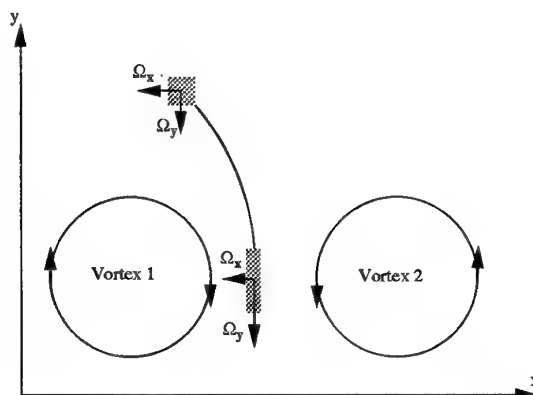
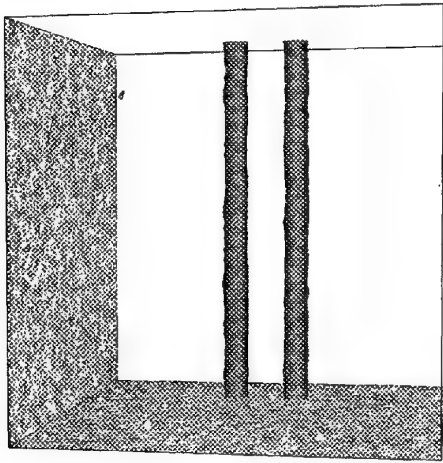
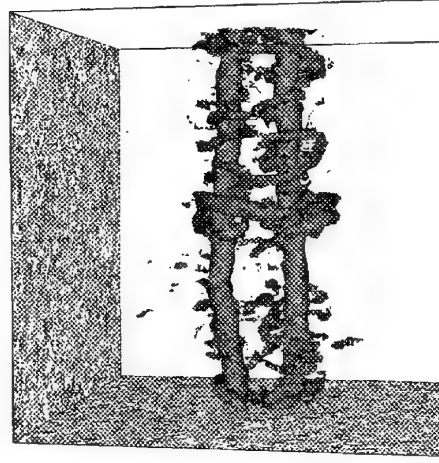


Figure 4: Vortex stretching

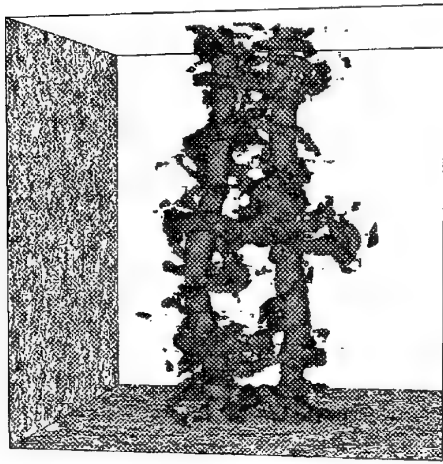
anism expressed by the first term of the right hand side of equation 15. The high value of the turbulence to vortices time scale ratio (see equation 12) implies that the turbulence is frozen on the time scale of the vortex evolution. For the velocity gradients $\partial U_i / \partial x_j$, the effect of turbulence is negligible and only the mean velocity has to be taken into account. The velocity field induced by the vortices compresses the fluid element in the x-direction and stretches it in the y-direction. In consequence, the magnitude of the vorticity in the y-direction Ω_y is increased ; but the sign of Ω_y could be either positive or negative since it is given by the initial turbulent stochastic



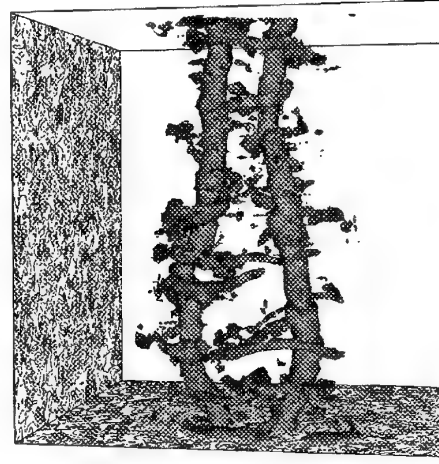
(a) $t^* = 0$



(b) $t^* = 48$

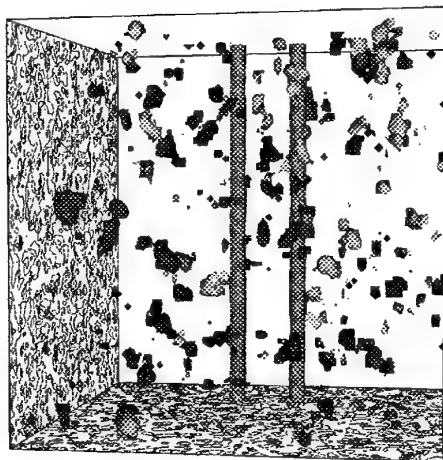


(c) $t^* = 96$

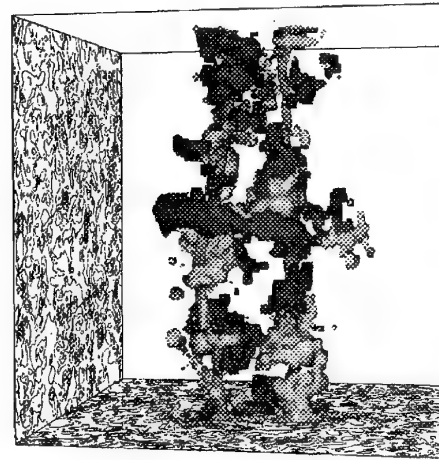


(d) $t^* = 144$

Figure 2: Iso-surface of vorticity magnitude



(a) $t^* = 0$



(b) $t^* = 96$

Figure 3: Iso-surface of axial velocity

conditions. Concurrently the magnitude of Ω_x tends to decrease. Then, after being moved between the vortices the eddy does not leave the pair on a symmetric trajectory. Because of the global motion of the pair, it is entrained around one of the vortices, and azimuthal tubes are formed.

In view to check this interpretation, a comparative analysis of the turbulence properties in two different regions of the flow has been performed. The location of these regions are defined relatively to the vortex pair and move with them (see table 2). The first one, referred as *far* zone, is sufficiently far to the vortices for considering that the turbulence is free. The second one, referred as *near* zone, is situated between the two vortices but out of the core regions.

A way to investigate the action of the vortex stretch-

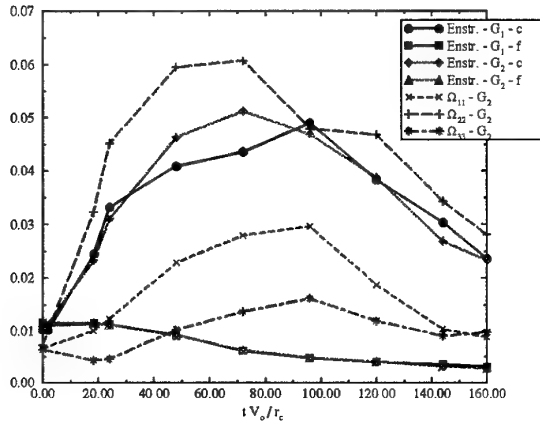


Figure 5: Enstrophy versus time

ing exerted by the vortex flow field on the turbulence consists to examine the evolution of the enstrophy in the neighbourhood of the pair. For this reason we define the enstrophy tensor $\Phi_{ij} = \Omega_i \Omega_j$. To evaluate the total amount of enstrophy, the classic scalar definition is used $F = 1/2 \sum_i \Phi_{ii}$ and to distinguish its distribution in each direction, the diagonal components Φ_{ii} are considered. Figure 5 presents the spatial average values in the *near* zone of the enstrophy for the simulations G_1 and G_2 . The evolutions of the average value in the *far* and in the *near* zone of Φ_{xx} , Φ_{yy} and Φ_{zz} are also presented but only for the case without axial core velocity (G_1).

At $t^* = 0$, in simulation G_1 , all the Φ_{ii} in the two zones are equal because all vorticity is due to the initial homogeneous and isotropic turbulence. Then, in the *far* zone, the three components decrease regularly and continue to be equal to each others. This confirms that the ambient turbulence is a still isotropic decaying turbulence. On the other hand, in the *near* zone, the total strain induced by the vortex pair stretch the turbulent eddies causing a rapid increase of the total amount of enstrophy F . The maximum of F is reached near $t^* = 70$. Afterwards, the general decay of the ambient turbulence exceeds the enstro-

phy production by the stretching of the vortices, and F begins to diminish. The analysis of the diagonal components in the *near* zone confirms the interpretation proposed before. Indeed, the augmentation of the enstrophy is mainly due to the increase of Φ_{yy} . A part of the increase of Φ_{xx} is caused by the fact that the stretching acts exactly in the y -direction only for eddies located in the median plane between the two vortices. Even, in the *near* zone as it has been defined, a fraction of the enstrophy produced by the vortex stretching process is given to the Φ_{xx} . Moreover, the mutual interactions of the turbulent eddies generate also a vortex stretching process which tends to redistribute energy between the different components of the fluctuations and lead to the spontaneous return to isotropy. That is the second cause for the increase of Φ_{xx} and the reason of the augmentation of Φ_{zz} . This redistribution goes on after Φ_{yy} has reached its maximum. In consequence, the maxima of Φ_{xx} and Φ_{zz} are reached later. Then, from $t^* = 140$, Φ_{xx} and Φ_{zz} have the same magnitude and decrease rapidly.

For simulation G_2 , only the total enstrophy F has been plotted in Figure 5. The presence of a strong axial velocity in the vortex core has no significant consequence on the observed phenomenon.

This strong production of vorticity in the plane normal to the z -direction explains the presence of intense axial velocities. Moreover, the fact that the initial length scale L_e associated to the most energetic eddies is greater than the vortex spacing d_0 leads to the formation of alternated sheet of axial velocities in the first part of the calculation. Indeed, when a turbulent eddy whose size is comparable to d_0 is stretched by the vortex induced velocity field, high axial velocity are created near each vortex; their magnitude is close but their sign is opposite. After t^* about 70, the structures disappear due to the decay of the turbulence.

Figure 6 features the evolution of the maximal axial

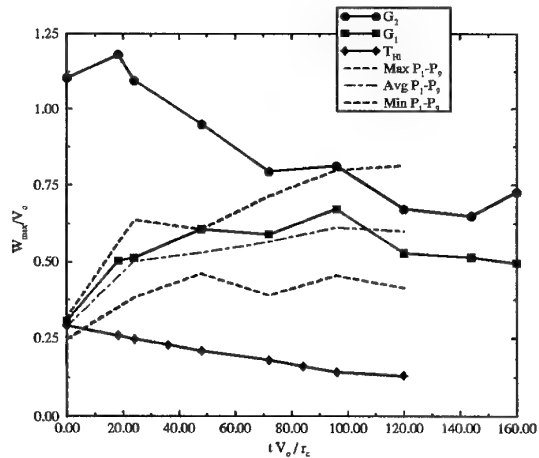


Figure 6: Axial velocity versus time

velocity over the whole flow field. At $t^* = 0$, for the

cases G_1 and P_{thi} , the only axial velocities are due to the turbulent fluctuations; their maximum have thus the same value of $0.3V_0$. During the simulations, the turbulent fluctuations of the case without vortices (P_{thi}) decrease continuously. At the opposite, in the case G_1 the maximal axial velocity increases for reaching a maximum close to $0.7V_0$. The locations of these high axial velocity remain always close to the pair and follow it during its displacement. For the case G_2 , the initial maximal velocity located at the vortex axis. Then, axial velocity in the core decreases because of the diffusion, the axial velocity created out of the core by the vortex stretching being predominant. From $t^* = 100$, the maximal velocity is due to the turbulent eddies. Its magnitude is greater than for the case G_1 ($0.8V_0$) but its location is in the same region.

4.1.3 Definitions of objective parameters for the vortex description

In this part, objective parameters for the description of the vortices are introduced. The goal is to perform a quantitative analysis of their evolution. For a complete characterisation, different aspects have to be investigated, namely: the displacement, the deformation and the decay. In the present situation, putting apart the curvature of the vortex axis which is an intrinsically three-dimensional phenomenon, the characteristic parameters of two-dimensional vortices can still be used for the description.

In the following the two vortices are denoted by the

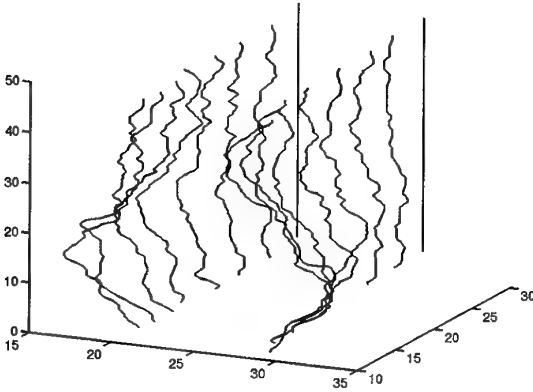


Figure 7: Vortex deformation - $t^* = 0$ to 160 , $\Delta t^* = 24$

subscripts $i = 1$ for the vortex whose vorticity vector is directed in the increasing z sense, and $i = 2$ for the other. At a given instant t , the plane Cartesian coordinates $(x_{c,i}, y_{c,i})$ of the vortex centre are determined by the location of the pressure minimum in each cross plane $z = c^{ste}$ (see Figure 7 for illustration). A line $(x_{c,i} = f_i(z), y_{c,i} = g_i(z))$ is thus obtained. Then, the position $(x_{t,i}, y_{t,i})$ of the equivalent two-dimensional vortex is defined by averaging in the z -direction. For the characterization of the decay, the core radius r_c and the maximal azimuthal velocity V_{max} have been chosen. Because of

the presence of turbulent fluctuations, their values cannot be directly obtained from the velocity field in each cross-plane. Thus, a two-dimensional flow is calculated by the averaging the flow in all the cross planes. But, before the averaging, the flow field in each cross plane $z = c^{ste}$ is moved by a translation of vector $(-x_{c,i}(z), -y_{c,i}(z))$. In this way, the effect of the deformation of the vortex axis is eliminated and only decay is taken into account. This operation is repeated independently for the two vortices, hence two equivalent two-dimensional vortices are obtained. Then, the evolution of the radial evolution of the azimuthal velocity $U_\theta(r)$, which is similar here to $U_x(y)$, is considered. Finally, the values of r_c and V_{max} are determined by minimisation of the mean squared difference between formula (1) summed for two vortices and the results of the simulation in the central region of the vortex. The main features of the vortex deformation can be obtained from the characteristics of the centre line $(x_{c,i}, y_{c,i})$. In the present work, attention is focused on the magnitude of the deformation. We define, for the x -direction, the peak magnitude:

$$\Delta_{x,i} = \max_z(x_{c,i}) - \min_z(x_{c,i}) \quad (16)$$

the standard deviation:

$$\delta_{x,i} = \left(\frac{1}{z_{max}} \int_0^{z_{max}} (x_{c,i}(z) - x_{t,i})^2 dz \right)^{1/2} \quad (17)$$

and the intercorrelation coefficient:

$$\delta_{xx} = \left(\frac{1}{z_{max} \delta_{x,1} \delta_{x,2}} \int_0^{z_{max}} (x_{c,1}(z) - x_{t,1})(x_{c,2}(z) - x_{t,2}) dz \right)^{1/2} \quad (18)$$

For the y -direction, similar definitions are used.

4.1.4 Instability of vortex pair

As expected, the velocity induced by each vortex near its companion causes the whole motion of the pair in the positive y -direction. The main effect of turbulence on this motion, represented by the variation of $(x_{t,i}, y_{t,i})$, is to vary their spacing in the x -direction. This has a direct consequence on the whole velocity. Here the vortices go away from each others and hence the pair slows down. On the other hand, their spacing in the y -direction seems not be influenced by the turbulence.

The vortex deformations are illustrated on the Figure 7. The centre lines of the vortices in the case G_1 are plotted for eight different instants with a regular time interval $\Delta t^* = 24$. In the initial condition the vortices are rectilinear. Then, perturbations appears. Short waves correspond to deformations in x - or in y -direction without preference.

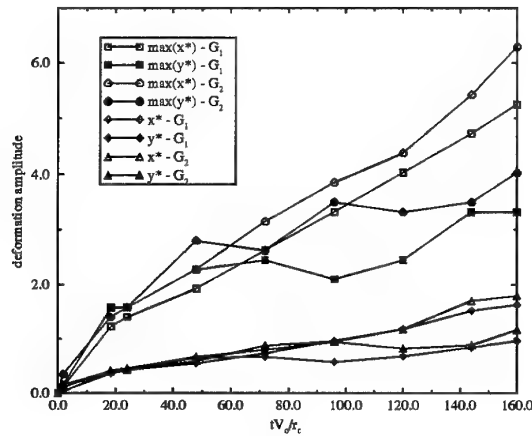


Figure 8: Deformation magnitude versus time

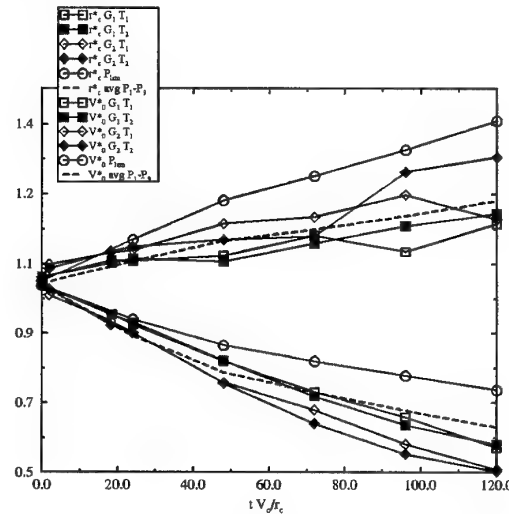
But the long-wave perturbation which appears correspond only to deformations in the direction joining the vortices (x-direction). The lines corresponding to the q-vortex (G_2 case) not presented here show a similar behaviour. The quantitative results about the deformation magnitudes are presented on Figure 8. For $t^* \leq 70$, the deformations are about the same magnitude in the two directions and for the two cases. At $t^* = 70$ the standards deviation δ^* are all close to 0.7–0.8 and the peak magnitude Δ^* are all in the range 2.5–3.0. But in the following, the amplitude become larger in the x-direction than in the y-direction and larger for q-vortex (G_2) than for the Lamb-Oseen (G_1). In the x-direction, the inter-correlations are always negative, although they are always positive in the y-direction.

For $t^* \leq 70$, the deformations due to the random turbulent perturbations predominate. Thus the deformation magnitude are the same in all directions and their wave lengths in the range of the turbulent eddies (from one to ten d_0). After $t^* = 70$, the magnitude of the deformations is now essentially due to the long wave perturbation whose wave length is equal to the domain size ($L^* = 46.9$). Its amplitude increases continuously up to the end of the simulation ($t^* = 160$), even though the turbulence decays. Hence, turbulence does not drive the vortex deformation any more. The turbulence fluctuations have initiated an unstable antisymmetric deformation of the vortex. That could be related to the work of Klein, Madja and Damodoran¹². These authors have studied theoretically the interaction of nearly parallel filaments for perturbations whose wave lengths are long in comparison with the vortex spacing d_0 . They show that for an antiparallel vortex pair, there is a finite-time collapse independent of the structure of the perturbation. Here, the ratio of the length wave to the vortex spacing is only about 2.9. Therefore, the theory does not rigorously apply but the mechanism is likely to be the same. Here, the waves developing have the maximal length allowed by the

finite domain, thus one can not conclude that it is the most unstable one. The deformations observed here after $t^* = 70$ suggest to extend the unconditional instability of counter rotating vortex pair in presence of turbulence and for finite length wave, but the quantitative results are not relevant for the case of an infinite medium. Furthermore, the presence of axial velocity in the vortex cores seems to increase the growth rate of the instability.

4.1.5 Aging of a vortex pair

The effect of the aging process is analysed from the radial distribution of the equivalent two-dimensional vortex defined in paragraph 4.1.3. The central region

Figure 9: Temporal variation of r_c^* and V_0^*

of the vortex ($0 \leq r^* \leq 3$) is accurately approximated by the analytic expression of the Lamb-Oseen pair. In the outer region of the vortex, the fitting does not apply correctly: for a same core set of parameters (radius and maximal velocity) the decay with the distance is faster here than for the laminar analytic solution of Lamb-Oseen. To improve the comparison between laminar and turbulent situations, Figure 9 features the evolutions of the core radius r_c^* and the maximal velocity V_0^* in the turbulent simulations (G_1 , G_2) and in the laminar one (P_{lam}). The case G_1 shows a stronger decay of the velocity V_{max}^* than the laminar case; this effect being more pronounced in presence of axial core velocity (G_2). As expected, the ambient turbulence accelerates the aging process of the vortex. The increasing of the core radius r_c is slower in presence of turbulence. This must not be interpreted as a smaller diffusion of the vorticity because r_c does not correspond to a point of constant velocity magnitude, but to the point where the instantaneous maximal velocity V_{max} is reached. Thus, turbulence does not simply accelerate the laminar diffusion process as suggested from an approach based on an increase of the bulk viscosity. The mechanisms induced by turbulence are radically different. The use of the natural

parameters r_c and V_{max} does not permit to show its main characteristics. In consequence, we introduce now another representation based upon another couple of parameters: a circulation Γ , and a vorticity Ω_{max} .

From the expression for one Lamb-Oseen vortex, the circulation at infinity is proportional to the product $r_c V_{max}$ (6) and the maximal vorticity Ω_{max} in the vortex centre is proportional to the ratio V_{max}/r_c (7). Here, we keep those definitions for Γ and Ω_{max} . For a pair of vortices, the circulation far from a vortex is not characteristic of its own evolution. Furthermore, the fitting by the Lamb-Oseen expression is not valid far from the vortex. Thus, the parameters Γ and Ω_{max} are meaningful only for the properties of the vortex core: Γ stands for the global circulation and Ω_{max} represents the maximal intensity.

Figure 10 (resp. 11) features the evolutions of Γ (resp.

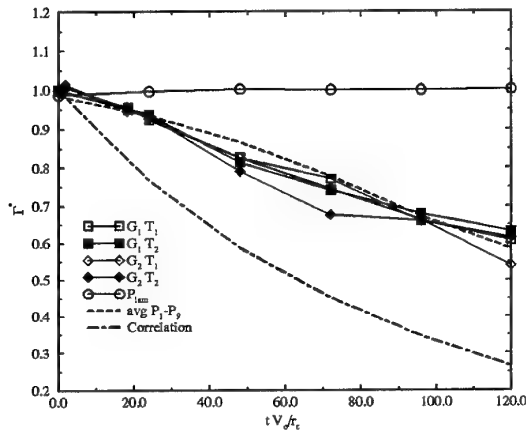


Figure 10: Temporal variation of circulation Γ^*

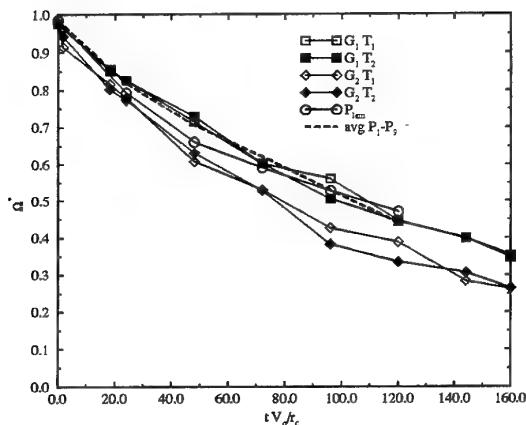


Figure 11: Temporal variation of vorticity Ω^*

Ω_{max}) in the two turbulent situations (G_1 , G_2) and for the laminar reference (P_{lam}). We added also the model of Donaldson and Bilanin:

$$\frac{d\Gamma}{dt} = -0.82 \frac{u'\Gamma_0}{b_0} \quad (19)$$

In the laminar case, the circulation Γ remains constant (Figure 10); each vortex behaves as if it was alone. That means, that in the absence of turbulence, the two vortices of the pair are sufficiently far from each other. In presence of turbulence, the circulation decreases, the axial velocity having no influence on this. On the other hand, the evolution of the maximal vorticity is similar in the laminar case to the one in the turbulent run (G_1); but the decay of the vorticity is faster in presence of axial velocity.

The parameters Γ and Ω_{max} are related to two different mechanisms of the aging process. In laminar situation, only one mechanism exists: the molecular diffusion. Hence, the evolution of the vortex is well represented by the maximal vorticity which is proportional to the velocity gradient. But, the action of turbulence should be decomposed in two parts.

The first is the turbulent transport of the vorticity which can be roughly understood as an increase of the effective diffusion. Its magnitude is controlled by the velocity gradient as in the laminar case. Its effect is essentially to accelerate the laminar process by increasing the rate of decay of Ω_{max} . In the simulation presented here (G_1), the decay of the maximal vorticity is the same as in the laminar situation. The reason is that the spatial resolution of the simulation ($\Delta x^* = 0.35$) is only about one third of the initial core radius, and the length scale corresponding to the peak wave number in the initial dissipation spectrum ($2\pi/k_d = 3.97r_0$) is about four times the initial core radius. In consequence, the turbulent diffusion can not act significantly on the scale of the core. The diffusion of the vorticity outside of the core is only due to molecular transport and the evolution of Ω_{max} is the same as in absence of turbulence. Moreover, in the simulation G_2 , the presence of the radial gradient of W causes a faster decay of Ω_{max} . In laminar situation, the diffusions of the axial velocity and of the radial velocity are independent. For this reason no laminar simulation of a q-vortex is presented here. For the decay of Ω_{max} the laminar reference of the case without axial velocity is relevant for doing the comparison with the case G_2 . But in presence of turbulence the evolution of axial and radial velocity are then coupled and even without small scale fluctuations able to induce turbulent diffusion of the vorticity, the presence of a gradient of axial velocity causes a faster decay of Ω_{max} than in the laminar simulation (P_{lam}) and in the case without axial velocity (G_1).

The second mechanism involved in the action of the turbulence is related to the phenomenon described in paragraph 4.1.2: the vortex stretching process transfers vorticity from the vortex to the ambient turbulence. This cause the decrease of the global intensity of the vortex core, and thus the circulation Γ decays. The vortex stretching is an inertial mechanism. It acts on all the turbulent scales, but the major part of the enstrophy is given to the large scales which are independent of the viscosity and can be significantly

stretched before reaching the dissipative scales. This is very different of the hypothesis of the diffusion model of Donaldson and Bilanin¹⁸ which overestimates the decay of the vortices.

4.2 Statistical approach

The results presented above correspond to a unique realisation of the stochastic initial turbulence. To establish their sensitivity to the initialization, nine simulations (P_{1-9}) have been performed in a smaller domain ($L^* = 28$); a grid of 81^3 nodes was used to conserve the same resolution. The only differences between these simulations are the random phases of the initial velocity fluctuations field in the spectral domain. That allows to carry out statistics on the parameter characteristics of the vortices: probability density distribution, average values, and also extrema which are fundamental for the hazard estimate. We proceed in two different ways. The first one consists in calculating the parameters from each realisation independently and then to perform the statistics on the values obtained.

First, let us go back to Figure 6 to examine the dispersion of results around the maximal axial velocity. The mean value obtained from the nine simulations is very close to those of the case G_1 . That means that the simulations G_1 , and G_2 which has the same initial turbulence, are representative. Nevertheless, the difference between the two extrema becomes large and increases regularly with time. Considering the diverse realisations, the axial velocity can go beyond $0.8V_0$ or remain fewer than $0.4V_0$. Therefore, the hazard related to the apparition of the horizontal vorticity tubes in one realisation is very difficult to be predict.

On the simulations G_1 , the two vortices move away

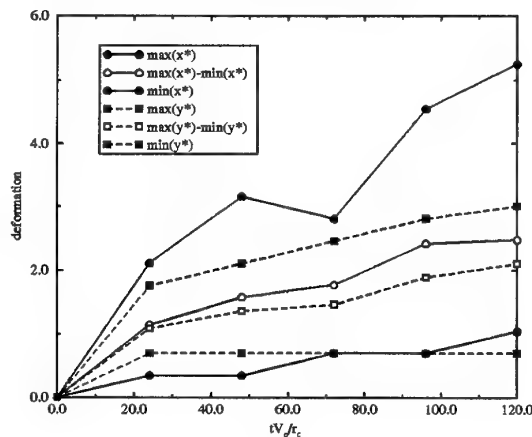


Figure 12: Statistics of deformation

from each other in the x- direction. The evolution of the mean value and the dispersion in the P_{1-9} runs do not confirm this feature: there is no tendency for the vortices to be nearer or further from each other. Thus, their spacing and the global motion of the pair is controlled by the random fluctuations. When

the spacing decreases the pair accelerates in the y- direction, when it increases the pair slows down. By the way, it is remarkable that the laminar prediction (P_{lam}) is in the range of the turbulent results.

The results concerning the deformation of the vortex axis are shown on the Figure 12. As explained in paragraph 4.1.2, their interpretation needs to take into account the effects of two phenomena : the turbulence and the long-wave instability. Here the turbulence has the same properties as for the case G_1 . But the domain is smaller ($L^* = 28$ vs 46.9), and the instability which develops has not the same length wave. Thus, the comparison with the calculation in the large domain is not valid. Nevertheless, it can be noticed that the dispersion of the results is very important: at $t^* = 120$ the peak to peak deformation ranges between 1 to 5.5, and the standard deviation between 0.5 to 3. About the aging process, the mean values of the core radius r_c , the maximal velocity V_0 , the maximal vorticity Ω_{max} , and the circulation Γ are presented on the Figures 9-11. At the opposite of the position and of the deformation, the dispersion on the characteristics of the vortex is very weak. In consequence, the mean values of all the parameters are very close to the results of the simulation G_1 . Hence, a unique calculation should be sufficient for determining their value.

4.3 Modelling

For the practical problem of the hazard caused by the wake vortices, simple models that can be used in real time in airports are needed. In this section, we use results obtain from the direct numerical simulations in view to help the design of such models.

The conclusions of this study seem to show that the aging process of the vortices is well described by the use of two parameters characteristic of classical two-dimensional vortices as the Lamb-Oseen one. Among all the possible couples, the choice of the maximal vorticity Ω_{max} and the global core circulation Γ is particularly judicious because it permits to separate the interaction between the vortices and the turbulence into two independent mechanisms. The evolution of Γ , which is related to the inertial vortex stretching process, involves essentially an interaction with the large turbulent scales (of order the vortex spacing d_0). The evolution of Ω_{max} is related to the diffusion mechanisms - molecular or turbulent - and involves the small turbulent eddies (smaller than the core radius r_c).

Let us now take into account scale considerations. The whole problem, as formulated in this work, involves seven physical parameters: the initial characteristics of the pair (r_0 , V_0 , d_0), those of the turbulence (kinetic energy k , dissipation ϵ), the kinematic viscosity ν and the time t . All these quantities can be expressed using two independent units (length and time). Hence the problem description required five independent dimensionless numbers. Following the conclusion just recalled, we postulate that the evo-

lutions of Γ and Ω are driven by two independent mechanisms. The problems is now to built the numbers relevant for this two processes.

For the vorticity the mechanisms of diffusion have to be examined. In laminar situation, the problem is entirely controlled by the Reynolds number: $Re = \Gamma_0/\nu$. In turbulent situation, the turbulent diffusion of the core vorticity has also to be taken into account. It is proportional to the square of the characteristic velocity $u'(r_0)$ of the eddies whose size are about of the core radius. Assuming that the core radius is included in the inertial turbulent subrange: $u'(r_0) = (\epsilon r_0)^{1/3}$. Thus, we introduce an other dimensionless number, the ratio between turbulent and molecular diffusion in the vortex core: $((\epsilon r_0)^{2/3})/(\nu V_0/r_0) = \epsilon^{2/3} r_0^{5/3}/\nu V_0$. Finally, we need to build a dimensionless time. For our presentation to be suitable for high turbulence level, we choose to use the turbulent scale: k/ϵ . Then, we propose for Ω the following expression:

$$\begin{aligned} \frac{\Omega}{\Omega_0} &= f\left(\frac{V_0 r_0}{\nu}, \frac{\epsilon^{2/3} r_0^{5/3}}{\nu V_0}, \frac{\epsilon t}{k}\right) \\ &= f\left(\frac{\Gamma_0}{\nu}, \frac{\epsilon^{2/3} \Gamma_0^{1/3}}{\nu \Omega_0^{4/3}}, \frac{\epsilon t}{k}\right) \end{aligned} \quad (20)$$

In the case an initial axial velocity W_0 in the vortex core, the gradient of $\Omega_w = W_0/r_0$ enhances the diffusion. The function f of (18) depends then also on the ratio of the two gradients: Ω_w/Ω_0 . Zeman²⁶ does not propose two mechanisms to explain the turbulent aging of trailing vortices, but we agree that the core spreading is mainly due to viscous diffusion (see eq. 20). His model does not predict the decay of the core circulation observed in field experiment.

The circulation Γ is controlled by the mutual stretching exerted between the vortices of the pair and the azimuthal turbulent eddies. This interaction occurs out of the core of the vortices. Actually the eddy located between the vortices are those which are preferentially involved in the process. Thus, as d_0 is in general one order of magnitude larger than r_0 , the vortex can be roughly considered as a filament only characterised by its circulation. Γ_e is a characteristic circulation of the eddies in interaction with the wake vortex, and if a is a length scale representative of their spacing to the vortex, a^2/Γ_e is the characteristic time scale of the action of the turbulence on the vortex. Reciprocally, a^2/Γ is the time scale of the action of the wake vortex on the turbulence. The ratio of these two time scales is the key parameter governing the evolution of Γ . For Γ_e , we can choose the product of the classical length scale $k^{3/2}/\epsilon$ by the root mean squared velocity $k^{1/2}$. That leads to the new number $\Gamma_0 \epsilon/k^2$. Actually, the eddies are essentially stretched in the region located between the two vortices of the pair. Thus, the ratio between the turbulent length scale $k^{3/2}/\epsilon$ and the vortex separation d_0 is very important. This introduces, the fifth

and last dimensionless number required: $d_0 \epsilon/k^{3/2}$. Therefore, the expression proposed for Γ is:

$$\begin{aligned} \frac{\Gamma}{\Gamma_0} &= g\left(\frac{\epsilon V_0 r_0}{k^2}, \frac{\epsilon d_0}{k^{3/2}}, \frac{kt}{\epsilon}\right) \\ &= g\left(\frac{\epsilon \Gamma_0}{k^2}, \frac{\epsilon d_0}{k^{3/2}}, \frac{kt}{\epsilon}\right) \end{aligned} \quad (21)$$

If the behaviour of Ω depends on the core circulation, the evolution of Γ is independent of the maximal vorticity. Fortunately, for the prediction of the hazard, the value of Γ is sufficient. Indeed, the maximal vorticity characterises the structures of the flow inside the core although Γ represents the global intensity of the vortex. Donaldson and Bilanin¹⁸ first proposed a model for the decay of the circulation Γ of a vortex in the atmospheric turbulence. But they considered that the evolution of Γ was driven by the turbulent diffusion as the more recent work of Zeman²⁶. We have shown in this work that this is not correct. Therefore we want to conclude by a warning: the prediction of the circulation is sufficient in practical problems but it is necessary to relate it to the vortex stretching mechanism as it is suggested in equation 21 and not to the properties of diffusion of the turbulence.

5 REBOUND WITH CROSSWIND

In the following the length are no more adimensionnalized by the core radius r_c but by the wingspan b . This parameter is more pertinent to consider the effect of the ground on the vortex pair behavior (see presentation of simulations section 3.3).

5.1 Two-dimensional laminar results

The work done in two-dimensional laminar flows has led to the definition of a "height of rebound" law which relates the altitude of rebound and the shear of the crosswind⁴¹ (see Figure 1 for geometry). To describe the effect of crosswind on the vortex bouncing, a relevant parameter is the vertical crosswind shear at an altitude of half the initial distance d_0 between the vortices $\sigma = \left. \frac{dU}{dy} \right|_{y=d_0/2}$. Since the altitude of rebound depends on core radius and initial strength of the vortices⁵, an appropriate dimensionless number is:

$$w_s = \frac{\sigma r_c}{u_{gmax}}$$

All the results are collected in Figure 13. Error bars are due to the determination of the minimum altitude in the computation. Linear fits have been performed for the results of Figure 13. These results lead to the following formulas:

- for the downwind vortex

$$\frac{h_{min}}{d_0} = 0.65 + 2.64 w_s \quad (22)$$

- for the upwind vortex

$$\frac{h_{min}}{d_0} = 0.65 - 1.61w_s \quad (23)$$

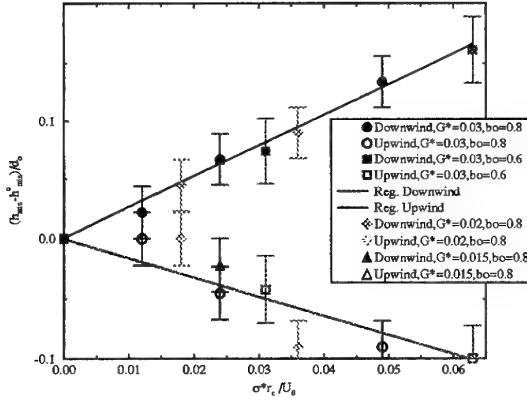


Figure 13: Minimum altitude versus $w_s = \sigma \times r_c / u_{\theta_{max}}$

5.2 Three-dimensional laminar results

The first goal of this study is to quantify the effect of the axial component of the wind on the altitude of rebound. Several computations have been made and their characteristics are summarized in Table 3.

5.2.1 Effects of three-dimensional wind

The first run SV has confirmed that there is no effect of the third dimension on the rebound phenomenon without wind. The altitude of rebound is the same as for the two-dimensional cases presented in section 5.1.

The interest of three-dimensional computations is to study the effect of a inhomogeneous crosswind on the trajectory of the vortices near the ground. The variation is imposed as indicated in equation 14. The maximal velocity difference is given in Table 3 with u'_{inf} . In the run R_0 , this variation leads to a maximal dimensionless crosswind at $y = y_{max}$ varying between 0.167 and 0.217. In order to facilitate the post-treatment of these computations, we use the works of Jeong and Hussain⁶¹ on the identification of a vortex: we compute the second eigenvalue λ_2 of the symmetric tensor $S^2 + \Omega^2$ where S and Ω are respectively the symmetric and antisymmetric parts of the velocity gradient tensor ∇u . In Figure 14, the isosurface of negative λ_2 is represented for $t^* = 4.8$. At that time the two secondary vortices are created due to viscous interaction between the primary vortices and the ground plane. But, as the primary vortices remain quite linear at this instant, the secondary vortices are curved. A second case R_{01} is computed using twice the number of point in the axial direction. There is no difference between the runs R_0 and R_{01} validating the use of coarse grid in the z -direction. To better study the three-dimensional

rebound mechanism, the altitude of the downwind primary vortex of the run R_0 is compared in Figure 15 with the results of the cases NZ_1 and NZ_2 . These two-dimensional cases correspond to the first

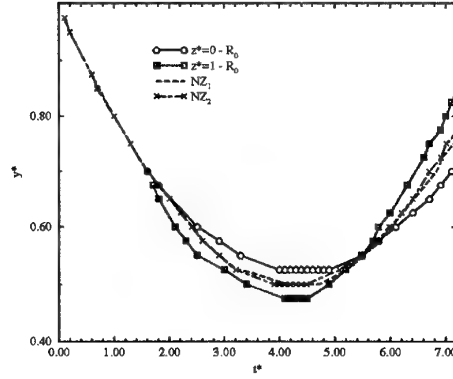


Figure 15: Altitude of downwind primary vortex versus time

and medium z -planes of the three-dimensional case. There is a large difference between the two-dimensional and the three-dimensional results. As explained in Corjon and Poinot⁴¹, the altitude of rebound is higher when the crosswind is higher for two-dimensional flows. But, in this three-dimensional run, the minimal altitude of rebound is obtained in the plane where the crosswind is maximal.

In Figures 16 and 17 are represented the paths of re-

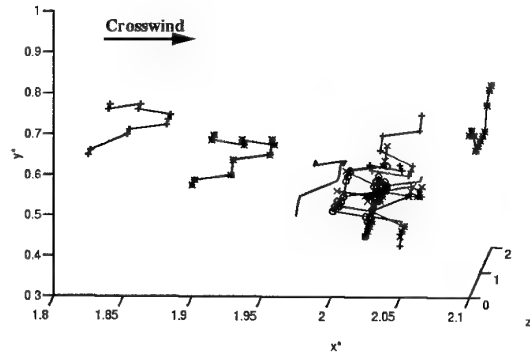
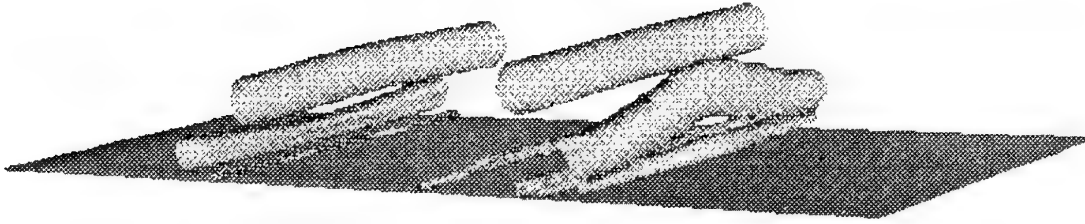


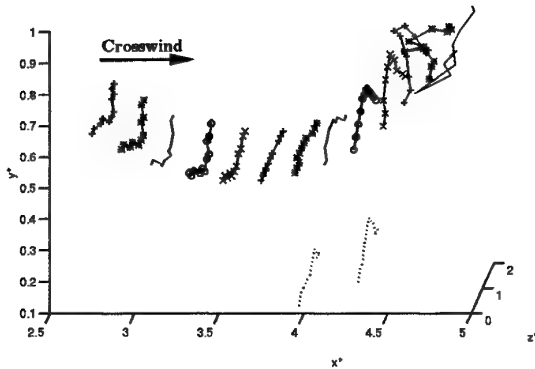
Figure 16: Position of upwind primary vortex centre - run R_0 - $t^* = 1.8$ to 9.0 , $\Delta t^* = 0.6$ from left to right

spectively the upwind and the downwind vortex. The variation of the crosswind along the vortex axis implies a small perturbation on the primary vortices. In Figure 17, we put also the position of secondary vortex center at $t^* = 4.5$ and 5.4 (dotted lines). These three-dimensional lines show that the primary vortex is initially perturbed by the variable crosswind and that this curvature will be inverted after the rebound. The viscous interaction does not occur simul-

Cases	Mesh grid	d_0	u_{inf}^*	u'_{inf}	w_{inf}
SV	241*81*11	0.74	0.00	0.0	0.00
NZ_1	241*81	0.74	0.167	NS	NS
NZ_2	241*81	0.74	0.217	NS	NS
R_0	241*81*11	0.74	0.167	0.3	0.00
R_{01}	241*81*21	0.74	0.167	0.3	0.00
R_1	241*81*11	0.74	0.167	0.3	0.167
R_2	241*81*11	0.74	0.100	0.3	0.167
R_3	310*104*11	0.57	0.167	0.3	0.167
R_4	241*81*11	0.74	0.167	0.3	0.083
R_5	241*81*11	0.74	0.167	0.1	0.00

Table 3: characteristics of the simulations of ground effect ($Re = 600$, $r_c^* = 0.1$)Figure 14: Isosurface of λ_2 - run R_0 - $t^* = 5.4$

taneously in each z -plane. For this run the rebound begins at the medium z -planes sooner than in the external z -plane. The secondary vortices are then curved at their creation and they amplify this curvature by self induction. The vortex sheet already separated enhances the separation of the other part. In the case R_1 , the total wind has an angle of 45 deg

Figure 17: Position of downwind primary vortex centre - run R_0 - $t^* = 1.8$ to 9.0 , $\Delta t^* = 0.6$ from left to right

with the vortex axis. The rebound phenomenon is the same: the strong vorticity sheet induced by the primary vortices becomes unstable and detaches from the wall creating curved secondary vortices. These secondary vortices roll over each primary vortex and make them rise up. The minimum altitude reached in the first and in the medium z -planes is presented in Table 4 with the results obtained for the other runs (R_2, R_3, R_4, R_5). We also put the average minimum altitude in this table. For R_1 , the minimum altitude is the same as in two-dimensional cases. There is also a curvature of the secondary vortices but opposite to the curvature observed for the run R_0 . For this case, the external z -planes begin to separate before the medium z -plane. The axial component of the wind decreases the altitude of rebound of the vortices. The grid is too coarse to accurately define this altitude, but the trend shows that the crosswind shear used in equations 22 and 23 should take into account the vorticity induced by the axial component of the wind.

We have computed the variation of the core radius size for the primary and the secondary vortices for the case R_0 . There is a fast growth of the secondary vortex core radius (as mentioned in Swearin-

Runs	h_0/d_0		
	$z = 0$	$z = 1$	Average
R_0	0.707	0.639	0.673
R_1	0.673	0.673	0.673
R_2	0.673	0.673	0.673
R_3	0.709	0.675	0.692
R_4	0.707	0.673	0.690
R_5	0.673	0.673	0.673
NZ_1	0.673	NS	NS
NZ_2	NS	0.673	NS

Table 4: Minimum altitude of rebound

gen, Crouch and Handler⁴⁹) and a slight increase of the primary vortex one.

5.2.2 Stability of primary-secondary vortex pair

The conclusions of Klein, Majda and Damoran¹² on the stability of anti-parallel vortex pair and the stability study of Swaeringen, Crouch and Handler⁴⁹ have led us to consider the later evolution of the two vortex pairs in the flowfield after the rebound. These authors have shown that a vortex pair is sensible to long wavelength perturbations and mainly the secondary vortex.

Once they begin to separate from the wall, the sec-

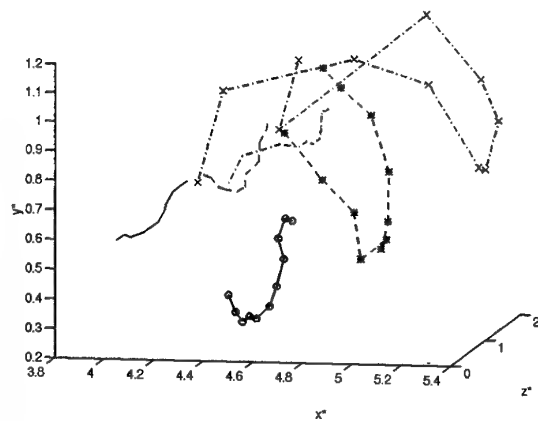


Figure 18: Center line of primary and secondary vortices - primary : solid line $t^* = 6.0$, dashed $t^* = 7.2$, dot-dashed $t^* = 8.4$ - secondary : \circ $t^* = 6.0$, \star $t^* = 7.2$, \times $t^* = 8.4$

ondary vortices are curved and their curvature continuously amplifies. The direction of curvature depends on the axial wind. If there is no axial wind the separation begin in the medium z -plane (see Figure 17), and at the external z -plane in the other case. As it can be seen in Figure 18 for the downwind pair of run R_1 , the curvature of the secondary vortex is continuously amplified. In this Figure, the lines without symbol represent the centre of the primary vortex at $t^* = 6.0, 7.2$ and 8.4 and the same lines with sym-

bols the center of the secondary vortex at the same instants (resp. \circ for $t^* = 6.0$, \star for $t^* = 7.2$ and \times for $t^* = 8.4$). The secondary vortex rolls around the primary one at different speeds in each z -plane. Figure 19 shows the negative isosurface of λ_2 for $t^* = 8.4$ with the same view angle. The reconnection between the primary and the secondary vortex occurs just after. The three projections of these paths are given in Figure 20 to 22.

The same phenomenon occurs for the upwind pair

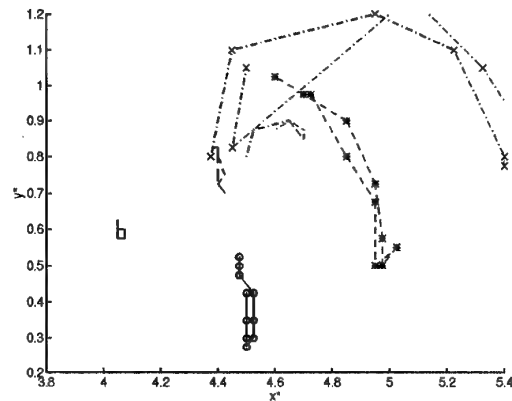


Figure 20: Center line of primary and secondary vortices - plane x, y

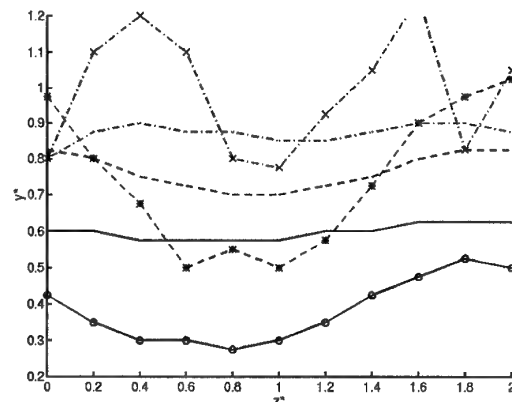
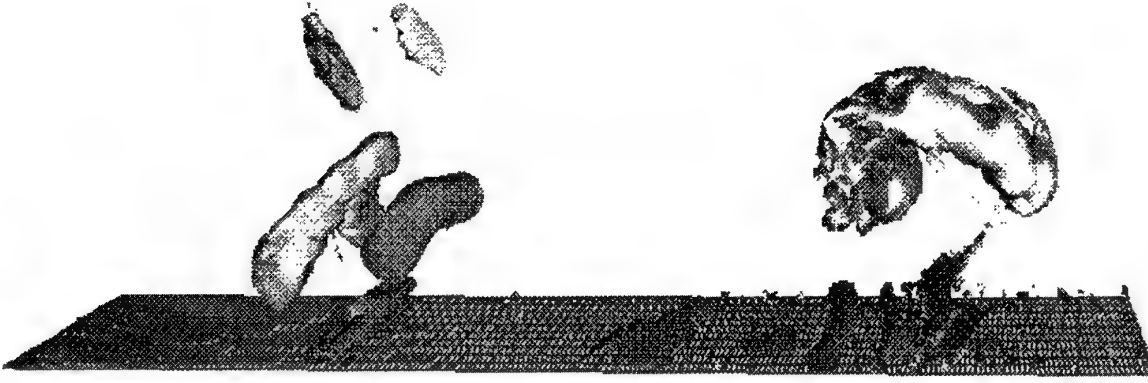
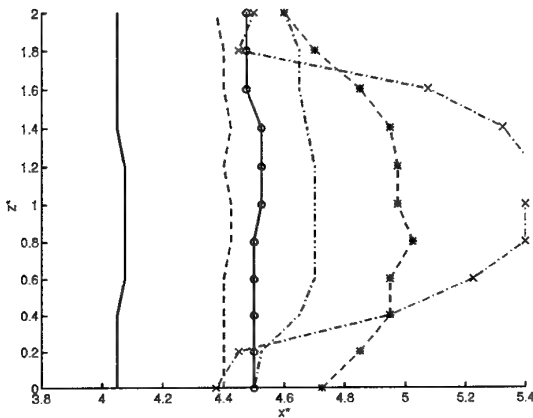


Figure 21: Center line of primary and secondary vortices - plane z, y

but later. This is due to the delay in the secondary vortex creation. The curvature of the upwind secondary vortex is always opposite to those of the downwind one. The reconnection between the primary and secondary vortices can explain the shortened wake lifetime observed when the vortices are in ground effect. The extension of the Crow theory proposed by Tombach and al.³² based on the interaction of the primary vortex and its image does not correspond to this type of instability. The theory of Klein and al. applies but their collapse time can not be computed because they only consider vortex filaments.

Figure 19: Isosurface of negative λ_2 - run $R_1 - t^* = 8.4$ Figure 22: Center line of primary and secondary vortices - plane x, z

The run R_5 , with a lower perturbation of the crosswind, leads to the same behavior but with a longer time of collapse. The axial component of the wind has the same effect. It increases the value of the linking time.

6 CONCLUSION

DNS of trailing vortices either embedded in isotropic homogeneous turbulence or bouncing near the ground have been performed.

Decay due to atmospheric turbulence

The effect of atmospheric turbulence on a vortex pair seems to imply independently the large scales ($O(d_0)$) and the small scales ($< r_c$). On one hand, the large scales cause the original mechanism of interaction between the vortices and the turbulence described here. This stretching exerted by the vortices create tubes of intense vorticity rolling up the vortices and produces high and hazardous axial velocity. In consequence, long-wave antisymmetric deformations of the vortex axis are induced. They are unstable and increase independently of the turbulence. The transfer of enstrophy from the vortices to the turbulence can be taken into account through the

global circulation Γ but has no influence on the diffusion of vorticity thus on the maximal vorticity Ω_{max} . The resulting vortex core has the same structure as the Lamb-Oseen vortex but with a slow increase of the core radius r_c and a fast decrease of the velocity V_{max} . On the other hand, the role of the small scale is to increase the diffusion mechanisms, but here the resolution is not accurate enough to allow the scales smaller than the core size to significantly diffuse the core vorticity. The comparisons between the nine turbulent realizations show that the two simulations G_1 and G_2 are representative for the decay and thus one can trust the conclusions derived from them in paragraph 4.1. Furthermore, the dispersion of the results has been estimated.

Rebound with three-dimensional wind

The first result is that the observed phenomenon is similar to the two-dimensional one. The mechanism of rebound is analogous but the axial component of the wind acts in decreasing the altitude of rebound. The inhomogeneity of crosswind is not equivalent to a superposition of two-dimensional rebounds along the z -axis. But the averaged minimum altitude of rebound is quite the same than for the equivalent two-dimensional cases.

The second result is the instability of the primary-secondary vortex pair initiated by this variation of crosswind. The secondary vortex is curved and this curvature leads to the reconnection between the primary and the secondary vortex. Then the primary vortex core bursts. The solitary vortex phenomenon could be observed if the crosswind is sufficiently high to counteract the creation of the upwind secondary vortex. In this case, the reconnection could occur only for the downwind pair.

Although they are only laminar, these results are important to understand the rebound phenomenon. Furthermore, we already do some preliminary turbulent computations near the ground: the viscous interaction seems to be modified as shown by Dommermuth⁴² for transitional vortices near a free surface. From the results of Section 4, we can expect that

azimuthal structures induced by turbulence could counteract the creation of the secondary vortex.

Future work

Several studies are in progress to continue the work presented here. For the decay due to turbulence, we will try to investigate the parameters of the decay model using both DNS and Large Eddy Simulations (LES). For the rebound, we will continue to study the mechanism and derive simple laws. LES will permit to deal with real test cases as the Idaho Falls trial⁶².

Acknowledgments

This work was supported by the STNA (Service Technique Navigation Aérienne) under research grant STNA/95/110. The authors would like to thank the CEA Saclay and CNUSC for the access to their IBM SP2, MEIKO for their access to CS2.

REFERENCES

1. Critchley, J. and Foot, P., "UK CAA wake vortex database : analysis of incidents reported between 1982 and 1990," PAPER-91, CAA, 1991.
2. Phillips, E., "Vortex tests may yield clues to USAIR crash," *Aviation Week and Space Technology*, May 1 1995.
3. Stough, H., Greene, G., Stewart, E., Stuever, R., Jordan, F., Rivers, R., and Vicroy, D., *NASA Wake Vortex Research*. American Institute of Aeronautics and Astronautics, Inc., 1993.
4. Greene, G., "An approximate model of vortex decay in the atmosphere," *J. AIRCRAFT*, Vol. 23, July 1986, pp. 566-573.
5. Corjon, A. and Poinot, T., "A model to define aircraft separations due to wake vortex encounter," *J. AIRCRAFT*, Vol. 33, May-June 1996.
6. Crow, S., "Stability theory for a pair of trailing vortices," *AIAA JOURNAL*, Vol. 8, No. 12, 1970.
7. Crow, S. and Bate, E. J., "Lifespan of trailing vortices in a turbulent atmosphere," *J. AIRCRAFT*, Vol. 13, No. 7, 1976, pp. 476-482.
8. Sarpkaya, T. and Daly, J., "Effect of ambient turbulence on trailing vortices," *J. AIRCRAFT*, Vol. 24, June 1987.
9. Liu, H., "Tow-tank simulation of vortex wake dynamics," in *FAA Proceedings of the aircraft wake vortices conference*, pp. 32-1, 32-26, October 29-31 1991.
10. Tombach, I., "Observations of atmospheric effects on vortex wake behavior," *J. of AIRCRAFT*, Vol. 10, November 1973, pp. 641-647.
11. Klein, R. and Majda, A., "An asymptotic theory for the nonlinear instability of antiparallel pairs of vortex filaments," *Phys. Fluids A*, Vol. 5, February 1993, pp. 369-379.
12. Klein, R., Majda, A., and Damodaran, K., "Simplified equations for the interaction of nearly parallel vortex filaments," *J. Fluid Mech.*, Vol. 288, 1995, pp. 201-248.
13. Rayleigh, J., *On the dynamics of revolving fluids*, Vol. Ser. A 93. Proc. R. Soc. Lond., 1916.
14. Lessen, M. and Paillet, F., "The stability of a trailing line vortex. Part 2: Viscous theory," *J. Fluid Mech.*, Vol. 65, No. 4, 1974, p. 769.
15. Ragab, S. and Sreedhar, M., "Numerical simulation of vortices with axial velocity deficits," *Phys. Fluids A*, Vol. 7, March 1995, pp. 549-558.
16. Virk, D., Hussain, F., and Kerr, R., "Compressible vortex reconnection," *J. Fluid Mech.*, Vol. 304, 1995, pp. 47-86.
17. Spalart, P., "On the motion of aircraft wakes in a stably stratified fluid," *J. Fluid Mech.*, 1996.
18. Donaldson, C. D. and Bilanin, A., "Vortex wakes of conventional aircraft," *AGARDograph*, May 1975.
19. Bilanin, A., Teske, M., and Hirsh, J., "Neutral atmospheric effects on the dissipation of aircraft vortex wakes," *AIAA JOURNAL*, Vol. 16, September 1978, pp. 956-961.
20. Robins, R. and Delisi, D., "Numerical study of vertical shear and stratification effects on the evolution of a vortex pair," *AIAA JOURNAL*, Vol. 28, April 1990, pp. 661-669.
21. Zheng, Z. and Ash, R., "Prediction of turbulent wake vortex motion near the ground," in *FED-vol.151, Transitional and turbulent compressible flows*, ASME, 1993.
22. Squire, H., "The growth of a vortex in turbulent flow," *Aeronautical Quarterly*, Vol. 16, 1965, pp. 302-306.
23. Owen, P., "The decay of a turbulent trailing vortex," *Aeronautical Quarterly*, Vol. 21, 1970, pp. 69-78.
24. Iversen, J., "Correlation of turbulent trailing vortex decay data," *J. AIRCRAFT*, Vol. 13, May 1976, pp. 338-342.
25. Phillips, W., "The turbulent trailing vortex during roll-up," *J. Fluid Mech.*, Vol. 105, 1981, pp. 451-467.

26. Zeman, O., "The persistence of trailing vortices: a modelling study," *Phys. Fluids A*, Vol. 7, January 1995, pp. 135-143.
27. Hill, F., "A numerical study of the descent of a vortex pair in a stably stratified atmosphere," *J. Fluid Mech.*, Vol. 71, 1975, pp. 1-13.
28. Sarpkaya, T., "Trailing vortices in homogeneous and density-stratified media," *J. Fluid Mech.*, Vol. 136, 1983, pp. 85-109.
29. Saffman, P., "The motion of a vortex pair in stratified atmosphere," *Stud. Appl. Math.*, Vol. 2, 1972, pp. 107-119.
30. Scorer, R. and Davenport, L., "Contrails and aircraft downwash," *J. Fluid Mech.*, Vol. 43, 1970, pp. 451-464.
31. Lissaman, P., Crow, S., MacCready, P., Tombach, I., and Bate, E., "Aircraft vortex wake descent and decay under real atmospheric effects," FAA-73-120, DOT, October 1973.
32. Tombach, I., Crow, S., and Bate, E., "Investigation of vortex wake stability near the ground," Final report AV-FR-538, AeroVironment, Pasadena (CA), July 1975.
33. Harvey, J. and Perry, F., "Flowfield produced by trailing vortices in the vicinity of the ground," *AIAA JOURNAL*, Vol. 9, August 1971, pp. 1659-1660.
34. Peace, A. and Riley, N., "A viscous vortex pair in ground effect," *J. Fluid Mech.*, Vol. 129, 1983, pp. 409-426.
35. Zheng, Z. and Ash, R., "Viscous effects on a vortex wake in ground effect," in *FAA Proceedings of the aircraft wake vortices conference*, October 29-31 1991.
36. Schilling, V., "Motion and decay of trailing vortices within the atmospheric surface boundary layer," *Beitr. Phys. Atmosph.*, Vol. 65, May 1992, pp. 157-169.
37. Teske, M., Quackenbush, T., Bilanin, A., and Wachpress, D., "Vortex roll-up, merging and decay with the uniwake computer program," in *FAA Proceedings of the aircraft wake vortices conference*, pp. 33-1, 33-20, October 29-31 1991.
38. Ash, R. and Zheng, Z., "Cross wind effects on turbulent aircraft wake vortices near the ground," in *25th AIAA Fluid Dynamics Conference, Colorado Springs (CO)*, No. AIAA-94-2381, June 20-23 1994.
39. Zheng, Z. and Ash, R., "Study of aircraft wake vortex behavior near the ground," *AIAA JOURNAL*, Vol. 34, March 1996, pp. 580-589.
40. Robins, R. and Delisi, D., "Potential hazard of aircraft wake vortices in ground effect with crosswind," *J. AIRCRAFT*, Vol. 30, March-April 1993, pp. 201-206.
41. Corjon, A. and Poinso, T., "Wake vortices behavior near the ground," in *Proceedings of 2nd International Workshop on Vortex Flows and Related Numerical Methods, Montréal (Canada)*, August 19-24 1995.
42. Dommermuth, D., "The laminar interactions of a pair of vortex tubes with a free surface," *J. Fluid Mech.*, Vol. 246, 1993, pp. 91-115.
43. Sarpkaya, T., Merrill, C., and Carroll, J., "Coherent structures in vortex/free-surface interaction," in *32nd Aerospace Sciences Meeting and Exhibit*, No. AIAA-94-0530, (Reno, NV), January 10-13 1994.
44. Chu, C. and Falco, R., "Vortex ring/viscous wall layer interaction model of the turbulence production process near the wall," *Experiments in Fluids*, Vol. 6, 1988, pp. 305-315.
45. Walker, J., Smith, C., Cerra, A., and Doligalski, T., "The impact of a vortex ring on a wall," *J. Fluid Mech.*, Vol. 181, 1987, pp. 99-140.
46. Doligalski, T., Smith, C., and Walker, J., "Vortex interactions with walls," *Annu. Rev. Fluid Mech.*, Vol. 26, 1994, pp. 573-616.
47. Orlandi, P., "Rebound of vortex dipole," *Phys. Fluids A*, 1990.
48. Smith, C., Walker, J., Haidari, A., and So-brun, U., "On the dynamics of near-wall turbulence," *Phil. Trans. R. Soc. Lond.*, Vol. 336, 1991, pp. 131-175.
49. Swearingen, J., Crouch, J., and Handler, R., "Dynamics and stability of a vortex ring impacting a solid boundary," *J. Fluid Mech.*, Vol. 297, 1995, pp. 1-28.
50. Risso, F., Corjon, A., and Stoessel, A., "Direct numerical simulation of trailing vortices in homogeneous turbulence," in *34th Aerospace Sciences Meeting and Exhibit, Reno (NV)*, No. AIAA-96-0802, January 15-18 1996.
51. Stoessel, A., "An Efficient Tool for the Study of 3D Turbulent Combustion Phenomena on MPP computers," in *Proc. of the HPCN 95 conference*, (Milan (Italy)), pp. 306-311, Springer-Verlag, 1995.
52. Lele, S. K., "Compact finite difference schemes with spectral-like resolution," *J. Comp. Phys.*, No. 103, 1992, pp. 16-42.

53. Poinso, T. and Lele, S., "Boundary conditions for direct simulations of compressible viscous flows," *J. Comp. Phys.*, Vol. 101, July 1992, pp. 104-129.
54. Stoessel, A. and Baum, M., "Direct Numerical Simulation of 2D Turbulent Combustion Using Domain Decomposition Methods," in *Proc. of the SCS High Performance Computing 1994 conference*, (La Jolla (CA-USA)), 1994.
55. Lamb, H., *Hydrodynamics*. New York: Dover publications, 1932.
56. Batchelor, G., "Axial flow in trailing line vortices," *J. Fluid Mech.*, Vol. 20, No. 4, 1964, pp. 645-658.
57. Betz, A., "Verhalten von WirbelSystemen," *ZAMM*, Vol. XII, No. 3, 1932, pp. 164-174.
58. Mayer, E. and Powell, K., "Viscous and inviscid instabilities of a trailing vortex," *J. Fluid Mech.*, Vol. 245, 1992.
59. Hinze, J., *Turbulence*. Mac Graw-Hill, 1959.
60. Melander, M. and Hussain, F., "Polarized vorticity dynamics on a vortex column," *Phys. Fluids A*, Vol. 5, August 1993, pp. 1992-2003.
61. Jeong, J. and Hussain, F., "On the identification of a vortex," *J. Fluid Mech.*, Vol. 285, 1995, pp. 69-94.
62. Garodz, L. J. and Clawson, K. L., "Vortex wake characteristics of B757-200 and B767-200 aircraft using the tower fly-by technique," ERL ARL-199 vol 1 and 2, NOAA, January 1993.

CARACTERISATION ET MODELISATION DU SILLAGE D'UN AVION A PARTIR D'ESSAIS EN VOL DE MAQUETTES EN LABORATOIRE

Patricia COTON
Division Mécanique du Vol
ONERA/IMFL
5Bd Paul PAINLEVE
59000 LILLE
FRANCE

RESUME

L'Institut de Mécanique des Fluides de Lille, établissement de l'ONERA, développe depuis de nombreuses années des méthodes expérimentales originales basées sur l'exploitation d'essais en vol de maquettes en laboratoire. Ces méthodes sont ici appliquées à la caractérisation, en vue de la modélisation, du sillage de l'avion de transport.

Cet article décrit tout d'abord la technique expérimentale puis les résultats obtenus au cours d'un certain nombre d'essais de visualisation par fumée puis bulles d'hélium du sillage d'une maquette d'AIRBUS A300B2. Les premiers éléments d'un modèle développé pour la mécanique du vol sont ensuite présentés ainsi que les développements ultérieurs de cette recherche. Enfin un certain nombre de voies d'investigation concernant d'autres techniques de mesure en particulier non intrusives sont évoquées.

La technique d'essais en vol de maquettes catapultées, appliquée ici à la caractérisation du sillage des avions, est particulièrement bien adaptée à l'étude du phénomène sur toute sa durée : formation, évolution et dégénérescence. Permettant d'accéder aux caractéristiques du champ aérodynamique lointain, elle est complémentaire de la soufflerie.

Les techniques de visualisation par fumée fournissent des informations sur la trajectoire et la vitesse des centres tourbillonnaires. Les visualisations par bulles d'hélium permettent d'obtenir des données sur le champ de vitesse dans le sillage et sur son évolution.

Ces techniques ont permis d'élaborer un premier modèle de sillage "utile" au sens de la mécanique du vol. Ces travaux de modélisation sont poursuivis actuellement par l'IMFL. En particulier une représentation des effets de proximité du sol ainsi que des effets liés à l'état de l'atmosphère va être développée. Les règles de transposition des résultats obtenus, du Reynolds de la maquette à celui de l'avion vont être analysées.

SUMMARY

The Fluid Mechanics Institute of Lille (IMFL), off-site centre of ONERA, has developed for many years specific experimental methods based on flight tests of scaled models performed in a laboratory. These methods are here applied to the characterization with a view to modelling of transport aircraft wake.

This paper firstly describes the experimental technique. Some tests conducted with an AIRBUS A300B2 model are

then presented. These tests are flow visualizations by means of smoke or helium bubbles. The first elements of a mathematical modelling of the wake behaviour which has been developed for flight mechanics purposes and the further developments of this research are described. Finally some prospecting directions concerning other non intrusive measurement methods are presented.

The experimental technique based on flight tests of scaled models, here applied to the characterization of aircraft wakes is particularly well adapted to the study of the phenomenon in its complete lifetime : formation, evolution and decay. Allowing access to the far-field characteristics of the flow, this technique is complementary to wind tunnel tests.

Flow visualizations by means of smoke give information about the trajectory and the velocity of the vortex centres. Flow visualizations by means of helium bubbles enable to obtain data on the velocity field in the wake and its evolution.

These techniques made it possible to elaborate a first modelling of the wake which is "useful" in a flight mechanics point of view. At the present time the modelling work is carried on by IMFL. In particular, a representation of ground effects as well as of effects due to atmosphere state will be developed. Transposition rules for the results, from the Reynolds number of the scaled model to the one of the aircraft, will be analysed.

1- INTRODUCTION

L'intensité des tourbillons marginaux est en premier lieu fonction de la portance de l'avion mais elle dépend également de la géométrie de l'aile. Ces effets de géométrie ne sont pas à l'heure actuelle parfaitement maîtrisés. Il a été constaté que certains avions génèrent un sillage à la fois plus intense, plus rapide et plus stable que d'autres appareils de même catégorie sans que l'on puisse en déterminer la cause de façon certaine (volets monoblocs ? position relative particulière des volets ? ...).

Ceci peut se révéler particulièrement critique pour les avions de transport futurs de grande capacité. Il est donc fondamental d'améliorer la connaissance des processus participant à la génération des turbulences de sillage surtout si, comme on peut le penser, l'évaluation de ces turbulences fera à terme partie de la procédure de certification.

L'Institut de Mécanique des Fluides de Lille (ONERA/IMFL) dispose d'un moyen d'essais original qui apporte une contribution intéressante à l'étude des sillages des avions et donne des éléments de base pour le

développement et la validation d'une modélisation. Ce moyen d'essais qui repose sur l'utilisation de maquettes catapultées est particulièrement bien adapté à l'étude de phénomènes instationnaires. Il offre :

- une représentation réaliste du comportement de l'avion et des phénomènes impliqués (pas d'interférence de montage ou de paroi, environnement bien reconnu),
- une complémentarité avec les essais en soufflerie basse vitesse,
- l'accès à la caractérisation des champs aérodynamiques proches et lointains autour de l'avion.

Dans ce contexte l'IMFL a engagé depuis quelques années des travaux de caractérisation et modélisation des sillages dont les premiers résultats vont être présentés dans cet article composé de cinq parties.

La description de la méthode expérimentale fait l'objet de la première de ces parties. Des essais effectués avec une maquette d'AIRBUS A300B2 et comportant des visualisations de sillage par fumée ou bulles d'hélium ont été réalisés dans le cadre d'un contrat passé par la Direction Générale de l'Aviation Civile. La présentation des résultats obtenus au cours de ces essais est faite dans les parties deux et trois de ce document. Les premiers éléments d'un modèle de sillage, développé pour la mécanique du vol, font l'objet de la quatrième partie. Enfin dans la cinquième partie sont présentées quelques directions de recherche concernant d'autres techniques de mesure et en particulier une technique de mesure par ultrasons dont le développement dans le cadre d'essais en vol de maquettes fait l'objet d'une coopération bilatérale avec la DLR-Göttingen.

2- TECHNIQUE EXPERIMENTALE D'ESSAIS EN VOL DE MAQUETTES

Cette technique expérimentale est basée sur l'utilisation de maquettes non motorisées catapultées. Les maquettes sont mises en vitesse au moyen d'une catapulte pneumatique préalablement positionnée en hauteur et en pente. Une fois larguées ces maquettes évoluent, libres de toute interaction de paroi ou de montage, dans un domaine d'observation de 30m de long, 10m de haut et 9m de large, avant d'être récupérées. Sur la vue générale de l'installation présentée fig. 1 on peut distinguer la zone de mise en vitesse de la maquette par la catapulte, le domaine d'évolution de la maquette et le dispositif de récupération. Les conditions initiales de pente, vitesse, incidence et dérapage sont ajustables. Les vols peuvent être réalisés dans l'air au repos ou en environnement perturbé : des rafales de vent, latérales ou verticales, de profils variés, peuvent être introduites le long de la trajectoire de la maquette au moyen de souffleries. Un plancher peut également être installé pour les études d'effet de sol. Tous ces essais peuvent être réalisés avec ou sans boucle interne de pilotage.

L'équipement de base embarqué dans les maquettes est composé d'un codeur PCM (30 voies de mesure, mots de 12 bits, fréquence d'échantillonnage 520Hz par voie), d'accéléromètres, de gyromètres et de mémoires statiques pour le stockage des données.

En fonction du type d'essai réalisé cet équipement est complété par une sonde de pression qui délivre des

informations sur l'incidence, le dérapage et la pression cinétique. Un micro-processeur pour le calcul de lois de pilotage ainsi que des actionneurs de gouvernes peuvent encore s'ajouter à cet équipement.

Les informations recueillies à bord de la maquette sont complétées par des mesures faites au sol. Une barrière de vitesse donne accès à la vitesse initiale du vol. Quatre bases optiques implantées tout au long de la zone d'évolution de la maquette et constituées chacune de deux appareils photographiques permettent d'obtenir les angles d'Euler et la position du centre de gravité de la maquette en quatre points du vol. La synchronisation des informations en provenance du sol et des mesures embarquées est assurée par l'activation, au moyen de flashes associés à chaque base optique, d'une photo-cellule équipant la maquette.

La trajectoire de vol est ensuite obtenue au travers d'une étude de cohérence entre les données en provenance de l'équipement embarqué et les informations en provenance du sol.

De plus amples détails concernant la technique expérimentale sont donnés en [1].

La maquette utilisée pour la présente étude est un AIRBUS A300B2 au 1/22 (envergure 2,04m). Cette maquette est en configuration atterrissage (becs braqués à 25°, volets braqués à 32,5°, trains d'atterrissage sortis). Son équipement embarqué est composé de 6 accéléromètres (3 verticaux, 2 latéraux et 1 longitudinal) ainsi que de 3 gyromètres (1 selon chaque axe de la maquette).

Les essais présentés ci-après ont été réalisés dans la configuration atterrissage décrite ci-dessus. Les vols effectués sont équilibrés. L'incidence de vol est égale à 6°, la pente vaut -4° et la vitesse est égale à 20m/s. Dans ces conditions le nombre de Reynolds des essais (calculé sur la corde moyenne de l'aile) est de $3,6 \cdot 10^5$.

3- VISUALISATION DU SILLAGE AU MOYEN DE FUMEE

Un rideau de fumée est généré dans un plan perpendiculaire à l'axe de vol de la maquette. Ce plan est éclairé par un projecteur de lumière froide de 2000W. La prise de vue se fait au moyen d'une caméra CCD noir et blanc située sous la catapulte. Les prises de vue sont réalisées à la cadence de 50 trames par seconde. Les images enregistrées durant le phénomène sont ensuite traitées par un logiciel permettant de déterminer la trajectoire et la vitesse de chaque tourbillon.

Au cours de la phase de formation du sillage on observe, au niveau de chaque demi-voilure, la présence d'un tourbillon de faible intensité prenant naissance à l'extrémité de l'aile et d'un tourbillon plus puissant se situant à l'extrémité du volet externe. Ces tourbillons interagissent puis s'amalgament rapidement en une seule grosse structure par demi-voilure. Le phénomène persiste longtemps après l'arrêt de la maquette (fig. 2).

La fig. 3 présente la trajectoire du centre de chacune de ces grosses structures dans le plan d'observation matérialisé par la fumée. Cette figure montre que les deux tourbillons contra-rotatifs sont animés d'un mouvement d'entraînement

vertical tout en s'écartant mutuellement.

Les historiques des vitesses latérales et verticales des centres tourbillonnaires droit et gauche sont donnés fig. 4. L'origine des temps indiqués en abscisse correspond au début de la phase de mise en vitesse de la maquette sous la catapulte. Dans ces conditions, l'instant daté de passage de la maquette dans le rideau de fumée est à 2,7s. Au vu de cette figure il apparaît deux phases. Au cours de la première phase, qui s'étend approximativement jusqu'à l'arrêt de la maquette, la vitesse verticale de chaque tourbillon décroît dans le temps et passe de 0,4m/s à 0,2m/s. La vitesse latérale quant à elle reste de l'ordre de 0,2m/s. Au cours de la seconde phase les historiques de vitesse sont plus bruités. Les taux de rotation restent élevés mais la cohérence dans le coeur de tourbillon diminue et le pointage du centre sur chaque image devient plus difficile.

4- VISUALISATION DU SILLAGE AU MOYEN DE BULLES D'HELIUM

Afin d'obtenir des informations sur les composantes du champ de vitesse dans l'écoulement, une autre technique de visualisation a été utilisée. Celle-ci repose sur l'utilisation de bulles de savon gonflées par un mélange air-hélium de façon à obtenir une masse volumique moyenne des bulles voisine de celle de l'air. Ces bulles sont émises par un générateur comprenant une tête émettrice et un pupitre de contrôle pour le débit des différents constituants. Le diamètre des bulles peut varier entre 1mm et 1cm et le débit peut être réglé de 20 bulles/s à 500 bulles/s.

Comme pour les visualisations par fumée, la prise de vue se fait au moyen d'une caméra CCD noir et blanc située sous la catapulte. La cadence de prise de vue est de 50 trames par seconde. Les bulles sont éclairées au moyen de deux projecteurs de lumière froide de 2000W chacun, l'un situé devant et l'autre derrière le plan d'émission des bulles.

Afin de pouvoir suivre sans ambiguïté la trajectoire de plusieurs bulles, la concentration en bulles doit être relativement faible. Le suivi, image par image, de chaque bulle permet alors d'accéder aux composantes de la vitesse de l'écoulement dans le plan d'observation. La fig. 5 donne un exemple de résultat obtenu pour les composantes latérale et verticale de la trajectoire de bulles suivies au cours d'un essai. Les fig. 6 et 7 présentent les composantes latérale et verticale des vitesses obtenues pour ces mêmes bulles.

Exprimées dans des axes liés au centre du tourbillon, les données décrites ci-dessus conduisent à des profils de vitesse tangentielle, fonction de la distance au centre tourbillonnaire, dont l'évolution dans le temps est présentée fig. 8. Le profil de la fig. 8a est obtenu 0,3s après que la maquette ait traversé le plan d'émission des bulles. Le maximum de la vitesse tangentielle, d'une valeur de 2,5m/s, est obtenu à une distance au centre égale à 20cm. Le profil de vitesse évolue peu pendant les 2 secondes suivantes. Ensuite le profil s'affaïsse.

5- DEVELOPPEMENT D'UN PREMIER MODELE POUR LA MECANIQUE DU VOL

L'objectif poursuivi ici est de développer un modèle de

représentation du sillage pour les besoins de la mécanique du vol, c'est-à-dire de développer un modèle de structure relativement simple pour permettre, en particulier, la simulation en temps réel. Dans sa forme finale un tel modèle servira à la prévision de l'évolution temporelle du sillage et au comportement de l'avion rencontrant une turbulence de sillage.

La première phase du travail de modélisation consiste donc à établir une structure de modèle pour le cas de base d'une atmosphère au repos. Ce premier modèle, qui ne comporte dans un premier temps aucun effet lié à la stratification thermique de l'atmosphère ou à la proximité du sol, sera ensuite complété. Des travaux sont actuellement en cours à l'IMFL pour développer une représentation des effets liés à la proximité du sol ainsi qu'à l'état de l'atmosphère.

La façon dont la structure de ce tout premier modèle est obtenue est présentée ci-après. Les paramètres de ce modèle seront ensuite recalés sur la base des résultats expérimentaux qui viennent d'être présentés.

Soit un système d'axes lié à l'avion dont le mouvement est rectiligne uniforme.

x, r, θ	repère cylindrique où x est l'axe de l'un des tourbillons
u, v, w	composantes de la vitesse moyenne dans le repère (x, r, θ)
u', v', w'	fluctuations de vitesse dans le repère cylindrique
p	pression statique moyenne
ν_c	viscosité cinématique
$\nu_{t,x}, \nu_{t,\theta}$	viscosités turbulentes

L'écoulement est supposé incompressible et localement axisymétrique au voisinage de chaque tourbillon. L'écoulement moyen est supposé stationnaire dans le référentiel utilisé qui par ailleurs est inertiel.

Alors au voisinage de chaque tourbillon :

$$\frac{\delta}{\delta x} \ll \frac{\delta}{\delta r} \quad \text{et} \quad v \ll u$$

d'où l'approximation quasi-cylindrique des équations de Navier Stokes :

- continuité

$$\frac{\delta u}{\delta x} + \frac{1}{r} \frac{\delta r v}{\delta r} = 0 \quad (1)$$

- transfert de la quantité de mouvement

$$u \frac{\delta u}{\delta x} + v \frac{\delta u}{\delta r} = - \frac{1}{\rho} \frac{\delta p}{\delta x} + \frac{1}{r} \frac{\delta}{\delta r} \left[v r^3 \frac{\delta u}{\delta r} - r u' v' \right] \quad (2)$$

$$\frac{w^2}{r} = \frac{\delta p}{\delta r} \quad (3)$$

$$u \frac{\delta w}{\delta x} + v \frac{\delta w}{\delta r} + \frac{vw}{r} = \frac{1}{r^2} \frac{\delta}{\delta r} \left[v r^3 \frac{\delta}{\delta r} \left(\frac{w}{r} \right) - r^2 v' w' \right] \quad (4)$$

Au frottement moléculaire s'ajoute donc un frottement apparent (frottement de Reynolds) dû à l'échange de quantité de mouvement par agitation turbulente.

La fermeture du système est obtenue en introduisant un modèle de turbulence. Si l'on choisit un modèle algébrique à longueur de mélange anisotrope, cela conduit dans le cas de l'approximation quasi-cylindrique à :

$$\overline{u'v'} = - v_{tr} \frac{\delta u}{\delta r}$$

$$\overline{v'w'} = - v_{tr} \frac{r \delta}{\delta r} \left(\frac{w}{r} \right)$$

Dans ces conditions l'équation (4) devient :

$$u \frac{\delta w}{\delta x} + v \frac{\delta w}{\delta r} + \frac{vw}{r} = \frac{1}{r^2} \frac{\delta}{\delta r} \left[r^3 (v_c + v_{tr}) \frac{\delta}{\delta r} \left(\frac{w}{r} \right) \right] \quad (5)$$

Si l'on admet maintenant que v_{tr} ne dépend pas de r , que v est négligeable et que $|u - V| \ll V$ l'équation (5) devient alors :

$$V \frac{\delta w}{\delta x} = \frac{(v_c + v_{tr})}{r^2} \frac{\delta}{\delta r} \left[r^3 \frac{\delta}{\delta r} \left(\frac{w}{r} \right) \right]$$

Cette dernière équation peut encore s'écrire

$$V \frac{\delta \Gamma}{\delta x} = (v_c + v_{tr}) r \frac{\delta}{\delta r} \left[\frac{1}{r} \frac{\delta \Gamma}{\delta r} \right] \quad (6)$$

avec $\Gamma = 2\pi r w$ = circulation sur un cercle de rayon r

La solution de (6) est de la forme :

$$\Gamma = 2\pi r w = \Gamma_0 \left[1 - \exp \left(- \frac{r^2 V}{4 (v_c + v_{tr}) x} \right) \right]$$

soit encore, en posant $x = Vt$

$$\Gamma = 2\pi r w = \Gamma_0 \left[1 - \exp \left(- \frac{r^2}{4 (v_c + v_{tr}) t} \right) \right]$$

Γ_0 est obtenu en exprimant la conservation de la circulation

$$\Gamma_0 = \int_0^\infty \frac{d\Gamma(r)}{dr} dr = \int_{\frac{b}{2}}^0 \frac{d\Gamma(y)}{dy} dy = \Gamma(y=0)$$

avec b envergure de l'aile.

Ceci donne finalement :

$$\Gamma_0 = \frac{C_z V b}{2 \lambda \int_0^1 \frac{\Gamma(y)}{\Gamma_0} dy}$$

où λ est l'allongement de l'aile.

Toujours sous l'hypothèse que $|u - V| \ll V$, la vitesse axiale est calculée par la formule de Batchelor [2]:

$$u = V - \frac{1}{8(v_c + v_{tr})x} \exp(-\eta) \left[\frac{1}{\pi \rho} + \frac{\Gamma_0^2}{4\pi^2} \left(\alpha + \log \frac{xV}{(v_c + v_{tr})} - 2 \log \frac{b_1 V}{(v_c + v_{tr})} \right) \right] + \frac{\Gamma_0^2}{4\pi^2} \frac{1}{8(v_c + v_{tr})x} Q_2(\eta)$$

$$\text{avec } \eta = \frac{V r^2}{4(v_c + v_{tr})x}$$

avec D la traînée totale, $\alpha \sim 1$, b_1 distance entre les deux tourbillons et $Q_2(\eta)$ donnée (cf [2]).

La distance séparant les deux tourbillons, une fois achevée la phase d'enroulement, est évaluée à partir de la méthode de Betz [3 et 4]. L'idée de cette méthode est de considérer que le résultat final de l'enroulement est une distribution de vorticit  axisym trique derri re chaque demi-voilure trait e comme une demi-voilure isol e. Cette vorticit  est constitu e et localis e de telle sorte que soient conserv s $d\Gamma/dy$ et les moments de $d\Gamma/dy$ derri re chaque demi-voilure. Ainsi le barycentre y_t de $d\Gamma/dy$ occupe une position fixe en envergure :

$$- \int_0^{\frac{b}{2}} \frac{d\Gamma}{dy} y dy = \Gamma_0 y_t$$

et donc la distance b_1 séparant les deux tourbillons lorsque l'enroulement est terminé vaut :

$$b_1 = b \int_0^1 \frac{\Gamma(Y)}{\Gamma_0} dy$$

L'écoulement final derrière l'avion est obtenu en composant les écoulements axisymétriques engendrés par chaque tourbillon.

Les paramètres de ce modèle vont être recalés sur la base des résultats expérimentaux présentés aux chapitres 3 et 4 de cet article. C'est ainsi que b_1 obtenu expérimentalement vaut 1,68m et que dans ce cas :

$$\int_0^1 \frac{\Gamma(Y)}{\Gamma_0} dy = \frac{b_1}{b} = 0,82$$

Dans les conditions d'essais réalisés :

$$\begin{aligned} V &= 20 \text{ m/s} \\ C_z &= 1,3 \quad \text{et donc} \quad \Gamma_0 = 4,2 \text{ m}^2 \text{ s}^{-1} \\ \lambda &= 7,7 \end{aligned}$$

Le profil de vitesse $w(r)$ finalement obtenu à partir des résultats présentés figure 8 est alors de la forme :

$$w = 0,67 \left[1 - \exp \left(- \frac{r^2}{0,03} \right) \right]$$

et ce profil de vitesse reste sensiblement le même de $T_0=0,3\text{s}$ après que la maquette ait traversé le plan d'émission des bulles à $T_0+2\text{s}$, c'est-à-dire de 1,5 à 22,5 envergures dans le sillage derrière la maquette (fig. 9). Pour $T_0+3\text{s}$, c'est-à-dire à 32.5 envergures derrière la maquette, le profil de vitesse prend la forme suivante (fig. 9e):

$$w = 0,67 \left[1 - \exp \left(- \frac{r^2}{0,05} \right) \right]$$

La vitesse maximale a donc diminuée de 23%. Quant au rayon correspondant à cette vitesse maximale, il a augmenté de 25%.

Les visualisations par fumée et bulles d'hélium fournissent

des informations semi-quantitatives sur la vitesse de l'écoulement, qui vont être complétées au moyen d'autres techniques de mesure dont les développements sont en cours. Ces nouvelles techniques vont être présentées dans le chapitre ci-après.

6- DEVELOPPEMENT DE NOUVELLES TECHNIQUES DE MESURE

Un certain nombre de directions de recherche concernant de nouvelles techniques de mesure non intrusives sont à l'heure actuelle explorées par L'IMFL, afin de compléter les techniques de semi-quantitatives de visualisation décrites aux chapitres 3 et 4 de cet article.

La vélocimétrie Doppler Globale (DGV) est l'une de ces techniques. Cette méthode optique non intrusive permet de quantifier des écoulements tridimensionnels complexes à la cadence de prise de vue d'une caméra. Contrairement aux méthodes classiques de vélocimétrie laser qui sont des méthodes de mesure point par point, cette technique permet d'accéder à la structure complète de l'écoulement à un instant donné dans le plan choisi pour l'observation. Le champ d'application de cette méthode s'ouvre donc parfaitement à la caractérisation du sillage des avions sur la base d'essais en vol de maquettes en laboratoire.

Les premiers travaux concernant la DGV ont débuté aux USA en 1992 [5 et 6]. Son principe est basé sur la mesure du décalage Doppler de la lumière diffusée par des particules ensemençant l'écoulement et éclairées par une nappe laser dont la fréquence est accordée sur la raie d'absorption de l'iode. Vue à travers une cellule remplie de vapeur d'iode, la variation de fréquence de la lumière diffusée est immédiatement traduite par une variation d'absorption de cette lumière. La variation locale d'intensité de la lumière est alors reliée à une composante donnée de la vitesse locale de l'écoulement.

Des améliorations notables ont été apportées à cette technique [7 et 8] en utilisant en particulier un laser à colorant accordable en fréquence sur une raie de faible largeur de la molécule gazeuse utilisée comme discriminateur de fréquence (fig. 10). Parallèlement, l'utilisation du brome en lieu et place de l'iode doit permettre d'effectuer des mesures de vitesse dans le domaine des quelques m/s rencontré dans le sillage des maquettes.

Les premiers essais de cette technique dans l'installation d'essais en vol de l'IMFL sont programmés pour le courant de 1996.

La seconde méthode de mesure envisagée est une méthode de mesure acoustique qui a été développée par la DLR-Göttingen [9 et 10]. Un signal ultrasonique est émis dans une direction donnée par un microphone situé en dehors de la zone de mesure. La vitesse de propagation de l'onde sonore se compose avec la vitesse de l'écoulement dans lequel elle se déplace. A température constante le temps de parcours du signal ultrasonique est donc fonction de la composante de la vitesse de l'écoulement suivant sa direction de propagation (fig. 11). Dans le cas où la température varie, un second signal ultrasonore est utilisé pour réaliser une compensation directe ou un calcul de

correction est introduit.

Un essai de faisabilité a été récemment réalisé dans le laboratoire d'essais en vol de l'IMFL. Le schéma de principe du montage utilisé est présenté fig 12a. Un laser dont le faisceau est dévié par le gradient de densité associé au passage de l'onde sonore permet de mesurer le temps que celle-ci met à parcourir le chemin d'intégration. La différence entre ce temps de parcours dans l'air au repos et dans le sillage de la maquette est ensuite calculée.

Un exemple typique de l'évolution de cette différence, enregistrée au cours d'un vol de maquette, est donné fig. 12b. Dans le cas d'un phénomène instationnaire, comme celui qui est mesuré ici, l'évolution de cette différence est d'une part due au mouvement de descente des tourbillons et d'autre part à la dégénérescence de ceux-ci.

L'analyse de ces informations permet ensuite, par le biais d'un modèle, de remonter aux caractéristiques du sillage (position, profil de vitesse).

7- CONCLUSION ET PERSPECTIVES

La technique d'essais en vol de maquettes catapultées, appliquée ici à la caractérisation du sillage des avions, est complémentaire de celle réalisée en soufflerie. Cette technique permet en effet d'accéder aux caractéristiques du sillage lointain derrière la maquette.

Les informations sur le champ de vitesse, issues de l'exploitation des visualisations par fumée et bulles d'hélium, ont permis de mesurer les caractéristiques des tourbillons et de jeter les bases d'une première modélisation. Ces travaux de modélisation vont être poursuivis. En particulier une représentation des effets de proximité du sol ainsi que des effets liés à l'état de l'atmosphère va être développée. Les règles de transposition des résultats obtenus, du Reynolds de la maquette à celui de l'avion, vont être analysées.

La prospection dans le domaine des méthodes de mesure globales et non intrusives applicables aux essais en vol de maquettes, dont deux exemples ont été présentés dans ce document, va être poursuivie.

En relation avec ces développements, deux domaines d'activités vont être prochainement abordés par l'IMFL. Il s'agit tout d'abord de l'étude de la phase de formation du sillage et de la maîtrise de la structure de celui-ci au moyen de dispositifs d'extrémité de voilure. Il s'agit également de l'étude de l'interaction du sillage sur l'avion suiveur, domaine dans lequel la technique d'essais en vol de maquettes peut apporter une contribution originale à la validation de modèles de comportement.

8- REFERENCES

- [1] Charon W., Verbrugge R.A., "Nouvelle technique d'essais sur maquettes libres en laboratoire pour la détermination de caractéristiques aérodynamiques"
AGARD CP 235 1978
- [2] Batchelor G. K., "Axial Flow in Trailing Ligne Vortices"
Journal of Fluid Mechanics (1964), Vol. 20, part 4, pp 645-658
- [3] Betz A., "Behavior of Vortex Systems"
NACA TM 713
translated from "Zeitschrift für Angewandte Mathematik und Mechanik" (1932), Vol. 12, n°3
- [4] Donaldson C. Du P., Snedeker R. S. And Sullivan R. D., "Calculation of Aircraft Wake Velocity Profiles and Comparison with Experimental Measurements"
Journal of Aircraft (1974), Vol.11, n°9, pp 547-555
- [5] Usry J. W., Meyers J. F., Miller L. S., "Doppler Global Velocimeter Measurements of the Vortical Flow Above a Thin Delta Wing"
AIAA 92-0005, January 1992
- [6] Lee J. W., Meyers J. F., Cavone A. A., Suzuki K. E., "Doppler Global Velocimeter Measurements of the Vortical Flow Above an F/A-18"
AIAA 93-0414, January 1993
- [7] Leporcq B., Le Roy J-F., Pinchemel B., Dufour C., "Improvement in Doppler Global Velocimetry : the Use of CW Dye Laser"
Eighth International Symposium on Application of Laser Techniques to Fluid Mechanics July 8-11 1996 Lisbon Portugal (to be published)
- [8] Leporcq B., Le Roy J-F., Pinchemel B., Dufour C., "Interest of CW Dye Laser in Doppler Global Velocimetry"
American Society of Mechanical Engineers, Fluid Engineering Division July 7-11 1996, San Diego California (to be published)
- [9] Schmidt D. W., Tilmann P. M., "Experimental Study of Sound-Wave Phase Fluctuations Caused by Turbulent Wakes"
The Journal of the Acoustical Society of America (1970), Vol. 47, pp 1310-1324
- [10] Engler R. H., Schmidt D. W., Wagner W.J., "Nondisturbing Acoustical Measurement of Flow Fields - New Developments and Applications"
The Journal of the Acoustical Society of America, Vol. 85, n° 1, January 1989

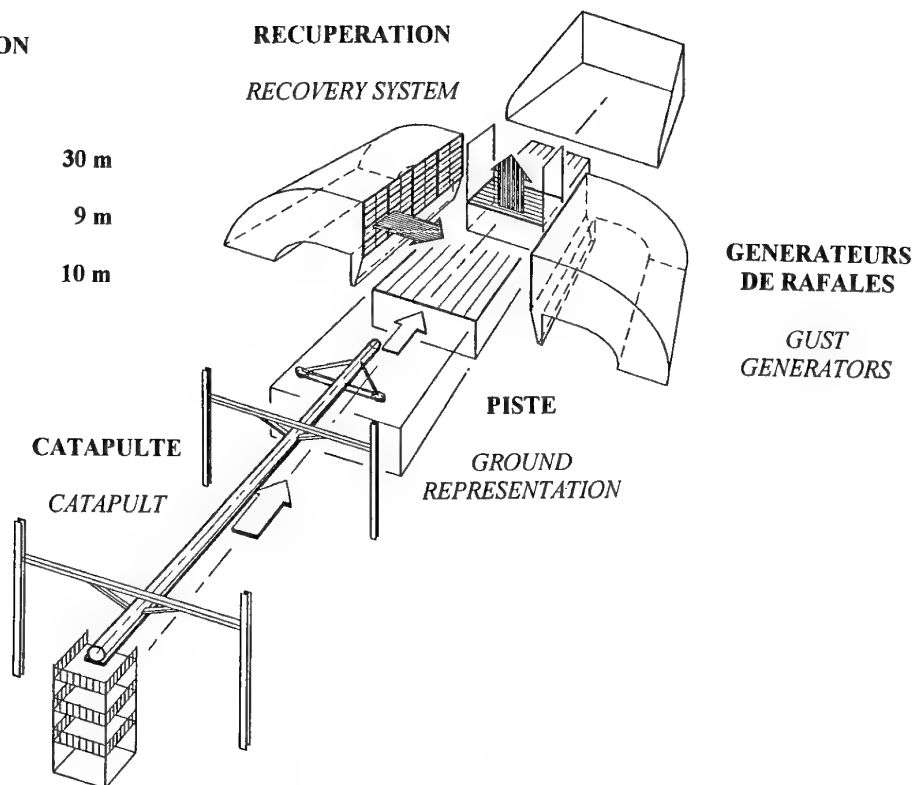
ZONE D'OBSERVATION**OBSERVATION AREA****Longueur (Length)** 30 m**Largeur (Width)** 9 m**Hauteur (Height)** 10 m

Figure 1 Vue générale du laboratoire d'essais en vol
General sketch of the flight test laboratory



1] T0



2] T0 + 0,1s



3] T0 + 0,22s



4] T0 + 0,46s

Figure 2 Visualisation du sillage par fumée
Wake visualization by means of smoke

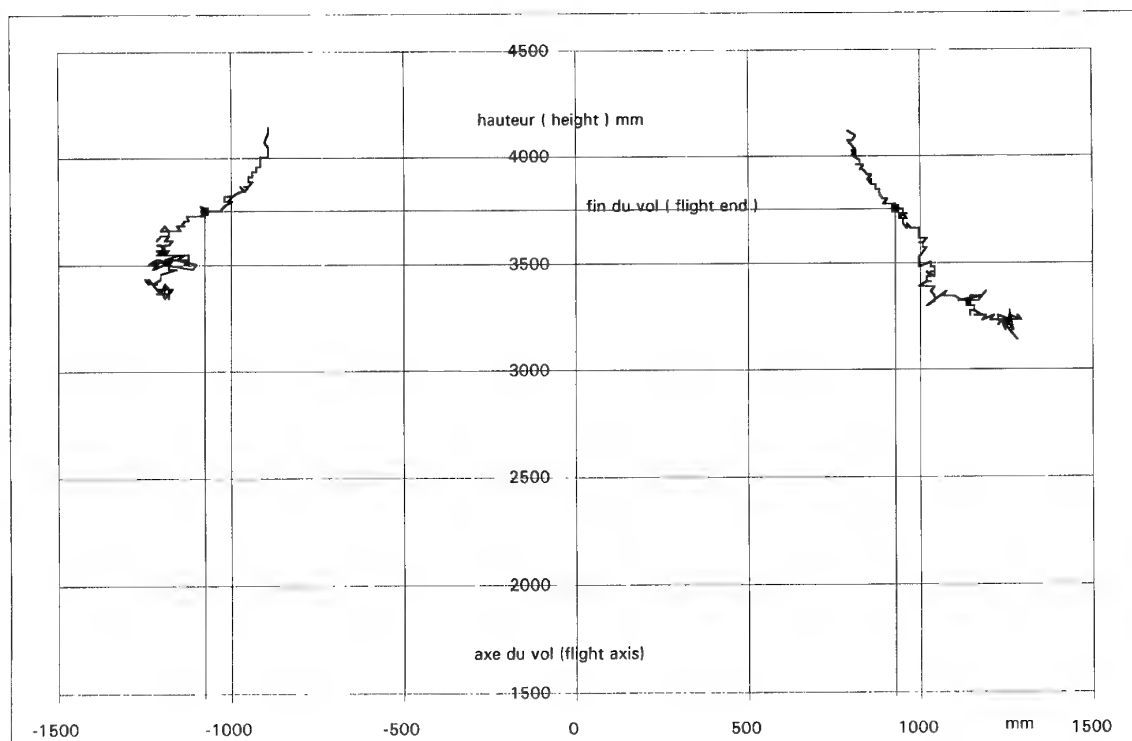


Figure 3 Trajectoire des centres des tourbillons dans le plan de fumée
Vortex centre trajectories on the smoke plan

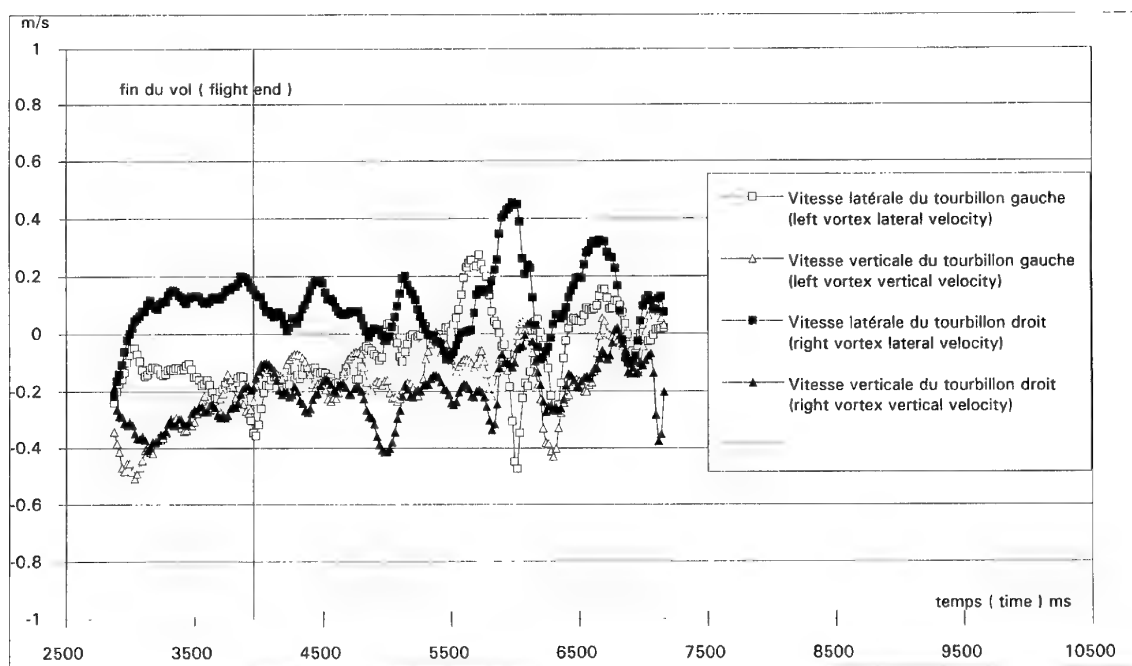


Figure 4 Evolution avec le temps des vitesses des centres des tourbillons dans le plan de fumée
Evolution with time of the vortex centre velocities on the smoke plan

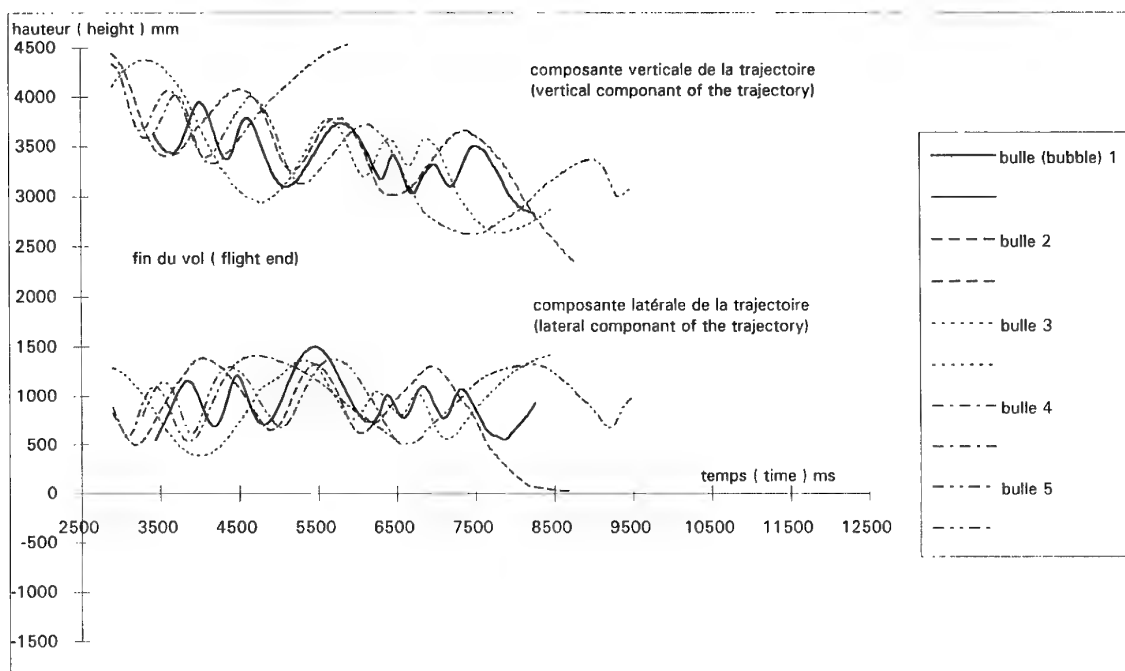


Figure 5 Exemple de trajectoires de bulle obtenues au cours d'un essai
Example of bubble trajectories obtained during a test

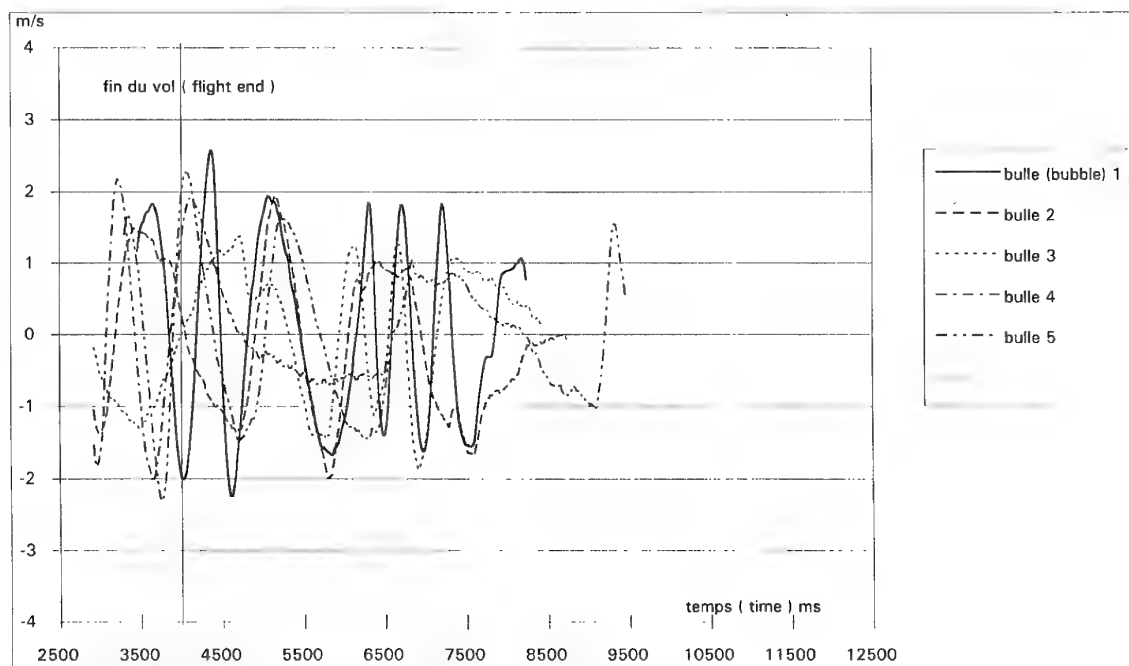


Figure 6 Exemple de vitesses latérales de bulle obtenues au cours d'un essai
Example of bubble lateral velocities obtained during a test

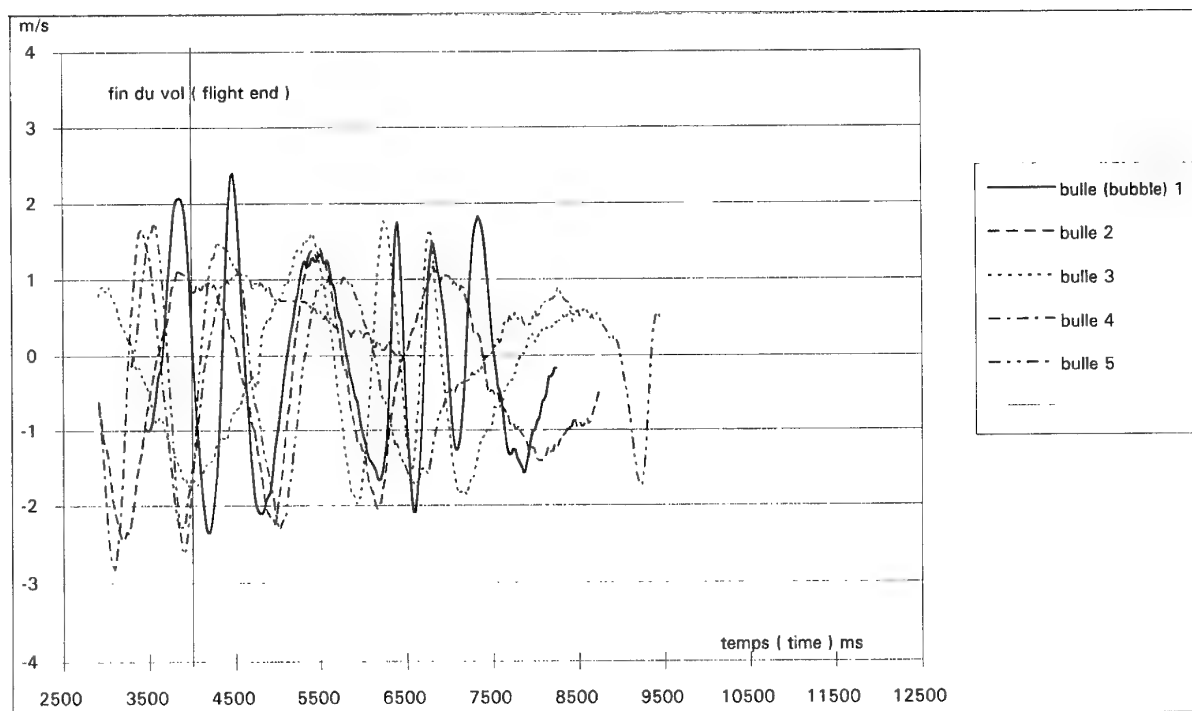
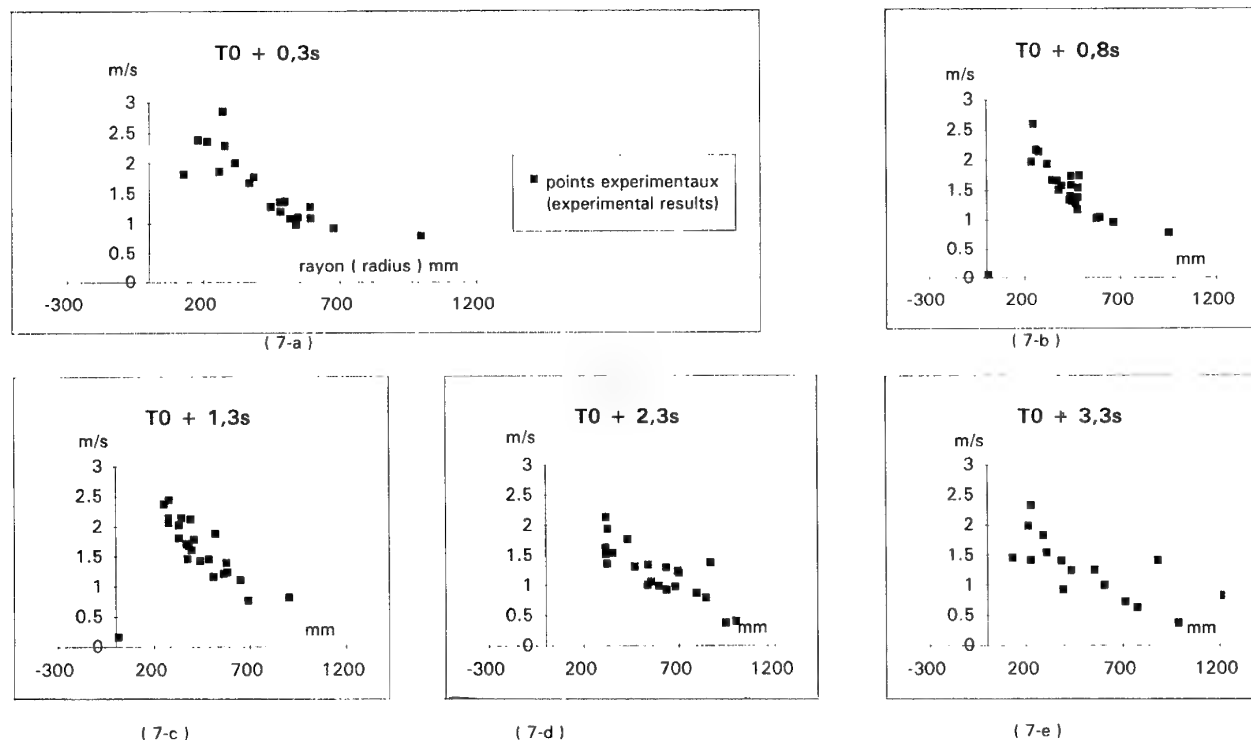
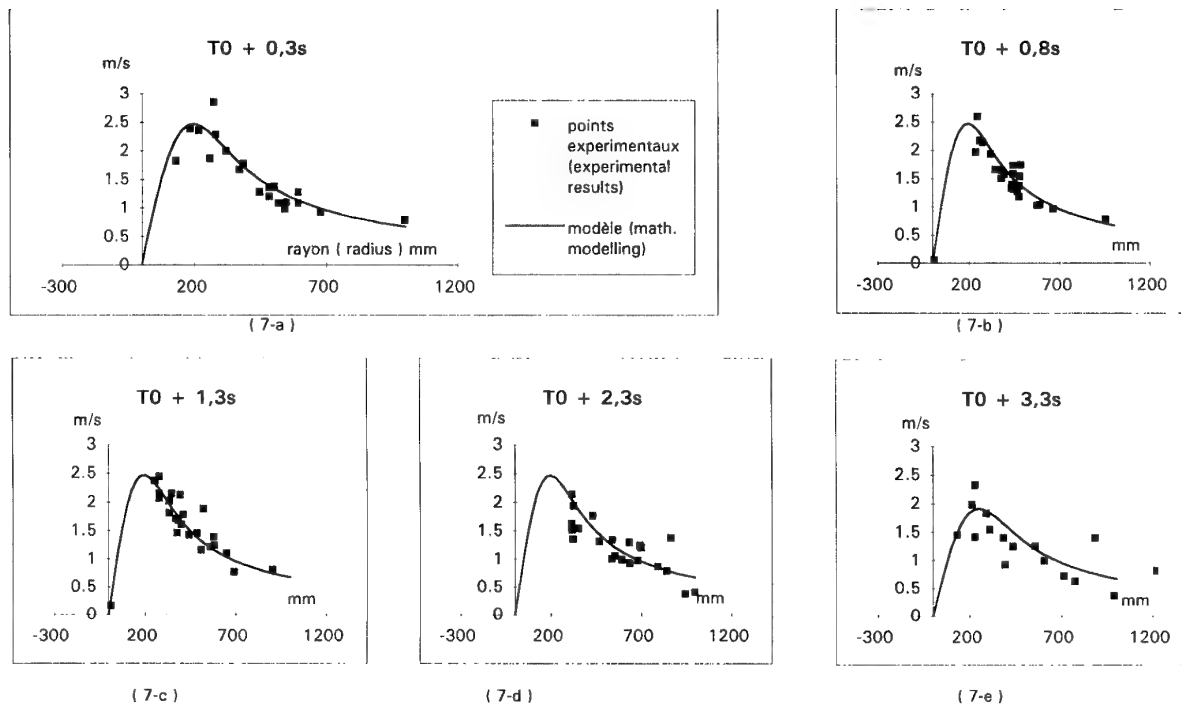


Figure 7 Exemple de vitesses verticales de bulle obtenues au cours d'un essai
Example of bubble vertical velocities obtained during a test



T0 temps de passage de la maquette dans le plan des bulles (the scaled model is passing through the bubble plan at T0)

Figure 8 Profils de vitesse tangentielle obtenus expérimentalement
Experimental tangential velocity profiles



T_0 temps de passage de la maquette dans le plan des bulles (the scaled model is passing through the bubble plan at T_0)

Figure 9 Profils de vitesse tangentielle - comparaison mesures et modèle
Tangential velocity profiles - comparison between measurement and modelling

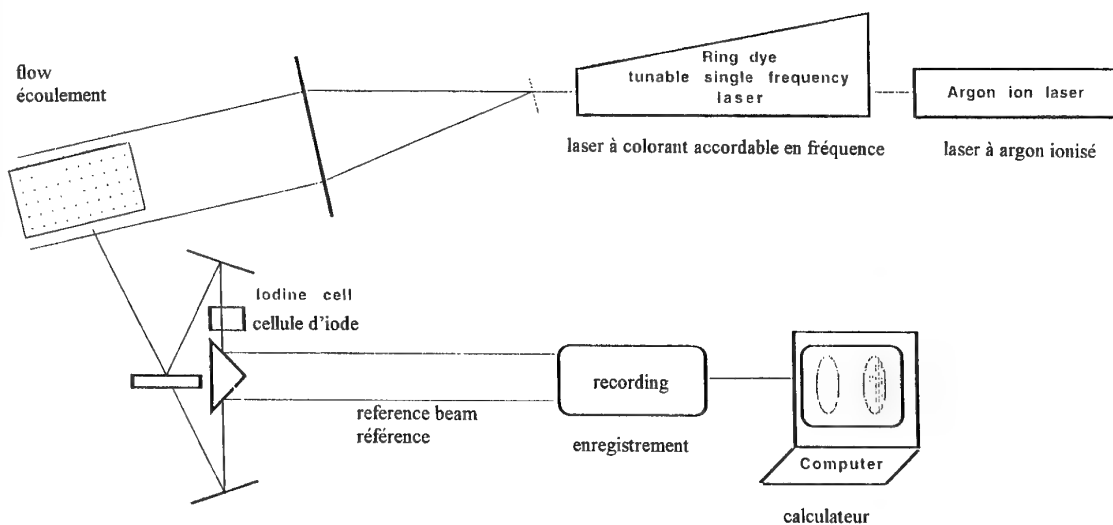
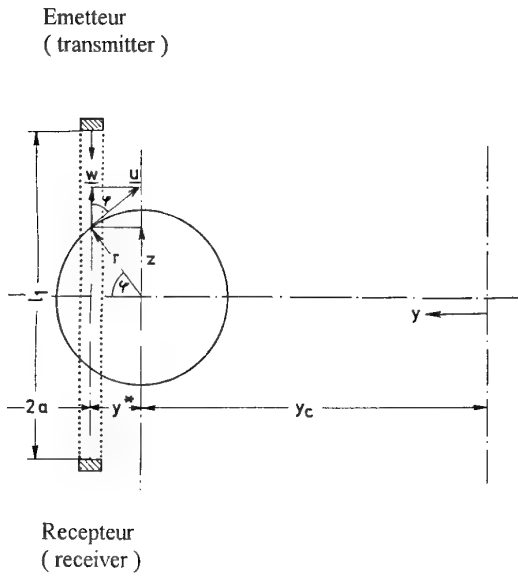


Figure 10 Principe de la Vélocimétrie Doppler Globale développée à l'IMFL
Principle of the Doppler Global Velocimetry developed by IMFL



$$t_1 = \int_{-\frac{l_1}{2}}^{\frac{l_1}{2}} \frac{dz}{c - w(y^*, z)} \quad c = \text{célérité du son (sound velocity)}$$

t_0 = temps de parcours en l'absence du tourbillon
(running time when no vortex)

$\Delta t = t_0 - t_1$ = différence de temps de parcours attribuée au tourbillon
(running time difference due to the vortex)

Figure 11 Principe de la méthode ultrasonique
Principle of the ultrasonic method

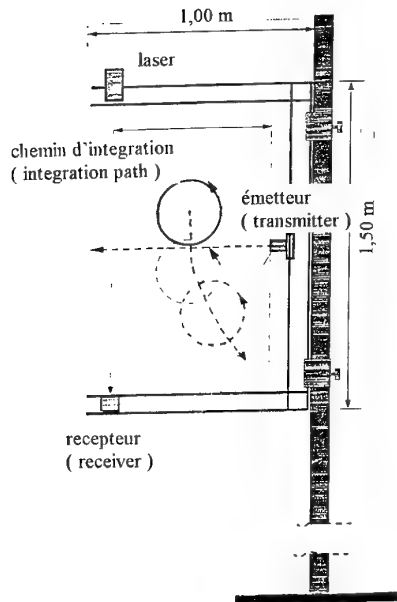
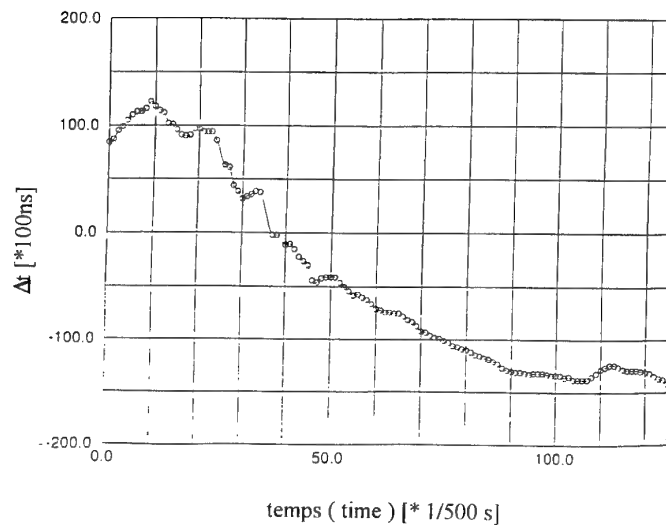


schéma de principe du dispositif
(sketch of the mounting system)



exemple de résultats obtenus
example of results

Figure 12 Application de la méthode ultrasonique au essais en vol de maquettes
Application of the ultrasonic method to flight tests of scaled models

Direct Numerical Simulation of the Breakdown of Aircraft Wake Vortices

S. C. Rennich

Department of Aeronautics and Astronautics
Stanford University
Stanford CA 94305-4035

S. K. Lele [†]

Department of Mechanical Engineering
Stanford University
Stanford CA 94305-4035

1 SUMMARY

An investigation is initiated that aims to improve the understanding of how disturbances to aircraft vortex wakes, applied at the wing, survive the roll-up process and eventually lead to destruction, or 'breakdown', of the wake. To efficiently perform this investigation, a numerical method is presented which accurately and efficiently computes flows in domains that are unbounded in two directions and periodic in the third, subject to the condition that vorticity is compactly distributed in the unbounded directions. This new code is used to compute the growth of symmetric disturbances on a pair of counter rotating columnar vortices. For high Reynolds number, the inviscid, linear vortex filament results of Crow [5] which predict the most unstable wavelength and its amplification rate, are reproduced well. From these computations an eigenfunction of the Crow instability as it exists in an evolving viscous vortex pair is extracted. The evolution of a perturbed plane wake due to an elliptically loaded wing is computed. It is observed that a perturbation of the correct wavelength rapidly evolves into the Crow instability and grows at approximately the predicted rate.

2 INTRODUCTION

The trailing vortices produced by large aircraft, especially during takeoff and landing, can be very hazardous to other aircraft. Since a reduction in this hazard could lead to increased safety and higher airport utilization, the problem has received considerable attention over the past twenty years but with little practical result. The possibility of new, very large commercial aircraft entering service has renewed interest in this area.

In 1970, Crow [5] (henceforth, this paper and its results will simply be referred to as Crow) analyzed the

stability of a pair of counter-rotating columnar vortices and identified the large-scale, inviscid instability which bears his name. Shortly thereafter, Crow [6] suggested the use of this instability as a means of alleviating the wake vortex hazard. The idea was to excite the most unstable wavelength with a large initial amplitude so that the wake would breakdown in an acceptable amount of time. Chevalier [3] and Bilanin & Widnall [2] demonstrated this mechanism in flight tests and water tunnel experiments. The results were encouraging since they showed a definite decrease in the time to breakdown. Since then, other researchers such as Rossow [8], using a vortex filament method, and Spalart [10], using a DNS method, have questioned the usefulness of the Crow instability, partly because it requires large energy input and the breakdown is not known to be sufficiently accelerated nor sufficiently robust. However, the question has hardly been put to rest. Issues including the effect of turbulence (atmospheric or body-generated), atmospheric stratification, the vorticity distribution in the vortex core, the effect of Reynolds number and the existence of systems of vortices more complex than just a single pair all conspire to prevent an easy answer. Since studies [1] have shown that rapid vortex breakdown can be achieved by control surface oscillations (however extreme), the task is not to determine if accelerated breakdown is possible, but to identify the best methods and document their effectiveness and cost.

3 OBJECTIVES

We approach this problem from a perspective closer to the one that might be taken by an aircraft designer wishing to alleviate any vortex hazard his aircraft might create.

It has been shown both experimentally and numerically that a perturbed wing wake, or a counter-rotating vortex pair, will breakdown via the Crow instability in approximately the time predicted by

[†]also affiliated with the Stanford University Department of Aeronautics and Astronautics

Crow. Further, to the best of our knowledge, no one has ever found a more unstable or faster-growing instability than the Crow instability for a counter-rotating vortex pair. Thus it appears that any successful alleviation scheme will be one that initiates the wake with a large amplitude perturbation that closely approximates the most unstable Crow eigenmode.

Since the aircraft designer must affect this perturbation at the wing, detailing how well any such perturbation survives the wake roll-up process and evolves to become the Crow instability is of interest. Also of interest would be a study detailing the sensitivity of the eventual Crow instability to the initial perturbation shape. We are not aware of any previous work in this area. Thus the primary objective of this research is to perform temporal DNS simulations of perturbed wing wakes (idealized but representative of realistic wakes) which roll up and evolve into a pair of counter-rotating vortices displaying the most unstable Crow eigenmode. These simulations will be analyzed to determine the extent to which the initial perturbation contributed to the Crow instability. Since we seek to understand these processes we begin with studies of the wake due to an elliptically loaded wing.

Actually achieving this objective requires extensive preliminary work. In order to perform DNS studies of the flows of interest in a reasonable amount of computer time, a new incompressible Navier-Stokes code for vortical flows with one periodic direction and two unbounded directions was developed [7]. Section 4 introduces the numerical method and demonstrates its convergence characteristics for several model problems. Section 5 uses this code to compute the evolution of a perturbed pair of counter-rotating vortices. This computation, distinct from our stated objective in that it does not begin with the roll-up of a plane wake, further verifies the performance of the code, provides some insight into Reynolds number effects on the Crow instability and allows the extraction of the Crow instability eigenmode as it exists in a viscous, three dimensional, counter-rotating vortex pair. Section 6 computes the roll-up of a 2D plane wake due to an elliptically loaded wing. This case further verifies the ability of the code as well as providing a baseline plane wake case for comparison. Section 7 addresses our objective by computing the 3D evolution of a perturbed plane wake due to an elliptically loaded wing. Section 8 offers some conclusions.

4 NUMERICAL METHOD

We require a domain that is unbounded in two directions because aircraft wakes exist in an essentially unbounded domain. The ground effect on the vortex wakes is not considered. Since the mean character of the wakes develops slowly in the direction of flight, we will only pursue temporal studies allowing a periodic boundary condition in the direction of flight. Several methods have been developed which allow

spectral methods to be applied to flows which are unbounded in one direction and periodic in the other two [12] [4] [9]. In these methods the assumptions of incompressibility and compact distribution of vorticity are used to represent the irrotational, far-field velocity analytically. This analytical far-field then provides the boundary condition for the domain of interest. The method due to Corral & Jiménez [4] and extended by Sondergaard [9] is particularly attractive. It retains all the resolution and efficiency characteristics of Fourier spectral methods and enforces the infinite boundary conditions exactly with little additional cost. Unfortunately, these 1-D unbounded methods can only be applied to vortex wake problems by extending a second direction suitably far and applying a periodic boundary condition. This limits the ability to represent the unbounded character and adds a large computational overhead. Despite its limitations, this approach has been successfully applied to vortex wake problems by Spalart [11].

The success of the method due to Corral and Jiménez in 1-D unbounded flows motivated us to extend the method to flows with two unbounded directions. This method is briefly presented here. A more complete description of the numerical method will be reported elsewhere [7].

4.1 Numerical Preliminaries

The governing equation for incompressible, unsteady flow can be written in vorticity form as

$$\frac{\partial \omega}{\partial t} = -\nabla \times (\omega \times \mathbf{u}) + \frac{1}{Re} \nabla^2 \omega \quad (1)$$

where \mathbf{u} is the velocity vector, ω is the vorticity vector and Re is the Reynolds number which is assumed constant. All quantities are nondimensionalized using the initial vortex radius, r_0 , defined as the radius of maximum velocity, and the total circulation in each vortex, Γ_0 . This nondimensionalization yields the circulation based Reynolds number $Re = \Gamma_0/\nu$ where ν is the kinematic viscosity. For simulations of evolving plane wakes, where there is no initial vortex radius, r_0 is taken as the approximate radius of the rolled-up vortex (defined in Section 6). Given an initial condition on vorticity, the difficulty in solving (1) lies in determining \mathbf{u} efficiently. Once \mathbf{u} is known, the fourth-order Runge-Kutta scheme is used to advance in time.

Before presenting the method it is useful to define three regions in the flow domain (see Figure 1). The first region is the internal domain, the space occupied by the circular cylinder large enough to contain all of the vorticity in the problem. The second region is the external domain which represents all space not in the internal domain. The periodic domain will be the space occupied by a square cylinder just large enough to contain the internal domain. Thus the internal and external domains are mutually exclusive and the periodic domain contains the entire internal domain and a part of the external domain.

Both the periodic domain and the cylindrical surface

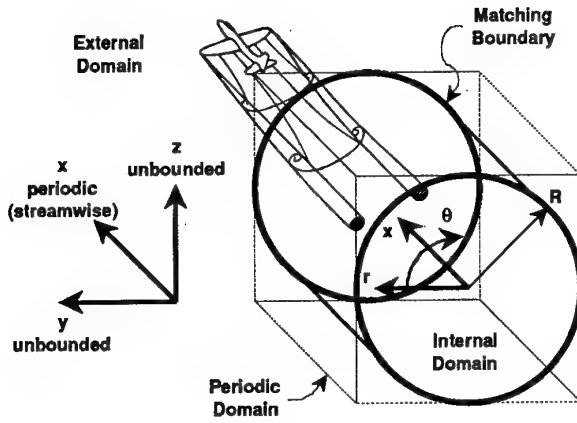


Figure 1: The three domains used in the velocity computation: internal, external and periodic.

require discretization. Consequently, both cartesian and cylindrical polar coordinate systems will be used in the ensuing discussion. The polar coordinate system will always be located such that the cylindrical matching surface is a surface of constant radius, R . These three domains and two coordinate systems are illustrated in Figure 1. In cartesian coordinates $\mathbf{u} = (u_x, u_y, u_z)$. In cylindrical polar coordinates $\mathbf{u} = (u_r, u_\theta, u_x)$. Note that the streamwise velocity u_x is the same in both systems. The symbols \mathbf{e}_r , \mathbf{e}_θ and \mathbf{e}_x will be used to represent the unit vectors in the r , θ and x directions.

4.2 Velocity Computation

The velocity computation begins by decomposing the complete velocity field, \mathbf{u} , into its vortical part \mathbf{u}_v , irrotational part $\nabla\phi$ and a part to accommodate the free-stream condition, \mathbf{u}_∞ :

$$\mathbf{u} = \mathbf{u}_v + \nabla\phi + \mathbf{u}_\infty \quad (2)$$

where \mathbf{u}_v and ϕ are field quantities and \mathbf{u}_∞ is a constant vector. Since \mathbf{u}_v is the only rotational component in (2), it can be computed from the vorticity-velocity relation

$$\nabla^2 \mathbf{u}_v = -\nabla \times \boldsymbol{\omega} \quad (3)$$

assuming periodic boundaries in all directions. In Fourier space this calculation is straightforward, accurate and efficient. The velocity due to the mean (over the 3d volume) component of axial vorticity, $\omega_{x \text{ mean}}$, for which (3) does not apply, is accounted for by adding a solid body rotation of angular velocity $1/2 \omega_{x \text{ mean}}$ about the center of the domain.

Since the vortical component of velocity, \mathbf{u}_v , was computed using periodic boundary conditions, it includes the effect of infinitely many image vortices. The velocity potential, ϕ can be thought of as a correction to \mathbf{u}_v which removes the effects of all the image vortices. The form of ϕ is arrived at analytically. Irrotational flow must satisfy, via continuity,

Laplace's equation

$$\nabla^2 \phi = 0. \quad (4)$$

Cast in cylindrical polar coordinates, (4) becomes

$$\frac{1}{r} \frac{\partial}{\partial r} \left(r \frac{\partial \phi}{\partial r} \right) + \frac{1}{r^2} \frac{\partial^2 \phi}{\partial \theta^2} + \frac{\partial^2 \phi}{\partial x^2} = 0. \quad (5)$$

Taking the Fourier series of ϕ in the periodic direction, x , and the azimuthal direction, θ , and substituting into (5) results in

$$r^2 \frac{\partial^2}{\partial r^2} (\hat{\phi}_{m,k_x}) + r \frac{\partial}{\partial r} (\hat{\phi}_{m,k_x}) - (k_x^2 r^2 + m^2) \hat{\phi}_{m,k_x} = 0 \quad (6)$$

for each axial wavenumber, k_x , and azimuthal wavenumber, m . For $k_x \neq 0$, (6) is Bessel's modified differential equation and thus the solutions are the modified Bessel functions of the first and second kind. Since the velocity must be finite everywhere, solutions involving the modified Bessel function of the first kind, I_m , apply to the internal domain. Solutions involving the modified Bessel function of the second kind, K_m , apply to the external domain. When $k_x = 0$, (6) becomes an Euler-Cauchy equation with solutions of the form $r^{|m|}$ and $r^{-|m|}$. Again, since the velocity must be finite everywhere, the $r^{|m|}$ solutions apply to the internal domain and the $r^{-|m|}$ solutions apply to the external domain.

The velocity potentials for the internal and external domains can be written as

$$\begin{aligned} \phi_{\text{internal}} = & \sum_{m=-N_\theta/2}^{N_\theta/2-1} \sum_{k_x=-N_x/2}^{N_x/2-1} C_{mk_x} I_m(k_x r) e^{i(m\theta + k_x x)} \\ & + \sum_{m=-N_\theta/2}^{N_\theta/2-1} C_{m,0} r^{|m|} e^{im\theta} \quad (7) \end{aligned}$$

$$\begin{aligned} \phi_{\text{external}} = & \sum_{m=-N_\theta/2}^{N_\theta/2-1} \sum_{k_x=-N_x/2}^{N_x/2-1} D_{mk_x} K_m(k_x r) e^{i(m\theta + k_x x)} \\ & + \sum_{m=-N_\theta/2}^{N_\theta/2-1} D_{m,0} r^{-|m|} e^{im\theta} \quad (8) \end{aligned}$$

and the velocities can be written as

$$\begin{aligned} \mathbf{u}_{\text{internal}} &= \mathbf{u}_v + \nabla\phi_{\text{internal}} + \mathbf{u}_\infty \\ \mathbf{u}_{\text{external}} &= \nabla\phi_{\text{external}} + \mathbf{u}_\infty \end{aligned} \quad (9)$$

Equations (9) contain $2N_\theta N_x$ unknown coefficients, C_{mk_x} and D_{mk_x} . These are determined by matching two components of the internal velocity with two components of the external velocity on the cylindrical interface between the internal and external

domains. Matching two components is sufficient to guarantee that all three components of velocity are continuous and smooth across the matching boundary.

The matching conditions are

$$[(\mathbf{u}_v + \nabla\phi_{\text{internal}}) \cdot \mathbf{e}_r]_{\text{boundary}} = [\nabla\phi_{\text{external}} \cdot \mathbf{e}_r]_{\text{boundary}} \quad (10)$$

$$[(\mathbf{u}_v + \nabla\phi_{\text{internal}}) \cdot \mathbf{e}_\theta]_{\text{boundary}} = [\nabla\phi_{\text{external}} \cdot \mathbf{e}_\theta]_{\text{boundary}} \quad (11)$$

and

$$[(\mathbf{u}_v + \nabla\phi_{\text{internal}}) \cdot \mathbf{e}_x]_{\text{boundary}} = [\nabla\phi_{\text{external}} \cdot \mathbf{e}_x]_{\text{boundary}}. \quad (12)$$

Substituting the series (7) and (8) into (10) - (12) allows the coefficients C_{m,k_x} to be found. With all the coefficients C_{m,k_x} and the vortical velocity known, the entire velocity field is defined. Commensurate with the vortical velocity calculation the generation of the potential velocities required $O(N^3 \log(N))$ operations. In practice, the cpu time required to compute the potential velocity component is approximately equal to the cpu time required to compute the vortical velocity component.

Although the vortical component of velocity is computed with spectral accuracy, the overall method is of fixed order. This is due to the interpolations required between the cartesian and polar coordinate systems and the Padé differencing used to compute the potential velocities from the non-periodic potential field. For this work, forth order interpolation and differencing schemes were used.

4.3 Validation

Before this method can be used, its accuracy and convergence characteristics must be established. The velocity computation will be validated here.

The test cases for the velocity computation were constructed by solving the linearized perturbation equations for an inviscid, incompressible, perturbation to an infinitely smooth, compact columnar vortex. Tests were conducted for many different combinations of axial perturbation mode, azimuthal perturbation mode and mean axial velocity. All tests were successful. The results shown here are only for the first azimuthal perturbation mode with zero axial velocity.

First the effect of increasing the number of azimuthal wavenumbers retained in the boundary matching procedure is examined. This is a good method for evaluating the effectiveness of the boundary treatment. With no boundary matching, the result will be equivalent to a standard Fourier solution on a periodic domain and will contain significant error. As more and more azimuthal wavenumbers are retained, the unbounded character becomes increasingly well

resolved and the result approaches the exact answer. Figure 2 shows that the error converges spectrally until saturation due to cartesian mesh resolution.

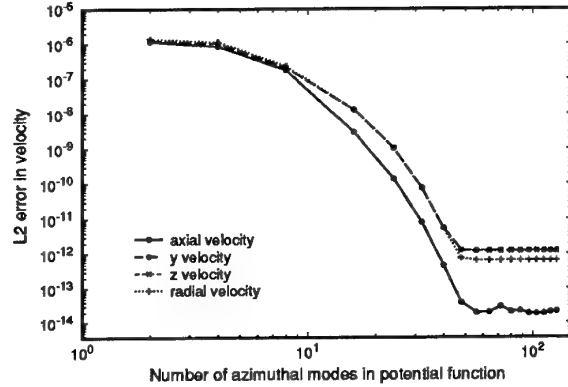


Figure 2: Effect of increasing the number of azimuthal modes in the potential function.

The second test examines the effect of increasing the size of the domain. When attempting to model boundaries at infinity, most conventional boundary treatments benefit from larger domains. Figure 3 shows that this is true for our method. The figure also shows the vast improvement in accuracy achieved by this boundary treatment versus merely extending the periodic domain.

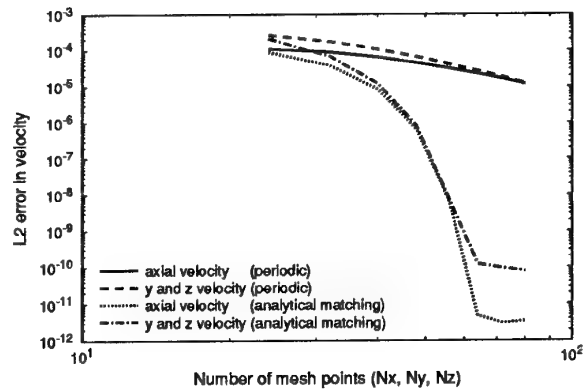


Figure 3: Effect of increasing the domain size on the error in velocity. The mesh spacing was kept constant, so increasing the domain corresponds to increasing the mesh size (but not density) as well. The number of azimuthal modes in the potential function was kept constant at 128.

Figure 4 shows how error decreases with increasing mesh density. The convergence is fourth order because fourth order methods are used in the interpolation between the cartesian and polar mesh and differentiation of the potential function to form velocities.

Tests have also been performed that examine the sensitivity of the method to non-zero vorticity on the matching boundary. These indicate that the method responds quite well and the resulting errors

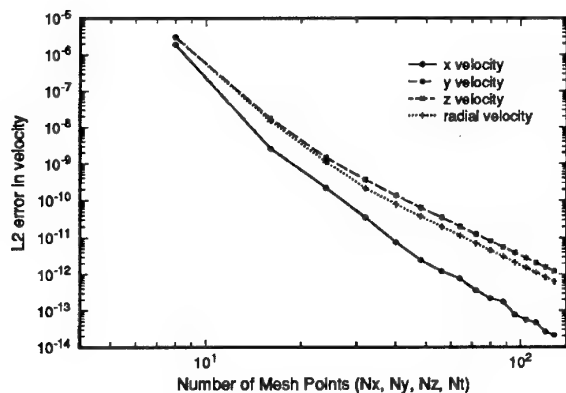


Figure 4: Effect of increasing the mesh density (cartesian and polar) with constant domain size.

in velocity have magnitudes of the same order as the magnitude of the vorticity on the boundary. These results are not shown here, but none of the simulations that follow have significant vorticity at the matching boundary.

5 CROW INSTABILITY

5.1 Baseline Case

Initial simulations were performed for a perturbed, counter rotating columnar vortex pair. These results allowed the extraction of the Crow instability eigenmode and demonstrated the effect of Reynolds number. The Reynolds number effect is important since detailed simulations at realistic Reynolds numbers are not feasible.

For the baseline case, we simply desire to compute the Crow instability for a representative condition. All quantities are nondimensionalized using the initial vortex radius, r_0 , defined as the radius of maximum azimuthal velocity and the magnitude of initial circulation in each vortex, Γ_0 . To make the computation representative of realistic aircraft, the estimated ratio of vortex core diameter to wingspan of 0.197 due to Spreiter and Sacks [13] is used, resulting in a vortex span of $b = 10.190^*$. Many researchers have disagreed with this estimate, but it will serve here. Following the analysis of Crow for vortices of this span, the most unstable perturbation wavenumber is $0.7358/b$, and the amplification rate is $0.736/2\pi b^2$. Since Crow's analysis assumes a Rankine profile in the vortex, these parameters need to be adjusted for the smooth vortices used in the simulation. This was done by adjusting the axial wavenumber so that the rotation rate for the $m = 1$ azimuthal mode obtained from the dispersion rela-

tion of the smooth vortex matched the rotation rate for a Rankine vortex perturbed at the wavenumber obtained from Crow's analysis. In this case the adjusted wavenumber is $0.7509/b$. The amplification rate should then match Crow's prediction.

Since we seek the eigenfunction of the Crow instability, it is desirable to perturb the initial columnar vortices with something close to what we expect the eigenfunction to be. This will minimize the contamination due to other instability modes and also minimize the computation time. For each vortex, the perturbation was generated by superposing two eigenfunctions of the desired axial wavenumber and $m = \pm 1$ obtained from the dispersion relation for a single columnar vortex. The relative phase of the two modes was adjusted to achieve the symmetric, sinusoidal perturbation with the planar angles predicted by Crow. The initial peak to peak perturbation in the vorticity centroid of each vortex was $0.015r_0$.

The computation was performed in three stages. Initially a domain of size $85.268 \times 20 \times 20$ discretized by a mesh of size $4 \times 128 \times 128$ was used. This was exactly the perturbation wavelength in the axial direction with a large enough cross plane to accommodate growth. There are enough points in the cross plane to fully resolve the vortices. Only enough points were carried in the axial direction (after de-aliasing) to resolve the mean flow and the fundamental perturbation. This was presumed sufficient during the linear growth of the perturbation and would conserve computer time. As the disturbance grew, the solution was interpolated to a mesh with 128 points in the axial direction so that any nonlinear interactions would be resolved. This first mesh resizing took place at $t = 1633.68$. As the two vortices approached reconnection the solution was further interpolated to a domain of size $85.268 \times 30 \times 30$ and a mesh of size $128 \times 192 \times 192$ to ensure that the vorticity did not approach the matching boundary. This second mesh resizing took place at $t = 3600.70$. The Reynolds number based on circulation for this case, $Re = \Gamma_0/\nu$, is 100,000.

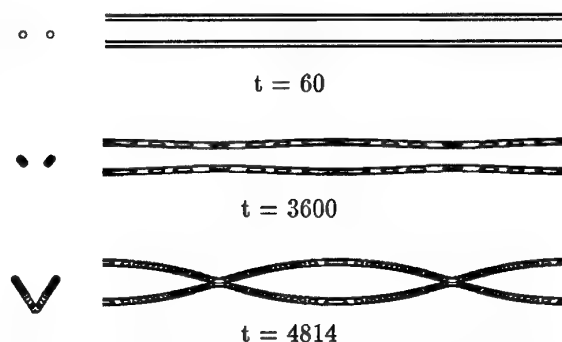


Figure 5: Vorticity contours, $|\omega| = 0.05$, for the baseline simulation. End and top views are shown.

To orient the reader, three snapshots of vorticity are

*The reader may note that if c , vortex diameter, is 2 and $c/b = .197$ then $b = 10.15$. In Crow's paper a quantity δ/β is formed and truncated to 0.063. It is from this number that $b = 10.190$ is obtained, and thus does not represent the estimate of Spreiter and Sacks to the number of digits reported. Regardless, $b = 10.190$ is fully sufficient for our purposes and is reported accurately for completeness.

shown in Figure 5. These clearly show how a pair of counter-rotating vortices, with an imperceptible initial perturbation, evolves into the familiar Crow instability. Figure 6 shows a perspective view of the vorticity at $t = 4814$. After that time, the simulation rapidly broke down due to insufficient resolution. This run consumed 28 hours of cpu time on a Cray C90. To quantify the accuracy of the simulation two invariants of the flow, linear and angular impulse, were tracked in time. For all runs presented here the total variation in linear and angular impulse was less than .1% of the mean.

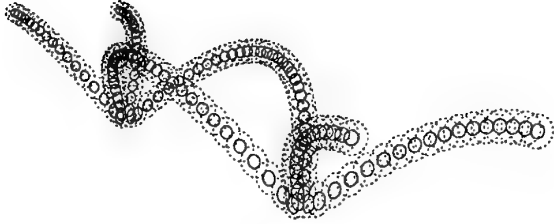


Figure 6: Perspective view of the fully developed Crow instability in the baseline case. Contours are of vorticity, $|\omega| = 0.05$ (dotted) and 0.25 (solid). $t = 4814$

5.2 Amplification Rates

Perhaps of greatest interest is the growth of different measures of the perturbation. We constructed five such measures. The first is the growth of the displacement of the vortex. This is defined as the maximum cross-plane (y - z) separation of the centroid of vorticity on each vortex and is essentially the quantity Crow measured in his analysis. Three other measures can be formed from the growth of the rms values of the three components of vorticity in the fundamental mode, defined as

$$\text{rms}(\omega_i) = \frac{L_x}{2} \left[\int_A |(\widehat{\omega}_i)_{k_x=1}|^2 dy dz \right]^{1/2} \quad (13)$$

where L_x is the domain length in the periodic direction, $(\widehat{\omega}_i)_{k_x=1}$ represents the fundamental axial mode Fourier coefficient of vorticity component ω_i and the integration is carried out over the yz plane. Finally, the kinetic energy in the fundamental mode can be computed and used as a measure of the perturbation. For this work, the energy is computed as

$$\text{energy} = \frac{L_x}{4} \int_{\text{internal domain}} (\widehat{u}_i)_{k_x=1} (\widehat{u}_i)_{k_x=1}^* dy dz \quad (14)$$

where $(\widehat{u}_i)_{k_x=1}$ represents the fundamental axial mode Fourier transform of the velocity. Note the sum over i and the fact that this integral is only carried out over that portion of the yz plane within the internal domain. The square root of this quantity

will be used in all figures to allow direct comparison.

Figure 7 shows the growth of the disturbance measures for the baseline case. The growth of the displacement measure follows Crow's predicted amplification rate remarkably well through almost three decades. The other measures indicate slightly lower amplification rates, most notably the amplification of the axial component of vorticity. We note that the addition of wavenumbers in the axial direction at $t = 1633.68$ shows only a very small effect on growth rate of the fundamental disturbance. Because of this insensitivity to the number of axial modes retained, later runs which were not carried into the nonlinear regime, were conducted with far fewer modes in the periodic direction.

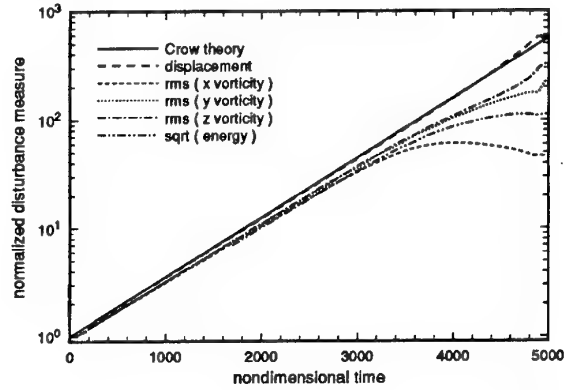


Figure 7: Growth of disturbance measures for the baseline case.

A more informative presentation is a plot of the amplification rates versus time for the disturbance measures shown in Figure 8. Here it is evident that the displacement undergoes a relatively large transient before following the predicted amplification rate very closely. All of the other measures display consistent amplification rates somewhat lower than Crow's prediction. This is presumably due to the effects of viscosity. At a time around 2400 the amplification rates begin to diverge indicating that nonlinear effects are becoming important. Interestingly, as the amplifications of the vorticity components fall due to nonlinear effects, the amplification rate of the displacement increases.

5.3 Disturbance shape

Figure 8 allows us to determine the 'most linear' parts of the linear growth of the Crow instability. Between times of approximately 1200 and 2200, relatively constant amplification rates indicate that the eigenfunction has evolved fully and has not yet been contaminated by nonlinear effects. The shape of the vorticity disturbance in the fundamental mode can be extracted and plotted at various times during the evolution. When normalized for amplitude growth, these shapes remain essentially constant for long times indicating that they represent the eigen-

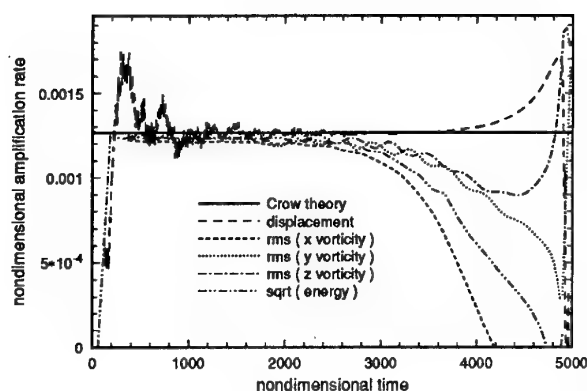


Figure 8: Amplification rates of disturbance measures for the baseline case.

function of the Crow instability. These can be plotted for ω_x , ω_y and ω_z at two different times to show their invariance with time. This is shown in Figures 9 - 11. All three comparisons show small variations, presumably due to viscous and nonlinear effects on the vorticity profiles, but the shapes are quite similar. Although not obvious from the figures, in physical space these mode shapes, when combined with the mean vorticity, produce a sinusoidally oscillating perturbation very similar to the disturbance shape predicted by Crow.

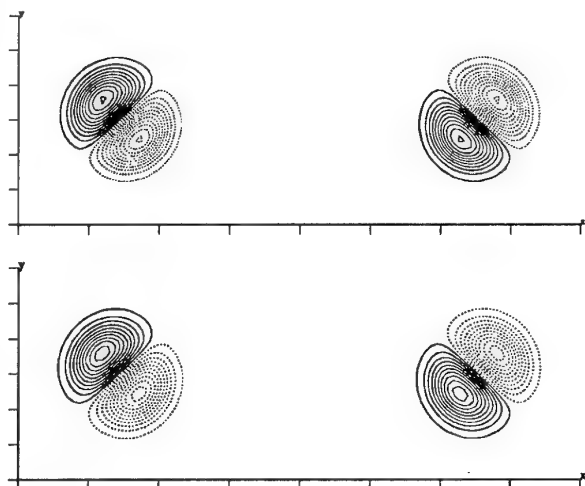


Figure 9: A comparison of the x vorticity in the fundamental mode of the baseline case at two different times. The top figure is for time $t = 1250.68$. The lower figure is for time $t = 2215.95$. The real part of the fundamental wavenumber axial transform of x vorticity is shown, normalized by the maximum of the real part of the fundamental wavenumber axial transform of y vorticity. Dotted and solid lines indicate vorticity of opposite sign. Contours are at intervals of 2.0

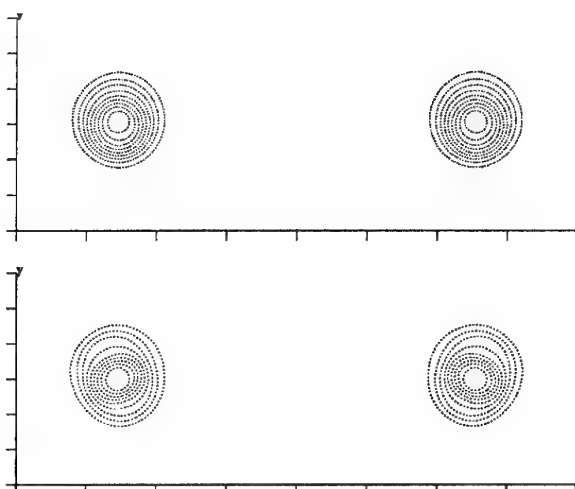


Figure 10: A comparison of the y vorticity in the fundamental mode of the baseline case at two different times. The top figure is for time $t = 1250.68$. The lower figure is for time $t = 2215.95$. The real part of the fundamental wavenumber axial transform of y vorticity is shown, normalized by its maximum. Dotted and solid lines indicate vorticity of opposite sign. Contours are at intervals of 0.1

5.4 Reynolds number effects

Using the same initial conditions as in the baseline case, two other runs were performed with different Reynolds numbers: $Re = 10,000$ and $Re = 1,000,000$. These two cases were both run in a $85.268 \times 20 \times 20$ domain with a $4 \times 128 \times 128$ mesh (again, just enough to resolve the fundamental mode). Consequently, these computations were limited to the linear amplification stage of the instability. Figure 12 shows the displacement growth rates for these different Reynolds number cases, and is presented to show how closely they all follow Crow's prediction.

Trends are more apparent in Figure 13 which shows the effect of Reynolds number on the amplification rates of all five disturbance measures, using Crow's prediction as a comparison. The amplification rates shown are the average amplification rates between times $t = 1100$ and $t = 2100$. Clearly all amplification rates approach Crow's prediction as Reynolds number is increased. The slight divergence of the displacement growth rate occurs due to lack of resolution for the high Reynolds number case. This is also the reason for omitting the y and z vorticity comparisons for that case. Those parameters were overwhelmed by noise in the simulation.

The disturbance measures are quite sensitive to Reynolds number with the striking exception of the displacement measure. This is encouraging because it is the displacement that leads to linking. It suggests that simulations using moderate Reynolds numbers are useful for investigating instabilities that might ultimately be applied to high Reynolds num-

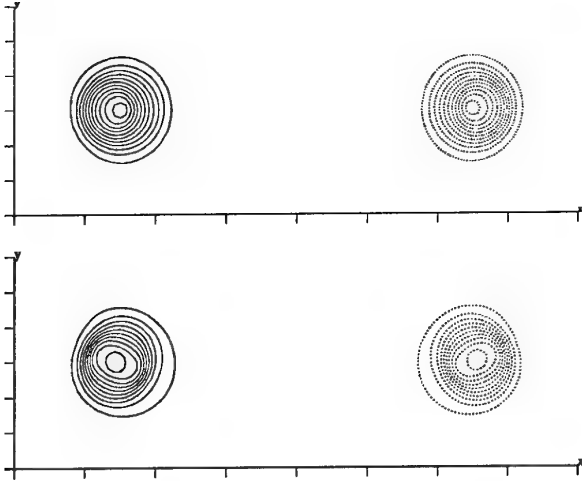


Figure 11: A comparison of the z vorticity in the fundamental mode of the baseline case at two different times. The top figure is for time $t = 1250.68$. The lower figure is for time $t = 2215.95$. The real part of the fundamental wavenumber axial transform of z vorticity is shown, normalized by the maximum of the real part of the fundamental wavenumber axial transform of y vorticity. Dotted and solid lines indicate vorticity of opposite sign. Contours are at intervals of 0.1

ber flows. Since we cannot perform simulations of cases at flight Reynolds number, this is important. All the computations of evolving plane wakes that follow will use a Reynolds number of 10,000.

6 2D ROLL-UP

As another intermediate step to our objective, we show here the two-dimensional rollup of a representative plane wake. Following the work of Spalart [11], for a given span b and root circulation Γ_0 , the elliptical lift distribution is

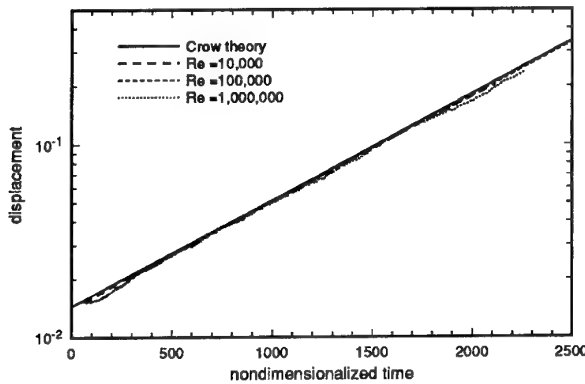


Figure 12: Amplification rates as a function of Reynolds number.

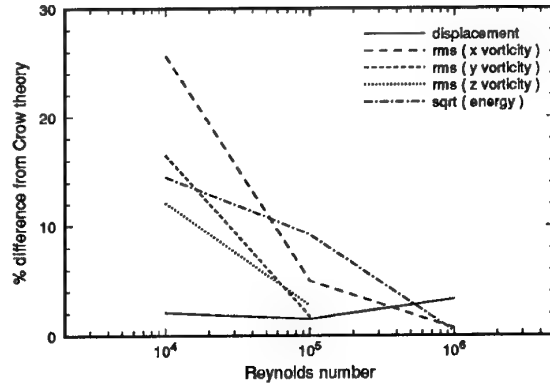


Figure 13: Displacement growth for Cases 0, 1 and 2.

$$\Gamma(y) = \begin{cases} \Gamma_0 \sqrt{1 - 4y^2/b^2}, & \text{if } y < b/2 \\ 0, & \text{if } y > b/2 \end{cases} \quad (15)$$

The axial vorticity shed by such a distribution is

$$\omega_x(y, z) = \frac{4\Gamma_0}{\pi\sigma^2 b^2} \int_{-b/2}^{b/2} \frac{s}{\sqrt{1 - 4s^2/b^2}} e^{-\left\{\frac{(y-s)^2 + z^2}{\sigma^2}\right\}} ds \quad (16)$$

where σ defines the thickness of the shed sheet of vorticity. For the 2D roll-up case studied, the parameters used are:

b	Γ_0	σ
12.9749	1.0	0.2

With these parameters, the effective span, b_0 , defined as

$$b_0 = \frac{1}{\Gamma_0} \int_{-b/2}^{b/2} \Gamma dy \quad (17)$$

is 10.1905. This is exactly the same as the separation (span) of the baseline columnar vortices and permits direct comparison. The root circulation and total lift are also unchanged from the baseline case. The Reynolds number based on circulation is 10,000. This circulation distribution is shown in Figure 14. Since we no longer have an initial columnar vortex, the length scale by which the problem is nondimensionalized needs to be clarified. We now nondimensionalize lengths based on $r_0 = .09813b_0$. This is the radius of the vortex that, according to the analysis of Spreiter and Sacks [13], would emerge after roll-up. This scaling was chosen to keep ratio of core radius to span, an important parameter in Crow's analysis, approximately constant. The degree of approximation is not critical, since during the roll-up process vorticity profiles vary substantially.

Figure 15 shows initial, short and long time snapshots of the roll-up of the wake due to an elliptical lift distribution.

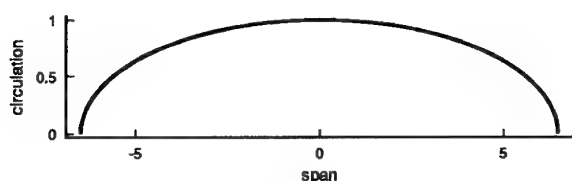


Figure 14: Circulation distribution for the two dimensional roll-up case.

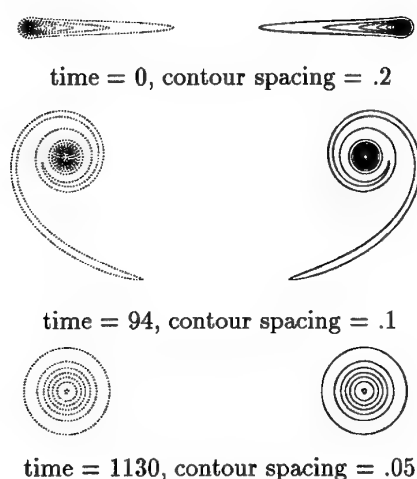


Figure 15: Two dimensional evolution of the vortex wake due to an elliptically loaded wing. Contours of axial vorticity are shown.

7 3D ROLL-UP

A three dimensional roll-up case was computed, corresponding to a perturbed elliptical configurations. The perturbed wake was formed as a sinusoidal oscillation between two prescribed distributions with the following parameters:

	b	Γ_0	σ
distribution 1	13.0074	0.9975	0.2
distribution 2	12.9425	1.0025	0.2

Again, in this case, the mean effective span is $b_0 = 10.1905$. The mean root circulation and total lift remain the same as in the baseline case. The Reynolds number based on circulation is 10,000. These distributions give peak to peak changes in the effective span of $.005 b_0$, which serves to initiate the instability. This small initial perturbation was chosen to allow a period of linear growth after the emergence of a dominant instability and before nonlinearities arise. An $8 \times 256 \times 256$ mesh was used for this case. The initial domain size was $85.268 \times 16 \times 16$. As the vorticity convected outward the solution was interpolated to larger domains. At time $t = 131$ the domain size was increased to $85.268 \times 20 \times 20$ and at time $t = 340$ the domain was increased to $85.268 \times 25 \times 25$.

Figure 16 shows the growth of the normalized dis-

turbance measures for this case. An initial period of strong nonlinearity is present which represents the bulk of the roll-up process. However, for later times, the displacement measure, the measure that is least affected by the low Reynolds number, follows Crow's predicted amplification rate well. Discontinuities can be seen in the vorticity measures at the times corresponding to domain enlargement which indicates that the resolution of this calculation is marginal. However, despite the jumps, the amplification rates of the disturbance measures do not appear significantly affected by the remeshing. This entire computation consumed 8.5 cpu hours on a Cray C90. More refined calculations are planned in the near future.

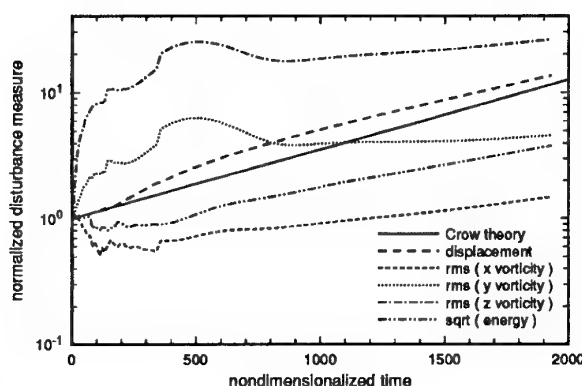


Figure 16: Growth of disturbance measures for the three dimensional evolution of the wake from a perturbed, elliptically loaded wing.

Figure 17 shows the shape of the vorticity disturbance in the fundamental axial mode at time $t = 1370$. They are scaled in the same manner as Figures 9 - 11 and show the evolution of a similar mode. This reinforces the conclusion that the initial perturbation did in fact give rise to the Crow instability. The differences between the shapes indicate that the Crow mode has not fully emerged from the roll-up process and the marginal resolution is apparent.

8 CONCLUSIONS

We are as yet a long way from a full understanding of the process by which a general perturbation, applied at the wing, evolves through the roll-up process and leads to the ultimate destruction of the wake. However, tools for efficiently conducting this investigation have been generated. Crow's inviscid, linear results have been shown to hold well for perturbed counter rotating columnar vortices at high Reynolds number and simulations of this case serve as a baseline for comparison. A plane wake due to an elliptically loaded wing with a perturbation that is a straightforward attempt to excite the Crow instability is simulated. The perturbation evolves rapidly during the roll-up process and results in an instability mode with approximately the amplification rate predicted by Crow's theory and approximately the

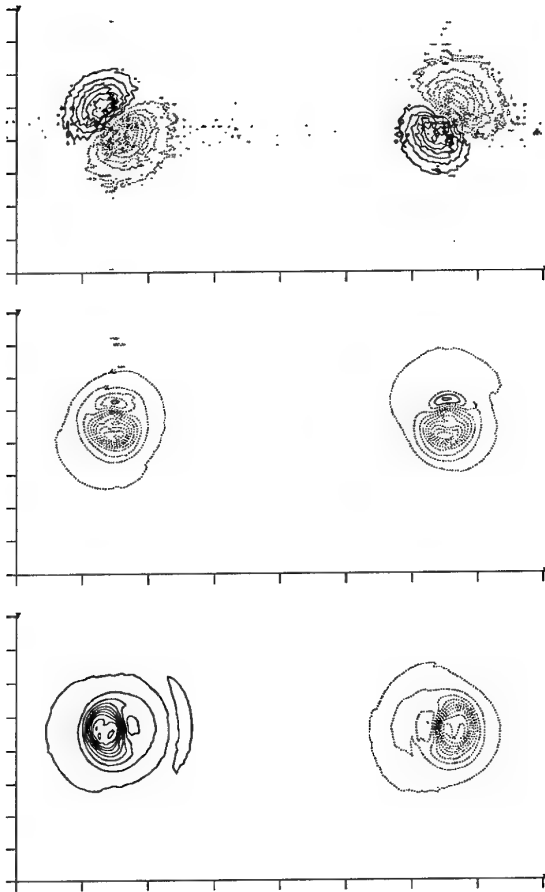


Figure 17: Profiles of vorticity in the fundamental mode of the rolled-up wake from a perturbed elliptically loaded wing at $t = 1370$. The real part of the fundamental wavenumber axial transform of the three vorticity components is shown, all normalized by the maximum of the real part of the fundamental wavenumber axial transform of y vorticity. Top = x vorticity, Middle = y vorticity, Bottom = z vorticity. Dotted and solid lines indicate vorticity of opposite sign. Contours are at intervals of 2.0 for the x vorticity and 0.1 for the y and z vorticities.

same mode shape as was observed in the simulations of the perturbed counter rotating vortex pair.

These results suggest that low energy perturbations to the aircraft wake which are applied at the wing might efficiently be used to excite the Crow instability in the developed wake and lead to breakdown in a predictable, if not reduced, time. Simulations of more realistic wakes with more general disturbances at higher Reynolds numbers and with greater resolution is left for the future.

9 Acknowledgements

This work was supported by the National Science Foundation and the Boeing Commercial Airplane Company under the PYI award to SKL. We would also like to acknowledge the Numerical Aerodynamic

Simulation Facility (NAS) and the San Diego Supercomputing Center (SDSC) for providing computer resources.

References

- [1] Marvin R. Barber and Joseph J. Tymczyszyn. Wake vortex attenuation flight tests: A status report. *NASA CP-2170*, 1980.
- [2] A. J. Bilanin and S. E. Widnall. Aircraft wake dissipation by sinusoidal instability and vortex breakdown. *AIAA 73-107*, 1973.
- [3] Howard Chevalier. Flight test studies of the formation and dissipation of trailing vortices. *Journal of Aircraft*, 10(1):2172-2179, 1973.
- [4] Roque Corral and Javier Jiménez. Fourier/Chebyshev Methods for the Incompressible Navier Stokes Equations in Infinite Domains. *Journal of Computational Physics*, 121:261-270, 1995.
- [5] S. C. Crow. Stability theory for a pair of trailing vortices. *AIAA Journal*, 8(12):2172-2179, 1970.
- [6] Steven C. Crow. Panel discussion. In John H. Olson, Arnold Goldburg, and Milton Rogers, editors, *Aircraft Wake Turbulence and Its Detection*, pages 577-583. Plenum Press, 1971.
- [7] Steven C. Rennich and Sanjiva K. Lele. Numerical method for incompressible flows with two unbounded directions using analytic matching. Manuscript in preparation.
- [8] Vernon J. Rossow. Prospects for destructive self-induced interactions in a vortex pair. *Journal of Aircraft*, 24(7):433-440, 1987.
- [9] Rolf Sondergaard, Nagi N. Mansour, and Brian J. Cantwell. The Effect of Initial Conditions on the Development of Temporally Evolving Planar Three Dimensional Incompressible Wakes. Technical Report AGARD-CP-551, AGARD, 1994.
- [10] Philippe R. Spalart. Wake vortices and turbulence. Fluid Mechanics Seminar - Stanford University, May 1995.
- [11] Philippe R. Spalart. On the motion of aircraft wakes in a stably stratified fluid. *Journal of Fluid Mechanics*, Submitted(1996).
- [12] Philippe R. Spalart, Robert D. Moser, and Michael M. Rogers. Spectral methods for the Navier-Stokes equations with one infinite and two periodic directions. *Journal of Computational Physics*, 96:297-324, 1991.
- [13] J. R. Spreiter and A. H. Sacks. The rolling up of the trailing vortex sheet and its effect on the downwash behind wings. *Journal of the Aeronautical Sciences*, 18(1):21-32, 1951.

The inviscid motion of a vortex pair in a compressible and stratified atmosphere

Roland Stüff

DLR-Institute for Fluid Mechanics
D-37073 Göttingen, Germany

SUMMARY

The movement of an inviscid vortex pair in a compressible atmosphere including buoyancy effects is described by analytic solutions. The effects of compressibility are dealt with in an isentropic atmosphere. The work of compression done by the atmosphere on the vortex is entirely consumed by the isentropic change of the thermodynamic state of the vortex pair. The acceleration of the accompanying and apparent mass is given by the displacement of the two vortices towards each other. The effects of buoyancy are investigated by means of a two-dimensional, incompressible, inviscid vortex pair which is heavier than the ambient fluid. It turns out that the condition of pressure continuity across the separating streamline can be achieved only by assuming an increase in circulation of the two vortices. The mass accompanying the vortex pair under the effect of non-conservative forces converts a fraction of its gravity potential into an increase of stagnation pressure. Both, the analytical formulas for compressibility and buoyancy, then, are combined to describe both effects simultaneously. Thus, inconsistencies of other papers are eliminated.

1. INTRODUCTION

Aircraft trailing vortices are considerably affected by atmospheric density and gravity stratification. The numerical code used by NASA in projects on wake research, see Vicroy¹ et al. 1994, is based on a paper by Greene². In the latter stratification effects due to buoyancy are accounted for by means of a theory by Saffman³. As stated by himself Saffman's theory of an inviscid vortex pair under the effect of gravity does not satisfy the condition of pressure continuity across the streamline which separates the accompanying from the surrounding mass. Of course, there cannot be a pressure jump inside an incompressible fluid. The formulas presented here satisfy the condition of pressure continuity by accounting for non-conservative forces. These forces exist due to the fact that the accompanying fluid has to cope with a time dependent external centrifugal force field and an increasing external stagnation pressure as shown by the author in a different paper⁴. As a consequence the circulation of the two vortices is a function of time too and its time rate of change is equal in magnitude to the increase of stagnation pressure in the accompanying fluid. A fraction of the gravity potential is consumed by this increase. As a result the acceleration of the vortex pair as a whole is less than predicted by Saffman³, who only

considered the inertia of the accompanying and apparent mass of the fluid. This paper, in addition to Saffman, also includes the compressibility of the vortex pair. Even in an isentropic atmosphere without buoyancy a descending vortex accelerates. The distance between the two vortices then is getting shorter and shorter. Thus, there is an increase in the velocity induced by both vortices at the two stagnation points and by one vortex at the center of the other. In this case the flow field can be decomposed into that one due to the compressibility and another one due to a quasisteady vortex pair. In addition, the acceleration of the vortex pair as a whole can be obtained by applying Kutta-Joukowski's rule to the displacement velocity of the vortex centers. The work of compression done by the atmosphere on the vortex pair is entirely consumed by the isentropic change of its thermodynamic state.

Both analytical solutions, the one for the buoyancy and the other one for the compressibility then are superposed to give both effects simultaneously in one solution. Compressibility so far seems not to have been considered in previous papers. In the case of buoyancy this paper predicts a lower speed than Saffman's³ 1972 paper. By now wake vortex research has been conducted for over thirty years by diverse groups such as FAA, NASA,

DLR, ONERA and aircraft manufacturers. Yet, as stated already by Widnall⁵ 1975 there still is a contradiction between numerical findings and data from in-flight tests. Of course, a theory including viscosity, turbulence, atmospheric wind and stratification cannot provide correct results if there is already a mistake in the inviscid part of it. The analytical solution presented here may serve as an initial solution to methods including instability, viscous, turbulent or atmospheric wind effects.

2. VORTEX PAIR IN ISENTROPIC ATMOSPHERE

A vortex pair descending in an isentropic atmosphere accelerates such that the velocity induced at the stagnation points and by one vortex at the center of the other is identical with the velocity of the vortex pair as a whole, see figure 1.

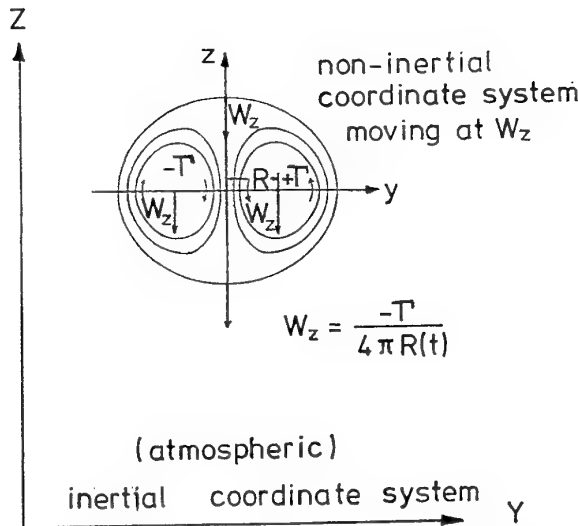


Fig. 1 – Twodimensional inviscid vortex pair descending in a dry isentropic atmosphere (constant potential temperature). X, Y, T coordinates of inertial system, x, y, t coordinates of non-inertial system moving at speed W_z .

The combined velocity field in this case is composed of a quasi-steady field due to the circulation and of another unsteady one due to the compression of the vortex pair. In the momentum equation the relationship between the acceleration of the vortex pair as a whole and the velocity fields due to circulation and compression is quite involved. Therefore, it is more convenient to start with the vorticity transport equation which can be derived from the momentum equation.

2.1 Basic equations

The vorticity transport equation for an isentropic flow is

$$\frac{d}{dT} \frac{\text{curl } v_{abs}}{\rho_0} = 0, \quad (2.1)$$

where ρ_0 is the instantaneous density and v_{abs} the velocity in the inertial coordinate system of the atmosphere. The absolute velocity is the vector sum of the velocity, W_z , of the non-inertial coordinate system and the velocity, v_0 , within the non-inertial coordinate system,

$$v_{abs} = W_z + v_0 \quad (2.2)$$

Integrating eq. (2.1) from an initial time designated by the subscript A to some later time,

$$\frac{\text{curl } v_{abs}}{\rho_0} = \frac{(\text{curl } v_{abs})_A}{\rho_A} = H(0, \pm R), \quad (2.3)$$

the relationship between vorticity and density is obtained. The Heaviside unit step function, H , assures that the curl is everywhere zero except at the vortex centers at $y = \pm R$. It should be noted that the circulation which follows from an integration of the vorticity over the vortex area remains constant, since the area enclosed by the same streamline goes with the inverse density. In the inertial coordinate system the vorticity equation

$$\frac{\partial}{\partial Y} v_{absz} - \frac{\partial}{\partial Z} v_{absy} = 0, \quad (2.4)$$

and the continuity equation,

$$\frac{1}{\rho_0} \frac{d\rho_0}{dT} + \frac{\partial}{\partial Z} v_{absz} + \frac{\partial}{\partial Y} v_{absy} = 0, \quad (2.5)$$

now constitute a complete set of differential equation. Z and Y are the vertical and lateral coordinates. With eq. (2.2) in eq. (2.4) the velocity of the non-inertial coordinate system, W_z , formally drops out,

$$\frac{\partial}{\partial Y} v_{0z} - \frac{\partial}{\partial Z} v_{0y} = 0, \quad (2.6)$$

because of being a function of only the time or Z . For the same reason equation (2.6) remains unchanged in the non-inertial system. Therefore, the inertial coordinates, Z, Y , may be replaced by those of the non-inertial system y, z .

With the assumption that the density differences inside the vortex pair are negligible the density also becomes a function of only the time. The continuity equation (2.5) then simplifies to the following one for the non-inertial system,

$$\frac{\partial}{\partial z} v_{0z} + \frac{\partial}{\partial y} v_{0y} = -\frac{1}{\rho_0} \frac{\partial \rho_0}{\partial t} \quad (2.7)$$

The vector field of v_0 which is the velocity field as seen by an observer in the origin of the non-inertial coordinate system is thought of as being composed of one field due to the vortex pair's quasisteady circulatory motion and of another one due to the compression by the ambient atmosphere,

$$v_0 = v_\Gamma + v_d, \quad (2.8)$$

where the subscript Γ designates the quasi-steady field induced by the circulation and the subscript d the dilatation due to the compression. With eqs. (2.6) through (2.8) continuity and vorticity equation now read,

$$\begin{aligned} \frac{\partial}{\partial z} (v_{\Gamma z} + v_{dz}) + \frac{\partial}{\partial y} (v_{\Gamma y} + v_{dy}) = \\ = -\frac{1}{\rho_0} \frac{\partial \rho_0}{\partial t} \end{aligned} \quad (2.9)$$

and

$$\frac{\partial}{\partial y} (v_{\Gamma z} + v_{dz}) - \frac{\partial}{\partial z} (v_{\Gamma y} + v_{dy}) = 0 \quad (2.10)$$

2.2 Velocity field of dilatation and circulation

The continuity equation of the dilatation is per definition,

$$\frac{\partial}{\partial z} v_{dz} + \frac{\partial}{\partial y} v_{dy} = -\frac{1}{\rho_0} \frac{\partial \rho_0}{\partial t}, \quad (2.11)$$

the continuity equation left over is with eqs. (2.9) and (2.11),

$$\frac{\partial}{\partial z} v_{\Gamma z} + \frac{\partial}{\partial y} v_{\Gamma y} = 0. \quad (2.12)$$

The velocity due to the dilatation is much smaller than that one due to circulation, $v_d \ll v_\Gamma$. Therefore, vorticity must be zero for either one

$$\frac{\partial}{\partial y} v_{\Gamma z} - \frac{\partial}{\partial z} v_{\Gamma y} = 0, \quad (2.13)$$

$$\frac{\partial}{\partial y} v_{dz} - \frac{\partial}{\partial z} v_{dy} = 0. \quad (2.14)$$

Because of the last equation the field of the dilatation can be described by a velocity potential $\phi(v_{dz} = \phi_z; v_{dy} = \phi_y)$. From eq. (2.11),

$$\phi_{zz} + \phi_{yy} = -\frac{1}{\rho_0} \frac{\partial \rho_0}{\partial t}, \quad (2.15)$$

a formal solution is found,

$$\phi = A(t)y^2 + B(t)z^2. \quad (2.16)$$

The field induced by the circulation can be described by either one a velocity potential or a streamfunction as can be seen from the Cauchy-Riemann differential equations (2.12) and (2.13). A streamfunction ($v_{\Gamma z} = -\psi_y; v_{\Gamma y} = \psi_z$) is chosen. With eq. (2.13) we have the Laplacian

$$\psi_{yy} + \psi_{zz} = 0. \quad (2.17)$$

A solution of eq. (2.17) is required which fulfills the boundary condition that $\psi = \text{const}$ is a surface in the three-dimensional space (t, y, z) and that the relationship

$$\begin{aligned} \frac{d\psi}{dt} = \frac{\partial \psi}{\partial t} + (v_{\Gamma y} + v_{dy}) \frac{\partial \psi}{\partial y} + \\ + (v_{\Gamma z} + v_{dz}) \frac{\partial \psi}{\partial z} = 0, \end{aligned} \quad (2.18)$$

holds for a surface which contains at all times the same particles. This means that the particles' paths in the combined flow are identical with the streamlines of the circulatory flow. Eq. (2.18) can be simplified further with the help of eqs. (2.16) and (2.17),

$$\frac{\partial \psi}{\partial t} + 2B(t)y\psi_y + 2C(t)z\psi_z = 0. \quad (2.19)$$

Reduced space coordinates are introduced with,

$$\bar{y} = f(t)y, \quad \bar{z} = f(t)z, \quad (2.20)$$

for the streamfunction such that

$$\psi(t, y, z) = \psi(\bar{y}, \bar{z}). \quad (2.21)$$

Laplace's equation (2.17) is formally unchanged

$$\psi_{\bar{y}\bar{y}} + \psi_{\bar{z}\bar{z}} = 0. \quad (2.22)$$

From eqs. (2.19) and (2.20) it follows that,

$$\ln f = -\int_{t_0}^t 2B(\bar{t})d\bar{t} = -\int_{t_0}^t 2C(\bar{t})d\bar{t}, \quad (2.23)$$

and from eqs. (2.15) through (2.23) that,

$$2B(t) = 2C(t) = \frac{-1}{2\rho_0} \frac{\partial \rho_0}{\partial t}, \quad (2.24)$$

and finally,

$$f = \sqrt{\frac{\rho_0}{\rho_A}}, \quad (2.25)$$

where ρ_A is the initial density. The streamfunction, now, is

$$\psi = \psi \left(\sqrt{\frac{\rho_0}{\rho_A}} y, \sqrt{\frac{\rho_0}{\rho_A}} z \right). \quad (2.26)$$

For a vortex pair it formally coincides with its steady counterpart

$$\psi = \frac{\Gamma}{2\pi} \left\{ \frac{\bar{y}}{2R_A} + \ln \frac{\bar{r}_1}{\bar{r}_2} \right\}, \quad (2.27)$$

where R_A is the initial distance of the vortex centers from the vertical z -axis and

$$\bar{r}_1^2 = (\bar{y} - R_A)^2 + \bar{z}^2; \quad \bar{r}_2^2 = (\bar{y} + R_A)^2 + \bar{z}^2 \quad (2.28)$$

The instantaneous distance of the vortex centers from the z -axis is

$$R(t) = R_A \sqrt{\frac{\rho_A}{\rho_0}}. \quad (2.29)$$

Eq. (2.29) in eq. (2.27) gives,

$$\psi = \frac{\Gamma}{2\pi} \left\{ \frac{y}{2R(t)} + \ln \frac{r_1}{r_2} \right\}, \quad (2.30)$$

with

$$\begin{aligned} r_1^2 &= (y - R(t))^2 + z^2; \\ r_2^2 &= (y + R(t))^2 + z^2. \end{aligned} \quad (2.31)$$

The combined flow field is constituted by that one due to compressibility and another one due to the quasi-steady flow as depicted in figure 2.

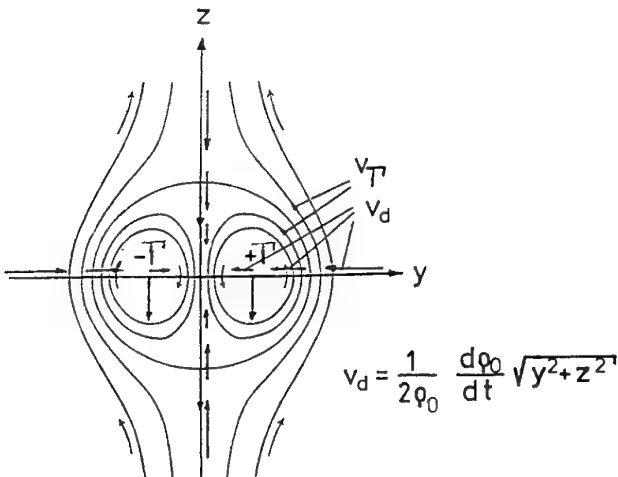


Fig. 2 – Combined velocity field of circulatory flow and of dilatation.

In the field of dilatation the velocity vector is always directed towards the origin of the

non-inertial coordinate system with its speed in proportion to the distance from the origin. The quasi steady flow field is that one of a two-dimensional vortex pair. Differentiating the instantaneous distance $R(t)$ of the vortex centers, eq. (2.29), with respect to time,

$$\frac{dR}{dt} = -\frac{1}{2\rho_0} \frac{\partial \rho_0}{\partial t} R(t), \quad (2.32)$$

the velocity vector of the dilatation at this center is obtained

$$\frac{dR}{dt} = v_{dc}. \quad (2.33)$$

The velocity of the vortex pair as a whole is,

$$W_z = \frac{-\Gamma}{4\pi R(t)}, \quad (2.34)$$

and the acceleration is with eqs. (2.32) and (2.24),

$$\frac{dW_z}{dt} = \frac{\Gamma}{4\pi R^2} v_{dc}. \quad (2.35)$$

It now will be shown that the acceleration, (dW_z/dt) , also can be obtained directly from the momentum equation. The equation is integrated over the area of one vortex, i.e. over one half vortex pair. For the non-inertial system Lamb's form is chosen,

$$\begin{aligned} \iint \rho_0 \frac{\partial}{\partial t} v_{abs} dF &= \\ &= \iint \frac{\rho_0}{2} \text{grad}(W_z^2 - v_0^2) dF - \\ &- \iint \text{grad } p dF + \iint \rho_0 v_0 \times \text{curl } v_{abs} dF. \end{aligned} \quad (2.36)$$

Carrying out the integration, the left hand side is,

$$\iint \rho_0 \frac{\partial}{\partial t} v_{abs} dF = \rho_0 \frac{F_0}{2} \frac{dW_z}{dt}. \quad (2.37)$$

The first term on the right hand side is zero. The pressure gradient represents the reaction force to the acceleration of the apparent mass,

$$\iint \text{grad } p dF = \alpha \rho_0 \frac{F_0}{2} \frac{dW_z}{dt}, \quad (2.38)$$

where α is the factor for the apparent mass. The last term contains a vortex singularity, see eq. (2.3). The velocity v_0 in this term reduces to the velocity of dilatation at the vortex singularity, so that

$$\iint \rho_0 v_0 \times \text{curl } v_{abs} dF = \quad (2.39)$$

$$= \rho_0 v_{dc} \iint \text{curl } v_{abs} dF = \rho_0 v_{dc} \Gamma,$$

which is Kutta-Joukowski's rule of lift force. With eqs. (2.37), (2.38), (2.39) in eq. (2.36) the acceleration is given by,

$$\frac{dW_z}{dt} = \frac{2v_{dc}\Gamma}{F_0(1+\alpha)}, \quad (2.40)$$

which says that the force necessary to accelerate the accompanying and apparent mass is equal to the lift force obtained from Kutta-Joukowski's rule. The area of one half vortex pair is

$$\frac{1}{2} F_0 = 4\pi R^2 \beta, \quad (2.41)$$

where

$$\beta = \frac{1}{4\pi} \int_0^\pi \zeta^2 d\theta, \quad (2.42)$$

with ζ and θ as polar coordinates. The result is

$$\beta = \frac{1}{1+\alpha}, \quad \alpha = \frac{2\pi}{3\sqrt{3}}, \quad (2.43)$$

so that

$$\frac{1}{2} F_0 = 4\pi R^2 \frac{1}{1+\alpha}. \quad (2.44)$$

This with eq. (2.40) gives

$$\frac{dW_z}{dt} = \frac{v_{dc}\Gamma}{4\pi R^2}. \quad (2.45)$$

The above equation is identical with eq. (2.35) q.e.d..

2.3 Energy considerations

The whole process is driven by the work done by the ambient atmosphere on the vortex pair. The ambient atmosphere is regarded as much greater than the mass accompanying the vortex pair. Therefore, the thermodynamic state of the atmosphere is assumed to be uninfluenced by the work it is doing.

Work of displacement is obtained by multiplying the Kutta-Joukowski force, eq. (2.39), (2.40) by the velocity W_z ,

$$W_z \cdot (\rho_0 v_{dc} \times \Gamma) = \rho_0 \frac{F_0}{2} (1+\alpha) W_z \frac{dW_z}{dt} \quad (2.46)$$

This represents the increase of the kinetic energy of the accompanying and apparent mass.

Isentropic work of compression increases the internal energy of the accompanying mass. The pressure encountered by the descending vortex pair is given by the static pressure at infinity but at same altitude plus the dynamic pressure, $P + \rho_0 W_z^2/2$, i.e. the stagnation pressure. In an ideal gas pressure, density and specific volume are related by,

$$\frac{p}{p_A} = \left(\frac{\rho_0}{\rho_A} \right)^\gamma = \left(\frac{v_A}{v} \right)^\gamma, \quad (2.47)$$

where the subscript A indicates quantities at some given initial altitude or time. γ is the ratio of the specific heats, c_p/c_v , at constant pressure and constant volume. With the ideal gas law ($p v = R T$, $c_v = R/(\gamma-1)$, $R \rightarrow$ gas constant of air) the increase of the internal energy finally is,

$$c_v(T - T_A) = \frac{1}{\gamma-1} (p v - p_A v_A). \quad (2.48)$$

3. VORTEX PAIR UNDER THE INFLUENCE OF BUOYANCY

The motion of a vortex pair under the influence of buoyancy forces is studied by means of an incompressible, inviscid, two-dimensional vortex pair. The accompanying fluid is assumed to be heavier than the surrounding $\rho_0 g > \rho_a g$, see figure 3.

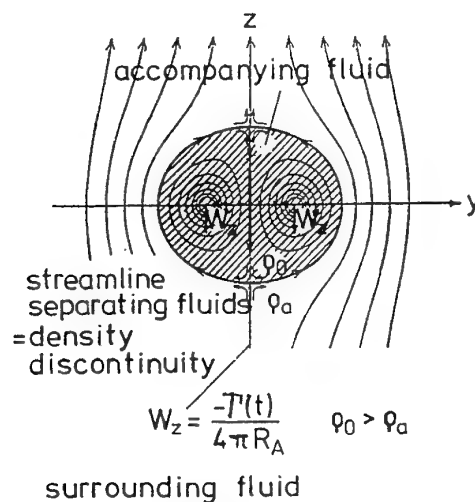


Fig. 3 – Twodimensional inviscid and incompressible vortex pair moving under the effect of gravity. ρ_0 density of accompanying fluid, ρ_a density of surrounding fluid.

3.1 Velocity of the vortex pair

The whole process is driven by the buoyancy force or the excess gravity potential,

$$F_b = (\rho_a - \rho_0)g S_0, \quad (3.1)$$

where S_0 is the area of the vortex pair. A first and second fraction of the force is consumed by the acceleration of the accompanying, $\rho_0(\partial W_z/\partial t)$, and apparent mass, $\alpha\rho_a(\partial W_z/\partial t)$. A third fraction of the excess gravity potential of F_b is consumed by the increasing stagnation pressure, $\rho_a(\partial W_z/\partial t)$, as most evidently can be seen from the stagnation points,

$$F_b = \left\{ \rho_0 \frac{dW_z}{dt} + \rho_a(1 + \alpha) \frac{dW_z}{dt} \right\} S_0. \quad (3.2)$$

The acceleration is,

$$\frac{dW_z}{dt} = \frac{(\frac{\rho_a}{\rho_0} - 1)g}{1 + \frac{\rho_a}{\rho_0}(1 + \alpha)} \quad (3.3)$$

The acceleration, (dW_z/dt) , is less than predicted by Saffman³ who did not account for the increase of stagnation pressure.

3.2 Surrounding flow

In considering the flow along the separating streamline the momentum equation can be formulated for both sides, see also ref.4. From the condition of pressure continuity it follows that in the non-inertial coordinate system at a fixed position on the streamline the acceleration of the surrounding flow is,

$$\rho_a \frac{\partial v_a}{\partial t} = -\rho_a(1 + \alpha) \left(\frac{dW_z}{dt} x\bar{n} \right) x\bar{n}, \quad (3.4)$$

where \bar{n} is the unit vector in the normal direction to the streamline. The local acceleration of the surrounding flow is given by the normal projection of its maximum velocity on to the separating streamline. The same rule applies to the velocity itself,

$$v_a = -(1 + \alpha)(W_z x\bar{n}) x\bar{n}, \quad (3.5)$$

see for example R.T. Jones⁶ textbook. Eqs. (3.4) and (3.5) are the same for a rigid body. Thus, the surrounding flow can be described by a velocity potential of an accelerating rigid body whose outline is given by the separating streamline,

$$\phi_B = 2R_0 W_z \left(\frac{z}{2R_0} - \arctg \frac{y - R_0}{z} + \arctg \frac{y + R_0}{z} \right), \quad (3.6)$$

where $2R_0$ is the distance between the vortex centers. The static pressure is the result of its share due to the quasi-steady flow and its share due to the acceleration of the apparent mass,

$$(p - p_\infty(z)) = \frac{\rho_a}{2} (W_z^2 - v_a^2) + \Delta p_{unst}, \quad (3.7)$$

where

$$\Delta p_{unst} = \rho_a \frac{dW_z}{dt} \frac{\partial \phi_B}{\partial W_z} - \rho_a \frac{dW_z}{dt} z, \quad (3.8)$$

see for example Lamb's⁷ textbook.

The above solution for the surrounding flow is in a formal accordance with the corresponding one of Saffman³. However, the velocity, W_z , and the acceleration, (dW_z/dt) , here are lower because of the increases in stagnation pressure, see eq. (3.3).

3.3 Free vortex sheet at dividing streamline

Saffman's³ theory implies that there is a bound vortex sheet at the separating streamline. However, in an incompressible fluid there cannot be a pressure jump. In the present paper a free vortex sheet with only a velocity jump is assumed to be at the separating streamline. Pressure continuity implies same static and dynamic pressure on either side of the separating streamline. For the same reason the time rate of change of static and dynamic pressure must be the same on either side, giving

$$\frac{\partial v_0}{\partial t} = \sqrt{\frac{\rho_a}{\rho_0}} \frac{\partial v_a}{\partial t}, \quad v_0 = \sqrt{\frac{\rho_a}{\rho_0}} v_a, \quad (3.9)$$

where v_0 and ρ_0 are velocity and density on the inside of the density discontinuity. v_a can be determined from eqs. (3.4), (3.5), (3.6). The theorem of Bjerknes⁸ says that circulation is created if density and pressure gradient are not parallel. This is the case across the separating streamline, i.e. across the density discontinuity. Evaluating the acceleration over a closed path the time rate of change of the vortex sheet intensity γ is obtained from Bjerknes theorem,

$$\begin{aligned} \frac{\partial \gamma}{\partial t} &= \\ &= - \left(1 - \sqrt{\frac{\rho_a}{\rho_0}} \right) (1 + \alpha) \left(\frac{dW_z}{dt} x \bar{n} \right) x \bar{n}, \end{aligned} \quad (3.10)$$

where

$$\gamma = \frac{\partial \Gamma_s}{\partial s}, \quad (3.11)$$

and Γ_s the circulation around the end of the vortex sheet cut off at s .

3.4 Accompanying fluid

Due to the condition of pressure continuity across the dividing streamline velocity and acceleration on the inside are given as a function of their respective quantities in the surrounding flow, see eq. (3.9). Therefore, the flow of the accompanying fluid can be described by a velocity potential which is given by the external velocity potential of eq. (3.6)

$$\begin{aligned} \phi_0 &= 2R_0 \sqrt{\frac{\rho_a}{\rho_0}} W_z \left(\frac{z}{2R_0} - \right. \\ &\quad \left. - \arctg \frac{y-R_0}{z} + \arctg \frac{y+R_0}{z} \right). \end{aligned} \quad (3.12)$$

The instantaneous circulation of the two vortices in the velocity potential above is

$$\Gamma = \sqrt{\frac{\rho_a}{\rho_0}} W_z 4\pi R_0. \quad (3.13)$$

Because of the time dependence of W_z the circulation Γ is a function of time too. Inside the vortex pair the non-conservation of stagnation pressure is inherently linked to non-conservative forces. The mechanism of vortex generation by non-conservative forces is dealt with by the author in a different paper⁴.

From eqs. (3.12) and (3.13) it can be seen that the velocity induced by the two single vortices at the two stagnation points and by one vortex at the center of the other is $\sqrt{\rho_a/\rho_0} W_z$ and not W_z . In the next section it will be shown that with the additional velocity induced by the vortex sheet the kinematic condition at the points mentioned above is fulfilled.

3.5 Additional flow field of vortex sheet

The additional flow field which is induced by the free vortex sheet can be elegantly described by a complex potential. The locally induced conjugate complex velocity is

$$v_z - iv_y = \frac{-i}{2\pi} \int \frac{\gamma(\zeta)}{z - \zeta} d\zeta, \quad (3.14)$$

where z and ζ are the complex coordinates of the observer and the vortex sheet. The intensity of the vortex sheet is with eq. (3.9)

$$\gamma = \bar{v}_a - \bar{v}_0 = \bar{v}_a(\zeta) \left(1 - \sqrt{\frac{\rho_a}{\rho_0}} \right), \quad (3.15)$$

with $\bar{v}_a(\zeta)$ as complex conjugate velocity from eq. (3.6),

$$\bar{v}_a(\zeta) = W_z \left\{ 1 + \frac{2R_0}{i} \left[\frac{1}{\zeta - iR_0} - \frac{1}{\zeta + iR_0} \right] \right\}. \quad (3.16)$$

With eqs. (3.15) and (3.16) eq. (3.14) can be rearranged,

$$\begin{aligned} v_z - iv_y &= \frac{(1 - \sqrt{\frac{\rho_a}{\rho_0}})}{2\pi i} W_z \left\{ \int \frac{d\zeta}{z - \zeta} - \right. \\ &\quad \left. - \frac{i2R_0}{z - iR_0} \left[\int \frac{d\zeta}{z - \zeta} + \int \frac{d\zeta}{\zeta - iR_0} \right] \right. \\ &\quad \left. + \frac{i2R_0}{z + iR_0} \left[\int \frac{d\zeta}{z - \zeta} + \int \frac{d\zeta}{\zeta + iR_0} \right] \right\}. \end{aligned} \quad (3.17)$$

The velocity field obtained from the above equation depends on whether it is evaluated for a point inside ($z < \zeta$) or outside ($z > \zeta$) the vortex pair. Inside the vortex pair the vector $(z - \zeta) = \mathcal{R} e^{i\theta}$ performs a complete revolution. Therefore

$$\int \frac{d\zeta}{z - \zeta} = -\ln(z - \zeta) \int_0^{2\pi} = -2\pi i. \quad (3.18)$$

For the same reason

$$\ln(\zeta - iR_0) \int_0^{2\pi} = \ln(\zeta + iR_0) \int_0^{2\pi} = 2\pi i. \quad (3.19)$$

Outside of the vortex pair at some point the vector $(z - \zeta)$ changes the sense of its turn and comes back to its initial angle, therefore

$$\ln(z - \zeta) \int_0^0 = 0 \quad (3.20)$$

for $z > \zeta$. With eqs. (3.18), (3.19), (3.20) in eq. (3.17) the additional velocity due to the vortex sheet in the surrounding flow is,

$$v_z - iv_y = \left(1 - \sqrt{\frac{\rho_a}{\rho_0}}\right) W_z 2r_0 \left\{ \frac{i}{z - iR_0} - \frac{i}{z + iR_0} \right\}. \quad (3.21)$$

Superposing this additional velocity field with that one induced by the two single vortices from eq. (3.12) it is found that the surrounding flow is the same as if there were two single vortices each with a circulation,

$$\Gamma = \pm W_z / \pi R_0, \quad (3.22)$$

and no vortex sheet. This also substantiates the replacement of the vortex pair by a rigid body as far as the surrounding flow is concerned. For the accompanying fluid ($z < \zeta$) it is found that everywhere inside the vortex pair the same vertical velocity is induced,

$$v_z = \left(1 - \sqrt{\frac{\rho_a}{\rho_0}}\right) W_z. \quad (3.23)$$

Together with the flow field induced by the two single vortices, eq. (3.12), the vertical velocity of eq. (3.23) results in the velocity W_z for the two stagnation points and the two vortex centers. Thus, the necessary kinematic condition is fulfilled at these points by the combined flow field.

4. COMBINED INFLUENCE OF COMPRESSIBILITY AND BUOYANCY

Reviewing the acceleration due to compressibility and buoyancy, eqs. (2.40), (3.3) it will be found that the instantaneous velocity, W_z , of the non-inertial coordinate system is in either case that one induced at the stagnation points and at the vortex centers. This, of course, applies if compressibility and buoyancy are acting simultaneously,

$$W_z = \frac{-\Gamma(t)}{4\pi R(t)}, \quad (4.1)$$

where contrary to the case of mere compressibility the circulation is a function of time and contrary to the case of mere buoyancy the vortex distance R is a function of time, too. Therefore, the acceleration of the non-inertial coordinate system now is,

$$\frac{dW_z}{dt} = \frac{\Gamma}{4\pi R^2} \frac{dR}{dt} - \frac{d\Gamma}{dt} \frac{1}{4\pi R}. \quad (4.2)$$

By comparison with eqs. (2.33), (2.35) and (2.40) the first term on the right hand side can be attributed to the effects of compressibility,

$$\left(\frac{dW_z}{dt}\right)_{comp} = \frac{\Gamma v_{dc}}{4\pi R^2} \quad (4.3)$$

The second term can be attributed solely to the effects of buoyancy,

$$\left(\frac{dW_z}{dt}\right)_b = \frac{-\frac{d\Gamma}{dt}}{4\pi R} = \frac{(\frac{\rho_a}{\rho_0} - 1)g}{(1 + \frac{\rho_a}{\rho_0} [1 + \alpha])}. \quad (4.4)$$

Nevertheless, since the circulation depends on the buoyancy the Kutta-Joukowski force contained in eq. (4.3) is enhanced if the acceleration due to buoyancy goes in the same direction. The circulation is given by an initial circulation, Γ_A , and its increase due to buoyancy, see eq. (4.4). With the instantaneous vortex distance, $R(t)$, known from the isentropic compression the instantaneous velocity, W_z , may be obtained from eq. (4.1).

5. VORTEX PAIR IN GROUND APPROACH

The scenario of a vortex pair in ground approach may be important for departing and arriving aircrafts. So far the hypothesis has been that the vortex pair maintains its identity and that the path of the vortex centers is given by the inductions from the vortex sheet and the other vortex. However, in ground approach the path is also affected by the induction from the image vortex pair. In a homogeneous atmosphere the path of the vortex centers in ground approach is given by,

$$\frac{1}{z_0^2} + \frac{1}{y_0^2} = \frac{1}{R^2}, \quad (5.1)$$

where y_0 and z_0 are the coordinates of the respective vortex center with z_0 as the vertical distance from the ground. The two vortices are parting from each other and at a large lateral distance each again becomes one half vortex pair. The path of the vortex centers, eq. (5.1), is unchanged if compressibility is neglected and buoyancy accounted for. But the velocity at which each vortex center moves along the curve of eq. (5.1) will be reduced according to eq. (3.3) if an inversion is encountered above the ground. The path given by eq. (5.1) is not a hyperbola even though being similar. There also seems to be some experimental evidence that a descending vortex pair regards a strong temperature inversion as a solid surface. In this case the image vortex pair has to be defined in terms of the temperature inversion.

6. NUMERICAL RESULTS

The mass of air accompanying the vortex pair always undergoes an isentropic (adiabatic) change of state even in the case of non-adiabatic stratification of the surrounding atmosphere. However, the density discontinuity at the separating streamline only disappears in the case of an isentropic stratification for which the compressibility effects will be studied in the absence of buoyancy forces. In addition, isentropic stratification does occur since it represents an indifferent equilibrium.

Thus, it may not seem unrealistic to assume a B-747 flying at 5000 m in an isentropically stratified atmosphere. The aircraft data such as weight and take off safety speed are taken from Davies⁹ ($W = 322050 \cdot g [kgm/s^2]$, $v_2 = 170 \text{ knots}$). At sea level the atmosphere's thermodynamic state is assumed to be, $310^\circ K$, 1030 hpa , 1.1575 kg/m^3 giving a density of $\rho_A = 0.75 \text{ kg/m}^3$ at 5000 m. The initial wake strength, i.e. the circulation is calculated from,

$$\Gamma = \frac{W}{\rho v_2 \sqrt{\frac{\rho_{seal}}{\rho}} \frac{\pi}{4} b}, \quad (6.1)$$

where the vortex spacing is found to be initially $(\pi/4)b = 2R_A = 47 \text{ m}$. Circulation and initial descent speed of the vortex pair are, $\Gamma = 822 \text{ m}^2/\text{s}$ and $W_{ZA} = 2.8 \text{ m/s}$. During the descent the velocities in the coordinate system attached to the vortex pair are given by the initial ones multiplied by the factor $\sqrt{\rho/\rho_A}$. They increase with the square root density ratio which is plotted in figure 4.

For a vortex pair arriving at the ground (sea level) this is $\sqrt{\rho/\rho_A} = 1.2387$. However, the forces are proportional to the dynamic pressure of the vortex pair and this goes with the density ratio, $\rho/\rho_A = 1.535$. In this estimation a constant equivalent airspeed (EAS) is already accounted for. The equivalent airspeed is the indicated airspeed (IAS) corrected for position error and compressibility error and the EAS is equal to the true airspeed (TAS) multiplied by the square root density ratio ($\text{EAS} = \text{TAS} \sqrt{\rho/\rho_{gr}}$). In the opinion of this author the 50% force increase is non-negligible.

From the instantaneous descent speed of the vortex pair a formula can be derived for the time, Δt , which has elapsed from the vortex production until to the arrival of the vortex pair at sea level,

$$\Delta t = \frac{T_{sealevel}}{W_{ZA} a 2.25} \left\{ 1 - \left(\frac{\rho}{\rho_{sealevel}} \right)^{0.9} \right\}, \quad (6.2)$$

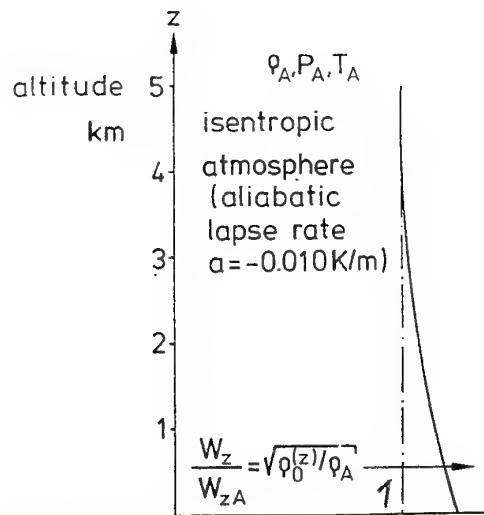


Fig. 4 – Amplification of velocities inside the descending vortex pair at constant circulation in an isentropic atmosphere by the factor $\sqrt{\rho_0/\rho_A}$. ρ_0 instantaneous density depending on altitude, ρ_A initial density at flight altitude.

where $a = -0.01^\circ K/m$ is the adiabatic (isentropic) lapse rate. The vortex wake produced at 5 km altitude according to the above equation arrives after 26.9 minutes at sea level. Assuming an unchanged descent speed 29.8 minutes are obtained, a 3 minutes difference. For a B-747 wake produced at 1 km altitude the figures are 7 and 7.12 minutes, a difference of approximately 7 seconds. Thus, for wakes produced by low flying aircrafts the time correction may be negligible. The whole process is reversed if a vortex pair ascends from sea level. It decelerates because of the downward Kutta-Joukowski force. In addition, it does isentropic work of expansion on the ambient atmosphere.

As an example for the simultaneous effects of compressibility and buoyancy a slightly overadiabatic lapse rate, $a = -0.0105^\circ K/m$, is taken. At flight altitude, 5000 m, the atmospheric state is assumed to be the same as in the previous example, $T_A = 261.2^\circ K$, $\rho_A = 0.75423 \text{ kg/m}^3$, $p_A = 565.5 \text{ hpa(mb)}$. Due to the overadiabatic lapse rate the atmospheric state at sea level is now different, $T = 313, 7^\circ K$; $\rho = 1.13962 \text{ kg/m}^3$; $p = 1026.2 \text{ hpa(mb)}$, from the previous case. The vortex pair is assumed to have been produced by the same aircraft, a B-747. The air accompanying the vortex pair now undergoes an adiabatic change of its state. Therefore the accompanying air is getting increasingly heavier than the surrounding air. From eq. (4.4) and by changing the variable of integration from T to Z with the help of eq. (4.1) the cir-

ulation can be found as a function of the altitude from,

$$\frac{\Gamma d\Gamma}{(4\pi R_A)^2} = \frac{\frac{\rho_A}{\rho_0} \left(\frac{\rho_A}{\rho_0} - 1 \right) g dZ}{\left(1 + \frac{\rho_A}{\rho_0} [1 + \alpha] \right)} \quad (6.3)$$

After the descent from 5000 *m* to sea level the circulation is found to be $\Gamma = 3784.4 \text{ m}^2/\text{s}$. This would result in a descent speed of 12.8 *m/s* for an incompressible vortex pair. However, due to the compressibility the descent speed at sea level is higher by the factor $(\rho_g/\rho_A)^{0.5} = 1.2388$ giving $W_z = 15.875 \text{ m/s}$. To the author such a high descent speed seems not to be unrealistic. Downbursts are known to exceed the above figure in some cases. Compared to the kinetic energy at sea level the initial one at 5000 *m* ($W_z = 2.8 \text{ m/s}$) seems to be marginal.

For the last case the underadiabatic stable lapse rate of the Standard Atmosphere, $a = -0.0065^\circ \text{ K/m}$ is chosen. All other parameters are the same at flight altitude. Due to the underadiabatic lapse rate the accompanying air is getting increasingly lighter than the surrounding. Buoyancy and compressibility are acting in opposite directions. The vortex pair descends until its instantaneous circulation is zero. Evaluating eq. (6.3) for this case it is found that the vortex pair will descend to 315 *m* below flight altitude and then slowly ascend. However, on ascent buoyancy and compressibility again are acting in opposite directions. Circulation and velocity of dilatation are changing their sign, so that the Kutta-Joukowski force still is directed downward while the buoyancy is directed upward.

7. CONCLUDING REMARKS

The wake of the B-747 chosen as an example of application for three different atmospheric stratifications drastically shows the effects of compressibility and buoyancy on the wake propagation. In all three cases the initial descent speed of the vortex pair was 2.8 *m/s* at 5000 *m* flight altitude. In an isentropically stratified atmosphere the wake arrives at sea level at approximately 3.5 *m/s*. A slightly overadiabatic stratification results in 15.9 *m/s* at sea level. The underadiabatic stratification of $a = -0.0065^\circ \text{ K/m}$ of the Standard Atmosphere leads to a preliminary stop and subsequent ascent of the vortex pair at 315 *m* below the flight path. For a still stratified atmosphere a complete analytic treatment has been presented. The effects of compressibility seem not to have been treated this way before as

far as aircraft wake research is concerned. In the case of buoyancy the non-conservation of stagnation pressure inside the vortex pair has been accounted for. Thus, the bound vortex sheet which exhibits a pressure jump inside an incompressible fluid according to Saffman's³ theory is replaced by a free vortex sheet with only a velocity jump. The formulas presented here are fairly simple and should be apt to account for more sophisticated atmospheric stratifications than those dealt with in the numerical examples. The Standard Atmosphere, then, may have no meaning. In conducting in-flight measurements the atmosphere should be monitored as closely as possible. Those data, unfortunately, were not available to the author. The theory presented here should provide a basic understanding of the stratification effects encountered during flights. Also, based on the physics explained here and in-flight data the analytical solutions may be modified, e.g. temperature inversion at some height above the ground. They also may serve as an initial solution to a theory including viscosity, turbulence and/or wind gradients.

REFERENCES

- 1 Vicroy, D., Bowles, R., Brandon, J.M., Greene, G.C., Jordan, jr., F.L., Rivers, R.A., Stewart, E.C., Stough, H.P., Stuever, R.A., "Nasa Wake Vortex Research", Proc. of ICAS 1994 paper No. ICAS-94-6.2.2. 1994, pp.519-528.
- 2 Greene, G.C., "An Approximate Model of Vortex Decay in the Atmosphere", J. of Aircraft, Vol. 23, No 7, July 1986.
- 3 Saffman, P.G., "The Motion of a Vortex Pair in a Stratified Atmosphere", Stud. Appl. Math., Vol. L1, No 2, 1972, pp.107-119.
- 4 Stuff, R., "A Non-viscous Mechanism of Vortex Generation by Non-conservative Forces", submitted to JFM.
- 5 Widnall, S.E., "The Structure and Dynamics of Vortex Filaments", Ann. Rev. Fl. Mech., 7, 1975, pp.141-165.
- 6 Jones, R.T., "Wing Theory", Princeton Uni. Pr. 1990.
- 7 Lamb, H., "Hydrodynamics", 1932 reprinted 1945 by Dover Inc., New York.
- 8 Bjerknes, V., "Das dynamische Prinzip der Circulationsbewegungen in der Atmosphäre", Meteorologische Zeitschrift 17, 1900, pp.97-106.
- 9 Davies, D.P., "Handling the big jets", Civil Aviation Authority, CAA-House, 45-59 Kingsway, London WC2B 6TE, 1990 edition.

Experimental and Numerical Results on Spiral Vortex Breakdown

Sven H. Backstein

Department of Aerospace Engineering
Aachen University of Technology
D-52062 Aachen

1. Summary

Experiments and numerical simulations have been performed to investigate the spiral breakdown of a wing tip vortex in flowfields of adverse axial pressure gradient. The basic idea was to stretch the transition domain between A and B (Fig.1) by a reduction of the imposed pressure gradient. Embedding the vortex in a flowfield with only gradual axial retardation, a stretching could be achieved in both, experiment and calculation,

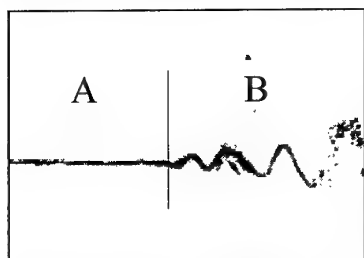


Fig.1: Spiral vortex breakdown

giving some interesting insight into the mechanism of vortex breakdown. The appearance of reversed axial flow, upstream of the spiral, is identified as the distinctive feature of vortex breakdown, that must lead to the loss of axial symmetry and to an unsteady flow.

2. Experimental Setup

The experimental setup consists of a halfmodel of a wing as a vortex generator and an apparatus which permits the variation of the pressure gradient in the outer field (Fig.2). The apparatus is a symmetrical arrangement of a pair of profiles (Fig.3). Their distance H and their angle of attack ϕ can be changed continuously creating a wide range of different pressure fields. By variation of only the parameter ϕ the axial pressure gradient can be decreased continuously down to zero (Fig.4). In the Göttingen-type water tunnel the vortex was visualized by small hydrogen bubbles which were produced at the wing tip by means of electrolysis.

3. Flow Picture

Due to their low density in comparison with the surrounding fluid, the bubbles suffer very low centrifugal forces. Thus they concentrate in the center of the vortex, where the pressure minimum resides. Even if the vortex axis is turned into a spiral path a clearly visible bubble line is conserved, showing neither a kink



Fig.2: Experimental setup

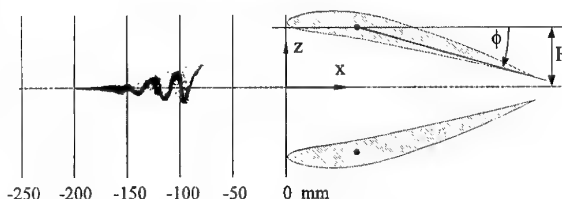


Fig.3: Pressure field generator

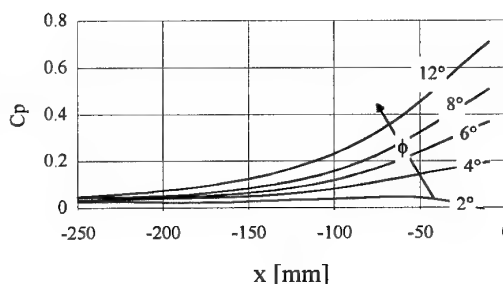


Fig.4: Pressure distribution along the axis

nor an abrupt expansion in space. As a function of pressure gradient, different spiral shapes were observed (Fig.5). For low values of the angle ϕ the vortex becomes a nearly straight line. If ϕ is increased, the vertex angle of the spiral also increases. The inclination of the vortex axis leads to a self-induction effect: Since

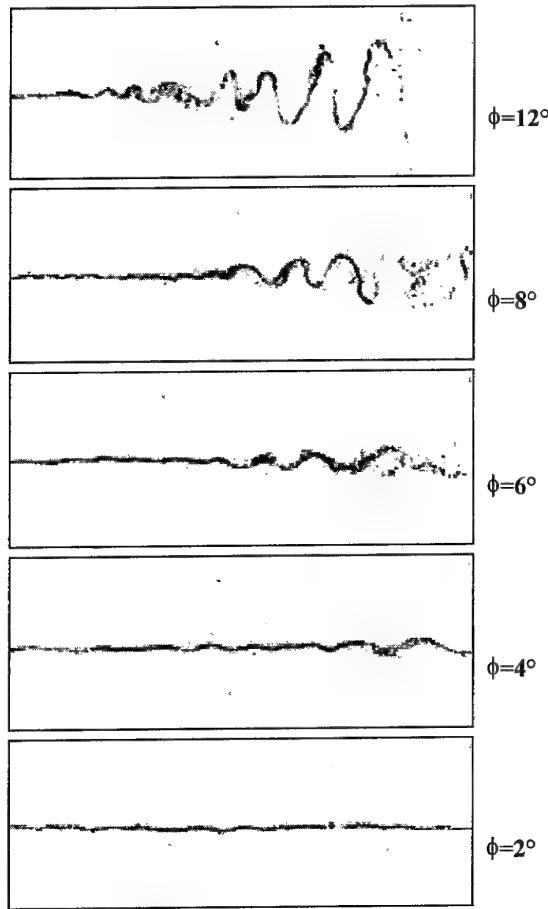


Fig.5: Spiral shape as a function of imposed pressure gradient, $U_\infty = 1.0 \text{ m/s}$

the tangential velocity has a component in axial direction, upstream velocities are induced which amplify the imposed flow deceleration on the spiral axis. A further result of self-induction is the appearance of stochastic distortions of the vortex center line. Stepping from one picture to the next an almost steady transition of the shapes of the vortex axes is found. If vortex breakdown is an abrupt change from one state to another, as usually assumed, the flow picture leads to the conclusion that a spatial expansion of the vortex core or its evading movement into a spiral path must be secondary effects, which may occur gradually.

4. Velocity Measurements

The above conclusion is supported by velocity measurements carried out using the LDV technique. Due to the unsteadiness of the flowfield, averaged velocity profiles, obtained by LDV, require an appropriate interpretation. Already the vortex upstream of the breakdown regime is subject to disturbances called 'vortex wandering', which is an unsteady stochastic motion of small amplitude in radial direction. The location (η, ζ) of the vortex center in a tunnel-fixed

coordinate system (Fig.6) is time dependent. One important consequence of this effect is, that the measured profile of the tangential velocity component, which is representative for the vortex structure, reveals lower maximum values than obtained in an undisturbed case. If a coordinate system is introduced in which the x-axis is approximately the center line of the straight part of the vortex (Fig.7), the connection between the

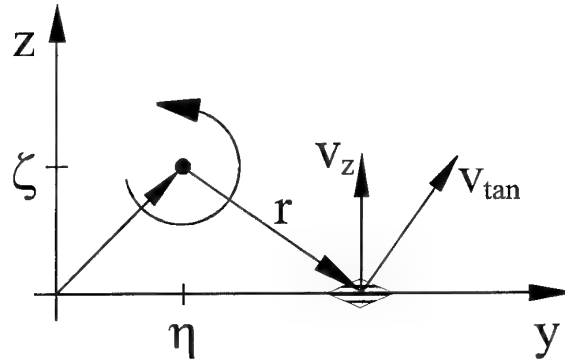


Fig.6: Vortex center position and measuring volume

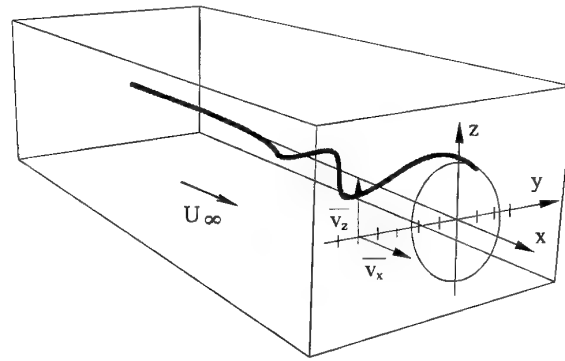


Fig.7: Coordinate System

measured mean vertical velocity profile $\bar{v}_z(y)$ and the true tangential velocity profile $v_{\tan}(r)$ can be given:

$$\bar{v}_z(y) = \int_{-\infty}^{\infty} \int_{-\infty}^{\infty} \frac{y - \eta}{r} v_{\tan}(r) \cdot p(\eta, \zeta) \cdot d\eta d\zeta \quad (1)$$

The probability distribution $p(\eta, \zeta)$ of the vortex center position was derived experimentally using a Laser Light Sheet to illuminate the bubbles in a plane $x = \text{const}$ over a long period of time and recording the flow picture on a video tape. The analysis of the recordings, performed with an automatic picture processing system, provided data which are in good agreement with a two dimensional Gaussian distribution:

$$p(\eta, \zeta) = \frac{1}{2\pi\sigma^2} \cdot e^{-\frac{\eta^2 + \zeta^2}{2\sigma^2}} \quad (2)$$

In the spiral domain a good approximation is obtained by a modified Gaussian distribution:

$$p(\eta, \zeta) = \frac{1}{4\pi^2\sigma^2} \int_0^{2\pi} e^{-\frac{(\eta - r_\sigma \cos\varphi)^2 + (\zeta - r_\sigma \sin\varphi)^2}{2\sigma^2}} d\varphi \quad (3)$$

where r_σ can be interpreted as the mean spiral radius. For $r_\sigma = 0$ Eq.(3) reduces to Eq.(2). If for the tangential velocity profile $v_{\tan}(r)$, the vortex model

$$v_{\tan}(r) = \frac{\Gamma}{2\pi \cdot r} \cdot \frac{r^2}{r^2 + r_c^2} \quad (4)$$

is chosen, which is especially suitable for wing tip vortices, the vortex structure can be obtained from a Least Squares Approximation:

$$\sum [\bar{v}_z(y_i) - \bar{v}_{z_{\text{reconstructed}}}(y_i)]^2 \rightarrow \min \quad (5)$$

Fig.8b shows the measured velocity profiles (marker points) and the reconstructed profiles (solid lines) of four planes normal to the axis. In plane ① and ② the vortex is approximately straight (Fig.8a), and the velocity profile is not significantly changed. Entering the spiral domain the maximum velocities are strongly reduced and the vortex core appears to be much wider than upstream of the spiral. This is mainly an effect of the stochastic motions of the vortex axis. The reconstructed vortex structure (Fig.8c) shows only slightly reduced maximum velocities in the spiral domain, together with a slightly increased core radius. In agreement with the visualization results a drastical core widening does not occur at the transition from the straight to the spiral domain.

Another feature, generally stated as distinctive for vortex breakdown, is the appearance of an internal stagnation point on or near the axis. LDV measurements of the mean axial velocity component $\bar{v}_x(y)$ show flow reversal on the spiral axis only for the strongest pressure gradient ($\Phi = 12^\circ$), whereas upstream of the spiral and for the weaker pressure gradients no reversed flow can be detected (Fig.9). This might lead to the conclusion that vortex breakdown can take place without stagnation, but it has to be kept in mind that averaging measurements in an unsteady flowfield fail to resolve events of small spatial and/or temporal extent.

5. Numerical Simulation

In addition to the experimental investigations, some numerical simulation of vortex breakdown at low pressure gradients has been carried out giving further interesting and surprising insight. On an equidistant staggered grid of $181 \times 101 \times 101$ grid points the 3D-Euler equations are solved using a 4-step Runge Kutta

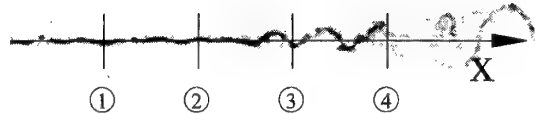


Fig.8a: Experimentally observed vortex center line in sideview, $U_\infty = 0.5 \text{ m/s}$

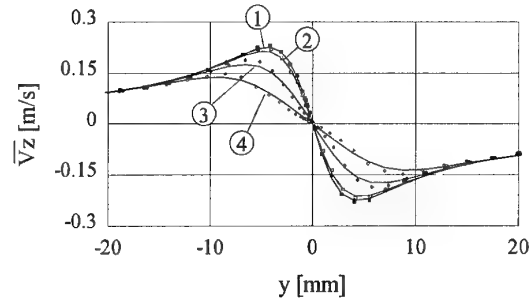


Fig.8b: Measured and reconstructed mean velocity profiles

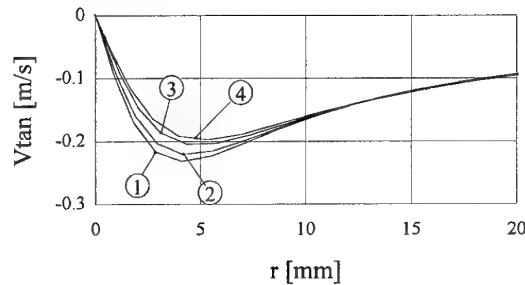


Fig.8c: Vortex structure at different axial stations

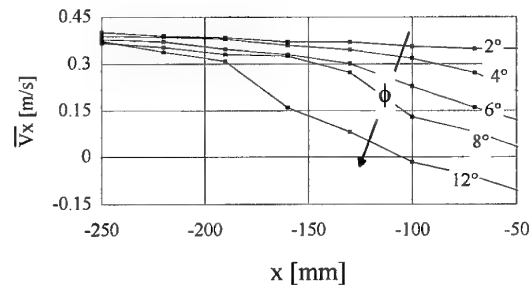


Fig.9: Axial velocity on the spiral axis in different pressure fields

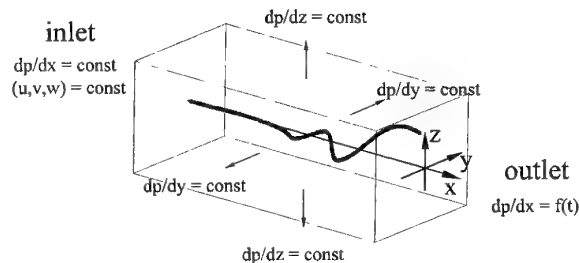


Fig.10: Control volume of the calculation

convection scheme. A grid resolution of $dx = dy = dz = r_c/4$ was chosen, based on the core radius in the inlet plane. Since the flow is not bounded by walls (Fig.10), a mass flux through the lateral boundaries is permitted. Neumann boundary conditions are used: At the inlet and lateral boundaries the normal pressure gradients $\partial p / \partial \bar{n}$ are kept constant during the calculation. They are derived at the beginning of the calculation by the momentum equation:

$$\frac{\partial v_n}{\partial t} + \frac{\partial}{\partial t}(u \cdot v_n) + \frac{\partial}{\partial t}(v \cdot v_n) + \frac{\partial}{\partial t}(w \cdot v_n) + \frac{\partial p}{\partial n} = 0 \quad (6),$$

assuming acceleration-free boundaries $\partial v_n / \partial t = 0$. In the outlet plane, $dp/d\bar{n}$ is calculated after each time step. As the initial flowfield, a straight vortex, embedded in a flow with retardation in axial direction, is given. The vortex, of wake type, is described analytically by Eq. (4) and in axial direction by:

$$v_x(r) = U_\infty \cdot \left(1 - \delta \cdot e^{-\left(\frac{r}{r_\delta}\right)^2}\right) \quad (7).$$

The parameters $\Gamma, r_c, U_\infty, \delta, r_\delta$ and the outer flowfield with axial retardation are derived from measurements permitting a comparison of experimental and numerical

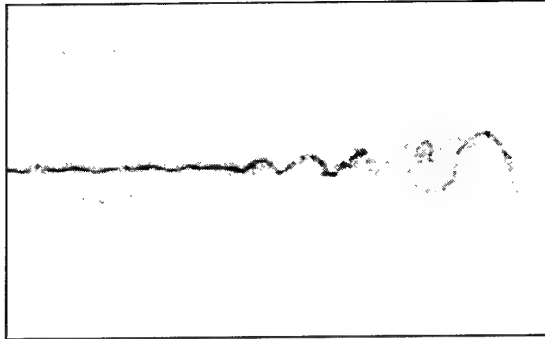


Fig.11a: Vortex center line as obtained from the experiment

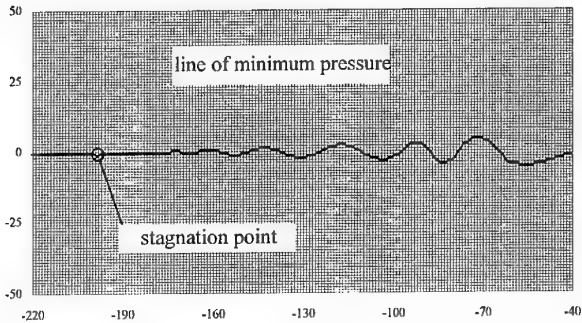


Fig.11b: Vortex center line as obtained from the calculation

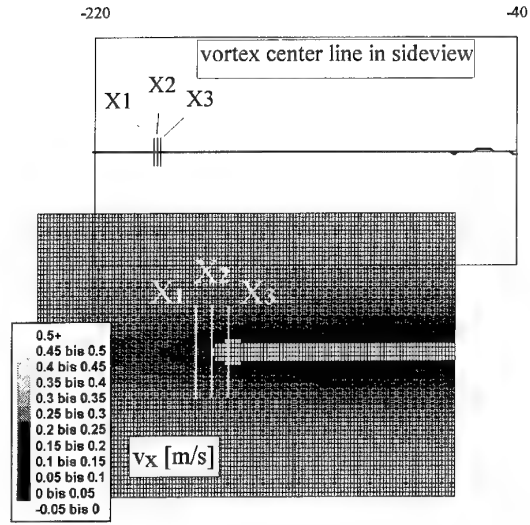


Fig.12: Stagnation of the axial flow far upstream of the spiral

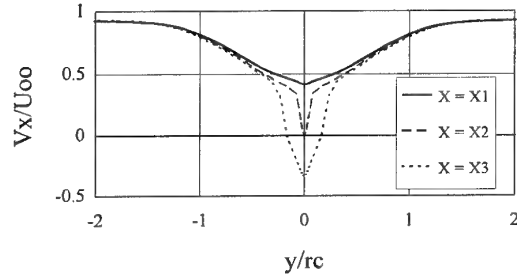


Fig.13: Profiles of axial velocity ($r_c = 4\text{mm}$)

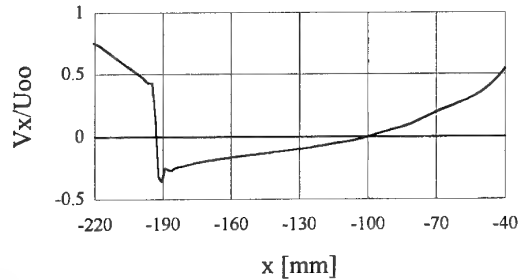


Fig.14a: Axial velocity on the vortex axis

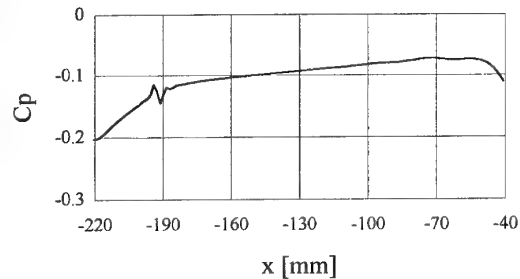


Fig.14b: Pressure on the vortex axis

results. An impression of the topology of the calculated flowfield can be obtained, considering the line of minimum pressure in sideview. Fig.11 shows the experimental and numerical results in equal scales. The calculated vortex center line shows a good agreement with one observed in the experiment. The formation of the spiral begins at about the same axial position, and also the observed spiral radius is reproduced by the calculation, except for the vicinity of the outlet plane.

The most interesting result of the calculation is the appearance of a stagnation point far upstream of the spiral (Fig.11b), which has not been found by the experiments. The measured axial velocities show reverse flow only in the fully developed spiral regime. At weaker pressure fields even spirals are observed without any stagnation. By analogy with the experiment, the imposed pressure gradient was varied in the calculation. Even in the case of a very weak pressure field a stagnation point appears. In this case only a slight spiral is formed far downstream of the stagnation point (Fig.12). The recirculation domain is axisymmetrical and has a bubble like shape. Fig.13 shows the development of the axial velocity profile in three sections near to the stagnation point. A drastical change of the velocity profiles takes place. The flow reversal is limited to a region very close to the vortex axis. Its maximum radial extent is only about the fourth part of the core radius. Consequently it could not be resolved by LDV measurements, since the measuring volume is of the same order of magnitude, and measurements are disturbed by vortex wandering.

The velocity distribution along the axis shows a change from a positive to a negative axial velocity of almost 'jump' like character. Far downstream of this jump the positive axial velocity is recovered, with a moderate gradient (Fig.14). The axial extent of the recirculation domain is very large in comparison with its radial extent.

6. Consideration of axial Momentum

For a better understanding of the results obtained from both experiment and flow calculation, a theoretical consideration is helpful, that derives, at which axial positions along the axis a steady flow is possible. A model of the axial velocity distribution on the axis is introduced, in which the flowfield is subdivided into four regions, depending on the signs of v_x and $\partial v_x / \partial x$ (Fig.15). The product of both terms plays an important role in the axial momentum equation, which will be considered in cylindrical coordinates:

$$\frac{\partial v_x}{\partial t} + \left(v_\varphi \cdot \frac{\partial v_x}{\partial \varphi} \right) + \left(v_r \cdot \frac{\partial v_x}{\partial r} \right) + \left(v_x \cdot \frac{\partial v_x}{\partial x} \right) + \frac{1}{\rho} \cdot \frac{\partial p}{\partial x} = 0 \quad (8)$$

In table 1 the terms of Eq.8 are evaluated on the axis. A steady solution requires that the first term: $\partial v_x / \partial t$ is

zero. If the solution is axisymmetrical, also the second

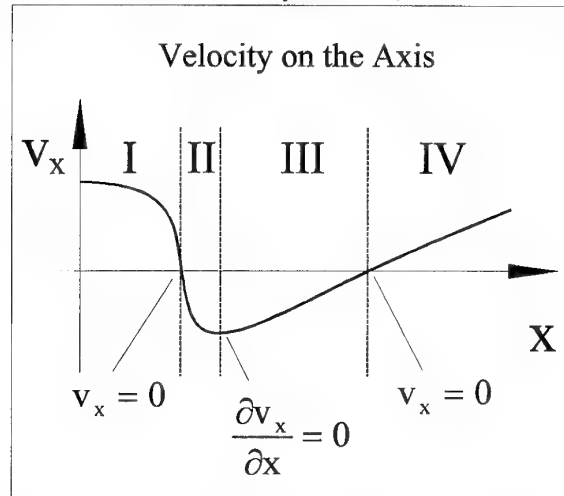


Fig.15: Model of the axial velocity distribution on the vortex axis

	$\frac{\partial v_x}{\partial t}$	$\left(v_\varphi \cdot \frac{\partial v_x}{\partial \varphi} \right)$	$\left(v_r \cdot \frac{\partial v_x}{\partial r} \right)$	$\left(v_x \cdot \frac{\partial v_x}{\partial x} \right)$	$\frac{\partial p}{\partial x}$	flow state
I	0	0	0	-	+	steady
II	-/0	0	0	+	+/-	unsteady/steady
III	0	0	0	-	+	steady
IV	≈ 0	$\neq 0$	$\neq 0$	+	+	unsteady

Table 1: Consideration of the axial momentum equation

and the third term must be zero. In this case the equilibrium must be balanced by only the fourth and the fifth term. Only if they are of opposite sign a steady and axisymmetrical solution is possible. This is the case in the regions I and III.

In region I the fourth term is negative, while due to the imposed pressure field the fifth term is positive. Thus the steady solution, obtained in the calculation, is justified.

Entering region II the fourth term becomes positive and, hence, cannot be compensated by a positive pressure gradient. Both a steady and an unsteady solution are possible, still conserving axial symmetry. In the steady case the axial pressure gradient must become negative. In the case of an unsteady solution the accelerative term $\partial v_x / \partial t$ becomes negative, leading to a further deceleration of the axial velocity.

In the calculation an almost steady position of the stagnation point is obtained, together with a large amount of the velocity gradient $\partial v_x / \partial x$. The velocity gradient stays nearly constant in time and the flow is almost axisymmetrical. Consequently a negative pressure gradient is obtained (Fig.16). The appearance of a negative pressure gradient is remarkable since the vortex is embedded in an outer flowfield of increasing pressure.

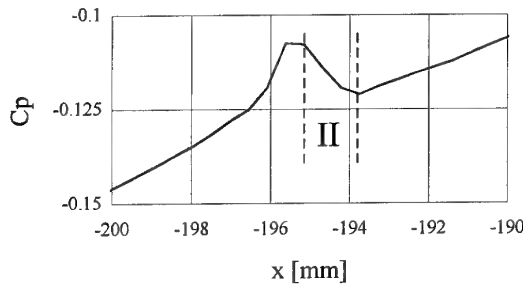


Fig. 16a: Pressure distribution along the vortex axis

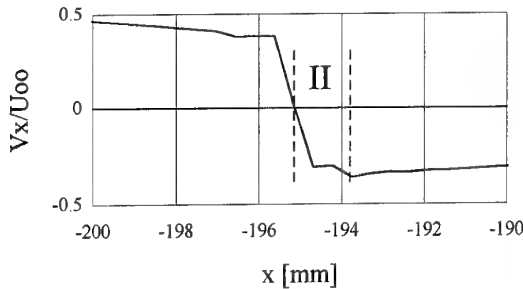


Fig. 16b: Axial velocity distribution along the vortex axis

In region III a steady solution requires a positive pressure gradient on the axis. As Fig. 14b shows, this requirement is satisfied in the calculation.

In region IV a steady axisymmetrical solution is not possible, because the fourth and the fifth term are of equal signs. If axisymmetry is conserved the accelerative term $\partial v_x / \partial t$ must become negative and, hence, the 'recovery point' must be moved downstream, leading to an extinction of region IV. If it should stay at a constant position, the second and/or the third term must become unequal zero, leading to a loss of axial symmetry. In the calculation the recovery point is slightly moved upstream and downstream but it stays at an almost constant averaged position. Downstream of it, an unsymmetrical solution is obtained. We find a low axial velocity gradient (see Fig. 14) and the evasive motion of the vortex axis into a spiral path (see Fig. 12).

It has to be emphasized that the loss of symmetry is a necessary consequence at the position where the reversal of axial flow ends. The bubble like recirculation domain of finite extent, which appears to be characteristic for vortex breakdown, must be followed by a spiral-like deformation of the vortex axis. Contributions on vortex breakdown found in literature are mostly focussed either on a bubble type breakdown or on a spiral type breakdown. This distinction between two breakdown modes does not seem to be appropriate, because both phenomena are coupled.

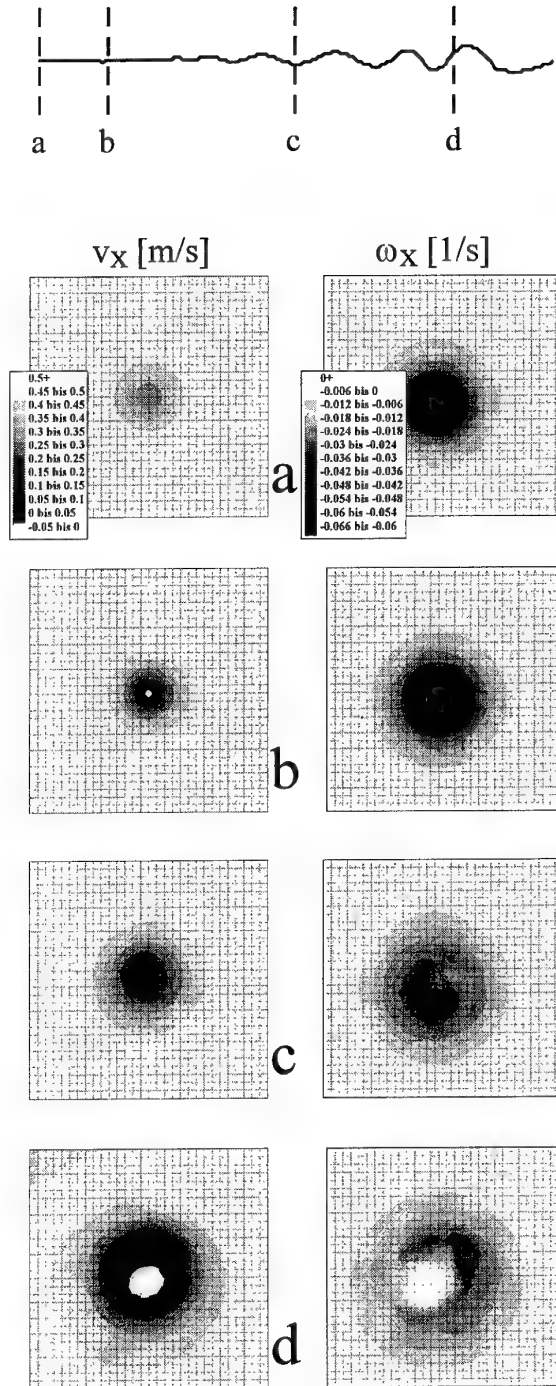


Fig. 17: Development of axial velocity and axial vorticity

In the spiral domain the vortical structure undergoes further significant changes, which shall not be discussed here in detail. Just to give an overview, the distributions of axial velocity and axial vorticity in four planes normal

to the spiral axis are presented, as obtained from the calculation (Fig.17).

7. Conclusions

- If tip vortices are embedded in pressure fields with a sufficient positive pressure gradient vortex breakdown of 'spiral type' is observed.
- A stretching of the transition from a straight to a spirally shaped vortex could be achieved by application of very weak pressure fields, permitting a spatial separation of characteristic phenomena of vortex breakdown, which were visualized and measured using LDV.
- The flow observed in the experiments could be simulated by numerical calculations, providing spiral breakdown of comparable topology. The more detailed resolution of the calculations reveals an axisymmetric recirculation bubble upstream of the spiral domain, which appears to be a prerequisite for the loss of axisymmetry.
- In the weak pressure fields considered here, the stagnation in the breakdown bubble appears in an almost jump-like manner and is of very small radial extent, which could not be resolved by LDV measurements.

8. Acknowledgement

This work was supported by the Deutsche Forschungsgemeinschaft (DFG) within the frame of the Sonderforschungsbereich 25 (SFB 25). The author is greatly indebted to Prof. Dr.-Ing. R. Staufenbiel and Dr.-Ing. D. Coors for their constructive comments, suggestions and valuable discussions.

Computational and Experimental Investigation of the Wakes shed from Flapping Airfoils and their Wake Interference/Impingement Characteristics

C.M. Dohring, M.F. Platzer, K.D. Jones, I.H. Tuncer
Department of Aeronautics and Astronautics
Naval Postgraduate School
Monterey, CA 93943

1. SUMMARY

Computational and experimental water tunnel investigations of the wakes shed from flapping airfoils are described. It is shown that there exists a critical non-dimensional plunge velocity above which the wake changes from a symmetric thrust-producing vortical structure to an asymmetric lift and thrust-producing one. Furthermore, it is found that the impingement of the wake generated by a flapping airfoil on a stationary airfoil produces a significant thrust augmentation on the flapping/stationary airfoil combination. Similarly, there exists a beneficial ground interference effect if the airfoil is flapping near a stationary wall. The experimental data are based on flow visualization using a two-color dye injection technique and laser-doppler velocimetry. The numerical results are obtained from an unsteady inviscid incompressible two-dimensional panel code and from a two-dimensional Navier-Stokes code. Comparisons between the experimental and numerical results show good agreement.

2. INTRODUCTION

Our interest in the flow physics of flapping airfoils and of flapping/stationary airfoil combinations derives from several fundamental and applied aspects. As first recognized by Knoller (1909) and Betz (1912), a flapping airfoil generates thrust. This Knoller-Betz effect was first confirmed experimentally by Katzmayer (1922). The first theoretical investigations of the aerodynamics of flapping airfoils were based on flat-plate airfoil theory, notably those of von Karman and Burgers (1935) and Garrick (1936), who showed that the propulsive efficiency of flapping airfoils is rather poor (not exceeding 50 percent) unless the airfoil is flapping rather slowly. Schmidt (1965) proposed the tandem airfoil arrangement and demonstrated

experimentally that a stationary airfoil positioned in the wake of a flapping airfoil nearly doubles the propulsive efficiency of the single flapping airfoil because the stationary airfoil converts the vortical energy generated by the flapping airfoil into additional thrust. This experimental finding was confirmed by Bosch (1978) who showed by means of an oscillatory flat-plate analysis that a sinusoidally flapping airfoil upstream of a stationary airfoil increases the propulsive efficiency of such an arrangement to almost 100 percent.

These inviscid flat-plate analyses represent, of course, only idealized flow features and leave unanswered questions about the effect of airfoil geometry and of real (viscous) fluid effects. For these reasons, we have performed water tunnel tests to obtain the necessary experimental data and we have developed potential flow panel codes, viscous-inviscid interaction solutions and Navier-Stokes solutions for single and two-foil systems for the systematic study of the wake characteristics and of the interaction effects with another airfoil or with a solid wall.

These computational and experimental investigations are described in the following sections.

3. COMPUTATIONAL APPROACHES

3.1 Unsteady Panel Code

The unsteady panel code models the wake by releasing a discrete vortex at each time step equal in magnitude and opposite in direction to the change in circulation about the airfoil from the previous time step. After release the vortex is convected downstream, influencing and being influenced by the airfoil and the other discrete wake vortices. This scheme is shown in Figure 1. In order to

enable visualization of the unsteady wake formation and evolution an interactive graphics animation interface was developed which greatly facilitates the understanding of the vortex shedding phenomena. Further details are given by Platzter et al (1993), Jones et al (1996), Jones & Center (1996), Teng (1987) and Pang (1988).

3.2 Navier-Stokes Code

The Navier-Stokes code is based on the strong conservation-law form of the compressible two-dimensional, thin-layer Navier-Stokes equations in a curvilinear coordinate system. The flow field is assumed to be laminar. The computational domain is discretized by C-grids. In the case of airfoils in tandem individual C-grids are first generated around each airfoil. Depending on the specified distance between the airfoils, the grids are then overlapped at the downstream edge of the upstream grid and the upstream edge of the downstream grid. Additional details are described by Tuncer & Platzter (1996).

3.3 Viscous-Inviscid Interaction Method

In the viscous-inviscid interaction solution, developed by Tuncer et al (1995), the two previous methods are combined in such a way that the computational domain is partitioned into two zones, a near field and a far field zone. The near field zone encompasses the viscous boundary layer and wake regions, and the neighbouring inviscid flowfield. An inner boundary is then placed in the inviscid flow region close to the outer boundary of the near field computational domain. Source and vortex panels are then placed on the inner boundary rather than on the airfoil surface for the solution of the potential flow equation. The flowfield in the far field is computed by the potential flow solution, which in turn computes the outer boundary conditions of the near field computational domain for the Navier-Stokes solution. A vortex shedding process similar to the one in the potential flow solution is modelled to account for the unsteady vortical wake.

4. EXPERIMENTAL APPROACH

4.1 Water Tunnel Tests

Experiments were carried out in the Naval Postgraduate School water tunnel facility to visualize and to measure the wake characteristics generated by flapping airfoils. This tunnel is a closed circuit, continuous flow facility with a contraction ratio of 6:1 and horizontal orientation as shown in Figure 2. The test section is 38 cm wide, 51 cm high, and 150 cm long. The flow velocity can be set in a range from 0 to 0.5 m/s. The flow visualization

experiments were conducted with a 1 cm chord length airfoil similar to a NACA 0012 foil. For the laser-doppler measurements a NACA 0012 airfoil with a chord length of 2 cm and 10 cm was used. Both airfoils have a wing span of 37 cm and stretch across the whole test section. The airfoils are attached to a vertical shaker which is mounted on the top of the test section. The frequency can be adjusted continuously from 5 Hz to 60 Hz. The amplitude can be adjusted from zero to a maximum value which depends on the frequency. The LDV measurements were performed with a dual beam frequency shifted 300 mW Argon Ion laser with a beam separation of 50 mm, a focal length of 350 mm and back scatter receiving optics. The vertical distribution of the mean streamwise velocity component was measured upstream and downstream of the flapping airfoil.

5. RESULTS

5.1 Wakes Shed from Single Flapping Airfoils

Qualitative and quantitative comparisons of the wake structures shed from a flapping airfoil are shown in Figure 3. The reduced flapping frequency is defined as

$$k = 2\pi f c/U$$

where f is the frequency of oscillation, c is the airfoil chord, and U is the flow velocity. If this reduced frequency is multiplied with the non-dimensional flapping amplitude h/c a non-dimensional maximum plunge velocity can be defined as $v_p = k(h/c)$.

Figure 3 shows the vortical wake produced by an airfoil which is flapping sinusoidally with a non-dimensional amplitude of $h/c = 0.2$ at a reduced frequency of 3.0. The flow velocity is 10.5 cm/s yielding a Reynolds number of 1040. It is seen that the wake is symmetric about the center line, and the wake vortices are evenly spaced. Note that the upper vortices are counter-clockwise and the lower ones are clockwise. Such a vortex pattern is indicative of a thrust producing pattern. This symmetric wake behavior is also observed for lower frequencies, the only difference being the vortical wave length. As the frequency increases, the wave length becomes shorter. However, there is an upper non-dimensional plunge velocity limit beyond which the vortical wake pattern changes from a symmetric pattern to an asymmetric one because the large eddies begin to pair up and travel away from the centerline. Tests with three different airfoil chords showed that this pairing and switching to an asymmetric wake occurs at a non-dimensional plunge velocity of approximately 1.

Before discussing the asymmetric wake behavior it is instructive to examine the symmetric case. In Figure 4 the results of computations of the time-averaged velocity profiles upstream and downstream of a flapping airfoil are shown using the unsteady panel code. The non-dimensional flapping amplitude is 0.1. The profiles are depicted at three different locations, 0.5 chord lengths upstream and 1.5 and 3 chord lengths downstream of the airfoil leading edge. The reduced frequency is 10. It can be seen that the airfoil produces a jet profile downstream of the trailing edge and that the maximum jet velocity exceeds the free-stream value by a factor of 2.4. The flapping airfoil therefore imparts a momentum increase to the fluid which manifests itself as airfoil thrust. It is also interesting to observe the amount of flow which is captured by the flapping foil, as manifested by the velocity distribution upstream of the leading edge. It is seen that the capturing area extends to roughly three chord lengths above and below the airfoil. In Figure 5 a comparison is given between the computed and measured time-averaged velocity profile at $0.75c$ downstream of an airfoil, flapping at a reduced frequency of 8.4 with a non-dimensional flapping amplitude of 0.088. It is seen that there is good agreement between the measurement and the computation.

If the product of reduced frequency and non-dimensional flapping amplitude is increased beyond a critical value, such that the non-dimensional maximum plunge velocity becomes approximately one, the vortical wake pattern becomes asymmetric, as shown in Figure 6. The vortical wake can be directed either upward or downward and therefore generates not only thrust but also a finite average lift. This experimentally observed asymmetric vortex pattern is also found in the numerical computations using the unsteady panel code. The inclination of the vortex pattern (up or down) is determined by the starting conditions used in the panel code. The qualitative agreement between the numerical and experimental wake structures is excellent. Even the small remnants of vorticity, visible at the bottom of Figure 6, that break off from the vortex pairs at higher frequencies are consistent in both approaches.

5.2 Flapping Wake Impingement Effect

As already shown by Garrick (1936), the propulsive efficiency of an airfoil which executes a pure flapping oscillation is rather poor unless the flapping occurs at small frequency. Therefore, there was little incentive to consider flapping foils for propulsive applications. However, as pointed out by Schmidt (1965) and Bosch (1978), the thrust and the propulsive efficiency of a tandem airfoil configuration exceed the values achievable

with a single flapping airfoil by a substantial amount if the stationary airfoil is positioned behind the flapping airfoil. This finding can be confirmed using both the unsteady panel code and the Navier-Stokes code. Figure 7 shows a comparison of such computations for a tandem NACA 0012 airfoil combination. As expected, the inviscid panel code predicts more optimistic values than the Navier-Stokes code. For further details of the Navier-Stokes computations we refer to Tuncer & Platzer (1996).

5.3 Wall Effect

Another interesting effect occurs if the airfoil executes a pure flapping oscillation in close proximity to a flat plate. Figure 8 presents a comparison of the measured time-averaged velocity distribution 0.75 chord length downstream of the trailing edge of a 20 mm chord airfoil which executes a flapping oscillation with a non-dimensional flapping amplitude of 0.088 at a reduced frequency of 57 (based on free-stream velocity). It is seen that there is a significant velocity increase as the airfoil is positioned closer to the wall (4 mm rather than 8.5 mm). Also shown, for comparison, is the velocity distribution without the flat plate. The leading edge of the airfoil was located 100 mm downstream of the leading edge of the flat plate. Therefore the airfoil was embedded in the laminar boundary layer of the flat plate. Figure 9 shows the achievable velocity increase due to the wall interference effect. It is seen that the velocity can be doubled if the airfoil is placed within the boundary layer.

This flow behaviour could be confirmed with Navier-Stokes calculations. Figure 10 depicts the computed thrust coefficient for an airfoil which is flapping with a non-dimensional amplitude of 0.088 and a reduced frequency of 4.2. It is seen that the thrust increases as the non-dimensional airfoil distance from the wall is decreased to values less than 1.5.

This wall effect can also be simulated to some extent by the inviscid unsteady panel code. It is well known that the aerodynamic characteristics of an airfoil flying close to the ground can be calculated by placing an image airfoil and computing the inviscid flow over the two-airfoil combination. Similarly, the ground effect on a flapping airfoil can be computed with the two-airfoil code described by Pang (1988) if the two airfoils are flapping in counter-phase. The application of this code produces the vortical wake patterns shown in Figure 11 and the thrust curves depicted in Figure 12. It is seen that there is a significant thrust increase generated by each airfoil if they are flapping in close proximity to each other. Furthermore, the thrust increases nonlinearly with reduced frequency. These results are quite consistent with the

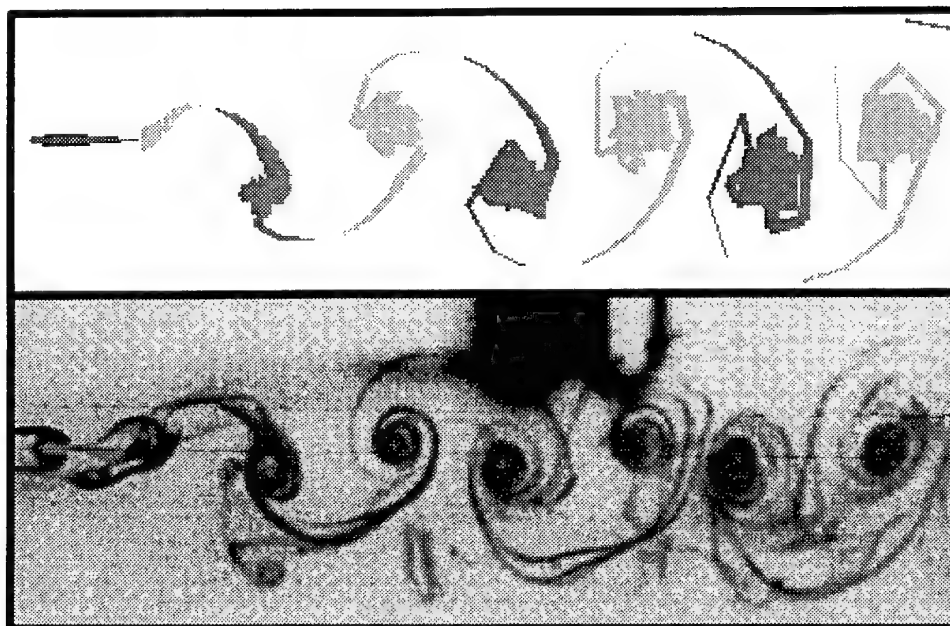


Fig. 3 Wake Comparison
 $k = 3.0$ $h/c = 0.2$

The upper figure shows the panel code computed wake.
 The lower figure shows the wake flow visualization.

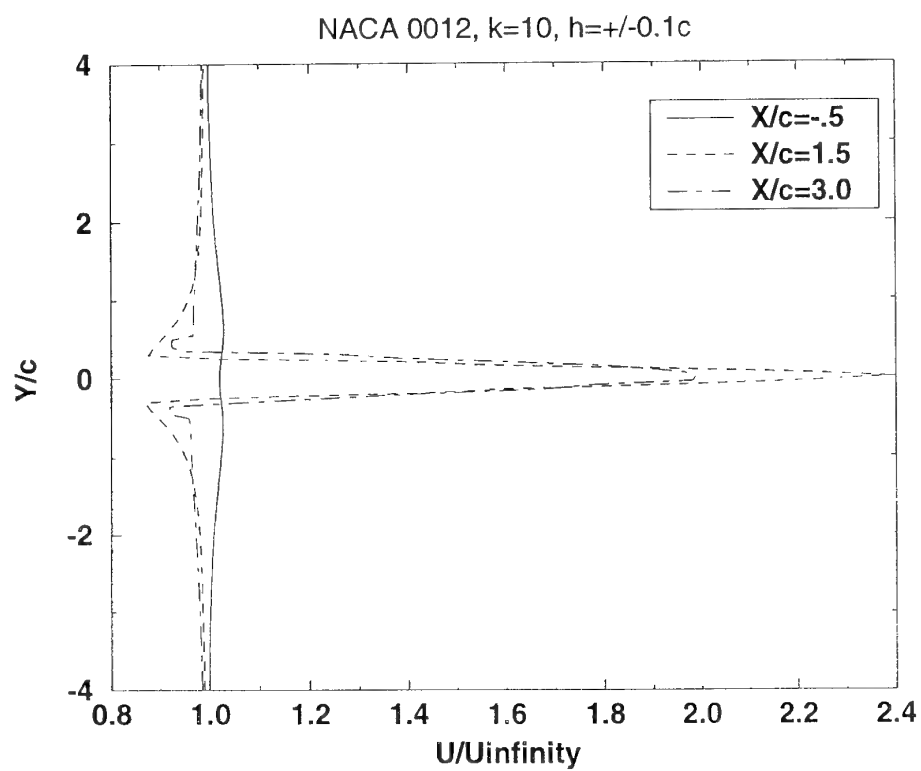


Fig. 4 Computed Velocity Profiles

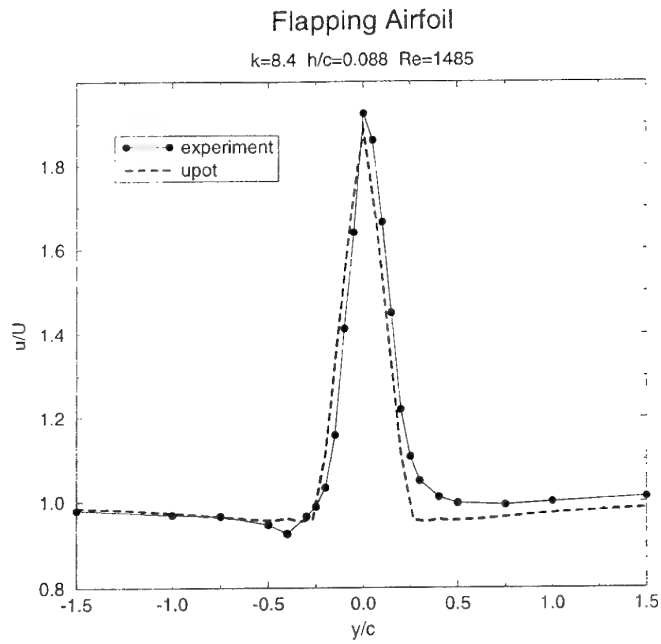


Fig. 5 Comparison of Time-Averaged Measured and Computed Velocity Profile

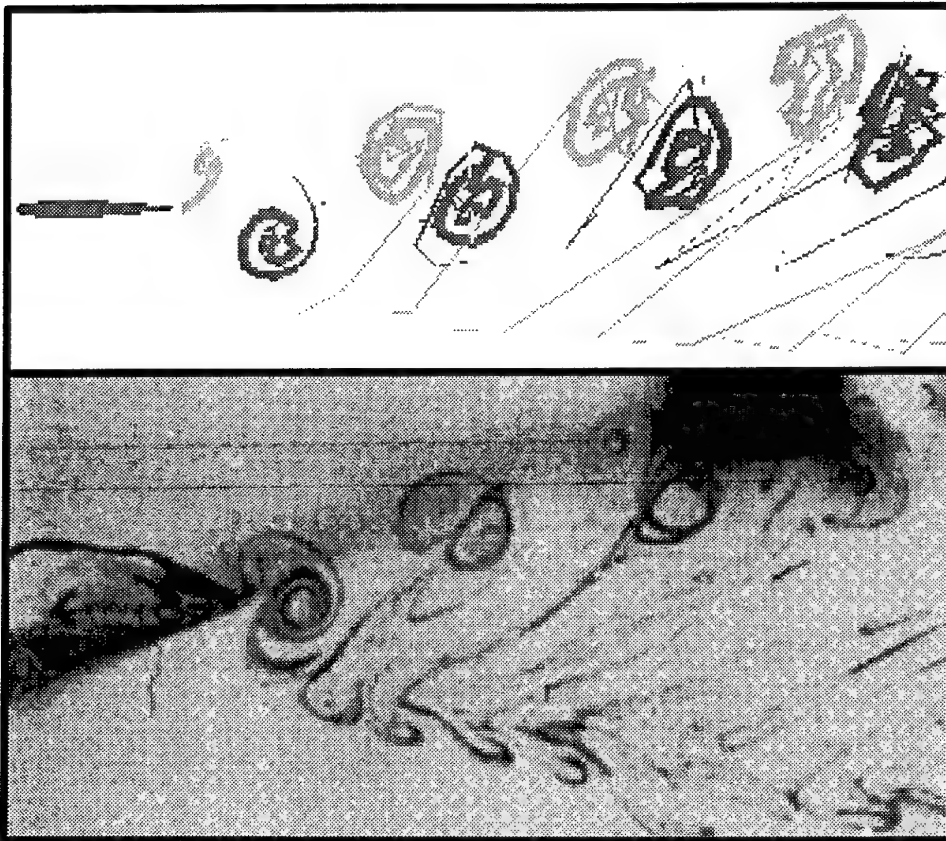


Fig. 6 Wake Comparison

$k = 10.1$ $h/c = 0.2$

The upper figure shows the panel code computed wake.
 The lower figure shows the wake flow visualization.

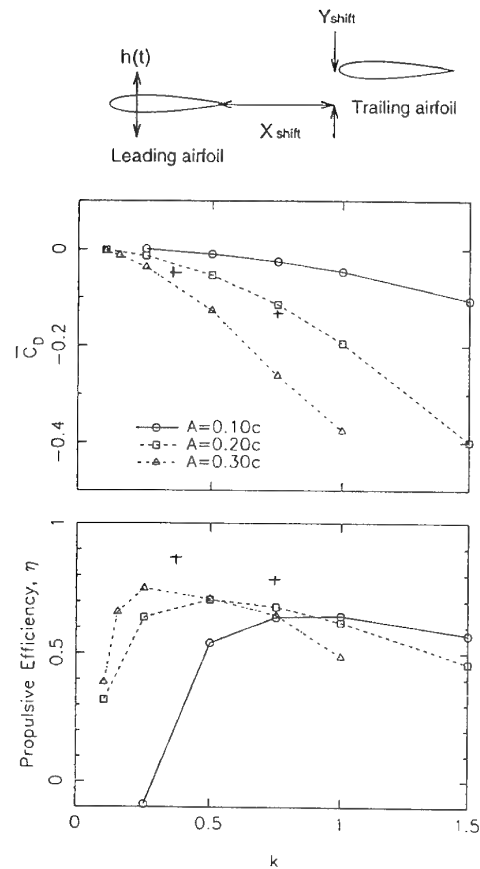


Fig. 7 Navier-Stokes Computed Thrust and Propulsive Efficiency
for Tandem Configuration
(+ indicates panel code computation)

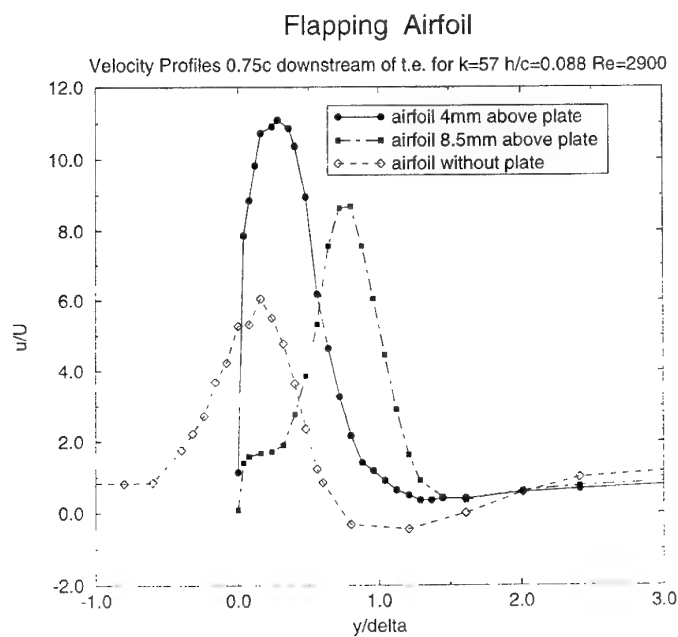


Fig. 8 Measured Velocity Profiles

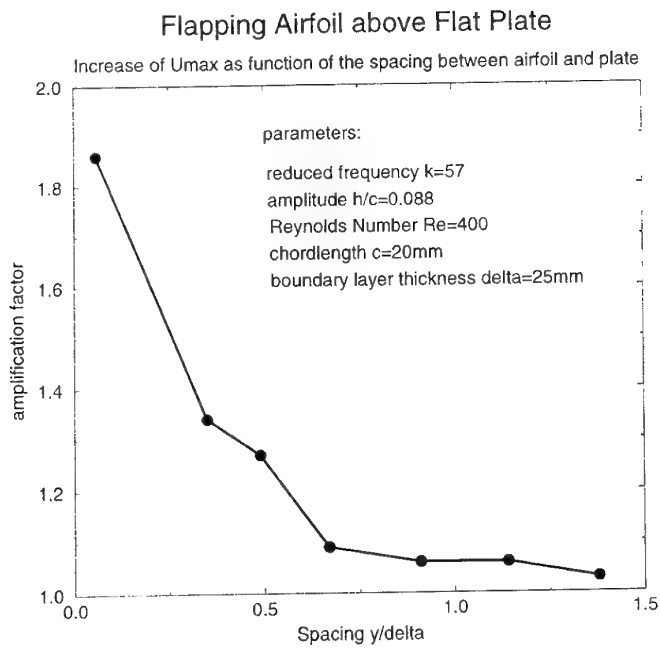


Fig. 9 Measured Maximum Velocity

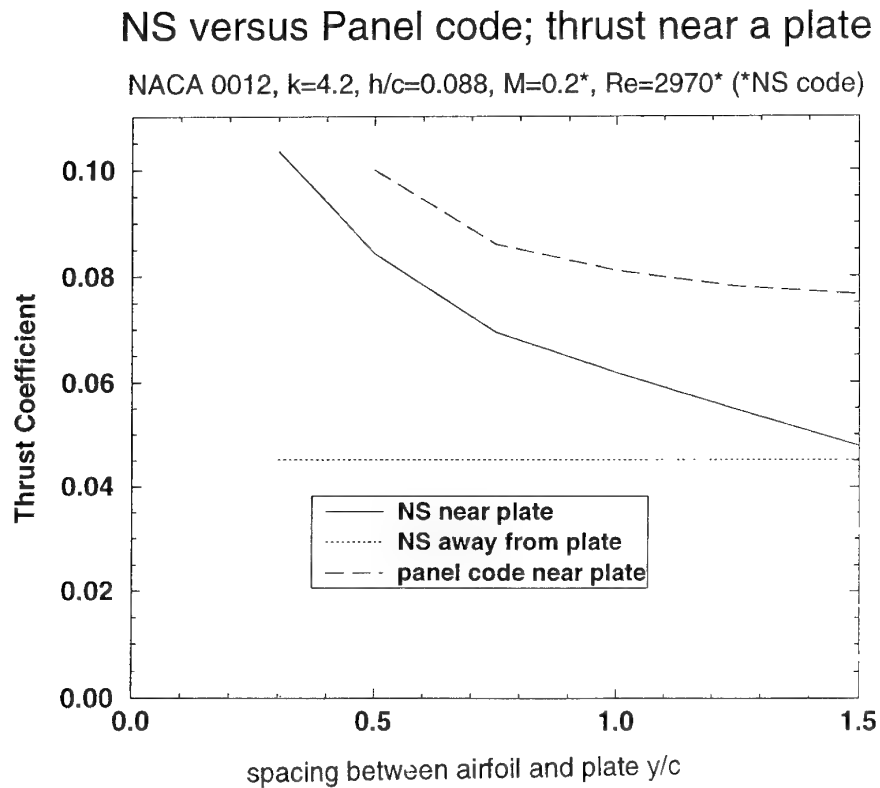


Fig. 10 Computed Thrust

Wake comparison in and out of GE

NACA 0012, $k=4.2$, $h=0.5$, $dh=\pm 0.088$

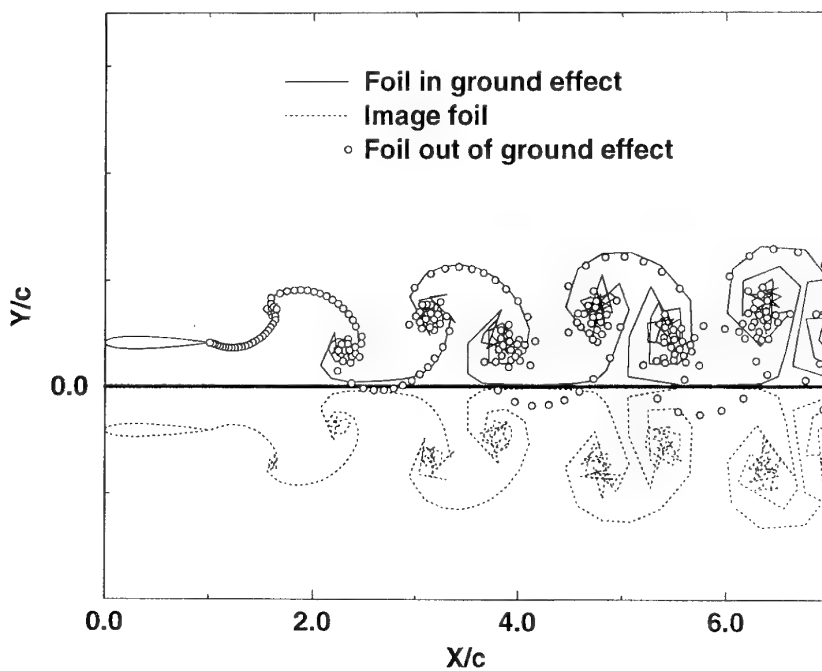


Fig. 11 Panel Code Computed Wake in Ground Effect

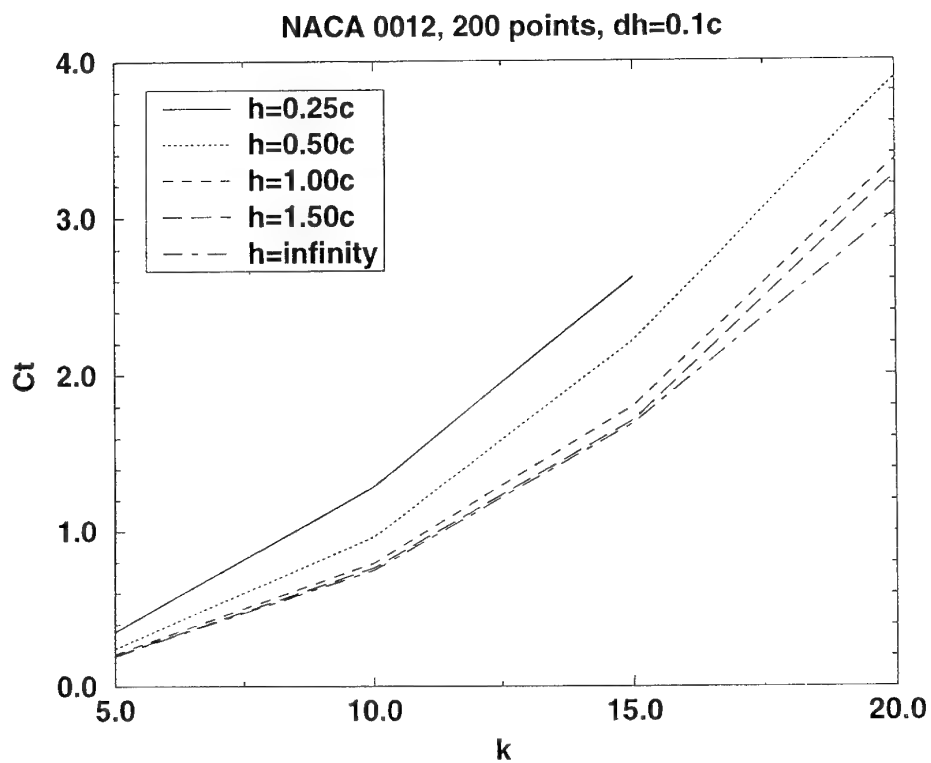


Fig. 12 Panel Code Computed Thrust

RECENT LABORATORY AND NUMERICAL TRAILING VORTEX STUDIES

Donald P. Delisi*, George C. Greene†, Robert E. Robins*, and Raminder Singh°

* Northwest Research Associates, Inc.
P.O. Box 3027
Bellevue, WA 98009
USA

† NASA Langley Research Center
Hampton, VA
USA

° Dept. of Mechanical Engineering, Indian Institute of Technology
Kanpur VP
India

SUMMARY

Results from two laboratory studies and two numerical studies are presented. In the first laboratory study, measurements of the strength of vortices from a three-dimensional (3-D) model wing are presented. The measurements follow the vortices as they evolve in time from a two-dimensional (2-D) line vortex pair to the development and migration of 3-D vortex rings. It is shown that the resulting vortex rings can contain up to 40 percent of the initial vortex circulation. Thus, the formation of vortex rings may not necessarily signal the end of the wake hazard to following aircraft.

In the second laboratory study, we present the results of an experiment which shows how the spanwise drag distribution affects wake-vortex evolution. In this experiment, we modified the spanwise drag distribution on a model wing while keeping the total lift and drag constant. The results show that adding drag on or near the centerline of the wing has a larger effect than adding drag at or near the wingtips. These measurements complement the results of NASA studies in the 1970s.

In the first numerical study, results of 3-D numerical calculations are presented which show that the vortex Reynolds number has a significant influence on the evolution and migration of wake vortices. When the Reynolds number is large, 3-D vortex rings evolve from the initially 2-D line vortex pairs. These vortex rings then migrate vertically. When the Reynolds number is lower, the transition of vorticity from 2-D to 3-D is delayed. When the Reynolds number is very low, the vortices never transition to 3-D, and the vertical migration is significantly reduced. It is suggested that this effect may have been important in previous laboratory wake-evolution studies. A second numerical study shows the influence that vertical wind shear can have on trailing vortex evolution.

1. INTRODUCTION

Researchers have a variety of tools to use to investigate wake vortices from lifting wings. These tools include full-scale field studies, laboratory experiments employing scale models, numerical studies using computer codes, and analytical studies. Of these, the field studies are the most

relevant, since they incorporate full-size or nearly full-size vehicles, and the resulting vortices are generated at large Reynolds numbers and evolve in a realistic environment. The difficulties in field studies are that they are expensive to run, the environment may not be what was desired, and the effects of the background may be difficult to control, and, therefore, the underlying physics may be difficult to isolate and to understand.

Because of the cost and complexity of field studies, many vortex studies are performed using laboratory and numerical models. These laboratory and computer model studies are less costly than field studies, and they allow for the investigation of complex interactions with the environment under controlled conditions. The underlying, but often unspoken, belief in these types of studies is that, although the details of the interactions may change in going from the laboratory or computer model results to the full-scale, the trends will be correct. In many cases, this belief appears to be justified.

In this paper, we will briefly examine four vortex studies that have recently been performed at Northwest Research Associates. Our objective is to give examples of the kinds of vortex studies that can be performed in the laboratory or with numerical models that in the field would be more difficult, less well controlled, or more expensive to perform.

2. LABORATORY MEASUREMENTS OF WAKE VORTEX STRENGTH BEHIND A TOWED WING MODEL

It is well known that the wake vortex system from an aircraft will descend with time and, under at least some conditions, will undergo a sinusoidal instability, changing the wake from a 2-D line vortex pair to a series of 3-D vortex rings. This instability was first analyzed by Crow¹.

In this study, we present results from a laboratory experiment in which we measured the evolution of the strength of trailing vortices from their generation as a line vortex pair through their migration as vortex rings. The experiments were performed in a nonstratified, nonturbulent fresh-water-filled towing tank measuring 9.9 m long, 0.9 m wide, and 1.0 m deep². The water depth was 0.9 m. The

wing was a flat plate that was cambered with a constant radius of curvature. The wing had a span of 3.81 cm, a chord of 1.91 cm, a uniform thickness of 0.056 cm, and an aspect ratio of 2.0. This low aspect ratio was used to give the maximum vertical distance from the wing to the bottom of the tank in units of b_0 , the initial vortex-separation distance. The nominal angle of attack of the wing was 13° , and the lift coefficient was 1.0. For this wing, the stall angle was around 24° . The wing was towed down the tank from a carriage which rode along tracks located above the water surface. The wing was connected to the carriage by a tapered strut measuring 1.3 cm in length and 0.16 cm in thickness tapering to .08 cm at the trailing edge. The wings were attached to one end of the strut and were submerged to a trailing-edge depth of 9.5 cm at a zero-degree angle of attack. The wing was towed down the tank at a speed of 250 cm/sec, yielding a chord Reynolds number of 47,600. From dye and particle visualizations, the vortices appeared turbulent. The lift and drag of the wing were measured with piezoelectric force sensors on the carriage.

The Digital Particle Image Velocimetry technique (DPIV)³ was used to measure in-plane velocity components in a vertical plane normal to, or aligned with, the direction of wing motion. The normal plane was used to measure the velocity field prior to Crow instability, while the along-track plane was used to measure the velocity field of the vortex rings. Particles made of Pliolite VT, with diameters of 180 to 355 μm , were used to seed the flow. Using DPIV, we measured vortex core separation, vertical migration, and circulation as a function of time (hence, depth below the wing).

Figure 1 shows a typical result. In this plot, H is nondimensional migration height, defined by $H = h/b_0$, where h is the dimensional vertical distance the vortices have migrated in a time t . Here, $h = 0$ and $t = 0$ correspond to the depth and time of the wing as it passes the measurement plane. The circulations of the left and right vortices have been normalized by the initial circulation, Γ_0 , which is given by

$$\Gamma_0 = \frac{L}{\rho U b_0} \quad (1)$$

where L is the lift measured by the lift sensor, ρ is density, and U is the towing speed. Figure 1 shows the data from eleven separate runs under nominally the same vortex conditions. For the eleven runs, the standard deviation in the lift was 1.0% of the average lift, and the standard deviation of the mean velocity was 0.3%.

To acquire the data shown in Figure 1, we towed the wing down the tank and recorded particle motions using a digital camera connected to a frame-grabber board in a personal computer. We typically recorded four or five image pairs during a run. For each run, the image window was only a few b_0 in height, to allow accurate estimates of circulation. The camera depth below the wing was varied to obtain information over a range of vortex depths. Figure 1 shows data from four camera depths. Data for H from zero to 8 was recorded in the plane normal to the wing track. Data for $H > 10$ was recorded in the along-track plane. Image pairs from each run were processed to yield the vortex separation as a function of depth and the circulation of each vortex in

the image. Several runs were performed at each camera depth to determine the scatter in the data. The initial vortex separation, b_0 , was also measured from the particle images, and was on the order of the wing span.

Figure 1 shows the decay of circulation of the vortices as they migrate vertically in the tank. Note that the values of circulation determined using DPIV are normalized by eqn. (1), which uses lift, towing speed, and the initial vortex separation. At early times (small H), these normalized values are near unity, indicating that the circulations derived from DPIV are in agreement with the value of Γ_0 determined from the lift, towing speed, and initial vortex separation. This agreement provides confirmation that the DPIV circulation values are credible.

For $H < 4$, Figure 1 shows that the two-dimensional vortices decay linearly. From other flow visualizations⁴, we have observed that the vortices begin to undergo Crow instability around $H \sim 4$. For H between 4 and 8, Figure 1 shows that the measured circulations range between around 80% of their initial value and zero. This large variation is caused by the random location of the measurement plane relative to the location of the linking of the vortices and the subsequent evolution of 3-D rings. If the plane is located in a region where the linking is or has just taken place, the measured circulations will be low. If the plane is in the middle of the ring, the circulations will be large.

For $H > 10$, the vorticity from the wing has evolved from a 2-D line vortex pair to a series of 3-D vortex rings⁴. Figure 1 follows two of these rings from $10 < H < 14$. Note that the stronger ring contains over 40% of the strength of the initial vortices. Thus, it is possible that, under some conditions, the vortices from a generating aircraft may still be a hazard to following aircraft even after the formation of 3-D vortex rings.

3. LABORATORY MEASUREMENTS OF THE EFFECT OF VARYING THE SPANWISE DRAG DISTRIBUTION ON FAR-FIELD VORTEX EVOLUTION

During the 1970s, NASA investigated the concept of adding various drag devices to the wings of an airplane in order to reduce the wake vortex hazard to following aircraft. The NASA studies included wind tunnel tests, towed model tests, and flight tests. The concept was to disrupt the vortex at or near the generation point, resulting either in a broadening of the vortex core, which would, hopefully, cause the vortex to decay sooner, or to perturb the vortex core, causing it to break down sooner. These devices proved mostly unsuccessful due, at least in part, to the weight and drag penalties they imposed on the aircraft⁵⁻⁷.

In this laboratory study, we used a 3-D model wing, similar to the one described in Section 2, to investigate the effect of varying the spanwise drag distribution on the far-field vortex evolution. Our goal was to examine how the drag distribution affects wake vortex evolution and, ultimately, to give guidelines to aircraft designers on how best to integrate wing and body designs into the most effective wake-vortex alleviation configuration.

Similar to the previous study, here we also towed a model wing at an angle of attack in a water-filled tank to generate wake vortices. In this study, we varied the spanwise drag

distribution on the wing by varying the spanwise location of local drag elements. The total lift, the total drag, the chord Reynolds number, and the angle of attack were all kept nearly constant. The result is a series of experiments where all of the fluid dynamic vortex-generation parameters are kept essentially constant except that the spanwise drag distribution is varied.

The experiments were performed in the fresh-water-filled towing tank described above. The wing was a flat plate that was cambered with a constant radius of 7.77 cm (Figure 2a), similar to the wing used above. The wing had a span of 10.11 cm, a chord of 5.13 cm, a uniform thickness of 0.08 cm, and an aspect ratio of 2.0. The nominal angle of attack was 7.1° , giving a lift coefficient of 0.7. The wing was connected to the carriage by a tapered strut measuring 2.5 cm in length and 0.32 cm in thickness tapering to 0.13 cm at the trailing edge. The wing was submerged to a trailing edge depth of 15.2 cm at a zero degree angle of attack. At this depth, the bottom floor was 7.5 spans below the wing. The wing was towed down the tank at a speed of 160 cm/sec, yielding a chord Reynolds number of 82,000. The drag of the strut holding the wing to the carriage was subtracted from the drag of the wing-strut combination, yielding the drag of the wing itself.

To vary the drag distribution, we added drag elements behind the trailing edge of the wing. These drag elements consisted of flat, circular-shaped disks oriented perpendicular to the upstream flow. The disks were located one chord length behind the trailing edge of the wing. Small stings were used to connect the center of the disk to the trailing edge (Figure 2b). The disks were located initially at the wingtips, and were then moved symmetrically to the centerline of the wing. When the sting was on the centerline, a single disk was used. With this configuration, the total lift and drag on the wing varied only slightly with the location of the disks. For these experiments, the lift-to-drag ratio was 3.2.

As the wings were towed down the tank at a positive angle of attack, vortices were generated which descended toward the floor. Dye was used to track the descent of the vortices, and small Pliolite particles lying on the floor of the tank were used to visualize the arrival of the vortices. Small velocity motions generated by the vortices caused the particles to move, and their motion was easily observed.

At least five, nominally identical runs were performed for each position of the disks. The results show that the time for the vortex system to reach the bottom floor of the tank depended on the spanwise position of the drag disks (Figure 3). When the disks were at or near the wingtips, the time of arrival of the vortices was nearly constant. When the disks were moved close to or on the wing centerline, the time of arrival was significantly longer (by up to ~75%), which implies more rapid decay. Without disks, the lift-to-drag ratio of the wing was 6.8 at the same angle of attack, and the time of arrival of the vortices to the floor was only slightly faster than when the disks were at or near the wingtips. Thus, the time for the vortices to travel 7.5 spans was nearly the same if there were no disks or when the disks were at or near the wingtips, although the lift-to-drag ratios for these two cases were different by more than a factor of 2. The time to migrate 7.5 spans was significantly longer only when the disks were at or near the wing centerline.

Previous NASA tests were based on the assumption that the most effective location of a drag device was just upstream of a vortex when it formed. Our new results complement the previous results by providing a systematic variation in the spanwise location of the drag device. Our results suggest that the above assumption on the most effective location of the drag device should be re-examined.

4. 3D NUMERICAL SIMULATIONS OF VORTEX EVOLUTION

For several years we have been using numerical studies in conjunction with laboratory and field studies to explore how environmental factors influence trailing vortex behavior. Results from 2-D numerical simulations were reported by Robins and Delisi^{8,9} and Delisi et al¹⁰, and recent 3-D results are reported by Robins and Delisi^{11,12}.

Because of restrictions on hardware size and other parameters, the effects of varying Reynolds number and core size on trailing vortex evolution can be difficult to study in the laboratory and the field. Although resolution requirements can place an upper bound on Reynolds number and a lower bound on core size, numerical studies of how these quantities affect vortex evolution can be quite informative.

In the first set of 3-D results presented below, we show that differences in Reynolds number can produce dramatic variations in how trailing vortices evolve. In these calculations, we used 256 grid points in the axial direction, 128 points in the cross-axial direction, and 144 grid points in the vertical direction. The corresponding box size was $20b_0 \times 10b_0 \times 11.2b_0$. Our 3-D numerical code uses pseudospectral approximation for horizontal variations and compact approximation for vertical variations. A projection method for the time-stepping ensures the incompressibility of the flow. The simulations were performed in an unstratified fluid with no ambient turbulence. Further details are available in Robins and Delisi¹¹.

Figure 4 shows the development of Crow instability for three initial vortex Reynolds numbers, defined by Γ_0/ν , where ν is the kinematic viscosity. (Note that in this figure, the vertical spacing of the vortices is not representative of the vertical migration in a given time; this information is shown in the next figure.) The initial vortices in each case are identical and are composed of a superposition of vortices having wavelengths ranging from 1.25 to $10b_0$. This range includes the wavelength of maximum initial perturbation growth, determined by Crow to be $8.6b_0$. The instability is energized by applying a small, random horizontal sinusoidal perturbation to the axis of each component vortex. The peak-to-peak amplitude of the perturbation is 2% of b_0 . This perturbation is imperceptible in the initial vortices shown in Figure 4.

The displays in Figure 4 show surfaces of constant vorticity magnitude viewed at an angle from above. The vorticity level shown is 20% of the peak vorticity in each display. The evolution is shown at nondimensional times, T , of 0, 7.5, 10, and 12.5, where $T = V_0 t / b_0$, where V_0 is the initial vortex descent rate defined as $\Gamma_0 / 2\pi b_0$. The results show that Crow instability is delayed when the Reynolds number is cut in half. When the Reynolds number is significantly reduced, Crow instability does not occur at sufficient

amplitudes to allow the vortices to link and form 3-D vortex rings.

Our previous 3-D numerical results have shown that larger initial core size will also delay the onset of linking¹¹. If we compare the evolutions in Figure 4 at the time of $T = 7.5$, we see larger cores for smaller Reynolds numbers, which implies that the growth rate of the core size increases as Reynolds number decreases. Thus, it appears that greater core sizes lead to slower linking, both for the case of an initially greater core size (ref. 11) or the case of smaller Reynolds number leading to greater core size (present study). Also, note for the case when Reynolds number = 366, where linking does not occur, that the core size continues to increase for later times.

The solid lines in Figure 5 show the vertical migration history, on an H vs T plot, for the cases shown in Figure 4. These curves are second-order fits to the numerical data points at intervals of $\Delta T = 2.5$. The three solid lines, for Reynolds numbers of 2930, 1465, and 366, show that decreasing the Reynolds number reduces the vertical migration of the vortex system. Also shown in Figure 5, as the symbols connected by dotted lines, are the results from two laboratory runs which were nominally identical to the runs shown in Figure 1. These data are in agreement with the numerical simulation for Reynolds number = 1465 up to $T \sim 10$, which is when the 3-D rings are forming in the numerical simulation (cf, Figure 4). For $T > 10$, the numerical simulation predicts a slightly larger vertical migration than the laboratory measurements.

Previous laboratory studies of vortex evolution from a 3-D wing reported that the 2-D line vortex pairs formed vortex rings which dissipated soon after formation, yielding a maximum vertical vortex migration of $H_{\max} < 7^{13}$. In our laboratory and numerical studies, the vortex rings migrate a long distance after formation, and H_{\max} is ~ 22 . Thus, the evolution observed in previous laboratory studies is consistent with a low Reynolds number vortex flow, and Reynolds number may have been an important factor in these previous studies.

A final 3-D numerical study shows the considerable effect that vertical wind shear can have on vortex evolution. Figure 6 illustrates the result of adding cross-stream vertical wind shear to the previous calculation for Reynolds number 2930 shown in Figure 4. The shear, U_s , is chosen so that the shear Froude number, $F_s (= V_\infty / U_s)$, is equal to 2, which corresponds to a shear of about 0.02 sec^{-1} for vortices from a cruising B-747. The figure shows that the shear increases the growth rate of the Crow instability, and that it deforms the resulting vortex rings.

5. CONCLUDING COMMENTS

The above laboratory and numerical investigations have allowed us to gain insights into the evolution of trailing vortices that would have been difficult and expensive to obtain from full-scale field tests. They have also provided tools and techniques that are useful in future vortex studies. Additional studies using these tools and techniques are in progress and will be reported at a later date.

ACKNOWLEDGMENTS

This work was supported by the U. S. Office of Naval Research and the Naval Sea Systems Command. The authors thank Dr. L. Patrick Purtell and Mr. Robert J. Lynch for their encouragement and support.

REFERENCES

1. Crow, S.C., "Stability theory for a pair of trailing vortices," *AIAA J.*, **8**, 1970, pp 2172-2179.
2. Delisi, D.P. and G.C. Greene, "Measurements and implications of vortex motions using two flow-visualization techniques," *J. Aircraft*, **27**, 1990, pp 968-971.
3. Willert, C.E. and M. Gharib, "Digital particle image velocimetry," *Experiments in Fluids*, **10**, 1991, pp 181-193.
4. Delisi, D.P., R.E. Robins, and D.B. Altman, "Laboratory and numerical studies of vortex evolution in ideal and realistic environments," in *Proceedings of the Aircraft Wake Vortices Conference. Volume 2*, edited by J.N. Hallock, U.S. Department of Transportation, Federal Aviation Administration Report DOT-FAA-5D-92-1.2, 1991, pp 30-1 to 30-28.
5. Dunham, R.E. Jr., "Unsuccessful concepts for aircraft wake vortex minimization," in *Wake Vortex Minimization*, NASA SP-409, 1977, pp 221-249.
6. Faery, H.F. Jr. and J.F. Marchman III, "Effect of whitcomb winglets and other wingtip modifications on wake vortices," in *Proceedings of the Aircraft Wake Vortices Conference: March 15-17, 1977*, FAA Report FAA-RD-77-68, 1977, pp 207-216.
7. Patterson, J.C., E.C. Hastings, and F.L. Jordan, "Ground development and flight correlation of the vortex attenuating spline device," in *Wake Vortex Minimization*, NASA SP-409, 1977, pp 271-303.
8. Robins, R.E. and D.P. Delisi, "Numerical study of vertical shear and stratification effects on the evolution of a vortex pair," *AIAA J.*, **28**, 1990, pp 661-669.
9. Robins, R.E. and D.P. Delisi, "Potential hazard of aircraft wake vortices in ground effect with crosswind," *J. Aircraft*, **30**, 1993, pp 201-206.
10. Delisi, D.P., R.E. Robins, and R.D. Lucas, "Initial laboratory observations of the evolution of a vortex pair in a stratified shear flow," *Phys. Fluids*, **3**, 1991, pp 2489-2491.
11. Robins, R.E. and D.P. Delisi, "Nonlinear development of sinusoidal instability for a pair of trailing vortices," 1995, submitted.
12. Robins, R.E. and D.P. Delisi, "Stratification effects on the 3-D evolution of trailing vortices," 1995, submitted.
13. Sarpkaya, T., "Trailing vortices in homogeneous and density-stratified media," *J. Fluid Mech.*, **136**, 1983, pp 85-109.

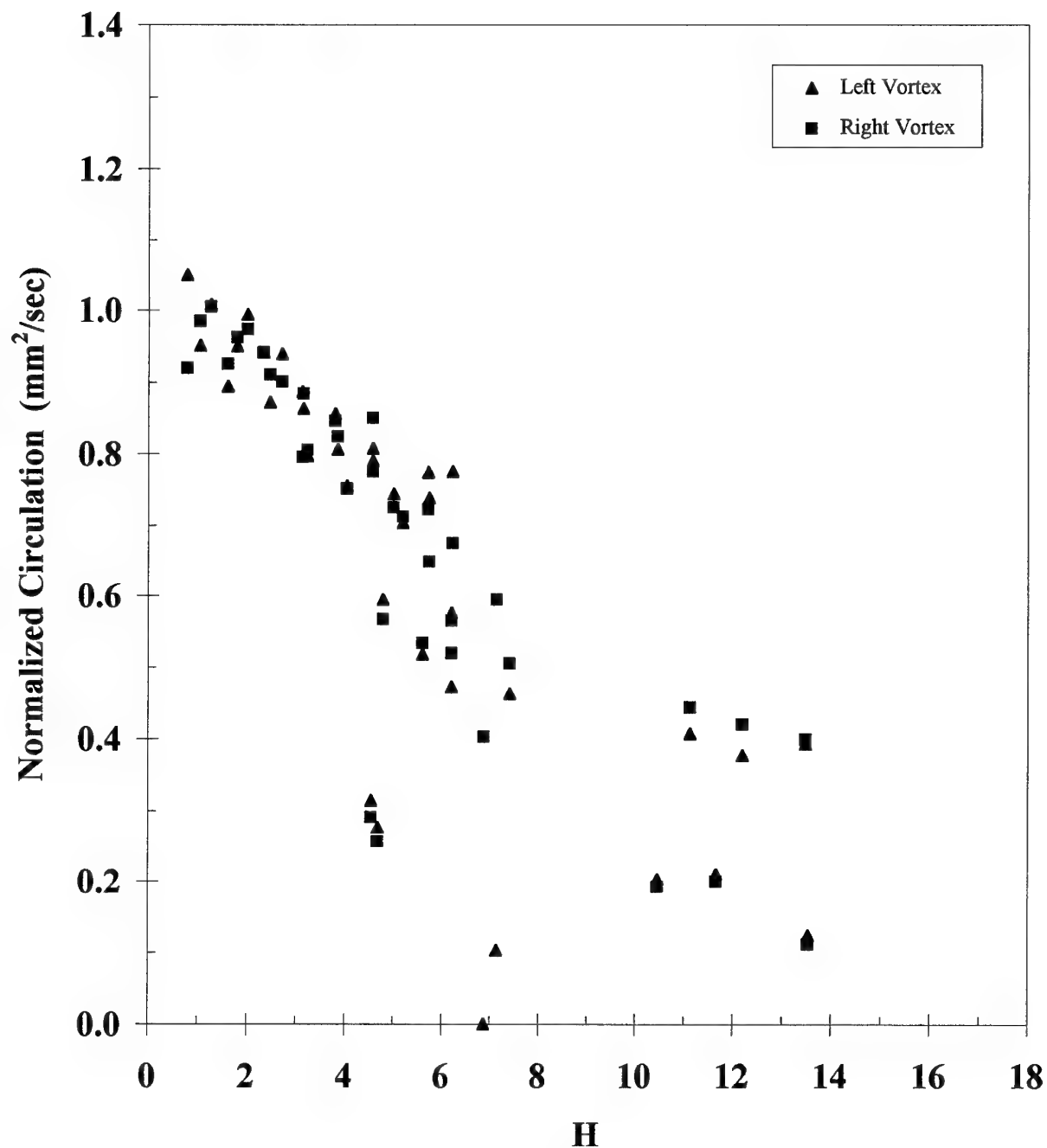


Figure 1. Normalized circulation behind a laboratory model wing as a function of normalized depth. Note the general decay of circulation with increasing depth (increasing H). 3-D rings form in this experiment around $H \sim 8 - 10$. Note that between $H = 10$ and $H = 14$, some vortex rings have circulation values around 40 percent of the initial circulation.

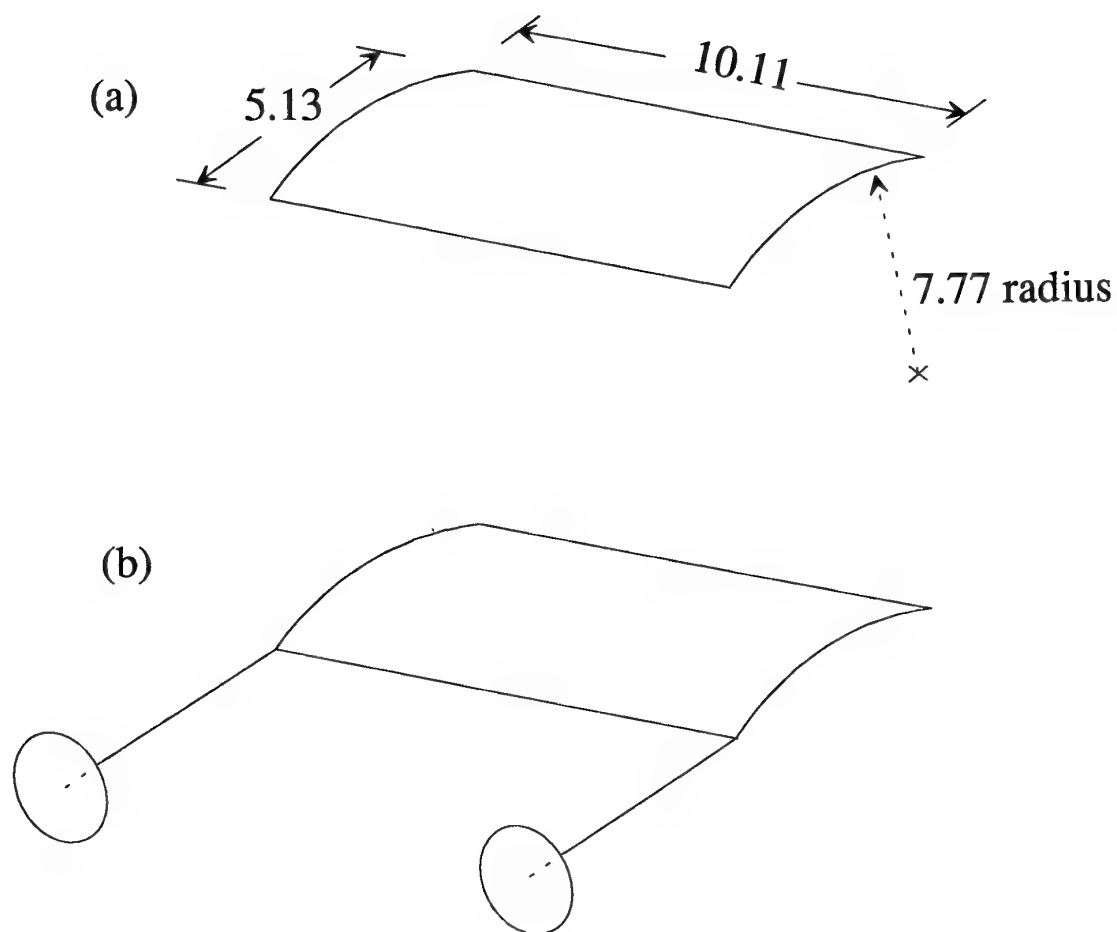


Figure 2. Drawings of the laboratory model wings used in the drag study. All dimensions are in cm. (a) The curved plate wing. (b) The curved plate wing with drag elements at the wingtips.

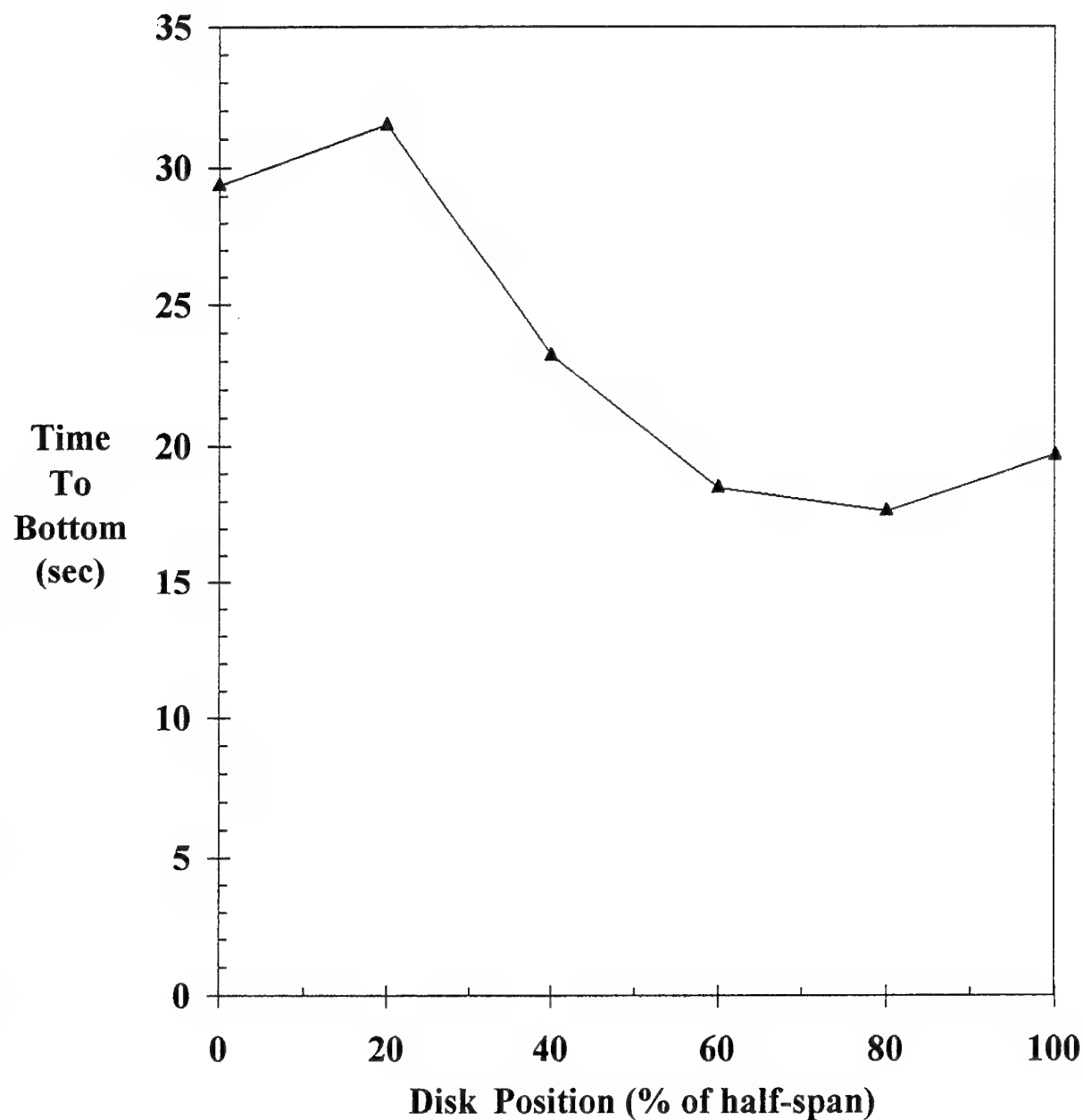


Figure 3. Time for the vortex system from a wing with drag disks to reach the bottom floor (located 7.5 spans below the wing) vs spanwise position of the disks. Each data point is the average of at least 5 runs.

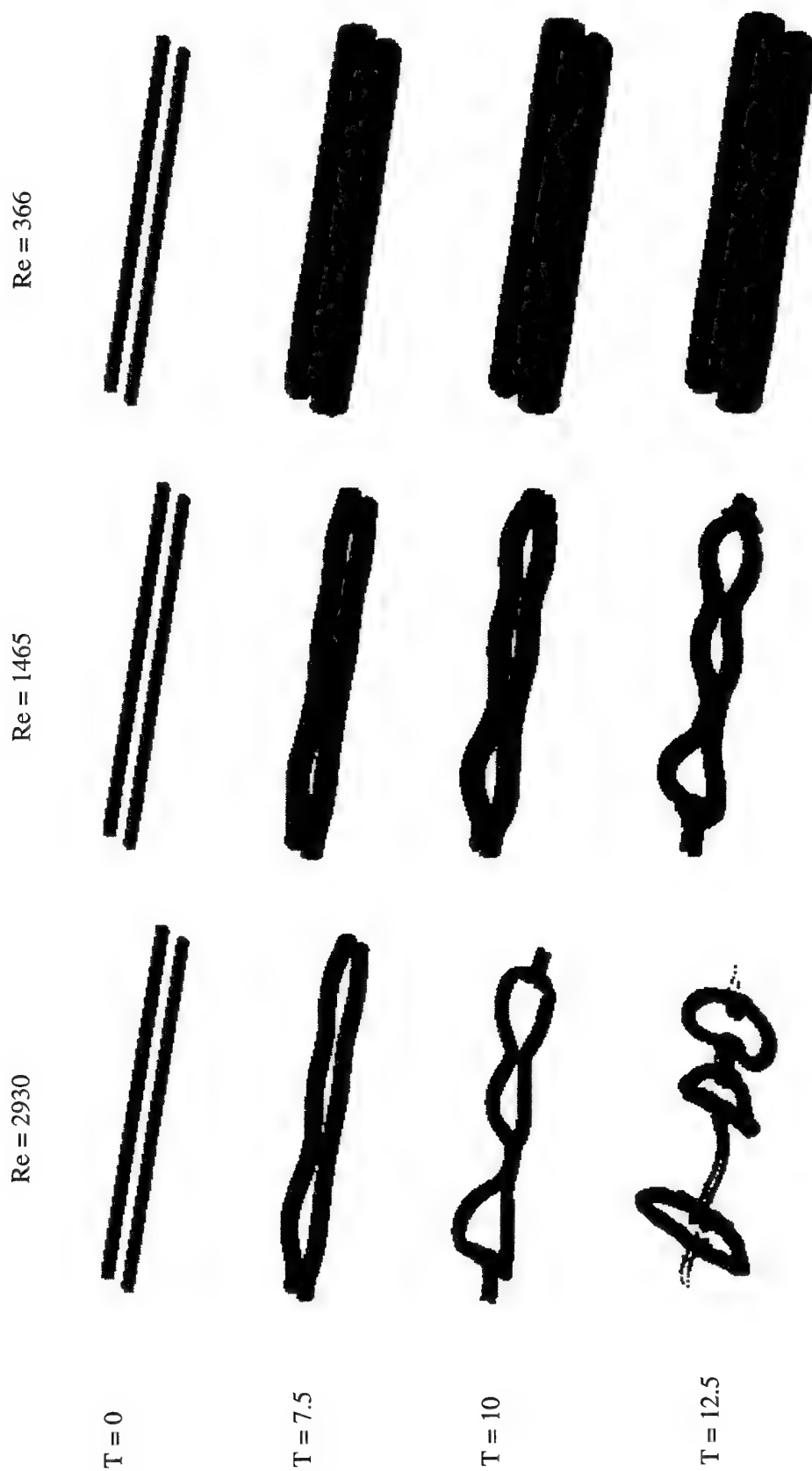


Figure 4. 3-D numerical results showing the effect of Reynolds number on trailing vortex evolution. Results are shown for Reynolds numbers ($= \Gamma \rho / \nu$) of 2930 (left), 1465 (middle), and 366 (right) at times of $T = 0, 7.5, 10$, and 12.5 . Vertical placement on this figure is for comparison purposes only; depth vs time information is shown on Figure 5.

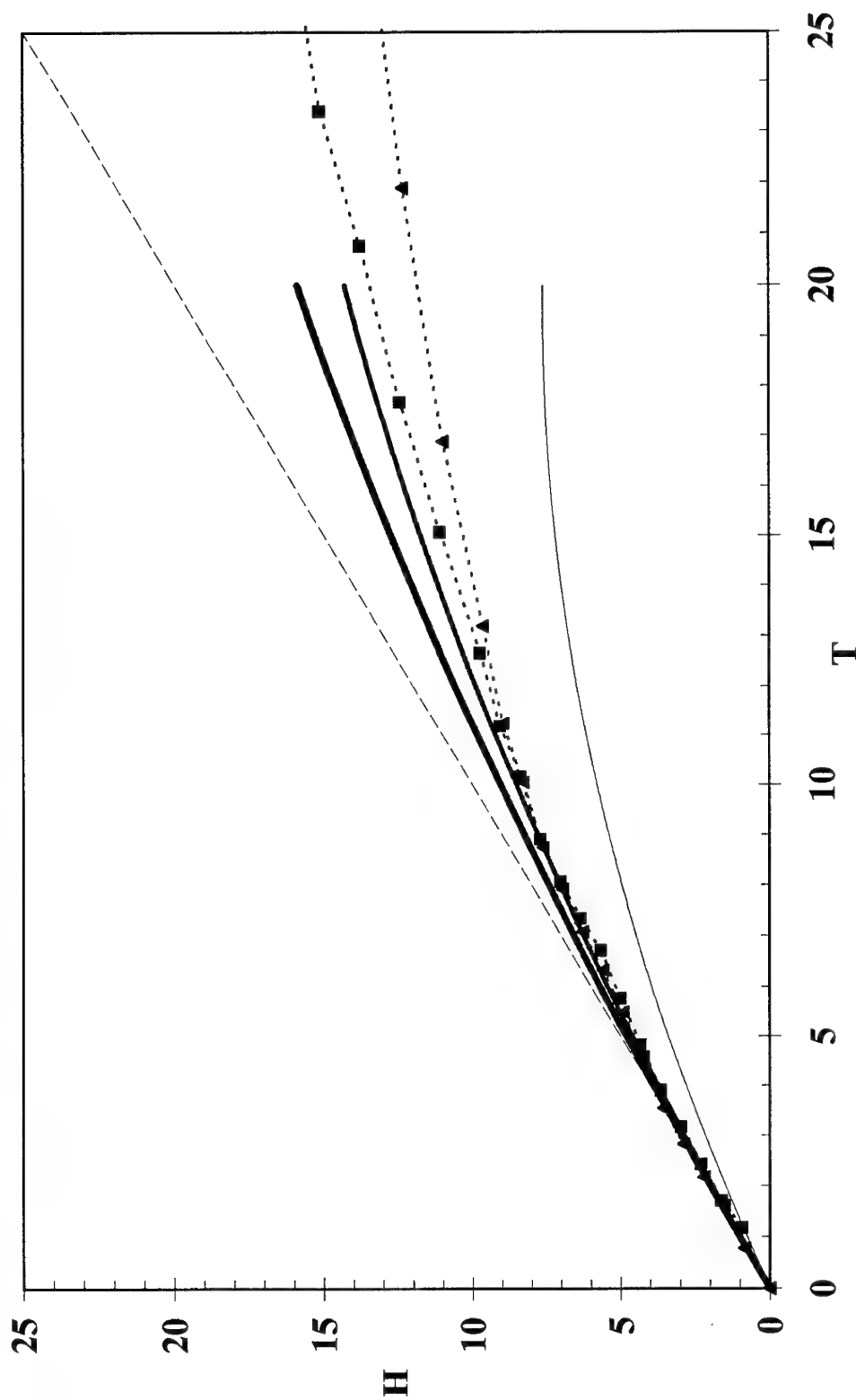


Figure 5. Nondimensional vertical migration distance vs nondimensional time. The three solid lines correspond to the numerical simulations shown in Figure 4; the heavy solid line is for a vortex Reynolds number (Re) = 2930, the medium solid line is for Re = 1465, and the thin solid line is for Re = 366. The dashed line is $H = T$. The two dotted lines with symbols are laboratory runs which were nominally identical to the runs shown in Figure 1.

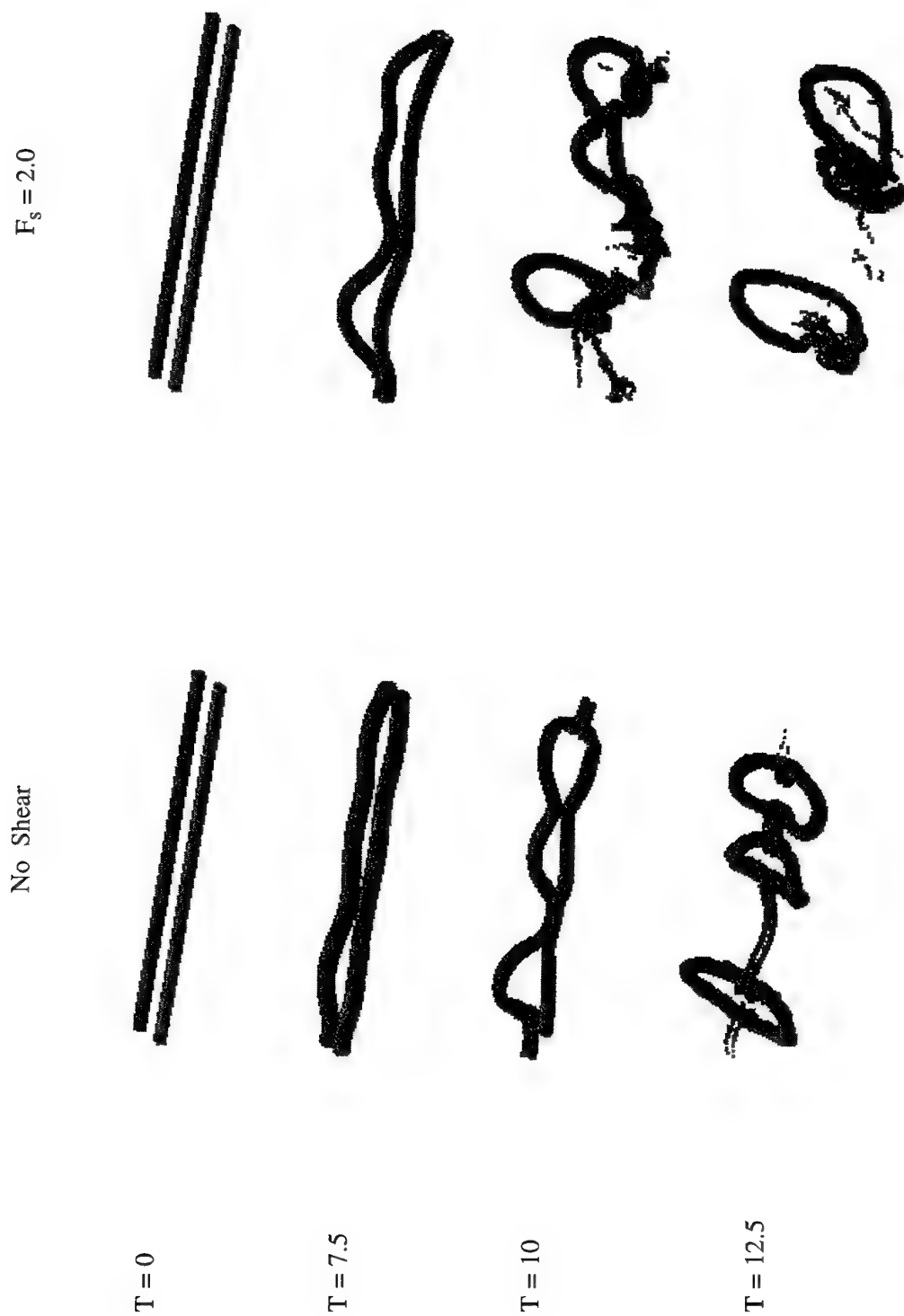


Figure 6. 3-D numerical results showing the effect of cross-stream vertical wind shear on trailing vortex evolution. Results are shown for Reynolds number 2930, with the no-shear case on the left and the case of $F_s (= V/U_z b_0)$ equal to 2 on the right.

Wake dynamics and exhaust distribution behind cruising aircraft

Thomas Gerz¹ and Thorsten Ehret²

¹ Institut für Physik der Atmosphäre, DLR Oberpfaffenhofen, D-82234 Weßling

² Institut für Strömungslehre und -maschinen, Universität Karlsruhe, D-76128 Karlsruhe

1. SUMMARY

By means of a vortex-filament technique and large-eddy simulations dynamics are discussed which control the distribution of the exhaust of a subsonic aircraft under cruising conditions from the nozzle exit to the distance where the trailing vortex pair starts to collapse into turbulence. Emphasis is first put on the method; second on the initial roll-up process and the phenomenon of "non-entrainment" of exhaust into the vortex cores. Third, the role of turbulence on the onset of the wingtip-vortex decay is considered; thereby it is distinguished between background atmospheric turbulence and turbulence stemming from the boundary-layer around the aircraft.

2. PURPOSE AND INTRODUCTION

Knowledge about the distribution of turbine exhaust behind aircraft, namely the entrainment into the wingtip vortices, the subsequent detrainment by baroclinicity and turbulence when the vortex pair descends in a stably stratified atmosphere, and the mixing when the vortices collapse, is requisite for understanding the chemical and microphysical processes in the aircraft wake and, hence, for assessing the impact of aircraft emissions on the atmosphere (Schumann 1994, WMO 1995).

Here, we discuss dynamical features behind subsonic aircraft under cruising conditions which control the distribution of the exhaust from the nozzle exit (jet regime) through the phase where the trailing vortices sink (vortex regime) until the organized vortex pair collapses (begin of dispersion regime). We use a vortex-filament technique (VFT) and large-eddy simulations (LES) as technical tools. The technical approach, the initialization procedures and the interface between the methods are outlined in detail in Sections 3 and 4. We focus on the roll-up process to illuminate its influence on the exhaust distribution during the early jet regime (in Section 5) and on the begin of the wake decay due to atmospheric turbulence and/or aircraft boundary-layer turbulence in a stably stratified atmosphere (in Section 6). A brief comparison with measured data concludes the study in Section 7.

Our study concentrates on a B-747 because the exhaust-distribution phenomenon described below seems to be typical for wide-body aircraft and since the B-747's alone account for about 50% of the NO_x emissions in the North-Atlantic flight corridor (from Hoinka *et al.* 1993) which is one of the most frequently used flight routes of the world.

3. METHODS

We compute the laminar roll-up of the lifting vortex sheet of a cruising B-747 by applying a VFT (Ehret and Oertel 1994). The dynamical evolution of the four exhaust jets is described by a jet-expansion model (Kärcher and Fabian 1994). We combine both dynamics by taking into account that the wake influences the exhaust positions but that the impact of the buoyant exhaust on the roll-up process is negligible (Jacquin and Garnier 1996, this issue).

According to the theorems of Kelvin and Helmholtz the change of the circulation distribution $d\Gamma/dy$ along the wing span y of an aircraft is modelled by proper positioning of vortex filaments along the wing. The filaments point into negative flight direction $-x$. Due to the mutual induction from each filament upon the other filaments the vortex sheet will roll up into the trailing vortices. The VFT simulates the flow field by discretizing the vortex filaments with finite thickness into segments of equal length and tracking their positions in a Lagrangian frame of reference. The required local velocity field in the aircraft wake is computed by integrating the Biot-Savart law. The integration proceeds in time according to the speed of the aircraft and the length of a segment. Numerical stability constraints define the radius of a filament (see Fell and Staufenbiel 1995), the segment length and timestep. For details of the filament method, see Ehret and Oertel (1994) and Ehret (1996, this issue). The emissions implemented in the roll-up simulation leave the nozzle exit plane every timestep at the proper wing positions as particle tracers and move within the induced velocity field. The particles carry the characteristics of freely evolving jets according to the jet model by Kärcher and Fabian (1994) with typical decays of axial velocity and temperature and species dilution.

It is the aim to follow the evolution of the vortex wake together with its thermodynamics and tracer distribution throughout the jet, vortex, and dispersion regimes in a stably stratified and turbulent atmosphere. Probably the most accurate but rather costly method to do so is the technique of LES. We apply such a code (Kaltenbach *et al.* 1994) and initialize it with the wake data provided by the VFT. The LES code works in an Eulerian space-fixed framework and solves the unstationary, incompressible, three-dimensional, Boussinesq-approximated Navier-Stokes equations for the velocity vector (u, v, w) , the energy equation for potential temperature θ' as an active scalar, and the conservation equation of a dynamically and chemi-

cally inactive exhaust concentration c' . The primes at θ and c mark deviations from the respective mean (background) states. The LES method resolves the large (*i.e.* energy-containing) eddies of the flow while the small-scale dynamics are parameterized. By this, a LES allows higher Reynolds numbers than the method of direct numerical simulation which covers all scales of motion. The subgrid-scale model follows the classical Smagorinsky approach and we account for anisotropic meshes according to the formula given by Scotti *et al.* (1993). Tests of other closures as documented in Gerz and Palma (1994a) for turbulence decay have shown that details of the closure are of minor importance here, since the subgrid-scale energy amounts to less than 5% of the resolved energy of the simulated flow only. The code integrates the discretized fields in space and time by second-order finite differencing. All boundaries of the computational domain are periodic.

In order to keep simulation costs at a minimum and the problem size small enough to fit into available computer resources, the size of the computational domain is kept as small as possible and increased in distinct steps when necessary. This requires a mapping of the fields from a given domain with high resolution into a larger one with coarser resolution. The domain size of the first simulation step covers in the directions of flight x , span y , and height z , $L_x \times L_y \times L_z = 160 \times 192 \times 180 \text{ m}^3$ with a grid volume of $\Delta x \times \Delta y \times \Delta z = 2.5 \times 0.5 \times 0.5 \text{ m}^3$, respectively. When the wake is 7s old the fields are mapped into a larger domain of size $408 \times 256 \times 540 \text{ m}^3$ where a mesh is $6.4 \times 1.0 \times 1.0 \text{ m}^3$ large. L_x is chosen to cover the most unstable mode for a B-747 according to Crow's theory (Crow 1970). Because the flow varies in flight direction at rather large scales (near-to-homogeneity during jet and early vortex regime), the mesh size Δx can be much larger than Δy or Δz . The numerical timestep varies between 0.004s and 0.024s. The LESs terminate at a wake age of 157s after 50 CPU hours, using 1 GByte memory on a Cray-J916 computer.

4. EXPERIMENTAL SET-UP

We select our input data such that they resemble a typical case in terms of aircraft, flight condition and atmospheric state. Such data have been measured during various *in-situ* and remote-sensing flight campaigns over South-Germany (Busen *et al.* 1994) and in the North-Atlantic flight corridor (Schumann *et al.* 1995).

Defining the aircraft conditions.

The B-747 aircraft has a span of 60m and a weight of $2.5 \times 10^6 \text{ N}$ which is about 75% of its maximum take-off weight. It cruises at a speed of 247m/s resulting in a maximum circulation of $\Gamma_0 = 600 \text{ m}^2/\text{s}$. We assume an elliptical wing loading. Our chain of simulations starts "from scratch": we use 50 vortex filaments for each wing, each of equal circulation strength $\Delta\Gamma = \Gamma_0/50$ which represent the vortex sheet of finite thickness along the wings and body of the aircraft. The spacing between two neighbored vortex filaments along the trailing edge of the wings is calculated by $\Delta y = \Delta\Gamma/(d\Gamma/dy)$. The filament ra-

dus is 6m, the length of a filament segment is 14.8m, the timestep is 0.06s. To account for the influence of the body of the aircraft the four or eight innermost vortex filaments rotate in the direction opposite to their respective wing neighbours.

The aircraft is propelled by four jet turbines of type CF6-80C2B1F, *i.e.* a turbine with core and bypass. As exhaust we assume a passive tracer, *e.g.* CO_2 . In order to simulate the distribution of exhaust during the roll-up process by VFT, we distinguish between hot burned species leaving the core of a turbine and warm air passing through the bypass. 12 particles represent the hot exhaust and 50 particles represent the bypass airflow from each turbine. Both sets of particles have uniform axial velocity and temperature excesses as listed in Table 1. Hence, at $t = 0\text{s}$, we neglect radial gradients. These data stem from engine emission calculations with a semi-empirical model based on the ICAO ground-emission data bank and a thermodynamic engine performance code for typical cruise altitudes (Deidewig 1992).

When the wake is 1s old we switch from VFT to LES. Therefore, an interface has to be established between the two methods as follows: The induced swirl-velocity field serves as initial data for the components (v, w) in the LES. Further, the tracer positions obtained by VFT are used to define the four jet core and bypass centres as well as the radii R_{jet} and R_{byp} of the inner and outer turbines. The jet axis and bypass values are obtained from the jet-model output at the plume age of 1s (Kärcher and Fabian 1994), see Table 1. In the LES the tracer particles are now represented in terms of normalized tracer concentration $c'/c'(0)$ with potential temperature θ' . Exhaust excesses of velocity, potential temperature and concentration enter the LES as two-dimensional fields with radial dependencies according to

$$f(1s, r) = f_{jet}(1s) \exp[-\ln(f_{jet}/f_{byp}) r_{jet}^2/R_{jet}^2] + f_{byp}(1s) \exp[-\ln(f_{jet}/f_{byp}) r_{byp}^2/R_{byp}^2], \quad (1)$$

for $f \in \{u, \theta', c'/c'(0)\}$ and $r \in \{r_{jet}, r_{byp}\}$ with $r = r(y - y_0, z - z_0)$ and jet centres at (y_0, z_0) for jet core and bypass, respectively.

The fields for u , v , w , θ' , and $c'/c'(0)$ are mapped onto the LES domain of size $160 \times 192 \times 180 \text{ m}^3$. The three-dimensionality is achieved by copying the information at 247m (1s) to all the grid points in the LES domain between 247m and 407m (1.6s) downstream. Thus, we make a small error by assuming a frozen flow state in the interval between 1 and 1.6s although the roll-up process is still in an evolving state. To check the accuracy of our interface, the filament simulations proceed up to 25 wingspans downstream, corresponding to a wake age of 6s. The overlap of 5s is used to check the quality of both methods in terms of vortex separation, maximum swirl velocity V_C at R_C and maximum downwash velocity. Table 2 lists the respective data obtained from VFT and LES after 1, 3, and 6s. We find that both methods yield good agreement in the key parameters of the roll-up process. Note that both methods deliver the correct final distance between the vortex cores of

Table 1: Initial jet core (Jet) and bypass (Byp.) excess data (background values and aircraft speed subtracted) at the turbine exit ($t = 0$, method as in Deidewig 1992) and after 1s (from jet model described in Kärcher and Fabian 1994); $c'(0)$ denotes the initial maximum concentration value.

		0 sec		1 sec	
		Jet	Byp.	Jet	Byp.
Radii $R_{jet/byp}$	[m]	0.20	0.80	1.0	3.7
Velocities $U'_{jet/byp}$	[m/s]	-219	-67	-18	-0.6
Absolute temperatures $T'_{jet/byp}$	[K]	330	31	10	1.5
Potential temperatures $\theta'_{jet/byp}$	[K]	514	49	15	2.3
Norm. concentrations $c'_{jet/byp}/c'(0)$		1	0	0.0278	0.00211

Table 2: Comparison of key data from vortex-filament technique and large-eddy simulation during the roll-up process of the wake a B-747 with 60m span, a weight of 2.5×10^6 N and a cruising speed of 247m/s. At the wake age of 1s, the LES is initialized with the VFT data.

		1 sec		3 sec		6 sec	
		VFT	LES	VFT	LES	VFT	LES
Vortex separation	[m]	53	53	49	49	47	47
Core radius R_C	[m]	4.0	4.0	4.0	4.0	3.5	3.5
Swirl velocity V_C	[m/s]	12.3	12.3	10.3	10.7	9.8	10.4
Downwash velocity	[m/s]	-11.6	-11.6	-11.8	-12.2	-11.5	-12.1

47m which is $\pi/4$ of the wingspan, a core radius of 3.5m, and a swirl velocity of about 10m/s. Note further, that in terms of vortex separation distance or trailing velocity the roll-up process is finished after 6s (25 wingspans) or a little earlier, in accordance with the findings of Quackenbush *et al.* (1996). The trailing velocity of the vortex pair is then -1.5m/s and agrees with theory. The Reynolds number of a LES is nominally infinity; subgrid motion, however, acts as friction. Typical resulting effective Reynolds numbers Γ_0/ν_{eff} , therefore, are about 600000 in the spatial average with a minimum value of 7000 at 7s increasing to 15000 at 157s for a case without turbulence. With background atmospheric turbulence we obtain 70000 and 1500 for average and minimum values, respectively.

In the turbine jets as well as around the aircraft's wing/body configuration turbulent boundary layers develop which quickly are incorporated into the trailing vortices. One can expect that like most of the exhaust mass also the largest turbulence fluctuations are situated around the vortex cores at distance R_C from the centres. Such turbulence increases mixing and may accelerate the decay process of the wake. As long as VFT is applied, the flow field is assumed to be always laminar. In the LES, however, we can model the boundary-layer turbulence by adding a three-dimensional random perturbation field (v_R, w_R) to the swirling flow (v, w) at $t=1s$, according to

$$(v_R, w_R)(x, y, z) = 0.16 V_C \exp(-(1 - r/R_C)^2) \times \text{ranf}(x, y, z), \quad (2)$$

where $r = r(y - y_{v0}, z - z_{v0})$ and ranf gives random numbers with zero mean and variance one. The vortex cores have coordinates (y_{v0}, z_{v0}) . Hence, the perturbation reaches its maximum value of $0.16V_C$ ($=2m/s$) at R_C and decays exponentially for smaller and larger radii. We add also a fluctuating velocity

field to the axial velocity u of the four jets with a maximum of $0.17U'_{jet}$ ($=-3m/s$) at the jet centres and depending on r as in Equation 1. The scalar fields are not disturbed.

Defining the atmospheric conditions.

We define the mean state of our model atmosphere in the tropopause region where civil-transport airliners typically cruise as motionless with a pressure of 215.9hPa at 11.3km height, a density of $0.35kg/m^3$, and an absolute temperature of 214.3K (potential temperature of 332.1K). During the first second (with VFT) the atmosphere is neutrally stratified. For LES we superimpose a background temperature gradient in terms of a constant Brunt-Väisälä frequency of $N = 0.014s^{-1}$ (oscillation period of about 7.5 minutes).

Besides the boundary-layer induced turbulence also background atmospheric turbulence amplifies the vortex decay. In designing atmospheric turbulence in our LES, we employ the data reported from a measurement campaign in the North-Atlantic flight corridor near the tropopause (Schumann *et al.* 1995). There, *in-situ* measurements show variances of the wind speed of $0.07 \pm 0.03m^2s^{-2}$ horizontally and $0.011 \pm 0.004 m^2s^{-2}$ vertically with vertical wind shear ranging between 0.001 and $0.006s^{-1}$. As upper bounds for the turbulent dissipation rate, Schumann *et al.* report small values of less than $10^{-7} m^2s^{-3}$. Although the measured variance spectra exhibit a slope close to -5/3, the vanishing dissipation rates suggest that the spectral turbulent energy transfer from large to small scales was almost entirely suppressed. Hence, turbulence activity is weak in general; variations in wind shear along flight tracks are only occasionally strong enough to produce active atmospheric turbulence events like clear-air turbulence (CAT). Mixing theories based on turbulent diffusion must therefore fail. Rather, such an at-

mospheric flow state at the microscale can be described by weak, anisotropic, and decaying turbulence in a stably stratified environment, where rather large and almost horizontally oriented eddies cause the mixing. Consequently, we design the LES to simulate decaying, weak, anisotropic turbulence under the background regime of stable stratification. The shape of the horizontal spectrum of the velocity variances reads

$$\frac{k_h^4}{k_p^5} \exp \left\{ -2 \left(\frac{k_h}{k_p} \right)^2 \right\}$$

where k_h and k_p denote the horizontal and peak wavenumbers. The initial (at $t=1s$) atmospheric turbulence velocities in the LES read 0.38m/s horizontally and 0.21m/s vertically and, thus, amount to 3.0% and 1.7% of V_C in Table 2. The most energetic eddies measure 60 to 90m horizontally (k_p between 11/100m and 7/100m). The turbulence is not forced and, thus, will decay in time. Details of the procedure to initiate a three-dimensional turbulence field with prescribed energy spectrum can be found in the papers by Gerz and Schumann (1989) and Dürbeck and Gerz (1995).

5. THE "NON-ENTRAINMENT" PHENOMENON

In previous studies it has been assumed that the dynamics of the exhaust jets and the roll-up process of the vortex sheet of cruising aircraft can be treated separately. It is often assumed that for subsonic aircraft with maximum take-off weight the roll-up is quick and usually finished within a downstream distance of about 10 wingspans (2.5 seconds for a B-747). Therefore, most wake modellers consider the incorporation of the exhaust by the *mature* trailing wingtip vortices. Consequently, such models predict that 100% of the exhaust will be trapped by the two vortices (e.g. Quackenbush *et al.* 1993, Miake-Lye *et al.* 1993) and released later by baroclinic and turbulent detrainment at the edge of the vortices descending in a stably stratified atmosphere.

However, observations of contrails induced by wide-body aircraft such as a B-747 indicate that, besides the well-known texture identifying the vortex cores, often another contrail forms *immediately* behind the aircraft which seems not being trapped by the vortices. Such a case is documented in Figure 1. The non-trapped portion of the exhaust stays at flight level and diffuses at a slow but constant rate, whereas the exhaust captured in the trailing vortices undergoes a very different history: It travels downward with the two vortices, highly concentrated first without substantial mixing but then released and dissolved suddenly when the vortices burst. Often the diffuse contrail lives much longer than the core trails. Needless to say that the cloud-forming microphysics and the chemistry of the exhaust differ in both wake regimes. Further, the maximum take-off weight of an aircraft for which a quick roll-up is assumed sets an upper limit; during flight the aircraft burns fuel which amounts to 25% of the maximum weight of a B-747. Therefore, the aircraft



Figure 1: Contrail of a B-747 aircraft during late vortex regime as seen from ground. The two thin contrails with high density mark the cores of the trailing vortex pair. Above them stays a broader diffuse cloud at flight level which has not been entrained by the vortices. (Photo: T. Hauf)

are typically lighter and the roll-up process takes typically longer than 2.5s, as documented in Table 2. Hence, it is desirable to simulate or model the roll-up process and the merging of the free exhaust jets with the vortex wake simultaneously. It has been recognized recently that this process is even more important for supersonic aircraft where the rolling-up is finished at about 50 wingspans (Quackenbush *et al.* 1996).

Before we analyze this phenomenon in detail we look at the state of the wake after 1s: Figure 2 shows the vortex filaments and the tracer particles in perspective, top and side views, respectively. The onset of roll-up can be recognized: The vortex sheet bends upwards at the wingtips such that the centers of the evolving cores still lay above flight level at this time. The exhaust clouds, however, stay below the nozzles' level due to the downwash. Figure 3 shows the same flow state in terms of swirl velocity of the wake and potential temperature excess of the four jets as initial fields for the LES in spanwise/vertical cross-sections. Both Figures illuminate that the hot exhaust from the turbine cores can be distinguished from the bypass air mass. Their relative positions reflect the action of buoyancy whereas the relative positions between inner and outer engine are determined by the vortex-induced flow.

Two possible explanations for the exhaust distribution as observed (Figure 1) are considered here: First, the aircraft's body disturbs the ideally elliptical loading of the wings which in turn modifies the roll-up process in the body region such that the downwash effect is smaller there than behind the wings. Second, the jet exhaust is hot (about 330 K warmer than the ambient air) which results in a relative upward motion of the particles due to buoyancy. Both effects may help portions of the exhaust to overcome the attracting force of the developing vortex cores. Figure 4 sketches the pressure-gradient force $P = -1/\rho_B(\partial p/\partial r)$ of the vortex and the buoyancy force $B = g\Delta T/T_B$ of the hot exhaust as the

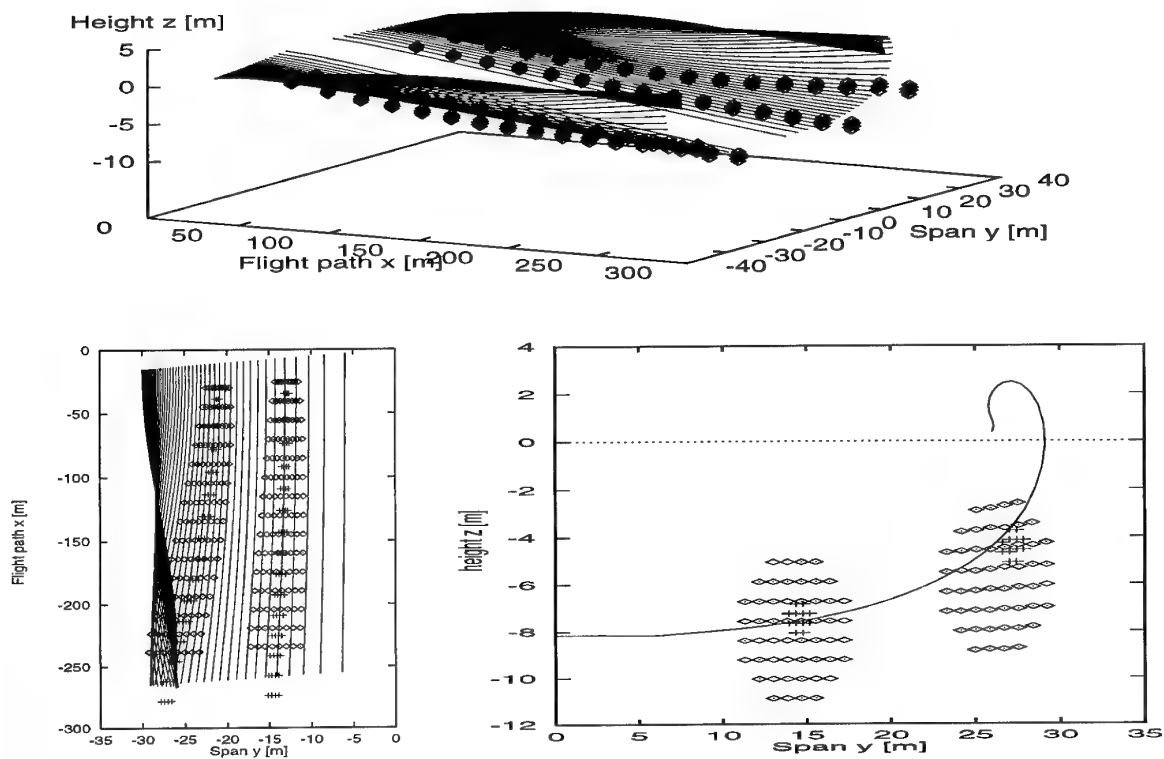
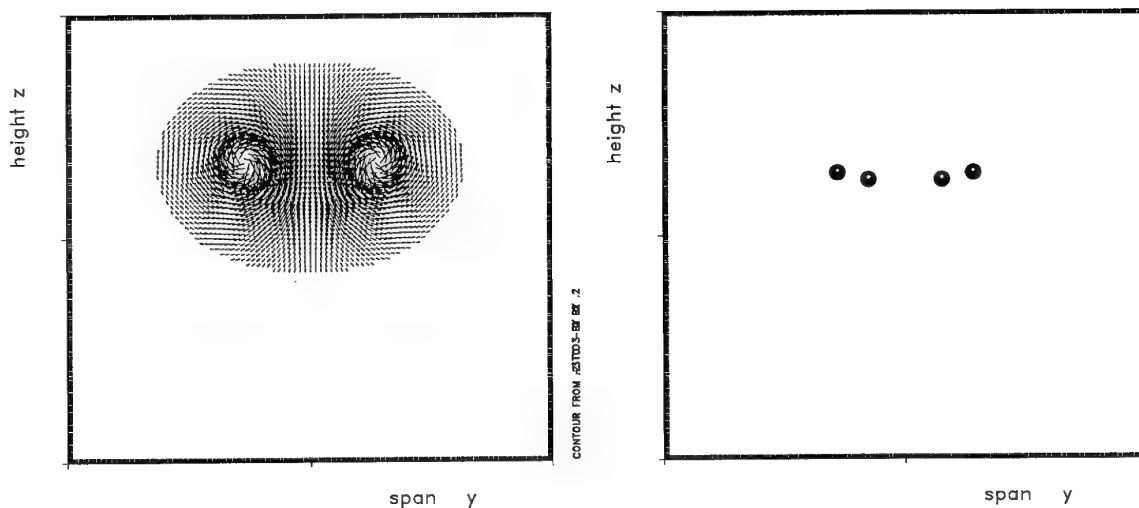


Figure 2: VFT: The wake of a B-747 aircraft in the period between 0 and 1s in terms of vortex filaments and exhaust particles. Top: perspective view; left: looking from above; right: looking from behind at the state after 1s. Particles from the core/bypass are marked by '+'/'◇'. The origin of the coordinates is defined by the axis of symmetry of the aircraft and the flight level.



P.138F62
xx5000 VECTOR

Figure 3: LES: The wake of a B-747 aircraft after 1s (4.1 spans) in terms of swirl-velocity components (v, w) (left) and potential temperature excess θ' of the four exhaust jets (right) in span-height cross-sections of size 192m \times 180m. Fields initialized with VFT data. Vectors are displayed every fourth gridpoint between 1.3 and 13m/s. The black contours of θ' range from 0.2 to 3K with increment of 0.2K and can be attributed to the bypass region; the white kernels inside approximately mark the jet cores with θ' between 3 and 15K.

dominant forces acting on the exit plane of a turbine, where ΔT is the temperature excess of the exhaust, g is the magnitude of the gravitational acceleration, ρ is the density, and index B marks the atmospheric background state. A necessary condition for the exhaust to escape vertically from the vortex attraction in distance d is that

$$B > P \cos(180^\circ - \alpha) \quad (3)$$

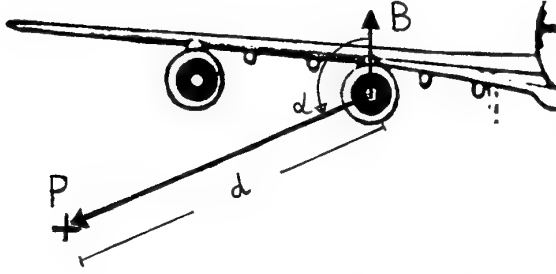


Figure 4: Sketch of forces P and B at a wing.

where α denotes the angle between both forces. For simplicity we now assume flow stationarity such that P equals the centrifugal force V_{swirl}^2/d at a distance d from the center of rotation and also relate the swirl velocity V_{swirl} to the maximum circulation Γ_0 by $\Gamma_0 = 2\pi d V_{swirl}$, which, however, only holds for a fully rolled-up vortex. Then, it follows as a first guess for the temperature excess ΔT necessary to overcome the vortex attraction in distance d

$$\Delta T > \frac{\Gamma_0^2 T_B}{4\pi^2 g} \frac{\cos(180^\circ - \alpha)}{d^3} \quad (4)$$

Hence, ΔT grows quadratically with the weight of an aircraft (being proportional to Γ_0) and decays cubically with the distance between vortex centre and turbine axis. Since the vortex centres are located near the wingtips we find that the exhaust of the inner turbines of a B-747, or the centre turbine of a DC-10 for example, need the lowest gas temperature to come free. Table 3 lists some typical values for d and α (obtained by VFT) for the inner turbines of a B-747 and the centre turbine of a DC-10 and the resulting values for ΔT after 0, 1, 3, and 6s: For both aircraft the necessary temperature excesses increase with time. However, they are quite small and may be observed until 1 or 2s (see Table 1). During early stages the vortex core lies above the wing (see Figure 2) and thus $\alpha < 90^\circ$ for the B-747. This results in even negative values for ΔT . Hence, in very short

distances behind the wing/turbine the exhaust has a good chance to escape from the wingtip vortices as indeed observed, this so much the more as the approximations in Equation 4 assume a fully developed vortex and, thus, Table 3 lists upper limits of ΔT .

In Figure 5 we apply now the VFT to the influences of body and hot exhaust on the early exhaust distribution. The Figure depicts the positions of the vortex filaments and of the exhaust particles after 741m (3s). Three cases are shown: In case (i) the particles are buoyant, the influence of the body is weak; in case (ii) the particles are again buoyant together with a strong influence of the body; in case (iii) finally both exhaust and body behave "neutrally". Only the particles from the jet core are shown. At this flow stage within the jet regime the roll-up process is about to finish (see Table 2) and the four jets are still clearly distinguishable. Obviously, the exhaust of the outer engines are influenced neither by the body nor by their buoyancy; they follow the attracting force of the evolving vortex cores. Also, the body has no remarkable influence on the exhaust distribution from the inner turbines. The right panel of Figure 5 illustrates that only the buoyancy of the particles of the inner engines causes a strong deviation in exhaust distribution compared to the case with non-buoyant exhaust. The effect, however, is such that buoyant exhaust is trapped even quicker by the vortices. We did not observe in our simulations that portions of the exhaust could overcome the attracting force of the vortices. This result is also found in the data from the LES. Howsoever, it is evident from the cases studied here that already the mutual inductions of the vortex sheet evolving into the wingtip vortices provide a force strong enough to influence the exhaust distribution.

6. TURBULENCE EFFECTS

In order to elaborate the effect of turbulence on the wake decay we look at three cases: neither boundary-layer nor atmospheric turbulence in case N, aircraft boundary-layer turbulence in case B, and weak atmospheric turbulence (together with boundary-layer turbulence) as the typical case along flight tracks in case A. The procedures are outlined in Section 4.

Figure 6 shows timeseries of wake and jet flow quantities from the exit to 157s for the cases N, B, and A. Depicted are the maximum values of the cross-stream and vertical velocity components, the pressure minimum as deviation from the ambient pressure, the distance travelled vertically by the vortex

Table 3: Upper limits of temperature excesses of the exhaust necessary to overcome the pressure-gradient force for $\Gamma_0 = 600\text{m}^2/\text{s}$ and $T_B = 214\text{K}$; acc. to Equation 4 and Sketch 4.

		B-747, inner turbine				DC-10, centre turbine			
		0 sec	1 sec	3 sec	6 sec	0 sec	1 sec	3 sec	6 sec
d	[m]	19	16	12	15	26	23	22	24
α	[°]	79	73	102	128	101	101	110	118
ΔT	[K]	<0	<0	24	36	2	3	6	8

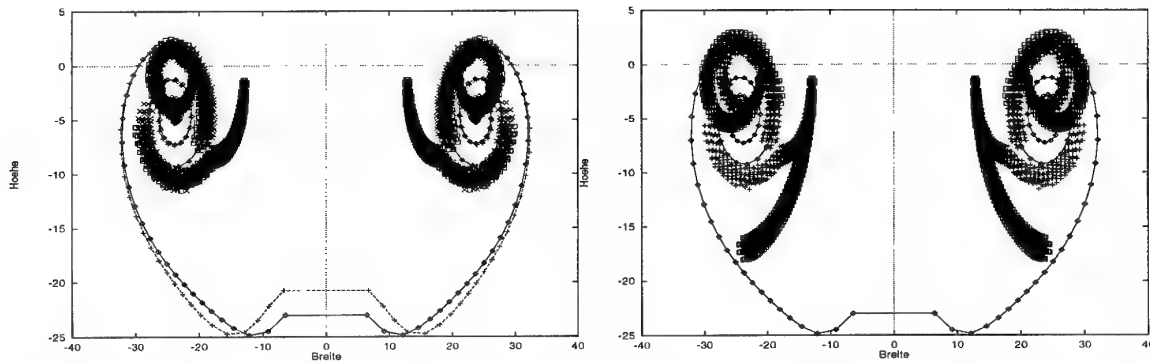


Figure 5: Positions of vortex filaments after 3s and particles exhausted between 0 and 3s in span-height cross-sections behind a B-747. Left panel: small (\diamond), large (+) body influence with buoyant particles (cases i and ii). Right panel: small body influence (\diamond) with buoyant (+), non-buoyant (\square) particles (cases i and iii).

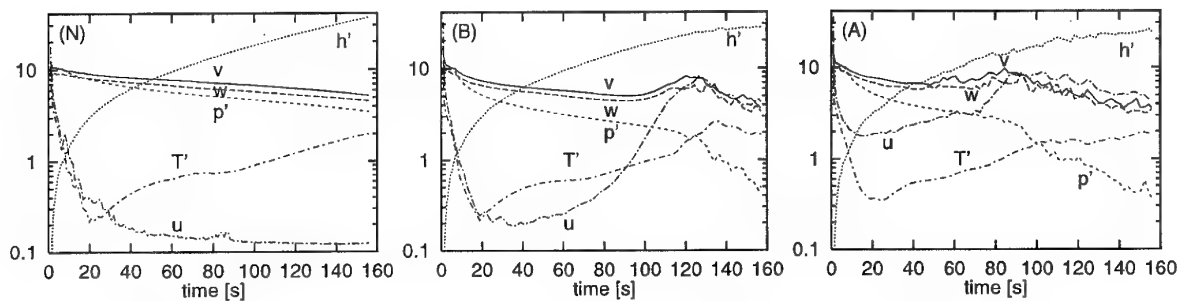


Figure 6: Timeseries of wake and jet flow quantities in a stably stratified atmosphere (from LES). N: no turbulence; B: aircraft boundary-layer turbulence; A: boundary-layer and atmospheric turbulence. Maximum velocity components v, w [m/s]; minimum pressure deviation p' [dPa]; downward travelled distance h' [dm]; maximum velocity against flight direction $-u$ [m/s]; maximum absolute temperature deviation T' [K].

pair, the maximum velocity in negative flight direction and the maximum absolute temperature excess of the exhaust. As long as the vortex cores are intact these quantities can be attributed to the vortex core and the jet dynamics, *i.e.* maximum values of (v, w) define $V_C(t)$ at R_C ; p' marks the vortex-core centre; from its position the travelled distance h' is deduced; in the vortex cores the warmest air is found and $-u$ describes the maximum jet speed. The component w is smaller than v because as the *upward* velocity component it is reduced by mutual induction of the *downward* trailing vortex pair.

First fact to notice for all cases is the very strong exponential decay of the jet properties (u and T') initially whereas the vortex core characteristics decay weakly. The temporal evolution of T' (as well as of the exhaust concentration, not shown) allows a very distinct definition of the end of the jet regime: T' decays during "free" jet expansion reaching almost ambient values but suddenly increases again when the exhaust is trapped by the vortices; now, the air mass within the cores is almost completely blocked from exchange with environmental air, the vortex descends and, thus, the air mass becomes warmer than the surrounding air. Hence, we can date the end of the jet regime to 20s of plume/wake age. The vortex pair trails downward at a constant speed of about 1.5m/s for all cases, see the linear growth

of h' . The effect of turbulence on the wake life cycle is prominent: In case N the flow becomes practically two-dimensional because the jet velocity $-u$ decays monotonously. In cases B and A, on the other hand, the superimposed turbulent fluctuations trigger a three-dimensional development, visible by the increase of $-u$, which naturally amplifies the vortex decay. When $-u$ increases it can no longer be associated with the jet velocity but reflects axial perturbations of the swirl flow. The onset of the vortex breakdown is also documented by the increase of the pressure minimum in the cores (decay of p' in Figure 6).

In comparison to case B we see that in presence of atmospheric turbulence (case A) the vortex starts to collapse earlier. Since the initial atmospheric perturbations are almost one order of magnitude smaller than the imposed boundary-layer turbulence we have to associate this effect (i) to the typical size of the largest eddy, which is 5 times larger than the vortex diameter, and/or (ii) to the fact that the atmospheric turbulence is present *outside* the vortices whereas the maximum of boundary-layer turbulence is situated at R_C , *i.e.* *inside* the vortices. This finding was documented also in a preliminary study with idealized wakes (Gerz and Palma 1994b).

Figure 7 depicts span-height cross-sections of x -

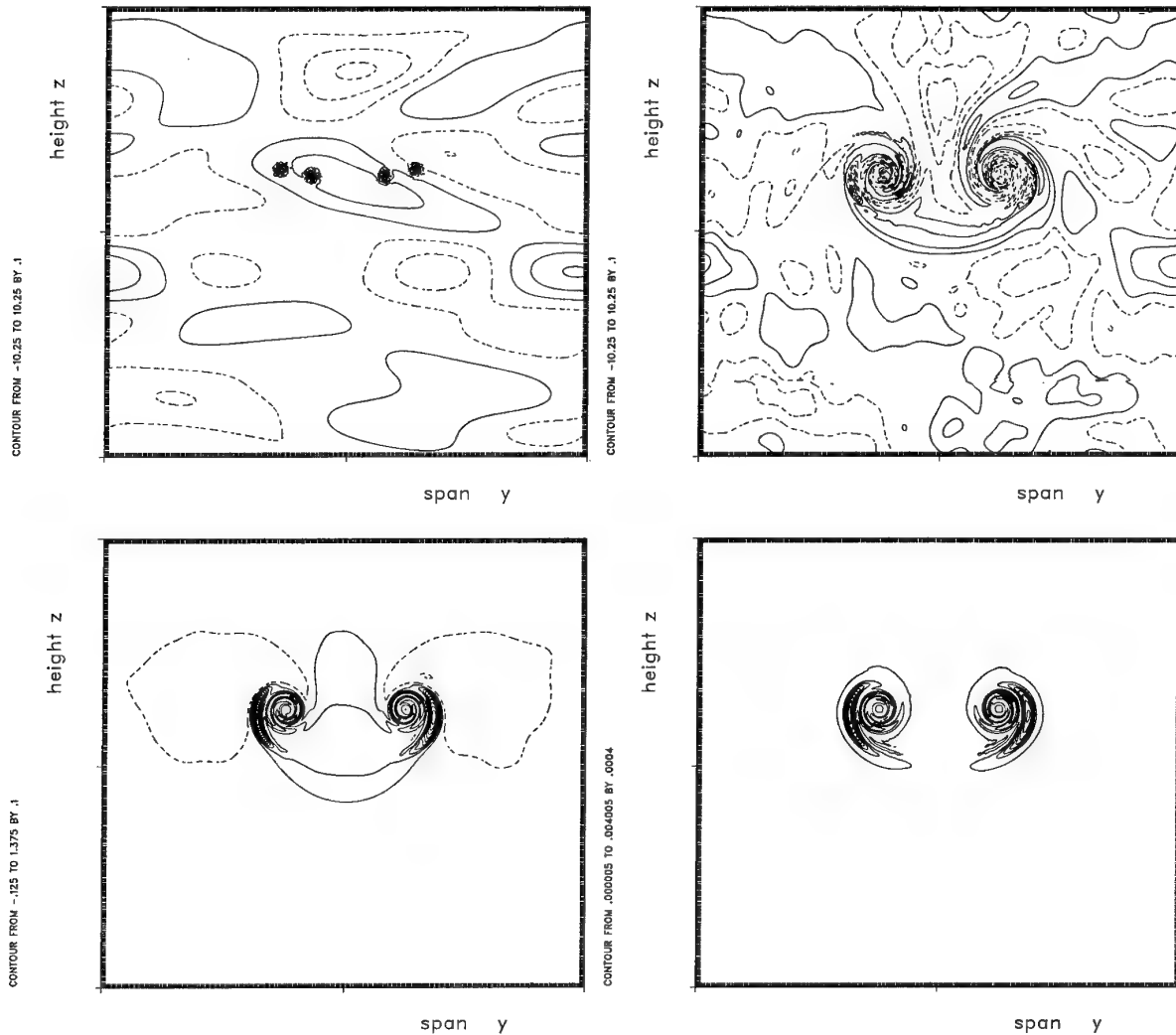


Figure 7: The wake of case A in the jet regime in terms of u (top left at 1s or 4.1 spans, top right at 6s or 24.7 spans), θ' (bottom left, 6s) and $c'/c'(0)$ (bottom right, 6s) in span-height cross-sections of size $192\text{m} \times 180\text{m}$. All quantities are averaged over meshes in x ($=$ flight) direction. Contours for u from $-17/-0.6$ (left/right) to 0.3m/s with interval 0.1m/s , contours for θ' from -0.125 to 1.4K with interval 0.1K , contours for $c'/c'(0)$ from 0.005×10^{-3} to 4×10^{-3} with increment 0.4×10^{-3} . Negative values are marked by dashed lines.

averaged fields of streamwise flow component u , potential temperature θ' , and species concentration $c'/c'(0)$ for case A. At 1s, the flow out of the four turbines into the turbulent atmosphere can clearly be recognized. The flow pattern attributed to atmospheric turbulence is similar to the one obtained by Spalart and Wray (1996, this issue) who considered the effect of isotropic turbulence on the wake lifespan. At 6s, the now fully developed vortex modifies the atmospheric turbulence such that the motion in the drainage area above the vortices becomes coherent and smaller-scale eddies develop around them. As also found and discussed in greater detail by Corjon *et al.* (1996, this issue), sheets of opposite sign of streamwise velocity component u wrap around each vortex. We see that together with the exhaust also ambient air is sucked into the trailing vortex pair. The upward flow left and right from the pair transports air from lower, *i.e.* potentially colder heights

into warmer regions, visible as the area enclosed by the dashed θ' contour. In the fields of θ' and $c'/c'(0)$ we can distinguish the exhaust from the outer engines from that of the inner ones: the former are already smoothed out around the cores, the latter are still higher concentrated in a half-moon like shape. Hence, we are still in the jet regime of the wake evolution. At this flow stage the cases N and B look the same (cf. Figure 6).

Figure 8 depicts the wakes of cases B and A after 87s. Case N is not shown because the differences to case B are minimal at this flow stage. (Note that we mapped the fields on a larger domain compared to the figures before.) After 87s, the vortex pair has travelled downward 148m in B, 141m in A leaving a wake behind, the so-called "secondary wake" (the wake of the wake) as visible in all quantities shown. The air inside the vortices becomes detrained due to

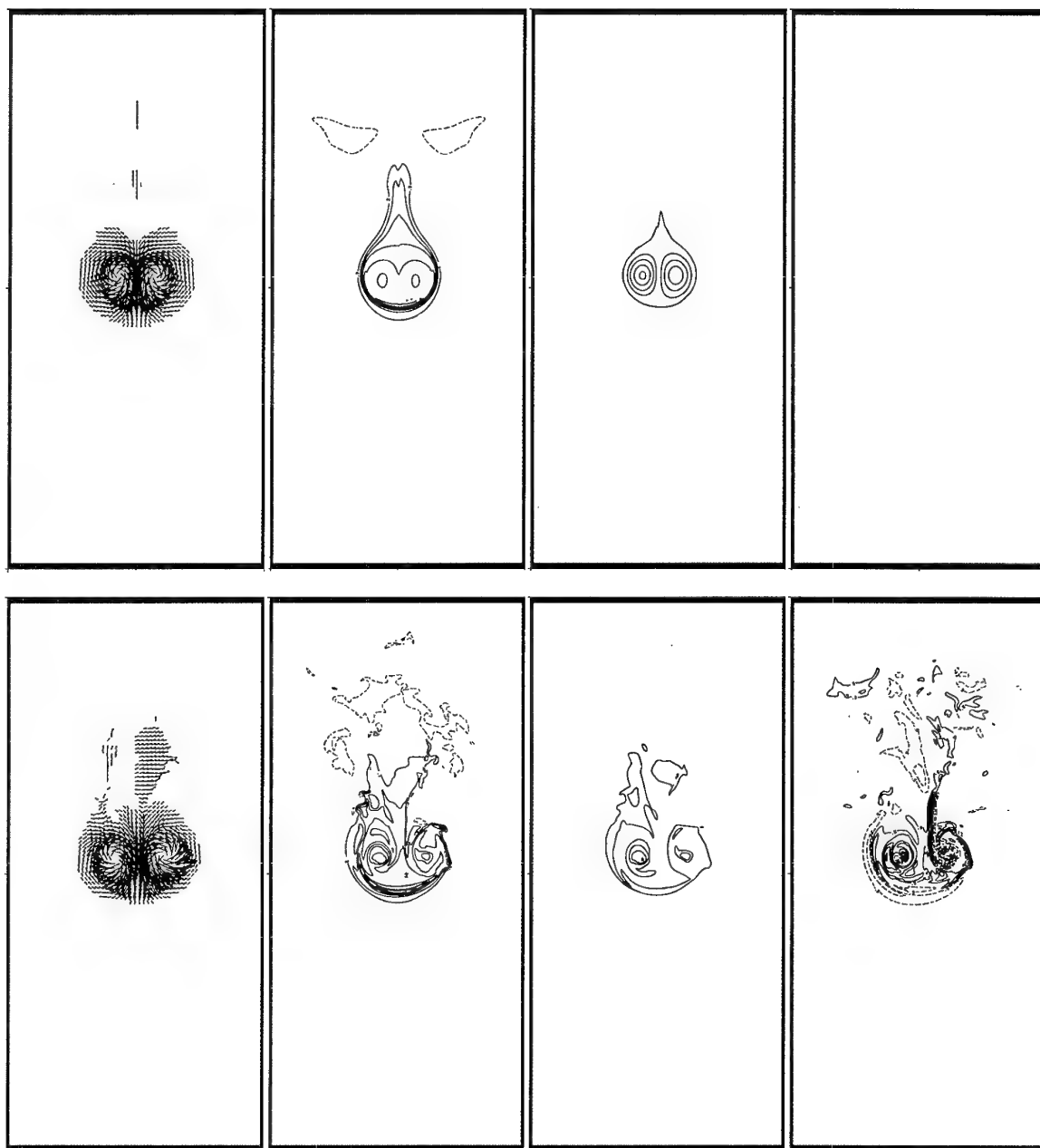


Figure 8: The instantaneous wakes of case B (top) and A (bottom) after 87s or 358 spans (vortex regime) in span-height cross-sections of size $256\text{m} \times 540\text{m}$. From left to right: (v, w) with magnitude $\geq 1\text{m/s}$; θ' from -0.2K with increment 0.2K ; $c'/c'(0)$ from 0.5×10^{-5} with increment 5×10^{-5} ; u from -3m/s with increment 0.5m/s . Negative values are marked by dashed lines. The data are not averaged.

baroclinicity as analyzed by Scorer and Davenport (1970) and by turbulent motions. If both mechanisms are absent in a viscous flow, all material stays in the vortex cores until they dissolve by the action of molecular friction. (We call to notice that the detrainment of previously entrained exhaust as visible here is different from the phenomenon outlined in the previous section.) Maxima of temperature and tracer concentration are found in the vortex cores. The upward motion of the relatively warm and, hence, buoyant material in the secondary wake amounts to about

1m/s . The instantaneous flow fields depicted in Figure 8 indicate that case A is in a more "advanced" state than case B. However, the fields averaged over meshes in x direction (not shown) reveal that the flow states of both B and A can still be attributed to the vortex regime for the vortex-pair structures are intact. Note that the atmospheric turbulence event has ceased in the meanwhile (see area below the vortices compared to Figure 7) but was sufficient to trigger strong shear layers in the streamwise flow component u . It is known that such axial flow disturbances

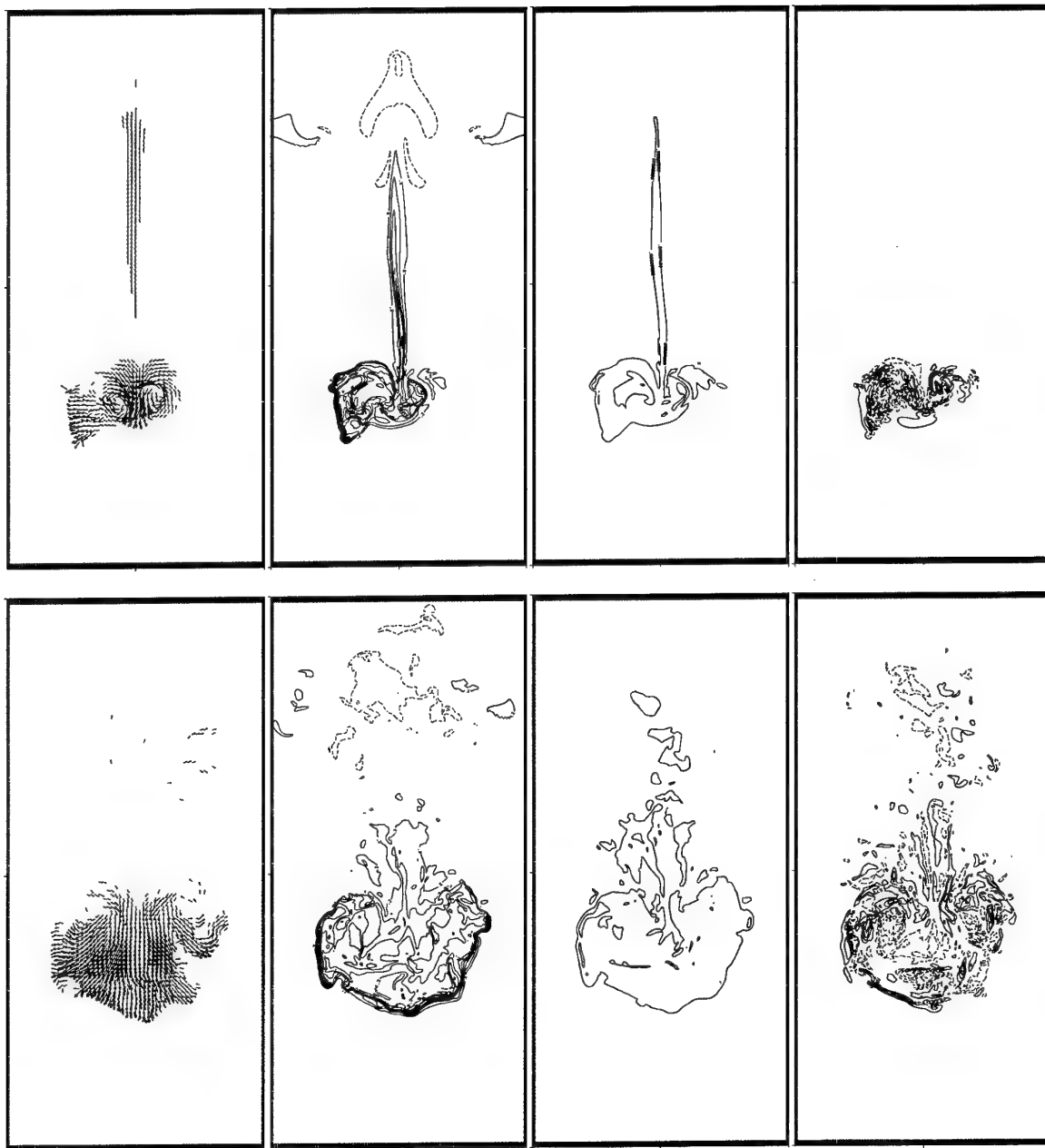


Figure 9: As Figure 8 after 146s or 601 spans corresponding to late vortex regime for B (top) and early dispersion regime for A (bottom).

quickly result in vortex instabilities like Crow instability (Crow 1970) or vortex bursting (see, e.g., Ragab and Sreedhar 1995 and references therein).

After 146s (Figure 9), the vortex pairs B and A have almost stopped their descent. The oscillation period of our model atmosphere is 7.5min. Hence, after about 130s, a quarter of the period, the vortices should stop trailing downwards when the translational kinetic energy of the vortices has decreased to a value necessary to work against gravity. The fact that they still move a little is due to the decreased vortex separation (see below) which increases the inductive

downward propagation. Even after a complete stop of the vortices they will not move upward again as long as their reservoir of rotational energy creates enough translational energy which compensates the work of buoyancy. But as a consequence, the rotational energy reservoir ceases quickly now resulting in vortex dissolution.

A remarkable difference between B and A is the character and size of the secondary wake. In B all field quantities show a rather coherent structure, namely a horizontally thin but vertically very elongated curtain of warm upwelling exhaust ($w \approx 1\text{m/s}$) de-

trained from the vortices below. The secondary wake of case A, on the other hand, is much more diffuse and broader. This difference becomes even more pronounced in the averaged fields.

In case N, a fully symmetric secondary wake develops which is qualitatively similar to case B. In contrast to the turbulent cases, however, the core region is still intact and the vortex pair continues to trail downward at this time, since its core separation is 23m now (*i.e.* half its initial value) which increases its translational energy. That substantial approach of the two vortices occurs in all cases with buoyancy because the baroclinic torque at the edge of the vortex detains vorticity from the core into the secondary wake. Then the two vortices have to approach each other in order to conserve their circulation (Scorer and Davenport 1970).

7. DISCUSSION AND CONCLUSION

By means of a vortex-filament technique (VFT) and large-eddy simulations (LES) we simulated the wake dynamics of a subsonic aircraft under cruising conditions from the nozzle exit to the distance where the trailing vortex pair begins to collapse. Within that dynamical frame, the distribution of the exhaust concentration has been described.

Special emphasis was given to the early exhaust distribution. The distortion of the circulation distribution by the body of the aircraft and the buoyancy force of the hot exhaust capable to overweight the attracting force of the swirling flow (Table 3) both could influence such a distribution. From the cases studied here we learned that already the initial mutual inductions of the vortex sheet provide a force strong enough to influence the exhaust distribution (Figure 5). The body has no significant effect on the distribution. Hot buoyant exhaust gets trapped even quicker than cold non-buoyant exhaust. Hence, the question how an exhaust distribution as depicted in Figure 1 may evolve remains open. During the first second (using VFT) we only considered the influence of the vortices on the tracer positions. The effect of the buoyant exhaust on the roll-up process can be neglected according to a study by Jacquin and Garnier (1996, this issue). A future analysis by VFT, however, should include the action of turbulence from the aircraft boundary-layer and the atmosphere.

Further, the early life path of the vortex wake was studied as it evolves in a stably stratified atmosphere. Since turbulence has a major impact on the dissolution of the organized vortex pair, we considered three cases: No turbulence at all (N), aircraft boundary-layer turbulence (B), and weak atmospheric turbulence (A) as the typical case along flight tracks in the region of the atmosphere's tropopause. Our simulations show that a cruising aircraft of type B-747 with a typical weight below maximum take-off weight develops a wake with a jet-regime duration of 20s, *i.e.* 5km or 83 wingspans downstream (Figure 6). The vortex sheet is fully rolled-up after 5 or 6s (Table 2). During the vortex regime all cases developed a secondary wake due to detrainment of vorticity, momentum, heat, and species from the vortex cores. The

detrainment is caused by baroclinicity and turbulence. Size and organization of the secondary wake, however, as well as the history of the vortex cores, as onset and evolution of the vortex instabilities, strongly depend on the character of the imposed turbulence. Thereby, we found that atmospheric turbulence — although being weak in amplitude — has the strongest capabilities to destroy the organized structure owing to the typical length scales of the atmospheric eddies which are larger than the vortex-core diameter.

From the data evaluated so far we can summarize that after 146s case N is still in the vortex regime, case B is about to leave it, and case A stays already in the dispersion regime. This reads in detail that after 146s two parallel vortex tubes exist in case N without a signature of distortion of the vortex axes, the two vortices experience a radial distortion of their axes but do not link yet in case B, and in case A finally the two vortices have linked and formed rings already.

The set-up of the simulations was oriented on *in-situ* measurements in wakes behind B-747 airliners. Busen *et al.* (1994) measured in the 1 min old contrail of a B-747 the cross-stream velocity components which revealed the existence of two counterrotating vortices, about 40m apart, with swirl velocities of 6 to 8m/s. The signals of temperature and relative humidity show two maximum peaks in the vortex centres and a relative minimum value between the vortices. Figure 6 and Figure 8 corroborate these measurements qualitatively and quantitatively very well. Moreover, the measured temperature increase of 1K inside the contrail puzzled the investigators since they assumed complete diffusion of heat after 60s. However, our simulations corroborate the measurement quite well (see Figure 6) and indicate that this temperature excess is due to the encapsulated air mass in the vortex cores trailing downward in a stably stratified atmosphere.

Measurements of nitrogen oxides concentrations in the 49 to 140s old wake behind a cruising B-747 also confirm our simulations at least qualitatively. The data deliver a concentration maximum at the height of the vortex cores and continuously smaller concentrations in the secondary wake up to flight level, see Figure 9. A study to quantify the comparison between *in-situ* measured and simulated data including chemical transformations in the wake is underway (Gerz *et al.* 1996).

It is documented in Figure 6 for cases B and A that during the onset of the vortex collapse the maximum values of the velocity components increase. This corroborates measurements in the NASA-Ames wind tunnel (Rossow 1996, this issue). Ongoing research will shed more light on the underlying instability process.

To our knowledge this is the first attempt to study the four-dimensional lifespan of an aircraft wake, starting at the wings and turbines and including density effects in the exhaust, atmospheric stratification,

and turbulence stemming from the boundary layer of the aircraft as well as from atmospheric motions. A similar work by means of LES has been set up recently by Lewellen and Lewellen (1996). They, however, start their calculations with essentially rolled-up vortices about 20 wingspans ($\approx 5s$) downstream and include the effect of cross-wind shear.

Acknowledgements.

The work was supported by the German Bundesministerium für Bildung, Wissenschaft, Forschung und Technologie (BMBF) within the project "Schadstoffe in der Luftfahrt" and by the Deutsche Forschungsgemeinschaft (DFG) within the project "Grundlagen der Auswirkungen der Luft- und Raumfahrt auf die Atmosphäre".

REFERENCES

- Busen R., Baumann R., Reinhardt M.E., Fimpel H., Kiemle C. and Quante M. 1994: Measurements of physical properties in the wake of commercial aircraft. In: *Impact of Emissions from Aircraft and Spacecraft upon the Atmosphere* (U. Schumann and D. Wurzel, eds.), DLR Mitteilung 94-06, Köln, 297-302.
- Corjon, A., Risso, F., Stoessel, A., Poinso, T. 1996: Three-dimensional direct numerical simulation of wake vortices: Atmospheric turbulence effects and rebound with crosswind. Paper 28 in this issue.
- Crow, S. C. 1970: Stability theory for a pair of trailing vortices. *AIAA Journal* **8**, 2172-2179.
- Deidewig, F. 1992: Schadstoffemissionen ziviler Flugtriebwerke am Beispiel des CFM56-3 und CF6-80C2. *Int. Bericht der DLR* **325-4/92**, pp. 89.
- Dürbeck T. and Gerz, T. 1995: Large-eddy simulation of aircraft exhaust plumes in the free atmosphere: effective diffusivities and cross-sections. *Geophys. Res. Letters* **22**, 3203-3206.
- Fell, S. and Staufenbiel, R. 1995: Formation and structure of vortex systems generated by unflapped and flapped wing configurations. *Z. Flugwiss. Weltraumforsch.* **19**, 366-379.
- Ehret, T. and Oertel, H. 1994: Numerical simulation of the dynamics and decay of trailing vortices including pollutants from air traffic. In: *Impact of Emissions from Aircraft and Spacecraft upon the Atmosphere* (U. Schumann and D. Wurzel, eds.), DLR Mitteilung 94-06, Köln, 268-273.
- Ehret, T. 1996: Stability theory of two wing tip vortices behind cruising aircraft. Paper 20 in this issue.
- Gerz, T. and Schumann, U. 1989: Influence of initial conditions on the development of stratified homogeneous turbulent shear flow. In: *Finite Approximations in Fluid Mechanics II, Notes on Numerical Fluid Dynamics* (E.H. Hirschel, ed.), Vieweg-Verlag, **25**, 142-156.
- Gerz, T. and Palma, J. M. L. M. 1994 (a): Sheared and stably stratified homogeneous turbulence: Comparison of DNS and LES. In: *Direct and Large-Eddy Simulation I* (P. Voke, L. Kleiser and J.-P. Chollet, eds.), Kluwer Dordrecht, 145-156.
- Gerz, T. and Palma, J. M. L. M. 1994 (b): Influence of atmospheric turbulence on the development of an idealized airplane wake: Numerical studies. In: *Impact of Emissions from Aircraft and Spacecraft upon the Atmosphere* (U. Schumann and D. Wurzel, eds.), DLR Mitteilung 94-06, Köln, 309-314.
- Gerz, T., Kärcher, B., Baumann, R., Beier, K., Deidewig, F., Dürbeck, T., Ehret, T., Haschberger, P., Konopka, P., Schlager, H. 1996: Transport and chemistry of emissions in the wake of subsonic aircraft. Part I: Jet and vortex regimes. To be submitted.
- Hoinka, K.-P., Reinhardt, M. E. and Metz, W. 1993: North atlantic air traffic within the lower stratosphere: cruising times and corresponding emissions. *J. Geophys. Res.* **98**, 23113-23131.
- Jacquín, L. and Garnier, F. 1996: On the dynamics of engine jets behind a transport aircraft. Paper 37 in this issue.
- Kärcher, B. and Fabian, P. 1994: Dynamics of aircraft exhaust plumes in the jet-regime. *Ann. Geophysicae* **12**, 911-919.
- Kaltenbach, H.-J., Gerz, T. and Schumann, U. 1994: Large-eddy simulation of homogeneous turbulence and diffusion in stably stratified shear flow. *J. Fluid Mech.* **280**, 1-40.
- Lewellen, D. C. and Lewellen, W. S. 1996: Large-eddy simulations of the vortex pair breakup in aircraft wakes. Subm. to *AIAA J.*
- Miake-Lye, R. C., Martinez-Sanchez, M., Brown, R. C. and Kolb, C. E. 1993: Plume and wake dynamics, mixing, and chemistry behind a high speed civil transport aircraft. *J. Aircraft* **30**, 467-479.
- Quackenbush, T. R., Teske, M. E. and Bilanin, A. J. 1993: Computation of wake/exhaust mixing downstream of advanced transport aircraft. *AIAA* **93-2944**, 15 pp.
- Quackenbush, T. R., Teske, M. E. and Bilanin, A. J. 1996: Dynamics of exhaust plume entrainment in aircraft vortex wakes. *AIAA* **96-0747**, 16 pp.
- Ragab S. and Sreedhar M. 1995: Numerical simulation of vortices with axial velocity deficits. *Phys. Fluids* **7**, 549-558.
- Robins, R. E. and Delisi D. P. 1990: Numerical study of vertical shear and stratification effects on the evolution of a vortex pair. *AIAA J.* **28**, 661-669.
- Robins, R. E. and Delisi, D. P. 1996: Nonlinear development of sinusoidal instability for a pair of trailing vortices. Subm. to *AIAA J.* in 1995.
- Rossow, V. J. 1996: Measurements in vortex wakes shed by conventional and modified subsonic aircraft. Paper 26 in this issue.
- Scorer, R. S. and Davenport, L. J. 1970: Contrails and aircraft downwash. *J. Fluid Mech.* **43**, 451-464.
- Scotti, A., Meneveau, C. and Lilly, D. K. 1993: Generalized Smagorinsky model for anisotropic grids. *Phys. Fluids A* **5**, 2306-2308.
- Schumann, U. 1994: On the effect of emissions from aircraft engines on the state of the atmosphere. *Ann. Geophysicae* **12**, 365-384.
- Schumann U., Konopka P., Baumann R., Busen R., Gerz T., Schlager H., Schulte P. and Volkert, H. 1995: Estimates of diffusion parameters of aircraft exhaust plumes near the tropopause from nitric oxide and turbulence measurements. *J. Geophys. Res.* **100**, 14147-14162.
- Spalart, P. R. and Wray, A. A. 1996: Initiation of the Crow instability by atmospheric turbulence. Paper 18 in this issue.
- WMO 1995: Scientific Assessment of Ozone Depletion 1994, Global Ozone Research and Monitoring Project - Report **37**, WMO, Geneva, Switzerland, 1995.

The Use of Aircraft Wakes to Achieve Power Reductions in Formation Flight

Prof. Dr.-Ing. D. Hummel

Institut für Strömungsmechanik
Technische Universität Braunschweig
Bienroder Weg 3, D-38106 Braunschweig
Germany

SUMMARY

Many migrating bird species fly in regular V-shaped formations. Each wing experiences an upwash field generated by all other wings in the formation and this leads to a reduction in flight power demand for each wing as well as for the whole formation. In this paper the aerodynamic interference is studied by means of aerodynamic theory. The total energy saving for the whole formation increases with the number of wings and with decreasing lateral distance. Local power reductions are highest in the inner parts of a formation and they decrease towards the apex and the side-edges. The technical realization of this principle is analysed for two airplanes. In calibration flights of gliders large distances have to be kept or the aerodynamic interference has to be taken into account. In formation flights of two airplanes a power reduction of 15% is obtainable for the rear airplane flying close to the wake of the front aircraft. The corresponding aileron and rudder deflections for compensation of the corresponding moments are small. Flight tests with two airplanes Do-28 show that the power reduction can be achieved in practical flight. The results are in excellent agreement with aerodynamic theory. In order to enable the rear airplane to find the proper position relative to the wake of the front airplane an automatic control system has been adapted. A formation flight controller has been designed which leads the upwash in the symmetry plane and the aileron deflections to maximum values. The application of this control system led to a considerable relief of the pilot and important power reductions could be achieved automatically.

1. INTRODUCTION

Migrating birds such as Swans, Geese, Pelicans and Cranes fly in regular V-shaped formations as shown in Fig. 1. The birds are located almost at the same flight level. They are ordered in swept lines and they keep so small spanwise distances that the wing tips of two adjoining individuals lie about one behind the other. Presently it is common understanding that this flight mode has two advantages: In these flight formations a power reduction takes place which leads to an aerodynamic benefit for all individuals. In addition in such regular formations exist good optical relations between the birds which lead to a communication benefit. Both aspects have been discussed by D. Hummel [1].

In the aeronautical sciences the problem of formation flight has been considered with respect to airplanes.

C. Wieselsberger [2] was the first to give the correct explanation for the power reduction in such formations. After the development of aerodynamic theory, see e.g. H. Schlichting, E. Truckenbrodt [3], H. Schlichting [4] performed calculations on the drag reduction in symmetrical V-shaped

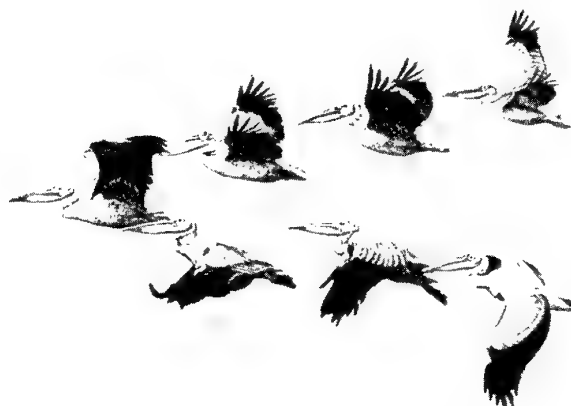


Fig. 1: Formation of migrating White Pelicans (*Pelecanus onocrotalus*). Drawing by James P. Smith.

flight formations of airplanes on the basis of Prandtl's lifting-line theory. Later P. B. S. Lissaman, C. A. Schollenberger [5] investigated optimum formation shapes and D. Hummel [6], [7], [8] extended the method of H. Schlichting [4] to arbitrarily shaped formations of wings having different span, weight and aspect ratio. More detailed investigations have been carried out by D. Hummel, K.-W. Bock [9] to include aileron deflections to compensate the rolling moment due to unsymmetric lift distribution. More recently formation flight has been studied theoretically on the basis of lifting-surface theory for unrolled, plane vortex sheets behind the wings by M. Beukenberg, D. Hummel [10] and for rolled-up vortex sheets by D. Hummel, M. Beukenberg [11]. All these theoretical investigations showed clearly that in formation flight considerable flight power reductions can be achieved. Some principles of aerodynamic interference and theoretical results for flight formations will be discussed subsequently in section 3.

Further investigations concerning the practicability of formation flights of airplanes have been carried out at TU Braunschweig. Calibration flights of gliders have been

analysed in detail and the corrections for proper single flight data have been given by means of aerodynamic theory. Concerning the power reduction formation flights have been performed with two airplanes Dornier Do-28. The shape of the formation has been documented from a third airplane Do-27 and the energy consumption has been measured in flight. Results of these flight tests as well as comparisons with theoretical predictions according to M. Beukenberg and D. Hummel [10], [12], [13] will be shown in section 4.

During the flight tests the pilot of the rear airplane had difficulties to maintain simultaneously the proper flight condition and the correct location relative to the wake of the front airplane. To overcome these problems an automatic control system has been adapted for the rear airplane. The control process was based on an existing 3-axes digital autopilot which was initiated by a guiding system to optimize the power reduction. For this purpose the upwash in the symmetry plane and the aileron deflection measured in flight were chosen to reach maximum values. The control system has been tested under simulated conditions as well as in practical flight [12], [13]. The results will be discussed in section 5.

2. NOTATIONS

2.1 Symbols

$A = b^2/S$	Aspect ratio
b	Span
b'	Reduced span, Equ. (8)
c	Chord
$c_L = L/qS$	Lift coefficient
$c_D = D/qS$	Drag coefficient
e	Local relative power reduction, Equ. (4)
E	Total relative power reduction, Equ. (7)
F	Thrust, throttle position
N	Flight power demand
$q = \rho V^2/2$	Dynamic pressure
$s = b/2$	Half span
S	Wing area
V	Flight speed
W	Weight
w	Upwash velocity, Equ. (1)
x, y, z	Rectangular coordinates, Fig. 2
$\Delta\xi = \Delta x/s$	Dimensionless distances in flight formations, Fig. 2
$\Delta\eta = \Delta y/s$	
$\Delta\zeta = \Delta z/s$	
α_w	Upwash angle, Equ. (1)
δ	Difference related to initial values
Γ	Circulation

2.2 Subscripts

c	Commanded quantity
ell	Elliptical circulation distribution
w	Pilot-controlled quantity
0	Single flight
1	Front airplane
2	Rear airplane
μ	Wing under consideration
v	Inducing wing
$-$	Mean value over wing span (section 3) or over time (section 4)

Further notations may be taken from section 3.1 and the text.

3. AERODYNAMICS OF FORMATION FLIGHT

3.1 Basic ideas

The investigations following here are concerned with arbitrarily shaped flight formations of different wings μ in horizontal flight at the same level according to Fig. 2. It is assumed that the shape of the formation remains constant with respect to time. This means that all wings fly at the same speed V . The corresponding dynamic pressure is $q = \rho V^2/2$. The different size of the wings is described by their span b_μ ($\mu = 1, 2, \dots, n$) where n is the total number of wings present in the formation. If all wing spans are related to a reference span b , the corresponding dimensionless parameter is $B_\mu = b_\mu/b$. The planform shape is characterized by the aspect ratio $A_\mu = b_\mu^2/S_\mu$. For given values of A_μ and B_μ the wing area is $S_\mu/b^2 = B_\mu^2/A_\mu$. In the various positions μ of the formation the wing loading W_μ/S_μ may be different. According to the balance of the vertical forces the corresponding dimensionless parameter is the lift coefficient $c_{L,\mu} = W_\mu/qS_\mu$ of each wing μ .

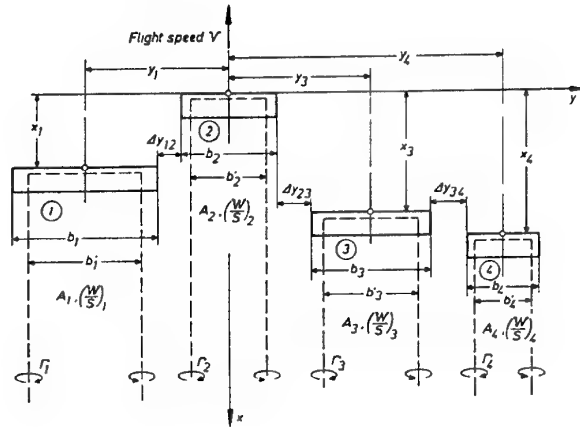


Fig. 2: Arrangement of wings in an arbitrarily shaped flight formation (example $n = 4$) and calculation of the interference effects by means of single horse-shoe vortices.

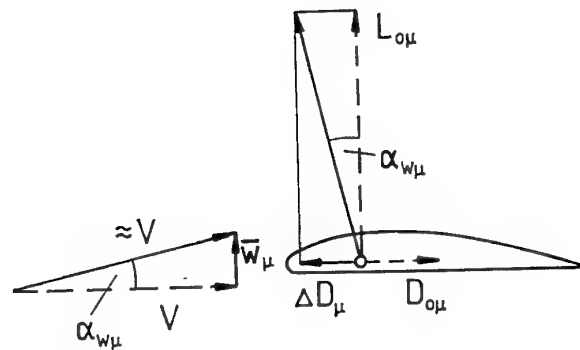


Fig. 3: Drag reduction ΔD_μ on wing μ due to upwash \bar{w}_μ .

In horizontal flight of a single wing μ (subscript 0) the lift $L_{0\mu}$ equals the weight W_μ and the power demand is $N_{0\mu} = D_{0\mu} \cdot V$, see Fig. 3. The drag consists of friction drag and of induced drag. The aerodynamic principle in flight formations is that each wing μ flies in an upwash field generated by all other wings v in the formation. In general the upwash is a function $w_\mu(y_\mu)$ of the spanwise coordinate y_μ of the wing μ under consideration. Its average value over the wing span is \bar{w}_μ . Due to this upwash the flow direction and thus the direction of lift ($L_\mu = L_{0\mu}$) is turned at an upwash angle

$$\alpha_{w\mu} = \frac{\bar{w}_\mu}{V} \quad (1)$$

as indicated in Fig. 3. This leads to a drag reduction at the wing μ

$$\Delta D_\mu = L_\mu \cdot \frac{\bar{w}_\mu}{V} = L_{0\mu} \cdot \frac{\bar{w}_\mu}{V} \quad (2)$$

and the corresponding reduction in flight power demand is

$$\Delta N_\mu = \Delta D_\mu \cdot V = L_{0\mu} \cdot \bar{w}_\mu \quad (3)$$

Based on the power demand for the same wing in single flight at the same speed V , the relative power reduction of wing μ is

$$e_\mu = \frac{\Delta N_\mu}{N_{0\mu}} = \frac{L_{0\mu} \cdot \bar{w}_\mu}{D_{0\mu} \cdot V} \quad (4)$$

The total reduction of flight power demand of the whole formation of n wings is

$$\Delta N = \sum_{\mu=1}^n \Delta N_\mu \quad (5)$$

and based on the power demand of all wings μ in single flight

$$N_0 = \sum_{\mu=1}^n N_{0\mu} \quad (6)$$

the relative power reduction of the whole formation can be expressed as

$$E = \frac{\Delta N}{N_0} \quad (7)$$

3.2 Calculation of the induced velocities

3.2.1 Horse-shoe vortex representation

The simplest analysis of flight formations can be achieved by replacing each inducing wing v according to Fig. 2 by a single horse-shoe vortex of span

$$b'_v = \frac{\pi}{4} b_v \quad (8)$$

and circulation

$$\Gamma_v = \frac{L_v}{\rho V b'_v} = \frac{2}{\pi} \frac{C_{L_v}}{A_v} V b_v \quad (9)$$

The induced upwash \bar{w}_μ at wing μ generated by all other

wings v of the formation is then easily calculated. This simple analysis has been applied by H. Schlichting [4] as well as by D. Hummel [1], [6], [7], [8].

3.2.2 Unrolled vortex sheet representation

If mean values \bar{w}_μ over the wing span of wing μ are used, the flow is symmetrical for each wing and no rolling moment occurs. To calculate the rolling moment due to asymmetrical upwash distribution and to compensate by means of proper aileron deflections, a more detailed analysis is necessary. In this case the wings and their wakes are replaced by plane vortex sheets with bound vorticity on the wing and a distribution of free vortices behind the wing. In the first step, the free vortex sheet is assumed to be unrolled and located in the plane of the wing. For the calculation of the induced velocities different approaches have been used by D. Hummel, K. W. Bock [9] and M. Beukenberg, D. Hummel [10]. From both theories, a rolling moment results due to the asymmetrical lift distribution against the wing span. For compensation some aileron deflections have been applied. For each wing this led to an asymmetric lift distribution against span which produced no rolling moment. Although the corresponding load distribution turned out to be non-elliptic, a considerable power reduction resulted, which was of the same order of magnitude as calculated by the simpler method. The calculation of the aerodynamic interference on the basis of a lifting-surface representation of the wing and for plane, unrolled free vortex sheets behind the wings has been extended by M. Beukenberg [12] to arbitrarily shaped formations of airplanes. In this method, the horizontal tails of the airplanes are also taken into account, pitching and rolling moments about the centre of gravity are balanced by proper deflections of the ailerons and the elevator and arbitrary locations of the airplanes including horizontal and vertical distances are possible.

3.2.3 Rolled-up vortex sheet representation

A detailed analysis of flight formations of Geese by L. L. Gould, F. Heppner [14] indicates some overlap of the wing tips. Observations showed that in flight formations of Cranes the leading individual flies at lowest level and the following birds are slightly staggered in height. Both details can be explained by the fact that the free vortex sheet behind a wing rolls up from both sides into two concentrated wing-tip vortices. Their distance is $b' < b$ as indicated in Fig. 2 and they are located above the plane of the wing. In the simple horse-shoe vortex representation according to Fig. 2, however, a certain overlap is possible up to a distance of $\Delta y = -b(4 - \pi)/8 < 0$. In this case the wing tip touches the free vortex of the adjacent wing. The details of the near wake behind the wing are not covered properly by this vortex model since the span b' according to equ. (8) is the asymptotic value related to elliptic load distribution [3] and the correct vertical location of the wing-tip vortex is not represented. If optimum flight formations are considered and if details of the lateral and vertical distance of the wings are discussed the rolled-up vortex sheet in the near wake has to be taken into account.

Fig. 4 shows a formation of $n = 2$ wings in which rolled up trailing vortex sheets are considered. In calculations carried out by D. Hummel, M. Beukenberg [11] the lifting-surface theory of C. Urban, R. Behr, S. Wagner [15] has been used. In this method the shape of the wake turns out by

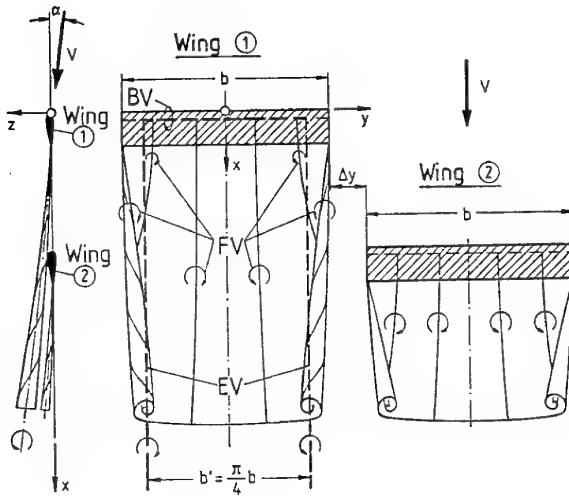


Fig. 4: Calculation of the interference effects by means of rolled-up vortex sheets, example $n = 2$ (BV bound vortex on the wing, FV free vortices behind the wing, EV equivalent single vortex, horse-shoe vortex).

means of an iteration procedure and the induced velocities generated by the non-planar vortex system are taken into account properly for the wing under consideration as well as for the evaluation of the mutual interference between the wings. Due to the iteration procedure calculations of this kind are extremely laborious. Some results are discussed subsequently.

3.3 Power reductions for wings

The power reduction in formation flight has been calculated according to different theoretical methods. Following here some typical results are shown in order to demonstrate the magnitude of the effects under consideration.

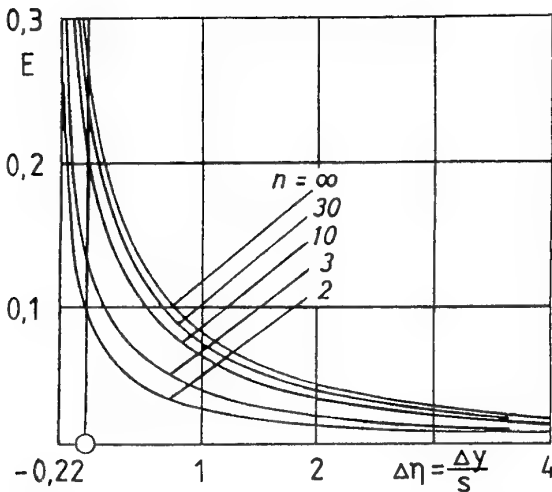


Fig. 5: Total power reduction in flight formations of equal wings as functions of spanwise distance and number of wings, $(c_{Di}/c_D)_0 = 0.5$.

In the case of equal wings the problem reduces considerably. In the simple horse-shoe vortex analysis the aspect ratio A_μ has not to be specified and the span ratio is $B_\mu = 1$. For each wing μ a quadratic polar

$$c_{D\mu} = c_{Dp\mu} + c_{Di\mu} = c_{Dp\mu} + \frac{c_{L\mu}^2}{\pi A_\mu} \quad (10)$$

is assumed, where c_{Dp} and c_{Di} denote the profile drag and the induced drag coefficients, respectively. For maximum range flight $c_{Di} = 0.5c_D$ and for minimum power demand $c_{Di} = 0.75c_D$ have to be considered. In the sample calculations $c_{Di} = 0.5c_D$ has been chosen. For minimum power demand the results should be multiplied by a factor of 1.5 [1].

Fig. 5 shows the total power reduction E in flight formations of equal wings as a function of spanwise distance $\Delta\eta = \Delta y/s$ and of the number of wings n . It turns out that the power reduction increases considerably with decreasing spanwise distance of the wings. The power reduction increases also with increasing number of wings n but there exists a limiting curve for $n \rightarrow \infty$ which has already been given by H. Schlichting [4]. The result according to Fig. 5 is independent of the actual shape of the formation. This is the well-known displacement theorem of M. M. Munk [16]. Thus it turns out that all flight formations having the same lateral distances between the wings and the same number of wings achieve the same total flight power reduction. For small spanwise distances the total flight power reduction reaches remarkable values. Even for two wings ($n = 2$) total flight power reductions in the order of magnitude of 10% for the maximum range condition and 15% for the minimum power condition are possible.

The distribution of the power reduction on the wings of the formation, however, depends strongly on the shape of the formation. Fig. 6 shows a typical example for formations of $n = 15$ equal wings at a spanwise distance $\Delta y = 0$. The wings are arranged on swept lines and the leading position n_1 is varied from $n_1 = 1$ (oblique line) over $n_1 = 4$ (unsymmetrical formation) to $n_1 = 8$ (symmetrical formation). The total power reduction $E = 0.23$ is the same for all these formations. In the leading position the power reduction is very low. This is due to the fact that the upwash decreases rapidly in upstream direction. The positions at both sides of the formation are also unfavourable since no neighbour-wings are present which would produce upwash. The worst position is those of the leading wing of a swept line formation ($n_1 = 1$) since both effects add. In the centre of straight lines the local power reduction lies over the average value.

If two wings are considered which fly side by side, the power reduction is equal for both wings. If one wing moves upstream the total power reduction for both wings remains constant according to Munk's theorem, but the front wing experiences a lower power reduction and the rear wing a larger one. In the limit of very large longitudinal distances the power reduction of the front wing tends to zero whereas the total power reduction, which is still present since a wake of the front wing exists, is concentrated on the rear wing. These results have been obtained on the basis of the simple horse-shoe vortex representation according to section 3.2.1. Further details may be taken from D. Hummel [6], [7], [8].

Improved calculations for flight formations have been carried out by D. Hummel, K.-W. Bock [9] in which the induced upwash $w_{\mu\nu}(y_\mu)$ has been taken into account and the

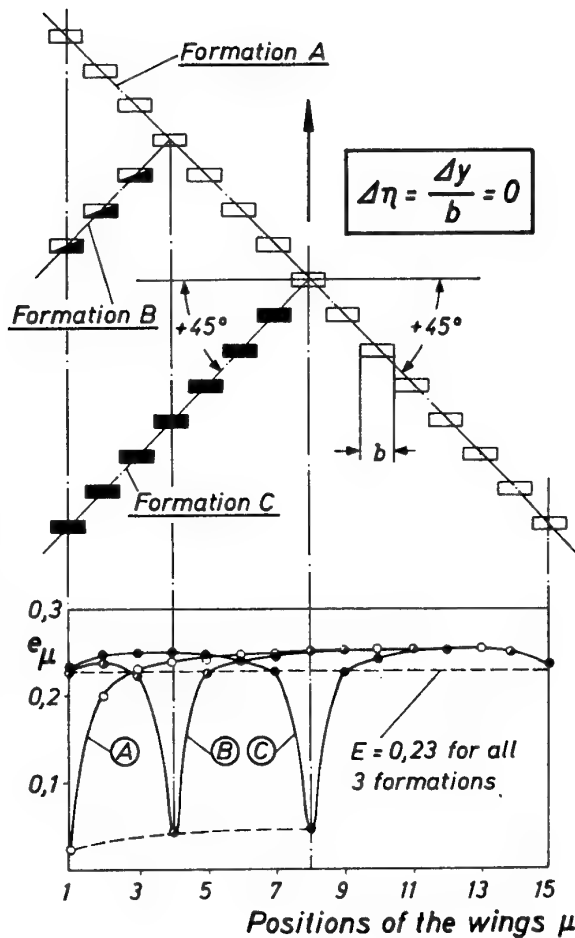


Fig. 6: Distribution of flight power reduction in 45° swept V-shaped formations of $n = 15$ equal wings at spanwise distance $\Delta y = 0$ and $c_{Di}/c_{D0} = 0.5$ for various leading positions n_1 .

Formation A = Oblique line, $n_1 = 1$
 Formation B = Unsymmetr. formation, $n_1 = 4$
 Formation C = Symmetrical formation, $n_1 = 8$.

resulting rolling moment has been compensated by aileron deflections. It turned out that the improved analysis led to slightly larger values of the calculated power reduction, especially for low spanwise distances. Results according to the simple horse-shoe vortex method may therefore be regarded as the minimum values of the power reduction which can be obtained.

Results for a more detailed analysis of the formation flight of two rectangular wings of aspect ratio $A = 6$, flying at a lift coefficient $c_L = 0.75$ and having a zero-lift drag coefficient $c_{D0} = 0.02$ are shown in Fig. 7. The longitudinal distance $\Delta\xi = \Delta x/s = 2$ is kept constant and the relative power reduction of the rear wing e_2 is plotted against the spanwise distance $\Delta\eta = \Delta y/s$. The dashed curve represents the results of the simple horse-shoe vortex method according to D. Hummel [1]. A certain overlap of the wing tips is possible and the adjacent free vortex is touched by the wing tip at $\Delta\eta = -0.22$. The results for a plane, unrolled vortex

sheet representation by means of lifting surface theory including aileron deflections for rolling moment compensation according to M. Beukenberg, D. Hummel [10] are also shown for comparison. In this case an overlap of the wing tips cannot be described. As mentioned already the calculated power reduction is slightly larger than that given by the simple horse-shoe vortex method. In addition results of calculations with a rolled-up vortex sheet representation are shown. In this case the free vortex sheet is located above the plane of the wing. From both sides wing-tip vortices roll up and the effective span of the vortex wake behind the wing is smaller than the wing span. Aileron deflections have not been taken into account in these calculations. If both wings are located in the same plane, $\Delta\zeta = \Delta z/s = 0$, the power reduction, obtained for the rear wing, is considerably smaller than that calculated from lifting-surface theory with unrolled vortex sheets. This is due to the fact that the rear wing is now located below the region of maximum upwash. For strong overlap the rear wing passes below the vortex wake of the front wing continuously into the region of downwash and a positive power reduction disappears at all. If the rear wing is slightly staggered in height relative to the front wing at $\Delta\zeta = 0.077$ the rear wing is still too low relative to the wake of the front wing, but the power reduction increases considerably, especially in the overlap region. For $\Delta\zeta = 0.155$ the rear wing is located aside the wing-tip vortex of the front wing and experiences maximum upwash. The power reduction too reaches a maximum for a certain small overlap. The comparison with the results according to lifting-surface theory with plane vortex sheet shows excellent agreement for $\Delta y > 0$. This means that calculations by means of the simpler theory are sufficient for positive spanwise distances, $\Delta y > 0$, whereas rolled-up vortex sheets have to be taken into account only for overlapping wing tips, $\Delta y < 0$. Further details may be taken from D. Hummel, M. Beukenberg [11].

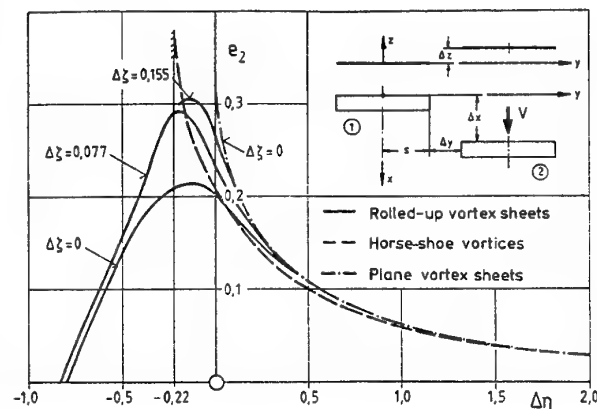


Fig. 7: Relative power reduction e_2 for the rear wing as function of the lateral distance $\Delta\eta = \Delta y/s$ for fixed longitudinal distance $\Delta\xi = \Delta x/s = 2$ and different vertical distances $\Delta\zeta = \Delta z/s$ for formations of two wings without and with overlaps of the wing tips. Comparison of the results according to different theories. (Wing parameters: aspect ratio $A_1 = A_2 = 6$, zero-lift drag coefficient $c_{D01} = c_{D02} = 0.02$, lift coefficients $c_{L1} = c_{L2} = 0.75$).

3.4 Power reductions for airplanes

Comprehensive sample calculations for formations of two equal airplanes have been carried out for realistic flight conditions. For this purpose the following data were chosen

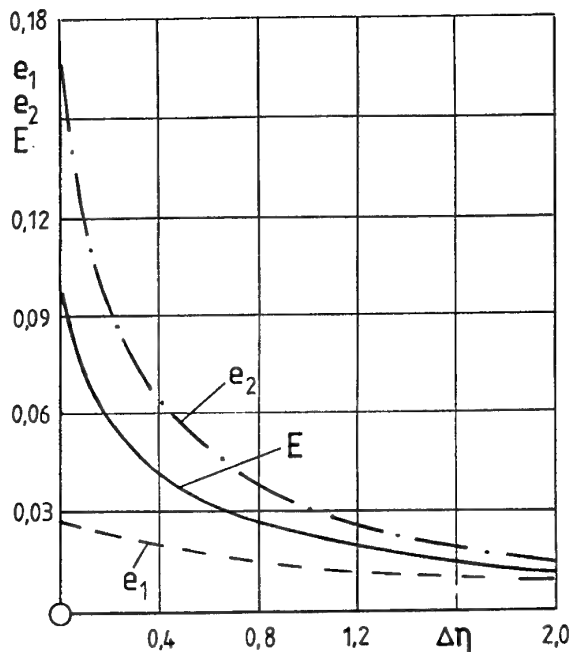
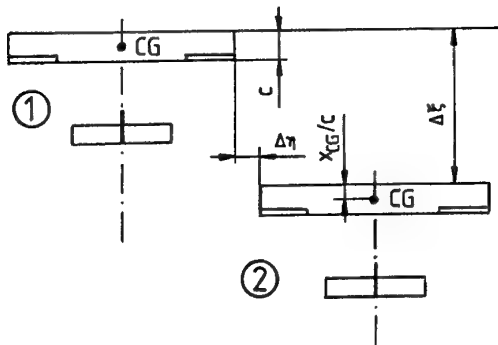
Wing: Rectangular wing $A_w = 6.0$
 Ailerons at } $\eta_Q = y_Q/b = 0.66$
 wing tip } $\lambda_K = c_K/c = 0.25$

Horizontal tail: Rectangular tail $A_T = 3.0$
 Size $b_T/b_w = 0.45$
 Position $\Delta\xi_T = \Delta x_T/s = 0.9$
 $\Delta\zeta_T = \Delta z_T/s = 0.1$
 Elevator: Free floating tail

Vertical tail: Aspect ratio $A_V = 1.5$
 Taper ratio $\lambda_V = 0.5$
 Leading-edge sweep $\varphi_V = 24^\circ$
 Size $b_V/b = 0.15$
 Rudder $c_K/c_i = 0.3$
 Position $\Delta\xi_V = \Delta x_V/s = 0.8$
 $\Delta\zeta_V = \Delta z_V/s = 0$

Centre of gravity position $x_{CG}/c = 0.25$

Zero-lift drag coefficient $c_{Dp} = 0.05$



Wings and tails in the formation have been taken into account by lifting-surface theory and plane vortex sheets. For each airplane the pitching moment about the centre of gravity was balanced by means of elevator deflections of the whole horizontal tail and the rolling moments due to unsymmetrical spanwise load distribution were compensated by means of aileron deflections. The resulting yawing moment again was balanced by corresponding deflections of the rudder of the vertical tail. More details about the geometry of the flight formations as well as on the calculation procedure may be taken from M. Beukenberg, D. Hummel [10] and M. Beukenberg [12].

The power reductions achieved in this flight formation at a constant lift coefficient $c_{L1} = c_{L2} = 0.7$ are shown in Fig. 8 as functions of the spanwise distance $\Delta\eta = \Delta y/s$ for a fixed longitudinal distance $\Delta\xi = \Delta x/s = 2$ and a fixed vertical distance $\Delta\zeta = \Delta z/s = 0$. The total power reduction for both airplanes is quite remarkable. For flight wing tip behind wing tip a total reduction of about 10% is achieved. Due to the longitudinal distance of both airplanes the power reduction is lower for the front airplane and higher for the rear airplane, reaching about 17% for flight with wing tip behind wing tip, $\Delta\eta = 0$.

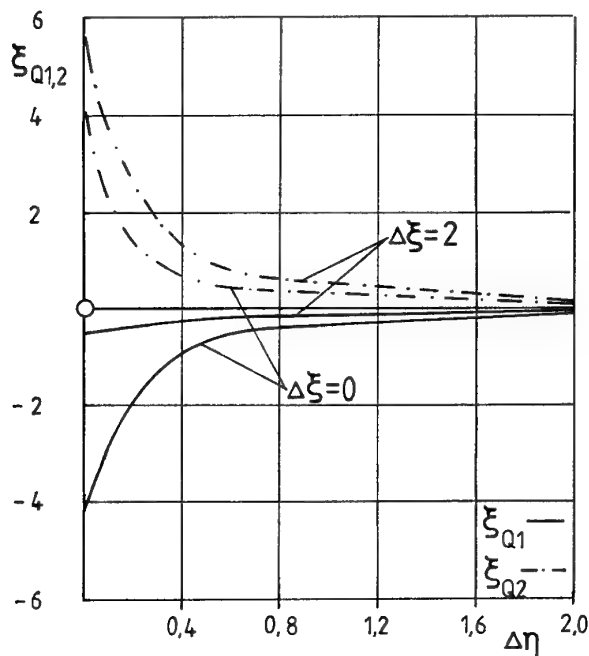


Fig. 9: Aileron deflections ξ_{Q1} , ξ_{Q2} as functions of the lateral distance $\Delta\eta = \Delta y/s$ for fixed longitudinal distance $\Delta\xi = \Delta x/s = 2$ and fixed vertical distance $\Delta\zeta = \Delta z/s = 0$ for formations of two sample airplanes. (Flight data as in Fig. 8).

Fig. 8: Relative power reductions E , e_1 , e_2 as functions of the lateral distance $\Delta\eta = \Delta y/s$ for fixed longitudinal distance $\Delta\xi = \Delta x/s = 2$ and fixed vertical distance $\Delta\zeta = \Delta z/s = 0$ for formations of two sample airplanes. (Flight parameters: Lift coefficients $c_{L1} = c_{L2} = 0.7$, zero-lift drag coefficients $c_{D01} = c_{D02} = 0.05$, centre of gravity position $x_{CG}/c = 0.25$).

The corresponding aileron deflections are shown in Fig. 9. They are opposite in sign for both airplanes and they are equal in size for flight side by side, $\Delta\xi = 0$, which is shown for comparison. For decreasing spanwise distance the aileron deflections increase. In the case of a longitudinal distance of both airplanes the aileron deflections are small for the front airplane and large for the rear airplane. The same applies in principle for the deflections of the rudder of the vertical tail, but the deflection angles are smaller; see M. Beukenberg [12].

Aileron deflection angles can be measured easily in flight. They can be used as a measure for the proper position of the rear airplane with respect to the wake of the front airplane. In an optimum flight formation the aileron deflections reach a maximum and this maximum can be used to find the proper positions.

4. FORMATION FLIGHT TESTS

4.1 Calibration flights of gliders

The determination of the performance of gliders is very laborious and expensive. There exist only a few planes for which the velocity polar, i. e. the sinking rate as function of airspeed, has been measured absolutely. These gliders are widely used as reference airplanes and all other new gliders are calibrated by means of comparison with such a reference glider and this is done in formation flight. The two gliders fly very close in spanwise direction and the formation is observed from a third airplane flying in far distance behind them at the same level. Different speeds are flown for a certain period of time, and the difference in sinking rate between the two gliders is determined from an evaluation of the photographs with respect to vertical positions and time. The velocity polar of the new glider is determined by adding the differences in sinking rate to the velocity polar of the absolutely calibrated reference glider. In such a simple evaluation procedure the aerodynamic interference is not considered.

Fig. 10 shows an extended evaluation scheme which takes into account the mutual interference of the two gliders. (A) represents the velocity polar diagram of the reference glider. For known shape of the formation the upwash induced at the reference glider by the second glider can be calculated and added, and this leads to the velocity polar (B)

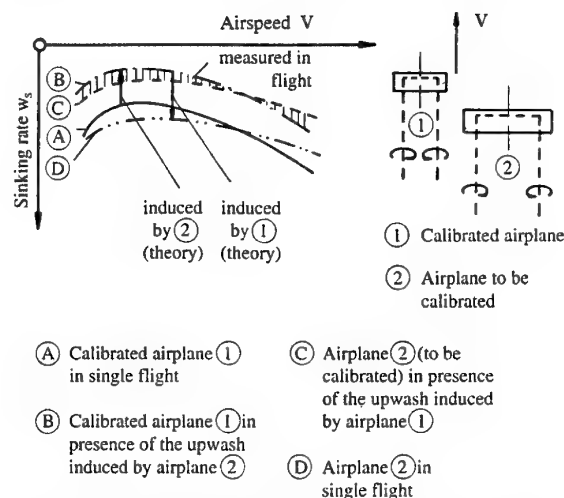


Fig. 10: Evaluation scheme for calibration flights of gliders.

of the reference glider in the presence of the second glider. The measured differences in the sinking rates between the two gliders, shown by hatching, are then added and this leads to the velocity polar (C) of the second glider in the presence of the reference glider. For known shape of the formation the effect of the reference glider on the second glider can again be calculated and subtracted, and this leads to the final velocity polar (D) of the second glider.

The discrepancy between the simple and the extended evaluation procedure is remarkable for gliders with different size and weight. An example is given in Fig. 11. The absolutely calibrated, small and medium weight glider of type CIRRUS performed formation flights with the very large and heavy glider SB-10 of Akaflieg Braunschweig. For typical shapes of the formation the mutual interference of the two gliders has been calculated. According to the scheme of Fig. 10 the sinking rates as well as the corresponding lift/drag ratios are given. If the interference is not considered the maximum lift/drag ratio of the SB-10 turned out to be 48.7 and from the improved evaluation scheme the maximum lift/drag ratio was 54.5. This is due to the fact that the large and heavy glider SB-10 favoured the reference glider CIRRUS more than itself was favoured by the reference glider.

The present investigations demonstrate that in calibration flights of gliders the spanwise distances should be so large that the mutual interference is negligibly small, and in this case the simple evaluation procedure can be applied. If, however, the spanwise distances of the two gliders are small in order to get accurate differences in the sinking rates, the mutual interference has to be taken into account.

Configuration	I				II	Calibrated glider
Aircraft type	② SB-10				① CIRRUS	
Wing span	26.0 m				17.74 m	
Aspect ratio	31.0				24.98	
Loading	36.1 kp/m ²				29.0 kp/m ²	
Airspeed	80	110	160	100	km/h	
Sinking rate w_s	(A)	0.620	0.920	2.240	0.770	m/s
	(B)	0.584	0.894	2.222	0.658	m/s
	Δw_s	-0.080	-0.270	-0.900	-0.200	m/s
	(C)	0.504	0.624	1.322	0.458	m/s
	(D)	0.512	0.630	1.326	0.510	m/s
without interference		0.540	0.650	1.340	0.570	m/s
Lift/drag ratio	with interference	43.37	48.51	33.51	54.5	-
	without interference	41.15	47.01	33.17	48.7	-

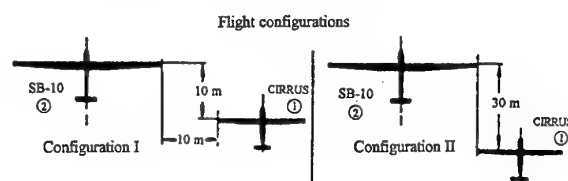


Fig. 11: Results of calibration flights of gliders with and without taking into account the mutual interference.

4.2 Measurements of power reductions

4.2.1 Testing techniques

Formations flights of two airplanes have been carried out in order to find out whether the large power reductions predicted by methods of theoretical aerodynamics can be realized in practical flight conditions. For this purpose two research aircraft Dornier Do-28 of Deutsche Forschungsanstalt für Luft- und Raumfahrt, Forschungszentrum Braunschweig, DLR (identification D-IFZB) and of Technische Universität Braunschweig (identification D-IBSW) were available. For the photographic documentation of the positions of the two aircraft relative to each other in formation flight a third aircraft Do-27 of DLR (identification D-EDFL) has been used.

The front airplane (D-IFZB) flew at constant flight level with constant velocity and acted as a "vortex generator" for the rear airplane, see Fig. 12. In addition the front airplane was equipped with a device which enabled the rear airplane to find the proper position. For this purpose a small (diameter 20cm, height 40cm) and light cone was carried along by means of a thin wire of variable length which could be adjusted to mark the longitudinal distance to be adopted by the rear airplane. In the correct longitudinal position the cone was located aside the rear airplane, and the cone could also be used to find the proper vertical position. For a certain period of time the rear airplane kept a constant position relative to the front airplane, and in this time its data acquisition system measured all quantities which are necessary for the evaluation of its flight state. During the measuring time photos of the formation were taken from the third accompanying aircraft Do-27 (D-EDFL) in order to be able to determine the actual positions of both aircraft by a quantitative evaluation. A photo of this kind is shown in Fig. 12.

During the flight tests the following technique was used. For given longitudinal distance a large lateral distance was used first to adjust the velocities of the two airplanes and this state was used as the reference state without interference. The lateral distance was then reduced to find a position with large interference effects. The wing tip behind wing tip position was adopted using some radio guidance from the third airplane. Concerning the vertical position the level of the wing tip vortices had to be found. For this purpose maximum interference effects were used. The flight

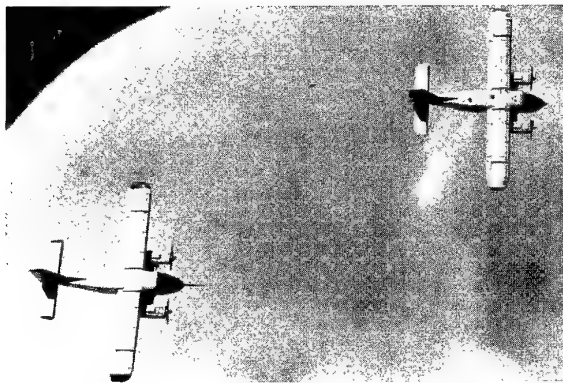


Fig. 12: Formation flight of two airplanes Do-28 at longitudinal distance $\Delta\xi = \Delta x/s = 4$ and lateral distance $\Delta\eta = \Delta y/s = 0$.

level of the rear airplane was adjusted in such a way that the throttle position for constant flight speed became a minimum and the aileron deflections reached a maximum. The corresponding position was kept for some minutes to collect the data and to document the positions. The lateral distance was then increased in steps and finally the reference position without interference effects was repeated. This technique was applied for various longitudinal distances. In addition the flight tests have been carried out for two different flight speeds $V = 80\text{ kts.}$ and $V = 100\text{ kts.}$ in order to vary also the lift coefficient.

From the data measured in flight the lift and drag coefficients have been evaluated from the equations of motion as

$$c_L = \frac{2\bar{m}g}{\rho V^2 S} \cos\gamma - \frac{N_{TW} \cdot \eta_P}{\rho V^3 S} \sin(\alpha + i_P) \quad (11)$$

$$c_D = \frac{N_{TW} \cdot \eta_P}{\rho V^3 S} \cos(\alpha + i_P) - \frac{2\bar{m}g}{\rho V^2 S} \sin\gamma - \frac{2\bar{m}}{\rho V^2 S} \frac{dV}{dt} \quad (12)$$

In these equations $\alpha + i_P$ is the angle between the free stream direction and the engine axis, N_{TW} the engine power, η_P the propeller efficiency, \bar{m} the aircraft mass in the measuring period under consideration and γ is the flight path inclination angle. Details for the determination of these quantities from the flight test data may be taken from [12], [13]. Equ. (11) and (12) have also been applied for flight conditions with large spanwise distances between the two aircraft. This led to data for the reference case without interference, and since a reliable polar diagram for the aircraft Do-28 was available, from these data the zero-lift drag coefficient of the aircraft in single flight, $c_{D0} = c_{Dp}$, could be determined. The relative power reduction according to equ. (4) has been calculated for the rear airplane (2) from

$$e_2 = \frac{\Delta N_2}{N_0} = 1 - \frac{N_2}{N_0} = 1 - \frac{c_{D2}}{c_{D0}} \quad (13)$$

where c_{D2} denotes the drag coefficient in formation flight. Results of the inflight tests showed, that some small angles of sideslip were present. Therefore the drag coefficients evaluated from equ. (12) as well as the aileron and rudder deflections include some contributions from the unsymmetrical flow. Therefore some corrections have been carried out to compensate this effect and to obtain results which are due to the interference effect only.

4.2.2 Results

The power reduction according to equ. (13) is obtained as the difference of two small drags, measured in flight. This can be done successfully, if the drag in single flight and the drag in formation flight are measured by the same procedure. For this reason, the drag characteristic in single flight was also measured during the formation flight tests and the measured characteristic for the aircraft Do-28 turned out in excellent agreement with the drag characteristic obtained by M. Beukenberg [13] and A. Redeker [17], [18].

Fig. 13 shows the relative power reduction of the rear airplane, e_2 , in formations of two equal airplanes Do-28 as function of the lateral distance $\Delta\eta$ for different longitudinal

distances $\Delta\xi$. For the lateral distance $\Delta\eta = 0$ a considerable power reduction e_2 of about 15% was obtained from the formation flight tests. With increasing lateral distance, the measured relative power reduction e_2 decreases rapidly. Included in Fig. 13 is the theoretical curve for a longitudinal distance $\Delta\xi = 4$. Due to the fact, that there is only a minor

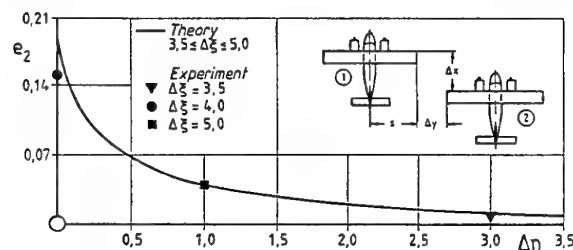


Fig. 13: Relative power reduction e_2 of the rear airplane as function of the lateral distance $\Delta\eta = \Delta y/s$ for different longitudinal distances $\Delta\xi = \Delta x/s$ for formations of two airplanes Do-28. Comparison between theory for $\Delta\xi = 4$ and experiment. (Flight parameters: $c_{L1} = 0.84$, $c_{L2} = 0.93$, $c_{D01} = c_{D02} = 0.0489$).

change in power reduction for longitudinal distances in the order of magnitude of $\Delta\xi = 4$ or more, it is worthwhile to compare all the measured values with this theoretical curve. Excellent agreement between theory and experiment for the relative power reduction e_2 as function of the lateral distance $\Delta\eta$ turns out.

A similar result is obtained for the aileron deflections of the rear airplane, plotted in Fig. 14 as function of the lateral distance $\Delta\eta$. The theoretical curve is included for the longitudinal distance $\Delta\xi = 4$. The aileron deflections decrease

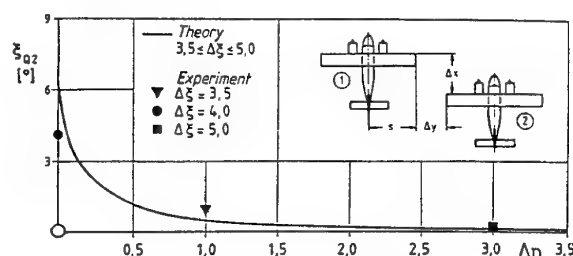


Fig. 14: Aileron deflections at the rear airplane as function of the lateral distance $\Delta\eta = \Delta y/s$ for constant longitudinal distance $\Delta\xi = 4$. Comparison between theory and experiment for two airplanes Do-28. (Flight parameters: $c_{L1} = 0.84$, $c_{L2} = 0.93$, $c_{D01} = c_{D02} = 0.0489$).

rapidly with increasing lateral distance, as mentioned earlier for the relative power reduction. The comparison of Fig. 13 and 14 shows evidently that the measured aileron deflections are a very sensitive criterion for the achieved power reduction.

Similar results have been obtained for higher lift coefficients and larger longitudinal distances. But in these cases the results yield larger differences between theory and experiment. These differences increase for higher lift coefficients c_L and larger longitudinal distances $\Delta\xi$. They are due to the fact that the pilot of the rear airplane had difficulties to

maintain simultaneously the proper flight condition and the correct location relative to the wake of the front airplane. To overcome these problems an automatic control system has been designed in order to be able to carry out formation flights by means of an autopilot. The basic ideas of the realization of this control system and the main results are discussed in the subsequent section.

5. AUTOMATIC CONTROL OF FORMATION FLIGHTS

5.1 Basic ideas

The optimum position of the rear airplane relative to the front airplane in lateral and longitudinal direction is defined by the maximum power reduction achieved by the rear airplane. Hence an autopilot for formation flight has to solve the problem to find and keep this optimum position for some time. In more detail it is necessary to search for the proper position of the rear airplane relative to the wake of the front airplane. This wake induces upwash velocities in its vicinity. If the rear airplane flies close to this wake, it achieves a power reduction which is especially high, if the induced upwash velocities are large. The optimum position in a flight formation is therefore characterized by a maximum induced upwash velocity along the wing span of the rear aircraft. Hence the criterion of optimum power reduction can be replaced by maximum induced upwash velocity along the wing span, when searching for the optimum position.

Taking into account all the informations about the wake of an aircraft and the known behaviour of an aircraft flying close to such a wake as well as the available sensor equipment of the experimental airplane, explained in detail by A. Redeker [17], [18], it is possible to realize an autopilot, solving the problem discussed above without big changes of the aircraft's equipment. For this purpose the decision was made to use an adaptive extremum controller. Such a technique means, that the aircraft has to perform always a motion to stay in the vicinity of the maximum power reduction and this leads to a loss in power reduction, compared to a stationary flight at the optimum. On the other hand the necessary technical expense is very small. The research aircraft Do-28 (D-IBSW) was equipped with a flight controller for the longitudinal motion according to A. Redeker [17]. This is a modern structured flight controller with state feedback, which can be used in different modes. For formation flights the modes "Altitude Hold" and "Altitude Acquire" are the most important ones. This flight controller has been extended by M. Beukenberg [12] to include also the lateral motion. The supplement was again a state feedback controller with the modes "Heading Hold" and "Position Line Hold" to be used in formation flights.

In formation flight the longitudinal distance of both aircraft has been kept constant by means of constant flight speeds of both aircraft. The vertical and lateral position of the rear aircraft relative to the wake of the front aircraft has been varied systematically in order to find the position for maximum power reduction of the rear aircraft. Instead of the power reduction itself related cost criteria have been applied. Concerning the vertical position of the rear aircraft the included upwash measured in the symmetry plane of the rear aircraft according to P. Vörsmann [19] has been used. This cost criterion reaches a maximum beside the trailing vortices of the front aircraft's wake. Unfortunately this crite-

tion cannot be used for the lateral position since the upwash in the symmetry plane of the rear aircraft still increases when its wing tip enters the downwash region of the front aircraft's wake and the power reduction decreases already. For this reason the aileron deflections as a very sensitive measure for the power reduction according to Figs. 13 and 14 have been used as cost criterion for the lateral position. The search motion is initiated by a new commanded flight level or position line. The measured values of the induced upwash and the aileron deflections are compared to the original ones and from the differences a new vertical or lateral position is determined. The corresponding steps decrease when the maximum of the power reduction is approached and they increase for departure from the extremum. The controller guides the aircraft into the new position and the procedure is repeated again and again. For more details see [12] and [13].

5.2 Results

5.2.1 Simulation tests

The performance of the formation flight controller has been checked by simulation tests. These investigations were based on the linearized differential equations of motion and the wake of the front airplane was simulated by a horse-shoe vortex system. The viscous core was taken into account in order to overcome the problem of infinite induced velocities. Details may be taken from M. Beukenberg [12].

Fig. 15 shows the behaviour of the formation flight controller for the longitudinal motion. Some variables plotted with respect to time are: distance in longitudinal direction δx and distance in vertical direction δz from the initial position, induced downwash velocity $-\delta w$ and thrust variation δF . At the initial position, the rear aircraft is located five wing spans ($\Delta x/b = 5$) behind and one wing span ($\Delta z/b = 1$) below the front aircraft and the lateral distance is $\Delta y/b = 0$. This means that the wing tip of the rear airplane is located next to the wake of the front aircraft. Starting from this position, the controller should guide the aircraft into a position relative to the wake with large power reduction. The motions of the aircraft commanded by the controller are clearly visible, e.g. by the variation of the vertical position. The relatively quick sequence of the commanded steps create the slightly rough outcome. It is clearly indicated, that the controller leads the rear aircraft within three steps into a favourable position relative to the wake of the front aircraft. Due to the continuous sequence of steps this favourable position can not be fixed. The process shows more or less large deviations from the optimum position. Favourable positions are characterized by a large induced upwash velocity together with a small throttle position δF . As an example, the time interval between $135 < t < 170$ s is chosen. The mean vertical position $\delta z = -15.39$ m shows only a small deviation from the optimum value $\delta z = -15$ m. Hence the rear aircraft achieves an upwash velocity of $w = 0.726$ m/s and a 14.3% smaller throttle position.

The behaviour of the extremum controller was also simulated for the lateral motion. At the initial position the rear aircraft was located five wing spans behind ($\Delta x/b = 5$) the front aircraft at the same altitude. The lateral distance was slightly larger than one wing span ($\Delta y/b = 1.3$). Fig. 16 shows the results of the simulation by some plotted variables for lateral position δy , aileron deflection $\delta \xi_Q$ and rudder deflection $\delta \zeta_S$. The optimum lateral position is included in

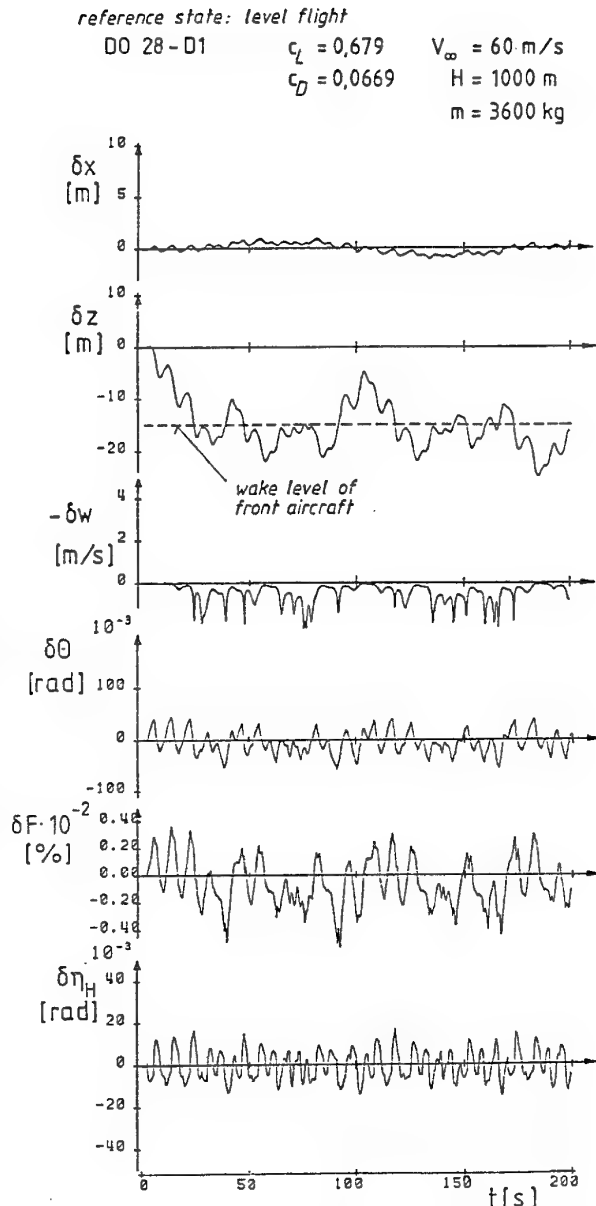


Fig. 15: Behaviour of the longitudinal part of the flight controller in formation flight. Results of simulation tests.

Fig. 16 as dashed line in the diagram for the lateral position. The approach of the rear airplane to the wake of the front airplane can be seen clearly by the change of the variables due to the commanded position changes. With decreasing distance from the wake in lateral direction the aileron deflection increases. This deflection is necessary to compensate the resulting rolling moment due to the nonuniform distribution of the induced upwash along the wing span. The size of the aileron deflection is in excellent agreement with the values calculated from the theory in section 3. After four cycles, the phase of approach has finished, because the rear airplane has reached a lateral position close to the wake. From now on, the formation flight controller holds the rear aircraft in a nearby position relative to the wake of the front airplane.

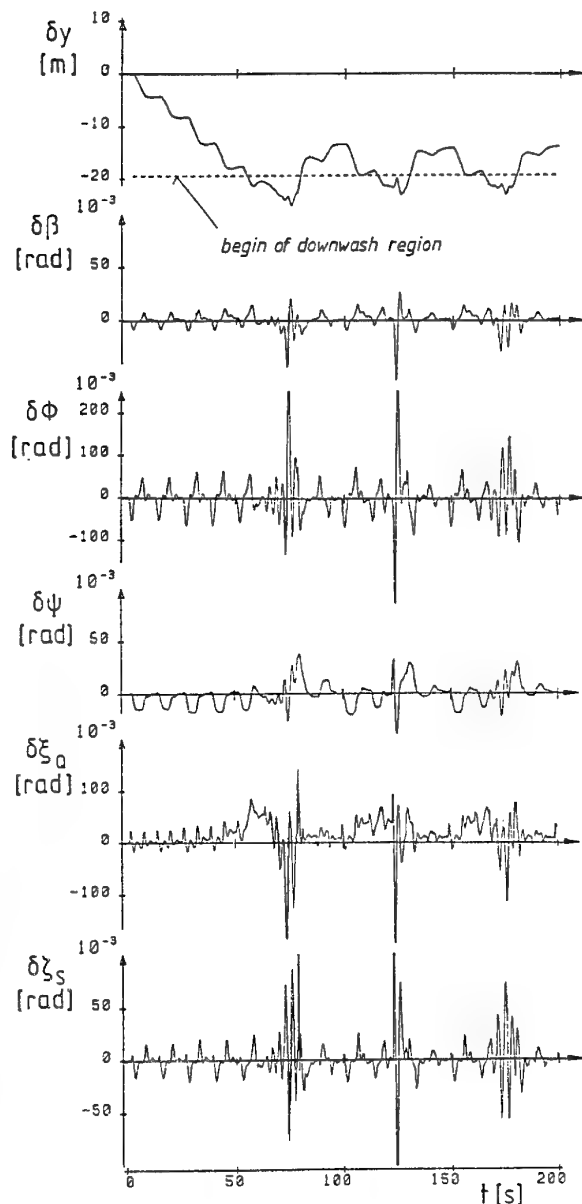


Fig. 16: Behaviour of the lateral part of the flight controller in formation flight. Results of simulation tests.

5.2.2 Flight tests

The controller was installed in the research aircraft Do-28 and tested in formation flight. Again the flight tests have been carried out in cooperation between TU Braunschweig and Deutsche Forschungs- und Versuchsanstalt für Luft- und Raumfahrt (DLR), Forschungszentrum Braunschweig. An airplane of type Do-228 of DLR (identification D-CODE) was available and acted as "vortex generator". The research aircraft Do-28 of Technische Universität Braunschweig (identification D-IBSW) completed the formation. For the photographic documentation of the positions of the two aircraft relative to each other in formation flight, a third aircraft Do-27 of DLR (identification D-EDFL) was available.

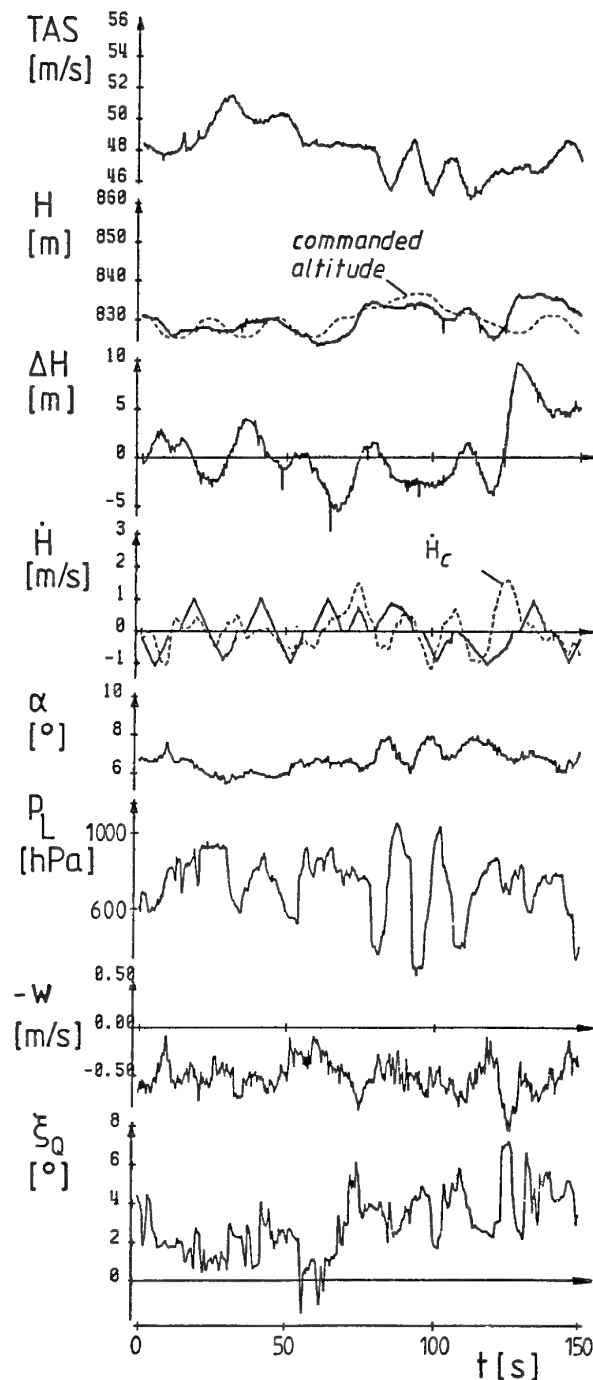


Fig. 17: Behaviour of the longitudinal part of the flight controller in formation flight during flight tests with two airplanes (Do-228 and Do-28).

After successful testing of the controller in single flight, some formation flight testing has been carried out. Fig. 17 shows a typical result. The longitudinal distance of the rear airplane relative to the leading airplane was approximately three wing spans and an average lift coefficient of $c_L = 0.875$ has been evaluated for that flight. The commanded altitude steps and the variations of the climb rate can be easily read off the time history for the flight altitude H , ΔH and the vertical speed $\dot{H} = dH/dt$ and simultaneously it is evident, that

the commanded values are in good agreement with the actual states. The air speed shows some variations. Since the air speed is used to fix the longitudinal distance, corresponding variations of this distance should be expected. But the evaluation of the photographs taken during the formation flights showed for the time interval under consideration only variations within one semi span. The most important variables in formation flight are aileron deflections and induced upwash velocity, because they are direct measures for the achieved power reduction. Fig. 17 indicates that large aileron deflections are combined with large upwash velocities at all times. This confirms the assumption, that the aileron deflections are a very good sensor for the induced upwash velocity along the wing span.

The corresponding power reduction was evaluated for the time interval of Fig. 17, using the method according to section 4.2. The result is shown in Fig. 18. As a scaling factor, the maximum theoretical power reduction for this formation at the optimum position is included. The power reduction was evaluated for those moments of time, when the controller measured the induced upwash, the engine inlet pressure and the aileron deflections in order to decide which size and direction the next step in search for the maximum should have. Within the time interval under consideration power reductions were obtained, which reached maximum values of more than 20%. The average value of the power reduction for the whole time interval has been evaluated as $e_2 = 10.24\%$. This value is also included as dashed line in Fig. 18.

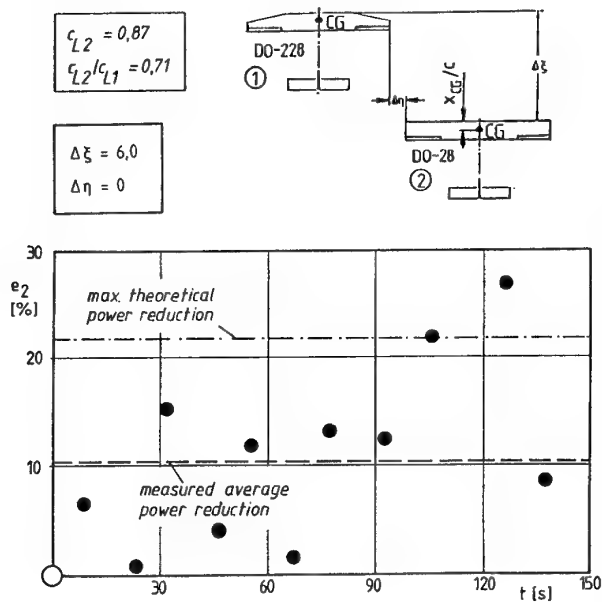


Fig. 18: Measured flight power reduction in autopilot-controlled formation flight with two airplanes (Do-228 and Do-28). Comparison between theory and experiment.

6. CONCLUSIONS

In the first part of this paper different methods of theoretical aerodynamics were applied to calculate the power reduction of flight formations. Methods using a simple horse-

shoe vortex model are compared with methods using a plane or a rolled-up vortex sheet. With the simple horse-shoe vortex method, the power reduction of even large formations can be estimated quite easily. The power reduction is smaller than the one obtained from calculations with a plane or a rolled-up vortex sheet. Taking into account the complicated geometry of a rolled-up vortex sheet, slightly different power reductions are calculated compared with the results for unrolled plane vortex sheets. The power reduction has been calculated also for whole aircrafts. Thereby wings and tails have been taken into account. For each airplane the pitching moment about the center of gravity was balanced by means of elevator deflections of the whole horizontal tail and the rolling moments were compensated by means of aileron deflections. The resulting yawing moment again has been balanced by corresponding rudder deflections. These results show that there is only a minor influence from the consideration of these details. Power reductions of 15% are obtainable for the rear aircraft in formations of two equal airplanes at the same altitude and small spanwise distances. The aileron and rudder deflection for the compensation of the corresponding moments are of moderate size.

In the second part formation flights of two airplanes have been analysed experimentally. In calibration flights of gliders the mutual interference of both aircraft may falsify the result. In the evaluation procedure for such flights, however, the mutual interference can be calculated by means of aerodynamic theory, and this leads to reliable results in such a situation. Furthermore the performance characteristics for formations of two aircraft Do-28 have been measured in flight and compared with theoretical predictions. Excellent agreement was found for the obtainable power reduction and the corresponding aileron deflections for different positions of the two airplanes relative to each other. The flight tests have demonstrated that the power reduction can be realized in practical flight formations of two airplanes.

On the other hand the pilot of the rear airplane had some difficulties to maintain simultaneously the proper flight conditions and the proper position relative to the wake of the front airplane. To overcome these problems, a control system has been adapted for the rear airplane. This is discussed in the third part of this paper. The basic controllers for the lateral and longitudinal motion have been realized as state feed back controllers. The essential formation flight controller works as an extremum controller. The results of the simulation tests showed, that such a controller is always able to find and hold favourable positions in a flight formation. This controller has been implemented and tested on board a research airplane of the Technische Universität Braunschweig. Preliminary tests in single flight confirmed the proper function of the basic controllers for the longitudinal and lateral aircraft motions. The formation flights have been carried out in cooperation with Deutsche Forschungsanstalt für Luft- und Raumfahrt (DLR). An aircraft of type Do-228 was used as front airplane. The formation flight controller showed an acceptable behaviour during formation flight tests. In horizontal flight a favourable position relative to the wake of the leading airplane could be found and held. Using the described formation flight controller, power reductions up to 10% could be obtained during flight tests and good agreement with theoretical values turned out.

REFERENCES

- [1] D. Hummel: Aerodynamic aspects of formation flight in birds. *J. theor. Biol.* **104** (1983), 321-347.
- [2] C. Wieselsberger: Beitrag zur Erklärung des Winkelfluges einiger Zugvögel. *Z. Flugtechnik u. Motorluftschiffahrt* **5** (1914), 225-229.
- [3] H. Schlichting, E. Truckenbrodt: Aerodynamics of the Airplane. Mc Graw-Hill, New York, 1979.
- [4] H. Schlichting: Leistungersparnis im Verbandsflug. *Mitt. dt. Akad. Luftfahrtforsch.*, H. 2 (1942), 97-139. See also: *Jb. 1942/43 dt. Akad. Luftfahrtforsch.*, 546-554.
- [5] P. B. S. Lissaman, C. A. Schollenberger: Formation flight of birds. *Science* **168** (1970), 1003-1005.
- [6] D. Hummel: Die Leistungersparnis beim Verbandsflug. *J. Orn.* **114** (1973), 259-282.
- [7] D. Hummel: Die Leistungersparnis in Flugformationen von Vögeln mit Unterschieden in Größe, Form und Gewicht. *J. Orn.* **119** (1978), 52-73.
- [8] D. Hummel: Recent aerodynamic contributions to problems of bird flight. *Proc. 11th Congr. Int. Council Aerospace Sci. (ICAS)*, Lisbon 1978, Vol. 1, 115-129.
- [9] D. Hummel, K.-W. Bock: Leistungersparnis durch Formationsflug. *Z. Flugwiss. Weltraumforsch.* **5** (1981), 148-162.
- [10] M. Beukenberg, D. Hummel: Flugversuche zur Messung der Leistungersparnis im Verbandsflug. *Jb. dt. Ges. Luft- und Raumfahrt (DGLR)* 1986, Bd. 1, 133-145.
- [11] D. Hummel, M. Beukenberg: Aerodynamische Interferenzeffekte beim Formationsflug von Vögeln. *J. Orn.* **130** (1989), 15-24.
- [12] M. Beukenberg: Beiträge zur Aerodynamik und Flugmechanik des Formationsfluges. Dissertation TU Braunschweig 1989.
- [13] M. Beukenberg, D. Hummel: Aerodynamics, performance and control of airplanes in formation flight. *Proc. 17th Congr. Int. Council Aerospace Sci. (ICAS)*, Stockholm 1990, Vol. 2, 1777-1794.
- [14] L. L. Gould, F. Heppner: The vee formation of Canada Geese. *Auk* **91** (1974), 494-506.
- [15] C. Urban, R. Behr, S. Wagner: Berechnung nichtlinearer aerodynamischer Charakteristika von interferierenden Tragflächen mittels eines Wirbelgitterverfahrens bei Unterschallströmung. *DGLR-Bericht* 86-3 (1986), 303-316.
- [16] M. M. Munk: Isoperimetrische Aufgaben aus der Theorie des Fluges. Dissertation Uni. Göttingen 1919.
- [17] A. Redeker: Beiträge zur Verbesserung der Führungsgenauigkeit von Flugreglern. Dissertation TU Braunschweig 1986.
- [18] A. Redeker: Computer-aided flight testing of a digital autopilot on board a research aircraft. *Proc. 14th Congr. Int. Council Aerospace Sci. (ICAS)*, Toulouse 1984, Vol. 1, 669-677.
- [19] P. Vörsmann: Ein Beitrag zur bordautonomen Windmessung. Dissertation TU Braunschweig 1985.

ACKNOWLEDGEMENT

These investigations have been partly supported by Deutsche Forschungsgemeinschaft under contract No. DFG-Hu 254/10.

On the Dynamics of Engine Jets behind a Transport Aircraft

L. Jacquin & F. Garnier

Office National d'Etudes et de Recherches Aéronautiques
29, avenue de la Division Leclerc, 92320 Châtillon-France

1. SUMMARY

The various mechanisms that contribute to the mixing and dispersion of the engine exhausts through their interaction with the vortex wake of an aircraft are discussed. The case of a typical large transport aircraft is considered. First, the interaction between the jets and the vortices is characterized by means of non dimensional parameters. When considering aircraft under cruise conditions, it is shown the jets have almost no effect on the vortex wake dynamics. We then consider the way the jet is changed by the vortices. This is evaluated by means of an integral model. Examples are given which show that the jet is captured by the vortices at very different distances behind the aircraft depending on the engine-wingtip separation. The model does not take into account the distortion of the jet plume by the vortex shearing which becomes significant when the jet reaches the vortex center region. Results of a numerical simulation of the convection-diffusion of a passive scalar field, as well as a visualisation realized during an experiment are presented in order to illustrate this point.

2. INTRODUCTION

The interaction of engine exhausts with the trailing vortices of an aircraft is an important topic for aviation impact on the atmosphere, wake vortex control or infrared detection of aircrafts. One generally admits that engine exhausts are trapped by the vortex wake, but a detailed modelisation of the phenomenon has never been accurately achieved.

The issue of the interaction between a jet and a vortex depends on the jet position with respect to the axis of the nearest vortex with which it interacts. The jet is first subjected to the action of turbulence generated at the plume/coflow interface. As it is expanding, the jet is then progressively deflected by the rotating component of the velocity, and it is convected toward the vortex axis by buoyancy. In the farfield, when the jet plume width has become sufficiently large, it spreads and rolls-up into the vortex cell under the action of differential convection, buoyancy and molecular diffusion.

In this paper, the nearfield dynamics of the jet/vortex interaction is studied by using an integral method. [The conservation laws of mass, momentum and energy are integrated on a jet section normal to its trajectory. This basic approach is used to identify and evaluate the various physical mechanisms that control the jet mixing

by the wake. It also offers a rapid method to describe the gross features of the flow for any set of flight conditions (e.g. wing circulation, engine locations, jet exit velocity and temperature)]. A similar approach has been used by Myake et al. (1991) to study the physics and chemistry of a high speed civil aircraft wake. In the dynamical part of the study by Myake et al. the jet growth and the vortex effects were treated separately. The nearfield of the jet was supposed to be equivalent to that of a buoyant round engine jet in a co-flowing airstream. Then the vortex effect was accounted for through a buoyant centripetal force acting on the hot plume at the end of the above mixing process. Thanks to this simplification Myake et al. were able to handle the problem analytically. The present model enables to take into account the vortex induced effects from the beginning of the jet expansion.

In such approaches, the vortex wake is represented by means of simple analytical tools (elliptic laws, Oseen formulae ...). This restricts them to cases of flight under cruise conditions. High loaded configurations (landing or take-off) will be only evoked in section 4, where global interaction parameters will be discussed.

Discussion on the various aspects of this problem will be illustrated by considering the case of a typical large scale aircraft (LTA) and that of a high speed civil transport (Concorde). Characteristic aerodynamic parameters are given in table 1. Subscript "0" denotes ambient conditions.

3. THE VORTEX WAKE

In the case of aircraft under cruise conditions, it is usually proposed to separate the vortex wake evolution into three different regimes (see e.g. CIAP Monograph, 1975). The first is the *formation regime* during which the vortices are built-up by the roll-up and merging of the vortex sheet issuing from the aircraft. A *decay regime* follows, where the vortices are eroded by "regular" turbulent and molecular diffusion. Then, a *dispersion regime* starts with the destabilisation and the disruption of the vortex system under the action of instability mechanisms (Crow instability, buoyancy, interaction with atmospheric turbulence). If V_0 denotes the aircraft speed, Γ_0 , the circulation, and b , the span, from dimensional arguments, the vortex wake evolution may be evaluated by means of the time and length scales $T_w = b^2/\Gamma_0$ and $X_w = V_0 T_w$. Values are given in table 1 for the case of an elliptic loading, for which $\Gamma_0 = \sigma V_0 b$,

with $\sigma = 2C_z / \pi AR$. These scales are often presented as being the characteristic scales of the *formation regime* (vorticity roll-up scales). But, as shown by laboratory experiments on trailing vortices, the latter seem to build-up soon behind the lifting surfaces. We may then suppose that the nominal circulation is almost established on scales smaller than those given above. Various studies devoted to the *dispersion regime* suggest that the break-up time of the wake is $T_{break} \approx 15 T_w$ (see CIAP Monograph, 1975), but this may vary on large proportion depending on the atmospheric conditions. The intermediate *diffusion regime* is also a matter of uncertainty. In particular, we do not know if, and how, turbulence participates in the vortex wake decay. Recent work on turbulence modeling suggests that the vortex induced rotation could prevent any turbulence from developing in such flows (see Zeman, 1995).

The impact of the engine jets on the vortex wake dynamics is usually ignored or neglected. This is justified as far as cruise conditions are considered, but, as shown for instance by Patterson and Jordan (1976), this could be inaccurate when take-off is considered. This problem is briefly discussed below.

4. INTERACTION PARAMETERS

Let consider an aircraft of span b , aspect ratio AR , lift coefficient C_z and drag coefficient C_x . The aircraft is propelled at a speed V_0 by means of N jets of exit area $A_j = \pi D_j^2 / 4$, exit velocity V_j and initial density ρ_j . It produces a vortex wake compounded by two rolled-up vortices of opposite circulation $\pm \Gamma_0$ and spacing $\tilde{b} = \pi b / 4$ (see figure 1). The wake vertical impulse $I_0 = \rho_0 \Gamma_0 \tilde{b}$ is equal to the aircraft weight.

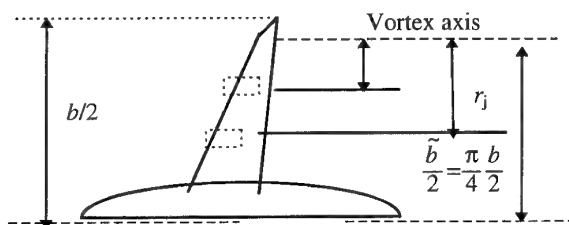


Figure 1 : Schematic view of the engine jet locations

Our first aim is to characterize the global impact of the jets on the vortex wake properties and to see if the jet may affect the vortex wake properties.

Various dimensionless parameters may be thought of. Here, we propose to consider the following global parameter :

$$R_1 = \frac{NJ}{I_0 V_0}, \quad (1)$$

which is the ratio between two invariant quantities : the excess of axial momentum of the jets ,

	Large Transport aircraft (LTA)		Supersonic Civil Transport (Concorde)
Heigh $H(km)$	10		16
$T_0 (^{\circ}K)$	220		205
$p_0 (bar)$	0.26		0.08
$\rho_0 (kg\ m^{-3})$	0.38		0.135
Span $b\ (m)$	60		25.5
Aspect Ratio AR	7.5		1.825
Surface $S\ (m^2)$	480		358
Lift Coef. C_z	0.42		0.123
Speed $V_0\ (m\ s^{-1})$	250		690
Elliptic coef. $\sigma=2C_z/\pi AR$	0.035		0.043
Circul. $\Gamma_0=\sigma V_0 b\ (m^2 s^{-1})$	540		760
Wake vortex time scale $T=b^2/\Gamma_0\ (s)$	5		0.85
Wake vortex length scale $X/b=V_0 T/b$	37		23
N engines	4		2
Jet diam. $D_j\ (m)$	0.6		1.76
Jet Temp. $T_j\ (^{\circ}K)$	580		460
Jet dens. $\rho_j\ (kg\ m^{-3})$	0.16		0.06
Jet speed $V_j\ (ms^{-1})$	480		1310
$J=\rho_j V_j (V_j-V_0) A_j\ (N)$	5000		118 550
$R_v=V_0/V_j$	0.52		0.49
$R_p=\rho_0/\rho_j$	2.4		2.05
Global interaction param $R_1=(1-R_v) T/L$	0.008		0.17
Global interaction param $R_2=J/\rho_0 \Gamma_0^2$	0.05		1.5
Engine/vortex axis $r_j\ (m)$	14	4	4.5

Table 1 : Characteristic aerodynamic parameters for a large transport aircraft (LTA) and a supersonic civil transport aircraft (Concorde).

$NJ = N \rho_j V_j (V_j - V_0) A_j$, and the flux of the vortex wake vertical impulse. R_1 may also read : $R_1 = (1 - R_v) T / L$, where $R_v = V_0 / V_j$, and where $L = C_z q_0 S$, $T = N \rho_j V_j^2 A_j$, denote the aircraft lift and thrust, with $q_0 = \rho_0 V_0^2 / 2$ and $S = b^2 / AR$. At cruise, the thrust counterbalances the drag, so that R_1 amounts to the drag to lift ratio, and is thus of order 10^{-2} for a LTA (a typical value for the velocity ratio R_v is 0.5; see table 1). During landing, R_1 decreases. In the two cases, the impact of the jets on the global properties of the vortex wake system may then be neglected. Stronger interactions can be expected during take-off, where R_1 increases. Higher values are obtained

for a HSCT which means that the jets could have more impacts on the vortex wake of this type of aircraft.

There are few theoretical and laboratory studies on jet/trailing vortex interaction. Most of them, are oriented towards the topic of vortex control, and they consider axisymmetrical cases with jets introduced in the central core region of the vortex. Several parameters may be identified in the literature to characterize this particular configuration. One is that of Long (1961), which, using our notations, amounts to

$$R_2 = \frac{J}{\rho_0 \Gamma_0^2} \quad (2)$$

This parameter has been introduced to characterize the coupling between azimuthal and axial velocity components in a jet-like, or in a wake like, trailing vortex. It was used, for instance, by Phillips and Graham (1984) to classify various experimental configurations where central jets or wakes were interacting with a vortex. The two parameters R_1 and R_2 are related by $R_2 / R_1 = \sigma / 4\pi N$. Phillips and Graham measurements show that the vortex core is affected as soon as $R_2 = O(1)$. For instance, it is shown that a strong jet, $R_2 \approx 5$, leads to a rapid turbulent decay of the azimuthal velocity profile of the flow, whereas a weak jet, $R_2 \approx 0.2$, lets the vortex almost unchanged. In our case, as shown in table 1, R_2 is order 10^{-2} , which means that if an engine jet were aligned with a vortex axis, it would have almost no effect on the vortex. Again, the HSCT is characterized by a much higher value of this interaction parameter.

Note that blowing is often characterized by the momentum flux ratio $C_\mu = \rho_j V_j^2 A_j / \rho_0 S$. This parameter is related to R_2 by $C_\mu = AR\sigma^2 R_2 / (1 - R_v)$ where $R_v = V_0 / V_j$. Considering that an efficient blowing corresponds to $R_2 \geq 1$, in the case of the wing tip vortices of a cruising LTA (table 1), one gets, typically, $C_\mu \geq 10^{-2}$. This amounts to a large expense of energy. Higher values are needed at higher C_z . However, low energy jet could perhaps participate to trigger the development of instabilities in the farfield (see Jacob et al., paper 27 of the present issue).

Now, we aim at characterizing what impact the vortex could have upon the jet dynamics. The parameters R_1 and R_2 give no detail on the local properties of jet/wake interaction process. The various regimes of this interaction must be analysed by considering the effect which the vortex wake field has on each individual jet at a scale equal to the jet width. This effect will depend on the location r_j of the jet with respect to the nearest vortex axis. The transversal interaction with the rotating component of the vortex field makes the present problem different from that of coflowing jets. Buoyancy must also be taken into account. From dynamical

arguments, at a given axial position x and radius r , interaction between the jet and the vortex momentums may be characterized by the ratio between the excess of axial momentum in the jet and the crossflow momentum flux across an area equivalent to that of the jet cross section. This gives :

$$R_3(x) = \frac{J}{\rho_0 V_\theta^2(r) A(x)} \quad (3)$$

V_θ denotes the downwash velocity induced by one vortex at the jet exit location r (figure 1). As the jet is expanding, the increase of its crossflow momentum is accounted for through the increase of $A(x)$ which is the area of the jet cross section. With respect to Long's parameter (2), R_3 is made dependent on the jet location (x, r) . Supposing that r is sufficiently large for a potential law $V_\theta = \Gamma_0 / 2\pi r$ to hold, one gets :

$$R_3(x) = 16\pi R_2 \left(\frac{r(x)}{D(x)} \right)^2 \quad (4)$$

One finds that at $x=0$ ($r=r_j$), $R_3(0)$ is very large, even for the HSCT. This means that the initial regime of the jets is poorly affected by the rotational component of the wake. Note that simpler parameters, such as the velocity ratios $V_j / V_\theta(r_j)$, or $V_0 / V_\theta(r_j)$, could also be used, but have less physical meaning than $R_3(0)$.

The jet evolution may then be split into two regimes : a *nearfield jet regime*, and a *deflection regime*. In accordance with the above discussion, the *nearfield jet regime* is equivalent to that of usual coflowing jets. Length scales of this regime are proportional to the jet exit diameter D_j . The *deflection regime* corresponds to the entrainment and captation of the jet by the vortex : as the jet spreads, it is progressively deflected by the continuous input of crossflow momentum and pressure induced effects, so that it acquires azimuthal and radial components of velocity. Azimuthal deflection becomes effective (end of the *nearfield*) when $R_3(x, r)$ becomes of the order of unity. In (4), a semi-empirical law is needed for the expansion ratio $D(x) / D_j$. An approximate evaluation is made in annexe 1. A characteristic distance X_{jet} is then deduced for the *nearfield jet regime* (see equation (A-2)). Distances of about one aircraft span are obtained for the LTA outboard engine, and five spans for the inboard engine.

The *deflection regime* is characterized by a competition between a pressure induced centripetal effect and the centrifugal force that takes place once the jet has been deflected. Gravity induced buoyancy must also be taken into account. These mechanisms are going to be detailed in the next section. Myake et al. (1991) have used a different approach : at the end of the *nearfield jet regime* (called "jet-dominated regime"), they considered that the jet plume was convected passively by the vortex and drifted radially towards the vortex center by buoyancy ("buoyant plume regime"). In the following,

we will consider a model that enables to treat continuously the two above defined regimes.

5. THE JET-WAKE INTERACTION : AN INTEGRAL MODEL

One considers the interaction between the jet and the wake on a period covering the *nearfield jet regime* and the *deflection regime*.

5.1. Basic equations

Referring to **figure 1**, let consider a jet element of unit length, transversal area $A = \pi D^2/4$, mass $m = \rho A$ and velocity $\vec{V}(V_x, V_r, V_\theta)$ in a polar coordinate system $(\vec{e}_x, \vec{e}_r, \vec{e}_\theta)$ attached to the center of mass of this element. The jet is developing in the velocity field $\vec{V}(\vec{V}_x, \vec{V}_r, \vec{V}_\theta)$ induced by a vortex pair of axis (o, \vec{e}_x) and of density $\hat{\rho}$ (external flow variables are denoted by a hat).

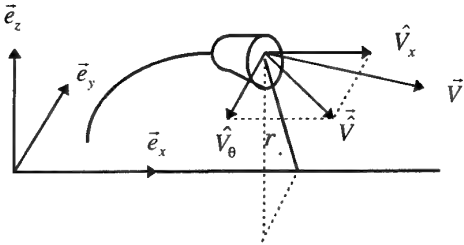


Figure 2 : Jet/wake interaction model : notations

The fundamental law of dynamics reads :

$$m\vec{\gamma} = \vec{F}_g + \vec{L} \quad (5)$$

where \vec{F}_g and \vec{L} are, respectively, vertical buoyancy and contact forces acting on the jet element surface. \vec{L} is split into a pressure and a viscous components :

$$\begin{aligned} \vec{F}_g &= (\hat{\rho} - \rho) A \vec{g} \vec{e}_z \\ \vec{L} &= \vec{P} + \vec{F}_e \end{aligned} \quad (6)$$

\vec{P} and \vec{F}_e are modeled according to the following hypothesis : i) the pressure on the jet surface is that of the external field, \hat{p} , ii) the jet width is small compared to the pressure gradient length scale, so that :

$$\vec{P} = -\oint_C \hat{p} \vec{n}_i dl = -\iint_A \vec{\nabla} \hat{p} d\sigma \approx -A \vec{\nabla} \hat{p} \quad (7)$$

where \vec{n}_i is the normal to the jet boundary; iii)

Following the approach of Morton-Taylor-Turner (1956), \vec{R} is set proportionnal to the difference between the velocity in the vortex and that of the jet :

$$\vec{F}_e = E (\vec{V} - \vec{V}) \quad (8)$$

where E is an entrainment function (see below). The acceleration $\vec{\gamma}$ at point P reads :

$$\vec{\gamma} = (\ddot{r} - r\dot{\theta}^2)\vec{e}_r + \frac{r^2\ddot{\theta}}{r}\vec{e}_\theta + \ddot{x}\vec{e}_x \quad (9)$$

where the dot denotes a temporal derivative. Introducing (6)-(9) into (5), one gets :

$$\begin{aligned} \rho A \dot{V}_x &= E(\hat{V}_x - V_x) \\ \rho A \dot{V}_r &= E(\hat{V}_r - V_r) + (\rho A \frac{V_\theta^2}{r} - A \frac{\partial \hat{p}}{\partial r}) + (\hat{\rho} - \rho) A g \sin \theta \\ \rho \frac{A}{r} \dot{V}_\theta r &= E(\hat{V}_\theta - V_\theta) - A \frac{1}{r} \frac{\partial \hat{p}}{\partial \theta} + (\hat{\rho} - \rho) A g \cos \theta \\ m \vec{\gamma} &= \underbrace{\vec{F}_e}_{\text{Entrainment}} + \underbrace{\vec{F}_c}_{\text{Inertia - pressure}} + \underbrace{\vec{F}_g}_{\text{Gravity}} \end{aligned} \quad (10)$$

The first terms on the right hand side (RHS) account for entrainment of momentum (see below). The second terms combine the inertial term $\rho A V_\theta^2/r$ and pressure force acting on the jet surface. This leads to a centripetal force which is responsible for the drift of the plumes towards the vortex centers. The last term accounts for gravity. This system is closed by considering the energy conservation. Following the same procedure as above, this equation is written for the total enthalpy H , under the form :

$$\rho A \dot{H} = E(\hat{H} - H) \quad (11)$$

The unknown variables are $\rho, A, V_x, V_r, V_\theta, r$ and θ .

The entrainment function E must be modeled.

5.2. Entrainment

In the model equations (10), (11), the "turbulent diffusion", and the effect it has on the jet growth and deflection, are accounted for by a single function E . Putting :

$$E = \frac{d}{ds} (\rho A V_s), \quad (12)$$

where subscript s denotes the component tangent to the jet path, the system (10) reads :

$$\begin{aligned} \frac{d}{ds} (\rho A V_s V_x) &= E \hat{V}_x \\ \frac{d}{ds} (\rho A V_s V_r) &= E \hat{V}_r + \rho A \frac{V_\theta^2}{r} - A \frac{\partial \hat{p}}{\partial r} + (\hat{\rho} - \rho) A g \sin \theta \\ \frac{d}{ds} (\rho A V_s V_\theta) + \rho A \frac{V_r V_\theta}{r} &= E \hat{V}_\theta - A \frac{1}{r} \frac{\partial \hat{p}}{\partial \theta} + (\hat{\rho} - \rho) A g \cos \theta \\ \frac{d}{ds} (\rho A V_s H) &= E \hat{H} \end{aligned} \quad (13)$$

where we have used $d/dt = V_s d/ds$. This shows that E amounts to an entrainment function which fixes the flux of external fluid that penetrates into the jet.

From dimensional arguments one may assume that $E \propto \hat{\rho} V_e L$, where V_e et L denote velocity and length scales characterizing the entrainment of external mass through the jet boundary. One can take L proportional to the jet diameter D , and split the entrainment velocity V_e into components colinear and normal to the jet path. One writes :

$$E = \hat{\rho} \left[\alpha_s (V_s - \hat{V}_s) + \alpha_n \sqrt{\hat{V}_n^2 + \hat{V}_b^2} \right] D \quad (14)$$

where subscript n and b denote the velocity components normal and binormal to the jet path. This formulation combines that of Prandtl for coflowing jets (first term) and that of Morton-Taylor-Turner for buoyant plumes. This expression is equivalent to that used by Myake et al.. It has also been used by Jacquin (1991) for modeling transversal jets. From experiments on coaxial jets, one may adopt a value of 0.15 for α_s . The model of Myake et al.; that focussed on the farfield region, corresponds to a much smaller value of α_s (≈ 0.05). Such a value is not suited for the nearfield of the jet. As for the transversal entrainment, experiments on transversal jets suggest that α_n is of order 1 (see [9]). The model under its final form is obtained by projecting (10), or (14), on the curvilinear frame $(\vec{s}, \vec{n}, \vec{b})$. This is detailed in annexe 2.

5.3. Dynamical balance

If considering a single vortex, for which

$$\vec{\nabla} \hat{p} = (\hat{\rho} \hat{V}_\theta^2 / r) \vec{e}_r, \text{ the various terms of system (10) may}$$

be evaluated at $x=0$. Comparisons between them confirm the findings of section 4. They show that the nearfield is dominated by the coaxial shearing. They also show that the weak transversal interaction is dominated by the transversal entrainment, and that the gravity force is initially larger than pressure induced centripetal force for the LTA inboard engine, the two being almost equivalent in the case of the outboard engine. As the jet expands and proceeds downstream, the efforts change together with the radial position of the jet. At the end of the *deflection regime*, the centripetal force reduces to a purely buoyant term $\vec{F}_c = (\hat{\rho} - \rho) A \hat{V}_\theta^2 / r$. The plume is convected at nearly the local speed of the vortex flow with a residual centripetal velocity component due to the above term. This corresponds to the "buoyant regime" of Myake et al. The present model reduces to their model on the long term, except that the shearing of the jet area by the vortex is not detailed here. This effect, will be characterized below (see section 6). Asymptotically, gravity and centripetal forces compares as follows :

$$\left\| \frac{\vec{F}_g}{\vec{F}_c} \right\| = \left(\frac{2\pi}{\sigma} \right)^2 Fr^2 \frac{b}{D_j} \left(\frac{r}{b} \right)^3. \quad (15)$$

where $Fr = \sqrt{g D_j} / \hat{V}_x$ is the Froude number. This

enables to define a region of radius r_{buoy} inside which centripetal effects are dominant. According to table 1, one obtains $r_{\text{buoy}} \approx 9\text{m}$ in the case of the LTA and $r_{\text{buoy}} \approx 11\text{m}$ in the case of the HSCT. Thus, the LTA outboard jets ($r_j = 4\text{m}$) and the HSCT jets ($r_j = 4.5\text{m}$) are immediately dominated by centripetal buoyancy. The LTA inboard jet is also rapidly influenced by this mechanism. Note that during half a revolution, when the jet is below the plane of the vortices, gravity participates to put the jet closer to the vortex center. Elsewhere, it has an opposite effect.

5.4. Vortex wake model

Several formulations may be found in the literature to modelize an aircraft vortex wake. They are all restricted to the farfield (see Maxworthy (1974), Greene (1988)). Here, the vortex wake is represented by the superposition of two gaussian vortices :

$$\vec{V}_\theta(r) = \frac{\Gamma_0}{2\pi} \left(\frac{1 - \exp(-1.256 \frac{r^2}{r_c^2})}{r} \vec{e}_\theta - \frac{1 - \exp(-1.256 \frac{r'^2}{r_c'^2})}{r'} \vec{e}_\theta' \right) \quad (16)$$

where r' denotes the separation distance between the point considered and the second vortex axis (see figure below) and where r_c is the viscous core radius.

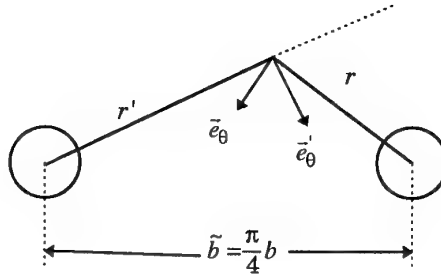


Figure 3 : Wake vortex as a superposition of two vortices : notations

Another important simplification is made here by supposing that the vortex wake amounts to regular vortices separated by \tilde{b} , and that this holds immediately behind the wings (see figure 1). A transition between b and \tilde{b} would be more convenient. But laboratory experiments show that this transition is rapid (within one or two wingspans). Moreover, if the jet is not too close to the vortex axis, we have seen that it is initially almost insensitive to the vortex field details. So that this hypothesis may not be too restrictive.

5.5. Results

The model equations given in annexe 2 are integrated by using a Runge-Kutta method. Inviscid relations are used to approximate the pressure gradients inside the vortex system. The viscous core radius r_c is taken arbitrarily constant, equal to 1m. The calculation is stopped when the jet boundary encounters the vortex axis. There, the plume has become largely dominated by the shearing and the model is inoperant (see next section). Typical results behind the starboard wing ($0 \leq y \leq b$) of a LTA are presented in figures 4 and 5. Mean jet paths and boundaries are plotted versus x/b . The vortex induced streamline originating from the engine exit is also shown, together with the vortex centerline. On figure 4, it is seen that the outboard engine jet is immediately captured by the vortex. This occurs on a distance of the order of one wing span. The inboard jet is rapidly deflected and its mean path nearly follows the vortex streamline. As shown on figure 5, its captation occurs on a much larger distance, within about 20 wing spans. The vortex streamlines descend under the mutual interaction of the vortices. Figure 6 shows the results obtained when considering a single vortex (cylindrical streamlines, horizontal axis). Comparisons with figure 5 show that the properties of the counterrotating system, descent and streamline patterns, make the captation process more efficient than in a single vortex.

6. SHEARING OF THE PLUME

The one-dimensional model described above does not account for the distortion of the jet interface by the vortex flow. This mechanism takes place as soon as the rotational component of the vortex velocity varies significantly across the plume width. This occurs far before the end of the calculations presented above. This is illustrated on figure 7 by an experimental result selected from those of a basic laboratory experiment conducted at ONERA, in which jets were emitted close to a vortex generated by two NACA 0012 profiles in opposite incidence $\pm 10^\circ$. These experiments aimed at studying the very first stage of a vortex/jet interaction, and was not specifically oriented towards the studying of the aircraft jet/wake problem. The winglet span is 500mm and the cord is 150mm. The external velocity is 17.5 ms^{-1} , and that of the jet, 40 ms^{-1} . The measured circulation is $\Gamma_0 = 1.3 \text{ m}^2 \text{ s}^{-1}$. Figure 7 shows the result of a smoke visualisation obtained in the case of a jet emitted at $r_j/b = 1/12$, that is very close to the wing tip ($b=1\text{m}$). The global interaction parameter R_1 (see (1)) is 4.10^{-3} and the local one (see (4)), $R_3(0, r_j) \approx 40$. These values are not far from those obtained in the case of a LTA outboard engine (see table 1). Visualisations were made by using the laser sheet method and by introducing smoke into the ejector. The picture shown in figure 7, corresponds to a perspective view from the tunnel glasses of a plane normal to the tunnel axis. The plane is located one half span behind the winglet trailing edge. It shows that even in the jet nearfield regime, where the jet still possesses a significant axial impulse, part of its fluid is already trapped into the vortex core. This picture is given as an illustration of this mechanism.

Another illustration is given in figure 8, which presents the results of a direct simulation of the two-dimensiona

convection-diffusion equation of a passive (non buoyant) scalar. The numerical method used is described in Laverdant and Candel (1988). A gaussian distribution of the scalar is introduced at time zero in the surrounding of a cylindrical Lamb vortex. The Peclet number is $\Gamma/\nu = 600$, the Prandtl number being equal to unity. The initial viscous core is $r_c = 0.016 b$. The plume shown in figure 8(a) is such that its 1% iso-concentration line encounters the vortex axis. Figures 8(b) to (c) shows the scalar isolines obtained at two subsequent times: $t = 0.13$ and $0.26 b^2/\Gamma$. The figure shows that the coupling between convection and diffusion leads to a rapid captation of the passive scalar plume into the vortex core. This occurs in spite of the absence of any buoyancy effect. The latter would then reinforce this captation process.

A more complete description of this regime is given in Gertz and Ehret, 1996 (paper 35, present issue).

7. CONCLUSIONS

Various aspects of the interaction between engine jets and a vortex wake behind an aircraft have been discussed. Characteristic parameters have been proposed in order to quantify the interaction. It has been shown that the engine jets poorly affect the global dynamics of the vortex wake of large transport aircrafts under cruise conditions. Supersonic transport aircraft wakes could be more sensitive to such effects. The vortex impact on the jet has been discussed by using an integral model, similar to that developed by Myake et al. (1991). The present model enables to describe continuously the jet trajectory from its emission up to its penetration into the vortex core. But the spreading of the jet gas by the vortex induced shearing and diffusion is not accounted for. An experimental example and results of a simplified numerical simulation of this problem indicate that this mechanism could play a dominant role on the overall dynamics during the jet deflection regime.

REFERENCES

1. Myake R., Martinez-Sanchez, Brown R. & Kolb C., "Plume and wake Dynamics, Mixing and Chemistry behind an HSCT aircraft, AIAA-91-3158, 1991.
2. CIAP Monograph, final report-DOT-TST-75-53, Dept. of transportation, Washington, 1975.
3. Zeman O., "The persistence of trailing vortices": a modeling study", *Phys. Fluids* 7 (1), 1995.
4. Long R.R., *J. Fluid Mech.*, 11, p-611-626, 1961
5. Phillips W.R.C. & Graham J.A.H., "Reynolds-stress measurements in a turbulent trailing vortex", *J. Fluid Mech.*, 147, p353-371, 1984.
6. Patterson & Jordan, in *Wake Vortex Minimization*, NASA SP-409, 1976.
7. Papamoschou D. & Roshko A., "The compressible turbulent shear layer: an experimental study", *J. Fluid Mech.*, 197, p453-477, 1988.

8. Morton B.R., Taylor G.I. and Turner J.S., "turbulent gravitational convection from maintained and instantaneous sources", Proc. Royal Soc. London A, **234**, p1-23, 1956.
9. Jacquin L., "Interaction de jets transversaux sur missiles-modélisation du jet", RTS 46/1147 AY, février 1991.
10. Jacquin L. "Phenomenological description and simplified modeling of the vortex wake issuing from a jet in a crossflow", La Recherche Aéronautique, **2**, 117-133, 1994.
11. Greene G.C. "An approximate model of vortex decay in the atmosphere", J.Aircraft, **23**, 7, 566-573, 1986
12. Maxworthy T. "The motion of aircraft trailing vortices", ASME Tran., Series E, Journal of Applied Mechanics, **42**, 2, 1975.
13. Laverdant A. & Candel S., "A numerical analysis of a diffusion flame-vortex interaction", Combustion science and technologie, vol. 60, p79-96, 1988.
14. Jacob J., Liepmann B. & Savas O., "Natural and forced growth characteristics of the far field vortex wake of a rectangular airfoil", paper n°27 present issue.
15. Gerz T. & Ehret T., "Wake dynamics and exhaust distribution behind cruising aircraft", paper n° 35, present issue.

$$\begin{cases} \vec{s} = \cos \gamma \cos \beta \vec{e}_x + \sin \gamma \vec{e}_r - \cos \gamma \sin \beta \vec{e}_\theta \\ \vec{n} = -\sin \gamma \cos \beta \vec{e}_x + \cos \gamma \vec{e}_r + \sin \gamma \sin \beta \vec{e}_\theta \\ \vec{b} = \sin \beta \vec{e}_x + \cos \beta \vec{e}_\theta \end{cases}$$

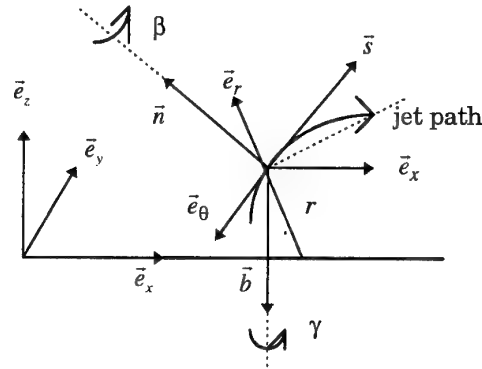


Figure A2-1 : Jet/wake interaction model : curvilinear frame.

This leads to :

$$\begin{cases} \frac{d}{ds}(\rho A V_s) = E \\ \frac{d}{ds}(\rho A V_s^2) = E \hat{V}_s - A \frac{\partial \hat{p}}{\partial r} \sin \gamma + \frac{A}{r} \frac{\partial \hat{p}}{\partial \theta} \cos \gamma \sin \beta \\ \rho A V_s^2 \frac{d\gamma}{ds} = E \hat{V}_n - A \frac{\partial \hat{p}}{\partial r} \cos \gamma - \frac{A}{r} \frac{\partial \hat{p}}{\partial \theta} \sin \gamma \sin \beta \\ \quad + \rho A \frac{V_s^2}{r} \cos \gamma \sin^2 \beta + (\hat{p} - \rho) A g \sin \theta \\ -\rho A V_s^2 \cos \gamma \frac{d\beta}{ds} = E \hat{V}_b - \frac{A}{r} \frac{\partial \hat{p}}{\partial \theta} \cos \beta \\ \quad + -\rho A \frac{V_s^2}{r} \cos \gamma \sin \gamma \sin \beta + (\hat{p} - \rho) A g \cos \theta \\ \frac{d}{ds}(\rho A V_s H) = E \hat{H} \end{cases}$$

The jet trajectory is then determined by :

$$\begin{cases} \frac{dr}{ds} = \sin \gamma \\ \frac{d\theta}{ds} = -\frac{\cos \gamma \sin \beta}{r} \end{cases}$$

ANNEXE 1 : EVALUATION OF THE NEARFIELD JET REGIME

If neglecting buoyancy, a similarity parameter for the nearfield regime is the ratio :

$$R_4 = \frac{(1 - R_v)(1 + \sqrt{R_p})}{1 + R_v \sqrt{R_p}}, \quad (\text{A-1})$$

which characterizes the initial expansion of mixing layers, if neglecting compressibility induced effects on the mixing (see Papamoschou & Roshko, 1988). It accounts for density effects through the density ratio R_p .

We propose to use also R_4 to characterize the expansion of the jets at large values of x/D_j , by considering an expansion law of the form $D(x) \propto a_4 R_4 x$ with a_4 of order 0.1. A characteristic distance for the nearfield jet regime, noted X_{jet} , is then obtained by putting $R_3=1$ and supposing $r=r_j$, in (4) :

$$\frac{X_{jet}}{D_j} = \frac{\sqrt{a_3}}{a_4 R_4} \left(\frac{r_j}{b} \right)^2 \quad (\text{A-2})$$

ANNEXE 2 : EQUATIONS OF THE MODEL

The system (13) is projected on the curvilinear frame $(\vec{s}, \vec{n}, \vec{b})$ by using the following geometrical relationships :

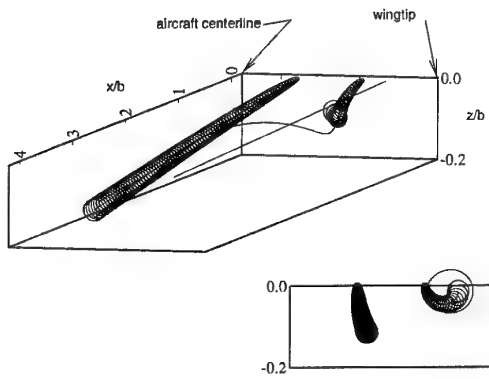


Figure 4 : Inboard-outboard jet plumes and vortex streamlines behind a large transport aircraft obtained using the integral model of section 5.

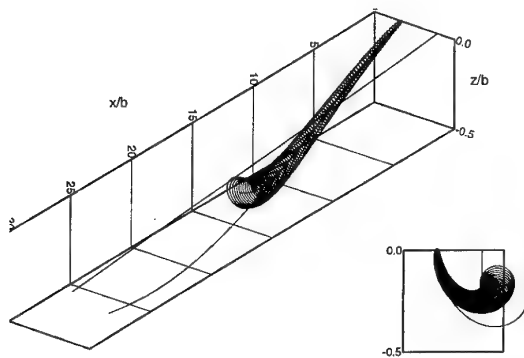


Figure 5 : Inboard jet plume and vortex streamlines on a larger distance.

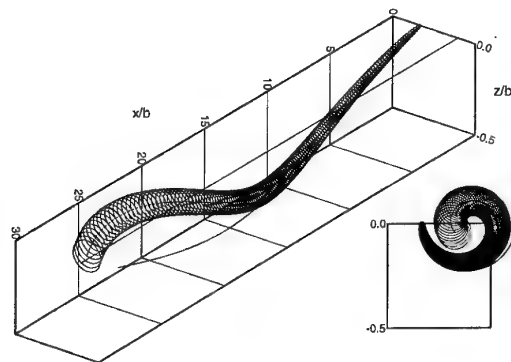


Figure 6 : Inboard jet plume and vortex streamlines when discarding the effects of the opposite vortex.

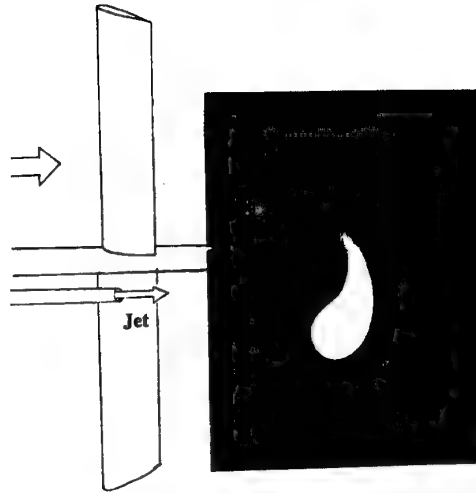


Figure 7 : Visualisation of a jet interacting with a vortex.

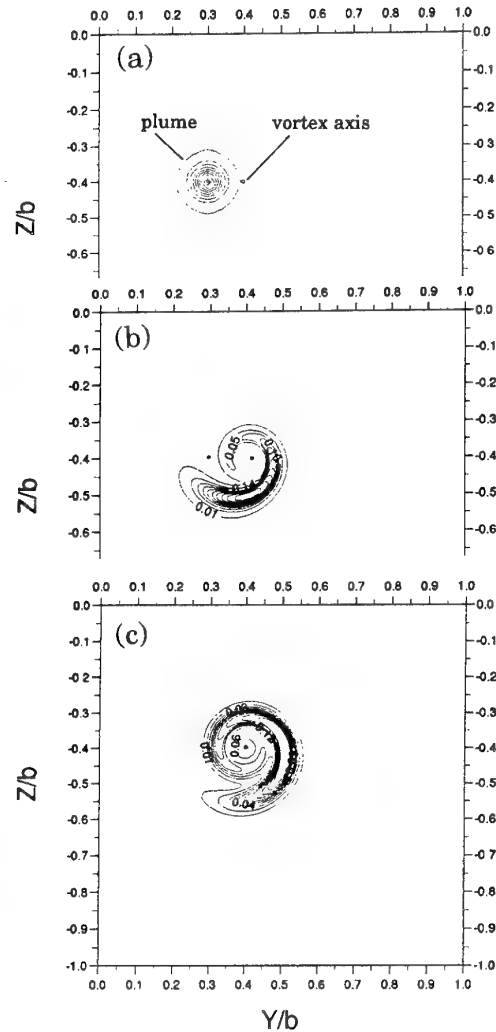


Figure 8 : Direct numerical simulation of a passive scalar convected and diffused into a vortex : (a) initial conditions, (b) $t=0.13T$, (c) $t=0.26T$.

GENERAL DISCUSSION
FDP Spring Meeting in Trondheim - Norway

Prof. Dr. G.E.A. Meier, DLR - Gottingen, Germany

First, I would like to thank all participants for the lively discussion during the whole conference. A lot of questions have been placed this way and have been answered by the authors already. The topic of wakes and vortices offers so many aspects, especially also for future research, that we are all now curious to know what our technical evaluator Dr. Jim McCroskey has found out about the content of the whole conference. Dr. McCroskey is employed at the Ames Research Center in California and is a well known expert in fluid dynamics.

He is certainly experienced enough because nearly 20 years of AGARD work makes him very able to perform such a Technical Evaluator's task. He recently got the von Karman Award of AGARD, and I think we can all congratulate him for this very great honor. Now, I ask Dr. McCroskey to begin with his Technical Evaluation.

Dr. W.J. McCroskey, Ames Research Center, U.S.A.

Thank you Professor Meier. Yes, it is one thing to sit through all the papers, but it is a nice alternative to sitting all the time in committee meetings. This Technical Evaluation is something that the Fluid Dynamics Panel typically does at the conclusion of each meeting. What is the job description for this? First, the Technical Evaluator ought to lead a cheer for the Program Committee, so cheers for the Program Committee. Then he tries to summarize why we came here, what we did and what we did not do, what is next, that is, recommendations, then say something controversial that will stimulate the discussion. In my case, I do not intend to give a synopsis for each paper or a grade for each paper. You have to pay extra for that.

Why did we come here? I won't run through all the detailed titles of the sessions because you have all read that. Probably what you didn't read is the theme printed at the top of the program. Basically, it says we are here to review and discuss wake research and the implications for air traffic regulations. It talks about aircraft separation, vortex decay and breakdown, and new tools and techniques. That gives the impression that the center of gravity of the Symposium would be on factors involving aircraft separation and the implications in air traffic. I have to say that I am still learning, absorbing, digesting, perhaps reeling with all of the information that has been presented here, so I will try to make some observations, put a few questions, and try to provide a framework for the general discussion to follow. In a sense, this presentation is work in progress, and we shall see how much clothes the emperor is actually wearing.

Now, my first observation is of a general nature, acknowledging that the theme and purpose of the meeting have some impact on how we should approach it. Consider, for example, if we were laying out a research program, or planning a conference or a book, about improving the performance of something, or perhaps the economics of a certain technology, or maybe just basic science and technology. Then there would be a certain logic or approach in formulating what to do, how to carry it out, and how to summarize it. However, the underlying theme of this meeting really is, "Avoiding a certain hazard". The way that we make plans to deal with hazards and avoiding them, or risk reduction, is usually different, whether the origin of the problem is natural, like earthquakes or floods,

or manmade, such as traffic accidents, wing flutter, cancer, or even canceled airline reservations. Finally, as a sign of the times, we have to think about where to focus our resources.

So, I have tried to organize this discussion within the context of vortex wakes being a serious hazard. First, we ask, "What is the problem?" Then in this hazard-avoiding scenario, "What are the consequences?" Next, it is very important to consider the relevant physics, which turns out to be the primary emphasis in this meeting, although important presentations were made in other areas as well. Having defined the problem, figured out how important it is, and laid out the relevant physics, we consider, "What, if anything, can be done about it?" This necessarily involves some kind of diagnostics, detection, or prediction. Here I am not talking about diagnostics in the usual laboratory sense, but in the real world. How do you know if the hazard is about to occur, and what kind of action do you need to take to avoid it?

I would like to start, then, by considering for this conference, "What is the problem?" It is a little out of the ordinary for AGARD, but we are really talking primarily about a civil problem -- the hazard of vortex wake encounters. That led us to focus primarily on vortex formation, evolution, decay, and breakdown, and some other related topics that were there for balance. The theme does mention the military problem of detection; but in fact, that did not materialize at the conference.

Certainly we all know the problem, and the consequences have been well stated in at least 7 papers on this subject. For safety reasons, we have to have large aircraft separations, and that leads to airport congestion and delays. Another unique feature of this meeting, and for this I think the Program Committee does deserve the cheer that I mentioned in the beginning, was including representatives of regulating agencies, the user community pilots and so on, manufacturers, and then a collection of research scientists looking at things like simulations, flight tests and experimental and theoretical fluid dynamics. The word synergism has fallen from favor, but nevertheless, I think the inclusion of this broad spectrum of people, not just as observers, but as active participants, has been a big plus in this meeting. Perhaps that is one of the factors that has resulted in a lot of discussion after every paper. We did have to cut off the discussion after almost every paper. That is gratifying.

I will talk a little about the relevant physics next. Again, principally we are dealing with strong concentrated vortices created by the generation of lift. The following physical aspects were emphasized in the different presentations: the initial formation and roll-up, ground and cross-wind interactions, instability and decay, breakdown, a little on forces and moments, (the consequences on the following aircraft), and finally, the exhaust and vortex interactions. There were at least 14 papers in this category dealing with theoretical or numerical studies. Ten or more with experiments, and at least 3 that had an important combinations of calculations, theory and experiments.

There is one aspect that I did want to mention, somewhat reflecting my own background and interests. The helicopter wake is also important. Actually, all kinds of rotating machinery generate vortices, whether they are marine propellers, turbomachinery, or helicopter rotors. They have vortex encounters all the time, generally occurring on the frequency of milliseconds to seconds, not the months or years between occurrences of the

significant aircraft-vortex interactions. There have been some important developments in the research on tip vortex development in the helicopter world that were not presented here, and the fixed-wing community should be aware of these.

Let me go back now to try to stimulate the discussion later on. I was struck with the questions of diagnosing this hazardous phenomenon. It occurred to me that detection sensors should be simple, rugged and reliable, but it has been pointed out that the simplest, rugged and most reliable ones often are restricted to being close to the ground and that might be a limitation. It seems to me that when detecting and using that detection information in the field for practical purposes, we are probably going to be looking at new issues in data management, dissemination and display. I will come back to that a little bit later. Also, it is going to be important to have theoretical and empirical models that can operate in real time, not on the lengthy times of either laboratory experiments or CFD.

One of the questions I posed in the beginning in this general category of hazard avoidance is, "what can we do about this phenomenon besides study it to death in laboratory environments"? One solution is to be patient and wait between successive landings, but economically that has certain consequences. Another solution is to modify the vortices, and there were 4 papers that particularly pointed out various aspects of trying to modify the vortices. Or, you can modify the flight procedures. There were at least 3 papers that concentrated on what to do in flight if you knew more about how the phenomenon were to evolve. Then finally, since we can't do everything that we would like to do, we have to ask ourselves where to concentrate our efforts in the future. Leading into the discussion in the next few minutes, I would like to elicit from the audience comments about what the relative proportion should be of the effort to modify vortices versus what should be put into detection and avoidance. It seems to me that, ultimately, the economics of waiting on the runway will be weighed against the performance penalties of modifying the vortices, and both will be weighed against the cost, complication, and reliability of detection equipment.

A few observations before I turn to some questions. I got the impression here that CFD, on the one hand, and LIDAR, on the other hand, are technologies that are really coming of age and promise to contribute to this situation in the future. I think that CFD has attained a demonstrated, mature capability that can be used today very significantly and in the immediate future for the initial vortex formation. In terms of the initial roll-up, CFD perhaps is becoming ready for this. Concerning the instabilities and breakups, we have seen some impressive calculations, but for the regions in between, there are some questions. In so far as the initial formation region is concerned, I don't think CFD capability was fully highlighted with the papers here, but this is an area which can be done in a reasonable amount of computation time with pretty high fidelity. Particularly, going to the next level of wing tips plus flaps, the initial formation and initial wake roll-up, I think that is probably the only way to get this process started. I think that the capability of predicting this near field with rather good fidelity for complex geometries is almost ready, (there have been a few demonstration calculations elsewhere), and we will be seeing them in the very near future. I think it is a very significant new capability. How to use it in this problem is going to require some creative thinking and some creative managing. I don't really see how - short of an Euler/Navier Stokes type of CFD analysis -

you are going to be able to calculate this kind of vortex development to get started into the roll-up stage downstream.

We also saw some very impressive calculations for the far field -- several examples of calculating the Crow instability as it is observed in practice. I think this approaches a breakthrough or a landmark, a milestone in the evolution of this type of technology towards contributing to real world problems. I think over the next two to five years, this type of thing, although it is expensive, should be and will be exploited.

My recommendation would be that program managers and funding agencies should not be timid about allowing people to undertake this work, although they need to keep a critical eye on it because it is very easy to go off in directions of limited usefulness. I can't help remembering that old adage about everyone believing an experiment except the person who did it, and no one believing a calculation except the person who did it. Anyway, I think these kinds of calculations are worth the price if you can get meaningful results. I think they can be meaningful. It behooves the researchers and the management to try to work together to be sure their effort is done. What about that range in between? Also what about emissions and chemistry? I think the level of maturity is increasing. I think that if we have a meeting five years from now, we will see a very different flavor of the results of CFD for Euler/Navier Stokes, for LES, and for direct numerical simulation. I think that will influence future flight experiments, although I have to say that I didn't see at this Conference great evidence of these kinds of CFD efforts having a direct impact up to now, either on the flight experiments or on the future of regulations.

I would like now to turn to some questions and comments from the audience, and perhaps I will be able to digest and include the information in my written comments to be done later on. The first of these is, "how is the best way to treat these ground and cross wind interactions?" I think this is much less clear than the initial vortex formation or the calculation of stability in the far field. I would be interested to see what some of you, the experts, would have to say on that. Secondly, what is the best way to treat the interaction or the effect of the vortex on the following aircraft? Because ultimately that seems to be what we are really interested in. Those vortices can run around and can do their things, and it is all very nice to be able to predict them, but what you really want to know is when does it become a real hazard. It is not at all clear to me what methodology should be invoked in answering that question after you know something about the structure of the disturbances that are out there. Thirdly, what kind of modifications should we be pursuing to try to improve the situation, if any. Is this an area that is only interesting and good for some Ph.D. theses, but won't really impact the ultimate problem? I think there is probably a good possibility for fruitful research here, but I would be interested in the audience views on what level of effort should go into this.

I am not well versed in the existing techniques and capabilities that are used for detection, but I would like to know what some of you in the audience have to say about the instrumentation and what levels of accuracy need to be invoked in this. My intuitive feeling is that it is a very different problem from the kind of laboratory measurements that I am more familiar with, where sometimes it makes sense to do an experiment and sometimes the accuracy issues preclude wasting your time to do it. I also have the intuitive feeling that we are looking at massive amounts of data being generated very rapidly. Is this data management really an issue or not? If it is an issue, Information

Technology really is a rapidly developing new field that is outside our current aeronautical way of thinking. Perhaps, it could be invoked, if data management is really a major problem here.

I would also be interested to know how science and technology from the laboratory works its way to the regulatory agencies. In that business, how do you determine whether this scientific hocus pocus is at all valid? Particularly, when you see conflicting results, and that is typically what happens when you are on the leading edge of new science, how do you translate this into regulations or procedures? Have you learned anything here this week that has helped?

Finally, I hear these concepts being thrown around about free flight, and again my intuition tells me that this is a potential nightmare if airplanes are allowed to fly anywhere they want and they just determine the best paths based on performance. It seems to me like there is a great likelihood for a lot more of these vortex encounters that we have been talking about avoiding.

This presentation is work in progress; this is about where I have progressed up to 2:30 this afternoon. I hope that this is the basis for some comments and discussions in the General Discussion period now, so I will stop at this point.

Prof. Meier

Thank you very much, Dr. McCroskey; I think this was really a very elucidating overview of topics and questions left at this Conference, and I think also that we should thank Dr. McCroskey for his efforts.

To structure our discussion I think we should take into account what Dr. McCroskey has proposed with respect to questions and also look to the topics of the Conference Program.

First of all, we will pick up the last point regarding regulations and the related use of scientific and research information. Are there any questions or statements about this?

Please remember that you have to use the microphone because everything is being recorded and will be printed later on.

Dr. Norman Malmuth, Rockwell International, U.S.A.

I would like to commend Jim on a good review. This is not targeted directly to the regulation aspect, but a couple of thoughts came to mind as I was listening to his review. Despite the tremendous advances in CFD for the near field, especially during the roll-up process, systematic asymptotic procedures should be combined with CFD. This could help improve the CFD formulation. More significantly, it could clarify the structure of the hazardous downstream region. Another comment, more consideration is needed of the Reynolds number scaling aspects. Lastly, I see the need for simpleminded tradeoff analyses. If the velocity field is redistributed in the wake, i.e., what is the best that can be done related to reducing rolling moments on trailing aircraft in relation to aircraft landing or other performance. Operationally, it would be useful to combine some of the deep theoretical studies with some of these performance aspects and tradeoffs.

Prof. Meier

Thank you for your comments. I think this was more or less already devoted to the next point I would like to make. This is about the physics in general and procedures we can use, but are there any other comments on the regulations matter? If not, we will proceed to the physical aspects.

I think we have to go a little deeper into the physical aspects, like the instability, vortex breakdown or what Dr. McCroskey has mentioned also, the ground effects, the crosswind problems, aircraft vortex interactions, and things like that. Are there any comments, remarks or questions?

Mr. J. Robinson, Boeing, U.S.A.

I would like to go back to topic number 5, "the regulatory agency issue". I interface with the FAA through Boeing. If we are going to see a benefit in the capacity-type issues, it would seem to me, where we could safely reduce separation, that we need to see an integral change on the scale of whole units of a nautical mile, not something that is partially integral or fractional. There may be some here who are involved with regulatory bodies, like John Greenwood, who could comment on that. As I listen to the different speakers and our collective understanding on the physical characterization of the wakes, I wonder about the efforts being made regarding the application of this research to reducing separation safely and on an integral scale. Such an effort would be of major interest and value when we talk about airport capacity issues. I wonder if someone can address that, and is there a consensus that it needs to be on an integral scale?

Prof. Meier

I think one answer would be if given you really had good measurement systems, precise information for the controllers about the wake of preceding vehicles, then you could really consider to reduce the distance or simply avoid the encounter, but what you need is precise information.

Mr. John Greenwood, National Air Traffic Services, U.K.

We have responsibility for determining the separation minima in the U.K. Firstly, to address Jerry Robinson's point on how complicated we can make the rules for controllers, of course that is a very open-ended question. If there are big capacity benefits in making the rules very complicated, then we can do that, and we can provide computer assistance, but at the moment we are not sure enough of the benefits of doing that, so we will stay with fairly simple rules I think. On the question of how do we know whether to believe all this very clever computational fluid dynamics and theory - well, historically we haven't believed it. We have changed separation minima in the U.K. four or five times since they were first introduced in the 1970's, but always on the basis of pilot encounter reports with wake vortices. We still run that reporting scheme and consistency with that is going to be very important for any future proposals to change regulations. The most likely thing to me for any change is going to be some model with quite a big empirical component, something like George Greene's, and if somebody looks at all of the flight tests, all of the experiments and finds more support for that, and then we test it out with some real full-scale detailed flight test results such as probes or LIDAR, then that is the way that science can optimize separation minima. That is the reason that we have funded the LIDAR work at Heathrow.

Prof. Meier

Thank you very much. Are there any other comments?

Dr. A. Corjon, Cerfacs, France

An important issue was forgotten during this meeting. If one day, we know exactly what is the behavior of the vortices in the atmospheric turbulence or the behavior of the vortices near ground (with or without a cross-wind), we must be able to forecast the meteorological conditions accurately to apply the separations that you can define precisely by CFD or another tool. If you can't forecast the meteorological condition, with enough accuracy, you cannot change the rules.

Prof. Meier

Thank you for this comment. I think you are right in one respect, but I think there is also one question which is left open. Dr. McCroskey has mentioned earlier, that there are also not really suitable measurement systems for the vortical wakes itself so local vortex or meteorological measurement may be another way to cope with this problem. But Dr. McCroskey has another comment.

Dr. McCroskey, U.S.A.

While we are on this subject, I want to ask clarification on something that I heard during the week. That is, that to be useful, these meteorological forecasts need to be projected maybe one hour in advance (from the audience, "20 minutes could be sufficient"). To me that seems a big difference - 20 minutes versus maybe more than one hour, so I am glad I asked the question.

Dr. O. Savas, University of California Berkeley, U.S.A.

This was a problem in the 70's and was discussed at great length and regulations were imposed which delayed it. Now, twenty years later we are discussing the same problem.

Obviously, by tightening the regulations, which means by identifying where the vortex is and how to deal with it, we will be able to postpone the problem for another twenty years. Then it will come back again. So, the obvious solution is that we do something about the vortices themselves, which is quite beyond the understanding of the physics of it. I see two routes: one is to use brute force. We don't know how this will work, and what the effects will be. The other one is to finesse very intricate, delicate methods. That should be one of the topics of this discussion.

Mr. Paul Herring, British Aerospace, U.K.

I think one of the problems with changing the airplane in some way to alleviate the wake problem is who is going to pay for it. The manufacturer has to sell an efficient airplane at the lowest possible price. If his airplane is in any way more expensive or less efficient than a competitor, the airlines won't buy it. So an airplane modified in some way may reduce the distance between take-offs, for example, but would an airline buy a Boeing if all it means is that the Airbus behind can take off a bit quicker?

Prof. Richard Kind, Carleton University, Canada

Maybe just a follow on comment to that. We do have landing charges and that sort of thing, and one can envision a scheme whereby an aircraft which leaves a more dangerous wake pays more in the sense that it uses the airport's capacity for longer.

Prof. Meier

There are similar ideas about the noise, so why not payment for the wake.

Mr. George Greene, NASA Langley, U.S.A.

One more follow on comment to that. It seems to me that things have changed somewhat in the past twenty years. With the hub and spoke system, we might now be in a situation, at least in the U.S., where in a number of cities the airports are essentially controlled by one airline which has most of the traffic. Now, if they choose to buy an airplane that is in some sense wake efficient, they can have more slots available. Since they are the primary user of an airport, then they are the primary beneficiary of spending the money to do that. It seems to me that we could be entering a stage somewhat like aircraft noise was twenty or so years ago. We paid very little attention to it because there was no commercial advantage. When airport curfews started, there was an economic advantage to having quiet airplanes. I wonder if the fact that we see a good representation of manufacturers here is an indication that airplanes with less wake hazard are beginning to be viewed as having a commercial advantage.

Prof. Meier

I think one main reason for our Conference, was to find out if there are measures to reduce wakes and vorticity.

Mr. V.J. Rossow, NASA Ames, U.S.A.

In response to Prof. Meier's question, I feel that several points should be made with regard to the modification of lift-generated wakes. NASA has been in the business of wake modification for over 25 years and is still working on the problem because we feel that a satisfactory solution for the reduction of the intensity or hazard caused by the wakes of subsonic transport aircraft has not yet been found. Yes, wake vortices can be changed considerably by various techniques, but the methods suggested so far carry unacceptable penalties with them. Based on my own ideas, and the comments of others on the subject, any acceptable modification technique will first need to have a negligible effect on the performance of the aircraft -- and should preferably have a beneficial effect. Secondly, the modification technique should have a sound theoretical and experimental basis so that it can be readily applied to a wide variety of aircraft with very low risk of failure or complications. The wing-fin concept described in my paper is probably one of the better ideas available at this time, but it fails both of the foregoing criteria.

I have probably been in the modification business longer than anybody here. The fact is I have probably been here longer than anybody, but that is beside the point. Anyway the rule I sort of work under, and in response to people criticizing my work, and I have had a lot of criticisms, most of them are well justified and I agree with. That is, if we come up with a modification, it should have certain requirements. First of all, it should have a negligible effect on the performance on the aircraft, and preferably be beneficial to the aircraft performance. That is a really tough thing to do. That is why I say we don't understand the wing fins well enough. I think that is the best thing going right now, but I don't think it is the solution. The other thing is that if we did come up with something that was really good and beneficial to the airplane, it probably would not be a big benefit, it would be in the order of a percent or two, if any at all. A friend of mine reminded me the other day that any change to the air traffic system or to airplanes has a very long time of implementation, on the order of 30 years, because airplanes last a long time, systems

take a long time, it takes a long time to train pilots, and the like, so it takes a long time. My answer to him was that I could perhaps celebrate that on my 100th birthday.

Prof. Meier

You are completely right. I think we talk about the measures of 2050 or something like that, but we have to do that, we have to think it over.

Dr. David Woodward, DRA, Farnborough, U.K.

A gentlemen over there said that the major beneficiary of any reduction in the separation distance would be the airport operator. Traditionally, airplanes land on runways which are statistically aligned with the prevailing wind, all for very good reasons. But the most interesting comment I heard this week was that a vortex in a cross-wind is very much older than a vortex that is aligned with the prevailing wind. How would it be if we persuaded the airport operators to realign the runways 15 degrees off the prevailing wind direction. If, and I don't know whether the answer is true or not, but if this would result in an aging of the vortex, and therefore a possible reduction in the separation distance, then the consequence for the aircraft designer is to design an airplane which can land in a higher cross-wind component. I might throw that into the pool for someone to comment on.

Prof. Meier

I think that is not such a bad idea, but cross wind would not only weaken the vortices, but also carry them away. Maybe there are some comments on this.

Dr. M. Vaughan, DRA Malvern, U.K.

Having spent quite a lot of time at Heathrow looking at aircraft coming in some very strong cross-winds, all I can say is that there are lots of strong cross-winds at Heathrow. one could establish the premise of the question by analyzing a vast amount of this real data. I perhaps should make the point, that to my mind, LIDAR now have the capability, provided you have high spectral resolution and high spatial resolution, to make very precise measurements at quite useful ranges and with aircraft in interesting positions, and at interesting distances in space behind aircraft. When that data is analyzed, particularly in these cross-winds that I indicated, I am sure some very valuable information will indeed come out of it.

Ir. Bram Elsenaar, NLR, Netherlands

Just a remark I will make with respect to the possibilities to weaken the vortex and the vortex strength. I start off quoting Harry Hoeijmakers, who should have given the keynote speech, that he wasn't quite sure he was able to modify the wakes in such a way that we would benefit from it. Calculating vortices is different from really understanding what is going on. What I am missing in the Conference is a good physical understanding of how a vortex works and what ways there are to promote the instability of a vortex so that it will break down earlier. What possibilities are there to take energy out of the vortex in a clever way, possibly by transferring energy from a transverse mode to a rotational mode or the other way around. It is a bit of a disappointment for me that better understanding of the physics of vortex flow hasn't shown up in this Conference. I think the future is that we should try to understand much better what is going on. I was pleased with some of the work which Boeing has been doing to increase the

understanding. I hope that maybe in the next Conference we will be able to understand in a much better way the physics in the vortices.

Prof. Meier

I think that we all ought to assist you in hoping that. But for my feeling, the vortical flows are at least as complicated as boundary layer flows and boundary layer has got much more attention over the last 100 years and the problem is still not solved completely.

M. Christian Dujarric, ESA, France

I would like to stress that AGARD is taking care of dual use technologies, that means both with military and civilian purposes. Here I see that we are discussing mostly civilian proposals, whereas in the announcement there was also the goal of detection of military aircraft. I don't know, but it seems that this topic has not been properly covered. Was it? Can someone comment on that?

Prof. Meier

I think I agree with you that there was not much attention on this aspect.

Mr. R. Stuff, DLR, Germany

I gave Prof. Meier a hand in preparing this meeting, and from what I have seen, there just were no papers offered.

M. Christian Dujarric, France

Does it mean that it was due to classification issues, or does it mean that there is no work.

Prof. Meier

I think the work is just starting. There are of course ideas in the industry, that vortical flows especially at high angle of attack are of very high importance. That one, for instance, can use vortices also for control purposes for fighters, and so on. So there is a lot of consideration, but maybe the people who are dealing with this have not seen their place right here because they do not see it as a wake problem. Maybe they see it as a local problem of the fighter environment really. Mainly that also this field is really in an initial stage, that is my feeling, especially the unsteady aspects that we have discussed previously.

Mr. Ronald Bengelink, Boeing, U.S.A.

I guess I would like to address the question, because as Christian said, we looked at it as being a dual purpose and we haven't seen it. But when I think about it more, it doesn't really matter, because what we are talking about here is two approaches. One needs to better understand the vortex so we can understand how to break it down or how to encourage the instabilities. The second is to figure out how to find it, how to detect its location. Once we get better at either of those two approaches, it will have total dual use applications. So, I am not too concerned about the fact that the focus of this Symposium was on the civil side. That happens to be where a lot of the interest is right now. But I think the solutions are going to have applications on both sides and in that sense, we are addressing the AGARD concern for military as well.

Prof. Meier

Yes, it is quite true, the physics is very similar for both applications.

Professor Decuyper

I would just like to add that fighter pilots are aware of that problem because they can experience very severe, undesired roll maneuvers, and the result can be so severe that the attacking aircraft can become the target and the escaping aircraft, the attacker.

Mr. Bengelink, U.S.A.

If we are spinning down, there was one thing that I wanted to address just a minute before we left and that was Jim McCroskey's last question about free flight. One of my concerns when I first heard about free flight was that there would be a possibility for a lot more problems, a lot more interactions between airplanes. One of the engineers, who is really a champion of this, pointed out to me that if you assume that there is a certain sphere around every aircraft that you have got to keep clear, then instead of operating the way we do today on flight paths intersecting at way points where you in essence bring everybody to a given point. You now let anybody go wherever they want to, therefore safety should go up. Conflict occurrences should go down because even with a very large increase in total fleet size compared with what we have today, there will still be a lot more empty space than airplane occupied space. As soon as we do not restrict airplanes to all cross the same point in the sky, we are going to improve safety rather than the other way around.

Prof. Meier

I think one has to be aware of the fact that such a wake is nearly something like a one dimensional distortion in space, and you have a lot of possibilities to come around that, but on the other hand, the dangerous thing is that if you hit such a line distortion, then you really have a problem. This vortex pair is something like a rope which is hanging somewhere in the air. The event of encounter you have nearly in no case, but once a year an airplane hits the vortex.

Dr. Woodward, U.K.

If I could bring us back to a detailed point that I noticed in some of the presentations. A lot of the experiments on trailing vorticity come from wings with cylindrical tip shapes. I was particularly struck in Mr. Easton's paper where he was calculating the vortex downstream. His calculation method showed, in many ways, classic symptoms of excessive numerical viscosity and he was unable to predict the separation of the viscous flow around the cylindrical wing tip. So that one detail of the flow, the suction peak towards the trailing edge around the tip, was not predicted. Now if you go back to what Harry Hooijmaekers was saying in the early paper that Bram presented, he would have been much better, in my opinion, if that wing tip shape had been a sharp line. Then you wouldn't have had this uncertainty about where the separation was on that wing tip. That ties in very clearly with the exercise that was done and reported in the last Vortex Aerodynamics Conference where we attempted to predict vortex flows using an Euler method. We have learned an awful lot there by comparing the calculations with vortex flows from a sharp edged delta. If we had tried to compare those calculations with the vortex flow from a delta with a round leading edge, we wouldn't have learned nearly so much, because we wouldn't have known where the separation was. So really, what I am

pleading for, is next time someone does a detailed experiment on a wing tip vortex, please can you make the wing tip sharp.

Dr. McCroskey, U.S.A.

I would like to make several small comments on that subject. The most important is that from the point of view of the wake roll-up and structure downstream, which is really the object of this Conference, I think it has been established by a few experiments and some calculations that you won't see the difference in the tip vortex structure one or two spans downstream. That is to say, to really make a major change in the vortex structure far downstream, you have to do more than just round or sharpen the tip. It is a big problem for the CFDer trying to make a detailed calculation in the near field, although we have some fairly recent results from the U.S. in which the separation on the rounded tip has now been calculated rather accurately and the suction peak is attained pretty accurately downstream of that. But again, compared to the changes that appear to be necessary to make a significant change far enough downstream to really have an impact either on helicopter blade vortex interaction or marine propeller tip vortex interaction with hulls, or the aircraft extreme problem that we are talking about here, that is a very small effect at best. There are some data available for wake measurements, a few body dimensions downstream with the identical wing at the same average loading, with square tips and rounded tips.

Prof. Meier

The tip is only important in the near field, but in the far field, I think it is the wing load which is determining the circulation.

Dr. McCroskey, U.S.A.

I will go out more on a limb and speculate that in terms of exciting Crow instabilities or something like that, that kind of detail, it is also probably not terribly important. On the other hand, it does seem to me that things like the flaps-down configuration compared to clean wing configuration, and maybe exploiting the way that the flap configuration is set, are ways that could have some major impact. That is what I was alluding to when I indicated that in my view, there is a great potential for some practical information to come out of CFD analyses in the next couple years or so.

Prof. Meier

The question of flap configurations is at present under consideration. On the one side, aerodynamicists tend to design a more continuous distribution of high lift devices along the span to avoid vibrations, but on the other hand, the slots and structured devices also tend to increase the instability of the vortex system in the wake, so I think up to now nobody knows the best direction to go.

Mr. Sven Backstein, RWTH, Aachen, Germany

I would like to make a remark especially on CFD computational fluid dynamics which is becoming more and more popular and which is a very challenging instrument, but we have to be careful because what we obtain, and indeed I also presented some CFD, some numerical results, today. We have to be careful because what we obtain from a CFD calculation is always a solution, but never an explanation. In many details we are still looking for explanations and understanding of phenomena we observe of the flow. In many points, we have not understood fully what happens and we are turning over to

CFD simulations thinking that we have everything under control because we can simulate it, but we should not forget to look for an understanding of the phenomena. Therefore, we still will have to use analytical mathematics. We should not forget about this.

Prof. Meier

And also the physics may not be forgotten.

Dr. Malmuth, U.S.A.

I would like to put in a plug for simplified aerodynamic inputs to optimization procedures. The paper by Graham from Cambridge on lifting line theory is one example.

He was trying to optimize the circulation distribution. This was also mentioned by my French colleague. I see a very interesting possibility to study the effects of varying the circulation distribution along the span. On the downstream roll-up process and the Crow instability, I think I only saw one paper related to this question. We ought to look at some systematic models of the far field development related to the effects of spanwise distribution on the minimization of problems induced rolling moments.

Prof. Meier

Thank you for that comment. If there are no other very urgent questions, I think the time for the discussion is up and I would like to thank all of you for your attention, especially the participants in the discussion for their interesting comments and questions. Finally, I would like to invite our FDP chairman, Prof. Ciray, to make some closing remarks to our Conference.

Prof. Dr. C. Ciray, Middle East Technical University, Turkey

Ladies and gentlemen, the symposium on "The Characterization and Modification of Wakes from Lifting Vehicles in Fluids" started on Monday, 20 May, at 9.00 and now, we come to the end of it.

The idea of this symposium was proposed some two to two and a half years ago in one of the meetings similar to this, that FDP holds regularly twice a year, in some place of some country of this great family of nations that we call the "Alliance". Thanks to the dedicated work of the Technical Programme Committee with Prof. Dr. G.E.A. Meier as the Chairman and Prof. R. Decuypere, Prof. R.J. Kind, Prof. M.A. Bonnet, Dr. B. Wagner, Prof. F. Sabetta, Prof. D.A. Poll, Mr. R.L. Bengelink and Dr. L.P. Purtell as members, this symposium became a reality. The technical content of the symposium created the reason for the gathering of a distinguished and very active audience like yours. I only hope that the outcome of this symposium is a rewarding one for each of you, and I also hope that it will be of use to the nations of the alliance, to the research community, to aviation industry and to the operators who run the airports.

I offer our cordial thanks to: the Technical Programme Committee, the authors who spent their days and nights to prepare manuscripts, the speakers who came to present the papers, the chairmen of the sessions, and I invite you to give a hand to these ladies and gentlemen who made this symposium a success.

I think you will concur with me that the technical evaluator, our past member and panel Chairman Dr. J. McCroskey, has done a remarkable job. We thank him for summing up the symposium and highlighting the critical issues to be discussed.

We extend our cordial thanks to the National delegation of Norway and the city of Trondheim who invited us so graciously to hold the Symposium and our Spring 1996 Activities in Norway, in Trondheim. Our cordial thanks are also extended to the President and the administrators of the Norwegian University of Science and Technology who allowed us to benefit from the use of the excellent facilities and premises of the University.

I think you would not like me to forget the name of the Company Marintech, which gave us the opportunity for a very interesting technical tour to their laboratories. You would not like me to forget, also, the name of Mr. Hansen, the Director of Marintech, who personally guided us through their laboratories and facilities. We thank very much Mr. Hansen and the Company Marintech for their hospitality.

I think it is time we express our sincere appreciation and extend our warm thanks to the person who made possible our 1996 Spring Activities to take place in Trondheim, Prof. Dr. Helge Norstrud, member of FDP, the good friend of any FDP member, and the Local Coordinator. I do not have any doubt that Helge deserves an ovation for his admirable, very thoughtful and sympathetic organizations. Mrs. Norstrud was no less active than Helge for taking care of the companions through the week. I congratulate them both and thank them for their hospitality, organizations and admirable warm reception they have shown. I invite you to give them a good hand.

I did not finish yet. We have a couple of people who came here before us, in order to see that everything is at FDP and AGARD standards. They were also at wherever was a personal or organizational problem. I am sure you know who I am talking of, the executive of FDP, Dr. J.K. Molloy and his secretary, Miss D. Pelat. I extend our warm thanks and appreciation to both of them, and we know that they deserve this.

Ladies and Gentlemen, perhaps it was easy for you to talk in the language that was convenient or listen to the presentations in the language that was suiting you. We had Mrs. Vioche, Mrs. Mazaud and Mrs. Couedic as interpreters and Mr. Crory and Mr. van Wick as the technicians between the speakers and listeners who made an arduous task to help us to appreciate the presentations and discussions. I invite you to express our appreciation and thanks to these wonderful people.

Ladies and Gentlemen, the symposium on the "Characterization and Modification of Wakes from Lifting Vehicles in Fluids" was one of the scheduled activities of FDP of AGARD. You know perfectly well that AGARD has become the name of a great institution since it has been conceived and founded by Prof. Theodore von Karman some 44 years ago. But AGARD is on the verge of changes. Indeed there are winds of change in the air; perhaps there are vortices.

By the way, vortices and wakes have been the subject of this symposium. During the discussion period, Mr. Masure proposed to modify the loading on the wings in a peculiar way to avoid tip vortices which turn out to be very strong during landing for obvious reasons. My proposition on the other hand is to start to think - to land the airplanes at higher speeds - it may be useful if feasible. Anyway, back to AGARD and changes. AGARD is going to change though the name may remain the same, but very likely in a different connotation. We, the FDP members, are

very pensive about these changes. We will do our best so that the new AGARD preserves FDP. Surely, the more important thing is that the spirit of AGARD as laid down by Prof. Th. von Karman and nourished by worthy "AGARDians" is preserved. We hope that it will be preserved.

While changes appear in the future, we also have programs of activities for the near future. As you may see in the vugraph, we will have our first Russian meeting in September 1996 in Moscow. AGARD has made a decision to hold meetings in Russia, and we have been the first victim. I say "victim" since the organization of this meeting and the way of deciding was slightly different from our customary procedures. So it took some time and required different activities of the Technical Programme Committee to organize it; also extra trips were needed to be made by a number of committee members and the executive of FDP to Moscow. But the indications are that this meeting is going to be a model for future activities of the same kind. The symposium will take place between 30 September and 3 October 1996, and the title is, "Aerodynamics of Wind Tunnel Circuits and Components". I recommend strongly to attend this meeting to those who have an interest in wind tunnels. There will be about thirty three papers; seventeen from the Alliance and sixteen from Russian scientists and engineers. I think the discussions will also be lively and rewarding. Furthermore, our hosts are organizing very interesting technical visits. I am assured that the cost will be reasonable. All in all, the meeting in Moscow seems to be an attractive and memorable one thanks to the efforts of the programme committee.

For 1997, two meetings are planned. The first one is very special. It has a unique character. This meeting will be produced with the joint effort of all panels forming AGARD. For the first time in the history of AGARD, all panels and other units forming AGARD will be at the same site to contribute to the symposium on, "Future Aerospace Technologies in Service to the Alliance". As it stands, AGARD has seven Panels, namely FVP, FDP, PEP, SMP, MSP, SPP and AMP. The first six panels will combine two by two to organize three technical sessions on three major themes which will run parallel in the famous "Ecole Polytechnique" in Paris. I am confident that this meeting and related Activities during the meeting will be rewarding. Just before the beginning of the joint symposium, FDP will run a workshop on "Hypersonic Experimental and Computational Capabilities" for two days, that means on the previous Thursday and Friday.

The second major activity of FDP in 1997 will be the symposium on "Advanced Aerodynamic Measurement Technology". This meeting is likely to be in September 1997, probably in the USA.

In addition to these activities, there will be two special courses run by VKI. In Spring 1997, the course on "Effect of Rain, Icing and de-Icing on Wing Performance" will take place at VKI. The other one is the course on "Turbulence in Compressible Flows", and it will take place both at VKI and Langley Research Center., USA.

Ladies and Gentlemen, now we really come to the end of our symposium. No technical activity of this sort is a successful one without a lively audience. My impression is that this symposium was a successful one thanks to the wonderful audience we had this week. Therefore, I thank you all for your interest to this symposium and for making it a successful one. I wish you all a safe trip back home.

REPORT DOCUMENTATION PAGE

1. Recipient's Reference	2. Originator's Reference AGARD-CP-584	3. Further Reference ISBN 92-836-0034-7	4. Security Classification of Document UNCLASSIFIED/ UNLIMITED												
5. Originator Advisory Group for Aerospace Research and Development North Atlantic Treaty Organization 7 rue Ancelle, 92200 Neuilly-sur-Seine, France															
6. Title The Characterisation & Modification of Wakes from Lifting Vehicles in Fluids															
7. Presented at/sponsored by The Fluid Dynamics Panel Symposium held in Trondheim, Norway, from 20-23 May 1996.															
8. Author(s)/Editor(s) Multiple			9. Date November 1996												
10. Author's/Editor's Address Multiple			11. Pages 428												
12. Distribution Statement There are no restrictions on the distribution of this document. Information about the availability of this and other AGARD unclassified publications is given on the back cover.															
13. Keywords/Descriptors <table border="0"><tr><td>Wakes</td><td>Detection</td></tr><tr><td>Vortices</td><td>Roll</td></tr><tr><td>Wake detection</td><td>Air traffic control</td></tr><tr><td>Reviews</td><td>Computational fluid dynamics</td></tr><tr><td>Aircraft</td><td>Aerodynamic stability</td></tr><tr><td>Separation</td><td></td></tr></table>				Wakes	Detection	Vortices	Roll	Wake detection	Air traffic control	Reviews	Computational fluid dynamics	Aircraft	Aerodynamic stability	Separation	
Wakes	Detection														
Vortices	Roll														
Wake detection	Air traffic control														
Reviews	Computational fluid dynamics														
Aircraft	Aerodynamic stability														
Separation															
14. Abstract <p>The papers prepared for the AGARD Fluid Dynamics Panel (FDP) Symposium on "The Characterisation & Modification of Wakes from Lifting Vehicles in Fluids", which was held 20-23 May in Trondheim, Norway are contained in this Report. In addition, a Technical Evaluator's Report aimed at assessing the success of the Symposium in meeting its objectives, and an edited transcript of the General Discussion held at the end of the Symposium are also included.</p> <p>Papers presented during the eight sessions addressed the following subjects:</p> <ul style="list-style-type: none">— Regulatory Viewpoints;— Vortex Wake Structures;— Aircraft/Vortex Interactions;— Vortex Instabilities;— Aircraft Spacing Considerations;— Atmospheric Effects on Wakes;— Vortex Breakdown;— Miscellaneous Issues.															

Aucun stock de publications n'a existé à AGARD. A partir de 1993, AGARD détiendra un stock limité des publications associées aux cycles de conférences et cours spéciaux ainsi que les AGARDographies et les rapports des groupes de travail, organisés et publiés à partir de 1993 inclus. Les demandes de renseignements doivent être adressées à AGARD par lettre ou par fax à l'adresse indiquée ci-dessus. *Veuillez ne pas téléphoner.* La diffusion initiale de toutes les publications de l'AGARD est effectuée auprès des pays membres de l'OTAN par l'intermédiaire des centres de distribution nationaux indiqués ci-dessous. Des exemplaires supplémentaires peuvent parfois être obtenus auprès de ces centres (à l'exception des États-Unis). Si vous souhaitez recevoir toutes les publications de l'AGARD, ou simplement celles qui concernent certains Panels, vous pouvez demander à être inclu sur la liste d'envoi de l'un de ces centres. Les publications de l'AGARD sont en vente auprès des agences indiquées ci-dessous, sous forme de photocopie ou de microfiche.

CENTRES DE DIFFUSION NATIONAUX

ALLEMAGNE

Fachinformationszentrum Karlsruhe
D-76344 Eggenstein-Leopoldshafen 2

BELGIQUE

Coordonnateur AGARD-VSL
Etat-major de la Force aérienne
Quartier Reine Elisabeth
Rue d'Evere, 1140 Bruxelles

CANADA

Directeur, Services d'information scientifique
Ministère de la Défense nationale
Ottawa, Ontario K1A 0K2

DANEMARK

Danish Defence Research Establishment
Ryvangs Allé 1
P.O. Box 2715
DK-2100 Copenhagen Ø

ESPAGNE

INTA (AGARD Publications)
Carretera de Torrejón a Ajalvir, Pk.4
28850 Torrejón de Ardoz - Madrid

ETATS-UNIS

NASA Goddard Space Flight Center
Code 230
Greenbelt, Maryland 20771

FRANCE

O.N.E.R.A. (Direction)
29, Avenue de la Division Leclerc
92322 Châtillon Cedex

GRECE

Hellenic Air Force
Air War College
Scientific and Technical Library
Dekelia Air Force Base
Dekelia, Athens TGA 1010

ISLANDE

Director of Aviation
c/o Flugrad
Reykjavik

ITALIE

Aeronautica Militare
Ufficio del Delegato Nazionale all'AGARD
Aeroporto Pratica di Mare
00040 Pomezia (Roma)

LUXEMBOURG

Voir Belgique

NORVEGE

Norwegian Defence Research Establishment
Attn: Biblioteket
P.O. Box 25
N-2007 Kjeller

PAYS-BAS

Netherlands Delegation to AGARD
National Aerospace Laboratory NLR
P.O. Box 90502
1006 BM Amsterdam

PORTUGAL

Estado Maior da Força Aérea
SDFA - Centro de Documentação
Alfragide
2700 Amadora

ROYAUME-UNI

Defence Research Information Centre
Kentigern House
65 Brown Street
Glasgow G2 8EX

TURQUIE

Millî Savunma Başkanlığı (MSB)
ARGE Dairesi Başkanlığı (MSB)
06650 Bakanlıklar-Ankara

Le centre de distribution national des Etats-Unis ne détient PAS de stocks des publications de l'AGARD.

D'éventuelles demandes de photocopies doivent être formulées directement auprès du NASA Center for AeroSpace Information (CASI) à l'adresse ci-dessous. Toute notification de changement d'adresse doit être fait également auprès de CASI.

AGENCES DE VENTE

NASA Center for AeroSpace Information
(CASI)
800 Elkridge Landing Road
Linthicum Heights, MD 21090-2934
Etats-Unis

The British Library
Document Supply Division
Boston Spa, Wetherby
West Yorkshire LS23 7BQ
Royaume-Uni

Les demandes de microfiches ou de photocopies de documents AGARD (y compris les demandes faites auprès du CASI) doivent comporter la dénomination AGARD, ainsi que le numéro de série d'AGARD (par exemple AGARD-AG-315). Des informations analogues, telles que le titre et la date de publication sont souhaitables. Veuillez noter qu'il y a lieu de spécifier AGARD-R-nnn et AGARD-AR-nnn lors de la commande des rapports AGARD et des rapports consultatifs AGARD respectivement. Des références bibliographiques complètes ainsi que des résumés des publications AGARD figurent dans les journaux suivants:

Scientific and Technical Aerospace Reports (STAR)
publié par la NASA Scientific and Technical
Information Division
NASA Langley Research Center
Hampton, Virginia 23681-0001
Etats-Unis

Government Reports Announcements and Index (GRA&I)
publié par le National Technical Information Service
Springfield
Virginia 22161
Etats-Unis
(accessible également en mode interactif dans la base de
données bibliographiques en ligne du NTIS, et sur CD-ROM)



AGARD holds limited quantities of the publications that accompanied Lecture Series and Special Courses held in 1993 or later, and of AGARDographs and Working Group reports published from 1993 onward. For details, write or send a telefax to the address given above. *Please do not telephone.*

AGARD does not hold stocks of publications that accompanied earlier Lecture Series or Courses or of any other publications. Initial distribution of all AGARD publications is made to NATO nations through the National Distribution Centres listed below. Further copies are sometimes available from these centres (except in the United States). If you have a need to receive all AGARD publications, or just those relating to one or more specific AGARD Panels, they may be willing to include you (or your organisation) on their distribution list. AGARD publications may be purchased from the Sales Agencies listed below, in photocopy or microfiche form.

NATIONAL DISTRIBUTION CENTRES

BELGIUM

Coordonnateur AGARD — VSL
Etat-major de la Force aérienne
Quartier Reine Elisabeth
Rue d'Evere, 1140 Bruxelles

CANADA

Director Scientific Information Services
Dept of National Defence
Ottawa, Ontario K1A 0K2

DENMARK

Danish Defence Research Establishment
Ryvangs Allé 1
P.O. Box 2715
DK-2100 Copenhagen Ø

FRANCE

O.N.E.R.A. (Direction)
29 Avenue de la Division Leclerc
92322 Châtillon Cedex

GERMANY

Fachinformationszentrum Karlsruhe
D-76344 Eggenstein-Leopoldshafen 2

GREECE

Hellenic Air Force
Air War College
Scientific and Technical Library
Dekelia Air Force Base
Dekelia, Athens TGA 1010

ICELAND

Director of Aviation
c/o Flugrad
Reykjavik

ITALY

Aeronautica Militare
Ufficio del Delegato Nazionale all'AGARD
Aeroporto Pratica di Mare
00040 Pomezia (Roma)

LUXEMBOURG

See Belgium

NETHERLANDS

Netherlands Delegation to AGARD
National Aerospace Laboratory, NLR
P.O. Box 90502
1006 BM Amsterdam

NORWAY

Norwegian Defence Research Establishment
Attn: Biblioteket
P.O. Box 25
N-2007 Kjeller

PORTUGAL

Estado Maior da Força Aérea
SDFA - Centro de Documentação
Alfragide
2700 Amadora

SPAIN

INTA (AGARD Publications)
Carretera de Torrejón a Ajalvir, Pk.4
28850 Torrejón de Ardoz - Madrid

TURKEY

Millî Savunma Başkanlığı (MSB)
ARGE Dairesi Başkanlığı (MSB)
06650 Bakanlıklar-Ankara

UNITED KINGDOM

Defence Research Information Centre
Kentigern House
65 Brown Street
Glasgow G2 8EX

UNITED STATES

NASA Goddard Space Flight Center
Code 230
Greenbelt, Maryland 20771

The United States National Distribution Centre does NOT hold stocks of AGARD publications.

Applications for copies should be made direct to the NASA Center for AeroSpace Information (CASI) at the address below.

Change of address requests should also go to CASI.

SALES AGENCIES

NASA Center for AeroSpace Information
(CASI)
800 Elkridge Landing Road
Linthicum Heights, MD 21090-2934
United States

The British Library
Document Supply Centre
Boston Spa, Wetherby
West Yorkshire LS23 7BQ
United Kingdom

Requests for microfiches or photocopies of AGARD documents (including requests to CASI) should include the word 'AGARD' and the AGARD serial number (for example AGARD-AG-315). Collateral information such as title and publication date is desirable. Note that AGARD Reports and Advisory Reports should be specified as AGARD-R-nnn and AGARD-AR-nnn, respectively. Full bibliographical references and abstracts of AGARD publications are given in the following journals:

Scientific and Technical Aerospace Reports (STAR)
published by NASA Scientific and Technical
Information Division
NASA Langley Research Center
Hampton, Virginia 23681-0001
United States

Government Reports Announcements and Index (GRA&I)
published by the National Technical Information Service
Springfield
Virginia 22161
United States
(also available online in the NTIS Bibliographic
Database or on CD-ROM)



Printed by Canada Communication Group
45 Sacré-Cœur Blvd., Hull (Québec), Canada K1A 0S7